NOVEL METHODS TO ADVANCE DIAGNOSTIC AND TREATMENT VALUE OF MEDICAL IMAGING FOR CARDIOVASCULAR DISEASE

EDITED BY: Zahra K. Motamed, Juan Carlos Del Alamo, Jolanda Wentzel, Danny Bluestein and Elazer Edelman

PUBLISHED IN: Frontiers in Cardiovascular Medicine and Frontiers in Bioengineering and Biotechnology

frontiers Research Topics

ISSN 1664-8714
ISBN 978-2-83250-201-3
DOI 10.3389/978-2-83250-201-3

About Frontiers

Frontiers is more than just an open-access publisher of scholarly articles: it is a pioneering approach to the world of academia, radically improving the way scholarly research is managed. The grand vision of Frontiers is a world where all people have an equal opportunity to seek, share and generate knowledge. Frontiers provides immediate and permanent online open access to all its publications, but this alone is not enough to realize our grand goals.

Frontiers Journal Series

The Frontiers Journal Series is a multi-tier and interdisciplinary set of open-access, online journals, promising a paradigm shift from the current review, selection and dissemination processes in academic publishing. All Frontiers journals are driven by researchers for researchers; therefore, they constitute a service to the scholarly community. At the same time, the Frontiers Journal Series operates on a revolutionary invention, the tiered publishing system, initially addressing specific communities of scholars, and gradually climbing up to broader public understanding, thus serving the interests of the lay society, too.

Dedication to Quality

Each Frontiers article is a landmark of the highest quality, thanks to genuinely collaborative interactions between authors and review editors, who include some of the world's best academicians. Research must be certified by peers before entering a stream of knowledge that may eventually reach the public - and shape society; therefore, Frontiers only applies the most rigorous and unbiased reviews.
Frontiers revolutionizes research publishing by freely delivering the most outstanding research, evaluated with no bias from both the academic and social point of view. By applying the most advanced information technologies, Frontiers is catapulting scholarly publishing into a new generation.

What are Frontiers Research Topics?

Frontiers Research Topics are very popular trademarks of the Frontiers Journals Series: they are collections of at least ten articles, all centered on a particular subject. With their unique mix of varied contributions from Original Research to Review Articles, Frontiers Research Topics unify the most influential researchers, the latest key findings and historical advances in a hot research area! Find out more on how to host your own Frontiers Research Topic or contribute to one as an author by contacting the Frontiers Editorial Office: frontiersin.org/about/contact

NOVEL METHODS TO ADVANCE DIAGNOSTIC AND TREATMENT VALUE OF MEDICAL IMAGING FOR CARDIOVASCULAR DISEASE

Topic Editors:
Zahra K. Motamed, McMaster University, Canada
Juan Carlos Del Alamo, University of Washington, United States
Jolanda Wentzel, Erasmus Medical Center, Netherlands
Danny Bluestein, Stony Brook University, United States
Elazer Edelman, Massachusetts Institute of Technology, United States

Citation: Motamed, Z. K., Del Alamo, J. C., Wentzel, J., Bluestein, D., Edelman, E., eds. (2022). Novel Methods to Advance Diagnostic and Treatment Value of Medical Imaging for Cardiovascular Disease.
Lausanne: Frontiers Media SA. doi: 10.3389/978-2-83250-201-3

Table of Contents

frontiers | Frontiers in Bioengineering and Biotechnology

TYPE Editorial
PUBLISHED 31 August 2022
DOI 10.3389/fbioe.2022.987326

OPEN ACCESS

EDITED AND REVIEWED BY
Markus O. Heller,
University of Southampton,
United Kingdom

*CORRESPONDENCE
Zahra Keshavarz-Motamed,
motamedz@mcmaster.ca

SPECIALTY SECTION
This article was submitted to Biomechanics, a section of the journal Frontiers in Bioengineering and Biotechnology

RECEIVED 06 July 2022
ACCEPTED 28 July 2022
PUBLISHED 31 August 2022

CITATION
Keshavarz-Motamed Z, Del Alamo JC, Bluestein D, Edelman ER and Wentzel JJ (2022), Editorial: Novel methods to advance diagnostic and treatment value of medical imaging for cardiovascular disease. *Front. Bioeng. Biotechnol.* 10:987326. doi: 10.3389/fbioe.2022.987326

Editorial: Novel methods to advance diagnostic and treatment value of medical imaging for cardiovascular disease

Zahra Keshavarz-Motamed[1,2]*, Juan C. Del Alamo[3,4], Danny Bluestein[5], Elazer R. Edelman[6] and Jolanda J. Wentzel[7]

[1]Department of Mechanical Engineering, McMaster University, Hamilton, ON, Canada, [2]School of Biomedical Engineering, McMaster University, Hamilton, ON, Canada, [3]Department of Mechanical Engineering, University of Washington, Seattle, WA, United States, [4]Center for Cardiovascular Biology, University of Washington, Seattle, WA, United States, [5]Department of Biomedical Engineering, Stony Brook University, Stony Brook, NY, United States, [6]Institute for Medical Engineering and Science, Massachusetts Institute of Technology, Cambridge, MA, United States, [7]Cardiology Department, Biomedical Engineering, Biomechanics Laboratory, Erasmus MC, Rotterdam, Netherlands

KEYWORDS

diagnostic methods, medical imaging, cardiovascular disease, monitoring, bioengineering

Editorial on the Research Topic
Novel methods to advance diagnostic and treatment value of medical imaging for cardiovascular disease

The use of medical imaging has substantially increased over the past decade, thanks to the technological advancements evident from the dramatic improvement in the sensitivity and spatial resolution of imaging modalities. Cardiovascular imaging has been at a crossroads regarding technological advances, with a shift in focus from single-modality diagnosis to an integrated multimodality approach that can provide comprehensive assessments of morphology, pathophysiology, and disease biology to stratify the patient risk and guide therapies. The wide inter-subject variability in cardiovascular anatomy and pathophysiology urges the design of personalized patient management, which can highly benefit from clinical imaging technologies. The remarkable advances in medical imaging have sparked the development of new image processing algorithms and image-based simulation tools. In addition to providing comprehensive diagnostic information, some tools can even predict intervention outcomes, thereby enabling personalized intervention planning. This Research Topic, *Novel Methods to Advance Diagnostic and Treatment Value of Medical Imaging for Cardiovascular Disease*, focuses on tools that augment the power of medical imaging to provide detailed quantification of cardiovascular disease. Here, we present a Research Topic of 21 research articles that provide the

reader with information regarding recent advancements in medical imaging improving diagnosis, prediction, monitoring, and treatment of cardiovascular disease.

Coronary disease

Accurate coronary blood flow quantification is crucial in the proper diagnosis and treatment planning in patients with coronary artery disease. Swine animal models are invaluable to study coronary flow and develop predictive tools for disease initiation and progression. Coronary hemodynamics play a fundamental role in these processes but the correspondence between human and swine coronary flow has not been previously demonstrated. De Nisco et al. confirmed the validity of swine-specific computational models to characterize coronary hemodynamics parameters and diseases such as atherosclerosis and their translation to human vascular disease. This validation was performed using a comparative computational fluid dynamics analysis (CFD) between swine-specific and human-specific models. The analysis involved several flow and anatomical features obtained through intravascular ultrasound and coronary computed tomography angiography.

A study by Hair et al. investigated the importance of using both patient-specific anatomic and flow information from magnetic resonance angiography in order to accurately assess the functional significance of coronary lesions. The purpose of the study was to investigate the effects of varying coronary flow reserve values on the calculation of fractional flow reserve. State-of-the-art CFD analyses of coronary flow are performed on high-resolution patient-specific coronary anatomies from CT but use flow rates obtained from population statistics and allosteric scaling as inlet boundary conditions. The authors demonstrated that this approach provides fractional flow reserve values that differ from those calculated by CFD with patient-specific flow rates derived from magnetic resonance angiography data, demonstrating the importance of patient-specific features on coronary disease evaluation.

Several studies have been performed which build upon current diagnostic imaging modalities. Blanken et al. developed a framework which quantifies coronary flow using accelerated 4D flow MRI with respiratory motion correction compressed sensing image reconstruction. The developed framework improves upon the current use of 2D flow MRI which is limited in clinical applicability. The proposed framework allows for diastolic quantification of left coronary flow which agrees with 2D flow MRI. Current intravascular ultrasound (IVUS) parameters cannot accurately diagnose intermediate coronary stenosis. By integrating IVUS parameters with lesion length, Li et al. demonstrated the potential for accurate diagnosis of intermediate coronary stenosis using IVUS parameters.

Dang et al. investigated the correlation between the quality of pericoronary adipose tissue (PCAT) derived from dual-layer spectral detector CT (SDCT) and the severity of coronary artery disease. PCAT is a known contributor to the development of atherosclerosis and the authors of this study suggest that the use of SDCT for PCAT may be an important feature to monitor in the development of coronary artery disease.

Valvular disease

Due to the wide range of differences in cardiovascular anatomy and pathophysiology, treatment planning for patients requiring valve repair or replacement calls for patient-specific approaches. Baiocchi et al. explored the effects of different imaging modalities, namely Doppler echocardiography and computed tomography, on a previously developed framework which diagnoses and monitors complex ventricular, vascular, and valvular disease for patients who undergo transcatheter aortic valve replacement (TAVR). Both of the mentioned imaging modalities along with the developed framework were compared against cardiac catheterization for patients with complex valvular, vascular, and ventricular disease who undergo TAVR in both pre and post-intervention. Schmid et al. investigated whether global indices of ventricular function measured by cardiac MRI pre-TAVR predict post-implantation outcomes. Magnetic resonance was right performed pre-TAVR to quantify volumetric function and global longitudinal and circumferential strain of both ventricles. The results of this study demonstrated that right ventricular function may play a role in predicting intermediate-term mortality in TAVR patients.

Dabiri et al. developed a near real-time, machine learning framework to predict the outcomes of MitraClip (MC) intervention for mitral regurgitation. Currently, fluid structure interaction simulations are used to predict outcomes of MC interventions, however, the high computational cost of these simulations make them unpractical in clinical settings. The machine learning method proposed in this study leverages patient-specific image data including 3D echocardiographic images, which are augmented using tools like principal component analysis to ultimately obtain stress maps and mitral regurgitation through the valve, enabling to predict the outcome of MC interventions in near real time.

Tetralogy of Fallot is a congenital heart defect which involves ventricular septal defect, pulmonary valve stenosis, aorta overriding, and right ventricular hypertrophy. Currently, this congenital disease is often surgically treated with pulmonary valve replacement (PVR) which carries risk as an open-heart operation. Yu et al. adapted computational biomechanical models to study the impact of PVR with five band insertions. Using CMR images, 147 computational bi-ventricle models were constructed to simulate right ventricle

cardiac functions and identify optimal band treatment options. The results from this study showed great potential of using active contraction bands to improve ventricular function in patients with Tetralogy of Fallot.

Vascular disease

Vascular disease in general is often onset due to abnormal interactions between vessel morphology and hemodynamics. De Marinis and Obrist developed a data assimilation methodology which can be used to improve spatial and temporal resolution of voxel-based flow data as obtained from biomedical imaging modalities. Combined with a CFD solver, this framework can be enhance the resolution of fine-scale flow features of cardiovascular flows.

Salmasi et al. investigated the impacts of blood flow patterns on the material properties of ascending thoracic aortic aneurysms from vascular remodeling. This was achieved by using image-based computational modelling to determine wall shear stresses along with *ex-vivo* measurements of tissue-derived mechanical and microstructural properties using segmental analysis.

An additional study by Saitta et al. explored the interactions between aortic morphology and hemodynamics in the development of type B aortic dissection (TBAD). Four patients with varying type B aortic dissection morphologies underwent both CT and 4D flow MRI imaging to perform flow visualization and quantitative analysis in the true and false lumens of the dissected aorta. This study demonstrated the clinical feasibility of 4D flow MRI in TBAD patients and its importance in assessing the hemodynamic footprint of this condition.

Lekavich et al. studied the effects of aerobic training compared to resistance training on cardiac and peripheral arterial capacity on cardiopulmonary and peripheral vascular function. Several parameters including strain-based variables, brachial artery flow-mediated dilation, as well as peak VO_2 and peak O_2 pulse were analyzed in sedentary and obese adults. The results of this study can lead to optimal choice of exercise modality to achieve specific clinical endpoints.

A crucial portion of the vascular system lies within the cranium to supply the brain with adequate oxygen. Image-based CFD analysis provides precise predictions of cerebral flow when supplied with inflow-outflow boundary conditions. However, the redundancy of flow paths offered by the circle of Willis makes it difficult to establish accurate patient-specific boundary conditions from anatomical images alone. Schollenberger et al. used arterial spin labeling MRI to solve this challenge in order to simulate cerebral hemodynamics in a patient-specific manner for patients suffering from cerebrovascular stenoses.

Myocardial/ventricular disease

Myocardial and ventricular disease have major implications on the entire cardiovascular system and must be treated promptly and properly in order to provide the best outcome for each patient. Huang et al. investigated alterations in left ventricular myocardial workload using the left ventricular pressure-strain loops in patients with type 2 diabetes mellitus. In this study, various biomechanical features including global longitudinal strain, global work index, global constructive work, and left ventricular ejection fraction were evaluated. Patient specific parameters were measured using echocardiography, 2-D speckle tracking echocardiography (STE), and LV pressure strain-loop (LVPSL) technology.

Myocardial infarction (MI) is caused by a lack of oxygen supplied to the myocardial cells and is a major cause of death and disability worldwide Kotronias et al. investigated the use of angiography-derived index of microcirculatory resistance to predict microvascular injury in patients with ST-segment-elevation MI. Current use of pressure-wire based methods to predict microvascular injury remain costly and procedurally complex. Peng et al. reviewed magnetic resonance texture analysis in MI, summarizing the outstanding challenges and clinical applications and illustrating how image-based metrics are increasingly used as biomarkers in the diagnosis and prognosis of cardiovascular diseases.

Medical imaging of myocardial fibrosis, which is associated with impaired contractility, increased stiffness, and electrophysiological alterations, is receiving increasing attention in recent years. A study performed by Sun et al. used both 2-D and 3-D STE to evaluate myocardial strain as well as determine which method is a more robust predictor of myocardial fibrosis in heart transplant recipients. This was accomplished by evaluating myocardial fibrosis by CMR extracellular volume fraction and its association with myocardial strain, measured using the methods originally mentioned. The results of this study demonstrated the potential of both 2-D and 3-D STE to monitor the development of fibrotic remodeling following heart transplant. An additional study performed by Cui et al. used the non-invasive LVPSL method to measure global myocardial work indices in patients with dilated cardiomyopathy. The results of the study demonstrated that the parameters measured by non-invasive LVPSL can be significant predictors of myocardial fibrosis in patients with dilated cardiomyopathy.

The idea of LV flow as a biomarker was explored using 4-D flow MRI by Kim et al., who studied patients with paroxysmal atrial fibrillation (PAF) and normal LV function imaged in sinus rhythm. The authors found LV blood particles take longer to transit the LV in PAF patients when compared to controls, suggesting that LV flow could be a sensitive biomarker that can detect subtle phenotypic differences.

Cardiomyopathy, as shown by Morita et al., can be heavily influenced based on genetic testing. Genetic testing carries socioeconomical and psychological burdens and it is therefore important to identify patients with cardiomyopathy who are more likely to have a positive genotype. The model developed in this study demonstrates superior accuracy to predict positive genotypes in patients with cardiomyopathy compared to standard methods. The developed framework involves a deep convolutional neural network algorithm to analyze echocardiographic images.

Conclusion and future directions

In the past 2 decades, the use of medical imaging has drastically increased, and medical imaging had astonishing advancements. Due to the increasing focus on personalized healthcare and the devastating effect of cardiovascular diseases, there has been rising interest in the field of patient-specific image-based cardiovascular *in silico* modelling. Such models have assisted researchers in gaining a deeper and more complete understanding of cardiovascular diseases and are beginning to assist clinicians in determining personalized and optimal treatments. Moving forward, one of the major challenges in cardiovascular modelling, covering not only fluid dynamics but also electrophysiological modelling for long term patient specific predictions. As the technology develops, researchers and physicians should envision the ultimate objective of a personalized cardiovascular model that incorporates personalized genomics, cellular behavior, tissue structure integrated with cardiovascular mechanics and fluid dynamics. We hope that our readers find the work published here both informative and stimulating in the endeavor to progress the therapy of cardiovascular disease.

Author contributions

All authors listed have made a substantial, direct and intellectual contribution to the work, and approved it for publication. ZK-M: Conception and design, manuscript writing, critical revision, led the effort and final approval of the manuscript. JCD, DB, ERE, and JJW: Critical revision and final approval of the manuscript.

Funding

ZK-M was supported by the NSERC Discovery Grant (RGPIN-2017-05349) and NSERC CRD Grant (CRDPJ 537352 - 18), JCD was supported by NIH grants R01 HD092216-01A1, 1R01 HL160024, NIH 1R01HL128630, 1R01HL130840, and Medtronic Inc., DB was supported by NIBIB U01EB026414, NHLBI U01HL131052 and NHLBI R42-HL134418, ERE was supported in part by R01 HL161069. Medtronic Inc. were not involved in the study design, collection, analysis, interpretation of data, the writing of this article or the decision to submit it for publication.

Acknowledgments

We thank all authors and reviewers for their invaluable contributions to this Research Topic.

Conflict of interest

The authors declare that the research was conducted in the absence of any commercial or financial relationships that could be construed as a potential conflict of interest.

Publisher's note

frontiers in Cardiovascular Medicine

ORIGINAL RESEARCH
published: 01 April 2021
doi: 10.3389/fcvm.2021.638929

Aerobic Versus Resistance Training Effects on Ventricular-Arterial Coupling and Vascular Function in the STRRIDE-AT/RT Trial

Carolyn L. Lekavich[1], Jason D. Allen[2], Daniel R. Bensimhon[3], Lori A. Bateman[4], Cris A. Slentz[1], Gregory P. Samsa[1], Aarti A. Kenjale[1], Brian D. Duscha[1], Pamela S. Douglas[1,5] and William E. Kraus[1,6]*

[1] Division of Cardiology, Duke University School of Medicine, Durham, NC, United States, [2] Division of Cardiovascular Medicine, Department of Kinesiology, University of Virginia, Charlottesville, VA, United States, [3] Cone Health and Vascular Center, Greensboro, NC, United States, [4] Department of Biostatistics, University of North Carolina at Chapel Hill, Chapel Hill, NC, United States, [5] Duke Clinical Research Institute, Durham, NC, United States, [6] Duke Molecular Physiology Institute, Durham, NC, United States

OPEN ACCESS

Edited by:
Zahra K. Motamed,
McMaster University, Canada

Reviewed by:
Ciro Santoro,
Federico II University Hospital, Italy
Haotian Gu,
King's College London,
United Kingdom
Trevor James King,
McMaster University, Canada

***Correspondence:**
Carolyn L. Lekavich
carolyn.lekavich@duke.edu

Specialty section:
This article was submitted to Cardiovascular Imaging, a section of the journal Frontiers in Cardiovascular Medicine

Received: 07 December 2020
Accepted: 08 March 2021
Published: 01 April 2021

Citation:
Lekavich CL, Allen JD, Bensimhon DR, Bateman LA, Slentz CA, Samsa GP, Kenjale AA, Duscha BD, Douglas PS and Kraus WE (2021) Aerobic Versus Resistance Training Effects on Ventricular-Arterial Coupling and Vascular Function in the STRRIDE-AT/RT Trial. Front. Cardiovasc. Med. 8:638929. doi: 10.3389/fcvm.2021.638929

Background: The goal was studying the differential effects of aerobic training (AT) vs. resistance training (RT) on cardiac and peripheral arterial capacity on cardiopulmonary (CP) and peripheral vascular (PV) function in sedentary and obese adults.

Methods: In a prospective randomized controlled trial, we studied the effects of 6 months of AT vs. RT in 21 subjects. Testing included cardiac and vascular ultrasoundography and serial CP for ventricular-arterial coupling (Ees/Ea), strain-based variables, brachial artery flow-mediated dilation (BAFMD), and peak VO_2 (pVO_2; mL/kg/min) and peak O_2-pulse (O_2p; mL/beat).

Results: Within the AT group ($n = 11$), there were significant increases in rVO_2 of 4.2 mL/kg/min (SD 0.93) ($p = 0.001$); O_2p of 1.9 mL/beat (SD 1.3) ($p = 0.008$) and the brachial artery post-hyperemia peak diameter 0.18 mm (SD 0.08) ($p = 0.05$). Within the RT group ($n = 10$) there was a significant increase in left ventricular end diastolic volume 7.0 mL (SD 9.8; $p = 0.05$) and percent flow-mediated dilation (1.8%) (SD 0.47) ($p = 0.004$). Comparing the AT and RT groups, post exercise, rVO_2 2.97, (SD 1.22), ($p = 0.03$), O_2p 0.01 (SD 1.3), ($p = 0.01$), peak hyperemic blood flow volume (1.77 mL) (SD 140.69) ($p = 0.009$), were higher in AT, but LVEDP 115 mL (SD 7.0) ($p = 0.05$) and Ees/Ea 0.68 mmHg/ml (SD 0.60) $p = 0.03$ were higher in RT.

Discussion: The differential effects of AT and RT in this hypothesis generating study have important implications for exercise modality and clinical endpoints.

Keywords: heart failure with preserved ejection fraction, ventricular-arterial coupling, brachial artery flow mediated dilatation, echocardiographic imaging, aerobic vs. resistance exercise training, ventricular-vascular coupling

HIGHLIGHTS

- The peripheral vascular and ventricular-arterial coupling interaction needs further exploration when considering targeted AT and RT exercise interventions.
- This prospective randomized control trial identified differential effects on structural adaptations relative to exercise type which may have significant implications when considering exercise prescriptions.

INTRODUCTION

Regular physical activity (PA) reduces the risk of cardiovascular disease, as well as cardiovascular and all-cause mortality (1–3). However, the central cardiac and peripheral vascular mechanisms whereby these significant health benefits are achieved, and how they differ with different modes of exercise remain unclear.

The effects of exercise training on left ventricular (LV) systolic function has been studied; but, the data are conflicting. Some studies show detectable improvements in LV function while others have failed to demonstrate changes (4–9). In addition, the exercise-induced effects on ventricular-arterial coupling and vascular physiology in exercise intervention clinical trials has been understudied, especially in training studies as long as 6 months (2, 9–13). Both aerobic and resistance exercise improve cardiac function; decrease arterial intima-medial thickness; and improve endothelial function, all of which are independently associated with risk of cardiovascular events and death (14–18). However, the relative effects of chronic aerobic exercise training (AT) and resistance exercise training (RT) on cardiac structural and functional, ventricular-arterial, and peripheral vascular adaptations to moderate term exercise training are not well-characterized.

As such, the purpose of this hypothesis generating sub-study of the Studies of a Targeted Risk Reduction Intervention through Defined Exercise (STRRIDE) Aerobic Training/Resistance Training (AT/RT study) (19, 20) was to compare the effects of long-term, 6 months of AT or RT (4 month control period, 2 month ramp up, 6 month training on changes in measures of cardiac and peripheral vascular morphology and function in those at elevated risk: sedentary, overweight and obese adults.

METHODS

Study Design

More details of the study design discussed below can be obtained in published form (21).

Subject Population

Subjects in the overall study were overweight, dyslipidemic, and sedentary men and women (exercising <1 time per week). Inclusion criteria were: age 18–70 years, body mass index 25–35 kg/m^2, LDL-C 130–190 mg/dL or HDL-C <45 mg/dL for women <40 mg/dL for men, fasting glucose <126 mg/dL (on no medications), resting BP <160/90 mm/Hg (on no medications), and sedentary (exercise <once/week). Exclusion criteria were overt presence of cardiovascular disease, current or planned use of weight loss diet regimens, use of potentially confounding medications (e.g., hypoglycemics, anti-hypertensives), pregnancy, other metabolic or musculoskeletal diseases, unwillingness or contra-indication to undergo exercise training or study testing.

Study Arms/Exercise Interventions

After completion of a 4-month control run-in period, subjects were randomized to one of two exercise training arms. All subjects provided verbal and written informed consent approved by the Duke University Institutional Review Board prior to participation.

Subjects were randomly assigned to either AT or RT groups using a block design for gender and race as described (22). For the AT group, subjects expended 2,000 kcal/week at 65–80% peak VO_2 using at least two of three modalities: stationary cycling, treadmill walking or stair climbing/elliptical training. For the RT group, subjects trained using a full-body RT regimen consisting of three sessions/week of three sets of 12–15 repetitions of nine resistance exercises at 70–85% 1RM. Both AT and RT required 2 months of ramp-up, followed by 6 months of training. Repeat CPET and vascular testing was performed within 48 h following the 6 months of training. All the participants were required not to participate in any exercise outside of that prescribed in the study.

For the AT group, at each session participants wore a Polar heart rate monitor with downloadable data, to verify that the intensity and duration fell within the guidelines of the program. Aerobic compliance was calculated as percentage of completed sessions over the number of prescribed sessions per week.

For the RT group, training was prescribed as three sessions per week of three sets of 8–12 repetitions on eight Cybex machines. This consisted of four upper body and four lower body exercises, designed to target major muscle groups. Throughout the training intervention, the amount of weight lifted on each machine was increased by five pounds when the participant performed 12 repetitions with proper form on all three sets during two consecutive workout sessions. All RT sessions were verified by use of the FitLinxx Strength Training PartnerTM, a touch screen "training-partner" computer system designed to monitor and track workouts electronically. RT compliance was calculated as percentage of completed sessions over the number of prescribed sessions per week.

All post-exercise training assessments for this study—CPET testing, vascular and echocardiographic measures—were performed within 24 h after a bout of exercise and before conclusion of the 6-month training program.

Cardiopulmonary Exercise Testing (CPET) with a 12-lead electrocardiogram and expired gas analysis was performed on a treadmill using a TrueMax 2400 Metabolic Card. The CPET protocol consisted of 2-min stages, increasing the workload by approximately one metabolic equivalent per stage. The two

Abbreviations: Ea, Arterial elastance (mmHg/ml); BAFMD, Brachial artery flow-mediated dilation (mm); CPET, Cardiopulmonary Exercise Testing; HFpEF, Heart failure with preserved ejection fraction; LVEDV, Left ventricular end diastolic volume; O_2p, Oxygen pulse; pVO_2, Peak oxygen uptake (L/min); STRRIDE, Studies of a Targeted Risk Reduction Intervention through Defined Exercise; Ees/Ea, Ventricular-arterial coupling; Ees, Ventricular elastance (mmHg/ml).

greatest, consecutive, 15-s readings from each test were averaged to determine absolute VO_2peak (L/min).

Standard Echocardiography

Resting transthoracic echocardiograms (TTE) were obtained at two time points: (1) after a 4-month control period but prior to the initiation of a 2 month ramp-up that preceded the 6-month exercise training program and (2) at the completion of the exercise training period. Echocardiographic studies were performed on a commercially available machine with a 2.5 MHz probe and digital storage capacity (GE Vivid 7). A complete study was performed in 2-D and tissue Doppler (TDI) modes. All TDI images were obtained at a frame rate of at least 100 frames/s. 2-D measurements included LV end diastolic and end systolic volumes with calculation of LV ejection fraction (biplane Simpson's rule). Pulsed Doppler imaging was used to interrogate trans-tricuspid, trans-mitral, pulmonary venous and LV outflow tract flows. The mitral inflow E and A wave velocities, pulmonary vein systolic (S) and diastolic (D) velocities and the mitral E wave deceleration time were measured. From these, the E/A and S/D ratios were calculated. Isovolumic relaxation time (IVRT) was also determined from the mitral inflow pattern. Tei index, a measure of the combined diastolic and systolic function was also calculated with the formula (ICT + IRT)/ET where ICT represents isovolumic contraction time, IRT represents isovolumic relaxation time, and ET represents ejection time (23). For all 2D and Doppler variables, three beats were measured and the average reported. For mitral annular velocities (mitral annular peak early (Ea), late (Aa), and systolic velocities (Sa), the sample volume (6 × 6 pixels) was placed at the septal and lateral mitral annulus.

Ventricular-Arterial Coupling

Arterial elastance (Ea), the measure of arterial elastance, was calculated as the ratio of end-systolic pressure to stroke volume (Ea = ESP/SV) (24). ESP was estimated as 0.90 multiplied times systolic blood pressure (SBP) by manual cuff at the time of echocardiogram as recommended (24). Stroke volume (SV, cm^3) was measured from the left ventricular outflow tract (LVOT) diameter at the pulse wave (PW) from the echo Doppler signal. Ees (ventricular elastance) was calculated using the single-beat method outlined by Chen et al. (24).

Ees(sb) = [DBP–(Endest*ESP)]/(SV*Endest)

Endest = 0.0275 – (0.165*EF) + 0.3656*(DBP/ESP) + (0.515*Endavg)

Endavg = 0.35695 + (-7.2266*tn) + (74.249*tn^2) + (-307.39*tn^3) + (684.54*tn^4) + (-856.92*tn^5) + (571.95*tn^6) + (-159.1*tn^7)

tn (ms) = R wave to flow onset time/R wave to flow end time; determined non-invasively from the echo Doppler signal in the LV outflow tract by pulse wave (24).

Tissue Doppler Strain Imaging Measurements

Analysis of myocardial wall velocities, strain and strain rate in the apical 4-chamber view was performed offline using customized computer software (EchoPac, Version 6.3, GE). Two-dimensional speckle tracking methods were used to extract left ventricular global longitudinal strain throughout the cardiac cycle, which was analyzed for measures of systolic and diastolic function. Peak global longitudinal, circumferential and radial strains and time to peak longitudinal strain were calculated. For an evaluation of diastology, we calculated peak early and late diastolic strain rate (SR_{Emax} and SR_{Amax}, respectively). In addition, peak diastolic strain rate deceleration time was calculated. See **Figure 1**. The echocardiograms and their analysis were performed before the current guidelines were in place and so provided somewhat limited stain information. Nevertheless, the strain derived from the 4ch view only approximates the global strain derived from the three views, especially in this instance in which each participant's compared to his or her own baseline data, acquired in the same way.

Brachial Artery Flow Mediated Dilation

Vascular testing occurred between 7 and 10 a.m. following an overnight fast and withholding all vasoactive medications. Additionally, no exercise was performed and no alcohol or tobacco products were consumed the day before or on the morning of testing. The BAFMD technique used a high-resolution ultrasound and an 8 MHz linear array transducer (Acuson Sequoia 512) to obtain images of the artery at baseline, during and following 5 min of forearm occlusion. Ultrasound brachial artery images were obtained in longitudinal view, just proximal to the olecranon process of the elbow. With the image depth set at 3 cm, zoom and gain setting were adjusted to provide an optimal view of the center of the vessel and the anterior and posterior walls of the artery. Once the settings were optimized, they were kept constant throughout the test and the probe was stabilized with a mechanical arm. In addition, to assure maximum laminar flow, Doppler flow velocity measurements were obtained by means of range gating focused on the center of the vessel using an angle of incidence of 60 degrees. All measurements were performed using the left arm with the subject in the supine position and the forearm extended and slightly supinated. All images were recorded on a magneto-optical disk for subsequent analysis.

The forearm occlusion condition consisted of inflation of a blood pressure cuff to 50 mmHg above systolic blood pressure for a period of 5 min. The cuff was positioned ∼2–3 centimeter (cm) distal to the olecranon process. Images of the brachial artery were obtained 1 min prior to inflation (baseline), during the 3rd min of inflation, and continuously for 2–3 min after cuff deflation. Throughout the brachial imaging procedure, heart rate and blood pressure were measured in order to account for any variation in central cardiovascular responses to the testing protocol. Arterial diameter and blood flow were measured from the digital recordings. Arterial diameters were determined from the anterior to posterior interface between the medial and adventitia (the "m" line), rather than between intimal layers. In addition, all diameters were end diastolic, as defined by the onset of the r-wave over at least three to four consecutive cardiac cycles using

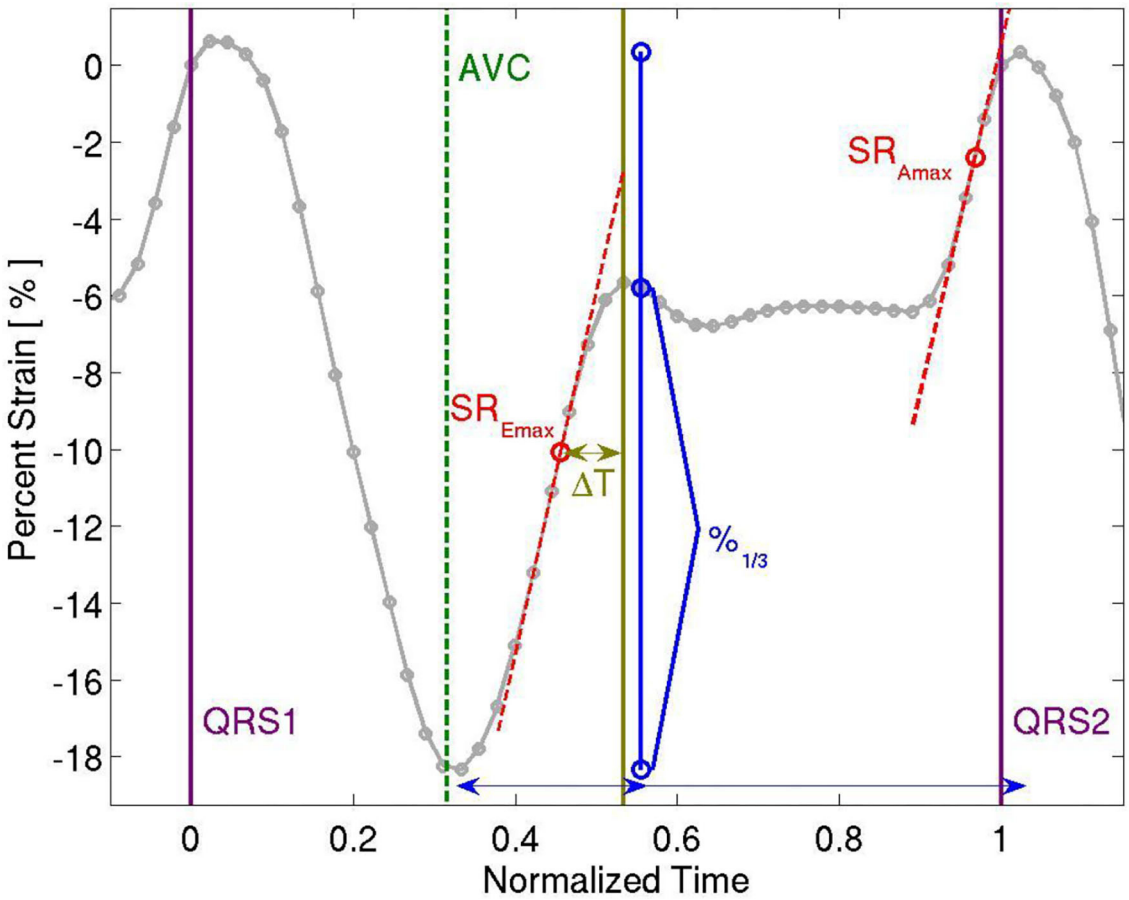

FIGURE 1 | Representative Strain Curve showing time to peak longitudinal strain, peak longitudinal strain, peak early and late diastolic strain rate (SR_{Emax} and SR_{Amax}, respectively), and peak diastolic strain rate deceleration time (ΔT).

specialized imaging software (Medical Imaging Applications). The reproducibility of this technique for our group has been reported previously (25).

The nitroglycerin (NTG)-stimulated brachial artery reactivity response was tested 10 min after performing the standard BAFMD testing. Participants were given a dose of 0.4 mg of NTG sublingually and images were obtained at 5 min post-NTG administration. Participants were monitored for up to 20 min before leaving; blood pressure was continuously monitored until BP returned to pre NTG values.

Doppler forearm blood flow velocities (peak and mean) were recorded during each experiment. Brachial artery blood flow (mL/min) was estimated by multiplying the velocity-time integral of the Doppler flow signal (corrected for angle) by heart rate and the vessel cross-sectional area. The percent change in brachial artery diameter, Doppler flow velocities, and blood flow was calculated by dividing the difference from baseline values by the baseline value prior to each condition.

Statistical Analysis

Baseline characteristics were described using mean and median for continuous variables and percentages for categorical variables. For between AT and RT groups comparisons, unpaired *T*-tests were used. For within group pre and post exercise training comparisons, paired *T*-tests were used. The across time mean vascular and physical performance measures for both AT and RT groups were analyzed using a *t*-test. Changes in strain derived variables were compared to conventional Doppler measures including the ratio of peak early (E) and late (A) diastolic mitral inflow velocities; early inflow to annular velocity ratio (E/e'); and isovolumic relaxation time (IVRT) using paired *T*-tests. To identify the association between baseline echocardiographic variables and exercise capacity, we performed univariable linear regression analyses with echocardiographic parameters as predictive variables and peak VO_2 (pVO_2) and peak O_2–pulse (O_2p) defined as peak absolute VO_2/peak heart rate as the outcome variables. A *p*-value of 0.05 was considered significant and all statistical tests were two-sided. Statistics were done using SPSS Statistics version 22, SAS version 9.4 or JMP

version 13.0. This study was conducted under the approval of the Duke Institutional Review Board.

RESULTS

Baseline Characteristics

Demographics

Twenty-one subjects were enrolled and completed the STRRIDE-AT/RT echocardiography/peripheral vascular sub-study. For the entire cohort, the mean age was 50.0 years; 48% were men and 86% were white, the percent of participants that were male did not differ by group X^2 (1, 7) = 0.12, $p > 0.05$, and the percentage of participants that are White did not differ by group X^2(1, 9) = 0.59, $p > 0.05$, mean body mass index (BMI) was 30.4 kg/m^2 and mean waist circumference was 104.3 cm. Mean systolic and diastolic blood pressures were 122.1 (SD 13.8) and 79.8 (SD 10.8) mmHg, respectively. There were no statistically significant differences between AT and RT group demographics (**Table 1**, AT/RT Demographics).

Baseline Echo and Exercise Capacity

Study Population Composition

Of the 21 subjects enrolled in the study, 11 were randomized to the AT group and 10 were randomized to the RT group. All AT and RT echocardiographic, pulsed Doppler imaging including trans tricuspid, trans mitral, pulmonary venous and LV outflow tract and vascular measures are presented in **Table 2A** (AT group) and **Table 2B** (RT group).

Correlation of Baseline Characteristics With Exercise Capacity

Since variables of baseline cardiac structure, systolic function, and diastolic function were similar in both groups, the data were combined and evaluated across both groups for correlation with baseline exercise capacity. No measures of baseline cardiac structure or diastolic function were significantly correlated with baseline exercise capacity measured as absolute (VO_2peak (L/min).

Exercise Effects, Changes in Cardiac and Peripheral Vascular Structure/Function

Within the AT Group

A significant exercise training effect was noted, with an increase in aVO_2 335 mL/min (SD 74.1) ($p = 0.001$), relative VO_2 (rVO_2) of 4.2 mL/kg/min (SD 0.93) ($p = 0.001$), and O_2p 1.9 mL/beat (SD 1.3) ($p = 0.008$). Of the peripheral vascular measures, the brachial artery post-hyperemia peak diameter increased 0.18 mm, (SD 0.08), ($p = 0.05$), but due to increased resting caliber of the vessel (0.13 mm, ns) there were no changes in flow-mediated dilation 0.09%, (SD) 1.0) ($p = 0$ 94). These structural changes showed a trend for post-training increased calculated peak blood flow volumes during reactive hyperemia by 104.5 ml/min (SD 168.3), ($p = 0.06$) (see **Table 2A**).

There was a consistent, significant correlation of time-to-peak longitudinal strain with peak VO_2 in the AT group both pre and post training ($r = -0.610$, $p = 0.020$; $r = -0.660$, $p = 0.010$; respectively). Other measures of ventricular-arterial coupling, myocardial and chamber systolic function such as circumferential, and radial strains did not show significant changes with exercise training. There were no significant changes in traditional or strain measures of diastolic function with exercise training (see **Table 2A**). AT Group Pre and Post Training Results and AT/RT pre/post training group comparisons.

Within the RT Group

No significant exercise training effects were observed in the RT group on pVO_2 or O_2p but there was a significant increase in LV end diastolic volume (LVEDP) 7.0 mL (SD 9.8) ($p = 0.05$) and modest but not significant increase in LV end systolic volume (LVESV) 3.5 mL (SD 5.2) ($p = 0.06$). There were no significant changes in brachial artery resting average diameter (−0.2 mm, $p = 0.51$), however, percentage flow-mediated dilation increased 1.8 mm (SD 0.47) ($p = 0.004$). Calculated resting and peak hyperemic blood flow volumes and resting and peak brachial artery shear rates were not different from baseline following exercise training. Other measures of ventricular-arterial coupling, myocardial and chamber systolic function did not show significant changes with exercise (See **Table 2B**).

Differential Responses in the AT and RT Groups

Measures of post-training cardiac structure, systolic function, and diastolic function, peripheral vascular and ventricular-arterial coupling were analyzed for correlation with post-training exercise capacity. When comparing the post exercise mean differences between AT and RT, the mean change in the AT group was significantly higher in rVO_2 2.97, (SD 1.22), ($p = 0.03$), O_2p 0.01 (SD 1.3), ($p = 0.01$), Ees/Ea 0.68 mmHg/ml (SD 0.60) $p = 0.03$ and the post-training LVEDP was higher in the RT group 7 mL (SD 3.1) ($p = 0.05$). There were no between group differences for brachial artery diameters in response to flow. However, peak hyperemic blood flow volume for the AT group was significantly greater than that of the RT group (177.8 mL) (SD 140.69) ($p = 0.009$) without any differences in shear rate. Nether group showed a significant brachial reactivity response to NTG (AT 26.2%, RT 21.8%, $p = 0.48$).

DISCUSSION

The unique aspects of this study illustrate significant central (cardiac) and peripheral vascular adaptations to AT and RT after 6 months of training in sedentary middle aged adults. However, the pattern of change is different. By intensively studying the coupling effects of central and peripheral vascular adaptations to moderate-length exercise training in at-risk humans, for the first time, relations among cardiorespiratory, cardiac and peripheral vascular measures have been integrated within the same study. Important new observations from this study are: (a) resistance and endurance exercise training have different but potentially congruent adaptations at the central (cardiac) and peripheral vascular levels resulting in differences in cardiorespiratory capacity, (b) with RT there was no increase in structural artery caliber or peak hyperemic blood flow or artery shear rates but there was an increase in flow mediated dilation coupled with increases in the ratio of ventricular-to-arterial elastance with

TABLE 1 | Aerobic Training (AT) and Resistance Training (RT) demographics.

	AT (Baseline) ($n = 11$)	RT (Baseline) ($n = 10$)	p-value	AT (Post-training) ($n = 11$)	RT (Post-training) ($n = 10$)	p-value
Age (years)	53.1 (6.4)	47.0 (12.3)	0.07			
Race (% white)	81.8	90.0	0.59			
Sex (%male)	64.3	30.0	0.12			
Height (cm)	169.7 (6.8)	171.2 (9.0)	0.65			
Weight (kg)	90.5 (10.4)	86.5 (12.7)	0.41	88.9 (10.6)	86.8 (13.2)	0.68
Waist circumference cm	105.7 (8.6)	102.8 (10.1)	0.46	105.0 (8.7)	101.9 (9.0)	0.40
BMI	31.7 (3.4)	29.3 (2.3)	0.07	31.1 (3.5)	29.3 (2.2)	0.12
SBP, mmHg	122.6 (9.5)	115.4 (15.9)	0.23	124.1 (8.7)	127.1 (9.5)	0.53
DBP, mmHg	83.3 (10.1)	79.7 (10.9)	0.44	82.8 (9.5)	79.7 (10.9	0.52
HR, bpm	60.0 (9.0)	66.6 (13.0)	0.20	60.0 (9.0)	66.6 (13.0)	0.20

All data presented as mean (SD), unless otherwise noted.

no concomitant increase in cardiorespiratory capacity, (c) with AT there was an increase in peak peripheral arterial structural caliber and blood flow with no increases in shear rate of the flow-mediated dilation. This increase in arterial caliber was matched with an increase in ventricular-arterial coupling and significant increases in cardiorespiratory capacity.

This study specifically links type of exercise intervention to cardiac and vascular responses that may contribute to improved cardiopulmonary performance in middle-aged, sedentary subjects and in fact, may be synergistic, as documented by Santoro et al. (26). As expected, the study showed improvements in peak aVO_2, peak rVO_2, and O_2p with AT, but not RT. Unique to this study, we observed that AT induced significant brachial artery absolute diameter and blood flow during hyperemia whereas, RT induced changes in vascular reactivity. These findings suggest harmonious adaptations to different exercise modes: AT changes vessel architecture and capacitance, whereas RT induces a stress response to exercise (vasodilation), without changing the vessel architecture (diameter).

Previous cross-sectional AT studies comparing both male (27) and female athletes (28) with healthy age-matched sedentary counterparts, report similar increases in artery caliber (29–31). Both animal and human studies, which tend to be aerobic-type trying, also demonstrate a transient increase in endothelial-mediated vasoreactivity followed by arteriogenesis in response to aerobic conditioning (25, 32, 33). However, these studies assessed changes in response to a relatively short-term training stimuli. To our knowledge, this is the first study of a longitudinal training design to observe changes in arterial structure in humans with intensive AT lasting 6 months and importantly this study included randomization to AT or RT after completion of a 4-month control run-in period.

If we consider the contrasting demands and mechanisms of blood flow delivery among AT vs. RT, this differential response is logical. Typically, RT subjects spent ∼1–2 min on each set of a specific lift with a rest period between sets. This created a short period of increased blood flow and shear stress on the arterial wall. In contrast, during AT, subjects performed less intense muscular contractions for up to 40 min per session; creating an increased blood flow demand by skeletal muscle for the entire exercise bout.

When linking the vascular and cardiac measures to exercise type, we found that the LVEDP increased significantly with RT and significantly higher post-training compared to AT and the post-training mean difference in Ees/Ea was higher in RT. Given that Ees/Ea measures LV volume, force and loading effects during contraction, it reflects the ventricular-arterial interaction (24). With AT, where the resting caliber of the vessel increased and architecture changed, Ees/Ea remained balanced reflecting a central and peripheral vascular physiologic balance. This finding suggests that RT affects the ventricular-vascular balance.

In addition, unique to this study, with AT, there was a significant negative correlation between peak rVO_2 and time-to-peak longitudinal strain ($p = 0.001$), a finding not previously reported. A shorter time to peak strain represents a more forceful myocardial contraction. There were no similar adaptations observed in the RT group. This may indicate that AT contributes to the balance of ventricular-arterial coupling while also having a training effect on myocardial contractility. Given that we observed substantive differences in the effects of AT and RT on cardiovascular structure and function, this may have important clinical implications for the use of exercise training in individuals with impaired cardiac relaxation finding, such as when considering an exercise prescription for patients with heart failure with preserved ejection fraction (HFpEF). Importantly, as physical activity interventions are tested, future studies should consider the myocardial and peripheral vascular interaction in human performance and cardiovascular health in middle-aged and elderly populations and the effects such changes may have on long-term cardiovascular health.

Strengths and Limitations

This study has unique strengths. To the best of our knowledge, this is the first study to compare two different modes of exercise of a 6-month training program in assessments of cardiac morphology, vascular function and cardiorespiratory fitness in adults of any age or cardiovascular risk. This provides the

TABLE 2A | AT group pre- and post-training results and AT/RT pre/post-training group comparisons.

	Baseline	Post-training	ΔTraining	*p*-value for AT pre- and post-training
Exercise capacity				
pVO_2 mL/min	2,448 (484.9)	2,784 (483.3)	335 (74.1)	**0.001***
mL/kg/min	26.85 (4.3)	31.09 (5.0)	4.2 (0.93)	**0.001***
O_2p mL/beat	14.40 (2.52)	16.34 (2.6)	1.9 (1.3)	**0.008***
mL/kg/beat	0.16 (0.02)	0.18 (0.02)	0.02 (0.02)	**0.0001***
Ve/VCO_2 slope	30.09 (4.5)	30.55 (3.5)	0.46 (0.78)	0.56
Vascular structure				
BaseAve (mm)	3.47 (0.49)	3.63 (0.47)	0.16 (0.09)	0.11
MaxDia (mm)	3.69 (0.47)	3.86 (0.47)	0.18 (0.08)	**0.05**
%ChgMax (%)	6.45 (2.89)	6.53 (2.31)	0.09 (1.1)	0.94
TimeToMax (ms)	44.45 (14.26)64 (24.6)	45.63 (18.56)	1.18 (7.10)	0.87
Rel Ave Shear Rate (s^{-1})	0.20 (0.08)	0.19 (0.04)	−0.01 (0.09)	0.62
Rel Peak Shear Rate (s^{-1})	0.34 (0.12)	0.34 (0.11)	0.00 (0014)	0.95
NTG mediated (%)	26.2 (11.2)	23.7 (8.9)	−1.15 (11.0)	0.93
Cardiac structure				
Heart Rate, bpm	6.0 (9.0)	60.0 (9.0)	0 (0.0)	1.0
LVEDV, mL	95.6 (18.7)	98.8 (14.5)	4.2 (3.0)	**0.20***
LVESV, mL	34.5 (7.4)	39.0 (8.8)	4.5(2.1)	0.06
Systolic function				
LVEF (%)	63.7 (4.5)	60.6 (5.4)	−3.1 (1.2)	**0.62***
Ea (mmHg/mL)	1.6 (0.1)	1.8 (0.3)	0.2 (0.1)	0.42
Ees (mmHg/mL)	1.9 (1.2)	2.5 (1.2)	0.67 (1.2)	0.68
Ees/Ea (ratio)	1.1 (0.8)	1.3 (0.4)	0.2 (0.6)	**0.77***
Tei Index	0.52 (0.07)	0.50 (0.07)	−0.02 (0.05)	0.14
Strain Indices				
Longitudinal global Peak Strain	−19.6 (0.64)	−17.3 (4.3)	−0.75 (5.0)	0.59
Time to peak longitudinal strain	0.40 (0.05)	0.38 (0.05)	−0.02 (0.04)	0.06
Strain rate (SR) $(seconds)^{-1}$	−83.6 (17.6)	−82.9 (26.1)	0.71 (33.7)	0.94
Time to peak SR	0.22 (0.05)	0.18 (0.05)	−0.04 (0.07)	0.06
Circumferential peak global strain	−19.3 (6.1)	−19.2 (5.6)	0.21 (6.7)	0.91
Radial peak global strain	−26.8 (14.7)	−37.2 (22.4)	−9.84 (24.5)	0.17
Diastolic function				
E	0.62 (0.09)	0.66 (0.11)	0.04 (0.13)	0.31
A	0.60 (0.12)	0.62 (0.14)	0.02 (0.11)	0.58
e'	0.11 (0.02)	0.10 (0.03)	−0.004 (0.02)	0.39
E/A	1.1 (0.33)	1.1 (0.24)	0.03 (0.27)	0.72
E/e'	5.8 (1.4)	6.8 (1.7)	0.71 (1.6)	0.11
MV Dec T	196.5 (28.0)	207.0 (31.1)	10.5 (43.5)	0.38
IVRT	95.7 (11.6)	89.3 (8.4)	−6.4 (13.6)	0.10
Peak early diastolic longitudinal strain (max)	0.32 (0.08)	0.31 (0.09)	−0.001 (0.10)	0.97
Time to peak early longitudinal strain (seconds)(max)	0.16 (0.04)	0.16 (0.04)	0.002 (0.06)	0.92
SRE Max	92.8 (22.7)	101.1 (27.4)	8.2 (23.3)	0.21
SRA Max	77.4 (21.0)	78.7 (34.0)	1.3 (34.6)	0.90

**Indicates training effect is significantly different between AT and RT.*

pVO_2, absolute peak VO_2; pO_2 pulse, absolute peak O_2 pulse; LVEDV, left ventricular end diastolic volume; LVESV, left ventricular end systolic volume; E, early trans-mitral LV filling (meters/second); A, late transmitral LV filling (meters/second); e', average tissue Doppler velocity of the septal and mitral annulus (meters/second); MV Dec T, Deceleration time of mitral inflow Doppler; IVRT, isovolumic relaxation time; SRE Max, strain rate diastolic E maximum; SRA Max, strain rate diastolic A maximum.

All data presented as mean (SD), unless otherwise noted. The bold values have significant p-values.

TABLE 2B | Characteristics pre- and post-training – RT group only.

	Baseline	Post-training	ΔTraining	*p*-value pre- and post-exercise
Exercise capacity				
pVO_2 mL/min	2,444 (480.3)	2,561(651.3)	117.5 (67.1)	0.11
mL/kg/min	28.3 (4.3)	29.6 (5.8)	1.3 (0.79)	0.14
O_2p mL/beat	13.7 (3.4)	14.3 (3.9)	0.65 (1.2)	0.12
mL/kg/beat	0.16 (0.03)	0.17 (0.03)	0.01 (0.01)	0.10
Ve/VCO_2 slope	31.1 (5.7)	32.7 (7.5)	1.6 (2.8)	0.11
Vascular structure				
BaseAve (mm)	3.28 (0.58)	3.33 (0.67)	0.06 (0.09)	0.54
MaxDia (mm)	3.48 (0.57)	3.59 (0.67)	0.11 (0.10)	0.30
%ChangeMax (%)	6.43 (2.16)	8.20 (2.30)	1.8 (0.47)	**0.004**
TimeToMax (ms)	40.80 (10.99)	38.20 (7.76)	−2.60 (3.49)	0.47
Rel Ave Shear Rate (s^{-1})	0.20 (0.09)	0.19 (0.08)	−0.01 (0.05)	0.54
Rel Peak Shear Rate (s^{-1})	0.35 (0.13)	0.31 (0.11)	−0.04 (0.12)	0.35
NTG mediated (%)	21.8 (7.6)	22.9 (9.0)	1.1 (2.2)	0.64
Cardiac structure				
Heart Rate, bpm	64.8 (10.1)	66.6 (13.0)	1.8 (7.3)	0.45
LVEDV, mL	108.9 (16.2)	115.9 (15.9)	7.0 (9.8)	**0.05**
LVESV, mL	38.7 (7.5)	42.2 (6.7)	3.5 (1.6)	0.06
Systolic function				
LVEF (%)	64.6 (3.6)	63.6 (4.4)	−1.0 (1.3)	0.47
Tei Index	0.50 (0.07)	0.52 (0.05)	0.01 (0.04)	0.43
Ea (mmHg/mL)	1.9 (0.5)	1.7 (0.3)	−0.2 (0.2)	0.26
Ees (mmHg/mL)	3.4 (1.2)	4.1 (1.2)	0.7 (0.9)	0.68
Ees/Ea (ratio)	1.7 (0.5)	2.3 (0.6)	0.6 (0.4)	0.29
Strain Indices				
Longitudinal global Peak Strain	−18.2 (2.9)	−18.8 (4.0)	−0.7 (5.4)	0.71
Time to peak longitudinal strain	0.41 (0.04)	0.40 (0.05)	−0.01 (0.06)	0.61
Strain rate (SR) (seconds) $^{-1}$	−88.3 (15.0)	−94.3 (16.1)	−5.9 (17.4)	0.31
Time to peak SR	0.22 (0.05)	0.21 (0.05)	−0.02 (0.09)	0.54
Circumferential peak global strain	−21.5 (5.2)	−20.0 (5.1)	1.6 (4.9)	0.33
Radial peak global strain	−40.6 (22.1)	−38.5 (20.3)	2.2 (23.1)	0.77
Diastolic function				
E	0.73 (0.14)	0.74 (0.13)	0.01 (0.04)	0.56
A	0.61 (0.17)	0.58 (0.18)	−0.03 (0.09)	0.39
e'	0.13 (0.04)	0.13 (0.03)	−0.002 (0.02)	0.76
E/A	1.37 (0.77)	1.40 (0.59)	0.03 (0.3)	0.79
E/e'	5.97 (1.27)	6.04 (1.15)	0.07 (0.98)	0.83
MV Dec T	186.3 (31.0)	198.4 (32.7)	12.1 (30.3)	0.24
IVRT	90.4 (16.2)	92.3 (15.6)	1.9 (11.0)	0.60
Peak early diastolic longitudinal strain (max)	0.26 (0.07)	0.26 (0.08)	−0.001 (0.08)	0.98
Time to peak early longitudinal strain (seconds)(max)	0.18 (0.03)	0.15 (0.04)	−0.03 (0.04)	0.04
SRE Max	115.6 (27.4)	118.6 (26.9)	3.0 (31.5)	0.77
SRA Max	68.9 (20.2)	71.6 (28.6)	2.7 (36.2)	0.82

pVO_2, absolute peak VO_2; pO_2, pulse, absolute peak O_2 pulse; LVEDV, left ventricular end diastolic volume; LVESV, left ventricular end systolic volume; E, early trans-mitral LV filling (meters/second); A, late transmitral LV filling (meters/second); e', average tissue Doppler velocity of the septal and mitral annulus (meters/second); MV Dec T, Deceleration time of mitral inflow Doppler; IVRT, isovolumic relaxation time; SRE Max, strain rate diastolic E maximum; SRA Max, strain rate diastolic A maximum.
All data presented as mean (SD), unless otherwise noted. The bold values have significant p-values.

unique opportunity to study the coupling of these components of cardiorespiratory health to two very different exercise exposures.

However, there exist also some limitations. While our older sedentary population was unique and the sample size was adequate to detect changes in cardiorespiratory physiology and fitness, in the future a larger sample size may be necessary to detect more subtle changes in vascular-arterial coupling and a more diverse study sample may provide unique phenotypic data. Our findings are thus hypothesis generating rather than definitive. In addition, all echocardiogram measurements were taken at rest as opposed to during an active state; therefore, we may have missed important dynamic myocardial adaptations that occur during submaximal and maximal exercise capacity that may include changes in ventricular-arterial coupling. Further, it is possible that, by assessing vascular changes only before and after the 6-month training program, we may have missed a critical period of physiologic and morphologic adaptation in the vascular reactivity change with AT, but captured the longer-term structural adaptations. That is, there may be a vascular reactivity change with AT, similar to that observed with 6 months of RT. This will require further investigation with measures taken at more intermediate time points.

Implications for Clinical Practice

This study addresses differences in physiologic adaptations to endurance (AT) and resistance exercise (RT). With AT, there were significant adaptive training effects in aerobic exercise capacity, and in peripheral arterial remodeling. Furthermore, the interaction of ventricular-arterial coupling remained balanced (adaptive) with AT; but demonstrated a significant increase post exercise for the RT group. These differential findings have important implications for the use of exercise training of various modalities to achieve specific clinical endpoints.

DATA AVAILABILITY STATEMENT

The raw data supporting the conclusions of this article will be made available by the authors, without undue reservation.

ETHICS STATEMENT

The studies involving human participants were reviewed and approved by Duke Institutional Review Board. The patients/participants provided their written informed consent to participate in this study.

AUTHOR CONTRIBUTIONS

WK, PD, JA, DB, and CL created the scientific conception and design of the paper. In addition, JA and AK provided key expertise to peripheral arterial physiology and measurement, PD to echocardiography, WK and BD to exercise physiology and measurement, and LB, GS, and CS to the biostatical analysis of the paper. All authors drafted, revised, authorized and made critically important contributions to the paper.

FUNDING

This work was supported by National Institutes of Health R01 HL57354 and National Institutes of Health/NINR T32NR00709.

REFERENCES

1. Kojda G, Hambrecht R. Molecular mechanisms of vascular adaptations to exercise. Physical activity as an effective antioxidant therapy? *Cardiovasc Res*. (2005) 67:187–97. doi: 10.1016/j.cardiores.2005.04.032
2. Douglas PS, O'Toole M. Aging and physical activity determine cardiac structure and function in the older athlete. *J Appl Physiol*. (1992) 72:1969–73. doi: 10.1152/jappl.1992.72.5.1969
3. Kraus WE, Powell KE, Haskell WL, Janz KF, Campbell WW, Jakicic JM, et al. Physical activity, all-cause and cardiovascular mortality, and cardiovascular disease. *Med Sci Sports Exerc*. (2019) 51:1270–81. doi: 10.1249/MSS.0000000000001939
4. Yilmaz DC, Buyukakilli B, Gurgul S, Rencuzogullari I. Adaptation of heart to training: a comparative study using echocardiography & impedance cardiography in male & female athletes. *Indian J Med Res*. (2013) 137:1111–20.
5. De Luca A, Stefani L, Pedrizzetti G, Pedri S, Galanti G. The effect of exercise training on left ventricular function in young elite athletes. *Cardiovasc Ultrasound*. (2011) 9:27. doi: 10.1186/1476-7120-9-27
6. Spence AL, Naylor LH, Carter HH, Buck CL, Dembo L, Murray CP, et al. A prospective randomised longitudinal MRI study of left ventricular adaptation to endurance and resistance exercise training in humans. *J Physiol*. (2011) 589:5443–52. doi: 10.1113/jphysiol.2011.217125
7. Sadaniantz A, Yurgalevitch S, Zmuda JM, Thompson PD. One year of exercise training does not alter resting left ventricular systolic or diastolic function. *Med Sci Sports Exerc*. (1996) 28:1345–50. doi: 10.1097/00005768-199611000-00001
8. Kelemen MH, Effron MB, Valenti SA, Stewart KJ. Exercise training combined with antihypertensive drug therapy. Effects on lipids, blood pressure, and left ventricular mass. *JAMA*. (1990) 263:2766–71. doi: 10.1001/jama.263.20.2766
9. Levy WC, Cerqueira MD, Abrass IB, Schwartz RS, Stratton JR. Endurance exercise training augments diastolic filling at rest and during exercise in healthy young and older men. *Circulation*. (1993) 88:116–26. doi: 10.1161/01.CIR.88.1.116
10. Arbab-Zadeh A, Dijk E, Prasad A, Fu Q, Torres P, Zhang R, et al. Effect of aging and physical activity on left ventricular compliance. *Circulation*. (2004) 110:1799–805. doi: 10.1161/01.CIR.0000142863.71285.74
11. Forman DE, Manning WJ, Hauser R, Gervino EV, Evans WJ, Wei JY. Enhanced left ventricular diastolic filling associated with long-term endurance training. *J Gerontol*. (1992) 47:M56–8. doi: 10.1093/geronj/47.2.M56
12. Takemoto KA, Bernstein L, Lopez JF, Marshak D, Rahimtoola SH, Chandraratna PA. Abnormalities of diastolic filling of the left ventricle associated with aging are less pronounced in exercise-trained individuals. *Am Heart J*. (1992) 124:143–8. doi: 10.1016/0002-8703(92)90932-L
13. Borlaug BA, Nishimura RA, Sorajja P, Lam CS, Redfield MM. Exercise hemodynamics enhance diagnosis of early heart failure with preserved ejection fraction. *Circ Heart Fail*. (2010) 3:588–95. doi: 10.1161/CIRCHEARTFAILURE.109.930701
14. Tuttle JL, Nachreiner RD, Bhuller AS, Condict KW, Connors BA, Herring BP, et al. Shear level influences resistance artery remodeling: wall dimensions, cell density, and eNOS expression. *Am J Physiol Heart Circ Physiol*. (2001) 281:H1380–9. doi: 10.1152/ajpheart.2001.281.3.H1380
15. Moreau KL, Donato AJ, Seals DR, Dinenno FA, Blackett SD, Hoetzer GL, et al. Arterial intima-media thickness: site-specific associations with HRT

and habitual exercise. *Am J Physiol Heart Circ Physiol*. (2002) 283:H1409–17. doi: 10.1152/ajpheart.00035.2002
16. Mann S, Beedie C, Jimenez A. Differential effects of aerobic exercise, resistance training and combined exercise modalities on cholesterol and the lipid profile: review, synthesis and recommendations. *Sports Med*. (2014) 44:211–21. doi: 10.1007/s40279-013-0110-5
17. Hellsten Y, Nyberg M. Cardiovascular adaptations to exercise training. *Compr Physiol*. (2015) 6:1–32. doi: 10.1002/cphy.c140080
18. Garber CE, Blissmer B, Deschenes MR, Franklin BA, Lamonte MJ, Lee IM, et al. American College of Sports Medicine position stand. Quantity and quality of exercise for developing and maintaining cardiorespiratory, musculoskeletal, and neuromotor fitness in apparently healthy adults: guidance for prescribing exercise. *Med Sci Sports Exerc*. (2011) 43:1334–59. doi: 10.1249/MSS.0b013e318213fefb
19. Kraus WE, Torgan CE, Duscha BD, Norris J, Brown SA, Cobb FR, et al. Studies of a targeted risk reduction intervention through defined exercise (STRRIDE). *Med Sci Sports Exerc*. (2001) 33:1774–84. doi: 10.1097/00005768-200110000-00025
20. Bales CW, Hawk VH, Granville EO, Rose SB, Shields T, Bateman L, et al. Aerobic and resistance training effects on energy intake: the STRRIDE-AT/RT study. *Med Sci Sports Exerc*. (2012) 44:2033–9. doi: 10.1249/MSS.0b013e318259479a
21. Slentz CA, Bateman LA, Willis LH, Shields AT, Tanner CJ, Piner LW, et al. Effects of aerobic vs. resistance training on visceral and liver fat stores, liver enzymes, and insulin resistance by HOMA in overweight adults from STRRIDE AT/RT. *Am J Physiol Endocrinol Metab*. (2011) 301:E1033–9. doi: 10.1152/ajpendo.00291.2011
22. Willis LH, Slentz CA, Bateman LA, Shields AT, Piner LW, Bales CW, et al. Effects of aerobic and/or resistance training on body mass and fat mass in overweight or obese adults. *J Appl Physiol*. (2012) 113:1831–7. doi: 10.1152/japplphysiol.01370.2011
23. Tei C, Ling LH, Hodge DO, Bailey KR, Oh JK, Rodeheffer RJ, et al. New index of combined systolic and diastolic myocardial performance: a simple and reproducible measure of cardiac function–a study in normals and dilated cardiomyopathy. *J Cardiol*. (1995) 26:357–66.
24. Chen CH, Fetics B, Nevo E, Rochitte CE, Chiou KR, Ding PA, et al. Noninvasive single-beat determination of left ventricular end-systolic elastance in humans. *J Am Coll Cardiol*. (2001) 38:2028–34. doi: 10.1016/S0735-1097(01)01651-5
25. Welsch MA, Allen JD, Geaghan JP. Stability and reproducibility of brachial artery flow-mediated dilation. *Med Sci Sports Exerc*. (2002) 34:960–5. doi: 10.1097/00005768-200206000-00009
26. Santoro C, Sorrentino R, Esposito R, Lembo M, Capone V, Rozza F, et al. Cardiopulmonary exercise testing and echocardiographic exam: an useful interaction. *Cardiovasc Ultrasound*. (2019) 17:29. doi: 10.1186/s12947-019-0180-0
27. Kasikcioglu E, Oflaz H, Kasikcioglu HA, Kayserilioglu A, Umman S, Meric M. Endothelial flow-mediated dilatation and exercise capacity in highly trained endurance athletes. *Tohoku J Exp Med*. (2005) 205:45–51. doi: 10.1620/tjem.205.45
28. Moe IT, Hoven H, Hetland EV, Rognmo O, Slordahl SA. Endothelial function in highly endurance-trained and sedentary, healthy young women. *Vasc Med*. (2005) 10:97–102. doi: 10.1191/1358863x05vm592oa
29. Shaw BS, Shaw I. Compatibility of concurrent aerobic and resistance training on maximal aerobic capacity in sedentary males. *Cardiovasc J Afr*. (2009) 20:104–6.
30. Daussin FN, Zoll J, Dufour SP, Ponsot E, Lonsdorfer-Wolf E, Doutreleau S, et al. Effect of interval versus continuous training on cardiorespiratory and mitochondrial functions: relationship to aerobic performance improvements in sedentary subjects. *Am J Physiol Regul Integr Comp Physiol*. (2008) 295:R264–72. doi: 10.1152/ajpregu.00875.2007
31. Roma MF, Busse AL, Betoni RA, Melo AC, Kong J, Santarem JM, et al. Effects of resistance training and aerobic exercise in elderly people concerning physical fitness and ability: a prospective clinical trial. *Einstein (Sao Paulo, Brazil)*. (2013) 11:153–7. doi: 10.1590/S1679-45082013000200003
32. Lash JM, Bohlen HG. Functional adaptations of rat skeletal muscle arterioles to aerobic exercise training. *J Appl Physiol (Bethesda, Md: 1985)*. (1992) 72:2052–62. doi: 10.1152/jappl.1992.72.6.2052
33. Laughlin MH. Endothelium-mediated control of coronary vascular tone after chronic exercise training. *Med Sci Sports Exerc*. (1995) 27:1135–44. doi: 10.1249/00005768-199508000-00006

Conflict of Interest: The authors declare that the research was conducted in the absence of any commercial or financial relationships that could be construed as a potential conflict of interest.

frontiers in Cardiovascular Medicine

ORIGINAL RESEARCH
published: 07 May 2021
doi: 10.3389/fcvm.2021.644500

Cardiac Magnetic Resonance Imaging Right Ventricular Longitudinal Strain Predicts Mortality in Patients Undergoing TAVI

Johannes Schmid[1], Claus Kamml[2], David Zweiker[2,3], Dominik Hatz[2], Albrecht Schmidt[2], Ursula Reiter[1], Gabor G. Toth[2], Michael Fuchsjäger[1], Andreas Zirlik[2], Josepha S. Binder[2] and Peter P. Rainer[2,4]**

[1] Division of General Radiology, Department of Radiology, Medical University of Graz, Graz, Austria, [2] Division of Cardiology, Department of Internal Medicine, Medical University of Graz, Graz, Austria, [3] Third Medical Department of Cardiology and Intensive Care, Wilhelminenhospital, Vienna, Austria, [4] BioTechMed Graz, Graz, Austria

OPEN ACCESS

Edited by:
Jolanda Wentzel,
Erasmus Medical Center, Netherlands

Reviewed by:
Richard Nethononda,
Chris Hani Baragwanath Hospital, South Africa
Jennifer Erley,
Deutsches Herzzentrum Berlin, Germany

***Correspondence:**
Johannes Schmid
johannes.schmid@medunigraz.at
Peter P. Rainer
peter.rainer@medunigraz.at

Specialty section:
This article was submitted to Cardiovascular Imaging, a section of the journal Frontiers in Cardiovascular Medicine

Received: 21 December 2020
Accepted: 19 March 2021
Published: 07 May 2021

Citation:
Schmid J, Kamml C, Zweiker D, Hatz D, Schmidt A, Reiter U, Toth GG, Fuchsjäger M, Zirlik A, Binder JS and Rainer PP (2021) Cardiac Magnetic Resonance Imaging Right Ventricular Longitudinal Strain Predicts Mortality in Patients Undergoing TAVI. Front. Cardiovasc. Med. 8:644500. doi: 10.3389/fcvm.2021.644500

Background: Right ventricular (RV) function predicts survival in numerous cardiac conditions, including left heart disease. The reference standard for non-invasive assessment of RV function is cardiac magnetic resonance imaging (CMR). The aim of this study was to investigate the association between pre-procedural CMR-derived RV functional parameters and mortality in patients undergoing transcatheter aortic valve implantation (TAVI).

Methods: Patients scheduled for TAVI were recruited to undergo pre-procedural CMR. Volumetric function and global longitudinal and circumferential strain (GLS and GCS) of the RV and left ventricle (LV) were measured. The association with the primary endpoint (1-year all-cause mortality) was analyzed with Cox regression.

Results: Of 133 patients undergoing CMR, 113 patients were included in the analysis. Mean age was 81.8 ± 5.8 years, and 65% were female. Median follow-up was 3.9 [IQR 2.3–4.7] years. All-cause and cardiovascular mortality was 14 and 12% at 1 year, and 28 and 20% at 3 years, respectively. One-year all-cause mortality was significantly predicted by RV GLS [HR = 1.109 (95% CI: 1.023–1.203); $p = 0.012$], RV ejection fraction [HR = 0.956 (95% CI: 0.929–0.985); $p = 0.003$], RV end-diastolic volume index [HR = 1.009 (95% CI: 1.001–1.018); $p = 0.025$], and RV end-systolic volume index [HR = 1.010 (95% CI: 1.003–1.017); $p = 0.005$]. In receiver operating characteristic (ROC) analysis for 1-year all-cause mortality, the area under the curve was 0.705 (RV GLS) and 0.673 (RV EF). Associations decreased in strength at longer follow-up. None of the LV parameters was associated with mortality.

Conclusions: RV function predicts intermediate-term mortality in TAVI patients while LV parameters were not associated with outcomes. Inclusion of easily obtainable RV GLS may improve future risk scores.

Keywords: transcatheter aortic valve implantation, aortic valve stenosis, magnetic resonance imaging, MRI, right ventricular function, strain, survival analysis, mortality

INTRODUCTION

Transcatheter aortic valve implantation (TAVI) is a minimally invasive treatment for patients suffering from severe aortic stenosis and is now available for more than a decade. Since then, procedure numbers are steadily increasing and are expected to rise further (1). While initially reserved for patients with a high-risk profile for surgical valve replacement, indications have been extended to intermediate-risk patients and trials already showed promising intermediate-term results in low-risk groups (2, 3). Predicting the outcome of patients undergoing TAVI is challenging as the commonly applied clinical risk scores perform only moderately (4, 5). Thus, adequate surrogate markers to improve outcome prediction are needed.

Until recently, the right ventricle (RV) has not received much attention in this respect. However, emerging evidence shows that the RV plays a key role in many cardiac conditions, including primary left heart disease (6). A prognostic value of RV function has not only been demonstrated in pulmonary hypertension (7) but also in heart failure with preserved and reduced ejection fraction (EF) (8, 9), dilated cardiomyopathy (10), or myocardial infarction (11). Echocardiographic studies indicate that RV dysfunction is frequent in patients with severe aortic stenosis and is associated with mortality (12–15).

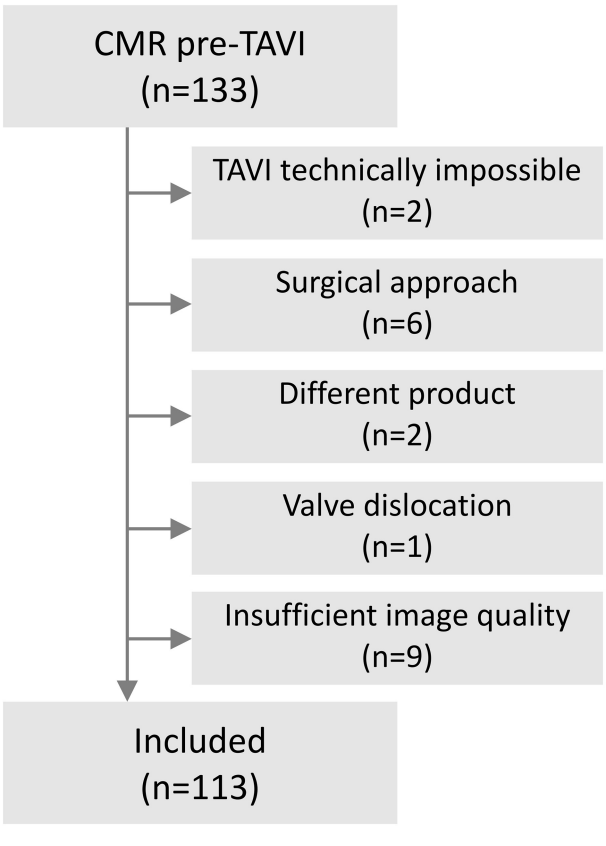

FIGURE 1 | Flow chart of included patients.

Due to the complex shape of the RV, standard echocardiography relies on tricuspid annular systolic excursion, fractional area change, or more recently strain as surrogates for RV function. Unlike echocardiography, cardiac magnetic resonance imaging (CMR) not only is capable of myocardial tissue characterization but also allows for more accurate measurement of cardiac chamber volumes. Measures of myocardial deformation derived from CMR feature tracking predict cardiovascular events (16). CMR is therefore regarded the reference standard for non-invasive assessment of RV volumes and function (17).

This study aims to elucidate the association between pre-procedural RV functional parameters derived from CMR and mortality in patients undergoing TAVI.

MATERIALS AND METHODS

In this single-center cohort study, patients with severe aortic stenosis scheduled for TAVI at the Division of Cardiology, Medical University of Graz were prospectively recruited to undergo pre-procedural CMR between May 2011 and March 2015, in the absence of CMR contraindications (incompatible metal implants such as pacemakers, severely reduced kidney function, claustrophobia). Patients who underwent a successful transfemoral TAVI procedure with a CoreValve (Medtronic) prosthesis were included in the study. Cases with a CMR image quality insufficient to allow reliable analysis were excluded.

The primary endpoint was all-cause mortality (18) at 1 year, which corresponds to the recommended minimum life expectancy for patients eligible for TAVI (19). Additionally, cardiovascular mortality was defined according to VARC-2 criteria (20) and served as a secondary endpoint. After a follow-up of at least 3 years, mortality data were gathered via review of medical records, via phone contact, or by request at the national death register. All patients gave written informed consent. The study was approved by the ethics committee of the Medical University of Graz (No. 25-437ex12/13) and complies with the Declaration of Helsinki.

Cardiac Magnetic Resonance Imaging

CMR was performed on a 1.5-Tesla scanner (Magnetom Sonata, Siemens Healthcare). Steady-state free precession cine sequences with retrospective electrocardiographic gating were acquired during free breathing in two-, three-, and four-chamber views and a stack of gapless slices in short-axis view to cover the entire left and right ventricle. Typical protocol parameters were: echo time 1.2 ms; measured temporal resolution 37–51 ms reconstructed to 30 phases; resolution $1.4 \times 1.7–2.0 \times 6$ mm^3 for long axes and $1.4 \times 2.2 \times 8$ mm^3 for short-axis views. To compensate for breathing artifacts, threefold averaging was used. Using dedicated software (cvi42, Version 5.6.5, Circle Cardiovascular Imaging), right and left ventricular (LV) end-diastolic and end-systolic volumes (EDV, ESV) were determined from a short-axis stack according to recommendations (21) and indexed to body surface area. Papillary muscles were included in the volumes. Global longitudinal and circumferential strains (GLS and GCS) were measured in both ventricles by means

TABLE 1 | Baseline characteristics according to 1-year mortality.

	All patients ($n = 113$)	Survived 1st year ($n = 97$)	Died in 1st year ($n = 16$)	p-value
Age, years	81.8 ± 5.8	81.4 ± 5.9	84.2 ± 5.0	0.071
Female sex	65% (73)	64.9% (63)	62.5% (10)	0.529
Body mass index	26.0 ± 4.8	26.3 ± 4.3	24.3 ± 6.9	0.280
CAD	78% (88)	75% (73)	94% (15)	0.117
CABG or PCI	38% (43)	38% (37)	38% (6)	0.961
PAD	27% (31)	25% (24)	44% (7)	0.114
Diabetes	26% (29)	25% (24)	31% (5)	0.552
Hypertension	83% (94)	84% (81)	81% (13)	0.731
Atrial fibrillation	41% (46)	38% (37)	56% (9)	0.172
NT-proBNP, ng/L	1,722 [654–3,515]	1,583 [624–3,515]	2,701 [2,152–3,871]	0.025*
Troponin T, ng/L	22 [12–38]	21 [12–38]	25 [16–65]	0.218
eGFR, ml/min/1.73 m^2	56.4 ± 16.9	57.1 ± 17.6	52.2 ± 11.0	0.280
AVA, cm^2	0.67 ± 0.17	0.67 ± 0.16	0.68 ± 0.19	0.832
STS score (%)	3.30 [2.55–5.33]	3.14 [2.48–5.18]	5.15 [3.83–6.65]	0.002*
EUROscore II (%)	4.77 [3.11–8.05]	4.77 [3.05–7.52]	5.94 [4.27–10.54]	0.096
mPAP, mmHg	29.4 ± 11.2	29.6 ± 11.7	28.5 ± 7.9	0.747
mPAP >25 mmHg	56.0% (51/91)	54.5% (42/77)	64.3% (9/14)	0.354
PCWP, mmHg	18.0 ± 8.3	18.1 ± 8.5	17.1 ± 7.4	0.679
CMR parameters				
RV-EF, %	54.7 ± 12.8	56.2 ± 11.1	45.5 ± 18.4	0.007*
RV-EDV, ml	131.5 [107.3–161.1]	131.5 [105.3–159.7]	134.0 [113.4–171.3]	0.168
RV-EDV index, ml/m^2	74.6 [63.3–92.5]	73.0 [62.0–91.8]	80.3 [65.8–97.6]	0.042*
RV-ESV, ml	59.6 [43.0–72.8]	55.7 [42.5–71.44]	67.2 [46.8–106.6]	0.023*
RV-ESV index, ml/m^2	33.2 [24.5–42.3]	32.1 [23.8–40.5]	40.1 [28.7–62.4]	0.059
RV-GLS, %	−21.3 ± 5.8	−21.9 ± 5.6	−17.7 ± 5.8	0.007*
RV-GCS, %	−13.5 ± 3.6	13.7 ± 3.5	−12.3 ± 4.5	0.158
LV-EF, %	52.5 ± 13.0	53.0 ± 11.9	49.5 ± 18.3	0.588
LV-EDV, ml	154.2 [117.1–198.3]	155.2 [118.6–198.1]	146.2 [114.8–214.8]	0.827
LV-EDV index, ml/m^2	88.7 [70.6–107.8]	90.0 [69.9–105.22]	81.1 [73.4–123.6]	0.446
LV-ESV, ml	69.7 [45.3–101.1]	69.8 [45.3–100.4]	60.1 [44.7–131.1]	0.726
LV-ESV index, ml/m^2	39.6 [27.4–54.1]	39.6 [27.4–54.0]	35.6 [28.2–71.7]	0.441
LV-GLS, %	−13.2 ± 3.9	−13.4 ± 3.8	−12.1 ± 4.8	0.227
LV-GCS, %	−17.2 ± 4.8	−17.4 ± 4.4	−16.2 ± 6.5	0.361
LV-GRS, %	30.3 ± 11.5	28.4 ± 15.1	30.0 ± 12.0	0.566
LV mass index, g/m^2	76.5 ± 18.2	76.8 ± 18.1	74.7 ± 19.3	0.675

Values are mean ± standard deviation, median [interquartile range] or percentage (absolute numbers).

CAD, coronary artery disease; CABG, coronary artery bypass graft; PCI, percutaneous coronary intervention; PAD, peripheral artery disease; NT-proBNP, N-terminal pro-brain natriuretic peptide; eGFR, estimated glomerular filtration rate; AVA, aortic valve area (from echocardiography); mPAP, mean pulmonary artery pressure; PCWP, pulmonary capillary wedge pressure; RV, right ventricle; LV, left ventricle; EF, ejection fraction; EDV, end-diastolic volume; ESV, end-systolic volume; GLS, global longitudinal strain; GCS, global circumferential strain; GRS, global radial strain; mPAP and PCWP from right heart catheterization (n = 91).

*p-values from Student's t-test or Fisher's exact test; variables transformed (logarithm or square root) if necessary. *$p < 0.05$.*

of feature tracking using the 2D model. RV free wall GLS and LV GLS were measured from a four-chamber slice. For GCS, the most basal and apical slices were rejected if tracking was inappropriate (assessed visually).

Statistics

Statistical analysis was performed using SPSS Statistics 25.0.0.1 (IBM). Parameters are presented as mean ± standard deviation, median [interquartile range] or percentage (absolute numbers). The primary endpoint was 1-year all-cause mortality; associations with mortality were analyzed in uni- and multivariate Cox regression models. To ensure acceptable proportional hazards in Cox regression, follow-up was truncated at 1 year. For Kaplan–Meier plots, variables were dichotomized at their median. Receiver operating characteristic (ROC) analysis was performed for 1-year all-cause mortality. Area under the curve was compared with the DeLong method using the package pROC in R 3.5.1 (The R Foundation for Statistical Computing). A p value of <0.05 was considered statistically significant.

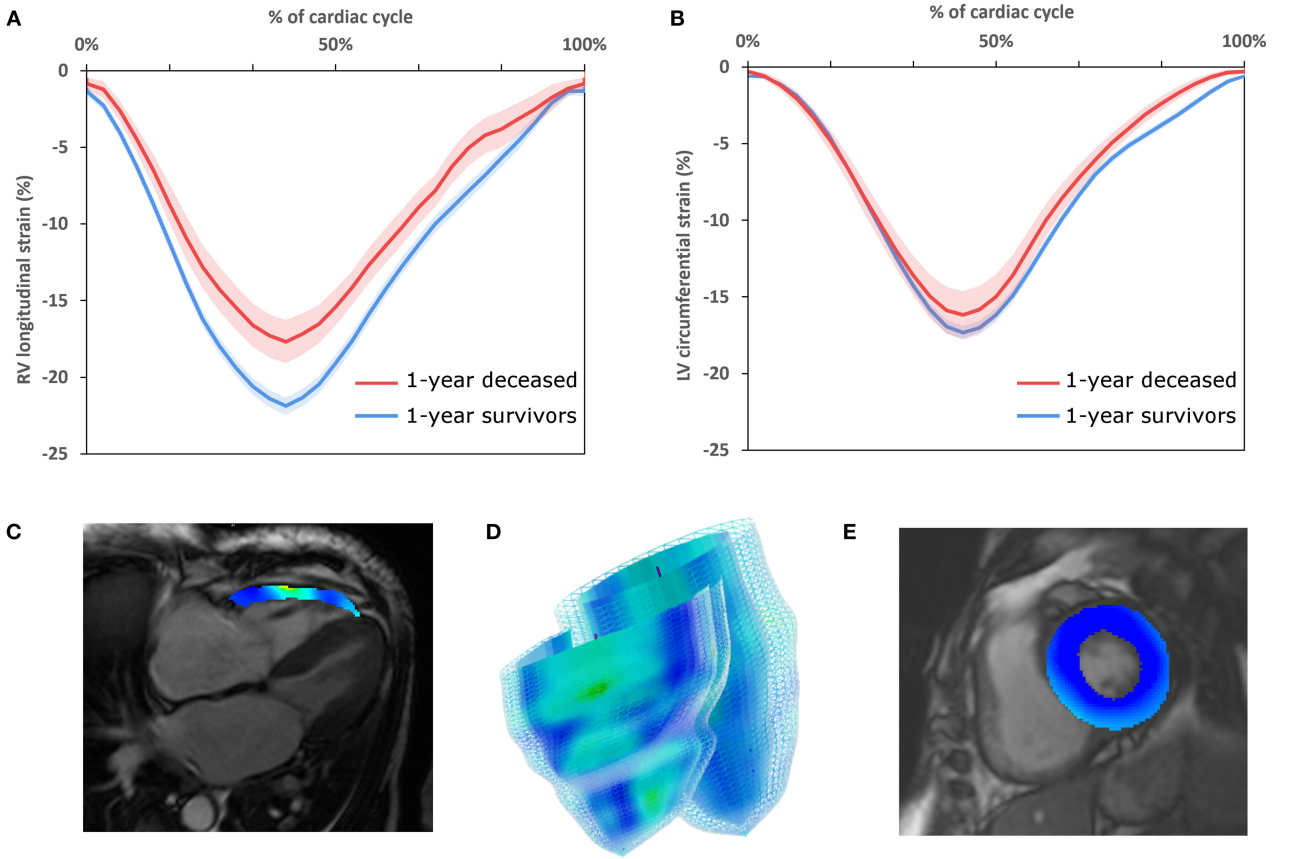

FIGURE 2 | Mean global strain curves of the cohort grouped by 1-year mortality. Individual global strain curves of the entire cohort are aligned at peak systolic strain and averaged in groups according to 1-year mortality. Mean and standard error of the mean are displayed for right ventricular longitudinal strain **(A)** and left ventricular circumferential strain **(B)**. Exemplary cardiac magnetic resonance images in end-systole with color-coded strain overlay **(C, E)** and a 3D model **(D)** are displayed.

RESULTS

Study Population

During the study period, a total of 296 patients underwent TAVI at our institution; of those, 133 patients had pre-procedural CMR (at a median of 2 [1–4] days before the procedure). Exclusion criteria were met by 20 patients, leaving 113 patients qualifying for analysis (**Figure 1**). The cohort comprised elderly patients with a mean age of 81.8 ± 5.8 years and a slight female predominance of 65%. Most of the patients suffered from high gradient severe aortic stenosis (81%); for the detailed distribution of types of aortic stenosis, see **Supplementary Figure 1** (19). The majority (80%) of the cohort underwent pre-procedural right heart catheterization. More than half (56%) of the patients suffered from pulmonary hypertension, defined as mPAP >25 mmHg, and even 74% if applying the recent 20 mm Hg definition (22) (details in **Supplementary Figure 2**). RV enlargement (elevated EDV index) was found in 8.8% (n = 10) and an enlarged LV in 32.7% (n = 37) (23). RV and LV EF was <50% in 28.3% (n = 32) and 32.7% (n = 37), respectively. Detailed baseline characteristics are presented in **Table 1**.

Survival Analysis

Patients were followed up for a median of 3.9 [2.3–4.7] years. Three-year follow-up was completed by all survivors. All-cause mortality was 14% (n = 16) and 28% (n = 32), and cardiovascular mortality was 12% (n = 13) and 20% (n = 23) at 1 and 3 years, respectively. Significant differences in RV EF, RV GLS, RV ESV, and RV EDV index were found between those who survived after 1 year and those who did not (**Table 1**, **Figure 2**). We also observed higher N-terminal pro-brain natriuretic peptide values in patients who did not survive 1 year. LV imaging parameters, however, did not differ between survivors and non-survivors. There was no significant difference in mortality between male and female patients.

Kaplan–Meier analyses revealed the impact of RV parameters on mortality especially during the first years of follow-up. This association was partially attenuated at extended follow-up

TABLE 2 | Univariate Cox regression of right and left ventricular parameters for 1-year all-cause mortality.

	HR (95% CI)	*p*-value
Right ventricle		
RV GLS (%)	1.109 (1.023–1.203)	0.012*
RV GCS (%)	1.099 (0.960–1.259)	0.169
RV EF (%)	0.956 (0.929–0.985)	0.003*
RV EDVi (ml/m^2)	1.009 (1.001–1.018)	0.025*
RV ESVi (ml/m^2)	1.010 (1.003–1.017)	0.005*
Left ventricle		
LV GLS (%)	1.073 (0.952–1.210)	0.245
LV GCS (%)	1.041 (0.942–1.150)	0.430
LV EF (%)	0.984 (0.950–1.020)	0.378
LV EDVi (ml/m^2)	1.008 (0.991–1.026)	0.365
LV ESVi (ml/m^2)	1.012 (0.996–1.028)	0.149
LV mass index (g/m^2)	0.993 (0.967–1.021)	0.633
Right heart catheterization ($n = 91$)		
mPAP > 25 mmHg	1.40 (0.47–4.18)	0.547
Right ventricular–pulmonary artery coupling ($n = 91$)		
RV GLS/mPAP	1.26 (0.44–3.64)	0.666

*EF, ejection fraction; GLS, global longitudinal strain; GCS, global circumferential strain; EDVi, end-diastolic volume index; ESVi, end-systolic volume index; mPAP, mean pulmonary artery pressure. *p < 0.05.*

(**Supplementary Figure 4**). To account for the non-proportional behavior of survival curves at long-term follow-up and better reflect intermediate-term outcomes, follow-up was truncated at 1 year for Cox regression analyses. Results from univariate Cox regressions of RV and LV parameters are given in **Table 2** and illustrated by Kaplan–Meier plots in **Figure 3**. RV GLS, RV EF, and RV volumes were significantly associated with 1-year all-cause mortality. In contrast to RV function, the corresponding LV parameters did not significantly predict mortality in the cohort.

We additionally performed several multivariate Cox regression models with RV GLS or RV EF adjusted for the relevant covariates STS score and NT-proBNP (**Table 3**). RV GLS and RV EF remained significant predictors of 1-year all-cause mortality independent of STS score; however, in models containing NT-proBNP, RV parameters did not reach significance.

On analysis of the secondary endpoints (**Supplementary Table 2**), RV EF and RV volumes significantly predicted 1-year and 3-year cardiovascular mortality as well as 3-year all-cause mortality, while RV GLS (though significant for 1-year cardiovascular mortality) just missed the significance level for 3-year all-cause and cardiovascular mortality ($p = 0.053$ and $p = 0.087$).

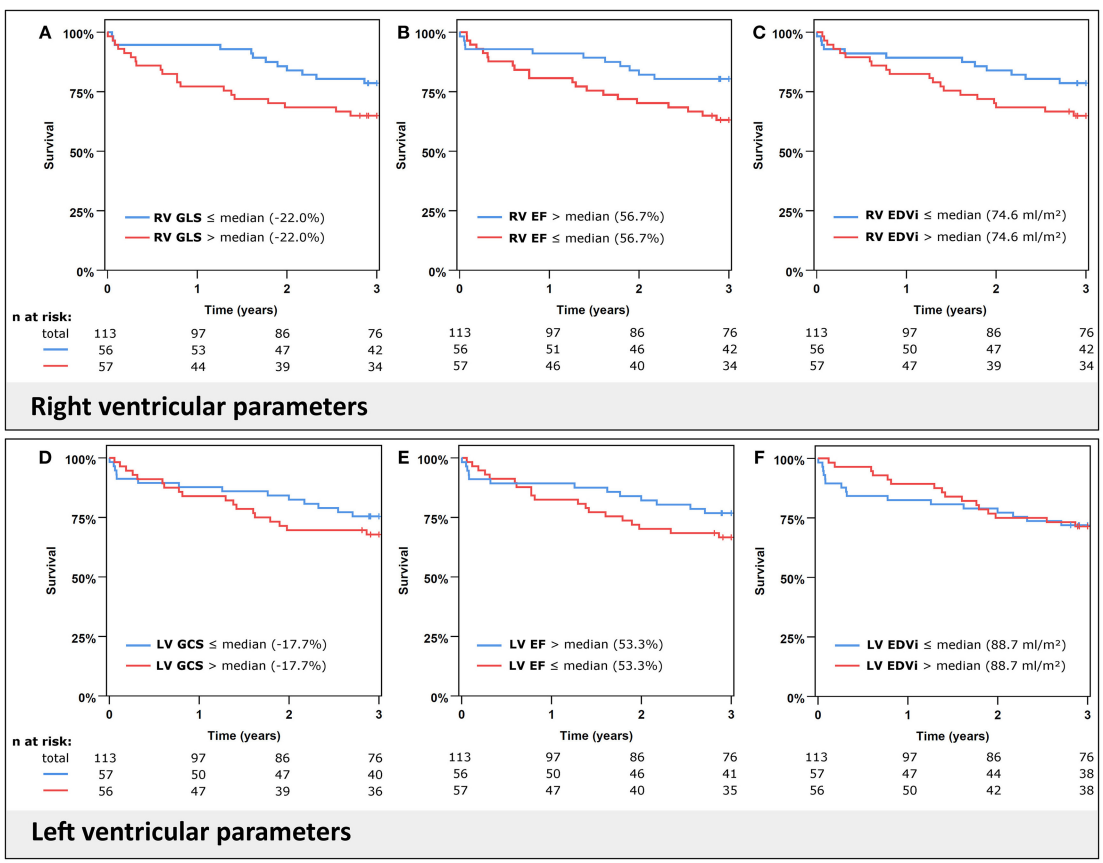

FIGURE 3 | Kaplan–Meier plots for all-cause mortality. Cumulative survival according to right ventricular (RV) global longitudinal strain (GLS) **(A)**, ejection fraction (EF) **(B)**, end-diastolic volume index (EDVi) **(C)** in the upper panels and left ventricular (LV) global circumferential strain (GCS) **(D)**, EF **(E)**, and EDVi **(F)** in the lower panels. Variables are stratified by their median.

We also assessed RV to pulmonary artery coupling using the ratio of RV GLS/invasive mean pulmonary artery pressure (mPAP), which was not significantly associated with mortality (**Table 2**). Interestingly, a modifying effect of elevated mPAP on RV GLS mortality prediction became apparent after 1 year of follow-up (**Supplementary Figure 5**). The survival curve of patients in the group with better (more negative) RV GLS but with elevated mPAP initially almost paralleled the curve of low mPAP patients during the first year, but then showed markedly increased mortality and aligned with the less negative RV GLS group.

Additional ROC analyses for 1-year all-cause mortality (**Figure 4**) illustrate a better diagnostic accuracy (area under the curve) of RV GLS and RV EF when compared to left ventricular parameters (RV GLS vs. LV GCS: $\Delta AUC = 0.167$, $p = 0.003$; RV EF vs. LV EF: $\Delta AUC = 0.145$, $p = 0.035$). The difference in the area under the curve was not significant for comparisons of RV GLS with RV EF ($\Delta AUC = 0.032$, $p = 0.663$), STS score ($\Delta AUC = -0.015$, $p = 0.860$), or NT-proBNP ($\Delta AUC = 0.044$, $p = 0.522$).

TABLE 3 | RV GLS in multivariate Cox regressions for 1-year all-cause mortality.

	HR (95% CI)	*p*-value
Model 1		
RV GLS (%)	1.094 (1.006–1.189)	0.035*
STS score (%)	1.164 (1.046–1.296)	0.005*
Model 2		
RV GLS (%)	1.076 (0.977–1.186)	0.136
NT-proBNP (log, ng/L)	1.911 (0.549–6.647)	0.309
Model 3		
RV EF (%)	0.960 (0.931–0.990)	0.010*
STS score (%)	1.170 (1.048–1.305)	0.005*
Model 4		
RV EF (%)	0.966 (0.929–1.003)	0.074
NT-proBNP (log, ng/L)	1.604 (0.453–5.675)	0.464

*RV, right ventricle; GLS, global longitudinal strain; EF, ejection fraction. *p < 0.05.*

DISCUSSION

Our data illustrate that RV functional parameters, especially RV GLS and RV EF, associate with intermediate-term outcomes in patients undergoing TAVI. Intriguingly, this association was much stronger than in corresponding LV parameters, which did not predict outcomes in our cohort.

When assessing the RV, the main advantage of CMR is its unique ability to accurately measure volumes, a task that is not easily achieved by echocardiography. Our study shows that both volumetric parameters (such as EF and EDV), as well as measures of RV myocardial contraction (RV GLS), predict mortality after TAVI. These associations were independent from multiparametric clinical risk scores. In contrast to the LV, longitudinal contraction pre-dominates RV function. Thus, GLS reflects RV function better than GCS, which was not associated with outcomes. Compared to volumetric parameters, RV GLS is easy to measure and, importantly, it can also be assessed by widely available echocardiography if acoustic windows permit. In line with our results, RV function assessed by echocardiography is also associated with mortality in patients with severe aortic stenosis (12, 24) and in patients undergoing TAVI (14, 25). Our study confirms these findings in prospectively enrolled patients using CMR as a reference standard.

Importantly, LV function, which is usually central in clinical assessment, did not predict mortality in our cohort. Consistent with our findings, other studies showed that LV EF predicted outcomes only in the subgroup of low gradient aortic stenosis (26, 27). In another large cohort study LV EF did predict 3-year mortality, but only in univariate analysis (28). One aspect that may contribute to the weak predictive power of LV function may be the differential response of the left ventricle with either

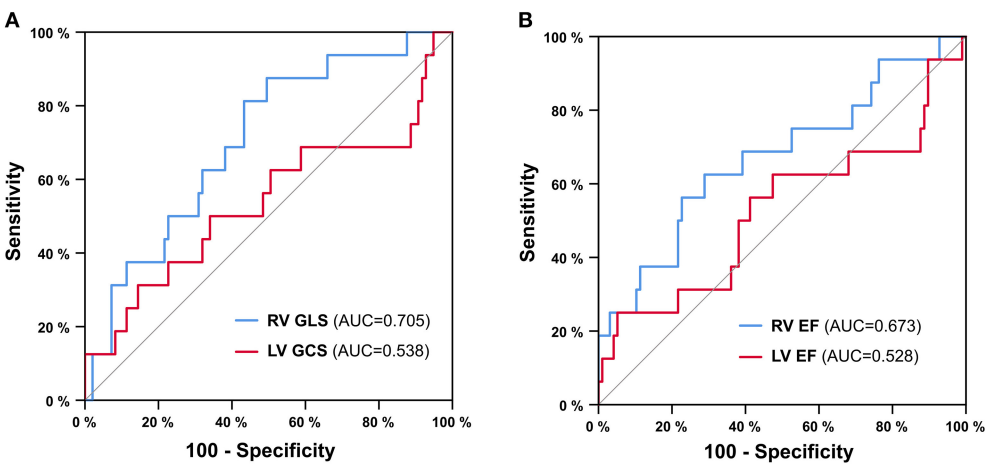

FIGURE 4 | ROC analysis for 1-year all-cause mortality. Right ventricular global longitudinal strain (RV GLS) vs. left ventricular global circumferential strain (LV GCS) **(A)** and right ventricular ejection fraction (RV EF) vs. left ventricular ejection fraction (LV EF) **(B)**. AUC = area under the curve.

concentric or eccentric remodeling or hypertrophy. Concentric geometry causes a reduction of ESV and thus tends to increase EF, which is based on the ratio of (EDV-ESV)/EDV. This mechanism may explain the complex and apparently non-linear association between LV function and survival with a reduced early survival of patients in the highest LV EF quartile observed in our cohort, as concentric phenotypes are associated with worse outcomes (29). Similarly, LV GCS or GLS is affected by different types of remodeling that may result in a more complex relationship with outcomes. Previous studies on the predictive ability of LV strains in TAVI patients yielded mixed results (30, 31). Though a high proportion of patients had increased LV mass index, this parameter was not significantly associated with 1-year mortality, similar to results of other large contemporary cohorts undergoing TAVI (32).

When assessing the prognostic value of pulmonary hypertension, we found that the mortality prediction of mPAP became only evident at longer follow-up. To further investigate the interdependency with the pulmonary vasculature, we related RV function assessed by CMR RV GLS to RV afterload using invasively measured mPAP and thereby assessed RV to pulmonary artery coupling. This approach was similarly applied before in other collectives but with estimating rather than directly measuring pulmonary artery pressures and relying on echocardiographic TAPSE (33, 34). Patients in the best (most negative) quartile of the coupling variable (RV GLS/mPAP) had markedly better survival (not shown). In patients with preserved RV GLS, those with pulmonary hypertension (mPAP >25 mmHg) initially had similar survival to those without, but, after 1-year survival, dropped to align with patients with reduced RV GLS. These data suggest that prognosis is worst if RV contractility impairment is already present at baseline with a delayed effect of pulmonary hypertension that precedes manifest RV GLS reduction. Patients with both preserved RV GLS and absent pulmonary hypertension had an excellent prognosis and 3-year survival reached 92%.

When analyzing the survival curves of the full available follow-up, long-term follow-up for more than 3 to 4 years increasingly attenuated survival prediction. This observation is likely explained by the age distribution of TAVI patients where non-procedure-related mortality is high and dominates after a few years.

Strengths and Limitations

This is the first study to comprehensively analyze the RV with gold standard CMR in patients undergoing TAVI including long-term follow-up and invasive hemodynamic assessment. This was accomplished in a reasonably sized cohort, although larger numbers might have allowed more extensive analyses with higher power for the detection of weaker associations. Our cohort reflects a typical TAVI cohort and mostly consisted of patients with high gradient aortic stenosis; thus, findings may be different in patients suffering from low gradient aortic stenosis where LV function may discriminate outcome better. The use of CMR (excluding patients with pacemakers and severely reduced kidney function) and the non-consecutive nature of our cohort may induce a certain selection bias in the study cohort.

Conclusion and Outlook

RV function predicts intermediate-term mortality after TAVI while LV-derived parameters do not. In particular, RV GLS is a promising parameter to stratify outcomes after TAVI, as the echocardiographic equivalent measures of longitudinal contraction (GLS and TAPSE) can be easily obtained and included in future prospectively validated clinical risk scores, which may help to improve patient selection.

DATA AVAILABILITY STATEMENT

The raw data supporting the conclusions of this article will be made available by the authors on request, without undue reservation.

ETHICS STATEMENT

The study involving human participants was reviewed and approved by the Ethics committee of the Medical University of Graz, Graz, Austria. The patients provided their written informed consent to participate in this study.

AUTHOR CONTRIBUTIONS

JS and PR conceptualized and designed the study. JS organized and collected data, performed statistical analyses and drafted the manuscript. CK analyzed cardiac magnetic resonance images. DZ and DH collected clinical and outcome data. UR acquired cardiac magnetic resonance images and wrote sections of the manuscript. JB recruited patients. PR, DZ, UR, GT, JB, AZ, MF, and AS revised the manuscript critically for important intellectual content. JS, JB, and PR supervised the study. All authors read and approved the submitted version.

ACKNOWLEDGMENTS

We would like to acknowledge all our colleagues that are involved in the clinical care of TAVI patients at our center.

SUPPLEMENTARY MATERIAL

The Supplementary Material for this article can be found online at: https://www.frontiersin.org/articles/10.3389/fcvm.2021.644500/full#supplementary-material

REFERENCES

1. Durko AP, Osnabrugge RL, Van Mieghem NM, Milojevic M, Mylotte D, Nkomo VT, et al. Annual number of candidates for transcatheter aortic valve implantation per country: current estimates and future projections. *Eur Heart J*. (2018) 39:2635–42. doi: 10.1093/eurheartj/ehy107
2. Mack MJ, Leon MB, Thourani VH, Makkar R, Kodali SK, Russo M, et al. Transcatheter aortic-valve replacement with a balloon-expandable valve in low-risk patients. *N Engl J Med.* (2019) 380:1695–705. doi: 10.1056/NEJMoa1814052
3. Popma JJ, Deeb GM, Yakubov SJ, Mumtaz M, Gada H, O'Hair D, et al. Transcatheter aortic-valve replacement with a self-expanding valve in low-risk patients. *N Engl J Med*. (2019) 380:1706–15. doi: 10.1056/NEJMoa1816885
4. Martin GP, Sperrin M, Ludman PF, de Belder MA, Gale CP, Toff WD, et al. Inadequacy of existing clinical prediction models for predicting mortality after transcatheter aortic valve implantation. *Am Heart J.* (2017)184:97–105. doi: 10.1016/j.ahj.2016.10.020
5. Wessler BS, Lundquist CM, Koethe B, Park JG, Brown K, Williamson T, et al. Clinical prediction models for valvular heart disease. *J Am Heart Assoc*. (2019) 8:e011972. doi: 10.1161/JAHA.119.011972
6. Amsallem M, Mercier O, Kobayashi Y, Moneghetti K, Haddad F. Forgotten no more: a focused update on the right ventricle in cardiovascular disease. *JACC Heart Fail*. (2018) 6:891–903. doi: 10.1016/j.jchf.2018.05.022
7. Swift AJ, Capener D, Johns C, Hamilton N, Rothman A, Elliot C, et al. Magnetic resonance imaging in the prognostic evaluation of patients with pulmonary arterial hypertension. *Am J Respir Crit Care Med*. (2017) 196:228–39. doi: 10.1164/rccm.201611-2365OC
8. Gorter TM, Hoendermis ES, van Veldhuisen DJ, Voors AA, Lam CSP, Geelhoed B, et al. Right ventricular dysfunction in heart failure with preserved ejection fraction: a systematic review and meta-analysis. *Eur J Heart Fail*. (2016) 18:1472–87. doi: 10.1002/ejhf.630
9. Meluzin J, Spinarová L, Hude P, Krejcí J, Dusek L, Vítovec J, et al. Combined right ventricular systolic and diastolic dysfunction represents a strong determinant of poor prognosis in patients with symptomatic heart failure. *Int J Cardiol.* (2005) 105:164–73. doi: 10.1016/j.ijcard.2004.12.031
10. Gulati A, Ismail TF, Jabbour A, Alpendurada F, Guha K, Ismail NA, et al. The prevalence and prognostic significance of right ventricular systolic dysfunction in nonischemic dilated cardiomyopathy. *Circulation.* (2013) 128:1623–33. doi: 10.1161/CIRCULATIONAHA.113.002518
11. Keskin M, Uzun AO, Hayiroglu MI, Kaya A, Çinar T, Kozan Ö. The association of right ventricular dysfunction with in-hospital and 1-year outcomes in anterior myocardial infarction. *Int J Cardiovasc Imaging.* (2019) 35:77–85. doi: 10.1007/s10554-018-1438-6
12. Dahou A, Clavel M-A, Capoulade R, Bartko PE, Magne J, Mundigler G, et al. Right ventricular longitudinal strain for risk stratification in low-flow, low-gradient aortic stenosis with low ejection fraction. *Heart*. (2016) 102:548–54. doi: 10.1136/heartjnl-2015-308309
13. Ren B, Spitzer E, Geleijnse ML, Zijlstra F, de Jaegere PPT, Van Mieghem NM, et al. Right ventricular systolic function in patients undergoing transcatheter aortic valve implantation: a systematic review and meta-analysis. *Int J Cardiol.* (2018) 257:40–5. doi: 10.1016/j.ijcard.2018.01.117
14. Asami M, Stortecky S, Praz F, Lanz J, Räber L, Franzone A, et al. Prognostic value of right ventricular dysfunction on clinical outcomes after transcatheter aortic valve replacement. *J Am Coll Cardiol Imaging*. (2019)12:577–87. doi: 10.1016/j.jcmg.2017.12.015
15. Pardo Sanz A, Santoro C, Hinojar R, Salido L, Rajjoub E-A, Monteagudo JM, et al. Right ventricle assessment in patients with severe aortic stenosis undergoing transcatheter aortic valve implantation. *Echocardiography*. (2020) 37:586–91. doi: 10.1111/echo.14633
16. Yang LT, Yamashita E, Nagata Y, Kado Y, Oshima S, Otsuji Y, et al. Prognostic value of biventricular mechanical parameters assessed using cardiac magnetic resonance feature-tracking analysis to predict future cardiac events: CMR Feature Tracking and Prognosis. *J Magn Reson Imaging*. (2017) 45:1034–45. doi: 10.1002/jmri.25433
17. Vasquez M, Nagel E. Clinical indications for cardiovascular magnetic resonance. *Heart Br Card Soc*. (2019) 105:1755–62. doi: 10.1136/heartjnl-2018-312971
18. Leon MB, Piazza N, Nikolsky E, Blackstone EH, Cutlip DE, Kappetein AP, et al. Standardized endpoint definitions for transcatheter aortic valve implantation clinical trials: a consensus report from the Valve Academic Research Consortium. *Eur Heart J.* (2011) 32:205–17. doi: 10.1093/eurheartj/ehq406
19. Baumgartner H, Falk V, Bax JJ, De Bonis M, Hamm C, Holm PJ, et al. 2017 ESC/EACTS Guidelines for the management of valvular heart disease. *Eur Heart J*. (2017) 38:2739–91. doi: 10.1093/eurheartj/ehx391
20. Kappetein AP, Head SJ, Généreux P, Piazza N, van Mieghem NM, Blackstone EH, et al. Updated standardized endpoint definitions for transcatheter aortic valve implantation: the Valve Academic Research Consortium-2 consensus document (VARC-2). *Eur J Cardiothorac Surg*. (2012) 42:S45–60. doi: 10.1093/ejcts/ezs533
21. Schulz-Menger J, Bluemke DA, Bremerich J, Flamm SD, Fogel MA, Friedrich MG, et al. Standardized image interpretation and post processing in cardiovascular magnetic resonance: Society for Cardiovascular Magnetic Resonance (SCMR) board of trustees task force on standardized post processing. *J Cardiovasc Magn Reson*. (2013) 15:35. doi: 10.1186/1532-429X-15-35
22. Simonneau G, Montani D, Celermajer DS, Denton CP, Gatzoulis MA, Krowka M, et al. Haemodynamic definitions and updated clinical classification of pulmonary hypertension. *Eur Respir J*. (2019) 53:1801913. doi: 10.1183/13993003.01913-2018
23. Petersen SE, Aung N, Sanghvi MM, Zemrak F, Fung K, Paiva JM, et al. Reference ranges for cardiac structure and function using cardiovascular magnetic resonance (CMR) in Caucasians from the UK Biobank population cohort. *J Cardiovasc Magn Reson.* (2017) 19:18. doi: 10.1186/s12968-017-0327-9
24. Galli E, Guirette Y, Feneon D, Daudin M, Fournet M, Leguerrier A, et al. Prevalence and prognostic value of right ventricular dysfunction in severe aortic stenosis. *Eur Heart J Cardiovasc Imaging*. (2015) 16:531–8. doi: 10.1093/ehjci/jeu290
25. Medvedofsky D, Koifman E, Miyoshi T, Rogers T, Wang Z, Goldstein SA, et al. Usefulness of longitudinal strain to assess remodeling of right and left cardiac chambers following transcatheter aortic valve implantation. *Am J Cardiol.* (2019) 124:253–61. doi: 10.1016/j.amjcard.2019.04.029
26. Malkin CJ, Long WR, Baxter PD, Gale CP, Wendler O, Monaghan M, et al. Impact of left ventricular function and transaortic gradient on outcomes from transcatheter aortic valve implantation: data from the UK TAVI Registry. *EuroIntervention*. (2016) 11:1161–9. doi: 10.4244/EIJY14M12_12
27. Puls M, Korte KP, Bleckmann A, Huenlich M, Danner BC, Schoendube F, et al. Long-term outcomes after TAVI in patients with different types of aortic stenosis: the conundrum of low flow, low gradient and low ejection fraction. *EuroIntervention*. (2017) 13:286–93. doi: 10.4244/EIJ-D-16-00801
28. Mangner N, Stachel G, Woitek F, Haussig S, Schlotter F, Höllriegel R, et al. Predictors of mortality and symptomatic outcome of patients with low-flow severe aortic stenosis undergoing transcatheter aortic valve replacement. *J Am Heart Assoc.* (2018) 7:e007977. doi: 10.1161/JAHA.117.007977
29. Duncan AI, Lowe BS, Garcia MJ, Xu M, Gillinov AM, Mihaljevic T, et al. Influence of concentric left ventricular remodeling on early mortality after aortic valve replacement. *Ann Thorac Surg*. (2008) 85:2030–9. doi: 10.1016/j.athoracsur.2008.02.075
30. Povlsen JA, Rasmussen VG, Vase H, Jensen KT, Terkelsen CJ, Christiansen EH, et al. Distribution and prognostic value of left ventricular global longitudinal strain in elderly patients with symptomatic severe aortic stenosis undergoing transcatheter aortic valve replacement. *BMC Cardiovasc Disord*. (2020) 20:506. doi: 10.1186/s12872-020-01791-9
31. Løgstrup BB, Andersen HR, Thuesen L, Christiansen EH, Terp K, Klaaborg K-E, et al. Left ventricular global systolic longitudinal deformation and prognosis 1 year after femoral and apical transcatheter aortic valve implantation. *J Am Soc Echocardiogr*. (2013) 26:246–54. doi: 10.1016/j.echo.2012.12.006
32. Varshney AS, Manandhar P, Vemulapalli S, Kirtane AJ, Mathew V, Shah B, et al. Left ventricular hypertrophy does not affect 1-year clinical outcomes in patients undergoing transcatheter aortic valve replacement. *JACC Cardiovasc Interv*. (2019) 12:373–82. doi: 10.1016/j.jcin.2018.11.013
33. Guazzi M, Dixon D, Labate V, Beussink-Nelson L, Bandera F, Cuttica MJ, et al. RV Contractile function and its coupling to pulmonary circulation in heart failure with preserved ejection fraction: stratification of clinical

phenotypes and outcomes. *J Am Coll Cardiol Img*. (2017) 10(10 Pt B):1211–21. doi: 10.1016/j.jcmg.2016.12.024

34. Sultan I, Cardounel A, Abdelkarim I, Kilic A, Althouse AD, Sharbaugh MS, et al. Right ventricle to pulmonary artery coupling in patients undergoing transcatheter aortic valve implantation. *Heart*. (2019) 105:117–21. doi: 10.1136/heartjnl-2018-313385

Conflict of Interest: GT received consultancy fees and unrestricted research support from Abbott, Medtronic, Biotronic and Boston Scientific, not related to this work.

The remaining authors declare that the research was conducted in the absence of any commercial or financial relationships that could be construed as a potential conflict of interest.

frontiers in Bioengineering and Biotechnology

ORIGINAL RESEARCH
published: 19 May 2021
doi: 10.3389/fbioe.2021.638934

A Novel Pulmonary Valve Replacement Surgery Strategy Using Contracting Band for Patients With Repaired Tetralogy of Fallot: An MRI-Based Multipatient Modeling Study

*Han Yu[1], Pedro J. del Nido[2,3], Tal Geva[4,5], Chun Yang[6], Zheyang Wu[6], Rahul H. Rathod[4,5], Xueying Huang[7], Kristen L. Billiar[8] and Dalin Tang[1,6]**

[1] School of Biological Science and Medical Engineering, Southeast University, Nanjing, China, [2] Department of Cardiac Surgery, Boston Children's Hospital, Boston, MA, United States, [3] Department of Surgery, Harvard Medical School, Boston, MA, United States, [4] Department of Cardiology, Boston Children's Hospital, Boston, MA, United States, [5] Department of Pediatrics, Harvard Medical School, Boston, MA, United States, [6] Mathematical Sciences Department, Worcester Polytechnic Institute, Worcester, MA, United States, [7] School of Mathematical Sciences, Xiamen University, Xiamen, China, [8] Department of Biomedical Engineering, Worcester Polytechnic Institute, Worcester, MA, United States

OPEN ACCESS

Edited by:
Zahra K. Motamed,
McMaster University, Canada

Reviewed by:
Alejandro Roldán-Alzate,
University of Wisconsin-Madison, United States
Virginie Le Rolle,
University of Rennes 1, France

***Correspondence:**
Dalin Tang
dtang@wpi.edu

Specialty section:
This article was submitted to Biomechanics, a section of the journal Frontiers in Bioengineering and Biotechnology

Received: 07 December 2020
Accepted: 08 April 2021
Published: 19 May 2021

Citation:
Yu H, del Nido PJ, Geva T, Yang C, Wu Z, Rathod RH, Huang X, Billiar KL and Tang D (2021) A Novel Pulmonary Valve Replacement Surgery Strategy Using Contracting Band for Patients With Repaired Tetralogy of Fallot: An MRI-Based Multipatient Modeling Study. Front. Bioeng. Biotechnol. 9:638934. doi: 10.3389/fbioe.2021.638934

Patients with repaired Tetralogy of Fallot (ToF), a congenital heart defect which includes a ventricular septal defect and severe right ventricular outflow obstruction, account for the majority of cases with late-onset right ventricle (RV) failure. Current surgery procedures, including pulmonary valve replacement (PVR) with right ventricle remodeling, yield mixed results. PVR with active band insertion was hypothesized to be of clinical usage on improving RV function measured by ejection fraction (EF). In lieu of risky open-heart surgeries and experiments on animal and human, computational biomechanical models were adapted to study the impact of PVR with five band insertion options. Cardiac magnetic resonance (CMR) images were acquired from seven TOF patients before PVR surgery for model construction. For each patient, five different surgery plans combined with passive and active contraction band with contraction ratio of 20, 15, and 10% were studied. Those five plans include three single-band plans with different band locations; one plan with two bands, and one plan with three bands. Including the seven no-band models, 147 computational bi-ventricle models were constructed to simulate RV cardiac functions and identify optimal band plans. Patient variations with different band plans were investigated. Surgery plan with three active contraction bands and band active contraction ratio of 20% had the best performance on improving RV function. The mean ± SD RV ejection fraction value from the seven patients was 42.90 ± 5.68%, presenting a 4.19% absolute improvement or a 10.82% relative improvement, when compared with the baseline models (38.71 ± 5.73%, $p = 0.016$). The EF improvements from the seven patients varied from 2.87 to 6.01%. Surgical procedures using active contraction bands have great potential to improve RV function measured by ejection

fraction for patients with repaired ToF. It is possible to have higher right ventricle ejection fraction improvement with more bands and higher band active contraction ratio. Our findings with computational models need to be further validated by animal experiments before clinical trial could become possible.

Keywords: right ventricle, Tetralogy of Fallot, ventricle mechanical model, surgery simulation, active contraction band

INTRODUCTION

Tetralogy of Fallot (TOF) is a common congenital heart disease. The symptoms include ventricular septal defect, pulmonary valve stenosis, aorta overriding, and right ventricular hypertrophy. Corrective surgery allows TOF patients to extend their life expectancy, and some patients manage to survive into adulthood (Murphy et al., 1993). Many repaired TOF survivors are left with some residual symptoms including pulmonary regurgitation causing progressive RV dysfunction and dilation (Geva et al., 2004; Kim and Emily, 2016). Anagnostopoulos et al. (2007) hypothesized that pulmonary valve cusp augmentation with pericardium would decrease pulmonary insufficiency and improve the early outcome for transatrial–transpulmonary TOF repair requiring transannular patch. Their procedure had some success in reducing the incidence of clinically significant postoperative pulmonary insufficiency (Anagnostopoulos et al., 2007). For pulmonary valve (PV) sparing repair procedure which may be associated with residual pulmonary stenosis, Sen et al. (2016) reported that valve-sparing transannular (VSTAR) repair had better short-term and comparable midterm results and may be appropriate for TOF repair in patients with small PV. For repaired TOF patients with pulmonary regurgitation or unsuitable for pulmonary valve sparing procedure, current surgical approach [pulmonary valve replacement (PVR)] yield mixed results with some patients failing to recover their RV function (Geva et al., 2004, 2010; Kim and Emily, 2016). Recent advanced techniques include transcatheter strategies and using tissue-engineered valves (Motta et al., 2017; Jones and Qureshi, 2018). Del Nido and Geva et al. (2004) proposed a RV remodeling surgery by trimming scar tissue on RV wall and replacing the original patch with a smaller one during the PVR. In a clinic trial (NIH 5P50HL074734, Geva, and del Nido), 34 TOF cases were randomly assigned to PVR and RV remodeling surgery as experimental group and other 30 TOF cases underwent PVR alone as control group. Results showed insignificant statistical difference in RV EF variance after the surgery between the two groups ($-2 \pm 7\%$ vs. $-1 \pm 7\%$; $p = 0.38$) (Geva et al., 2004). In search for innovative PVR surgical procedures to improve postsurgery RV cardiac functions, computational simulations for a PVR procedure with active contracting band insertions were performed using cardiac magnetic resonance (CMR) data from one TOF patient to investigate the effect of band material stiffness variations, band length, and active contraction ratios (Yang et al., 2013). The initial modeling results were promising (Tang et al., 2013; Yang et al., 2013).

Recent development in computational modeling made it possible for patient-specific ventricle models to be used for heart disease study and surgical optimizations. Peskin (1977, 1989) pioneered ventricle models with free moving boundaries and introduced early cardiac simulation models using immersed boundary method. McCulloch et al. (1992) developed a three-dimensional finite element method for large elastic deformations of ventricular myocardium, presenting the first practical opportunity to solve large-scale anatomically detailed models for cardiac stress analysis. Kerckhoffs et al. (2007) presented a novel method to couple the finite element cardiac mechanical model into a closed-loop lumped circulation models. Sacks and Chuong (1993) and Billiar and Sacks (2000) used biaxial mechanical test to acquire ventricle anisotropic material properties. Saber et al. (2001) and Axel (2002) proposed early magnetic resonance imaging (MRI)-based ventricle mechanical analysis. Nordsletten et al. (2011) developed a solid/fluid coupled left ventricle model to quantitate blood flow, pressure distributions, and mechanical energy loss caused by viscous dissipation.

Efforts were also made in moving ventricular computational models closer to clinical and surgical applications (Tang et al., 2008, 2013; Yang et al., 2013; Deng et al., 2018; Yu et al., 2019, 2020). Using CT-based mechanical fluid-solid interaction (FSI) ventricle model, Deng et al. (2018) studied systolic anterior motion of the mitral valve in hypertrophic obstructive cardiomyopathy. Our previous work included using bi-ventricular model to search surgical options, identify possible factors for post-PVR outcome prediction, estimate right ventricle myocardium stiffness, and study the impact of patch size, scar tissue removal, and RV remodeling on right ventricular function (Tang et al., 2008, 2013; Yang et al., 2013; Yu et al., 2019). Our pilot study using ventricle mechanical model of one TOF patient showed the surgery plan of inserting three bands with band active contraction ratio of 20% could improve RV ejection fraction from 37.38 to 41.58% (Yu et al., 2020).

We hypothesized that PVR with active contracting bands would improve RV cardiac function measured by ejection fraction (EF). RV EF was selected since it is easy to calculate and it is the single most commonly used measure for RV cardiac function in clinical practice. It is sufficient for the RV function assessment of our preliminary study. The normal RV EF range is 47–68% for a healthy male and 50–72% for a healthy female, respectively (Alfakih et al., 2010). In lieu of risky surgery with animals or TOF patients, patient-specific computational ventricle models based on CMR imaging data were used to quantify ventricle motion and evaluate RV ejection fraction before and after the band insert surgery. CMR data from seven repaired TOF patients were used to construct a total of 147 models combining five different band insertion options and four different contraction ratios. Results from these models were analyzed to seek optimized band insertion options with the best post-PVR outcome.

MATERIALS AND METHODS

Data Acquisition

Boston Children's Hospital Committee on Clinical Investigation approved this study. The approval number is IRB-CRM09-04-0237. Written informed consent was obtained from participants. CMR data was acquired from seven TOF patients 6 months before and after PVR (four males, average age: 31.81 years). Demographic and ejection fraction (EF) data of the seven TOF patients are given in **Table 1**. Post-PVR EF data served as a benchmark for us to check if the new surgery strategy with active contracting bands could provide better post-PVR cardiac outcome. CMR image segmentation was performed at Children's Hospital-Boston, Harvard Medical School using a commercial software QMass (Medis Medical Imaging Systems, Leiden, the Netherlands). The locations of patch, scar, and valve were identified based on cine MRI, flow velocity data, and delayed enhancement CMR and with inspections by cardiac surgeon Dr. del Nido (PJdN, over 30 years of experience) who performed the PVR surgeries. Each acquired cardiac cycle data set included 30 discrete time points, and each time point had a 3D CMR image data. End-diastolic volume (EDV) and end-systolic volume (ESV) were computed with Simpson's method. **Figure 1** gives two sample CMR image slices at end ejection, their segmented contours, constructed 3D RV/LV model with scar, patch, and myocardium fiber orientation and recorded RV pressure *via* cardiac catheterization procedures.

Five PVR Surgical Plans With Active Contracting Bands and Band Active Contraction

Five band insertion plans with band location and number variations are proposed to find optimal surgical plan using active contracting bands. An illustration of the five band plans is given by **Figure 2**. The five band plans included three plans with single band at different band locations, one plan with two bands, and one plan with three bands (**Figure 2** and **Table 2**). The details were introduced in our previous publication (Yu et al., 2020). These five band plans led to 20 models for each patient with one passive band model and three active band models with different contraction ratios. Including the no-band baseline model, 21 models were constructed for each patient. Since we used seven TOF patients, a total of 147 models were included in our paper.

The innovative PVR surgical plan using active contracting band was motivated by the fact that poor RV cardiac function indicated by low EF values were caused partially by RV's weak contraction ability due to RV dilation. The contracting bands were used with the expectation that they would help RV to contract and improve its cardiac function. Passive elastic bands would not help since while they seem to be able to help RV to contract, they would hold the ventricle during its expansion (diastole) and defeat the purpose. Active contracting bands could help the ventricle to contract through active contraction and also allow the ventricle to re-expand through active relaxation. It is commonly known that myocardium active contraction is achieved by sarcomere shortening. However, active relaxation is equally important for the band models to work. **Figure 3** gives plots of selected band zero-stress lengths in systole and diastole and band stress/strain curves in a cardiac cycle. When transitioning from diastole to systole (active contraction), the band zero-stress length changes from its diastole zero-stress length to systole zero-stress length (shortening) which results in strain and stress increases. When transitioning from systole to diastole (active relaxation), the band zero-stress length changed from its systole zero-stress length to diastole zero-stress length results in strain and stress decreases. Band material stress-strain curves are given in section "The RV/LV/Patch/Band Model and Material Models for Ventricle, Patch and Band."

The RV/LV/Patch/Band Model and Material Models for Ventricle, Patch, and Band

The RV/LV/patch/band model includes governing equations, boundary conditions, and material models for ventricle tissue, scar tissue, patch, and bands. The governing equations are the same for all structure components (Tang et al., 2008, 2013; Yang et al., 2013; Yu et al., 2019):

$$\rho v_{i,tt} = \sigma_{ij,j},\ i,j = 1,2,3;\ \text{sum over } j. \tag{1}$$

$$\varepsilon_{ij} = \frac{1}{2}\left(v_{i,j} + v_{j,i} + v_{\alpha,i}v_{\alpha,j}\right),\ i,j,\alpha = 1,2,3. \tag{2}$$

TABLE 1 | Patient demographic and CMR data.

Patient no.	Gender	Age (year)	Weight (kg)	Maximumpressure (mmHg)	RV EDV (ml)	RV ESV (ml)	RV EF (%)	PVR ΔEF (%)
P1	M	22.5	80	31.4	406.91	254.49	37.5%	1.49%
P2	M	47.7	95	31	408.76	254.79	37.7%	−2.56%
P3	M	43.5	123	65	665.06	464.05	30.2%	−15.22%
P4	F	38.5	49	28	328.79	195.97	40.4%	−3.35%
P5	M	11.6	38	36	204.17	121.26	40.6%	−8.41%
P6	F	14.3	58.5	29	204.00	104.30	48.8%	5.57%
P7	F	44.6	57.1	50	299.00	186.00	37.8%	−12.32%
Mean ± SD	–	31.81 ± 15.27	71.5 ± 29.7	38.63 ± 15.27	359.53 ± 158.61	225.84 ± 120.13	39.00 ± 5.53%	−4.97 ± 7.44%

PVR, pulmonary valve replacement.
PVR ΔEF = post-PVR EF – pre-PVR RV.

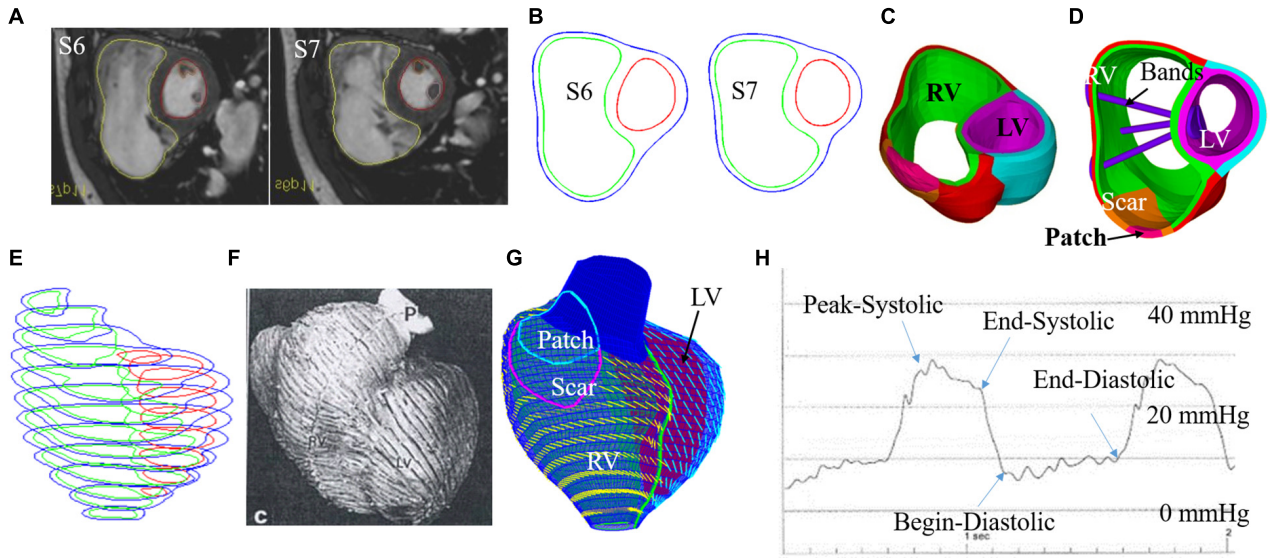

FIGURE 1 | CMR-based model construction process and pressure conditions. **(A)** Selected CMR slices from a patient, end of systole. **(B)** Segmented contours. **(C)** Two-layer structure. **(D)**. Ventricle with three bands inserted. **(E)** Stacked contours. **(F)** RV fiber orientation from a TOF patient. **(G)** Model with fiber orientations. **(H)** Recorded RV pressure profile (Tang et al., 2008, 2013; Yang et al., 2013; Yu et al., 2019, 2020).

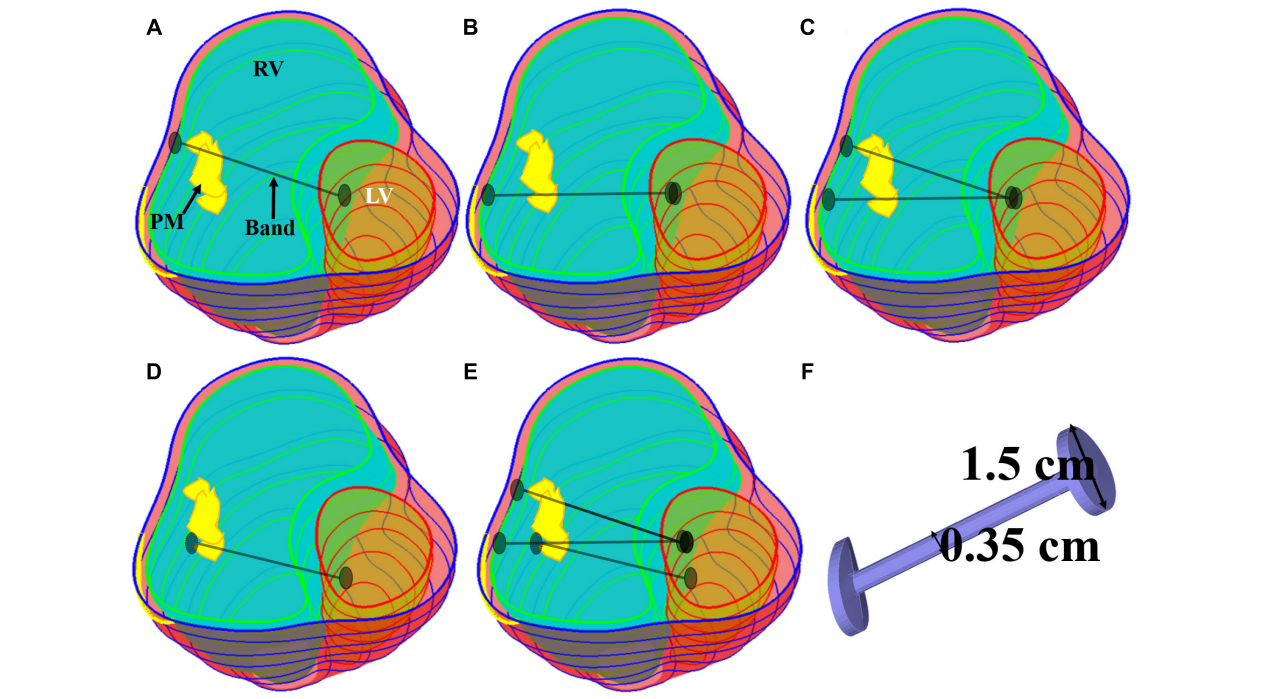

FIGURE 2 | Five band insertion surgical plans. **(A)** Plan A: a band at anterior to the middle of papillary muscle (PM). **(B)** Plan B: a band at posterior to the middle of PM. **(C)** Plan C: double bands, plans A and B combined. **(D)** Plan D: a band at the base of the PM. **(E)** Plan E: combination of plans C and D. **(F)** Inserted band. PM, papillary muscle (Yu et al., 2020).

RV/LV combined geometry for each patient was obtained from CMR data and reconstructed following established procedures (Yang et al., 2013). Patch and scar locations were determined by our cardiac surgeon (PJ del Nido) and radiologist (T. Geva). No-slip conditions and natural boundary conditions were imposed automatically by ADINA (ADINA R&D, Watertown, MA, United States) at all interfaces of different structure components (ventricle, band, scar, and patch). RV and

TABLE 2 | Band model summary, band location and numbers, contraction ratios, and zero-load band length for all 21 RV/LV models.

Models	Plan	Band number	Contraction ratio	Zero-load band length (cm)	Band location
Baseline	–	0	–	–	–
A000	A	1	Passive	100%L	Anterior to the middle of PM
A010	A	1	10%	90%L	Anterior to the middle of PM
A015	A	1	15%	85%L	Anterior to the middle of PM
A020	A	1	20%	80%L	Anterior to the middle of PM
P000	B	1	Passive	100%L	Posterior to the middle of PM
P010	B	1	10%	90%L	Posterior to the middle of PM
P015	B	1	15%	85%L	Posterior to the middle of PM
P020	B	1	20%	80%L	Posterior to the middle of PM
AP000	C	2	Passive	100%L	Plan A and B combined
AP010	C	2	10%	90%L	Plan A and B combined
AP015	C	2	15%	85%L	Plan A and B combined
AP020	C	2	20%	80%L	Plan A and B combined
B000	D	1	Passive	100%L	The base of the PM
B010	D	1	10%	90%L	The base of the PM
B015	D	1	15%	85%L	The base of the PM
B020	D	1	20%	80%L	The base of the PM
APB000	E	3	Passive	100%L	Combination of plan C and D
APB010	E	3	10%	90%L	Combination of plan C and D
APB015	E	3	15%	85%L	Combination of plan C and D
APB020	E	3	20%	80%L	Combination of plan C and D

Plan A models are models with a band at anterior to the middle of PM. They are named as AXXX, where A is short for anterior, and XXX represents band active contraction ratio, for example, 010 = 10%. Plan B models are models with a band at posterior to the middle of PM. They are named PXXX, where P is short for posterior. Plan D models has a band at the base of PM. They are called BXXX, where B is short for base. For multiband plans, plan C models are named as APXXX since plan C is the combination of A and B; and Plan E is named as APBXXX because plan E is the combination of A, P, and B. PM, papillary muscle.

LV inner-pressure conditions were prescribed as (Tang et al., 2008, 2013; Yang et al., 2013; Yu et al., 2019, 2020):

$$p\big|_{RV} = p_{RV}(t), p\big|_{LV} = p_{\mathrm{LV}}(t) \tag{3}$$

where p_{RV} and p_{LV} were blood pressure conditions specified on RV and LV inner surfaces. Pressure on the RV/LV out-surface was set to be zero. Patch, scar, and band materials were assumed to be hyper-elastic, isotropic, nearly incompressible, and homogeneous. The isotropic Mooney–Rivlin strain energy function is given by (Tang et al., 2008, 2013; Yang et al., 2013; Yu et al., 2019, 2020),

$$W_{\mathrm{iso}} = c_1(I_1-3) + c_2(I_2-3) + D_1[\exp(D_2(I_1-3))-1] \tag{4}$$

where c_1, c_2, D_1, and D_2 are material constants and I_1 and I_2 are the first and second invariants of Cauchy–Green strain,

$$I_1 = \sum C_{ii}, I_2 = \frac{1}{2}(I_1^2 - C_{ij}C_{ij}) \tag{5}$$

where C_{ij} is the Cauchy–Green deformation tensor. Ventricle tissue material was assumed to be hyper-elastic, anisotropic, nearly incompressible, and homogeneous. The non-linear anisotropic modified Mooney–Rivlin model was obtained by adding an additional anisotropic term in Eq. (4) (Yang et al., 2013):

$$W = W_{\mathrm{iso}} + W_{\mathrm{aniso}} \tag{6}$$

$$W_{\mathrm{aniso}} = \frac{K_1}{K_2}(\exp(I_4-1)^2-1) \tag{7}$$

where $I_4 = C_{ij}(n_f)_i(n_f)_j$, n_f is the fiber direction, and K_1 and K_2 are material constants. With parameters chosen properly, the modified Mooney–Rivlin model described in Eq. (6) could fit the directly measured myocardium stress-strain data from our biaxial test experiment (Yang et al., 2013; Yu et al., 2019, 2020). In our models, patent-specific ventricle material parameter values were selected to match CMR-measured volume data.

A two-layer construction process was used to make our RV/LV models to take myocardium fiber orientations into consideration (see **Figure 1D**). Patient-specific fiber orientation data was not available for our study. Fiber orientation data from available literature were used in our models (Sanchez-Quintana et al., 1996; Nash and Hunter, 2000; Hunter et al., 2003). Fiber orientations were specified for every element on the inner and outer layers of our models. For left ventricle, the fiber orientation was approximately −60° (relative to circumferential direction) at the outer layer and +80° at the inner layer. RV fiber orientation was −45° at the outer layer and +40° at the inner layer (see **Figure 1**).

Preshrink Process to Obtain Ventricle Zero-Load Geometries and Patient-Specific Ventricle Material Parameter Quantification

Patient ventricle CMR images were obtained under *in vivo* conditions. Zero-load ventricular geometries were not available from *in vivo* CMR images and were obtained using a preshrink iterative process. In our modeling process, the approximate zero-load geometries were obtained by shrinking segmented

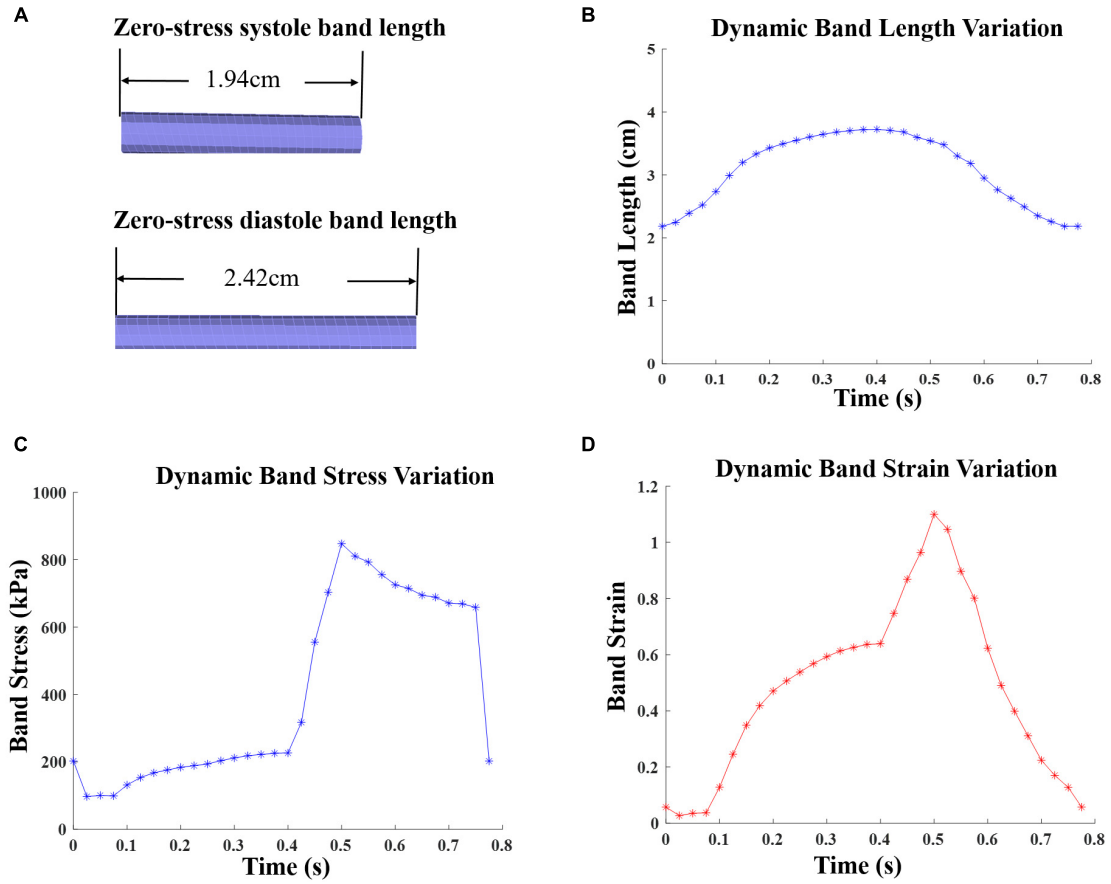

FIGURE 3 | Zero-stress band length and dynamic band stress/strain variations for patient 5 surgery plan D model with 20% active contraction ratio in the entire cardiac cycle. **(A)** Zero-load band length at systole and diastole. **(B)** Dynamic band length variation. **(C)** Dynamic band stress variation. **(D)** Dynamic band strain variation.

contours on each slice (short-axis direction) with a short-axis shrinking rate and reducing distance between each slice (long-axis direction) with a long-axis shrinking rate (3%). The shrink ratio for inner contours was 2–3% based on the RV end-systole volume (minimum volume in a cardiac cycle) and the corresponding RV pressure. The outer contours shrink ratio was determined to meet the conservation of mass of the total ventricular wall. **Figure 4** gives an illustration of the preshrink process. Three material parameter values c_1, d_1, and K_1 in Eqs. (4)–(7) were adjusted iteratively until the relative error between the pressurized computational RV volume and CMR-measured *in vivo* volume data was less than 0.2%. This process was done semiautomatically using a secant method for fast convergence to *in vivo* RV volume. **Figure 5** shows stress-stretch relations of patient 5 RV tissue, patch, scar, and band at begin filling and begin ejection, respectively. The corresponding material parameter values for those material models are shown in **Table 3**. For our seven no-band baseline models, the mean ± SD RV volume was 226.84 ± 121.20 ml at begin filling (same as end-systole volume ESV) and 359.19 ± 158.41 ml at begin ejection (same as end-diastole volume EDV), in agreement with the CMR data: 225.84 ± 120.13 ml at begin filling (p = 0.313) and 359.53 ± 158.61 ml at begin ejection (p = 0.438). Details were described in Tang et al. (2013, 2008), Yang et al. (2013), and Yu et al. (2019, 2020).

Solution Methods, Data Extraction, and Statistical Analysis

The 147 models were constructed and solved with ADINA using unstructured finite elements and the Newton–Raphson iteration method (Tang et al., 2008, 2013; Yang et al., 2013; Yu et al., 2019; Yu et al., 2020). Simulations were performed for several cardiac cycles until the solution relative differences between the last two cycles in L_2 norm were less than 0.1%. The L_2 norm of a given function F was computed with:

$$\| F\|_{L_2} = \sqrt{\int_{T_k}^{T_{k+1}} \left(\iiint_V F^2 \mathrm{d}V \right) \mathrm{d}t}, \tag{8}$$

where T is the period (one cardiac cycle), F will be $|S(t)-S(t+T)|$ as the function difference over one period where $S(t)$ stands for either stress-P_1 (maximum principal stress) or strain-P_1 (maximum principal strain), the integration is taken over the

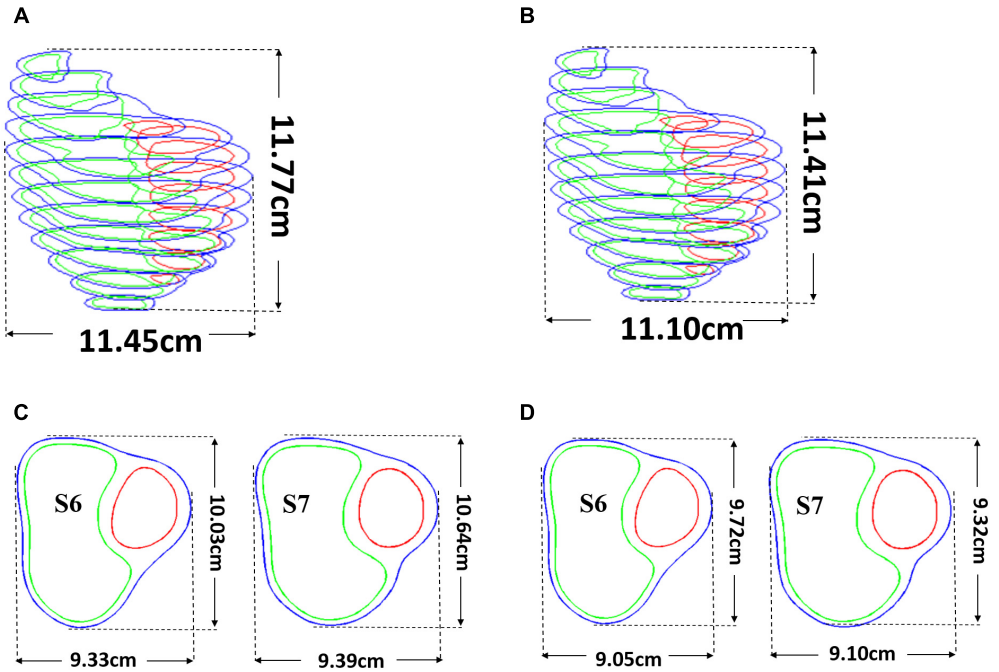

FIGURE 4 | Pre-shrink process. **(A)** Stacked contours before pre-shrink. **(B)** Stacked contours after preshrink with a long-axis shrinking rate (3%). **(C)** Slices 6 and 7 before preshrink. **(D)** Slices 6 and 7 after preshrink, the shrink ratio for inner contours was 2–3%. The outer contours shrink ratio was determined to meet the conservation of mass of the total ventricular wall.

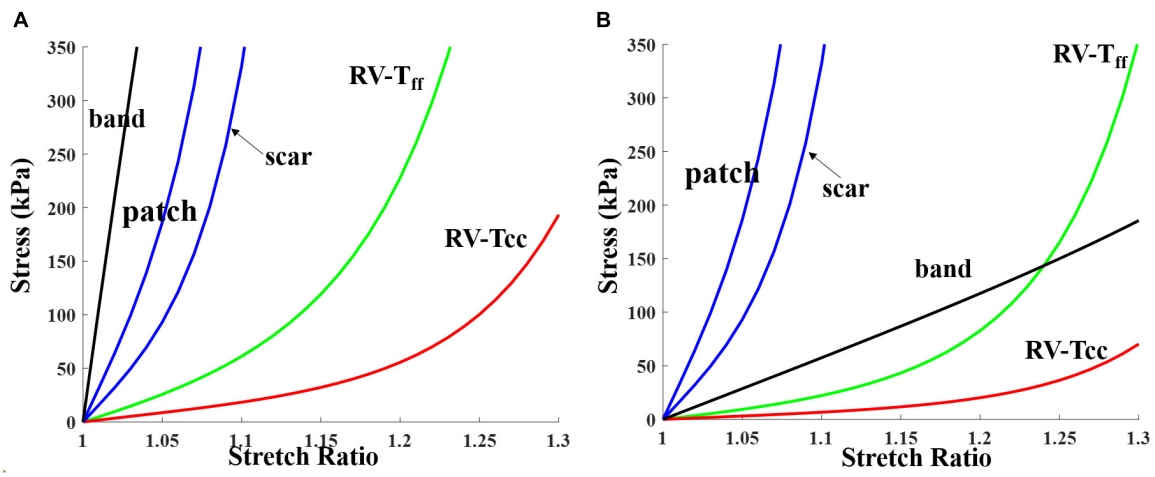

FIGURE 5 | Stress-stretch curves for patch, scar, band, and myocardium tissue for RV inner layer (patient 5). Material parameter values are given in **Table 3**. **(A)** End systole. **(B)** End diastole. RV-T_{ff}, RV stress in fiber direction; RV-T_{cc}, RV stress in direction perpendicular to fiber direction.

entire RV domain and one cardiac cycle with discretization performed utilizing all available nodes and time steps. The results from the last period were recorded for analysis. For all 147 simulations, only three cycles were needed to obtain the solution. For each model, stress and strain data from 100 evenly spaced points for each slice of RV inner surface were extracted. Maximum principal stress and strain values were chosen to represent the stress and strain state of these points, and their mean values at begin filling (BF) and begin ejection (BE) were recorded as the stress and strain value of this model. RV Ejection fraction was used as the index (marker) for evaluating ventricle cardiac function. RV ejection fraction (EF) is defined as:

$$\mathrm{EF} = \frac{\text{RV EDV} - \text{RV ESV}}{\text{RV EDV}} \times 100\% \tag{9}$$

where RV EDV is right ventricle end-diastole volume and RV ESV is right ventricle end-systole volume. Higher EF value indicates that the ventricle is more efficient in pumping blood.

TABLE 3 | Summary of parameter values of the Mooney–Rivlin models for patient 5 patch, scar, RV tissue, and band (c_2 = 0 kPa).

Material/model	c_1 (kPa)	D_1 (kPa)	D_2	K_1 (kPa)	K_2
Patch (isotropic)	26.52	26.52	9.0	0	–
Scar (isotropic)	13.26	13.26	9.0	0	–
Band (isotropic, end ejection)	900	0	–	0	–
Band (isotropic, end filling)	70	0	–	0	–
Myocardium, end ejection					
RV/LV inner layer (anisotropic)	7.64	2.41	3.0	36.55	3.0
RV/LV outer layer (anisotropic)	8.72	2.24	3.0	35.52	3.2
Myocardium, end filling					
RV/LV inner layer (anisotropic)	2.78	0.87	3.0	13.29	3.0
RV/LV outer layer (anisotropic)	3.17	0.82	3.0	12.92	3.2

Difference between pre- and post-PVR EF denoted by △EF was used to measure PVR (with and without active contracting bands) improvement:

$$\triangle \text{ EF} = \text{post-PVR EF} - \text{pre-PVR EF}. \quad (10)$$

Preoperation (no-band) RV/LV models were regarded as the baseline model. The paired test Wilcoxon signed rank test was used to compare the differences of EF, stress, and strain values between band and baseline models and the differences between different surgery plans. The test was performed using the function: p = signrank(a,b) from MATLAB statistical tool box.

RESULTS

Three-Band Surgical Option Had Best Improvement for RV Ejection Fraction

Simulation results from the seven patients using five band options with band contraction ratio of 20% are given in **Table 4**. Surgery plan with three active bands (plan E) had the best RV EF improvement among the five band plans. The mean ± SD RV ejection fraction value from the seven patients with plan E was 42.90 ± 5.68%, representing a 4.19% absolute improvement or 10.82% relative improvement over the mean value of the baseline no-band models (38.71 ± 5.73%, $p = 0.016$). Absolute EF improvements for each patient varied from 2.87 to 6%. Mean ± SD ΔEF values of the seven patients for band options A–D were 2.51 ± 0.80%, 2.13 ± 0.53%, 3.36 ± 1.07%, 1.90 ± 0.40%, respectively. The two-band plan (option C) had the second best performance. Similar results were also found when the band active contraction ratio was 15 or 10%, respectively.

Higher Band Contraction Ratio Had Better RV EF Improvement

Table 5 summarizes results from the seven patients using band option E (three-band model) with 0, 10, 15, and 20% band contraction ratios and their EF differences compared with the no-band baseline model. The models with 0% contraction ratio corresponded to models with passive bands. Mean ± SD ΔEF values of the seven patients for 10 and 15% band contraction ratio were 3.19 ± 1.00 and 2.27 ± 0.89%, respectively. Considering the results given in section "Three-Band Surgical Option had Best Improvement for RV Ejection Fraction": mean ± SD ΔEF of seven patients for 20% band contraction ratio were 4.19 ± 1.11%, models with 20% band contraction ratio had higher ΔEF and EF values than that with 15 and 10% band contraction ratios. Higher band contraction ratio improved RV EF more.

Intuitively, it might be reasonable to expect that a passive elastic band may be able to improve ejection fraction since elastic bands would help the ventricle to contract. Our simulations indicated that that was not the case. Mean ΔEF of models with surgery option E and passive bands was −3.27%, and ΔEF values ranged from −5.67 to −1.93%. For surgery option A–D, mean ± SD ΔEF were −1.37 ± 0.50, −1.04 ± 0.44, −2.32 ± 0.85, and −1.23 ± 0.79%, respectively. RV EF decreased after passive bands were inserted. The reason is actually simple: passive elastic bands would not "relax" by themselves after they contracted. The bands would actually hold the ventricle and became resistance for ventricle expansion. Mean ± SD volume values of surgery options A–D with passive bands at begin ejection were 349.76 ± 158.75, 352.08 ± 157.36, 344.56 ± 157.62, 350.83 ± 157.53, and 339.24 ± 157.82 ml, respectively, whereas the baseline model was 359.19 ± 158.41 ml. On the other hand, active bands help ventricle to contract by active contraction and would not resist ventricle expansion since active bands would "relax" through active relaxation (**Table 6**).

Stress/Strain Patterns Were Complex in Right Ventricle

Figures 6, **7** provides begin-ejection (maximum pressure) and begin-filling (minimum pressure) stress and strain plots on RV inner surface from four band models of patient 5. Stress and strain distributions have complex patterns. Band insertion changed local stress and strain distributions. **Figures 6**, **7** show that stress and strain values of RV tissues near band insert locations increased, whereas stress and strain relatively away from band decreased. Mean stress and strain values are given in **Tables 2**, **4**, **5**, showing variations due to band options, contraction ratios, and patient variations. There were very noticeable patient variations in stress/strain values. RV mean stress values from plan A varied from 46.61 kPa (P2)

TABLE 4 | RV ejection fraction (EF) and wall stress/strain data from models with band active contraction ratio of 20%.

Patients	Begin filling			Begin ejection			EF	ΔEF
	RV vol (ml)	Stress (kPa)	Strain	RV vol (ml)	Stress (kPa)	Strain		
Plan A (1 band, option A)								
P1	244.90	3.17	0.033	406.15	61.64	0.291	39.70%	2.32%
P2	248.20	3.20	0.029	408.42	46.61	0.314	39.23%	1.79%
P3	454.35	7.70	0.020	665.47	77.62	0.194	31.72%	2.12%
P4	186.00	3.46	0.019	327.59	54.74	0.308	43.22%	2.98%
P5	113.82	4.26	0.026	204.64	54.68	0.287	44.38%	4.11%
P6	100.39	3.13	0.022	204.14	58.03	0.418	50.82%	1.94%
P7	181.45	7.44	0.017	299.87	89.02	0.267	39.49%	2.41%
Mean ± SD	218.44 ± 118.7	4.62 ± 2.05	0.024 ± 0.006	359.47 ± 158.58	63.19 ± 14.85	0.297 ± 0.067	41.22 ± 5.85%	2.51 ± 0.80%
Plan B (1 band, option B)								
P1	246.47	3.16	0.032	407.07	64.72	0.285	39.45%	2.07%
P2	248.86	3.13	0.028	409.31	48.72	0.318	39.20%	1.76%
P3	455.69	6.99	0.019	662.07	76.83	0.192	31.17%	1.57%
P4	187.73	3.86	0.026	327.81	54.61	0.309	42.73%	2.49%
P5	115.45	4.52	0.030	203.80	54.03	0.287	43.35%	3.08%
P6	100.53	3.14	0.022	203.41	58.49	0.417	50.58%	1.70%
P7	181.57	7.30	0.018	299.74	88.49	0.266	39.43%	2.35%
Mean ± SD	219.47 ± 118.89	4.59 ± 1.82	0.025 ± 0.006	359.03 ± 157.84	63.70 ± 14.23	0.296 ± 0.067	40.84 ± 5.84%	2.13 ± 0.53%
Plan C (2 bands, option C)								
P1	240.64	3.21	0.033	405.83	63.98	0.289	40.70%	3.32%
P2	246.21	3.37	0.033	408.79	49.39	0.313	39.77%	2.33%
P3	447.69	8.10	0.022	664.29	79.06	0.199	32.61%	3.01%
P4	180.69	3.76	0.025	327.32	59.38	0.312	44.80%	4.56%
P5	111.12	3.31	0.025	203.22	51.38	0.286	45.32%	5.05%
P6	99.36	3.32	0.025	203.19	57.93	0.418	51.10%	2.22%
P7	179.26	7.91	0.020	299.65	89.08	0.266	40.18%	3.10%
Mean ± SD	214.99 ± 117.19	4.71 ± 2.26	0.026 ± 0.005	358.90 ± 158.61	64.32 ± 14.64	0.298 ± 0.066	42.07 ± 5.77%	3.36 ± 1.07%
Plan D (1 band, option D)								
P1	243.71	2.92	0.031	400.63	64.86	0.306	39.17%	1.79%
P2	248.88	2.88	0.026	407.35	46.87	0.310	38.90%	1.46%
P3	455.90	6.70	0.021	663.89	77.39	0.199	31.33%	1.73%
P4	189.25	4.33	0.026	327.44	58.42	0.305	42.20%	1.96%
P5	116.50	4.92	0.030	204.46	53.37	0.283	43.02%	2.75%
P6	100.97	3.24	0.024	204.56	56.94	0.419	50.64%	1.76%
P7	182.88	6.72	0.017	299.91	86.88	0.265	39.02%	1.94%
Mean ± SD	219.73 ± 118.5	4.53 ± 1.67	0.025 ± 0.005	358.32 ± 157.72	63.53 ± 14.08	0.298 ± 0.066	40.61 ± 5.81%	1.90 ± 0.40%
Plan E (3 bands, option E)								
P1	235.13	3.39	0.035	402.45	67.76	0.302	41.58%	4.20%
P2	243.04	3.53	0.037	408.20	51.56	0.315	40.46%	3.02%
P3	441.93	8.40	0.025	665.31	79.89	0.200	33.58%	3.98%
P4	178.64	4.11	0.028	327.18	59.69	0.312	45.40%	5.16%
P5	109.43	3.69	0.027	203.71	57.02	0.307	46.28%	6.01%
P6	98.20	3.73	0.030	203.52	59.39	0.423	51.75%	2.87%
P7	175.77	8.39	0.024	299.37	88.86	0.267	41.29%	4.21%
Mean ± SD	211.73 ± 115.66	5.03 ± 2.30	0.029 ± 0.005	358.53 ± 158.63	66.31 ± 13.48	0.304 ± 0.067	42.90 ± 5.68%	4.19 ± 1.11%

ΔEF, difference between the current model EF and EF from baseline no-band model. Stress/strain values are mean values from all RV inner surface data points, 100 points per image slice.

to 89.02 kPa (P7), a 91% increase. RV mean strain values from plan A varied from 0.194 (P3) to 0.418 (P6), a 115% increase. Patient mean stress/strain value variations for other band options were similar.

It should be noted that mean stress/strain values (average of seven patients) had very small variations for all five band options. At begin ejection, stress and strain values from models with active band were close to the baseline.

TABLE 5 | RV EF and wall stress/strain data of plan E models (3 bands) with 0, 10, 15, and 20% band contraction ratios.

Patients	Begin filling			Begin ejection			EF	ΔEF
	RV vol (ml)	Stress (kPa)	Strain	RV vol (ml)	Stress (kPa)	Strain		
Passive bands								
P1	248.83	2.82	0.028	375.78	54.60	0.278	33.78%	−3.60%
P2	254.60	2.51	0.019	394.09	42.87	0.310	35.40%	−2.04%
P3	466.38	6.09	0.017	644.83	76.66	0.197	27.67%	−1.93%
P4	191.92	3.44	0.018	307.01	49.67	0.295	37.49%	−2.75%
P5	118.11	3.77	0.025	180.59	41.78	0.266	34.60%	−5.67%
P6	103.77	2.53	0.015	190.01	50.33	0.407	45.39%	−3.49%
P7	187.09	5.87	0.012	282.35	77.11	0.253	33.74%	−3.34%
Mean ± SD	224.39 ± 121.35	3.86 ± 1.52	0.019 ± 0.006	339.24 ± 157.82	56.15 ± 14.84	0.287 ± 0.064	35.44 ± 5.32%	−3.27 ± 1.26%
Band active contraction ratio: 10%								
P1	242.37	3.01	0.030	402.81	67.33	0.301	39.83%	2.45%
P2	249.85	2.79	0.025	407.67	48.72	0.314	38.71%	1.27%
P3	455.54	6.57	0.018	665.33	78.99	0.200	31.53%	1.93%
P4	186.16	3.54	0.021	327.86	58.67	0.313	43.22%	2.98%
P5	114.05	3.60	0.025	203.88	55.88	0.306	44.06%	3.79%
P6	101.27	2.90	0.020	203.72	58.17	0.422	50.29%	1.41%
P7	182.07	6.32	0.015	299.44	87.98	0.267	39.20%	2.12%
Mean ± SD	218.76 ± 118.86	4.10 ± 1.63	0.022 ± 0.005	358.67 ± 158.54	65.11 ± 13.93	0.303 ± 0.066	40.98 ± 5.77%	2.27 ± 0.89%
Band active contraction ratio: 15%								
P1	238.86	3.18	0.032	402.66	67.47	0.301	40.68%	3.30%
P2	246.70	3.14	0.031	407.99	50.66	0.315	39.53%	2.09%
P3	449.11	7.37	0.021	665.58	79.25	0.200	32.52%	2.92%
P4	182.61	3.80	0.024	327.52	58.99	0.312	44.24%	4.00%
P5	111.80	3.61	0.025	203.81	56.41	0.306	45.15%	4.88%
P6	99.80	3.29	0.025	203.63	58.74	0.422	50.99%	2.11%
P7	179.07	7.23	0.019	299.54	88.72	0.267	40.22%	3.14%
Mean ± SD	215.42 ± 117.36	4.52 ± 1.92	0.025 ± 0.005	358.68 ± 158.66	65.75 ± 13.68	0.303 ± 0.066	41.90 ± 5.72%	3.19 ± 1.00%
Band active contraction ratio: 20%								
P1	235.13	3.39	0.035	402.45	67.76	0.302	41.58%	4.20%
P2	243.04	3.53	0.037	408.20	51.56	0.315	40.46%	3.02%
P3	441.93	8.40	0.025	665.31	79.89	0.200	33.58%	3.98%
P4	178.64	4.11	0.028	327.18	59.69	0.312	45.40%	5.16%
P5	109.43	3.69	0.027	203.71	57.02	0.307	46.28%	6.01%
P6	98.20	3.73	0.030	203.52	59.39	0.423	51.75%	2.87%
P7	175.77	8.39	0.024	299.37	88.86	0.267	41.29%	4.21%
Mean ± SD	211.73 ± 115.66	5.03 ± 2.30	0.029 ± 0.005	358.53 ± 158.63	66.31 ± 13.48	0.304 ± 0.067	42.90 ± 5.68%	4.19 ± 1.11%

RV, right ventricle; EF, ejection fraction. ΔEF is the difference between the current model EF and EF from baseline no-band model.

RV mean ± SD stress values of the five plans with 20% band contraction ratio were 63.19 ± 14.85, 63.70 ± 14.23, 64.32 ± 14.64, 63.53 ± 14.08, and 66.31 ± 13.48 kPa, respectively. Meanwhile, baseline stress value was 62.89 ± 14.81 kPa. RV mean ± SD strain values of options A–E with 20% band contraction ratio were 0.297 ± 0.067, 0.296 ± 0.067, 0.298 ± 0.066, 0.298 ± 0.066, and 0.304 ± 0.067, which were also close to mean ± SD stress value of baseline models: 0.292 ± 0.062.

Table 5 comparing stress/strain values from models with different band contraction ratios. At begin ejection, average stress and strain values (seven patients) from models with 10% band contraction ratio were 16 and 5.6% higher than that from the passive band models. Average stress and strain values from models with 10, 15, and 20% band contraction ratios showed practically no differences (difference <2%).

DISCUSSION

Motivation of the Innovative PVR With Active Contracting Band Insertion Procedures

How to manage the residual symptoms for repaired ToF cases such as pulmonary regurgitation has gradually become a great challenge for clinicians. Even though PVR could be an effective treatment for pulmonary regurgitation, other symptoms such as

TABLE 6 | Mean ± SD RV ejection fraction and wall stress/strain data of seven TOF patients from 140 RV/LV models with active or passive band(s) and seven models without band.

Plan	Begin filling			Begin ejection			EF	ΔEF
	RV vol (ml)	Stress (kPa)	Strain	RV vol (ml)	Stress (kPa)	Strain		
Baseline	226.84 ± 121.2	4.22 ± 1.63	0.022 ± 0.008	359.19 ± 158.41	62.89 ± 14.81	0.292 ± 0.062	38.71 ľ 5.73%	
A000	225.48 ± 121.6	4.05 ± 1.56	0.020 ± 0.006	349.76 ± 158.75	60.13 ± 14.82	0.291 ± 0.065	37.34 ± 5.56%	−1.37 ± 0.50%
A010	222.19 ± 120.26	4.19 ± 1.69	0.021 ± 0.006	359.66 ± 158.55	63.35 ± 14.52	0.297 ± 0.067	40.21 ± 5.86%	1.50 ± 0.63%
A015	220.41 ± 119.53	4.38 ± 1.84	0.022 ± 0.005	359.41 ± 158.49	63.41 ± 14.52	0.297 ± 0.067	40.67 ± 5.87%	1.96 ± 0.75%
A020	218.44 ± 118.7	4.62 ± 2.05	0.024 ± 0.006	359.47 ± 158.58	63.19 ± 14.85	0.297 ± 0.067	41.22 ± 5.85%	2.51 ± 0.80%
P000	226.01 ± 144.44	4.17 ± 1.58	0.021 ± 0.007	352.08 ± 157.36	61.01 ± 14.74	0.293 ± 0.065	37.67 ± 5.52%	−1.04 ± 0.44%
P010	223.02 ± 120.21	4.17 ± 1.56	0.022 ± 0.006	359.43 ± 157.91	63.45 ± 14.26	0.297 ± 0.067	39.89 ± 5.83%	1.18 ± 0.37%
P015	221.34 ± 119.58	4.34 ± 1.66	0.023 ± 0.006	359.12 ± 157.82	63.57 ± 14.23	0.296 ± 0.067	40.33 ± 5.84%	1.62 ± 0.44%
P020	219.47 ± 118.89	4.59 ± 1.82	0.025 ± 0.006	359.03 ± 157.84	63.70 ± 14.23	0.296 ± 0.067	40.84 ± 5.84%	2.13 ± 0.53%
AP000	225.02 ± 121.37	3.88 ± 1.59	0.019 ± 0.006	344.56 ± 157.62	57.99 ± 15.86	0.287 ± 0.064	36.39 ± 5.43%	−2.32 ± 0.85%
AP010	220.54 ± 119.53	4.03 ± 1.73	0.021 ± 0.005	358.93 ± 158.60	63.49 ± 14.89	0.297 ± 0.066	40.52 ± 5.79%	1.81 ± 0.77%
AP015	217.91 ± 118.43	4.32 ± 1.95	0.023 ± 0.005	359.10 ± 158.72	63.95 ± 14.70	0.298 ± 0.066	41.28 ± 5.77%	2.57 ± 0.91%
AP020	214.99 ± 117.19	4.71 ± 2.26	0.026 ± 0.005	358.90 ± 158.61	64.32 ± 14.64	0.298 ± 0.066	42.07 ± 5.77%	3.36 ± 1.07%
B000	225.72 ± 121.25	4.08 ± 1.58	0.021 ± 0.006	350.83 ± 157.53	59.57 ± 14.05	0.293 ± 0.066	37.48 ± 5.76%	−1.23 ± 0.79%
B010	223.21 ± 120.01	4.14 ± 1.54	0.022 ± 0.006	358.94 ± 157.96	63.17 ± 14.05	0.298 ± 0.066	39.73 ± 5.82%	1.02 ± 0.32%
B015	221.48 ± 119.34	4.30 ± 1.59	0.023 ± 0.005	358.76 ± 157.84	63.11 ± 14.10	0.297 ± 0.066	40.19 ± 5.8%	1.48 ± 0.35%
B020	219.73 ± 118.5	4.53 ± 1.67	0.025 ± 0.005	358.32 ± 157.72	63.53 ± 14.08	0.298 ± 0.066	40.61 ± 5.81%	1.90 ± 0.40%
APB000	224.39 ± 121.35	3.86 ± 1.52	0.019 ± 0.006	339.24 ± 157.82	56.15 ± 14.84	0.287 ± 0.064	35.44 ± 5.32%	−3.27 ± 1.26%
APB010	218.76 ± 118.86	4.10 ± 1.63	0.022 ± 0.005	358.67 ± 158.54	65.11 ± 13.93	0.303 ± 0.066	40.98 ± 5.77%	2.27 ± 0.89%
APB015	215.42 ± 117.36	4.52 ± 1.92	0.025 ± 0.005	358.68 ± 158.66	65.75 ± 13.68	0.303 ± 0.066	41.90 ± 5.72%	3.19 ± 1.00%
APB020	211.73 ± 115.66	5.03 ± 2.30	0.029 ± 0.005	358.53 ± 158.63	66.31 ± 13.48	0.304 ± 0.067	42.90 ± 5.68%	4.19 ± 1.11%

RV dysfunction may sometimes be irreversible after the PVR surgery (Geva et al., 2004, 2010; Kim and Emily, 2016). del Nido and Geva et al. (2010) proposed an aggressive surgical treatment including removing scar tissue and remodeling RV in order to improve RV function after PVR. However, the randomized clinical trial showed that the addition of surgical remodeling of the RV during PVR resulted in no measurable improvement in RV function (Geva et al., 2010).

PVR with active contracting band insertion aims to improve RV EF by assisting the ventricle to contract. In theory, the band should actively contract during systole, decreasing RV volume, and yet, the band should also be able to relax during diastole. These processes were reflected in our models: the mean ± SD RV volume values of models E020 at end ejection/begin filling were 211.73 ± 115.66 ml, which was lower than that of baseline models (226.84 ± 121.20 ml, p = 0.016). At end filling/begin ejection, no significant difference was found between E020 and baseline RV volume values (358.53 ± 158.63 ml vs. 359.19 ± 158.41 ml, p = 0.813) since the active bands were able to relax and did not resist the ventricle to expand in diastole phase (filling phase). Compared with our previous work on band insert surgery simulation, 147 models were constructed for seven patients with repaired TOF in this paper, vs. only one patient was used in previous paper (Yu et al., 2020). The purpose of this study was to demonstrate patient variations in post-PVR outcome using the proposed active contraction band options. Results from this seven-patient study were consistent with previous findings: RV ejection fraction values of all seven patients increased after the surgery with active contraction band insertion. The mean ± SD RV △EF value from the seven patients with plan E was 4.19 ± 1.11%, which is a significant improvement. Meanwhile, among all seven studied TOF patients, only two of them had increased EF values after pulmonary valve surgery (P1 and P6). The clinical mean ± SD ΔEF was -4.97 ± 7.44% based on actual patient pre- and post-PVR data. This is the proof of the concept that PVR with active contraction band insertion may have the potential to improve post-PVR RV cardiac function measured by ejection fraction for repaired ToF patients.

Availability of Active Contracting Band

The idea of active band is completely theoretical currently. Our simulation provided the possible outcome of the surgery if such active contraction band could be made available. There are potential techniques that could be applied to manufacture active contracting band in the future including (a) using stem cells to cultivate muscle or (b) artificial mechanical muscle (Chou and Hannaford, 1996; Baar et al., 2005; Proulx et al., 2011; Sugimoto et al., 2017; Thomalla and Van deVen, 2018). Baar et al. (2005) used neonatal rat cardiomyogenic cells to construct a cylinder formed by cardiomyocytes which could be electrically induced to contract and showed positive inotropy and chronotropy (Baar et al., 2005). Proulx et al. (2011) described a band made by seeding human mesenchymal stem cells onto bundled fibrin microthreads and stitched through a collagen gel. Another viable solution is to use mechanical artificial active contraction device such as hydraulic or pneumatic McKibben actuator. McKibben actuator, also known as McKibben artificial muscle, is assembled with an internal elastic deformable tube

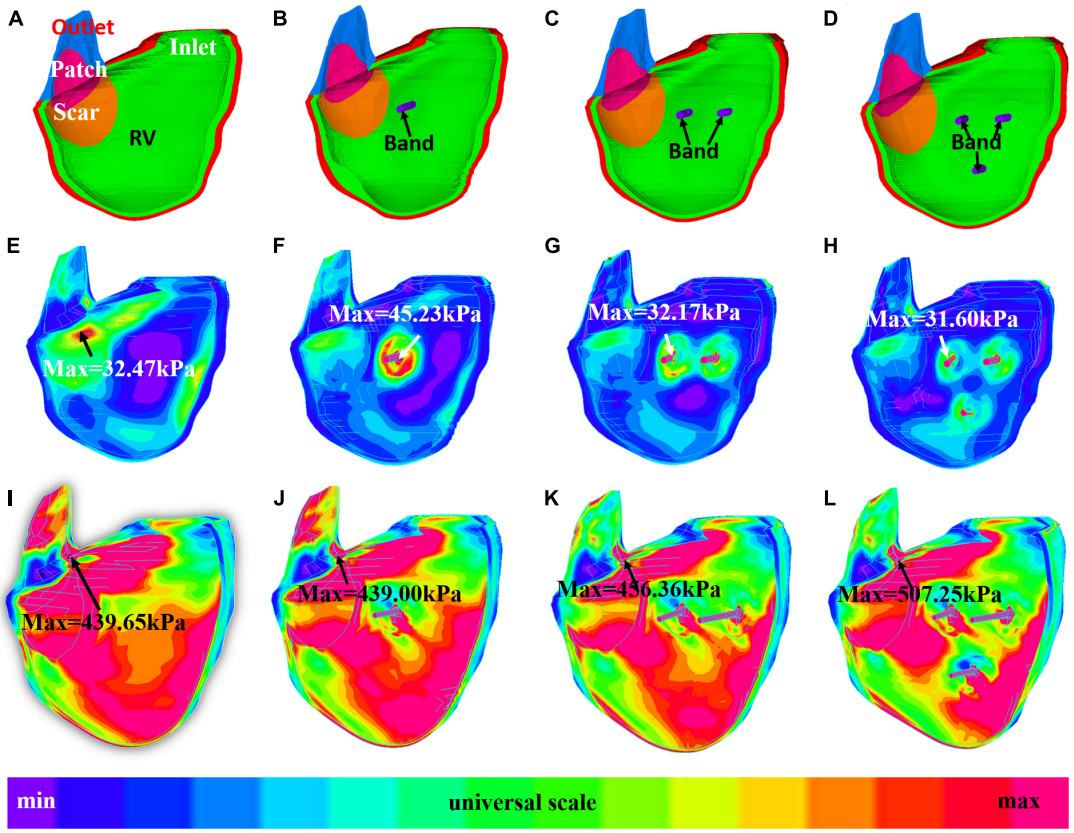

FIGURE 6 | Stress plots of patient 5 from the no-band model and three active band models with band contraction ratio of 20%. **(A)** Model with no band, zero load. **(B)** Plan A: model with one band, zero load. **(C)** Plan C: model with two bands, zero-load. **(D)** Plan E: model with three bands, zero load. **(E)** Model with no band, begin filling. **(F)** Plan A: model with one band, begin filling. **(G)** Plan C: model with two bands, begin filling. **(H)** Plan E: model with three bands, begin filling. **(I)** Model with no band, begin ejection. **(J)** Plan A: model with one band, begin ejection. **(K)** Plan C: model with two bands, begin ejection. **(L)** Plan E: model with three bands, begin ejection.

surrounded by non-extensible threads weaved into an external mesh shell (Chou and Hannaford, 1996; Sugimoto et al., 2017; Thomalla and Van deVen, 2018). Such actuators were already widely used in robot technology. Takuma et al. designed a robot with McKibben actuators which could operate periodic motions including walking (Sugimoto et al., 2017). Maximum active contraction ratio of McKibben actuator could reach about 30% (Chou and Hannaford, 1996; Thomalla and Van deVen, 2018), which would be enough to meet the contracting requirement of our active contraction band used in PVR surgeries.

Use of Ejection Fraction as a Measure of Surgical Outcome

RV EF was used as the measure of RV function in this paper because it is commonly used in practice and by many investigators, and it serves our demonstration purpose well. The concept is simple and calculation is easy. Outcome comparisons of different band options using a single indicator (EF) are straightforward and easy to understand. However, since it is only one number, it is lacking detailed local information for more careful evaluation of RV functions. 3D stress/strain distributions could compensate RV EV when detailed analysis is desired. RV kinetic energy due to its deformation in systole can be calculated as needed for a more detailed analysis. Since we currently have structure-only models, we would not be able to calculate the energy from the flow side and perform the analysis for that part. We are currently working on the corresponding fluid-structure interaction models. Full analysis from both structure and flow side will be reported when results become available. Those details will be helpful in band design and development of related tissue regeneration techniques (Tang et al., 2013).

It is true that EF is a crude measure of ventricular function (LV and RV), does not reliably reflect the functional status of the myocardium, and is sensitive to preload and afterload (so-called loading conditions). Despite these well-known limitations, EF has remained n inexplicably strong predictor of clinical outcomes in numerous diseases that affect the RV (e.g., repaired TOF) and the LV (e.g., aortic stenosis, hypertension, ischemic heart disease). These observation have been confirmed by numerous large studies. However, why EF is such a strong predictor of clinical outcomes is not fully understood. So, if the goal is to detect subtle abnormalities of heart muscle function, there are more sensitive tools. If the goal is to use it as a predictor of

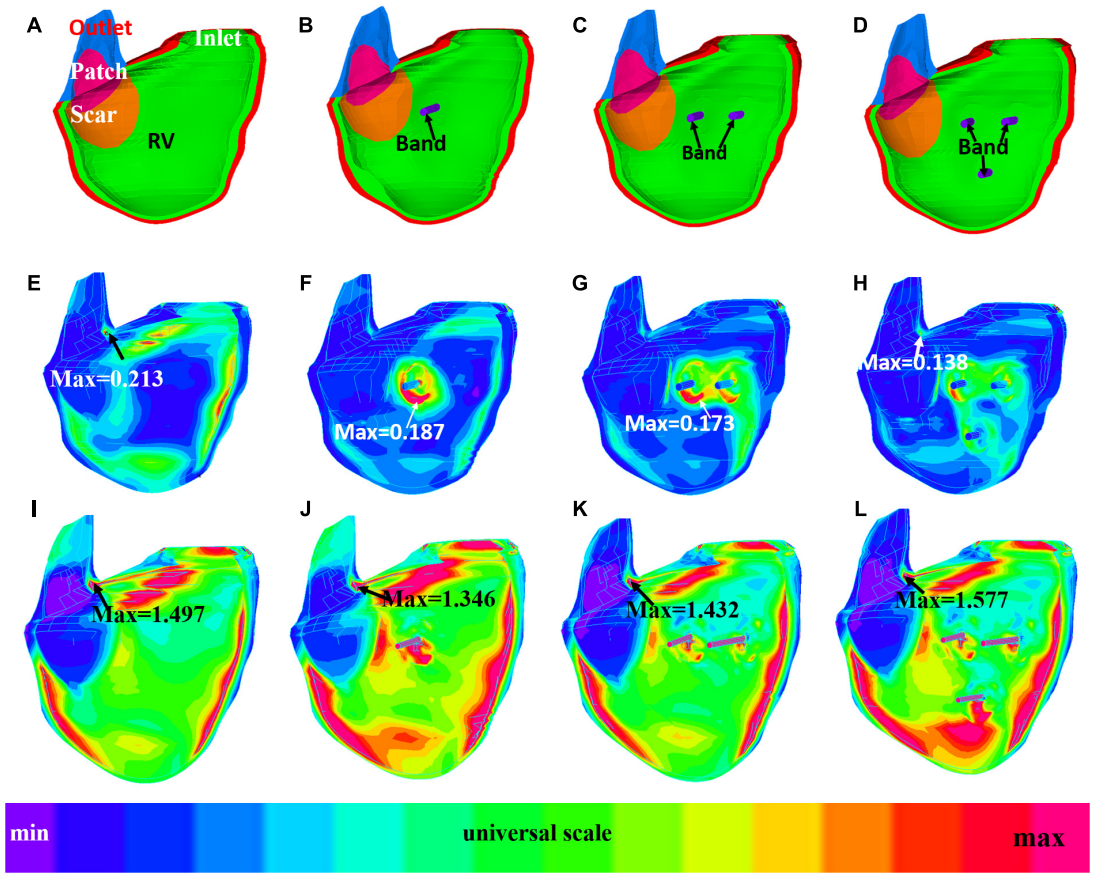

FIGURE 7 | Strain plots of patient 5 from the no-band model and three active band models with band contraction ratio of 20%. **(A)** Model with no band, zero load. **(B)** Plan A: model with one band, zero load. **(C)** Plan C: model with two bands, zero load. **(D)** Plan E: model with three bands, zero-load. **(E)** Model with no band, begin filling. **(F)** Plan A: model with one band, begin filling. **(G)** Plan C: model with two bands, begin filling. **(H)** Plan E: model with three bands, begin filling. **(I)** Model with no band, begin ejection. **(J)** Plan A: model with one band, begin ejection. **(K)** Plan C: model with two bands, begin ejection. **(L)** Plan E: model with three bands, begin ejection.

clinical outcomes (which is what ultimately matters), EF is an excellent marker.

Validations

Validation is always ideal for computational modeling effort. It should be noted that the parameter determination process is a self-validation process in some sense. Our pre-PVR models were self-validated since patient-specific tissue material parameter values were carefully adjusted to match MRI-measured ventricle volume data. Since the ventricles remained to be the same post-PVR, using the same parameter values was natural for our post-PVR band models. Without actual clinical post-PVR data, using pre-PVR material properties gave us the best-effort approximations for our band models. Accuracies of simulation results including calculation of ventricle volumes and ejection fractions should be interpreted with that understanding.

Since materials with active-contraction properties are not currently available, direct validations using either patients or animal models are not possible at present time. Researchers have been working on myocardium regeneration for many years and encouraging progresses have been made. Clinical application of the active contraction band is what we would like to achieve in the future.

Potential Clinical Applications

Possible potential clinical implementation of PVR with active contracting bands primarily depends on the availability of the availability of the active contracting bands. This modeling study is the proof of the concept that PVR with active contraction band insertion may improve post-PVR RV cardiac function measured by ejection fraction for repaired ToF patients. The mean ± SD RV △EF value from the seven patients with plan E was 4.19 ± 1.11% (all patients had improved EF), which is a significant improvement over the actual PVR surgery data $\Delta EF = -4.97 \pm 7.44\%$. Meanwhile, among all seven studied TOF patients, only two of them had improved EF values after PVR (P1 and P6). A 9.16% average increase in RVEF compares favorably with published drug trials to treat heart failure where an improvement in LVEF of 3–4% resulted in a significant improvement in functional capacity (Aleksova et al., 2012).

Limitations

This paper used structure-only models to save model construction manpower and computing time (147 3D models). Fluid-structure interaction did not include algorithm that allows a more realistic simulation. Clearly, FSI models will provide a more complete structural and flow information. However, for our purpose, EF was used to measure surgical outcome for the surgical strategies under investigation. The model parameters in both structure-only and FSI will be adjusted to match MRI-measured ventricle volume data. Therefore, structure-only or FSI models will give the same EF. Another reason that structure-only model could be used as a good approximation to calculate EF is that ventricle volume is mainly determined by the flow pressure acting on the ventricle inner surface. The flow stress activating on ventricle inner surface could be decomposed into pressure (normal component) and flow shear stress (shear component). The magnitude of flow shear stress is nearly negligible compared with pressure. That was the reason we used structure-only models to save time. FSI models will take far more time to construct and will be needed when we investigate flow behaviors, valve functions, ventricle remodeling, etc.

Lack of validation is definitely a limitation. This was discussed in section "Use of Ejection Fraction as a Measure of Surgical Outcome."

Several other limitations exist in our modeling study: (a) patient-specific TOF RV/LV myofibril orientations should be included if available in the future; (b) localized tissue material properties were not available; and (c) flow behaviors and valve dynamics were not included in this study. We are working hard to obtain better ventricle data and improve our models.

DATA AVAILABILITY STATEMENT

The raw data supporting the conclusions of this article will be made available by the authors, without undue reservation.

ETHICS STATEMENT

The studies involving human participants were reviewed and approved by the Boston Children's Hospital Committee on Clinical Investigation. Written informed consent to participate in this study was provided by the participants' legal guardian/next of kin.

AUTHOR CONTRIBUTIONS

TG, RR, and PN collected the CMR and blood pressure data. KB did the biaxial test. HY, CY, XH, ZW, and DT did model construction. HY did statistical analysis. HY and DT wrote and revised the manuscript. All authors contributed to the article and approved the submitted version.

FUNDING

This research was supported in part by the National Natural Science Foundation of China (grants 11672001 and 81571691 to DT). Postgraduate Research & Practice Innovation Program of Jiangsu Province KYCX19_0110 (HY).

REFERENCES

Aleksova, A., Masson, S., Maggioni, A. P., Lucci, D., Urso, R., Staszewsky, L., et al. (2012). Effects of candesartan on left ventricular function, aldosterone and bnp in chronic heart failure. *Cardiovasc. Drugs Ther.* 26, 131–143. doi: 10.1007/s10557-012-6370-8

Alfakih, K., Plein, S., Thiele, H., Jones, T., Ridgway, J. P., and Sivananthan, M. U. (2010). Normal human left and right ventricular dimensions for MRI as assessed by turbo gradient echo and steady-state free precession imaging sequences. *J. Magn. Resonan. Imaging* 17, 323–329. doi: 10.1002/jmri.10262

Anagnostopoulos, P., Azakie, A., Natarajan, S., Alphonso, N., Brook, M. M., and Karl, T. R. (2007). Pulmonary valve cusp augmentation with autologous pericardium may improve early outcome for tetralogy of Fallot. *J. Thorac. Cardiovasc. Surg.* 133, 640–647. doi: 10.1016/j.jtcvs.2006.10.039

Axel, L. (2002). Biomechanical dynamics of the heart with MRI. *Annu. Rev. Biomed. Eng.* 4, 321–347. doi: 10.1146/annurev.bioeng.4.020702.153434

Baar, K., Birla, R., Boluyt, M. O., Borschel, G. H., Arruda, E. M., and Dennis, R. G. (2005). Self-organization of rat cardiac cells into contractile 3-D cardiac tissue. *FASEB J.* 19, 275–277.

Billiar, K. L., and Sacks, M. S. (2000). Biaxial mechanical properties of the natural and glutaraldehyde treated aortic valve cusp–Part I: experimental results. *J. Biomech. Eng.* 122, 23–30. doi: 10.1115/1.429624

Chou, C. P., and Hannaford, B. (1996). Measurement and modeling of mckibben pneumatic artificial muscles. *IEEE Trans. Robot. Autom.* 12, 90–102. doi: 10.1109/70.481753

Deng, L., Huang, X., Yang, C., Lyu, B., Duan, F., Tang, D., et al. (2018). Numerical simulation study on systolic anterior motion of the mitral valve in hypertrophic obstructive cardiomyopathy. *Int. J. Cardiol.* 266, 167–173. doi: 10.1016/j.ijcard.2018.01.062

Geva, T., Gauvreau, K., Powell, A. J., Cecchin, F., Rhodes, J., Geva, J., et al. (2010). Randomized trial of pulmonary valve replacement with and without right ventricular remodeling surgery. *Circulation* 122, S201–S208.

Geva, T., Sandweiss, B. M., Gauvreau, K., Lock, J. E., and Powell, A. J. (2004). Factors associated with impaired clinical status in long-term survivors of tetralogy of Fallot repair evaluated by magnetic resonance imaging. *J. Am. Coll. Cardiol.* 43, 1068–1074. doi: 10.1016/j.jacc.2003.10.045

Hunter, P. J., Pullan, A. J., and Smaill, B. H. (2003). Modeling total heart function. *Annu. Rev. Biomed. Eng.* 5, 147–177. doi: 10.1146/annurev.bioeng.5.040202.121537

Jones, M. I., and Qureshi, S. A. (2018). Recent advances in transcatheter management of pulmonary regurgitation after surgical repair of tetralogy of Fallot. *F1000Res.* 7:679. doi: 10.12688/f1000research.14301.1

Kerckhoffs, R. C., Neal, M. L., Gu, Q., Bassingthwaighte, J. B., Omens, J. H., and McCulloch, A. D. (2007). Coupling of a 3D finite element model of cardiac ventricular mechanics to lumped systems models of the systemic and pulmonic circulation. *Ann. Biomed. Eng.* 35, 1–18. doi: 10.1007/s10439-006-9212-7

Kim, Y. Y., and Emily, Rl (2016). Approach to residual pulmonary valve dysfunction in adults with repaired tetralogy of Fallot. *Heart* 102, 1520–1526. doi: 10.1136/heartjnl-2015-309067

McCulloch, A. D., Waldman, L., Rogers, J., and Guccione, J. M. (1992). Large-scale finite element analysis of the beating heart. *Crit. Rev. Biomed. Eng.* 20, 427–449.

Motta, S. E., Lintas, V., Fioretta, E. S., Hoerstrup, S. P., and Emmert, M. (2017). Off-the-shelf tissue engineered heart valves for in situ regeneration: current state, challenges and future directions. *Expert Rev. Med. Devices* 15, 35–45. doi: 10.1080/17434440.2018.1419865

Murphy, J. G., Gersh, B. J., Mair, D. D., Fuster, V., McGoon, M. D., Kirklin, J. W., et al. (1993). Long-term outcome in patients undergoing surgical repair of tetralogy of Fallot. *N. Engl. J. Med.* 329, 593–599. doi: 10.1056/nejm199308263290901

Nash, M. P., and Hunter, P. J. (2000). Computational mechanics of the heart, from tissue structure to ventricular function. *J. Elastic.* 61, 113–141. doi: 10.1007/0-306-48389-0_4

Nordsletten, D., McCormick, M., Kilner, P. J., Hunter, P., Kay, D., and Smith, N. P. (2011). Fluid–solid coupling for the investigation of diastolic and systolic human left ventricular function. *Int. J. Numeric. Methods Biomed. Eng.* 27, 1017–1039. doi: 10.1002/cnm.1405

Peskin, C. S. (1977). Numerical analysis of blood flow in the heart. *J. Com. Phys.* 25, 220–252. doi: 10.1016/0021-9991(77)90100-0

Peskin, C. S. (1989). A three-dimensional computational method for blood flow in the heart. *J. Comp. Phys.* 81, 372–405. doi: 10.1016/0021-9991(89)90213-1

Proulx, M. K., Carey, S. P., Ditroia, L. M., Jones, C. M., Fakharzadeh, M., Guyette, J. P., et al. (2011). Fibrin microthreads support mesenchymal stem cell growth while maintaining differentiation potential. *J. Biomed. Mater. Res. A.* 96, 301–312. doi: 10.1002/jbm.a.32978

Saber, N. R., Gosman, A. D., Wood, N. B., Kilner, P. J., Charrier, C. L., and Firman, D. N. (2001). Computational flow modeling of the left ventricle based on in vivo MRI data: initial experience. *Ann. Biomech. Eng.* 29, 275–283. doi: 10.1114/1.1359452

Sacks, M. S., and Chuong, C. J. (1993). Biaxial mechanical properties of passive right ventricular free wall myocardium. *J. Biomech. Eng.* 115, 202–205. doi: 10.1115/1.2894122

Sanchez-Quintana, D., Anderson, R. H., and Ho, S. Y. (1996). Ventricular myoarchitecture in tetralogy of Fallot. *Heart* 17, 280–286. doi: 10.1136/hrt.76.3.280

Sen, D. G., Najjar, M., Yimaz, B., Levasseur, S. M., Kalessan, B., Quaegebeur, J., et al. (2016). Aiming to preserve pulmonary valve function in tetralogy of fallot repair: comparing a new approach to traditional management. *Pediatr. Cardiol.* 37, 818–825. doi: 10.1007/s00246-016-1355-1

Sugimoto, Y., Nakanishi, D., Nakanishi, M., and Osuka, K. (2017). Stability and joint stiffness analysis of legged robot's periodic motion driven by McKibben pneumatic actuator. *Adv. Robot.* 31, 441–452. doi: 10.1080/01691864.2016.1273135

Tang, D., Yang, C., Geva, T., and del Nido, P. J. (2008). Patient-specific MRI-based 3D FSI RV/LV/Patch models for pulmonary valve replacement surgery and patch optimization. *J. Biomech. Eng.* 130:041010.

Tang, D., Yang, C., Geva, T., Rathod, R. H., Yamauchi, H., Gooty, V., et al. (2013). A multiphysics modeling approach to develop right ventricle pulmonary valve replacement surgical procedures with a contracting band to improve ventricle ejection fraction. *Comput. Struct.* 122, 78–87. doi: 10.1016/j.compstruc.2012.11.016

Thomalla, S. D., and Van deVen, J. D. (2018). Modeling and Implementation of the Mckibben actuator in hydraulic systems. *IEEE Trans. Robot.* 34, 1593–1602.

Yang, C., Tang, D., Geva, T., Rathod, R. H., Yamauchi, H., Gooty, V., et al. (2013). Using contracting band to improve right ventricle ejection fraction for patients with repaired tetralogy of fallot, a modeling study using patient-specific cmr-based two-layer anisotropic models of human right and left ventricles. *J. Thorac. Cardiovasc. Surg.* 145, 285–293. doi: 10.1016/j.jtcvs.2012.03.009

Yu, H., del Nido, P. J., Geva, T., Yang, C., Wu, Z., Rathod, R. H., et al. (2020). Multi-band surgery for repaired tetralogy of fallot patients with reduced right ventricle ejection fraction: a pilot study. *Front. Physiol.* 11:198. doi: 10.3389/fphys.2020.00198

Yu, H., Tang, D., Geva, T., Yang, C., Wu, Z., Rathod, R. H., et al. (2019). Patient-specific in vivo right ventricle material parameter estimation for patients with tetralogy of fallot using mri-based models with different zero-load diastole and systole morphologies. *Int. J. Cardiol.* 276, 93–99. doi: 10.1016/j.ijcard.2018.09.030

Conflict of Interest: The authors declare that the research was conducted in the absence of any commercial or financial relationships that could be construed as a potential conflict of interest.

The reviewer AR-A declared a past collaboration with the authors TG and RR to the handling editor.

frontiers in Cardiovascular Medicine

ORIGINAL RESEARCH
published: 02 July 2021
doi: 10.3389/fcvm.2021.663767

Effect of Patient-Specific Coronary Flow Reserve Values on the Accuracy of MRI-Based Virtual Fractional Flow Reserve

Jackson Hair[1,2], *Lucas Timmins*[3,4], *Retta El Sayed*[2], *Habib Samady*[5] *and John Oshinski*[1,2]*

[1] Department of Radiology and Imaging Sciences, Emory University School of Medicine, Atlanta, GA, United States, [2] Department of Biomedical Engineering, Georgia Institute of Technology and Emory University, Atlanta, GA, United States, [3] Department of Biomedical Engineering, University of Utah, Salt Lake City, UT, United States, [4] Scientific Computing and Imaging Institute, University of Utah, Salt Lake City, UT, United States, [5] Division of Cardiology, Department of Medicine, Emory School of Medicine, Atlanta, GA, United States

OPEN ACCESS

Edited by:
Jolanda Wentzel,
Erasmus Medical Center, Netherlands

Reviewed by:
Erhan Tenekecioglu,
University of Health Sciences, Turkey
Kelvin Kian Loong Wong,
University of Adelaide, Australia

***Correspondence:**
John Oshinski
jnoshin@emory.edu

Specialty section:
This article was submitted to Cardiovascular Imaging, a section of the journal Frontiers in Cardiovascular Medicine

Received: 03 February 2021
Accepted: 28 May 2021
Published: 02 July 2021

Citation:
Hair J, Timmins L, El Sayed R, Samady H and Oshinski J (2021) Effect of Patient-Specific Coronary Flow Reserve Values on the Accuracy of MRI-Based Virtual Fractional Flow Reserve. Front. Cardiovasc. Med. 8:663767. doi: 10.3389/fcvm.2021.663767

The purpose of this study is to investigate the effect of varying coronary flow reserve (CFR) values on the calculation of computationally-derived fractional flow reserve (FFR). CFR reflects both vessel resistance due to an epicardial stenosis, and resistance in the distal microvascular tissue. Patients may have a wide range of CFR related to the tissue substrate that is independent of epicardial stenosis levels. Most computationally based virtual FFR values such as FFR_{CT} do not measure patient specific CFR values but use a population-average value to create hyperemic flow conditions. In this study, a coronary arterial computational geometry was constructed using magnetic resonance angiography (MRA) data acquired in a patient with moderate CAD. Coronary flow waveforms under rest and stress conditions were acquired in 13 patients with phase-contrast magnetic resonance (PCMR) to calculate CFR, and these flow waveforms and CFR values were applied as inlet flow boundary conditions to determine FFR based on computational fluid dynamics (CFD) simulations. The stress flow waveform gave a measure of the functional significance of the vessel when evaluated with the physiologically-accurate behavior with the patient-specific CFR. The resting flow waveform was then scaled by a series of CFR values determined in the 13 patients to simulate how hyperemic flow and CFR affects FFR values. We found that FFR values calculated using non–patient-specific CFR values did not accurately predict those calculated with the true hyperemic flow waveform. This indicates that both patient-specific anatomic and flow information are required to accurately non-invasively assess the functional significance of coronary lesions.

Keywords: CFR, FFR, MRI, CFD, vFFR

INTRODUCTION

Coronary artery disease (CAD) is responsible for half of all deaths attributed to cardiovascular disease, making it a leading cause of death globally (1, 2). Not all patients with CAD are at risk for adverse events, and it is therefore important to be able to correctly identify which patients would benefit from percutaneous coronary intervention (PCI). The gold standard for making this determination is through assessment of the functional significance of the stenosis by fractional flow reserve (FFR), which is approximated in the catheterization lab as the ratio of the pressure distal to a lesion over the proximal pressure (3). The pressure is expected to scale linearly with the flow rate if the resistance is constant and minimized, which is achieved through induction of hyperemia using an injected vasodilator—such as adenosine—and averaging measurements across multiple cardiac cycles (3). Therefore, this pressure ratio provides an approximation for the flow reduction caused by the plaque. Several studies have shown the benefits and efficacy of FFR in deciding who would benefit from PCI (4, 5), and FFR is the only diagnostic method for guiding coronary intervention that has shown any benefit to patient outcomes to date. Unfortunately, despite its proven efficacy, survey data from coronary interventions of intermediate stenoses have shown that FFR is used in only 6.1% of patients while 73.6% of patients are evaluated with angiography alone (6, 7). This underutilization can be attributed largely to the extra time and cost of the pressure wire, as well as the small but non-negligible risk to the patient. Therefore, there have been considerable efforts in recent years to develop non-invasive alternative methods of determining FFR.

A complimentary coronary physiologic measure to FFR is coronary flow reserve (CFR), which is defined as the ratio of hyperemic flow to basal flow (8). In healthy individuals, CFR has been shown to be ∼4.8, which indicates hyperemic flow is almost five times greater than basal flow (8, 9). Unlike FFR, CFR is affected by both epicardial vessel resistance due to stenoses and distal tissue bed vascular function (10). Because CFR is affected by total vascular resistance and FFR only reflects epicardial vessel resistance, *CFR value can vary substantially between patients with the same FFR values* (**Figure 1**) (10–13). CFR can be measured clinically through magnetic resonance imaging (MRI) and positron emission tomography (PET) and can be estimated through single-proton emission computed tomography (SPECT).

Virtual fractional flow reserve (vFFR) combines non-invasive coronary imaging with computational fluid dynamics (CFD) to estimate FFR. To compute vFFR, certain boundary conditions must be defined in the patient-specific model, including: the lateral wall geometry which describes the coronary luminal boundary; the inlet flow rate to simulate hyperemic coronary blood flow; and flow-splitting ratios at vessel branch points. Computed tomography (CT) has proven to be an attractive modality for defining these boundary conditions due to its excellent spatial resolution which can characterize the coronary arterial geometry (14). However, it cannot quantify the other boundary conditions directly due to its inability to measure flow. With CT-derived vFFR (FFR_{CT}), the total myocardial mass of the individual can be estimated from the CT image data, which allows for an estimation of the patient-specific basal coronary arterial flow, or the flow through the coronary arteries when the subject is at *rest*, through allometric scaling (14). The rationale behind this is that the rate of myocardial blood flow should be proportionate to the amount of myocardial tissue (15). This relationship, however, only applies to *basal* coronary flow, while FFR is defined only during hyperemic, or stress, flow conditions.

To account for this requirement of hyperemic flow, the predicted basal flow must be artificially scaled by an estimated CFR value, which has been done through direct modification of the resistances within the model (14). The epicardial resistance is automatically adjusted through the presence of a stenosis, but CFR is determined by both the epicardial and microvascular responses to stress, and CT has no means through which it can estimate patient-specific microvascular resistance. Therefore, the microvascular resistance must be scaled using a *population-average* response rather than a *patient-specific* one (14). Because FFR quantifies the pressure drop across the stenotic lesion and the pressure gradient is directly related to the flow rate *via* Ohm's Law, it follows that any linear change in the inlet flow would likely result in a proportionate change in the calculated vFFR. *Therefore, it is hypothesized that basal flow scaled by patient-non-specific CFR cannot accurately calculate vFFR.*

The purpose of this study is to investigate the effect of varying CFR values on the calculated vFFR value. A coronary geometry exhibiting an intermediate stenosis was acquired through magnetic resonance angiography (MRA) and produced a constant epicardial resistance for a series of computational simulations. Basal and hyperemic (under adenosine administration) coronary flow waveforms were acquired in a series of 13 patients using phase-contrast MRI (PCMR) which enabled calculation of CFR. Flow through the coronary geometry was simulated at a range of hyperemic flow conditions determined by the measured CFR values and enabled determination of the resulting vFFR.

METHODS

Overview of Methodology

An overview of the experimental approach is presented below, followed by a detailed explanation of each component of the methodology. First, a coronary arterial computational model was constructed using MRA image data acquired from a patient presenting with moderate CAD. Second, resting and hyperemic time-dependent flows through the coronary sinus were measured in a separate cohort of patients ($n = 13$) undergoing clinically indicated stress cardiovascular MRI exam. Third, CFD was used to determine vFFR values with various applied hyperemic flow conditions, including: (i) *in vivo* hyperemic flow by PCMR measurement (true vFFR), (ii) basal flow scaled by the patient-specific CFR (patient-scaled vFFR), and (iii) basal flow scaled by population-average CFR estimates (cohort-scaled vFFR). These scaled vFFR values were compared with the true vFFR values to assess correlation and concordance, thereby evaluating how changing the hyperemic flow response—as measured by CFR—as well as time-dependent flow patterns affect vFFR prediction with

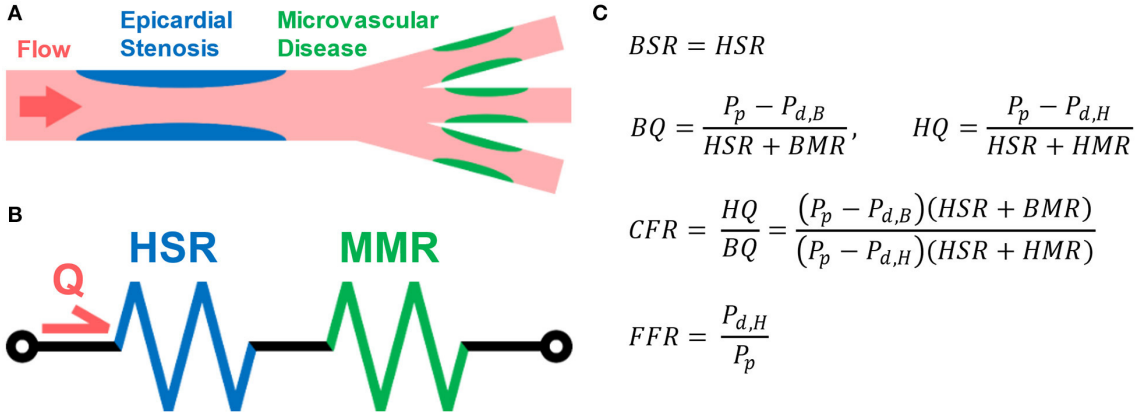

FIGURE 1 | Illustration of Coronary Flow Reserve (CFR). **(A)** Coronary arterial blood flow travels through both epicardial vessels and microvasculature. Each can contribute to the total resistance. The resistance due to the epicardial vessels (blue) is the stenotic resistance (SR), and the resistance due to the microvasculature (green) is the myocardial microvascular resistance (MMR). **(B)** The flow can be modeled using a circuit analogy in which the total resistance is the sum of the SR and MR. **(C)** MR during basal (BMR) and hyperemic (HMR) flow conditions should vary, but SR should remain the same in both (HSR). The basal flow rate (BQ) can be estimated as the difference in the proximal pressure (P_p) and distal, basal pressure ($P_{d,B}$) divided by the total basal resistance. Similarly, the hyperemic flow rate (HQ) can be estimated using the distal, hyperemic pressure ($P_{d,H}$) and total hyperemic resistance. CFR is defined as the ratio of HQ to BQ, while FFR is the ratio of $P_{d,H}$ to P_p. Through these equations, the theoretical interdependence of CFR and FFR can be seen.

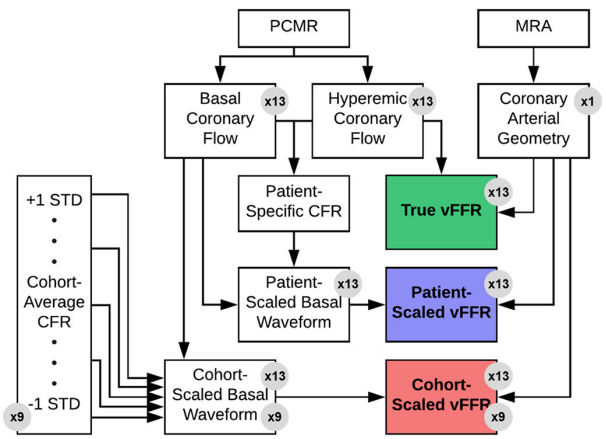

FIGURE 2 | Overview of experimental design. A single left coronary artery tree was acquired from an MRA of a patient with a 50% stenosis in the LAD. Hyperemic and basal flow waveforms were measured in patients ($n = 13$) using PCMR. Each hyperemic flow waveform was applied as an inflow boundary conditions for the anatomic model to determine the true vFFR value *via* CFD. Each basal flow waveform was then scaled by either the patient-specific or one of nine estimated CFR value to approximate the hyperemic flow. These scaled flow rates were then applied as inflow boundary CFD simulations to estimate vFFR—i.e., patient-scaled vFFR or cohort-scaled vFFR. These scaled vFFR values were then compared to the corresponding true vFFR values.

a constant geometry. A graphical flowchart of these methods can be seen in **Figure 2**. The study was approved by the university's Institutional Review Board.

The purpose of this study was to investigate the effects of flow conditions on vFFR, not specifically to validate vFFR measurements against an invasive gold standard. Because the variable of interest in this study is the simulated hyperemic flow, the arterial geometry was maintained as a constant to isolate the effect of the flow behavior. Therefore, the calculated vFFR values are not intended to be representative of any particular subject's true functional significance; rather, they are only meant to be compared against other non-invasive estimates to see how the predicted values change with variable flow.

Coronary Anatomy Model Geometry

A patient presenting with NYHA class III ischemic heart failure was imaged prior to cardiac resynchronization therapy as part of an IRB-approved study (16). Imaging was performed on a 3 T MRI scanner (MAGNETOM Trio, Siemens Healthcare) using a six-element phased-array cardiac coil. A 3D, whole-heart, navigator- and ECG-gated inversion-recovery FLASH sequence with a centric *k*-space trajectory acquired coronary images in the transverse plane at a resolution of $0.64 \times 0.64 \times 0.75$ mm^3. Images were acquired in diastole during the slow infusion of a gadolinium-based contrast agent (17). The left main (LM), left anterior descending (LAD), and left circumflex (LCX) arteries were segmented from the image data using a Frangi vessel enhancing post-processing filter followed by a colliding fronts segmentation algorithm (Vascular Modeling Toolkit) (18–20). The resulting triangulated surface geometry was imported into Geomagic (Geomagic, Inc.) to generate a smooth 3D surface. This surface was imported into ICEM meshing software (ANSYS, Inc.) to generate the 3D computational mesh. Flow extensions were added to the inlet and each outlet by projecting the edge contour in line with the local trajectory of the boundary surface (**Figure 3**). The model was generated with ~100,000 tetrahedral elements and 150,000 six-node pentahedral elements comprising eight boundary layers with a linear growth factor of 1.1 such that each innermost element was approximately the same volume as

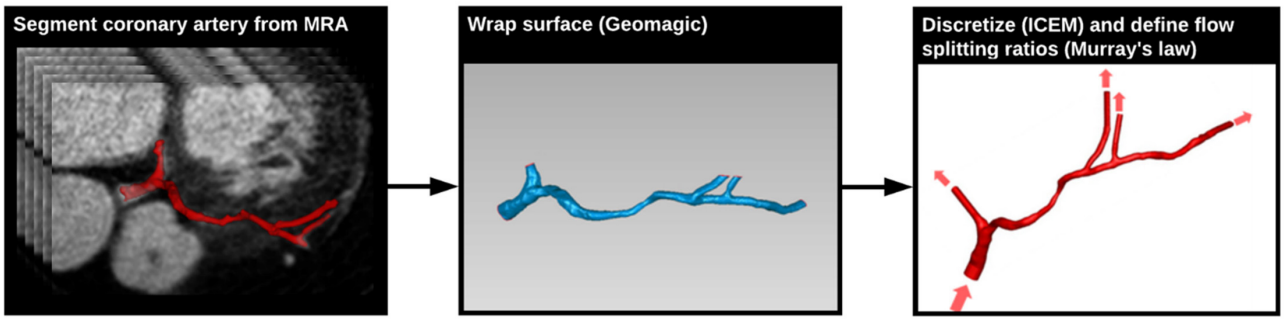

FIGURE 3 | Generation of coronary arterial geometry from MRA data. The left main (LM), left anterior descending (LAD), and left circumflex (LCX) arteries were segmented from a 3D MRA dataset data using the Vascular Modeling Toolkit (VMTK) **(left)**. The resulting surface geometry was imported into Geomagic to generate a smooth 3D surface **(center)**. This surface was imported into ICEM meshing software to generate the 3D computational mesh, and transient CFD simulations were run using Fluent **(right)**. Flow boundary conditions were based on PCMR measured flows.

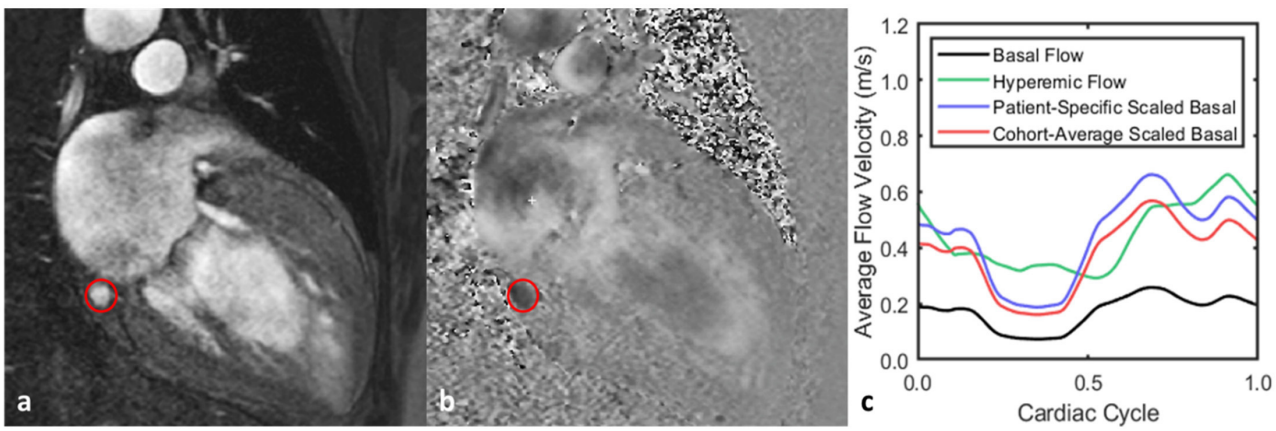

FIGURE 4 | Representative flow waveform measurement for one patient. **(a,b)** Magnitude and phase images acquired from PCMR acquisition with the coronary sinus outlined. **(c)** Both the basal and hyperemic flows were acquired using PCMR, and the basal flow was then scaled by a range of CFR values. When the basal flow is scaled by the patient-specific CFR—2.8—, the time-average flow rate is the same for both it and the hyperemic flow. Scaling the basal flow by the cohort-average CFR—2.2—produces the same basal waveform but with a different time-average flow rate from the hyperemic flow.

the adjacent tetrahedral element. Previously analysis of patient-specific models of epicardial coronary vessels has demonstrated solution independence at this mesh density (21).

Coronary Flow Measurements

Coronary sinus flow measurements were acquired in patients (n = 13) who had been clinically indicated for a cardiac stress MRI at Emory University Hospital on a 1.5 T scanner (MAGNETOM Avanto^{fit}, Siemens Healthcare) using a twenty-element phased-array cardiac coil (22–24). As part of the routine scan, a low-resolution axial 3D volume was first acquired for planning purposes. Multiplanar reformation of this volume determined a plane which perpendicularly intersected the proximal coronary sinus immediately adjacent to its ostium into the right atrium (**Figures 4A,B**). An ECG-gated, 2D PCMR cine was acquired on this plane during a breath-hold with a field-of-view of 350 × 306 mm, an in-plane pixel spacing of 0.68 mm, and a slice thickness of 6 mm. The velocity-encoding value (VENC) in each scan was initially set at 60 cm · s^{-1} and adjusted if aliasing was observed in the velocity-encoded image. Each patient was imaged once during a resting state and again following a 3 min infusion of intravenous adenosine at a rate of 140 μg · kg^{-1} · min^{-1} to induce maximal coronary hyperemia.

Following data acquisition, images were exported offline and analyzed using the freely available software, Segment version 2.0 (25). For each image stack, the magnitude and phase images were coupled and used to identify the luminal contours of the target vessel. A constant region-of-interest (ROI) was used across each temporal phase, and the ROI size was maintained when evaluating repeated measurements of the same vessel. Static tissue regions at the chest walls were automatically identified and used to calculate a second-order polynomial map to represent the estimated phase error and correct for this (25). The through-plane velocities of the pixels contained within the ROI were then added to provide a time-dependent flow waveform. This procedure was repeated for images acquired both during rest

and during stress. Based on previously reported measurements of coronary arterial flow rates (26–28), the left coronary arterial flow rate was assumed to comprise ∼2 thirds of the total coronary flow. The measured coronary sinus flow waveforms were then scaled by this value to give an estimation of the inflow waveform of the LM.

Hyperemic Flow Conditions for CFD Simulations

Various hyperemic flow conditions were applied to evaluate their effects on computed vFFR values. The first condition was the pulsatile hyperemic flow measured *in vivo* for each patient, which was used to define the true vFFR against which the other predicted vFFR values would be compared. Next, the patient-specific CFR value was calculated by taking the ratio of time-averaged, hyperemic-to-basal flow rates across the cardiac cycle. For each patient, the measured basal flow was scaled by the patient-specific CFR value to give a flow waveform with the same time-averaged flow rate as the measured hyperemic flow (**Figure 4**). This flow was used to compute the patient-scaled vFFR. Lastly, the basal flow rate was scaled by a series of global estimates of the CFR which were not specific to the patient but were representative of the cohort as a whole. In total, nine patient-non-specific CFR values were used to cover the range of one standard deviation above and below the cohort average value. Each of these computed waveforms were used to compute a cohort-scaled vFFR value for the patients.

CFD and vFFR Calculation

Transient (i.e., pulsatile) CFD simulations were run using Fluent (ANSYS, Inc.). There were 13 patients on whom coronary flow measurements were obtained, and for each of these patients 11 vFFR values were computed: the true vFFR found using the actual hyperemic flow waveform, the patient-scaled vFFR found by scaling the basal waveform with the patient-specific CFR, and nine cohort-scaled vFFR values found using the patient-non-specific CFR estimates and the basal waveform. These patient-non-specific CFR estimates were constant across the entire cohort.

For each case, the simulated hyperemic flow rate was prescribed as a time-varying blunt inlet flow boundary condition, inlet pressure was set at 100 mmHg, and mass flow splits, which were derived from Murrays law, were applied at each outlet flow surface (29). The transient solution was computed across three pulsatile cardiac cycles comprising 300 time steps, each at a heart rate of 60 beats per minute. Blood was modeled as Newtonian with a density of $1{,}060\,\mathrm{kg}\cdot\mathrm{m}^{-3}$ and dynamic viscosity of $0.0035\,\mathrm{Pa}\cdot\mathrm{s}$. Because the PCMR flow measurements were acquired across only 18 temporal phases, the waveforms were resampled to 300 time steps using a first order linear interpolation scheme followed by a lowpass filter to create a smooth waveform with the same time-averaged flow rate. We used the SIMPLE algorithm for pressure-velocity coupling and second-order Green-Gauss node-based discretization for momentum and pressure. For each time step, convergence was achieved once the residuals of momentum and continuity fell below 10^{-5}. The computed pressure was then sampled along the centerline of the vessel and divided by the inlet pressure to calculate vFFR along the length of the vessel, in accordance with clinical practice. The clinically relevant vFFR value—found 4 mm distal to the region of minimal lumen area—was then time averaged and recorded.

Statistical Analysis

Across all tested CFR values—both patient-specific and patient-non-specific—, the error of the computed scaled vFFR was calculated in relation to the true vFFR found with the corresponding hyperemic waveform. Within each simulated CFR group, a two-tailed, paired *t*-test was used to evaluate that error at a significance level of 0.05. Correlation between each scaled vFFR value and its corresponding true vFFR value was calculated through the Pearson correlation coefficient, and concordance was evaluated through a Bland–Altman analysis and calculation of Lin's concordance correlation coefficient (30, 31).

RESULTS

The CFR values for the cohort ranged from 1.2 to 4.1 with a mean value of 2.2 ± 0.98. The difference between the various scaled vFFR values and the true vFFR (termed vFFR error) was determined across all 13 patients. Paired comparison of the patient-specific vFFR with the true vFFR produced a mean vFFR error of -0.02 ± 0.02 with a *p*-value of 0.004; scaling the basal flow waveforms by the cohort-average CFR of 2.2, however, gave an average error of -0.03 ± 0.1 and a *p*-value of 0.236 (**Figure 5A**). Mean vFFR error was seen to monotonically decrease with increasing simulated CFR value, and, in general, the distribution of the error was seen to be larger with deviation from the cohort-average CFR, and increasing significance was observed on either end of the range of tested values (**Figure 5A**). The patient-specific vFFR produced the smallest error variance with the true vFFR, and their relationship was seen to be strongly linear; conversely, the cohort-average vFFR showed a very weak linearity when plotted against true vFFR (**Figure 5B**). None of the patient-non-specific CFR values were able to produce a coefficient of determination >0.34 (**Table 1**). Similarly, the patient-specific vFFR showed a strong concordance with true vFFR, while the cohort-average showed a very weak concordance (**Figure 5C**). Across all patient-non-specific CFR values simulated, the concordance correlation coefficient was seen to be between 0.14 and 0.34 (**Table 1**).

DISCUSSION

The major findings of this study are: (1) scaling the basal coronary flow waveform by a patient-non-specific CFR estimate *cannot* provide predictive results for all individuals within a cohort, and (2) using the patient-specific CFR to scale the basal waveform yields vFFR values which are strongly predictive of those found with the hyperemic flow waveform.

Myocardial ischemia can result from epicardial disease, microvascular disease, or a combination of both. Clinical

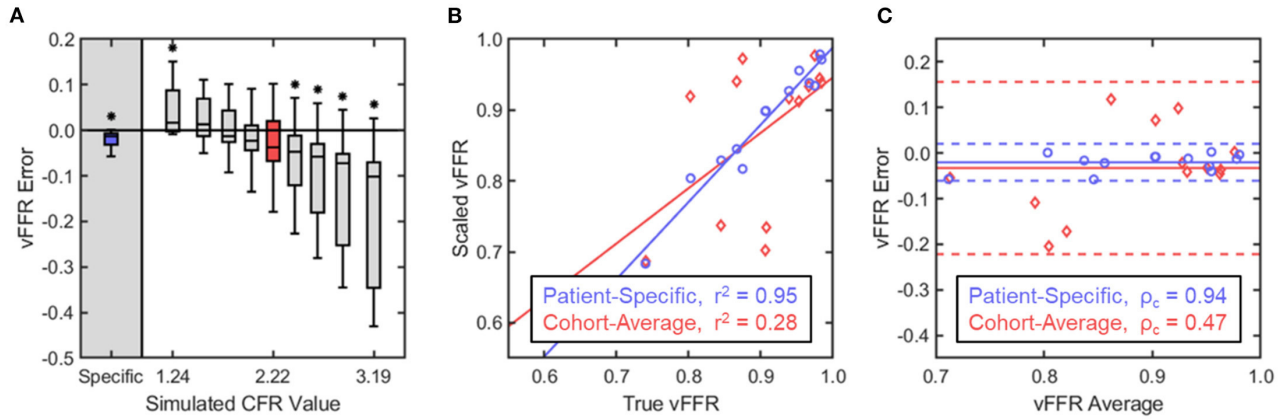

FIGURE 5 | Statistical analysis of vFFR estimation with variable flow conditions. **(A)** vFFR error was defined as the difference in the scaled vFFR value calculated with the basal waveform and the true vFFR value calculated with the hyperemic waveform. Within each group, the boxes represent the interquartile range and median while the whiskers indicate the 10 and 90th percentiles. Comparison within each simulated CFR group against the true vFFR was performed through a paired, two-way *t*-test, with significance determined for $p < 0.05$. **(B)** Scaled vFFR values were plotted against the corresponding true vFFR values for two CFR groups: (1) the patient-specific CFR values and (2) the cohort-average CFR value of 2.2. Linear regression determined a line of best-fit for each group, and Pearson's correlation coefficient determined the linearity of the relationship. **(C)** A Bland–Altman analysis and calculation of Lin's concordance correlation coefficient was performed to assess the concordance of the relationship. For each match-pair of true vFFR and scaled vFFR, the difference between the two values was plotted against their average. The solid lines indicate the mean vFFR error while the dashed lines indicate two standard deviations from the mean.

TABLE 1 | Statistical results for all simulated CFR values.

	Patient-specific					**Cohort-average**				
CFR		1.24	1.54	1.78	2.01	***2.22***	2.43	2.66	2.89	3.19
p-value	**0.004**	0.019	0.191	0.883	0.400	**0.236**	0.043	0.018	0.009	0.005
Pearson's r^2	**0.95**	0.34	0.34	0.34	0.34	**0.28**	0.34	0.34	0.34	0.34
Lin's ρ_c	**0.91**	0.21	0.31	0.34	0.33	**0.25**	0.25	0.21	0.17	0.14

Patient-specific and Cohort-average columns are bold for emphasis.

indication for intervention in epicardial stenosis has been shown to be most successful when guided by the FFR, which approximates the reduction in flow through a given vessel due to an anatomic narrowing. Accurate measurement of this flow reduction relies on the assumption of maximal hyperemia, in which the downstream microvascular resistance is minimized. The physiologic response to hyperemia is, however, patient-specific, and depends on both the stenotic resistance contributed by the epicardial vessels and the downstream hyperemic microvascular resistance. Though it is possible to estimate the value of hyperemic stenotic resistance (HSR) through anatomic measurements and allometric scaling, the hyperemic myocardial resistance (HMR) can only be measured through direct quantification of flow (10). The comorbidity of both epicardial and microvascular coronary disease is not uncommon; however, the presence or severity of one cannot be used as a direct indicator of the presence or severity of the other. In 2017 it was shown that as few as 68% of patients with moderate coronary stenosis had concordant FFR and CFR findings (10).

vFFR is an emerging methodology that seeks to provide a non-invasive alternative to invasive catheter-based FFR. Arguably the most well-known of these approaches is FFR_{CT} (14). As CT is incapable of quantifying the CFR or HMR, its flow boundary conditions rely on population-average physiologic responses to hyperemia. Though results of this methodology for vFFR have shown some success in predicting invasive FFR, the correlation between the two measurements does not indicate strong correlation ($r^2 = 0.54$), and its diagnostic accuracy has shown to suffer substantially when predicting FFR values near the clinical cutoff (0.80) where specificity is most needed by clinicians (32). It is possible that these limitations in efficacy are due at least in part to the assumptions made regarding HMR and, by extension, CFR.

Scaling the basal flow waveform by the time-averaged, patient-specific CFR does not replicate the exact hyperemic time-dependent flow waveform for a given patient. This is due to the interactions between the myocardium and the microvasculature, resulting in phasic fluctuations of the intracoronary resistance (33). Since the intracoronary resistance is not uniform across the cardiac cycle during resting flow, it has varying levels of response to hyperemic induction as well, resulting in a time-dependent CFR (**Figure 4C**). However, because FFR is calculated as the time-averaged ratio of distal and proximal pressure in the coronary arteries, it was expected to be insensitive to temporal

fluctuations and depend only on the time-averaged flow rate and epicardial anatomy. By scaling the basal flow waveform by the patient-specific CFR, the resulting vFFR values were seen to show very strong correlation and concordance with those calculated using the hyperemic waveform, which would indicate support for this hypothesis. However, the significant paired differences between the two groups does suggest that these waveforms may not be completely interchangeable for all populations. In general, across all CFR values tested, we observed an underestimation for vFFR when using the basal waveforms from the patients, which would indicate that differences in the temporal behavior between these two waveforms can result in significantly different vFFR calculations. Though the concordance and correlation values for this cohort were high, these results suggest that vFFR is not completely insensitive to time-dependent behaviors, and therefore more thorough testing should be performed to investigate which populations can interchangeably use a basal or hyperemic waveform for the calculation of vFFR.

Scaling the basal flow by some non-patient-specific CFR values near the population average produced vFFR values that were, on average, not significantly different from hyperemic vFFR, but deviation from the population average resulted in increasingly large deviations in estimating vFFR. Predictive power of CFR-scaled vFFR for hyperemic vFFR was never strong for any estimated CFR value, and correlation was mostly independent of the estimated CFR as well. This indicates that patient-specific characterization of the hyperemic flow rate needs to be used to accurately predict vFFR. Therefore, the choice in imaging modalities is limited to those that can measure both anatomy and flow. One could use a combination of imaging modalities to accomplish this, such as using both CT—to acquire the coronary anatomy and estimate the basal coronary flow rate through allometric scaling as described by Choy and Kassab (15)—and positron emission tomography (PET)—to assess the patient-specific CFR and determine the hyperemic response (34). Perhaps a more feasible clinical solution would be to use MRI which can acquire both anatomy and flow directly (35, 36). The use of PCMR to directly estimate the pressure gradient across a coronary stenosis has also been shown to be feasible, which has the potential to eliminate the need for CFD flow simulations altogether (37).

There are some limitations to this study. All comparisons were made between artificial vFFR values without direct comparison with an invasive FFR measure. As was stated previously, such a comparison would not be valid for this study, as the coronary geometry was maintained as a constant so that the effects of flow variation could be isolated. The results presented here strongly indicate that calculating vFFR without patient-specific hyperemic flow conditions can produce inaccurate results. It is possible that other sources of error may exist estimating FFR through vFFR, including inaccuracies within the coronary geometry or the outflow boundary conditions. Additional studies to test each of these variables would be needed to draw such conclusions. It is acknowledged that blood is a non-Newtonian fluid; however, the Reynolds (Re) numbers in these computational models were moderate (Re $\approx$ 250–400), and the impact of the non-Newtonian behavior of blood on the hemodynamic environment is minimal (38). Finally, the computational models assumed a rigid coronary wall. We acknowledge that the presented models only approximate the *in vivo* conditions, and that application of a validated fluid-structure interaction (FSI) computational framework may provide improve accuracy in the predicted hemodynamics measures.

The coronary inlet flow rates used within this study were not directly measured from the patients' coronary arteries but were linearly scaled waveforms acquired from the coronary sinuses. This approximation was used as direct arterial flow measurement through PCMR could not be feasibly integrated into the clinical protocol. Though the arterial flow and the coronary sinus flow rates do not exhibit identical temporal behaviors, the functional behavior of one should give an indication of the other due to their similarities. Due to the aforementioned suspected temporal dependence of vFFR, it is possible that this approximation may have resulted in the patient-specific scaled vFFR group performing better or worse than the equivalent arterial flow waveform would have in estimating the true vFFR; however, this approximation should not undercut the conclusion that using patient-non-specific hyperemic response cannot give a strongly predictive estimation of the true vFFR.

This study found that scaling the basal flow waveform by an estimated patient-non-specific CFR will not accurately predict the vFFR calculated using the actual hyperemic flow waveform; using the patient-specific CFR, however, was seen to provide more consistent and accurate measurements of vFFR. The necessity for having patient-specific hyperemic flow behavior means that assumptions about CFR cannot be used to scale the patient's basal flow prior to its use as a boundary condition without significantly sacrificing the model's predictive power. It is recommended to execute additional studies to identify the extent to which the temporal behavior affects the computed vFFR.

DATA AVAILABILITY STATEMENT

The raw data supporting the conclusions of this article will be made available by the authors, without undue reservation.

ETHICS STATEMENT

The studies involving human participants were reviewed and approved by Emory University Institutional Review Board. The patients/participants provided their written informed consent to participate in this study.

AUTHOR CONTRIBUTIONS

JH and JO developed the hypothesis and planned the methodology. JH oversaw the image acquisition and constructed the vessel geometry. RE performed the computational simulations with oversight from JH and LT. HS provided

clinical perspectives to help inform the discussion. All authors reviewed and approved the final manuscript.

FUNDING

This work was supported by National Science Foundation Graduate Research Fellowship (Hair) and National Institute of Biomedical Imaging and Bioengineering, grant numbers R01-EB027774 (JO) and R01-HL150608 (LT).

ACKNOWLEDGMENTS

We would also like to thank Deborah Painter and Varuna for technical support provided during image acquisition.

REFERENCES

1. Mozaffarian D, Benjamin EJ, Go AS, Arnett DK, Blaha MJ, Cushman M, et al. Heart disease and stroke statistics—2015 update: a report from the American Heart Association. *Circulation*. (2015) 131:e29–322. doi: 10.1161/CIR.0000000000000152
2. Harold JG, Bass TA, Bashore TM, Brindis RG, Brush JE Jr, Burke JA, et al. ACCF/AHA/SCAI 2013 update of the clinical competence statement on coronary artery interventional procedures: a report of the American College of Cardiology Foundation/American Heart Association/American College of Physicians Task Force on Clinical Competence and Training (Writing Committee to Revise the 2007 Clinical Competence Statement on Cardiac Interventional Procedures). *J Am Coll Cardiol*. (2013) 62:357–96. doi: 10.1161/CIR.0b013e318299cd8a
3. Pijls NH, Van Gelder B, Van der Voort P, Peels K, Bracke FA, Bonnier HJ, et al. Fractional flow reserve a useful index to evaluate the influence of an epicardial coronary stenosis on myocardial blood flow. *Circulation*. (1995) 92:3183–93. doi: 10.1161/01.CIR.92.11.3183
4. Pijls NH, van Schaardenburgh P, Manoharan G, Boersma E, Bech JW, van't Veer M, et al. Percutaneous coronary intervention of functionally nonsignificant stenosis: 5-year follow-up of the DEFER Study. *J Am Coll Cardiol*. (2007) 49:2105–11. doi: 10.1016/j.jacc.2007.01.087
5. De Bruyne B, Pijls NH, Kalesan B, Barbato E, Tonino PA, Piroth Z, et al. Fractional flow reserve-guided PCI versus medical therapy in stable coronary disease. *N Engl J Med*. (2012) 367:991–1001. doi: 10.1056/NEJMoa1205361
6. Dattilo PB, Prasad A, Honeycutt E, Wang TY, Messenger JC. Contemporary patterns of fractional flow reserve and intravascular ultrasound use among patients undergoing percutaneous coronary intervention in the United States: Insights from the National Cardiovascular Data Registry. *J Am Coll Cardiol*. (2012) 60:2337–9. doi: 10.1016/j.jacc.2012.08.990
7. Shaw LJ, Berman DS, Maron DJ, Mancini GB, Hayes SW, Hartigan PM, et al. Optimal medical therapy with or without percutaneous coronary intervention to reduce ischemic burden: results from the Clinical Outcomes Utilizing Revascularization and Aggressive Drug Evaluation (COURAGE) trial nuclear substudy. *Circulation*. (2008) 117:1283–91. doi: 10.1161/CIRCULATIONAHA.107.743963
8. Gould KL, Lipscomb K, Hamilton GW. Physiologic basis for assessing critical coronary stenosis. Instantaneous flow response and regional distribution during coronary hyperemia as measures of coronary flow reserve. *Am J Cardiol*. (1974) 33:87–94. doi: 10.1016/0002-9149(74)90743-7
9. Wilson RF, Wyche K, Christensen BV, Zimmer S, Laxson DD. Effects of adenosine on human coronary arterial circulation. *Circulation*. (1990) 82:1595–606. doi: 10.1161/01.CIR.82.5.1595
10. Ahn SG, Suh J, Hung OY, Lee HS, Bouchi YH, Zeng W, et al. Discordance between fractional flow reserve and coronary flow reserve: insights from intracoronary imaging and physiological assessment. *JACC Cardiovasc Interv*. (2017) 10:999–1007. doi: 10.1016/j.jcin.2017.03.006
11. Johnson NP, Kirkeeide RL, Gould KL. Is discordance of coronary flow reserve and fractional flow reserve due to methodology or clinically relevant coronary pathophysiology? *JACC Cardiovasc Imaging*. (2012) 5:193–202. doi: 10.1016/j.jcmg.2011.09.020
12. Gould KL, Johnson NP, Bateman TM, Beanlands RS, Bengel FM, Bober R, et al. Anatomic versus physiologic assessment of coronary artery disease: role of coronary flow reserve, fractional flow reserve, and positron emission tomography imaging in revascularization decision-making. *J Am Coll Cardiol*. (2013) 62:1639–53. doi: 10.1016/j.jacc.2013.07.076
13. De Bruyne B, Fearon WF, Pijls NH, Barbato E, Tonino P, Piroth Z, et al. Fractional flow reserve–guided PCI for stable coronary artery disease. *N Engl J Med*. (2014) 371:1208–17. doi: 10.1056/NEJMoa1408758
14. Taylor CA, Fonte TA, Min JK. Computational fluid dynamics applied to cardiac computed tomography for noninvasive quantification of fractional flow reserve: scientific basis. *J Am Coll Cardiol*. (2013) 61:2233–41. doi: 10.1016/j.jacc.2012.11.083
15. Choy JS, Kassab GS. Scaling of myocardial mass to flow and morphometry of coronary arteries. *J Appl Physiol*. (1985) (2008) 104:1281–6. doi: 10.1152/japplphysiol.01261.2007
16. Hartlage GR, Suever JD, Clement-Guinaudeau S, Strickland PT, Ghasemzadeh N, Magrath RP III, et al. Prediction of response to cardiac resynchronization therapy using left ventricular pacing lead position and cardiovascular magnetic resonance derived wall motion patterns: a prospective cohort study. *J Cardiovasc Magn Reson*. (2015) 17:57. doi: 10.1186/s12968-015-0158-5
17. Yang Q, Li K, Liu X, Bi X, Liu Z, An J, et al. Contrast-enhanced whole-heart coronary magnetic resonance angiography at 3.0-T: a comparative study with X-ray angiography in a single center. *J Am Coll Cardiol*. (2009) 54:69–76. doi: 10.1016/j.jacc.2009.03.016
18. Sethian JA. A fast marching level set method for monotonically advancing fronts. *Proc Natl Acad Sci USA*. (1996) 93:1591–5. doi: 10.1073/pnas.93.4.1591
19. Sethian JA. *Level Set Methods and Fast Marching Methods: Evolving Interfaces in Computational Geometry, Fluid Mechanics, Computer Vision, and Materials Science. Vol. 3*. Cambridge: Cambridge University Press (1999).
20. Antiga L, Ene-Iordache B, Remuzzi A. Computational geometry for patient-specific reconstruction and meshing of blood vessels from MR and CT angiography. *IEEE Trans Med Imaging*. (2003) 22:674–84. doi: 10.1109/TMI.2003.812261
21. Timmins LH, Molony DS, Eshtehardi P, McDaniel MC, Oshinski JN, Samady H, et al. Focal association between wall shear stress and clinical coronary artery disease progression. *Ann Biomed Eng*. (2015) 43:94–106. doi: 10.1007/s10439-014-1155-9
22. Sakuma H, Kawada N, Takeda K, Higgins CB. MR measurement of coronary blood flow. *J Magnet Reson Imag Off J Int Soc Magnet Reson Med*. (1999) 10:728–33. doi: 10.1002/(SICI)1522-2586(199911)10:5<728::AID-JMRI17>3.0.CO;2-X
23. Kawada N, Sakuma H, Yamakado T, Takeda K, Isaka N, Nakano T, et al. Hypertrophic cardiomyopathy: MR measurement of coronary blood flow and vasodilator flow reserve in patients and healthy subjects. *Radiology*. (1999) 211:129–35. doi: 10.1148/radiology.211.1.r99ap36129
24. Hundley WG, Hillis LD, Hamilton CA, Applegate RJ, Herrington DM, Clarke GD, et al. Assessment of coronary arterial restenosis with phase-contrast magnetic resonance imaging measurements of coronary flow reserve. *Circulation*. (2000) 101:2375–81. doi: 10.1161/01.CIR.101.20.2375
25. Heiberg E, Sjögren J, Ugander M, Carlsson M, Engblom H, Arheden H. Design and validation of Segment-freely available software for cardiovascular image analysis. *BMC Med Imaging*. (2010) 10:1. doi: 10.1186/1471-2342-10-1
26. Johnson K, Sharma P, Oshinski J. Coronary artery flow measurement using navigator echo gated phase contrast magnetic resonance velocity mapping at 3.0 T. *J Biomech*. (2008) 41:595–602. doi: 10.1016/j.jbiomech.2007.10.010
27. Schiemann M, Bakhtiary F, Hietschold V, Koch A, Esmaeili A, Ackermann H, et al. MR-based coronary artery blood velocity measurements in patients without coronary artery disease. *Eur Radiol*. (2006) 16:1124–30. doi: 10.1007/s00330-005-0039-7

28. Marcus JT, Smeenk HG, Kuijer JP, Van der Geest RJ, Heethaar RM, Van Rossum AC. Flow profiles in the left anterior descending and the right coronary artery assessed by MR velocity quantification: effects of through-plane and in-plane motion of the heart. *J Comp Assist Tomogr*. (1999) 23:567–76. doi: 10.1097/00004728-199907000-00017
29. Murray CD. The physiological principle of minimum work: I. The vascular system and the cost of blood volume. *Proc Natl Acad Sci USA*. (1926) 12:207–14. doi: 10.1073/pnas.12.3.207
30. Bland JM, Altman DG. Statistical methods for assessing agreement between two methods of clinical measurement. *Lancet*. (1986) 327:307–10. doi: 10.1016/S0140-6736(86)90837-8
31. Lin LIK. A concordance correlation coefficient to evaluate reproducibility. *Biometrics*. (1989) 45:255–68. doi: 10.2307/2532051
32. Cook CM, Petraco R, Shun-Shin MJ, Ahmad Y, Nijjer S, Al-Lamee R, et al. Diagnostic accuracy of computed tomography-derived fractional flow reserve: a systematic review. *JAMA Cardiol*. (2017) 2:803–10. doi: 10.1001/jamacardio.2017.1314
33. Davies JE, Whinnett ZI, Francis DP, Willson K, Foale RA, Malik IS, et al. Use of simultaneous pressure and velocity measurements to estimate arterial wave speed at a single site in humans. *Am J Physiol Heart Circ Physiol*. (2006) 290:H878–H88. doi: 10.1152/ajpheart.00751
34. Nakazato R, Heo R, Leipsic J, Min JK. CFR and FFR assessment with PET and CTA: strengths and limitations. *Curr Cardiol Rep*. (2014) 16:484. doi: 10.1007/s11886-014-0484-5
35. Rivera-Rivera LA, Johnson KM, Turski PA, Wieben O. Pressure mapping and hemodynamic assessment of intracranial dural sinuses and dural arteriovenous fistulas with 4D flow MRI. *Am J Neuroradiol*. (2018) 39:485–7. doi: 10.3174/ajnr.A5494
36. Zhang L, Song X, Dong L, Li J, Dou R, Fan Z, et al. Additive value of 3T cardiovascular magnetic resonance coronary angiography for detecting coronary artery disease. *J Cardiovasc Magnet Reson*. (2018) 20:1–8. doi: 10.1186/s12968-018-0450-2
37. Deng Z, Fan Z, Lee SE, Nguyen C, Xie Y, Pang J, et al. Noninvasive measurement of pressure gradient across a coronary stenosis using phase contrast (PC)-MRI: a feasibility study. *Magn Reson Med*. (2017) 77:529–37. doi: 10.1002/mrm.26579
38. Ku DN. Blood flow in arteries. *Ann Rev Fluid Mech*. (1997) 29:399–434. doi: 10.1146/annurev.fluid.29.1.399

Conflict of Interest: The authors declare that the research was conducted in the absence of any commercial or financial relationships that could be construed as a potential conflict of interest.

frontiers in Bioengineering and Biotechnology

ORIGINAL RESEARCH
published: 08 July 2021
doi: 10.3389/fbioe.2021.643453

Effects of Choice of Medical Imaging Modalities on a Non-invasive Diagnostic and Monitoring Computational Framework for Patients With Complex Valvular, Vascular, and Ventricular Diseases Who Undergo Transcatheter Aortic Valve Replacement

*Melissa Baiocchi[1†], Shirley Barsoum[1†], Seyedvahid Khodaei[1], Jose M. de la Torre Hernandez[2], Sydney E. Valentino[3], Emily C. Dunford[3], Maureen J. MacDonald[3] and Zahra Keshavarz-Motamed[1,4,5]**

[1] Department of Mechanical Engineering, McMaster University, Hamilton, ON, Canada, [2] Hospital Universitario Marques de Valdecilla, IDIVAL, Santander, Spain, [3] Department of Kinesiology, McMaster University, Hamilton, ON, Canada, [4] School of Biomedical Engineering, McMaster University, Hamilton, ON, Canada, [5] School of Computational Science and Engineering, McMaster University, Hamilton, ON, Canada

OPEN ACCESS

Edited by:
Philippe Sucosky,
Kennesaw State University,
United States

Reviewed by:
Alejandro Roldán-Alzate,
University of Wisconsin-Madison,
United States
Jason Andrew Shar,
Wright State University, United States

***Correspondence:**
Zahra Keshavarz-Motamed
motamedz@mcmaster.ca

[†]These authors have contributed equally to this work

Specialty section:
This article was submitted to Biomechanics, a section of the journal Frontiers in Bioengineering and Biotechnology

Received: 18 December 2020
Accepted: 19 April 2021
Published: 08 July 2021

Citation:
Baiocchi M, Barsoum S, Khodaei S, de la Torre Hernandez JM, Valentino SE, Dunford EC, MacDonald MJ and Keshavarz-Motamed Z (2021) Effects of Choice of Medical Imaging Modalities on a Non-invasive Diagnostic and Monitoring Computational Framework for Patients With Complex Valvular, Vascular, and Ventricular Diseases Who Undergo Transcatheter Aortic Valve Replacement. Front. Bioeng. Biotechnol. 9:643453. doi: 10.3389/fbioe.2021.643453

Due to the high individual differences in the anatomy and pathophysiology of patients, planning individualized treatment requires patient-specific diagnosis. Indeed, hemodynamic quantification can be immensely valuable for accurate diagnosis, however, we still lack precise diagnostic methods for numerous cardiovascular diseases including complex (and mixed) valvular, vascular, and ventricular interactions (C3VI) which is a complicated situation made even more challenging in the face of other cardiovascular pathologies. Transcatheter aortic valve replacement (TAVR) is a new less invasive intervention and is a growing alternative for patients with aortic stenosis. In a recent paper, we developed a non-invasive and Doppler-based diagnostic and monitoring computational mechanics framework for C3VI, called C3VI-DE that uses input parameters measured reliably using Doppler echocardiography. In the present work, we have developed another computational-mechanics framework for C3VI (called C3VI-CT). C3VI-CT uses the same lumped-parameter model core as C3VI-DE but its input parameters are measured using computed tomography and a sphygmomanometer. Both frameworks can quantify: (1) global hemodynamics (metrics of cardiac function); (2) local hemodynamics (metrics of circulatory function). We compared accuracy of the results obtained using C3VI-DE and C3VI-CT against catheterization data (gold standard) using a C3VI dataset ($N = 49$) for patients with C3VI

who undergo TAVR in both pre and post-TAVR with a high variability. Because of the dataset variability and the broad range of diseases that it covers, it enables determining which framework can yield the most accurate results. In contrast with C3VI-CT, C3VI-DE tracks both the cardiac and vascular status and is in great agreement with cardiac catheter data.

Keywords: computational model, local hemodynamics, global hemodynamics, workload, diagnostic tool, doppler echocardiography, computed tomography

INTRODUCTION

Cardiovascular disease remains the primary cause of death worldwide and produces immense health and economic burdens (Roth et al., 2017; Ritchie and Roser, 2018; Benjamin et al., 2019). Cardiovascular disease is prevalent in 48.0% of adults and was responsible for 31.8% of all deaths in 2017 (Ritchie and Roser, 2018; Benjamin et al., 2019) and will remain the first cause of death globally by 2030. In the most general condition, several diseases of the valves, ventricles and the vascular system mechanically interact with one another and their combination exacerbate adverse effect of each isolated disease on the cardiovascular system (Généreux et al., 2013; Nombela-Franco et al., 2014; Blanke et al., 2016; Sotiropoulos et al., 2016). *This complex (and mixed) valvular, vascular and ventricular interactions (C3VI) is a complicated situation made even more challenging in the face of other cardiovascular pathologies.* C3VI represent situations in which a number of vascular, valvular and ventricular pathologies have mechanical interactions with each other. C3VI includes diseases of the heart valves such as stenosis and regurgitation of aortic and mitral valves, ventricular pathologies such as hypertrophy and heart failure, diseases of the vascular system such as hypertension as well as anatomical alterations due to interventions for C3VI such as transcatheter and surgical valve replacement (Elmariah et al., 2013; Généreux et al., 2013; Nombela-Franco et al., 2014; Pibarot et al., 2015; Ben-Assa et al., 2019).

"Cardiology is flow"(Richter and Edelman, 2006) and indeed quantifications of hemodynamics can be immensely valuable for precise diagnosis, however, we still lack precise diagnostic tools for various cardiovascular diseases (Di Carli et al., 2016). There has been an emerging conclusion by many researchers that valvular disease is a complex and mixed disease that also depends on the ventricle and the vascular system states (Yin, 1987; Burkhoff et al., 2005; Borlaug and Kass, 2008; Taylor and Steinman, 2010; Dweck et al., 2012; Antonini-Canterin et al., 2013; Keshavarz-Motamed et al., 2014, 2016; Ben-Assa et al., 2019; Ikonomidis et al., 2019; Keshavarz-Motamed et al., 2020; Sadeghi et al., 2020; Khodaei et al., 2021a,b). Indeed, the quantitative investigations of hemodynamics in patients with C3VI should take into account the interactive coupling of the valves, ventricle, and the vascular system. The conclusions and recommendations made in the previous studies can be boiled down to define the following two hemodynamics quantification capabilities that computational diagnostic frameworks are required to have to be clinically useful for patients with C3VI. The required quantities are local and global hemodynamics metrics (Yin, 1987; Burkhoff et al., 2005; Borlaug and Kass, 2008; Taylor and Steinman, 2010; Dweck et al., 2012; Antonini-Canterin et al., 2013; Ky et al., 2013; Keshavarz-Motamed et al., 2014, 2016; Ben-Assa et al., 2019; Ikonomidis et al., 2019; Seemann et al., 2019; Keshavarz-Motamed et al., 2020; Sadeghi et al., 2020) as follows: (1) *Metrics of circulatory function (local)*, e.g., fluid dynamics of the circulatory system, and (2) *Metrics of cardiac function (global)*, e.g., heart workload and its breakdown to the contributing disease components. Assessments of hemodynamics, if available, would offer valued information about the cardiac health condition and could be used for planning C3VI interventions and making critical clinical decisions with life-threatening risks. Presently, *there are no tools available to invasively or non-invasively quantify local and global hemodynamics.* Phase-contrast magnetic resonance imaging (MRI) can offer the fluid dynamics. However, MRI has a lower temporal resolution than doppler echocardiography (DE) (Elkins and Alley, 2007; Kilner et al., 2007). It is important to note that, due to the high risk of the magnetic field of the machine for patients with implanted devices, MRI cannot be used for patients with most implanted medical devices except safely for MRI-conditional devices (Orwat et al., 2014). Computed tomography (CT) has a high spatial resolution and can provide anatomical information with a high accuracy (Villarraga-Gómez et al., 2018), however, it has a low temporal resolution (Maleki and Esmaeilzadeh, 2012; Watson et al., 2018; Rehman and Makaryus, 2019) and cannot measure any (local and global) hemodynamic parameters. Furthermore, CT uses ionizing radiation (Burgstahler and Schroeder, 2007; Fleischmann et al., 2008) so receiving multiple scans increases the risk of developing cancer (Edwards and Arthurs, 2011; Pearce et al., 2012; Power et al., 2016; Rigsby et al., 2018). Cardiac catheterization is the gold standard for evaluating cardiac function but it is invasive and carries high risk (Omran et al., 2003) so it not practical for diagnosis in patients with cardiovascular diseases in regular clinical practice. Most importantly, cardiac catheterization offers access to flow and pressure only in very limited regions. Doppler echocardiography (DE) is risk-free, has high temporal resolution and can be used to investigate cardiac function in real time. Despite DE's potential advantages, there is no DE methods to quantify global hemodynamics and there is no method to quantify local hemodynamics accurately.

In this work, we seek for a method that can quantify global hemodynamics in addition to measures of local hemodynamics. Currently only lumped-parameter models have these capabilities due to the complexity of the cardiovascular system and

the unmanageable computational cost that 3-D models of hemodynamics in the entire cardiovascular system has. A diagnostic lumped parameter model framework that can quantify both *local* and *global* hemodynamics in patients with cardiovascular diseases should meet the following 2 conditions:

(1) The computational diagnostic framework should be developed based on the clinical patient-specific input parameters (e.g., hemodynamic metrics, clinical data and imaging). Upon development of a diagnostic lumped parameter model, its results should be validated against clinical data obtained using DE, MRI, and more specifically cardiac catheterization.
(2) The patient-specific input parameters for such development should be obtained *non-invasively* in each patient. It is critical to note that obtaining the input parameters invasively in patient refutes the entire purpose of the diagnostic computational mechanics framework.

There have been attempts for quantifying hemodynamics and for fundamental understanding of cardiovascular mechanics using lumped parameter modeling (Segers et al., 2003; Geven et al., 2004; Tanné et al., 2008; Garcia et al., 2009, 2005; Keshavarz-Motamed et al., 2011, 2014, 2015, 2016; Mynard et al., 2012; Broomé et al., 2013; de Canete et al., 2013; Revie et al., 2013; Benevento et al., 2015; Frolov et al., 2016; Mihalef et al., 2017; Duanmu et al., 2018; Li et al., 2018; Pant et al., 2018; Ben-Assa et al., 2019; Mao et al., 2019; Keshavarz-Motamed, 2020; Keshavarz-Motamed et al., 2020). All of these models [except (Keshavarz-Motamed et al., 2016; Keshavarz-Motamed, 2020)] cannot satisfy Requirements #1 and #2 above, although they were very important to provide fundamental understandings using idealized or hypothetical cases (Segers et al., 2003; Geven et al., 2004; Tanné et al., 2008; Garcia et al., 2009, 2005; Keshavarz-Motamed et al., 2011, 2014, 2015; Mynard et al., 2012; Broomé et al., 2013; de Canete et al., 2013; Revie et al., 2013; Benevento et al., 2015; Frolov et al., 2016; Mihalef et al., 2017; Duanmu et al., 2018; Li et al., 2018; Pant et al., 2018; Ben-Assa et al., 2019; Mao et al., 2019; Keshavarz-Motamed et al., 2020). Among all of the previous studies, the only lumped-parameter models that satisfy both Requirements #1 and #2 are one on coarctation of the aorta (Keshavarz-Motamed et al., 2016) and the other one on C3VI (Keshavarz-Motamed, 2020).

Transcatheter aortic valve replacement (TAVR) is an emerging minimally invasive intervention for patients with aortic stenosis across a broad risk spectrum. In this study, we contributed to proceeding computational mechanics as an influential revenue to augment clinical data and measurements, and medical imaging to develop diagnostic methods for monitoring, treatment planning and risk assessment in patients with C3VI who undergo TAVR in both pre and post TAVR states at no risk to the patient. *In patients with C3VI and TAVR, DE and CT are commonly used but MRI is not usually used due the risk of the magnetic field interactions with the implanted devices in the body of these patients.* We recently developed (Keshavarz-Motamed, 2020) a highly innovative, Doppler-based, non-invasive, image-based, patient-specific diagnostic and monitoring lumped parameter model framework for C3VI (called C3VI-DE) which uses input parameters, measured reliably using DE and a sphygmomanometer and satisfy both Requirements (#1 & #2). C3VI-DE, which has a lumped-parameter model at its core, quantifies (1) local hemodynamics (e.g., details of the physiological pulsatile flow and pressure in the heart and circulatory system); (2) global hemodynamics (e.g., cardiac function hemodynamic metrics, LV workload, instantaneous LV pressure and volume) and most importantly the individual share of each disease constituent on the global hemodynamics. *Currently, in clinical practice, none of these metrics can be acquired in patients non-invasively and if invasive procedures using cardiac catherization are conducted, the measured metrics are not complete.* Additionally, in the present work, we have developed another computational-mechanics framework for C3VI (called C3VI-CT). C3VI-CT uses the same lumped-parameter model core as C3VI-DE and was coupled with input parameters measured using CT and a sphygmomanometer (for simplicity, we called this latter framework C3VI-CT). The two frameworks differ in terms of the modality used for collecting the input parameters for the core lumped-parameter model. In the present work, we compared accuracy of the results obtained from C3VI-DE and C3VI-CT against cardiac catheterization data in forty-nine C3VI patients who underwent TAVR to determine which framework can yield the most accurate results. To the best of our knowledge, this is the first study that investigates the effects of choice of medical imaging modalities on the accuracy of a computational diagnostic framework for patients with C3VI in terms of local and global hemodynamic.

MATERIALS AND METHODS

Our recent non-invasive diagnostic and monitoring computational-mechanics framework for C3VI (called C3VI-DE) (Keshavarz-Motamed, 2020) uses limited input parameters, measured reliably using Doppler echocardiography and a sphygmomanometer. In this study, we have developed another computational-mechanics framework for C3VI (called C3VI-CT). C3VI-CT uses the same lumped-parameter model core as C3VI-DE and was coupled with input parameters measured using CT and a sphygmomanometer (**Figure 1**; Schematic diagrams of C3VI-DE and C3VI-CT). The developed algorithm (for both C3VI-DE and C3VI-CT) uses the following input parameters: systolic and diastolic brachial blood pressures, forward left ventricular outflow tract stroke volume, cardiac cycle duration, ejection time, ascending aorta area, left ventricular outflow tract area, aortic valve effective orifice area, mitral valve effective orifice area, and grading of the severity of aortic and mitral valves regurgitation. The algorithm consists of a parameter estimation algorithm and a lumped-parameter model that incorporates several sub-models to analyze any combination of mixed and complex valvular, vascular and ventricular diseases in

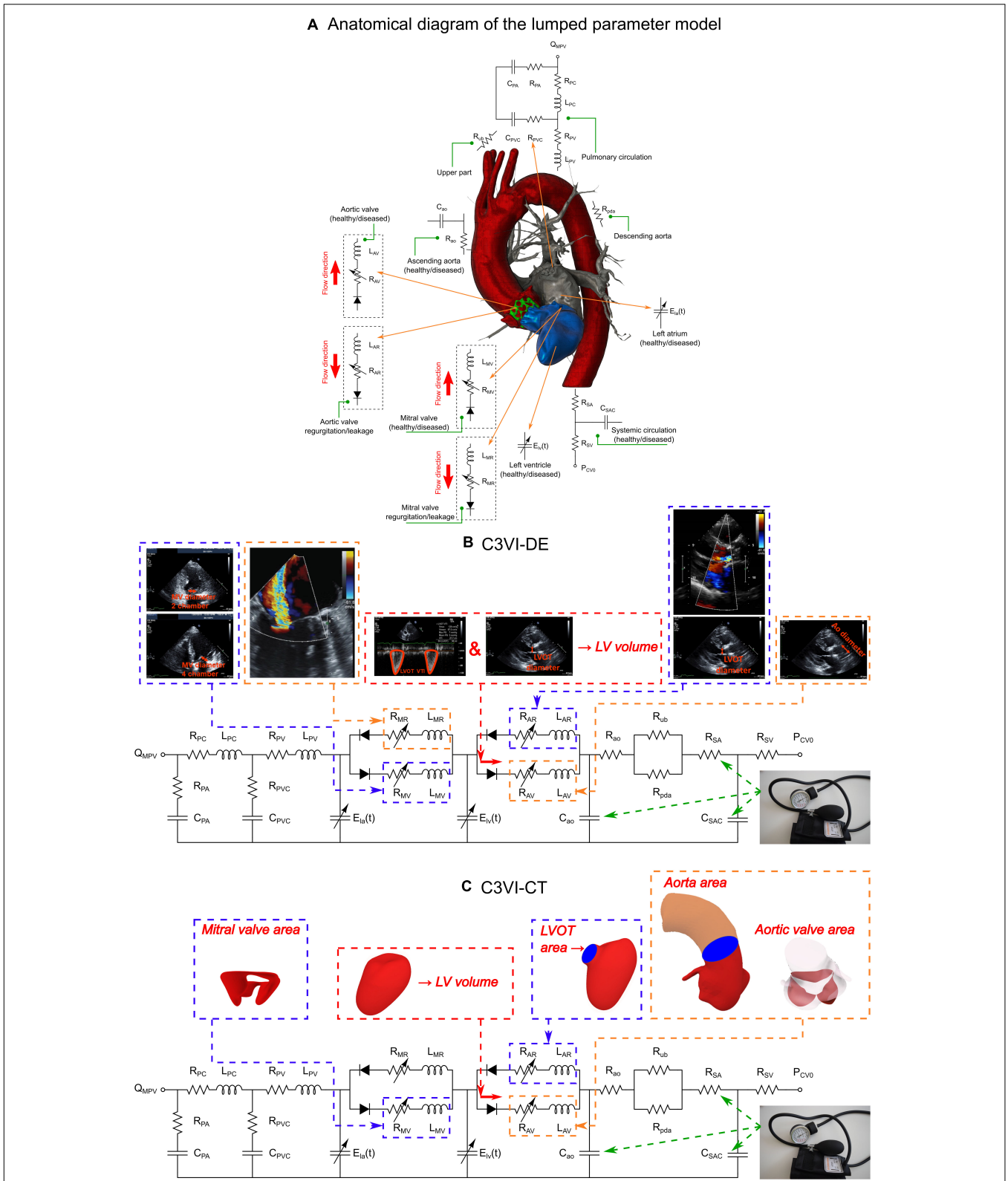

FIGURE 1 | Schematic diagram of the lumped parameter modeling. **(A)** Anatomical representation. **(B)** Electrical representation of C3VI-DE. This model includes four sub-models. (1) left atrium, (2) left ventricle, (3) aortic valve, (4) mitral valve, (5) systemic circulation, and (6) pulmonary circulation (**Table 1**, abbreviations). C3VI-DE input parameters were measured using DE and sphygmomanometer. **(C)** Electrical representation of C3VI-CT. Input parameters of C3VI-CT were measured using CT and sphygmomanometer.

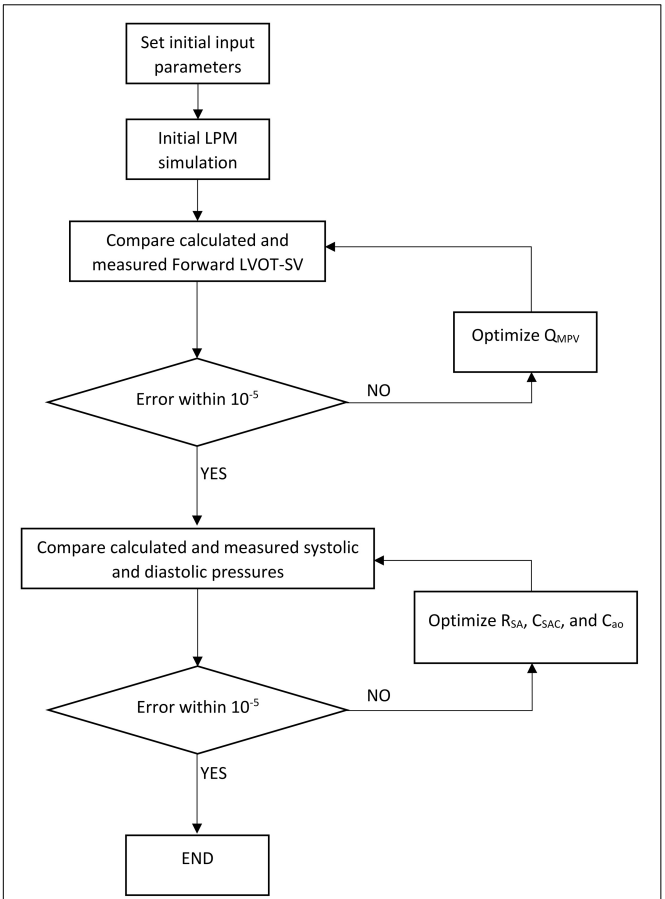

FIGURE 2 | Patient-specific response optimization flow chart. This flow chart was used for both C3VI-DE and C3VI-CT.

both pre and post interventional status (see **Figure 1** for Schematic diagrams; **Figure 2** for Flow chart; **Table 1** for Cardiovascular parameters).

Lumped Parameter Model

Cardiac-Arterial Model

Left ventricle

LV pressure and LV volume were coupled using a time varying elastance E(t) as follows:

$$E(t) = \frac{P_{LV}(t)}{V(t) - V_0} \tag{1}$$

where, $P_{LV}(t)$, $V(t)$, and V_0 are the LV time-varying pressure, time-varying volume, and unloaded volume, respectively (Keshavarz-Motamed et al., 2016). As explained by Keshavarz-Motamed (2020), to represent the normalized elastance function of the LV, we observed that among summation of Gaussian functions (Pironet et al., 2013; Chaudhry, 2015), Boltzmann Distribution (McDowell, 1999), double Hill function (Mynard et al., 2012; Broomé et al., 2013), and the latter provided the most physiologically accurate results (e.g., pressure, volume, and flow waveforms). The double Hill function which is a cooperative process (Moss et al., 2004), as physiologically expected from myocyte recruitment during preload and is modeled by a sigmoidal Hill function.

$$E(t) = N\left(\frac{\left(\frac{t}{\tau_1}\right)^{m_1}}{1+\left(\frac{t}{\tau_1}\right)^{m_1}}\right)\left(\frac{1}{1+\left(\frac{t}{\tau_2}\right)^{m_2}}\right) + E_{min} \tag{2}$$

$$N = \frac{E_{max} - E_{min}}{2} \tag{3}$$

where, N, τ_1, τ_2, m_1, m_2, and $E_{\min}$ are elastane normalization, ascending time translation, descending time translation, ascending gradient, descending gradient, and minimum elastance, respectively (see **Table 1**). A double Hill function was modeled the contraction and relaxation in the heart chambers (equation 2); the first term in brackets resembles to the contraction of the chamber and the second term in brackets resembles to the relaxation of the chamber. τ_1, τ_2, m_1, m_2 govern the time translation and gradient of the elastance function, respectively: (1) τ_1 and τ_2 are parameters that are functions of the cardiac cycle duration (T) and are calculated in each patient using the equations provided in **Table 1**; (2) m_1, m_2 are constant for all patients (see **Table 1** for more details). Parameter values used for the elastance function were adapted from Gleason and Braunwald (1962); Van de Werf et al. (1984); Brown and Ditchey (1988); Dell'Italia and Walsh (1988); Kass et al. (1988); Takeuchi et al. (1992); Senzaki et al. (1996); Stergiopulos et al. (1996); Maniar et al. (2003); Liang et al. (2009) to obtain physiologically waveforms (**Table 1**).

Left atrium

Left atrium pressure and LA volume were coupled using time varying elastance E(t), following the same method described above for the LV model (defined in equations 2 and 3) (Mynard et al., 2012; Broomé et al., 2013; **Table 1**). Additionally, a phase lag was used in the LA elastance function to account for the relative onset of contractions between LA and LV (Mynard et al., 2012). In Particular, LV contraction was introduced at T = 0, and LA contraction was launched at 0.85 T (Mynard et al., 2012), causing in a time delay of 0.15 T.

Modeling Heart Valves

Aortic valve

Aortic valve was modeled using the net pressure gradient formulation (PG_{net}) through the aortic valve as follows:

$$PG_{net}|_{AV} = \frac{2\pi\rho}{\sqrt{E_L Co|_{AV}}}\frac{\partial Q(t)}{\partial t} + \frac{\rho}{2\,E_L Co|_{AV}^2}Q^2(t) \tag{4}$$

and

$$E_L Co|_{AV} = \frac{(EOA|_{AV})A_{AO}}{A_{AO} - EOA|_{AV}} \tag{5}$$

where, $E_L Co|_{AV}$, $EOA|_{AV}$, A_{AO}, ρ, and $Q$are the valvular energy loss coefficient, effective orifice area, ascending aorta cross sectional area, fluid density, and transvalvular flow rate, respectively.

TABLE 1 | Cardiovascular parameters.

Description	Abbreviation	Value
Valve parameters		
Effective orifice area	EOA	Measured using DE and CT
Inertance (mitral valve)	M_{MV}	Constant value: 0.53 gcm^{-2} (Flachskampf et al., 1993; Tanné et al., 2008; Keshavarz-Motamed, 2020) Defined by Flachskampf et al. (1993)
Systematic circulation parameters		
Aortic resistance	R_{ao}	Constant value: 0.05 $mmHg.s.mL^{-1}$ (Keshavarz-Motamed et al., 2011, 2014, 2016; Keshavarz-Motamed, 2020)
Aortic compliance	C_{ao}	0.6 C_{SAC} (Stergiopulos et al., 1999) Initial value: 0.5 mL/mmHg (Keshavarz-Motamed et al., 2011, 2014, 2016; Keshavarz-Motamed, 2020) Optimized based on brachial pressures *(Systolic and diastolic brachial pressures are optimization constraints)*
Systemic vein resistance	R_{SV}	0.05 $mmHg.s.mL^{-1}$ (Keshavarz-Motamed et al., 2011, 2014, 2016; Keshavarz-Motamed, 2020)
Systemic arteries and veins compliance	C_{SAC}	Initial value: 2 mL/mmHg (Keshavarz-Motamed et al., 2011, 2014, 2016; Keshavarz-Motamed, 2020) Optimized based on brachial pressures *(Systolic and diastolic brachial pressures are optimization constraints)*
systemic arteries resistance (including arteries, arterioles and capillaries)	R_{SA}	Initial value: 0.8 $mmHg.s.mL^{-1}$ (Keshavarz-Motamed et al., 2011, 2014, 2016; Keshavarz-Motamed, 2020) Optimized based on brachial pressures *(Systolic and diastolic brachial pressures are optimization constraints)*
Upper body resistance	R_{ub}	Adjusted to have 15% of total flow rate in healthy case (Keshavarz-Motamed et al., 2016)
Proximal descending aorta resistance	R_{pda}	Constant value: 0.05 $mmHg.s.mL^{-1}$ (Keshavarz-Motamed et al., 2016; Keshavarz-Motamed, 2020)
Elastance Function*		
Maximum Elastance	E_{max}	2.1 (LV) 0.17 (LA)
Minimum Elastance	E_{min}	0.06 (LV, LA)
Elastance ascending gradient	m_1	1.32 (LV, LA)
Elastance descending gradient	m_2	27.4 (LV) 13.1 (LA)
Elastance ascending time translation	τ_1	0.269 T (LV) 0.110 T (LA)
Elastance descending time translation	τ_2	0.452 T (LV) 0.18 T (LA)
Pulmonary circulation parameters		
Pulmonary Vein Inertance	L_{PV}	Constant value:0.0005 $mmHg{\cdot}s^2{\cdot}mL^{-1}$ (Tanné et al., 2008; Keshavarz-Motamed, 2020)
Pulmonary Vein Resistance	R_{PV}	Constant value: 0.002 $mmHg{\cdot}s{\cdot}mL^{-1}$ (Tanné et al., 2008; Keshavarz-Motamed, 2020)
Pulmonary Vein and capillary Resistance	R_{PVC}	Constant value: 0.001 $mmHg{\cdot}s{\cdot}mL^{-1}$ (Tanné et al., 2008; Keshavarz-Motamed, 2020)
Pulmonary Vein and Capillary Compliance	C_{PVC}	Constant value: 40 mL/mmHg (Tanné et al., 2008; Keshavarz-Motamed, 2020)
Pulmonary Capillary Inertance	L_{PC}	Constant value: 0.0003 $mmHg{\cdot}s^2{\cdot}mL^{-1}$ (Tanné et al., 2008; Keshavarz-Motamed, 2020)
Pulmonary Capillary Resistance	R_{PC}	Constant value: 0.21 $mmHg{\cdot}s{\cdot}mL^{-1}$ (Tanné et al., 2008; Keshavarz-Motamed, 2020)
Pulmonary Arterial Resistance	R_{PA}	Constant value: 0.01 $mmHg{\cdot}s{\cdot}mL^{-1}$ (Tanné et al., 2008; Keshavarz-Motamed, 2020)
Pulmonary Arterial Compliance	C_{PA}	Constant value: 4 mL/mmHg (Tanné et al., 2008; Keshavarz-Motamed, 2020)
Mean Flow Rate of Pulmonary Valve	Q_{MPV}	*Forward LVOT-SV* is the only input flow condition. *Q_{MPV} is a flow parameter that was optimized so that the lump-parameter model could reproduce the desirable measured Forward LVOT-SV*
Input flow condition		
Forward left ventricular outflow tract stroke volume	Forward LVOT-SV	Measured using DE and CT
Output condition		
Central venous pressure	P_{CV0}	Constant value: 4 mmHg (Keshavarz-Motamed et al., 2011, 2014, 2016; Keshavarz-Motamed, 2020)
Other		
Constant blood density	ρ	Constant value: 1050 kg/m^3 (Keshavarz-Motamed et al., 2011, 2014, 2016; Keshavarz-Motamed, 2020)
Cardiac cycle duration	T	Measured using DE and CT
Systolic End Ejection time	T_{EJ}	Measured using DE and CT

Summarized parameters used in the lumped parameter modeling to simulate all patient-specific cases.

Aortic regurgitation

Aortic regurgitation (AR) was modeled using the similar formulation as the aortic valve:

$$PG_{net}|_{AR} = \frac{2\pi\rho}{\sqrt{E_L Co|_{AR}}}\frac{\partial Q(t)}{\partial t} + \frac{\rho}{2\ E_L Co|_{AR}^2}Q^2(t) \quad (6A)$$

and

$$E_L Co|_{AR} = \frac{EOA_{AR}A_{LVOT}}{A_{LVOT} - EOA_{AR}} \quad (6B)$$

where, $E_L Co|_{AR}$, EOA_{AR}, and A_{LVOT} are regurgitation energy loss coefficient, regurgitant effective orifice area and LVOT area, respectively. AR pressure gradient is the difference between aorta pressure and LV pressure during diastole.

Mitral valve

Mitral valve (MV) was modeled using the analytical formulation for the net pressure gradient ($PG_{net}|_{MV}$) across the MV during LA ejection. $PG_{net}|_{MV}$ was expressed as a function of ρ, Q_{MV}, EOA_{MV} and M_{MV}, represent the fluid density, transvalvular flow rate, effective orifice area and inertance, respectively.

$$PG_{net}|_{MR} = \frac{M_{MV}}{EOA_{MV}}\frac{\partial Q_{MV}(t)}{\partial t} + \frac{\rho}{2\ EOA|_{MV}^2}Q_{MV}^2(t) \quad (7)$$

Mitral regurgitation

Mitral regurgitation (MR) pressure gradient is the difference between mitral pressure and LA pressure during systole and was modeled using the following equation:

$$PG_{net}|_{MR} = \frac{M_{MV}}{EOA_{MR}}\frac{\partial Q(t)}{\partial t} + \frac{\rho}{2\ EOA|_{MR}^2}Q^2(t) \quad (8)$$

where, $EOA|_{MR}$ is MR effective orifice area.

Pulmonary flow

The pulmonary valve flow waveform was modeled using a rectified sine curve with duration t_{ee} and amplitude Q_{MPV} as follows:

$$Q_{PV}(t) = Q_{MPV}\sin\left(\frac{\pi t}{t_{ee}}\right), t \le t_{ee}; Q_{PV}(t) = 0, tee < t \le T \quad (9)$$

where, Q_{MPV}, t_{ee} and T are mean flow rate of the pulmonary valve, end-ejection time and cardiac cycle duration, respectively. Forward left ventricular outflow tract stroke volume (*Forward LVOT-SV*) was the sole input flow condition in this study. Indeed, the mean flow rate of the pulmonary valve (Q_{MPV}) was optimized so that the lump-parameter algorithm replicates the measured *Forward LVOT*-SV.

Input Parameters and Patient-Specific Parameter Estimation

Both C3VI-CT and C3VI-DE algorithms use the following input parameters: forward left ventricular outflow tract stroke volume (*Forward LVOT-SV*), cardiac cycle duration (T), ejection time (T_{EJ}), ascending aorta area (A_{AO}), left ventricle outflow tract area (A_{LVOT}), aortic valve effective orifice area ($EOA|_{AV}$), mitral valve effective orifice area ($EOA|_{MV}$), grading of the severity of aortic, and mitral valves regurgitation and systolic and diastolic blood pressures.

Flow inputs

Both C3VI-CT and C3VI-DE use only one measured flow parameter as an input: forward left ventricle stroke volume (*Forward LVOT-SV*). *Forward LVOT-SV* is defined as the volume of blood that passes through the LVOT cross sectional area every time the heart beats.

C3VI-CT

Forward LVOT-SV measured using CT is defined (Equation 10) as follows:

$$Forward\ LVOT - SV = EDV - ESV \quad (10)$$

where, *EDV* and *ESV* are the end diastolic volume and the end systolic volume, respectively. Using CT data, we have estimated end diastole phase and end systole phase by tracking the images and the spatial position of the mitral valve and aortic valve leaflets as well as the left ventricle. Therefore, the very first image after aortic-valve closure was deemed as the end systole (beginning of diastole) and the very first image after mitral-valve closure was considered as the end diastole (beginning of systole). We segmented and reconstructed the 3-D geometries of the complete ventricle in patients in both pre and post-TAVR using CT images and ITK-SNAP (version 3.8.0-BETA) (Yushkevich et al., 2006), a 3-D image processing and model generation software package (**Figure 1C**). We then, using an in house Matlab code, calculated the left ventricle volume at the end systole and end diastole after reconstructing the 3-D shape using CT data. We used smoothing procedure for the surfaces. The smoothing procedure mainly removed the effect of trabeculae and papillary muscles, which has been shown to have negligible influence on the ventricle hemodynamics (Vedula et al., 2016). Change in the volume due to smoothing was less than 3% in all patients.

C3VI-DE

Forward LV-SV measured using DE is defined as the following (Keshavarz-Motamed, 2020):

$$Forward\ LV - SV = A_{LVOT}\ VTI_{LVOT} = \frac{\pi(D_{LVOT})^2}{4}VTI_{LVOT} \quad (11)$$

where, D_{LVOT}, A_{LVOT}, and VTI_{LVOT} are LVOT diameter, LVOT area, and LVOT velocity-time integral, respectively.

Time inputs

Cardiac cycle time (T) and ejection time (T_{EJ}) were measured using Doppler echocardiography and ECG-Gated CT to be used in C3VI-DE and C3VI-CT, respectively.

Aortic valve and mitral valve inputs

To model blood flow in forward direction, both C3VI-CT and C3VI-DE require aortic valve effective orifice area ($EOA|_{AV}$), mitral valve effective orifice area ($EOA|_{MV}$), ascending aorta area (A_{AO}) and left ventricle outflow tract area (A_{LVOT}).

C3VI-CT

We segmented and reconstructed the 3-D geometries of the aortic and mitral valves, ascending aorta and LVOT section in C3VI patients in both pre and post-TAVR using CT images and ITK-SNAP (version 3.8.0-BETA) (Yushkevich et al., 2006) (**Figure 1C**). We calculated $EOA|_{AV}$, $EOA|_{MV}$, A_{AO} *and* A_{LVOT} using an in house Matlab code, after reconstructing the 3-D shape using CT data.

C3VI-DE

$EOA|_{AV}$, A_{AO}, A_{LVOT} were calculated using the following equations (Keshavarz-Motamed, 2020):

$$EOA|_{AV} = \frac{Forward\ LVOT - SV}{VTI_{AO}} \tag{12}$$

$$A_{AO} = \frac{\pi(D_{AO})^2}{4} \tag{13}$$

$$A_{LVOT} = \frac{\pi(D_{LVOT})^2}{4} \tag{14}$$

where, VTI_{AO}, D_{AO}, and D_{LVOT} are the velocity time integral in the ascending aorta (amount of the blood flow going through the aorta), ascending aorta diameter and LVOT diameter, respectively.

Moreover, mitral valve is approximately an ellipse and its area was quantified using the following equation where d_1 and d_2 are mitral-valve diameters measured in the apical two-chamber and apical four-chamber views, respectively (Keshavarz-Motamed, 2020).

$$EOA|_{MV} = \frac{\pi d_1 d_2}{4} \tag{15}$$

Grading of aortic and mitral valve regurgitation severity inputs

To model blood flow in the reverse direction, both C3VI-CT and C3VI-DE require grading of aortic and mitral valve regurgitation severity (e.g., regurgitant effective orifice area of aortic valve and regurgitant effective orifice area of mitral valve) [(see Keshavarz-Motamed, 2020) for all details)]. C3VI-CT uses CT data for all the mentioned input parameters, however, it cannot provide measurements for grading of aortic and mitral valve regurgitation severity, which are measured using DE (Keshavarz-Motamed, 2020). We therefore use grading of aortic and mitral valve regurgitation severity measured by DE for both C3VI-CT and C3VI-DE.

Systolic and diastolic blood pressures

Systolic and diastolic blood pressures measured using a sphygmomanometer are additional input parameters for both C3VI-CT and C3VI-DE.

Parameter estimation for systemic circulation

Parameters R_{SA}, C_{SAC}, and C_{ao} were optimized so that the aorta pressure calculated using the model matched the patient's systolic and diastolic brachial pressures measured using a sphygmomanometer (see section "Computational Algorithm" and section "Patient-Specific Response Optimization" for details) for both C3VI-CT and C3VI-DE.

Simulation execution

Please see the section "Computational Algorithm" for both C3VI-CT and C3VI-DE calculations.

Computational Algorithm

The lumped-parameter algorithm was analyzed numerically by creating and solving a system of ordinary differential equations in Matlab Simscape (MathWorks, Inc.), supplemented by additional functions written in Matlab and Simscape. Matlab's ode23t trapezoidal rule variable-step solver was used to solve the system of differential equations with an initial time step of 0.1 milliseconds. The convergence residual criterion was set to 10^{-6}. Initial voltages and currents of capacitors and inductors were set to zero. The model was run for several cycles (around 50 cycles) to reach steady state before starting the response optimization process described below. In order to generate a signal to model LV elastance, a double Hill function representation of a normalized elastance curve for human adults was used (Mynard et al., 2012; Broomé et al., 2013). This elastance formulation was shown to completely represent the LV function independent of its pathological condition. Simulations started at the onset of isovolumic contraction. The instantaneous LV volume, V(t), was calculated using the time varying elastance (Equation 1) and LV pressure, P_{LV}. Subsequently, the LV flow rate was calculated as the time derivative of the instantaneous LV volume. The same method was used to obtain the left-atrium volume, pressure and flow rate. P_{LV} was initially calculated using the initial values of the model input parameters from **Table 1**. The *Forward LVOT-SV* was calculated using the lumped-parameter model and then fitted to the one measured (Equation 10) by optimizing Q_{MPV} (as detailed below). Finally, for each patient R_{SA}, C_{SAC}, and C_{ao} were optimized to fit the aortic pressure from the model to the patient systolic and diastolic pressures measured using a sphygmomanometer.

Patient-Specific Response Optimization

The parameters of the lumped parameter algorithm are listed in **Table 1**. Some of the parameters were considered constant based on the previous studies in the literature or based on the rationale given below and their values are reported in **Table 1**. Additionally, the parameters that were measured in each patient are indicated in that table. To precisely replicate the body conditions of individual patients, as described below, four parameters of the lumped parameter algorithm were optimized so that the model replicated the physiological measurements performed in the patient. Simulink Design Optimization toolbox was used to optimize the response of the lumped-parameter model using the trust region reflective algorithm implemented in Matlab fmincon function. The response optimization was performed in two consecutive steps with tolerances of 10^{-6} (**Figure 2**, flow chart).

The mean flow rate of the pulmonary valve, Q_{MPV}, could not be measured or computed using CT and cannot be reliably measured using Doppler echocardiography. However, because *Forward LVOT-SV* can be measured reliably using Doppler echocardiography and can be computed using CT, in the first step of optimization, Q_{MPV} was optimized to minimize the

error between the *Forward LVOT-SV* calculated by the lumped-parameter algorithm and the one measured in each patient reliable using DE.

In the second step, R_{SA}, C_{SAC}, and C_{ao} were optimized so that maximum and minimum of the aorta pressures were equal to the systolic pressure and diastolic pressure, respectively, measured using a sphygmomanometer in each patient. Because the left ventricle confronts the total systemic resistance and not the specific resistances, and the systemic arteries resistance (R_{SA}) is one order of magnitude greater than both the aortic resistance (R_{ao}) and systemic vein resistance (R_{SV}), we considered R_{ao} and R_{SV} as constants and optimized R_{SA} as the main contributor of the total systemic resistance (Keshavarz-Motamed et al., 2011, 2012, 2014, 2015; Benevento et al., 2015; Keshavarz-Motamed, 2020; Sadeghi et al., 2020). C_{ao} was considered to be 0.6 of C_{SAC} because 60% of the total arterial compliance lives in the proximal aorta (Stergiopulos et al., 1999).

In addition, we performed a comprehensive parameter sensitivity analysis that discovered negligible effects of changes in the pulmonary parameters (e.g., C_{PVC}) on the lumped parameter model output variables (Keshavarz-Motamed, 2020). Therefore, we did not include these pulmonary parameters in the parameter-optimization process and counted them as constants (**Table 1**).

Study Population

Forty-nine deidentified and anonymous C3VI patients with severe aortic valve stenosis who underwent TAVR (see **Table 2** for patients characteristics) between 2011 and 2018 at St. Joseph's Healthcare and Hamilton General Hospital (Hamilton, ON, Canada) and Hospital Universitario Marques de Valdecilla (IDIVAL, Santander, Spain) were considered (Keshavarz-Motamed, 2020; Keshavarz-Motamed et al., 2020). The selections were done by operators blinded to the objectives and contents of this study. Informed consent was obtained from all participants. The protocols were reviewed and approved by the Institutional Review Boards of each institution as follows: the Hamilton Integrated Research Ethics Board (HiREB) of Hamilton Health Sciences and St. Joseph's Healthcare, both affiliated to McMaster University and Comité de ética de la investigación con medicamentos de Cantabria of the Hospital Universitario Marques de Valdecilla. All methods and measurements were conducted in accordance with pertinent guidelines and regulations, e.g., guidelines of the American College of Cardiology and American Heart Association. Cardiac catheterizations were performed only in pre intervention status. The patient medical records were used to collect demographic and procedural data (see **Table 1** for details). Data was acquired at two time points: pre-procedure and 90-days post-procedure.

Statistical Analysis

All results were expressed as mean ± standard deviations (SD). Statistical analyses were performed using SigmaStat software (Version 3.1, Systat Software, San Jose, CA, United States). Coefficient of determination, R^2, was used to quantify the quality of linear regressions. Statistically significant differences between two datasets were assessed using two-sample *t*-test at 1% significance level.

RESULTS

C3VI-DE and C3VI-CT vs. Clinical Cardiac Catheterization Data

Validation with clinical cardiac catheterization is a gold standard and the highest-level validation that is possible in patients in the field of cardiovascular mechanics. However, because of its invasive nature, catheter data are rare and collecting a useable dataset are incredibly rare. It is important to note that from a fluid mechanics point of view, in incompressible flow the relationship between pressure and velocity is well defined and therefore from catheter pressure data, the velocity can be easily obtained. In the complex time-varying cardiovascular system, in which many phenomena interact with one another, having a model that replicates the catheter data in each patient, shows the validity of the model to the highest degree. Our results show that C3VI-DE can non-invasively quantify pulsatile flow and pressure throughout the heart in C3VI patients and provide instantaneous quantities such as left ventricle and aorta pressures. Conversely, C3VI-CT cannot accurately obtain these quantities (**Figures 3**, **4**).

Pressure Waveforms

The instantaneous pressure computed by C3VI-DE were compared with clinical cardiac catheter pressure measurements in all forty-nine C3VI patients. **Figure 3** shows the comparison of C3VI-DE calculations with catheter data in 3 of the 49 patients (Patients #1, #2, and #3). C3VI-DE results are in qualitative agreement with catheter measurements, e.g., similar waveform shape as well as specific wave elements such as the amplitude and timing of the systolic peak. Quantitatively, results computed by C3VI-DE had an average RMS error of 11.8 mmHg and 9.9 mmHg in the LV and aorta pressures, respectively ($n = 49$). Conversely, results from C3VI-CT do not precisely agree with catheter measurements with the average RMS errors of 64.5 mmHg and 12.7 mmHg in the left ventricle and aorta pressures, respectively ($n = 49$).

Peak Pressure

The peak pressures obtained from C3VI-DE (LV: 164.5 ± 30.7 mmHg; aorta: 133.88 ± 14.25 mmHg) are in close agreement with catheter measurements (LV: 165.9 ± 30.9 mmHg, aorta: 133.75 ± 14.67 mmHg) in all forty-nice C3VI patients (**Figure 4**). The high coefficients of determination (LV: $R^2 = 0.982$; aorta: $R^2 = 0.933$; **Figure 4**) indicate a strong correlation between C3VI-DE and cardiac catheter measurements, with maximum relative errors of 4.49% for aorta pressure and 4.33% for LV pressure in all forty-nine patients. In contrast with those obtained from C3VI-DE, peak pressures obtained from C3VI-CT (LV: 143.4 ± 27.5 mmHg, aorta: 134.4 ± 14.5 mmHg) are incompatible with the catheter measurements. Its low coefficients of determination (LV: $R^2 = 0.63$; aorta: $R^2 = 0.83$; **Figure 4**) indicate a weak correlation between C3VI-CT and catheter measurements, with maximum relative errors of 31.4% and 7.8% for LV and aortic pressures, respectively, in all C3VI subjects.

TABLE 2 | Patient characteristics.

	Pre interventionMean ± SD (n = 49)	Post interventionMean ± SD (n = 49)
Ventricular indices – DE findings		
Ejection fraction, %	53.5 ± 12.7	61 ± 14.6
Heart rate, bpm	70.7 ± 9.5	68 ± 11.8
Stroke volume, mL	48.3 ± 11.7	44.5 ± 15.5
NYHA classifications ≥ grade 2	82%	76%
Valvular indices – DE findings		
Aortic valve effective orifice area (cm^2)	0.58 ± 0.16	1.75 ± 0.4
Mean aortic valve gradient, mmHg	51.52 ± 13.6	11.1 ± 6.1
Maximum aortic valve gradient, mmHg	84.5 ± 21.32	20.4 ± 10.28
Aortic valve disease type	Tricuspid: 46; Bicuspid: 3	None
Aortic valve regurgitation ≥ grade 2	48%	5%
Mitral valve regurgitation ≥ grade 2	19%	20%
Vascular indices – Sphygmomanometer		
Brachial systolic blood pressure, mmHg	139 ± 22.5	135 ± 16.8
Brachial diastolic blood pressure, mmHg	79 ± 11.7	68 ± 10.3
Patient description		
Mean age, years; Gender	64.5 ± 5.5; (Female: 36%)	Same as pre TAVR
Mean weight, kg; Mean height, cm	73.4 ± 12.8; 165.7 ± 9.6	71.6 ± 10.5; 165.7 ± 9.6
Body surface area, m^2	1.73 ± 0.14	Not available
Body mass index, kg/m^2	31.9 ± 21.5	Not available
EuroScore II	7.2 ± 5.33	Not available
STS mortality rate	6.89 ± 4.45	Not available
Associated cardiovascular lesions		
Previous percutaneous coronary intervention	39%	Same as pre TAVR
Previous coronary artery bypass grafting	30%	Same as pre TAVR
Previous myocardial infarction	19%	Same as pre TAVR
Previous stroke	1%	Same as pre TAVR
Atrial fibrillation	26%	Same as pre TAVR
Cerebrovascular accident	5%	Same as pre TAVR
Peripheral vascular disease	38%	Same as pre TAVR
Hypertension	82%	78%

Changes in hemodynamic metrics from baseline to post-intervention.

C3VI-DE vs. C3VI-CT: Input Parameters to the Model

The developed algorithm uses the following input parameters: forward LVOT stroke volume, cardiac cycle duration, ascending aorta area, LVOT area, aortic valve effective orifice area, mitral valve effective orifice area, and grading of aortic and mitral valves regurgitation severity. While for C3VI-DE all of these parameters are reliably measured using DE, for C3VI-CT they are measured using CT, except for grading of aortic and mitral valve regurgitation severity, which are measured using DE since CT cannot provide these measurements. The other input parameters of the model are systolic and diastolic blood pressures, which are measured using a sphygmomanometer for both C3VI-DE and C3VI-CT. **Figure 5** shows that when the measurements of the input parameters were performed using CT data, aortic valve effective orifice area, LVOT area, and ascending aorta area were significantly higher than those measured using DE, while the forward LVOT stroke volume and mitral valve effective area were lower than the ones measured using DE. **Table 3** shows the maximum variations of the computed LV workload and LV peak pressure, averaged over all patients, obtained from one-parameter-at-a-time sensitivity analysis of ±30% relative to the baseline. As shown in **Table 3**, the LV worklaod and LV peak pressure are greatly sensitive to the forward LVOT stroke volume, among all of the input parameters of the model, and consequently the underestimated forward LVOT stroke volume obtained from the CT data can introduce an error in the calculated LV workload.

C3VI-DE vs. C3VI-CT: Model Outputs (Hemodynamics Metrics of Circulatory and Cardiac Function)

Figure 6 shows that the calculated hemodynamics metrics of circulatory and cardiac function (e.g., LV workload, LV peak pressure and peak to peak pressure gradient) were substantially different when the measurements of the input parameters were performed using DE rather than CT. Compared to C3VI-DE, C3VI-CT underestimates the LV workload, LV peak pressure and peak to peak pressure gradient (the difference between LV peak pressure and aorta peak pressure) by 18%, 16%, and 55%,

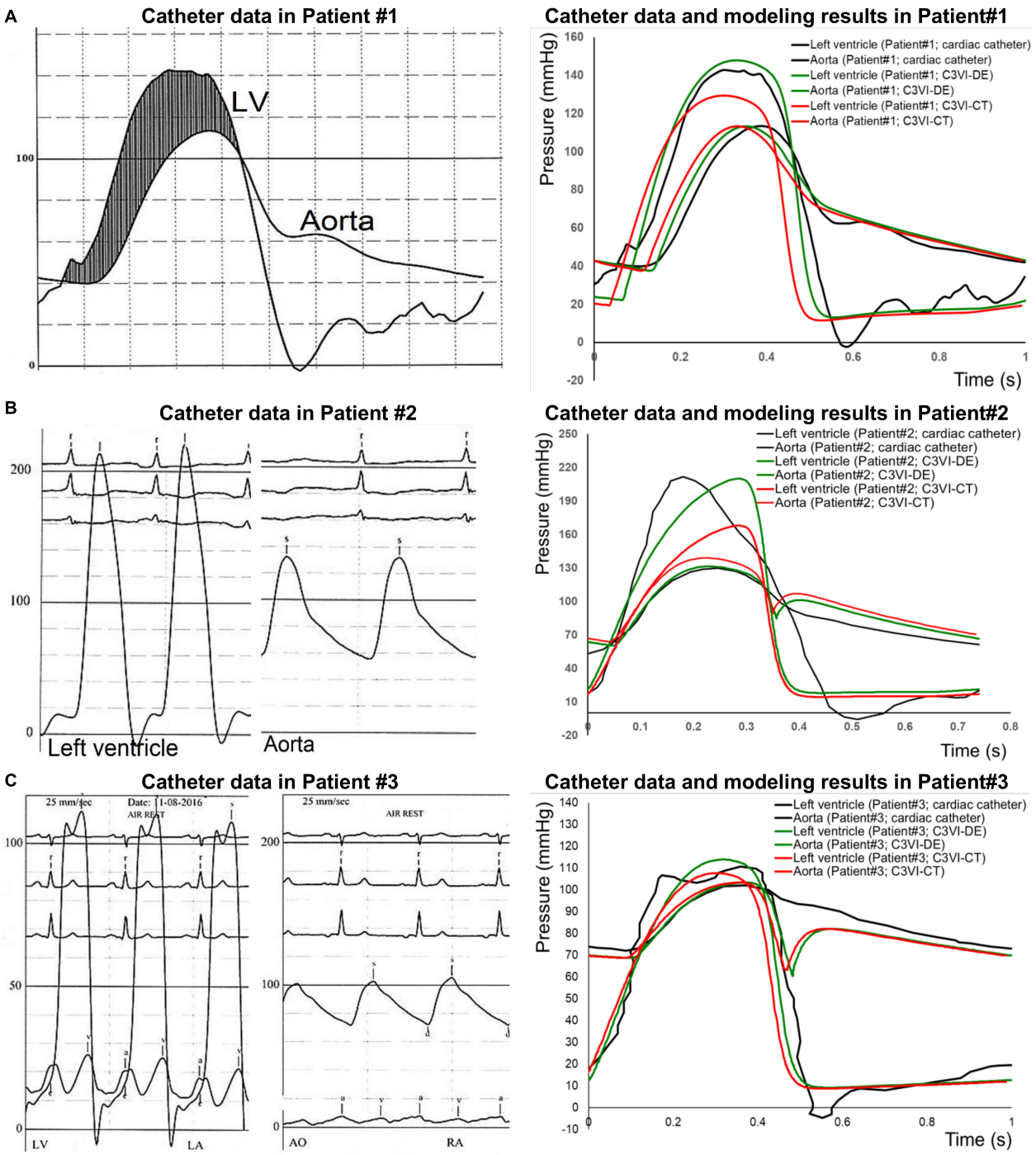

FIGURE 3 | Pressure waveform comparison (C3VI-CT & C3VI-DE *vs.* cardiac catheter): The instantaneous C3VI-DE pressure compared favorably with cardiac catheter pressure in all subjects. Conversely, results from C3VI-CT do not precisely agree with catheter measurements. **(A)** Patient #1; **(B)** Patient #2; **(C)** Patient #3.

respectively (average in $N = 49$). Moreover, we used the pre-intervention states (both from DE and CT) of the patients, virtually performed intervention in the models and used our framework to predict the patient state post intervention. **Figure 7** compares the actual post-intervention LV workload with the LV workload that our framework predicted that all patients would have after the intervention (patients with C3VI underwent TAVR; $N = 49$). We observed quantitative agreement, resulted from, between the post-intervention LV workload predicted using C3VI-DE and the actual post-intervention LV workload in all C3VI subjects (error of average: 0.4%, $N = 49$; **Figure 7**) which demonstrates the validity of the C3VI-DE model and

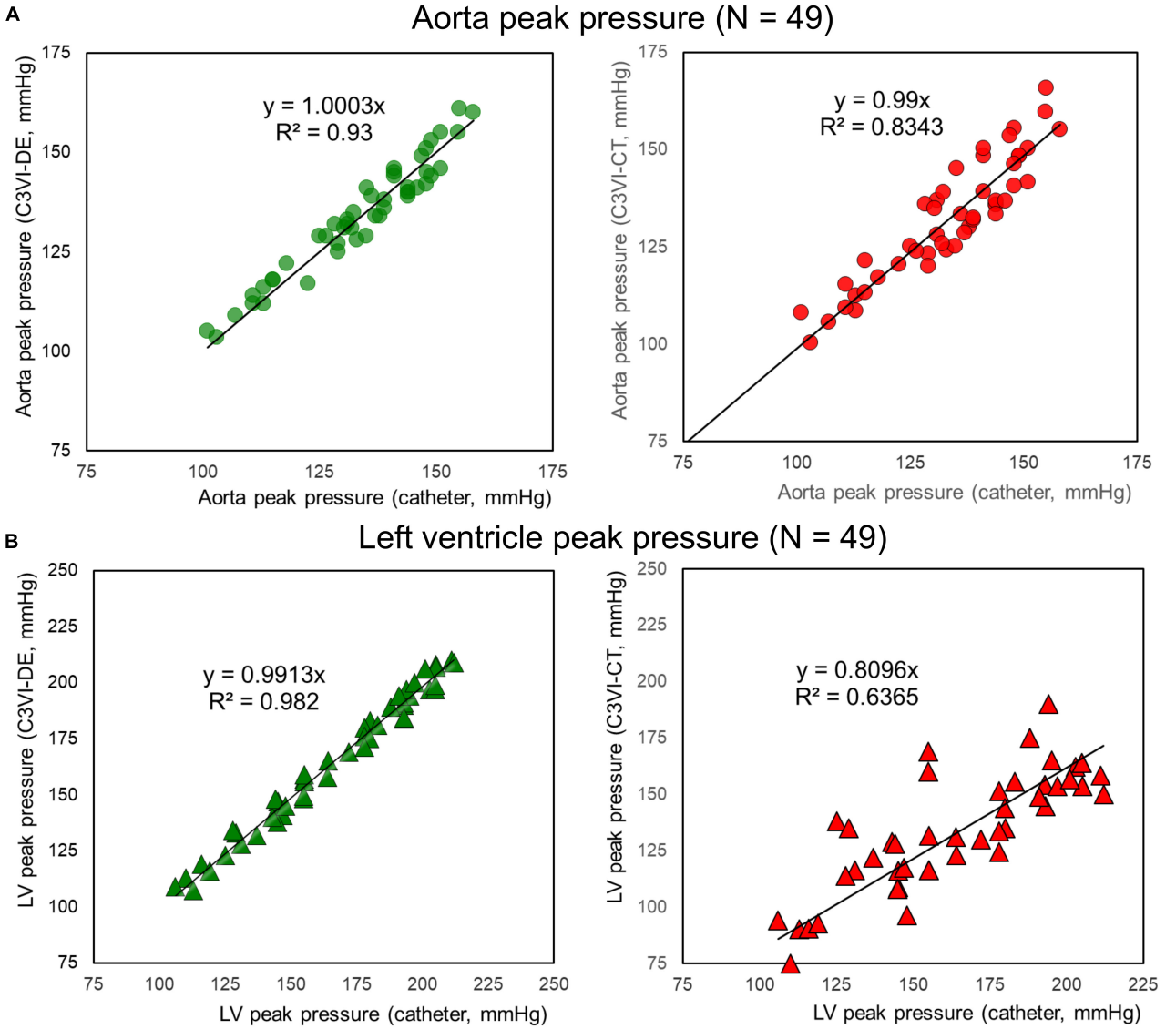

FIGURE 4 | Peak pressure correlation (C3VI-CT & C3VI-DE *vs.* cardiac catheter). Peak pressures calculated by C3VI-DE correlated well with catheter measurements in all forty-nine C3VI patients, described by high coefficients of determination. In contrast with C3VI-DE, peak pressures obtained from C3VI-CT are incompatible with the catheter measurements, described by low coefficients of determination. **(A)** Aorta. **(B)** Left ventricle.

its predictive capability. However, there is no firm quantitative agreement between the post-intervention LV workload predicted using C3VI-CT and the actual post-intervention LV workload in C3VI patients (error of average: 11.4%, $N = 49$; **Figure 7**).

DISCUSSION

Because of high individual differences in the anatomy and pathophysiology of patients, planning individualized treatment requires patient-specific diagnosis. Hemodynamics quantification in C3VI plays an essential role in precise and early diagnosis (Marsden, 2013; Khalafvand et al., 2014; Di Carli et al., 2016), however, present diagnostic methods are limited and cannot quantify hemodynamics of C3VI (Marsden, 2013; Di Carli et al., 2016; Anvari et al., 2021).

As the need for patient-specific diagnostic methods continues to be studied, understanding the strengths and limitations of imaging modalities is crucial toward creating accurate diagnostic tools. Over the past decade, the use of medical imaging has exponentially increased (Smith-Bindman et al., 2012; Blecker et al., 2013), likely due to its technological advancements which is evident through the miniaturization of imaging devices and the dramatic increase in sensitivity and spatial resolution (Fleischmann et al., 2008; Smith-Bindman et al., 2012; Di Carli et al., 2016). In spite of astonishing advancements in medical imaging, medical imaging on its own cannot quantify local and global hemodynamics: (1) Phase-contrast magnetic resonance

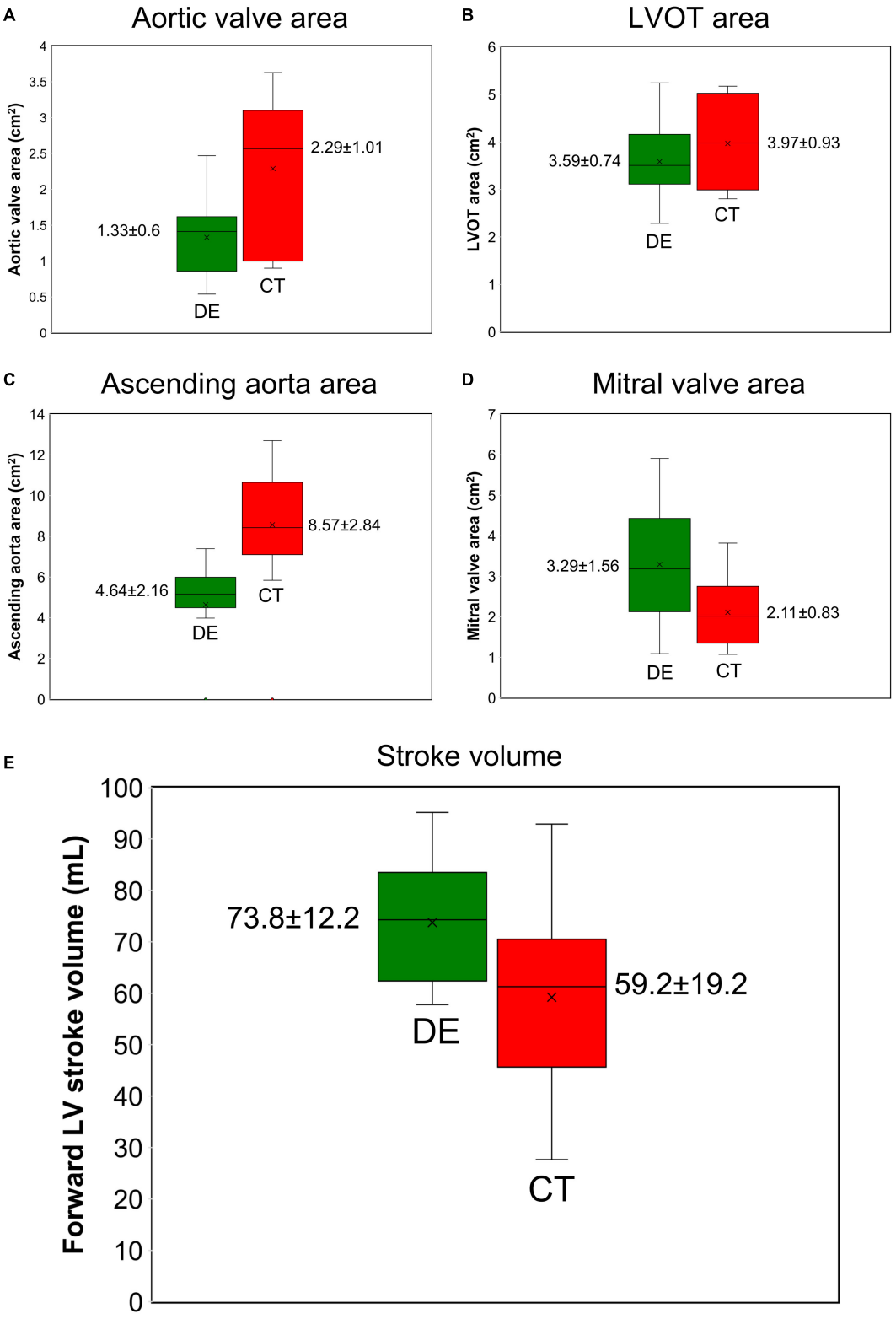

FIGURE 5 | Doppler echocardiography measurements *vs.* computed tomography measurements ($N = 49$). **(A)** aortic valve effective orifice area; **(B)** LVOT area; **(C)** ascending aorta area; **(D)** mitral valve effective orifice area; **(E)** forward LVOT stroke volume. DE and CT generated significantly different results for aortic valve effective orifice area, LVOT area, ascending aorta area, mitral valve effective orifice area, and forward LVOT stroke volume as the two sample *t*-test rejected the null hypothesis at 0.01 significance level.

TABLE 3 | Maximum variation of the computed LV workload and LV peak pressure.

Input parameters of the algorithm measured using CT or DE	Abbreviation	Maximum variations of computed LV workload and LV peak pressure ($N = 49$)
Forward left ventricular outflow tract stroke volume	Forward LVOT-SV	58% and 51%
Cardiac cycle duration	T	14.5% and 11%
Ascending aorta area	A_{AO}	0.68% and 0.5%
LVOT area	A_{LVOT}	0.7% and 0.65%
Aortic valve effective orifice area	EOA_{AV}	14% and 18%
Mitral valve effective orifice area	EOA_{MV}	1.4% and 0.9%
Input parameters of the algorithm measured using DE		
Regurgitant effective orifice area of the aortic valve	EOA_{AR}	19% and 10.6%
Regurgitant effective orifice area of the mitral valve	EOA_{MR}	11.5% and 4.5%
Input parameters of the algorithm measured using sphygmomanometers		
Systolic pressure	P_{SYS}	1.2% and 0.85%
Diastolic pressure	P_{DIAS}	1% and 0.9%

Results were obtained from one-parameter-at-a-time sensitivity analysis (±30%) relative to the baseline, averaged over all patients (N = 49). LV workload, the integral of LV pressure and its volume change, is greatly sensitive to the forward LVOT stroke volume, among all of the input parameters of the algorithm.

imaging (MRI): MRI can provide 3-D velocity and volumetric data throughout the cardiac cycle, making it a great tool for characterizing flow throughout the volume with a relatively high spatial resolution (Fleischmann et al., 2008; Shen et al., 2021). On the downside, MRI has a lower temporal resolution (20 ms highest) than Doppler echocardiography does, and is the most costly of the compared imaging modalities (Picano, 2005; Watson et al., 2018). In addition, Gadolinium contrast agent, used in approximately 1 in 3 MRI scans to increase the image clarity, is toxic and may lead to the development of Nephrogenic Systemic Fibrosis in patients with severe renal failure (Kuo et al., 2007; Paterson et al., 2013). However, 4D flow MRI is an emerging technology to allow comprehensive assessment of cardiac function, vascular and valvular function (Zhong et al., 2019). Most importantly, although use MRI is limited in patients with implanted medical devices as they remain a major risk during the examination (Orwat et al., 2014), some devices [e.g., MRI-conditional pacemakers; Saunderson et al. (2020) and (Saunderson et al., 2020)] may be used in MRI environment if certain conditions are fulfilled. However, the possibility, safety and reliability of 4-D flow MRI remain to be confirmed in patients with implanted cardiac devices. As Saunderson et al. (Saunderson et al., 2020) mentioned, larger studies are required to fully evaluate safety of 4D flow MRI across a wider range of cardiovascular implanted devices; (2) Computed tomography (CT): CT scans allows for 3D and 4D visualization and measurement of complex anatomy as well as flexible structures at high spatial resolution (Villarraga-Gómez et al., 2018). Dual source CT has poor temporal resolution with the highest resolution outputs of 83 ms, which is the lowest of the compared modalities, thus requiring slow and steady heart rates to yield a clear image (Lin and Alessio, 2009; Sabarudin and Sun, 2013; Watson et al., 2018). Additionally, due to the ionizing radiation, receiving multiple scans increases the risk of developing cancer by 2.7–12% for the general population and up to triple the risk of brain tumors and leukemia for pediatric patients. Furthermore, CT typically requires the use of an iodine-based contrast agent which, in rare cases, may induce anaphylaxis or contrast-induced nephropathy (Andreucci et al., 2014; Faggioni and Mehran, 2016; Rehman and Makaryus, 2019). More importantly, CT cannot measure any (local and global) hemodynamic parameters; (3) Doppler echocardiography (DE): DE provides functional, real-time information regarding cardiac geometry, instantaneous flow and pressure gradients (Anavekar and Oh, 2009; Steeds, 2011). DE can detect structural abnormalities as well as assess contractility and ejection fraction, at an excellent temporal resolution of < 4 ms and has an infinitesimal risk-to-benefit ratio (Papolos et al., 2016). As a result, DE remains the gold standard for assessing cardiac function, and is essential for basic and clinical cardiovascular research (Anavekar and Oh, 2009; Steeds, 2011; Parra and Vera, 2012). Moreover, DE is the least costly of the compared imaging modalities as well as the most widely available. Despite its versatility and potential, DE cannot precisely evaluate local and global hemodynamics, or provide breakdown contributions of each component in cardiovascular disease (Anavekar and Oh, 2009; Scantlebury Dawn et al., 2013). Such information has a high clinical importance for planning advanced treatments for C3VI patients.

We recently developed a non-invasive, image-based, patient-specific diagnostic and monitoring lumped parameter modeling framework for C3VI patients (called C3VI-DE) which uses limited input parameters, measured using DE reliably and a sphygmomanometer (Keshavarz-Motamed, 2020). Additionally, in this study, we have developed another computational framework that used the same lumped-parameter model core in conjunction with input parameters measured using CT and a sphygmomanometer (called C3VI-CT). *In this study, we focused on comparing data generated from DE and CT as they are commonly used in clinics for patients with C3VI and severe aortic stenosis who received TAVR.* In this paper, we compared accuracy of the results obtained using C3VI-DE and C3VI-CT against catheterization data in forty-nine C3VI patients with severe aortic stenosis who underwent TAVR with substantial inter- and

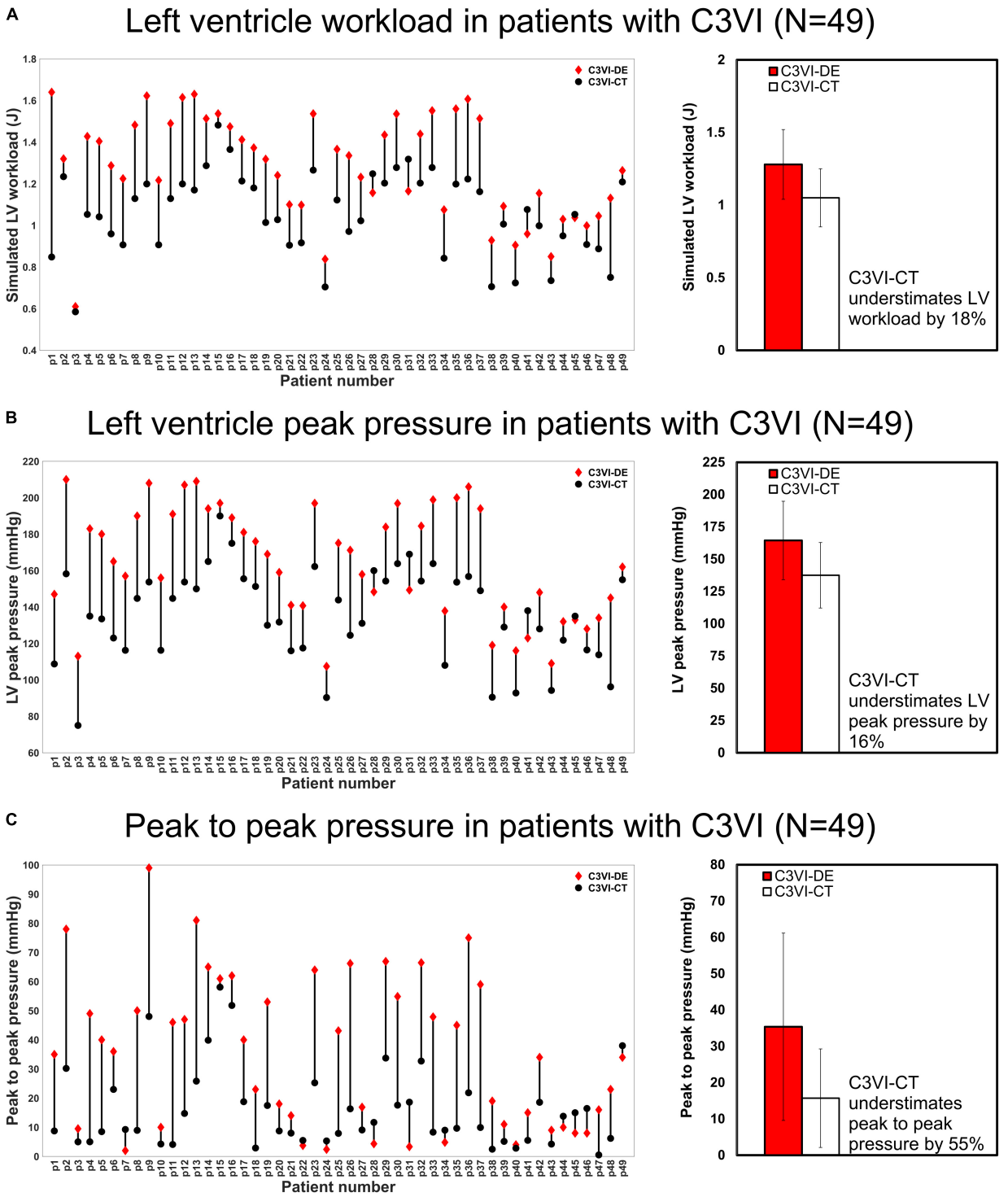

FIGURE 6 | Changes in hemodynamics assessments calculated by C3VI-DE and C3VI-CT in patients with C3VI ($N = 49$). **(A)** LV workload; **(B)** LV peak pressure; **(C)** Peak to peak pressure. Two-sample *t*-test showed that calculations of C3VI-DE and C3VI-CT for all three variables (LV workload, LV peak pressure and peak to peak pressure) are significantly different at 0.01 significance level.

intra-patient variability covering a wide range of diseases to determine with which modality the framework can yield the most accurate results. Based on our analysis, we found that results from C3VI-DE are in qualitative and quantitative agreement with catheter measurements, whereas results from C3VI-CT do not agree with catheter measurements.

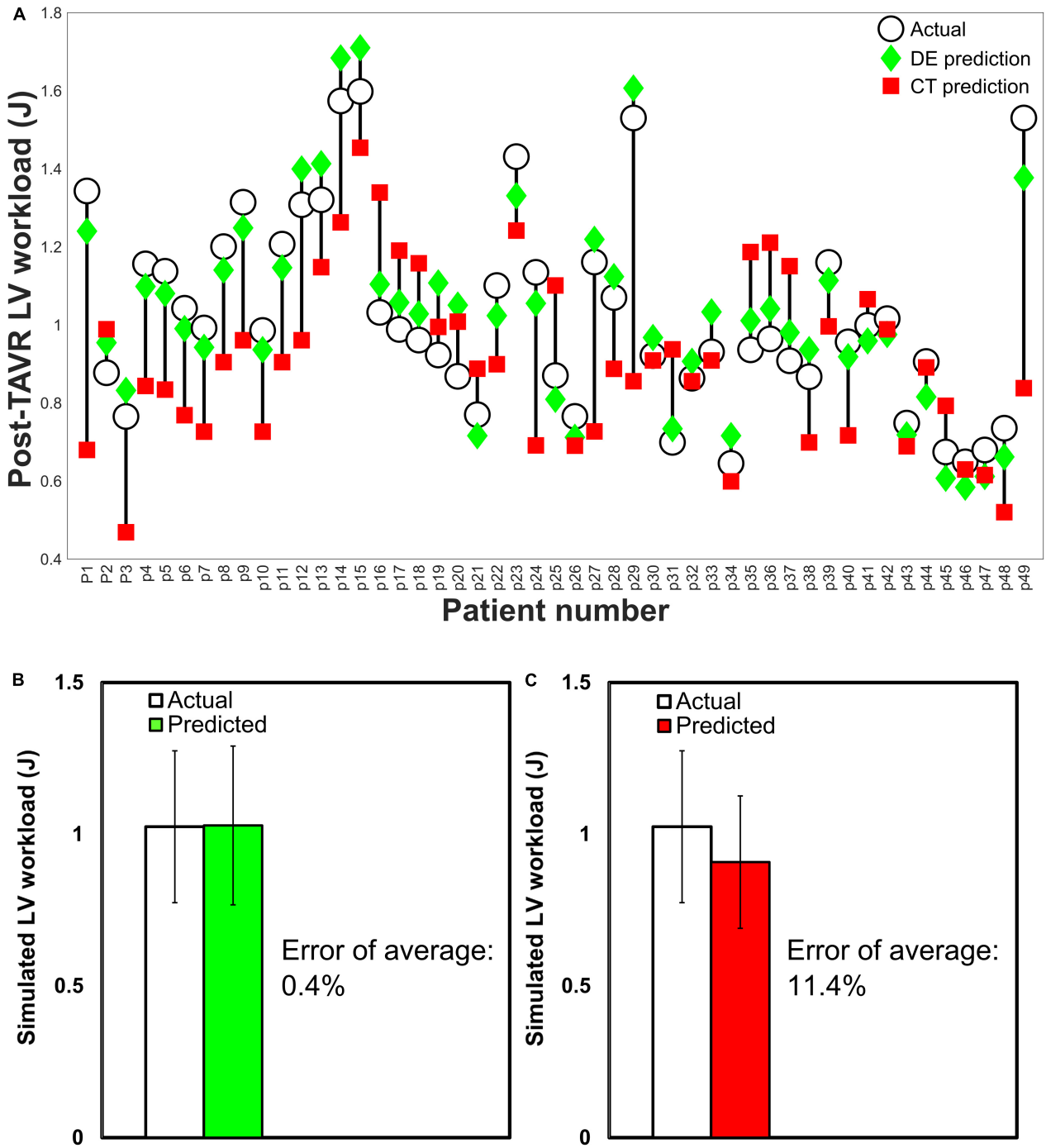

FIGURE 7 | Changes in predicted LV workload after intervention and actual post-intervention LV workload in patients with C3VI ($N = 49$). **(A)** Computed by C3VI-DE and C3VI-CT. **(B)** Computed by C3VI-DE. **(C)** Computed by C3VI-CT. The two-sample *t*-test rejects the null hypothesis that the prediction and the actual values of the post-intervention LV workload have equal means for C3VI-CT predictions but not for C3VI-DE predictions at 0.01 significance.

Although DE suffers from operator dependence and is only able to provide a single component of the flow velocity, the input parameters that are used in C3VI-DE (detailed in section "Materials and Methods") can be reliably measured using DE. Furthermore, our proposed method decreases the operator dependence of DE by providing many quantitative measures

that are obtained independent from the operator and are not accessible otherwise by any other method or imaging modality. CT has a high spatial resolution and can provide anatomical information with a high accuracy (Villarraga-Gómez et al., 2018), however, it has a low temporal resolution (Maleki and Esmaeilzadeh, 2012; Watson et al., 2018; Rehman and Makaryus, 2019). All input parameters obtained from CT images to be used in C3VI-CT (detailed in section" Materials and Methods") were measured at the closest instance to end systole and end diastole but because of poor time resolution, the situation of the left ventricle and valves are not known at the exact end systole and end diastole instances. we have estimated end diastole phase and end systole phase by tracking the images and the spatial position of the mitral valve and aortic valve leaflets as well as the left ventricle. Therefore, the very first image after aortic-valve closure was deemed as the end systole (beginning of diastole) and the very first image after mitral-valve closure was considered as the end diastole (beginning of systole). Although DE images do not have as high spatial resolution as CT images, the input parameters that are required for C3VI-DE are among the quantities that can be reliably measured in DE images. Furthermore because of high temporal resolution of DE, the end diastole and end systole instances can be accurately determined. We believe that reliably measured input parameters at a high temporal resolution using DE enabled more accurate results in C3VI-DE than the ones obtained from C3VI-CT based on input parameters that were affected by the poor temporal resolution of CT. Please note in this study, all measurements of the input parameters for both C3VI-DE and C3VI-CT were verified by two cardiologists.

The C3VI-DE framework is an innovative non-invasive diagnostic and monitoring tool that can investigate and quantify effects of C3VI components on cardiac function and the circulatory system. C3VI-DE is centered around calculations of local hemodynamics (fluid dynamics of the circulatory system) and global hemodynamics (cardiac function and hemodynamics). Furthermore, by decomposing the global hemodynamics into the individual contributions of each C3VI disease constituent, it can help predicting the effects of interventions as well as planning for the suitable sequence of interventions and for making critical clinical decisions with life-threatening risks. C3VI-DE is capable of monitoring both the cardiac and vascular conditions and can be used for their diagnosis with direct clinical relevance.

LIMITATIONS

This study was performed using data collected in 49 patients with C3VI. Future studies must confirm the conclusion of this study about C3VI-DE and C3VI-CT in a larger population of C3VI patients. In addition, future studies should further investigate the C3VI-CT algorithm with a higher temporal resolution of CT data (if becomes available).

DATA AVAILABILITY STATEMENT

The raw data supporting the conclusions of this article will be made available by the correspondence author upon request.

ETHICS STATEMENT

The studies involving human participants were reviewed and approved by the Institutional Review Boards of each institution as follows: the Hamilton Integrated Research Ethics Board (HiREB) of Hamilton Health Sciences and St. Joseph's Healthcare, both affiliated to McMaster University and Comité de ética de la investigación con medicamentos de Cantabria of the Hospital Universitario Marques de Valdecilla. The patients/participants provided their written informed consent to participate in this study.

AUTHOR CONTRIBUTIONS

MB and SB: data collection and analysis, interpretation of data, and manuscript writing. SK, JT, SV, ED, and MM: clinical data collection and analysis. ZK-M: conception and design, algorithm development (both C3VI-DE and C3VI-CT), data analysis, interpretation of data, manuscript writing, critical revision final approval of the manuscript, and supervise the research. All authors read and approved the final manuscript.

FUNDING

This work was supported by NSERC Discovery Grant (RGPIN-2017-05349) (https://www.nserc-crsng.gc.ca/index_eng.asp). MB, SB, and SK were supported by NSERC Discovery Grant (RGPIN-2017-05349). NSERC as the funders had no role in study design, data collection and analysis, decision to publish, or preparation of the manuscript.

ACKNOWLEDGMENTS

We are thankful of great comments of two reviewers that helped us to improve the quality of the manuscript.

REFERENCES

Anavekar, N. S., and Oh, J. K. (2009). Doppler echocardiography: a contemporary review. *J. Cardiol.* 54, 347–358. doi: 10.1016/j.jjcc.2009.10.001

Andreucci, M., Solomon, R., and Tasanarong, A. (2014). Side effects of radiographic contrast media: pathogenesis, risk factors, and prevention. *BioMed Res. Int.* 2014, 741018. doi: 10.1155/2014/741018

Antonini-Canterin, F., Poli, S., Vriz, O., Pavan, D., Bello, V. D., and Nicolosi, G. L. (2013). The Ventricular-Arterial Coupling: From Basic Pathophysiology to Clinical Application in the Echocardiography Laboratory. *J. Cardiovasc. Echography* 23, 91–95. doi: 10.4103/2211-4122.127408

Anvari, S., Nambiar, S., Pang, J., and Maftoon, N. (2021). Computational Models and Simulations of Cancer Metastasis. *Arch. Comput. Methods Eng.* doi: 10.1007/s11831-021-09554-1

Ben-Assa, E., Brown, J., Keshavarz-Motamed, Z., de la Torre Hernandez, J. M., Leiden, B., Olender, M., et al. (2019). Ventricular stroke work and vascular impedance refine the characterization of patients with aortic stenosis. *Sci. Transl. Med.* 11, doi: 10.1126/scitranslmed.aaw0181

Benevento, E., Djebbari, A., Keshavarz-Motamed, Z., Cecere, R., and Kadem, L. (2015). Hemodynamic Changes following Aortic Valve Bypass: A Mathematical Approach. *PLoS ONE* 10, doi: 10.1371/journal.pone.0123000

Benjamin, E. J., Muntner, P., Alonso, A., Bittencourt, M. S., Callaway, C. W., Carson, A. P., et al. (2019). Heart Disease and Stroke Statistics—2019 Update: A Report From the American Heart Association. *Circulation* 139, e56–e528. doi: 10.1161/CIR.0000000000000659

Blanke, P., Naoum, C., Dvir, D., Bapat, V., Ong, K., Muller, D., et al. (2016). *Predicting LVOT Obstruction in Transcatheter Mitral Valve Implantation: Concept of the Neo-LVOT. JACC Cardiovasc. Imaging*. Available online at: http://www.sciencedirect.com/science/article/pii/S1936878X16000395 [Accessed September 17, 2016]

Blecker, S., Bhatia, R. S., You, J. J., Lee, D. S., Alter, D. A., Wang, J. T., et al. (2013). Temporal trends in the utilization of echocardiography in Ontario, 2001 to 2009. *JACC Cardiovasc. Imaging* 6, 515–522. doi: 10.1016/j.jcmg.2012.10.026

Borlaug, B. A., and Kass, D. A. (2008). Ventricular-Vascular Interaction in Heart Failure. *Heart Fail. Clin.* 4, 23–36. doi: 10.1016/j.hfc.2007.10.001

Broomé, M., Maksuti, E., Bjällmark, A., Frenckner, B., and Janerot-Sjöberg, B. (2013). Closed-loop real-time simulation model of hemodynamics and oxygen transport in the cardiovascular system. *Biomed. Eng. Online* 12, 69. doi: 10.1186/1475-925X-12-69

Brown, K. A., and Ditchey, R. V. (1988). Human right ventricular end-systolic pressure-volume relation defined by maximal elastance. *Circulation* 78, 81–91.

Burgstahler, C., and Schroeder, S. (2007). Magnetic resonance imaging versus computed tomography for the detection of coronary stenosis: do we really have to focus on "stenoses"? *Heart* 93, 1322–1324. doi: 10.1136/hrt.2006.113910

Burkhoff, D., Mirsky, I., and Suga, H. (2005). Assessment of systolic and diastolic ventricular properties via pressure-volume analysis: a guide for clinical, translational, and basic researchers. *Am. J. Physiol. Heart Circ. Physiol.* 289, H501–H512. doi: 10.1152/ajpheart.00138.2005

Chaudhry, Q. A. (2015). A Gaussian function model for simulation of complex environmental sensing. *Complex Adapt. Syst. Model.* 3, 3. doi: 10.1186/s40294-015-0009-0

de Canete, J. F., del Saz-Orozco, P., Moreno-Boza, D., and Duran-Venegas, E. (2013). Object-oriented modeling and simulation of the closed loop cardiovascular system by using SIMSCAPE. *Comput. Biol. Med.* 43, 323–333. doi: 10.1016/j.compbiomed.2013.01.007

Dell'Italia, L. J., and Walsh, R. A. (1988). Application of a time varying elastance model to right ventricular performance in man. *Cardiovasc. Res.* 22, 864–874.

Di Carli, M. F., Geva, T., and Davidoff, R. (2016). The Future of Cardiovascular Imaging. *Circulation* 133, 2640–2661.

Duanmu, Z., Yin, M., Fan, X., Yang, X., and Luo, X. (2018). A patient-specific lumped-parameter model of coronary circulation. *in Scientific Reports* doi: 10.1038/s41598-018-19164-w

Dweck, M. R., Boon, N. A., and Newby, D. E. (2012). Calcific aortic stenosis: a disease of the valve and the myocardium. *J. Am. Coll. Cardiol.* 60, 1854–1863. doi: 10.1016/j.jacc.2012.02.093

Edwards, A. D., and Arthurs, O. J. (2011). Paediatric MRI under sedation: is it necessary? What is the evidence for the alternatives? *Pediatr. Radiol.* 41, 1353. doi: 10.1007/s00247-011-2147-7

Elkins, C. J., and Alley, M. T. (2007). Magnetic resonance velocimetry: applications of magnetic resonance imaging in the measurement of fluid motion. *Exp. Fluids* 43, 823–858. doi: 10.1007/s00348-007-0383-2

Elmariah, S., Palacios, I. F., McAndrew, T., Hueter, I., Inglessis, I., Baker, J. N., et al. (2013). Outcomes of Transcatheter and Surgical Aortic Valve Replacement in High-Risk Patients With Aortic Stenosis and Left Ventricular Dysfunction Results From the Placement of Aortic Transcatheter Valves (PARTNER) Trial (Cohort A). *Circ. Cardiovasc. Interv.* 6, 604–614.

Faggioni, M., and Mehran, R. (2016). Preventing Contrast-induced Renal Failure: A Guide. *Interv. Cardiol. Rev.* 11, 98–104. doi: 10.15420/icr.2016:10:2

Flachskampf, F. A., Rodriguez, L., Chen, C., Guerrero, J. L., Weyman, A. E., and Thomas, J. D. (1993). Analysis of mitral inertance: a factor critical for early transmitral filling. *J. Am. Soc. Echocardiogr. Off. Publ. Am. Soc. Echocardiogr.* 6, 422–432. doi: 10.1016/s0894-7317(14)80241-1

Fleischmann, D., Liang, D. H., and Herfkens, R. J. (2008). Technical advances in cardiovascular imaging. *Semin. Thorac. Cardiovasc. Surg.* 20, 333–339. doi: 10.1053/j.semtcvs.2008.11.015

Frolov, S. V., Sindeev, S. V., Lischouk, V. A., Gazizova, D. S., Liepsch, D., and Balasso, A. (2016). A lumped parameter model of cardiovascular system with pulsating heart for diagnostic studies. *J. Mech. Med. Biol.* 17, 1750056. doi: 10.1142/S0219519417500567

Garcia, D., Barenbrug, P. J. C., Pibarot, P., Dekker, A. L. A. J., van der Veen, F. H., Maessen, J. G., et al. (2005). A ventricular-vascular coupling model in presence of aortic stenosis. *Am. J. Physiol. Heart Circ. Physiol.* 288, H1874–H1884. doi: 10.1152/ajpheart.00754.2004

Garcia, D., Camici, P. G., Durand, L.-G., Rajappan, K., Gaillard, E., Rimoldi, O. E., et al. (2009). Impairment of coronary flow reserve in aortic stenosis. *J. Appl. Physiol. Bethesda Md* 1985 106, 113–121. doi: 10.1152/japplphysiol.00049.2008

Généreux, P., Head, S. J., Hahn, R., Daneault, B., Kodali, S., Williams, M. R., et al. (2013). Paravalvular leak after transcatheter aortic valve replacement: the new Achilles' heel? A comprehensive review of the literature. *J. Am. Coll. Cardiol.* 61, 1125–1136.

Geven, M. C. F., Bohté, V. N., Aarnoudse, W. H., van den Berg, P. M. J., Rutten, M. C. M., Pijls, N. H. J., et al. (2004). A physiologically representative in vitro model of the coronary circulation. *Physiol. Meas.* 25, 891–904. doi: 10.1088/0967-3334/25/4/009

Gleason, W. L., and Braunwald, E. (1962). Studies on the first derivative of the ventricular pressure pulse in man. *J. Clin. Invest.* 41, 80–91. doi: 10.1172/JCI104469

Ikonomidis, I., Aboyans, V., Blacher, J., Brodmann, M., Brutsaert, D. L., Chirinos, J. A., et al. (2019). The role of ventricular–arterial coupling in cardiac disease and heart failure: assessment, clinical implications and therapeutic interventions. A consensus document of the European Society of Cardiology Working Group on Aorta & Peripheral Vascular Diseases, European Association of Cardiovascular Imaging, and Heart Failure Association. *Eur. J. Heart Fail.* 21, 402–424. doi: 10.1002/ejhf.1436

Kass, D. A., Midei, M., Graves, W., Brinker, J. A., and Maughan, W. L. (1988). Use of a conductance (volume) catheter and transient inferior vena caval occlusion for rapid determination of pressure-volume relationships in man. *Cathet. Cardiovasc. Diagn.* 15, 192–202.

Keshavarz-Motamed, Z. (2020). A diagnostic, monitoring, and predictive tool for patients with complex valvular, vascular and ventricular diseases. *Sci. Rep.* 10, 1–19. doi: 10.1038/s41598-020-63728-8

Keshavarz-Motamed, Z., Edelman, E. R., Motamed, P. K., Garcia, J., Dahdah, N., and Kadem, L. (2015). The role of aortic compliance in determination of coarctation severity: Lumped parameter modeling, in vitro study and clinical evaluation. *J. Biomech.* 48, 4229–4237.

Keshavarz-Motamed, Z., Garcia, J., Gaillard, E., Capoulade, R., Ven, F. L., Cloutier, G., et al. (2014). Non-Invasive Determination of Left Ventricular Workload in Patients with Aortic Stenosis Using Magnetic Resonance Imaging and Doppler Echocardiography. *PLoS One* 9:e86793. doi: 10.1371/journal.pone.0086793

Keshavarz-Motamed, Z., Garcia, J., Maftoon, N., Bedard, E., Chetaille, P., and Kadem, L. (2012). A new approach for the evaluation of the severity of coarctation of the aorta using Doppler velocity index and effective orifice area: in vitro validation and clinical implications. *J. Biomech.* 45, 1239–1245.

Keshavarz-Motamed, Z., Garcia, J., Pibarot, P., Larose, E., and Kadem, L. (2011). Modeling the impact of concomitant aortic stenosis and coarctation of the aorta on left ventricular workload. *J. Biomech.* 44, 2817–2825. doi: 10.1016/j.jbiomech.2011.08.001

Keshavarz-Motamed, Z., Rikhtegar Nezami, F., Partida, R. A., Nakamura, K., Staziaki, P. V., Ben-Assa, E., et al. (2016). Elimination of trans-coarctation pressure gradients has no impact on left ventricular function or aortic shear stress post intervention in patients with mild coarctation. *JACC Cardiovasc. Interv.* 9, 1953–1965.

Keshavarz-Motamed, Z., Khodaei, S., Rikhtegar Nezami, F., Amrute, J., Lee Suk, J., Brown, J., et al. (2020). Mixed Valvular Disease Following Transcatheter Aortic Valve Replacement: Quantification and Systematic Differentiation Using Clinical Measurements and Image-Based Patient-Specific In Silico Modeling. *J. Am. Heart Assoc.* 9, e015063. doi: 10.1161/JAHA.119.015063

Khalafvand, S. S., Zhong, L., and Ng, E. Y. K. (2014). Three-dimensional CFD/MRI modeling reveals that ventricular surgical restoration improves ventricular

function by modifying intraventricular blood flow. *Int. J. Numer. Methods Biomed. Eng.* 30, 1044–1056. doi: 10.1002/cnm.2643

Khodaei, S., Henstock, A., Sadeghi, R., Sellers, S., Blanke, P., Leipsic, J., et al. (2021a). Personalized intervention cardiology with transcatheter aortic valve replacement made possible with a non-invasive monitoring and diagnostic framework. *Sci. Rep.* 11, 10888. doi: 10.1038/s41598-021-85500-2

Khodaei, S., Sadeghi, R., Blanke, P., Leipsic, J., Emadi, A., and Keshavarz-Motamed, Z. (2021b). Towards a non-invasive computational diagnostic framework for personalized cardiology of transcatheter aortic valve replacement in interactions with complex valvular, ventricular and vascular disease. *Int. J. Mech. Sci.* 202–203, 106506. doi: 10.1016/j.ijmecsci.2021.106506

Kilner, P. J., Gatehouse, P. D., and Firmin, D. N. (2007). Flow Measurement by Magnetic Resonance: A Unique Asset Worth Optimising. *J. Cardiovasc. Magn. Reson.* 9, 723–728. doi: 10.1080/10976640701465090

Kuo, P. H., Kanal, E., Abu-Alfa, A. K., and Cowper, S. E. (2007). Gadolinium-based MR Contrast Agents and Nephrogenic Systemic Fibrosis. *Radiology* 242, 647–649. doi: 10.1148/radiol.2423061640

Ky, B., French, B., May Khan, A., Plappert, T., Wang, A., Chirinos, J. A., et al. (2013). Ventricular-arterial coupling, remodeling, and prognosis in chronic heart failure. *J. Am. Coll. Cardiol.* 62, 1165–1172. doi: 10.1016/j.jacc.2013.03.085

Li, B., Wang, W., Mao, B., and Liu, Y. (2018). A Method to Personalize the Lumped Parameter Model of Coronary Artery. *Int. J. Comput. Methods* 16, 1842004. doi: 10.1142/S0219876218420045

Liang, F., Takagi, S., Himeno, R., and Liu, H. (2009). A Lumped Parameter Model Of Cardiovascular System With Pulsating Heart For Diagnostic Studies. *Med. Biol. Eng. Comput.* 47, 743–755. doi: 10.1007/s11517-009-0449-9

Lin, E., and Alessio, A. (2009). What are the basic concepts of temporal, contrast, and spatial resolution in cardiac CT? *J. Cardiovasc. Comput. Tomogr.* 3, 403–408. doi: 10.1016/j.jcct.2009.07.003

Maleki, M., and Esmaeilzadeh, M. (2012). The Evolutionary Development of Echocardiography. *Iran. J. Med. Sci.* 37, 222–232.

Maniar, H. S., Prasad, S. M., Gaynor, S. L., Chu, C. M., Steendijk, P., and Moon, M. R. (2003). Impact of pericardial restraint on right atrial mechanics during acute right ventricular pressure load. *Am. J. Physiol. Heart Circ. Physiol.* 284, H350–H357. doi: 10.1152/ajpheart.00444.2002

Mao, B., Feng, Y., Li, B., Liu, J., Feng, Y., and Liu, Y. (2019). Lumped parameter model based surgical planning for CABG. *Med. Nov. Technol. Devices* 2, 100014. doi: 10.1016/j.medntd.2019.100014

Marsden, A. L. (2013). Simulation based planning of surgical interventions in pediatric cardiology. *Phys. Fluids 1994-Present* 25, 101303.

McDowell, S. A. C. (1999). A Simple Derivation of the Boltzmann Distribution. *J. Chem. Educ.* 76, 1393. doi: 10.1021/ed076p1393

Mihalef, V., Itu, L., Mansi, T., and Sharma, P. (2017). "Lumped Parameter Whole Body Circulation Modelling," in *Patient-specific Hemodynamic Computations: Application to Personalized Diagnosis of Cardiovascular Pathologies*, eds L. M. Itu, P. Sharma, and C. Suciu (Cham: Springer International Publishing), 111–152. doi: 10.1007/978-3-319-56853-9_5

Moss, R. L., Razumova, M., and Fitzsimons, D. P. (2004). Myosin crossbridge activation of cardiac thin filaments: implications for myocardial function in health and disease. *Circ. Res.* 94, 1290–1300. doi: 10.1161/01.RES.0000127125.61647.4F

Mynard, J. P., Davidson, M. R., Penny, D. J., and Smolich, J. J. (2012). A simple, versatile valve model for use in lumped parameter and one-dimensional cardiovascular models. *Int. J. Numer. Methods Biomed. Eng.* 28, 626–641. doi: 10.1002/cnm.1466

Nombela-Franco, L., Ribeiro, H. B., Urena, M., Allende, R., Amat-Santos, I., DeLarochellière, R., et al. (2014). Significant mitral regurgitation left untreated at the time of aortic valve replacement: a comprehensive review of a frequent entity in the transcatheter aortic valve replacement era. *J. Am. Coll. Cardiol.* 63, 2643–2658.

Omran, H., Schmidt, H., Hackenbroch, M., Illien, S., Bernhardt, P., von der Recke, G., et al. (2003). Silent and apparent cerebral embolism after retrograde catheterisation of the aortic valve in valvular stenosis: a prospective, randomised study. *The Lancet* 361, 1241–1246.

Orwat, S., Diller, G.-P., and Baumgartner, H. (2014). Imaging of congenital heart disease in adults: choice of modalities. *Eur. Heart J. Cardiovasc. Imaging* 15, 6–17. doi: 10.1093/ehjci/jet124

Pant, S., Corsini, C., Baker, C., Hsia, T.-Y., Pennati, G., and Vignon-Clementel, I. E. (2018). A Lumped Parameter Model to Study Atrioventricular Valve Regurgitation in Stage 1 and Changes Across Stage 2 Surgery in Single Ventricle Patients. *IEEE Trans. Biomed. Eng.* 65, 2450–2458. doi: 10.1109/TBME.2018.2797999

Papolos, A., Narula, J., Bavishi, C., Chaudhry, F. A., and Sengupta, P. P. (2016). U.S. Hospital Use of Echocardiography: Insights From the Nationwide Inpatient Sample. *J. Am. Coll. Cardiol.* 67, 502–511. doi: 10.1016/j.jacc.2015.10.090

Parra, D. A., and Vera, K. (2012). New imaging modalities to assess cardiac function: not just pretty pictures. *Curr. Opin. Pediatr.* 24, 557–564. doi: 10.1097/MOP.0b013e328357bae3

Paterson, I., Mielniczuk, L. M., O'Meara, E., So, A., and White, J. A. (2013). Imaging Heart Failure: Current and Future Applications. *Can. J. Cardiol.* 29, 317–328. doi: 10.1016/j.cjca.2013.01.006

Pearce, M. S., Salotti, J. A., Little, M. P., McHugh, K., Lee, C., Kim, K. P., et al. (2012). Radiation exposure from CT scans in childhood and subsequent risk of leukaemia and brain tumours: a retrospective cohort study. *The Lancet* 380, 499–505. doi: 10.1016/S0140-6736(12)60815-0

Pibarot, P., Hahn, R. T., Weissman, N. J., and Monaghan, M. J. (2015). Assessment of paravalvular regurgitation following TAVR: a proposal of unifying grading scheme. *JACC Cardiovasc. Imaging* 8, 340–360. doi: 10.1016/j.jcmg.2015.01.008

Picano, E. (2005). Economic and biological costs of cardiac imaging. *Cardiovasc. Ultrasound* 3, 13. doi: 10.1186/1476-7120-3-13

Pironet, A., Dauby, P. C., Paeme, S., Kosta, S., Chase, J. G., and Desaive, T. (2013). Simulation of Left Atrial Function Using a Multi-Scale Model of the Cardiovascular System. *PLoS One* 8:e65146. doi: 10.1371/journal.pone.0065146

Power, S. P., Moloney, F., Twomey, M., James, K., O'Connor, O. J., and Maher, M. M. (2016). Computed tomography and patient risk: Facts, perceptions and uncertainties. *World J. Radiol.* 8, 902–915. doi: 10.4329/wjr.v8.i12.902

Rehman, R., and Makaryus, A. N. (2019). *"Cardiac Imaging," in StatPearls (Treasure Island (FL): StatPearls Publishing)*. Available online at: http://www.ncbi.nlm.nih.gov/books/NBK448128/ [Accessed July 3, 2019]

Revie, J. A., Stevenson, D., Chase, J. G., Pretty, C. J., Lambermont, B. C., Ghuysen, A., et al. (2013). Evaluation of a Model-Based Hemodynamic Monitoring Method in a Porcine Study of Septic Shock. *Comput. Math. Methods Med.* 2013, e505417. doi: 10.1155/2013/505417

Richter, Y., and Edelman, E. R. (2006). Cardiology is flow. *Circulation* 113, 2679–2682.

Rigsby, C. K., McKenney, S. E., Hill, K. D., Chelliah, A., Einstein, A. J., Han, B. K., et al. (2018). Radiation Dose Management for Pediatric Cardiac Computed Tomography: A Report from the Image Gently "Have-A-Heart" Campaign. *Pediatr. Radiol.* 48, 5–20. doi: 10.1007/s00247-017-3991-x

Ritchie, H., and Roser, M. (2018). *Causes of Death. Our World Data*. Available online at: https://ourworldindata.org/causes-of-death [Accessed June 27, 2019].

Roth, G. A., Johnson, C., Abajobir, A., Abd-Allah, F., Abera, S. F., Abyu, G., et al. (2017). Global, Regional, and National Burden of Cardiovascular Diseases for 10 Causes, 1990 to 2015. *J. Am. Coll. Cardiol.* 70, 1–25. doi: 10.1016/j.jacc.2017.04.052

Sabarudin, A., and Sun, Z. (2013). Beta-blocker administration protocol for prospectively ECG-triggered coronary CT angiography. *World J. Cardiol.* 5, 453–458. doi: 10.4330/wjc.v5.i12.453

Sadeghi, R., Khodaei, S., Ganame, J., and Keshavarz-Motamed, Z. (2020). Towards non-invasive computational-mechanics and imaging-based diagnostic framework for personalized cardiology for coarctation. *Sci. Rep.* 10, 9048. doi: 10.1038/s41598-020-65576-y

Saunderson, C. E. D., Paton, M. F., Chowdhary, A., Brown, L. A. E., Gierula, J., Sengupta, A., et al. (2020). Feasibility and validation of trans-valvular flow derived by four-dimensional flow cardiovascular magnetic resonance imaging in pacemaker recipients. *Magn. Reson. Imaging* 74, 46–55. doi: 10.1016/j.mri.2020.08.024

Scantlebury Dawn, C., Geske Jeffrey, B., and Nishimura Rick, A. (2013). Limitations of Doppler Echocardiography in the Evaluation of Serial Stenoses. *Circ. Cardiovasc. Imaging* 6, 850–852. doi: 10.1161/CIRCIMAGING.113.000575

Seemann, F., Arvidsson, P., Nordlund, D., Kopic, S., Carlsson, M., Arheden, H., et al. (2019). Noninvasive Quantification of Pressure-Volume Loops From

Brachial Pressure and Cardiovascular Magnetic Resonance. *Circ. Cardiovasc. Imaging* 12, e008493. doi: 10.1161/CIRCIMAGING.118.008493

Segers, P., Stergiopulos, N., Westerhof, N., Wouters, P., Kolh, P., and Verdonck, P. (2003). Systemic and pulmonary hemodynamics assessed with a lumped-parameter heart-arterial interaction model. *J. Eng. Math.* 47, 185–199. doi: 10.1023/B:ENGI.0000007975.27377.9c

Senzaki, H., Chen, C. H., and Kass, D. A. (1996). Single-beat estimation of end-systolic pressure-volume relation in humans. A new method with the potential for noninvasive application. *Circulation* 94, 2497–2506.

Shen, J., Faruqi, A. H., Jiang, Y., and Maftoon, N. (2021). Mathematical Reconstruction of Patient-Specific Vascular Networks Based on Clinical Images and Global Optimization. *IEEE Access* 9, 20648–20661. doi: 10.1109/ACCESS.2021.3052501

Smith-Bindman, R., Miglioretti, D. L., Johnson, E., Lee, C., Feigelson, H. S., Flynn, M., et al. (2012). Use of diagnostic imaging studies and associated radiation exposure for patients enrolled in large integrated health care systems, 1996-2010. *JAMA* 307, 2400–2409. doi: 10.1001/jama.2012.5960

Sotiropoulos, F., Le, T. B., and Gilmanov, A. (2016). Fluid mechanics of heart valves and their replacements. *Annu. Rev. Fluid Mech.* 48, 259–283.

Steeds, R. P. (2011). Echocardiography: frontier imaging in cardiology. *Br. J. Radiol. 84 Spec No* 3, S237–S245. doi: 10.1259/bjr/77730594

Stergiopulos, N., Meister, J. J., and Westerhof, N. (1996). Determinants of stroke volume and systolic and diastolic aortic pressure. *Am. J. Physiol.* 270, H2050–H2059. doi: 10.1152/ajpheart.1996.270.6.H2050

Stergiopulos, N., Segers, P., and Westerhof, N. (1999). Use of pulse pressure method for estimating total arterial compliance in vivo. *Am. J. Physiol.* 276, H424–H428. doi: 10.1152/ajpheart.1999.276.2.H424

Takeuchi, M., Odake, M., Takaoka, H., Hayashi, Y., and Yokoyama, M. (1992). Comparison between preload recruitable stroke work and the end-systolic pressure–volume relationship in man. *Eur. Heart J.* 13, 80–84. doi: 10.1093/eurheartj/13.suppl_E.80

Tanné, D., Kadem, L., Rieu, R., and Pibarot, P. (2008). Hemodynamic impact of mitral prosthesis-patient mismatch on pulmonary hypertension: an in silico study. *J. Appl. Physiol.* 105, 1916–1926.

Taylor, C. A., and Steinman, D. A. (2010). Image-based modeling of blood flow and vessel wall dynamics: applications, methods and future directions. *Ann. Biomed. Eng.* 38, 1188–1203.

Van de Werf, F., Boel, A., Geboers, J., Minten, J., Willems, J., Geest, H. D., et al. (1984). Diastolic properties of the left ventricle in normal adults and in patients with third heart sounds. *Circulation* 69, 1070–1078. doi: 10.1161/01.CIR.69.6.1070

Vedula, V., Seo, J., Lardo, A. C., and Mittal, R. (2016). Effect of trabeculae and papillary muscles on the hemodynamics of the left ventricle. *Theoretical and Computational Fluid Dynamics volume* 30, ages3–ages21.

Villarraga-Gómez, H., Lee, C., and Smith, S. T. (2018). Dimensional metrology with X-ray CT: A comparison with CMM measurements on internal features and compliant structures. *Precis. Eng.* 51, 291–307. doi: 10.1016/j.precisioneng.2017.08.021

Watson, S. R., Dormer, J. D., and Fei, B. (2018). Imaging technologies for cardiac fiber and heart failure: a review. *Heart Fail. Rev.* 23, 273–289. doi: 10.1007/s10741-018-9684-1

Yin, F. C. P. (ed.) (1987). *Ventricular/Vascular Coupling: Clinical, Physiological, and Engineering Aspects*. New York: Springer-Verlag, doi: 10.1007/978-1-4613-8634-6

Yushkevich, P. A., Piven, J., Hazlett, H. C., Smith, R. G., Ho, S., Gee, J. C., et al. (2006). User-guided 3D active contour segmentation of anatomical structures: significantly improved efficiency and reliability. *NeuroImage* 31, 1116–1128. doi: 10.1016/j.neuroimage.2006.01.015

Zhong, L., Schrauben, E. M., Garcia, J., Uribe, S., Grieve, S. M., Elbaz, M. S. M., et al. (2019). Intracardiac 4D Flow MRI in Congenital Heart Disease: Recommendations on Behalf of the ISMRM Flow & Motion Study Group. *J. Magn. Reson. Imaging* 50, 677–681. doi: 10.1002/jmri.26858

Conflict of Interest: The authors declare that the research was conducted in the absence of any commercial or financial relationships that could be construed as a potential conflict of interest.

frontiers in Bioengineering and Biotechnology

ORIGINAL RESEARCH
published: 02 August 2021
doi: 10.3389/fbioe.2021.731924

Comparison of Swine and Human Computational Hemodynamics Models for the Study of Coronary Atherosclerosis

*Giuseppe De Nisco[1], Claudio Chiastra[1], Eline M. J. Hartman[2], Ayla Hoogendoorn[2], Joost Daemen[2], Karol Calò[1], Diego Gallo[1], Umberto Morbiducci[1] and Jolanda J. Wentzel[2]**

[1]PoliTo[BIO]Med Lab, Department of Mechanical and Aerospace Engineering, Politecnico di Torino, Turin, Italy, [2]Department of Cardiology, Biomedical Engineering, Erasmus MC, Rotterdam, Netherlands

OPEN ACCESS

Edited by:
Philippe Sucosky, Kennesaw State University, United States

Reviewed by:
Mauro Malvè, Public University of Navarre, Spain
Sónia Isabel Silva Pinto, University of Porto, Portugal

***Correspondence:**
Jolanda J. Wentzel
j.wentzel@erasmusmc.nl

Specialty section:
This article was submitted to Biomechanics, a section of the journal Frontiers in Bioengineering and Biotechnology

Received: *28 June 2021*
Accepted: *22 July 2021*
Published: *02 August 2021*

Citation:
De Nisco G, Chiastra C, Hartman EMJ, Hoogendoorn A, Daemen J, Calò K, Gallo D, Morbiducci U and Wentzel JJ (2021) Comparison of Swine and Human Computational Hemodynamics Models for the Study of Coronary Atherosclerosis. Front. Bioeng. Biotechnol. 9:731924. doi: 10.3389/fbioe.2021.731924

Coronary atherosclerosis is a leading cause of illness and death in Western World and its mechanisms are still non completely understood. Several animal models have been used to 1) study coronary atherosclerosis natural history and 2) propose predictive tools for this disease, that is asymptomatic for a long time, aiming for a direct translation of their findings to human coronary arteries. Among them, swine models are largely used due to the observed anatomical and pathophysiological similarities to humans. However, a direct comparison between swine and human models in terms of coronary hemodynamics, known to influence atherosclerotic onset/development, is still lacking. In this context, we performed a detailed comparative analysis between swine- and human-specific computational hemodynamic models of coronary arteries. The analysis involved several near-wall and intravascular flow descriptors, previously emerged as markers of coronary atherosclerosis initiation/progression, as well as anatomical features. To do that, non-culprit coronary arteries (18 right–RCA, 18 left anterior descending–LAD, 13 left circumflex–LCX coronary artery) from patients presenting with acute coronary syndrome were imaged by intravascular ultrasound and coronary computed tomography angiography. Similarly, the three main coronary arteries of ten adult mini-pigs were also imaged (10 RCA, 10 LAD, 10 LCX). The geometries of the imaged coronary arteries were reconstructed (49 human, 30 swine), and computational fluid dynamic simulations were performed by imposing individualized boundary conditions. Overall, no relevant differences in 1) wall shear stress-based quantities, 2) intravascular hemodynamics (in terms of helical flow features), and 3) anatomical features emerged between human- and swine-specific models. The findings of this study strongly support the use of swine-specific computational models to study and characterize the hemodynamic features linked to coronary atherosclerosis, sustaining the reliability of their translation to human vascular disease.

Keywords: coronary artery disease, computational fluid dynamics, patient-specific modeling, wall shear stress, helical flow

INTRODUCTION

Coronary atherosclerosis is a major cause of morbidity and mortality in Western World (Virani et al., 2021), consisting of the build-up of an atherosclerotic plaque in the wall of coronary arteries, possibly leading to severe stenosis and/or thrombus formation, with vascular lumen occlusion and death (Lusis, 2000).

The natural history of the coronary atherosclerotic disease is driven by a complex interplay of several local biological, systemic and biomechanical factors, with a still incomplete understanding of the underlying mechanisms (Chatzizisis et al., 2007; Wentzel et al., 2012; Kwak et al., 2014; Morbiducci et al., 2016; Zaromytidou et al., 2016). Although several large *in vivo* human studies have provided valuable insights into the initiation and progression of coronary atherosclerosis (Stone et al., 2012; Cheng et al., 2014), these studies remain often limited to short durations and limited number of imaging moments, mainly due to ethical reasons (Millon et al., 2014). Therefore, they lack the time scales necessary for the development of this pathology and might not capture all phenomena present during this complex, multifactorial disease (Daugherty et al., 2017). Such limitations may affect the *in vivo* investigation of innovative clinical strategies for coronary atherosclerotic treatment in humans (Xiangdong et al., 2011; Millon et al., 2014; Daugherty et al., 2017).

Animal models of coronary atherosclerosis have the potential to overcome many of these inherent restrictions of human studies (Xiangdong et al., 2011; Millon et al., 2014; Daugherty et al., 2017), facilitating the analysis of the coronary atherosclerotic disease at different stages (Daugherty et al., 2017). For this reason, several large animal models based on the use of rabbits, pigs, or non-human primates, have been adopted to e.g.: 1) study coronary atherosclerosis natural history (Getz and Reardon, 2012; Daugherty et al., 2017); 2) evaluate the efficacy of clinical treatment procedures (Shin et al., 2021); 3) identify predictive tools for the evolution of the disease, which most of the time is asymptomatic (De Nisco et al., 2020; Hoogendoorn et al., 2020; Mazzi et al., 2021). Most of the animal model-based studies on atherosclerosis onset and progression imply that their findings reliably inform human studies, sometimes suggesting a direct translation to humans. However, the value of animal models in identifying hemodynamic factors involved in the atherosclerotic disease or in predicting the effectiveness of treatment strategies in clinical trials has remained not fully clarified.

In relation to coronary atherosclerotic disease, the capability of an animal model to mimic the complexity of the human coronary pathophysiology plays a critical role (Daugherty et al., 2017; Shin et al., 2021). In this regard, due to their similarities to humans in terms of anatomy (i.e., size and distribution) (Weaver et al., 1986; Lelovas et al., 2014), pathophysiology (Lelovas et al., 2014; Shim et al., 2016), lipoprotein profile (Mahley et al., 1975), and site of lesion formation (Shim et al., 2016), swine models are massively applied to study coronary atherosclerosis (Xiangdong et al., 2011; Daugherty et al., 2017). In particular, swine models of familial hypercholesterolemia with a mutation in genes coding for apolipoproteins and low-density lipoproteins receptor allows studying sustained atherosclerotic plaques onset/progression because of their capability to develop advanced atherosclerotic lesions within 12–18 months when fed a high fat diet (Thim et al., 2010; Daugherty et al., 2017).

Besides the already investigated differences/similarities between human and swine models, a direct comparison in terms of coronary hemodynamics, a well-established biomechanical factor influencing atherosclerotic onset/development (Wentzel et al., 2012; Morbiducci et al., 2016), is still lacking. This may limit the translation to human models of previous findings suggesting the role of near-wall and intravascular hemodynamic descriptors as markers of coronary atherosclerosis initiation/progression in swine-specific models (Chatzizisis et al., 2008; De Nisco et al., 2019, 2020; Hoogendoorn et al., 2020).

Aiming to bridge this gap of knowledge, in this study we perform, for the first time, a detailed comparative analysis between swine- and human-specific computational hemodynamic models of the three main coronary arteries, in terms of several descriptors of 1) near-wall and 2) intravascular flow quantities, and 3) vessel morphology, that have been already identified as biomechanical risk factors in the initiation/progression of coronary atherosclerotic plaques (Stone et al., 2012; Wentzel et al., 2012).

MATERIALS AND METHODS

Human Population

Forty-eight hemodynamically stable patients from the IMPACT study data set (Hartman et al., 2020) were involved in the analysis. Clinical characteristics are listed in **Table 1**. The IMPACT study enrolled patients with acute coronary syndrome and with at least one non-stented non-culprit coronary segment accessible for intracoronary imaging study. The presence of previous coronary artery bypass graft surgery, 3-vessel disease, renal insufficiency (creatinine clearing <50 ml/min), left ventricular ejection fraction <30%, and atrial fibrillation, were considered as exclusion criteria. All patients underwent percutaneous coronary

TABLE 1 | - Human dataset clinical characteristics.

Clinical characteristics	
N = 48 subjects	
Age (years)	61.3 ± 9
Men (%)	43 (90%)
Body mass index	27.0 ± 4.5
Diabetes mellitus, n (%)	8 (17%)
Hypertension, n (%)	14 (29%)
Dyslipidemia, n (%)	23 (48%)
Smokers, n (%)	36 (75%)
Positive family history, n (%)	19 (40%)
Previous MI, n (%)	9 (19%)
Previous PCI, n (%)	11 (23%)
LDL (mmol/L)	2.84 ± 1.02

MI: myocardial infarction; PCI: percutaneous coronary intervention; LDL: low-density lipoproteins.

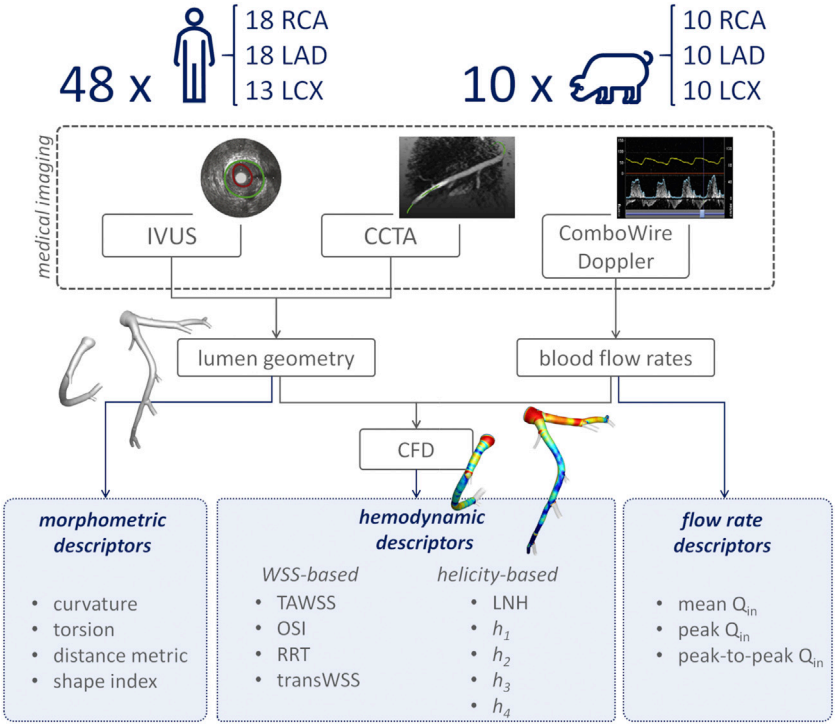

FIGURE 1 | Schematic diagram of the study design, showing how imaging data contribute to define vessel geometry and hemodynamic, morphometric, and flow variables. RCA, LAD, and LCX denote right, left anterior descending, and left circumflex coronary artery, respectively. IVUS: intravascular ultrasound; CCTA: coronary computed tomography angiography; CFD: computational fluid dynamics; TAWSS: time-averaged wall shear stress; OSI: oscillatory shear index; RRT: relative residence time; transWSS: transverse wall shear stress; LNH: local normalized helicity; h_1: average helicity; h_2: average helicity intensity; h_3: signed balance of counter rotating helical flow structures; h_4: unsigned balance of counter rotating helical flow structures; Q_{in}: inflow rate.

intervention of the culprit coronary vessel. After successful treatment, a non-culprit coronary segment (right–RCA, left anterior descending–LAD, or left circumflex–LCX coronary artery) was imaged and used for the study.

All patients gave their informed consent. The study was approved by the local medical ethical committee of the Erasmus MC (MEC 2015-535, NL54519.078.15), was registered (ISCRTN:43,170,100) and conducted in accordance with the World Medical Association Declaration of Helsinki (64th WMA General Assembly, Fortaleza, Brazil, October 2013) and Medical Research Involving Human Subject Act (WMO).

Animal Model

Ten adult familial hypercholesterolemia Bretoncelles Meishan mini-pigs with a low-density lipoprotein receptor mutation were enrolled in the analysis. The study involved the three main coronary arteries (i.e., RCA, LAD, and LCX) of each animal at 3 months after the start of a high fat diet. At this stage, the animals were considered ostensibly healthy.

The study was approved by the local animal ethics committee of the Erasmus MC (EMC nr. 109-14-10) and performed according to the National Institute of Health guide for the Care and Use of Laboratory animals (Council, 2011).

Medical Imaging and Geometry Reconstruction

An overview of the methods is provided in **Figure 1**. The same imaging protocol was applied to human- and swine-specific coronary segments. Each coronary artery was imaged by computed coronary tomography angiography (CCTA) (SOMATOM Force, Siemens Healthineers, Germany) and intravascular ultrasound (IVUS) (InfraRedX, Burlington, MA, United States), as detailed elsewhere (De Nisco et al., 2019, 2020; Hartman et al., 2020; Hoogendoorn et al., 2020). Coronary lumen contours were segmented on IVUS images (QCU-CMS, Medis Medical Imaging, Leiden) and aligned along the 3D CCTA centerline in order to reconstruct the 3D vessel geometry. Additional luminal regions proximally (up to the aorta) and at least two diameters distally to the IVUS-imaged segment were reconstructed using CCTA images (De Nisco et al., 2019, 2020; Hartman et al., 2020; Hoogendoorn et al., 2020). The 79 reconstructed luminal surfaces of the coronary arteries (49 human-specific models: 18 RCA, 18 LAD, and 13 LCX; 30 swine-specific models: 10 RCA, 10 LAD, and 10 LCX) are presented in **Figure 2** and **Figure 3** for humans and animal models, respectively. The 3D geometries were reconstructed including the side branches.

Combowire Doppler (Phillips Volcano, Zaventem, Belgium) flow velocity measurements were acquired in each coronary

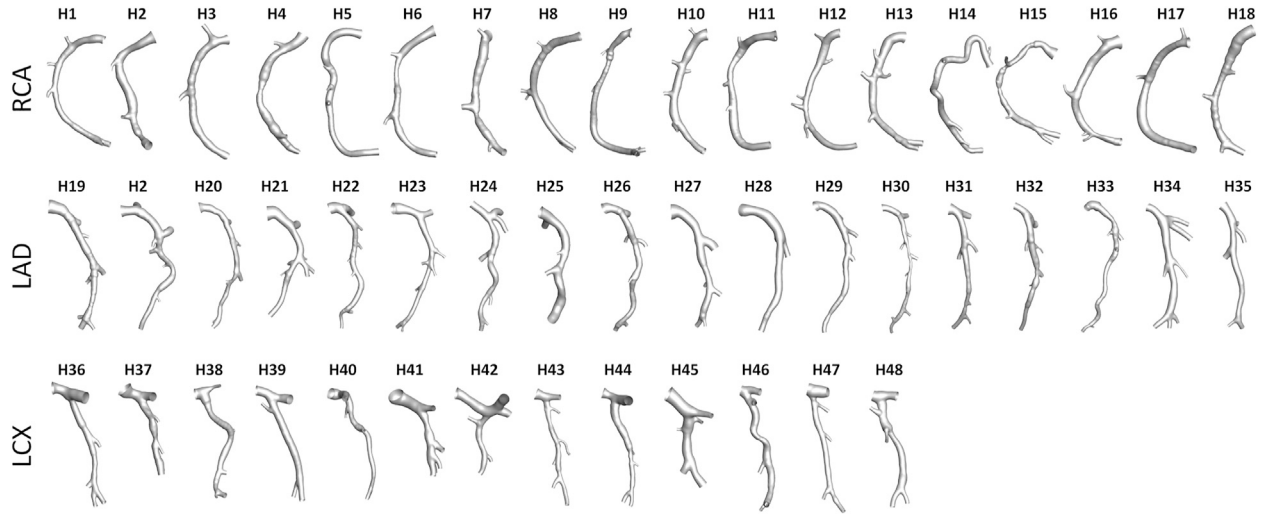

FIGURE 2 | Geometry of the 49 human coronary artery models. Labels from H1 to H48 identify the single patient. Right (RCA), left anterior descending (LAD), and left circumflex (LCX) coronary artery geometries are grouped.

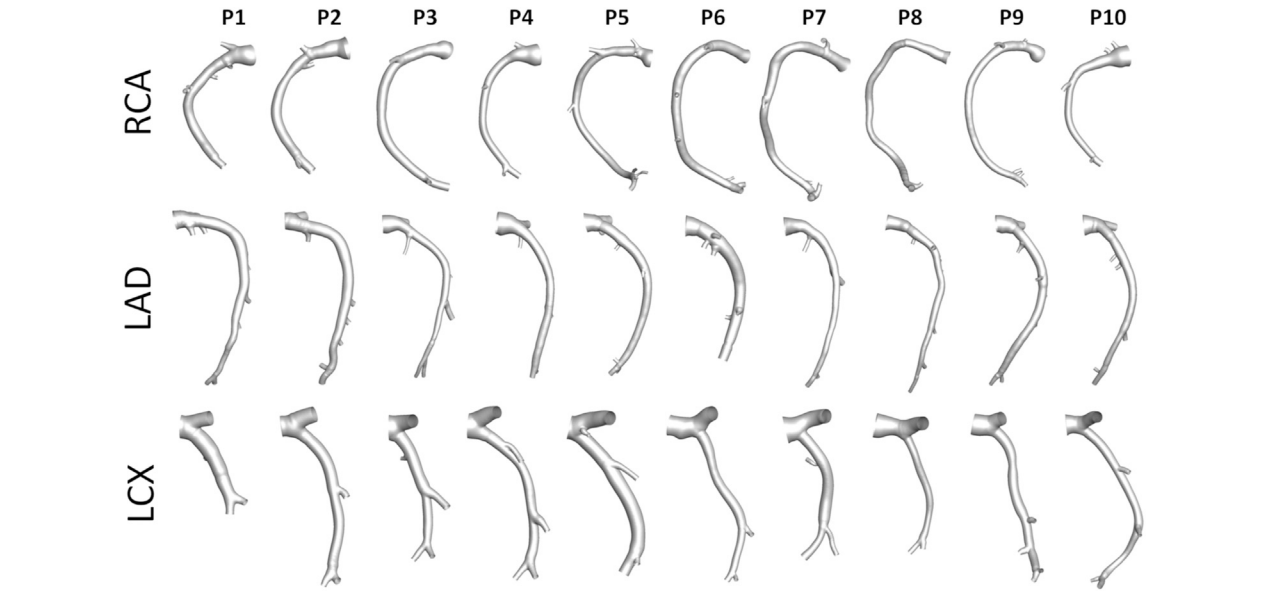

FIGURE 3 | Geometry of the 30 swine coronary artery models. Labels from P1 to P10 identify the single pig. Right (RCA), left anterior descending (LAD), and left circumflex (LCX) coronary artery geometries are grouped.

artery at the inflow section and immediately upstream and downstream of each side branch, as extensively detailed elsewhere (De Nisco et al., 2019, 2020; Hartman et al., 2020; Hoogendoorn et al., 2020).

Computational Hemodynamics

The reconstructed vessel geometries were discretized, and unsteady-state computational fluid dynamics (CFD) simulations were performed to characterize coronary hemodynamics (**Figure 1**). The governing equations of fluid motion were numerically solved in Fluent environment (ANSYS Inc. Canonsburg, PA, United States of America), by using the finite volume method. All the CFD settings are extensively detailed elsewhere (De Nisco et al., 2019, 2020; Hartman et al., 2020; Hoogendoorn et al., 2020). Briefly, blood was assumed as an incompressible, homogeneous, non-Newtonian fluid (Chiastra et al., 2017). No-slip condition was assumed at the arterial wall. *In vivo* ComboWire Doppler velocity measurements were used to derive individualized (specific for each human and

TABLE 2 | - Definition of hemodynamic descriptors involved in the analysis.

WSS-based descriptors	
Time-Averaged WSS (TAWSS)	$\mathrm{TAWSS} = \frac{1}{T}\int_0^T \lvert\mathbf{WSS}\rvert\, dt$
Oscillatory Shear Index (OSI)	$\mathrm{OSI} = 0.5\left[1 - \left(\frac{\left\lvert\int_0^T \mathbf{WSS}\, dt\right\rvert}{\int_0^T \lvert\mathbf{WSS}\rvert\, dt}\right)\right]$
Relative Residence Time (RRT)	$\mathrm{RRT} = \frac{1}{\mathrm{TAWSS}\cdot(1-2\cdot\mathrm{OSI})} = \frac{1}{\frac{1}{T}\left\lvert\int_0^T \mathbf{WSS}\, dt\right\rvert}$
Transverse WSS (transWSS)	$\mathrm{transWSS} = \frac{1}{T}\int_0^T \left\lvert\mathbf{WSS}\cdot\left(\mathbf{n}\times\frac{\int_0^T \mathbf{WSS}\, dt}{\left\lvert\int_0^T \mathbf{WSS}\, dt\right\rvert}\right)\right\rvert dt$
Helicity-based descriptors	
Local Normalized Helicity (LNH)	$\mathrm{LNH} = \frac{\mathbf{v}\cdot\boldsymbol{\omega}}{\lvert\mathbf{v}\rvert\cdot\lvert\boldsymbol{\omega}\rvert} = \cos\gamma$
Average helicity (h_1)	$h_1 = \frac{1}{TV}\int_T\int_V \mathbf{v}\cdot\boldsymbol{\omega}\, dV\, dt$
Average helicity intensity (h_2)	$h_2 = \frac{1}{TV}\int_T\int_V \lvert\mathbf{v}\cdot\boldsymbol{\omega}\rvert\, dV\, dt$
Signed balance of counter-rotating helical flow structures (h_3)	$h_3 = \frac{h_1}{h_2} \quad -1 \le h_3 \le 1$
Unsigned balance of counter-rotating helical flow structures (h_4)	$h_4 = \frac{\lvert h_1\rvert}{h_2} \quad 0 \le h_4 \le 1$

WSS *is the WSS vector; T is the period of the cardiac cycle;* **n** *is the unit vector normal to the arterial surface at each element;* **v** *is the velocity vector;* **ω** *is the vorticity vector;* γ *is the angle between velocity and vorticity vectors; V is the arterial volume.*

swine model, as reported elsewhere (De Nisco et al., 2019, 2020; Hartman et al., 2020; Hoogendoorn et al., 2020)) boundary conditions (BCs) as follows: 1) the inlet flow rate was estimated from the most proximal Doppler velocity measurement, and prescribed as inlet boundary condition in terms of time-dependent flat velocity profile; 2) side branches perfusion was quantified as the difference between upstream and downstream Doppler velocity-based flow rate measurements and applied as outflow condition in terms of measured flow ratio. If velocity-based flow measurements were inaccurate or not available, a generalized flow rate (van der Giessen et al., 2011) was prescribed as inflow BC, while a proper diameter-based scaling law for human- (van der Giessen et al., 2011) and swine-specific (Huo and Kassab, 2012) models was applied to estimate the flow ratio at the outflow section (De Nisco et al., 2019, 2020; Hartman et al., 2020; Hoogendoorn et al., 2020).

Hemodynamic Descriptors

Near-wall and intravascular hemodynamics were analyzed by computing the hemodynamic quantities listed in **Table 2**.

Near-wall hemodynamics was characterized in terms of the three canonical WSS-based descriptors, namely time-averaged wall shear stress (TAWSS), oscillatory shear index (OSI) (Ku et al., 1985), and relative residence time (RRT) (Himburg et al., 2004). Additionally, the transversal WSS (transWSS) (Peiffer et al., 2013), a descriptor of WSS multidirectionality, was also considered. The transWSS represents the average WSS component acting orthogonal to the time-average WSS vector direction (**Table 2**).

Based on the recently-emerged atheroprotective role of physiological helical-shaped blood flow structures in coronary arteries (De Nisco et al., 2019, 2020), intravascular hemodynamics was investigated in terms of helical flow, quantified through the quantities summarized in **Table 2**. In detail, the local normalized helicity (LNH) (Morbiducci et al., 2007), representing the cosine of the angle between local velocity (**v**) and vorticity (**ω**) vectors (**Table 2**), was used to visualize right- and left-handed helical blood flow patterns (positive and negative LNH values, respectively) (Gallo et al., 2012; Morbiducci et al., 2013) inside the coronary artery models. Furthermore, four additional helicity-based descriptors (Gallo et al., 2012; Morbiducci et al., 2013) were applied to characterize the strength, size and relative rotational direction of helical flow in the 79 coronary artery models (**Table 2**): cycle-average helicity (h_1) and helicity intensity (h_2), indicating the net amount and the intensity of helical flow, respectively; signed (h_3) and unsigned helical rotation balance (h_4), measuring the prevalence (identified by the sign of descriptor h_3) or only the strength of relative rotations of helical flow patterns, respectively.

The hemodynamics of each coronary vessel was characterized also in terms of inflow rate (Q_{in}), as given by its mean, peak, and peak-to-peak values (**Figure 1**). Peak-to-peak Q_{in} was defined as the difference between the maximum and the minimum values of the inflow rate.

TABLE 3 | - Definition of the geometric quantities adopted for characterizing coronary vessels morphometry.

Morphometric descriptors		
Curvature (κ)	$\kappa(s) = \frac{\lvert\mathbf{C}'(s)\times\mathbf{C}''(s)\rvert}{\lvert\mathbf{C}'(s)\rvert^3}$	
Torsion (τ)	$\tau(s) = \frac{[\mathbf{C}'(s)\times\mathbf{C}''(s)]\cdot\mathbf{C}'''(s)}{\lvert\mathbf{C}'(s)\times\mathbf{C}''(s)\rvert^2}$	
Distance Metric (DM)	$\mathrm{DM} = \frac{L}{l}$	$\mathrm{DM} \ge 1$
Shape Index (SI)	$\mathrm{SI}(s) = \frac{d(s)}{D(s)}$	$0 \le \mathrm{SI} \le 1$

C′, ***C″***, *and* ***C‴*** *are the first, second, and third derivative of the centerline curve* ***C****, respectively; s is the curvilinear abscissa; L and l are the curvilinear and Euclidean distance between the centerline curve endpoints, respectively; d and D are the minimum and maximum diameter of arterial cross-section, respectively.*

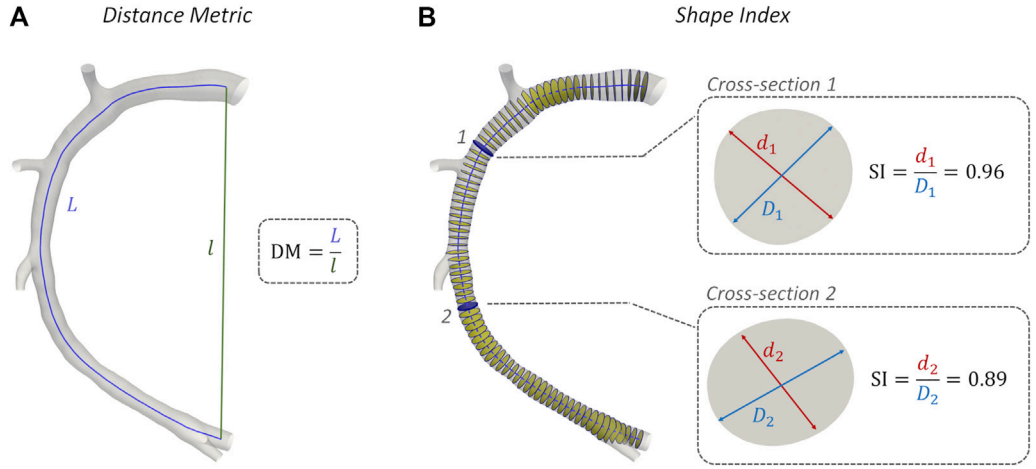

FIGURE 4 | Methodology of Distance Metric (DM) and Shape Index (SI) assessment. Model H1 was taken as explanatory example. **(A)** DM computing: *L* and *l* are the curvilinear (blue) and Euclidean (green) distance between the centerline curve endpoints; **(B)** SI computation at two explanatory coronary cross-sections along the vessel centerline: *d* and *D* are the minimum and maximum diameter of arterial cross-section, respectively.

Morphometry

The geometric quantities summarized in **Table 3** were adopted for characterizing coronary vessel morphometry. In detail, a robust centerline-based analysis was performed, where vessel curvature (κ) and torsion (τ) were assessed according to an approach proposed elsewhere (Gallo et al., 2015). Briefly, after extracting the main vessel centerline (defined as the geometrical locus of the centers of maximum inscribed spheres) in the Vascular Modeling Toolkit (VMTK, Orobix, Bergamo, Italy, http://www.vmtk.org/) environment, its continuous, noise-free analytical formulation (**C**) was obtained by adopting free-knots regression splines (Sangalli et al., 2009). Coronary curvature and torsion were then calculated by differentiation of the free-knots regression, spline centerline representation (**Table 3**). Here the average values of curvature ($\overline{\kappa}$) and torsion ($\overline{\tau}$) along the main vessel were considered, which are known to have an influence on arterial hemodynamics (Gallo et al., 2015). Additionally, the degree of tortuosity of coronary vessels was assessed by computing the standard Distance Metric index (DM, **Table 3**) (Vorobtsova et al., 2016; Ciurică et al., 2019). DM, computed as the ratio between the curvilinear (*L*) and Euclidean (*l*) distance between the centerline curve endpoints (**Figure 4A**), quantifies the "lengthening effect" of coronary tortuosity. Finally, coronary cross-section eccentricity along the main vessel centerline was measured by computing the Shape Index (SI), as the ratio between the local cross-section minimum (*d*) and the maximum (*D*) diameter (Finotello et al., 2020). To calculate the SI, the opensource Vascular Modelling Toolkit software (VMTK, Orobix, Bergamo, Italy, http://www.vmtk.org/) was used. SI ranges between 0 and 1, where one indicates a perfectly circular cross-sectional shape (**Figure 4B**). Like for κ and τ, the average value of Shape Index ($\overline{SI}$) along the main vessel was considered for the analysis.

Statistical Analysis

Data analysis was performed in the main branch of the RCA, LAD and LCX segments only, by removing coronary side branches in the post-processing step using VMTK. Hemodynamic and morphometric data were grouped according to the population (humans *vs* animals) and the coronary vessel type (i.e., RCA, LAD, or LCX). Differences between the two populations were investigated in Matlab environment (The MathWorks Inc. United States of America) by the Mann-Whitney *U*-test. Statistical significance was assumed for $p < 0.05$.

RESULTS

Near-Wall and Intravascular Flow Features Visualization

Helical blood flow patterns developing in human and swine coronary models were visualized in **Figure 5** and **Figure 6**, respectively, using the cycle-average LNH isosurface values (blue and red colors indicate left-handed and right-handed helical flow patterns, respectively). Despite intra- and inter-species variations, the intravascular hemodynamics of both human and swine coronary arteries were markedly characterized by the presence of two distinguishable counter-rotating helical flow patterns.

Intra- and inter-species differences were analyzed by visual inspection also in terms of TAWSS luminal distribution, presented in **Figure 7** and **Figure 8** for human and swine models, respectively. In detail, the luminal surface of some of the human coronary arteries were largely exposed to low TAWSS values (red color in figure, e.g., cases H2-RCA, H21-LAD, and H38-LCX), whereas other human arteries were not (e.g., cases H5-RCA, H28-LAD, and H39-LCX). The same observations on intra-species variability can also be extended to swine models (**Figure 8**), with some individual cases exposed to low TAWSS values over most of the luminal surface (e.g., cases P5-RCA, P10-LAD, and P7-LCX) and other ones presenting with low TAWSS luminal regions of

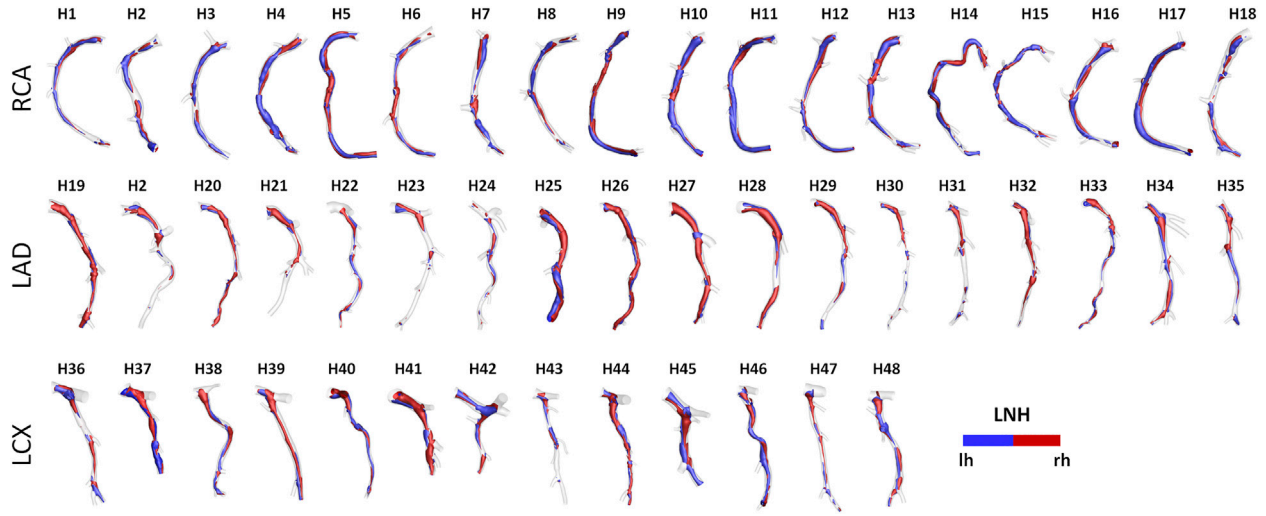

FIGURE 5 | Intravascular fluid structures in the 49 human coronary arteries. For each case, isosurfaces of cycle-average LNH are presented. Distinguishable left-handed (lh - LNH < 0) and right-handed (rh - LNH > 0) helical flow structures can be observed in all coronary arteries. Labels from H1 to H48 identify the single patient. Right (RCA), left anterior descending (LAD), and left circumflex (LCX) coronary artery geometries are grouped.

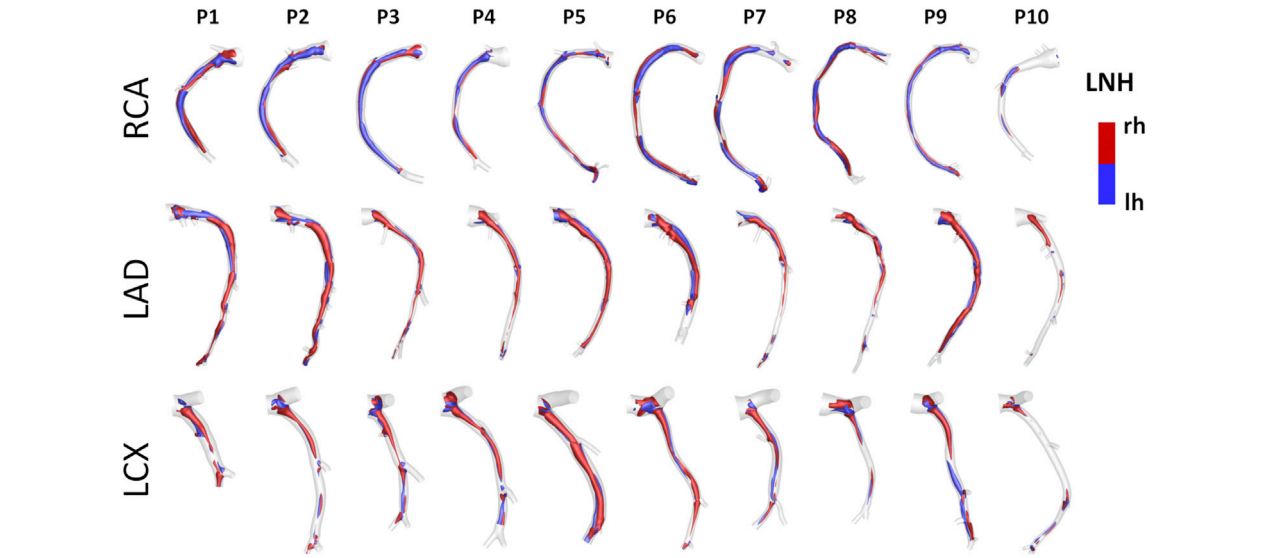

FIGURE 6 | Intravascular fluid structures in the 30 swine coronary arteries. For each case, isosurfaces of cycle-average LNH are presented. Distinguishable left-handed (lh - LNH < 0) and right-handed (rh - LNH > 0) helical flow structures can be observed in all coronary arteries. Labels from P1 to P10 identify the single pig. Right (RCA), left anterior descending (LAD), and left circumflex (LCX) coronary artery geometries are grouped.

moderate extension (e.g., cases P8-RCA, P9-LAD, and P4-LCX).

Hemodynamics: Quantitative Analysis

A detailed quantitative comparison between human and swine models is presented in **Figure 9** in terms of hemodynamics and morphometry. Human and swine models were grouped per species and per coronary vessel. Among the WSS-based descriptors, no significant difference emerged between the two species (*WSS* column in **Figure 9**) in terms of TAWSS (confirming the qualitative results presented in **Figures 7**, **8**), RRT, and transWSS. Contrarily, a significant inter-species difference emerged for OSI but only for the LADs ($p < 0.001$), with swine LADs characterized by higher median value and larger interquartile range than human LADs (0.0005 [0.0004, 0.0007] and 0.0023 [0.0013, 0.0057] for human and swine models, respectively). Interestingly, an overall poor WSS multidirectionality emerged in both species, with OSI values lower than 0.08 (0.0005 [0.0003, 0.0009] and 0.0009 [0.0006, 0.0022] for human and swine models, respectively), and

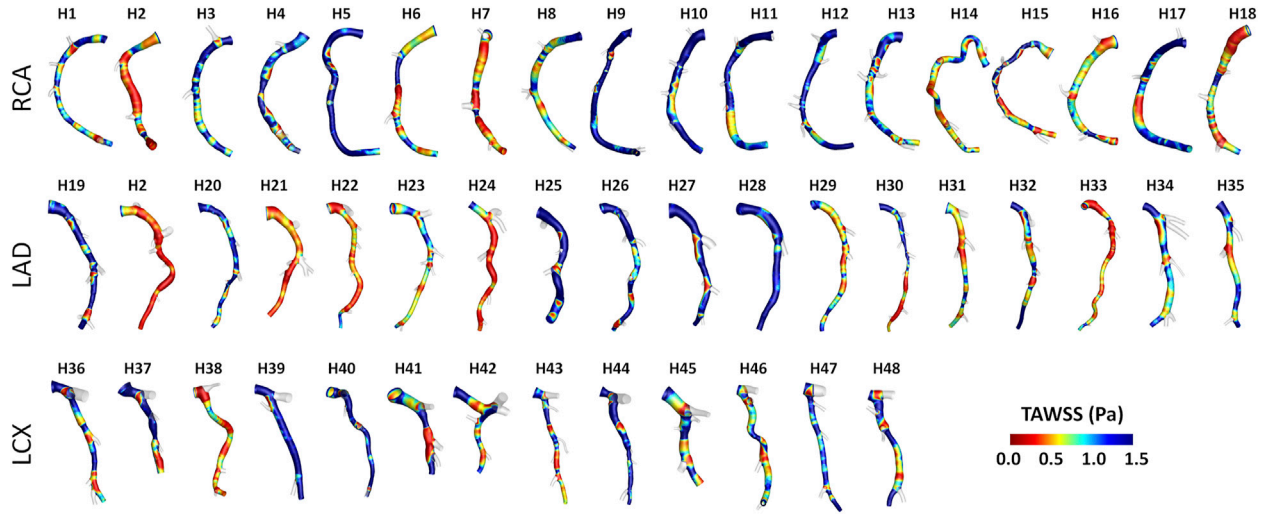

FIGURE 7 | TAWSS distribution at the luminal surface of the 49 human coronary arteries. Red color highlights luminal regions exposed to low TAWSS values. Labels from H1 to H48 identify the single patient. Right (RCA), left anterior descending (LAD), and left circumflex (LCX) coronary artery geometries are grouped.

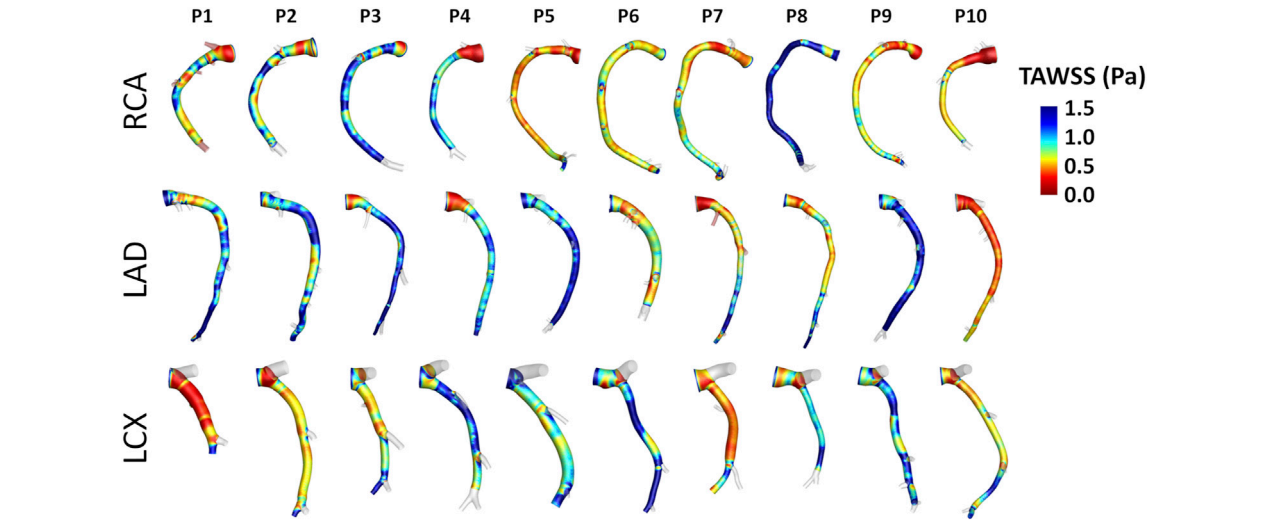

FIGURE 8 | TAWSS distribution at the luminal surface of the 30 swine coronary arteries. Red color highlights luminal regions exposed to low TAWSS values. Labels from P1 to P10 identify the single pig. Right (RCA), left anterior descending (LAD), and left circumflex (LCX) coronary artery geometries are grouped.

transWSS values lower than 0.10 Pa (0.03 [0.02, 0.05] and 0.03 [0.02, 0.04] Pa for human and swine models, respectively).

The quantitative analysis of the intravascular flow patterns, based on helicity-based descriptors (*Helicity* column in **Figure 9**), highlighted a significant inter-species difference for helical flow intensity in RCA ($p < 0.05$) and LCX ($p < 0.01$). In detail, human RCA and LCX vessels (2.53 [0.83, 3.76] and 2.33 [1.73, 4.63] m/s^2 for human RCA and LCX, respectively) exhibited higher h_2 values compared to the respective swine vessels (0.71 [0.35, 1.33] and 0.46 [0.20, 1.40] m/s^2 for swine RCA and LCX, respectively), and larger intra-species variability. Of note, no significant inter-species difference emerged for topological quantities h_3 and h_4, suggesting an overall similar configuration of the counter-rotating helical flow patterns developing in human and swine coronary arteries, presented in **Figures 5**, **6**.

The analysis of the hemodynamics is completed by the *Flow* column in **Figure 9**. Overall, human and swine coronary vessels were characterized by similar mean, peak, and peak-to-peak values of measured inflow rate, except for the LAD, where swine models presented significantly higher Q_{in} maximum values ($2.52.10^{-5}$ [$1.95.10^{-5}$, $3.87.10^{-5}$] and $5.20.10^{-5}$ [$3.36.10^{-5}$, $7.95.10^{-5}$] m^3/s for human and swine models, respectively; $p < 0.05$) and larger dynamics ($1.86.10^{-6}$ [$1.48.10^{-6}$, $3.09.10^{-6}$] and $4.97.10^{-6}$ [$3.01.10^{-6}$, $7.09.10^{-6}$] m^3/s

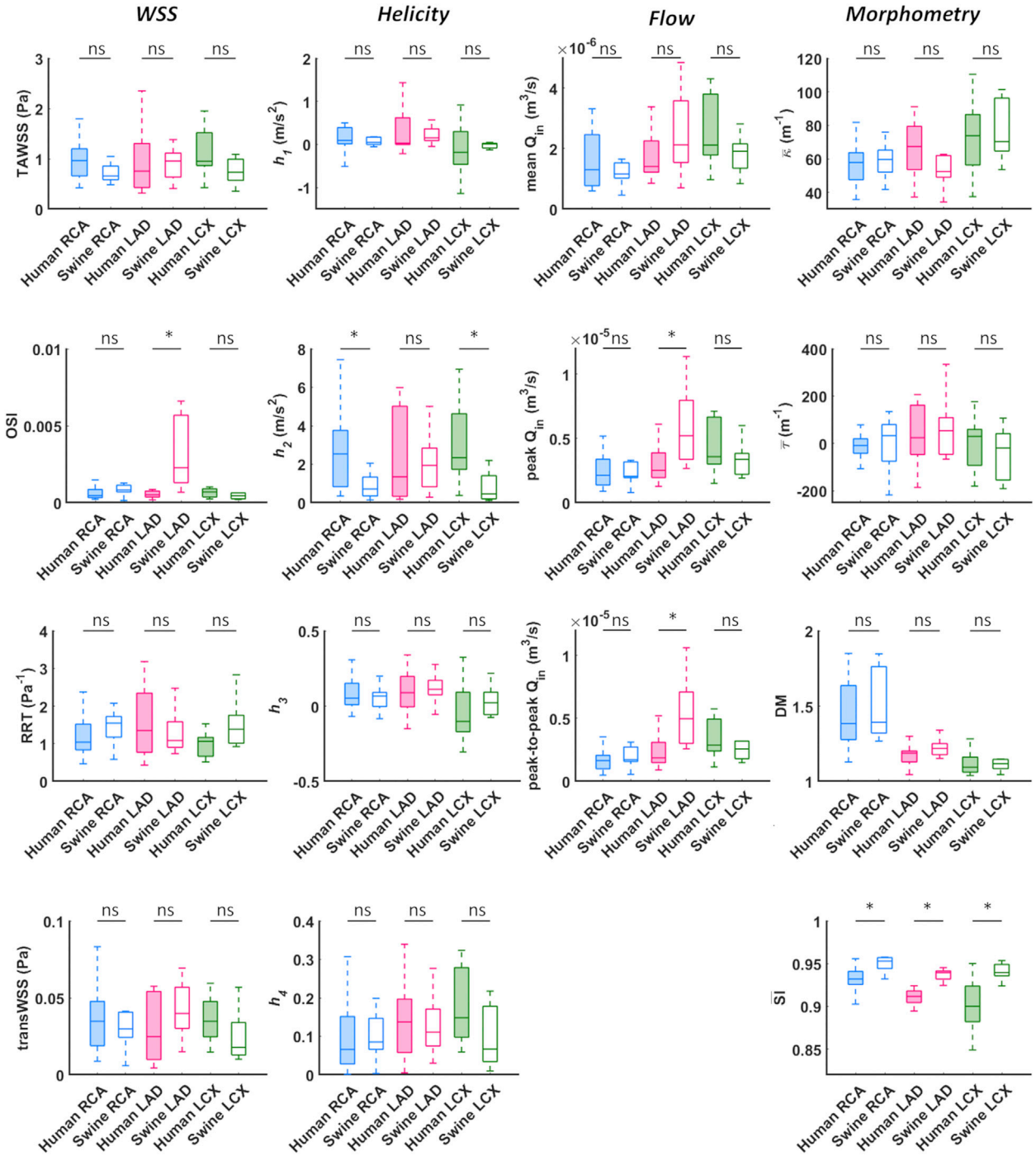

FIGURE 9 | Box plots comparing WSS, helicity, flow rate, and morphometry in human and swine coronary arteries. For each population, right (RCA), left anterior descending (LAD), and left circumflex (LCX) coronary artery geometries are grouped and distinguished by box color (blue, magenta, and green, respectively). *WSS* column: TAWSS - time-average wall shear stress, OSI - oscillatory shear index, RRT - relative residence time, transWSS - transverse wall shear stress; *Helicity* column: h_1 - average helicity, h_2 - average helicity intensity, h_3 - signed balance of counter rotating helical flow structures, h_4 - unsigned balance of counter rotating helical flow structures; *Flow* column: Q_{in} - inflow rate; *Morphometry* column: κ - curvature, τ - torsion, DM - distance metric, SI - similarity index. Median and interquartile range are displayed for each descriptor. *$p < 0.05$.

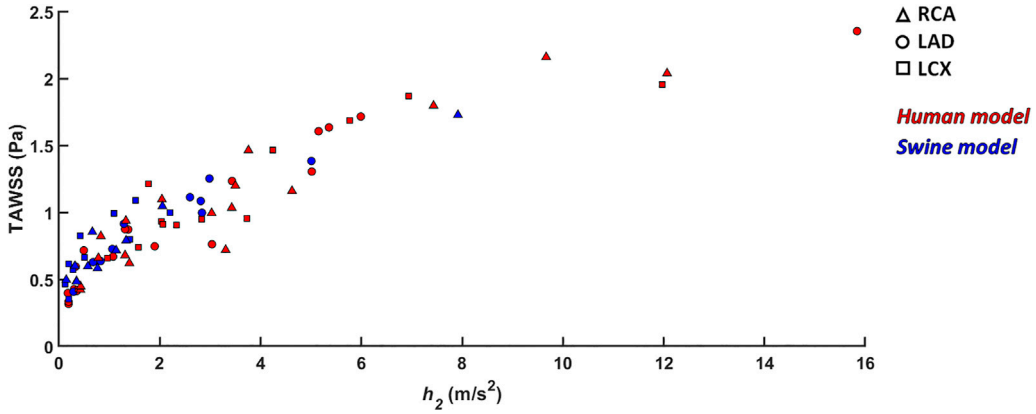

FIGURE 10 | Scatter plots of helicity intensity h_2 vs TAWSS. Red color indicates human models; blue color indicates swine models. Right (RCA), left anterior descending (LAD), and left circumflex (LCX) coronary artery geometries are distinguished by marker shape.

for human and swine models, respectively; $p < 0.01$) than human models.

Morphometry: Quantitative Analysis

No significant inter-species difference emerged in vessel curvature, torsion, and tortuosity (*Morphometry* column in **Figure 9**). In both populations, RCA models were characterized by higher DM values and larger intra-species variability, compared to LAD and LCX vessels. Conversely, a significant inter-species difference emerged in coronary vessels eccentricity, as measured by the shape index ($p < 0.01$). In detail, the cross-section of human coronary arteries presented with a more elliptical shape than swine arteries (**Figure 4B** and **Figure 9**), as highlighted by the lower $\overline{SI}$ values.

DISCUSSION

Swine models have contributed to a deeper understanding of the natural history of coronary atherosclerosis, with a valuable application to multiple research fields, such as the study of novel clinical treatment procedures efficacy (Getz and Reardon, 2012; Daugherty et al., 2017; Shin et al., 2021). The translation of results obtained in swine models to the patient situation is mainly based on intra-species comparisons of the coronary anatomy (Weaver et al., 1986; Lelovas et al., 2014), pathophysiology (Lelovas et al., 2014; Shim et al., 2016), cholesterol levels (Mahley et al., 1975) and sites of lesion formation (Shim et al., 2016). However, a direct comparison in terms of coronary local hemodynamics, a recognized risk factor of atherosclerosis (Chatzizisis et al., 2007; Wentzel et al., 2012; Kwak et al., 2014; Morbiducci et al., 2016; Zaromytidou et al., 2016), is still lacking.

Here a detailed comparative analysis between 49 human- and 30 swine-specific computational hemodynamic models of coronary arteries is presented in terms of coronary near-wall and intravascular hemodynamics, and morphometry. The study highlighted that overall human and swine coronary models present equivalent near-wall and intravascular hemodynamics, as well as equivalent geometrical features, with some minor exceptions, as discussed below.

Hemodynamics

No significant inter-species difference emerged in terms of TAWSS, RRT, and transWSS in the three main coronary arteries. The two populations differed only in terms of OSI of the LAD coronary segment, with swine vessels presenting with significantly higher OSI median values than the human ones (0.0023 [0.0013, 0.0057] and 0.0005 [0.0004, 0.0007] for swine and human models, respectively, $p < 0.001$). Such inter-species difference can be interpreted as a consequence of the observed inter-species difference in the measured inflow rates at LAD coronary arteries, presenting with significantly larger peak and peak-to-peak values in swine than human models ($p < 0.05$ and $p < 0.01$, respectively), thus physically precipitating oscillations of the WSS vector along the cardiac cycle (Ku et al., 1985; Soulis et al., 2006; Gallo et al., 2018).

As previous research has shown (De Nisco et al., 2019, 2020), relatively low WSS multidirectionality is present in coronary arteries of both ostensibly healthy swine and human coronary arteries, as reflected by the observed very low OSI and transWSS values (*WSS* column in **Figure 9**). Even though low multidirectionality was observed, plaque progression was proven to be significantly related to multidirectional WSS parameters (Hoogendoorn et al., 2020). However, multidirectional WSS seems to be more relevant for atherosclerotic plaque development in later stages of the disease and therefore this inter-species observed difference in OSI in the LAD is of less relevance for studies on atherosclerotic plaque initiation (Gallo et al., 2018; Kok et al., 2019; Hoogendoorn et al., 2020).

An overall inter-species equivalence emerged also in terms of intravascular hemodynamics, characterized by the presence of distinguishable counter-rotating helical flow patterns (**Figures 5**, **6**). The evident similarity of helical flow features in human and swine coronary models finds confirmation in average helicity

(h_1), and in the balance between counter-rotating helical flow patterns (h_3 and h_4, respectively) in the three main coronary arteries (*Helicity* column in **Figure 9**). Significant inter-species differences emerged only for the helical flow intensity (h_2), being higher in human RCAs ($p < 0.05$) and LCXs ($p < 0.01$) compared to the swine ones (*Helicity* column in **Figure 9**). However, despite the emerged significant difference in helical flow intensity, the relationship between the latter and WSS in coronary arteries, as previously reported for swine models (De Nisco et al., 2019), was also observed in human coronary arteries. Physiological high values of helical flow intensity keep TAWSS values within a physiological, atheroprotective range (**Figure 10**), and thereby prevent atherosclerotic plaque progression, which was also demonstrated by a direct association between plaque progression and helical flow intensity (De Nisco et al., 2020). Hence, the emerged inter-species difference in helical flow intensity does not cancel out but confirms previous findings on its physiological significance in swine coronary arteries (De Nisco et al., 2019, 2020), and remarks upon its possible use as surrogate marker of cardiovascular flow disturbances (Morbiducci et al., 2009, 2013; Gallo et al., 2012, 2015, 2018; Liu et al., 2015).

Morphometry

The comparative analysis between human and swine coronary anatomical features confirmed the strong inter-species similarity. In addition to the already observed equivalence in vessel size and distribution (Weaver et al., 1986; Lelovas et al., 2014), human and swine coronary arteries are characterized by comparable values of mean curvature, mean torsion and tortuosity of the three main coronary arteries (*Morphometry* column in **Figure 9**). Interestingly, the emerged significant inter-species difference in coronary eccentricity ($\overline{SI}$), revealed that the luminal section of human coronary arteries is more elliptical than that of swine coronary arteries.

Limitations

Several limitations could weaken the findings of this study. Computational hemodynamic modelling suffers from assumptions and uncertainties. Among them, the assumption of rigid vascular wall might affect WSS estimation. However, studies applying fluid-structure interaction approaches reported that WSS spatial distribution is preserved when using rigid walls (Torii et al., 2009; Malvè et al., 2012). Additionally, the cardiac-induced motion of coronary arteries was neglected. This idealization was based on previous evidences reporting the minor effect of myocardial motion on coronary flow and WSS distribution with respect to the blood pressure pulse (Zeng et al., 2003; Theodorakakos et al., 2008). Moreover, cardiac-induced motion could markedly affect instantaneous WSS distribution, but it has a minor effect on cycle-average WSS quantities as the ones considered in the present study (Torii et al., 2010). Finally, the limitations above affect swine as well as human populations. Hence, even not knowing whether their influence is species-independent, it might be negligible on the outcome of this study.

CONCLUSION

Atherosclerosis is a multifactorial disease with hemodynamics as one of the main determinants of atherosclerotic plaque localization and progression. This study demonstrates that individual swine computational hemodynamic models of the three main coronary arteries are representative of the human hemodynamics in the same vessels. In detail, the study points out that swine and human coronary arteries present the same near-wall and intravascular hemodynamic features, as well as demonstrate anatomical similarities. These findings thus support the application of swine-specific computational models to investigate the hemodynamic-related risk of coronary atherosclerosis and have a high potential to translate directly into human coronary artery disease.

DATA AVAILABILITY STATEMENT

The data analyzed in this study is subject to the following licenses/restrictions: the data can be shared upon request. Requests to access these datasets should be directed to j.wentzel@erasmusmc.nl.

ETHICS STATEMENT

The study involving human participants was reviewed and approved by the METC (MEC-2015-535; positief besluit NL54519.078.15, v02). The patients/participants provided their written informed consent to participate in this study. The animal study was reviewed and approved by DEC: dier experimentele commissie (EMC nr 109-14-10).

AUTHOR CONTRIBUTIONS

Conceptualization: GDN, DG, CC, UM, and JW; Data curation: GDN, AH, KC, and EH; Simulations: GDN, KC; Post-processing of the results: GDN; Interpretation of data: GDN, DG, CC, UM, and JW; Supervision: UM, JW; Writing - original draft preparation: GDN, UM, DG, CC, UM, and JW. All authors discussed the results and reviewed the manuscript.

FUNDING

CC, DG, and UM were supported by the Italian Ministry of Education, University and Research (FISR 2019_03221, CECOMES). EH, AH, and JW were supported by the European Research Council (grant number 310457).

REFERENCES

Chatzizisis, Y. S., Coskun, A. U., Jonas, M., Edelman, E. R., Feldman, C. L., and Stone, P. H. (2007). Role of Endothelial Shear Stress in the Natural History of Coronary Atherosclerosis and Vascular Remodeling: Molecular, Cellular, and Vascular Behavior. *J. Am. Coll. Cardiol.* 49, 2379–2393. doi:10.1016/j.jacc.2007.02.059

Chatzizisis, Y. S., Jonas, M., Coskun, A. U., Beigel, R., Stone, B. V., Maynard, C., et al. (2008). Prediction of the Localization of High-Risk Coronary Atherosclerotic Plaques on the Basis of Low Endothelial Shear Stress: an Intravascular Ultrasound and Histopathology Natural History Study. *Circulation* 117, 993–1002. doi:10.1161/CIRCULATIONAHA.107.695254

Cheng, J. M., Garcia-Garcia, H. M., de Boer, S. P. M., Kardys, I., Heo, J. H., Akkerhuis, K. M., et al. (2014). *In Vivo* detection of High-Risk Coronary Plaques by Radiofrequency Intravascular Ultrasound and Cardiovascular Outcome: Results of the ATHEROREMO-IVUS Study. *Eur. Heart J.* 35, 639–647. doi:10.1093/eurheartj/eht484

Chiastra, C., Gallo, D., Tasso, P., Iannaccone, F., Migliavacca, F., Wentzel, J. J., et al. (2017). Healthy and Diseased Coronary Bifurcation Geometries Influence Near-wall and Intravascular Flow: A Computational Exploration of the Hemodynamic Risk. *J. Biomech.* 58, 79–88. doi:10.1016/j.jbiomech.2017.04.016

Ciurică, S., Lopez-Sublet, M., Loeys, B. L., Radhouani, I., Natarajan, N., Vikkula, M., et al. (2019). Arterial Tortuosity. *Hypertens. (Dallas, Tex. 1979)* 73, 951–960. doi:10.1161/HYPERTENSIONAHA.118.11647

Council, N. R. (2011). *Guide for the Care and Use of Laboratory Animals*. Eighth Edition. Washington, DC: The National Academies Press. doi:10.17226/12910

Daugherty, A., Tall, A. R., Daemen, M. J. A. P., Falk, E., Fisher, E. A., García-Cardeña, G., et al. (2017). Recommendation on Design, Execution, and Reporting of Animal Atherosclerosis Studies: A Scientific Statement from the American Heart Association. *Arterioscler. Thromb. Vasc. Biol.* 37, e131–e157. doi:10.1161/ATV.0000000000000062

De Nisco, G., Hoogendoorn, A., Chiastra, C., Gallo, D., Kok, A. M., Morbiducci, U., et al. (2020). The Impact of Helical Flow on Coronary Atherosclerotic Plaque Development. *Atherosclerosis* 300, 39–46. doi:10.1016/J.ATHEROSCLEROSIS.2020.01.027

De Nisco, G., Kok, A. M., Chiastra, C., Gallo, D., Hoogendoorn, A., Migliavacca, F., et al. (2019). The Atheroprotective Nature of Helical Flow in Coronary Arteries. *Ann. Biomed. Eng.* 47, 425–438. doi:10.1007/s10439-018-02169-x

Finotello, A., Faggiano, E., Conti, M., Spinella, G., Pane, B., Palombo, D., et al. (2020). Medical Image Analysis to Measure the Follow-Up Geometry of Thoraco-Abdominal Aortic Aneurysms Treated with Multilayer Flow Modulator Stent. *Comput. Methods Biomech. Biomed. Eng. Imaging Vis.* 8, 126–133. doi:10.1080/21681163.2019.1617195

Gallo, D., Bijari, P. B., Morbiducci, U., Qiao, Y., Xie, Y., Joyce), et al. (2018). Segment-specific Associations between Local Haemodynamic and Imaging Markers of Early Atherosclerosis at the Carotid Artery: an *In Vivo* Human Study. *J. R. Soc. Interf.* 15, 20180352. doi:10.1098/rsif.2018.0352

Gallo, D., Steinman, D. A., Bijari, P. B., and Morbiducci, U. (2012). Helical Flow in Carotid Bifurcation as Surrogate Marker of Exposure to Disturbed Shear. *J. Biomech.* 45, 2398–2404. doi:10.1016/j.jbiomech.2012.07.007

Gallo, D., Steinman, D. A., and Morbiducci, U. (2015). An Insight into the Mechanistic Role of the Common Carotid Artery on the Hemodynamics at the Carotid Bifurcation. *Ann. Biomed. Eng.* 43, 68–81. doi:10.1007/s10439-014-1119-0

Getz, G. S., and Reardon, C. A. (2012). Animal Models of Atherosclerosis. *Arterioscler. Thromb. Vasc. Biol.* 32, 1104–1115. doi:10.1161/ATVBAHA.111.237693

Hartman, E. M. J., De Nisco, G., Kok, A. M., Hoogendoorn, A., Coenen, A., Mastik, F., et al. (2020). Lipid-rich Plaques Detected by Near-Infrared Spectroscopy Are More Frequently Exposed to High Shear Stress. *J. Cardiovasc. Transl. Res.* 14, 416–425. doi:10.1007/s12265-020-10072-x

Himburg, H. A., Grzybowski, D. M., Hazel, A. L., LaMack, J. A., Li, X.-M., and Friedman, M. H. (2004). Spatial Comparison between wall Shear Stress Measures and Porcine Arterial Endothelial Permeability. *Am. J. Physiol. Heart Circ. Physiol.* 286, H1916–H1922. doi:10.1152/ajpheart.00897.2003

Hoogendoorn, A., Kok, A. M., Hartman, E. M. J., de Nisco, G., Casadonte, L., Chiastra, C., et al. (2020). Multidirectional wall Shear Stress Promotes Advanced Coronary Plaque Development: Comparing Five Shear Stress Metrics. *Cardiovasc. Res.* 116, 1136–1146. doi:10.1093/cvr/cvz212

Huo, Y., and Kassab, G. S. (2012). Intraspecific Scaling Laws of Vascular Trees. *J. R. Soc. Interf.* 9, 190–200. doi:10.1098/rsif.2011.0270

Kok, A. M., Molony, D. S., Timmins, L. H., Ko, Y.-A., Boersma, E., Eshtehardi, P., et al. (2019). The Influence of Multidirectional Shear Stress on Plaque Progression and Composition Changes in Human Coronary Arteries. *EuroIntervention* 15, 692–699. doi:10.4244/eij-d-18-00529

Ku, D. N., Giddens, D. P., Zarins, C. K., and Glagov, S. (1985). Pulsatile Flow and Atherosclerosis in the Human Carotid Bifurcation. Positive Correlation between Plaque Location and Low Oscillating Shear Stress. *Arteriosclerosis* 5, 293–302. doi:10.1161/01.ATV.5.3.293

Kwak, B. R., Bäck, M., Bochaton-Piallat, M.-L., Caligiuri, G., Daemen, M. J. A. P., Davies, P. F., et al. (2014). Biomechanical Factors in Atherosclerosis: Mechanisms and Clinical Implications. *Eur. Heart J.* 35, 3013–3020d. doi:10.1093/eurheartj/ehu353

Lelovas, P. P., Kostomitsopoulos, N. G., and Xanthos, T. T. (2014). A Comparative Anatomic and Physiologic Overview of the Porcine Heart. *J. Am. Assoc. Lab. Anim. Sci.* 53, 432–438.

Liu, X., Sun, A., Fan, Y., and Deng, X. (2015). Physiological Significance of Helical Flow in the Arterial System and its Potential Clinical Applications. *Ann. Biomed. Eng.* 43, 3–15. doi:10.1007/s10439-014-1097-2

Lusis, A. J. (2000). Atherosclerosis. *Nature* 407, 233–241. doi:10.1038/35025203

Mahley, R. W., Weisgraber, K. H., Innerarity, T., Brewer, H. B. J., and Assmann, G. (1975). Swine Lipoproteins and Atherosclerosis. Changes in the Plasma Lipoproteins and Apoproteins Induced by Cholesterol Feeding. *Biochemistry* 14, 2817–2823. doi:10.1021/bi00684a005

Malvè, M., García, A., Ohayon, J., and Martínez, M. A. (2012). Unsteady Blood Flow and Mass Transfer of a Human Left Coronary Artery Bifurcation: FSI vs. CFD. *Int. Commun. Heat Mass. Transf* 39, 745–751. doi:10.1016/j.icheatmasstransfer.2012.04.009

Mazzi, V., De Nisco, G., Hoogendoorn, A., Calò, K., Chiastra, C., Gallo, D., et al. (2021). Early Atherosclerotic Changes in Coronary Arteries Are Associated with Endothelium Shear Stress Contraction/Expansion Variability. *Ann. Biomed. Eng.*. in press. doi:10.1007/s10439-021-02829-5

Millon, A., Canet-Soulas, E., Boussel, L., Fayad, Z., and Douek, P. (2014). Animal Models of Atherosclerosis and Magnetic Resonance Imaging for Monitoring Plaque Progression. *Vascular* 22, 221–237. doi:10.1177/1708538113478758

Morbiducci, U., Kok, A. M., Kwak, B. R., Stone, P. H., Steinman, D. A., and Wentzel, J. J. (2016). Atherosclerosis at Arterial Bifurcations: Evidence for the Role of Haemodynamics and Geometry. *Thromb. Haemost.* 115, 484–492. doi:10.1160/TH15-07-0597

Morbiducci, U., Ponzini, R., Gallo, D., Bignardi, C., and Rizzo, G. (2013). Inflow Boundary Conditions for Image-Based Computational Hemodynamics: Impact of Idealized versus Measured Velocity Profiles in the Human Aorta. *J. Biomech.* 46, 102–109. doi:10.1016/j.jbiomech.2012.10.012

Morbiducci, U., Ponzini, R., Grigioni, M., and Redaelli, A. (2007). Helical Flow as Fluid Dynamic Signature for Atherogenesis Risk in Aortocoronary Bypass. A Numeric Study. *J. Biomech.* 40, 519–534. doi:10.1016/j.jbiomech.2006.02.017

Morbiducci, U., Ponzini, R., Rizzo, G., Cadioli, M., Esposito, A., De Cobelli, F., et al. (2009). *In Vivo* quantification of Helical Blood Flow in Human Aorta by Time-Resolved Three-Dimensional Cine Phase Contrast Magnetic Resonance Imaging. *Ann. Biomed. Eng.* 37, 516–531. doi:10.1007/s10439-008-9609-6

Peiffer, V., Sherwin, S. J., and Weinberg, P. D. (2013). Computation in the Rabbit Aorta of a New Metric - the Transverse wall Shear Stress - to Quantify the Multidirectional Character of Disturbed Blood Flow. *J. Biomech.* 46, 2651–2658. doi:10.1016/j.jbiomech.2013.08.003

Sangalli, L. M., Secchi, P., Vantini, S., and Veneziani, A. (2009). Efficient Estimation of Three-Dimensional Curves and Their Derivatives by Free-Knot Regression Splines, Applied to the Analysis of Inner Carotid Artery Centrelines. *J. R. Stat. Soc. Ser. C (Applied Stat.* 58, 285–306. doi:10.1111/j.1467-9876.2008.00653.x

Shim, J., Al-Mashhadi, R. H., Sørensen, C. B., and Bentzon, J. F. (2016). Large Animal Models of Atherosclerosis-Nnew Tools for Persistent Problems in Cardiovascular Medicine. *J. Pathol.* 238, 257–266. doi:10.1002/path.4646

Shin, H. S., Shin, H. H., and Shudo, Y. (2021). Current Status and Limitations of Myocardial Infarction Large Animal Models in Cardiovascular Translational Research. *Front. Bioeng. Biotechnol.* 9, 321. doi:10.3389/fbioe.2021.673683

Soulis, J. V., Giannoglou, G. D., Chatzizisis, Y. S., Farmakis, T. M., Giannakoulas, G. A., Parcharidis, G. E., et al. (2006). Spatial and Phasic Oscillation of Non-newtonian wall Shear Stress in Human Left Coronary Artery Bifurcation: an Insight to Atherogenesis. *Coron. Artery Dis.* 17, 351–358. doi:10.1097/00019501-200606000-00005

Stone, P. H., Saito, S., Takahashi, S., Makita, Y., Nakamura, S., Kawasaki, T., et al. (2012). Prediction of Progression of Coronary Artery Disease and Clinical Outcomes Using Vascular Profiling of Endothelial Shear Stress and Arterial Plaque Characteristics: the PREDICTION Study. *Circulation* 126, 172–181. doi:10.1161/CIRCULATIONAHA.112.096438

Theodorakakos, A., Gavaises, M., Andriotis, A., Zifan, A., Liatsis, P., Pantos, I., et al. (2008). Simulation of Cardiac Motion on Non-newtonian, Pulsating Flow Development in the Human Left Anterior Descending Coronary Artery. *Phys. Med. Biol.* 53, 4875–4892. doi:10.1088/0031-9155/53/18/002

Thim, T., Hagensen, M. K., Drouet, L., Bal Dit Sollier, C., Bonneau, M., Granada, J. F., et al. (2010). Familial Hypercholesterolaemic Downsized Pig with Human-like Coronary Atherosclerosis: a Model for Preclinical Studies. *EuroIntervention* 6, 261–268. doi:10.4244/EIJV6I2A42

Torii, R., Keegan, J., Wood, N. B., Dowsey, A. W., Hughes, A. D., Yang, G.-Z., et al. (2010). MR Image-Based Geometric and Hemodynamic Investigation of the Right Coronary Artery with Dynamic Vessel Motion. *Ann. Biomed. Eng.* 38, 2606–2620. doi:10.1007/s10439-010-0008-4

Torii, R., Wood, N., Hadjiloizou, N., Dowsey, A., Wright, A., Hughes, A., et al. (2009). Fluid-structure Interaction Analysis of a Patient-specific Right Coronary Artery with Physiological Velocity and Pressure Waveforms. *Commun. Numer. Methods Eng.* 25, 565–580. doi:10.1002/cnm.1231

van der Giessen, A. G., Groen, H. C., Doriot, P.-A., de Feyter, P. J., van der Steen, A. F. W., van de Vosse, F. N., et al. (2011). The Influence of Boundary Conditions on wall Shear Stress Distribution in Patients Specific Coronary Trees. *J. Biomech.* 44, 1089–1095. doi:10.1016/j.jbiomech.2011.01.036

Virani, S. S., Alonso, A., Aparicio, H. J., Benjamin, E. J., Bittencourt, M. S., Callaway, C. W., et al. (2021). Heart Disease and Stroke Statistics-2021 Update: A Report from the American Heart Association. *Circulation* 143, e254–e743. doi:10.1161/CIR.0000000000000950

Vorobtsova, N., Chiastra, C., Stremler, M. A., Sane, D. C., Migliavacca, F., and Vlachos, P. (2016). Effects of Vessel Tortuosity on Coronary Hemodynamics: An Idealized and Patient-specific Computational Study. *Ann. Biomed. Eng.* 44, 2228–2239. doi:10.1007/s10439-015-1492-3

Weaver, M. E., Pantely, G. A., Bristow, J. D., and Ladley, H. D. (1986). A Quantitative Study of the Anatomy and Distribution of Coronary Arteries in Swine in Comparison with Other Animals and Man. *Cardiovasc. Res.* 20, 907–917. doi:10.1093/cvr/20.12.907

Wentzel, J. J., Chatzizisis, Y. S., Gijsen, F. J. H., Giannoglou, G. D., Feldman, C. L., and Stone, P. H. (2012). Endothelial Shear Stress in the Evolution of Coronary Atherosclerotic Plaque and Vascular Remodelling: Current Understanding and Remaining Questions. *Cardiovasc. Res.* 96, 234–243. doi:10.1093/cvr/cvs217

Xiangdong, L., Yuanwu, L., Hua, Z., Liming, R., Qiuyan, L., and Ning, L. (2011). Animal Models for the Atherosclerosis Research: a Review. *Protein Cell* 2, 189–201. doi:10.1007/s13238-011-1016-3

Zaromytidou, M., Siasos, G., Coskun, A. U., Lucier, M., Antoniadis, A. P., Papafaklis, M. I., et al. (2016). Intravascular Hemodynamics and Coronary Artery Disease: New Insights and Clinical Implications. *Hell. J. Cardiol.* 57, 389–400. doi:10.1016/j.hjc.2016.11.019

Zeng, D., Ding, Z., Friedman, M. H., and Ethier, C. R. (2003). Effects of Cardiac Motion on Right Coronary Artery Hemodynamics. *Ann. Biomed. Eng.* 31, 420–429. doi:10.1114/1.1560631

Conflict of Interest: The authors declare that the research was conducted in the absence of any commercial or financial relationships that could be construed as a potential conflict of interest.

Publisher's Note: All claims expressed in this article are solely those of the authors and do not necessarily represent those of their affiliated organizations, or those of the publisher, the editors and the reviewers. Any product that may be evaluated in this article, or claim that may be made by its manufacturer, is not guaranteed or endorsed by the publisher.

frontiers in Cardiovascular Medicine

ORIGINAL RESEARCH
published: 16 August 2021
doi: 10.3389/fcvm.2021.704251

Association Between Echocardiographic Non-invasive Myocardial Work Indices and Myocardial Fibrosis in Patients With Dilated Cardiomyopathy

*Cunying Cui[1], Yanan Li[1], Yuanyuan Liu[1], Danqing Huang[1], Yanbin Hu[1], Ying Wang[1], Lijia Ma[2] and Lin Liu[1]**

[1] Department of Ultrasound, The People's Hospital of Zhengzhou University, Henan Provincial People's Hospital, Fuwai Central China Cardiovascular Hospital, Zhengzhou, China, [2] Department of Radiology, The People's Hospital of Zhengzhou University, Henan Provincial People's Hospital, Zhengzhou, China

OPEN ACCESS

Edited by:
Zahra K. Motamed,
McMaster University, Canada

Reviewed by:
Matthias Schneider,
Charité – Universitätsmedizin Berlin, Germany
Özge Özden Tok,
Memorial Bahçelievler Hospital, Turkey

***Correspondence:**
Lin Liu
liulin_819@126.com

Specialty section:
This article was submitted to Cardiovascular Imaging, a section of the journal Frontiers in Cardiovascular Medicine

Received: 02 May 2021
Accepted: 26 July 2021
Published: 16 August 2021

Citation:
Cui C, Li Y, Liu Y, Huang D, Hu Y, Wang Y, Ma L and Liu L (2021) Association Between Echocardiographic Non-invasive Myocardial Work Indices and Myocardial Fibrosis in Patients With Dilated Cardiomyopathy. Front. Cardiovasc. Med. 8:704251. doi: 10.3389/fcvm.2021.704251

Objectives: To analyze the association between global myocardial work indices evaluated by non-invasive left ventricular (LV) pressure-strain loop (PSL) and LV myocardial fibrosis in patients with dilated cardiomyopathy (DCM).

Methods: A total of 57 patients with DCM were included in this prospective study. Global work index (GWI), global constructive work (GCW), global wasted work (GWW), global work efficiency (GWE) and global longitudinal strain (GLS) were measured using LVPSL. LV volumes and LV ejection fraction (LVEF) were evaluated using cardiac magnetic resonance imaging (CMRI), LV myocardial fibrosis was estimated at CMRI by qualitative assessment of late gadolinium enhancement (LGE). According to the CMRI, the studied population was divided into two groups, namely: patients without LGE (LGE-) and patients with LGE (LGE+).

Results: The LGE+ group presented with increased age, LV end systolic volume (LVESV) index and reduced GWI, GCW, GWE, GLS, CMRI-derived LVEF ($LVEF_{CMRI}$), the differences between the two groups were statistically significant ($P < 0.05$). After correcting for age and LVESV index, $LVEF_{CMRI}$, GLS, GWI, GCW, and GWE retained independent associations with LV myocardial fibrosis. According to receiver operating characteristics (ROC) analysis, $LVEF_{CMRI}$, and GCW showed larger AUC and higher accuracy, sensitivity, and specificity than GLS, the accuracy of predicting LV myocardial fibrosis ranged from high to low as: $LVEF_{CMRI}$, GCW, GWE, GWI, and GLS.

Conclusions: $LVEF_{CMRI}$, GWI, GCW, GWE, and GLS remained significant predictors of LV myocardial fibrosis. $LVEF_{CMRI}$, and GCW appeared to better predict LV myocardial fibrosis compared with GLS.

Keywords: dilated cardiomyopathy, myocardial work, left ventricular systolic function, myocardial fibrosis, magnetic resonance imaging, echocardiography

INTRODUCTION

Dilated cardiomyopathy (DCM) is defined as the dilatation and dysfunction of one or both ventricles in the absence of abnormal loading or coronary heart disease (CHD) (1, 2). This disease can occur in all age groups but is more common in young adults. The incidence rate in men is higher than that in women (3). With progression of the disease, it can lead to various complications, such as heart failure, shock, arrhythmia, and even sudden death (4). Accurate assessment of left ventricular function in DCM patients is extremely important for clinical diagnosis, treatment, and prognosis (5).

Cardiac magnetic resonance imaging (CMRI) is the gold standard for the measurement of cardiac function parameters (6, 7). In addition, the application of late gadolinium enhancement (LGE) is currently the most reliable method for non-invasive detection of localized myocardial fibrosis, which is helpful for the diagnosis of DCM and significantly related to its prognosis (8, 9). However, CMRI takes longer and is expensive, it is difficult to be used as a routine examination in clinical practice.

The left ventricular ejection fraction (LVEF) and global longitudinal strain (GLS) measured using echocardiography are often recommended for the evaluation of left ventricular systolic function (LVSF) (10). However, LVEF and GLS are susceptible to cardiac load. The myocardial work index derived from the left ventricular pressure-strain loop (LVPSL) is a new method for non-invasive assessment of LVSF (11). This technique is derived from the 2D speckle tracking technique, and it considers the effect of afterload on strain. The method is simple, easy, and non-invasive, and it could be widely used in clinical practice.

Previous studies by Chan et al. and the author confirmed the feasibility of the myocardial work index to evaluate LVSF in patients with DCM (12, 13). The present study aimed to analyze the correlation between global myocardial work indices and LV myocardial fibrosis in patients with DCM.

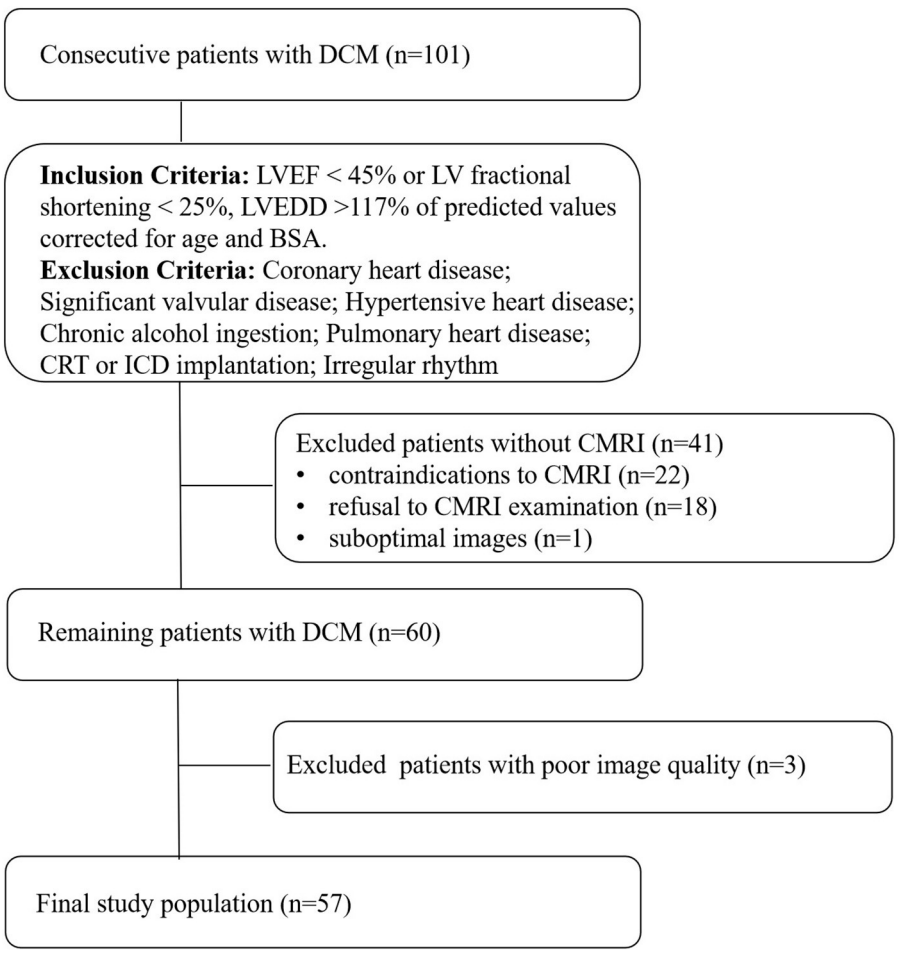

FIGURE 1 | Flow chart detailing the identification of the study cohort. Contraindications to CMRI include incompatible metallic devices, contrast medium allergy, or claustrophobia. Significant valvular disease was defined as valvular stenosis or > mild functional regurgitation. Functional mitral regurgitation was secondary to left ventricular remodeling, mitral valve anatomy was normal. DCM, dilated cardiomyopathy, LVEF, left ventricular ejection fraction, LVEDD, left ventricular end-diastolic diameter, BSA, body surface area, CMRI, cardiac magnetic resonance imaging, CRT, cardiac resynchronisation therapy, ICD, implantable cardioverter defibrillator.

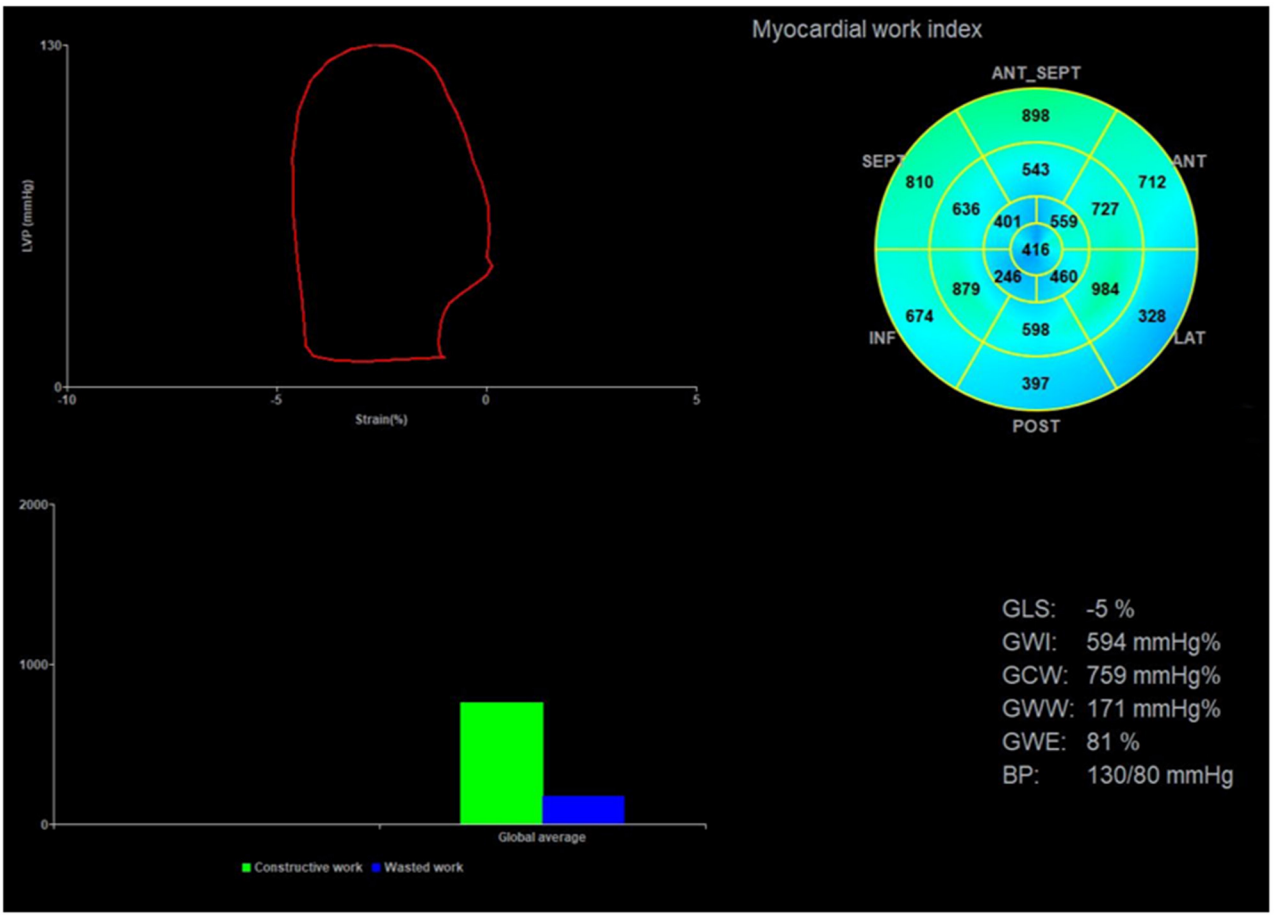

FIGURE 2 | Image analysis for myocardial work. The upper left corner of the image is the left ventricular PSL curve, the upper right corner is the 17-segment myocardial work index bull's eye diagram, and the lower right corner displays the left ventricular global myocardial work indices obtained from the PSL curve. PSL, pressure-strain loop.

MATERIALS AND METHODS

Study Population

We conducted a prospective study on 101 consecutive patients with DCM in the heart failure department of Fuwai Central China Cardiovascular Hospital from January 2019 to February 2021. The diagnosis of DCM was established according to current guidelines (14). The inclusion criteria were: (1) LV ejection fraction (LVEF) $\leq$ 45% or LV fractional shortening $<$ 25%; (2) LV end-diastolic diameter $>$ 117% of predicted values corrected for age and body surface area (BSA), both echo-determined. Patients with coronary heart disease ($>$ 50% angiographical stenosis in any epicardial coronary artery, and patients with an ischemic scar at cardiac MRI), hypertensive heart disease, significant valvular disease (valvular stenosis or $>$ mild functional regurgitation), chronic alcohol ingestion, pulmonary heart disease, congenital heart disease, a history of cardiac resynchronisation therapy (CRT) and implantable cardioverter defibrillator (ICD) implantation, or irregular rhythm were excluded. The 41 patients who had not undergone a CMRI were excluded. Finally, 3 patients were excluded from this study because of poor image quality. The final analysis included 57 DCM patients (**Figure 1**).

We recorded medical history, including New York Heart Association (NYHA) functional class; biomarkers; cardiovascular risk factors; current medications and 12-lead electrocardiography (ECG). ECG, Transthoracic echocardiography and CMRI were performed within 24 h.

Transthoracic Echocardiography

All echocardiographic examinations were performed on a Vivid E95 ultrasound system (GE Vingmed Ultrasound AS, Horten, Norway) equipped with an M5Sc-D 1.4–4.6 MHz transducer. All the study subjects were placed in a left-side position and synchronously connected to the electrocardiogram. The average frame rate of the 2D image was 59 $\pm$ 7 frames/sec. The LVEF of each patient was measured using the biplane Simpson method. The peak velocity of the mitral valve in early diastolic period (E peak), and the average velocity of the mitral annulus (e') were

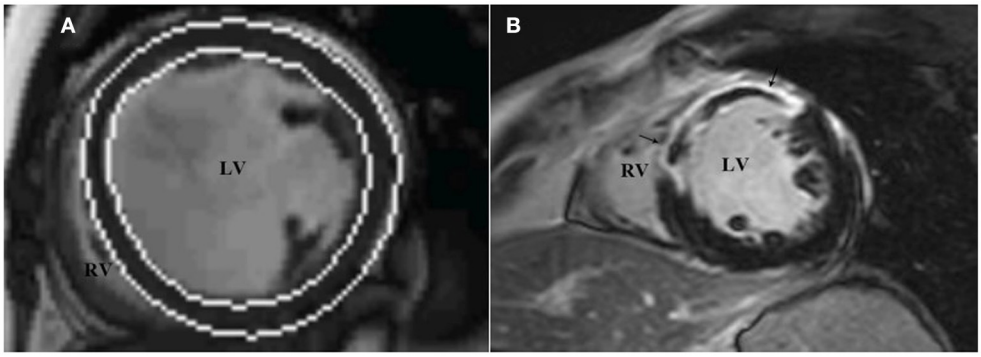

FIGURE 3 | LV function and LGE analysis via cardiac magnetic resonance imaging. The analysis software automatically tracks the left ventricular endocardium and epicardium to measure left ventricular volume **(A)**, and assesses the presence and distribution of left ventricular LGE through short-axis images **(B)**, which show high signal intensity in the middle segment of the left ventricular septum, anterior wall. LGE, late gadolinium enhancement.

measured, and E/e′ was calculated. Apical four-, three-, and two-chamber images were continuously acquired for at least three cardiac cycles, and the Doppler blood flow spectrum of the aortic and mitral valves was obtained. The original data images were saved to a hard disk for analysis.

Image Analysis for Myocardial Work

Echopac version 203 (GE Vingmed Ultrasound AS, Horten, Norway) was used for image analysis. According to the Doppler flow spectrum of the aortic valve and mitral valve, valvular event time was determined. Tracking was automatic, but if the tracking was not satisfactory, tracking points were adjusted manually to determine segmental and global longitudinal strain. After entering the cuff blood pressure value, the software automatically generated the LVPSL curve, GLS, and myocardial work parameters. The absolute value of GLS was recorded and the global myocardial work parameters included global work index (GWI), global constructive work (GCW), global wasted work (GWW), and global work efficiency (GWE). GWI is equivalent to the area of the PSL, GCW is a sign of active contraction of the left ventricular myocardium, GWW is a sign of energy loss, and GWE is the percentage of GCW in the sum of GCW and GWW (**Figure 2**).

Cardiac Magnetic Resonance Imaging

A Siemens MAGNETOM Skyra 3.0 MR scanner (Magnetom Symphony, Siemens Medical Solutions, Erlanger, Germany), an 18-channel phased array coil for heart, and chest lead ECG gating technology were used for CMRI. The short- and long-axis images of the left ventricle were collected using a balance steady-state free procession sequence with the following parameters: TR, 3.3 ms; TE, 1.43 ms; FOV, 340 × 340 mm; matrix, 208 × 166; layer thickness, 8 mm; layer spacing, 2 mm; reversal angle, 80°; and dynamic breath-hold scanning, one cardiac cycle. A total of 25 images were collected.

For LGE image acquisition, a high-pressure syringe was used for elbow vein bolus injection of gadolinium (gadoterate meglumine, Dotarem, Guerbet, Aulnay-sous-Bois, France; 0.15 mmol/kg; flow rate of 4 mL/s). Segmented inversion was adopted to restore the gradient echo sequence. The collected short-axis images of first pass perfusion and delay period had the following parameters: layer thickness, 8 mm; TR, 6.1 ms; TE, 2.9 ms; and reversal angle, 25°. A proper reversal time was chosen to suppress normal myocardial signals.

LV Function and LGE Analysis via Cardiac Magnetic Resonance Imaging

All images were reevaluated by two experienced observers, and all clinical data were blinded for analysis. By using Siemens Argus post-processing software (Argus software, Siemens Healthcare Erlangen, Germany), the left ventricular endocardium and epicardium were automatically tracked and contoured on the image (**Figure 3A**). The left ventricular cavity contained trabecular and papillary muscles. The recognition errors were corrected manually. Left ventricular end diastolic volume (LVEDV), left ventricular end systolic volume (LVESV) and left ventricular mass (LVM) were measured, and LVEF was calculated:

$$\mathrm{LVEF} = (\mathrm{LVEDV} - \mathrm{LVESV})/\mathrm{LVEDV}. \quad (1)$$

LVEDV, LVESV, and LVM were corrected as indices using BSA.

In accordance with the recommendation of the American Heart Association in 2002 (15), the left ventricular myocardium was divided into 17 segments, and the presence and distribution of LGE were evaluated using short-axis images. LGE (+) was defined as the myocardial signal at the LGE enhancement site higher than the 5SD threshold of the average signal intensity of the distal normal myocardium (**Figure 3B**). According to the CMRI data, the studied population was divided into two groups: patients without LGE (LGE-) and patients with LGE (LGE+).

Biochemical Evaluation

Blood samples of patients were drawn to measure the level of N-terminal pro-brain natriuretic peptide (NT-proBNP). Analysis was conducted in the clinical laboratory.

TABLE 1 | Baseline characteristics of the study population and according to presence of LGE.

Clinical characteristics	All patients $n = 57$	LGE+ group $n = 32$	LGE– group $n = 25$	*P*-value
Age, years	43.9 ± 12.7	47.5 ± 12.5	39.4 ± 11.5	0.02
Male, *n* (%)	45 (78.95)	25 (78.12)	20 (80.00)	0.86
BSA, m²	2.00 ± 0.19	2.02 ± 0.20	1.98 ± 0.20	0.54
Heart rate, bpm	74.26 ± 5.42	73.53 ± 5.56	75.20 ± 5.20	0.25
Systolic blood pressure, mm Hg	118.24 ± 12.46	120.44 ± 12.95	115.44 ± 11.43	0.13
Diastolic blood pressure, mm Hg	75.47 ± 8.88	75.47 ± 9.31	75.48 ± 8.49	0.99
Diabetes mellitus, *n* (%)	12 (21.05)	6 (18.75)	6 (24.00)	0.63
Dyslipidemia, *n* (%)	21 (36.84)	12 (37.50)	9 (36.00)	0.91
NYHA functional class II/III/IV, *n*	11/25/21	6/12/14	5/13/7	0.40
NT-proBNP, pg/mL	1560 (764, 2826.5)	1672 (985.75, 3173.00)	764 (374.50, 1515.00)	0.23

BSA, body surface area; NYHA, New York Heart Association; NT-proBNP, N-terminal pro-Brain Natriuretic Peptide. Data are expressed as mean ± SD, median (IQR), or number (percentage).

TABLE 2 | Echocardiography parameters for the overall population and according to presence of LGE.

Variables	All patients $n = 57$	LGE+ group $n = 32$	LGE– group $n = 25$	*P*-value
LAV index, mL/m^2	40.65 ± 2.35	41.14 ± 2.17	40.02 ± 2.45	0.07
E/e′	16.15 ± 3.26	16.70 ± 2.87	15.44 ± 3.64	0.15
$LVEF_{Simpson}$, %	29.32 ± 7.45	27.09 ± 5.59	29.76 ± 4.88	0.07
GWI, mm Hg%	633.61 ± 257.74	507.78 ± 172.75	794.68 ± 261.38	<0.001
GCW, mm Hg%	817.67 ± 323.58	642.25 ± 200.43	1042.20 ± 324.45	<0.001
GWW, mm Hg%	169 (123.50, 276.50)	183 (134.00, 298.25)	141 (105.50, 219.00)	0.05
GWE, %	79.26 ± 10.13	74.22 ± 9.94	85.72 ± 5.87	<0.001
GLS, %	6 (5.00, 8.00)	5 (4.00, 6.75)	8 (5.50, 11.00)	<0.001

LAV, left atrial volume; E/e', ratio of the peak mitral flow velocity (E peak) to the average velocity of the mitral annulus (e'); GWI, global work index; GCW, global constructive work; GWW, global wasted work; GWE, global work efficiency; GLS, global longitudinal strain; $LVEF_{Simpson}$, left ventricular ejection fraction measured using the biplane Simpson method; LGE, late gadolinium enhancement; Data are expressed as mean ± SD, median (IQR).

TABLE 3 | Cardiac magnetic resonance imaging parameters for the overall population and according to presence of LGE.

Variables	All patients $n = 57$	LGE+ group $n = 32$	LGE– group $n = 25$	*P*-value
LVEDV index, mL/m^2	157.37 ± 39.93	165.45 ± 34.80	147.04 ± 44.24	0.08
LVESV index, mL/m^2	126.79 ± 36.66	139.36 ± 30.84	110.70 ± 37.78	0.003
$LVEF_{CMRI}$, %	20.09 ± 7.16	15.86 ± 3.85	25.52 ± 6.79	<0.001
LVM index, g/m^2	110.19 ± 31.45	112.49 ± 31.19	107.26 ± 32.17	0.54

LVEDV, left ventricular end diastolic volume; LVESV, left ventricular end systolic volume; $LVEF_{CMRI}$, cardiac magnetic resonance imaging-derived left ventricular ejection fraction; LVM, left ventricular mass; LGE, late gadolinium enhancement; Data are expressed as mean ± SD.

Statistical Analysis

Continuous variables were expressed by mean ± standard deviation when the variables obeyed normal distribution; otherwise, the median (quartile) was used. Categorical variables are presented as number (%). Baseline characteristics among patients with and without LGE were compared by chi-square or Fisher's exact test (categorical variables), and independent sample *t*-test or Wilcoxon signed rank test (continuous variables) as appropriate. To investigate the associations between variables and LV myocardial fibrosis, univariate and multivariate logistic regression analyses were performed. Correlations between independent variables were examined by Pearson correlation coefficients. For collinearity reasons (Pearson's coefficient > 0.6), several multivariate logistic regression models were built. A value of $P < 0.05$ was considered statistically significant.

Receiver operating characteristics (ROC) curve analyses were used to determine optimal cutoff points for variables in predicting LV myocardial fibrosis, and to calculate the area under the curve (AUC), sensitivity, specificity and accuracy. Intra-observer variability and inter-observer variability of myocardial work indices were assessed in 20 patients and tested using intraclass correlation coefficients (ICCs).

All statistical analyses were performed using a standard statistical software program (SPSS Version 20.0, IBM, Chicago, IL, USA).

RESULTS

Study Population and Clinical Characteristics

As depicted in **Figures 1**, 101 patients were enrolled, 57 patients were included in the final analysis. They were divided in two groups: the LGE+ group ($n = 32/57$, 56.1%) and LGE - group ($n = 25/57$, 43.9%).

Baseline characteristics are presented in **Table 1**. Medications and electrocardiographic characteristics are shown in **Supplementary Table 1**. In the overall population ($n = 57$), mean age was 43.9 ± 12.7 years, 45 (78.95%) patients were males. QRS duration 108 (99.50, 130.50) ms, 19 (33.33%) patients had wide QRS (duration ≥120 ms). Eight (14.04%) patients had left bundle branch block, The LGE+ group presented with increased age and the difference between the two groups was statistically significant ($P < 0.001$). There were no statistically significant differences in sex, BSA, heart rate, blood pressure, NYHA functional class, NT-proBNP, concomitant diseases, medications, or electrocardiographic parameters between the two groups ($P > 0.05$).

Parameters Measured by Echocardiography and Cardiac Magnetic Resonance Imaging

As shown in **Tables 2**, **3**, the LGE+ group presented with increased LVESV index ($P < 0.05$) and reduced $LVEF_{CMRI}$, GLS, GWI, GCW, and GWE. The differences between the two groups were statistically significant ($P < 0.001$). There were no statistically significant differences in LAV index, $LVEF_{Simpson}$, E/e', or LVM index between the two groups ($P > 0.05$).

Association Between Parameters and LV Myocardial Fibrosis

The univariate logistic regression analysis showed an association between LV myocardial fibrosis and the following parameters (**Table 4**): Age, LVESV index, $LVEF_{CMRI}$, GLS, GWI, GCW, and GWE. There was no significant correlation between age, LVESV index and parameters of LV function, including $LVEF_{CMRI}$, GLS, GWI, GCW, and GWE. Considering the significant correlations among parameters of LV function, several multivariate logistic regression models with one parameter of LV function and age, and LVESV index were built (**Table 5**). After correcting for age and LVESV index, $LVEF_{CMRI}$, GLS, GWI, GCW, and GWE retained independent associations with LV myocardial fibrosis.

According to ROC analysis, the AUC of $LVEF_{CMRI}$ was larger than that of GLS, GWI, GCW, and GWE, as shown in **Figure 4**. According to the Youden index, the cutoff point of $LVEF_{CMRI}$ was 20.50%, the corresponding sensitivity was 93.80%, the specificity was 72.00%, and the accuracy was 84.21%. The cutoff point of GWE was 78.50%, the corresponding sensitivity was 65.60%, the specificity was 88.00%, and the accuracy was 75.43%. The cutoff points and corresponding sensitivity, specificity, accuracy of GWI, GCW, and GLS are shown in **Supplementary Table 2**, $LVEF_{CMRI}$, GCW showed larger AUC and higher accuracy, sensitivity, and specificity than GLS, the accuracy of predicting LV myocardial fibrosis ranged from high to low as: $LVEF_{CMRI}$, GCW, GWE, GWI, and GLS.

TABLE 4 | Univariate logistic regression analysis to identify the determinants of LV myocardial fibrosis at late gadolinium enhancement.

Variables	OR (95% CI)	*P*-value
Age	1.057 (1.009∼1.108)	0.002
Sex, male	0.893 (0.246∼3.242)	0.86
NYHA functional class	1.380 (0.668∼2.848)	0.38
NT-proBNP	1.000 (1.000∼1.001)	0.19
LVESV index	1.026 (1.007∼1.045)	0.01
$LVEF_{CMRI}$, %	0.649 (0.508∼0.829)	0.001
$LVEF_{Simpson}$	0.907 (0.817∼1.008)	0.07
GWI	0.994 (0.990∼0.997)	0.001
GCW	0.994 (0.991∼0.997)	<0.001
GWE	0.807 (0.715∼0.911)	0.001
GLS	0.541 (0.376∼0.779)	0.001

OR, odds ratio; 95% CI, 95% Confidence Interval; NYHA, New York Heart Association; NT-proBNP, N-terminal pro-Brain Natriuretic Peptide; LVESV, left ventricular end systolic volume; $LVEF_{CMRI}$, cardiac magnetic resonance imaging-derived left ventricular ejection fraction; $LVEF_{Simpson}$, left ventricular ejection fraction measured using the biplane Simpson method; GWI, global work index; GCW, global constructive work; GWE, global work efficiency; GLS, global longitudinal strain.

TABLE 5 | Multivariate logistic regression models to predict LV myocardial fibrosis.

Multivariate models		OR (95% CI)	*P*-value
Model 1	Age	1.073 (0.999∼1.153)	0.05
	LVESV index	1.002 (0.975∼1.029)	0.90
	$LVEF_{CMRI}$	0.627 (0.465∼0.844)	0.002
Model 2	Age	1.051 (0.999∼1.041)	0.09
	LVESV index	1.016 (0.770∼0.966)	0.15
	GLS	0.626 (0.429∼0.912)	0.02
Model 3	Age	1.053 (0.993∼1.117)	0.08
	LVESV index	1.019 (0.997∼1.042)	0.09
	GWI	0.995 (0.992∼0.999)	0.01
Model 4	Age	1.037 (0.976∼1.101)	0.24
	LVESV index	1.014 (0.992∼1.038)	0.21
	GCW	0.995 (0.992∼0.999)	0.004
Model 5	Age	1.034 (0.974∼1.096)	0.27
	LVESV index	1.016 (0.994∼1.038)	0.15
	GWE	0.837 (0.737∼0.951)	0.01

OR, odds ratio; 95% CI, 95% Confidence Interval.

Reproducibility of Myocardial Work Indices

Intra-observer variability and inter-observer variability of GWI, GCW, GWW, and GWE are presented in **Supplementary Table 3**. Intra-observer variability and inter-observer variability were the lowest for GWI, represented by the

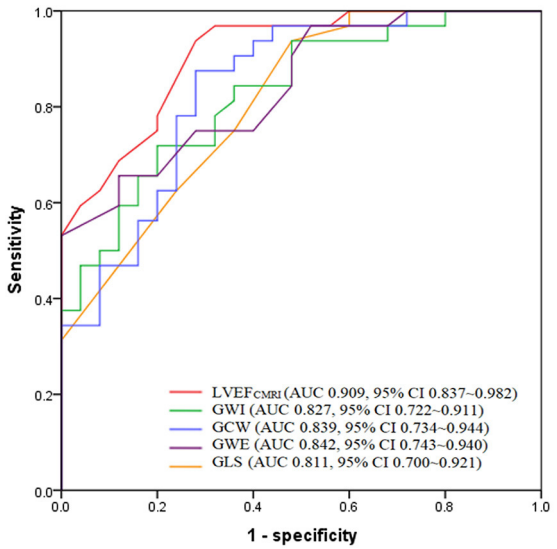

FIGURE 4 | Receiver operating characteristic analysis of $LVEF_{CMRI}$, GWI, GCW, GWE, and GLS for predicting LV myocardial fibrosis. $LVEF_{CMRI}$, cardiac magnetic resonance imaging-derived left ventricular ejection fraction; GWI, Global work index; GCW, Global constructive work; GWE, Global work efficiency; GLS, Global longitudinal strain.

highest ICCs, ICCs were 0.910 for inter-observer and 0.961 for intra-observer measurements.

DISCUSSION

This study was the first to analyze the correlation between myocardial work indices and myocardial fibrosis in patients with DCM. We found that $LVEF_{CMRI}$, GWI, GCW, GWE, and GLS remained significant predictors of LV myocardial fibrosis. $LVEF_{CMRI}$, and GCW showed larger AUC and higher accuracy, sensitivity, and specificity than GLS, the accuracy of predicting LV myocardial fibrosis ranged from high to low as: $LVEF_{CMRI}$, GCW, GWE, GWI, and GLS.

Prognostic Value of Myocardial Fibrosis in Patients With DCM

The pathological bases of DCM are myocardial degeneration, atrophy, and fibrosis. Myocardial fibrosis is associated with increased risk for mortality, arrhythmia events, hospitalizations, and sudden death, therefore, detection of myocardial fibrosis has important clinical value in evaluating prognosis (16). CMRI with LGE detects myocardial fibrosis with high sensitivity and specificity. Presence of LGE is significantly associated with adverse outcome and is recommended for risk stratification of DCM patients (17). Absence of LGE is independently correlated with LV reverse remodeling, irrespective of the severity of LV dilatation and dysfunction (18). Progressive myocardial fibrosis is associated with a more than 3-fold higher risk for mortality and heart failure outcomes (19).

The association between non-invasive myocardial work indices and LV myocardial fibrosis in patients with DCM has not yet been reported. In our study, we found that global myocardial work indices, including GWI, GCW, GWE, remained significant predictors of LGE in DCM patients, indicating that these parameters may be potential surrogate markers for the detection of fibrosis when CMRI is contraindicated (significant chronic renal disease, incompatible metallic devices, or claustrophobia).

Association Between Myocardial Dysfunction and Myocardial Fibrosis in Patients With DCM

Myocardial fibrosis leads to the decrease in ability of myocardial movement and deformation, manifested as impairment of myocardial global systolic function (4, 5, 20). Myocardial dysfunction is closely related to fibrosis in DCM patients. Previous studies have found that LVEF is significantly negatively correlated with myocardial fibrosis in DCM patients (21), while progressive fibrosis is associated with minimal change in LVEF (19), and GLS in the LGE+ group is lower than that in LGE- group (22). In this study, the LGE+ group presented with reduced GWI, GCW, GWE, GLS, and $LVEF_{CMRI}$. These findings confirmed the association between myocardial dysfunction and fibrosis.

Additionally, in our study, multivariate logistic regression analysis showed that GWI, GCW, GWE, and GLS were independent predictors for myocardial fibrosis in addition to $LVEF_{CMRI.}$ $LVEF_{CMRI}$, and GCW showed larger AUC and higher accuracy, sensitivity, and specificity than GLS, the accuracy of predicting LV myocardial fibrosis ranged from high to low as: $LVEF_{CMRI}$, GCW, GWE, GWI, and GLS. Therefore, apart from CMRI, LV myocardial work indices may provide further insights into LV myocardial fibrosis in patients with DCM. The optimal cutoff points of $LVEF_{CMRI}$, GWI, GCW, GWE, and GLS might provide valuable information. Galli et al. (23) found that GCW was significantly correlated with myocardial fibrosis in patients with hypertrophic cardiomyopathy. In future work, the application value of LV myocardial work indices in other cardiovascular diseases will be further explored to verify its clinical value.

Wide QRS (duration $\geq$120 ms) on the ECG represents intraventricular conduction delay. In the study, there was no statistically significant difference in QRS duration between LGE- and LGE+ patients, indicating no significant association between QRS duration and LV myocardial fibrosis. A previous study (24) found that the combination of wide QRS and LGE can provide additional risk stratification compared with LGE status alone in DCM patients.

Limitations

This study was conducted in a single center with a small number of samples and needs to be expanded for further study. A previous study (25) found that LV midwall LGE showed an excellent predictive value in identifying high-risk DCM patients, but the correlation between the localization of LGE (sub-endocardial, mid-segment, sub-epicardial) and myocardial

work parameters in this study were not explored. In addition, the accuracy of myocardial work indices in the evaluation of therapeutic response to medications were not analyzed. Further studies with extended follow-up are needed to verify the results of this study.

CONCLUSION

$LVEF_{CMRI}$, GWI, GCW, GWE, and GLS remained significant predictors of LV myocardial fibrosis. $LVEF_{CMRI}$, and GCW appeared to better predict LV myocardial fibrosis compared with GLS. LV myocardial work indices may be potential surrogate markers for the detection of fibrosis in addition to $LVEF_{CMRI}$.

DATA AVAILABILITY STATEMENT

The original contributions presented in the study are included in the article/**Supplementary Material**, further inquiries can be directed to the corresponding author/s.

ETHICS STATEMENT

The studies involving human participants were reviewed and approved by the ethics committee of Fuwai Central China Cardiovascular Hospital. The patients/participants provided their written informed consent to participate in this study. Written informed consent was obtained from the individual(s) for the publication of any potentially identifiable images or data included in this article.

AUTHOR CONTRIBUTIONS

CC and LL designed the study, analyzed data, wrote the manuscript, and reviewed and edited the manuscript. YLi, YLiu, DH, YH, YW, and LM performed this study. All authors read and approved the manuscript.

FUNDING

This study was supported by National Natural Science Foundation of China (82071950), National Natural Science Foundation of Henan for Excellet Young Scientists (202300410364), Medical Science and Technology Project of Henan Province (SB201901099), and Henan Provincial Medical Science and Technology Research Project (LHGJ20190805, LHGJ20200084).

ACKNOWLEDGMENTS

The authors wish to thank the members of the research team, namely, Liu Songyan, Liu Ruijie, Zhao Qingqing, and Zhu Huizhen. Additionally, we thank International Science Editing (http://www.internationalscienceediting.com) for editing this manuscript.

SUPPLEMENTARY MATERIAL

The Supplementary Material for this article can be found online at: https://www.frontiersin.org/articles/10.3389/fcvm.2021.704251/full#supplementary-material

REFERENCES

1. Pinto YM, Elliott PM, Arbustini E, Adler Y, Anastasakis A, Bohm M, et al. Proposal for a revised definition of dilated cardiomyopathy, hypokinetic non-dilated cardiomyopathy, and its implications for clinical practice: a position statement of the ESC working group on myocardial and pericardial diseases. *Eur Heart J.* (2016) 37:1850–8. doi: 10.1093/eurheartj/ehv727
2. Braunwald E. Cardiomyopathies: An Overview. *CIRC Res.* (2017) 121:711–21. doi: 10.1161/CIRCRESAHA.117.311812
3. Halliday BP, Gulati A, Ali A, Newsome S, Lota A, Tayal U, et al. Sex- and age-based differences in the natural history and outcome of dilated cardiomyopathy. *Eur J Heart Fail.* (2018) 20:1392–400. doi: 10.1002/ejhf.1216
4. Weintraub RG, Semsarian C, Macdonald P. Dilated cardiomyopathy. *Lancet.* (2017) 390:400–14. doi: 10.1016/S0140-6736(16)31713-5
5. Japp AG, Gulati A, Cook SA, Cowie MR, Prasad SK. The diagnosis and evaluation of dilated cardiomyopathy. *J Am Coll Cardiol.* (2016) 67:2996–3010. doi: 10.1016/j.jacc.2016.03.590
6. Pedrotti P, Pedretti S, Imazio M, Quattrocchi G, Sormani P, Quarta G. [Clinical applications of cardiac magnetic resonance imaging: heart failure and cardiomyopathies]. *G Ital Cardiol.* (2018) 19:679–91. doi: 10.1714/3027.30252
7. Lee SE, Nguyen C, Xie Y, Deng Z, Zhou Z, Li D, et al. Recent advances in cardiac magnetic resonance imaging. *Korean Circ J.* (2019) 49:146–59. doi: 10.4070/kcj.2018.0246
8. Pi SH, Kim SM, Choi JO, Kim EK, Chang SA, Choe YH, et al. Prognostic value of myocardial strain and late gadolinium enhancement on cardiovascular magnetic resonance imaging in patients with idiopathic dilated cardiomyopathy with moderate to severely reduced ejection fraction. *J Cardiovasc Magn Reson.* (2018) 20:36. doi: 10.1186/s12968-018-0466-7
9. Alba AC, Gaztanaga J, Foroutan F, Thavendiranathan P, Merlo M, Alonso-Rodriguez D, et al. Prognostic value of late gadolinium enhancement for the prediction of cardiovascular outcomes in dilated cardiomyopathy: an international, multi-Institutional study of the MINICOR group. *Circ Cardiovasc Imaging.* (2020) 13:e010105. doi: 10.1161/CIRCIMAGING.119.010105
10. Bayram E, Gulcu O, Aksu U, Aksakal E, Birdal O, Kalkan K. Evaluating the association between the three different ejection fraction measurement techniques and left ventricle global strain. *Eurasian J Med.* (2018) 50:173–7. doi: 10.5152/eurasianjmed.2018.17409
11. Boe E, Skulstad H, Smiseth OA. Myocardial work by echocardiography: a novel method ready for clinical testing. *Eur Heart J Cardiovasc Imaging.* (2019) 20:18–20. doi: 10.1093/ehjci/jey156
12. Chan J, Edwards N, Khandheria BK, Shiino K, Sabapathy S, Anderson B, et al. A new approach to assess myocardial work by non-invasive left ventricular pressure-strain relations in hypertension and dilated cardiomyopathy. *Eur Heart J Cardiovasc Imaging.* (2019) 20:31–9. doi: 10.1093/ehjci/jey131
13. Cui C, Liu L, Li Y, Liu Y, Huang D, Hu Y, et al. Left ventricular pressure-Strain loop-Based quantitative examination of the global and regional myocardial work of patients with dilated cardiomyopathy. *Ultrasound Med Biol.* (2020) 46:2834–45. doi: 10.1016/j.ultrasmedbio.2020.06.008
14. Mathew T, Williams L, Navaratnam G, Rana B, Wheeler R, Collins K, et al. Diagnosis and assessment of dilated cardiomyopathy: a guideline protocol

from the British society of echocardiography. *Echo Res Pract.* (2017) 4:G1–13. doi: 10.1530/ERP-16-0037
15. Chen MS, Bhatt DL. Highlights of the 2002 update to the 2000 American college of cardiology/American heart association acute coronary syndrome guidelines. *Cardiol Rev.* (2003) 11:113–21. doi: 10.1097/01.CRD.0000064422.16013.ED
16. Centurion OA, Alderete JF, Torales JM, Garcia LB, Scavenius KE, Mino LM. Myocardial fibrosis as a pathway of prediction of ventricular arrhythmias and sudden cardiac death in patients with nonischemic dilated cardiomyopathy. *Crit Pathw Cardiol.* (2019) 18:89–97. doi: 10.1097/HPC.0000000000000171
17. Gulati A, Jabbour A, Ismail TF, Guha K, Khwaja J, Raza S, et al. Association of fibrosis with mortality and sudden cardiac death in patients with nonischemic dilated cardiomyopathy. *JAMA.* (2013) 309:896–908. doi: 10.1001/jama.2013.1363
18. Masci PG, Schuurman R, Andrea B, Ripoli A, Coceani M, Chiappino S, et al. Myocardial fibrosis as a key determinant of left ventricular remodeling in idiopathic dilated cardiomyopathy: a contrast-enhanced cardiovascular magnetic study. *Circ Cardiovasc Imaging.* (2013) 6:790–9. doi: 10.1161/CIRCIMAGING.113.000438
19. Mandawat A, Chattranukulchai P, Mandawat A, Blood AJ, Ambati S, Hayes B, et al. Progression of myocardial fibrosis in nonischemic DCM and association with mortality and heart failure outcomes. *JACC Cardiovasc Imaging.* (2021) 14:1338–50. doi: 10.1016/j.jcmg.2020.11.006
20. Schultheiss HP, Fairweather D, Caforio A, Escher F, Hershberger RE, Lipshultz SE, et al. Dilated cardiomyopathy. *Nat Rev Dis Primers.* (2019) 5:32. doi: 10.1038/s41572-019-0084-1
21. Shao XN, Jin YN, Sun YJ, Zhang WB, Cheng JL. Evaluation of the correlation between myocardial fibrosis and ejection fraction in dilated cardiomyopathy using magnetic resonance T1 mapping. *Eur Rev Med Pharmacol Sci.* (2020) 24:12300–5. doi: 10.26355/eurrev_202012_24022
22. Ota S, Hozumi T, Tanimoto T, Takemoto K, Wada T, Kashiwagi M, et al. Global longitudinal strain evaluated by speckle-tracking echocardiography as a surrogate marker for predicting replacement fibrosis detected by magnetic resonance-late gadolinium enhancement in patients with nonischemic cardiomyopathy. *J Clin Ultrasound.* (2021) 49:479–87. doi: 10.1002/jcu.22983
23. Galli E, Vitel E, Schnell F, Le Rolle V, Hubert A, Lederlin M, et al. Myocardial constructive work is impaired in hypertrophic cardiomyopathy and predicts left ventricular fibrosis. *Echocardiography.* (2019) 36:74–82. doi: 10.1111/echo.14210
24. Marume K, Noguchi T, Tateishi E, Morita Y, Kamakura T, Ishibashi K, et al. Mortality and sudden cardiac death risk stratification using the noninvasive combination of wide QRS duration and late gadolinium enhancement in idiopathic dilated cardiomyopathy. *Circ Arrhythm Electrophysiol.* (2018) 11:e006233. doi: 10.1161/CIRCEP.117.006233
25. Wang J, Yang F, Wan K, Mui D, Han Y, Chen Y. Left ventricular midwall fibrosis as a predictor of sudden cardiac death in non-ischaemic dilated cardiomyopathy: a meta-analysis. *ESC Heart Fail.* (2020) 7:2184–92. doi: 10.1002/ehf2.12865

Conflict of Interest: The authors declare that the research was conducted in the absence of any commercial or financial relationships that could be construed as a potential conflict of interest.

Publisher's Note: All claims expressed in this article are solely those of the authors and do not necessarily represent those of their affiliated organizations, or those of the publisher, the editors and the reviewers. Any product that may be evaluated in this article, or claim that may be made by its manufacturer, is not guaranteed or endorsed by the publisher.

frontiers in Bioengineering and Biotechnology

ORIGINAL RESEARCH
published: 17 August 2021
doi: 10.3389/fbioe.2021.725833

Coronary Flow Assessment Using Accelerated 4D Flow MRI With Respiratory Motion Correction

Carmen P. S. Blanken[1], Eric M. Schrauben[1], Eva S. Peper[1], Lukas M. Gottwald[1], Bram F. Coolen[2], Diederik F. van Wijk[3], Jan J. Piek[4], Gustav J. Strijkers[2], R. Nils Planken[1], Pim van Ooij[1] and Aart J. Nederveen[1]*

[1]Department of Radiology and Nuclear Medicine, Amsterdam University Medical Centers, Amsterdam, Netherlands, [2]Department of Biomedical Engineering and Physics, Amsterdam University Medical Centers, Amsterdam, Netherlands, [3]Department of Cardiology, Noordwest Ziekenhuisgroep, Alkmaar, Netherlands, [4]Department of Cardiology, Amsterdam University Medical Centers, Amsterdam, Netherlands

OPEN ACCESS

Edited by:
Jolanda Wentzel, Erasmus Medical Center, Netherlands

Reviewed by:
Natalya Kizilova, Warsaw University of Technology, Poland
Aike Qiao, Beijing University of Technology, China

***Correspondence:**
Pim van Ooij
p.vanooij@amsterdamumc.nl

Specialty section:
This article was submitted to Biomechanics, a section of the journal Frontiers in Bioengineering and Biotechnology

Received: *15 June 2021*
Accepted: *02 August 2021*
Published: *17 August 2021*

Citation:
Blanken CPS, Schrauben EM, Peper ES, Gottwald LM, Coolen BF, van Wijk DF, Piek JJ, Strijkers GJ, Planken RN, van Ooij P and Nederveen AJ (2021) Coronary Flow Assessment Using Accelerated 4D Flow MRI With Respiratory Motion Correction. Front. Bioeng. Biotechnol. 9:725833. doi: 10.3389/fbioe.2021.725833

Magnetic resonance imaging (MRI) can potentially be used for non-invasive screening of patients with stable angina pectoris to identify probable obstructive coronary artery disease. MRI-based coronary blood flow quantification has to date only been performed in a 2D fashion, limiting its clinical applicability. In this study, we propose a framework for coronary blood flow quantification using accelerated 4D flow MRI with respiratory motion correction and compressed sensing image reconstruction. We investigate its feasibility and repeatability in healthy subjects at rest. Fourteen healthy subjects received 8 times-accelerated 4D flow MRI covering the left coronary artery (LCA) with an isotropic spatial resolution of 1.0 mm^3. Respiratory motion correction was performed based on 1) lung-liver navigator signal, 2) real-time monitoring of foot-head motion of the liver and LCA by a separate acquisition, and 3) rigid image registration to correct for anterior-posterior motion. Time-averaged diastolic LCA flow was determined, as well as time-averaged diastolic maximal velocity (V_{MAX}) and diastolic peak velocity (V_{PEAK}). 2D flow MRI scans of the LCA were acquired for reference. Scan-rescan repeatability and agreement between 4D flow MRI and 2D flow MRI were assessed in terms of concordance correlation coefficient (CCC) and coefficient of variation (CV). The protocol resulted in good visibility of the LCA in 11 out of 14 subjects (six female, five male, aged 28 ± 4 years). The other 3 subjects were excluded from analysis. Time-averaged diastolic LCA flow measured by 4D flow MRI was 1.30 ± 0.39 ml/s and demonstrated good scan-rescan repeatability (CCC/CV = 0.79/20.4%). Time-averaged diastolic V_{MAX} (17.2 ± 3.0 cm/s) and diastolic V_{PEAK} (24.4 ± 6.5 cm/s) demonstrated moderate repeatability (CCC/CV = 0.52/19.0% and 0.68/23.0%, respectively). 4D flow- and 2D flow-based diastolic LCA flow agreed well (CCC/CV = 0.75/20.1%). Agreement between 4D flow MRI and 2D flow MRI was moderate for both diastolic V_{MAX} and V_{PEAK} (CCC/CV = 0.68/20.3% and 0.53/27.0%, respectively). In conclusion, the proposed framework of accelerated 4D flow MRI equipped with respiratory motion correction and compressed sensing image reconstruction enables repeatable diastolic LCA flow quantification that agrees well with 2D flow MRI.

Keywords: left coronary artery, blood flow quantification, 4D flow MRI, 2D flow MRI, respiratory motion correction

INTRODUCTION

The clinical evaluation of obstructive coronary artery disease (CAD) relies on a combined approach of catheter-based coronary artery angiography (CAG) and physiological testing with for example fractional flow reserve (FFR) or instantaneous wave-free ratio (iFR). Current guidelines recommend non-invasive testing in patients with stable angina pectoris (SAP) to identify probable obstructive CAD before performing invasive CAG (Fihn et al., 2012; Montalescot et al., 2013).

MRI is a non-invasive, non-ionizing imaging technique that can reliably provide prognostic information in patients with CAD using stress-induced perfusion imaging (Motwani et al., 2018). In fact, MRI provides detailed anatomical information (Albrecht et al., 2018; Bustin et al., 2019; Roy et al., 2021) and can also measure coronary flow (Hofman et al., 1996; Davis et al., 1997; Marcus et al., 1999; Johnson et al., 2008; Zhu et al., 2021), potentially enabling assessment of the coronary flow reserve (CFR). The CFR is a measure for the adaptive capacity of the coronary vascular bed to meet the myocardial oxygen demand during increased oxygen consumption of the myocardium. Large-scale studies have shown that a CFR of less than 2.0 is an independent predictor of cardiac mortality and major adverse cardiac events and has greater prognostic value than FFR (Murthy et al., 2011; van de Hoef et al., 2014; Kato et al., 2017). The potential of MRI to concurrently assess coronary anatomy, CFR and myocardial perfusion makes it a potential screening modality for accurate selection and planning of patients with SAP for percutaneous coronary intervention (PCI).

To date, MRI-based coronary flow quantification has only been reported using 2D flow MRI (Hofman et al., 1996; Davis et al., 1997; Marcus et al., 1999; Johnson et al., 2008), which has limitations for clinical use. It requires prior knowledge of the desired measurement location(s) and its accuracy depends highly on correct planning of the imaging slice, i.e. perpendicular to the vessel, distal to the stenosis of interest. In contrast, 4D flow MRI (time-resolved three-dimensional three-directional phase-contrast MRI) provides volumetric coverage (Markl et al., 2012). Therefore, the acquisition is easy to plan, analysis planes can be placed after image acquisition and the flow can be quantified at multiple locations from a single dataset. Yet, coronary flow quantification using 4D flow MRI has never been reported, presumably because the small size of the coronary arteries necessitates the use of a high spatial resolution (~1 mm^3), leading to unrealistically long scan times that make it nearly impossible to avoid patient movement causing image deterioration.

High spatial resolution 4D flow MRI at clinically feasible scan times requires sparse sampling. Pseudo-spiral Cartesian undersampling with compressed sensing image reconstruction has previously made intracranial flow quantification possible with good accuracy and repeatability (Gottwald et al., 2020a). Application of this technique to the coronary arteries is promising, provided that we can correct for respiratory motion.

In the current study, we therefore investigate the feasibility and repeatability of accelerated, high spatial resolution 4D flow MRI with respiratory motion correction for flow quantification in the left coronary artery (LCA) of healthy subjects at rest. We hypothesize that respiratory motion correction results in improved visibility of the LCA compared to non-corrected data, and that 4D flow MRI-based measurements of LCA flow agree well with 2D flow MRI-based measurements.

MATERIALS AND METHODS

Image Acquisition

Fourteen healthy subjects (eight female, six male, aged 28 ± 4 years) underwent cardiac MRI at 3T (Ingenia Philips, Best, the Netherlands). The study was approved by the local institutional review board (METC) of Amsterdam UMC and all participants gave written informed consent. A Dixon cardiac angiogram with isotropic spatial resolution of 1.5 mm^3 was acquired for planning purposes using electrocardiographic (ECG) gating to mid-diastole and respiratory gating using a lung-liver navigator with an end-expiration acceptance window of 7 mm. Next, a 4D flow MRI acquisition was performed with an isotropic spatial resolution of 1.0 mm^3, covering the LCA in a 30-mm thick transversal slab. This acquisition was directly followed by a 2D flow MRI acquisition planned perpendicular to the LCA, with a spatial resolution of 1.0 × 1.0 mm^2 and 6.0 mm slice thickness. For the purpose of repeatability testing, the sequence of the aforementioned 4D and 2D acquisitions was performed once more with identical settings.

4D flow MRI was acquired using 8 times-accelerated pseudo-spiral undersampling (Gottwald et al., 2020b; Peper et al., 2020). Three-directional velocity-encoding sensitivity (VENC) was set to 50 cm/s and retrospective ECG-gating enabled cardiac binning into 24 phases. A pencil beam navigator was played out on the lung-liver interface to monitor respiratory motion at a sampling frequency of 2 Hz. To reject outliers caused by deep inspiration, an acceptance window of 20 mm was employed. Breath-held 2D flow MRI was acquired using parallel imaging with a SENSE factor of 2. Through-plane VENC was set to 35 cm/s (lower than for the 4D flow MRI, since the larger slice thickness causes spatial velocity averaging which in our experience conceals local peak velocities observed in the 4D flow MRI acquisition).

Lastly, a real-time coronal balanced steady state free precession (bSSFP) series was run for ~50 s to monitor foot-head respiratory motion of the LCA with respect to the motion of the liver. This scan was ECG-triggered to mid-diastole and had a spatial resolution of 2.0 × 2.0 mm^2 and slice thickness of 8.0 mm.

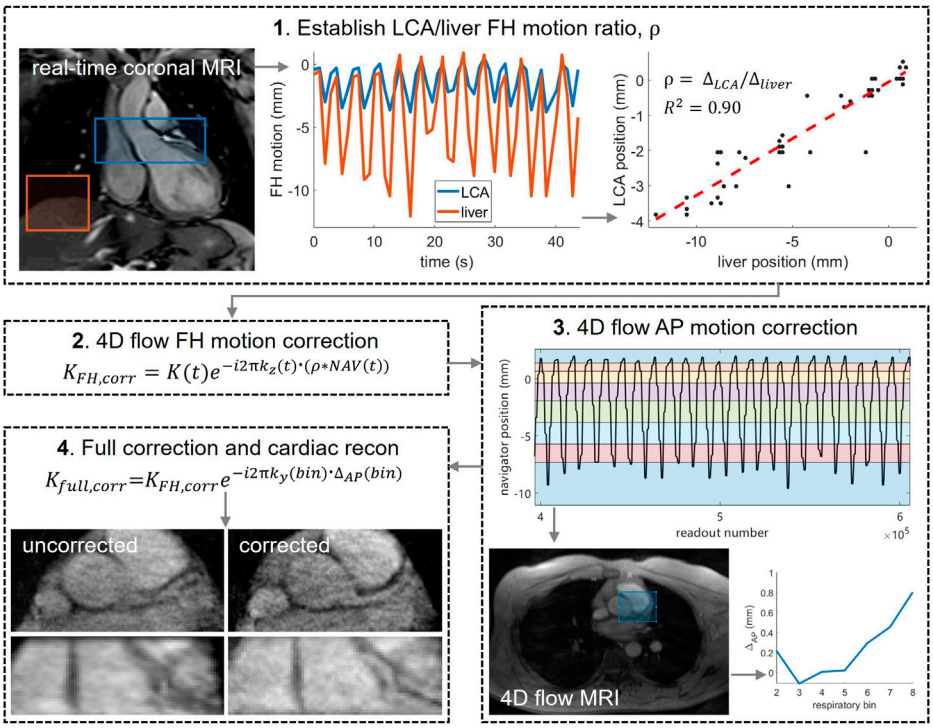

FIGURE 1 | Post-processing pipeline used to correct for respiratory motion in the 4D flow MRI acquisitions. **1)** a real-time ECG-triggered scan was used to determine the ratio ρ between the motion of LCA and liver motion in foot-head (FH) direction. Motion curves were determined by rigid image registration on two separate regions of interest: over the LCA (blue) and over the liver (red). LCA and liver positions were plotted against each other and a linear fit was made, the slope of which is equal to ρ. **2)** LCA offsets, calculated by multiplying liver offsets *NAV*(*t*) with ρ, were converted into time-dependent phase shifts by multiplying the normalized k-space coordinate in the FH direction k_z (t) with the corresponding LCA offset. The complex raw k-space data *K*(t) was then multiplied with these phase shifts. **3)** *NAV*(t) was binned into 8 respiratory phases with equal amounts of data and bin-specific images (time-averaged over mid-diastolic time frames) were reconstructed from the FH motion-corrected raw data. Rigid image registration of bins 2–8 to bin 1 (end-expiration) was performed over a central region including the LCA, producing AP offsets per bin. **4)** AP offsets were corrected in the complex raw k-space data and final image reconstruction was performed.

Respiratory Motion Correction and Image Reconstruction

Prior to reconstruction of the final images, respiration-induced motion of the LCA was corrected in both the foot-head (FH) and anterior-posterior (AP) directions. The methodology is schematically depicted in **Figure 1**.

Motion Correction in Foot-Head Direction

FH motion correction was based on the 4D flow respiratory navigator signal in combination with the real-time coronal scan. In short, the real-time scan was used to determine the ratio ρ between the motion of LCA and liver motion in FH direction, to be able to estimate LCA motion at every k-space readout and correct for it prior to image reconstruction. LCA and liver motion curves were determined by rigid image registration on two separate regions of interest, and their end-expiration heights were aligned. LCA and liver positions were plotted against each other and a linear fit was made, the slope of which is equal to ρ. Next, the lung-liver navigator positions were interpolated to give a position at the time of every imaging readout. The resulting navigator positions will be referred to as *NAV*(t). Offsets from end-expiration were determined and converted into LCA position offsets by multiplication with ρ. To correct for these offsets, readout-specific phase shifts were calculated by multiplying the normalized k-space coordinate in the FH direction $k_z(t)$ with the corresponding LCA offset. The complex raw k-space data *K*(t) was then multiplied with these phase shifts.

Motion Correction in Anterior-Posterior Direction

After sorting *NAV*(t) into 8 independent respiratory phase bins with equal amounts of data, bin-specific, time-averaged images were reconstructed from the FH motion-corrected raw 4D flow data, using only k-space samples that were acquired during mid-diastole. From each reconstruction, five central slices were averaged to remove any remaining unresolved FH motion, and rigid image registration of bins 2–8 to bin 1 (end-expiration) was performed over a central region including the LCA. This produced AP offsets per bin, which were corrected in the complex raw k-space data in a similar manner as described for the FH offsets. Right-left offsets were expected to be small and were thus ignored.

Image Reconstruction

Compressed sensing image reconstruction was performed in Matlab R2019b (The MathWorks, Inc., Natick, MA), making

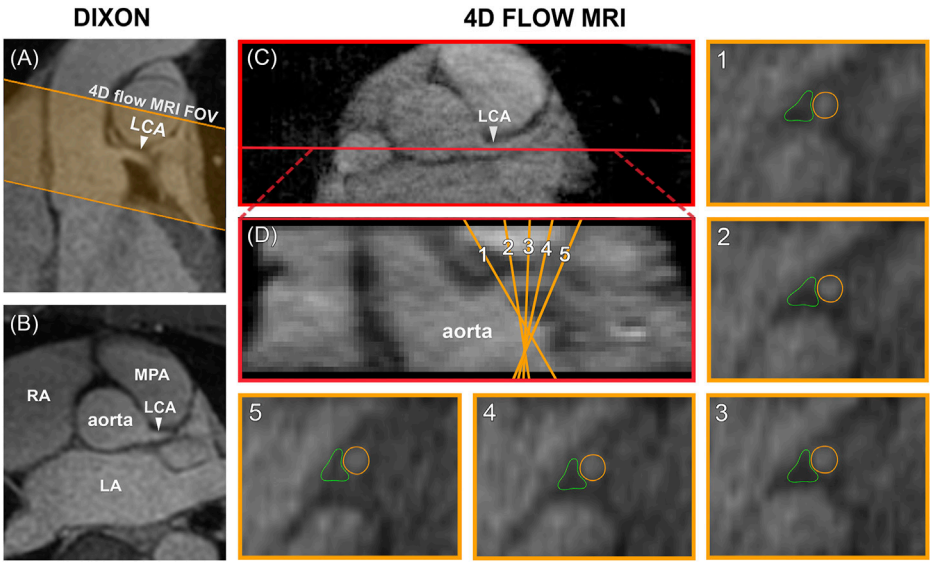

FIGURE 2 | (A) Planning of the 4D flow MRI field of view (orange) on the Dixon water image. **(B)** Transversal view of the Dixon water image. **(C)** The LCA is identified on a transversal 4D flow MRI magnitude image and a longitudinal cross-section is made (shown in red). **(D)** The resulting coronal view is used to place five analysis planes perpendicular to the LCA. **1–5)** In these planes, measurement contours are placed around the LCA lumen and in adjacent pericardial fat. FOV = field of view, LCA = left coronary artery, LA = left atrium, RA = right atrium, MPA = main pulmonary artery.

use of a sparsifying total variation transform in time with a regularization parameter $r = 0.001$ and 20 iteration steps using MRecon (Gyrotools, Zürich, Switzerland) and the Berkeley Advanced Reconstruction Toolbox (BART) (Uecker, 2015). To assess the effect of the respiratory motion correction on the images, non-corrected images were reconstructed as well.

Data Analysis

Data analysis was performed in GTFlow V3.2.15 (Gyrotools, Zürich, Switzerland). 4D flow MRI magnitude images were used to localize the LCA branching off from the aorta in a mid-diastolic time frame and to make a longitudinal cross-section, see **Figure 2**. The longitudinal view was used to place 5 equidistant analysis planes perpendicular to the LCA, approximately 1.5 mm apart, to be able to check for consistency of the measurements over the length of the LCA. Next, the LCA was visually identified in each plane and measurement contours were drawn around the lumen. Additional reference contours were drawn in the adjacent pericardial fat to verify that the measurements would amount to zero flow here, see **Figure 2**. Both the LCA and the reference contours were copied to all mid-diastolic time frames and onto the corresponding velocity images. Other time frames in which the LCA could not be identified because of blurring due to myocardial contraction and relaxation were discarded. Diastolic flow curves were calculated for each contour, as well as streamlines for visualization. Contour-averaged flow curves were calculated for each subject and averaged over all subjects. For comparison with velocities reported in echocardiographic and 2D flow MRI studies, maximal velocity (V_{MAX}) was determined for each contour and each time frame by selecting the voxel with the highest signal within the contour. Next, time-averaged diastolic V_{MAX} and diastolic peak velocity (V_{PEAK}) were determined for each subject.

Scan-rescan repeatability of time-averaged diastolic flow, time-averaged diastolic V_{MAX} and diastolic V_{PEAK} was evaluated by means of Bland-Altman analysis, coefficient of variation (CV) and smallest detectable difference. Furthermore, concordance correlation coefficients (CCC) were determined based on absolute agreement and a two-way mixed-effects model (Chen and Barnhart, 2013). CCC was classified as: poor (<0.5), moderate (0.5–0.75), good (0.75–0.9) and excellent (>0.9) (Koo and Li, 2016). CV was defined as the standard deviation of the scan-rescan differences divided by the mean of all scan and rescan measurements. The smallest detectable difference was defined as 1.96 times the standard deviation of the scan-rescan differences. A paired *t*-test was used to compare measured flows and velocities with 2D flow MRI and pericardial fat control measurements. Flow values will be presented as mean ± SD.

RESULTS

4D Flow MRI

Median scan time was 12:20 min per 4D flow MRI scan (IQR: 11:30–13:15 min) with a respiratory gating efficiency of approximately 90%. Three subjects were excluded because of insufficient visibility of the LCA in both the original and motion-corrected reconstructions. In these subjects, a pattern of relatively long inspiration phases and no clear skewness towards end-expiration was observed. In the remaining eleven subjects (six female, five male, aged 28 ± 4 years), the LCA was identified in the

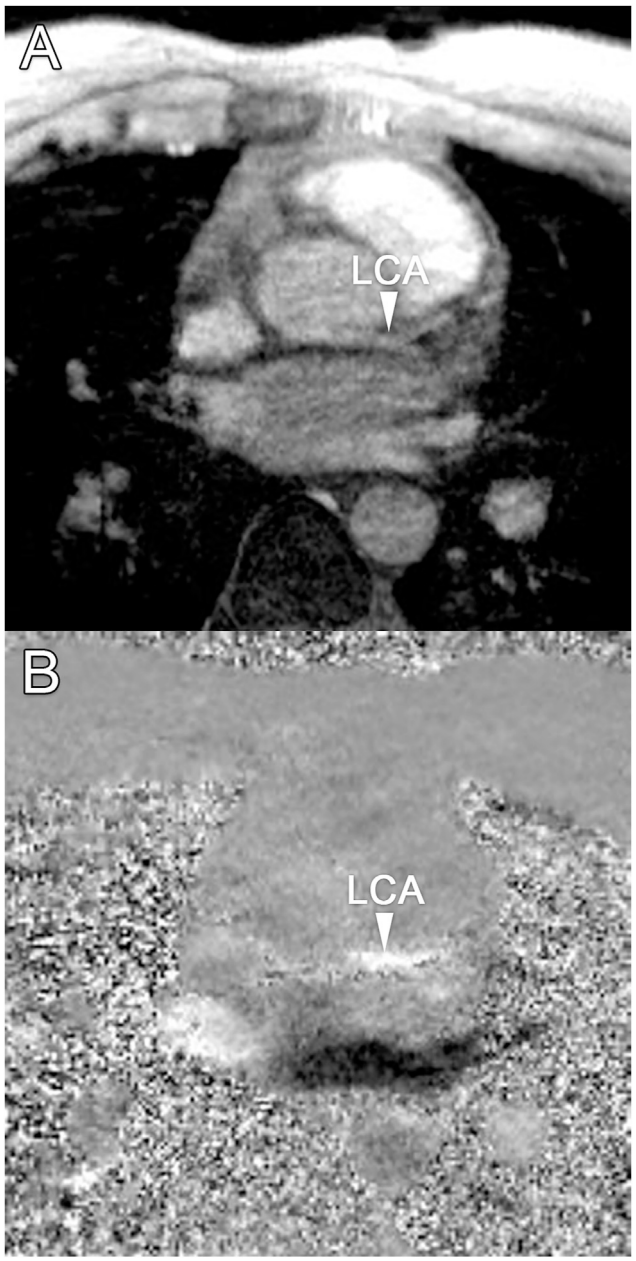

FIGURE 3 | (A) Transversal 4D flow MRI magnitude image and **(B)** phase image showing velocities in right-left direction during mid-diastole. Arrows indicate the location of the left coronary artery, where velocity signal can be observed.

magnitude images and velocity signal in the phase images. An overview of all original and corrected reconstructions can be found in **Supplementary Figure S1**. **Figure 3** shows example images of phase-contrast magnitude and velocity in right-left direction. **Figure 4** shows streamlines in the LCA, splitting into left anterior descending (LAD) and left circumflex (LCX) coronary artery. A video of the streamlines can be found in **Supplementary Video S1**. Flow curves from this acquisition are presented in **Figure 5** (top). Seven out of 24 time frames were examined in this subject. In the other subjects, the number of examined cardiac frames ranged from 5 to 8.

Averaged over all subjects, time-averaged diastolic flows of 1.30 ± 0.39 ml/s in the LCA and 0.11 ± 0.14 ml/s in adjacent pericardial fat were measured, see **Figure 5** (bottom). Mean scan-rescan difference and limits of agreement were −0.05 [−0.57; 0.47] ml/s in the LCA - resulting in a smallest detectable difference of 0.52 ml/s - and −0.04 [−0.59; 0.51] ml/s in the pericardial fat (**Figure 6**). LCA and pericardial fat control measurements of diastolic flow differed significantly ($p < 0.001$). Averaged over all subjects, time-averaged diastolic V_{MAX} in the LCA was 17.2 ± 3.0 cm/s and diastolic V_{PEAK} was 24.4 ± 6.5 cm/s. Statistical results regarding repeatability and agreement between 4D flow MRI and 2D flow MRI are summarized in **Table 1**. 4D flow-based diastolic LCA flow measurements had good scan-rescan repeatability (CCC = 0.79, CV = 20.4%). Time-averaged diastolic V_{MAX} measurements were moderately repeatable (CCC = 0.52, CV = 19.0%), as were diastolic V_{PEAK} measurements (CCC = 0.68, CV = 23.0%).

2D Flow MRI

Time-averaged diastolic LCA flow as measured by 2D flow MRI was 1.47 ± 0.50 ml/s (**Figure 5**). Mean scan-rescan difference and limits of agreement were −0.08 [−0.63; 0.48] ml/s (**Figure 6**), resulting in a smallest detectable difference of 0.56 ml/s. Time-averaged diastolic V_{MAX} in the LCA was 17.8 ± 5.6 cm/s and diastolic V_{PEAK} was 22.1 ± 7.0 cm/s. 2D flow-based diastolic LCA flow measurements had good scan-rescan repeatability (CCC = 0.84, CV = 19.4%), time-averaged diastolic V_{MAX} measurements were excellently repeatable (CCC = 0.92, CV = 11.2%) and diastolic V_{PEAK} measurements demonstrated good repeatability (CCC = 0.81, CV = 20.5%) (**Table 1**).

4D flow- and 2D flow-based diastolic LCA flow agreed well (CCC = 0.75, CV = 20.1%) and did not significantly differ (p =

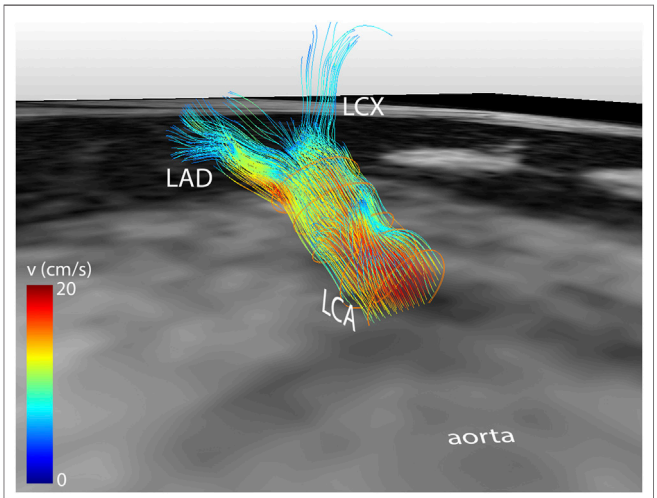

FIGURE 4 | Streamline reconstruction of 4D flow MRI-derived velocities in the LCA for a mid-diastolic time frame. Streamlines initiate from five contours placed in the LCA and split into LAD and LCX. Velocity color-coding shows that the measured velocities in the LAD and LCX are lower than in the LCA.

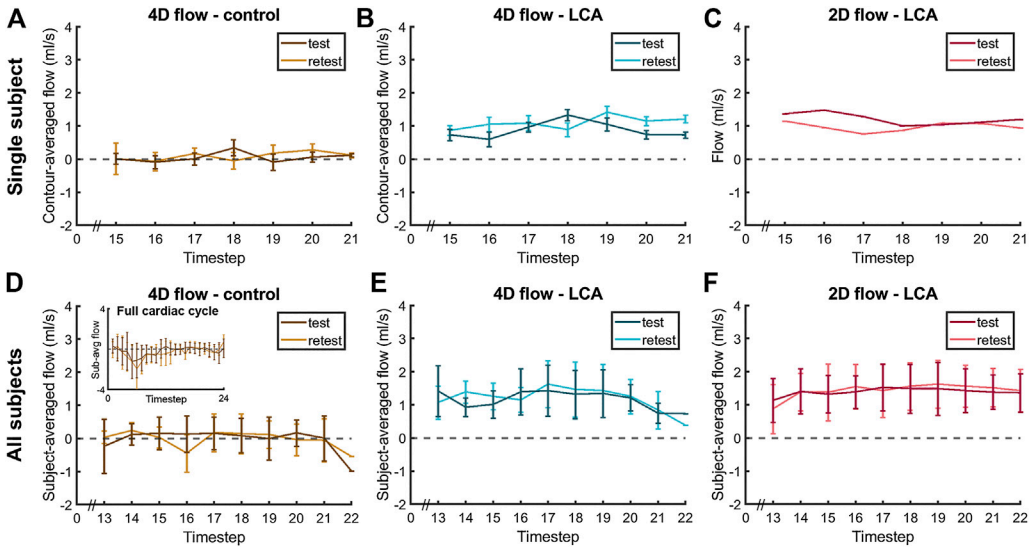

FIGURE 5 | Diastolic flow measured by 4D flow MRI and 2D flow MRI in the LCA and by 4D flow MRI in the adjacent pericardial fat ("4D flow - control") in a single subject **(A–C)**, same subject as in **Figure 4**) and averaged over all subjects **(D–F)**, displayed for scan and rescan 4D flow MRI acquisitions. Single-subject flow curves are the result of averaging over all five measurement contours. All-subjects flow curves are the average over all eleven subject-specific (contour-averaged) flow curves.

0.07), despite a trend towards higher measurements by 2D flow MRI as compared to 4D flow MRI (mean difference and limits of agreement: 0.17 [−0.38; 0.71] ml/s). Moderate agreement and no significant differences between 4D flow MRI and 2D flow MRI were found in measurements of time-averaged diastolic V_{MAX} (CCC = 0.68, CV = 20.3%, $p = 0.60$) and diastolic V_{PEAK} (CCC = 0.53, CV = 27.0%, $p = 0.25$).

DISCUSSION

In this study, we investigated the feasibility and repeatability of accelerated 4D flow MRI for blood flow quantification in the LCA of healthy subjects at rest. Prospective 8-fold undersampling, respiratory motion correction and compressed sensing image reconstruction facilitated 4D flow MRI-based LCA flow quantification during mid-diastolic time frames. Flow measurements were repeatable and agreed well with 2D flow MRI-based measurements.

CFR assessment is a possible application of the non-invasive LCA flow measurement performed in the current study. Based on the scan-rescan repeatability found in this study, the difference of baseline flow and hyperemic flow should at least be 0.52 ml/s to be detected using the current MRI protocol. Given that the CFR is 4–5 (i.e. an increase from roughly 1.5 to 6.5 ml/s in the LCA) in healthy subjects and around 2 in patients (i.e. an increase from roughly 1.5 to 3.0 ml/s in the LCA), the actual difference will be well above the detection threshold of the presented method.

The observation that 4D flow MRI demonstrates lower repeatability in maximal velocity measurement than 2D flow MRI may be explained by the inherently lower signal-to-noise ratio of the 4D flow MRI acquisition due to smaller voxel size along the length of the LCA (1.0 vs 6.0 mm for 2D flow MRI). Furthermore, unlike 2D flow MRI, 4D flow MRI does not benefit from the slice in-flow effect. The measured velocities were also less repeatable than has been reported for Doppler echocardiography (Hozumi et al., 1998; Kasprzak et al., 2000; Pizzuto et al., 2001; Ciampi et al., 2019).

Literature on healthy LCA diastolic peak velocities is limited. In the early 90's, studies appeared using transesophageal echocardiography for LCA flow quantification. These studies report baseline values - under general anesthesia - of 29 ± 12 cm/s, 34 ± 8 cm/s and 71 ± 19 cm/s in patients without left main coronary artery stenosis (Yamagishi et al., 1991; Yasu et al., 1993; Kasprzak et al., 2000). More recent studies focus on the LAD using transthoracic echocardiography (Hozumi et al., 1998; Pizzuto et al., 2001; Wittfeldt et al., 2016; Ciampi et al., 2019) or LAD, LCX and RCA using intracoronary Doppler (Ofili et al., 1993; Anderson et al., 2000; van de Hoef et al., 2015) and no longer report LCA velocities. The 24.4 ± 6.5 cm/s (4D flow MRI) and 22.1 ± 7.0 cm/s (2D flow MRI) peak velocities we measured in the LCA are lower than previously reported in studies using transesophageal echocardiography (Yamagishi et al., 1991; Yasu et al., 1993; Kasprzak et al., 2000), but similar to values measured using 2D flow MRI (Schiemann et al., 2006).

Studies using 2D flow MRI that measured LAD - as opposed to LCA - flow have reported time-averaged values of 0.5–1.4 ml/s (Davis et al., 1997; Marcus et al., 1999; Johnson et al., 2008; Zhu et al., 2021). Other studies measured LAD peak flow velocities with 2D flow MRI to determine the CFR and found good correlations with CFR obtained by Doppler guide wire (in patients) and by PET (in healthy subjects) (Hundley et al., 1996; Shibata et al., 1999; Sakuma et al., 2000; Bedaux et al., 2002; Nagel et al., 2003). Interestingly, measured peak velocities were significantly lower by 2D flow MRI than by Doppler guide wire, despite the good correlation between CFRs by the two

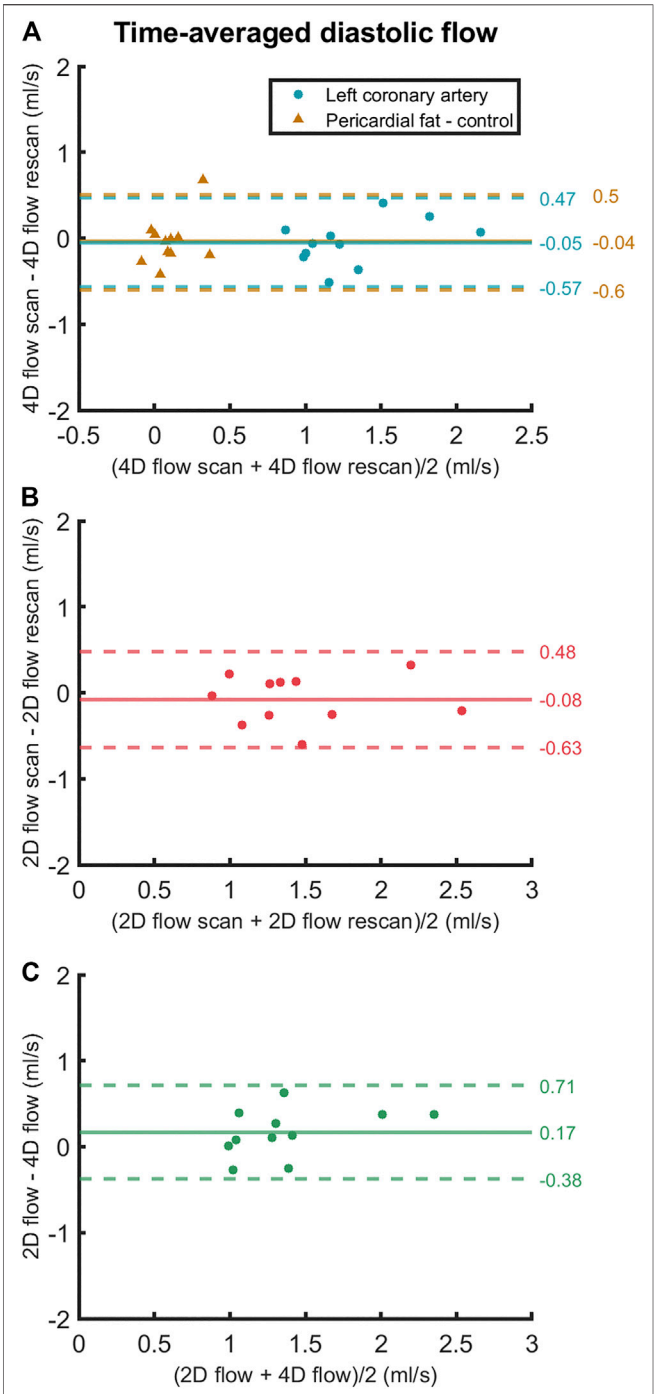

FIGURE 6 | Bland-Altman plots of **(A)** scan and rescan 4D flow MRI measurements, **(B)** scan and rescan 2D flow MRI measurements and **(C)** 4D flow MRI and 2D flow MRI scan-rescan-averaged measurements of time-averaged diastolic LCA flow. Data points are subject-specific. Mean differences and 95% limits of agreement are indicated on the right.

techniques (Shibata et al., 1999; Bedaux et al., 2002; Nagel et al., 2003; Keegan et al., 2015). These differences were probably a result of the different nature of the two measurements: Doppler guide wire measures velocities along a line whereas in phase-contrast MRI, velocity profiles are spatially smoothed when averaged over the volume of a voxel. Other MRI studies have focused on global CFR assessment based on velocity or flow measurement in the coronary sinus or based on myocardial perfusion by contrast-enhanced MRI (Ibrahim et al., 2002; Lund et al., 2003; Aras et al., 2007; Kato et al., 2017). In short, a variety of studies has reported on coronary flows and velocities, but differences in modalities and anatomical locations of measurement complicate meaningful comparison between studies.

We quantified LCA flow at rest only. For CFR assessment, the flow should also be quantified in the hyperemic state, which may introduce more blurring due to a higher heart rate and heavier breathing, but may also result in higher SNR due to higher velocities and a larger luminal area. Hyperemia can be induced in different ways, the most common being administration of a vasodilatory drug. Another possibility is physical exercise testing with the use of an MRI-compatible ergometer, but this introduces subject motion and has a smaller effect on the myocardial blood flow than a vasodilatory drug. Furthermore, inducing hypercapnia, an increased arterial CO_2-pressure, with the use of a gas control breathing mask has been shown to have an effect similar to physical exercise (Pelletier-Galarneau et al., 2018).

Not only MRI, but also CT, PET-CT, and myocardial perfusion scintigraphy are potentially available non-invasive techniques to investigate different and sometimes overlapping characteristics of coronary artery disease (CAD) (Heo et al., 2014; Alexanderson-Rosas et al., 2015; Smulders et al., 2017). PET-CT is a powerful technique because it can combine anatomical evaluation and corresponding functional status including coronary flow velocity (reserve) and the assessment of microvascular resistance. However, the limited availability, use of ionizing radiation and costs of PET-CT has prevented its widespread application in clinical practice. MRI may provide a more accessible alternative.

Recent developments in the field of cardiac MRI have enabled whole-heart 5D (4D + a respiratory motion dimension) flow imaging, 5D anatomical imaging of the heart including the coronary arteries, and high-resolution coronary angiography (Feng et al., 2018; Bustin et al., 2019; Ma et al., 2020). The current study is the first to combine and implement high spatial resolution imaging, 3D time-resolved velocity encoding, and 2D respiratory motion correction to achieve coronary flow quantification. Vital to the successful combination of these assets are a number of design elements of the proposed framework. First, the use of pseudo-spiral Cartesian k-space sampling allows for a targeted FH field of view to enable 1.0 mm^3 resolution at a scan time of approximately 12 min. In contrast, Ma et al. (2020) and Feng et al. (2018) employ a radial phyllotaxis sampling scheme which requires a cubic field of view. This sampling strategy is relatively efficient for high-resolution respiratory motion-resolved whole-heart application (2.5 mm^3 at a scan time of 8 min, or 1.15 mm^3 at a scan time of 14 min with the aid of MR contrast), but would require impractically long scan

TABLE 1 | Statistical results regarding scan-rescan repeatability and agreement between 4D flow MRI and 2D flow MRI.

	4D flow - LCA		2D flow - LCA		LCA		4D flow - control	
Statistic	**Scan**	**Rescan**	**Scan**	**Rescan**	**4D flow**	**2D flow**	**Scan**	**Rescan**
Time-averaged diastolic flow (ml/s)								
Mean ± SD [ml/s]	1.27 ± 0.46	1.32 ± 0.36	1.43 ± 0.53	1.51 ± 0.52	1.30 ± 0.39	1.47 ± 0.50	0.09 ± 0.23	0.12 ± 0.15
Mean diff. [ml/s]	−0.05		−0.08		0.17		−0.04	
LOA [ml/s]	−0.57; 0.47		−0.63; 0.48		−0.38; 0.71		−0.59; 0.51	
CV [%]	20.4		19.4		20.1		n/a	
CCC	0.79		0.84		0.75		n/a	
SDD [ml/s]	0.52		0.56		n/a		n/a	
Time-averaged diastolic V_{MAX} (cm/s)								
Mean ± SD [cm/s]	17.6 ± 4.0	16.8 ± 2.6	17.3 ± 5.4	18.3 ± 5.9	17.2 ± 3.0	17.8 ± 5.6		
Mean diff. [cm/s]	0.83		−1.03		0.58			
LOA [cm/s]	−5.56; 7.22		−4.92; 2.86		−6.38; 7.54			
CV [%]	19.0		11.2		20.3			
CCC	0.52		0.92		0.68			
SDD [cm/s]	6.39		3.89		n/a			
Diastolic V_{PEAK} (cm/s)								
Mean ± SD [cm/s]	24.8 ± 6.7	24.1 ± 7.5	21.9 ± 7.3	22.4 ± 7.4	24.4 ± 6.5	22.1 ± 7.0		
Mean diff. [cm/s]	0.66		−0.50		−2.33			
LOA [cm/s]	−10.37; 11.69		−9.37; 8.38		−14.66; 10.0			
CV [%]	23.0		20.5		27.0			
CCC	0.68		0.81		0.53			
SDD [cm/s]	11.0		8.9		n/a			

LOA, limits of agreement; CV, coefficient of variation; CCC, concordance correlation coefficient; SDD, smallest detectable difference; control, pericardial fat reference measurements.

times for 1.0 mm^3 resolution coronary application. For coronary angiography, Bustin et al. (2019) employed a k-space sampling scheme similar to the current one, however their approach was optimized for diastolic vessel depiction instead of time-resolved flow measurement. Another important design element is the two-dimensional respiratory motion correction based on a one-dimensional navigator in combination with rigid image registration. Multi-dimensional motion correction or resolution is typically achieved using self-navigation (Feng et al., 2018; Bustin et al., 2019; Ma et al., 2020), which requires frequent sampling of the k-space center making it not readily compatible with non-radial sequences. A disadvantage of the 1D navigator-based approach we introduced is the necessary acquisition of an extra scan, prolonging the total scan time by approximately 1 min. Furthermore, our motion correction pipeline is not fully automated and AP motion correction based on image registration requires interim image reconstruction. These aspects further prolong reconstruction time.

The current proof of concept study has a couple of limitations. Firstly, we performed measurements in the LCA only. For meaningful clinical measurements, the approach should be extended to also encompass the LAD and LCX, as well as the right coronary artery (RCA). However, the spatial resolution employed in our study does not allow for accurate measurements in these smaller diameter (2.9–3.9 mm) vessels considering the fact that the luminal area should contain at least 16 voxels to keep the measurement error below 10% (Dodge et al., 1992; Tang et al., 1993). An average LCA has a lumen diameter of 4.5 ± 0.5 mm and fits exactly 16 voxels of the size we used in this study (Dodge et al., 1992). Hence, a higher spatial resolution has to be achieved for clinical application.

Secondly, we only considered diastolic time frames because of the presence of myocardial contraction- and relaxation-induced blurring of the LCA in the systolic images. To resolve this issue, a higher temporal resolution must be achieved while maintaining high spatial resolution. To date, this has only been achieved in single-slice through-plane flow imaging with an efficient k-space sampling scheme (Zhu et al., 2021). Nevertheless, for CFR assessment, diastolic flow values should suffice to determine the ratio between resting flow and hyperemic flow.

Lastly, we tested for repeatability by performing two 4D flow MRI acquisitions in direct succession, without repositioning the subject. Consequently, differences in patient position or acquisition planning were not accounted for.

In general, the main difficulty with high-resolution 4D flow MRI applied to small diameter vessels is that it is prone to motion artifacts, due to the long acquisition time needed. The acquisitions may contain (involuntary) patient movement resulting in image blurring, and breathing motion may induce blurring or ghosting despite respiratory motion compensation, as opposed to single breathhold acquisition used in 2D flow MRI (Dyverfeldt and Ebbers, 2017). A recent advancement, called focused navigation, enables non-rigid image registration in 3D, and can in the future potentially be applied to flow imaging (Roy et al., 2021). Non-Cartesian k-space sampling, in

combination with a high temporal resolution, might make the acquisition more robust against motion in general (Glover and Pauly, 1992). This way, systolic time frames might be taken into account as well and flow curves over the entire cardiac cycle can be obtained.

CONCLUSION

The proposed framework of accelerated 4D flow MRI with respiratory motion correction and compressed sensing image reconstruction enables non-invasive, diastolic LCA flow quantification that agrees well with 2D flow MRI. Important assets of the developed methodology are the use of pseudo-spiral k-space sampling which allows for a targeted FH field of view, and the 2D respiratory motion correction based on a 1D navigator. Opportunities for further optimization exist in enhancing the temporal resolution, automating the entire reconstruction pipeline, and improving robustness for atypical breathing patterns using more advanced k-space sampling and motion correction schemes. The observed scan-rescan repeatability justifies future experiments on quantification of hyperemic LCA flow, to investigate whether the current acquisition can be used to determine CFR.

DATA AVAILABILITY STATEMENT

The raw data supporting the conclusions of this article will be made available by the authors, without undue reservation. All 4D flow data were acquired using our in-house developed Amsterdam UMC "PROspective Undersampling in multiple Dimensions" (PROUD) patch. A compiled version of this patch is available on reasonable request.

ETHICS STATEMENT

The studies involving human participants were reviewed and approved by the local institutional review board (METC) of Amsterdam UMC. The participants provided their written informed consent to participate in this study.

AUTHOR CONTRIBUTIONS

All authors contributed to conception and design of the study. CB and ES worked on the acquisition and postprocessing of the data. CB performed the statistical analysis and wrote the first draft of the manuscript. All authors contributed to manuscript revision, read, and approved the submitted version.

ACKNOWLEDGMENTS

We thank Pit Spee, BSc, for his assistance in setting up the scan protocol and data analysis protocol.

SUPPLEMENTARY MATERIAL

The Supplementary Material for this article can be found online at: https://www.frontiersin.org/articles/10.3389/fbioe.2021.725833/full#supplementary-material

REFERENCES

Albrecht, M. H., Varga-Szemes, A., Schoepf, U. J., Apfaltrer, G., Xu, J., Jin, K.-N., et al. (2018). Coronary Artery Assessment Using Self-Navigated Free-Breathing Radial Whole-Heart Magnetic Resonance Angiography in Patients with Congenital Heart Disease. *Eur. Radiol.* 28 (3), 1267–1275. doi:10.1007/s00330-017-5035-1

Alexanderson-Rosas, E., Guinto-Nishimura, G. Y., Cruz-Mendoza, J. R., Oropeza-Aguilar, M., De La Fuente-Mancera, J. C., Barrero-Mier, A. F., et al. (2015). Current and Future Trends in Multimodality Imaging of Coronary Artery Disease. *Expert Rev. Cardiovasc. Ther.* 13 (6), 715–731. doi:10.1586/14779072.2015.1039991

Anderson, H. V., Stokes, M. J., Leon, M., Abu-Halawa, S. A., Stuart, Y., and Kirkeeide, R. L. (2000). Coronary Artery Flow Velocity Is Related to Lumen Area and Regional Left Ventricular Mass. *Circulation* 102 (1), 48–54. doi:10.1161/01.CIR.102.1.48

Aras, A., Anik, Y., Demirci, A., Balci, N. C., Kozdag, G., Ural, D., et al. (2007). Magnetic Resonance Imaging Measurement of Left Ventricular Blood Flow and Coronary Flow reserve in Patients with Chronic Heart Failure Due to Coronary Artery Disease. *Acta Radiol.* 48 (10), 1092–1100. doi:10.1080/02841850701545748

Bedaux, W. L. F., Hofman, M. B. M., de Cock, C. C., Stoel, M. G., Visser, C. A., and van Rossum, A. C. (2002). Magnetic Resonance Imaging versus Doppler Guide Wire in the Assessment of Coronary Flow reserve in Patients with Coronary Artery Disease. *Coron. Artery Dis.* 13 (7), 365–372. doi:10.1097/00019501-200211000-00003

Bustin, A., Ginami, G., Cruz, G., Correia, T., Ismail, T. F., Rashid, I., et al. (2019). Five-minute Whole-Heart Coronary MRA with Sub-millimeter Isotropic Resolution, 100% Respiratory Scan Efficiency, and 3D-PROST Reconstruction. *Magn. Reson. Med.* 81 (1), 102–115. doi:10.1002/mrm.27354

Chen, C.-C., and Barnhart, H. X. (2013). Assessing Agreement with Intraclass Correlation Coefficient and Concordance Correlation Coefficient for Data with Repeated Measures. *Comput. Stat. Data Anal.* 60 (1), 132–145. doi:10.1016/j.csda.2012.11.004

Ciampi, Q., Zagatina, A., Cortigiani, L., Gaibazzi, N., Borguezan Daros, C., Zhuravskaya, N., et al. (2019). Functional, Anatomical, and Prognostic Correlates of Coronary Flow Velocity Reserve during Stress Echocardiography. *J. Am. Coll. Cardiol.* 74 (18), 2278–2291. doi:10.1016/j.jacc.2019.08.1046

Davis, C. P., Liu, P.-F., Hauser, M., Göhde, S. C., Von Schulthess, G. K., and Debatin, J. F. (1997). Coronary Flow and Coronary Flow reserve Measurements in Humans with Breath-Held Magnetic Resonance Phase Contrast Velocity Mapping. *Magn. Reson. Med.* 37 (4), 537–544. doi:10.1002/mrm.1910370410

Dodge, J. T., Brown, B. G., Bolson, E. L., and Dodge, H. T. (1992). Lumen Diameter of normal Human Coronary Arteries. Influence of Age, Sex, Anatomic Variation, and Left Ventricular Hypertrophy or Dilation. *Circulation* 86 (1), 232–246. doi:10.1161/01.cir.86.1.232

Dyverfeldt, P., and Ebbers, T. (2017). Comparison of Respiratory Motion Suppression Techniques for 4D Flow MRI. *Magn. Reson. Med.* 78 (5), 1877–1882. doi:10.1002/mrm.26574

Feng, L., Coppo, S., Piccini, D., Yerly, J., Lim, R. P., Masci, P. G., et al. (2018). 5D Whole-Heart Sparse MRI. *Magn. Reson. Med.* 79, 826–838. doi:10.1002/mrm.26745

Fihn, S. D., Gardin, J. M., Abrams, J., Berra, K., Blankenship, J. C., Dallas, A. P., et al. (2012). 2012 ACCF/AHA/ACP/AATS/PCNA/SCAI/STS Guideline for the

Diagnosis and Management of Patients with Stable Ischemic Heart Disease. *J. Am. Coll. Cardiol.* 60 (24), e44–e164. doi:10.1016/j.jacc.2012.07.013

Glover, G. H., and Pauly, J. M. (1992). Projection Reconstruction Techniques for Reduction of Motion Effects in MRI. *Magn. Reson. Med.* 28 (2), 275–289. doi:10.1002/mrm.1910280209

Gottwald, L. M., Peper, E. S., Zhang, Q., Coolen, B. F., Strijkers, G. J., Nederveen, A. J., et al. (2020). Pseudo-spiral Sampling and Compressed Sensing Reconstruction Provides Flexibility of Temporal Resolution in Accelerated Aortic 4D Flow MRI: A Comparison with K-T Principal Component Analysis. *NMR Biomed.* 33 (4), e4255. doi:10.1002/nbm.4255

Gottwald, L. M., Töger, J., Markenroth Bloch, K., Peper, E. S., Coolen, B. F., Strijkers, G. J., et al. (2020). High Spatiotemporal Resolution 4D Flow MRI of Intracranial Aneurysms at 7T in 10 minutes. *AJNR Am. J.*41, 1201–1208. doi:10.3174/ajnr.A6603

Heo, R., Nakazato, R., Kalra, D., and Min, J. K. (2014). Noninvasive Imaging in Coronary Artery Disease. *Semin. Nucl. Med.* 44 (5), 398–409. doi:10.1053/j.semnuclmed.2014.05.004

Hofman, M. B. M., van Rossum, A. C., Sprenger, M., and Westerhof, N. (1996). Assessment of Flow in the Right Human Coronary Artery by Magnetic Resonance Phase Contrast Velocity Measurement: Effects of Cardiac and Respiratory Motion. *Magn. Reson. Med.* 35 (4), 521–531. doi:10.1002/mrm.1910350411

Hozumi, T., Yoshida, K., Ogata, Y., Akasaka, T., Asami, Y., Takagi, T., et al. (1998). Noninvasive Assessment of Significant Left Anterior Descending Coronary Artery Stenosis by Coronary Flow Velocity Reserve with Transthoracic Color Doppler Echocardiography. *Circulation* 97 (16), 1557–1562. doi:10.1161/01.CIR.97.16.1557

Hundley, W. G., Lange, R. A., Clarke, G. D., Meshack, B. M., Payne, J., Landau, C., et al. (1996). Assessment of Coronary Arterial Flow and Flow Reserve in Humans with Magnetic Resonance Imaging. *Circulation* 93 (8), 1502–1508. doi:10.1161/01.CIR.93.8.1502

Ibrahim, T., Nekolla, S. G., Schreiber, K., Odaka, K., Volz, S., Mehilli, J., et al. (2002). Assessment of Coronary Flow reserve: Comparison between Contrast-Enhanced Magnetic Resonance Imaging and Positron Emission Tomography. *J. Am. Coll. Cardiol.* 39 (5), 864–870. doi:10.1016/S0735-1097(01)01829-0

Johnson, K., Sharma, P., and Oshinski, J. (2008). Coronary Artery Flow Measurement Using Navigator echo Gated Phase Contrast Magnetic Resonance Velocity Mapping at 3.0T. *J. Biomech.* 41 (3), 595–602. doi:10.1016/j.jbiomech.2007.10.010

Kasprzak, J. D., Drożdż, J., Peruga, J. Z., Rafalska, K., and Krzemińska-pakuła, M. (2000). Definition of Flow Parameters in Proximal Nonstenotic Coronary Arteries Using Transesophageal Doppler Echocardiography. *Echocardiography* 17 (2), 141–150. doi:10.1111/j.1540-8175.2000.tb01115.x

Kato, S., Saito, N., Nakachi, T., Fukui, K., Iwasawa, T., Taguri, M., et al. (2017). Stress Perfusion Coronary Flow Reserve versus Cardiac Magnetic Resonance for Known or Suspected CAD. *J. Am. Coll. Cardiol.* 70 (7), 869–879. doi:10.1016/j.jacc.2017.06.028

Keegan, J., Raphael, C. E., Parker, K., Simpson, R. M., Strain, S., de Silva, R., et al. (2015). Validation of High Temporal Resolution Spiral Phase Velocity Mapping of Temporal Patterns of Left and Right Coronary Artery Blood Flow against Doppler Guidewire. *J. Cardiovasc. Magn. Reson.* 17, 85. doi:10.1186/s12968-015-0189-y

Koo, T. K., and Li, M. Y. (2016). A Guideline of Selecting and Reporting Intraclass Correlation Coefficients for Reliability Research. *J. Chiropractic Med.* 15 (2), 155–163. doi:10.1016/j.jcm.2016.02.012

Lund, G. K., Watzinger, N., Saeed, M., Reddy, G. P., Yang, M., Araoz, P. A., et al. (2003). Chronic Heart Failure: Global Left Ventricular Perfusion and Coronary Flow Reserve with Velocity-Encoded Cine MR Imaging: Initial Results. *Radiology* 227 (1), 209–215. doi:10.1148/radiol.2271012156

Ma, L. E., Yerly, J., Piccini, D., Di Sopra, L., Roy, C. W., Carr, J. C., et al. (2020). 5D Flow MRI: A Fully Self-Gated, Free-Running Framework for Cardiac and Respiratory Motion-Resolved 3D Hemodynamics. *Radiol. Cardiothorac. Imaging* 2, e200219. doi:10.1148/ryct.2020200219

Marcus, J. T., Kuijer, J. P., Van der Geest, R. J., Heethaar, R. M., and Van Rossum, A. C. (1999). Flow Profiles in the Left Anterior Descending and the Right Coronary Artery Assessed by MR Velocity Quantification: Effects of Through-Plane and In-Plane Motion of the Heart. *J. Comput. Assist. Tomogr* 23 (4), 567–576. doi:10.1097/00004728-199907000-00017

Markl, M., Frydrychowicz, A., Kozerke, S., Hope, M., and Wieben, O. (2012). 4D Flow MRI. *J. Magn. Reson. Imaging* 36 (5), 1015–1036. doi:10.1002/jmri.23632

Montalescot, G., Montalescot, G., Sechtem, U., Achenbach, S., Andreotti, F., Arden, C., et al. (2013). 2013 ESC Guidelines on the Management of Stable Coronary Artery Disease: the Task Force on the Management of Stable Coronary Artery Disease of the European Society of Cardiology. *Eur. Heart J.* 34 (38), 2949–3003. doi:10.1093/eurheartj/eht296

Motwani, M., Swoboda, P. P., Plein, S., and Greenwood, J. P. (2018). Role of Cardiovascular Magnetic Resonance in the Management of Patients with Stable Coronary Artery Disease. *Heart* 104 (11), 888–894. doi:10.1136/heartjnl-2017-311658

Murthy, V. L., Naya, M., Foster, C. R., Hainer, J., Gaber, M., Di Carli, G., et al. (2011). Improved Cardiac Risk Assessment with Noninvasive Measures of Coronary Flow Reserve. *Circulation* 124 (20), 2215–2224. doi:10.1161/CIRCULATIONAHA.111.050427

Nagel, E., Thouet, T., Klein, C., Schalla, S., Bornstedt, A., Schnackenburg, B., et al. (2003). Noninvasive Determination of Coronary Blood Flow Velocity with Cardiovascular Magnetic Resonance in Patients after Stent Deployment. *Circulation* 107 (13), 1738–1743. doi:10.1161/01.CIR.0000060542.79482.81

Ofili, E. O., Labovitz, A. J., and Kern, M. J. (1993). Coronary Flow Velocity Dynamics in normal and Diseased Arteries. *Am. J. Cardiol.* 71 (14), D3–D9. doi:10.1016/0002-9149(93)90128-Y

Pelletier-Galarneau, M., DeKemp, R. A., Hunter, C. R. R. N., Klein, R., Klein, M., Ironstone, J., et al. (2018). Effects of Hypercapnia on Myocardial Blood Flow in Healthy Human Subjects. *J. Nucl. Med.* 59 (1), 100–106. doi:10.2967/jnumed.117.194308

Peper, E. S., Gottwald, L. M., Zhang, Q., Coolen, B. F., van Ooij, P., Nederveen, A. J., et al. (2020). Highly Accelerated 4D Flow Cardiovascular Magnetic Resonance Using a Pseudo-spiral Cartesian Acquisition and Compressed Sensing Reconstruction for Carotid Flow and wall Shear Stress. *J. Cardiovasc. Magn. Reson.* 22 (1), 7. doi:10.1186/s12968-019-0582-z

Pizzuto, F., Voci, P., Mariano, E., Emilio Puddu, P., Sardella, G., and Nigri, A. (2001). Assessment of Flow Velocity reserve by Transthoracic Doppler Echocardiography and Venous Adenosine Infusion before and after Left Anterior Descending Coronary Artery Stenting. *J. Am. Coll. Cardiol.* 38 (1), 155–162. doi:10.1016/S0735-1097(01)01333-X

Roy, C. W., Heerfordt, J., Piccini, D., Rossi, G., Pavon, A. G., Schwitter, J., et al. (2021). Motion Compensated Whole-Heart Coronary Cardiovascular Magnetic Resonance Angiography Using Focused Navigation (fNAV). *J. Cardiovasc. Magn. Reson.* 23 (1), 33. doi:10.1186/s12968-021-00717-4

Sakuma, H., Koskenvuo, J. W., Niemi, P., Kawada, N., Toikka, J. O., Knuuti, J., et al. (2000). Assessment of Coronary Flow Reserve Using Fast Velocity-Encoded Cine MR Imaging. *Am. J. Roentgenology* 175 (4), 1029–1033. doi:10.2214/ajr.175.4.1751029

Schiemann, M., Bakhtiary, F., Hietschold, V., Koch, A., Esmaeili, A., Ackermann, H., et al. (2006). MR-based Coronary Artery Blood Velocity Measurements in Patients without Coronary Artery Disease. *Eur. Radiol.* 16 (5), 1124–1130. doi:10.1007/s00330-005-0039-7

Shibata, M., Sakuma, H., Isaka, N., Takeda, K., Higgins, C. B., and Nakano, T. (1999). Assessment of Coronary Flow reserve with Fast Cine Phase Contrast Magnetic Resonance Imaging: Comparison with Measurement by Doppler Guide Wire. *J. Magn. Reson. Imaging* 10 (4), 563–568. doi:10.1002/(sici)1522-2586(199910)10:4<563::aid-jmri9>3.0.co;2-h

Smulders, M. W., Jaarsma, C., Nelemans, P. J., Bekkers, S. C. A. M., Bucerius, J., Leiner, T., et al. (2017). Comparison of the Prognostic Value of Negative Non-invasive Cardiac Investigations in Patients with Suspected or Known Coronary Artery Disease-A Meta-Analysis. *Eur. Hear. J. - Cardiovasc. Imaging* 18 (9), 980–987. doi:10.1093/ehjci/jex014

Tang, C., Blatter, D. D., and Parker, D. L. (1993). Accuracy of Phase-Contrast Flow Measurements in the Presence of Partial-Volume Effects. *J. Magn. Reson. Imaging* 3 (2), 377–385. doi:10.1002/jmri.1880030213

Uecker, M. (2015). "Berkeley Advanced Reconstruction Toolbox," in Proceedings of the 23rd Annual Meeting of ISMRM, Toronto, Canada, Vol. 23, 2486.

van de Hoef, T. P., Echavarría-Pinto, M., van Lavieren, M. A., Meuwissen, M., Serruys, P. W. J. C., Tijssen, J. G. P., et al. (2015). Diagnostic and Prognostic Implications of Coronary Flow Capacity. *JACC: Cardiovasc. Interventions* 8 (13), 1670–1680. doi:10.1016/j.jcin.2015.05.032

van de Hoef, T. P., van Lavieren, M. A., Damman, P., Delewi, R., Piek, M. A., Chamuleau, S. A. J., et al. (2014). Physiological Basis and Long-Term Clinical Outcome of Discordance between Fractional Flow Reserve and Coronary Flow Velocity Reserve in Coronary Stenoses of Intermediate Severity. *Circ. Cardiovasc. Interv.* 7 (3), 301–311. doi:10.1161/CIRCINTERVENTIONS.113.001049

Wittfeldt, A., Jeppsson, A., and Gan, L.-M. (2016). Effects of Nitroglycerine on Coronary Flow Velocity before and during Adenosine Provocation. *Cardiovasc. Ultrasound* 14 (1), 48. doi:10.1186/s12947-016-0091-2

Yamagishi, M., Yasu, T., Ohara, K., Kuro, M., and Miyatake, K. (1991). Detection of Coronary Blood Flow Associated with Left Main Coronary Artery Stenosis by Transesophageal Doppler Color Flow Echocardiography. *J. Am. Coll. Cardiol.* 17 (1), 87–93. doi:10.1016/0735-1097(91)90708-H

Yasu, T., Yamagishi, M., Beppu, S., Nagata, S., and Miyatake, K. (1993). Left Main Coronary Flow Velocity Associated with Stenosis. *Chest* 104 (3), 690–693. doi:10.1378/chest.104.3.690

Zhu, D., Bonanno, G., Hays, A. G., Weiss, R. G., and Schär, M. (2021). Phase Contrast Coronary Blood Velocity Mapping with Both High Temporal and Spatial Resolution Using Triggered Golden Angle Rotated Spiral K-T Sparse Parallel Imaging (GASSP) with Shifted Binning. *Magn. Reson. Med.* 86, 1929–1943. doi:10.1002/mrm.28837

Conflict of Interest: The authors declare that the research was conducted in the absence of any commercial or financial relationships that could be construed as a potential conflict of interest.

Publisher's Note: All claims expressed in this article are solely those of the authors and do not necessarily represent those of their affiliated organizations, or those of the publisher, the editors and the reviewers. Any product that may be evaluated in this article, or claim that may be made by its manufacturer, is not guaranteed or endorsed by the publisher.

frontiers in Bioengineering and Biotechnology

ORIGINAL RESEARCH
published: 17 August 2021
doi: 10.3389/fbioe.2021.722445

A Combined Computational Fluid Dynamics and Arterial Spin Labeling MRI Modeling Strategy to Quantify Patient-Specific Cerebral Hemodynamics in Cerebrovascular Occlusive Disease

Jonas Schollenberger[1]*, *Nicholas H. Osborne*[2], *Luis Hernandez-Garcia*[1,3] and *C. Alberto Figueroa*[1,2]

[1]Department of Biomedical Engineering, University of Michigan, Ann Arbor, MI, United States, [2]Department of Surgery, University of Michigan, Ann Arbor, MI, United States, [3]Functional MRI Laboratory, University of Michigan, Ann Arbor, MI, United States

OPEN ACCESS

Edited by:
Zahra K. Motamed,
McMaster University, Canada

Reviewed by:
Dalin Tang,
Worcester Polytechnic Institute, United States
Amirhossein Arzani,
Northern Arizona University, United States

***Correspondence:**
Jonas Schollenberger
scjonas@umich.edu

Specialty section:
This article was submitted to Biomechanics, a section of the journal Frontiers in Bioengineering and Biotechnology

Received: 08 June 2021
Accepted: 19 July 2021
Published: 17 August 2021

Citation:
Schollenberger J, Osborne NH, Hernandez-Garcia L and Figueroa CA (2021) A Combined Computational Fluid Dynamics and Arterial Spin Labeling MRI Modeling Strategy to Quantify Patient-Specific Cerebral Hemodynamics in Cerebrovascular Occlusive Disease. Front. Bioeng. Biotechnol. 9:722445. doi: 10.3389/fbioe.2021.722445

Cerebral hemodynamics in the presence of cerebrovascular occlusive disease (CVOD) are influenced by the anatomy of the intracranial arteries, the degree of stenosis, the patency of collateral pathways, and the condition of the cerebral microvasculature. Accurate characterization of cerebral hemodynamics is a challenging problem. In this work, we present a strategy to quantify cerebral hemodynamics using computational fluid dynamics (CFD) in combination with arterial spin labeling MRI (ASL). First, we calibrated patient-specific CFD outflow boundary conditions using ASL-derived flow splits in the Circle of Willis. Following, we validated the calibrated CFD model by evaluating the fractional blood supply from the main neck arteries to the vascular territories using Lagrangian particle tracking and comparing the results against vessel-selective ASL (VS-ASL). Finally, the feasibility and capability of our proposed method were demonstrated in two patients with CVOD and a healthy control subject. We showed that the calibrated CFD model accurately reproduced the fractional blood supply to the vascular territories, as obtained from VS-ASL. The two patients revealed significant differences in pressure drop over the stenosis, collateral flow, and resistance of the distal vasculature, despite similar degrees of clinical stenosis severity. Our results demonstrated the advantages of a patient-specific CFD analysis for assessing the hemodynamic impact of stenosis.

Keywords: arterial spin labeling, computational fluid dynamics, cerebral hemodynamics, cerebrovascular occlusive disease, circle of willis, collateral flow, carotid stenosis

INTRODUCTION

Cerebrovascular occlusive disease (CVOD), characterized by the presence of stenosis in the arteries supplying the brain, is a major risk factor for ischemic stroke. Clinical diagnosis and stratification of CVOD patients relies routinely on measuring the maximum narrowing of the lumen based on duplex ultrasound or computed tomography angiography (CTA). However, the degree of luminal stenosis is only one factor in the assessment of stroke risk. Plaque characteristics, downstream brain perfusion,

and patency of collateral pathways also play an important role in the overall risk evaluation of cerebral ischemia (Saba et al., 2018; Liebeskind, 2003; Liebeskind and Feldmann, 2012). Collateral flow in the circle of Willis (CoW) has been associated with reduced stroke risk in patients with severe carotid stenosis (Henderson et al., 2000; Bisschops et al., 2003; Hendrikse et al., 2001). Collateral flow is highly dependent on the cerebral vasculature anatomy, availability of collateral pathways, degree of stenosis in the arteries supplying the brain and, critically, the condition of the cerebral microcirculation and its autoregulatory response (Ramsay et al., 1991; Russell et al., 2008).

The clinical gold standard for evaluating collateral flow is digital subtraction angiography (DSA). Despite providing high-resolution images of blood supply in the cerebral arteries, the procedure is invasive and strictly qualitative. MRI arterial spin labeling (ASL) has become an increasingly popular method for measuring cerebral perfusion, and it provides a non-invasive quantitative alternative to DSA. In non-selective ASL (NS-ASL), brain tissue perfusion is measured by magnetically labeling blood in the neck arteries and acquiring a series of slices of the brain after a short transit delay (Alsop et al., 2014). More recently, ASL has been extended to vessel-selective labeling to measure the perfusion territory of individual arteries (Helle et al., 2010; Schollenberger et al., 2020). The diagnostic capabilities of vessel-selective ASL (VS-ASL) have previously been demonstrated in patients with extracranial stenosis and arteriovenous malformation (Richter et al., 2017; Helle et al., 2013). Additionally, cerebral angiograms have been performed based on VS-ASL to visualize blood supply in the cerebral arteries (Jensen-Kondering et al., 2015), rendering similar qualitative information on cerebral flow patterns as DSA. Nevertheless, the information provided by VS-ASL on collateral flow patterns has thus far been qualitative.

Image-based computational fluid dynamics (CFD) provides a powerful tool for analyzing cerebral hemodynamics. Compared to experimental approaches, CFD renders velocity, pressure, wall shear stress, etc. throughout entire vascular territories with arbitrarily high spatial and temporal resolutions. The feasibility of CFD to assess cerebral hemodynamics has been previously demonstrated for intracranial stenoses (Liu et al., 2017; Leng et al., 2014) and aneurysms (Castro et al., 2006; Rayz et al., 2008; Raschi et al., 2012). However, patient-specific calibration of cerebral blood flow CFD models remains challenging. Previous studies have heavily relied on literature data for determining flow splits in the CoW (Xiao et al., 2013; Mukherjee et al., 2016) or used simplistic allometric scaling assumptions to calibrate outflow boundary conditions (Bockman et al., 2012).

In this paper, we propose a novel strategy to quantitatively characterize regional cerebral blood flow and perfusion using CFD in combination with PC-MRI and ASL data. First, a method to calibrate the cerebral blood flow CFD model based on NS-ASL perfusion data is presented. The calibration includes estimation of flow splits in the CoW from non-selective perfusion images and total inflow to the CoW from PC-MRI, followed by tuning of the outflow boundary conditions to match the estimated flow splits. Second, the calibrated CFD model is validated against territorial perfusion maps from VS-ASL based on the blood supply to each cerebral territory using Lagrangian particle tracking (LPT). Lastly, the proposed strategy is demonstrated *via* an in-depth quantification of patient-specific cerebral hemodynamics in a healthy control subject and two CVOD patients.

MATERIALS AND METHODS

Patient Details

Two CVOD patients and a healthy control subject were enrolled in a feasibility study and underwent a research MRI exam. The protocol was approved by the local Institutional Review Board and all subjects provided informed written consent (HUM00114275 and HUM00018426). The reconstructed geometric models of the three subjects are illustrated in **Figure 1**. The models include the ascending and proximal descending thoracic aorta, its upper branches (brachiocephalic trunk, left carotid and left subclavian), the main neck arteries (internal and external carotids, vertebral arteries), and the main intracranial arteries including the CoW. The healthy control and patient 1 were reconstructed based on magnetic resonance angiography (MRA) and patient 2 based on CTA.

The healthy control subject (male, 28 years old) presented without evidence of CVOD. The CoW anatomy was incomplete with both right and left posterior communicating arteries hypoplasia. Patient 1 (female, 55 years old) presented with an asymptomatic 70–99% stenosis (duplex ultrasound, velocity criteria) in the right proximal internal carotid artery (RICA). The left internal carotid artery (LICA) was patent with no evidence of hemodynamically significant stenosis. Patient 1 has a complete CoW anatomy. Patient 2 (male, 64 years old) presented with asymptomatic bilateral carotid stenosis. The RICA revealed a tandem stenosis of 80–90% (CTA, ECST criteria), stretching from the carotid bifurcation to the distal end of the carotid bulb. The LICA showed a 60% stenosis (CTA, ECST criteria). Patient 2 has an incomplete CoW anatomy with right P1 segment and distal right vertebral artery (RVA) hypoplasia.

Imaging Data

All subjects underwent an MRI study to collect data on vascular anatomy, brain tissue perfusion, and flow. The protocol was performed at 3T (MR750; GE Healthcare, Waukesha, WI) with a 32-channel receive-only head coil for the head and neck and the scanner's build-in coil for the upper chest. At the end of the study, the subject's blood pressure was measured in the upper arm in the supine position.

Anatomy

Anatomical information from the ascending thoracic aorta to the carotid bifurcation level was acquired with a 2D T1-weighted spoiled gradient echo sequence (voxel size = $0.58 \times 0.58 \times 2$ mm^3, TR/TE = 75/3.3 ms). The remaining anatomy from the neck to the CoW was acquired with a 3D Time-of-Flight sequence (voxel size = $0.42 \times 0.42 \times 1.5$ mm^3, TR/TE = 21/2.5 ms). Additionally,

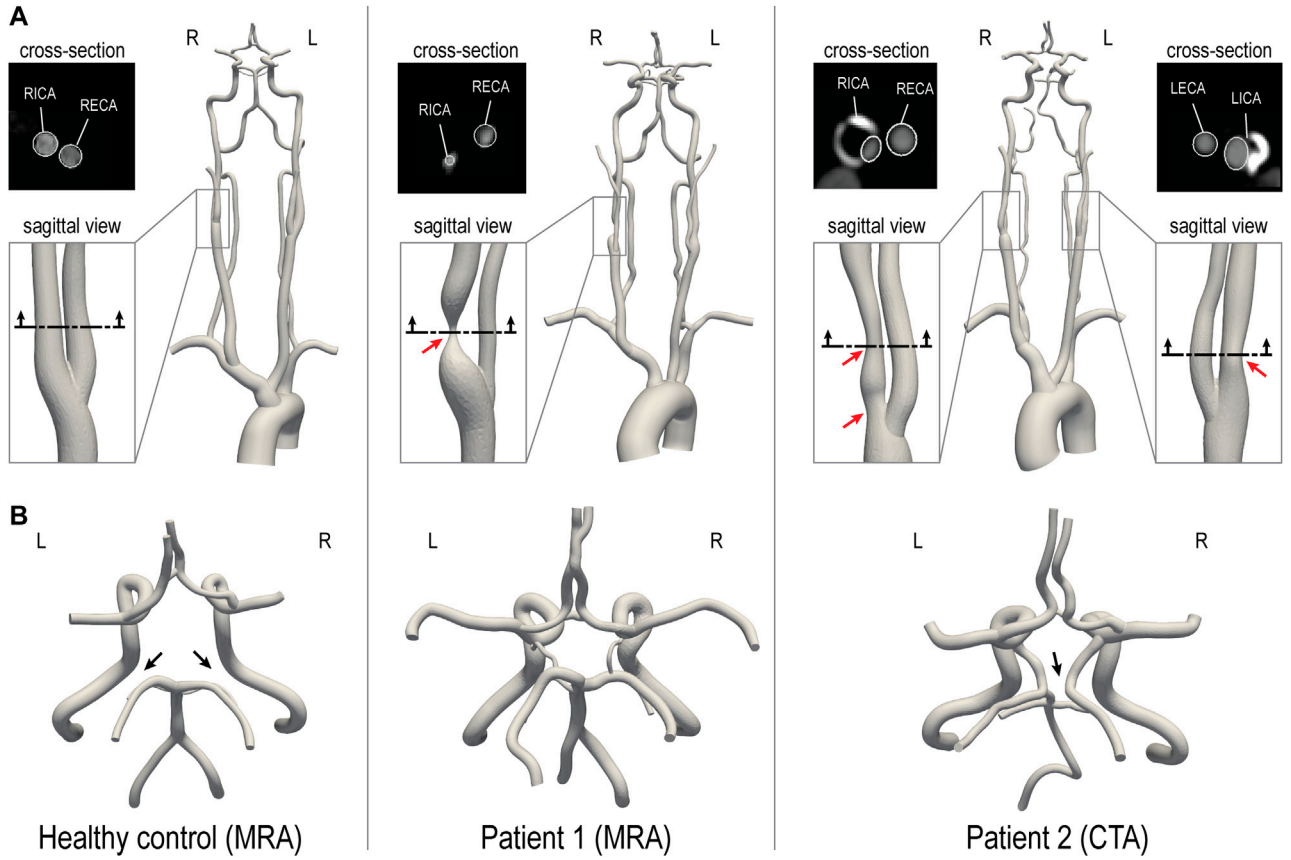

FIGURE 1 | 3D-reconstructed geometric models of a healthy control and two CVOD patients. **(A)** For each patient, a close-up of the stenosis is shown. The red arrows indicate the location of the stenosis. An axial cross-section of the stenosis illustrates a comparison between image data and model contours (this comparison is also shown for the healthy volunteer). **(B)** Posterior view of the CoW. The black arrows indicate variations in the CoW anatomy. RICA, right internal carotid artery; RECA, right external carotid artery; LICA, left internal carotid artery; LECA, left external carotid artery. R and L indicate the right and left side from the subject's perspective.

structural images of the brain were collected with a 2D T1-weighted spoiled gradient echo sequence (voxel size = 0.46 × 0.46 × 7 mm^3, TR/TE = 100/3.0 ms). For patient 2, an additional CTA data of the neck and head vasculature was available (voxel size = 0.39 × 0.39 × 0.62 mm^3). For patient 2, the CTA dataset was chosen over the MRA for reconstruction due to the higher resolution.

Brain Tissue Perfusion

Using a pseudo-continuous ASL scheme, non-selective and vessel-selective cerebral perfusion images were collected. Prior to image acquisition, an off-resonance calibration pre-scan was performed to correct for B0-inhomogeneity in the label plane. For the NS-ASL acquisition, sequence parameters were set following consensus recommendations (Alsop et al., 2014): Label duration = 1,800 ms, post-labeling delay = 2,000 ms, TR/TE = 4,600/4, voxel size = 3.75 × 3.75 × 7 mm^3, 3D spiral acquisition, 18 slices, 8 pairs of label/control images. The slice prescription was the same as for the T1-weighted structural images. The label plane was positioned above the carotid bifurcation where the arteries of interest (carotid and vertebral) run perpendicular to the plane and with a maximum distance between them. The start of the labeling period was cardiac-triggered to reduce pulsatility artifacts. A proton density image was collected, followed by a non-selective perfusion scan. Subsequently, four VS-ASL scans of the vertebral and carotid arteries were collected. The position of vertebral and carotid arteries within the label plane was determined from the Time-of-Flight acquisition. Keeping all parameters of the NS-ASL scan unchanged, vessel-selective labeling was performed based on a super-selective labeling scheme (Helle et al., 2010), whereby additional in-plane gradients rotate clockwise every radiofrequency pulse to create a circular labeling spot. Finally, the vessel-selective labeling efficiency was measured by collecting an image 2 cm above the labeling plane 10 ms after labeling for 500 ms. Image reconstruction was performed in MATLAB to a resolution of 128 × 128 using zero-padding in k-space. The ASL perfusion signal was calculated by subtracting label and control images and averaging over all acquired pairs. A detailed explanation of the sequence setup and parameters can be found elsewhere (Schollenberger et al., 2020).

Flow

Volumetric blood flow waveforms were measured using 2D cardiac-gated phase-contrast (PC-MRI) at the level of the ascending aorta (voxel size = 0.58 × 0.58 × 5 mm^3, TR/TE = 5.2/3.1 ms, velocity encoding = 130 cm/s) and above the carotid bifurcation (voxel size = 0.31 × 0.31 × 5 mm^3, TR/TE = 6.0/3.7 ms, velocity encoding = 100 cm/s). The slice was positioned perpendicular to the arteries of interest and velocity was encoded in the through-plane direction. PC-MRI data were processed in MATLAB to calculate flow rates.

Computational Modeling

The key computational modeling tasks, namely three-dimensional anatomical reconstruction, mesh generation, boundary condition specification, and finite element analysis were performed using the validated open-source computational hemodynamics framework CRIMSON (Arthurs et al., 2021).

Anatomical Reconstruction and Mesh Generation

3D geometric models of the aorta and head and neck vessels, including the CoW, were reconstructed from the anatomical imaging data. Briefly, centerlines and 2D vessel contours were defined for each vessel of interest. Contours were then lofted to create an analytical representation of each vessel and ultimately define a 3D geometric model of the vasculature (Xiao et al., 2013). This 3D model was then discretized using linear tetrahedral elements. A mesh-adaptation algorithm (Sahni et al., 2006) was used to refine the mesh locally based on local velocity gradients. The final mesh sizes for healthy subject, patient 1, and patient 2 consisted of 2.16×10^6, 1.84×10^6, and 2.39×10^6 elements, respectively. Mesh-independence was evaluated for patient 1 by creating an additional highly-refined mesh with 6.86×10^6 elements, which resulted in a difference of less than 1% for the flow rates at each outlet and a maximum difference of 2% for peak velocity in the center of the stenosis.

Boundary Conditions

A pulsatile inflow waveform reconstructed from PC-MRI was mapped to a parabolic velocity profile and prescribed at the inlet of the ascending aorta for each geometric model. Each vessel outlet was coupled to a three-element Windkessel model, which consists of a proximal resistance (R_p), a distal resistance (R_d), and a capacitor (C) (Vignon-Clementel et al., 2010). For each subject, the total arterial resistance is $R_T = P_{mean}/Q_T$, where the mean pressure $P_{mean} = 1/3\ P_{systolic} + 2/3\ P_{diastolic}$ and Q_T is total cardiac output. The total arterial compliance is $C_T = (Q_{T,max}-Q_{T,min})/(P_{systolic}-P_{diastolic})*\Delta t$, where $Q_{T,max}$ and $Q_{T,min}$ are maximum and minimum values of aortic inflow, and Δt is the time lapse between these values. Initial estimates for the Windkessel model parameters were obtained by distributing R_T and C_T among the different outlets, to obtain R_i and C_i for vessel i = 1,. . .,13, as described in (Xiao et al., 2014). The Windkessel parameters were then iteratively adjusted following the scheme described in detail in ***Patient-specific calibration of outflow boundary conditions for the CFD models***. Lastly, a no-slip boundary condition was assigned to all vessel walls.

Finite Element Analysis

Blood was modeled as an incompressible Newtonian fluid with a dynamic viscosity of 0.004 $kg\,m^{-1}s^{-1}$ and a density of 1,060 $kg\,m^{-3}$. A stabilized finite-element formulation for the incompressible Navier-Stokes equations was employed to solve for blood flow velocity and pressure in the models (Whiting and Jansen, 2001). Computations were performed using 80 cores on a high-performance computing cluster. Simulations were run using a time step size of 0.1 ms until cycle-to-cycle periodicity was achieved, typically after 5 cardiac cycles.

Patient-Specific Calibration of Outflow Boundary Conditions for the CFD Models

Calculation of Mean Flow at Model Outlets

Intracranial Arteries

The flow distribution among cerebral and cerebellar arteries was derived from the NS-ASL perfusion images, a cerebral territory atlas, and the total inflow to the brain as illustrated in **Figure 2**. First, the NS-ASL perfusion images were mapped into a standardized template space (Montreal Neurological Institute ch2better) using the toolbox SPM12 (Wellcome Trust Center for Neuroimaging, London, United Kingdom). Next, the standardized perfusion images were segmented using a vascular territory atlas. The atlas was extended to include the cerebellum. This extended vascular territory atlas with a resolution of 370 × 301 × 316 is given as a NIfTI dataset in the **Supplementary Materials**. In this work, we assumed the following relationship between eight intracranial arteries and seven vascular territories (see **Figure 2**): 1) RACA territory, perfused by the RACA (yellow); 2) LACA territory, perfused by the LACA (magenta); 3) RMCA territory, perfused by the RMCA (green); 4) LMCA territory, perfused by the LMCA (light blue); 5) RPCA territory, perfused by the RPCA (orange); 6) LPCA territory, perfused by the LPCA (dark blue); 7) Cerebellum territory, perfused evenly by RSCA and LSCA (red). A perfusion split ps_j was then calculated by dividing the integral of perfusion signal over the volume of each territory j = 1,. . .,7 by the integral of perfusion signal over the entire brain volume. The total mean inflow to the CoW ($\bar{Q}_{CoW}$) was calculated from the PC-MRI data on left and right ICAs and VAs. Mean flow rates through each intracranial vessel ($\bar{Q}_{target,i}$) were calculated as the product of the total mean inflow to the CoW and the perfusion split ps_j corresponding to the territory perfused by vessel i = 1,. . .,8.

Extracranial Arteries

Mean flow rates in the external carotid arteries were calculated from PC-MRI. In the subclavian arteries, we assumed a mean flow rate of 5.6% of cardiac-output (Xiao et al., 2013). Finally, the difference between inflow and intracranial, external carotid arteries, and subclavian arteries flow was assigned to the descending thoracic aorta.

Calibration of Windkessel Model Parameters

Patient-specific calibration of the Windkessel model parameters for each outflow branch was performed in three stages. *Stage 1*: the distal resistance R_d was iteratively adjusted during simulation

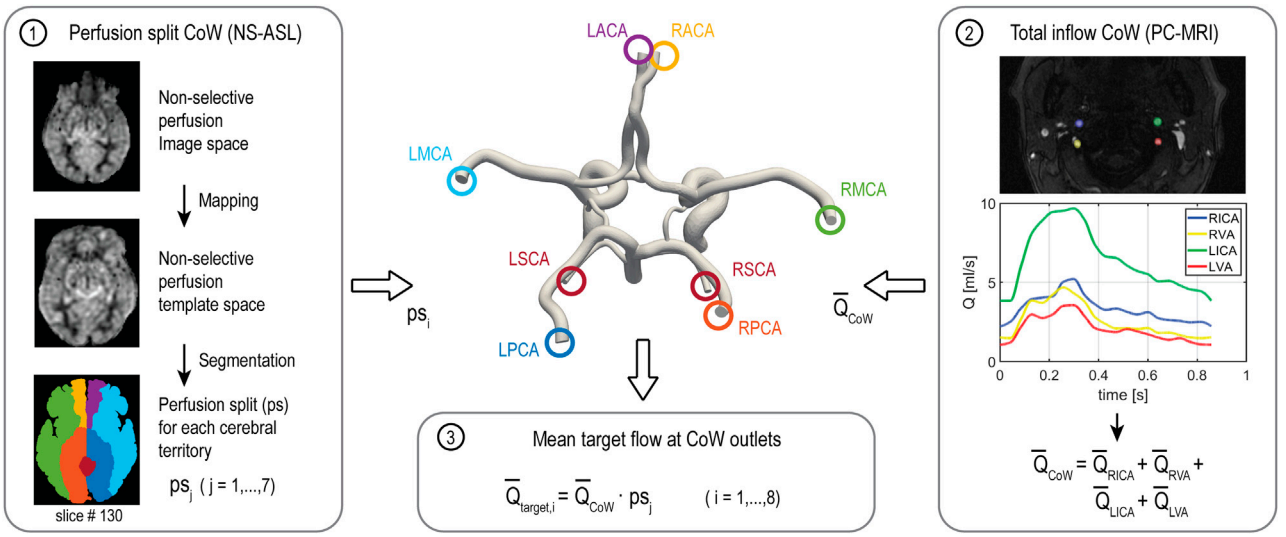

FIGURE 2 | Workflow of calculating the flow split among the arteries of the CoW based on NS-ASL perfusion imaging, a vascular territory atlas, and total inflow to the CoW from PC-MRI. RACA/LACA, right/left anterior cerebral artery; RMCA/LMCA, right/left middle cerebral artery; RPCA/LPCA, right/left posterior cerebral artery; RSCA/LSCA, right/left superior cerebellar artery.

runtime using Python controller scripts (Arthurs et al., 2016) to match the target mean flow rates. At each simulation time step, R_d was adjusted proportional to the error between the current mean flow and the target flow. Simulations were terminated once the flow at each outlet was fully converged (error <1%). *Stage 2:* The ratio of R_p/R_d was adjusted for each cerebral and cerebellar branch such that the computed and measured PC-MRI flow waveforms in the ICAs and VAs had similar pulsatility. The total resistance $R_i = R_p + R_d$ at each outlet was kept constant to preserve mean flow. *Stage 3:* Measurements of brachial pressure ($P_{systolic}$ and $P_{diastolic}$) were matched by adjusting R_T and C_T. The percentage change in R_T and C_T through the iterations was proportionally assigned to R_i and C_i at each outlet i = 1,. . .,13. The final Windkessel parameters are summarized in **Supplementary Table S1**.

Validation of the Calibrated CFD Models

The calibrated CFD models were validated against VS-ASL by comparing the fractional blood supply (FBS) in each vascular territory. We defined the fractional blood supply for a vascular territory *j* from a neck artery *k* as $FBS_{j,k} = Q_{j,k}/\Sigma_k Q_{j,k}$, where *j* = 1,. . .,7 is the vascular territory index and *k* = 1,. . .,4 is the neck artery index (1:RIVA, 2:RVA, 3:LVA, 4:LICA), and $Q_{j,k}$ is the flow contribution from the neck artery *k* to the vascular territory *j*. The process for calculating $FBS_{j,k}$ from VS-ASL and CFD data is described next.

Fractional Blood Supply Based on VS-ASL

The process for calculating $FBS_{j,k}$ from VS-ASL images is outlined in **Figure 3**. The perfusion signal in the VS-ASL images is determined by the blood supply from a single neck artery to the vascular territories. The signal in the VS-ASL images was first scaled based on the measured labeling efficiency. Then, scaled VS-ASL images were transformed into the standardized template space (panel 1). The sum of all scaled VS-ASL images produces the total perfusion image. The $FBS_{j,k}$ maps were then calculated by dividing each scaled VS-ASL image by the total perfusion image on a voxel-by-voxel basis (panel 2). Then, the $FBS_{j,k}$ maps were segmented into different territories using the vascular territory atlas. Lastly, due to noise in the raw ASL data, negative values of $FBS_{j,k}$ distribution are possible on a given voxel. Therefore, we characterize the $FBS_{j,k}$ distribution by its median (M) and median absolute deviation (MAD) (see panel 3).

Fractional Blood Supply Based on CFD Lagrangian Particle Tracking

To validate the CFD results using the VS-ASL data, one must develop a method to assess the fractional blood supply of the intracranial arteries/territories and compare it with the median (M) of the $FBS_{j,k}$ obtained with VS-ASL for each artery/territory. This can be achieved *via* a further post-processing analysis on the CFD data, known as "Lagrangian particle tracking" (LPT), whereby virtual boluses of blood are created by seeding mass-less particles in different regions of the vasculature and advected by the velocity field over multiple cardiac cycles. This is an established technique with multiple applications in cardiovascular flows (Di Achille et al., 2014; Van Bakel et al., 2018; Nauta et al., 2017; Suh et al., 2011; Arzani et al., 2014).

In this work, particles were seeded continuously at the base of the carotid and vertebral arteries. LPT was performed individually for each carotid and vertebral artery over 4 cardiac cycles (**Supplementary Figure S1**). The number of particles seeded in each artery, over multiple re-injections over the 4 cardiac cycles, was proportional to the flow rate of

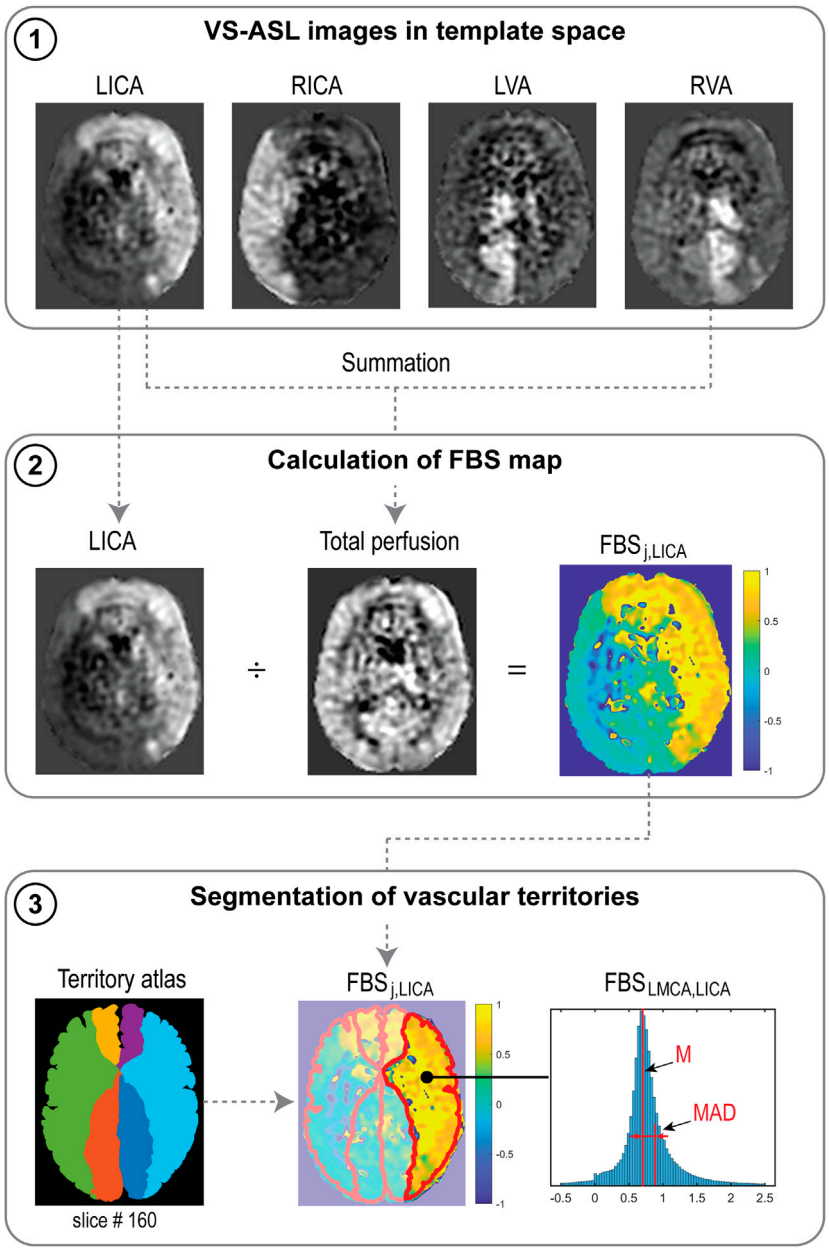

FIGURE 3 | Processes to calculate $FBS_{j,k}$ from VS-ASL images, illustrated for the LICA. (1) Scaled VS-ASL perfusion images in standardized template space. (2) Calculation of spatial $FBS_{j,k}$ maps. (3) Segmentation of territories using a vascular territory atlas and calculation of median (M) and median absolute deviation (MAD) from the $FBS_{j,k}$ distribution in each territory.

each artery. Particles were then counted at each outlet of the intracranial arteries, and once cycle-to-cycle periodicity in the number of tracked particles was achieved, the total number of particles collected per vessel over a full cardiac cycle was extracted. Lastly, for each intracranial vessel, assigned to a vascular territory j, its fractional blood supply $FBS_{j,k}$ from each neck artery k was calculated by dividing the particle count of the LPT analysis for neck artery k by the sum of the particle counts of each of the four LPT analyses of the neck arteries.

RESULTS

Validation of Calibrated CFD Model

Fractional Blood Supply: CFD LPT Versus VS-ASL

Qualitative Analysis

A qualitative comparison between FBS obtained from VS-ASL and CFD LPT is illustrated in **Figure 4**. The VS-ASL images (**Figure 4A**) show the perfusion territories of the four neck arteries, from the inferior region of the cranium (bottom row slices) to the superior region (top row slices). Each image voxel was color-coded based on

the FBS of the neck arteries. For visualization purposes, we limited the FBS in each voxel to positive fraction values between 0 and 1 (cf. **Figure 3** panel 3). LPT analyses results (**Figure 4B**) show maps of the advection of particles, color-coded based on the seeding artery in the neck, as well as temporal histograms of particles collected at the outflow of selected intracranial arteries.

1. Middle cerebral arteries: The VS-ASL data revealed that the perfusion territories of the RMCA (arrow 1) and LMCA (arrow 2) were primarily supplied by the ipsilateral carotid artery for all subjects regardless of the degree of stenosis. This perfusion pattern was also replicated in the LPT analyses, where particles exiting the RMCA primarily originated in the RICA (green particles) and particles leaving the LMCA predominantly originated in the LICA (blue particles).
2. Anterior cerebral arteries: All three subjects displayed flow compensation from the LICA to the RACA territory (arrow 3) in the VS-ASL images. The LPT analysis also reproduced this flow compensation in the RACA *via* the anterior communicating artery (AComA) for all subjects. The histograms of LPT RACA particles illustrate clear differences in the amount of compensation among subjects. The healthy control subject revealed significant blood supply from the LICA (blue particles) to the RACA, despite the absence of stenosis. The severe RICA stenosis in patient 1 resulted in the RACA being predominantly supplied by the LICA. In contrast, the severe stenosis in the RICA and the mild stenosis in the LICA in patient 2 only led to a small amount of collateral flow in the RACA.
3. Posterior cerebral arteries: The VS-ASL images revealed large differences in blood supply in the RPCA (arrow 4) and LPCA (arrow 5) territories between subjects. These differences in blood supply were also replicated in the LPT analyses. In the healthy control subject, the posterior circulation received mixed supply from both vertebral arteries as seen in the LPCA histogram. In patient 1, the RPCA territory was predominantly perfused by the LVA whereas the LPCA territory was predominantly perfused by the RVA (see histogram). The VS-ASL data revealed a switch in blood supply to the posterior circulation between right and left hemisphere, a switch also mirrored in the LPT analysis which shows vortex-like flow patterns in the basilar artery resulting in crossing of particles originating in the VAs. In patient 2, the posterior circulation was supplied by the ipsilateral carotid arteries. In this patient, the VAs did not contribute to cerebral blood flow. Instead, the LVA supplied most of the cerebellum flow with some small contribution from the LICA, as also apparent in the VS-ASL data (arrow 6).

Quantitative Analysis

A quantitative comparison of $FBS_{j,k}$ obtained with VS-ASL and CFD LPT is summarized in **Figure 5**. For each vascular territory *j*, the percentage supply contributions from the neck arteries *k*, obtained from VS-ASL (red bars) and LPT (blue bars), are shown. VS-ASL data includes the median absolute deviation. Due to noise in the VS-ASL signal, FBS results show small negative values in territories for which the perfusion contribution from a given neck artery *k* is small. Conversely, the LPT data is "noise-free" and given by a single value of FBS, instead of by a distribution. Overall, VS-ASL and LPT estimates of $FBS_{j,k}$ agreed well for all subjects. The LPT analysis correctly identified the artery contributing the largest % of perfusion in vascular territories predominately perfused by a single neck artery in all subjects (e.g., LACA, LMCA, RMCA). Furthermore, the magnitude of flow compensation from the LICA to the RACA territory was correctly reflected in the LPT analyses for all subjects. The main sources of perfusion in the RPCA and LPCA territories were correctly identified by the LPT in both patients and only partially matched in the healthy control subject.

A correlation coefficient of $FBS_{j,k}$ between VS-ASL and LPT was calculated for each subject over all vascular territories *j* and neck arteries *k* (**Figure 6**). The correlation coefficients were R = 0.92, R = 0.94, and R = 0.95 for the healthy subject, patient 1, and patient 2, respectively.

Flow: CFD Versus PC-MRI

Mean flow rates from the calibrated CFD model were compared to PC-MRI flow data in the vertebral and carotid arteries above the carotid bifurcation. The difference in mean flow rates in each neck artery was smaller than 10% for all subjects. A comparison of the flow waveforms in the vertebral and carotid arteries between CFD and PC-MRI is shown in **Figure 7** for patient 1, **Figure 8** for patient 2, and **Supplementary Figure S2** for the healthy control subject.

CFD-Based Quantification of Patient-specific Cerebral Hemodynamics

Once the validation of the CFD results using VS-ASL and PC-MRI data was established, we used the calibrated models to assess alterations in cerebral hemodynamics. Specifically, pressure and flow waveforms, the hemodynamic impact of the carotid stenoses, and the resistances of the distal cerebral vascular territories were quantified in the two patients of the study.

Figure 7 shows pressure and flow waveforms in six arteries of the neck and head for patient 1. The mean pressure drop over the stenosis was defined as $\Delta\overline{P} = \overline{P}_{prox}\text{-}\overline{P}_{dist}$, where $\overline{P}_{prox}$ and $\overline{P}_{dist}$ are the mean cross-sectional-averaged pressures 2 cm proximal and distal to the maximum diameter reduction, respectively. The mean pressure drop over the RICA was $\Delta\overline{P}_{RICA}$ = 26.25 mmHg, compared to a $\Delta\overline{P}_{LICA}$ = 0.58 mmHg mean pressure drop over the unstenosed LICA. Another metric of the hemodynamic significance of the stenosis is given by the fractional flow (FF) index (Liebeskind and Feldmann, 2012; Liu et al., 2017; Miao et al., 2016), defined as $FF = \overline{P}_{dist}/\overline{P}_{prox}$. This index produced FF_{RICA} = 0.71 and FF_{LICA} = 0.99. The stenosis resulted in a substantial difference in flow between the RICA and LICA, with mean flow rates of $\overline{Q}_{RICA}$ = 3.25 ml/s and $\overline{Q}_{LICA}$ = 6.79 ml/s. In the CoW, the RMCA and LMCA exhibit substantially different mean values of pressure ($\overline{P}_{RMCA}$ = 47.62 mmHg, $\overline{P}_{LMCA}$ = 74.91 mmHg, mean difference: 27.29 mmHg). Despite the pressure difference between hemispheres, the mean flow rates in the RMCA and LMCA were comparable with $\overline{Q}_{RMCA}$ = 3.74 ml/s and $\overline{Q}_{LMCA}$ = 3.92 ml/s. This preservation of flow at the RMCA was achieved through a reduction in the total resistance of its distal vasculature, resulting

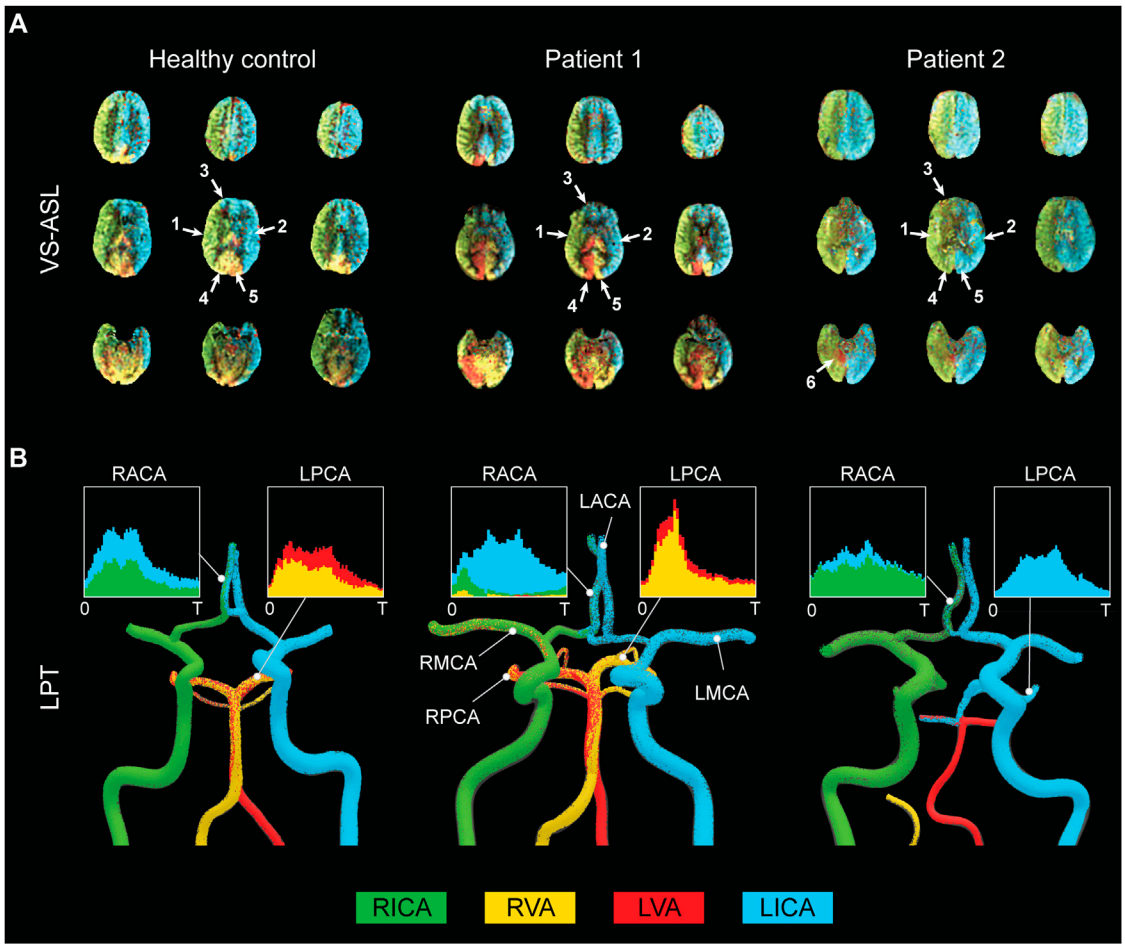

FIGURE 4 | Qualitative comparison between FBS obtained from VS-ASL and CFD LPT **(A)** VS-ASL images show the perfusion territories of the main neck arteries from the inferior of the cranium **(bottom row slices)** to the superior **(top row slices)**. The images were created by color-coding the FBS maps of the main neck arteries on a voxel-by-voxel basis. For visualization purposes, we limited the fractional contributions of each neck artery to a positive range between 0 and 1. The arrows indicate the vascular territories of the 1) RMCA, 2) LMCA, 3) RACA, 4) RPCA, 5) LPCA, and 6) cerebellum. **(B)** LPT analyses show the advection of particles in the large arteries of the CoW. Particles are color-coded based on the artery of origin in the neck. Histograms demonstrate mixed supply in the RACA and LPCA over the cardiac cycle T.

in $R_{RMCA} = 1.7 \times 10^9$ Pa s m^{-3} compared to $R_{LMCA} = 2.54 \times 10^9$ Pa s m^{-3} at the contralateral LMCA.

Figure 8 shows the pressure and flow waveforms for patient 2. The mean pressure drop over the stenoses and *FF* indices in the RICA and LICA were $\Delta\overline{P}_{RICA} = 1.75$ mmHg, $\Delta\overline{P}_{LICA} = 0.71$ mmHg, $FF_{RICA} = 0.98$, and $FF_{LICA} = 0.99$, respectively. The mean flow rates in the RICA and LICA were $\overline{Q}_{RICA} = 4.00$ ml/s and $\overline{Q}_{LICA} = 5.25$ ml/s. Despite the severe RICA stenosis and moderate LICA stenosis, the mean pressure at the RMCA and LMCA were similar ($\overline{P}_{RMCA} = 106.42$ mmHg, $\overline{P}_{LMCA} = 106.37$ mmHg, mean difference: 0.05 mmHg). The mean flow rates, as well as the corresponding total resistances, at the outlets of the RMCA and LMCA were comparable with $\overline{Q}_{RMCA} = 2.50$ ml/s and $\overline{Q}_{LMCA} = 2.60$ ml/s, and $R_{RMCA} = 5.64 \times 10^9$ Pa s m^{-3} and $R_{LMCA} = 5.44 \times 10^9$ Pa s m^{-3}, respectively.

Pressure and flow waveforms for the healthy control subject are provided in **Supplementary Figure S2**.

DISCUSSION

Patient-specific Calibration of Outflow Boundary Conditions

We presented a strategy for calibrating patient-specific outflow boundary conditions in the CoW. Our strategy relies on deriving mean flow splits in the main arteries of the CoW using ASL perfusion data, and on knowledge of the total flow to the head given by PC-MRI data in the neck arteries. The perfusion data in the different cerebral territories is the result of the spatial distribution of blood supply to the brain tissue, which is determined by the overall distal microvascular resistance and potentially cerebral auto-regulatory effects that seek to compensate deficits in flow in a region of the brain. Therefore, the calibrated outflow boundary condition parameters include the effect of all these mechanisms. Cerebral auto-regulatory compensation was apparent in patient 1, where the ASL-derived flow rates in the right and left MCA of the

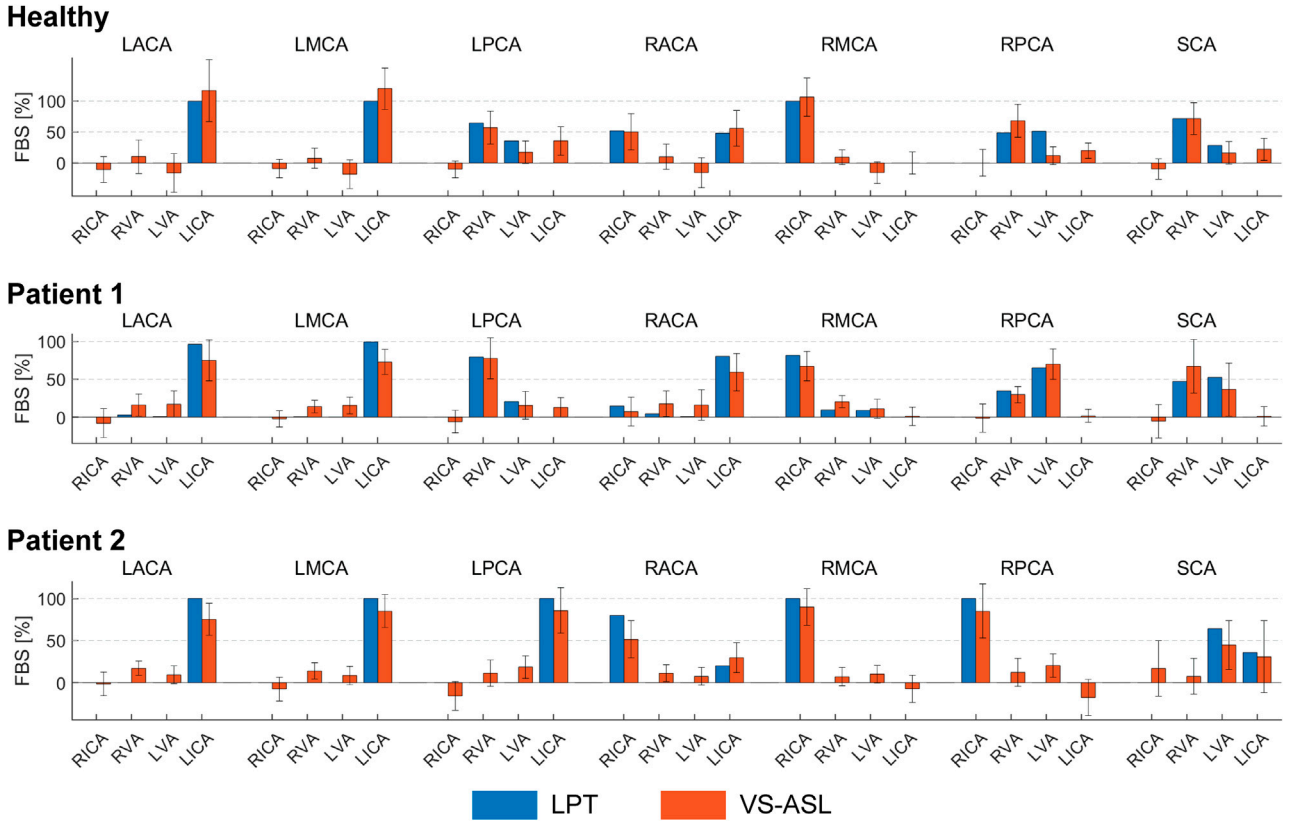

FIGURE 5 | Comparison of the $FBS_{j,k}$, obtained from VS-ASL and LPT, in each vascular territory *j* and for each neck artery *k*. For VS-ASL, values of $FBS_{j,k}$ represent the median of the $FBS_{j,k}$ distribution in each vascular territory. The error bar represents the median absolute deviation. For LPT, values of $FBS_{j,k}$ were calculated based on the particle count at each outlet of the CoW. RACA/LACA, right/left anterior cerebral artery; RMCA/LMCA, right/left middle cerebral artery; RPCA/LPCA, right/left posterior cerebral artery; SCA, superior cerebellar arteries; RVA/LVA, right/left vertebral artery; RICA/LICA, right/left internal carotid artery.

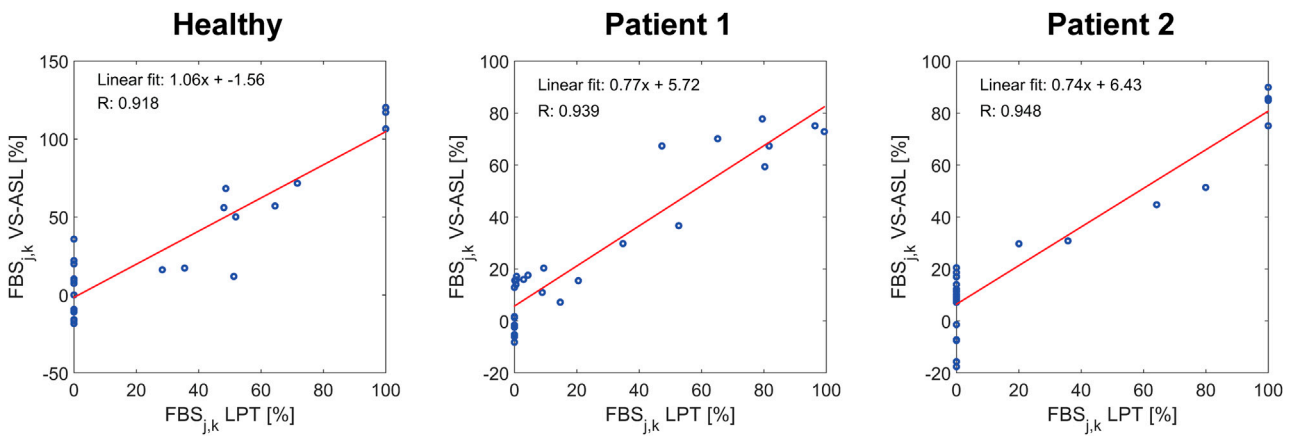

FIGURE 6 | Correlation of $FBS_{j,k}$ between VS-ASL and LPT. For each subject, the correlation coefficient and linear fit of $FBS_{j,k}$ over all territories *j* and neck arteries *k* was calculated.

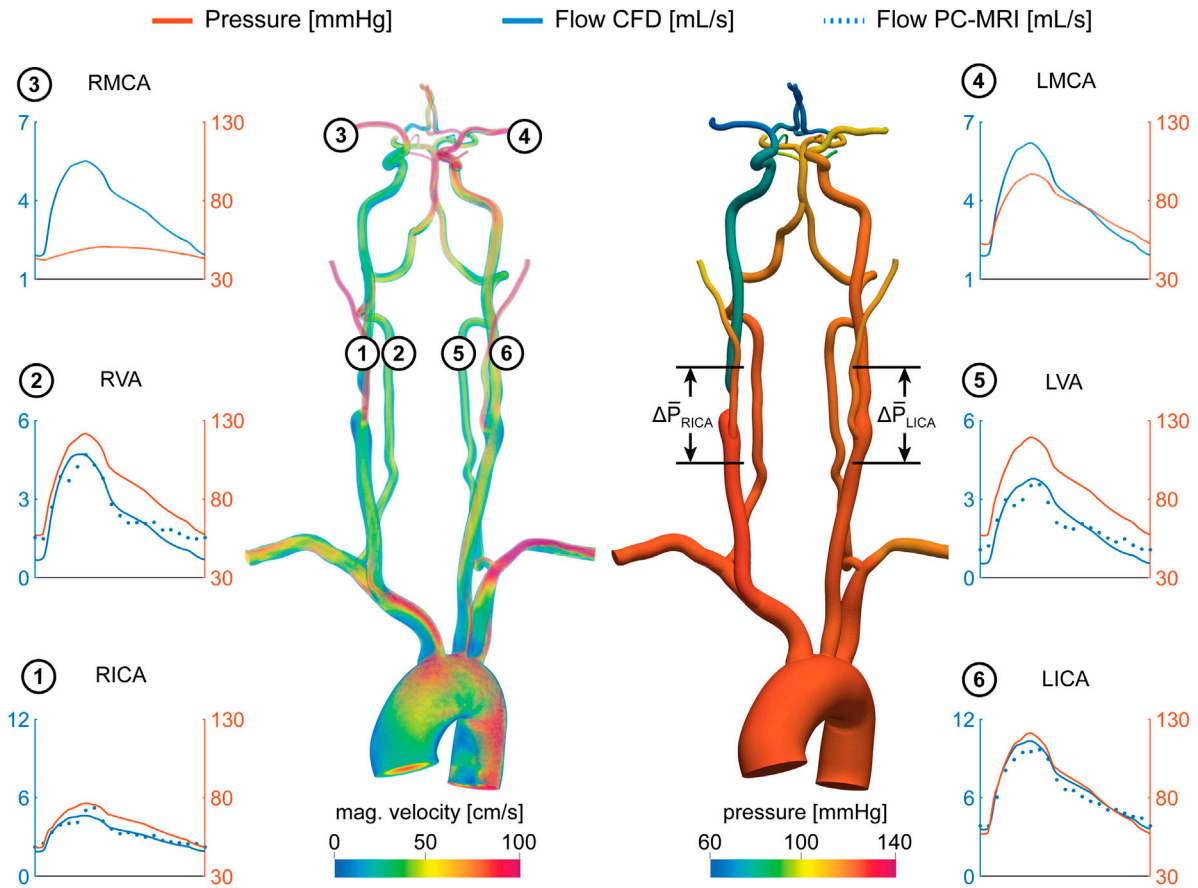

FIGURE 7 | Velocity and pressure fields at peak systole for patient 1. Flow and pressure waveforms are evaluated in the internal carotid (ICA), vertebral (VA), and middle cerebral arteries (MCA). The flow waveforms in the neck arteries are compared to PC-MRI measurements above the carotid bifurcation (dotted lines). The mean pressure drop $\Delta\bar{P} = \bar{P}_{prox} - \bar{P}_{dist}$ was calculated over the RICA stenosis and the same vessel segment in the LICA.

CoW were comparable despite a severe RICA stenosis. To match the ASL-derived mean flow rates in the CFD analysis, the distal resistance of each Windkessel model for the vessels in the CoW was iteratively adjusted during stage 1 of the calibration (cf. ***Calibration of Windkessel model parameters***). The calibrated RMCA resistance was significantly lower than its LMCA counterpart. This finding points to a substantial vasodilation of the distal vasculature of the RMCA to maintain adequate blood supply to the brain tissue.

Previous CFD modeling studies of cerebral blood flow have relied primarily on assumptions on the flow distribution in the CoW, either based on literature data of healthy vasculatures (Xiao et al., 2013; Mukherjee et al., 2016) or allometric scaling laws (Bockman et al., 2012). However, in situations of cerebrovascular disease, the distribution of flow between the different vessels of the CoW may be substantially different from that given by idealized allometric scaling principles based on healthy data. Ultimately, incorrect values of flow in the vessels of the CoW will affect the quality of the CFD results. Zhang et al. (2016) previously presented a calibrated 1D-0D computational model of cerebral blood using single photon emission computed tomography (SPECT) to estimate the flow distribution in the CoW (Yamada et al., 2014). In this work, we built on this approach by acquiring non-invasive and non-radioactive NS-ASL perfusion images and using 3D models of blood flow, given by the incompressible Navier-Stokes equations, which are essential to capture complex hemodynamics around the stenosis and in the small and tortuous vessels of the CoW.

Validation of Calibrated CFD Model

In this work, we demonstrated that our CFD calibration strategy of using NS-ASL perfusion images, in combination with a vascular territory atlas and PC-MRI, can accurately characterize flow in the main arteries of the CoW in a small group of subjects. The LPT analysis performed using the calibrated CFD model was validated using VS-ASL data by comparing their respective values of FBS in each vascular territory. Results showed an overall good agreement between LPT and VS-ASL with high correlation coefficients.

Bockman et al. (2012) developed a CFD model of the vertebrobasilar system with outflow boundary conditions defined *via* allometric scaling on healthy subjects without flow-altering CVOD. They studied the agreement in the laterality of the VA blood supply for the cerebral and cerebellar circulations between CFD and vessel-encoded ASL. ASL perfusion data was therefore not used to calibrate the outflow BC of the CFD model. Here, we

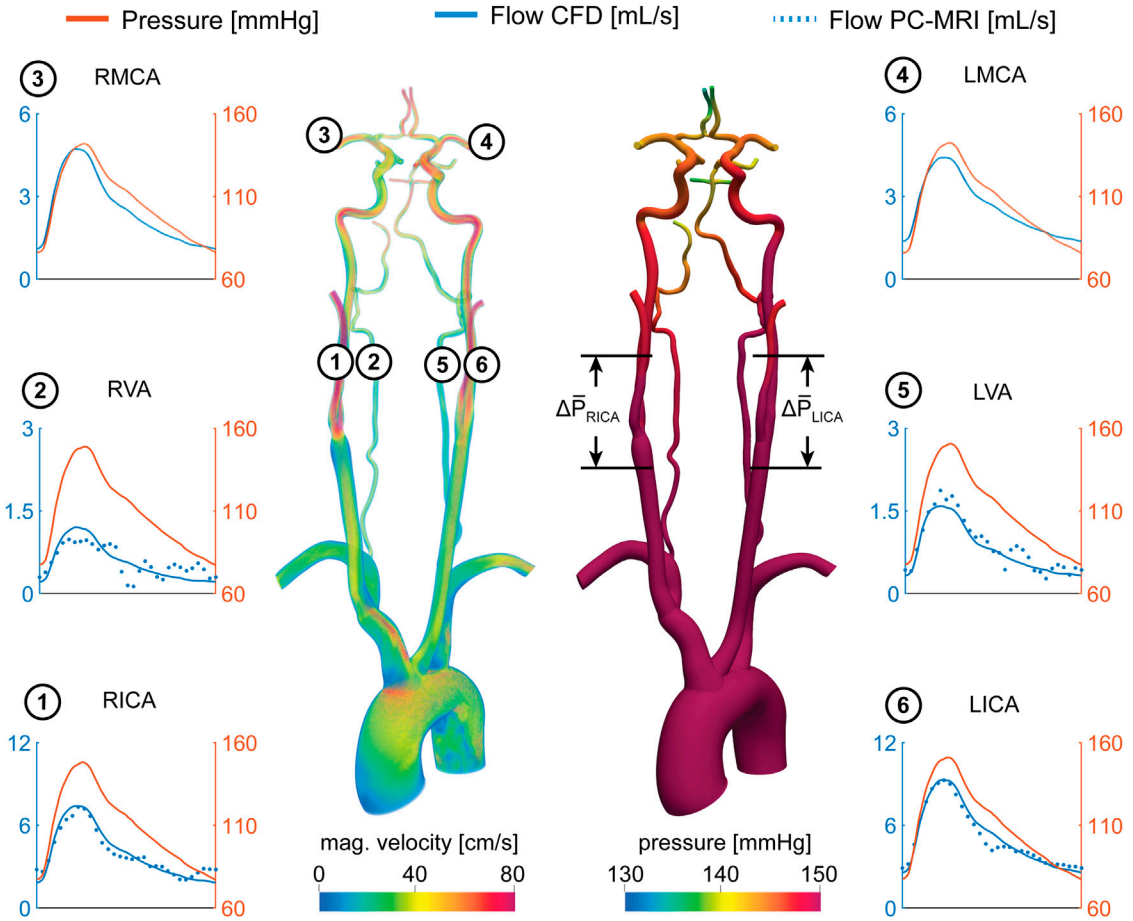

FIGURE 8 | Velocity and pressure fields at peak systole for patient 2. Flow and pressure waveforms are evaluated in the internal carotid (ICA), vertebral (VA), and middle cerebral arteries (MCA). The flow waveforms in the neck arteries are compared to PC-MRI measurements above the carotid bifurcation (dotted lines). The mean pressure drop $\Delta\bar{P} = \bar{P}_{prox} - \bar{P}_{dist}$ was calculated over the RICA and LICA stenosis.

modeled the entire CoW and validated blood supply to each vascular territory in both healthy and CVOD subjects. Furthermore, we demonstrated that the calibrated CFD models captured the collateral flow observed in the VS-ASL data.

Assessment of Patient-Specific Cerebral Hemodynamics

Using the validated CFD model, we performed an in-depth quantification of cerebral hemodynamics in the two CVOD patients. Both patients presented with a severe RICA stenosis (70–99% diameter reduction) according to the velocity criteria (Patient 1), which correlates the peak systolic velocity measured with Duplex Ultrasound to a percentage diameter reduction, and the ECST criteria (Patient 2), which is defined as the diameter reduction relative to the original vessel diameter based on CTA. Despite similar degrees of clinical stenosis severity, the cerebral hemodynamics varied significantly between these two patients. In patient 1, the RICA stenosis led to severe ipsilateral pressure and flow drop compared to the contralateral unstenosed LICA. Despite the pressure difference between right and left hemisphere, there was no significant difference in flow between the right and left MCA due to collateral flow compensation and vasodilation of the distal vasculature. In contrast, the RICA stenosis in patient 2 did not result in a notable drop in ipsilateral pressure or flow. Consequently, the flow compensation between hemispheres was small. The difference in flow compensation between the two patients is explained by the much smaller stenosis diameter of patient 1 (1.4 mm in our geometric model, 74.7% diameter reduction relative to the distal diameter) compared to patient 2 (3.0 mm, 52.3% diameter reduction relative to distal diameter), see **Figure 1**. Flow compensation is highly dependent on accurate characterizations of the degree of stenosis, the cerebral anatomy, and the cerebrovascular reserve and can vary significantly between patients.

Medical imaging used for cerebral hemodynamics assessment (e.g. Transcranial Doppler, 4D Flow MRI, etc.) only provide information on velocity. However, the above results (similar cerebral flow between the two subjects while having substantial differences in pressure) highlight the shortcomings

of describing the hemodynamic significance of CVOD lesions purely from the perspective of velocity. In contrast, blood pressure is highly sensitive to changes in vascular resistance induced by the stenosis, as illustrated in patient 1. Therefore, substantial changes in cerebral blood pressure may be a more sensitive marker for diminished vascular flow reserve. While pressure catheter measurements are commonly acquired in other vascular territories (e.g. coronary arteries), cerebral blood pressure is generally not acquired during clinical assessment of CVOD patients due to increased stroke risk. While there have been efforts to derive pressure gradients from 4D Flow MRI data, application in the small and tortuous CoW arteries remains challenging due to limited spatial resolution (Vali et al., 2019). In contrast, patient-specific CFD overcomes these shortcomings by providing highly resolved velocity and pressure.

To quantify the stenosis hemodynamic significance, we calculated the fractional flow index, defined as the ratio of the pressures distal and proximal to the stenosis under baseline flow conditions (e.g., non-hyperemic). The fractional flow in the RICA stenosis was $FF_{RICA} = 0.71$ for patient 1 and $FF_{RICA} = 0.98$ for patient 2. Using a threshold of FF = 0.8 (Miao et al., 2016), only the RICA stenosis in patient 1 would be deemed to be hemodynamically significant. While the clinical metric of diameter reduction resulted in a similar value of 70–99% in the RICA for both patients, the fractional flow index captured better the large differences in cerebral hemodynamics between the patients. The metric of fractional flow reserve (FFR) has become widely used in coronary artery disease (CAD) to evaluate the risk for myocardial ischemia. FFR-guided intervention has been shown to reduce myocardial ischemia, rate of death, and revascularization compared to anatomical-based intervention (Tonino et al., 2009; De Bruyne et al., 2014). However, the use of fractional flow for the risk assessment of ischemic stroke in CVOD has not yet been established.

In this work, the CFD analysis focused primarily on assessing the hemodynamic effects of carotid stenosis on flow and pressure, as well as the cerebral vasculature's capacity to compensate flow. However, it is important to note that the formation of emboli from the carotid plaque is thought to be the major mechanism of ischemic stroke in patients with carotid stenosis, especially in asymptomatic patients (King et al., 2011). The assessment of plaque composition, in particular the size of the lipid-rich necrotic core and the fibrous cap, is key to determining plaque vulnerability and embolic stroke risk. However, hemodynamic factors (e.g. wall shear stress and blood pressure) are suspected to also play an important role in plaque vulnerability (Chen et al., 2020).

FBS obtained from CFD and LPT provided important information about collateral flow in the anterior circulation and mixed VA supply in the posterior circulation. Beyond flow compensation, FBS in the cerebral vascular territories can provide clinically relevant information about the etiology of embolic stroke. Even after thorough diagnostic evaluation, the cause of embolic stroke remains uncertain in one third of cases (Nouh et al., 2016). It is common that multiple atherosclerotic lesions within the same patient are identified. Evaluation of FBS in the region of the stroke could help to determine the source of emboli and ultimately guide clinical treatment.

These results illustrate the level of insight on hemodynamic assessment of CVOD patients that calibrated patient-specific CFD analysis can bring.

Limitations

Vascular Territory Atlas

In this work, the flow splits between the main intracranial arteries were estimated from non-selective ASL perfusion images. The segmentation of the perfusion images relied on knowledge of the vascular territories corresponding to the intracranial arteries. Since the precise location of the territories was not available, which is generally the case, a vascular territory atlas was used to define the boundaries of each territory. Vascular territory atlases are routinely used in the radiologic assessment of infarctions to investigate the stroke mechanism and to guide further therapy (Phan et al., 2005). A major limitation of most available atlases (Tatu et al., 2012) is the small sample size of subjects used to derive territory maps, resulting in large uncertainties in the border zones. The atlas used in this work was recently developed by Kim et al. based on a large population study of 1,160 stroke patients with intracranial stenosis (Kim et al., 2018). In their study, the authors showed that the border zones of the derived atlas were much narrower than previously assumed, which justified assigning territory boundaries based on the probability of each image voxel of being associated with each intracranial artery. However, some degree of variability in the vascular territories is expected among patients. For example, the formation of leptomeningeal collaterals between the distal branches of the CoW can lead to changes in the vascular territories (Tariq and Khatri, 2008). In the presence of patent leptomeningeal collaterals, the additional pathways would have to be accounted for in the geometric model and in the segmentation of the territories.

VS-ASL

The acquisition of VS-ASL images is generally challenging due to the inherently low signal-to-noise ratio. Cardiac pulsatility, B_0-field inhomogeneity, and subject movement can lead to further artifacts in the territorial perfusion maps (Schollenberger et al., 2020). For example, signal fluctuations between label and control images can result in spurious perfusion signal in vascular territories not perfused by the labeled neck artery. Previous applications of VS-ASL have been limited to a qualitative description of territorial perfusion. In this work, we quantified VS-ASL image data by deriving the fractional blood supply. To account for the spatial variability of FBS within a vascular territory due to noise and image artifacts, we included the median absolute deviation in the data as shown in **Figure 5**.

PC-MRI

Estimation of mean flow rates in the intracranial arteries relies on knowledge of the total flow to the CoW. However, PC-MRI flow measurements in the neck arteries might not always be available. As an alternative approach, intracranial flow rates

could be estimated exclusively from the non-selective ASL data. In this work, we quantified the ASL image data by calculating the averaged signal difference between control and label images. While the signal difference is proportional to perfusion, the units are arbitrary. However, one of the advantages of ASL is the ability to quantify the difference images in units of perfusion (e.g. ml/min/100 g). This can be achieved by using for example a single compartment model (Buxton et al., 1998). Once the perfusion images are quantified, mean intracranial flow rates can be derived by integrating perfusion over each segmented territory using the vascular territory atlas and multiplying with the brain tissue density. While the resulting total flow to the CoW might be different from the one measured with PC-MRI, the ratio of flow rates across the intracranial arteries and consequently the collateral flow would be maintained.

CONCLUSION

In this work, we presented a strategy to quantify cerebral hemodynamics using CFD in combination with ASL and PC-MRI data. We demonstrated that our calibrated CFD model accurately reproduced the fractional blood supply to the vascular territories, as obtained from VS-ASL. In particular, the flow compensation between hemispheres was captured well by the calibrated CFD models. The assessment of cerebral hemodynamics in two CVOD patients using calibrated patient-specific CFD analysis showed significant differences in cerebral hemodynamics between the patients despite similar degrees of clinical stenosis severity. We further illustrated the advantages of CFD-based pressure data for assessing the hemodynamic significance of carotid stenosis. Future studies are needed to investigate the benefits of using of a hemodynamic-based metric (fractional flow) versus an anatomy-based metric (diameter reduction) for the risk assessment of CVOD patients.

DATA AVAILABILITY STATEMENT

The raw data supporting the conclusions of this article will be made available by the authors, without undue reservation.

ETHICS STATEMENT

The studies involving human participants were reviewed and approved by the University of Michigan institutional review board. The patients/participants provided their written informed consent to participate in this study. Written informed consent was obtained from the individual(s) for the publication of any potentially identifiable images or data included in this article.

AUTHOR CONTRIBUTIONS

JS: conceptualization, methodology, software, formal analysis, investigation, data curation, writing (original draft), and visualization. NO: resources and writing (review and editing). LH-G: conceptualization, validation, resources, writing (review and editing), and supervision. CF: conceptualization, validation, resources, writing (review and editing), supervision, and funding acquisition.

FUNDING

This work was supported by the Predoctoral Fellowship (Rackham Graduate School, University of Michigan) and the Edward B. Diethrich Professorship.

ACKNOWLEDGMENTS

The authors would like to acknowledge Heather Golden for her help with patient enrollment.

SUPPLEMENTARY MATERIAL

The Supplementary Material for this article can be found online at: https://www.frontiersin.org/articles/10.3389/fbioe.2021.722445/full#supplementary-material

REFERENCES

Alsop, D. C., Detre, J. A., Golay, X., Günther, M., Hendrikse, J., Hernandez-Garcia, L., et al. (2014). Recommended Implementation of Arterial Spin-Labeled Perfusion MRI for Clinical Applications: A Consensus of the ISMRM Perfusion Study Group and the European Consortium for ASL in Dementia. *Magn. Reson. Med.* 73, 102–116. doi:10.1002/mrm.25197

Arthurs, C. J., Khlebnikov, R., Melville, A., Marčan, M., Gomez, A., Dillon-Murphy, D., et al. (2021). CRIMSON: An Open-Source Software Framework for Cardiovascular Integrated Modelling and Simulation. *PLOS Comput. Biol.* 17, e1008881. doi:10.1371/journal.pcbi.1008881

Arthurs, C. J., Lau, K. D., Asrress, K. N., Redwood, S. R., and Figueroa, C. A. (2016). A Mathematical Model of Coronary Blood Flow Control: Simulation of Patient-specific Three-Dimensional Hemodynamics during Exercise. *Am. J. Physiology-Heart Circulatory Physiol.* 310, H1242–H1258. doi:10.1152/ajpheart.00517.2015

Arzani, A., Les, A. S., Dalman, R. L., and Shadden, S. C. (2014). Effect of Exercise on Patient Specific Abdominal Aortic Aneurysm Flow Topology and Mixing. *Int. J. Numer. Meth. Biomed. Engng.* 30, 280–295. doi:10.1002/cnm10.1002/cnm.2601

Bisschops, R. H. C., Klijn, C. J. M., Kappelle, L. J., Van Huffelen, A. C., and Van der Grond, J. (2003). Collateral Flow and Ischemic Brain Lesions in Patients with Unilateral Carotid Artery Occlusion. *Neurology* 60, 1435–1441. doi:10.1212/01.WNL.0000061616.96745.90

Bockman, M. D., Kansagra, A. P., Shadden, S. C., Wong, E. C., and Marsden, A. L. (2012). Fluid Mechanics of Mixing in the Vertebrobasilar System: Comparison of Simulation and MRI. *Cardiovasc. Eng. Tech.* 3, 450–461. doi:10.1007/s13239-012-0112-8

Buxton, R. B., Frank, L. R., Wong, E. C., Siewert, B., Warach, S., and Edelman, R. R. (1998). A General Kinetic Model for Quantitative Perfusion Imaging with Arterial Spin Labeling. *Magn. Reson. Med.* 40, 383–396. doi:10.1002/mrm.1910400308

Castro, M. A., Putman, C. M., and Cebral, J. R. (2006). Computational Fluid Dynamics Modeling of Intracranial Aneurysms: Effects of Parent Artery

Segmentation on Intra-aneurysmal Hemodynamics. *AJNR Am. J. Neuroradiol* 27, 1703–1709.

Chen, Z., Qin, H., Liu, J., Wu, B., Cheng, Z., Jiang, Y., et al. (2020). Characteristics of Wall Shear Stress and Pressure of Intracranial Atherosclerosis Analyzed by a Computational Fluid Dynamics Model: A Pilot Study. *Front. Neurol.* 10, 1–9. doi:10.3389/fneur.2019.01372

De Bruyne, B., Fearon, W. F., Pijls, N. H. J., Barbato, E., Tonino, P., Piroth, Z., et al. (2014). Fractional Flow Reserve-Guided PCI for Stable Coronary Artery Disease. *N. Engl. J. Med.* 371, 1208–1217. doi:10.1056/NEJMoa1408758

Di Achille, P., Tellides, G., Figueroa, C. A., and Humphrey, J. D. (2014). A Haemodynamic Predictor of Intraluminal Thrombus Formation in Abdominal Aortic Aneurysms. *Proc. R. Soc. A.* 470, 20140163. doi:10.1098/rspa.2014.0163

Helle, M., Norris, D. G., Rüfer, S., Alfke, K., Jansen, O., and Van Osch, M. J. P. (2010). Superselective Pseudocontinuous Arterial Spin Labeling. *Magn. Reson. Med.* 64, 777–786. doi:10.1002/mrm.22451

Helle, M., Rüfer, S., Van Osch, M. J. P., Nabavi, A., Alfke, K., Norris, D. G., et al. (2013). Superselective Arterial Spin Labeling Applied for Flow Territory Mapping in Various Cerebrovascular Diseases. *J. Magn. Reson. Imaging* 38, 496–503. doi:10.1002/jmri.24041

Henderson, R. D., Eliasziw, M., Fox, A. J., Rothwell, P. M., and Barnett, H. J. M. (2000). Angiographically Defined Collateral Circulation and Risk of Stroke in Patients with Severe Carotid Artery Stenosis. *Stroke* 31, 128–132. doi:10.1161/01.STR.31.1.128

Hendrikse, J., Hartkamp, M. J., Hillen, B., Mali, W. P. T. M., and Grond, J. v. d. (2001). Collateral Ability of the Circle of Willis in Patients with Unilateral Internal Carotid Artery Occlusion. *Stroke* 32, 2768–2773. doi:10.1161/hs1201.099892

Jensen-Kondering, U., Lindner, T., van Osch, M. J. P., Rohr, A., Jansen, O., and Helle, M. (2015). Superselective Pseudo-continuous Arterial Spin Labeling Angiography. *Eur. J. Radiol.* 84, 1758–1767. doi:10.1016/j.ejrad.2015.05.034

Kim, D.-E., Park, J.-H., Schellingerhout, D., Ryu, W.-S., Lee, S.-K., Jang, M. U., et al. (2019). Mapping the Supratentorial Cerebral Arterial Territories Using 1160 Large Artery Infarcts. *JAMA Neurol.* 76, 72. doi:10.1001/jamaneurol.2018.2808

King, A., Serena, J., Bornstein, N. M., and Markus, H. S. (2011). Does Impaired Cerebrovascular Reactivity Predict Stroke Risk in Asymptomatic Carotid Stenosis?. *Stroke* 42, 1550–1555. doi:10.1161/STROKEAHA.110.609057

Leng, X., Scalzo, F., Ip, H. L., Johnson, M., Fong, A. K., Fan, F. S. Y., et al. (2014). Computational Fluid Dynamics Modeling of Symptomatic Intracranial Atherosclerosis May Predict Risk of Stroke Recurrence. *PLoS One* 9, e97531–8. doi:10.1371/journal.pone.0097531

Liebeskind, D. S. (2003). Collateral Circulation. *Stroke* 34, 2279–2284. doi:10.1161/01.STR.0000086465.41263.06

Liebeskind, D. S., and Feldmann, E. (2012). Fractional Flow in Cerebrovascular Disorders. *Intervent Neurol.* 1, 87–99. doi:10.1159/000346803

Liu, J., Yan, Z., Pu, Y., Shiu, W.-S., Wu, J., Chen, R., et al. (2017). Functional Assessment of Cerebral Artery Stenosis: A Pilot Study Based on Computational Fluid Dynamics. *J. Cereb. Blood Flow Metab.* 37, 2567–2576. doi:10.1177/0271678X16671321

Miao, Z., Liebeskind, D. S., Lo, W., Liu, L., Pu, Y., Leng, X., et al. (2016). Fractional Flow Assessment for the Evaluation of Intracranial Atherosclerosis: A Feasibility Study. *Intervent Neurol.* 5, 65–75. doi:10.1159/000444333

Mukherjee, D., Jani, N. D., Selvaganesan, K., Weng, C. L., and Shadden, S. C. (2016). Computational Assessment of the Relation between Embolism Source and Embolus Distribution to the Circle of Willis for Improved Understanding of Stroke Etiology. *J. Biomech. Eng.* 138, 81008. doi:10.1115/1.4033986

Nauta, F. J. H., Lau, K. D., Arthurs, C. J., Eagle, K. A., Williams, D. M., Trimarchi, S., et al. (2017). Computational Fluid Dynamics and Aortic Thrombus Formation Following Thoracic Endovascular Aortic Repair. *Ann. Thorac. Surg.* 103, 1914–1921. doi:10.1016/j.athoracsur.2016.09.067

Nouh, A., Hussain, M., Mehta, T., and Yaghi, S. (2016). Embolic Strokes of Unknown Source and Cryptogenic Stroke: Implications in Clinical Practice. *Front. Neurol.* 7, 1–16. doi:10.3389/fneur.2016.00037

Phan, T. G., Donnan, G. A., Wright, P. M., and Reutens, D. C. (2005). A Digital Map of Middle Cerebral Artery Infarcts Associated with Middle Cerebral Artery Trunk and Branch Occlusion. *Stroke* 36, 986–991. doi:10.1161/01.STR.0000163087.66828.e9

Ramsay, S. C., Yeates, M. G., Lord, R. S., Hille, N., Yeates, P., Eberl, S., et al. (1991). Use of Technetium-HMPAO to Demonstrate Changes in Cerebral Blood Flow reserve Following Carotid Endarterectomy. *J. Nucl. Med.* 32, 1382–1386.

Raschi, M., Mut, F., Byrne, G., Putman, C. M., Tateshima, S., Viñuela, F., et al. (2012). CFD and PIV Analysis of Hemodynamics in a Growing Intracranial Aneurysm. *Int. J. Numer. Meth. Biomed. Engng.* 28, 214–228. doi:10.1002/cnm.1459

Rayz, V. L., Boussel, L., Acevedo-Bolton, G., Martin, A. J., Young, W. L., Lawton, M. T., et al. (2008). Numerical Simulations of Flow in Cerebral Aneurysms: Comparison of CFD Results and *In Vivo* MRI Measurements. *J. Biomech. Eng.* 130, 1–9. doi:10.1115/1.2970056

Richter, V., Helle, M., van Osch, M. J. P., Lindner, T., Gersing, A. S., Tsantilas, P., et al. (2017). MR Imaging of Individual Perfusion Reorganization Using Superselective Pseudocontinuous Arterial Spin-Labeling in Patients with Complex Extracranial Steno-Occlusive Disease. *AJNR Am. J. Neuroradiol* 38, 703–711. doi:10.3174/ajnr.a5090

Russell, S. M., Woo, H. H., Siller, K., Panasci, D., and LeRoux, P. D. (2008). Evaluating Middle Cerebral Artery Collateral Blood Flow reserve Using Acetazolamide Transcranial Doppler Ultrasound in Patients with Carotid Occlusive Disease. *Surg. Neurol.* 70, 466–470. doi:10.1016/j.surneu.2007.10.030

Saba, L., Yuan, C., Hatsukami, T. S., Balu, N., Qiao, Y., DeMarco, J. K., et al. (2018). Carotid Artery Wall Imaging: Perspective and Guidelines from the ASNR Vessel Wall Imaging Study Group and Expert Consensus Recommendations of the American Society of Neuroradiology. *AJNR Am. J. Neuroradiol.* 39, E9–E31. doi:10.3174/ajnr.A5488

Sahni, O., Müller, J., Jansen, K. E., Shephard, M. S., and Taylor, C. A. (2006). Efficient Anisotropic Adaptive Discretization of the Cardiovascular System. *Comp. Methods Appl. Mech. Eng.* 195, 5634–5655. doi:10.1016/j.cma.2005.10.018

Schollenberger, J., Figueroa, C. A., Nielsen, J. F., and Hernandez-Garcia, L. (2020). Practical Considerations for Territorial Perfusion Mapping in the Cerebral Circulation Using Super-selective Pseudo-continuous Arterial Spin Labeling. *Magn. Reson. Med.* 83, 492–504. doi:10.1002/mrm.27936

Suh, G.-Y., Les, A. S., Tenforde, A. S., Shadden, S. C., Spilker, R. L., Yeung, J. J., et al. (2011). Quantification of Particle Residence Time in Abdominal Aortic Aneurysms Using Magnetic Resonance Imaging and Computational Fluid Dynamics. *Ann. Biomed. Eng.* 39, 864–883. doi:10.1007/s10439-010-0202-4

Tariq, N., and Khatri, R. (2008). Leptomeningeal Collaterals in Acute Ischemic Stroke. *J. Vasc. Interv. Neurol.* 1, 91–95.

Tatu, L., Moulin, T., Vuillier, F., and Bogousslavsky, J. (2012). "Arterial Territories of the Human Brain," in *The Human Brain* (Vienna: Springer Vienna), 99–110. doi:10.1159/000333602

Tonino, P. A. L., De Bruyne, B., Pijls, N. H. J., Siebert, U., Ikeno, F., van `t Veer, M., et al. (2009). Fractional Flow Reserve versus Angiography for Guiding Percutaneous Coronary Intervention. *N. Engl. J. Med.* 360, 213–224. doi:10.1056/NEJMoa0807611

Vali, A., Aristova, M., Vakil, P., Abdalla, R., Prabhakaran, S., Markl, M., et al. (2019). Semi-automated Analysis of 4D Flow MRI to Assess the Hemodynamic Impact of Intracranial Atherosclerotic Disease. *Magn. Reson. Med.* 82, 749–762. doi:10.1002/mrm.27747

Van Bakel, T. M., Arthurs, C. J., Van Herwaarden, J. A., Moll, F. L., Eagle, K. A., Patel, H. J., et al. (2018). A Computational Analysis of Different Endograft Designs for Zone 0 Aortic Arch Repair†. *Eur. J. Cardio-thoracic Surg.* 54, 389–396. doi:10.1093/ejcts/ezy068

Vignon-Clementel, I. E., Figueroa, C. A., Jansen, K. E., and Taylor, C. A. (2010). Outflow Boundary Conditions for 3D Simulations of Non-periodic Blood Flow and Pressure fields in Deformable Arteries. *Comp. Methods Biomech. Biomed. Eng.* 13, 625–640. doi:10.1080/10255840903413565

Whiting, C. H., and Jansen, K. E. (2001). A Stabilized Finite Element Method for the Incompressible Navier-Stokes Equations Using a Hierarchical Basis. *Int. J. Numer. Meth. Fluids* 35, 93–116. doi:10.1002/1097-0363(20010115)35:1<93::aid-fld85>3.0.co;2-g

Xiao, N., Alastruey, J., and Alberto Figueroa, C. (2014). A Systematic Comparison between 1-D and 3-D Hemodynamics in Compliant Arterial Models. *Int. J. Numer. Meth. Biomed. Engng.* 30, 204–231. doi:10.1002/cnm.2598

Xiao, N., Humphrey, J. D., and Figueroa, C. A. (2013). Multi-scale Computational Model of Three-Dimensional Hemodynamics within a Deformable Full-Body Arterial Network. *J. Comput. Phys.* 244, 22–40. doi:10.1016/j.jcp.2012.09.016

Yamada, S., Kobayashi, M., Watanabe, Y., Miyake, H., and Oshima, M. (2014). Quantitative Measurement of Blood Flow Volume in the Major Intracranial Arteries by Using 123I-Iodoamphetamine SPECT. *Clin. Nucl. Med.* 39, 868–873. doi:10.1097/RLU.0000000000000555

Zhang, H., Fujiwara, N., Kobayashi, M., Yamada, S., Liang, F., Takagi, S., et al. (2016). Development of a Numerical Method for Patient-specific Cerebral Circulation Using 1D-0D Simulation of the Entire Cardiovascular System with SPECT Data. *Ann. Biomed. Eng.* 44, 2351–2363. doi:10.1007/s10439-015-1544-8

Conflict of Interest: The authors declare that the research was conducted in the absence of any commercial or financial relationships that could be construed as a potential conflict of interest.

Publisher's Note: All claims expressed in this article are solely those of the authors and do not necessarily represent those of their affiliated organizations, or those of the publisher, the editors and the reviewers. Any product that may be evaluated in this article, or claim that may be made by its manufacturer, is not guaranteed or endorsed by the publisher.

frontiers in Cardiovascular Medicine

ORIGINAL RESEARCH
published: 27 August 2021
doi: 10.3389/fcvm.2021.669860

Deep Learning Analysis of Echocardiographic Images to Predict Positive Genotype in Patients With Hypertrophic Cardiomyopathy

Sae X. Morita[1†], Kenya Kusunose[2†], Akihiro Haga[3], Masataka Sata[2], Kohei Hasegawa[4], Yoshihiko Raita[4], Muredach P. Reilly[1,5], Michael A. Fifer[6], Mathew S. Maurer[1] and Yuichi J. Shimada[1]*

[1] Division of Cardiology, Department of Medicine, Columbia University Irving Medical Center, New York, NY, United States, [2] Department of Cardiovascular Medicine, Tokushima University, Tokushima, Japan, [3] Department of Medical Image Informatics, Graduate School of Biomedical Sciences, Tokushima University, Tokushima, Japan, [4] Department of Emergency Medicine, Massachusetts General Hospital, Boston, MA, United States, [5] Irving Institute for Clinical and Translational Research, Columbia University Irving Medical Center, New York, NY, United States, [6] Cardiology Division, Department of Medicine, Massachusetts General Hospital, Boston, MA, United States

OPEN ACCESS

Edited by:
Zahra K. Motamed,
McMaster University, Canada

Reviewed by:
Emmanuel Androulakis,
Royal Brompton and Harefield NHS Foundation Trust, United Kingdom
Max Olender,
Massachusetts Institute of Technology, United States

***Correspondence:**
Yuichi J. Shimada
ys3053@cumc.columbia.edu

[†]These authors have contributed equally to this work and share first authorship

Specialty section:
This article was submitted to Cardiovascular Imaging, a section of the journal Frontiers in Cardiovascular Medicine

Received: 19 February 2021
Accepted: 09 August 2021
Published: 27 August 2021

Citation:
Morita SX, Kusunose K, Haga A, Sata M, Hasegawa K, Raita Y, Reilly MP, Fifer MA, Maurer MS and Shimada YJ (2021) Deep Learning Analysis of Echocardiographic Images to Predict Positive Genotype in Patients With Hypertrophic Cardiomyopathy. Front. Cardiovasc. Med. 8:669860. doi: 10.3389/fcvm.2021.669860

Genetic testing provides valuable insights into family screening strategies, diagnosis, and prognosis in patients with hypertrophic cardiomyopathy (HCM). On the other hand, genetic testing carries socio-economical and psychological burdens. It is therefore important to identify patients with HCM who are more likely to have positive genotype. However, conventional prediction models based on clinical and echocardiographic parameters offer only modest accuracy and are subject to intra- and inter-observer variability. We therefore hypothesized that deep convolutional neural network (DCNN, a type of deep learning) analysis of echocardiographic images improves the predictive accuracy of positive genotype in patients with HCM. In each case, we obtained parasternal short- and long-axis as well as apical 2-, 3-, 4-, and 5-chamber views. We employed DCNN algorithm to predict positive genotype based on the input echocardiographic images. We performed 5-fold cross-validations. We used 2 reference models—the Mayo HCM Genotype Predictor score (Mayo score) and the Toronto HCM Genotype score (Toronto score). We compared the area under the receiver-operating-characteristic curve (AUC) between a combined model using the reference model plus DCNN-derived probability and the reference model. We calculated the *p*-value by performing 1,000 bootstrapping. We calculated sensitivity, specificity, positive predictive value (PPV), and negative predictive value (NPV). In addition, we examined the net reclassification improvement. We included 99 adults with HCM who underwent genetic testing. Overall, 45 patients (45%) had positive genotype. The new model combining Mayo score and DCNN-derived probability significantly outperformed Mayo score (AUC 0.86 [95% CI 0.79–0.93] vs. 0.72 [0.61–0.82]; $p < 0.001$). Similarly, the new model combining Toronto score and DCNN-derived probability exhibited a higher AUC compared to Toronto score alone (AUC 0.84 [0.76–0.92] vs. 0.75 [0.65–0.85];

$p = 0.03$). An improvement in the sensitivity, specificity, PPV, and NPV was also achieved, along with significant net reclassification improvement. In conclusion, compared to the conventional models, our new model combining the conventional and DCNN-derived models demonstrated superior accuracy to predict positive genotype in patients with HCM.

Keywords: hypertrophic cardiomyopathy, echocardiography, deep learning, genotype, prediction

INTRODUCTION

Hypertrophic cardiomyopathy (HCM) is the most common genetic cardiac disease, affecting ∼1 in 200–500 people (1). HCM is caused by mutations in the genes coding for proteins constructing the contractile apparatus of the myocardium (2). Investigators have documented dozens of genes and >1,000 gene mutations associated with HCM pathogenesis (2). Genetic testing has now become a powerful tool for family screening, diagnosis, and prognostication in HCM (3, 4). For example, genetic testing can determine whether each of the first-degree relatives is at risk of developing HCM (3, 5). Genetic testing can also help clinicians establish the diagnosis of HCM in patients with atypical clinical features (5). Furthermore, positive genotype carries a significant prognostic impact (6). On the other hand, genetic testing is time- and resource-intensive, and can introduce substantial financial (7, 8), social (e.g., insurability) (9), and psychological burdens (10). Thus, it is important to precisely determine the pre-test probability in each patient with HCM prior to performing genetic testing.

Several prediction tools have been developed to predict positive genotype in HCM—e.g., the Mayo HCM Genotype Predictor score ("the Mayo score" in this manuscript), the Toronto HCM Genotype score ("the Toronto score") (11, 12). These scoring systems are based on a limited number of clinical parameters including echocardiographic features [e.g., left ventricular (LV) wall thickness, interventricular septal morphology] (11, 12). However, these measurements can be subjective and are prone to intra- and inter-observer variability. Further, these scoring systems only offer limited predictive accuracy (11–15).

Deep learning is a rapidly evolving approach in a variety of medical settings including cardiovascular imaging (16–20). This technology has the potential to overcome the aforementioned human limitations (21). In the HCM population, a previous study demonstrated that deep learning-derived classification model using echocardiographic images can distinguish HCM from other cardiovascular diseases (22). Nonetheless, no previous studies examined the ability of deep learning to predict positive genotype in HCM. We therefore designed the present study to investigate, in patients with HCM, whether deep convolutional neural network (DCNN, a type of deep learning) analysis of echocardiographic images improves the ability to predict positive genotype compared to the conventional models based only on clinical parameters.

METHODS

Study Design and Population

We prospectively enrolled patients who were seen at the Center for Advanced Cardiac Care at Columbia University Medical Center (New York, NY, USA) and ≥18 years of age with a clinical diagnosis of HCM between 1988 and 2018. We diagnosed HCM if there was echocardiographic evidence of LV hypertrophy—i.e., max LV wall thickness ≥15 mm—out of proportion to systemic loading conditions and a non-dilated LV (3, 23, 24). We excluded patients based on the following criteria; (1) Patients who have never had genetic testing; (2) Patients with HCM phenocopies such as Fabry disease and cardiac amyloidosis confirmed with appropriate testing (3); and (3) Patients who underwent septal reduction therapy—i.e., septal myectomy, alcohol septal ablation—or heart transplant before enrollment. We collected baseline characteristics of the study sample including medical and family history, medication use, and echocardiographic parameters at the time of genetic testing. The institutional review boards of Columbia University Irving Medical Center and Tokushima University Hospital approved this study.

Outcome Measure

The primary outcome was positive genotype. By convention, variants categorized as "definitely pathogenic" or "likely pathogenic" were regarded positive in the present analysis (6, 11, 12). Variants classified as "variant of uncertain significance," "likely benign," or "benign" were considered negative (6, 11, 12). This definition of positive genotype was used in the present study because only these mutations are clinically actionable (i.e., allow treating physicians and the proband's family members to proceed with cascade genetic screening) and carry diagnostic and prognostic impact (3–5). All the patients were offered genetic testing for HCM using one of the commercially available testing kits (e.g., GeneDx, Invitae). Genetic testing kit was chosen based on available insurance reimbursement and patient preference. A sensitivity analysis was also performed after excluding patients with variant of uncertain significance.

The Reference Models

We used 2 reference models: (1) the Mayo score and (2) the Toronto score. To calculate the Mayo score, we assigned 1 point for the presence of the following variables: age at diagnosis ≤45 years, maximal LV wall thickness ≥20 mm on transthoracic echocardiography, reverse curve

septal morphology on transthoracic echocardiography, positive family history of HCM, and positive family history of sudden cardiac death (11). We subtracted 1 point from the score if hypertension was present (11). We made the diagnosis of hypertension based on past medical history, blood pressure measurements, and antihypertensive medication use. We did not count antihypertensives solely used for non-antihypertensive purposes—e.g., β-blockers and/or non-dihydropyridine calcium channel blockers for symptomatic relief of obstructive HCM and/or rate control of atrial fibrillation. For the calculation of the Toronto score, we used the following weighted variables: age at diagnosis, sex, hypertension, family history of HCM, septal morphological subtype (i.e., reverse or neutral), and the ratio of maximal LV wall thickness to posterior wall thickness (12).

Acquisition of Echocardiographic Images

Standard echocardiographic examinations were performed using a commercially available ultrasound system (iE33, Philips Healthcare, Amsterdam, The Netherlands) as a part of routine clinical care according to the guideline recommendations (25). The 2-dimensional echocardiographic images of all subjects were obtained from the parasternal short- (SAX) and long-axis (LAX) views as well as the apical 2- (AP2), 3- (AP3), 4- (AP4), and 5-chamber (AP5) views. We selected cases with good or adequate imaging quality on the basis of the visualization of the LV walls and endocardial borders. Echocardiographic images were stored digitally as a DICOM file and analyzed offline.

Import of the Echocardiographic Images

Echocardiographic images from the SAX, LAX, AP2, AP3, AP4, and AP5 views were analyzed. All DICOM images were rigidly registered and rescaled into a reference image to adjust the size of the echocardiographic images. The images were cut and down-sampled to 18.07 × 18.07 cm with 120 × 120 monochrome pixels. Simultaneously, metadata presented in the periphery of the images were removed. To adjust for differences in frame rate and heart rate between patients, 10 equally-spaced images per 1 cardiac cycle were chosen with the use of a semi-automatic heartbeat analysis algorithm. The starting frame was defined by the R wave on the electrocardiogram as a recording of echocardiographic images are triggered by the R wave. The methodological details are provided in **Supplementary Methods** and have been published previously (16).

Deep Learning Algorithm

Figure 1 visualizes the processing steps of DCNN. Positive genotype was predicted by a DCNN algorithm using the 6 views (SAX, LAX, AP2, AP3, AP4, and AP5). All data were randomly divided into 5 groups and 4 of the groups were used as the training set to develop the model, and the rest was used as the test set to examine the model performance (i.e., 5-fold cross-validation; **Supplementary Figure 1**). To avoid an unexpected extraction of undesired features for the evaluation, training data were augmented in each dataset. The output was the probability of positive genotype. Model training was performed on a graphics processing unit (GeForce GTX 1080 Ti, NVIDIA, Santa Clara, California, USA). The Adam optimizer was used for training (**Supplementary Figure 2**) (26). The details are provided in **Supplementary Methods**. Deep learning was performed with the Python 3.6 programming language with Keras 2.1.5. Additionally, to visually display which part of the heart the DCNN-based models were focused on, gradient-weighted class activation mapping (grad-CAM) analysis was performed (27).

Statistical Analysis

For comparisons of the baseline characteristics between patients with positive and negative genotype, Fisher's exact test, Student's *t*-test, or chi-squared test was used, as appropriate. The following steps were taken to compare the area under the receiver operating characteristics curve (AUC) of one of the reference models (i.e., the Mayo score or the Toronto score) and that of a

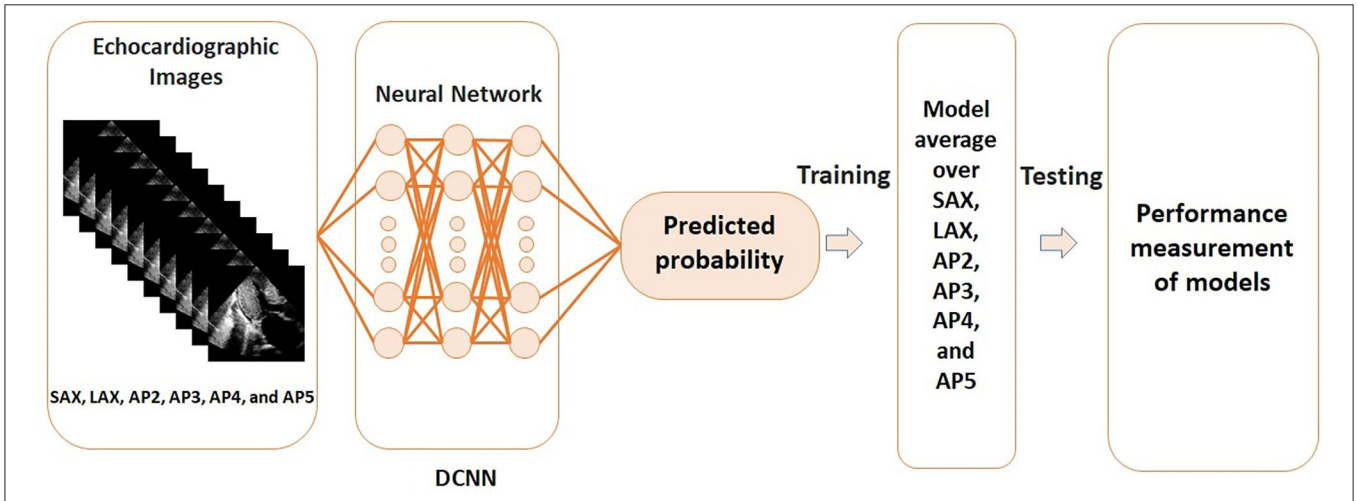

FIGURE 1 | Steps of the deep convoluted neural network analysis using echocardiographic images. DCNN, deep convoluted neural network; AP2, apical 2-chamber view; AP3, apical 3-chamber view; AP4, apical 4-chamber view; AP5, apical 5-chamber view; LAX, parasternal long-axis view; SAX, parasternal short-axis view.

TABLE 1 | Baseline clinical characteristics of the study sample.

Characteristics*	Genotype		*P*-value
	Positive *n* = 45	Negative *n* = 54	
Demographics			
Age (year)	40 ± 17	55 ± 22	<0.001
Female	17 (38)	18 (33)	0.80
NYHA functional class	1 [1–2]	1 [1–2]	0.70
Race/ethnicity			0.77
Caucasian	36 (80)	46 (85)	
African-American	1 (2)	2 (4)	
Asian	1 (2)	0 (0)	
Other or unidentified	7 (16)	6 (11)	
Medical history			
Prior AF	26 (58)	29 (54)	0.83
Prior sustained VT/VF	8 (18)	3 (6)	0.10
Prior non-sustained VT	13 (29)	9 (17)	0.49
Prior syncope	9 (20)	6 (11)	0.34
Family history of sudden cardiac death	10 (22)	7 (16)	0.34
Family history of HCM	21 (47)	6 (13)	<0.001
Medications			
β-blocker	26 (58)	29 (54)	0.83
Calcium channel blocker	11 (24)	21 (39)	0.19
ACE inhibitor	2 (4)	8 (15)	0.10
ARB	1 (2)	10 (19)	0.02
Diuretic			
Loop diuretic	4 (9)	7 (13)	0.74
Thiazide	1 (2)	11 (20)	0.01
Potassium-sparing diuretic	1 (2)	7 (13)	0.07
Disopyramide	17 (38)	5 (9)	0.001
Amiodarone	2 (4)	4 (2)	0.69
Echocardiographic measurements			
Left atrial diameter (mm)	43 ± 8	44 ± 8	0.65
Systolic blood pressure (mmHg)	117 ± 17	129 ± 19	0.001
Diastolic blood pressure (mmHg)	71 ± 10	74 ± 11	0.17
Interventricular septum thickness (mm)	19 ± 5	18 ± 5	0.38
Posterior wall thickness (mm)	12 ± 3	13 ± 3	0.08
Left ventricular outflow tract gradient (mmHg) at rest	18 [0–25]	26 [0–40]	0.18
Left ventricular outflow tract gradient (mmHg) with Valsalva maneuver	35 [0–51]	38 [0–64]	0.79
Left ventricular ejection fraction (%)	60 ± 10	60 ± 12	0.97
Left ventricular end-diastolic diameter (mm)	43 ± 7	44 ± 9	0.65
Left ventricular end-systolic diameter (mm)	29 ± 7	28 ± 9	0.80
Systolic anterior motion of mitral valve leaflet	24 (53)	29 (54)	>0.99
Degree of mitral regurgitation†	1 [1–2]	1 [1–2]	0.67
Genotype			–
MYBPC3	20 (44)	–	
MYH7	12 (27)	–	
TNNT2	5 (11)	–	
MYL2	3 (7)	–	
ACTN2	1 (2)	–	
THBD	1 (2)	–	
Multiple	1 (2)	–	
Other	2 (4)	–	

(Continued)

TABLE 1 | Continued

Characteristics*	Genotype		*P*-value
	Positive *n* = 45	Negative *n* = 54	
Predictors of positive genotype			
Age at diagnosis	34 ± 17	49 ± 21	<0.001
Reverse septal contour	21 (47)	13 (24)	0.03
Maximal left ventricular wall thickness	19 ± 5	18 ± 5	0.38
Hypertension	26 (58)	34 (63)	0.74
Ratio of maximal wall thickness to posterior wall thickness			0.03
<1.46	16 (36)	33 (61)	
1.47–1.70	13 (29)	9 (17)	
1.71–1.92	9 (20)	5 (9)	
1.93–2.26	4 (9)	4 (7)	
>2.27	3 (7)	3 (6)	

**Data were expressed as number (percentage), mean ± standard deviation, or median [interquartile range].*
† Degree of mitral regurgitation was converted to numerical values according to the following rule: none = 0, trace = 1, trace to mild = 1.5, mild = 2, mild to moderate = 2.5, moderate = 3, moderate to severe = 3.5, severe = 4.
ACE, angiotensin converting enzyme; AF, atrial fibrillation; ARB, angiotensin II receptor blocker; HCM, hypertrophic cardiomyopathy; NYHA, New York Heart Association; VT/VF, ventricular tachycardia or ventricular fibrillation.

TABLE 2 | Predictive performance of Mayo score and a new model combining Mayo score and deep convolutional neural network-based probability to predict positive genotype in patients with hypertrophic cardiomyopathy.

Prediction model	AUC	*P*-value*	NRI†	*P*-value†	Sensitivity (%)	Specificity (%)	PPV (%)	NPV (%)
Mayo score (reference)	0.72 (0.61–0.82)	Reference	Reference	Reference	71 (56–84)	81 (69–91)	76 (61–87)	77 (63–88)
Mayo score + DCNN	0.86 (0.79–0.93)	<0.001	0.71 (0.30–1.24)	<0.001	71 (56–84)	81 (69–91)	76 (61–87)	77 (63–88)

**P-value was calculated to compare AUC of the reference model with that of the combined model.*
† Continuous NRI and associated p-values were displayed.
AUC, area under the receiver-operating-characteristic curve; DCNN, deep convoluted neural network; NPV, negative predictive value; NRI, net reclassification improvement; PPV, positive predictive value.

new model combining the reference model with the DCNN-derived model. First, logistic regression model was constructed to estimate the coefficient values and the constant to combine the reference model and the DCNN-derived probability. Second, the AUC of the reference model and that of the combined model were compared using non-parametric receiver operating characteristic estimation with 1,000 bootstrapping. The Stata command *rocreg* with *auc* option was used to perform this step. Additionally, the net reclassification improvement was examined using the Stata command *incrisk*. The sensitivity, specificity, positive predictive value (PPV), and negative predictive value (NPV) were also calculated. Statistical significance was declared if the 2-sided *p*-value was <0.05. These analyses were performed using Stata Statistical Software: Release 12 (StataCorp LP, College Station, TX).

RESULTS

Initially, 105 patients with HCM who underwent genetic testing and had at least 1 echocardiographic study were screened. In this cohort, six patients were excluded based on the exclusion criteria. The most common reasons for exclusion were prior septal reduction therapy and prior heart transplant. As a result, 99 patients were included in the analysis. A total of 45 (45%) patients had positive genotype. This proportion is similar to what has been reported in the literature (6). Baseline patient characteristics are shown in **Table 1**. Patients with positive genotype were younger and more likely to have family history of HCM as well as reverse septal contour, and had lower systolic blood pressure.

The DCNN-predicted probability showed the AUC of 0.76 (95% CI 0.66–0.86). The AUC of the Mayo score was 0.72 (95% CI 0.61–0.82). **Table 2** summarizes the net reclassification improvement, sensitivity, specificity, PPV, and NPV using the Mayo score as the reference model. The new model combining the Mayo score with the DCNN-predicted probability significantly improved the predictive accuracy compared to the Mayo score (AUC = 0.86; 95% CI 0.79–0.93; $p < 0.001$; **Figure 2**). There was also a significant net reclassification improvement (**Table 2**), indicating that a larger number of patients were reclassified in the right direction compared to the number of patients who were reclassified in the wrong direction. The coefficients and constant to construct the combined model are

shown in **Supplementary Results**. The sensitivity analysis after excluding patients with variant of uncertain significance showed similar findings; the AUC of the Mayo score was 0.73, whereas that of the combined model was 0.87 ($p = 0.0002$).

When the Toronto score was used as the reference model, the AUC was 0.75 (95% CI 0.65–0.85; **Table 3**). The new model combining the Toronto score with the DCNN-predicted probability exhibited significant improvement in the AUC compared to the Toronto score alone (AUC 0.84, 95% CI 0.76–0.92, $p = 0.03$; **Figure 2**). A significant net reclassification improvement was also achieved along with improvement in the sensitivity, specificity, PPV, and NPV (**Table 3**). After excluding patients with variant of uncertain significance, the AUC of the Toronto score was 0.74 and that of the combined model was 0.85 ($p = 0.01$).

To improve the interpretability of DCNN models, representative visualizations generated by grad-CAM are shown in **Figure 3**. This visualization method revealed that the DCNN-based models applied a large weight on the LV walls (e.g., the interventricular septum and posterior wall) and the left atrium.

DISCUSSION

Summary of Findings

In this study that examined the incremental value of deep learning-based models to predict positive genotype, the predictive ability of our novel models combining the conventional model and the deep learning-based probability significantly outperformed that of the conventional models. The present study serves as the first investigation demonstrating the additional value of deep learning-based analysis of echocardiographic images in predicting positive genotype in patients with HCM.

Impact of Positive Genotype on Family Screening, Diagnosis, and Prognostication

Genetic testing is useful in determining family screening strategies in HCM. Without genetic testing, first-degree relatives have to undergo phenotypic screening with electrocardiogram and echocardiography every 5 years, and more frequently if the age is <18 years (3, 5). This burden can be relieved if the proband has positive genotype and the family member does not carry the identified gene mutation (3, 5). Furthermore, genetic testing has both diagnostic and prognostic values. In patients with suspected HCM, positive genotype confirms the diagnosis of HCM (2). With regard to prognostication, patients with positive genotype had a 2-fold higher risk of adverse outcomes (e.g., heart failure, atrial fibrillation) compared to those with negative phenotype in a prospective cohort study of patients with HCM (6). Thus, positive genotype can have a substantial impact on the clinical management of patients with HCM and their family members.

On the other hand, genetic testing can carry substantial financial and social burdens. For example, genetic testing costs a few thousand dollars in the US, and the proportion of the patient's out-of-pocket payment depends on the insurance type and plan. With regard to the social burden of genetic testing, while the Genetic Information Non-discrimination Act prohibits

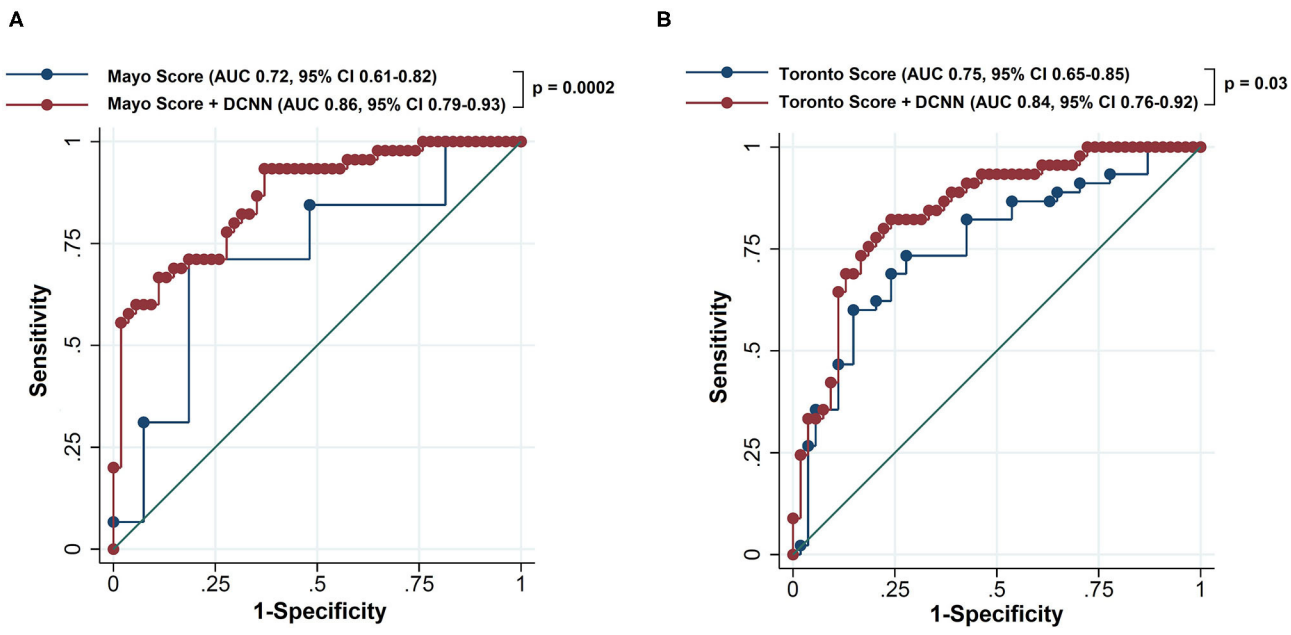

FIGURE 2 | Receiver operating characteristics curve of the reference scoring system and new model combining the reference scoring system and deep convolutional neural network-based probability to predict positive genotype in patients with hypertrophic cardiomyopathy. The reference scoring system was the Mayo score in **(A)** and the Toronto score in **(B)**. The dots represent different threshold levels. DCNN, deep convoluted neural network; AUC, area under the receiver operating characteristic curve; CI, confidence interval.

TABLE 3 | Predictive performance of Toronto score and a new model combining Toronto score and deep convolutional neural network-based probability to predict positive genotype in patients with hypertrophic cardiomyopathy.

Prediction model	AUC	*P*-value*	NRI†	*P*-value†	Sensitivity (%)	Specificity (%)	PPV (%)	NPV (%)
Toronto score (reference)	0.75 (0.65–0.85)	Reference	Reference	Reference	73 (58–85)	72 (58–84)	69 (54–82)	76 (62–86)
Toronto score + DCNN	0.84 (0.76–0.92)	0.03	0.64 (0.34–1.22)	<0.001	80 (65–90)	78 (64–88)	75 (61–88)	82 (69–91)

**P-value was calculated to compare AUC of the reference model with that of the combined model.*
† Continuous NRI and associated p-values were displayed.
AUC, area under the receiver-operating-characteristic curve; DCNN, deep convoluted neural network; NPV, negative predictive values; NRI, net reclassification improvement; PPV, positive predictive value.

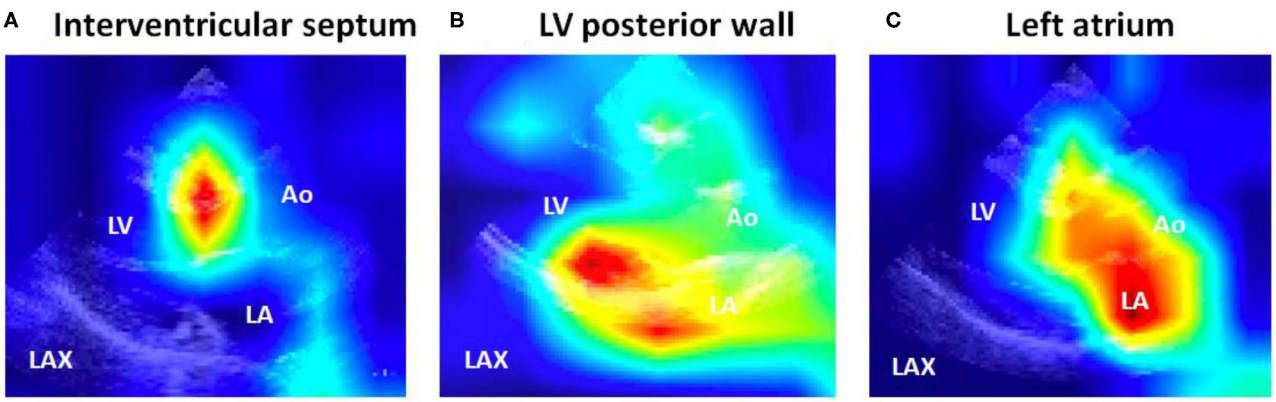

FIGURE 3 | Spatial display of important features detected by the deep convoluted neural network analysis models. Note that the important features were localized to **(A)** the interventricular septum, **(B)** the LV posterior wall, and **(C)** the left atrium. Ao, aorta; LA, left atrium; LAX: parasternal long-axis view; LV, left ventricular/ventricle.

discrimination of insurability based on genetic testing results, the law is silent regarding life, disability, and long-term care insurance (9, 28, 29). As such, genetic testing can result in non-negligible burdens, and accurate identification of patients with HCM who have high pre-test probability carries clinical, socio-economical, and psychological importance.

Nevertheless, the currently available conventional models—i.e., the Mayo score, the Toronto score—offer only modest ability to predict positive genotype. The AUCs of these scoring systems have been reported to be ∼0.75 (11–15), which is in agreement with those in the present study (0.72 with the Mayo score and 0.75 with the Toronto score). In this context, findings in the current analysis add to the body of knowledge by demonstrating that the deep learning-based analysis of echocardiographic images provides incremental value to the conventional models in predicting positive genotype in patients with HCM.

Advantages of Deep Learning-Based Approach Over the Conventional Prediction Methods

The Mayo and Toronto scoring systems include a limited number of parameters determined by echocardiography—e.g., maximal LV wall thickness, septal morphological subtypes. However, these parameters have been known to have large intra- and inter-observer variability (11, 30). It is a time- and cost-intensive process to train physicians until they can accurately measure the wall thickness and classify the septal morphology (31). Even after going through such specialized trainings, the interpretation of echocardiographic images still remains interpreter-dependent and subjective, and can be affected by fatigue (31). Moreover, these parameters used in the conventional models do not account for dynamic (i.e., non-static) image information.

By contrast, deep learning has a potential to overcome such variability in human assessment of echocardiographic measurements (32). Deep learning is also able to extract information that is not readily apparent to humans (33). Thus, deep learning-based models can offer a new avenue to generate an accurate, consistent, rapid, and automated interpretation of echocardiographic images while reducing the risk of human errors. Its application has shown a high potential to revolutionize the process of diagnosis and prognostication, with promising results in the fields of dermatology (34), radiology (35), and cardiology (16, 36). In the HCM population, a prior study reported that a deep learning-derived classification model using echocardiographic images can differentiate HCM from cardiac amyloidosis and pulmonary arterial hypertension (22). Furthermore, our DCNN approach utilizes not only spatial but also temporal information by incorporating the additional dimension of time.

Despite the potential usefulness, no prior studies have applied deep learning-based methods to predict positive genotype in HCM. The present analysis represents the first study to

exhibit the incremental value of deep learning-based analysis of echocardiographic images in addition to the conventional clinical parameters to predict positive genotype in the HCM population. The ability of our deep learning-based approach to analyze echocardiographic images obtained in routine clinical care—as opposed to "research-quality" images gained for investigational purposes—further underscores the feasibility and generalizability of this novel method.

Spatial Visualization of Important Features to Identify Genotype-Positive Patients

Deep learning technology is frequently referred to as a black box—i.e., it does not provide information as to which features are mainly used for the development of discrimination models. Our deep learning method is not an exception. To address this issue, in the present study, we have performed the grad-CAM analysis and provided visualization of the important features that the deep learning models focused on, which greatly enhances the interpretability (27). This analysis demonstrated an interesting finding—in addition to the LV, features spatially located in the left atrium were frequently used to distinguish between patients with positive and negative genotype in HCM. This observation is consistent with our prior knowledge; the left atrial diameter has been known to predict sudden cardiac death (37) and cardiovascular death in the HCM population (38). The inferences from our study suggest that echocardiographic parameters related to the left atrium—e.g., left atrial diameter, volume, and ejection fraction—have a potential to predict positive genotype in the HCM population.

Potential Limitations

Findings in the present study should be interpreted with several limitations in mind. First, the present study is subject to selection bias. The study sample was limited to patients with HCM who underwent genetic testing. Second, positive genotype was defined by the currently available classification of mutations; however, the classification of each mutation can change in the future. Third, validation with external samples was not performed. This study should prompt model validation with a new cohort. Last, the study samples were relatively homogeneous in terms of race and sex. Further, there is a possibility that the spectrum of mutations observed in the study samples may not exactly represent those in the general HCM population. Therefore, generalizability of the results to other HCM populations (e.g., those who are not followed at HCM referral centers) needs to be established.

Conclusions

Compared to the conventional models based on clinical and echocardiographic parameters, our new models integrating the conventional and deep learning-based analysis of echocardiographic images demonstrated a superior ability to predict positive genotype in patients with HCM. For patients and treating physicians, the novel deep learning-based method introduced in the present study can be used as an assistive technology to inform the decision-making process of performing genetic testing; deep learning coupled to human expertise can provide more accurate pre-test probability. For researchers, the current analysis would prompt further investigation into developing a better deep learning model to predict positive genotype in patients with HCM.

DATA AVAILABILITY STATEMENT

The original contributions presented in the study are included in the article/**Supplementary Materials**. Further inquiries can be directed to the corresponding author.

ETHICS STATEMENT

The studies involving human participants were reviewed and approved by the institutional review boards of Columbia University Irving Medical Center and Tokushima University Hospital. The patients/participants provided their written informed consent to participate in this study.

AUTHOR CONTRIBUTIONS

SM wrote the manuscript. KK and YS conceived the idea for the manuscript. KK and AH performed the deep learning analyses of echocardiographic images. YS was guarantor and performed the statistical analyses. SM and YS contributed to data acquisition. MS, KH, YR, MR, MF, MM, and YS contributed to interpreting the data and revising the work critically for intellectual content. All authors made the decision to submit.

FUNDING

YS was supported by research grants from the National Institute of Health (Bethesda, MD; R01 HL157216), American Heart Association (Dallas, TX) National Clinical and Population Research Awards and Career Development Award, The Feldstein Medical Foundation (Clifton, NJ) Medical Research Grant, Korea Institute of Oriental Medicine (Daejeon, Republic of Korea), and Columbia University Irving Medical Center Irving Institute for Clinical & Translational Research (New York, NY) Precision Medicine Pilot Award. MM was supported by the National Institute of Health (K24 AG036778). MR was supported by the National Institute of Health (UL1 TR001873 and K24 HL107643). The funding organizations did not have any role in the study design, collection, analysis, or interpretation of data, in writing of the manuscript, or in the decision to submit the article for publication. The researchers were independent from the funding organizations.

SUPPLEMENTARY MATERIAL

The Supplementary Material for this article can be found online at: https://www.frontiersin.org/articles/10.3389/fcvm.2021.669860/full#supplementary-material

REFERENCES

1. Maron BJ. Clinical course and management of hypertrophic cardiomyopathy. *N Engl J Med.* (2018) 379:655–68. doi: 10.1056/NEJMra1710575
2. Seidman CE, Seidman JG. Identifying sarcomere gene mutations in hypertrophic cardiomyopathy: a personal history. *Circ Res.* (2011) 108:743–50. doi: 10.1161/CIRCRESAHA.110.223834
3. Ommen SR, Mital S, Burke MA, Day SM, Deswal A, Elliott P, et al. 2020 AHA/ACC Guideline for the diagnosis and treatment of patients with hypertrophic cardiomyopathy. *Circulation.* (2020) 142:e558–631. doi: 10.1161/CIR.0000000000000937
4. Elliott PM, Anastasakis A, Borger MA, Borggrefe M, Cecchi F, Charron P, et al. 2014 ESC Guidelines on diagnosis and management of hypertrophic cardiomyopathy. *Eur Heart J.* (2014) 35:2733–79. doi: 10.1093/eurheartj/ehu284
5. Veselka J, Anavekar NS, Charron P. Hypertrophic obstructive cardiomyopathy. *Lancet.* (2017) 389:1253–67. doi: 10.1016/S0140-6736(16)31321-6
6. Ho CY, Day SM, Ashley EA, Michels M, Pereira AC, Jacoby D, et al. Genotype and lifetime burden of disease in hypertrophic cardiomyopathy: insights from the Sarcomeric Human Cardiomyopathy Registry (SHaRe). *Circulation.* (2018) 138:1387–98.
7. Andersen PS, Havndrup O, Hougs L, Sorensen KM, Jensen M, Larsen LA, et al. Diagnostic yield, interpretation, and clinical utility of mutation screening of sarcomere encoding genes in Danish hypertrophic cardiomyopathy patients and relatives. *Hum Mutat.* (2009) 30:363–70. doi: 10.1002/humu.20862
8. Hoss S, Habib M, Silver J, Care M, Chan RH, Hanneman K, et al. Genetic testing for diagnosis of hypertrophic cardiomyopathy mimics: yield and clinical significance. *Circ Genom Precis Med.* (2020) 13:e002748. doi: 10.1161/CIRCGEN.119.002748
9. Mohammed S, Lim Z, Dean PH, Potts JE, Tang JN, Etheridge SP, et al. Genetic insurance discrimination in sudden arrhythmia death syndromes: Empirical evidence from a cross-sectional survey in North America. *Circ Cardiovasc Genet.* (2017) 10:e001442. doi: 10.1161/CIRCGENETICS.116.001442
10. Wynn J, Holland DT, Duong J, Ahimaz P, Chung WK. Examining the psychosocial impact of genetic testing for cardiomyopathies. *J Genet Couns.* (2018) 27:927–34. doi: 10.1007/s10897-017-0186-4
11. Bos JM, Will ML, Gersh BJ, Kruisselbrink TM, Ommen SR, Ackerman MJ. Characterization of a phenotype-based genetic test prediction score for unrelated patients with hypertrophic cardiomyopathy. *Mayo Clin Proc.* (2014) 89:727–37. doi: 10.1016/j.mayocp.2014.01.025
12. Gruner C, Ivanov J, Care M, Williams L, Moravsky G, Yang H, et al. Toronto hypertrophic cardiomyopathy genotype score for prediction of a positive genotype in hypertrophic cardiomyopathy. *Circ Cardiovasc Genet.* (2013) 6:19–26. doi: 10.1161/CIRCGENETICS.112.963363
13. Bonaventura J, Norambuena P, Tomasov P, Jindrova D, Sediva H, Macek M, et al., et al. The utility of the Mayo Score for predicting the yield of genetic testing in patients with hypertrophic cardiomyopathy. *Arch Med Sci.* (2019) 15:641–9. doi: 10.5114/aoms.2018.78767
14. Murphy SL, Anderson JH, Kapplinger JD, Kruisselbrink TM, Gersh BJ, Ommen SR, et al. Evaluation of the Mayo Clinic Phenotype-Based Genotype Predictor Score in patients with clinically diagnosed hypertrophic cardiomyopathy. *J Cardiovasc Transl Res.* (2016) 9:153–61. doi: 10.1007/s12265-016-9681-5
15. Newman R, Jefferies JL, Chin C, He H, Shikany A, Miller EM, et al. Hypertrophic cardiomyopathy genotype prediction models in a pediatric population. *Pediatr Cardiol.* (2018) 39:709–17. doi: 10.1007/s00246-018-1810-2
16. Kusunose K, Haga A, Inoue M, Fukuda D, Yamada H, Sata M. Clinically feasible and accurate view classification of echocardiographic images using deep learning. *Biomolecules.* (2020) 10. doi: 10.3390/biom10050665
17. Nagendran M, Chen Y, Lovejoy CA, Gordon AC, Komorowski M, Harvey H, et al. Artificial intelligence versus clinicians: systematic review of design, reporting standards, and claims of deep learning studies. *BMJ.* (2020) 368:m689. doi: 10.1136/bmj.m689
18. Xu B, Kocyigit D, Grimm R, Griffin BP, Cheng F. Applications of artificial intelligence in multimodality cardiovascular imaging: a state-of-the-art review. *Prog Cardiovasc Dis.* (2020) 63:367–76. doi: 10.1016/j.pcad.2020.03.003
19. Kusunose K, Haga A, Abe T, Sata M. Utilization of artificial intelligence in echocardiography. *Circ J.* (2019) 83:1623–29. doi: 10.1253/circj.CJ-19-0420
20. Kusunose K, Abe T, Haga A, Fukuda D, Yamada H, Harada M, et al. A deep learning approach for assessment of regional wall motion abnormality from echocardiographic images. *J Am Coll Cardiol Img.* (2020) 13:374–81. doi: 10.1016/j.jcmg.2019.02.024
21. Davis A, Billick K, Horton K, Jankowski M, Knoll P, Marshall JE, et al. Artificial intelligence and echocardiography: a primer for cardiac sonographers. *J Am Soc Echocardiogr. J Am Soc Echocardiogr.* (2020) 33:1061–6. doi: 10.1016/j.echo.2020.04.025
22. Zhang J, Gajjala S, Agrawal P, Tison GH, Hallock LA, Beussink-Nelson L, et al. Fully automated echocardiogram interpretation in clinical practice. *Circulation.* (2018) 138:1623–35. doi: 10.1161/CIRCULATIONAHA.118.034338
23. Shimada YJ, Hasegawa K, Kochav SM, Mohajer P, Jung J, Maurer MS, et al. Application of proteomics profiling for biomarker discovery in hypertrophic cardiomyopathy. *J Cardiovasc Transl Res.* (2019) 12:569–79. doi: 10.1007/s12265-019-09896-z
24. Shimada YJ, Hoeger CW, Latif F, Takayama H, Ginns J, Maurer MS. Myocardial contraction fraction predicts cardiovascular events in patients with hypertrophic cardiomyopathy and normal ejection fraction. *J Card Fail.* (2019) 25:450–6. doi: 10.1016/j.cardfail.2019.03.016
25. Mitchell C, Rahko PS, Blauwet LA, Canaday B, Finstuen JA, Foster MC, et al. Guidelines for performing a comprehensive transthoracic echocardiographic examination in adults: recommendations from the American Society of Echocardiography. *J Am Soc Echocardiogr.* (2019) 32:1–64. doi: 10.1016/j.echo.2018.06.004
26. Kusunose K, Haga A, Yamaguchi N, Abe T, Fukuda D, Yamada H, et al. Deep learning for assessment of left ventricular ejection fraction from echocardiographic images. *J Am Soc Echocardiogr.* (2020) 33:632–5el. doi: 10.1016/j.echo.2020.01.009
27. Selvaraju RR, Cogswell M, Das A, Vedantam R, Parikh D, Batra D. Grad-CAM: visual explanations from deep networks via gradient-based localization. *IEEE I Conf Comp Vis.* (2017) 618–26. doi: 10.1109/ICCV.2017.74
28. Christiaans I, Kok TM, van Langen IM, Birnie E, Bonsel GJ, Wilde AA, et al. Obtaining insurance after DNA diagnostics: a survey among hypertrophic cardiomyopathy mutation carriers. *Eur J Hum Genet.* (2010) 18:251–3. doi: 10.1038/ejhg.2009.145
29. Prince AER. Political economy, stakeholder voices, and saliency: lessons from international policies regulating insurer use of genetic information. *J Law Biosci.* (2018) 5:461–94. doi: 10.1093/jlb/lsz001
30. Urbano-Moral JA, Gonzalez-Gonzalez AM, Maldonado G, Gutierrez-Garcia-Moreno L, Vivancos-Delgado R, De Mora-Martin M, et al. Contrast-enhanced echocardiographic measurement of left ventricular wall thickness in hypertrophic cardiomyopathy: comparison with standard echocardiography and cardiac magnetic resonance. *J Am Soc Echocardiogr.* (2020) 33:1106–15. doi: 10.1016/j.echo.2020.04.009
31. Krittanawong C, Johnson KW, Rosenson RS, Wang Z, Aydar M, Baber U, et al. Deep learning for cardiovascular medicine: a practical primer. *Eur Heart J.* (2019) 40:2058–73. doi: 10.1093/eurheartj/ehz056
32. Ouyang D, He B, Ghorbani A, Yuan N, Ebinger J, Langlotz CP, et al. Video-based AI for beat-to-beat assessment of cardiac function. *Nature.* (2020) 580:252–6. doi: 10.1038/s41586-020-2145-8
33. Kusunose K. Radiomics in echocardiography: deep learning and echocardiographic analysis. *Curr Cardiol Rep.* (2020) 22:89. doi: 10.1007/s11886-020-01348-4
34. Haenssle HA, Fink C, Schneiderbauer R, Toberer F, Buhl T, Blum A, et al. Man against machine: diagnostic performance of a deep learning convolutional neural network for dermoscopic melanoma recognition in comparison to 58 dermatologists. *Ann Oncol.* (2018) 29:1836–42. doi: 10.1093/annonc/mdy166
35. Ueda D, Shimazaki A, Miki Y. Technical and clinical overview of deep learning in radiology. *Jpn J Radiol.* (2019) 37:15–33. doi: 10.1007/s11604-018-0795-3

36. Litjens G, Ciompi F, Wolterink JM, de Vos BD, Leiner T, Teuwen J, et al. State-of-the-art deep learning in cardiovascular image analysis. *J Am Coll Cardiol Img.* (2019) 12:1549–65. doi: 10.1016/j.jcmg.2019.06.009
37. O'Mahony C, Jichi F, Pavlou M, Monserrat L, Anastasakis A, Rapezzi C, et al. A novel clinical risk prediction model for sudden cardiac death in hypertrophic cardiomyopathy (HCM risk-SCD). *Eur Heart J.* (2014) 35:2010–20. doi: 10.1093/eurheartj/eht439
38. Liu Q, Li D, Berger AE, Johns RA, Gao L. Survival and prognostic factors in hypertrophic cardiomyopathy: a meta-analysis. *Sci Rep.* (2017) 7:11957. doi: 10.1038/s41598-017-12289-4

Conflict of Interest: The authors declare that the research was conducted in the absence of any commercial or financial relationships that could be construed as a potential conflict of interest.

frontiers in Cardiovascular Medicine

ORIGINAL RESEARCH
published: 07 September 2021
doi: 10.3389/fcvm.2021.717114

Long-Term Clinical Outcomes in Patients With an Acute ST-Segment-Elevation Myocardial Infarction Stratified by Angiography-Derived Index of Microcirculatory Resistance

Rafail A. Kotronias[1], Dimitrios Terentes-Printzios[1], Mayooran Shanmuganathan[1,2], Federico Marin[1], Roberto Scarsini[1,3], James Bradley-Watson[1], Jeremy P. Langrish[1], Andrew J. Lucking[1], Robin Choudhury[1], Rajesh K. Kharbanda[1], Hector M. Garcia-Garcia[4], Keith M. Channon[1], Adrian P. Banning[1] and Giovanni Luigi De Maria[1] On behalf of Oxford Acute Myocardial Infarction (OxAMI) Study investigators*

[1] Oxford Heart Centre, NIHR Biomedical Research Centre, Oxford University Hospitals, Oxford, United Kingdom, [2] OCMR, Radcliffe Department of Medicine, University of Oxford, Oxford, United Kingdom, [3] Division of Cardiology, Department of Medicine, University of Verona, Verona, Italy, [4] MedStar Washington Hospital Centre, Washington, DC, United States

OPEN ACCESS

Edited by:
Jolanda Wentzel,
Erasmus Medical Centre, Netherlands

Reviewed by:
Emmanuel Androulakis,
Royal Brompton and Harefield NHS Foundation Trust, United Kingdom
Grigorios M. Chatzantonis,
University Hospital Münster, Germany

***Correspondence:**
Giovanni Luigi De Maria
Giovanniluigi.Demaria@ouh.nhs.uk

Specialty section:
This article was submitted to Cardiovascular Imaging, a section of the journal Frontiers in Cardiovascular Medicine

Received: 30 May 2021
Accepted: 02 August 2021
Published: 07 September 2021

Citation:
Kotronias RA, Terentes-Printzios D, Shanmuganathan M, Marin F, Scarsini R, Bradley-Watson J, Langrish JP, Lucking AJ, Choudhury R, Kharbanda RK, Garcia-Garcia HM, Channon KM, Banning AP and De Maria GL (2021) Long-Term Clinical Outcomes in Patients With an Acute ST-Segment-Elevation Myocardial Infarction Stratified by Angiography-Derived Index of Microcirculatory Resistance. Front. Cardiovasc. Med. 8:717114. doi: 10.3389/fcvm.2021.717114

Aims: Despite the prognostic value of coronary microvascular dysfunction (CMD) in patients with ST-segment-elevation myocardial infarction (STEMI), its assessment with pressure-wire-based methods remains limited due to cost, technical and procedural complexities. The non-hyperaemic angiography-derived index of microcirculatory resistance (NH IMR_{angio}) has been shown to reliably predict microvascular injury in patients with STEMI. We investigated the prognostic potential of NH IMR_{angio} as a pressure-wire and adenosine-free tool.

Methods and Results: NH IMR_{angio} was retrospectively derived on the infarct-related artery at completion of primary percutaneous coronary intervention (pPCI) in 262 prospectively recruited STEMI patients. Invasive pressure-wire-based assessment of the index of microcirculatory resistance (IMR) was performed. The combination of all-cause mortality, resuscitated cardiac arrest and new heart failure was the primary endpoint. NH IMR_{angio} showed good diagnostic performance in identifying CMD (IMR $>$ 40U); AUC 0.78 (95%CI: 0.72–0.84, $p < 0.0001$) with an optimal cut-off at 43U. The primary endpoint occurred in 38 (16%) patients at a median follow-up of 4.2 (2.0–6.5) years. On survival analysis, NH IMR_{angio} $>$ 43U (log-rank test, $p < 0.001$) was equivalent to an IMR $>$ 40U(log-rank test, $p = 0.02$) in predicting the primary endpoint (hazard ratio comparison $p = 0.91$). NH IMRangio $>$ 43U was an independent predictor of the primary endpoint (adjusted HR 2.13, 95% CI: 1.01–4.48, $p = 0.047$).

Conclusion: NH IMR_{angio} is prognostically equivalent to invasively measured IMR and can be a feasible alternative to IMR for risk stratification in patients presenting with STEMI.

Keywords: STEMI, NH IMRangio, IMR, prognosis, coronary angiography, coronary physiology

INTRODUCTION

Coronary microvascular dysfunction in patients admitted with ST-segment-elevation myocardial infarction (STEMI) is biologically (1) and prognostically relevant (2, 3). An early assessment of CMD in the catheterisation laboratory is desirable to triage additional therapies and/or plan *ad-hoc* clinical care strategies. This can be achieved by measuring the index of microvascular resistance (IMR) with a conventional pressure-wire and thermodilution technique (4). Our group and others have previously shown the good diagnostic performance of IMR in predicting microvascular injury diagnosed by cardiac magnetic resonance (CMR) imaging (1, 5). Contemporary studies highlight the early- and long-term prognostic implications of an IMR > 40U in patients with STEMI (6, 7). Recently, IMR has also been proposed as a tool to triage novel or additional therapies in STEMI, with promising clinical and research implications (8, 9).

Despite its proposed role as a prognostic biomarker (9) the clinical adoption of IMR remains limited. Additional cost, procedural time, an extra—though small—procedural risk associated with the manipulation of a pressure wire in the infarct related artery (IRA) and patient discomfort due to intravenous adenosine infusion, are amongst some of the barriers to its widespread use. The recent development and application of computational flow dynamics to three-dimensional modeling of the coronary artery represents an excellent opportunity to derive angiographic indices of coronary physiology (such as fractional flow reserve (FFR) or IMR) avoiding the use of a pressure wire (10). Our group has recently described a novel, angiography-derived, pressure-wire free index of microcirculatory resistance (IMR_{angio}) (11). This index showed a good diagnostic performance in predicting an invasive IMR > 40U in patients with STEMI. Whilst IMR_{angio} accurately diagnoses CMD in patients with STEMI, it would be desirable to have an adenosine free angiographic index of CMD. It is reported that in most patients with STEMI the vasodilatory capacity of the microvascular coronary bed is blunted and consequently the response of coronary microcirculation to adenosine is often minimal or incomplete. (12, 13). In this regard, we have recently described the non-hyperaemic version of IMR_{angio}–NH IMR_{angio}, and shown it retains its diagnostic reliability in most patients with STEMI (14). Thus, we hypothesized that NH IMR_{angio} would provide similar prognostic information to invasively-measured IMR.

The aim of this work was to evaluate the prognostic performance of NH IMR_{angio} in patients with STEMI.

METHODS

Patient Population

Patients with a diagnosis of STEMI presenting between January 2010 and March 2020 with STEMI at the Oxford Heart Centre were enrolled in the prospective OxAMI (Oxford Acute Myocardial Infarction) cohort study (15). The current study is based on prospectively enrolled participants who had pressure-wire based IMR measurements, unless they met any specific exclusion criteria for enrolment (**Supplementary Material**, **Supplementary Figure 1**). This analysis includes all participants on whom both invasive IMR measurement and angiography-derived coronary physiology assessment was possible.

Primary percutaneous coronary intervention (pPCI) was performed in standard fashion with the use of adjunctive therapies (manual thrombectomy, glycoprotein IIb/IIIa) and choice of stenting technique at the operator's discretion. ST-segment resolution was calculated using surface electrocardiography acquired before and at 90 min after pPCI as described previously (16), and defined as complete if ≥70%. Post-pPCI left ventricular ejection fraction (LVEF) was derived from echocardiogram performed prior to hospital discharge.

The study protocol was approved by the local ethics committee (10/H0408/24) and conducted in accordance with the Declaration of Helsinki.

Non-hyperaemic IMR_{angio} Measurement

The methodology for the derivation of NH IMR_{angio} and its reproducibility have been published previously (14). According to the published methodology, we measured NH IMR_{angio} on the IRA, using two dedicated coronary angiographic projections acquired at the end of the pPCI procedure. Angiographic views were acquired at resting conditions (not during adenosine intravenous infusion). In brief, three-dimensional quantitative coronary angiography and quantitative flow ratio (QFR) analyses were performed using QAngio® XA 3D software (Medis, Leiden, the Netherlands). NH IMR_{angio} was computed using the following formula:

$$NH\ IMRangio = Pa(resting) \times QFR \times \frac{Nframes}{fps}$$

where *Pa* was the post PCI mean aortic pressure at resting conditions, *Nframes* was the number of angiographic frames from contrast dye to travel from the guiding catheter to a distal reference (placed at the distal third of the IRA) in resting conditions and fps was the frame-acquisition rate (**Figure 1**).

All analyses were performed at the OxACT core lab (University of Oxford, Oxford Heart Centre, Oxford, UK) by independent operators blinded to physiology and clinical outcome data.

Invasive Measurement of Coronary Physiology Indices

Invasive assessment of coronary physiology indices on the IRA was performed with pressure-wire technology (Pressure Wire X, Abbott, California, US or Certus, St. Jude Medical, Minnesota, US) and thermodilution technique at the end of the pPCI as previously reported (**Supplementary Material**) (15). We routinely collected IMR, coronary flow reserve (CFR) and

Abbreviations: CFR, coronary flow reserve; CMD, coronary microvascular dysfunction; IMR, index of microcirculatory resistance; LVEF, left ventricle ejection fraction; NH IMR_{angio}, non-hyperaemic IMR_{angio}; pPCI, primary percutaneous coronary intervention; QFR, quantitative flow ratio; RRR, resistive reserve ratio; STEMI, ST-segment elevation myocardial infarction.

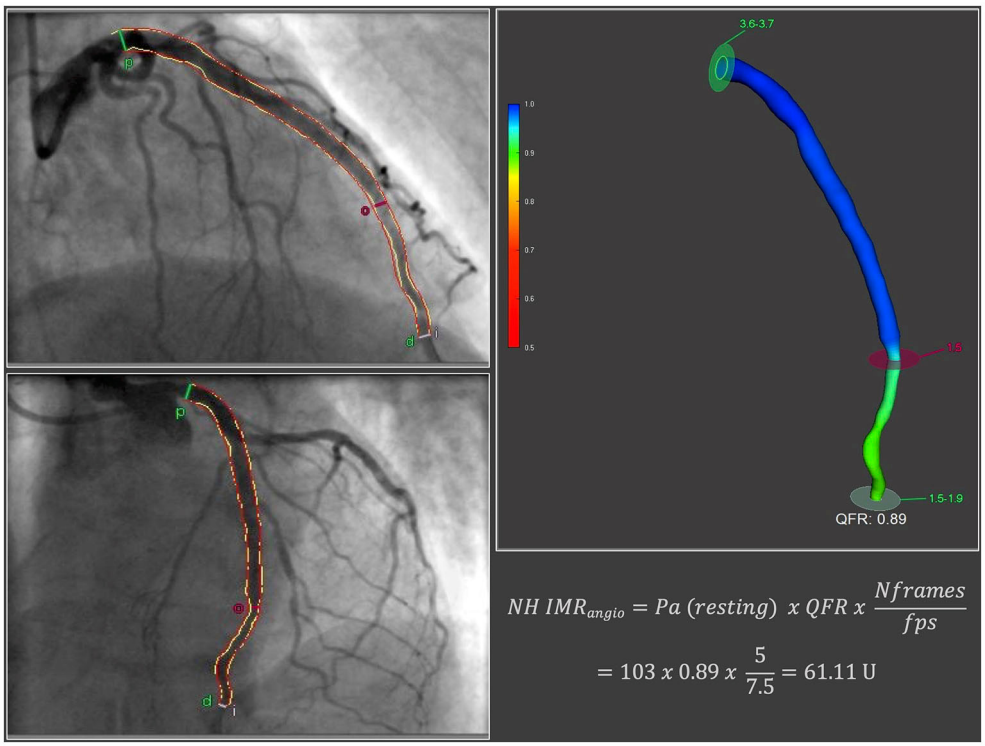

FIGURE 1 | NH IMR_{angio} derivation. fps, frames per second; Nframes, number of angiographic frames from contrast dye to travel from the guiding catheter to a distal reference in resting conditions; NH IMR_{angio}, non-hyperaemic IMR_{angio}; Pa, post percutaneous coronary intervention mean aortic pressure at resting conditions; QFR, quantitative flow ratio.

resistive reserve ratio (RRR) data. Based on established literature, IMR and CFR were dichotomized using thresholds of 40U and 2.0, respectively (5).

Clinical Follow-Up

The primary clinical outcome of the study was the composite endpoint of all-cause mortality, resuscitated cardiac arrest and new heart failure diagnosis. The secondary clinical outcome of the study was the composite endpoint of cardiac mortality, resuscitated cardiac arrest and new heart failure diagnosis. Heart failure was defined as the development of new heart failure symptomatology and/or prescription of diuretics in conjunction with supporting new non-invasive imaging findings of left ventricular systolic dysfunction (LVEF) $<$ 50% and/or raised levels of brain natriuretic peptide. Outcome data was collected from scheduled study follow-up visits and annual telephone calls and review of electronic case records and contacting the participants' General Practitioners.

Statistical Analysis

We tested the normality assumption of continuous variables with statistical (Shapiro-Wilk test) and graphical (histogram) means. We expressed continuous variables as mean $\pm$ standard deviation or median (25–75 percentile) as appropriate and categorical variables as numbers (percentage). Between-group comparisons for categorical variables were performed using Pearson's χ^2 or Fisher's exact test as appropriate, while continuous variables were compared using Student's *t*-test, Mann-Whitney U test or Kruskal-Wallis test. Correlations between variables were expressed using Spearman rho coefficients.

We used receiver operator characteristic curve analysis to explore the diagnostic utility of NH IMR_{angio} to predict an IMR $>$ 40U. We then selected the optimal NH IMR_{angio} cut-off value by identifying the value that maximizes the Youden's *J* statistic.

We subsequently performed survival analyses for the primary and secondary endpoints stratified according to (i) NH IMR_{angio}, (ii) IMR and (iii) CFR (expressed as dichotomous variables) using Kaplan Meier and Cox proportional hazard regression modeling methods. We compared the hazard ratios of dichotomised NH IMR_{angio}, IMR and CFR with paired Student's *t*-tests (17).

To evaluate the prognostic utility of NH IMR_{angio} (as a dichotomous variable) for our primary endpoint we constructed multivariate Cox regression models adjusted for clinical, procedural, angiographic and echocardiographic variables. We measured the goodness of fit using concordance (C-statistic) statistics. By adding NH IMR_{angio} in a baseline multivariate model, we assessed for improvement in model performance by performing a likelihood ratio test.

Statistical analyses were performed with SPSS version 26 (IBM Inc. New York USA) and R studio version 1.3 (*survival*, *survminer*, *forestplot* and *survcomp* packages). All tests were two-sided and α was set at 0.05.

RESULTS

Study Population

A total of 262 patients with both post pPCI invasive IMR and NH IMR_{angio} assessment were included in the current analysis. Complete follow-up data was available for 241 participants (92%) with a median follow-up of 4.2 (2.0–6.5) years. Baseline clinical, procedural, imaging and post pPCI coronary physiology data are reported in **Tables 1**, **2**. The median IMR and NH IMR_{angio} values at the end of the procedure were 33 (20–55) and 43 (30–59) units respectively.

TABLE 1 | Clinical, procedural and echocardiographic characteristics.

	All
Total number	**262**
Clinical	
Age, years	62 ± 11
Male gender, *n* (%)	215 (82)
Hypertension, *n* (%)	119 (46)
Hypercholesterolemia, *n* (%)	101 (39)
Diabetes, *n* (%)	41 (16)
Smoker, *n* (%)	110 (42)
Previous cardiology history, *n* (%)	37 (14)
Family history of IHD, *n* (%)	101 (39)
Procedural	
Ischemic time (minutes)	180 (122, 317)
Target vessel	
LAD, *n* (%)	119 (45)
LCX, *n* (%)	25 (10)
RCA, *n* (%)	109 (42)
Other, *n* (%)	9 (3)
TIMI flow—pre-PCI	
0	197 (75)
1	22 (8)
2	30 (12)
3	13 (5)
TIMI flow—post-PCI	
0	0 (0)
1	3 (1)
2	33 (13)
3	226 (86)
Myocardial Blush Grade	
0	21 (8)
1	46 (18)
2	106 (40)
3	89 (34)
Complete ST segment resolution, *n* (%)	151 (73)
Discharge echocardiography LVEF (%)	50 (45, 56)

IHD, ischaemic heart disease; LAD, left anterior descending artery; LCx, left circumflex artery; LVEF, left ventricle ejection fraction; PCI, percutaneous coronary intervention; RCA, right coronary artery; TIMI, the Thrombolysis in Myocardial Infarction.

Diagnostic Performance of NH IMR_{angio}

NH IMR_{angio} was significantly correlated with IMR (rho = 0.50, $p < 0.0001$) and predicted an IMR > 40U with an AUC of 0.78 (95% CI: 0.72–0.84, $p < 0.0001$) (**Supplementary Figure 2**). The optimal NH IMR_{angio} cut-off to predict an IMR > 40U was 43U (Sensitivity: 77%, Specificity: 67%, Diagnostic accuracy: 70%) coinciding with the median NH IMR_{angio} value of 43U observed in the overall study cohort. Patients with a high NH IMR_{angio} (>43U) were characterized by longer ischaemic times, worse post pPCI TIMI flow grade, lower occurrence of complete ST-segment resolution, and lower left ventricular ejection fraction at discharge than patients with a low NH IMR_{angio} (**Supplementary Table 1**). A high NH IMR_{angio} (>43U) was associated with a significantly higher degree of invasively assessed microvascular dysfunction (expressed by either IMR, CFR or RRR) than a low NH IMR_{angio} (**Supplementary Table 2**).

Prognostic Value of NH IMR_{angio}

At 7 years of follow-up, the primary and secondary endpoints occurred in 38 (16%) and 30 (12%) participants respectively. All-cause death occurred in 13 (5%) participants (4 cardiac, 1 sepsis-related and 6 neoplasm-related deaths), two (1%) had a resuscitated cardiac arrest and 28 (12%) had a new diagnosis of heart failure. Cox regression analyses showed that a post pPCI NH IMR_{angio} >43U was significantly associated with a higher risk of both the primary and secondary endpoints,

TABLE 2 | Post PCI pressure-wire- and angiography-derived coronary physiology indices.

	All
Total number	**262**
Pressure-wire-derived	
Resting Pa, mmHg	92 ± 18
Resting transit time, s	0.69 (0.48, 1.13)
Hyperaemic Pa, mmHg	83 ± 16
Hyperaemic Pd, mmHg	76 (67, 87)
Hyperaemic transit time, s	0.43 (0.28, 0.78)
FFR	0.94 (0.90, 0.98)
IMR	33 (20, 55)
CFR	1.5 (1.1, 2)
RRR	1.7 (1.3, 2.3)
Angiography-derived	
NH IMR_{angio}	43 (30, 59)
Fixed flow QFR	0.95 (0.90, 0.98)
Contrast QFR	0.96 (0.90, 0.99)

CFR, coronary flow reserve; FFR, fractional flow reserve; IMR, index of microvascular resistance; NH IMR_{angio}, non-hyperaemic IMR_{angio}; Pa, aortic pressure; Pd, distal pressure; PCI, percutaneous coronary intervention; QFR, quantitative flow ratio; RRR, resistive reserve ratio.

(HR 3.43, 95% CI: 1.67–7.07, $p = 0.001$ and HR 3.32, 95% CI: 1.48–7.47, $p = 0.004$, respectively). A post pPCI IMR >40U was also significantly associated with a higher risk of the primary and secondary endpoints (HR 2.07, 95% CI: 1.09–3.92, $p < 0.03$ and HR 2.17, 95% CI 1.06–4.48, $p < 0.04$, respectively). The comparison of the hazard ratio estimates of NH IMR_{angio} > 43U and IMR > 40U did not yield a statistically significant difference for either endpoint ($p = 0.91$ and $p = 0.85$).

In an exploratory analysis, a CFR ≤ 2.0 was significantly associated with a higher risk of the primary and secondary endpoints (HR 3.82, 95% CI 1.17–12.43, $p < 0.03$ and HR 4.56, 95% CI 1.08–19.18, $p < 0.04$, respectively). Pairwise comparisons of CFR ≤ 2.0 with IMR > 40U and NH IMR_{angio} > 43U hazard ratios were not statistically significant.

The Kaplan Meier curves displaying the relationship between survival-free from the primary and secondary endpoints for participants with high vs. low NH IMR_{angio} and IMR have a similar profile (**Figures 2**, **3** respectively). The analysis of participants dichotomised according to low vs. high CFR yield similar Kaplan Meier survival curve profiles to the profiles observed when participants were dichotomised according to IMR and NH IMR_{angio} for both endpoints (**Supplementary Figures 3**, **4**). In a landmark analysis excluding participants who experienced a primary or secondary endpoint event at 30 days, survival free from a primary and secondary endpoint was significantly lower in participants with an NH IMR_{angio} > 43U (**Figure 4**). In a further sub-analysis excluding patients with post pPCI TIMI Flow grade <3, NH IMR_{angio} > 43U was significantly associated with a higher risk of the primary endpoint (**Supplementary Figure 5**).

To further evaluate the prognostic utility of NH IMR_{angio} >43U a multivariate Cox regression analysis was performed. The univariate and multivariate predictors of the primary endpoint are listed in **Table 3**. Post pPCI TIMI flow grade <3, myocardial blush grade <3 and incomplete ST-segment resolution were not significant predictors (**Table 3**). NH IMR_{angio} >43U was an independent predictor of the primary endpoint (adjusted HR 2.13, 95% CI: 1.01–4.48, $p = 0.047$) alongside age, ischaemic time, and discharge LVEF (**Figure 5**). NH IMRangio >43U was an independent predictor of long-term outcome even when patients with post pPCI TIMI flow <3 were excluded from the analysis (adjusted HR 2.82, 95% CI: 1.28–6.19, $p = 0.01$). The addition of NH IMR_{angio} >43U as a variable to a cox regression model including age, ischaemic time and discharge LVEF% yielded a good model (C-statistic 0.82, χ^2: 67) with a significant improvement in predictive performance (χ^2 difference: 4.30, $p = 0.04$).

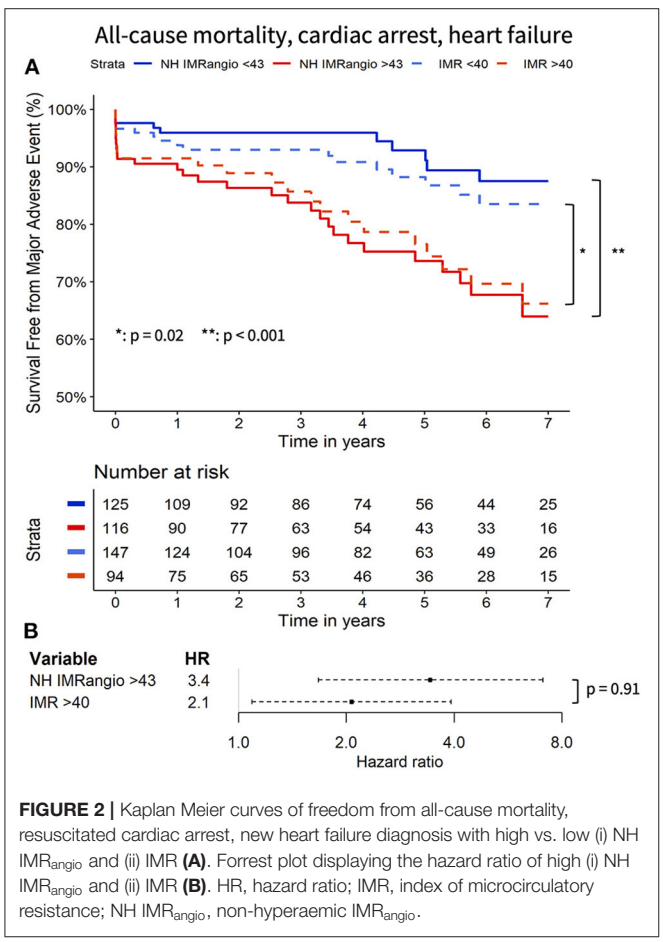

FIGURE 2 | Kaplan Meier curves of freedom from all-cause mortality, resuscitated cardiac arrest, new heart failure diagnosis with high vs. low (i) NH IMR_{angio} and (ii) IMR **(A)**. Forrest plot displaying the hazard ratio of high (i) NH IMR_{angio} and (ii) IMR **(B)**. HR, hazard ratio; IMR, index of microcirculatory resistance; NH IMR_{angio}, non-hyperaemic IMR_{angio}.

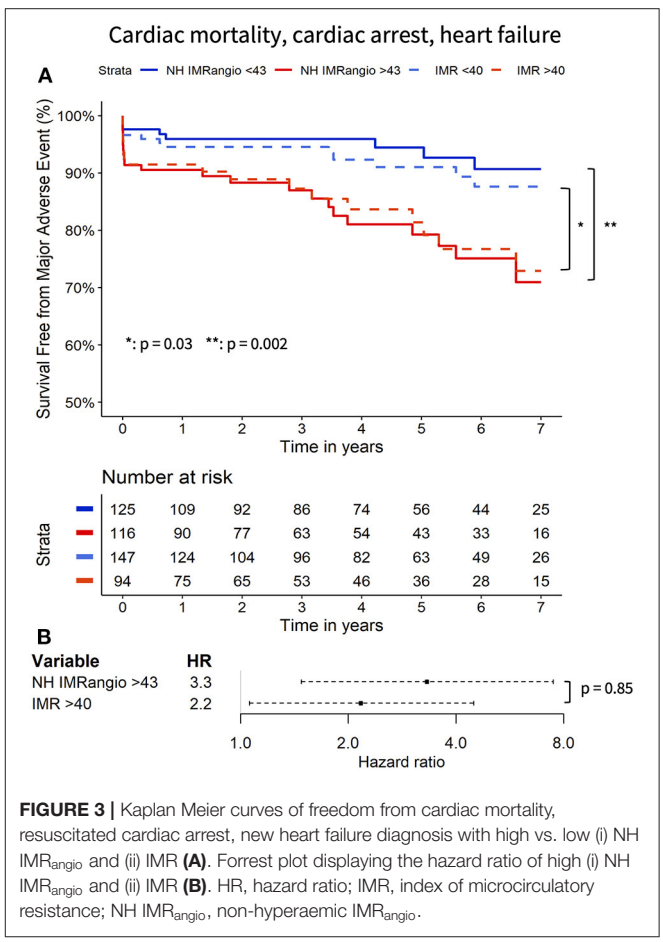

FIGURE 3 | Kaplan Meier curves of freedom from cardiac mortality, resuscitated cardiac arrest, new heart failure diagnosis with high vs. low (i) NH IMR_{angio} and (ii) IMR **(A)**. Forrest plot displaying the hazard ratio of high (i) NH IMR_{angio} and (ii) IMR **(B)**. HR, hazard ratio; IMR, index of microcirculatory resistance; NH IMR_{angio}, non-hyperaemic IMR_{angio}.

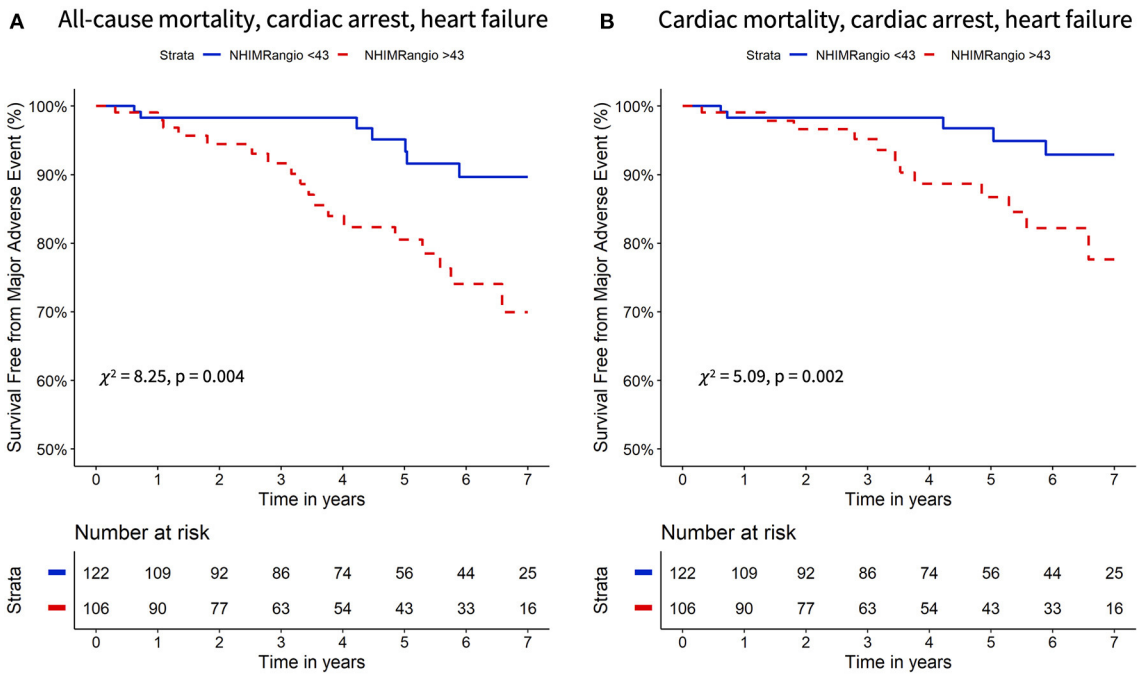

FIGURE 4 | Landmark analysis (30 days onward) Kaplan Meier curves of freedom from all-cause mortality, resuscitated cardiac arrest, new heart failure diagnosis **(A)** and cardiac mortality, resuscitated cardiac arrest and new heart failure diagnosis **(B)** stratified according to high versus low NH IMR_{angio}. NH IMR_{angio}, non-hyperaemic IMR_{angio}.

DISCUSSION

This study extends our preliminary findings (14) and explores the prognostic value of a dedicated pressure-wire and adenosine-free angiographic index (NH IMR_{angio}) for the assessment of CMD in patients with STEMI.

Coronary microvascular dysfunction in STEMI is prognostically important (2, 7) due to the resulting poor structural and functional myocardial recovery (1, 18). Physiological measurements derived from invasive assessment of coronary microvascular function at the time of pPCI (e.g. IMR) provide a grading of the severity of CMD and correlate well with CMR-defined structural microvascular injury (1, 4). However, the routine clinical adoption of IMR remains limited due to a number of factors including additional cost and procedural time. These constraints can be overcome with angiography-derived, pressure wire-free indices of coronary physiology indices. Our recent validation of the non-hyperaemic angiography-derived index of microcirculatory resistance (NH IMR_{angio}) against pressure-wire-based IMR represented a preliminary dataset (14).

Diagnostic Performance of NH IMR_{angio}

In the current analysis, we expand our preliminary findings to a larger cohort and show that the non-hyperaemic version of IMR_{angio}–NH IMR_{angio} reliably predicts CMD as defined by an IMR >40U in the IRA of patients with STEMI. Using a non-hyperaemic index to evaluate CMD in the IRA of patients with STEMI could have a certain value, as the response of coronary microcirculation to a vasodilatory agent is highly likely to be blunted and compromised as a reflection of distal embolisation and ischaemia-reperfusion injury (5, 13). As a confirmation of this hypothesis, in our cohort, the median value of RRR—a dedicated index to express the vasodilatory capacity of the coronary microcirculation—was 1.7. This value is suggestive of a depressed coronary microvascular vasodilatory capacity in this cohort of patients with STEMI, a finding consistent with previous reports (12, 13). This depressed vasodilatory capacity can explain why, particularly in patients with STEMI, a non-hyperaemic index such as NH IMR_{angio} retains some diagnostic accuracy in identifying microvascular injury (14).

Prognostic Value of NH IMR_{angio}

The main finding of the current study is the observation that an NH IMR_{angio} >43U, measured in the IRA of patients with STEMI at the end of pPCI, is equivalent to an IMR >40U in predicting long-term adverse events. The survival curves of patients stratified according to low or high values of IMR or NH IMR_{angio} present a similar profile, while the stratification is prognostically significant for both indices. The hazard ratios of a high IMR (>40U) or NH IMR_{angio} (>43U) are not significantly different, further supporting the prognostic equivalence of the two indices. The prognostic equivalence is also maintained when analysing a stricter cardiac endpoint excluding non-cardiac mortality. These findings are consistent with the results and effect

TABLE 3 | Univariate and multivariate analysis results for predictors of all-cause mortality, resuscitated cardiac arrest, new heart failure.

Univariate predictors	Hazard ratio	95% CI	p-value
Age (per 1 year increase)	1.07	1.03–1.10	**<0.01**
Male gender	2.02	1.00–4.07	0.05
LAD as IRA	2.09	1.09–4.00	**0.03**
Ischaemic time (per 1 min delay)	1.00	1.00–1.00	**0.04**
Incomplete ST segment resolution	2.20	0.82–5.91	0.12
TIMI Flow Grade < 3	1.32	0.58–3.00	0.51
Myocardial Blush Grade < 3	1.61	0.76–3.39	0.22
IMR > 40	2.07	1.09–3.92	**<0.03**
CFR ≤ 2.0	3.82	1.17–12.43	**<0.03**
Discharge echocardiography LVEF (per % increase)	0.91	0.89–0.94	**<0.01**
NH IMR_{angio} > 43U	3.43	1.67–7.07	**<0.01**
Multivariate predictors			
Age (per 1 year increase)	1.07	1.03–1.11	**<0.01**
Ischaemic time (per 1 min delay)	1.00	1.00–1.00	**0.03**
Discharge echocardiography LVEF (per % increase)	0.92	0.90–0.95	**<0.01**
NH IMR_{angio} > 43U	2.13	1.01–4.48	**<0.05**

CI, confidence interval; CFR, coronary flow reserve; IMR, index of microvascular resistance; IRA, infarct related artery; LAD, left anterior descending artery; LVEF, left ventricle ejection fraction; NH IMR_{angio}, non-hyperaemic IMR_{angio}; TIMI, Thrombolysis in Myocardial Infarction. Values in bold denote a statistically significant result (p-value <0.05).

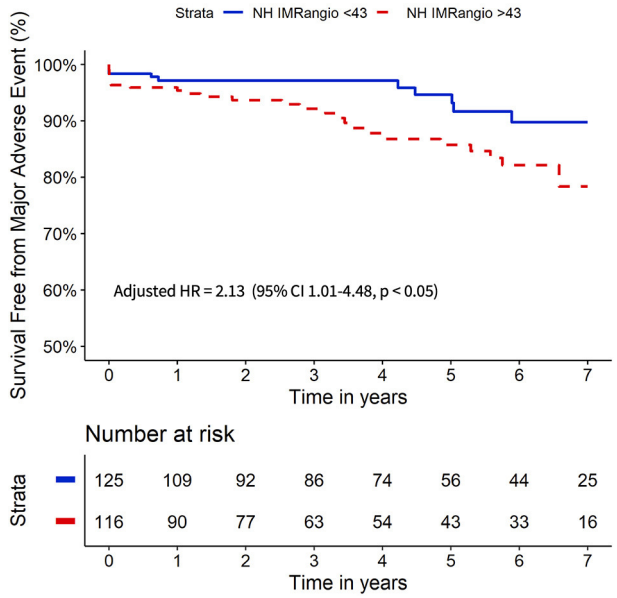

FIGURE 5 | Kaplan Meier curves of freedom from all-cause mortality, resuscitated cardiac arrest, new heart failure diagnosis with high vs. low NH IMR_{angio} adjusted for age, ischaemic time, LVEF%. HR, hazard ratio; CI, confidence interval; LVEF, left ventricle ejection fraction; NH IMR_{angio}, non-hyperaemic IMR_{angio}.

estimates reported in the previous work by Fearon et al. on the prognostic role of invasive and pressure-wire based IMR in patients with STEMI (7).

Kaplan-Meier survival curves separate early on, suggesting a prognostic role of NH IMR_{angio} for early cardiac complications; a finding corroborated by previous IMR based work (6). Since this early separation could influence our analysis, we conducted a landmark analysis from 30 day onwards. An NH IMR_{angio} >43U retained its significance in this landmark analysis suggesting that the long-term prognostic performance is not exclusively driven by early events. This may be explained by the significant contribution of new heart failure diagnoses to our combined study endpoints. In our previous work, we have already shown that non-hyperaemic IMR_{angio} is significantly elevated in patients with clinically significant microvascular obstruction assessed by cardiac magnetic resonance (14). This provides a further biologically plausible explanation for the prognostic significance of NH IMR_{angio} we report herein (14).

Finally, this study suggests that an NH IMR_{angio} >43U is an independent predictor of adverse events, with an associated two-fold increased risk of a poor clinical outcome at 7 years follow-up. Our findings resonate with previously published findings of the independent prognostic value of an IMR > 40U in predicting long-term outcomes in patients with STEMI (5, 7). Specifically, adding NH IMR_{angio} into a model with other clinically relevant and universally available variables incrementally improved the predictive performance of the model itself, supporting the independent and incremental prognostic significance of NH IMR_{angio} as a novel alternative tool for risk stratification.

Limitations

Firstly, we acknowledge that the relatively small sample size, low number of cardiac events and single-centre origin of our study is amongst the limitations of our work. For this reason, further testing in larger and external cohorts is needed to corroborate and to increase the precision of the findings. We also recognize that our cohort study might have been subject to selection bias due to the exclusive inclusion of patients in whom invasive coronary physiology measurements were performed. This might have led to the unintentional inclusion of a relatively intermediate-low risk cohort of patients with STEMI, as reflected by the relative low rate of adverse events at follow up. However, on a practical level it must also be considered that the real unmet need is to improve risk-stratification in patients at intermediate risk of adverse events. Patients presenting with high-risk features (multiple comorbidities, haemodynamic instability, complex coronary anatomy) have already "declared" their risk category, whilst it is the majority of "intermediate risk" patients (like the patients included in our analysis) that may benefit the most from personalized and stratified medicine approaches (19).

In addition, we recognize the limitations arising from the use of a non-hyperaemic index to study coronary microvascular function. A future large-scale, prospective study assessing the prognostic value of the hyperaemic angiography-derived index is indeed needed, and it could abate the limitations of the current analysis focused on a non-hyperaemic version of the index. Nonetheless, it must be acknowledged that in the current

study, NH IMR_{angio} resulted prognostically equivalent to invasive IMR. Whilst this observation is evident in STEMI patients, we do not anticipate that a non-hyperaemic index will work as well in patients with coronary syndromes characterized by a lesser degree of CMD, as also already recently reported (14). Finally, a limitation of this work is the off-line evaluation of NH IMR_{angio} and our ability to perform the analysis in 71% of patients. Even though our tool should be formally evaluated in a "real-time" setting, there is little doubt about its suitability as a real-time catheterisation laboratory tool. A large body of evidence suggests that real-time measurement of QFR is not only feasible but significantly quicker than pressure-wire based coronary physiology evaluation (20). Indeed, we expect that dedicated acquisitions for real-time assessment of NH IMR_{angio} in a prospective study would enable analysis in >95% of cases.

CONCLUSION

In an analysis of 262 patients with STEMI, NH IMR_{angio} is reliable at predicting CMD defined as an IMR >40U. An NH IMR_{angio} of >43U was an independent multivariate associate of long-term all-cause mortality, resuscitated cardiac arrest and new heart failure diagnosis. Since the prognostic profile of NH IMR_{angio} was equivalent to that of IMR, it can be a feasible alternative to IMR for catheterisation laboratory assessment of CMD and long-term risk stratification.

DATA AVAILABILITY STATEMENT

The datasets presented in this article are not readily available because a patent based on some of the data included in this article has been filed. Requests to access the datasets should be directed to Giovanni Luigi De Maria, GiovanniLuigi.Demaria@ouh.nhs.uk.

ETHICS STATEMENT

The studies involving human participants were reviewed and approved by the local ethics committee (10/H0408/24). The patients/participants provided their written informed consent to participate in this study.

AUTHOR CONTRIBUTIONS

RAK: methodology, investigation, formal analysis, writing—original draft, visualisation, writing—review and editing, project administration, and funding acquisition. DT-P, FM, RS, JB-W, JL, AL, RC, and RAK: investigation and writing—review and editing. MS: investigation, writing—review and editing, and funding acquisition. OxAMI Study Investigators: investigation, methodology, resources, project administration, and funding acquisition. HG-G: conceptualisation, methodology, and writing—review and editing. KC: conceptualisation, methodology, investigation, resources, writing—review and editing, project administration, and funding acquisition. AB: conceptualisation, methodology, investigation, resources, writing—review and editing, and funding acquisition. GD: conceptualisation, methodology, investigation, resources, writing—original draft, writing—review and editing, supervision, project administration, and funding acquisition. All authors contributed to the article and approved the submitted version.

FUNDING

This study was Supported by British Heart Foundation (BHF; grant CH/16/1/32013), BHF Centre of Research Excellence, Oxford (RG/13/1/30181), Oxfordshire Health Services Research Committee and the National Institute for Health Research (NIHR) Oxford Biomedical Research Centre. RAK, Academic Clinical Fellow is funded by Health Education England (HEE) /National Institute for Health Research (NIHR) for this research project. MS is in receipt of the Alison Brading Memorial Scholarship in Medical Science, Lady Margaret Hall, University of Oxford.

ACKNOWLEDGMENTS

The authors would like to acknowledge the Oxford Heart Centre Catherisation Laboratory team, Lisa Gaughran, and Yujun Ng for their support of the study.

SUPPLEMENTARY MATERIAL

The Supplementary Material for this article can be found online at: https://www.frontiersin.org/articles/10.3389/fcvm.2021.717114/full#supplementary-material

REFERENCES

1. De Maria GL, Alkhalil M, Wolfrum M, Fahrni G, Borlotti A, Gaughran L, et al. Index of microcirculatory resistance as a tool to characterize microvascular obstruction and to predict infarct size regression in patients with STEMI undergoing primary PCI. *JACC Cardiovasc Imaging.* (2019) 12:837–48. doi: 10.1016/j.jcmg.2018.02.018
2. Herzog BA, Husmann L, Valenta I, Gaemperli O, Siegrist PT, Tay FM, et al. Long-term prognostic value of 13N-ammonia myocardial perfusion positron emission tomography added value of coronary flow reserve. *J Am Coll Cardiol.* (2009) 54:150–6. doi: 10.1016/j.jacc.2009.02.069
3. Scarsini R, Shanmuganathan M, De Maria GL, Borlotti A, Kotronias RA, Burrage MK, et al. Coronary microvascular dysfunction assessed by pressure wire and CMR after STEMI predicts long-term outcomes. *JACC Cardiovasc Imaging*. (2021). doi: 10.1016/j.jcmg.2021.02.023. [Epub ahead of print].
4. McGeoch R, Watkins S, Berry C, Steedman T, Davie A, Byrne J, et al. The index of microcirculatory resistance measured acutely predicts the extent and severity of myocardial infarction in patients with ST-segment elevation myocardial infarction. *JACC Cardiovasc Interv*. (2010) 3:715–22. doi: 10.1016/j.jcin.2010.04.009
5. Carrick D, Haig C, Ahmed N, Carberry J, Yue May VT, McEntegart M, et al. Comparative prognostic utility of indexes of microvascular

function alone or in combination in patients with an acute ST-segment-elevation myocardial infarction. *Circulation*. (2016) 134:1833–47. doi: 10.1161/CIRCULATIONAHA.116.022603
6. Fahrni G, Wolfrum M, De Maria GL, Cuculi F, Dawkins S, Alkhalil M, et al. Index of microcirculatory resistance at the time of primary percutaneous coronary intervention predicts early cardiac complications: insights from the OxAMI (Oxford Study in Acute Myocardial Infarction) Cohort. *J Am Heart Assoc*. (2017) 6: e005409. doi: 10.1161/JAHA.116.005409
7. Fearon WF, Low AF, Yong AS, McGeoch R, Berry C, Shah MG, et al. Prognostic value of the index of microcirculatory resistance measured after primary percutaneous coronary intervention. *Circulation*. (2013) 127:2436–41. doi: 10.1161/CIRCULATIONAHA.112.000298
8. De Maria GL, Alkhalil M, Borlotti A, Wolfrum M, Gaughran L, Dall'Armellina E, et al. Index of microcirculatory resistance-guided therapy with pressure-controlled intermittent coronary sinus occlusion improves coronary microvascular function and reduces infarct size in patients with ST-elevation myocardial infarction: the Oxford Acute Myocardial Infarction-Pressure-controlled Intermittent Coronary Sinus Occlusion study (OxAMI-PICSO study). *EuroIntervention*. (2018) 14:e352–9. doi: 10.4244/EIJ-D-18-00378
9. De Maria GL, Garcia-Garcia HM, Scarsini R, Finn A, Sato Y, Virmani R, et al. Novel device-based therapies to improve outcome in ST-segment elevation myocardial infarction. *Eur Heart J Acute Cardiovasc Care*. (2021). doi: 10.1093/ehjacc/zuab012. [Epub ahead of print].
10. Tu S, Westra J, Yang J, von Birgelen C, Ferrara A, Pellicano M, et al. Diagnostic accuracy of fast computational approaches to derive fractional flow reserve from diagnostic coronary angiography: the international multicenter FAVOR pilot study. *JACC Cardiovasc Interv*. (2016) 9:2024–35. doi: 10.1016/j.jcin.2016.07.013
11. De Maria GL, Scarsini R, Shanmuganathan M, Kotronias RA, Terentes-Printzios D, Borlotti A, et al. Angiography-derived index of microcirculatory resistance as a novel, pressure-wire-free tool to assess coronary microcirculation in ST elevation myocardial infarction. *Int J Cardiovasc Imaging*. (2020) 36:1395–406. doi: 10.1007/s10554-020-01831-7
12. Maznyczka AM, McCartney PJ, Oldroyd KG, Lindsay M, McEntegart M, Eteiba H, et al. Effects of intracoronary alteplase on microvascular function in acute myocardial infarction. *J Am Heart Assoc*. (2020) 9:e014066. doi: 10.1161/JAHA.119.014066
13. Scarsini R, De Maria GL, Borlotti A, Kotronias RA, Langrish JP, Lucking AJ, et al. Incremental value of coronary microcirculation resistive reserve ratio in predicting the extent of myocardial infarction in patients with STEMI. Insights from the Oxford Acute Myocardial Infarction (OxAMI) study. *Cardiovasc Revasc Med*. (2019) 20:1148–55. doi: 10.1016/j.carrev.2019.01.022
14. Scarsini R, Shanmuganathan M, Kotronias RA, Terentes-Printzios D, Borlotti A, Langrish JP, et al. Angiography-derived index of microcirculatory resistance (IMRangio) as a novel pressure-wire-free tool to assess coronary microvascular dysfunction across the spectrum of coronary syndromes. *Int J Cardiovasc Imaging*. (2021) 37:1801–13. doi: 10.1007/s10554-021-02254-8
15. De Maria GL, Cuculi F, Patel N, Dawkins S, Fahrni G, Kassimis G, et al. How does coronary stent implantation impact on the status of the microcirculation during primary percutaneous coronary intervention in patients with ST-elevation myocardial infarction? *Eur Heart J*. (2015) 36:3165–77. doi: 10.1093/eurheartj/ehv353
16. Schröder R. Prognostic impact of early ST-segment resolution in acute ST-elevation myocardial infarction. *Circulation*. (2004) 110:e506–10. doi: 10.1161/01.CIR.0000147778.05979.E6
17. Haibe-Kains B, Desmedt C, Sotiriou C, Bontempi G. A comparative study of survival models for breast cancer prognostication based on microarray data: does a single gene beat them all? *Bioinformatics*. (2008) 24:2200–8. doi: 10.1093/bioinformatics/btn374
18. Sezer M, Aslanger EK, Cimen AO, Yormaz E, Turkmen C, Umman B, et al. Concurrent microvascular and infarct remodeling after successful reperfusion of ST-elevation acute myocardial infarction. *Circ Cardiovasc Interv*. (2010) 3:208–15. doi: 10.1161/CIRCINTERVENTIONS.109.891739
19. Crosby DB, Brocklehurst P, Chamberlain P, Dive C, Holmes C, Isaacs C, et al. *The MRC Framework for the Development, Design and Analysis of Stratified Medicine Research*. London: Medical Research Council (2015).
20. Westra J, Andersen BK, Campo G, Matsuo H, Koltowski L, Eftekhari A, et al. Diagnostic performance of in-procedure angiography-derived quantitative flow reserve compared to pressure-derived fractional flow reserve: the FAVOR II Europe-Japan study. *J Am Heart Assoc*. (2018) 7:e009603. doi: 10.1161/JAHA.118.009603

Author Disclaimer: The views expressed in this publication are those of the authors and not necessarily those of the NIHR, NHS or the UK Department of Health and Social Care.

Conflict of Interest: GD reports grants from Miracor Medical SA, outside the submitted work. In addition, GD has a patent PCT/US20/55240 pending. AB reports grants from Boston Scientific, personal fees from Boston Scientific, personal fees from Abbott, personal fees from Medtronic, personal fees from Phillips, outside the submitted work. HG-G reports institutional research grants from Medtronic, Boston Scientific, Abbott, Biotronik, Neovasc, Corflow, Shockwave, Chiesi, outside the submitted work.

The remaining authors declare that the research was conducted in the absence of any commercial or financial relationships that could be construed as a potential conflict of interest.

Publisher's Note: All claims expressed in this article are solely those of the authors and do not necessarily represent those of their affiliated organizations, or those of the publisher, the editors and the reviewers. Any product that may be evaluated in this article, or claim that may be made by its manufacturer, is not guaranteed or endorsed by the publisher.

frontiers in Cardiovascular Medicine

ORIGINAL RESEARCH
published: 30 September 2021
doi: 10.3389/fcvm.2021.720127

Association of Pericoronary Adipose Tissue Quality Determined by Dual-Layer Spectral Detector CT With Severity of Coronary Artery Disease: A Preliminary Study

Yuxue Dang[1], Xujiao Chen[1], Shaowei Ma[2], Yue Ma[1], Quanmei Ma[1], Ke Zhou[3], Ting Liu[4], Kunhua Wang[5†] and Yang Hou[1*†]*

[1] Department of Radiology, Shengjing Hospital of China Medical University, Shenyang, China, [2] Department of Cardiology, Shengjing Hospital of China Medical University, Shenyang, China, [3] Department of Cardiac Surgery, Shengjing Hospital of China Medical University, Shenyang, China, [4] Department of Radiology, The First Affiliated Hospital of China Medical University, Shenyang, China, [5] Department of Radiology, The People's Hospital of Liaoning Province, Shenyang, China

OPEN ACCESS

Edited by:
Zahra K. Motamed, McMaster University, Canada

Reviewed by:
Mariana Vasconcelos, São João University Hospital Center, Portugal
Filippo Cademartiri, Gabriele Monasterio Tuscany Foundation (CNR), Italy

***Correspondence:**
Kunhua Wang
wang-christina@163.com
Yang Hou
houyang1973@163.com

[†] These authors have contributed equally to this work

Specialty section:
This article was submitted to Cardiovascular Imaging, a section of the journal Frontiers in Cardiovascular Medicine

Received: 03 June 2021
Accepted: 06 September 2021
Published: 30 September 2021

Citation:
Dang Y, Chen X, Ma S, Ma Y, Ma Q, Zhou K, Liu T, Wang K and Hou Y (2021) Association of Pericoronary Adipose Tissue Quality Determined by Dual-Layer Spectral Detector CT With Severity of Coronary Artery Disease: A Preliminary Study. Front. Cardiovasc. Med. 8:720127. doi: 10.3389/fcvm.2021.720127

Background: Pericoronary adipose tissue (PCAT) is considered as a source of inflammatory mediators, leading to the development of coronary atherosclerosis. The study aimed to investigate the correlation between PCAT quality derived from dual-layer spectral detector CT (SDCT) and the severity of coronary artery disease (CAD), and whether PCAT parameters were independently associated with the presence of CAD.

Materials and Methods: A total of 403 patients with symptoms of chest pain who underwent SDCT were included. PCAT quality including fat attenuation index (FAI) measured from conventional polychromatic CT images (FAI_{120kvp}) and spectral virtual mono-energetic images at 40 keV (FAI_{40keV}), slope of spectral HU curve (λ_{HU}), and effective atomic number (Eff-Z) were measured around the lesions representing the maximal degree of vascular stenosis in each patient. Meanwhile, overall epicardial adipose tissue (EAT) attenuation was acquired in the conventional polychromatic energy imaging.

Results: FAI_{40keV}, λ_{HU}, Eff-Z, and FAI_{120kvp} increased along with the degree of CAD in general and were superior to the overall EAT attenuation for detecting the presence of CAD. Multivariate logistic regression analysis indicated that FAI_{40keV} was the most powerful independent indicator (odds ratio 1.058, 95% CI 1.044–1.073; $p < 0.001$) of CAD among these parameters. Using an optimal cut-off (−131.8 HU), FAI_{40keV} showed higher diagnostic accuracy of 80.6% compared with the other parameters.

Conclusions: These preliminary findings suggest that FAI_{40keV} on SDCT may be an appealing surrogate maker to allow monitoring of PCAT changes in the development of CAD.

Keywords: pericoronary adipose tissue, dual-layer spectral detector CT, coronary artery disease, fat attenuation index, epicardial adipose tissue

INTRODUCTION

It is widely recognized that epicardial adipose tissue (EAT) plays a crucial role in the development of coronary artery disease (CAD) (1–3). Compared with EAT volume, EAT attenuation is more sensitive in showing the pathological changes of EAT, such as inhibition of adipocyte differentiation, interstitial fibrosis and microvascular proliferation (4, 5). Although EAT attenuation was associated with CAD risk factors and the presence of CAD, it was not associated with the presence of a significant coronary artery lesion (6). As an important component of EAT, pericoronary adipose tissue (PCAT) wrapping around coronary arteries secretes the inflammatory cytokines which may affect the adjacent vessel wall, and the resulting vascular inflammation leads to the formation and progress of coronary atherosclerosis (7–9). This complex interplay between vascular inflammation revealed by PCAT attenuation and coronary stenosis caused by atherosclerosis has been a focus of recent research. PCAT attenuation had been found to be associated with hemodynamically significant lesions, an increased risk of acute coronary syndrome, cardiac mortality and poor prognosis (10–13). Yu et al. found that perivascular fat attenuation index (FAI) provided incremental value to diameter stenosis for identifying hemodynamically significant lesions (11). However, this study included only patients with moderate to severe stenosis. The relationship between PCAT changes and the degree of coronary stenosis is still uncertain. Therefore, we conducted a preliminary study to investigate the association of PCAT attenuation and EAT attenuation with different stages of CAD in a large cohort of patients with chest pain.

Dual-layer spectral detector CT (SDCT) was introduced in recent years, which has shown to be highly suitable for coronary CTA in a clinical setting (14, 15). The use of spectral reconstructions such as virtual monochromatic imaging (VMI) at the low energy level of 40 keV can increase the contrast of soft tissue significantly (15–17). Effective atomic number (Eff-Z) and the slope of the spectral HU curve (λ_{HU}) are important energy spectrum parameters, which can help to differentiate the tissue characteristics (18, 19). Based on the knowledge learned above, we hypothesized that the index of PCAT on SDCT may be more sensitive and accurate than conventional CT to reflect the changes of PCAT.

To the best of our knowledge, there are no reports of relationship of PCAT quality derived from SDCT with different degrees of CAD. Therefore, the current study aimed to (i) investigate the association between PCAT index derived from SDCT and severity of CAD, and (ii) explore whether the PCAT index can be used as an independent risk factor for CAD.

MATERIALS AND METHODS

Patients

This retrospective study was approved by the institutional review board of Shengjing Hospital of China Medical University (NO.2020PS231K). Because it was a retrospective study and the scans were performed as part of clinical routine, informed consent was exempted. Data from 468 patients with chest pain and suspected coronary artery disease who underwent coronary CT angiography (coronary CTA) on a spectral detector CT between April 2018 and July 2020 were reviewed in this study. The exclusion criteria were as follows: (1) patients with incomplete clinical records; (2) poor image quality; (3) previous history of percutaneous coronary intervention (PCI) or coronary artery bypass grafting (CABG); and (4) patients suffering from malignancy or cardiomyopathies. As a result, a total of 403 patients were included in this study (**Figure 1**). Among them, 121 patients were diagnosed with moderate or severe stenosis by coronary CTA, and catheter coronary angiography (CAG) was performed to further confirm the extent of lesions.

The relevant clinical data of the patients was collected by reviewing the electronic medical database. Body mass index (BMI) was calculated as weight (kg)/height^2 (m^2). Patients on insulin therapy or oral anti-diabetic drugs, or showing HbA1c $\geq$ 6.5%, fasting glucose $\geq$ 126 mg/dL or non-fasting glucose $\geq$ 200 mg/dL were considered to have Diabetes Mellitus Type 2. Systolic blood pressure $\geq$ 140 mm Hg, or diastolic blood pressure $\geq$ 90 mm Hg, or use of antihypertensive drugs was considered as an indication of hypertension. Current and previous smoking and drinking histories were reviewed. Total cholesterol (TC), triglycerides (TG), high-density lipoprotein (HDL), and low-density lipoprotein (LDL) were collected.

CT Acquisition and Reconstruction

The coronary computed tomography angiography (coronary CTA) scans were performed on a spectral detector CT scanner (IQon, Philips Healthcare, Best, The Netherlands) using prospective electrocardiogram (ECG) gating (Step & Shoot Cardiac). The scans were performed with the following parameters: 120 kVp, 0.27s rotation time, 64 $\times$ 0.625 mm slice collimation, and the Dose Right Index set to 13. The scan trigger was centered around a physiologic cardiac phase of ventricular diastasis corresponding to 78% of the R–R interval, with a $\pm$3% buffer used. Patients with a heart rate >70 bpm received intravenous ß-receptor blocker before the scan regularly (see **Supplementary Material** for detailed information).

Raw data were reconstructed using spectral iterative reconstruction algorithm with the spectral reconstruction level set to 4 (Philips Healthcare). Axial images were reconstructed at a slice thickness of 0.9 mm with an overlapping increment of 0.45 mm. The resulting spectral base image (SBI) datasets included the true conventional polychromatic (120 kVp) images along with a wide variety of spectral reconstructions. The SBI corresponding to the best cardiac phase was identified from which VMI were generated—for the purpose of image assessment, VMIs from 40 to 70 keV in steps of 10 keV were assessed.

According to the degree of coronary stenosis from CCTA and CAG, all patients were first divided into non-CAD group [< 50% luminal diameter stenosis (DS)] and CAD group ($\geq$ 50% DS). In order to further explore the relationship of PCAT index on degrees of DS, the patients were then divided into four subgroups: Group A (minimal stenosis, < 25% DS), Group B (mild stenosis, 25%-49% DS), Group C (moderate stenosis, 50%-69% DS) and Group D (severe stenosis, $\geq$ 70% DS) according to the 2014

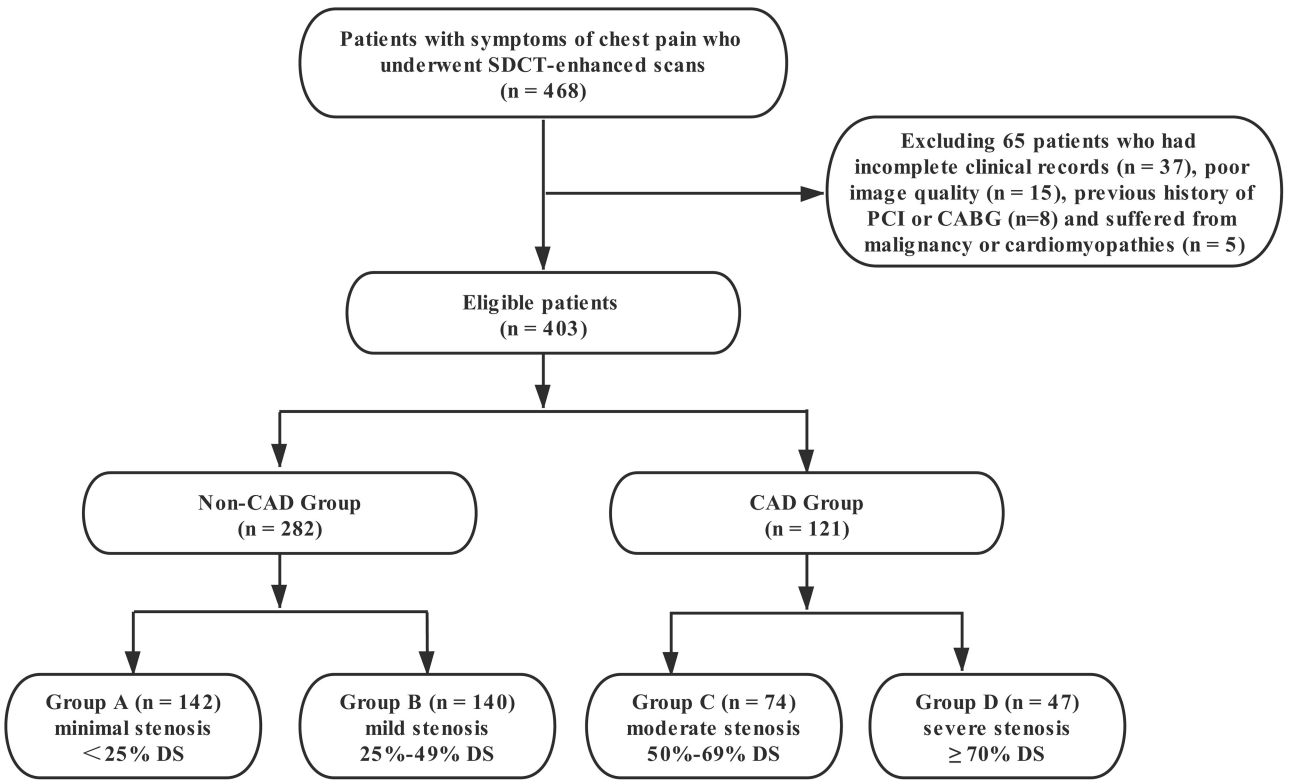

FIGURE 1 | Flow diagram of patient recruitment and grouping. PCI, percutaneous coronary intervention; CABG, coronary artery bypass graft; DS, diameter stenosis.

guidelines provided by the Society of Cardiovascular Computed Tomography (SCCT) (20). Furthermore, the coronary plaques of the maximal coronary stenosis were divided into calcified, non-calcified, and mixed plaques (21). The PCAT indices in the different plaque groups were further analyzed.

Quantification of EAT and PCAT Measures

The EAT attenuation was assessed using the semi-automated software (cardiac risk assessment version 1.2.0, Siemens Healthineer, Germany). Attenuation values within −190 HU to −30 HU were considered to represent adipose tissue (13). See **Supplementary Material** for details on EAT attenuation measurement.

PCAT was sampled in three-dimensional layers radially outwards from the outer vessel wall and measured (7, 13). Adipose tissue was identified as all voxels with attenuation thresholds of −190 to −30 HU in conventional polychromatic energy imaging, −280 to −40 HU in VMI at 40 keV, and −220 to −30 HU in VMI at 70 keV, respectively (22). PCAT analysis was performed in the adipose tissue around the plaque that caused the maximal degree of vascular stenosis in each patient (**Figure 2**). FAI was measured within the predefined volume of interest at the following energy levels: conventional 120 kVp, and at spectral VMI levels of 40 keV and 70 keV using the semi-automated software (Dr. Wise® Coronary Artery CT Aided Diagnosis Software V200831), reported as FAI_{120kvp}, FAI_{40keV}, FAI_{70keV}, respectively and the slope of the spectral HU curve (λ_{HU}) was calculated using the formula: $\lambda_{HU} = (FAI_{40keV}\text{-}FAI_{70keV})/30$. The effective atomic number (Eff-Z) was measured using the dedicated workstation (IntelliSpace Portal Version 6.5, Philips Healthcare).

All measurements were repeated three times by a radiologist with 8 years of experience in coronary CTA and averaged in order to ensure the accuracy of the data, and the investigator was blinded to clinical information and grouping situation. In order to verify the repeatability of the PCAT measures, 60 cases were randomly selected in a blinded manner and re-measured by the same investigator after 6 weeks.

Statistical Analysis

Datasets were analyzed using commercially available software (SPSS version 20.0, USA and MedCalc Statistical Software, version 15.2). Continuous variables were presented as means ± standard deviation. Inter-group comparisons were performed with independent–samples *t*-test or ANOVA. Welch's *t*-test was used in data with heterogeneity of variance among multiple groups. And the LSD or Dunnett's T3 test was used for paired comparison. Multivariate binary logistic regression was used to evaluate the association of EAT and PCAT measures with coronary stenosis. In order to compare the relative weight values of EAT and PCAT measures, each variable was standardized, and then performing multivariate logistic regression analysis

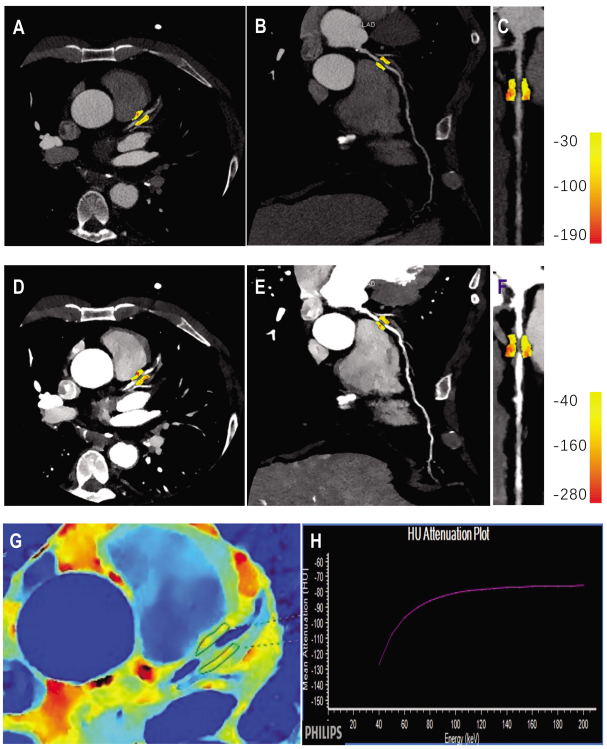

FIGURE 2 | Quantitative PCAT analysis in a case example of a 56-years old male patient with significant coronary artery stenosis (severe stenosis in proximal LAD). Axial view and the corresponding curved multiplane and straightened view of PCAT of the proximal LAD in the conventional 120 kVp **(A–C)** and 40 keV VMI **(D–F)**. **(G,H)** Represented the corresponding panels of Eff-Z imaging and spectral attenuation curve, respectively. LAD, left anterior descending artery; VMI, virtual monochromatic images.

to compare the standard partial regression coefficient of each variable. The receiver-operating characteristic (ROC) curve was drawn and the corresponding optimal cut-off value for predicting the presence of CAD was determined. The intra-class correlation coefficient (ICC) was used to evaluate intra-reader reliability of PCAT measurements. Generally, an ICC value ≥ 0.75 indicates excellent reliability, between 0.40 and 0.75 indicates fair to moderate reliability, and < 0.40 indicates poor reliability (23). A two-sided $p < 0.05$ was considered significant.

RESULTS

Patients

There were 403 subjects included in this study. Clinical characteristics in different groups of the study cohort are shown in **Table 1**.

Comparison of the EAT Attenuation and PCAT Parameters on SDCT in Patients With and Without CAD

All PCAT indices showed excellent reliability (ICC > 0.75) (**Supplementary Table 1**). The FAI_{40keV}, λ_{HU}, Eff-z, and FAI_{120kvp} were significantly larger in patients with CAD than those in non-CAD group (both $p < 0.001$). EAT attenuation in the two groups were also statistically different ($p < 0.001$) (**Figure 3**).

PCAT Parameters and EAT Attenuation From SDCT With Relation to the Degree of Coronary Stenosis

Patients were further divided into four subgroups according to the degree of coronary stenosis, Group A (minimal), Group B (mild), Group C (moderate), and Group D (severe) (see Methods). Lesion characteristics are shown in **Table 2**. There were significant differences in PCAT index and EAT attenuation among the groups. In view of the overall situation, FAI_{40keV}, λ_{HU}, Eff-Z, FAI_{120kvp}, and EAT attenuation all showed an increasing trend along with an increased degree of vascular stenosis (**Table 3**). Additionally, significant differences were seen in FAI_{40keV} and λ_{HU} between Groups C and D, with no significant differences seen in the other parameters of the two groups.

Furthermore, FAI_{40keV} was larger in the maximal stenosis segments with the non-calcified or mixed plaques than those with the calcified plaques in CAD group ($p < 0.05$, **Figure 4A**). While no significant difference was observed between the patients with non-calcified and mixed plaques. Interestingly, the opposite results were obtained in non-CAD group, which showed that FAI_{40keV} adjacent to non-calcified plaques was the lowest (**Figure 4B**). However, there were no significant differences in FAI_{40keV} between patients with different type of plaques.

The Association of PCAT and EAT Measures With the Presence of CAD

On multivariate binary logistic analysis, after adjusting the conventional cardiovascular risk factors (age, gender, BMI, Diabetes Mellitus Type 2, hypertension, smoking, drinking, TC, TG, HDL, LDL) and type of plaques, FAI_{40keV}, λ_{HU}, Eff-Z, FAI_{120kvp}, and EAT attenuation were found to be significantly associated with the presence of CAD (**Table 4**). It should be noted that due to the collinearity between the above-mentioned PCAT-related parameters (FAI_{40keV}, λ_{HU}, Eff-Z, FAI_{120kvp}, and EAT attenuation), we, respectively, substituted these parameters into the regression equation for analysis. According to the standard partial regression coefficient, among these parameters, FAI_{40keV} was the most powerful independent indicator.

ROC Analysis for Prediction of CAD

The ROC curve for FAI_{40keV}, λ_{HU}, Eff-Z, and FAI_{120kvp} showed them as superior predictors of CAD with the corresponding areas under curve (AUC) 0.811, 0.756, 0.646, and 0.731, respectively, which were greater than AUC of EAT attenuation (0.614) (**Figure 5** and **Table 5**). FAI_{40keV} showed the highest AUC with the optimal cutoff value of −131.8 HU to predict CAD, with a diagnostic accuracy of 80.6% compared to the other parameters.

TABLE 1 | Baseline characteristics of study cohort ($n = 403$).

	All patients ($n = 403$)	Non-CAD ($n = 282$)	CAD ($n = 121$)	*p*
Age (years)	57.4 ± 10.1	56.0 ± 10.6	60.5 ± 8.1	< 0.001*
Males (%)	229 (56.8)	145 (51.4)	84 (69.4)	0.001*
BMI (kg/m2)	25.5 ± 3.8	24.9 ± 3.6	26.9 ± 3.9	< 0.001*
History				
Smoking (%)	116 (28.8)	70 (24.8)	46 (38.0)	0.011*
Drinking (%)	98 (24.3)	58 (20.6)	40 (33.1)	0.012*
Diabetes mellitus (%)	121 (30.0)	78 (27.7)	43 (35.5)	0.125
Hypertension (%)	142(35.2)	86 (30.5)	56 (46.3)	0.003*
Laboratory index				
Total cholesterol (mmol/L)	4.76 ± 1.10	4.71 ± 1.00	4.86 ± 1.29	0.273
Triglycerides (mmol/L)	1.40 ± 1.02	1.33 ± 0.74	1.58 ± 1.46	0.074
HDL -cholesterol (mmol/L)	1.11 ± 0.44	1.17 ± 0.46	0.96 ± 0.36	< 0.001*
LDL -cholesterol (mmol/L)	2.97 ± 0.94	2.82 ± 0.86	3.33 ± 1.01	< 0.001*

Compared with the non-CAD group, $^{*}p < 0.05$ was statistically significant.

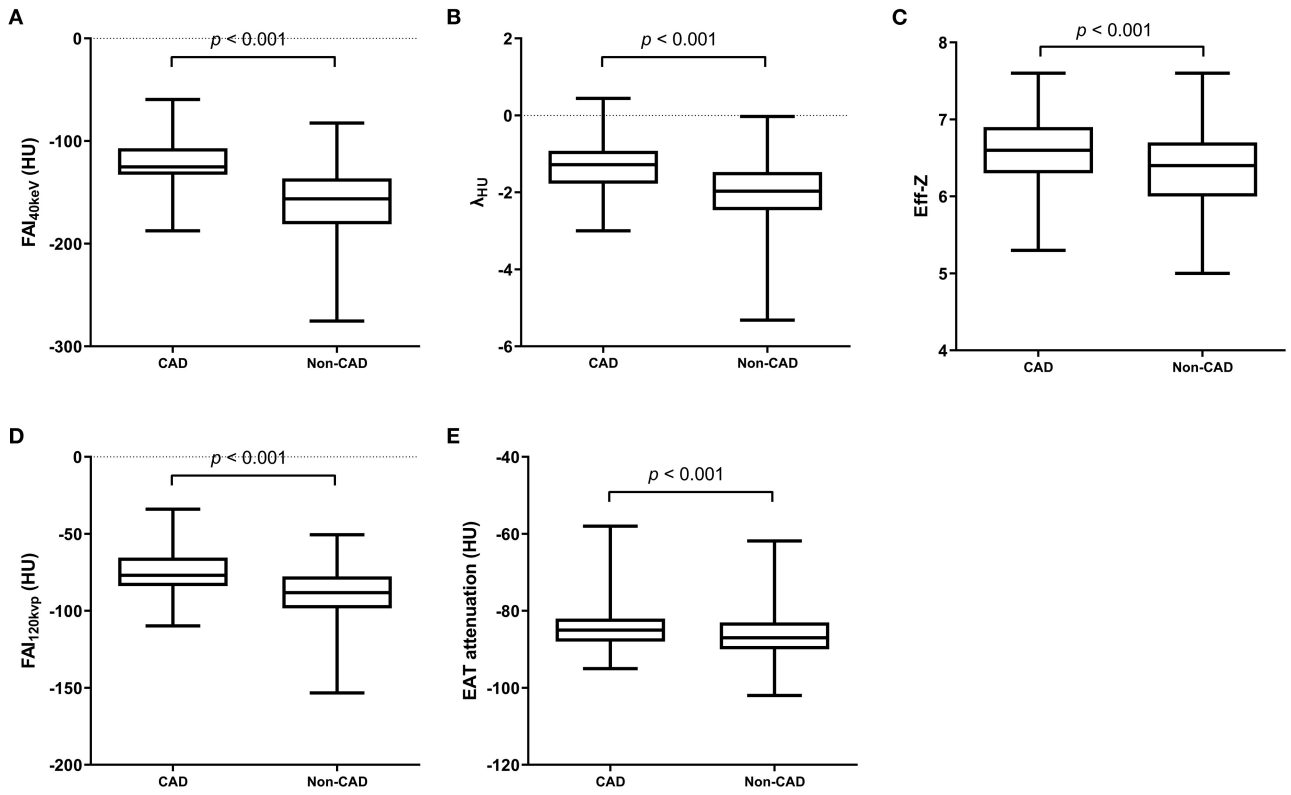

FIGURE 3 | SDCT-related parameters of PCAT and EAT attenuation in CAD and non-CAD groups. FAI40keV **(A)**, λHU **(B)**, Eff-z **(C)** and FAI120kvp **(D)** and EAT attenuation **(E)** were significantly larger in patients with CAD than those in non-CAD group (both $p < 0.001$). A value of $p < 0.05$ indicated statistical significance.

DISCUSSION

Our preliminary findings demonstrated that FAI_{40keV} and λ_{HU} obtained from SDCT were superior to conventional polychromatic CT for detecting the pathologic changes of PCAT during the development and progression of coronary atherosclerosis. Furthermore, PCAT index on SDCT was independently associated with the presence of CAD and FAI_{40keV} was found to be the most powerful independent indictor for CAD.

To the best of our knowledge, this is the first study exploring the relationship between PCAT indicators derived from SDCT

TABLE 2 | Lesion characteristics of coronary CTA in the four subgroups.

Characteristics	Group A	Group B	Group C	Group D
Number of cases	142	140	74	47
Number of lesion branches				
Single-vessel lesion	73	50	6	7
Double-vessel lesions	46	25	7	10
Triple-vessel/ LM lesions	23	65	61	30
Localization of the most serious lesions				
LM	4	6	3	0
LAD	70	77	47	30
LCX	13	7	4	3
RCA	55	50	20	14
Types of plaques characters of the maximal coronary stenosis				
Non-calcified plaques	53	40	29	14
Mixed plaques	11	41	32	25
Calcified plaques	78	59	13	8

Group A, minimal stenosis; Group B, mild stenosis; Group C, moderate stenosis; and Group D, severe stenosis.
Number of lesion branches: the presence of any plaque in the coronary artery (LAD, LCX, RCA and LM), irrespective of the degree of stenosis.
LM, Left main coronary artery; LAD, left anterior descending artery; LCX, Left circumflex coronary artery; RCA, Right coronary artery.

TABLE 3 | SDCT-related parameters of PCAT and EAT attenuation in different degree of stenosis groups.

	Group A	Group B	Group C	Group D	*F*	*p*
PCAT indices on SDCT						
FAI_{40keV} (HU)	$-159.6 \pm 32.5^{\#}$	$-160.9 \pm 35.4^{\#}$	$-131.0 \pm 25.3^{*\#}$	$-113.0 \pm 22.5^{*}$	57.168	< 0.001
λ_{HU}	$-2.0 \pm 0.8^{\#}$	$-2.1 \pm 0.8^{\#}$	$-1.5 \pm 0.7^{*\#}$	$-1.2 \pm 0.6^{*}$	25.692	< 0.001
Eff-Z	$6.3 \pm 0.5^{\#}$	$6.3 \pm 0.5^{\#}$	$6.6 \pm 0.4^{*}$	$6.6 \pm 0.5^{*}$	8.187	< 0.001
FAI_{120kvp} (HU)	$-89.8 \pm 15.3^{\#}$	$-88.3 \pm 18.4^{\#}$	$-77.7 \pm 13.0^{*}$	$-71.4 \pm 14.8^{*}$	26.381	< 0.001
EAT attenuation (HU)	$-86.5 \pm 5.5^{\#}$	$-87.6 \pm 6.0^{\#}$	$-83.4 \pm 8.9^{*}$	$-82.1 \pm 9.5^{*}$	7.818	< 0.001

$^{*}p < 0.05$ *vs. Group A;* $^{\#}p < 0.05$ *vs. Group D.*

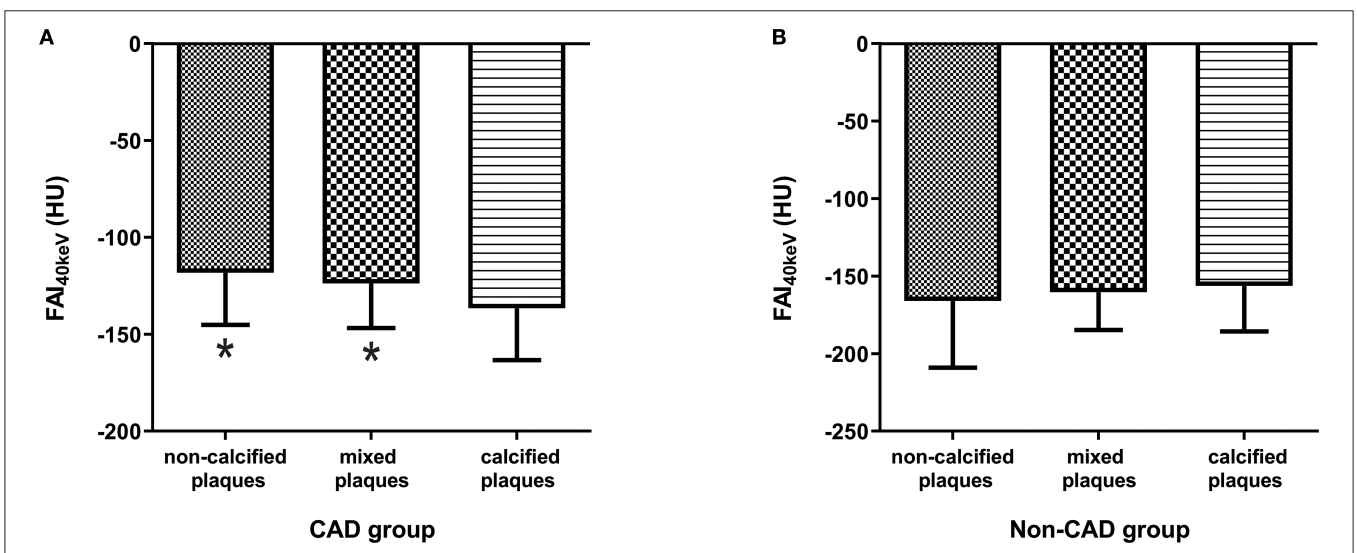

FIGURE 4 | Comparison of FAI40keV (HU) based on plaque type in CAD group **(A)** and non-CAD group **(B)**. $^{*}p < 0.05$ compared to calcified plaques.

TABLE 4 | The association of PCAT measures and EAT attenuation with the presence of CAD.

Analyses	Standard partial regression coefficient	OR (95% CI)	*p*
1st: FAI_{40keV} (HU)	2.029	1.058 (1.044–1.073)	<0.001
2nd: λ_{HU}	1.429	5.733 (3.514–9.352)	<0.001
3rd: Eff-Z	0.752	4.857 (2.449–9.635)	<0.001
4th: FAI_{120kvp} (HU)	1.265	1.076 (1.054–1.099)	<0.001
5th: EAT attenuation (HU)	0.688	1.100 (1.056–1.146)	<0.001

OR, odds ratio; CI, confidence interval. p < 0.05 was regarded as indicating statistical significance.

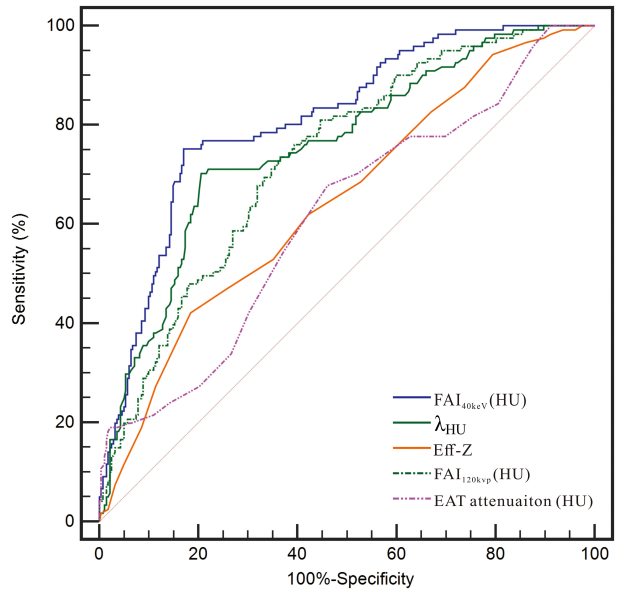

FIGURE 5 | Receiver operating characteristic (ROC) curve analysis showed that compared with other parameters, the FAI_{40kev} had the highest the area under curve (AUC).

with coronary stenosis. The present study showed statistical differences in FAI_{40keV}, FAI_{120kvp}, and EAT attenuation between the non-CAD and CAD groups. The results are consistent with previous studies (6, 24), which found EAT attenuation was significantly higher in the CAD group than that in the non-CAD group. In the early stage of atherosclerosis, perhaps due to the expansion of adipose tissue and accumulation of lipid (25), FAI is relatively low. With the progression of coronary atherosclerosis, as there exists a complex, bidirectional interplay between the vascular wall and perivascular fat (26), pro-inflammatory cytokines released from the vessel wall diffuse directly into the surrounding peri-coronary fat the resulting perivascular inflammation promotes the adipose tissue remodeling and fibrosis (27, 28). Meanwhile, the maturity of the adipocytes and accumulation of intracellular lipids are inhibited (29–31), the adipocyte size get smaller, the lipid droplet content are reduced (10, 32), resulting in FAI increases. In the late stage of coronary atherosclerosis, fibrosis of adipose tissue could aggravate the increase in FAI. As a result, the more severe the coronary stenosis, the higher FAI level.

Furthermore, significant differences were seen in the values of FAI_{40keV} and λ_{HU} between the moderate and severe stenosis groups, with no significant differences between the FAI_{120kvp} and EAT attenuation between the two groups. Correspondingly, the AUCs for FAI_{40keV} and λ_{HU} were higher than those of FAI_{120kvp} and EAT attenuation. Based on the results, it is speculated that the spectral information from SDCT is superior to conventional polychromatic CT in detecting subtle changes in adipose tissue caused by PCAT remodeling during atherosclerosis progression. SDCT is an imaging technology introduced in recent years, which addresses the limitation of conventional polychromatic CT which assess coronary lesions only from a morphological point of view, by providing spectral results such as VMI at a wide range of energy levels (33). In addition, SDCT enables multiple quantitative results, including λ_{HU} and Eff-Z, which make it possible to perform tissue characterization (34, 35). With the capability of simultaneous, homologous and isotropic information, and not requiring any a priori scan decisions, the SDCT provides workflow benefits making it more convenient for routine clinical use. Compared with the values obtained from a polychromatic beam, the CT value under single energy can more accurately reflect the X-ray absorption characteristics of the materials (36). We suggest that the PCAT derived from single energy reconstructions at the low end of the spectrum (corresponding to 40 keV) can better differentiate the fat densities. This is consistent with prior work of Rodriguez-Granillo et al. that showed that VMI at low energy levels (40 keV) can detect differences of fat densities in different locations (22). In our work, we also observed a similar trend in λ_{HU} and Eff-Z. Since PCAT itself is a fat component, the energy spectrum curve is a curve with the back of the arch arched upwards, and the attenuation increased with higher keV. λ_{HU} in the energy range of 40 to 70 keV is negative, and it is significantly higher in the CAD group than that in the non-CAD group. λ_{HU} may be one of the markers reflecting the inflammatory state of PCAT. However, Eff-Z is not sensitive to FAI_{40keV} and λ_{HU} in reflecting pathological changes of PCAT because of its insufficient resolution. These findings highlight the potential value of SDCT in displaying fine changes of PCAT adjacent to plaques that could not be observed using conventional polychromatic CT. Our preliminary results suggest that FAI_{40keV} and λ_{HU} could be the novel surrogate image-markers reflecting the remodeling of PCAT.

Our findings also suggest that PCAT has a better ability to predict vascular stenosis than overall EAT. The possible reasons can be interpreted from the following aspects: Firstly, in terms of pathophysiology, PCAT could act adjacent coronary arteries directly contributing to the development of atherosclerosis through secretion of a large number of pro-inflammatory adipocytokines relating to energy metabolism and causing inflammation in a paracrine and vasocrine manner more than as a systemic inflammatory effect (3, 37), whereas EAT attenuation more reflects the effect of abnormal lipid metabolism on

TABLE 5 | Cut-off values of PCAT indices and EAT attenuation for the detection of CAD.

Parameters	Cut-off value	AUC (95% CI)	Sensitivity (%)	Specificity (%)	Accuracy (%)
FAI_{40keV} (HU)	−131.8	0.811 (0.769–0.848)	75.2	83.0	80.6
λ_{HU}	−1.4	0.756 (0.712–0.798)	70.3	79.4	77.2
Eff-Z	6.7	0.646 (0.597–0.693)	42.2	81.6	66.0
FAI_{120kvp} (HU)	−83.0	0.731 (0.685–0.774)	73.6	63.5	66.5
EAT attenuation (HU)	−87.0	0.614 (0.564–0.662)	67.8	53.9	54.6

AUC, area under the curve.

atherosclerosis, that is, it reflects its role as a visceral fat bank rather than local inflammatory effects. Additionally, when the lesion is mainly on a single coronary artery, the predictive value of global EAT attenuation for vascular stenosis may be weakened as the peri-coronary fat around normal or non-significantly stenosis vessels was relatively normal.

Marwan et al. (38) support a hypothesis of different types or activity of PCAT, the more metabolically active of which might exert local effects on the coronary vessels, thus contributing to atherogenesis. The current study showed that FAI_{40keV} was significantly higher in the maximal stenosis segments with non-calcified or mixed plaques than those with the calcified plaques in CAD cases. This may suggest that PCAT surrounding the atherosclerotic plaques with non-calcified component has higher metabolically activity. This may be related to the characteristic of highly inflamed atherosclerotic plaque, which has been discussed in detail in another separate work of our research team (39). Interestingly, the opposite results were obtained in non-CAD cases, which showed that FAI_{40keV} adjacent to non-calcified plaques was the lowest, although the differences between the groups were not statistically significant. The reason might be that low-stage inflammation causing more lipid droplets accumulated in adipocytes and an increase in cell size (40, 41) in the early stage of atherosclerotic plaque formation. Previous research (21, 42) has shown that EAT volume was significantly greater in coronary segments with non-calcified or mixed plaques compared than those with calcified plaques. This may lead to the low attenuation of PCAT adjacent non-calcified plaques. The results seemed to suggest that the effect of different types of plaque on the adjacent PCAT is not invariable with the progress of atherosclerosis.

Recent studies (10) show that FAI can non-invasively monitor the vascular inflammation and the development of CAD *in vivo*. Our results demonstrated that FAI_{40keV} was the best predictor for CAD with the optimal cut-off value of −131.8 HU. FAI_{40keV} achieved higher AUC, sensitivity and accuracy than other parameters because of its higher sensitivity in detecting adipose attenuation differences. And with the degree of atherosclerotic lesion, FAI_{40keV} tended to increase as mentioned in the above discussion, which reflected that FAI_{40keV} could detect the subtle changes of PCAT around the lesions in different stages of CAD. Monitoring changes in FAI_{40keV} during at different phases of CAD may help to better understand the mechanism of PCAT promotes atherogenesis. This may make FAI_{40keV} a new promising imaging marker to identify and monitor the course of coronary atherosclerosis. However, there are few studies on PCAT based on SDCT, and it is difficult for us to compare with other studies.

Several limitations should be noted. First, this study is only a single-center retrospective study with limited sample size. The results need to be verified in a large prospective cohort. Second, this was a cross-sectional study, with the initial state of the study subjects unknown, and a longitudinal study would be more helpful to reveal the relationship between progression of atherosclerosis and PCAT. And lastly, the optimal cut-offs of identified need further validation.

CONCLUSIONS

Our preliminary results support the superiority of the FAI derived from spectral CT images (FAI_{40keV}) along with the slope of the spectral attenuation curve (λ_{HU}) over the corresponding index from conventional polychromatic CT reconstructions (FAI_{120kvp}) and EAT attenuation for detecting the pathologic changes of PCAT during the development and progression of atherosclerosis. FAI_{40keV} could be a novel dynamic surrogate imaging marker of vascular inflammation and if its potential value was further verified in larger clinical trials with outcomes data, this could be a powerful indicator of a potential occurrence, development and prognostic information of a coronary lesion.

DATA AVAILABILITY STATEMENT

The original contributions presented in the study are included in the article/**Supplementary Material**, further inquiries can be directed to the corresponding authors.

ETHICS STATEMENT

The study was approved by institutional review board of Shengjing Hospital of China Medical University. Written informed consent for participation was not required for this study in accordance with the national legislation and the institutional requirements.

AUTHOR CONTRIBUTIONS

YD, KW, and YH participated in conceiving and designing of the study. YD, XC, SM, YM, QM, KZ, and TL contributed to collecting and assembling of data. YD, XC, KW, and YH

contributed to analyzing and interpreting of data. YD, XC, and YH contributed to drafting of the manuscript. All authors approved the final version of manuscript for publication.

FUNDING

This study has received funding by the National Natural Science Foundation of China (Grant Nos. 82071920 and 81901741), the Key Research and Development Plan of Liaoning Province (No. 2020JH2/10300037) and 345 Talent Project in Shengjing Hospital of China Medical University.

ACKNOWLEDGMENTS

The authors would like to acknowledge Mani Vembar, Hui Yao, Zheng Jia, Xiaomei Lu and Xiaoliang Xiong for their assistance with CT technology and data measurement.

SUPPLEMENTARY MATERIAL

The Supplementary Material for this article can be found online at: https://www.frontiersin.org/articles/10.3389/fcvm.2021.720127/full#supplementary-material

REFERENCES

1. Madonna R, Massaro M, Scoditti E, Pescetelli I, De Caterina R. The epicardial adipose tissue and the coronary arteries: dangerous liaisons. *Cardiovasc Res*. (2019) 115:1013–25. doi: 10.1093/cvr/cvz062
2. Hirata Y, Tabata M, Kurobe H, Motoki T, Akaike M, Nishio C, et al. Coronary atherosclerosis is associated with macrophage polarization in epicardial adipose tissue. *J Am College Cardiol*. (2011) 58:248–55. doi: 10.1016/j.jacc.2011.01.048
3. Wu Y, Zhang A, Hamilton DJ, Deng T. Epicardial fat in the maintenance of cardiovascular health. *Methodist DeBakey Cardiovas J*. (2017) 13:20–4. doi: 10.14797/mdcj-13-1-20
4. Franssens BT, Nathoe HM, Leiner T, van der Graaf Y, Visseren FL, group Ss. Relation between cardiovascular disease risk factors and epicardial adipose tissue density on cardiac computed tomography in patients at high risk of cardiovascular events. *Eur J Prevent Cardiol*. (2017) 24:660–70. doi: 10.1177/2047487316679524
5. Mahabadi AA, Balcer B, Dykun I, Forsting M, Schlosser T, Heusch G, et al. Cardiac computed tomography-derived epicardial fat volume and attenuation independently distinguish patients with and without myocardial infarction. *PLoS ONE*. (2017) 12:e0183514. doi: 10.1371/journal.pone.0183514
6. Liu Z, Wang S, Wang Y, Zhou N, Shu J, Stamm C, et al. Association of epicardial adipose tissue attenuation with coronary atherosclerosis in patients with a high risk of coronary artery disease. *Atherosclerosis*. (2019) 284:230–6. doi: 10.1016/j.atherosclerosis.2019.01.033
7. Goeller M, Tamarappoo BK, Kwan AC, Cadet S, Commandeur F, Razipour A, et al. Relationship between changes in pericoronary adipose tissue attenuation and coronary plaque burden quantified from coronary computed tomography angiography. *Eur Heart J Cardiovasc Imaging*. (2019) 20:636–43. doi: 10.1093/ehjci/jez013
8. Mancio J, Oikonomou EK, Antoniades C. Perivascular adipose tissue and coronary atherosclerosis. *Heart*. (2018) 104:1654–62. doi: 10.1136/heartjnl-2017-312324
9. Fernandez-Alfonso MS, Gil-Ortega M, Aranguez I, Souza D, Dreifaldt M, Somoza B, et al. Role of PVAT in coronary atherosclerosis and vein graft patency: friend or foe? *Br J Pharmacol*. (2017) 174:3561–72. doi: 10.1111/bph.13734
10. Antonopoulos AS, Sanna F, Sabharwal N, Thomas S, Oikonomou EK, Herdman L, et al. Detecting human coronary inflammation by imaging perivascular fat. *Sci Transl Med*. (2017) 9:398. doi: 10.1126/scitranslmed.aal2658
11. Yu M, Dai X, Deng J, Lu Z, Shen C, Zhang J. Diagnostic performance of perivascular fat attenuation index to predict hemodynamic significance of coronary stenosis: a preliminary coronary computed tomography angiography study. *Eur Radiol*. (2020) 30:673–81. doi: 10.1007/s00330-019-06400-8
12. Oikonomou EK, Marwan M, Desai MY, Mancio J, Alashi A, Hutt Centeno E, et al. Non-invasive detection of coronary inflammation using computed tomography and prediction of residual cardiovascular risk (the CRISP CT study): a post-hoc analysis of prospective outcome data. *Lancet*. (2018) 392:929–39. doi: 10.1016/S0140-6736(18)31114-0
13. Goeller M, Achenbach S, Cadet S, Kwan AC, Commandeur F, Slomka PJ, et al. Pericoronary adipose tissue computed tomography attenuation and high-risk plaque characteristics in acute coronary syndrome compared with stable coronary artery disease. *JAMA Cardiol*. (2018) 3:858–63. doi: 10.1001/jamacardio.2018.1997
14. Huang X, Gao S, Ma Y, Lu X, Jia Z, Hou Y. The optimal monoenergetic spectral image level of coronary computed tomography (CT) angiography on a dual-layer spectral detector CT with half-dose contrast media. *Quant Imaging Med Surg*. (2020) 10:592–603. doi: 10.21037/qims.2020.02.17
15. Yi Y, Zhao XM, Wu RZ, Wang Y, Vembar M, Jin ZY, et al. Low Dose and low contrast medium coronary CT angiography using dual-layer spectral detector CT. *Int Heart J*. (2019) 60:608–17. doi: 10.1536/ihj.18-340
16. Zopfs D, Lennartz S, Laukamp K, Grosse Hokamp N, Mpotsaris A, Maintz D, et al. Improved depiction of atherosclerotic carotid artery stenosis in virtual monoenergetic reconstructions of venous phase dual-layer computed tomography in comparison to polyenergetic reconstructions. *Eur J Radiol*. (2018) 100:36–42. doi: 10.1016/j.ejrad.2018.01.008
17. Neuhaus V, Abdullayev N, Grosse Hokamp N, Pahn G, Kabbasch C, Mpotsaris A, et al. Improvement of image quality in unenhanced dual-layer CT of the head using virtual monoenergetic images compared with polyenergetic single-energy CT. *Invest Radiol*. (2017) 52:470–6. doi: 10.1097/RLI.0000000000000367
18. Taguchi N, Oda S, Kobayashi T, Naoe H, Sasaki Y, Imuta M, et al. Advanced parametric imaging for evaluation of Crohn's disease using dual-energy computed tomography enterography. *Radiol Case Rep*. (2018) 13:709–12. doi: 10.1016/j.radcr.2018.04.002
19. Ma Q, Hu J, Yang W, Hou Y. Dual-layer detector spectral CT versus magnetic resonance imaging for the assessment of iron overload in myelodysplastic syndromes and aplastic anemia. *Jpn J Radiol*. (2020) 38:374–81. doi: 10.1007/s11604-020-00921-9
20. Raff GL, Chinnaiyan KM, Cury RC, Garcia MT, Hecht HS, Hollander JE, et al. SCCT guidelines on the use of coronary computed tomographic angiography for patients presenting with acute chest pain to the emergency department: a report of the Society of Cardiovascular Computed Tomography Guidelines Committee. *J Cardiovas Computed Tomogr*. (2014) 8:254–71. doi: 10.1016/j.jcct.2014.06.002
21. Hassan M, Said K, Rizk H, ElMogy F, Donya M, Houseni M, et al. Segmental peri-coronary epicardial adipose tissue volume and coronary plaque characteristics. *Eur Heart J Cardiovasc Imaging*. (2016) 17:1169–77. doi: 10.1093/ehjci/jev298
22. Rodriguez-Granillo GA, Capunay C, Deviggiano A, De Zan M, Carrascosa P. Regional differences of fat depot attenuation using non-contrast, contrast-enhanced, and delayed-enhanced cardiac CT. *Acta Radiol*. (2019) 60:459–67. doi: 10.1177/0284185118787356
23. Sampat MP, Whitman GJ, Stephens TW, Broemeling LD, Heger NA, Bovik AC, et al. The reliability of measuring physical characteristics of spiculated masses on mammography. *Br J Radiol*. (2006) 79:S134–40. doi: 10.1259/bjr/96723280

24. Pracon R, Kruk M, Kepka C, Pregowski J, Opolski MP, Dzielinska Z, et al. Epicardial adipose tissue radiodensity is independently related to coronary atherosclerosis. A multidetector computed tomography study. *Circulation J.* (2011) 75:391–7. doi: 10.1253/circj.CJ-10-0441
25. Mahabadi AA, Lehmann N, Kalsch H, Robens T, Bauer M, Dykun I, et al. Association of epicardial adipose tissue with progression of coronary artery calcification is more pronounced in the early phase of atherosclerosis: results from the Heinz Nixdorf recall study. *JACC Cardiovas Imaging.* (2014) 7:909–16. doi: 10.1016/j.jcmg.2014.07.002
26. Lin A, Dey D, Wong DTL, Nerlekar N. Perivascular adipose tissue and coronary atherosclerosis: from biology to imaging phenotyping. *Curr Atheroscler Rep.* (2019) 21:47. doi: 10.1007/s11883-019-0817-3
27. Wernstedt Asterholm I, Tao C, Morley TS, Wang QA, Delgado-Lopez F, Wang ZV, et al. Adipocyte inflammation is essential for healthy adipose tissue expansion and remodeling. *Cell Metabol.* (2014) 20:103–18. doi: 10.1016/j.cmet.2014.05.005
28. Numaguchi R, Furuhashi M, Matsumoto M, Sato H, Yanase Y, Kuroda Y, et al. Differential phenotypes in perivascular adipose tissue surrounding the internal thoracic artery and diseased coronary artery. *J Am Heart Assoc.* (2019) 8:e011147. doi: 10.1161/JAHA.118.011147
29. Skiba DS, Nosalski R, Mikolajczyk TP, Siedlinski M, Rios FJ, Montezano AC, et al. Anti-atherosclerotic effect of the angiotensin 1-7 mimetic AVE0991 is mediated by inhibition of perivascular and plaque inflammation in early atherosclerosis. *Br J Pharmacol.* (2017) 174:4055–69. doi: 10.1111/bph.13685
30. Quesada I, Cejas J, Garcia R, Cannizzo B, Redondo A, Castro C. Vascular dysfunction elicited by a cross talk between periaortic adipose tissue and the vascular wall is reversed by pioglitazone. *Cardiovas Therapeut.* (2018) 36:e12322. doi: 10.1111/1755-5922.12322
31. Qi XY, Qu SL, Xiong WH, Rom O, Chang L, Jiang ZS. Perivascular adipose tissue (PVAT) in atherosclerosis: a double-edged sword. *Cardiovasc Diabetol.* (2018) 17:134. doi: 10.1186/s12933-018-0777-x
32. Back M, Yurdagul A Jr, Tabas I, Oorni K, Kovanen PT. Inflammation and its resolution in atherosclerosis: mediators and therapeutic opportunities. *Nat Rev Cardiol.* (2019) 16:389–406. doi: 10.1038/s41569-019-0169-2
33. Marin D, Fananapazir G, Mileto A, Choudhury KR, Wilson JM, Nelson RC. Dual-energy multi-detector row CT with virtual monochromatic imaging for improving patient-to-patient uniformity of aortic enhancement during CT angiography: an in vitro and in vivo study. *Radiology.* (2014) 272:895–902. doi: 10.1148/radiol.14132857
34. Jia Y, Xiao X, Sun Q, Jiang H. CT spectral parameters and serum tumour markers to differentiate histological types of cancer histology. *Clin Radiol.* (2018) 73:1033–40. doi: 10.1016/j.crad.2018.07.104
35. Goo HW, Goo JM. Dual-Energy CT: new Horizon in medical imaging. *Korean J Radiol.* (2017) 18:555–69. doi: 10.3348/kjr.2017.18.4.555
36. Matsumoto K, Jinzaki M, Tanami Y, Ueno A, Yamada M, Kuribayashi S. Virtual monochromatic spectral imaging with fast kilovoltage switching: improved image quality as compared with that obtained with conventional 120-kVp CT. *Radiology.* (2011) 259:257–62. doi: 10.1148/radiol.11100978
37. Noyes AM, Dua K, Devadoss R, Chhabra L. Cardiac adipose tissue and its relationship to diabetes mellitus and cardiovascular disease. *World J Diabetes.* (2014) 5:868–76. doi: 10.4239/wjd.v5.i6.868
38. Marwan M, Hell M, Schuhback A, Gauss S, Bittner D, Pflederer T, et al. CT Attenuation of pericoronary adipose tissue in normal versus atherosclerotic coronary segments as defined by intravascular ultrasound. *J Computer Assisted Tomogr.* (2017) 41:762–7. doi: 10.1097/RCT.0000000000000589
39. Chen X, Dang Y, Hu H, Ma S, Ma Y, Wang K, et al. Pericoronary adipose tissue attenuation assessed by dual-layer spectral detector computed tomography is a sensitive imaging marker of high-risk plaques. *Quant Imaging Med Surgery.* (2021) 11:2093–103. doi: 10.21037/qims-20-860
40. Aldiss P, Davies G, Woods R, Budge H, Sacks HS, Symonds ME. 'Browning' the cardiac and peri-vascular adipose tissues to modulate cardiovascular risk. *Int J Cardiol.* (2017) 228:265–74. doi: 10.1016/j.ijcard.2016.11.074
41. Sun K, Kusminski CM, Scherer PE. Adipose tissue remodeling and obesity. *J Clin Invest.* (2011) 121:2094–101. doi: 10.1172/JCI45887
42. Alexopoulos N, McLean DS, Janik M, Arepalli CD, Stillman AE, Raggi P. Epicardial adipose tissue and coronary artery plaque characteristics. *Atherosclerosis.* (2010) 210:150–4. doi: 10.1016/j.atherosclerosis.2009.11.020

Conflict of Interest: The authors declare that the research was conducted in the absence of any commercial or financial relationships that could be construed as a potential conflict of interest.

frontiers in Cardiovascular Medicine

ORIGINAL RESEARCH
published: 30 September 2021
doi: 10.3389/fcvm.2021.715514

Lesion Length Improves Diagnostic Accuracy of Intravascular Ultrasound for Detecting Functional Intermediate Coronary Stenosis Evaluated With Coronary Angiography-Derived Fractional Flow Reserve in Non-left Main Artery

Menghuan Li[1], *Iokfai Cheang*[1], *Yuan He*[1], *Shengen Liao*[1], *Hui Wang*[1]* and *Xiangqing Kong*[1,2]*

[1] Department of Cardiology, The First Affiliated Hospital of Nanjing Medical University, Nanjing, China, [2] Gusu School, Nanjing Medical University, Suzhou, China

OPEN ACCESS

Edited by:
Juan Carlos Del Alamo,
University of Washington,
United States

Reviewed by:
Dalin Tang,
Worcester Polytechnic Institute,
United States
Erhan Tenekecioglu,
University of Health Sciences, Turkey

***Correspondence:**
Xiangqing Kong
kongxq@njmu.edu.cn
Hui Wang
Wangnuo@188.com

Specialty section:
This article was submitted to Cardiovascular Imaging, a section of the journal Frontiers in Cardiovascular Medicine

Received: 27 May 2021
Accepted: 20 August 2021
Published: 30 September 2021

Citation:
Li M, Cheang I, He Y, Liao S, Wang H and Kong X (2021) Lesion Length Improves Diagnostic Accuracy of Intravascular Ultrasound for Detecting Functional Intermediate Coronary Stenosis Evaluated With Coronary Angiography-Derived Fractional Flow Reserve in Non-left Main Artery. Front. Cardiovasc. Med. 8:715514. doi: 10.3389/fcvm.2021.715514

Objective: Intravascular ultrasound (IVUS) parameters, for example, minimal lumen area (MLA) and area stenosis (AS), poorly identified functional intermediate coronary stenosis (ICS). For detecting functional ICS defined by coronary angiography-derived fractional flow reserve (caFFR), our study aims to determine whether IVUS parameters integrated with lesion length (LL) by three-dimensional quantitative coronary analysis (3D-QCA) could improve diagnostic value.

Methods: A total of 111 patients with 122 ICS lesions in the non-left main artery were enrolled. MLA and AS were calculated in all lesions by IVUS. Diameter stenosis (DS%) and LL were measured by 3D-QCA. caFFR was computed by the proprietary fluid dynamic algorithm, a caFFR $\leq$ 0.8 was considered as functional stenosis. Receiver-operating curve analyses were used to compare the diagnostic accuracy among indices to predict functional stenoses.

Results: Mean caFFR values in all lesions were 0.86 $\pm$ 0.09. Lesions with caFFR $\leq$ 0.8 showed lower MLA and higher AS (MLA: 3.3 $\pm$ 0.8 vs. 4.1 $\pm$ 1.2, $P = 0.002$; AS: 71.3 $\pm$ 9.6% vs. 63.5 $\pm$ 1.3%, $P = 0.007$). DS% and LL were more severe in lesions with caFFR $\leq$ 0.8 (DS%: 45.5 $\pm$ 9.6% vs. 35.5 $\pm$ 8.2%, $P < 0.001$; LL: 31.6 $\pm$ 12.9 vs. 21.0 $\pm$ 12.8, $P < 0.001$). caFFR were correlated with MLA, AS, and LL (MLA: $r = 0.36$, $P < 0.001$; AS: $r = -0.36$, $P < 0.001$; LL: $r = -0.41$, $P < 0.001$). Moreover, a multiple linear regression analysis demonstrated that MLA ($\beta = 0.218$, $P = 0.013$), AS ($\beta = -0.197$, $P = 0.029$), and LL ($\beta = -0.306$, $P > 0.001$) contributed significantly to the variation in caFFR. The best cutoff value of MLA, AS, and LL for predicting caFFR $\leq$ 0.8 were 3.6 mm^2, 73%, and 26 mm, with area under the curve (AUC) of 0.714, 0.688, and 0.767, respectively. Combined with MLA, AS, and LL for identifying functional ICS, the accuracy was the highest among study methods (AUC: 0.845, $P < 0.001$), and was significantly higher than each single method (All $P < 0.05$).

Conclusion: Lesion length can improve the diagnostic accuracy of IVUS-derived parameters for detecting functional ICS.

Keywords: intravascular ultrasound, computational angiography-derived fractional flow reserve, intermediate coronary artery stenosis, three dimensional quantitative coronary angiography, diagnostic accuracy

INSTRUCTIONS

Intermediate coronary artery lesion refers to stenoses with 40–70% of stenosis severity found by coronary angiography (1). Currently, percutaneous coronary intervention (PCI) is one of the most common invasive therapeutic techniques worldwide, showing a tremendous survival benefit in patients with acute coronary syndromes and patients with significant stenosis deemed myocardial ischemia (2–4). However, the decision of revascularization or medical therapy remains controversial in patients with intermediate coronary stenosis (ICS), in which the optimal assessment method of these functional significances was essential.

Functional assessment was essential to explore myocardial perfusion for ICS lesion. Fractional flow reserve (FFR) is a validated index for evaluating functional severity of coronary artery lesions (3, 5). FFR < 0.8 is usually considered as a positive functional stenosis, which indicates myocardial ischemia. Functional assessment of ICS by FFR was shown to be superior to visual assessment for therapeutic strategy-making (5). However, the use of invasive pressure wire and induction of hyperemia are required during the measurement of FFR, causing patient discomfort and limiting its clinical use (6). In recent years, computational approaches-derived FFR indices have been developed to detect functional coronary stenosis noninvasively. FLASH FFR study showed good diagnostic performance of a novel coronary angiography-derived FFR (caFFR), with a diagnostic accuracy of 95.7%, sensitivity of 90.4%, specificity of 98.6%, and the area under the curve of 0.979, to detect an invasive FFR ≤ 0.8 (7).

Intravascular ultrasound (IVUS) is a common method to evaluate functional intermediate stenosis in clinical practice. However, several studies demonstrated that minimal lumen area (MLA) and area stenosis (AS) had a weak-moderate correlation with FFR (1, 8–10). In addition, the best threshold of IVUS-MLA or IVUS-AS for detecting functional ICS remains controversial. The accuracy of identifying functional stenosis by IVUS parameters was not satisfied compared with FFR.

A previous study reported that lesion length (LL) calculated with quantitative coronary angiography (QCA) was associated with myocardial ischemia (11). In this study, we hypothesized that integrating LL could improve accuracy for detecting functional ICS. Our study aims to determine whether IVUS parameters, including MLA and AS, integrated with LL measured by three-dimensional QCA (3D-QCA) could improve diagnostic value for detecting caFFR ≤ 0.8.

METHODS

Study Population

This observational retrospective single-center study enrolled patients with ICS who underwent IVUS evaluation from January 2014 to January 2019. ICS was defined as 40–70% diameter stenosis on visual estimation. Exclude criteria were: left main coronary artery (LMCA) lesions, bypass graft lesions, true bifurcation lesions, poor quality of coronary angiogram precluding caFFR computation (e.g., substantial foreshortening or overlap of the vessels, absence of two angiographic projections with the view of at least 30° apart, insufficient contrast flush), ostial lesions in a major artery, and incomplete data of IVUS parameters.

Study protocol was approved by the independent institutional ethical committee of the First Affiliated Hospital of Nanjing Medical University. The study complied with the Declaration of Helsinki. Written informed consents were obtained from all participants before examinations.

IVUS Imaging

IVUS imaging was performed after intracoronary administration of 200 ug nitroglycerin using a 20-MHz phased-array transducer (Eagle Eye Gold^{TM}) coupled with an imaging console (Volcano, Rancho Cordova, CA). The transducer was introduced to the distal portion of target lesions and was pulled back to the proximal vessel at a speed of 0.5–1.0 mm/s. MLA was analyzed at the site of most stenosis with the smallest lumen area. The reference vessel cross-sectional area was measured by identifying the edge of the adventitia. AS was calculated as reference cross-sectional area minus MLA and divided by reference cross-sectional area.

caFFR Measurement

The operator who performed caFFR computation (Rainmed Ltd., Suzhou, China) was blind to IVUS results. To assess caFFR, two angiographic images of the target vessel excluding overlapped or foreshortening vessels, separated by at least 30° apart were selected to reconstruct a three-dimension (3D) model of the coronary artery. The model provided 3D-QCA data, including LL, diameter stenosis fraction (DS%), and flow speed. Invasive aortic blood pressure was reviewed from the data of the institutional catheter center and was input to the FlashAngio console. Resting flow velocities were determined by TIMI Frame Count and anatomical information was derived from the 3D model. caFFR were calculated by FlashAngio software with a proprietary fluid dynamic algorithm. Similar to FFR, a caFFR of $\leq$0.8 was considered significant.

Statistical Analysis

Data distribution was assessed by the Kolgormonov-Smirnov test. Numerical variables with normal distribution were presented as the mean ± standard deviation and were compared by independent sample student's *t*-test. Non-normally distributed continuous variables were presented as median with interquartile range (IQR) and compared by non-parametric Mann–Whitney *U* test. Categorical variables were calculated using counts and percentages, and were evaluated by Chi-square test or Fisher exact test as appropriate. The correlation between caFFR and MLA, AS, and LL was analyzed by calculating Pearson R correlation coefficients for variables with normal distribution or Spearman rank's correlation coefficients for variables with non-normal distribution. Linear regression analysis was conducted to evaluate the effect of MLA, AS, and LL on caFFR. Receiver operation curves (ROC) analysis was applied to assess the best cutoff values of MLA, AS, and LL predicting caFFR $\leq$ 0.8 using MedCalc (version 18.2.1, Mariakerke, Belgium). The best cutoff value was calculated using the Youden index. Sensitivity, specificity, positive predictive value, and negative predictive value with 95% confidence intervals were determined for each cutoff value. The combined diagnostic power of MLA, AS, and LL was estimated with ROC by adding a new variable calculating by binary logistic regression. $P < 0.05$ was considered statistically significant. Statistical analyses were performed by

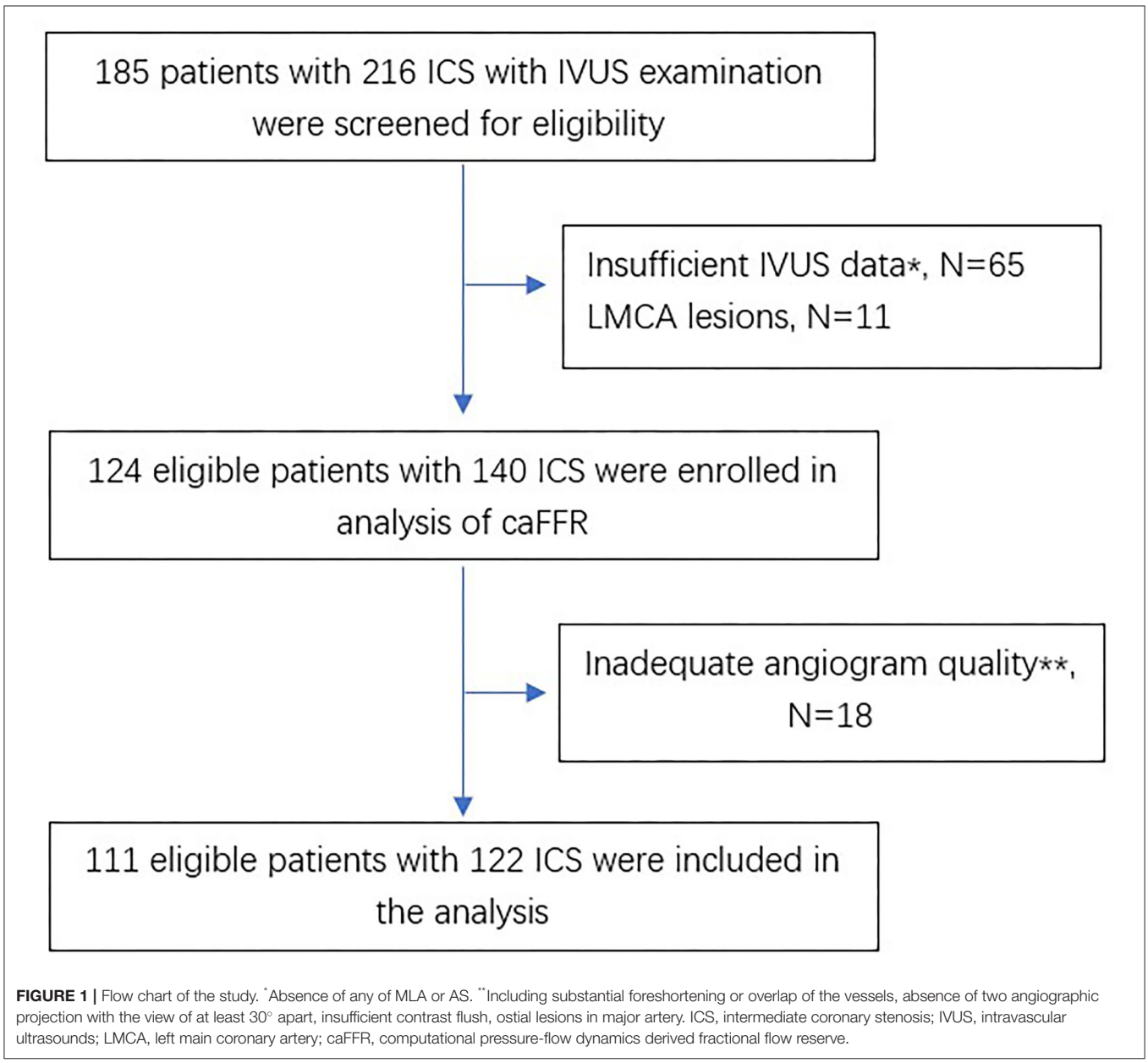

FIGURE 1 | Flow chart of the study. *Absence of any of MLA or AS. **Including substantial foreshortening or overlap of the vessels, absence of two angiographic projection with the view of at least 30° apart, insufficient contrast flush, ostial lesions in major artery. ICS, intermediate coronary stenosis; IVUS, intravascular ultrasounds; LMCA, left main coronary artery; caFFR, computational pressure-flow dynamics derived fractional flow reserve.

TABLE 1 | Clinical characteristics of patients between the caFFR ≤ 0.8 group and the caFFR > 0.8 group.

Patient characteristics	All *N* = 111	caFFR ≤ 0.8 *N* = 22	caFFR > 0.8 *N* = 89	*P* value
Age (years)	63.61 ± 0.4	64.31 ± 0.0	63.51 ± 0.6	0.755
Male	79 (71.2)	16 (72.7)	63 (70.8)	0.857
Hypertension	69 (62.2)	16 (72.7)	53 (59.6)	0.254
Diabetes mellitus	24 (21.6)	6 (27.3)	18 (20.3)	0.472
Hyperlipidemia	9(8.1)	1 (4.5)	8 (9.0)	0.685
Stroke	11 (9.9)	5 (22.7)	6 (6.7)	0.025
Smoking	41 (36.9)	12 (54.5)	29 (32.6)	0.056
Previous PCI	7 (6.3)	3 (13.6)	4 (4.5)	0.138
LVEF (%)	63.54 ± 0.6	62.46 ± 0.9	63.74 ± 0.1	0.347
Diagnoses				0.171
SAP	40 (36.0)	12 (54.5)	28 (31.5)	
UAP	59(53.2)	8 (36.4)	51 (57.3)	
STEMI	9(8.1)	2 (9.1)	7 (7.9)	
NSTEMI	3 (2.7)	0 (0)	3 (3.4)	
Invasive blood pressure				
SBP (mmHg)	1252 ± 0	1222 ± 1	1252 ± 0	0.500
DBP (mmHg)	821 ± 3	801 ± 5	821 ± 2	0.374

PCI, percutaneous coronary intervention; LVEF, left ventricular ejection fraction; SAP, stable angina pectoris; UAP, unstable angina pectoris; STEMI, ST segment elevated myocardial infarction; NSTEMI, non-ST-segment elevated myocardial infarction; SBP, systolic blood pressure; DBP, diastolic blood pressure.

Statistical Program for Social Sciences 21.0 software (SPSS, Inc., Chicago, IL).

RESULTS

Figure 1 shows the flow chart of this study. A total of 185 patients with 216 ICS lesions assessed by IVUS were screened for eligibility. There were 140 lesions enrolled in the analysis of caFFR, of which, 111 patients with 122 ICS lesions completed 3D-QCA and caFFR analysis. The main reasons for screening failure were insufficient IVUS data (65 lesions, 30.1%), LMCA lesions (11 lesions, 5.1%), and inadequate angiogram quality (18 lesions, 8.3%).

Clinical characteristics of patients are presented in **Table 1**. Mean age was 63.6 ± 10.4 years, 71.2% were male. Risk factors including hypertension, diabetes mellitus, hyperlipidemia, and smoking had no significant differences between the caFFR ≤ 0.8 group and the caFFR > 0.8 group; while stroke was more frequent in patients with caFFR ≤ 0.8. Forty patients were diagnosed as stable angina pectoris (SAP), 59 as unstable angina pectoris (UAP), nine as ST-segment elevated myocardial infarction (STEMI), and three as non-ST-segment elevated myocardial infarction (NSTEMI). No significant difference of distribution among the presentation of patients was shown between groups.

Mean caFFR value in all lesions was 0.86 ± 0.09. Lesions with caFFR ≤ 0.8 showed lower MLA and higher AS compared with

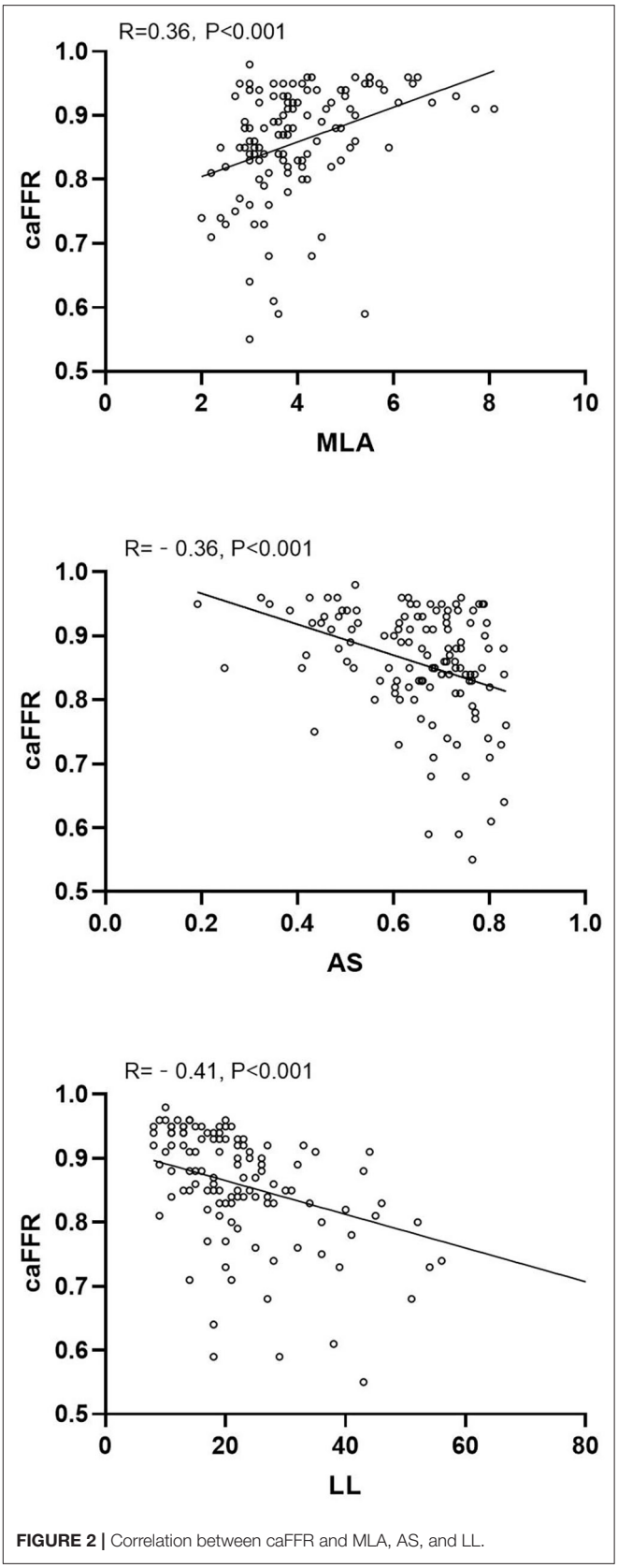

FIGURE 2 | Correlation between caFFR and MLA, AS, and LL.

TABLE 2 | Lesion characteristics between the caFFR ≤ 0.8 group and the caFFR > 0.8 group.

Lesion characteristics	All $N = 122$	caFFR ≤ 0.8 $N = 24$	caFF > 0.8 $N = 98$	*P* value
IVUS-parameters				
MLA (mm^2)	4.01 ± 0.2	3.30 ± 0.8	4.11 ± 0.2	0.002
AS (%)	65.11 ± 0.3	71.39 ± 0.6	63.51 ± 0.3	0.007
3D-QCA parameters				
Diameter stenosis (%)	37.59 ± 0.4	45.59 ± 0.6	35.58 ± 0.2	<0.001
Lesion length (mm)	23.01 ± 3.5	31.61 ± 2.9	21.01 ± 2.8	<0.001
Flow speed (cm/s)	144.55 ± 2.7	159.34 ± 8.1	140.15 ± 3.3	0.126
Target vessels				1.000
LAD	97 (79.5)	19 (79.2)	78 (79.6)	
LCX	6 (4.9)	1 (4.2)	5 (5.1)	
RCA	19 (15.6)	4 (16.7)	15 (15.3)	
Treatment				0.082
Stenting	52 (42.6)	14 (58.3)	38 (38.8)	
Medical treatment only	70 (57.4)	10 (41.7)	60 (61.2)	
caFFR value	0.860 ± 0.09	0.720 ± 0.07	0.890 ± 0.05	<0.001

IVUS, intravascular ultrasound; MLA, minimal lumen area; AS, area stenosis; 3D-QCA, three-dimensional quantitative coronary angiography; LAD, left anterior descending branch; LCX, left circumflex artery; RCA, right coronary artery.

TABLE 3 | Linear regression analysis of the effect of MLA, AS, and LL on caFFR.

	Univariate analysis			Multivariate analysis		
Variables	***β***	**95% CI**	***P* value**	***β***	**95% CI**	***P* value**
Intercept				0.924	0.818–1.013	<0.001
MLA	0.361	0.014–0.039	<0.001	0.218	0.004–0.029	0.013
AS	0.352	−0.311–−0.108	<0.001	−0.197	−0.249–−0.014	0.029
LL	−0.423	−0.003–−0.001	<0.001	−0.306	−0.003–−0.001	<0.001

β, standardized regression coefficient; CI, confidence interval; MLA, minimal lumen area; AS, area stenosis; LL, lesion length.

TABLE 4 | Diagnostic value of different variables.

Index	Positive threshold	Area	Sen	Spe	PPV	NPV	*P* value
MLA	≤3.6	0.714	75	63	33	91	<0.001
AS	>73%	0.688	54	77	36	87	0.002
LL	>26	0.767	58	82	44	89	<0.001
MLA+AS+LL		0.845	83	73	44	95	<0.001

MLA, minimal lumen area; AS, area stenosis; LL, lesion length; Sen, sensitivity; Spe, specificity; PPV, positive predictive value; NPV, negative predictive value.

caFFR > 0.8 (MLA: 3.3 ± 0.8 vs. 4.1 ± 1.2, $P = 0.002$; AS: 71.3 ± 9.6% vs. 63.5 ± 1.3%, $P = 0.007$). Diameter stenosis (DS%) and lesion length (LL) evaluated by 3D-QCA were more severe in the group of caFFR ≤ 0.8 (DS%: 45.5 ± 9.6% vs. 35.5 ± 8.2%, $P < 0.001$; LL: 31.6 ± 12.9 vs. 21.0 ± 12.8, $P < 0.001$) (**Table 2**).

caFFR showed moderate correlations with MLA, AS, and LL (MLA: $r = 0.36$, $P < 0.001$; AS: $r = -0.36$, $P < 0.001$; LL: $r = -0.41$, $P < 0.001$) (**Figure 2**). Moreover, a multiple linear regression analysis demonstrated that MLA ($\beta = 0.218$, $P = 0.013$), AS ($\beta = -0.197$, $P = 0.029$), and LL ($\beta = -0.306$, $P < 0.001$) contributed significantly to the variation in caFFR (**Table 3**). When defined caFFR ≤ 0.8 as the threshold for myocardial ischemia, the best cutoff value of MLA to detect functional ICS was 3.6 mm^2, with the area under the curve (AUC) of 0.714, sensitivity of 75%, specificity of 63%, positive predictive value (PPV) of 33%, and negative predictive value (NPV) of 91%. In addition, the best cutoff value of AS to identify functional ICS was 73%, with AUC, sensitivity, specificity, PPV, and NPV of 0.688, 54, 77, 36, and 87%, respectively. The diagnostic accuracy of LL to determine caFFR ≤ 0.8 was ideal (AUC 0.767, sensitivity 58%, specificity 82%, PPV 44%, NPV 89%, $P < 0.001$).

Moreover, when combined MLA, AS, and LL for identifying functional ICS, the accuracy was higher than all other single measures (AUC: 0.845, sensitivity 83%, specificity 73%, PPV 44%, NPV 95%, $P < 0.001$, **Table 4**). The ROC showed that the accuracy of the combined method was significantly higher compared with every single method alone (**Figure 3**).

DISCUSSION

The present study correlated IVUS-parameters and LL assessed by 3D-QCA with caFFR in intermediate stenosis of non-LMCA. MLA, AS, and LL demonstrated a weak correlation with caFFR. We identified that MLA ≤ 3.6 mm^2, AS >73%, and LL >26 mm as the highest diagnostic accuracy to reveal functional ICS confirmed by caFFR. The combination of these three parameters provides an incremental diagnostic accuracy to each measure separately.

In clinical practice, although IVUS examination is commonly used for assisting management strategies in ICS lesions, the cutoff value of the parameters for detecting functional ICS remained controversial. A previous study suggested that IVUS-MLA ≤ 4 mm^2 was considered as functional stenosis which may require revascularization (12). Ben-Dor et al. identified an MLA < 3.6 mm^2 as the best threshold value (AUC 0.70) in lesions with reference vessels diameter larger than 3.5 mm for FFR < 0.8 (1). Takagi et al. analyzed 51 lesions with coronary stenosis with both IVUS and FFR, concluding that an MLA < 3.0 mm^2 and AS > 60% showed the highest accuracy (AUC 0.74) (13). In this study, we found that MLA ≤ 3.6 mm^2 and AS >73% presented the best diagnostic power for predicting functional ischemia defined by caFFR (AUC 0.714 for MLA, AUC 0.688 for AS). The accuracy of IVUS parameters differed greatly among studies (1, 10, 12). On the other hand, MLA or AS is one of many factors that influence coronary flow, which only reflect a single dimensional anatomic change and could not reflect other factors such as the amount of segmental lesion (13).

Quantitative angiography-derived parameters correlated weakly to moderately with functional ICS. Kang et al. demonstrated a significant but weak correlation between LL and FFR in lesion with lumen area < 3 mm^2 ($r = -0.47$)

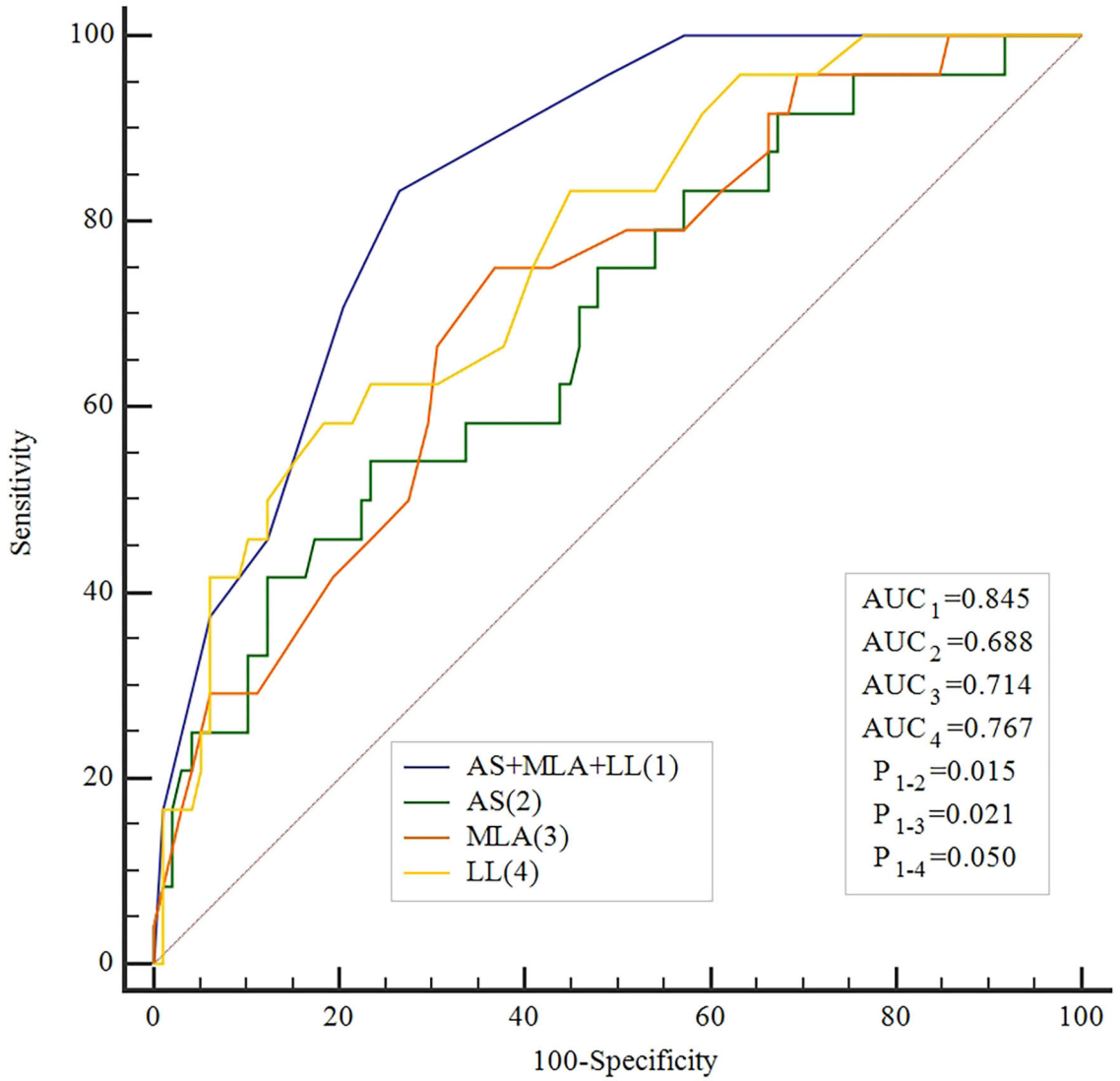

FIGURE 3 | Receiving operator curve for caFFR and MLA, AS, LL, and their combination.

(9). Naganuma et al. also showed a weak linear correlation between LL and FFR ($r = -0.348$) (14). In our study, LL was weakly correlated with caFFR, which was consistent with the previous study. Furthermore, our result showed LL $>$ 26 mm powered a functional significance. However, Kang et al. demonstrated that the best cutoff value of LL for predicting FFR $<$ 0.8 was 3.1 mm (9). In this study, the mean LL was only 4.6 $\pm$ 6.0 mm, which could explain the very low threshold of LL in functional lesions. Lopez-Palop et al. revealed that long lesions (>20 mm) with moderate angiographic stenosis might be one of the determinants of functional significance (11). Moreover, Koo studied the effect of lesion characteristics on the diagnostic performance of machine learning-based computed tomography-derived fractional flow reserve (ML-FFR), showing a downward trend of ML-FFR along with an increase in lesion length (15). Thus, we concluded that LL should be considered when judging the benefit of revascularization.

Although MLA, AS, and LL had a certain role in identifying functional ischemia, their diagnostic efficiency was still of concern. The FIRST study showed an AUC of 0.65 with an MLA $<$ 3.07 mm^2 to predict FFR $<$ 0.8, which was a quite low diagnostic power (10). Moreover, Lopez-Palop et al. illustrated a better diagnostic power of LL in determining FFR $<$ 0.8 (AUC 0.78) (11).

As an essential variable influencing the pressure difference between the proximal to the distal lesion, MLA subjected to the heterogeneity of the reference vessel diameter, and the effect of AS on blood flow should also be considered. Moreover, in the principle of fluid dynamics (16), LL is a crucial variable affecting the flow of the vessels. Therefore, a model combining the three indexes was constructed in our study to acquire higher accuracy.

After the combination of MLA, AS, and LL, the AUC elevated to 0.845, which is greater than each index measure alone. We present a high overall sensitivity of 83% showing a combined model could identify more positive lesions, but PPV is only 44%, indicating that revascularization should be under cautious consideration when the combined model shows positive results. In this case, physicians need to obtain more information, like FFR or radionuclide myocardial perfusion. Furthermore, the specificity of the combined model is passable, but the NPV is as high as 95% allowing revascularization to be deferred with greater confidence when MLA is larger, AS is lower, and/or LL is short enough.

In summary, although anatomic features assessed by IVUS or 3D-QCA have a certain role in predicting myocardial ischemia, their accuracy was unsatisfactory in clinical practice. By integrated MLA, AS, and LL to evaluate overall diagnostic power, a combined method provides higher accuracy than each measure alone.

LIMITATIONS

There are several limitations of this study. First, this is a single center, retrospective study. Although we consecutively screened eligible patients, around 43.5% of them were excluded, selective bias was inevitable. Second, the number of analyzed vessels from LCX or RCA was insufficient. Finally, caFFR values were assessed offline, aortic pressure was input with the invasive blood pressure reviewed from the record of operation. A large multi-center prospective cohort study with a larger number of LCX and RCA should be conducted.

DATA AVAILABILITY STATEMENT

The raw data supporting the conclusions of this article will be made available by the authors, without undue reservation.

ETHICS STATEMENT

The studies involving human participants were reviewed and approved by the Independent Institutional Ethical Committee of The First Affiliated Hospital of Nanjing Medical University. The patients/participants provided their written informed consent to participate in this study.

AUTHOR CONTRIBUTIONS

ML: conceptualization, methodology, investigation, formal analysis, and writing—original draft. XK: validation and supervision. HW: conceptualization and investigation. YH and IC: writing—review and editing. SL: formal analysis. All authors contributed to the article and approved the submitted version.

FUNDING

This paper was funded by Science Foundation of Gusu School (GSKY20210105) and Natural Science Foundation of Jiangsu Province (BK2012648 to HW). The funding body played no role in the design, writing, or decision to publish this paper.

ACKNOWLEDGMENTS

The authors acknowledge the Rainmed Ltd for supporting the computation of the caFFR value.

REFERENCES

1. Ben-Dor I, Torguson R, Deksissa T, Bui AB, Xue Z, Satler LF, et al. Intravascular ultrasound lumen area parameters for assessment of physiological ischemia by fractional flow reserve in intermediate coronary artery stenosis. *Cardiovasc Revascularization Med.* (2012) 13:177–82. doi: 10.1016/j.carrev.2011.12.003
2. Shaw LJ, Berman DS, Maron DJ, Mancini GB, Hayes SW, Hartigan PM, et al. Optimal medical therapy with or without percutaneous coronary intervention to reduce ischemic burden: results from the Clinical Outcomes Utilizing Revascularization and Aggressive Drug Evaluation (COURAGE) trial nuclear substudy. *Circulation.* (2008) 117:1283–91. doi: 10.1161/CIRCULATIONAHA.107.743963
3. Pijls NH, van Schaardenburgh P, Manoharan G, Boersma E, Bech JW. van't Veer M, et al. Percutaneous coronary intervention of functionally nonsignificant stenosis: 5-year follow-up of the DEFER Study. *J Am Coll Cardiol.* (2007) 49:2105–11. doi: 10.1016/j.jacc.2007.01.087
4. Erne P, Schoenenberger AW, Burckhardt D, Zuber M, Kiowski W, Buser PT, et al. Effects of percutaneous coronary interventions in silent ischemia after myocardial infarction: the SWISSI II randomized controlled trial. *Jama.* (2007) 297:1985–91. doi: 10.1001/jama.297.18.1985
5. Pijls NH, Fearon WF, Tonino PA, Siebert U, Ikeno F, Bornschein B, et al. Fractional flow reserve versus angiography for guiding percutaneous coronary intervention in patients with multivessel coronary artery disease: 2-year follow-up of the FAME (Fractional Flow Reserve Versus Angiography for Multivessel Evaluation) study. *J Am Coll Cardiol.* (2010) 56:177–84. doi: 10.1016/j.jacc.2010.04.012
6. Curzen N, Rana O, Nicholas Z, Golledge P, Zaman A, Oldroyd K, et al. Does routine pressure wire assessment influence management strategy at coronary angiography for diagnosis of chest pain? : the RIPCORD study. *Circ Cardiovasc Interv.* (2014) 7:248–55. doi: 10.1161/CIRCINTERVENTIONS.113.000978
7. Li J, Gong Y, Wang W, Yang Q, Liu B, Lu Y, et al. Accuracy of computational pressure-fluid dynamics applied to coronary angiography to derive fractional flow reserve: FLASH FFR. *Cardiovasc Res.* (2020) 116:1349–56. doi: 10.1093/cvr/cvz289
8. Ben-Dor I, Torguson R, Gaglia MA. Jr. <jabb>, Gonzalez MA, Maluenda G, Bui AB, et al. Correlation between fractional flow reserve and intravascular ultrasound lumen area in intermediate coronary artery stenosis. *EuroIntervention.* (2011) 7:225–33. doi: 10.4244/EIJV7I2A37
9. Kang SJ, Lee JY, Ahn JM, Mintz GS, Kim WJ, Park DW, et al. Validation of intravascular ultrasound-derived parameters with fractional flow reserve for assessment of coronary stenosis severity. *Circ Cardiovasc Interv.* (2011) 4:65–71. doi: 10.1161/CIRCINTERVENTIONS.110.959148
10. Waksman R, Legutko J, Singh J, Orlando Q, Marso S, Schloss T, et al. FIRST: fractional flow reserve and intravascular ultrasound relationship study. *J Am Coll Cardiol.* (2013) 61:917–23. doi: 10.1016/j.jacc.2012.12.012
11. Lopez-Palop R, Carrillo P, Cordero A, Frutos A, Mateo I, Mashlab S, et al. Effect of lesion length on functional significance of

intermediate long coronary lesions. *Catheter Cardiovasc Interv.* (2013) 81:E186–94. doi: 10.1002/ccd.24459
12. Stone GW, Maehara A, Lansky AJ, de Bruyne B, Cristea E, Mintz GS, et al. A prospective natural-history study of coronary atherosclerosis. *N Engl J Med.* (2011) 364:226–35. doi: 10.1056/NEJMoa1002358
13. Takagi A, Tsurumi Y, Ishii Y, Suzuki K, Kawana M, Kasanuki H. Clinical potential of intravascular ultrasound for physiological assessment of coronary stenosis: relationship between quantitative ultrasound tomography and pressure-derived fractional flow reserve. *Circulation.* (1999) 100:250–5. doi: 10.1161/01.CIR.100.3.250
14. Naganuma T, Latib A, Costopoulos C, Takagi K, Naim C, Sato K, et al. The role of intravascular ultrasound and quantitative angiography in the functional assessment of intermediate coronary lesions: correlation with fractional flow reserve. *Cardiovasc Revasc Med.* (2014) 15:3–7. doi: 10.1016/j.carrev.2013.11.002
15. Koo HJ, Kang JW, Kang SJ, Kweon J, Lee JG, Ahn JM, et al. Impact of coronary calcium score and lesion characteristics on the diagnostic performance of machine-learning-based computed tomography-derived fractional flow reserve. *Eur Heart J Cardiovasc Imaging.* (2021). doi: 10.1093/ehjci/jeab062
16. Qiao A, Hou Y, Yang H. Finite element analysis of the influence of morphology of coronary artery stenosis on fractional flow reserve. *Chinese J. Biomed. Eng.* (2015). doi: 10.3969/j.issn.0258-8021.2015.02.010

Conflict of Interest: The authors declare that the research was conducted in the absence of any commercial or financial relationships that could be construed as a potential conflict of interest.

Publisher's Note: All claims expressed in this article are solely those of the authors and do not necessarily represent those of their affiliated organizations, or those of the publisher, the editors and the reviewers. Any product that may be evaluated in this article, or claim that may be made by its manufacturer, is not guaranteed or endorsed by the publisher.

frontiers in Cardiovascular Medicine

ORIGINAL RESEARCH
published: 01 October 2021
doi: 10.3389/fcvm.2021.733339

Quantitative Analysis of Myocardial Work by Non-invasive Left Ventricular Pressure-Strain Loop in Patients With Type 2 Diabetes Mellitus

Danqing Huang[1†], Cunying Cui[1†], Qiang Zheng[2], Yanan Li[1], Yuanyuan Liu[1], Yanbin Hu[1], Ying Wang[1], Ruijie Liu[1] and Lin Liu[1]*

[1] Department of Ultrasound, Fuwai Central China Cardiovascular Hospital, Central China Fuwai Hospital of Zhengzhou University, Henan Provincial People's Hospital, People's Hospital of Zhengzhou University, Zhengzhou, China, [2] School of Computer and Control Engineering, Yantai University, Yantai, China

OPEN ACCESS

Edited by:
Juan Carlos Del Alamo, University of Washington, United States

Reviewed by:
Ernst Wellnhofer, Charité—Universitätsmedizin Berlin, Germany
Francesco Sturla, IRCCS Policlinico San Donato, Italy

***Correspondence:**
Lin Liu
liulin@zzu.edu.cn

[†]These authors have contributed equally to this work

Specialty section:
This article was submitted to Cardiovascular Imaging, a section of the journal Frontiers in Cardiovascular Medicine

Received: 30 June 2021
Accepted: 08 September 2021
Published: 01 October 2021

Citation:
Huang D, Cui C, Zheng Q, Li Y, Liu Y, Hu Y, Wang Y, Liu R and Liu L (2021) Quantitative Analysis of Myocardial Work by Non-invasive Left Ventricular Pressure-Strain Loop in Patients With Type 2 Diabetes Mellitus. Front. Cardiovasc. Med. 8:733339. doi: 10.3389/fcvm.2021.733339

Background: Type 2 diabetes mellitus (T2DM) is a common risk factor for cardiovascular diseases. The aims of this study were to evaluate the changes in the left ventricular myocardial work in T2DM patients using the left ventricular pressure-strain loop (PSL) technique, and to explore the risk factors for the left ventricular myocardial work impairment.

Methods: Fifty patients with T2DM and 50 normal controls (NCs) were included in the study. In addition to conventional echocardiography and two-dimensional speckle tracking echocardiography, the left ventricular myocardial work parameters were measured using PSL technology.

Results: The absolute value for global longitudinal strain (GLS), global work index (GWI) and, global constructive work (GCW) were significantly decreased in the T2DM group ($P < 0.05$), while the left ventricular ejection fraction (LVEF) was not significantly different between the T2DM and NC groups. Multivariable linear regression analysis showed that hemoglobin A1c (HbA1c) was independently related to GWI ($\beta = -0.452$, $P < 0.05$), while HbA1c and the diabetes duration were independently related to GCW ($\beta = -0.393$, $P < 0.05$ and $\beta = -0.298$, $P < 0.05$, respectively).

Conclusions: Changes in the left ventricular myocardial systolic function in T2DM patients were identified using PSL technology. HbA1c was shown to be an independent risk factor affecting GWI, while HbA1c and diabetes duration were demonstrated to be independent risk factors affecting GCW.

Keywords: type 2 diabetes mellitus, echocardiography, myocardial work, pressure-strain loop, left ventricle function

INTRODUCTION

Diabetes is a common clinical metabolic disease. Type 2 diabetes mellitus (T2DM) accounts for more than 90% of diabetic patients (1). The incidence of cardiovascular disease is 2-3 times higher in T2DM patients compared to healthy individuals (2). Therefore, the evaluation of left ventricular systolic function in T2DM patients at an early stage is important for treatment and prognosis.

Left ventricular ejection fraction (LVEF) and two-dimensional speckle tracking technology are commonly used to evaluate the left ventricular systolic function, but these methods are load-dependent (3). Recently, a new non-invasive left ventricular pressure-strain loop (PSL) technology has been developed based on two-dimensional speckle tracking technology to assess the changes in left ventricular myocardial function. PSL technology combines the ventricular deformation and pressure, and the influence of cardiac afterload on traditional myocardial strain measurement is considered (4–6). Hubert et al. invasively measured the left ventricular pressure in patients implanted with a bi-ventricular pace-maker, and blood pressure was measured by brachial artery cuff-pressure for estimating the left ventricular pressure. They found that the maximum systolic value was different between measured and estimated pressures, but the estimated and measured PSL and global myocardial work indices were strongly correlated, with an $R^2 > 0.88$. The major reason is that the temporal integration induces a smoothing of the difference between measured and estimated works, so the deducted estimation of left ventricular work is accurate (7).

A previous study showed that the level of hemoglobin A1c (HbA1c) was independently associated with decreased left ventricular strain in T2DM patients with preserved LVEF (8). However, the relationship between HbA1c and left ventricular PSL parameters in T2DM patients with normal LVEF is unclear. We hypothesized that HbA1c is independently associated with left ventricular PSL parameters in T2DM patients with normal LVEF.

The aims of the present study were to evaluate the changes in the left ventricular myocardial work in T2DM patients using the left ventricular PSL technique, and to explore the clinical factors impairing the left ventricular myocardial work.

METHODS

Study Population

A total of 100 participants were consecutively enrolled in Fuwai Central China Cardiovascular Hospital between May and December of 2020, of which 50 were in the T2DM group (26/24, male/female) and 50 age- and gender-matched healthy individuals were in the normal control (NC) group (29/21, male/female) (**Figure 1**). The inclusion criteria for all T2DM patients were set according to the 2020 guidelines of the American Diabetes Association (9). Participants with any one of the following conditions were excluded: LVEF < 50%, heart failure, arterial hypertension, valvular heart disease, arrhythmia, congenital heart disease, or poor ultrasound image quality. In view of relatively higher incidence of coronary heart disease in T2DM patients, the recent examination of coronary angiography or computerized tomography were performed in all participants. Those who suffered from obvious atherosclerotic stenosis should also be excluded. The study was approved by the ethics committee of Fuwai Central China Cardiovascular Hospital and informed consents was obtained before participation.

Laboratory Analyses

Total cholesterol (TC), triglyceride (TG), high-density lipoprotein cholesterol (HDL-C), low-density lipoprotein cholesterol (LDL-C), and HbA1c levels were measured <2 weeks before the echocardiographic evaluation using standard laboratory techniques. Fasting plasma glucose (FPG) and 2-h postprandial plasma glucose (2h-PPG) levels were measured in T2DM patients.

Echocardiographic Examination

Transthoracic echocardiography was performed using a Vivid E95 system (GE Vingmed Ultrasound AS, Horten, Norway) equipped with an M5Sc-D probe (1.4-4.6 MHz). All study participants were scanned in the left lateral position with continuous electrocardiogram monitoring. Left atrial diameter (LAD), left ventricular end diastolic diameter (LVDd), left ventricular end diastolic volume (LVEDV), left ventricular end systolic diameter (LVDs), left ventricular end systolic volume (LVESV), and LVEF were measured in the parasternal long-axis view of the left ventricle. Doppler spectrum images of the aortic and mitral valves were collected from apical five- and four-chamber views. Two-dimensional images consisting of three cardiac cycles from the apical four-, three-, and two-chamber views were acquired at frame rates between 57 and 68 frames/s (mean, 65 ± 6 frames/s). All images were stored on a hard disk for offline analysis.

Left Ventricular Strain and Myocardial Work Quantification

Echopac version 203 software (GE vingmed ultra sound, Horten, Norway) was used for image analysis. Three index points were used to define the mitral annulus and left ventricular apex at the end-systolic frame in each apical view. Automated tracking of myocardial motion was performed with the region of interest adjusted by correcting the endocardial border or width if necessary. The software calculated global longitudinal strain (GLS) from the weighted average of the peak systolic longitudinal strain of the 17 segments. Peak systolic left ventricular pressure was assumed to be equal to the peak arterial pressure, which was recorded from the brachial cuff blood pressure measured immediately before the echocardiographic recordings. A non-invasive left ventricular pressure curve was constructed using the strain and blood pressure data, and a normalized reference curve adjusted according to the duration of isovolumic and ejection phases defined by the timing of aortic and mitral valve opening and closing events on Doppler spectrum images (10). Left ventricular myocardial work parameters was subsequently computed by the differentiation of the strain values over time multiplying the instantaneous LV pressure (**Figure 2**). The myocardial work parameters are as follows:

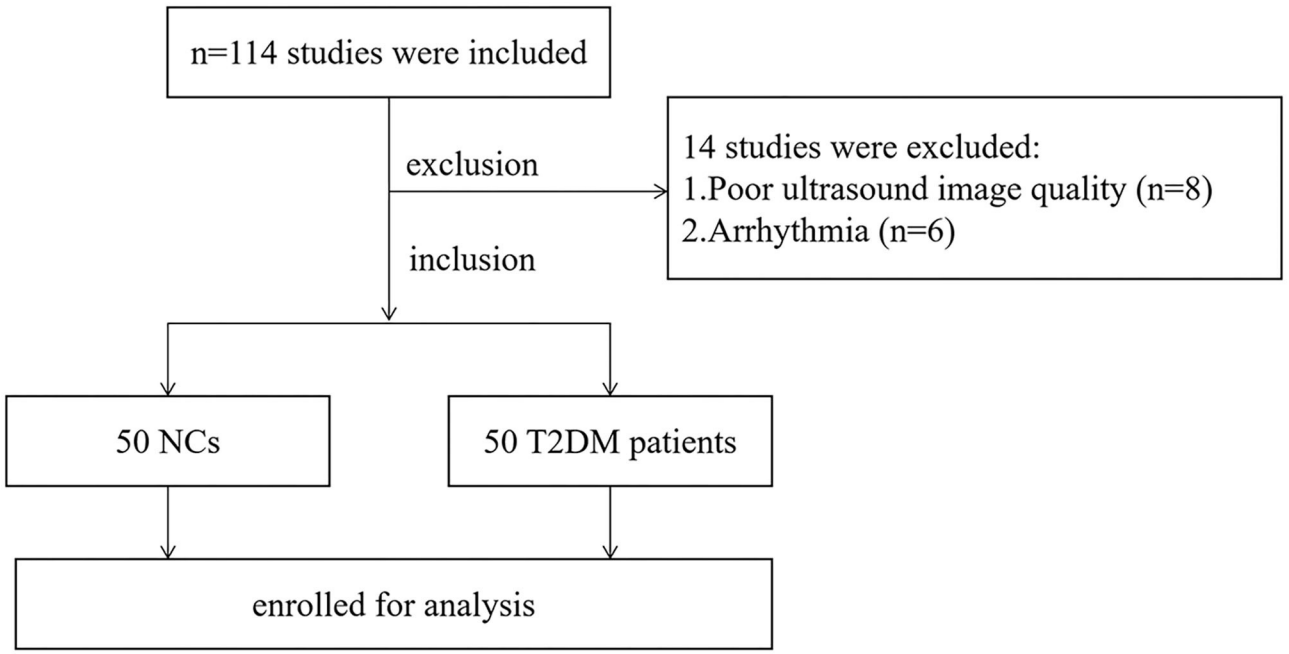

FIGURE 1 | Flow chart of participants inclusion in the T2DM and NC groups. T2DM, type 2 diabetes mellitus; NC, normal control.

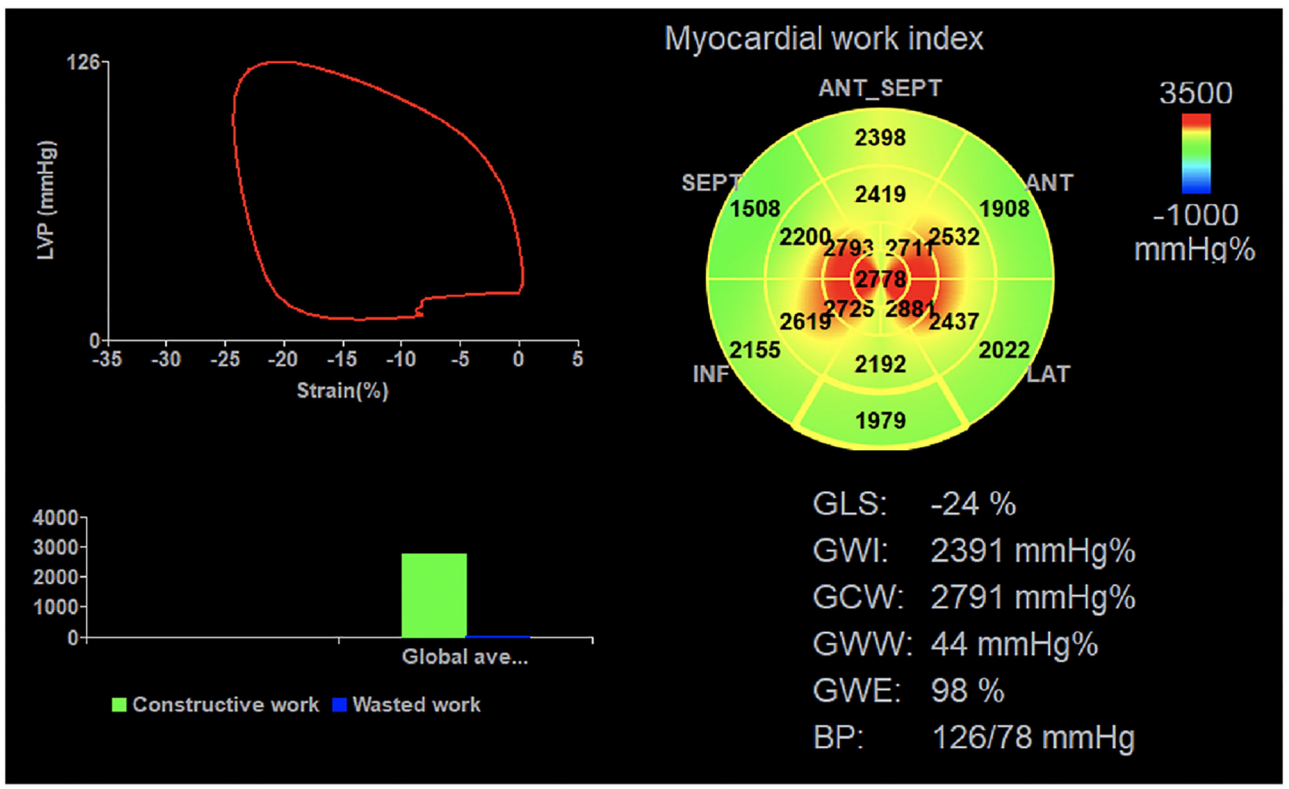

FIGURE 2 | Left ventricular myocardial work parameters were measured using the non-invasive PSL technique. Cuff contraction pressure is represented on the ordinate and longitudinal strain on the abscissa. PSL, pressure-strain loop; GLS, global longitudinal strain; GWI, global work index; GCW, global constructive work; GWW, global wasted work; GWE, global work efficiency, BP blood pressure.

(1) Global work index (GWI): total work within the area of the left ventricular PSL calculated from mitral valve closure to mitral valve opening.
(2) Global constructive work (GCW): work performed by during left ventricular shortening in systole and lengthening during the isovolumic relaxation phase.
(3) Global wasted work (GWW): the negative work performed during left ventricular lengthening in systole and shortening in isolvolumic relaxation phase.
(4) Global work efficiency (GWE): the percentage of constructive work divided by the sum of constructive and wasted work.

TABLE 1 | Statistical comparisons of demographic characteristics and clinical parameters between NC and T2DM groups.

Parameters	**NC group *n* = 50**	**T2DM group *n* = 50**		
			χ^2	***P*-value**
Male gender, *n* (%)	29 (58%)	26 (52%)	0.364	0.546
Smoking, *n* (%)	12 (24%)	14 (28%)	0.208	0.648
			t	***P*-value**
Age (years)	46.88 ± 10.60	50.20 ± 9.73	−1.632	0.106
BMI (kg/m^2)	24.32 ± 3.67	26.09 ± 3.80	−2.370	0.020
BSA (m²)	1.72 ± 0.16	1.83 ± 0.24	−2.449	0.016
SBP (mm Hg)	118.84 ± 3.94	120.68 ± 6.00	−1.813	0.073
DBP (mm Hg)	77.70 ± 6.31	79.24 ± 7.40	−1.120	0.265
pulse pressure (mm Hg)	41.14 ± 7.13	41.44 ± 8.85	−0.187	0.852
Heart rate (bpm)	67.82 ± 8.37	71.02 ± 9.41	−1.797	0.075
TC (mmol/L)	4.33 ± 0.61	4.50 ± 1.01	−0.957	0.341
TG (mmol/L)	1.65 ± 0.64	2.17 ± 1.04	−2.296	0.004
LDL-C (mmol/L)	2.48 ± 0.70	2.79 ± 0.66	−2.196	0.030
HbA1c (%)	5.24 ± 0.36	8.06 ± 1.37	−10.350	<0.001
			Z	***P*-value**
HDL-C (mmol/L)	1.01 (0.30)	1.03 (0.23)	−0.259	0.796
FPG (mmol/L)	–	7.88 ± 1.49	–	–
2h-PPG (mmol/L)	–	11.60 ± 2.32	–	–
Diabetes duration (years)	–	2.50 (9.37)	–	–
Oral antihyperglycemic agent, *n* (%)	–	23 (46%)	–	–
Insulin, *n* (%)	–	3 (6%)	–	–
Oral antihyperglycemic agent + insulin, *n* (%)	–	14 (28%)	–	–
Complications, *n* (%)	–	11 (22%)	–	–
Cardiovascular medications, *n* (%)	–	13 (26%)	–	–

T2DM, type 2 diabetes mellitus; NC, normal control; BMI, body mass index;BSA, body surface area; SBP, systolic blood pressure; DBP, diastolic blood pressure; HbA1c, hemoglobin A1c; FPG, fasting plasma glucose; 2h-PPG, 2-h postprandial plasma glucose; TC, total cholesterol; TG, triglyceride; HDL-C, high-density lipoprotein cholesterol; LDL-C, low-density lipoprotein cholesterol.

TABLE 2 | Statistical comparisons of conventional echocardiographic parameters and GLS between NC and T2DM groups.

Parameters	**NC group *n* = 50**	**T2DM group *n* = 50**		
			t	***P*-value**
LAD (mm)	33.38 ± 3.46	34.62 ± 3.45	−1.795	0.076
LVDd (mm)	45.76 ± 2.62	45.54 ± 2.11	0.463	0.645
LVEDV (ml)	98.00 ± 12.58	96.80 ± 10.68	0.514	0.608
			Z	***P*-value**
LVDs (mm)	30.00 (2.00)	30.00 (2.00)	−0.267	0.790
LVESV (ml)	35.50 (5.00)	35.00 (6.00)	−0.253	0.801
LVEF (%)	63.50 (3.25)	62.00 (4.00)	1.552	0.121
GLS (%)	−19.50 (3.00)	−17.00 (3.00)	−4.509	<0.001

T2DM, type 2 diabetes mellitus; NC, normal control; LAD, left atrial diameter; LVDd, left ventricular end diastolic diameter; LVEDV, left ventricular end diastolic volume; LVDs, left ventricular end systolic diameter; LVESV, left ventricular end systolic volume; LVEF, left ventricular ejection fraction; GLS, global longitudinal strain.

Statistical Analysis

The statistical analyses were performed using SPSS 26.0 software (IBM, Armonk, NY, USA). *P*-value <0.05 was considered statistically significant. Continuous variables were expressed as mean ± standard deviation for normally distributed data, or as median (interquartile range) for non-normally distributed data. Categorical variables were expressed as frequencies and percentages.

The statistical analysis was performed using the Student's *t*-test, Mann-Whitney *U*-test, and χ^2 test as appropriate to compare the T2DM and NC groups. Pearson's correlation coefficient was used for determining the correlation between GLS and myocardial work parameters. The clinical factors with *P*-value <0.05 in univariable linear regression outcomes were incorporated into the multivariable linear regression analysis models by means of stepwise selection to detect the independent predictors of abnormal myocardial function in T2DM patients. There was no multicollinearity between variables in these models. Ten subjects were randomly selected and re-measured the global myocardial work parameters by two observers. Intra-observer and inter-observer variability was assessed in 20 randomly selected subjects using the Bland-Altman analyses.

RESULTS

Study Population Characteristics

Body mass index (BMI), body surface area (BSA), HbA1c, TG, and LDL-C in the T2DM group were significantly increased compared to the NC group ($P < 0.05$) (**Table 1**). There were no significant differences in gender, age, heart rate, systolic blood pressure (SBP), diastolic blood pressure (DBP), TC, HDL-C, and smoking history between the two groups ($P > 0.05$).

Comparison of Conventional Echocardiographic Parameters and GLS

The absolute value of GLS in the T2DM group was significant lower compared to the NC group ($P < 0.05$). No significant difference was observed in LAD, LVDd, LVEDV, LVDs, LVESV, and LVEF between the T2DM and NC groups ($P > 0.05$) (**Table 2**).

Comparison of Myocardial Work

The GWI and GCW in the T2DM group were significantly decreased compared to the NC group ($P < 0.05$) (**Table 3**;

TABLE 3 | Statistical comparisons of global myocardial work parameters between NC and T2DM groups.

Parameters	NC group *n* = 50	T2DM group *n* = 50		
			t	***P*-value**
GWI (mm Hg%)	1899.84 ± 173.47	1712.80 ± 249.44	4.353	<0.001
GCW (mm Hg%)	2151.08 ± 196.17	1934.58 ± 266.64	4.625	<0.001
			Z	***P*-value**
GWW (mm Hg%)	34.50 (26.50)	45.00 (38.50)	−1.421	0.155
GWE (%)	98.00 (1.00)	97.00 (2.00)	−1.848	0.065

T2DM, type 2 diabetes mellitus; NC, normal control; GWI, global work index; GCW, global constructive work; GWW, global wasted work; GWE, global work efficiency.

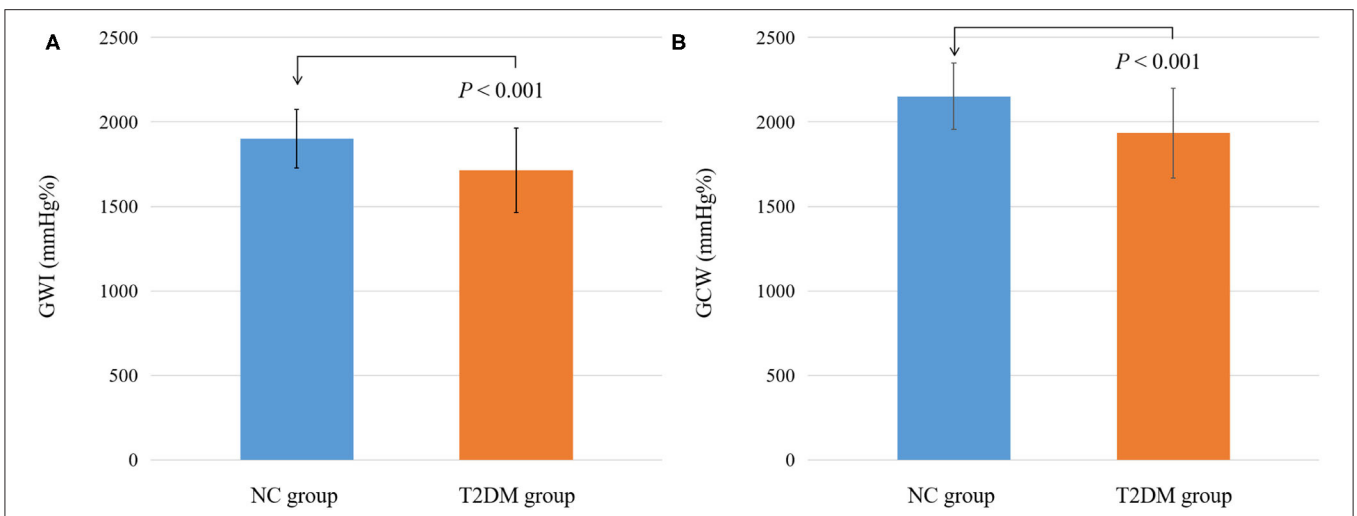

FIGURE 3 | Differential changes of myocardial work parameters between NC and T2DM groups. **(A)** Differential changes of GWI between NC and T2DM groups. **(B)** Differential changes of GCW between NC and T2DM groups.T2DM, type 2 diabetes mellitus; NC, normal control; GWI, global work index; GCW, global constructive work.

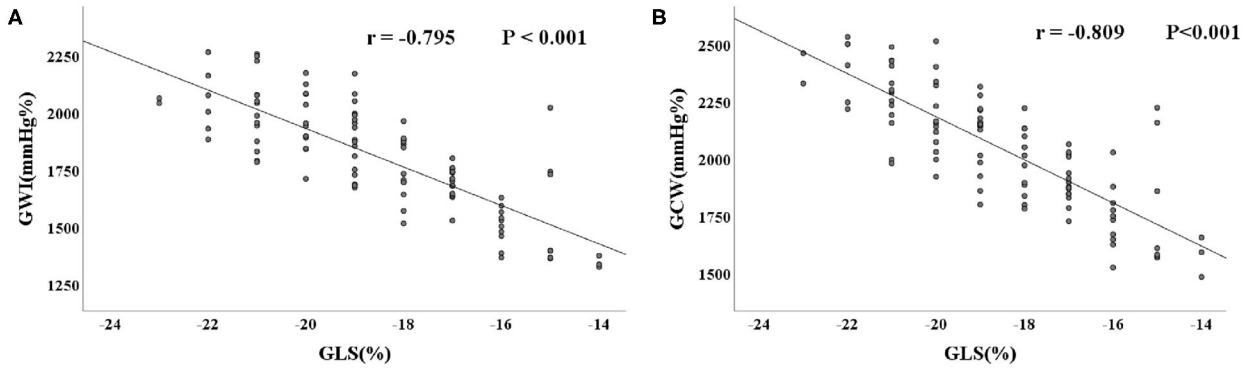

FIGURE 4 | Correlation between myocardial work parameters and GLS. **(A)** Correlation between GWI and GSL. **(B)** Correlation between GCW and GSL. PSL, pressure-strain loop; GLS, global longitudinal strain; GWI, global work index; GCW, global constructive work.

TABLE 4 | Univariable and multivariable linear regression analysis of GWI in T2DM patients.

	Univariable analysis		Multivariable analysis	
	β	***P*–value**	*β*	***P*–value**
Age (years)	−0.065	0.654	–	–
BSA (m^2)	−0.340	0.016	–	–
Heart rate (bpm)	−0.191	0.183	–	–
SBP (mm Hg)	0.178	0.217	–	–
DBP (mm Hg)	−0.130	0.367	–	–
Pulse pressure (mm Hg)	0.229	0.109	–	–
TC (mmol/L)	−0.209	0.149	–	–
TG (mmol/L)	0.060	0.677	–	–
HDL–C (mmol/L)	0.123	0.397	–	–
LDL–C (mmol/L)	−0.205	0.152	–	–
HbA1c (%)	−0.452	0.001	−0.452	−0.001
FPG (mmol/L)	−0.304	0.032	–	–
2h–PPG (mmol/L)	−0.124	0.391	–	–
Diabetes duration (years)	−0.357	0.011	–	–
R^2				0.204
Adjusted R^2				0.187

T2DM, type 2 diabetes mellitus; BSA, body surface area; SBP, systolic blood pressure; DBP, diastolic blood pressure; HbA1c, hemoglobin A1c; FPG, fasting plasma glucose; 2h–PPG, 2–h postprandial plasma glucose; TG, triglyceride; TC, total cholesterol; HDL–C, high–density lipoprotein cholesterol; LDL–C, low–density lipoprotein cholesterol; GWI, global work index; R^2, coefficient of determination; β, standardized regression coefficients.

Figure 3). However, there were no significant differences in GWW and GWE between the two groups ($P > 0.05$).

Correlation Between GLS and Myocardial Work Parameters

GLS showed a good correlation with GWI and GCW ($r = -0.795$, $P < 0.001$ and $r = -0.809$, $P < 0.001$, respectively) (**Figure 4**).

Risk Factor Analysis for Left Ventricular Myocardial Work Impairment in T2DM Patients

BSA, HbA1c, FPG, and diabetes duration were incorporated into the multivariate linear regression model of GWI and GCW by means of stepwise selection based on the univariate linear regression analysis results. HbA1c was independently associated with GWI, while HbA1c and the diabetes duration were independently associated with GCW ($P < 0.05$) (**Tables 4**, **5**).

Reproducibility Test

Intra-observer and inter-observer variability for global myocardial work parameters are summarized in **Table 6**. Bland-Altman analyses showed good repeatability and reproducibility in global myocardial work parameters.

DISCUSSION

The main findings of this study showed that GWI and GCW were significantly different between the NC and T2DM groups. PSL

TABLE 5 | Univariable and multivariable linear regression analysis of GCW in T2DM patients.

	Univariable analysis		Multivariable analysis	
	β	***P*-value**	*β*	***P*-value**
Age (years)	−0.192	0.183	–	–
BSA (m^2)	−0.355	0.011	–	–
Heart rate (bpm)	−0.135	0.349	–	–
SBP (mm Hg)	0.210	0.143	-	–
DBP (mm Hg)	−0.080	0.579	–	–
Pulse pressure (mm Hg)	0.209	0.144	–	–
TC (mmol/L)	−0.130	0.369	–	–
TG (mmol/L)	0.123	0.395	–	–
HDL-C (mmol/L)	0.125	0.385	–	–
LDL-C (mmol/L)	−0.206	0.151	–	–
HbA1c (%)	−0.517	<0.001	−0.393	0.004
FPG (mmol/L)	−0.347	0.013	–	–
2h-PPG (mmol/L)	−0.153	0.289	–	–
Diabetes duration (years)	−0.461	0.001	−0.298	0.027
R^2				0.340
Adjusted R^2				0.312

T2DM, type 2 diabetes mellitus; BSA, body surface area; SBP, systolic blood pressure; DBP, diastolic blood pressure; HbA1c, hemoglobin A1c; FPG, fasting plasma glucose; 2h-PPG, 2-h postprandial plasma glucose; TG, triglyceride; TC, total cholesterol; HDL-C, high-density lipoprotein cholesterol; LDL-C, low-density lipoprotein cholesterol; GCW, global constructive work; R^2, coefficient of determination; β, standardized regression coefficients.

TABLE 6 | Repeatability and reproducibility of myocardial work parameters.

Parameters	Mean ± SD	Mean ± SD	Bias	95%LOA
Intraobserver				
GWI (mm Hg%)	1,784.70 ± 248.05	1,797.40 ± 239.75	20.70	−50.57–91.97
GCW (mm Hg%)	1,965.95 ± 262.88	2,009.05 ± 262.523	43.10	−128.58–214.78
GWW (mm Hg%)	36.65 ± 15.28	39.90 ± 16.37	3.25	−4.96–11.46
GWE (%)	97.40 ± 0.88	97.45 ± 0.76	0.05	−0.95–1.05
Interobserver				
GWI (mm Hg%)	1,784.70 ± 248.05	1,783.65 ± 220.39	−8.35	−128.20–111.50
GCW (mm Hg%)	1,965.95 ± 262.88	1,991.60 ± 258.02	25.65	−110.66–161.96
GWW (mm Hg%)	36.65 ± 15.28	38.75 ± 12.78	2.30	−10.29–14.89
GWE (%)	97.40 ± 0.88	97.25 ± 0.79	−0.15	−1.11–0.81

SD, standard deviation; LOA, limits of agreement; SD, standard deviation. GWI, global work index; GCW, global constructive work; GWW, global wasted work; GWE, global work efficiency.

technology was able to assess the impairment of left ventricular systolic function in T2DM patients. Multivariable linear regression analysis confirmed that HbA1c was independently related to GWI, while HbA1c and diabetes duration were independently related to GCW.

The HbA1c level in the T2DM group was higher than that in the NC group. HbA1c has been widely used as an indicator of diabetes control and it is correlated with FPG and 2h-PPG (11, 12). T2DM patients often suffer from insulin deficiency or insulin resistance, and the body fails to make full use of glucose to produce energy. Then, the lipid and protein metabolism is enhanced, resulting in weight loss. However, our results showed that the BMI in the T2DM group was higher than that in the NC group. This finding may be related to individual lifestyle and medication regimen (13). In addition, the levels of TG and LDL-C in the T2DM group were higher than those in the NC group. The free fatty acids produced by TG were able to further reduce insulin sensitivity, forming a vicious circle between TG levels and insulin resistance (14–16).

The absolute value of GLS in the T2DM group was lower compared to that in the NC group, while the LVEF was similar. Consistent with previous studies (17, 18), this result indicates that the left ventricular longitudinal systolic function is impaired in T2DM patients, and GLS is more sensitive than LVEF in reflecting the subtle change in myocardial function.

Several prior studies have shown that T2DM is closely related to vascular arteriosclerosis, which can elevate pulse pressure (19, 20). A widened pulse pressure may increase left ventricular afterload (21). Tadic M et al. found GWI was higher in hypertensive patients than in controls, and even higher in subjects with both hypertension and diabetes (22). Interestingly, our results showed GWI and GCW in T2DM patients were significantly reduced. This finding may be related to pulse pressure. We have excluded patients with hypertension in our study. Our results showed that there was no significant difference in pulse pressure between NC and T2DM groups. Therefore, the increase of the left ventricular afterload and the compensatory increase of the left ventricular pump function were insignificant. In our study, there was no significant difference in LVEF between T2DM patients and normal control group, but the absolute value of GLS, GWI, and GCW were significantly decreased in the T2DM group. Considering the influence of afterload on strain measurement results, PSL technology combined with ventricular strain and arterial pressure is more accurate in evaluating left ventricular systolic function than using GLS technology alone (23). Oberhoffer FS et al. showed that blood pressure and GLS were not significantly difference between Turner syndrome patients and healthy controls, but the GWI and GCW were significantly higher in Turner syndrome patients (24). Therefore, PSL technology is more sensitive and comprehensive than global strain and LVEF in evaluating early impairment of ventricular function. We also found that GLS have a good correlation with GWI and GCW. Reproducibility testing results for GWI, GCW, GWW, and GWE in the present study suggested a good repeatability.

HbA1c is an independent risk factor affecting GWI, while HbA1c and the diabetes duration are the independent risk factors affecting GCW, which may be related to the long-term hyperglycaemic environment. The potentially pathogenic conditions, such as endothelial dysfunction and oxidative stress, may impair the left ventricular systolic function (25–27). Previous studies have shown that diabetes duration is independently related to left ventricular diastolic dysfunction (28, 29). Another important finding in the present study was that the diabetes duration is independently related to GCW, further confirming that the diabetes course can also lead to left ventricular systolic dysfunction.

LIMITATIONS

The limitations of this study are as follows. The present investigation was a cross-sectional research study performed at a single center with a relatively small sample size. PSL technology is based on two-dimensional speckle tracking imaging, which requires a high-quality ultrasound image. The follow-up data for prognostic effects in T2DM patients are lacking, so the relationship between PSL related parameters and left ventricular systolic dysfunction needs further longitudinal study.

CONCLUSIONS

In conclusion, combined with the cardiac afterload, PSL technology can evaluate the changes in the left ventricular myocardial systolic function in T2DM patients with normal LVEF. HbA1c is an independent risk factor affecting GWI, while HbA1c and diabetes duration are the independent risk factors affecting GCW. Therefore, T2DM patients should be treated as soon as possible and the HbA1c level should be strictly controlled.

DATA AVAILABILITY STATEMENT

The raw data supporting the conclusions of this article will be made available by the authors, without undue reservation.

ETHICS STATEMENT

The studies involving human participants were reviewed and approved by the Ethics Committee of Fuwai Central China Cardiovascular Hospital. The patients/participants provided their written informed consent to participate in this study.

AUTHOR CONTRIBUTIONS

DH and CC designed the study, analyzed the data, and wrote the manuscript. CC, YLi, YLiu, YH, YW, and RL assisted recruitment and manuscript revision. LL, QZ, and CC assisted in study design, data interpretation, and manuscript revision. All authors had read and approved the final manuscript.

FUNDING

This study was supported by National Natural Science Foundation of China (82071950), National Natural Science Foundation of Henan for Excellent Young Scientists (202300410364), Medical Science and Technology Project of Henan Province (SB201901099), and Henan Provincial Medical Science and Technology Research Project (LHGJ20190805 and LHGJ20200084).

SUPPLEMENTARY MATERIAL

The Supplementary Material for this article can be found online at: https://www.frontiersin.org/articles/10.3389/fcvm.2021.733339/full#supplementary-material

REFERENCES

1. Kazeminia M, Salari N, Mohammadi M. Prevalence of cardiovascular disease in patients with type 2 diabetes mellitus in Iran: a systematic review and meta-analysis. *J Diabetes Res.* (2020) 2020:1–9. doi: 10.1155/2020/3069867
2. Chen X, Guo H, Yang Q, Fang J, Kang X. Quantitative evaluation of subclinical left ventricular dysfunction in patients with type 2 diabetes mellitus by three-dimensional echocardiography. *Int J Cardiovasc Imaging.* (2020) 36:1311–9. doi: 10.1007/s10554-020-01833-5
3. Cui C, Liu L, Li Y, Liu Y, Huang D, Hu Y, et al. Left ventricular pressure-strain loop-based quantitative examination of the global and regional myocardial work of patients with dilated cardiomyopathy. *Ultrasound Med Biol.* (2020) 46:2834–45. doi: 10.1016/j.ultrasmedbio.2020.06.008
4. Manganaro R, Marchetta S, Dulgheru R, Sugimoto T, Tsugu T, Ilardi F, et al. Correlation between non-invasive myocardial work indices and main parameters of systolic and diastolic function: results from the EACVI NORRE study. *Eur Heart J Cardiovasc Imaging.* (2020) 21:533–41. doi: 10.1093/ehjci/jez203
5. Wang CL, Chan YH, Wu VC, Lee HF, Hsiao FC, Chu PH. Incremental prognostic value of global myocardial work over ejection fraction and global longitudinal strain in patients with heart failure and reduced ejection fraction. *Eur Heart J Cardiovasc Imaging.* (2021) 22:348–56. doi: 10.1093/ehjci/jeaa162
6. Sahiti F, Morbach C, Cejka V, Albert J, Eichner FA, Gelbrich G, et al. Left ventricular remodeling and myocardial work: results from the population-based STAAB cohort study. *Front Cardiovasc Med.* (2021) 8:669335. doi: 10.3389/fcvm.2021.669335
7. Hubert A, Rolle VL, Leclercq C, Galli E, Samset E, Casset C, et al. Estimation of myocardial work from pressure–strain loops analysis: an experimental evaluation. *Eur Heart J Cardiovasc Imaging.* (2018) 19:1372–9. doi: 10.1093/ehjci/jey024
8. Zhang X, Wei X, Liang Y, Liu M, Li C, Tang H. Differential changes of left ventricular myocardial deformation in diabetic patients with controlled and uncontrolled blood glucose: a three-dimensional speckle-tracking echocardiography–based study. *J Am Soc Echocardiogr.* (2013) 26:499–506. doi: 10.1016/j.echo.2013.02.016
9. Classification and diagnosis of diabetes: standards of medical care in diabetes-2020. *Diabetes Care.* (2020) 43(Suppl 1):14-31. doi: 10.2337/dc21-S002
10. El Mahdiui M, van der Bijl P, Abou R, Ajmone Marsan N, Delgado V, Bax JJ. Global left ventricular myocardial work efficiency in healthy individuals and patients with cardiovascular disease. *J Am Soc Echocardiogr.* (2019) 32:1120–7. doi: 10.1016/j.echo.2019.05.002
11. Ketema EB, Kibret KT. Correlation of fasting and postprandial plasma glucose with HbA1c in assessing glycemic control; systematic review and meta-analysis. *Arch Public Health.* (2015) 73:43–51. doi: 10.1186/s13690-015-0088-6
12. Haddadinezhad S, Ghazaleh N. Relation of fasting and postprandial and plasma glucose with hemoglobinA1c in diabetics. *Int J Diabetes Dev Ctries.* (2010) 30:8–10. doi: 10.4103/0973-3930.60002
13. Heller S. Weight gain during insulin therapy in patients with type 2 diabetes mellitus. *Diabetes Res Clin Pract.* (2004) 65(Suppl 1):23–7. doi: 10.1016/j.diabres.2004.07.005
14. Li X, Li G, Cheng T, Liu J, Song G, Ma H. Association between triglyceride-glucose index and risk of incident diabetes: a secondary analysis based on a Chinese cohort study: TyG index and incident diabetes. *Lipids Health Dis.* (2020) 19:236–46. doi: 10.1186/s12944-020-01403-7
15. Tian X, Zuo Y, Chen S, Liu Q, Tao B, Wu S, et al. Triglyceride-glucose index is associated with the risk of myocardial infarction: an 11-year prospective study in the Kailuan cohort. *Cardiovasc Diabetol.* (2021) 20:19–28. doi: 10.1186/s12933-020-01210-5
16. Ke JF, Wang JW, Zhang ZH, Chen MY, Lu JX, Li LX. Insulin therapy is associated with an increased risk of carotid plaque in type 2 diabetes: a real-world study. *Front Cardiovasc Med.* (2021) 8:599545. doi: 10.3389/fcvm.2021.599545
17. Bogdanović J, Ašanin M, Krljanac G, Lalić NM, Jotić A, Stanković S, et al. Impact of acute hyperglycemia on layer-specific left ventricular strain in asymptomatic diabetic patients: an analysis based on two-dimensional speckle tracking echocardiography. *Cardiovasc Diabetol.* (2019) 18:68–79. doi: 10.1186/s12933-019-0876-3
18. Vukomanovic V, Suzic-Lazic J, Celic V, Cuspidi C, Petrovic T, Grassi G, et al. The relationship between functional capacity and left ventricular strain in patients with uncomplicated type 2 diabetes. *J Hypertens.* (2019) 37:1871–6. doi: 10.1097/HJH.0000000000002125
19. Jankowski P, Bilo G, Kawecka-Jaszcz K. The pulsatile component of blood pressure: its role in the pathogenesis of atherosclerosis. *Blood Press.* (2007) 16:238–45. doi: 10.1080/08037050701428166
20. Prenner SB, Chirinos JA. Arterial stiffness in diabetes mellitus. *Atherosclerosis.* (2015) 238:370–9. doi: 10.1016/j.atherosclerosis.2014.12.023
21. Glasser SP, Krasikov T, Devereux RB, Oberman A, Patki A, Kitzman DW, et al. Subclinical, hemodynamic, and echocardiographic abnormalities of high pulse pressure in hypertensive and non-hypertensive adults. *Am J Cardiovasc Dis.* (2012) 2:309–17.
22. Tadic M, Cuspidi C, Pencic B, Grassi G, Celic V. Myocardial work in hypertensive patients with and without diabetes: an echocardiographic study. *J Clin Hypertens.* (2020) 22:2121–7. doi: 10.1111/jch.14053
23. Smiseth OA, Donal E, Penicka M, Sletten OJ. How to measure left ventricular myocardial work by pressure–strain loops. *Eur Heart J Cardiovasc Imaging.* (2020) 22:259–61. doi: 10.1093/ehjci/jeaa301
24. Oberhoffer FS, Abdul-Khaliq H, Jung AM, Zemlin M, Rohrer TR, Abd El Rahman M. Assessment of left ventricular myocardial work in Turner syndrome patients: insights from the novel non-invasive pressure-strain loop analysis method. *Quant Imaging Med Surg.* (2020) 10:15–25. doi: 10.21037/qims.2019.09.19
25. Parim B, Sathibabu Uddandrao VV, Saravanan G. Diabetic cardiomyopathy: molecular mechanisms, detrimental effects of conventional treatment, and beneficial effects of natural therapy. *Heart Fail Rev.* (2019) 24:279–99. doi: 10.1007/s10741-018-9749-1
26. Zamora M, Villena JA. Contribution of impaired insulin signaling to the pathogenesis of diabetic cardiomyopathy. *Int J Mol Sci.* (2019) 20:2833. doi: 10.3390/ijms20112833
27. Mochizuki Y, Tanaka H, Matsumoto K, Sano H, Toki H, Shimoura H, et al. Clinical features of subclinical left ventricular systolic dysfunction in patients with diabetes mellitus. *Cardiovasc Diabetol.* (2015) 14:37–46. doi: 10.1186/s12933-015-0201-8
28. Bajraktari G, Qirko S, Rexhepaj N, Bakalli A, Beqiri A, Elezi S, et al. Non-insulin dependent diabetes as an independent predictor of asymptomatic left ventricular diastolic dysfunction. *Croat Med J.* (2005) 46:225–31.
29. Kim Y, Shin MS, Kim YS, Kang WC, Kim BR, Moon J, et al. The impact of diabetes duration on left ventricular diastolic function and cardiovascular disease. *Postgrad Med J.* (2012) 88:189–93. doi: 10.1136/postgradmedj-2011-130439

Conflict of Interest: The authors declare that the research was conducted in the absence of any commercial or financial relationships that could be construed as a potential conflict of interest.

frontiers in Bioengineering and Biotechnology

ORIGINAL RESEARCH
published: 08 October 2021
doi: 10.3389/fbioe.2021.742985

Qualitative and Quantitative Assessments of Blood Flow on Tears in Type B Aortic Dissection With Different Morphologies

Simone Saitta[1,2†], Baolei Guo[3†], Selene Pirola[1], Claudia Menichini[1], Daqiao Guo[3], Yan Shan[4], Zhihui Dong[3], Xiao Yun Xu[1*] and Weiguo Fu[3*]*

[1]Department of Chemical Engineering, Imperial College London, London, United Kingdom, [2]Department of Electronics Information and Bioengineering, Politecnico di Milano, Milan, Italy, [3]Department of Vascular Surgery, Zhongshan Hospital, Institute of Vascular Surgery, Fudan University, Shanghai, China, [4]Department of Radiology, Zhongshan Hospital, Fudan University, Shanghai, China

OPEN ACCESS

Edited by:
Zahra K. Motamed,
McMaster University, Canada

Reviewed by:
Lisa Prahl Wittberg,
Royal Institute of Technology, Sweden
Luísa Sousa,
University of Porto, Portugal

***Correspondence:**
Baolei Guo
guo.baolei@zs-hospital.sh.cn
Xiao Yun Xu
yun.xu@imperial.ac.uk
Weiguo Fu
fu.weiguo@zs-hospital.sh.cn

[†]These authors have contributed equally to this work

Specialty section:
This article was submitted to Biomechanics, a section of the journal Frontiers in Bioengineering and Biotechnology

Received: 17 July 2021
Accepted: 21 September 2021
Published: 08 October 2021

Citation:
Saitta S, Guo B, Pirola S, Menichini C, Guo D, Shan Y, Dong Z, Xu XY and Fu W (2021) Qualitative and Quantitative Assessments of Blood Flow on Tears in Type B Aortic Dissection With Different Morphologies. Front. Bioeng. Biotechnol. 9:742985. doi: 10.3389/fbioe.2021.742985

Objective: The interactions between aortic morphology and hemodynamics play a key role in determining type B aortic dissection (TBAD) progression and remodeling. The study aimed to provide qualitative and quantitative hemodynamic assessment in four different TBAD morphologies based on 4D flow MRI analysis.

Materials and Methods: Four patients with different TBAD morphologies underwent CT and 4D flow MRI scans. Qualitative blood flow evaluation was performed by visualizing velocity streamlines and flow directionality near the tears. Quantitative analysis included flow rate, velocity and reverse flow index (RFI) measurements. Statistical analysis was performed to evaluate hemodynamic differences between the true lumen (TL) and false lumen (FL) of patients.

Results: Qualitative analysis revealed blood flow splitting near the primary entry tears (PETs), often causing the formation of vortices in the FL. All patients exhibited clear hemodynamic differences between TL and FL, with the TL generally showing higher velocities and flow rates, and lower RFIs. Average velocity magnitude measurements were significantly different for Patient 1 (t = 5.61, p = 0.001), Patient 2 (t = 3.09, p = 0.02) and Patient 4 (t = 2.81, p = 0.03). At follow-up, Patient three suffered from left renal ischemia because of FL collapse. This patient presented a complex morphology with two FLs and marked flow differences between TL and FLs. In Patient 4, left renal artery malperfusion was observed at the 32-months follow-up, due to FL thrombosis growing after PET repair.

Conclusion: The study demonstrates the clinical feasibility of using 4D flow MRI in the context of TBAD. Detailed patient-specific hemodynamics assessment before treatment may provide useful insights to better understand this pathology in the future.

Keywords: type B aortic dissection, 4D flow MRI, aortic remodeling, flow imaging, thoracic endovascular aortic repair (TEVAR)

INTRODUCTION

Approximately 30% of patients with aortic dissection have one or more ischemic complications of the peripheral vasculature, including stroke, paraplegia, loss of peripheral pulses, and compromised renal or mesenteric perfusion (Nienaber et al., 2016). With regards to Stanford type B aortic dissection (TBAD), the presence of a dissecting aneurysm or the occurrence of organ ischemia requires immediate treatment. In recent years, primary entry closure with thoracic endovascular aortic repair (TEVAR) has been performed as the first-line strategy for complicated TBAD (Nienaber et al., 2013). The primary goal of TEVAR is to reduce flow and pressure in the false lumen (FL). Aortic remodeling is facilitated in most cases, causing the FL to regress and thrombose (Nienaber et al., 2013). However, this is a highly complex pathology and each dissection has the anatomical morphology of its own, with different dissection propagation lengths, numbers of secondary tears, volumes of true lumen (TL) and FL and even some cases with multiple FLs. These morphological features are of critical importance for aortic remodeling in both acute and chronic dissections and are strictly related to hemodynamics (Xu et al., 2017).

Limited by the complex interactions between hemodynamics and geometry in TBAD, little effort has been spent on understanding the hemodynamic mechanisms leading to visceral ischemia and asymptomatic cases with malperfusion following the primary entry tear (PET) closure. Moreover, current risk stratification methods rely on anatomic rather than hemodynamic characteristics (Evangelista et al., 2012; Allen et al., 2019). Incorporating hemodynamics in patient risk stratification could improve TBAD development predictions and, eventually, treatment (François et al., 2013).

Until recently, hemodynamic parameters could not be easily measured, and patient-specific flow alterations are not yet clearly understood. Sophisticated numerical simulations studies have evaluated blood flow in TBAD using computational fluid dynamics (CFD) and four-dimensional phase-contrast magnetic resonance imaging (4D flow MRI) (Pirola et al., 2019). In particular, 4D flow MRI allows to measure blood flow velocities in the aorta at any anatomic location of interest (Markl et al., 2016), enabling quantitative functional assessment of blood flow (Youssefi et al., 2017; Soulat et al., 2020). Based on this imaging technique, previous studies have demonstrated the feasibility of evaluating hemodynamic alterations in the TL and FL (François et al., 2013; Liu et al., 2018; Allen et al., 2019). These similar studies provide valuable information about the complex hemodynamics involved in TBAD. Nonetheless, they did not provide insights into how much hemodynamics can vary among patients with different aortic morphologies. In fact, despite the constant research efforts, the complex interactions between patient-specific hemodynamics and aortic morphology make it difficult to fully understand the causalities of this disease and to relate such factors to TBAD progression. It is thus necessary to further investigate patient-specific TL and FL hemodynamic alterations. Accordingly, 4D flow MRI assessment of blood flow in TBADs may improve patient risk assessment and allow additional procedures to be targeted to patients with organ malperfusion (Adriaans et al., 2019; Zilber et al., 2021).

In the present study, four acute TBAD patients with different aortic morphologies were evaluated through 4D flow MRI analysis and aortic remodeling after TEVAR was assessed at 12-, 24- or 32 months follow-up. The main goal of this study was to analyze pre-TEVAR blood flow dynamics in the TL and FL of a diverse set of aortic morphologies, with special attention to flow distributions at the entry/re-entry tear (RT) sites. Additionally, we provide new insights into the possible relationships between pre-TEVAR aortic hemodynamics and aortic remodeling that occurred following TEVAR, suggesting that lower FL flow rates concurrently with branch vessel perfusion through RTs may represent a risk factor for the development of malperfusion after TEVAR.

MATERIALS AND METHODS

Study Design

In this study, a total of four patients (45–59 years-old, 3 males and 1 female) with acute complicated TBAD were included. Preoperative computed tomography (CT) and 4D flow MRI scans were performed on all patients. Different aortic morphologies were observed among the four cases during CT imaging analysis. The geometric parameters before TEVAR are reported in **Table 1**. This study was approved by the Ethics Committee of Zhongshan Hospital, Fudan University, Shanghai, China (Ethics approval number Y2017-056).

Computed tomography Scanning Protocol and Post-Processing

Patients underwent CT scans using a 320-row volumetric scanner (Aquilion ONE, Toshiba Medical System, Japan), generating axial images with 0.7 mm isotropic pixel spacing and 1 mm-thick sections from the top of the aortic arch to the bilateral iliac artery. Non-ionic contrast agent iopamidol 370 (iopamidol, Bracco, Milan, Italy) of 1.2 ml/kg followed by a saline flush of 25 ml was administered via antecubital vein using an automated injection system (Vistron CT Injection System, Medrad, Warrendale, PA, United States) at a flow rate of 4 ml/s. The trigger threshold was set at 200 HU (Aquilion ONE) within the descending aorta. For all patients, manual segmentation of the aortic geometries was performed by an expert operator using 3D Slicer (Kikinis et al., 2014). 3D renderings of the aortic anatomies are shown in **Figure 1** together with tear locations and stent-graft positioning at follow-up. A set of geometric measurements associated with TBAD were taken from the CT images; these included PET area, re-entry tear (RT) maximum diameter, maximum FL cross-sectional area and TL and FL volumes. Perfusion of celiac artery, superior mesenteric artery, right and left renal arteries was assessed.

Geometric measurements taken from CT scans are reported in **Table 1**. For Patient 4, the FL covered a large portion of the abdominal aorta, even below the iliac bifurcation; therefore, TL and FL volumes were calculated from the PET to the celiac artery (CA) root.

TABLE 1 | Aortic dissection morphologic measurements of interest for the four patients.

Geometric variable	Patient 1	Patient 2	Patient 3	Patient 4
PET maximum diameter (mm)	22	10	4 (FL1) + 5 (FL2)	11.3
RT maximum diameter (mm)	10.01 (RT1)	4.89 (RT1) 4.66 (RT2) 4.91 (RT3)	9.31 (RT1; FL1 to TL)	4.24 (RT1) 7.03 (RT2)
Celiac artery	TL	FL	TL	FL
Superior mesenteric artery	TL	FL	TL	TL
Right renal artery	FL	TL	TL	TL
Left renal artery	TL	TL + FL	TL (dynamic ischemia)	FL
Maximum FL cross-sectional area (mm^2)	684	467	305 (FL1) + 827 (FL2)	970
TL volume (cm^3)	18	49.1	44.8	86.0
FL volume (cm^3)	81	143	64.3 (FL1), 159.4 (FL2)	198.7

FL, false lumen; PET, primary entry tear; RT, re-entry tear; TL, true lumen.

4D Flow MRI Acquisition and Post-processing

4D flow MRI images were acquired using a 3-T clinical MR scanner (Magnetom Avanto; Siemens Medical Solutions, Erlangen, Germany) using the following parameters: flip angle 7°; velocity encoding 150 cm/s in all directions; spatial resolution $1.85 \times 1.85 \times 2.5\,mm^3$; and temporal resolution 47–61 ms. Retrospective electrocardiographic gating was used to reconstruct 12–20 frames/cardiac cycle. Using custom-built MATLAB code, the volumes segmented from CT scans were registered onto the 4D flow image volumes (Saitta et al., 2019). Data were visualized and further post-processed with Paraview (Kitware, NY, United States). Five cross-sectional planes were selected along the aorta for hemodynamics quantification (**Figure 2**).

Endovascular Procedures

TEVAR was performed on all patients under general anesthesia using Valiant Capitivia (Medtronic, Minneapolis, MN) or C-TAG (W. L. Gore & Associates, Flagstaff, AZ) through the unilateral common femoral artery with a percutaneous puncture secured by two ProGlide stitches (Abbott Vascular, Abbott Park, IL). As previously reported (Guo et al., 2018), Patient 3, whose CT scan showed a TBAD with three-channel morphology, underwent TEVAR with a provisional extension to induce complete attachment (PETTICOAT) procedure (Melissano et al., 2012). Endograft oversizing was 0–5% according to the distance from the adventitia to the proximal landing zone. PETs were covered with a single 15- to 20 cm-long endograft. The proximal landing zone in Patient 1 was measured < 15 mm, the left subclavian artery was intentionally covered, as the right vertebral artery was patent and the left one was not dominant.

Statistics

Hemodynamic and geometric measurements were entered into the statistical analysis software GraphPad Prism 8.1 (GraphPad Software, La Jolla, CA, United States of America). Variations in mean flow rate, peak flow rate, peak velocity magnitude and reverse flow index (RFI) in the TL and FL were compared using the paired *t*-test. A *p*-value of less than 0.05 was considered statistically significant.

RESULTS

Qualitative assessment of blood flow in the four patients was performed through visualization of streamlines within the aorta at mid-systole, emphasizing blood flow directionality around the PETs and RTs (**Figure 3**). Quantitative analysis of blood flow included the calculation of plane-averaged velocity magnitude, peak flow rate, peak velocity magnitude and RFI at five cross-sections along the aorta (**Figure 2**).

4D Flow-Based Qualitative Assessment

For all patients, visualization of streamlines revealed a clear difference in blood flow velocities within TL and FL, with TLs experiencing generally higher velocities. In Patient 1, flow patterns observed around the PET revealed the presence of a flow split, with a higher TL velocity due to compression, and lower velocity recirculating around the tear and entering the FL (**Figure 3**). Distal to the PET, no secondary tears were present, resulting in little flow disturbance in the TL. Blood flow acceleration was observed around the RET, with the formation of a high velocity stream re-entering the TL and causing helical flow formation.

In Patient 2, streamlines visualization showed a high velocity jet across the PET. This caused rapid deceleration of the flow jet in the proximal FL through the formation of vortical flow. Distal to the PET, the TL experienced significantly higher velocities due to the curvature of the aorta. In this case, both the CA and the superior mesenteric artery (SMA) were perfused by the FL. High velocity flow was observed entering the SMA from the FL through a re-entry tear (**Figure 3**).

Patient 3 featured a stark difference between FLs and TL in blood flow velocity along the aorta (**Figure 3**). In this case, the high velocity flow crossing the PET split three-ways, entering both FL1 and FL2 through the connected intimal tears. The high velocity flow leaving the TL and perfusing the SMA is shown in **Figure 3**; at this location, a re-entry tear (from FL1 to TL) was present.

Patient 4 presented a dissection with the PET located distal to the aortic arch. The high velocity flow in the TL at the arch and proximal to the PET entered the FL hitting the outer wall. A portion of the flow filled the upper region of the FL and the other

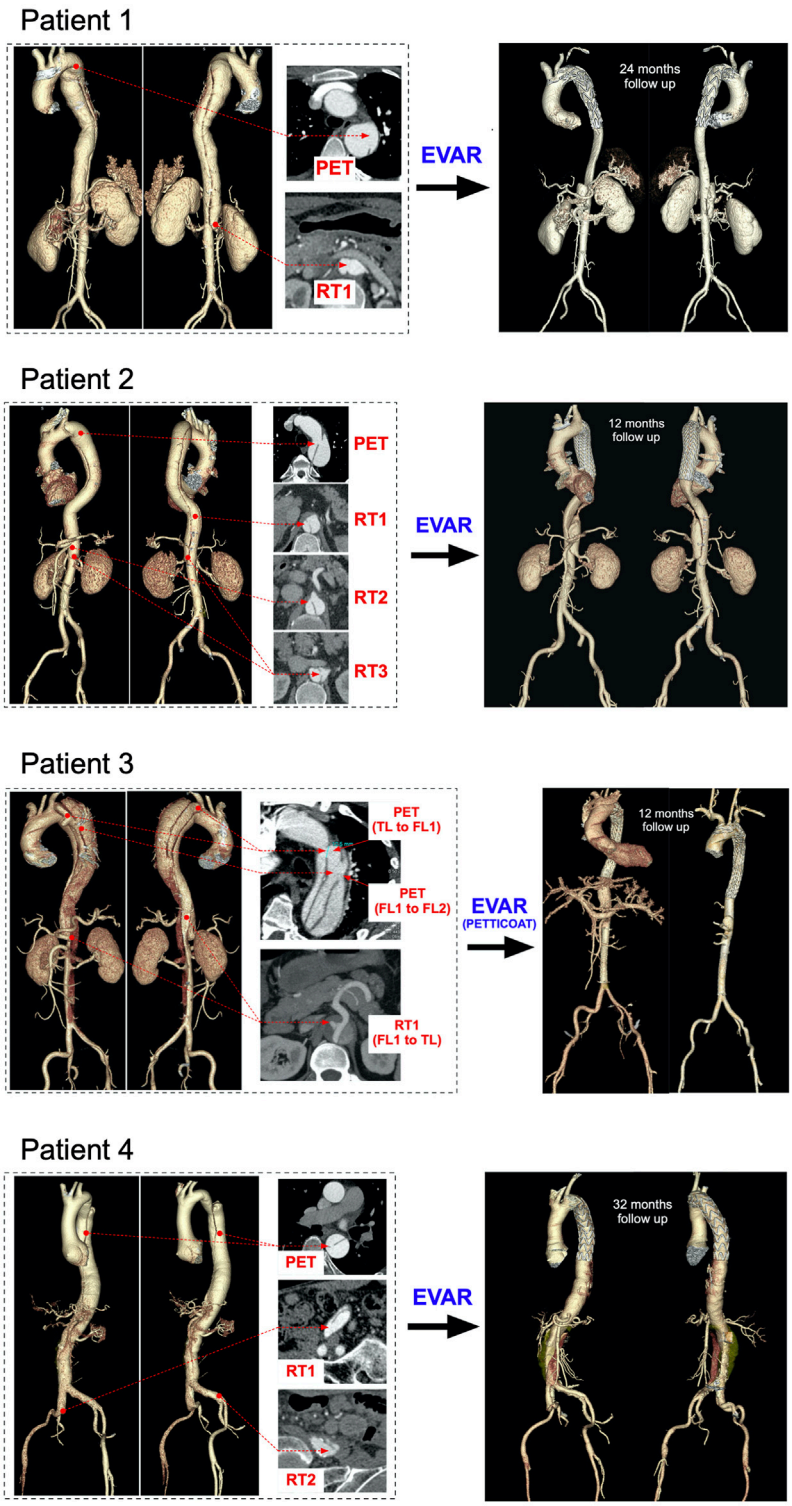

FIGURE 1 | Aortic reconstructions **(Left)** pre-TEVAR volumetric aortic reconstructions for the four patients with selected cross-sections to point the visible primary entry tears (PET), re-entry tears (RT), true lumens (TL) and false lumens (FL) **(Right)** post-TEVAR volumetric aortic reconstructions for the four patients at 12-, 24- and 32 months follow-ups, respectively.

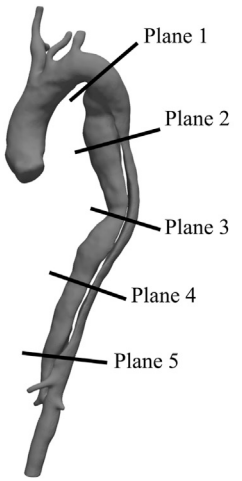

Plane 1: above the primary entry tear (PET)

Plane 2: 2 cm distal to the PET

Plane 3: at the end of the potential stent-graft (15 cm in length)

Plane 4: at the end of the potential stent-graft (20 cm in length)

Plane 5: 2 cm proximal to the celiac artery

FIGURE 2 | Cross-sections exemplification for post-processing **(Right)** Exemplification of the five cross-sectional planes selected along the aorta for 4D flow MRI analysis **(Left)** Volumetric reconstruction of a post-TEVAR aortic geometry (Patient 1) with stent-graft end pointed in red.

portion flowed downstream. Stagnant flow was visible in the upper FL region (light blue streamline region in **Figure 3**).

4D Flow MRI-Based Quantitative Assessment

Hemodynamic quantities of interest calculated on the five selected planes are reported in **Table 2**. For each plane, flow rate was calculated by taking the dot product between velocity and normal vectors and integrating the result over the plane area. In this way, a flow rate waveform was obtained for the cardiac cycle, from which peak and average values were computed. RFI was calculated as the fraction of negative area of the flow rate curve over the whole area under the curve (Birjiniuk et al., 2020).

$$RFI = \frac{\left|\int_0^T Q_r dt\right|}{\left|\int_0^T Q_a dt\right| + \left|\int_0^T Q_r dt\right|} \times 100\%, \quad (1)$$

where Q_r and Q_a are the total retrograde and antegrade flow rates, and T is the cardiac cycle period. Flowrate waveforms over time for planes 2 and 5 are plotted in **Figure 4** for both TLs and FLs of the four patients.

On plane 1, proximal to the PET, the measured average velocity magnitudes varied between 10 and 22.7 cm/s. Null RFIs were found on plane 1 for Patients 1, 2 and 3, while a RFI = 6.3% was found for Patient 4. Such detail can also be appreciated in **Figure 4**, where null RFIs correspond to TL flow rate curves staying above the horizontal axis for the whole cardiac cycle.

For Patient 1, differences between TL and FL average velocity magnitudes increased with the distance from the PET and were equal to 3.85, 5.55, 5.99 and 6.30 cm/s for planes 2, 3, 4 and 5 respectively. Through all selected planes, peak flow rate values were larger in the FL than in the TL, with differences ranging from 0.19 to 1.76 L/min. TL peak velocity magnitudes were greater than FL values by 6.21, 5.69, 3.53 and 7.43 cm/s for planes 2, 3, 4 and 5, respectively.

For Patient 2, TL average velocity magnitudes were higher than FL values by 10.0, 3.93, 2.30 and 8.22 cm/s for planes 2 to 5. Peak flow rates were consistently higher in the FL, with differences ranging from −5.89 to −1 L/min. TL peak velocity magnitudes exceeded FL values by 12.8, 11.4, 6.84, and 17.2 cm/s for planes 2 to 5.

Patient 3 exhibited larger differences in average velocities between the TL and FL, with values ranging from 14.9 (on plane 2) to 114 cm/s (on plane 5). Peak flow rates were higher in the FL on planes 2 and 4 by 2.53 and 0.46 L/min respectively, whereas they were higher in the TL on planes 3 and 5 by 1.12 and 4.21 L/min. On all selected planes, peak velocity magnitudes were higher in the TL, with the largest difference of 185 cm/s found on plane 5. In this special case of TBAD, FL1 and FL2 average velocity magnitudes were averaged, while maximum values were considered for considering peak flow rates and peak velocity magnitudes.

For Patient 4, average velocity magnitude was higher in the TL for all planes, with values ranging from 5.06 (on plane 5) to 15.1 cm/s (on plane 4). On planes 2 and 3, TL peak flow rates were higher than FL values by 11.6 and 0.35 L/min, while on planes 4 and 5, FL values where greater than TL ones by 0.85 and 0.67 L/min, respectively. On all planes, peak velocity magnitudes were higher in the TL than in the FL, with differences ranging from 0.840 (on plane 3) to 92.2 cm/s (on plane 4).

Note that, given a VENC of 150 cm/s, fluid regions characterized by lower velocities are affected by noise in the velocity measurement around 7.50 cm/s (at 5% VENC).

False Lumens Retrograde Flow Analysis

Differences between TL and FL can be visualized in **Figure 4**, where flow rates over time through planes 2 and 5 are plotted for the four patients. Negative flow rate curve areas correspond to non-zero RFI values. Patient 1 had null retrograde flow in the TL throughout the whole cardiac cycle. Retrograde flow in the FL during diastole resulted in 11.7 and 15% RFIs through planes 2 and 5. For Patient 2, a 7.5% RFI through plane 2 in the FL corresponded to retrograde flow during diastole, while a RFI of

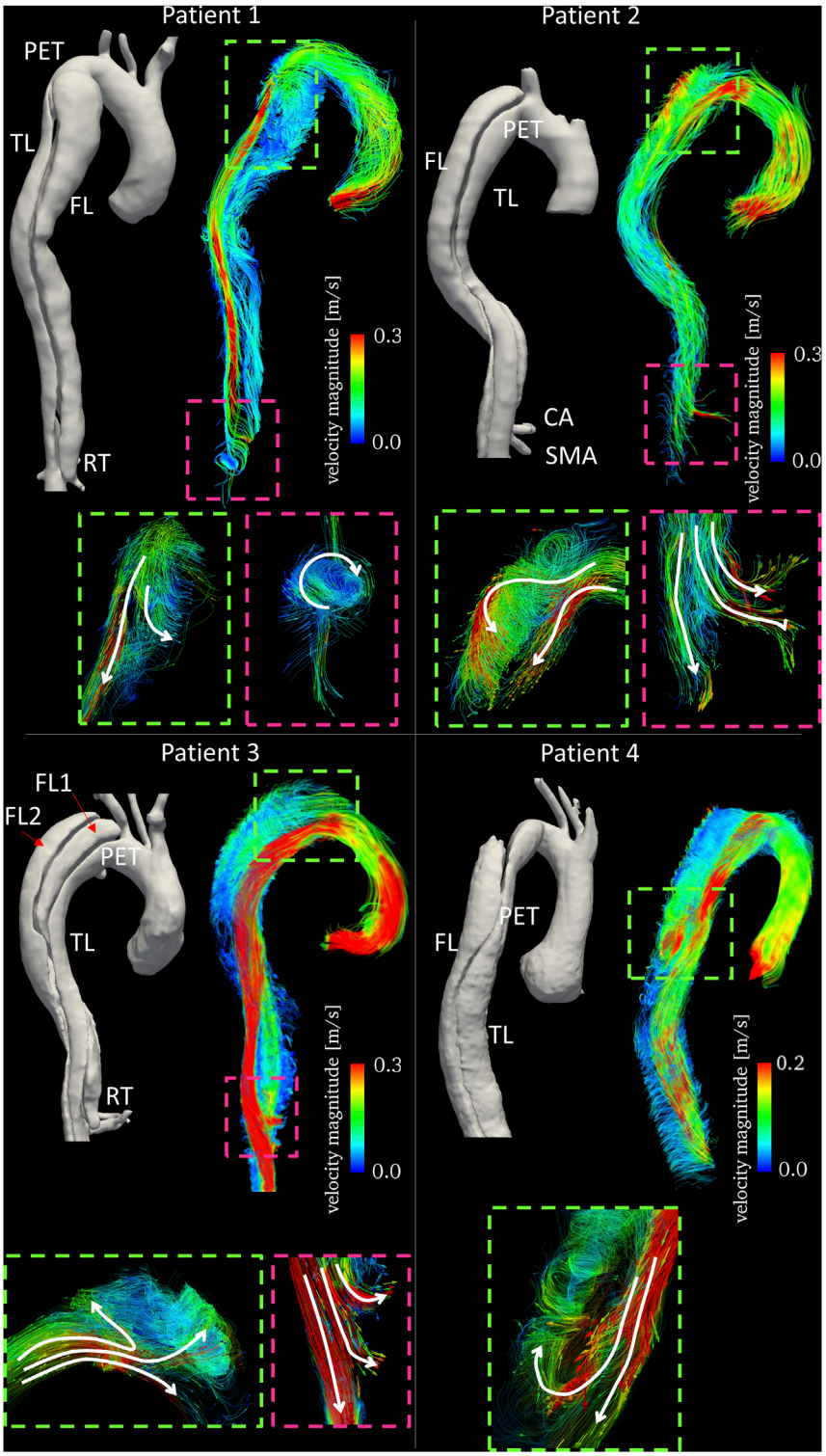

FIGURE 3 | Time averaged velocity streamlines color-coded by velocity magnitude together with 3D aortic reconstructions for the four patients. Text labels indicating primary entry tears (PETs), true lumen (TL), false lumen (FL), celiac artery (CA) and superior mesenteric artery (SMA) are in white. Enlarged subfigures are shown at the primary entry tears (dashed green boxes) and re-entry tears (dashed pink boxes) with arrows to emphasize flow directionality.

TABLE 2 | Blood flow measurements computed from 4D flow on the selected cross-sectional planes for the four patients.

Variable			Patient 1	Patient 2	Patient 3	Patient 4
Average velocity magnitude (cm/s)	plane 1	TL	13.2	13.6	22.7	10.0
	plane 2	TL	12.3	19.8	23.5	13.1
		FL	8.45	9.76	11.8 (FL1), 5.35 (FL2)	2.98
	plane 3	TL	10.5	12.3	37.0	9.00
		FL	4.95	8.37	14.0 (FL1), 3.76 (FL2)	8.76
	plane 4	TL	12.8	12.4	39.6	15.1
		FL	6.81	10.1	4.97 (FL1), 6.66 (FL2)	5.10
	plane 5	TL	13.5	14.3	124	5.06
		FL	7.20	6.08	8.48 (FL1), 10.8 (FL2)	1.22
Peak flow rate (L/min)	plane 1	TL	7.54	15.3	11.0	11.5
	plane 2	TL	2.35	6.46	7.25	13.0
		FL	2.55	8.29	5.73 (FL1), 4.04 (FL2)	1.40
	plane 3	TL	2.92	4.01	6.78	6.15
		FL	4.69	9.90	2.32 (FL1), 3.29 (FL2)	5.80
	plane 4	TL	2.52	4.58	5.19	6.17
		FL	4.24	10.0	2.87 (FL1), 2.79 (FL2)	7.03
	plane 5	TL	2.36	4.64	5.99	6.29
		FL	2.96	5.69	0.87 (FL1), 0.90 (FL2)	6.92
Peak velocity magnitude (cm/s)	plane 1	TL	30.8	39.7	40.6	29.9
	plane 2	TL	21.7	42.4	44.3	33.5
		FL	15.5	29.6	24.9 (FL1), 7.07 (FL2)	4.13
	plane 3	TL	21.6	38.8	70.5	23.3
		FL	15.9	27.4	24.6 (FL1), 6.72 (FL2)	22.4
	plane 4	TL	24.7	41.4	82.8	45.2
		FL	21.1	34.5	11.3 (FL1), 12.9 (FL2)	14.3
	plane 5	TL	27.1	37.8	208	160
		FL	19.6	20.7	15.8 (FL1), 23.0 (FL2)	67.8
Reverse flow fraction (%)	plane 1	TL	0	0	0	6.31
	plane 2	TL	0	0	0	6.17
		FL	11.7	7.51	5.51 (FL1), 0 (FL2)	0
	plane 3	TL	0	5.73	0	17.8
		FL	22.3	4.54	4.39 (FL1), 51.3 (FL2)	51.5
	plane 4	TL	0	10.0	0	7.64
		FL	9.37	1.87	3.35 (FL1), 59.4 (FL2)	61.4
	plane 5	TL	0	20.3	0	12.6
		FL	15.0	5.70	46.0 (FL1), 39.6 (FL2)	69.4

FL, false lumen; TL, true lumen.

zero was found through plane 2 in the TL. An opposite trend was observed through plane 5, where retrograde diastolic flow was larger in the TL. TL and FL RFIs were 20 and 5.7%, respectively. For Patient 3, no retrograde flow was found in the TL across all planes. Similar flow rate waveforms were found for the two FLs at plane 5, where a peak value of 0.90 L/min was observed in FL1 and RFIs of 46 and 40% were found for FL1 and FL2, respectively. Higher FL flow rates were found across plane 2 than plane 5 throughout the cardiac cycle. Such a difference could be attributed to the fact that plane 2 is close to the PET where the flow is affected by the higher velocity in the TL.

Flow rate through Patient 4's plane 2 in the TL displayed the typical aortic flow waveform, with clearly distinguishable systolic and diastolic phases. At plane 2, 80% of the total mean flow rate was carried by the TL and RFI = 0 was found in the FL. With respect to plane 2, the TL flow rate peak was observed after 0.11 s on plane 5, where retrograde diastolic flow corresponded to RFIs of 12.6 and 69.4% for the TL and FL, respectively.

Analysis of retrograde flow fraction revealed that patients 2 and 4 who had visceral branches perfused by the FL had non-zero RFIs in the TL.

Statistical Analysis: Difference Between False Lumens and True Lumen

The results of the statistical analysis to evaluate the differences in hemodynamics between TL and FL are reported in **Table 3**; **Figure 5**. Average velocity magnitude was significantly higher in the TL for Patient 1 ($p < 0.005$), Patient 2 ($p < 0.05$) and Patient 4 ($p < 0.05$), and higher, but not statistically significant, for Patient 3 ($p = 0.08$). For Patient 2, peak flow rate was larger in the FL ($p < 0.05$), whereas for Patient 3 it was found to be greater in the TL ($p < 0.05$). For all patients, peak velocity magnitude was higher in the TL, with statistically significant difference in Patient 1 ($p < 0.05$) and Patient 2 ($p < 0.05$). Patient 2 had higher TL RFIs, while all other patients exhibited greater RFIs in the FL ($p < 0.005$ for Patient 1, $p < 0.05$ for Patient 3 and $p = 0.072$ for Patient 4).

Aortic Remodeling at Follow-Up

The four patients underwent midterm follow-up (12–32 months) CT scans (**Figure 1**). CT imaging demonstrated the good position of all endografts, obliteration of all FLs in the thoracic aorta, nearly complete thrombosis of the FLs, expansion of the TL, and no endoleak. In Patient 1 and Patient 2, the FL was almost thrombosed apart from the

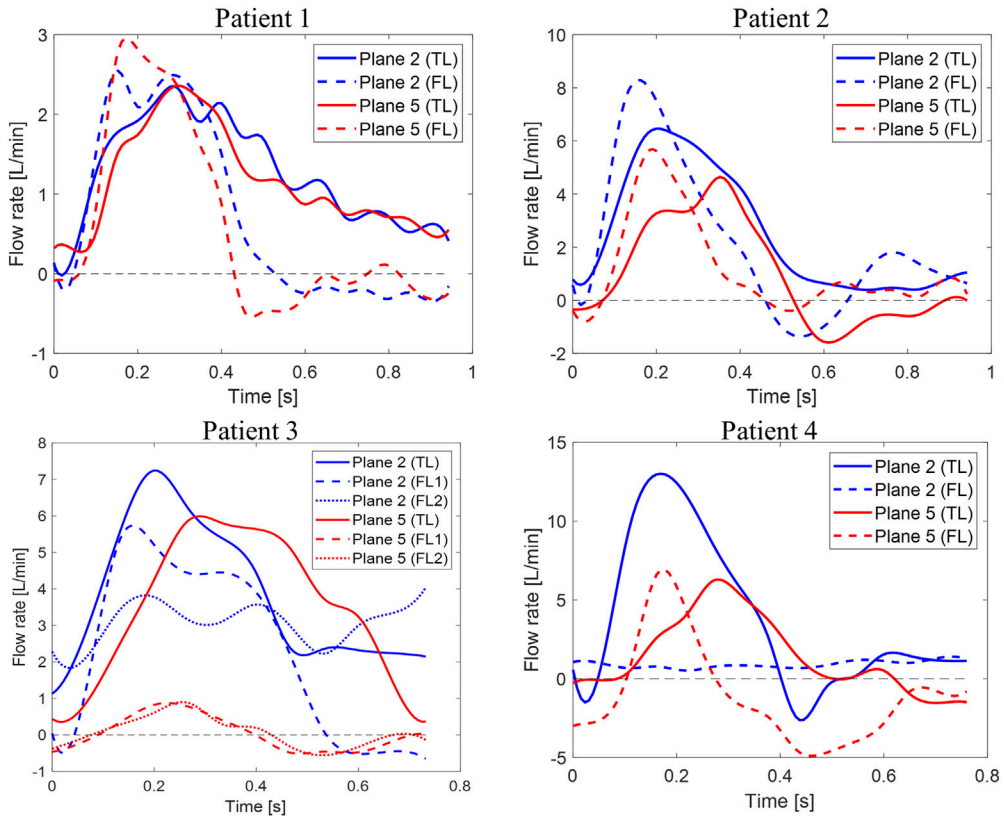

FIGURE 4 | Flow rate waveforms. Time plots of flow rates calculated through planes two and five in the TL and FL for the four patients. *Y*-axis limits were adjusted to better show each patient's waveforms.

TABLE 3 | Comparison of 4D flow analysis in the TL and FL among the four patients.

Variable		Patient 1	Patient 2	Patient 3	Patient 4
Average velocity magnitude [cm/s]	TL	12.3 ± 1.28	14.7 ± 3.52	56.03 ± 45.9	10.6 ± 4.46
	FL	6.85 ± 1.45	8.58 ± 1.83	8.23 ± 1.67[c]	4.52 ± 3.24
	T	5.61	3.09	2.08	2.81
	P	0.001[a]	0.02[a]	0.08	0.03[a]
Peak flow rate [L/min]	TL	2.54 ± 0.27	4.92 ± 1.06	6.30 ± 0.9	7.91 ± 3.40
	FL	3.61 ± 1.02	8.47 ± 2.02	3.20 ± 1.99[b]	5.29 ± 2.65
	T	2.03	3.12	2.85	1.22
	P	0.088	0.021[a]	0.029[a]	0.27
Peak velocity magnitude [cm/s]	TL	23.75 ± 2.62	40.10 ± 2.11	101.4 ± 73	65.5 ± 64
	FL	18.04 ± 2.79	28.05 ± 5.74	21.35 ± 5.69[b]	27.2 ± 28.1
	T	2.99	3.94	2.19	1.10
	P	0.024[a]	0.007[a]	0.07	0.31
RFI [%]	TL	0.004 ± 0.009	9.0 ± 8.56	0	11.0 ± 5.26
	FL	14.6 ± 5.65	4.9 ± 2.36	43.9 ± 0.26[c]	45.6 ± 31.3
	T	5.17	0.92	3.39	2.18
	P	0.002[a]	0.391	0.0146[a]	0.072

FL, false lumen; RFI, reverse flow index; TL, true lumen.

[a]*Represents a statistically significant difference (p < 0.05). For Patient 3, a single asterisk*

[b]*Indicates that the mean of values calculated in the two FLs is reported, while a double asterisk*

[c]*Indicates that the maximum value between the two FLs is reported.*

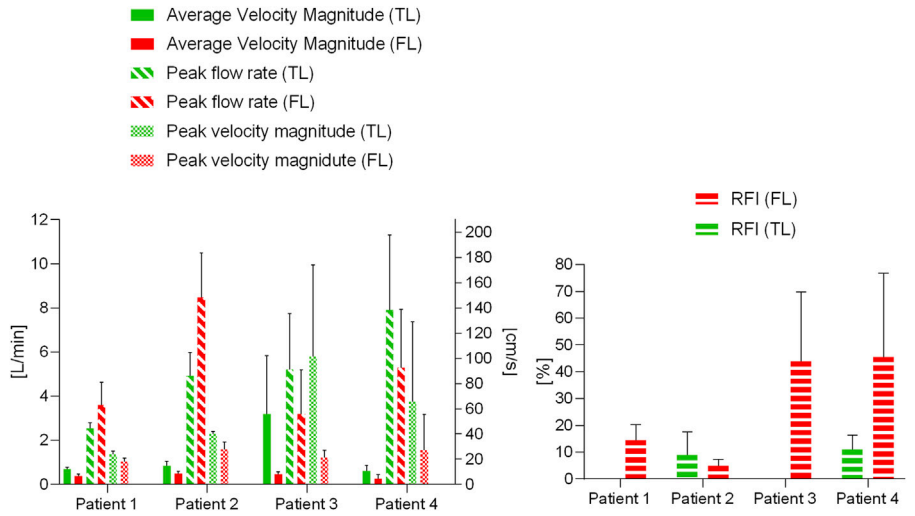

FIGURE 5 | Blood flow parameter variations for the four patients in the TL and FL. Average velocity magnitude, peak flow rate and peak velocity magnitude are plotted on the left, reverse flow index (RFI) variations are plotted on the right.

TABLE 4 | Geometric analysis for the four kind of aortic dissection post-TEVAR.

Variable	Patient 1	Patient 2	Patient 3	Patient 4
Follow up	24 months	12 months	12 months	32 months
PET maximum diameter	Covered	Covered	Covered	Covered
RT maximum diameter (mm)	8.98 (RT1)	8.51 (RT1) 4.37 (RT2) 5.27 (RT3)	Covered	4.44 (RT1) 7.14 (RT2)
Celiac artery	Perfused	Perfused by FL	Perfused	Perfused
Superior mesenteric artery	Perfused	Perfused by RT2	Perfused	Perfused
Right renal artery	Perfused through RT1	Perfused	Perfused	Perfused
Left renal artery	Perfused	Perfused through RT3	Malperfused static ischemia	Malperfused
FL area	Decreased	Decreased	Collapsed	Decreased
TL volume	Increased	Increased	Increased with remodeling	Increased
FL volume	Almost thrombosed apart from the area near the RT1	Partially thrombosed	Collapsed	Completely thrombosed in TA, and partially thrombosed in AA

FL, false lumen; PET, primary entry tear; RT, re-entry tear; TL, true lumen; TA, thoracic aorta; AA, abdominal aorta.

area near the distal re-entry tear. The right renal artery in Patient 1 was perfused by the FL with the flow from TL through the re-retry tear (RT1). In Patient 2, the re-entry tears (RT2 and RT3) played important roles in the blood flow exchange between TL and FL after TEVAR. This patient did not suffer malperfusion syndrome during follow up despite the CA and SMA were both perfused by FL. The FL collapsed and completely thrombosed in Patient 3 after the TEVAR with PETTICOAT procedure. However, a dynamic ischemia in the left renal artery became a static ischemia. Patient 4 had a better TL remodeling in thoracic aorta than the abdominal aorta. The abdominal FL was perfused through the two distal re-entry tears in the iliac arteries and partial thrombosed. Unfortunately, the left renal artery was malperfused during follow up. The post-TEVAR analysis is listed in **Table 4**.

DISCUSSION

Current guidelines suggest that non-invasive methods based on CFD and MRI can provide additional dynamic information regarding entry tear flow or arterial vessel involvement (François et al., 2013; Riambau et al., 2017). However, it is still unclear how blood flow distributes at the entry/re-entry tear sites in TBAD. In the present study, four cases of TBAD with different morphologies were analyzed using 4D flow MRI for qualitative and quantitative blood flow assessment. Additionally, observations related to aortic remodeling for the four patients post-TEVAR were reported. This analysis demonstrates the added value of using 4D flow MRI to provide clinically relevant information for better understanding of blood flow

alterations in the TL and FL, which can vary among different types of TBADs.

Patient-specific analyses using flow visualization and quantification would aid physicians understand the complex pathologic changes of TBAD with different morphologies. However, interpreting the meaning of different hemodynamic measures is particularly challenging, and most studies report analyses for only one or a few patients with no follow-up for validation (Müller-Eschner et al., 2011).

This study confirms the feasibility of using 4D flow MRI to assess hemodynamic differences between TL and FL. The presence of blood flow in the FL has been shown to be the most important risk factor for FL enlargement (Sueyoshi et al., 2004). In particular, Inoue et al. (Inoue et al., 2000) found volume flow rate in the FL to be a significant predictor of FL growth; the larger the flow rate, the faster was the FL expansion. In the present study, 4D flow-derived velocity streamlines showed the formation of vortical flow structures in the FL near the PETs caused by an acceleration of blood flow entering the FL. These observations are in agreement with findings by François et al. (2013) and Müller-Eschner et al. (2011), who reported the presence of abnormal, complex flow patterns in the FL. In general, blood flow in the FL was characterized by lower velocities and higher RFIs. In our study, average velocity magnitude was found to be significantly higher ($p < 0.05$) in the TL for three of the four patients analyzed (t = 5.61, 3.09 and 2.81 m/s for Patients 1, 2 and 4 respectively). Similar results were found by Liu et al. (2018), who analyzed a cohort of 16 patients and reported higher average velocities in the TL (t = 7.64) and higher RFIs in the FL (t = 5.01).

A second key finding of this study was based on the retrograde flow analysis performed on the four patients. RFIs were significantly higher in the FL ($p < 0.05$) for Patient 1 (t = 5.17) and Patient 3 (t = 3.39). Interestingly, a correlation between RFIs and pre-TEVAR side branches perfusion was found. No reversed flow was observed in the TL of Patients 1 and 3, who concurrently had the CA perfused by the TL. On the other hand, Patients 2 and 4 exhibited non-zero TL RFIs and had the CA and left renal artery perfused by the FL. These findings support the previously postulated hypothesis that reversed flow may be related to distal reentry pathways into the FL with higher pressure, causing disturbances of blood stream and retrograde flow in the TL (Catapano et al., 2020). This correlation is further backed up by the overall higher RFI in the TL than in the FL of Patient 2 (**Figure 5**). In this case in fact, perfusion of CA, SMA and left renal artery was provided by the FL.

An additional aim of this study was to explore whether specific hemodynamic conditions pre-TEVAR could potentially be related to aortic remodeling post-TEVAR. It seems likely that incorporating hemodynamic parameters obtained with 4D flow MRI will improve predictions. A recent 4D flow MRI-based patient-specific study by Takei et al. (2019) revealed that flow rate at the re-entry site and in the FL can have important effects on FL volume change. To better manage distal re-entry tears and avoid malperfusion, fenestrated and branched stent grafts have been used to treat patients (Oikonomou et al., 2014; Pellenc et al., 2019). In two of the four cases examined here, aortic complications such as partial thrombosis of FL and organ malperfusion were observed during follow-up. The limited number of patients in our study did not allow for a predictive analysis. However, they did provide useful insights about hemodynamics and potential associations with aortic remodeling during follow-up. Patients 1 and 2, had similar TL and FL flow rate waveforms (and peaks) during systole, but differed during diastole (**Figure 3**). In both patients, peak flow rates were higher in the FL than in the TL. On the other hand, the remarkable difference in pre-intervention flow rates observed in Patient 3 (especially on Plane 5), could be linked to the static ischemia developed in this patient. In this case, pre-TEVAR TL blood flow was characterized by significantly higher average velocities and flow rates and lower RFIs. The low FL flow rate and the intricate double FL morphology led to the complete collapse of the FL after TEVAR with distal bare stents placement preventing perfusion of the left renal artery and eventually leading to ischemia at follow-up. Similarly, Patient 4 was characterized by a lower peak flow rate in the FL with respect to the TL (**Figure 5**). In this case, the left renal artery was perfused by the FL pre-TEVAR and suffered from malperfusion after intervention. Our findings suggest that if peak flow rate before TEVAR is lower in the FL than in the TL, the FL may collapse or thrombose after occlusion of the PET by the graft; if this condition occurs concurrently with branch vessel perfusion by FL through a RT, malperfusion might be observed at follow-up.

Aortic hemodynamics is the key to aortic remodeling in both acute and chronic TBAD, as well as aortic-related complications after TEVAR (Tsai et al., 2007). Therefore, identifying and validating imaging biomarkers of aortic remodeling would have significant clinical implications. In our current study, it is difficult to draw robust conclusions on which specific hemodynamic parameters are associated with the clinical outcomes observed at follow-up. Future studies will include a larger patient cohort to further investigate potential predictive blood flow features using 4D flow MRI or CFD, with the goal of helping clinicians in treatment planning for TBAD patients.

Despite providing key information about patient-specific hemodynamics, 4D flow MRI presents some inherent limitations. The relatively high *VENC* of 150 cm/s, necessary to avoid aliasing in the TL, leads to lower signal-to-noise ratio in the FL which is characterized by lower velocities (François et al., 2013). The use of multi-*VENC* 4D flow MRI, could potentially solve this problem, and it seems especially necessary to evaluate blood flow in TBADs (Nett et al., 2012; Ha et al., 2016). Additionally, 4D flow MRI techniques are affected by errors due to noise and limited spatial and temporal resolution (Markl et al., 2016). Limitations in spatial resolution have been shown to have a significant effect on near-wall flow parameters such as wall shear stress (Piatti et al., 2017). Nonetheless, directly measured parameters such as flow rate through a plane are less sensitive to this constraint and can be estimated with reasonable accuracy (David et al., 2019). On the other hand, a low temporal resolution may lead to underestimations of the true peak velocity and flow rate. In this regard, new phase-contrast MR sequences hold the potential to increase temporal resolution while keeping scan

time to a minimum. Finally, the accuracy of geometric measurements taken on CT images inevitably depends on the image voxel size (Horner et al., 2019). Nonetheless, since no quantitative correlations were made between geometric features and flow parameters, our analyses are not significantly affected by intrinsic errors due to voxel size.

This study demonstrated the clinical applicability of 4D flow MRI in the context of TBAD, paving the way for future studies involving larger patient cohorts. Through 4D flow analysis, it was possible to quantify hemodynamics of TL vs. FL, showing the importance of retrograde flow in relation to visceral branch vessel perfusion. Our results confirm the potential of 4D flow MR imaging to be used as a non-invasive technique for patient risk stratification and treatment planning.

DATA AVAILABILITY STATEMENT

The data that support the findings of this study are available from the corresponding author, BG, upon reasonable request.

ETHICS STATEMENT

The studies involving human participants were reviewed and approved by This study was approved by the Ethics Committee of Zhongshan Hospital, Fudan University, Shanghai, China (Ethics approval number Y2017-056). The patients/participants provided their written informed consent to participate in this study. Written informed consent was obtained from the individual(s) for the publication of any potentially identifiable images or data included in this article.

AUTHOR CONTRIBUTIONS

SS "Formal Analysis, Methodology, Visualization, Writing original draft, Writing review and editing," BG "Conceptualization, Funding acquisition, Data curation, Supervision, Methodology, Writing original draft, Writing review and; editing," SP "Formal Analysis, Methodology, Visualization" CM "Formal Analysis, Methodology, Visualization," DG "Investigation, Supervision YS Data curation, Methodology," ZD "Data curation, Investigation, Project administration XX Conceptualization, Investigation, Project administration, Supervision, Writing review and; editing," WF—Funding acquisition, Investigation, Supervision.

FUNDING

Sponsored by the National Natural Science Foundation of China (82000436, 81770474), The Science and Technology of Shanghai (21410710500, 201409004800) and The Royal Society, United Kingdom (IE161052).

REFERENCES

Adriaans, B. P., Wildberger, J. E., Westenberg, J. J. M., Lamb, H. J., and Schalla, S. (2019). Predictive Imaging for Thoracic Aortic Dissection and Rupture: Moving beyond Diameters. *Eur. Radiol.* 29 (12), 6396–6404. doi:10.1007/s00330-019-06320-7

Allen, B. D., Aouad, P. J., Burris, N. S., Rahsepar, A. A., Jarvis, K. B., François, C. J., et al. (2019). Detection and Hemodynamic Evaluation of Flap Fenestrations in Type B Aortic Dissection with 4D Flow MRI: Comparison with Conventional MRI and CT Angiography. *Radiol. Cardiothorac. Imaging* 1 (1), e180009. doi:10.1148/ryct.2019180009

Birjiniuk, J., Oshinski, J. N., Ku, D. N., and Veeraswamy, R. K. (2020). Endograft Exclusion of the False Lumen Restores Local Hemodynamics in a Model of Type B Aortic Dissection. *J. Vasc. Surg.* 71 (6), 2108–2118. doi:10.1016/j.jvs.2019.06.222

Catapano, F., Pambianchi, G., Cundari, G., Rebelo, J., Cilia, F., Carbone, I., et al. (2020). 4D Flow Imaging of the Thoracic Aorta: Is There an Added Clinical Value. *Cardiovasc. Diagn. Ther.* 10 (4), 1068–1089. doi:10.21037/cdt-20-452

David, A., Le Touze, D., Warin-Fresse, K., Paul-Gilloteaux, P., Bonnefoy, F., Idier, J., et al. (2019). *In-vitro* Validation of 4D Flow MRI Measurements with an Experimental Pulsatile Flow Model. *Diagn. Interv. Imaging* 100 (1), 17–23. doi:10.1016/j.diii.2018.08.012

Evangelista, A., Salas, A., Ribera, A., Ferreira-González, I., Cuellar, H., Pineda, V., et al. (2012). Long-Term Outcome of Aortic Dissection with Patent False Lumen. *Circulation* 125 (25), 3133–3141. doi:10.1161/circulationaha.111.090266

François, C. J., Markl, M., Schiebler, M. L., Niespodzany, E., Landgraf, B. R., Schlensak, C., et al. (2013). Four-dimensional, Flow-Sensitive Magnetic Resonance Imaging of Blood Flow Patterns in Thoracic Aortic Dissections. *J. Thorac. Cardiovasc. Surg.* 145 (5), 1359–1366. doi:10.1016/j.jtcvs.2012.07.019

Guo, B., Pirola, S., Guo, D., Dong, Z., Xu, X. Y., and Fu, W. (2018). Hemodynamic Evaluation Using Four-Dimensional Flow Magnetic Resonance Imaging for a Patient with Multichanneled Aortic Dissection. *J. Vasc. Surg. Cases, Innov. Tech.* 4 (1), 67–71. doi:10.1016/j.jvscit.2017.11.005

Ha, H., Kim, G. B., Kweon, J., Kim, Y.-H., Kim, N., Yang, D. H., et al. (2016). Multi-VENC Acquisition of Four-Dimensional Phase-Contrast MRI to Improve Precision of Velocity Field Measurement. *Magn. Reson. Med.* 75 (5), 1909–1919. doi:10.1002/mrm.25715

Horner, M., Luke, S. M., Genc, K. O., Pietila, T. M., Cotton, R. T., Ache, B. A., et al. (2019). Towards Estimating the Uncertainty Associated with Three-Dimensional Geometry Reconstructed from Medical Image Data. *J. verification, validation, uncertainty quantification* 4 (4). doi:10.1115/1.4045487

Inoue, T., Watanabe, S., Sakurada, H., Ono, K., Urano, M., Hijikata, Y., et al. (2000). Evaluation of Flow Volume and Flow Patterns in the Patent False Lumen of Chronic Aortic Dissections Using Velocity-Encoded Cine Magnetic Resonance Imaging. *Jpn. Circ. J.* 64 (10), 760–764. doi:10.1253/jcj.64.760

Kikinis, R., Pieper, S. D., and Vosburgh, K. G. (2014). 3D Slicer: a Platform for Subject-specific Image Analysis, Visualization, and Clinical Support. Intraoperative Imaging and Image-Guided Therapy. *Springer*, 277–289. doi:10.1007/978-1-4614-7657-3_19

Liu, D., Fan, Z., Li, Y., Zhang, N., Sun, Z., An, J., et al. (2018). Quantitative Study of Abdominal Blood Flow Patterns in Patients with Aortic Dissection by 4-dimensional Flow MRI. *Sci. Rep.* 8 (1), 9111–9118. doi:10.1038/s41598-018-27249-9

Markl, M., Schnell, S., Wu, C., Bollache, E., Jarvis, K., Barker, A. J., et al. (2016). Advanced Flow MRI: Emerging Techniques and Applications. *Clin. Radiol.* 71 (8), 779–795. doi:10.1016/j.crad.2016.01.011

Melissano, G., Bertoglio, L., Rinaldi, E., Civilini, E., Tshomba, Y., Kahlberg, A., et al. (2012). Volume Changes in Aortic True and False Lumen after the "PETTICOAT" Procedure for Type B Aortic Dissection. *J. Vasc. Surg.* 55 (3), 641–651. doi:10.1016/j.jvs.2011.10.025

Müller-Eschner, M., Rengier, F., Partovi, S., Unterhinninghofen, R., Böckler, D., Ley, S., et al. (2011). Tridirectional Phase-Contrast Magnetic Resonance Velocity Mapping Depicts Severe Hemodynamic Alterations in a Patient with Aortic Dissection Type Stanford B. *J. Vasc. Surg.* 54 (2), 559–562. doi:10.1016/j.jvs.2011.02.017

Nett, E. J., Johnson, K. M., Frydrychowicz, A., Del Rio, A. M., Schrauben, E., Francois, C. J., et al. (2012). Four-dimensional Phase Contrast MRI with Accelerated Dual Velocity Encoding. *J. Magn. Reson. Imaging* 35 (6), 1462–1471. doi:10.1002/jmri.23588

Nienaber, C. A., Clough, R. E., Sakalihasan, N., Suzuki, T., Gibbs, R., Mussa, F., et al. (2016). Aortic Dissection. *Nat. Rev. Dis. Primers* 2 (1), 1–18. doi:10.1038/nrdp.2016.71

Nienaber, C. A., Kische, S., Rousseau, H., Eggebrecht, H., Rehders, T. C., Kundt, G., et al. (2013). Endovascular Repair of Type B Aortic Dissection. *Circ. Cardiovasc. Interv.* 6 (4), 407–416. doi:10.1161/circinterventions.113.000463

Oikonomou, K., Kopp, R., Katsargyris, A., Pfister, K., Verhoeven, E. L., and Kasprzak, P. (2014). Outcomes of Fenestrated/branched Endografting in post-dissection Thoracoabdominal Aortic Aneurysms. *Eur. J. Vasc. Endovascular Surg.* 48 (6), 641–648. doi:10.1016/j.ejvs.2014.07.005

Pellenc, Q., Roussel, A., De Blic, R., Girault, A., Cerceau, P., Ben Abdallah, I., et al. (2019). False Lumen Embolization in Chronic Aortic Dissection Promotes Thoracic Aortic Remodeling at Midterm Follow-Up. *J. Vasc. Surg.* 70 (3), 710–717. doi:10.1016/j.jvs.2018.11.038

Piatti, F., Sturla, F., Bissell, M. M., Pirola, S., Lombardi, M., Nesteruk, I., et al. (2017). 4D Flow Analysis of BAV-Related Fluid-Dynamic Alterations: Evidences of wall Shear Stress Alterations in Absence of Clinically-Relevant Aortic Anatomical Remodeling. *Front. Physiol.* 8, 441. doi:10.3389/fphys.2017.00441

Pirola, S., Guo, B., Menichini, C., Saitta, S., Fu, W., Dong, Z., et al. (2019). 4-D Flow MRI-Based Computational Analysis of Blood Flow in Patient-specific Aortic Dissection. *IEEE Trans. Biomed. Eng.* 66 (12), 3411–3419. doi:10.1109/tbme.2019.2904885

Riambau, V., Böckler, D., Brunkwall, J., Cao, P., Chiesa, R., Coppi, G., et al. (2017). Editor's Choice - Management of Descending Thoracic Aorta Diseases. *Eur. J. Vasc. Endovascular Surg.* 53 (1), 4–52. doi:10.1016/j.ejvs.2016.06.005

Saitta, S., Pirola, S., Piatti, F., Votta, E., Lucherini, F., Pluchinotta, F., et al. (2019). Evaluation of 4D Flow MRI-Based Non-invasive Pressure Assessment in Aortic Coarctations. *J. Biomech.* 94, 13–21. doi:10.1016/j.jbiomech.2019.07.004

Soulat, G., McCarthy, P., and Markl, M. (2020). 4D Flow with MRI. *Annu. Rev. Biomed. Eng.* 22, 103–126. doi:10.1146/annurev-bioeng-100219-110055

Sueyoshi, E., Sakamoto, I., Hayashi, K., Yamaguchi, T., and Imada, T. (2004). Growth Rate of Aortic Diameter in Patients with Type B Aortic Dissection during the Chronic Phase. *Circulation* 110 (11_Suppl. l_1), II–256. doi:10.1161/01.cir.0000138386.48852.b6

Takei, Y., Itatani, K., Miyazaki, S., Shibasaki, I., and Fukuda, H. (2019). Four-dimensional Flow Magnetic Resonance Imaging Analysis before and after Thoracic Endovascular Aortic Repair of Chronic Type B Aortic Dissection. *Interactive Cardiovasc. Thorac. Surg.* 28 (3), 413–420. doi:10.1093/icvts/ivy271

Tsai, T. T., Evangelista, A., Nienaber, C. A., Myrmel, T., Meinhardt, G., Cooper, J. V., et al. (2007). Partial Thrombosis of the False Lumen in Patients with Acute Type B Aortic Dissection. *N. Engl. J. Med.* 357 (4), 349–359. doi:10.1056/nejmoa063232

Xu, H., Li, Z., Dong, H., Zhang, Y., Wei, J., Watton, P. N., et al. (2017). Hemodynamic Parameters that May Predict False-Lumen Growth in Type-B Aortic Dissection after Endovascular Repair: A Preliminary Study on Long-Term Multiple Follow-Ups. *Med. Eng. Phys.* 50, 12–21. doi:10.1016/j.medengphy.2017.08.011

Youssefi, P., Sharma, R., Figueroa, C. A., and Jahangiri, M. (2017). Functional Assessment of Thoracic Aortic Aneurysms - the Future of Risk Prediction. *Br. Med. Bull.* 121 (1), 61–71. doi:10.1093/bmb/ldw049

Zilber, Z. A., Boddu, A., Malaisrie, S. C., Hoel, A. W., Mehta, C. K., Vassallo, P., et al. (2021). Noninvasive Morphologic and Hemodynamic Evaluation of Type B Aortic Dissection: State of the Art and Future Perspectives. *Radiol. Cardiothorac. Imaging* 3 (3), e200456. doi:10.1148/ryct.2021200456

Conflict of Interest: The authors declare that the research was conducted in the absence of any commercial or financial relationships that could be construed as a potential conflict of interest.

Publisher's Note: All claims expressed in this article are solely those of the authors and do not necessarily represent those of their affiliated organizations, or those of the publisher, the editors and the reviewers. Any product that may be evaluated in this article, orclaim that may be made by its manufacturer, is not guaranteed or endorsed by the publisher.

frontiers in Bioengineering and Biotechnology

ORIGINAL RESEARCH
published: 18 October 2021
doi: 10.3389/fbioe.2021.750656

High Wall Shear Stress can Predict Wall Degradation in Ascending Aortic Aneurysms: An Integrated Biomechanics Study

M. Yousuf Salmasi[1†], Selene Pirola[2†], Sumesh Sasidharan[3], Serena M. Fisichella[2,4], Alberto Redaelli[4], Omar A. Jarral[1], Declan P. O'Regan[5], Aung Ye Oo[6], James E. Moore Jr[3], Xiao Yun Xu[2] and Thanos Athanasiou[1]*

[1]Department of Surgery and Cancer, Imperial College London, London, United Kingdom, [2]Department of Chemical Engineering, Imperial College London, London, United Kingdom, [3]Department of Bioengineering, Imperial College London, London, United Kingdom, [4]Politecnico di Milano, Milan, Italy, [5]MRC London Institute of Medical Sciences, Imperial College London, London, United Kingdom, [6]Barts Heart Centre, London, United Kingdom

OPEN ACCESS

Edited by:
Jolanda Wentzel,
Erasmus Medical Center, Netherlands

Reviewed by:
Natalya Kizilova,
Warsaw University of Technology, Poland
Harvey Ho,
The University of Auckland, New Zealand

***Correspondence:**
M. Yousuf Salmasi
y.salmasi@imperial.ac.uk

[†]These authors have contributed equally to this work and share first authorship

Specialty section:
This article was submitted to Biomechanics, a section of the journal Frontiers in Bioengineering and Biotechnology

Received: 30 July 2021
Accepted: 24 September 2021
Published: 18 October 2021

Citation:
Salmasi MY, Pirola S, Sasidharan S, Fisichella SM, Redaelli A, Jarral OA, O'Regan DP, Oo AY, Moore JE, Xu XY and Athanasiou T (2021) High Wall Shear Stress can Predict Wall Degradation in Ascending Aortic Aneurysms: An Integrated Biomechanics Study. Front. Bioeng. Biotechnol. 9:750656. doi: 10.3389/fbioe.2021.750656

Background: Blood flow patterns can alter material properties of ascending thoracic aortic aneurysms (ATAA) via vascular wall remodeling. This study examines the relationship between wall shear stress (WSS) obtained from image-based computational modelling with tissue-derived mechanical and microstructural properties of the ATAA wall using segmental analysis.

Methods: Ten patients undergoing surgery for ATAA were recruited. Exclusions: bicuspid aortopathy, connective tissue disease. All patients had pre-operative 4-dimensional flow magnetic resonance imaging (4D-MRI), allowing for patient-specific computational fluid dynamics (CFD) analysis and anatomically precise WSS mapping of ATAA regions (6–12 segments per patient). ATAA samples were obtained from surgery and subjected to region-specific tensile and peel testing (matched to WSS segments). Computational pathology was used to characterize elastin/collagen abundance and smooth muscle cell (SMC) count.

Results: Elevated values of WSS were predictive of: reduced wall thickness [coef –0.0489, 95% CI (–0.0905, –0.00727), p = 0.022] and dissection energy function (longitudinal) [–15,0, 95% CI (–33.00, –2.98), p = 0.048]. High WSS values also predicted higher ultimate tensile strength [coef 0.136, 95% CI (0 0.001, 0.270), p = 0.048]. Additionally, elevated WSS also predicted a reduction in elastin levels [coef –0.276, 95% (CI –0.531, –0.020), p = 0.035] and lower SMC count ([oef –6.19, 95% CI (–11.41, –0.98), p = 0.021]. WSS was found to have no effect on collagen abundance or circumferential mechanical properties.

Conclusions: Our study suggests an association between elevated WSS values and aortic wall degradation in ATAA disease. Further studies might help identify threshold values to predict acute aortic events.

Keywords: aortic surgery, aneurysm, computational fluid dynamics, CFD, magnetic resonance imaging, wall shear stress, computational pathology, vascular biomechanics

INTRODUCTION

Ascending thoracic aortic aneurysm (ATAA) is a permanent and irreversible dilatation of the thoracic aorta. Many patients remain asymptomatic until acute presentation with rupture or dissection (AD), which is associated with a 50% early mortality rate (Howard et al., 2013). Death from aortic aneurysm-related emergencies occurs at a rate of 2.4/100,000, and is one of the most common causes of death amongst conditions requiring emergency surgery in high-income countries (Stewart et al., 2014). Survivors of acute events often need repeat intervention and have high rates of stroke and renal failure. This has a huge impact on their quality-of-life, and carries significant societal burden (Tsai et al., 2006).

The evolution in our understanding of the disease from large observational studies has led to the reliance on ATAA diameter as the primary predictor of future AD. Intervention is recommended in patients who have a maximal aortic diameter ≥55 mm, with lower thresholds (≥50 mm) for those with bicuspid aortic valves (BAV) or connective tissue disease (Hiratzka et al., 2010; Erbel et al., 2014). Interventions in ATAA can be complex and not without risk, involving open surgery (particularly for ascending and arch aneurysms), endovascular stenting, or a combination of both. This drives the need for an accurate prognostic prediction prior to subjecting patients to treatment that involves moderate risk. However, isolated ATAA diameter measurements are inadequate predictors of acute aortic events. International registry data (>4,400 dissection patients) has highlighted that 40% of dissections occur below 50 mm (and up to 60% below 55 mm) (Pape et al., 2007). In this light, clinicians at present are unable to accurately predict the prognosis of enlarged thoracic aortas from routine imaging. Indeed, diameter alone fails to take into account local flow patterns, aortic wall stresses, mechanical properties and wall thickness. A patient specific approach is required.

Despite having the potential to predict disease progression, biomechanical assessment of the aorta remains experimental with limited translation into clinical practice. Biomechanically, AD occurs when haemodynamic forces exceed the aortic wall strength leading to intimal tear and false lumen propagation. It is possible that long-term exposure to certain blood flow patterns lead to changes in aortic wall structure (i.e., remodeling) that predispose wall degradation and a higher risk of AD. The identification of which flow patterns correlate with changes in aortic wall structure might lead to a more rational and useful patient-specific predictor (Geiger et al., 2012; Condemi et al., 2017; Piatti et al., 2017; Bollache et al., 2018).

The degradation of extracellular matrix (ECM) structures in ATAA is well reported. Methods to quantify degeneration center around computational histology techniques to characterize microstructural elements, such as elastin and collagen. Studies employing these methods have linked abnormal WSS patterns to disruption of the aortic microarchitecture (Guzzardi et al., 2015; Bollache et al., 2018). However, studies that use flow-to-tissue spatial registration (that incorporate the whole aneurysm) have been limited.

This study aims to explore the relationship between haemodynamic parameters, material properties and composition of the aortic wall in ATAA using whole aneurysm samples, with a view to assess the predictive ability of flow on aortic wall degeneration. We hypothesize elevated WSS in ATAAs is associated with accelerated degenerative disease.

MATERIALS AND METHODS

The study was ethically approved (17/NI/0160) by the Health Research Authority (HRA) in the United Kingdom and was sponsored by the Imperial College London Joint Research and Compliance Office, as defined under the sponsorship requirements of the Research Governance Framework (2005). The study was designed as a cohort study during the years 2018-2020, incorporating computational flow analysis, *in-vitro* vascular wall mechanical testing and microstructural quantification. Patients and public were involved in the design, conduct, reporting, and dissemination plans of our research via the London Aortic Mechanobiology Working Group.

Study Population

A total of 10 patients undergoing proximal aortic surgery (either aortic root, ascending aorta, proximal arch replacements, or a combination of these) were recruited into this cohort study. The main exclusion criteria were: connective tissue disease (i.e. Marfans, Ehler-Danlos, Loeys-Dietz), bicuspid aortic valve and redo-aortic surgery. Patient characteristics were ascertained from clinic letters and pre-operative echocardiography. Recruited patients provided informed consent for participation in the study, which involved the additional MR imaging and provision of tissue sample from surgery.

MRI Acquisition

Patients were scheduled to undergo cardiac gated magnetic resonance imaging (MRI) scanning at a time point prior to surgery (range 1–90 days) using a 3T MRI scanner (Siemens Healthcare, Erlangen, Germany). The addition of a time-resolved 3-dimensional sequence (4D-flow) visualized and measured temporal changes and flow-patterns throughout the whole volume of the thoracic aorta.

Aneurysm Tissue Characterization

Patient-matched aneurysm specimens were obtained *en-bloc* and acquired immediately after surgical excision in the operating theatre. Rectangular or dog-bone shaped subsections aligned in either the longitudinal or circumferential direction were punched out at specific locations (**Figure 1A**) and assessed for tensile mechanical properties, peel strength and strain inhomogeneities (Olchanyi et al., 2020). In particular, for each patient, the aneurysm region was unfolded at the outer wall and subdivided into up to six (depending on the size of the collected sample) circumferential anatomical regions to the right (R1, R2, R3) and left (L1, L2, L3) of the midline (**Figure 1B**). These were further divided into upper and lower regions, giving 6 to 12 segments in total per patient (**Figure 1B**). These segments were

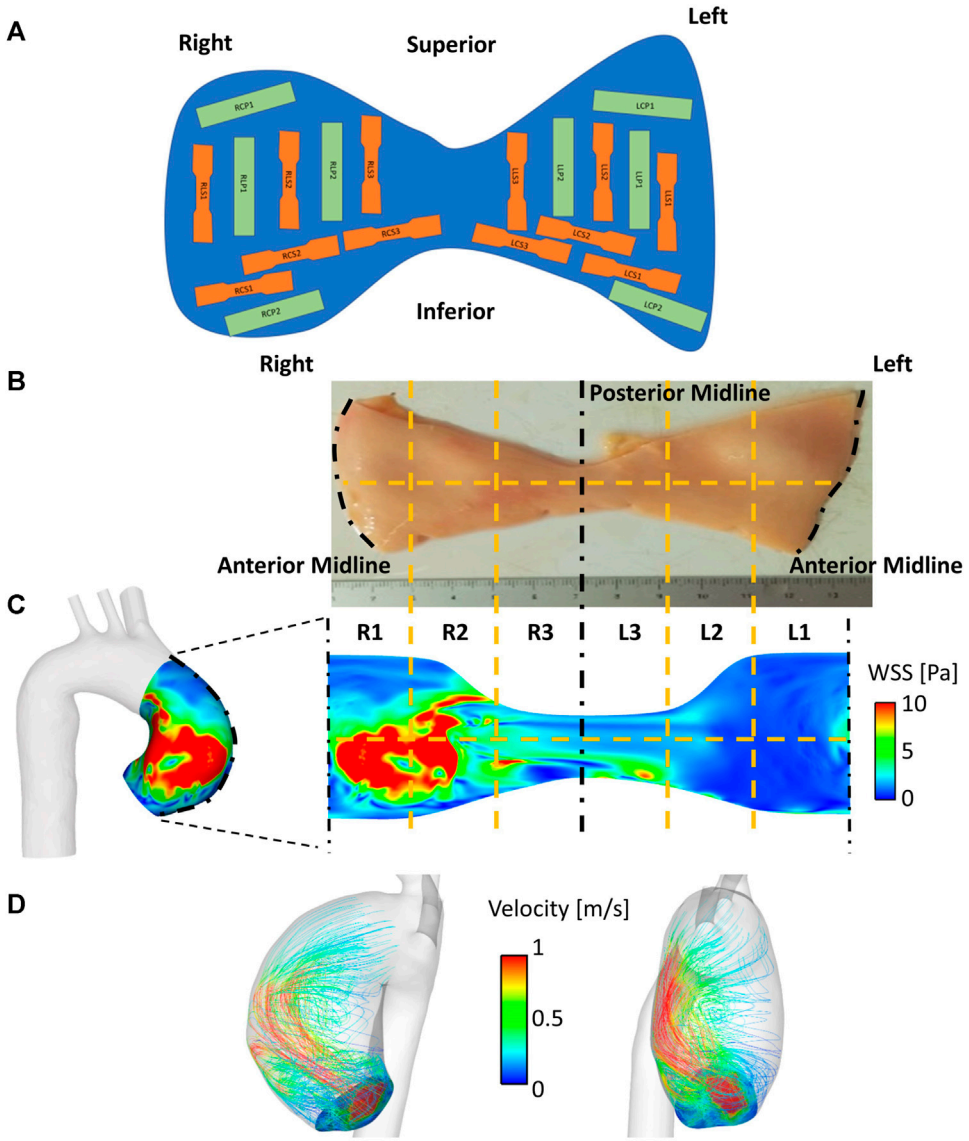

FIGURE 1 | Matching flow to material properties. **(A)** Reference map used for collection of samples throughout the whole aortic specimen. Segments are classified using alphanumeric codes in which the first letter and number denote the position (R = right, L = left), the second letter denotes the sample orientation (C = circumferential, L = longitudinal), the third letter denotes the sample type (S = dogbone, P = rectangular) **(B–C)** WSS mapping on to aneurysmal wall surface, which is unraveled by division along the anterior. This is subdivided into six circumferential regions (R1-R3, L1-L3), with a horizontal dividing line (12 segments total). **(D)** Streamlines demonstrating haemodynamic flow derived from CFD within an anatomically (patient-specific) segmented aortic wall.

matched to the 6–12 segmental regions undergoing computational WSS mapping (Section 2.4; **Figure 1C**), using the anterior midline (widest region of the aneurysm region in the vertical plane) as the common frame of reference. Whole-aneurysm tissue specimens underwent thickness mapping (~0.01 µm resolution using a bench top device - Litematic VL-50-B Mitutoyo Ltd.).

Sharp stencils were used to create 20 mm × 5 mm dogbone samples (for uniaxial testing). The dogbone shaped tissue provided larger shoulders for easier gripping, whereas the narrower gauge section in the center provided a smaller cross-sectional area for a focused region of deformation and failure. The samples for peel testing required a different shape: the width of the peeling sample needed to be kept constant throughout the peeling arc. As such rectangular stencils were used (5 mm × 20 mm) to obtain eight further samples from both halves of the aneurysm specimen (both circumferential and longitudinal) –these would be used for peel testing.

Uniaxial tensile tests were performed on all dog-bone shaped subsections using a Test Resources R-Series Controller with a 44 N load cell. All tests were conducted in an environmental chamber containing phosphate buffered saline (PBS), maintained at 37°C. Tensile force-elongation data were used to provide estimations of region specific ultimate tensile strength (UTS)

and maximum tangential stiffness (MTS) as described by previous groups (Vorp et al., 2003). Peel testing allowed estimation of peel force (F_{peel}) and dissection energy function (DEF) for rectangular subsections.

Computational Fluid Dynamics (CFD)

Image-based CFD modelling was used to evaluate pre-operative aneurysmal WSS distribution in a patient-specific and region-specific fashion. To this aim, the 3D thoracic aortic geometry, including the arch branches, of each patient was reconstructed from MRI data (bright blood). Reconstructed geometries (**Figures 1C, D**) started upstream of the aneurysm, in the aortic root between mid-sinus and STJ levels, and ended distally, in the descending thoracic aorta at the level of the pulmonary artery.

Patient-specific geometries were discretized using unstructured meshes (**Supplementary Figure S1**) with a tetrahedral core and 10 prismatic layers at the walls. Local mesh refinements were prescribed at the aneurysm wall and arch branches. Mesh refinement in the region of interest (i.e. aneurysm wall) was guided by flow features observed from 4D flow MRI data (i.e. a finer mesh was designed where higher velocity gradients were observed). Sensitivity analyses were conducted to ensure mesh-independent results. Final meshes consisted of 5.5–16.6 million elements (Pirola et al., 2019).

For each patient, 3D subject-specific velocity profiles of the aortic valve were incorporated at the computational model inlet from 4D flow MR images (Armour et al., 2021). This therefore took into account the patient-to-patient variation in the ascending aorta hemodynamics which arise due to differences in left ventricular outflow tract and aortic valve anatomy (**Figure 1D**). Model outlets, located distal to the aneurysm, consisted of the descending aorta outlet and the arch branches. 3-element Windkessel model was applied at all outlets; model parameters were tuned using patient-specific central mean aortic pressure and blood flow rates evaluated using 4D flow MRI data (Pirola et al., 2017; 2019). Briefly, the total resistance (R_T) of the 3-element Windkessel model was calculated as $R_T = P_m/Q_m$ (Les et al., 2010). P_m is the mean central pressure of the patient, which was measured ~30 min before the MR scan using a BP Plus device (BP Plus, Uscom, Australia). Q_m is the mean flow through the outlet. This was evaluated using 4D flow MR images. The proximal resistance was evaluated as $R_1 = \rho c/A$ (Xiao et al., 2014, where ρ is the blood density, c is the pulse wave speed and A is the outlet cross-sectional area. The pulse wave speed was evaluated as $c = 13.3/(2r)^{0.3}$ Reymond et al. (2009)), where r is the outlet radius. The distal resistance was evaluated as $R_2 = R_T\text{-}R_1$ (LaDisa et al., 2011). Total vasculature compliance was calculated as $C = \tau/R_T$, where τ is the time-constant of the exponential diastolic pressure-fall (Xiao et al. (2014)). This was assumed equal to 1.79 and 1.92 s for normotensive and hypertensive subjects, respectively (Simon et al., 1979).

Simulations were run in ANSYS CFX (v 15.0). The aortic wall was assumed to be rigid with a no-slip condition. Blood was modelled as an incompressible Newtonian fluid, with a density of 1,060 kg m^{-3} and viscosity of $4{\cdot}10^{-3}$ Pa s. High-resolution advection scheme and second-order Backward Euler scheme were employed for spatial and temporal discretization of the Navier-Stokes equations, respectively. A fixed timestep of 10^{-3} s was used, and the maximum RMS residual was set to 10^{-5} as a convergence criterion. The shear stress transport transitional (SST-Tran) model was used to account for the transitional nature of the aortic flow (Tan et al., 2009), with a 1% turbulence level prescribed as the inlet boundary condition. The patient-specific central diastolic pressure was used as the initial condition. Simulations were run for the number of cycles necessary to achieve periodicity. The period of the cardiac cycle of each patient was recorded during 4D flow MR acquisition and stored in the image header. Periodicity was considered as achieved when differences in pulse pressure and pressure maxima between two consecutive heartbeats were less than 3 and 1%, respectively, at each model outlet. Results from the last cycle only were analyzed. Before proceeding with result analysis, for each patient, predicted blood flow features were checked against 4D flow MR acquired features.

Computational result postprocessing workflow was designed to coincide with tissue processing for mechanical and histological testing: for each patient, the aneurysm region was unfolded at the outer wall and subdivided into segments corresponding to the aortic aneurysm tissue segments used to characterize the material properties (**Figures 1B,C**). Results were analyzed in ANSYS EnSight.

The primary derived measurement from CFD analysis was the magnitude of the wall shear stress (WSS) vector. For each anatomical region, several WSS-derived parameters were evaluated. These are summarized in **Table 1**. Briefly, WSS values are reported as maxima in time (WSS_{max}, WSS_{mean}) and time-averaged ($TAWSS_{max}$, $TAWSS_{mean}$, WSS_{Max}^{Tmean}). *Mean* and max subscripts refer to spatial mean and maxima, respectively. *Tmean* superscript refers to temporal mean. The spatial mean value was calculated over each segment (R1, R2, R3, L1, L2, L3, upper and lower).

Computational Pathology

Full circumferential rings of tissue were obtained from the inferior border of the ATAA specimen (**Figure 2A**). Whole slide imaging was performed using a high-resolution digital optical system (Hamamatsu TM) and uploaded onto the digital processing software QuPath (https://qupath.github.io). Cross-sectional images of each ATAA ring were divided into six circumferential regions (**Figure 2B**), matching the right-to-left segments used in the CFD and mechanical analyses (**Figures 1B, C**). Using a pre-defined workflow (**Figure 2C**), microstructural density calculation of medial structural proteins was conducted, namely of elastin (from slides stained with Elastin Van Gieson) and collagen (slides stained with picrosirius red). Using the H&E stained slides (**Figure 2D**), the thresholding function was used to highlight the stained cells of the medial layer. Setting the range of particle size from 20 to 100 μm the total cell count was extracted and divided by the total area to obtain the density.

Statistical Analysis

Amongst the 10 recruited patients, a total of 371 ATAA anatomical samples had matched CFD, material properties and

TABLE 1 | Calculated wall shear stress (WSS) parameters from computational fluid dynamics (CFD) analysis.

Short name	Description	Formula
WSS_{max}	Maximum in time and space of the WSS magnitude	$\text{Time Max}(\text{Spatial Max}(\lvert WSS\rvert))$.
WSS_{mean}	Maximum in time of the spatial mean of the WSS magnitude	$\text{TimeMax}\left(\frac{\sum_{\lvert WSS\rvert_i \cdot A_i}}{\sum A_i}\right)$ Where i refers to the surface mesh element at the aortic wall and A_i is the area of the surface mesh element. The mean value was calculated over each sub-segment
WSS_{Max}^{Tmean}	Mean in time of the spatial maximum of the WSS magnitude	$\frac{\sum(\text{SpatialMax}(\lvert WSS\rvert))_j}{j}$ Where j is the number of time points
TAWSS	Time average of the magnitude of the WSS	$TAWSS = \frac{1}{T}\int_0^T \lvert WSS\rvert dt$
$TAWSS_{max}$	Spatial maximum of the TAWSS	$\text{SpatialMax}(TAWSS)$
$TAWSS_{mean}$	Spatial mean of the TAWSS	$\frac{\sum TAWSS_i \cdot A_i}{\sum A_i}$

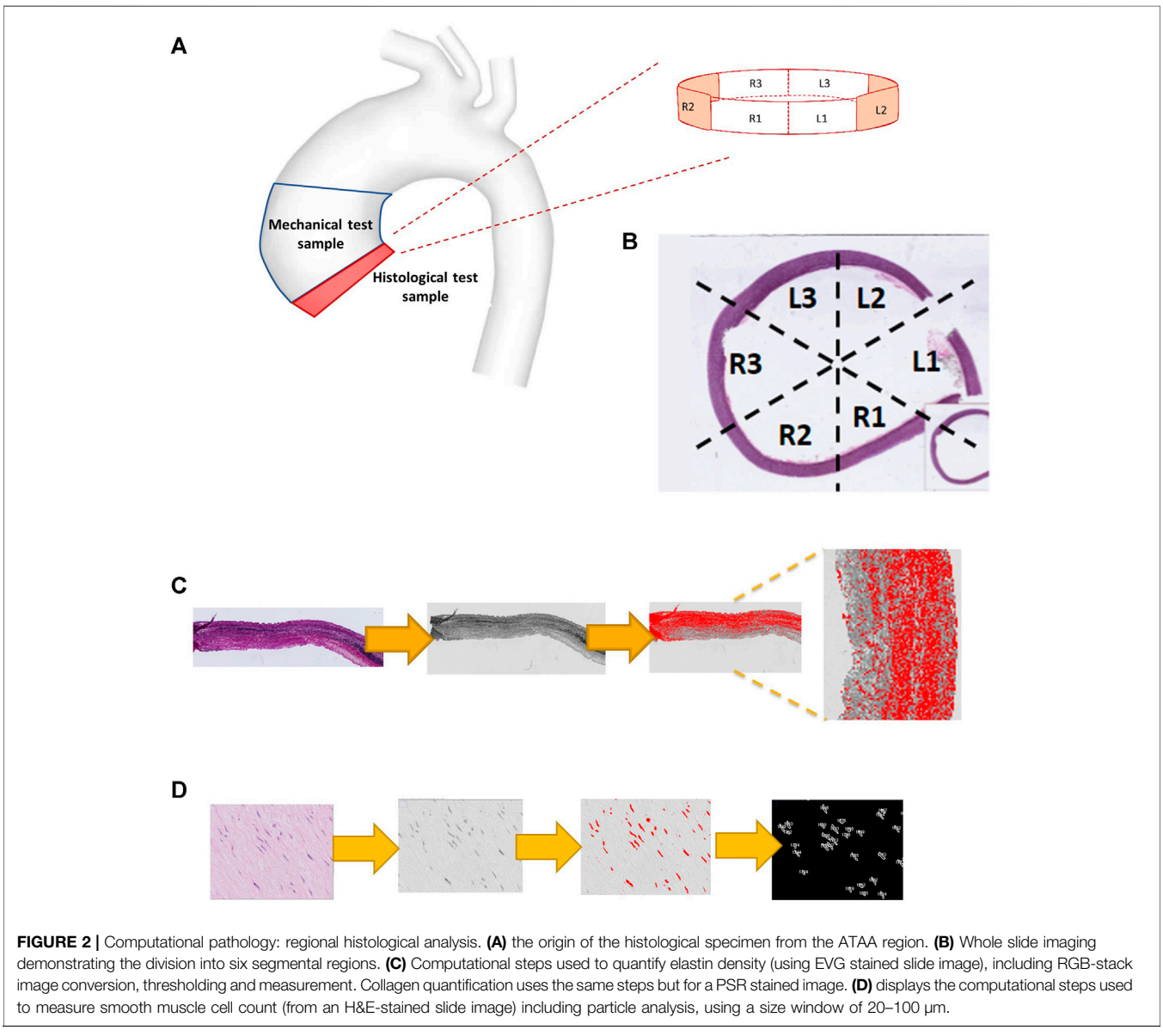

FIGURE 2 | Computational pathology: regional histological analysis. **(A)** the origin of the histological specimen from the ATAA region. **(B)** Whole slide imaging demonstrating the division into six segmental regions. **(C)** Computational steps used to quantify elastin density (using EVG stained slide image), including RGB-stack image conversion, thresholding and measurement. Collagen quantification uses the same steps but for a PSR stained image. **(D)** displays the computational steps used to measure smooth muscle cell count (from an H&E-stained slide image) including particle analysis, using a size window of 20–100 μm.

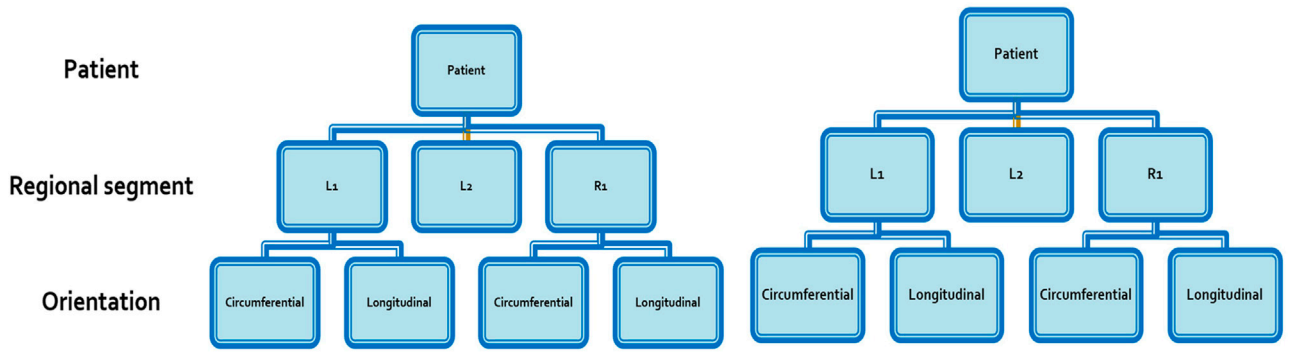

FIGURE 3 | Hierarchical structure of data arising from each aortic segment.

microstructural features, and were thus included in the analysis, being treated as separate data points. Of these samples, thickness was measured in 102 samples, 63 samples (29 longitudinal, 34 circumferential) were used for tensile testing, 63 samples (30 longitudinal, 33 circumferential) for peel testing, 143 for histological analyses (60, 35 and 48 for elastin, collagen and SMCs, respectively). All haemodynamic parameters were acquired as continuous variables, as were the histological and mechanical data. Where relevant, data were reported as means and standard deviations, being averaged across the whole patient cohort. All statistical analysis were conducted using STATA 13.0 (Stata Corp. College Station, TX, United States).

Univariable linear regression analysis was used to explore the effect of WSS on acquired material parameters (including mechanical and histological). These models tested the hypothesis of a flow-mediated degenerative process in the aortic wall giving rise to altered material properties. Results of regression analysis were reported as standardized beta-coefficients with 95% confidence intervals. The significance level was set at $\alpha = 0.05$. Values of longitudinal F_{peel}, longitudinal DEF, UTS and MTS were positively skewed; values of elastin abundance were negatively skewed. Therefore, logarithmic transformation with skewness correction was applied in STATA to these datasets.

Scatter plots and trendlines have been generated using Microsoft Excel, using $\log_{10}$ transformation for longitudinal DEF and UTS, and $\log_{10}$ (90-x) transformation for elastin abundance.

Multilevel Mixed Effects (Hierarchical) Linear Models

As the aortic segments arose from among 10 different subjects, multilevel mixed-effect linear regression models were further constructed to account for the hierarchical structure of the data points. The data arising from each aortic segment was nested into a clustered hierarchical structure using two levels in the model: 1) patient; and 2) orientation of the subsection (circumferential versus longitudinal) (**Figure 3**). Univariate regression was again carried out, assessing the effect of WSS separately on wall thickness, UTS, MTS and histological parameters. The significance level for all models was set at $\alpha = 0.05$.

RESULTS

Of the cohort of 10 patients, the majority were male (8/10), and of Caucasian ethnicity (8/10). Patient age was (mean ± standard deviation) 63.9years ±6.6 (**Table 2**). Whilst none had syndromic disease, 3 reported a family history of aortic disease. The mean aneurysm diameter was 54.7 mm ± 7.5. Three patients had root aneurysms, two patients had arch aneurysms, with the remaining patients having isolated ascending aorta aneurysms. All patients had good ventricular function (mean left ventricular ejection fraction 57.2% ± 9.0) with 3 patients suffering from severe aortic regurgitation. Maxima of jet velocity and area-averaged velocity at the model inlet were 1.86 ± 0.93 m/s and 0.51 ± 0.13 m/s (mean ± standard deviation), respectively.

WSS Distribution

The patient-specific TAWSS distribution maps for all 10 patients are shown in **Figure 4**. The R1 segment (outer right wall) was the region yielding the highest values of WSS (**Table 3**), including temporal maximum WSS values (WSS_{max} and WSS_{mean}) as well as time-averaged values ($TAWSS_{max}$ and $TAWSS_{mean}$). The highest value for WSS_{max} (24.98 ± 7.79 Pa) in the R1 region contrasted to the lowest value yielded from the inner curve (10.18 ± 4.14 Pa). When measuring the (peak in time) WSS averaged over space (WSS_{mean}), the R1 region still yielded the highest value (11.68 ± 6.42 Pa). For $TAWSS_{max}$, R1, also the region of highest WSS values, was 4.85Pa ± 2.07, compared to the inner curve (2.67 ± 0.81 Pa). This indicated that as well as the asymmetric peak flow patterns reached in systole acting on the potentially fragile intima in ATAA, the sustained stress over the cardiac cycle, as displayed by the TAWSS, was also asymmetrical and affecting the outer curve more intensely.

Comparing WSS With Aortic Material Properties

In order to test the hypothesis of flow mediated wall degeneration, WSS was compared with material properties of the aortic wall. Statistically significant linear regression analysis results are summarized in **Table 4**. Scatter plots and trendlines showing

TABLE 2 | Summary of clinical covariates for recruited patients. AR = aortic regurgitation.

Covariate	Mean ± standard deviation	Covariate	N/10
Age (years)	63.9 ± 6.6	Female	2
		Peripheral vascular disease	2
Height (cm)	174.5 ± 12.5	Arch aneurysm	2
Weight (Kg)	84.7 ± 27.4	Root aneurysm	3
Body mass index (kg m^{-2})	27.2 ± 5.7	Severe AR	3
Body surface area (m^2)	1.99 ± 0.27	—	—
		Smoking (current or ex-)	3
Left ventricular ejection fraction (%)	57.2 ± 9.0	Caucasian ethnicity	8
Mean arterial pressure (mmHg)	105.3 ± 19.3	Relevant family history	3
		Hypertension	4
Pulse wave velocity (m/s)	5.8 ± 0.7	Diabetes	0
Max aneurysm diameter (mm)	54.7 ± 7.5	Chronic airway disease	2

the relationship between WSS and aortic wall material properties are shown in **Figure 5**.

Wall Thickness

The data on measured wall thickness was normally distributed. Linear regression analysis was conducted which showed a statistically significant influence ($p < 0.05$) of $TAWSS_{max}$ and WSS_{Max}^{Tmean} parameters on wall thickness (**Table 4**). These yielded negative coefficients of variance, indicating that higher WSS values are associated with aortic wall thinning (**Table 4**; **Figures 5A,B**).

Peeling Properties

Peeling force (F_{peel}) and dissection energy function (DEF) (as measured from tissue mechanical testing) provide a surrogate for the likelihood of dissection (i.e. separation of the medial layers) per region of interest. These were obtained from ATAA specimens in both the circumferential and longitudinal directions. Regression analysis (**Table 4**) comparing log transformed DEF values in the longitudinal orientation (DEF_{long}) with $TAWSS_{Mean}$ yielded a statistically significant relationship [coef −0.211, 95% CI (−0.427, −0.062), $p = 0.048$]. This relationship displayed a negative coefficient result: higher WSS values were associated with lower DEF_{long} values (as can also be observed in **Figure 5C**). In contrast, in the circumferential direction F_{peel} and DEF values showed an opposite trend, with higher values corresponding to higher WSS. However, results for F_{peel} (both longitudinal and circumferential) and circumferential DEF were not statistically significant.

Tensile Properties: Ultimate Tensile Strength (UTS) and Maximum Tangential Stiffness (MTS)

The comparison of log-transformed UTS data to $TAWSS_{max}$ revealed a statistically significant positive correlation (coef 0.136, 95% CI [0 0.001, 0.270], $p = 0.048$) (**Table 4**; **Figure 5D**). A comparison of log-transformed MTS data to WSS revealed a nonsignificant trend toward higher values of WSS leading to stiffer aortic tissue (coef 0.120, 95% CI [-0.009, 0.248], $p = 0.068$). Comparisons to other WSS measures failed to show statistical significance. These results together suggest that high WSS leads to stiffer aortic tissue with higher tensile strength, but the statistical significance is marginal.

Microstructural Features

Elastin abundance was found to be lower in areas with higher $TAWSS_{Max}$ [coef −0.276, 95% CI (−0.531, −0.020), $p = 0.035$] (**Table 4**; **Figure 5E**). An opposing, but statistically insignificant, trend was found for collagen abundance, i.e., higher TAWSS showed some association with areas of high collagen content. Higher WSS levels were also associated with lower counts of SMCs [$TAWSS_{Max}$: coef −6.19, 95% CI (−11.41, −0.98), $p = 0.021$; WSS_{Max}^{Tmean}: coef −5.87, 95% CI (−10.12, −1.62), $p = 0.008$] (**Table 4** and **Figures 5F,G**).

Multi-Level Mixed Effects Regression

Significant results of multilevel mixed-effects linear models are reported in **Tables 5**, **6**.

Tissue Thickness

The fixed effects part of the model (i.e. the effect of $TAWSS_{Max}$ on tissue thickness) was found to be non-significant (coef -0.016, 95% CI [-0.063, 0.031], $p = 0.496$) (**Table 5**). Thus, despite the linear relationship observed earlier between WSS and thickness, the data variance evident at the patient level remains significant.

Mechanical Properties: MTS and UTS.

In the case of UTS, the results trended towards a higher UTS in response to higher WSS, although this relationship was non-significant ($p = 0.08$). There was no evidence of influence of the patient or aortic tissue orientation on the WSS-UTS relationship. $TAWSS_{max}$ was found to have no significant influence on MTS ($p = 0.115$).

Microstructural Features: SMC Count

$TAWSS_{max}$ was found to have a persistently negative influence on SMC count [coef −4.87, 95% CI (−9.26, −0.48), $p = 0.030$]. The multi-level model found WSS_{Max}^{Tmean} to be a stronger fit to the SMC count data than patient variance (**Table 6**). Multi-level mixed effects regression however found no significant association between the evaluated WSS parameters and elastin/collagen.

DISCUSSION

Computational modelling of thoracic aortic disease has expanded the repertoire of aneurysm diagnostics in recent years. Whilst

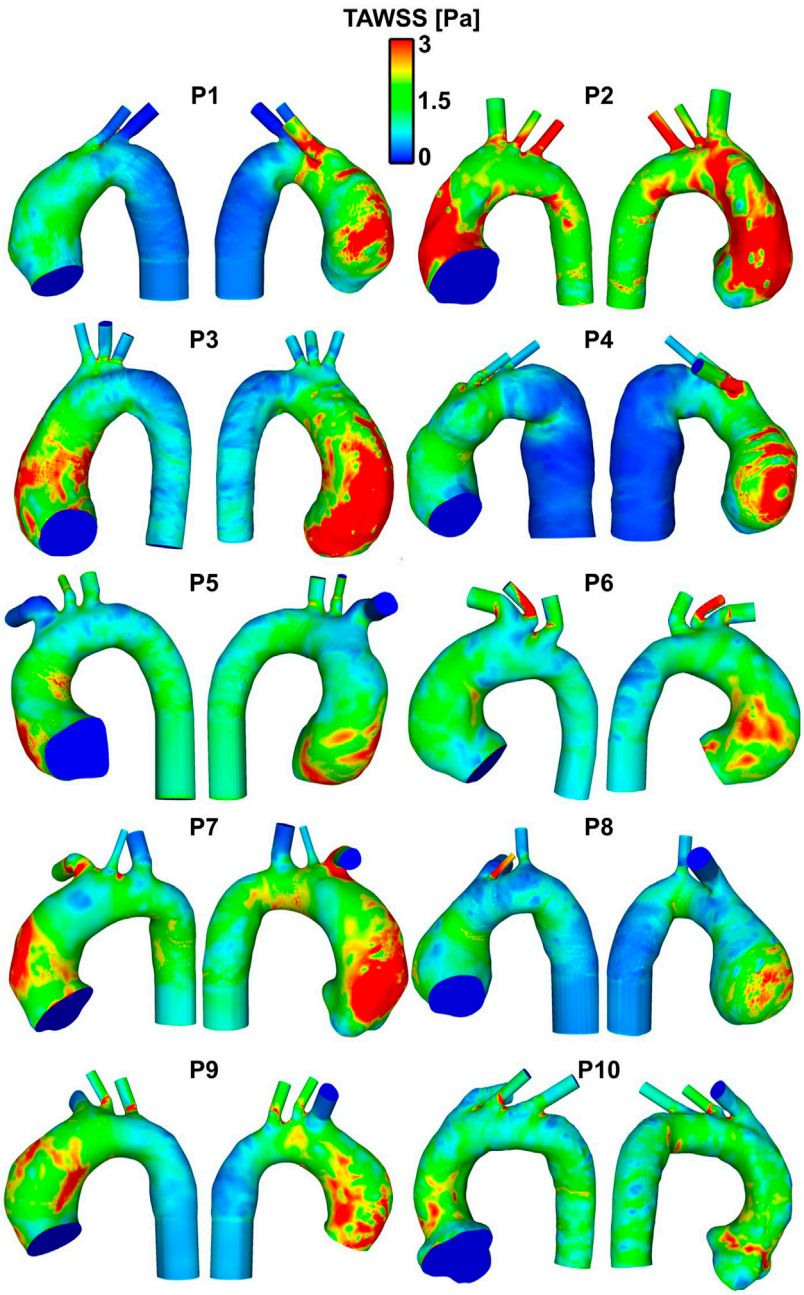

FIGURE 4 | Patient-specific TAWSS distribution maps in the ten patients with ATAA. Regions in red indicate TAWSS >3 Pa, which, on gross inspection, are localized to the aneurysmal aorta, and particularly to the outer curve.

several *in vivo* parameters related to aortic wall mechanics can be obtained from such models, their association with aortic wall mechanobiology, and in the pathogenesis of ATAA remains poorly understood. Further developments in this field may allow disease severity, progression, and acute events to be predicted at an individual patient level. This is required as isolated size measurements of the aorta are inadequate (Pape et al., 2007). Existing studies have associated abnormal WSS in the ATAA with aneurysm growth and wall degeneration (Geiger et al., 2012; Guzzardi et al., 2015; Condemi et al., 2017; Bollache et al., 2018). This study builds on such work, utilizing state of the art imaging, modelling, and biomechanical methods. However, because of the availability of pathologic human aortic specimens and the ability to assess their local properties, we made a more concerted effort to divide the aortic anatomy into finer areas for analysis, specifically including up to six regions circumferentially and a further upper and lower division (up to 12 in total).

TABLE 3 | Mean wall shear stress (WSS) parameters (±standard deviation) in anatomical regions around the aneurysm (averaged over 10 patients). All values are in Pascals (Pa).

	—	TAWSS $_{max}$	TAWSS $_{mean}$	WSS $_{max}$	WSS $_{mean}$
Lower	L1	4.15±1.30	2.29±0.99	22.31±5.05	8.49±4.17
	L2	3.12±1.37	1.71±0.74	16.03±6.66	5.69±3.33
	L3	3.06±1.28	1.83±0.87	13.95±8.08	6.22±4.12
Upper	L1	4.23±1.61	2.58±1.07	22.72±9.66	9.86±6.52
	L2	3.33±1.90	1.85±0.83	17.59±10.82	6.45±4.07
	L3	2.67±0.81	1.77±0.54	10.18±4.14	5.16±2.61
Lower	R1	4.85±2.07	2.60±1.03	24.98±7.79	10.11±4.90
	R2	4.63±2.21	2.23±0.87	23.73±11.47	8.51±5.04
	R3	3.04±1.07	1.56±0.38	14.51±7.54	4.27±1.69
Upper	R1	4.84±2.20	2.48±1.11	24.88±12.56	11.68±6.42
	R2	3.75±1.50	2.00±0.48	18.87±8.69	6.82±3.14
	R3	2.60±0.35	1.77±0.29	12.99±7.21	4.65±1.46

Elevated WSS on the Outer Curve

The WSS distribution in the ascending aorta is dominated by the curvature of the aortic arch, which forces blood emanating from the heart to change its direction. Fluid at the centre of the vessel is more difficult to displace as it is travelling at a higher velocity compared to that closer to the wall, so it is displaced to a greater degree (Caballero et al., 2013). Thus, blood is skewed towards the outer curvature of the bend.

Our findings agree with several previous studies assessing flow in ATAA, which also noted the highest WSS on the outer curve (Bieging et al., 2011; Bürk et al., 2012; Van Ooij et al., 2015).

WSS and Wall Thickness

Owing to the low temporo-spatial resolution of cross-sectional imaging and difficulty in tracking the motion of the aortic wall (<2.5 mm thickness), estimations of stress distribution within the aneurysm wall are reliant on important assumptions of aortic wall thickness (commonly assumed to be constant) and material properties (commonly not patient- or even disease-specific) (Martin et al., 2015; Gomez et al., 2020). Our results have identified a potential link between areas of high WSS and aortic wall thinning. Reduced wall thickness in areas of high WSS has been previously shown in femoral artery bifurcation by Kornet et al. (1999), who explained this finding with the link between low WSS, increased influx of substances into the aortic wall (through an increase in blood residence time) and increased release of vasoactive molecules potentially causing thickness increase of the intima-media layer.

These results represents a step towards the incorporation of wall thickness inferences from baseline imaging that can be incorporated into fluid-structure interaction models and estimations of wall stress distribution. These results also help to strengthen the flow-mediated degeneration hypothesis, whereby persistently elevated WSS throughout the cardiac cycle exposes mechanocytes within the aortic wall to prolonged stimuli and downstream potentially maladaptive remodeling (Humphrey et al., 2015). However, the conducted hierarchical analysis also suggests that data variance at the patient level remains significant.

WSS and Aortic Wall Mechanical Properties

Our analyses on the effect of WSS on wall mechanical properties produced two main findings. Firstly, higher WSS was associated with a reduced DEF in the longitudinal direction. This contrasted with circumferential DEF, which showed an insignificant increasing trend. This further exemplifies the anisotropic nature of the aortic wall and suggests that it extends to influence both tear direction and location in aneurysm dissection (Manopoulos et al., 2018). Secondly, the aortic wall had significantly higher values for UTS with higher WSS, indicating a reduced likelihood for wall rupture in response to elevated WSS. In addition, the aorta might be stiffer in response to high WSS, as suggested by elevated values for MTS. This result, however, was not statistically significant.

WSS and Microstructural Features: Implications for Mechanobiology

Higher WSS levels were found to be associated with a reduction in both elastin abundance and smooth muscle cell (SMC) count. Loss of elastin integrity and relative increase in collagen describes the reduced compliance and increased stiffness of the aorta seen in ageing (Wagenseil et al., 2009). Studies have shown that global increases in vascular structural stiffness reflect increased central pulse pressures and pulse wave velocities (Lacolley et al., 2009; Safar et al., 2010) that pathologically increase proximal aortic loading. Collagen deposition in many cases of ATAA has been observed to be higher, reflecting the compensatory fibrotic changes as a result of the disease process (Wågsäter et al., 2013; Meng et al., 2014). The microstructural response to elevated WSS therefore explains these changes (Humphrey et al., 2015), and describes the resulting aortic wall stiffness

TABLE 4 | Linear regression analysis: comparison of measurements of WSS per ATAA segment and tissue-derived parameters of corresponding segment from patient-specific excised tissue. circ = circumferential, long = longitudinal, SMC = smooth muscle cell. All results are statistically significant (p-value < 0.05).

Tissue measurement	WSS parameter	Coef	Standard error	95% CI	p-value
Tissue thickness	$TAWSS_{Max}$	–0.0489	0.0209	–0.090–0.007	0.022
	WSS_{Max}^{Tmean}	–0.0421	0.0187	–0.079–0.005	0.026
Log dissection energy function (long)	$TAWSS_{Mean}$	–0.211	0.106	–0.427–0.062	0.048
Log Ultimate tensile strength	$TAWSS_{Max}$	0.136	0.067	0 0.001–0.270	0.048
Log Elastin abundance	$TAWSS_{Max}$	–0.276	0.128	–0.531–0.020	0.035
SMC count	$TAWSS_{Max}$	–6.19	2.59	–11.41–0.98	0.021
	WSS_{Max}^{Tmean}	–5.87	2.11	–10.12–1.62	0.008

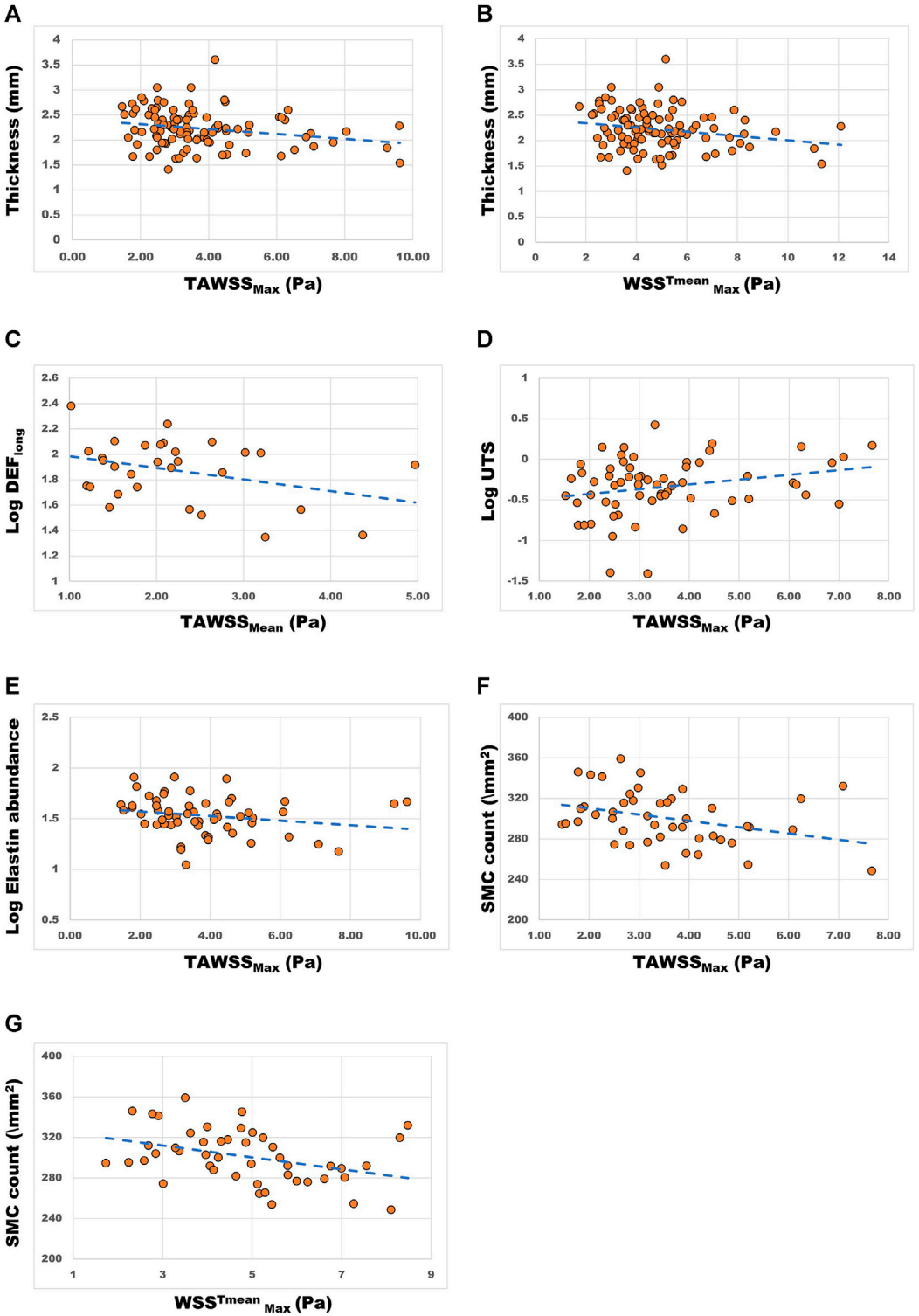

FIGURE 5 | Scatter plots and trendlines demonstrating the relationship between WSS parameters (*x*-axes) and aortic wall material properties. **(A)** aortic wall thickness (mm) vs $TAWSS_{max}$ (Pa) and **(B)** WSS^{Tmean}_{Max} (Pa); **(C)** longitudinal dissection energy function (log_{10} transformed, Log DEF_{long}) vs $TAWSS_{mean}$ (Pa); **(D)** ultimate tensile strength (log_{10} transformed, Log UTS) vs $TAWSS_{max}$ (Pa); **(E)** Elastin abundance (log_{10} (90-x) transformed) vs $TAWSS_{max}$ (Pa); **(F)** Smooth muscle cell (SMC) count (\mm^2) vs $TAWSS_{max}$ (Pa) and **(G)** WSS^{Tmean}_{Max} (Pa).

TABLE 5 | Results of multilevel mixed-effects linear model for the main outcome of tissue thickness. The fixed effects part of the model tested the influence of $TAWSS_{max}$ on thickness, whilst the random effect part of the model tested the influence of the patient. From these results, the influence of WSS alone on thickness does not occur in isolation and the variance occurring at the patient level is an important influencing factor.

	Coef	Standard error	95% CI	*p* Value
$TAWSS_{max}$	–0.016	0.024	–0.063–0.031	0.496
Patient	0.032	0.019	0.010–0.105	—
Var (estimate tissue thickness)	0.100	0.015	0.074–0.133	—
Likelihood ratio test vs linear model	—	—	—	0.0002

TABLE 6 | Multilevel mixed effects linear regression: association between wall shear stress (WSS_{Max}^{Tmean}) and smooth muscle cell (SMC) count. The fixed effects part of the model tests the effect of WSS_{Max}^{Tmean} on SMC count. Random effects part of the model tests the effect of the data being nested with the patient domain.

	Coef	Standard error	95% CI	*p* Value
WSS_{Max}^{Tmean}	–4.87	2.240	–9.26–0.48	0.030
Patient	62.94	84.2	4.58–865.54	—
Var (estimate SMC count)	504.31	116.15	321.11–792.05	—
Likelihood ratio test vs linear model	—	—	—	0.167

and delamination potential, thus increasing the likelihood of dissection (Phillippi et al., 2011).

In addition to endothelial cells and fibroblasts, SMCs are part of the repertoire of crucial mechano-sensing and -regulating cells in the aortic wall. These cells display adaptive remodeling in response to shear stress encountered by endothelial cells, which they detect with integrins, glyclocalyx, membrane microdomains, cytoskeleton, receptor tyrosine kinases and others. The direct link between WSS level and SMC found in the present study is likely to result from mechanodysregulation in response to elevated WSS, involving a disruption of cell matrix connections which are vital to aortic wall integrity (Michel et al., 2018). Dysfunctional mechanosensing can lead to cellular apoptosis and/or an atrophic remodeling response, thus disturbing the structural integrity of the aortic wall (Leung et al., 1976). Whilst there are a number of possible intracellular and matrix signaling pathways associated with the process that we have not tested for, they are likely to culminate in a final common pathway, leading to cellular loss and matrix degeneration.

Strengths and Limitations

This study benefits from a robust method of ATAA flow-to-tissue patient-specific association, which arises from segmental aneurysm analysis. Conducting the tissue characterization and CFD portions of work separately has helped reduce the risk of bias, that could result from basing aortic tissue acquisition on findings from flow analysis retrospectively (Guzzardi et al., 2015). Our statistical methods have aimed to appreciate the spread of data and made use of multilevel regression models, which have not been utilized in similar studies. Altogether this aims to improve the validity of the findings.

The study is limited by its small sample size. This may perhaps explain the lack of significance in some relationships. Larger studies would also help deal with potential confounders such patient covariates and valve function. In addition, CFD simulations were conducted under rigid wall assumption (i.e. aortic wall compliance was not taken into account). Including aortic wall compliance could further improve WSS estimation. However, this would significantly increase the computational time required to conduct patient-specific simulation further decreasing the likelihood of adoption of this technique into the clinic. Rigid wall is therefore a common assumption is several computational studies (Morbiducci et al., 2013) with a translational goal. In addition, we do not expect WSS results to be significantly affected by this assumption. Firstly, because our mechanical test results suggest increased stiffness in regions of enhanced WSS. Secondly, previous imaging studies have shown a reduction in aneurysm wall compliance when compared with healthy tissues. Larger sample sizes and the incorporation of computational methods to couple flow and wall material properties will form the basis of future work.

CONCLUSION

Our findings make a strong case for the co-localization of elevated WSS and patterns of medial degeneration, the hallmark of TAA disease. This is likely a result of the negative remodeling process of the aortic wall in response to chronic exposure to locally higher shear forces. Detailed wall shear stress analysis could predict areas of altered vascular wall mechanics and microstructural features in ascending aortic aneurysms. Presented findings further validate 4D-flow MRI and computational fluid dynamics as powerful tools for risk stratification in aneurysmal disease. This can improve precision in the timing and planning of intervention in at-risk patients.

DATA AVAILABILITY STATEMENT

The raw data supporting the conclusions of this article will be made available by the authors, without undue reservation.

ETHICS STATEMENT

The studies involving human participants were reviewed and approved by (17/NI/0160) the Health Research Authority (HRA) in the United Kingdom and was sponsored by the Imperial College London Joint Research and Compliance Office, as defined under the sponsorship requirements of the Research Governance Framework (2005). The patients/participants provided their written informed consent to participate in this study.

AUTHOR CONTRIBUTIONS

MS: conception, recruitment, analysis, statistics, writing, review; SP: conception, analysis, writing, review; SS: analysis, writing, review; SF: analysis, review; AR: review; OJ: writing, review; DO: writing, review; AO: review; JM: writing, review; XX: conception, review; TA: conception, review.

FUNDING

This work was supported by the NIHR Imperial College BRC (P69559) and the British Heart Foundation Centre for Research Excellence (Imperial College) (RE/18/4/34215). DPO is funded by the Medical Research Council.

ACKNOWLEDGMENTS

The authors would like to thank additional surgeons who agreed to participate in this study (Royal Brompton and Harefield) Fabio De Robertis, Shahzad Raja, Toufan Bahrami, (Hammersmith Hospital) Jon Anderson, Andrew Chukwuemeka, (Barts Heart Centre) John Yap, Rakesh Uppal, Kulvinder Lall.The authors also thank staff at the Robert Steiner MRI Unit who conducted the 4D-flow MRI sequences, including Ben Statton, Marina Quinlan, Alaine Berry and Faiza Ahmed. We also thank the Cardiovascular Histopathology Unit who helped in the preparation and staining of pathology slides, including Pratibha Shah, Alex Bowman and Toyin Adefila-Ideozu.

SUPPLEMENTARY MATERIAL

The Supplementary Material for this article can be found online at: https://www.frontiersin.org/articles/10.3389/fbioe.2021.750656/full#supplementary-material

Supplementary Figure 1S | Example of unstructured mesh used for geometry discretization. The image shows details of the tetrahedral core and 10 prismatic layers at the wall **(A)** and of local mesh refinements. These were prescribed at the arch branches and the aneurysm wall, where a finer mesh was designed where higher velocity gradients were observed from 4D flow MRI data. Smooth transition between finer and coarser regions was ensured by prescribing small growth ratios and verified through mesh expansion factor (Ansys ICEM) **(B)**.

REFERENCES

Armour, C. H., Guo, B., Pirola, S., Saitta, S., Liu, Y., Dong, Z., et al. (2021). The Influence of Inlet Velocity Profile on Predicted Flow in Type B Aortic Dissection. *Bio. Model. Mech.* 20, 481–490. doi:10.1007/s10237-020-01395-4

Bieging, E. T., Frydrychowicz, A., Wentland, A., Landgraf, B. R., Johnson, K. M., Wieben, O., et al. (2011). *In Vivo* Three-Dimensional MR wall Shear Stress Estimation in Ascending Aortic Dilatation. *J. Magn. Reson. Imaging* 33 (3), 589–597. doi:10.1002/jmri.22485

Bollache, E., Guzzardi, D. G., Sattari, S., Olsen, K. E., Di Martino, E. S., Malaisrie, S. C., et al. (2018). Aortic Valve-Mediated wall Shear Stress Is Heterogeneous and Predicts Regional Aortic Elastic Fiber Thinning in Bicuspid Aortic Valve-Associated Aortopathy. *J. Thorac. Cardiovasc. Surg.* 156 (6), 2112–2120. doi:10.1016/j.jtcvs.2018.05.095

Bürk, J., Blanke, P., Stankovic, Z., Barker, A., Frydrychowicz, A., Russe, J., et al. (2012). Evaluation of 3D Blood Flow Patterns and wall Shear Stress in the normal and Dilated Thoracic Aorta Using Flow-Sensitive 4D CMR. *J. Cardiovasc. Magn. Reson.* 14 (1), 84. doi:10.1186/1532-429x-14-84

Caballero, A. D., and Laín, S. (2013). A Review on Computational Fluid Dynamics Modelling in Human Thoracic Aorta. *Cardiovasc. Eng. Tech.* 4 (2), 103–130. doi:10.1007/s13239-013-0146-6

Condemi, F., Campisi, S., Viallon, M., Troalen, T., Xuexin, G., Barker, A. J., et al. (2017). Fluid- and Biomechanical Analysis of Ascending Thoracic Aorta Aneurysm with Concomitant Aortic Insufficiency. *Ann. Biomed. Eng.* 45 (12), 2921–2932. doi:10.1007/s10439-017-1913-6

Erbel, R., Aboyans, V., Boileau, C., Bossone, E., Bartolomeo, R. Di., Eggebrecht, H., et al. (2014). 2014 ESC Guidelines on the Diagnosis and Treatment of Aortic Diseases. *Eur. Heart J.* 35 (41), 2873–2926. doi:10.1093/eurheartj/ehu281

Geiger, J., Markl, M., Herzer, L., Hirtler, D., Loeffelbein, F., and Stiller, B. (2012). Aortic Flow Patterns in Patients with Marfan Syndrome Assessed by Flow-Sensitive Four-Dimensional MRI. *J. Magn. Reson. Imaging* 35 (3), 594–600. doi:10.1002/jmri.23500

Gomez, A., Wang, Z., Xuan, Y., Wisneski, A. D., Hope, M. D., Saloner, D. A., et al. (2020). Wall Stress Distribution in Bicuspid Aortic Valve–Associated Ascending Thoracic Aortic Aneurysms. *Ann. Thorac. Surg.* 110 (3), 807–814. doi:10.1016/j.athoracsur.2019.12.035

Guzzardi, D. G., Barker, A. J., Van Ooij, P., Malaisrie, S. C., Puthumana, J. J., Belke, D. D., et al. (2015). Valve-Related Hemodynamics Mediate Human Bicuspid Aortopathy: Insights from Wall Shear Stress Mapping. *J. Am. Coll. Cardiol.* 66 (8), 892–900. doi:10.1016/j.jacc.2015.06.1310

Hiratzka, L. F., Bakris, G. L., Beckman, J. A., Bersin, R. M., Carr, V. F., Casey, D. E., et al. (2010). ACCF/AHA/AATS/ACR/ASA/SCA/SCAI/SIR/STS/SVM Guidelines for the Diagnosis and Management of Patients with Thoracic Aortic Disease. *Circulation* 121 (13). doi:10.1161/CIR.0b013e3181d4739e

Howard, D. P. J., Banerjee, A., Fairhead, J. F., Perkins, J., Silver, L. E., and Rothwell, P. M. (2013). Population-Based Study of Incidence and Outcome of Acute Aortic Dissection and Pre-morbid Risk-Factor Control: 10-Year Results from the Oxford Vascular Study. *Circulation* 127 (20), 2031–2037. doi:10.1161/circulationaha.112.000483

Humphrey, J. D., Schwartz, M. A., Tellides, G., and Milewicz, D. M. (2015). Role of Mechanotransduction in Vascular Biology: Focus on Thoracic Aortic Aneurysms and Dissections. *Circ. Res.* 116 (8), 1448–1461. doi:10.1161/circresaha.114.304936

Kornet, L., Hoeks, A. P. G., Lambregts, J., and Reneman, R. S. (1999). In the Femoral Artery Bifurcation, Differences in Mean wall Shear Stress within Subjects Are Associated with Different Intima-media Thicknesses. *Arterioscler Thromb. Vasc. Biol.* 19 (12), 2933–2939. doi:10.1161/01.atv.19.12.2933

Lacolley, P., Challande, P., Osborne-Pellegrin, M., and Regnault, V. (2009). Genetics and Pathophysiology of Arterial Stiffness. *Cardiovasc. Res.* 81 (4), 637–648. doi:10.1093/cvr/cvn353

LaDisa, J. F., Figueroa, C. A., Vignon-Clementel, I. E., Kim, H. J., Xiao, N., Ellwein, L. M., et al. (2011). Computational Simulations for Aortic Coarctation: Representative Results from a Sampling of Patients. *J. Biomech. Eng.* 133, 091008. doi:10.1115/1.4004996

Les, A. S., Shadden, S. C., Figueroa, C. A., Park, J. M., Tedesco, M. M., Herfkens, R. J., et al. (2010). Quantification of Hemodynamics in Abdominal Aortic Aneurysms during Rest and Exercise Using Magnetic Resonance Imaging and Computational Fluid Dynamics. *Ann. Biomed. Eng.* 38, 1288–1313. doi:10.1007/s10439-010-9949-x

Leung, D. Y. M., Glagov, S., and Mathews, M. B. (1976). Cyclic Stretching Stimulates Synthesis of Matrix Components by Arterial Smooth Muscle Cells *In Vitro*. *Science* 191, 475–477. doi:10.1126/science.128820

Manopoulos, C., Karathanasis, I., Kouerinis, I., Angouras, D. C., Lazaris, A., Tsangaris, S., et al. Identification of Regional/layer Differences in Failure Properties and Thickness as Important Biomechanical Factors Responsible for the Initiation of Aortic Dissections. *J. Biomech.* 2018. 80:102–110. doi:10.1016/j.jbiomech.2018.08.024

Martin, C., Sun, W., and Elefteriades, J. (2015). Patient-specific Finite Element Analysis of Ascending Aorta Aneurysms. *Am. J. Physiol. - Hear. Circ. Physiol.* 308 (10), H1306–H1316. doi:10.1152/ajpheart.00908.2014

Meng, Y., Tian, C., Liu, L., Wang, L., and Chang, Q. (2014). Elevated Expression of Connective Tissue Growth Factor, Osteopontin and Increased Collagen Content in Human Ascending Thoracic Aortic Aneurysms. *Vascular* 22 (1), 20–27. doi:10.1177/1708538112472282

Michel, J. B., Jondeau, G., and Milewicz, Di. M. (2018). From Genetics to Response to Injury: Vascular Smooth Muscle Cells in Aneurysms and Dissections of the Ascending Aorta. *Cardiovasc. Res.* 114 (4), 578–589. doi:10.1093/cvr/cvy006

Morbiducci, U., Ponzini, R., Gallo, D., Bignardi, C., and Rizzo, G. (2013). Inflow Boundary Conditions for Image-Based Computational Hemodynamics: Impact of Idealized versus Measured Velocity Profiles in the Human Aorta. *J. Biomech.* 46 (1), 102–109. doi:10.1016/j.jbiomech.2012.10.012

Olchanyi, M. D., Sadikov, A., Frattolin, J., Sasidharan, S., Yousuf Salmasi, M., Edgar, L. T., et al. (2020). Validation of Markerless Strain-Field Optical Tracking Approach for Soft Tissue Mechanical Assessment. *J. Biomech.* 116 (2021), 110196. doi:10.1016/j.jbiomech.2020.110196

Pape, L. A., Tsai, T. T., Isselbacher, E. M., Oh, J. K., O'Gara, P. T., Evangelista, A., et al. (2007). Aortic Diameter ≥5.5 Cm Is Not a Good Predictor of Type A Aortic Dissection: Observations from the International Registry of Acute Aortic Dissection (IRAD). *Circulation* 116 (10), 1120–1127. doi:10.1161/circulationaha.107.702720

Phillippi, J. A., Pasta, S., and Vorp, D. A. (2011). "Biomechanics and Pathobiology of Aortic Aneurysms," in *Biomechanics and Mechanobiology of Aneurysms* (New York, NY, USA: Springer). doi:10.1007/8415_2011_84

Piatti, F., Sturla, F., Bissell, M. M., Pirola, S., Lombardi, M., Nesteruk, I., et al. (2017). 4D Flow Analysis of BAV-Related Fluid-Dynamic Alterations: Evidences of wall Shear Stress Alterations in Absence of Clinically-Relevant Aortic Anatomical Remodeling. *Front. Physiol.* 8, 441. doi:10.3389/fphys.2017.00441

Pirola, S., Cheng, Z., Jarral, O. A., O'Regan, D. P., Pepper, J. R., Athanasiou, T., et al. (2017). On the Choice of Outlet Boundary Conditions for Patient-specific Analysis of Aortic Flow Using Computational Fluid Dynamics. *J. Biomech.* 60, 15–21. doi:10.1016/j.jbiomech.2017.06.005

Pirola, S., Guo, B., Menichini, C., Saitta, S., Fu, W., Dong, Z., et al. (2019). 4-D Flow MRI-Based Computational Analysis of Blood Flow in Patient-specific Aortic Dissection. *IEEE Trans. Biomed. Eng.* 66 (12), 3411–3419. doi:10.1109/tbme.2019.2904885

Reymond, P., Merenda, F., Perren, F., Rüfenacht, D., and Stergiopulos, N. (2009). Validation of a One-Dimensional Model of the Systemic Arterial Tree. *Am. J. Physiol.-Heart Circulatory Physiol.* 297, H208–H222. doi:10.1152/ajpheart.00037.2009

Safar, M. E. (2010). Arterial Aging-Hemodynamic Changes and Therapeutic Options. *Nat. Rev. Cardiol.* 7 (8), 442. doi:10.1038/nrcardio.2010.96

Stewart, B., Khanduri, P., McCord, C., Ohene-Yeboah, M., Uranues, S., Vega Rivera, F., et al. (2014). Global Disease burden of Conditions Requiring Emergency Surgery. *Br. J. Surg.* 101, e9–22. doi:10.1002/bjs.9329

Simon, A. C., Safar, M. E., Levenson, J. A., London, G. M., Levy, B. I., Chau, N. P., et al. (1979). An Evaluation of Large Arteries Compliance in Man. *Am. J. Physiol.* 237 (5), H550–H554. doi:10.1152/ajpheart.1979.237.5.H550

Tan, F., Borghi, A., Mohiaddin, R., Wood, N., Thom, S., and Xu, Y. X. (2009). Analysis of Flow Patterns in a Patient-specific Thoracic Aortic Aneurysm Model. *Comput. Structures* 87, 680–690. doi:10.1016/j.compstruc.2008.09.007

Tsai, T. T., Evangelista, A., Nienaber, C. A., Trimarchi, S., Sechtem, U., Fattori, R., et al. (2006). Long-term Survival in Patients Presenting with Type A Acute Aortic Dissection: Insights from the International Registry of Acute Aortic Dissection (IRAD). *Circulation* 114 (1), 350–357. doi:10.1161/CIRCULATIONAHA.105.000497

Van, O. P., Potters, W. V., Nederveen, A. J., Allen, B. D., Collins, J., Carr, J., et al. (2015). A Methodology to Detect Abnormal Relative wall Shear Stress on the Full Surface of the Thoracic Aorta Using Four-Dimensional Flow MRI. *Magn. Reson. Med.* 73 (3), 1216–1227. doi:10.1002/mrm.25224

Vorp, D. A., Schiro, B. J., Ehrlich, M. P., Juvonen, T. S., Ergin, M. A., and Griffith, B. P. (2003). Effect of Aneurysm on the Tensile Strength and Biomechanical Behavior of the Ascending Thoracic Aorta. *Ann. Thorac. Surg.* 75 (4), 1210–1214. doi:10.1016/s0003-4975(02)04711-2

Wagenseil, J. E., and Mecham, R. P. (2009). Vascular Extracellular Matrix and Arterial Mechanics. *Physiol. Rev.* 89 (3), 957–989. doi:10.1152/physrev.00041.2008

Wågsäter, D., Paloschi, V., Hanemaaijer, R., Hultenby, K., Bank, R. A., Franco-Cereceda, A., et al. (2013). Impaired Collagen Biosynthesis and Cross-Linking in Aorta of Patients with Bicuspid Aortic Valve. *J. Am. Heart Assoc.* 2 (1), e000034. doi:10.1161/JAHA.112.000034

Xiao, N., Alastruey, J., and Figueroa, C. A. (2014). A Systematic Comparison between 1-d and 3-d Hemodynamics in Compliant Arterial Models. *Int. J. Numer. Meth. Biomed. Eng.* 30, 204–231. doi:10.1002/cnm.2598

Conflict of Interest: The authors declare that the research was conducted in the absence of any commercial or financial relationships that could be construed as a potential conflict of interest.

Publisher's Note: All claims expressed in this article are solely those of the authors and do not necessarily represent those of their affiliated organizations, or those of the publisher, the editors and the reviewers. Any product that may be evaluated in this article, or claim that may be made by its manufacturer, is not guaranteed or endorsed by the publisher.

frontiers in Cardiovascular Medicine

REVIEW
published: 28 October 2021
doi: 10.3389/fcvm.2021.724271

Magnetic Resonance Texture Analysis in Myocardial Infarction

Fei Peng[1], Tian Zheng[1], Xiaoping Tang[1], Qiao Liu[1], Zijing Sun[1], Zhaofeng Feng[1], Heng Zhao[2] and Lianggeng Gong[1]**

[1] Department of Medical Imaging Center, Second Affiliated Hospital of Nanchang University, Nanchang, China, [2] Department of Radiology, The First Affiliated Hospital, Hengyang Medical School, University of South China, Hengyang, China*

Texture analysis (TA) is a newly arisen field that can detect the invisible MRI signal changes among image pixels. Myocardial infarction (MI) is cardiomyocyte necrosis caused by myocardial ischemia and hypoxia, becoming the primary cause of death and disability worldwide. In recent years, various TA studies have been performed in patients with MI and show a good clinical application prospect. This review briefly presents the main pathogenesis and pathophysiology of MI, introduces the overview and workflow of TA, and summarizes multiple magnetic resonance TA (MRTA) clinical applications in MI. We also discuss the facing challenges currently for clinical utilization and propose the prospect.

Keywords: magnetic resonance imaging, myocardial infarction, texture analysis (TA), machine learning, stratifying risk

OPEN ACCESS

Edited by:
Juan Carlos Del Alamo, University of Washington, United States

Reviewed by:
Shady Abohashem, Massachusetts General Hospital and Harvard Medical School, United States
Mariana Paiva, Centro Hospitalar Universitário de São João (CHUSJ), Portugal

****Correspondence:***
Heng Zhao
angerh9@126.com
Lianggeng Gong
gong111999@126.com

Specialty section:
This article was submitted to Cardiovascular Imaging, a section of the journal Frontiers in Cardiovascular Medicine

Received: *12 June 2021*
Accepted: *27 September 2021*
Published: *28 October 2021*

Citation:
Peng F, Zheng T, Tang XP, Liu Q, Sun ZJ, Feng ZF, Zhao H and Gong LG (2021) Magnetic Resonance Texture Analysis in Myocardial Infarction. Front. Cardiovasc. Med. 8:724271. doi: 10.3389/fcvm.2021.724271

INTRODUCTION

Myocardial infarction (MI) is myocardial necrosis caused by ischemia and hypoxia of cardiomyocytes, an imbalance between oxygen offering and myocardial requirement. It belongs to a part of the clinical manifestation of the acute coronary syndrome (ACS) (1). MI is a major cause of death and disability worldwide and brings about approximately one-third of all deaths in patients over 35 years old (2, 3).

The European Society of Cardiology (ESC) has conducted the fourth universal definition of MI from cardiac troponin values (cTn) and clinical myocardial ischemia evidence that is ranging from symptoms of myocardial ischemia, ECG abnormalities, and new imaging evidence (4). However, clinical ischemic symptoms are not specific for myocardial ischemia and may be misdiagnosed as other medical conditions (5). Early mortality and morbidity can be decreased by accurate diagnosis, better prevention, and management, then life expectancy and quality of life will be enhanced (6). So, more sensitive, precise, and specific techniques are required for the diagnosis and characterization of MI.

As the imaging techniques evolve, it plays a more and more important role in MI. Cardiac magnetic resonance (CMR) has advantages, such as non-Radiative, multiparameters and sequences, multiplanar reconstruction capabilities, and high tissue resolution, which composes the "gold standard" tool for evaluating the cardiac structure and function non-invasively and becomes the best available imaging technique for detection of MI (7, 8). Meanwhile, CMR has essential significance in stratifying risk, predicting prognosis, predicting response to therapy, detecting complications, etc., in MI (8). Nevertheless, the traditional visual inspection of images may not recognize subtle differences and detect invisible signal changes (9, 10). Magnetic resonance texture analysis (MRTA), which belongs to radiomics, includes extensive technologies modeling the spatial distribution of pixel grayscale for data recognition, classification, and segmentation based on the

latent texture. Furthermore, MRTA is capable of detecting subtle signal changes and obtaining underlying image information that remains imperceptible to eyes to provide tissue characteristics (9, 11–13). More importantly, MRTA has the potential further to strengthen the diagnostic and prognostic value of imaging (14, 15).

This article concentrates on the role of MRTA in MI. In this study, we review the major pathogenesis and pathophysiology of MI, the basic concepts and types of MRTA, the clinical applications of MRTA in MI, current challenges, and potential prospects.

PATHOGENESIS AND PATHOPHYSIOLOGY OF MI

Myocardial infarction is most commonly owing to coronary thrombosis from the rupture of an atherosclerotic plaque (16). When the blood is exposed to the thrombogenic lipids, the platelets and coagulation factors are activated, which become the precipitating factor of the plaque disruption (3). The coronary plaques with lipid-rich core and thin fibrous cap occupy the highest risk of rupture (17). However, in addition to atherosclerosis, there are several etiologies of MI, such as intracardiac thrombus or valvular vegetation that led to coronary artery embolism, cocaine use, coronary dissection, hypotension, anemia, Kawasaki's syndrome, trauma, metabolic disease, congenital coronary anomalies, and complications of angiography (3, 17).

In MI, once the onset of myocardial ischemia, there is a subsequent decrease in myocardial perfusion, bringing about the reduction of tissue oxygenation, which transforms the hypoxia cardiomyocytes from aerobic to anaerobic metabolism, bringing about edema of cardiomyocyte and ultimately tissue necrosis (5).

The myocardial necrosis process resembles a "wavefront" phenomenon that is ranging from the endocardium to the epicardium (18) (**Figure 1**). Within about 15 min, the myocardium shows ischemia with no infarct. At approximately 40 min, it appears subendocardial infarction. Roughly at 3 h, the subendocardial infarct extends to the mid myocardium. Beyond 6 h, the infarction extends to subepicardial layers and develops into transmural. After approximately 2 months, scar tissues replace the piece, inflammatory cells, and edema, leading to shrinking of the necrotic tissue and myocardial thinning (5, 19).

TEXTURE ANALYSIS

Texture analysis (TA) is a part of radiomics. Through image post-Processing technology, the distribution and relationship of pixel or voxel gray are analyzed to extract many quantitative texture features that are not visible by the naked eyes in medical images (20). The image texture represents the gray-level variation rule of pixels in images (21). Changes in image intensity owing to persistent ischemia and hypoxia may be reflected as textural patterns near or after cardiomyocyte death (**Figure 2**). **Figure 3** exhibits a simplified workflow about the clinical application of MRTA. A schematic diagram illustrating the whole TA applied on CMR is shown in **Figure 4**. In the light of the means applied to assess the inter-relationships of the pixels, the forms of texture analyses can be classified as below: statistical, structural, model-based, and transform methods (13, 14).

Types of TA

With high gray and spatial resolution, MRI images possess extensive and similar image information. Therefore, the statistical method becomes the most commonly used method in MRTA. For statistical-based TA, various properties control the distribution and relations of gray-scale values in images to represent texture (14). First-order statistical TA, also called a histogram, extracts the image intensity values from the region of interest (ROI). A histogram can be derived by calculating the frequency count of the number of pixels of each gray value (22). Second-order statistics analyze the spatial relationship or co-occurrence of the pixel intensity values. The two most commonly used methods are gray-level co-occurrence matrix (GLCM) and gray-level run-length matrix (GLRLM). Through the calculation of the neighborhood gray difference matrix, high-order statistics study the spatial relationship among three or more pixels and reflect the change of intensity in a specific area or the distribution of homogeneous areas. The common calculation method includes neighborhood gray-tone difference matrix (NGTDM) and gray-level size zone matrix (GLSZM) (23).

Structural-based TA catches intensity changes between the central and adjacent voxels. Local binary patterns (LBP) are a non-Parametric algorithm and also the most frequently used method that depicts the local features of gray-scale connection between image pixels and neighboring pixels (24).

Model-based TA explicates texture in an image with sophisticated mathematical models, for example, stochastic or fractal models. The model parameters are estimated and applied to image analysis. Due to a lack of direction selectivity, this method is unsuited for depicting local image structures (13).

Transform-based TA enables the spatial information of images to convert into spatial frequencies. It contains Gabor, Fourier, and Wavelet transform. As the most widespread method, Wavelet transform can analyze the frequency content of images in different spatial frequency resolutions (25).

Machine Learning

Artificial intelligence (AI) is rapidly gaining importance in the medical imaging field and is likely to gradually turn into clinical practice in the next few years (26, 27). According to the data derived from AI, machine learning is a rapidly growing area that concentrates on building systems that make accurate predictions according to the data (28). Machine learning is mainly applied to establish the diagnosis of MI and assists differential diagnosis of acute mesenteric ischemia (AMI) and chronic mesenteric ischemia (CMI) that cannot be identified by the naked eyes (15, 29, 30). The application of machine learning in medical imaging can be briefly summarized into three types: supervised, unsupervised, and semisupervised learning (31). Supervised learning intends to recognize the relationship between characteristics relevant to the learning objectives and

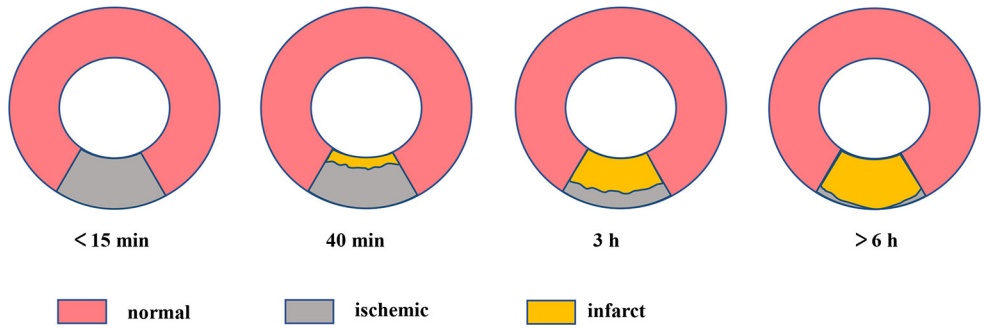

FIGURE 1 | The "wavefront" of myocardial ischemic necrosis, necrosis of cardiomyocytes progresses from the subendocardium to the subepicardium over time if ischemia persists and ultimately becoming transmural infarct.

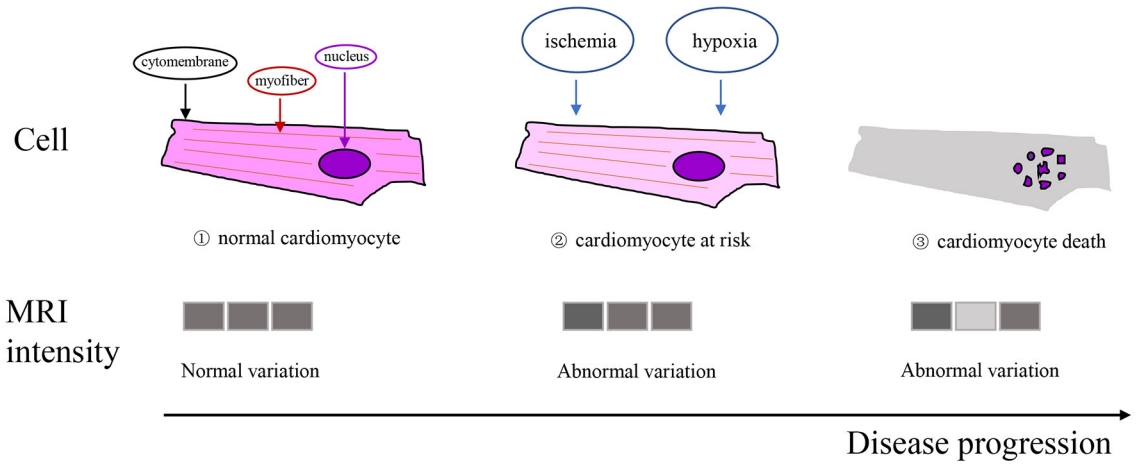

FIGURE 2 | Schematic illustration of the texture working hypothesis in myocardial infarction (MI). Top row: ischemia and hypoxia may cause cardiomyocyte at risk or death; (1), (2), and (3) represent normal cardiomyocyte, cardiomyocyte at risk, and cardiomyocyte death, respectively. Bottom row: changes in the statistical properties of the image intensities due to the persistent ischemia and hypoxia of cardiomyocytes may be reflected as certain textural patterns.

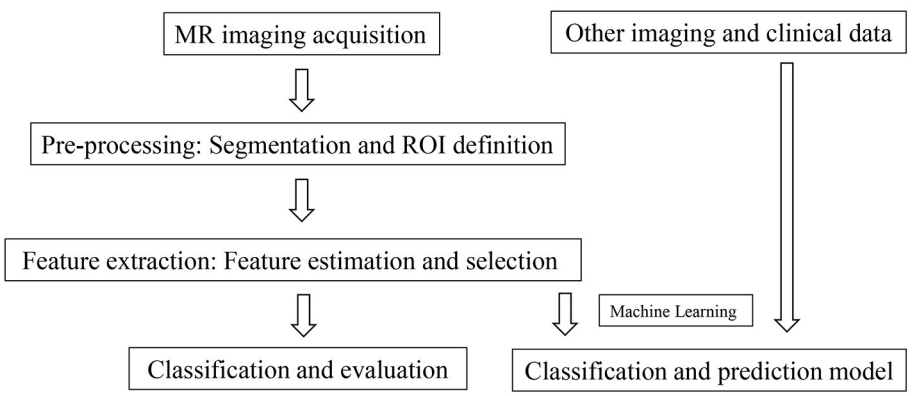

FIGURE 3 | Overview of the MRTA simplified workflow. MRTA, magnetic resonance texture analysis.

the expected result indicators in a dataset for classification. Unsupervised learning intends to identify and establish potential patterns through the use of unlabeled data from a computer. By combining supervised and unsupervised learning, semisupervised learning utilizes the amount of unlabeled data and few labeled data for training. At present, the most relevant

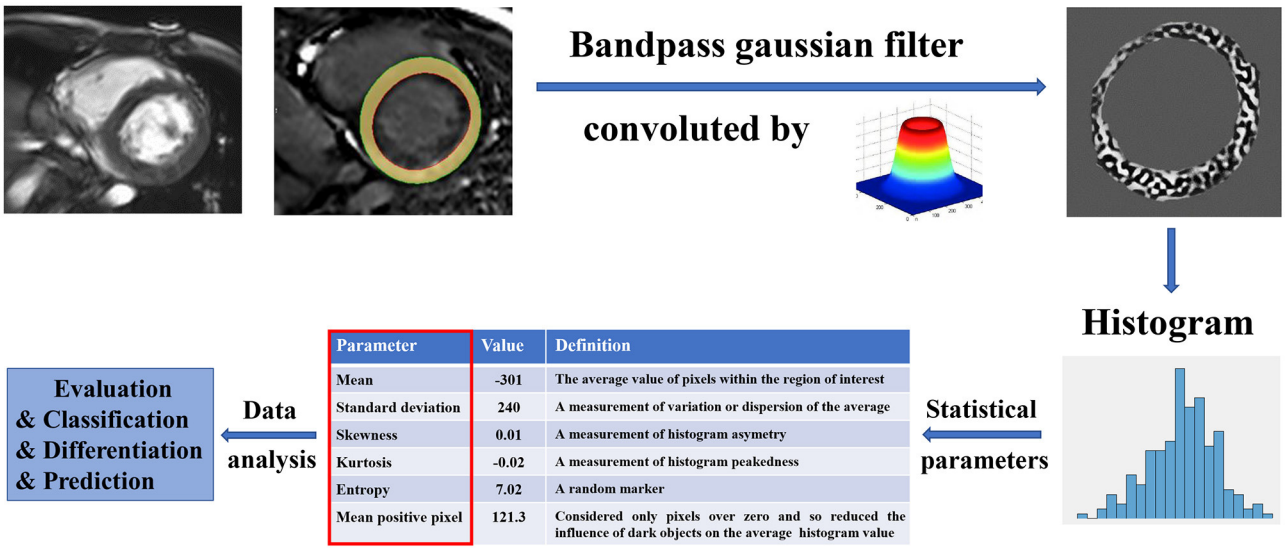

FIGURE 4 | A schematic diagram illustrating the whole texture analysis (TA) applied on CMR. The myocardium in a CMR image was convolved by a bandpass Gaussian filter to enhance the image and highlight the variance. The histogram of the enhanced myocardium was computed to obtain a couple of statistic parameters, such as mean, SD, skewness, kurtosis, entropy, and mean positive pixel. These parameters were furthermore analyzed among different patients for evaluation, classification, differentiation, and prediction. CMR, Cardiac magnetic resonance.

to cardiovascular imaging are supervised and unsupervised learning (32).

MRTA CLINICAL APPLICATIONS IN MI

Magnetic resonance texture analysis clinical applications in MI emerge as a promising research domain, and many findings have presented encouraging results. The series of studies can be divided into three broad categories: establishing the diagnosis, determining the age of infarct, stratifying risk (**Table 1**).

Establishing Diagnosis

Despite the relative importance of various MRI technologies vary, MRI plays a significant role in establishing a diagnosis for both AMI and CMI (7). The rapid application of TA in medical imaging provides a new method for diagnosing MI. Baessler et al. (15) performed TA in 120 patients with MI using histogram, GLCM, GLRLM, absolute gradient, autoregressive model, and wavelet transform. Taking late gadolinium enhancement (LGE) as a reference standard, five texture features [Teta1, WavEnHH.s-3, Perc.01, S (5,5) Sum Entrp, and Variance] enabled distinguishing scarred myocardium from normal myocardium on non-Enhanced cine MRI independently. Moreover, multiple logistic regression showed that Teta1 and Perc.01 achieved the highest diagnostic performance for small and sizeable myocardial scars with the area under the curve (AUC) were 0.92 and 0.93, respectively. Therefore, MRTA may provide an extra mean for the diagnosis of MI with gadolinium-free enhancement imaging, which may be helpful for patient groups with accompanying chronic kidney disease who have an added risk of gadolinium-related complications.

Determining the Age of Infarct

Apart from being a useful diagnostic tool, MRI can also be applied for differentiation between acute and chronic infarction, which is especially helpful when the patient has multi-infarct in different vascular areas or when an infarct occurs with no clinical symptoms. Distinguishing AMI from CMI has vital clinical significance for treatment and follow-up, especially in patients with pre-Existing CMI, and the probability of locating acute lesions by ECG or coronary angiography is limited. The management of two types of infarcts differs. It is crucial to determine the infarct age, especially when both infarction entities coexist, complicating that will complicate the therapeutic plan and follow-up after treatment. Several imaging features involving the identification of AMI and CMI in previous studies, such as wall thickening and thinning (40), microvascular obstruction (MVO) (41), edema on T2-weighted images (42, 43), and hyper-enhancement in contrast-enhanced MRI (44). However, some of these imaging features lack insufficient sensitivity and specificity, and technical limitations still exist (7, 29).

Compared with those current technologies that rely on image visual evaluation, the quantitative character of TA is a unique advantage. Edema of AMI and fibrosis of CMI hold the most essential characteristics of cardiac pathological changes correspondingly and affect the internal structure of tissues, which indicates there may be some inherent texture discrepancy in the images of tissues influenced by AMI and CMI. Larroza et al. (29) performed TA in 44 patients with MI (22 with AMI and 22 with CMI) by using histogram, GLCM, GLRLM, absolute gradient, autoregressive model, and wavelet transform, 279 texture features extracted from cine, and LGE MRI were used to distinguish AMI from CMI alone. A nested cross-validation approach combining a feature

TABLE 1 | Magnetic resonance texture analysis (MRTA) clinical applications in myocardial infarction (MI).

Clinical application	References	Study size	Acquisition	Type of TA	Modeling methods	Results
Establishing diagnosis	Baessler et al. (15)	120	CMR, 1.5T	Histogram, GLCM, GLRLM, absolute gradient, wavelet autoregressive model,	Multiple logistic regression	Combining the texture features Teta1 and Perc.01 obtain the highest accuracy for diagnosing large and small MI on CMR with an area under the curve of 0.93 and 0.92 respectively
Determining age of infarct	Larroza et al. (29)	44	LGE, CMR, 1.5T	Histogram, GLCM, GLRLM, absolute gradient, wavelet autoregressive model,	Random forest algorithm SVM	The polynomial SVM yielded the best classification performance (AUC = 0.86 ± 0.06 on LGE and AUC = 0.82 ± 0.06 on cine MRI)
	Chen et al. (33)	70	T1 mapping, LGE, CMR, 3.0T	Histogram, GLCM Difference entropy, GLRLM	Random forest algorithm	GLRLM features (horizontal fraction) extracted from of ECV demonstrated a significantly higher AUC (0.91) than other texture features in differentiation of unsalvageable infarction and salvageable myocardium
Risk stratification	Larroza et al. (34)	50	Cine, CMR,1.5T	GLCM, GLRLM, GLSZM, NGTDM, LBP	SVM	Evaluation of myocardial segmental viability based on transmural extension: LBP features using a 2D + t approach achieved high discrimination (AUC > 0.8) of non-Viable, viable and remote segments, with sensitivity 92, 72, and 85%, respectively
	Ma et al. (35)	68	T1 mapping, CMR, 3.0 T	Histogram, GLCM, wavelet	Multiple logistic regression	The combination of TA and T1 mapping native T1 values could provide high diagnostic accuracy for transmurality (AUC = 0.84) and MVO (AUC = 0.86)
	Kotu et al. (36)	22	LGE, CMR, 1.5T	Dictionary-based texture, dc-values	MLE-Bayes	TA aided with intensity values gives better segmentation of scar from myocardium with high sensitivity (82.32%) and specificity (89.05%)
	Kotu et al. (37)	44	LGE, CMR,1.5T	Dictionary-based texture	FTCM	Pixel with larger Rp values is more likely to be the border area of scar
	Engan et al. (38)	24	LGE, CMR	GLCM	MLE-Bayes	Combination of image texture and statistical features on scar may have potential discriminative power between high and low risk of serious ventricular arrhythmias groups
	Gibbs et al. (39)	76	LGE, CMR, 1.5 T	Histogram	Kaplan-Meier analysis	Patients suffering arrhythmic events with significantly higher kurtosis and lower skewness compared with those suffering no arrhythmic events

CMR, cardiac magnetic resonance; LGE, late gadolinium enhancement; GLCM, gray-level co-occurrence matrix; GLRLM, gray-level run-length matrix; GLSZM, gray-level size zone matrix; NGTDM, neighborhood gray-tone difference matrix; SVM, support vector machine; MLE, maximum likelihood estimator; LBP, local binary patterns; ECV, extracellular volume; MVO, microvascular obstruction; AUC, area under the curve; TA, texture analysis; FTCM, Frame texture classification method.

selection technology called multiple support vector machine recursive feature elimination (MSVM-RFE) was applied to test the diagnosis efficiency, the results showed that the polynomial SVM achieved the optimum classification performance (AUC = 0.86 ± 0.06 on LGE MRI and AUC = 0.82 ± 0.06 on cine MRI). However, the discrimination is not straightforward and demands the use of machine learning, especially in cases where the infarction is not readily visually perceptible in standard cine MRI.

Stratifying Risk

In recent years, MRTA plays a new role in identifying multiple prognostic indicators that guide risk stratification and prognosis prediction in patients with MI. The applications mainly involve five sub-aspects: (1) differentiation of reversible from irreversible myocardial injury; (2) evaluation of transmurality; (3) detection of MVO; (4) assessment of scar size combined with segmentation; and (5) identification of scar heterogeneity.

Differentiation of Reversible From Irreversible Injury

Differentiating reversible from irreversible myocardial damage is valuable for prognosis prediction. The salvaged myocardium is an independent predictor of prognosis and is associated with mortality, representing the risk area but can be rescued or rescued through revascularization (45). The myocardial salvage index (formula: T2-weighted edema area-delayed enhanced area/T2-weighted edema area) (45), T1 mapping techniques (46, 47), blood oxygen-level dependent (BOLD) (48), etc., have been studied to evaluate the severity of the ischemic myocardial injury. Nevertheless, the traditional visual quantification of the average intensity level for ROI is insufficient because it easily ignores subtle changes and remains subjective (49). TA may overcome some of the above limitations by utilizing specific imaging information to obtain tissue features and quantitatively analyze the relationship between pixels and gray patterns in images.

One promising result about the differentiation of reversible from irreversible myocardial injury based on MRTA was reported by Bing-Hua Chen et al. (33). They examined TA of extracellular volume (ECV) mapping from the calculation of native and post-Contrast T1 mapping images in 70 patients with ST-elevation MI. Five texture features [one co-occurrence matrix features S (0,1) difference entropy, two histogram indexes (mean and perci.99%), and run-length matrix features (horizontal fraction and vertical fraction)] were selected for analysis. The results showed that the horizontal fraction demonstrated a significantly higher AUC (0.91) than other texture features in identifying unsalvageable and salvageable myocardium.

Evaluation of Transmurality

The transmurality of infarction possesses an independent prognostic value in measuring the recovery of contractile function after treatment, and a greater transmural extent is related to poorer recovery (50, 51).

Magnetic resonance texture analysis shows several promising results in the evaluation of transmurality. Ma et al. (35) combined T1 mapping and TA for the assessment of myocardial segmental transmurality in 68 patients with AMI, the combination of native T1 values and four features {histogram (mean), GLCM [S(0,1) Correlat, S(1,-1) SumEntrp, and S(2,0) Correlat]} achieved good diagnostic performance (AUC = 0.84). In addition, taking the transmural extension on LGE as the standard judgment of infarcted segmental viability, Larroza et al. (34) applied MRTA to distinguish infarcted viable, non-Viable, and remote segments in 50 patients suffering CMI. Features derived from four matrix-based TA (GLCM, GLRLM, GLSZM, and NGTDM) and LBP methods were extracted from the segments on cine MRI, by combining SVM classifier, LBP using a 2D + t method achieved high discrimination (AUC > 0.8), with sensitivity 92% (non-Viable), 72% (viable), and 85% (remote), respectively. Hence, MRTA may have the potential to provide a new way to detect the myocardial segmental transmurality and assess myocardial segmental viability by the gadolinium-free method.

Detection of MVO

Microvascular obstruction appears in severe microcirculation damage caused by myocyte death, overflow of intracellular substances, severe stasis, and occlusion of end arteries and capillaries (7). Moreover, MVO often indicates transmural MI and correlates with adverse remodeling and poor prognosis (52).

Ma et al. (35) applied MRTA for the detection of MVO in 68 patients with AMI. Through combination of native T1 values and eight texture features {[histogram(Perc. 90%), GLCM [S(1,0) Entropy, S(0,1) Correlation, S(4,0) SumVarnc, S(5,0) DifEntrp], and wavelets (WavEnLL_s-1, WavEnLL_s-2, WavEnLL_s-3)]} that are extracted from T1 mapping, it reached a high diagnostic performance (AUC = 0.86) for MVO. Thus, MRTA may provide a more accurate means for diagnosing the severity of the acute myocardial injury.

Assessment of Scar Size Combined With Segmentation

The extent of infarct can predict left ventricular adverse remodeling (LVAR) and correlates negatively with prognosis (53–55). Besides that, since the scar is a cause of arrhythmia, infarct size is a better predictor of ventricular tachycardia than left ventricular (LV) ejection fraction (EF) or LV volumes (56, 57). Previous reports suggest the scar size assessed by MRI has the potential to predict survival and mortality independent of LVEF (58–60). Thus, segmentation of scar is a first step to explore the internal information in the scar.

Magnetic resonance texture analysis-combined segmentation can better provide the signal intensity features of the scar, then to help better segment the scar and assess scar size. Kotu et al. (36) segmented scar from normal myocardium on LGE MRI using intensity-based TA in 22 post-MI patients. Through maximum likelihood estimator (MLE)-based Bayes classification, the dictionary-based texture features and dc-values were applied to segment scarred and normal myocardium. Compared with manual segmentation by cardiologists, TA aided with intensity values achieved better segmentation of scar with high sensitivity (82.32%) and specificity (89.05%), thus may be helpful to reduce small missed infarcts that not even affect LVEF but can lead to arrhythmic events (61–63).

Identification of Scar Heterogeneity

After MI, the necrotic tissue is gradually replaced by granulation and fibrous tissue and finally, develops into scar tissue. The myocardium presents heterogeneous nature owing to scarring, and the scar tissue is complex on a histopathological level. In addition, numerous studies have shown that the degree of scar heterogeneity correlates directly with the risk of arrhythmia events, thereby, better guide the implantation of an implantable cardioverter defibrillator (ICD) (64, 65). In previous research, the myocardial heterogeneity visualization is mainly based on thresholds that are defined at intensity levels corresponding to the percentage of the max intensity level in scar area (57, 66). TA allows for quantization of patterns and relations among pixels inside images occasionally invisible to human eyes, thus, acquiring an additional measure of heterogeneity.

The scar can be described as two areas: (1) the core area, which consists of fibrous tissue and the myocardial fibers which are in a state of complete death, does not respond to the electrical signals transmitted by the myocardium to tell the heart to contract;

(2) the border area, also known as peri-infarct area or gray zone area, contains heterogeneous tissue composed of necrotic tissue mix with bundles of viable cardiomyocytes; the electrical signals in these areas will be disturbed, which may lead to reentry and sometimes arrhythmias (37, 39, 57). It is believed that accurately defining and visualizing border areas may be helpful to give insight into better risk stratification for patients with MI. A probability mapping technique based on texture and intensity features was proposed by Kotu et al. (37) to describe the heterogeneity of myocardial scar in CMR images after MI. On dictionary-based textural features, the result showed that the pixel with larger Rp values was more likely to be the border area of the scar but not necessarily in scar core, which may offer an additional valuable means to identify border areas in scarred myocardium to help predict arrhythmia events.

Some studies reveal that MRTA helps to identify arrhythmias events for patients with previous MI. Engan et al. (38) performed data analysis of image texture (based on GLCM) and statistical features on 24 implanted ICD patients with myocardial scars in CMR. Using maximum likelihood estimation (MLE)-based Bayes classifiers, the results showed that a combination of texture and statistical features might have potential discriminative power between the high and low risk of severe ventricular arrhythmias groups. Similar findings were reported by Gibbs et al. (39) who applied MRTA by using filtration histogram technique to assess LGE images in 76 patients with previous MI and evaluated the characteristics of the scar heterogeneity. The average follow-up time was 371.5 days to observe the ventricular arrhythmic events. The results suggested that patients who are suffering from arrhythmia presented higher kurtosis and lower skewness compared with those suffering no arrhythmia; furthermore, Kaplan-Meier analysis revealed that higher coarse kurtosis and lower fine skewness possessed a particular ability to forecast the increased incidence of ventricular arrhythmic events.

DISCUSSION

Challenges of MRTA

Despite these superiorities, extensive clinical application of MRTA in MI remains challenging. First, most of the studies are small sample pilot exploration in a single center, and almost all of them are retrospective studies. The conclusions obtained lack extensive verification support, and the clinical evidence is not sufficient. Therefore, prospective, multicenter, and large sample studies are needed. Second, at present, medical imaging equipment lacks the same image acquisition and imaging algorithm standard, and different acquisition times of the same MR machine and acquisition of different MR machines can affect the stability of radiomics features, and the reproducibility is low. Consequently, strict protocols and standardized methodologies should be followed to maximize the validity of future research. Third, there are many feature parameters in TA, and the prediction accuracy is affected by feature parameters, feature selection methods, and classifiers. In addition, MRTA software is manifold, and there is no evidence to show which software is superior at present. However, 3D TA includes more spatial information and is superior to 2D TA but applies less due to increased complexity. Thus, more accurate and widely applicable feature selection and pattern recognition methods will become the development direction of MRTA.

Comparison of MRTA and CMR

In the era of big data, TA has become a research hotspot in the field of precision medicine and AI (25). Compared with CMR, MRTA has many advantages as follows. First, MRTA can detect tissue changes that are not easily perceptible to the naked eyes by quantifying gray-level patterns and pixel interrelationships in images, thus can compensate the deficiency of traditional image analysis methods and strengthen the utilization value of CMR images simultaneously (10). Second, MRTA can recognize subtle differences in textural information and further strengthen the diagnostic, prognostic, and predictive values of CMR imaging (67). In addition, MRTA has several shortcomings when compared with CMR, lack of standardization has become the main reason that limits its widespread clinical application (68); besides, TA software needs to be purchased for an additional fee and thus causes increased costs. Although the development of MRTA is still at an early stage and faces many challenges, MRTA shows good clinical application prospects in the cardiovascular field.

Prospects

Although multiple MRTA clinical applications in MI have shown encouraging results, some aspects are not or rarely referred to and may become future developments.

In traditional imaging, the following factors are also related to risk stratification and prognosis in patients with MI that may be helpful for MRTA clinical application, for instance, (1) hemorrhage in the core of infarct has been demonstrated as an adverse prognostic indicator that is relevant to LVAR, large infarct size, and increased LV end-systolic volume (69); (2) ischemia may help to identify the individuals at high risk of non-Fatal MI; moreover, compared with patients with no peri-infarct ischemia, the existence of peri-infarct ischemia correlates with a higher incidence of cardiovascular events (70); (3) the right ventricle (RV) function evaluated late after MI is also a significant prognostic indicator (71). In the future study, MRTA applications in evaluating hemorrhage in the core of infarct, ischemia, and the RV function, etc., may be of potential value for risk stratification and prognosis prediction in MI. Besides, predicting response to therapy and detecting complications are also a new clinical application aspect of MRTA in MI.

In addition to the above future developments that MRTA has potential in risk stratification and prognosis prediction in MI, the combined application with MRTA also has a certain prospect. First, except for the cine, mapping, and LGE, applying MRTA to other CMR quantitative techniques, such as strain, diffusion tensor imaging (DTI), perfusion-weighted imaging (PWI), and intravoxel incoherent motion (IVIM), can enrich the clinical research methods of MI. Second, MRTA combined with other imaging techniques, such as ECG, echocardiography, and myocardial radionuclide tomographic imaging may improve early MI diagnosis and prognosis. Third, cTn is the most diagnostic biochemical marker for MI, the combination of MRTA

and cTn will increase the understanding of the connection between texture change and progression of MI. Fourth, the combination of radiomics characteristics and genomic data is described as radiogenomics (11). Gene regulation plays an important role in the occurrence of MI and cardiac remodeling after MI (72, 73). In the future, combinations of TA features and genomic data may have potential clinical application value in MI.

CONCLUSION

At present, the inferential diagnosis of MI is based on the combination of biochemical markers, ischemic symptoms, or ECG changes. We are entering an era of combined imaging and clinical assessment in disease detection and diagnosis. MRTA can detect the invisible signal changes, thus, provides an additional non-Invasive method to establish the diagnosis, determine the age of infarct, and stratify risk and predict prognosis in MI. Although its current application for MI imaging faces some challenges, MRTA shows good clinical application prospects in MI.

AUTHOR CONTRIBUTIONS

FP conducted the reference analysis and wrote the manuscript. LGG and HZ contributed to the topic conception, manuscript revision, and decision to submit for publication and are the co-corresponding authors. The remaining authors contributed to the reference collection and helped in the revision of the manuscript. All authors contributed to the article and approved the submitted version.

FUNDING

This study was supported by the National Natural Science Foundation of China (Grand No. 81860316).

REFERENCES

1. Anderson JL, Morrow DA. Acute Myocardial Infarction. *N Engl J Med.* (2017) 376:2053–64. doi: 10.1056/NEJMra1606915
2. Mozaffarian D, Benjamin EJ, Go AS, Arnett DK, Blaha MJ, Cushman M, et al. Heart disease and stroke statistics-2016 update: a report from the American heart association. *Circulation.* (2016) 133:e38–360. doi: 10.1161/CIR.0000000000000350
3. Saleh M, Ambrose JA. Understanding myocardial infarction. *F1000Res.* (2018) 7:F1000 Faculty Rev-1378. doi: 10.12688/f1000research.15096.1
4. Thygesen K, Alpert JS, Jaffe AS, Chaitman BR, Bax JJ, Morrow DA, et al. Fourth Universal Definition of Myocardial infarction. *Circulation.* (2018) 138:e618–51. doi: 10.1161/CIR.0000000000000617
5. Moore A, Goerne H, Rajiah P, Tanabe Y, Saboo S, Abbara S. Acute myocardial infarct. *Radiol Clin North Am.* (2019) 57:45–55. doi: 10.1016/j.rcl.2018.08.006
6. Mizuno Y, Sakakura K, Yamamoto K, Taniguchi Y, Tsukui T, Seguchi M, et al. Determinants of periprocedural myocardial infarction in current elective percutaneous coronary interventions. *Int Heart J.* (2020) 61:1121–8. doi: 10.1536/ihj.20-215
7. Rajiah P, Desai MY, Kwon D, Flamm SD. MR imaging of myocardial infarction. *Radiographics.* (2013) 33:1383–412. doi: 10.1148/rg.335125722
8. Lobeek M, Badings E, Lenssen M, Uijlings R, Koster K, van 't Riet E, et al. Diagnostic value of the electrocardiogram in the assessment of prior myocardial infarction. *Neth Heart J.* (2020) 29:142–50. doi: 10.1007/s12471-020-01515-w
9. Baessler B, Luecke C, Lurz J, Klingel K, von Roeder M, de Waha S, et al. Cardiac MRI texture analysis of T1 and T2 maps in patients with infarctlike acute myocarditis. *Radiology.* (2018) 289:357–65. doi: 10.1148/radiol.2018180411
10. Hassani C, Saremi F, Varghese BA, Duddalwar V. Myocardial radiomics in cardiac MRI. *AJR Am J Roentgenol.* (2020) 214:536–45. doi: 10.2214/AJR.19.21986
11. Gillies RJ, Kinahan PE, Hricak H. Radiomics: Images are more than pictures, they are data. *Radiology.* (2016) 278:563–77. doi: 10.1148/radiol.2015151169
12. Neisius U, El-Rewaidy H, Nakamori S, Rodriguez J, Manning WJ, Nezafat R. Radiomic analysis of myocardial native T1 imaging discriminates between hypertensive heart disease and hypertrophic cardiomyopathy. *JACC Cardiovasc Imaging.* (2019) 12:1946–54. doi: 10.1016/j.jcmg.2018.11.024
13. Cai JH, He Y, Zhong XL, Lei H, Wang F, Luo GH, et al. Magnetic resonance texture analysis in Alzheimer's disease. *Acad Radiol.* (2020) 27:1774–83. doi: 10.1016/j.acra.2020.01.006
14. Castellano G, Bonilha L, Li LM, Cendes F. Texture analysis of medical images. *Clin Radiol.* (2004) 59:1061–9. doi: 10.1016/j.crad.2004.07.008
15. Baessler B, Mannil M, Oebel S, Maintz D, Alkadhi H, Manka R. Subacute and chronic left ventricular myocardial scar: accuracy of texture analysis on nonenhanced cine MR images. *Radiology.* (2018) 286:103–12. doi: 10.1148/radiol.2017170213
16. Heusch G, Gersh BJ. The pathophysiology of acute myocardial infarction and strategies of protection beyond reperfusion: a continual challenge. *Eur Heart J.* (2017) 38:774–84. doi: 10.1093/eurheartj/ehw224
17. Boateng S, Sanborn T. Acute myocardial infarction. *Dis Mon.* (2013) 59:83–96. doi: 10.1016/j.disamonth.2012.12.004
18. Frangogiannis NG. Pathophysiology of myocardial infarction. *Compr Physiol.* (2015) 5:1841–75. doi: 10.1002/cphy.c150006
19. Ibanez B, Aletras AH, Arai AE, Arheden H, Bax J, Berry C, et al. Cardiac MRI Endpoints in myocardial infarction experimental and clinical trials: JACC scientific expert panel. *J Am Coll Cardiol.* (2019) 74:238–56. doi: 10.1016/j.jacc.2019.05.024
20. de Carvalho Alegro M, Valotta Silva A, Yumi Bando S, de Deus Lopes R, Martins de Castro LH, Hungtsu W, et al. Texture analysis of high resolution MRI allows discrimination between febrile and afebrile initial precipitating injury in mesial temporal sclerosis. *Magn Reson Med.* (2012) 68:1647–53. doi: 10.1002/mrm.24174
21. Alobaidli S, McQuaid S, South C, Prakash V, Evans P, Nisbet A. The role of texture analysis in imaging as an outcome predictor and potential tool in radiotherapy treatment planning. *Br J Radiol.* (2014) 87:20140369. doi: 10.1259/bjr.20140369
22. Dragić M, Zarić M, Mitrović N, Nedeljković N, Grković I. Application of gray level co-occurrence matrix analysis as a new method for enzyme histochemistry quantification. *Microsc Microanal.* (2019) 25:690–8. doi: 10.1017/S1431927618016306
23. Patel N, Henry A, Scarsbrook A. The value of MR textural analysis in prostate cancer. *Clin Radiol.* (2019) 74:876–85. doi: 10.1016/j.crad.2018.11.007
24. Sørensen L, Shaker SB, de Bruijne M. Quantitative analysis of pulmonary emphysema using local binary patterns. *IEEE Trans Med Imaging.* (2010) 29:559–69. doi: 10.1109/TMI.2009.2038575
25. Mannil M, Eberhard M, von Spiczak J, Heindel W, Alkadhi H, Baessler B. Artificial intelligence and texture analysis in cardiac imaging. *Curr Cardiol Rep.* (2020) 22:131. doi: 10.1007/s11886-020-01402-1
26. Miller DD, Brown EW. Artificial intelligence in medical practice: the question to the answer? *Am J Med.* (2018) 131:129–33. doi: 10.1016/j.amjmed.2017.10.035
27. Leiner T, Rueckert D, Suinesiaputra A, Baeßler B, Nezafat R, Išgum I, et al. Machine learning in cardiovascular magnetic resonance: basic concepts and applications. *J Cardiovasc Magn Reson.* (2019) 21:61. doi: 10.1186/s12968-019-0575-y

28. Henglin M, Stein G, Hushcha PV, Snoek J, Wiltschko AB, Cheng S. Machine learning approaches in cardiovascular imaging. *Circ Cardiovasc Imaging*. (2017) 10:e005614. doi: 10.1161/CIRCIMAGING.117.005614
29. Larroza A, Materka A, López-Lereu MP, Monmeneu JV, Bodí V, Moratal D. Differentiation between acute and chronic myocardial infarction by means of texture analysis of late gadolinium enhancement and cine cardiac magnetic resonance imaging. *Eur J Radiol.* (2017) 92:78–83. doi: 10.1016/j.ejrad.2017.04.024
30. Jiang B, Guo N, Ge Y, Zhang L, Oudkerk M, Xie X. Development and application of artificial intelligence in cardiac imaging. *Br J Radiol.* (2020) 93:20190812. doi: 10.1259/bjr.20190812
31. Handelman GS, Kok HK, Chandra RV, Razavi AH, Lee MJ, Asadi H. eDoctor: machine learning and the future of medicine. *J Intern Med.* (2018) 284:603–19. doi: 10.1111/joim.12822
32. O'Regan DP. Putting machine learning into motion: applications in cardiovascular imaging. *Clin Radiol.* (2020) 75:33–7. doi: 10.1016/j.crad.2019.04.008
33. Chen BH, An DA, He J, Wu CW, Yue T, Wu R, et al. Myocardial extracellular volume fraction radiomics analysis for differentiation of reversible versus irreversible myocardial damage and prediction of left ventricular adverse remodeling after ST-elevation myocardial infarction. *Eur Radiol.* (2020) 31:504–14. doi: 10.1007/s00330-020-07117-9
34. Larroza A, López-Lereu MP, Monmeneu JV, Gavara J, Chorro FJ, Bodí V, et al. Texture analysis of cardiac cine magnetic resonance imaging to detect nonviable segments in patients with chronic myocardial infarction. *Med Phys.* (2018) 45:1471–80. doi: 10.1002/mp.12783
35. Ma Q, Ma Y, Yu T, Sun Z, Hou Y. Radiomics of non-contrast-enhanced T1 mapping: diagnostic and predictive performance for myocardial injury in acute ST-segment-elevation myocardial infarction. *Korean J Radiol.* (2021) 22:535–46. doi: 10.3348/kjr.2019.0969
36. Kotu LP, Engan K, Eftestøl T, Ørn S, Woie L. Segmentation of scarred and non-scarred myocardium in LG enhanced CMR images using intensity-based textural analysis. *Annu Int Conf IEEE Eng Med Biol Soc.* (2011) 2011:5698–701. doi: 10.1109/IEMBS.2011.6091379
37. Kotu LP, Engan K, Skretting K, Måløy F, Orn S, Woie L, et al. Probability mapping of scarred myocardium using texture and intensity features in CMR images. *Biomed Eng Online*. (2013) 12:91. doi: 10.1186/1475-925X-12-91
38. Engan K, Eftestol T, Orn S, Kvaloy JT, Woie L. Exploratory data analysis of image texture and statistical features on myocardium and infarction areas in cardiac magnetic resonance images. *Annu Int Conf IEEE Eng Med Biol Soc.* (2010) 2010:5728–31. doi: 10.1109/IEMBS.2010.5627866
39. Gibbs T, Villa ADM, Sammut E, Jeyabraba S, Carr-White G, Ismail TF, et al. Quantitative assessment of myocardial scar heterogeneity using cardiovascular magnetic resonance texture analysis to risk stratify patients post-myocardial infarction. *Clin Radiol*. (2018) 73:1059.e1017–59. doi: 10.1016/j.crad.2018.08.012
40. Abdel-Aty H, Zagrosek A, Schulz-Menger J, Taylor AJ, Messroghli D, Kumar A, et al. Delayed enhancement and T2-weighted cardiovascular magnetic resonance imaging differentiate acute from chronic myocardial infarction. *Circulation.* (2004) 109:2411–6. doi: 10.1161/01.CIR.0000127428.10985.C6
41. Nijveldt R, Hofman MB, Hirsch A, Beek AM, Umans VA, Algra PR, et al. Assessment of microvascular obstruction and prediction of short-term remodeling after acute myocardial infarction: cardiac MR imaging study. *Radiology*. (2009) 250:363–70. doi: 10.1148/radiol.2502080739
42. Abdel-Aty H, Simonetti O, Friedrich MG. T2-weighted cardiovascular magnetic resonance imaging. *J Magn Reson Imaging*. (2007) 26:452–9. doi: 10.1002/jmri.21028
43. Monmeneu JV, Bodí V, Sanchis J, López-Lereu MP, Mainar L, Núñez J, et al. Cardiac magnetic resonance evaluation of edema after ST-elevation acute myocardial infarction. *Rev Esp Cardiol.* (2009) 62:858–66. doi: 10.1016/S1885-5857(09)72650-7
44. Kim KA, Seo JB, Do KH, Heo JN, Lee YK, Song JW, et al. Differentiation of recently infarcted myocardium from chronic myocardial scar: the value of contrast-enhanced SSFP-based cine MR imaging. *Korean J Radiol.* (2006) 7:14–9. doi: 10.3348/kjr.2006.7.1.14
45. Eitel I, Desch S, Fuernau G, Hildebrand L, Gutberlet M, Schuler G, et al. Prognostic significance and determinants of myocardial salvage assessed by cardiovascular magnetic resonance in acute reperfused myocardial infarction. *J Am Coll Cardiol.* (2010) 55:2470–9. doi: 10.1016/j.jacc.2010.01.049
46. Dall'Armellina E, Ferreira VM, Kharbanda RK, Prendergast B, Piechnik SK, Robson MD, et al. Diagnostic value of pre-contrast T1 mapping in acute and chronic myocardial infarction. *JACC Cardiovasc Imaging*. (2013) 6:739–42. doi: 10.1016/j.jcmg.2012.11.020
47. White SK, Sado DM, Fontana M, Banypersad SM, Maestrini V, Flett AS, et al. T1 mapping for myocardial extracellular volume measurement by CMR: bolus only versus primed infusion technique. *JACC Cardiovasc Imaging*. (2013) 6:955–62. doi: 10.1016/j.jcmg.2013.01.011
48. Chen BH, Shi RY, An DA, Wu R, Wu CW, Hu J, et al. BOLD cardiac MRI for differentiating reversible and irreversible myocardial damage in ST segment elevation myocardial infarction. *Eur Radiol.* (2019) 29:951–62. doi: 10.1007/s00330-018-5612-y
49. Robinson AA, Chow K, Salerno M. Myocardial T1 and ECV measurement: underlying concepts and technical considerations. *JACC Cardiovasc Imaging*. (2019) 12:2332–44. doi: 10.1016/j.jcmg.2019.06.031
50. Kim RJ, Wu E, Rafael A, Chen EL, Parker MA, Simonetti O, et al. The use of contrast-enhanced magnetic resonance imaging to identify reversible myocardial dysfunction. *N Engl J Med.* (2000) 343:1445–53. doi: 10.1056/NEJM200011163432003
51. Choi KM, Kim RJ, Gubernikoff G, Vargas JD, Parker M, Judd RM. Transmural extent of acute myocardial infarction predicts long-term improvement in contractile function. *Circulation.* (2001) 104:1101–7. doi: 10.1161/hc3501.096798
52. Shin JM, Choi EY, Park CH, Han K, Kim TH. Quantitative T1 mapping for detecting microvascular obstruction in reperfused acute myocardial infarction: comparison with late gadolinium enhancement imaging. *Korean J Radiol.* (2020) 21:978–86. doi: 10.3348/kjr.2019.0736
53. Orn S, Manhenke C, Anand IS, Squire I, Nagel E, Edvardsen T, et al. Effect of left ventricular scar size, location, and transmurality on left ventricular remodeling with healed myocardial infarction. *Am J Cardiol.* (2007) 99:1109–14. doi: 10.1016/j.amjcard.2006.11.059
54. Kaandorp TA, Lamb HJ, Viergever EP, Poldermans D, Boersma E, van der Wall EE, et al. Scar tissue on contrast-enhanced MRI predicts left ventricular remodelling after acute infarction. *Heart.* (2007) 93:375–6. doi: 10.1136/hrt.2006.097675
55. Wu E, Ortiz JT, Tejedor P, Lee DC, Bucciarelli-Ducci C, Kansal P, et al. Infarct size by contrast enhanced cardiac magnetic resonance is a stronger predictor of outcomes than left ventricular ejection fraction or end-systolic volume index: prospective cohort study. *Heart.* (2008) 94:730–6. doi: 10.1136/hrt.2007.122622
56. Bello D, Fieno DS, Kim RJ, Pereles FS, Passman R, Song G, et al. Infarct morphology identifies patients with substrate for sustained ventricular tachycardia. *J Am Coll Cardiol.* (2005) 45:1104–8. doi: 10.1016/j.jacc.2004.12.057
57. Schmidt A, Azevedo CF, Cheng A, Gupta SN, Bluemke DA, Foo TK, et al. Infarct tissue heterogeneity by magnetic resonance imaging identifies enhanced cardiac arrhythmia susceptibility in patients with left ventricular dysfunction. *Circulation.* (2007) 115:2006–14. doi: 10.1161/CIRCULATIONAHA.106.653568
58. Kwon DH, Halley CM, Carrigan TP, Zysek V, Popovic ZB, Setser R, et al. Extent of left ventricular scar predicts outcomes in ischemic cardiomyopathy patients with significantly reduced systolic function: a delayed hyperenhancement cardiac magnetic resonance study. *JACC Cardiovasc Imaging.* (2009) 2:34–44. doi: 10.1016/j.jcmg.2008.09.010
59. Cheong BY, Muthupillai R, Wilson JM, Sung A, Huber S, Amin S, et al. Prognostic significance of delayed-enhancement magnetic resonance imaging: survival of 857 patients with and without left ventricular dysfunction. *Circulation.* (2009) 120:2069–76. doi: 10.1161/CIRCULATIONAHA.109.852517
60. Roes SD, Kelle S, Kaandorp TA, Kokocinski T, Poldermans D, Lamb HJ, et al. Comparison of myocardial infarct size assessed with contrast-enhanced magnetic resonance imaging and left ventricular function and volumes to predict mortality in patients with healed myocardial infarction. *Am J Cardiol.* (2007) 100:930–6. doi: 10.1016/j.amjcard.2007.04.029
61. Kwong RY, Chan AK, Brown KA, Chan CW, Reynolds HG, Tsang S, et al. Impact of unrecognized myocardial scar detected by cardiac magnetic

resonance imaging on event-free survival in patients presenting with signs or symptoms of coronary artery disease. *Circulation.* (2006) 113:2733–43. doi: 10.1161/CIRCULATIONAHA.105.570648
62. Kwong RY, Sattar H, Wu H, Vorobiof G, Gandla V, Steel K, et al. Incidence and prognostic implication of unrecognized myocardial scar characterized by cardiac magnetic resonance in diabetic patients without clinical evidence of myocardial infarction. *Circulation.* (2008) 118:1011–20. doi: 10.1161/CIRCULATIONAHA.107.727826
63. Kwok CS, Mallen CD. Missed acute myocardial infarction: an underrecognized problem that contributes to poor patient outcomes. *Coron Artery Dis.* (2020) 32:345–9. doi: 10.1097/MCA.0000000000000975
64. Verma A, Marrouche NF, Schweikert RA, Saliba W, Wazni O, Cummings J, et al. Relationship between successful ablation sites and the scar border zone defined by substrate mapping for ventricular tachycardia post-myocardial infarction. *J Cardiovasc Electrophysiol.* (2005) 16:465–71. doi: 10.1046/j.1540-8167.2005.40443.x
65. Kazbanov IV. ten Tusscher KHW, Panfilov AV. Effects of heterogeneous diffuse fibrosis on arrhythmia dynamics and mechanism. *Sci Rep.* (2016) 6:20835. doi: 10.1038/srep20835
66. Roes SD, Borleffs CJ, van der Geest RJ, Westenberg JJ, Marsan NA, Kaandorp TA, et al. Infarct tissue heterogeneity assessed with contrast-enhanced MRI predicts spontaneous ventricular arrhythmia in patients with ischemic cardiomyopathy and implantable cardioverter-defibrillator. *Circ Cardiovasc Imaging.* (2009) 2:183–90. doi: 10.1161/CIRCIMAGING.108.826529
67. Raisi-Estabragh Z, Gkontra P, Jaggi A, Cooper J, Augusto J, Bhuva AN, et al. Repeatability of cardiac magnetic resonance radiomics: a multi-centre multi-vendor test-retest study. *Front Cardiovasc Med.* (2020) 2:586236. doi: 10.3389/fcvm.2020.586236
68. Van Timmeren JE, Cester D, Tanadini-Lang S, Alkadhi H, Baessler B. Radiomics in medical imaging-"how-to" guide and critical reflection. *Insights Imaging.* (2020) 11:91. doi: 10.1186/s13244-020-00887-2
69. Ganame J, Messalli G, Dymarkowski S, Rademakers FE, Desmet W, Van de Werf F, et al. Impact of myocardial haemorrhage on left ventricular function and remodelling in patients with reperfused acute myocardial infarction. *Eur Heart J.* (2009) 30:1440–9. doi: 10.1093/eurheartj/ehp093
70. Tsukiji M, Nguyen P, Narayan G, Hellinger J, Chan F, Herfkens R, et al. Peri-infarct ischemia determined by cardiovascular magnetic resonance evaluation of myocardial viability and stress perfusion predicts future cardiovascular events in patients with severe ischemic cardiomyopathy. *J Cardiovasc Magn Reson.* (2006) 8:773–9. doi: 10.1080/10976640600737615
71. Kim HW, Farzaneh-Far A, Kim RJ. Cardiovascular magnetic resonance in patients with myocardial infarction: current and emerging applications. *J Am Coll Cardiol.* (2009) 55:1–16. doi: 10.1016/j.jacc.2009.06.059
72. Liang Y, Luo S, Schooling CM, Au Yeung SL. Genetically predicted fibroblast growth factor 23 and major cardiovascular diseases, their risk factors, kidney function, and longevity: a two-sample mendelian randomization study. *Front Genet.* (2021) 23:699455. doi: 10.3389/fgene.2021.699455
73. Önalan Etem E, Diş Ö, Tektemur A, Korkmaz H, Buran Kavuran I. Common single nucleotide polymorphisms in the FNDC5 gene and serum irisin levels in acute myocardial infarction. *Anatol J Cardiol.* (2021) 25:528–35. doi: 10.5152/AnatolJCardiol.2021.36214

Conflict of Interest: The authors declare that the research was conducted in the absence of any commercial or financial relationships that could be construed as a potential conflict of interest.

frontiers in Cardiovascular Medicine

ORIGINAL RESEARCH
published: 02 November 2021
doi: 10.3389/fcvm.2021.742110

Data Assimilation by Stochastic Ensemble Kalman Filtering to Enhance Turbulent Cardiovascular Flow Data From Under-Resolved Observations

Dario De Marinis [1,2]* *and Dominik Obrist* [1]

[1] *ARTORG Center for Biomedical Engineering Research, University of Bern, Bern, Switzerland,* [2] *Dipartimento di Meccanica, Matematica e Management and Centro di Eccellenza in Meccanica Computazionale, Politecnico di Bari, Bari, Italy*

We propose a data assimilation methodology that can be used to enhance the spatial and temporal resolution of voxel-based data as it may be obtained from biomedical imaging modalities. It can be used to improve the assessment of turbulent blood flow in large vessels by combining observed data with a computational fluid dynamics solver. The methodology is based on a Stochastic Ensemble Kalman Filter (SEnKF) approach and geared toward pulsatile and turbulent flow configurations. We describe the observed flow fields by a mean value and its covariance. These flow fields are combined with forecasts obtained from a direct numerical simulation of the flow field. The method is validated against canonical pulsatile and turbulent flows. Finally, it is applied to a clinically relevant configuration, namely the flow downstream of a bioprosthetic valve in an aorta phantom. It is demonstrated how the 4D flow field obtained from experimental observations can be enhanced by the data assimilation algorithm. Results show that the presented method is promising for future use with *in vivo* data from 4D Flow Magnetic Resonance Imaging (4D Flow MRI). 4D Flow MRI returns spatially and temporally averaged flow fields that are limited by the spatial and the temporal resolution of the tool. These averaged flow fields and the associated uncertainty might be used as observation data in the context of the proposed methodology.

Keywords: data assimilation, Ensemble Kalman Filter, cardiovascular flow, turbulence, ensemble averaging

OPEN ACCESS

Edited by:
Zahra K. Motamed, McMaster University, Canada

Reviewed by:
Humberto Godinez, Los Alamos National Laboratory (DOE), United States
Amirhossein Arzani, Northern Arizona University, United States
Pierre Sagaut, Aix Marseille Universita, France

***Correspondence:**
Dario De Marinis
dario.demarinis@poliba.it

Specialty section:
This article was submitted to Cardiovascular Imaging, a section of the journal Frontiers in Cardiovascular Medicine

Received: *15 July 2021*
Accepted: *06 October 2021*
Published: *02 November 2021*

Citation:
De Marinis D and Obrist D (2021) Data Assimilation by Stochastic Ensemble Kalman Filtering to Enhance Turbulent Cardiovascular Flow Data From Under-Resolved Observations. Front. Cardiovasc. Med. 8:742110. doi: 10.3389/fcvm.2021.742110

1. INTRODUCTION

The clinical relevance of 4D Flow Magnetic Resonance Imaging (4D Flow MRI) for quantifying pulsatile and turbulent blood flow in the ascending aorta is limited by spatial and temporal resolution which are in general insufficient for a precise assessment of flow related parameters such as turbulent kinetic energy (TKE), Reynolds shear stress (RSS) and wall shear stress. In recent years, models to overcome these limits have been proposed, e.g., to quantify TKE for assessing aortic stenosis severity (1).

Data Assimilation (DA) can help to enhance the quality of these parameters. In DA, sparse and noisy measurement data (observations) are combined with the forecast solution computed by a

numerical (forward) model in order to obtain an improved prediction of the true state of the system. A widely used and well-known technique for DA is the Kalman Filter (KF) proposed by Kalman (2). Computation of an appropriate filter is based on the uncertainties of the observations and of the forward model. These uncertainties can be described by covariances of specific variables that are typically not known *a priori*, such that the appropriate design of a filter requires modeling. The original KF can be applied to a wide range of applications if the physical system can be described by a linear model and data observed from measurements are affected by normally distributed noise. In this context, the forecast computed by the linear model is perturbed by the error of the model, and the forecast mean depends linearly only on the previous time step since the error has zero mean. The covariance of the error is not zero, therefore it also appears in the forecast covariance matrix computation.

In nonlinear systems, the forecast mean and covariance cannot be calculated directly from the previous time step anymore, because of the nonlinear nature of the model operator. This limitation led to enhancements of the basic KF theory. A first example is the Extended Kalman Filter (3) which linearizes the original nonlinear dynamics around the previous state estimates. The ensemble KF (EnKF) (4) replaces the forecast covariance matrix by a sample covariance and estimates the forecast mean and covariance from an ensemble of states of system, which represents the evolution of the state probability density function. This makes the EnKF an important DA tool for ensemble forecasting. If the observations can be interpreted as the result of an ensemble of samples, the noise covariance is replaced by the sample covariance which results in the Stochastic Ensemble Kalman Filter (SEnKF) (5, 6) also known as Ensemble Kalman Filter with perturbed observations.

Many examples of KF techniques applied to fluid dynamics problems have been reported in the literature. Hœpffner et al. (7) used a KF based on the linearized Navier–Stokes equations to reconstruct the relevant statistics of the initial conditions in transitional wall-bounded flow systems. The study has been extended to turbulent wall-bounded flows to estimate the mean turbulent flow profile in the near-wall region by using noisy observations on the wall (8) and to capture the turbulent flow state at the outer boundary of the buffer region of turbulent boundary layer by using an EnKF (9). Gu and Oliver (10) proposed an EnKF to investigate multiphase flows in porous media. Harlim and Majda (11) compare different methods for filtering sparsely observed turbulent geophysical flows in the atmosphere and ocean regimes. Suzuki (12) developed a hybrid unsteady-flow simulation technique combining particle tracking velocimetry (PTV) and direct numerical simulation (DNS) by using a reduced-order KF. Recently, a reduced-order model based on KF has been proposed for turbulent flow configurations showing a successful improvement of the prediction of turbulent features even when the observation is provided only in a limited region (13).

DA using methods different from KF have been also applied to fluid dynamics problems. A variational DA technique based on the minimization of the error between observations and numerical solution in the context of Reynolds Averaged Navier–Stokes (RANS) equations has been applied successfully to reconstruct the mean flow field around a cylinder in laminar regime (14). The variational DA technique has been used to combine mean velocity from 2D PIV observations of flow over an idealized airfoil and a numerical solver for RANS Equation (15).

Both variational and KF-based DA techniques for computational fluid dynamics have been reviewed and compared for unsteady viscous flow applications (16). These techniques are powerful tools, because the coupling of observed data with computational models can remove errors which cannot be identified by using only one of these scientific methodologies alone. However, reliable tools for accurate prediction of complex flow configurations are still lacking.

In the field of cardiovascular flows, DA and Kalman filter have been used in order to improve the accuracy and reliability of physical modeling and to reduce the uncertainty due to the lack of information about boundary conditions, patient-specific geometries and blood viscosity. Gaidzik et al. (17) improved hemodynamic flow prediction by merging Phase-Contrast MRI data with CFD simulations for an idealized aneurysm model where well-controlled laminar flow can be obtained. Canuto et al. (18) implemented an EnKF for the purpose of estimating parameters in cardiovascular models, i.e., a fully zero-dimensional model of the right heart and pulmonary circulation and a coupled 0D–1D model of the lower leg, through the assimilation of clinical measurements of specific patients. DeVault et al. (19) proposed a model for the blood flow in a vital subnetwork of the cerebral vasculature, namely the Circle of Willis. In this model the parameters of the outflow conditions were calibrated using a subset of clinical measurements through EnKF techniques. Arnold et al. (20) used EnKF to estimate the inlet flow waveform in patient-specific arterial network models. Habibi et al. (21) used a reduced-order modeling Kalman filter to provide blood flow data that were more accurate than the computational and synthetic voxel-based experimental datasets with the aim of improving near-wall hemodynamics quantification. In their recent review, Arzani and Dawson (22) present and compare different variational and KF-based DA for modeling cardiovascular flows. Some other studies on merging CFD and 4D flow MRI data using data assimilation are reported here for completeness (23–27).

The aim of this paper is to propose a DA methodology based on the SEnKF approach that can be used to enhance the spatial and temporal resolution of voxel-based flow observations of turbulent pulsatile flow (as in 4D Flow MRI) to improve the assessment of turbulent blood flow in large vessels. To the best of the authors' knowledge, the current work seems to be the first study that tackles turbulence modeling in blood flow with KF-based DA techniques. We propose to consider voxel-based observed data as the result of a volumetric averaging of the true state over the voxel size. The associated sample covariance will take into account the presence of turbulence as well as the noise. The present problem of DA could also be addressed by the 4D-Var method (28, 29) or the Ensemble Kalman Smoother (30) which cope with problems presenting nonlinearity and strong sensitivity to initial conditions as in turbulent flows. Here, we only aim at finding the correct covariance matrix of these

fluctuations rather than trying to predict exact, instantaneous fluctuations. The sensitivity to initial conditions ensures that every simulated pulse results in a slightly different realization of the turbulent flow field. The average of this ensemble of flow realizations corresponds to the mean flow in the Reynolds decomposition and the covariance matrix then corresponds to the Reynolds stress tensor. We will apply the SEnKF method mainly for these analogies with the Reynolds decomposition of turbulent flows.

The used forward model comprises a high-order finite-difference flow solver for the Navier–Stokes equations for the Direct Numerical Simulation (DNS) of turbulent incompressible flow (31) which is thoroughly validated and has been used for several complex flow configurations (32–34) and recently for the study of fluid-structure interaction problems (35, 36). The numerical forecast provided by the forward model are decomposed in an expectation value (ensemble-average) and its fluctuations. Such expectation values can be interpreted as a RANS flow field and the associated covariance matrix as the Reynolds stresses (RSS). In that spirit, our SEnKF algorithm applies a correction to the numerical forecast based on its covariance (RSS) and on a set of observed data and their associated covariances.

The remainder of this paper is organized as follows: the section 2 provides a brief description of the theoretical background of turbulent flows, EnKF and SEnKF approaches, and the proposed DA methodology that will estimate the enhanced flow fields. In the section 3, the proposed DA methodology is applied to three cases: Unsteady flow past a circular cylinder confined in a channel; Wall-bounded turbulent flow in a channel; Flow downstream of an aortic valve. The paper concludes with a discussion on the accuracy, efficiency, and versatility of the DA methodology based on these results.

2. METHODS

2.1. Ensemble Averaging

We model incompressible flow of a homogeneous Newtonian fluid with the Navier–Stokes equations

$$\vec{\nabla} \cdot \vec{u}\left(\vec{x},t\right) = 0, \tag{1}$$

$$\frac{\partial \vec{u}\left(\vec{x},t\right)}{\partial t} + \left(\vec{u}\left(\vec{x},t\right)\cdot\vec{\nabla}\right)\vec{u}\left(\vec{x},t\right) + \frac{1}{\rho}\vec{\nabla}p\left(\vec{x},t\right) - \nu\nabla^2\vec{u}\left(\vec{x},t\right) - \vec{f}\left(\vec{x},t\right) = 0, \tag{2}$$

where $\vec{x} = \{x, y, z\}$ are Cartesian coordinates, and t is the time. The variables ρ and ν are the fluid density and the kinematic viscosity, respectively; p is the fluid pressure; $\vec{u}$ and $\vec{f}$ are the fluid velocity and the volumetric forcing, respectively.

In the case of turbulent flows, the pressure and velocity fields present chaotic, unsteady changes due to the nonlinear nature of the system and exhibit strong sensitivity to the initial conditions. In practice, this leads to non-reproducible flow fields despite the deterministic nature of the Navier–Stokes (Equation 2) and a statistical approach is often used to study turbulent flow systems. Therefore, we will not aim at predicting exact turbulent fluctuations from noisy observations. Rather, we will formulate a data assimilation scheme to predict statistical properties of the turbulent flow comprising the mean flow and the second moment of the turbulent fluctuations.

The expectation value of a specific turbulent flow quantity may be estimated from an ensemble of multiple realizations of the flow field, i.e., multiple states-of-system. Each realization r of the flow field $\vec{u}\left(\vec{x},t\right)_{(r)}$ can be decomposed in an ensemble-averaged field $\langle\vec{u}\left(\vec{x},t\right)\rangle$ and the fluctuations $\vec{u'}\left(\vec{x},t\right)_{(r)}$ according to the Reynolds decomposition

$$\vec{u}\left(\vec{x},t\right)_{(r)} = \langle\vec{u}\left(\vec{x},t\right)\rangle + \vec{u'}\left(\vec{x},t\right)_{(r)}, \tag{3}$$

with the ensemble-average on the s states-of-system defined as

$$\langle\vec{u}\left(\vec{x},t\right)\rangle \coloneqq \lim_{s\to\infty}\frac{1}{s}\sum_{r=1}^{s}\vec{u}\left(\vec{x},t\right)_{(r)}. \tag{4}$$

This leads to the following Reynolds-averaged Navier–Stokes (RANS) equations for incompressible flows:

$$\vec{\nabla}\cdot\langle\vec{u}\left(\vec{x},t\right)\rangle = 0 \tag{5}$$

$$\frac{\partial\langle\vec{u}\left(\vec{x},t\right)\rangle}{\partial t} + \left(\langle\vec{u}\left(\vec{x},t\right)\rangle\cdot\vec{\nabla}\right)\langle\vec{u}\left(\vec{x},t\right)\rangle + \frac{1}{\rho}\vec{\nabla}\langle p\left(\vec{x},t\right)\rangle - \nu\nabla^2\langle\vec{u}\left(\vec{x},t\right)\rangle - \langle\vec{f}\left(\vec{x},t\right)\rangle = -\vec{\nabla}\cdot\langle\vec{u'}\left(\vec{x},t\right)\vec{u'}\left(\vec{x},t\right)^{\mathrm{T}}\rangle. \tag{6}$$

Equations (5) and (6) have the same form as the original (Equations 1, 2) except for the additional term on the right-hand side of Equation (6) comprising the so-called Reynolds Stresses (RSS) $-\rho\langle\vec{u'}\left(\vec{x},t\right)\vec{u'}\left(\vec{x},t\right)^{\mathrm{T}}\rangle$.

In pulsatile flows, the flow configurations are repeated with period T, and a generic time t_n can be written as

$$t_n = t_{(r),\phi} = t_\phi + (r-1)\,T, \tag{7}$$

where t_ϕ is the phase time and r is the number of the pulse. The description of the pulsatile dynamics can be reduced to the study of the flow configurations of the basic pulse period. Nonetheless, in presence of turbulence, the periodically subsequent configurations of the pulsatile flow will show differences due to the turbulent fluctuations. Information about the turbulent dynamics of pulsatile flows can be captured decomposing the flow field by phase-averaging, that is obtained by building the ensemble of states-of-system from the periodically subsequent configurations. Thus, the ensemble definition (Equation 4) assumes the following form

$$\langle\vec{u}\left(\vec{x},t_n\right)\rangle_\phi \coloneqq \lim_{s\to\infty}\frac{1}{s}\sum_{r=1}^{s}\vec{u}\left(\vec{x},t_\phi+(r-1)\,T\right) \tag{8}$$

where $\langle\cdot\rangle_\phi$ is the phase-average operation on the periodically subsequent configurations related to the basic time t_ϕ. The

pulsatile turbulent dynamics is then described at each basic time t_ϕ by the phase-averaged flow field $\langle \vec{u}\left(\vec{x}, t_\phi\right)\rangle_\phi$ and its covariance $\langle \vec{u'}\left(\vec{x}, t_\phi\right) \vec{u'}\left(\vec{x}, t_\phi\right)^{\mathrm{T}}\rangle_\phi$.

In turbulent configurations presenting a statistically-steady behavior, a time-average corresponds to an ensemble-average. Thus, the ensemble definition (Equation 4) assumes the following form

$$\langle \vec{u}\left(\vec{x}, t\right)\rangle_t \coloneqq \lim_{s\to\infty} \frac{1}{s} \sum_{r=1}^{s} \vec{u}\left(\vec{x}, t_0 + (r-1)\,\Delta\tau\right) \tag{9}$$

where $\langle\cdot\rangle_t$ is the time-average operation, t_0 is the initial time value and $\Delta\tau$ a chosen time increment. The statistically-steady turbulent dynamics is then described by the time-averaged flow field $\langle \vec{u}\left(\vec{x}, t\right)\rangle_t$ and its covariance $\langle \vec{u'}\left(\vec{x}, t\right) \vec{u'}\left(\vec{x}, t\right)^{\mathrm{T}}\rangle_t$. Note that the definition of the time-average operation (Equation 9) is formally identical to the definition ensemble average (Equation 8) if the number of phases describing the flow is equal to 1 and $\Delta\tau$ corresponds the time period T.

In spatially-homogeneous turbulent flows the turbulent features are statistically the same in the flow domain such that the ensemble-average (Equation 4) can be replaced by a volume-average,

$$\overline{\vec{u}\left(\vec{x}, t\right)} \coloneqq \frac{1}{V} \iiint_V \vec{u}\left(\vec{\xi}, t\right) \mathrm{d}\vec{\xi} \tag{10}$$

where $\overline{\cdot}$ stands for the volume-average operation over the volume V. The spatially-homogeneous turbulent dynamics is then described by the volume-averaged flow field $\overline{\vec{u}\left(\vec{x}, t\right)}$ and its associated covariance $\overline{\vec{u'}\left(\vec{x}, t\right) \vec{u'}\left(\vec{x}, t\right)^{\mathrm{T}}}$.

In summary, the ensemble used for statistical characterization of a turbulent flow can be built in different ways depending on the physical behavior of the turbulent flow configuration (statistically-steady, periodic, spatially-homogeneous) leading to different forms of Equation (4). Equations (8)–(10) can be seen as special cases of the following most general form of the ensemble definition Equation (4)

$$\langle \overline{\vec{u}\left(\vec{x}, t_n\right)}\rangle_\phi \coloneqq \lim_{s\to\infty} \frac{1}{s} \sum_{r=1}^{s} \overline{\vec{u}\left(\vec{x}, t_{(r),\phi}\right)}. \tag{11}$$

2.2. Stochastic Ensemble Kalman Filtering Approach

The SEnKF approach is used to estimate the state of the system by filtering an ensemble forecast with observations over time. Hereafter, a brief introduction to KF algorithms and then to the SenKF is presented. Details of the algorithms are available in the original papers (2, 4, 5).

The true state-of-system at time t_n is denoted by the state-vector $\vec{u}_n$. The observation of this state is denoted by the vector $\vec{d}_n$ which depends on $\vec{u}_n$ through the observation operator $\mathbf{H}$ that describes the measurement tool used for the acquisition of the data, such that

$$\vec{d}_n = \mathbf{H}\vec{u}_n + \vec{r}_n, \tag{12}$$

where $\vec{r}_n$ is the observation noise described by a normal distribution $\vec{r}_n \sim \mathcal{N}(\vec{0}, \mathbf{R}_n)$ with zero mean and covariance $\mathbf{R}_n$. The forward model is defined through the operator $\mathbf{M}_n$ such that

$$\vec{u}_n = \mathbf{M}_n\vec{u}_{n-1} + \vec{q}_n, \tag{13}$$

where the error $\vec{q}_n$ follows a normal distribution $\vec{q}_n \sim \mathcal{N}(\vec{0}, \mathbf{Q}_n)$ with zero mean and covariance $\mathbf{Q}_n$. The operator $\mathbf{M}_n$ models the physical behavior of the system and can be of linear or nonlinear nature.

To estimate the state at time level n, we assume that the state of the system $\vec{u}_{n-1}$ given all past observations to that time step $\vec{d}_{1:n-1}$ follows a normal distribution with mean $\vec{\mu}^a_{n-1}$ and with covariance $\mathbf{P}^a_{n-1}$, such that

$$\vec{u}_{n-1}|\vec{d}_{1:n-1} \sim \mathcal{N}\left(\vec{\mu}^a_{n-1}, \mathbf{P}^a_{n-1}\right). \tag{14}$$

Starting from this assumption on the previous time level $n-1$, we can estimate a forecast of the state vector $\vec{u}_n$ as

$$\vec{u}_n|\vec{d}_{1:n-1} \sim \mathcal{N}\left(\vec{\mu}^f_n, \mathbf{P}^f_n\right), \tag{15}$$

where the superscript f stands for the *forecast* step that is the prior update obtained from the forward model. In the following, the superscript a denotes the *analysis* step that is the posteriori update of the system obtained by taking into account also the observations at that time step.

The basic idea of the EnKF algorithms (4) is to estimate $\vec{\mu}^f_n$ and $\mathbf{P}^f_n$ from an ensemble of s states $\vec{u}^f_{(r),n}$ with $r = 1, 2, \ldots, s$,

$$\vec{u}^f_{(r),n} = \mathbf{M}\left(\vec{u}^a_{(r),n-1}, t_n\right) \tag{16}$$

$$\vec{\mu}^f_n = \frac{1}{s}\sum_{r=1}^{s} \vec{u}^f_{(r),n} \tag{17}$$

$$\mathbf{P}^f_n = \frac{1}{s}\sum_{r=1}^{s} \left(\vec{u}^f_{(r),n} - \vec{\mu}^f_n\right)\left(\vec{u}^f_{(r),n} - \vec{\mu}^f_n\right)^{\mathrm{T}}. \tag{18}$$

If the observations $\vec{d}_n$ can be treated as the result of an ensemble of s samples $\vec{d}_{(r),n}$, the observation noise covariance is replaced by a sample covariance, which leads to the following relations for the SEnKF algorithm (5):

$$\vec{d}_{(r),n} = \mathbf{H}\vec{u}_{(r),n} + \vec{r}_{(r),n} \tag{19}$$

$$\vec{d}_n = \frac{1}{s}\sum_{r=1}^{s} \vec{d}_{(r),n} \tag{20}$$

$$\mathbf{R}_n = \frac{1}{s}\sum_{r=1}^{s} \left(\vec{d}_{(r),n} - \vec{d}_n\right)\left(\vec{d}_{(r),n} - \vec{d}_n\right)^{\mathrm{T}}. \tag{21}$$

After the prior update obtained from the forecast step (Equations 16–18), the SEnKF algorithms proceeds with the analysis step

which updates the state-vector using the observations:

$$\vec{u}^a_{(r),n} = \vec{u}^f_{(r),n} + \mathbf{K}_n \left(\vec{d}_{(r),n} - \mathbf{H}\vec{u}^f_{(r),n} \right) \quad (22)$$

$$\vec{\mu}^a_n = \frac{1}{s} \sum_{r=1}^{s} \vec{u}^a_{(r),n}, \quad (23)$$

$$\mathbf{P}^a_n = \frac{1}{s} \sum_{r=1}^{s} \left(\vec{u}^a_{(r),n} - \vec{\mu}^a_n \right) \left(\vec{u}^a_{(r),n} - \vec{\mu}^a_n \right)^{\mathrm{T}}. \quad (24)$$

Equation (22) defines the correction of the forecast $\vec{u}^f_{(r),n}$ to the state estimate $\vec{u}^a_{(r),n}$ through the so-called Kalman gain $\mathbf{K}_n$ which depends on the observation uncertainty $\mathbf{R}_n$ and the uncertainty of the forecast estimate $\mathbf{P}^f_n$ according to

$$\mathbf{K}_n = \mathbf{P}^f_n \mathbf{H}^{\mathrm{T}} \left(\mathbf{H}\mathbf{P}^f_n \mathbf{H}^{\mathrm{T}} + \mathbf{R}_n \right)^{-1}. \quad (25)$$

For the limiting case, where the observations are assumed to be perfect, i.e., $\mathbf{H}_n = \mathbf{I}$ and $\mathbf{R}_n \to \mathbf{0}$ (where $\mathbf{I}$ is the identity matrix), the Kalmain gain reduces to $\mathbf{K}_n = \mathbf{I}$ such taht the analysis step becomes $\vec{u}^a_{(r),n} = \vec{d}_{(r),n}$. This limiting case illustrates that the state estimate $\vec{u}^a_{(r),n}$ tends to be dominated by the observations $\vec{d}_{(r),n}$ if $\mathbf{R}_n$ is small. In contrast, $\mathbf{K}_n \to \mathbf{0}$ if the prior covariance $\mathbf{P}^f_n$ tends to zero, i.e., if the level of forecast certainty is high. In that case, the filter ignores the observations and $\vec{u}^a_{(r),n} \approx \vec{u}^f_{(r),n}$.

2.3. Data Assimilation Methodology for Pulsatile Turbulent Flows

In the following, we extend the SEnKF approach to formulate a DA methodology for pulsatile, turbulent flows.

2.3.1. Data Acquisition

In the present context, we assume that observations of pulsatile, turbulent flows are available as voxel-based data with voxel size h. Often small turbulent length scales cannot be captured by such observations. The measured data can be seen as the result of a volumetric average over the voxel volume according to Equation (10). Moreover, if the observations are run for p repetitive pulses, the voxel data can also be phase averaged to obtain estimates of mean and a covariance according to Equation (11). Each observed voxel(v)-based data $\vec{d}_{v;(s),\phi}$ measured in the pulse s has an error $\vec{r}_{v;(s),\phi}$ whose covariance will be considered as the result of a voxel-phase-average. This leads to the following definitions of the data $\vec{d}_{v;(s),\phi}$, the associated mean $\vec{d}_{v;\phi}$ and sample covariance $\mathbf{r}_{v;\phi}$:

$$\vec{d}_{v;(s),\phi} = \overline{\vec{u}\left(\vec{x}, t_{(s),\phi}\right)} \quad (26)$$

$$\vec{d}_{v;\phi} = \langle \overline{\vec{u}\left(\vec{x}, t_\phi\right)} \rangle_\phi = \frac{1}{p} \sum_{s=1}^{p} \vec{d}_{v;(s),\phi}, \quad (27)$$

$$\begin{aligned} \mathbf{r}_{v;\phi} &= \langle \overline{\vec{u}\left(\vec{x}, t_\phi\right)}' \, \overline{\vec{u}\left(\vec{x}, t_\phi\right)}'^{\mathrm{T}} \rangle_\phi \\ &= \frac{1}{p} \sum_{s=1}^{p} \left(\vec{d}_{v;(s),\phi} - \vec{d}_{v;\phi} \right) \left(\vec{d}_{v;(s),\phi} - \vec{d}_{v;\phi} \right)^{\mathrm{T}}. \end{aligned} \quad (28)$$

In the classical relation (Equation 21), the covariance matrix is written with respect to the entire state-vector $\vec{d}_n$. Here for simplicity we assume that covariance between velocities of different voxels is zero; thus, we define the covariance matrix $\mathbf{r}_v$ independently for each voxel v.

2.3.2. Forecast Solution

The forecast solution is computed using a Navier–Stokes solver for direct numerical simulation (DNS). In the EnKF formalism, this solver represents the nonlinear forward model ($\mathbf{M} = \mathbf{DNS}$) between two subsequent update steps $n-1$ and n such that

$$\vec{u}_n = \mathbf{DNS}\left(\vec{u}_{n-1}, t_n\right) + \vec{q}_n, \quad (29)$$

$$\vec{u}^f_{(r),n} = \mathbf{DNS}\left(\vec{u}^a_{(r),n-1}, t_n\right). \quad (30)$$

The Kalman time step $\Delta t_{KF} = t_{n+1} - t_n$ between two subsequent updates should not be confused with the DNS time step of the Navier–Stokes solver. Even though the DNS Equation 30 returns a deterministic solution $\vec{u}^f_{(r),n}$ affected only by a numerical error, we know that turbulent flows have a stochastic behavior that can be investigated *a posteriori* by using an ensemble-average approach in order to evaluate the effect of the turbulent fluctuations. The deterministic solution $\vec{u}^f_{(r),n}$ differs from the ground-truth solution $\vec{u}_n$ of Equation 29 because of the error $\vec{q}_n$ which is composed of three contributions of different nature: a numerical error $\vec{q}_{n_{NUM}}$ due to the limited numerical accuracy of the discretized Navier–Stokes equations; an uncertainty $\vec{q}_{n_{TUR}}$ due to the stochastic nature of turbulent fluctuations; and a modeling error $\vec{q}_{n_{MOD}}$ due to the uncertainty error (e.g., unknown boundary conditions, viscosity) typical of blood flow physical modeling:

$$\vec{q}_n = \vec{q}_{n_{NUM}} + \vec{q}_{n_{TUR}} + \vec{q}_{n_{MOD}}. \quad (31)$$

Here, the numerical error $\vec{q}_{n_{NUM}}$ is assumed to be negligible, because in a DNS its magnitude must be lower than the magnitude of turbulent fluctuations. In the case of blood flow simulations, the error $\vec{q}_{n_{MOD}}$ will add additional uncertainty that will affect the forecast solution.

In the present work, the DNS data $\vec{u}^f_{(r),n}$ is considered as a stochastic realization of the ground truth, i.e., it comprises a mean flow component and a random turbulent fluctuation. In the language of the Kalman filter theory, the mean flow is the ground truth and the Reynolds stress tensor is the covariance matrix $\mathbf{P}$ of the forecast noise. This interpretation neglects the effect of numerical noise and modeling uncertainty. The appropriate choice of the forcast ensemble for the SEnKF algorithm is important for obtaining a good filter for the specific flow configuration. For pulsatile turbulent configurations, we propose to build the ensemble of states from multiple pulses, i.e., each pulse is considered a different realization. First, the pulse period T is divided in a number of intervals N_Φ defined by the basic time $t_\phi = t_1, t_2, \ldots, t_{N_\phi}$ with $t_{N_\phi} = T$. We generate an increasingly large ensemble by running the forward model for multiple pulses. This is a significant deviation from the standard SEnKF concept, where the ensemble is typically built from multiple computations of the forward model with slightly different initial conditions.

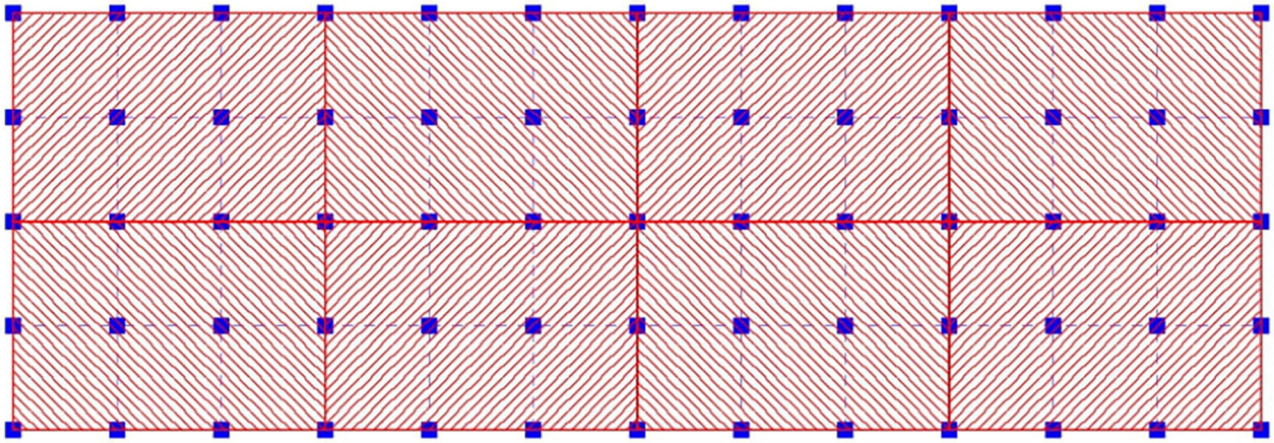

FIGURE 1 | Overlapping of a 2D voxel grid (red) with respect to the 2D computational grid (blue) for $g_v = 4 \times 3 = 12$.

In accordance with Equations (16)–(18), the forecast state-vector, its mean and associated sample covariance at each computational grid node g are then computed as:

$$\vec{u}^f_{g;(s),\phi} \equiv \vec{u}^f\left(\vec{x}_g, t_{(s),\phi}\right), \tag{32}$$

$$\vec{\mu}^f_{g;(s),\phi} \equiv \langle \vec{u}^f\left(\vec{x}_g, t\right)\rangle_{(s),\phi} = \frac{1}{s}\sum_{r=1}^{s} \vec{u}^f_{g;(r),\phi}, \tag{33}$$

$$\langle \vec{u}'^f\left(\vec{x}_g, t\right)\vec{u}'^f\left(\vec{x}_g, t\right)\rangle_{(s),\phi} = \frac{1}{s}\sum_{r=1}^{s}\left(\vec{u}^f_{g;(r),\phi} - \vec{\mu}^f_{g;(s),\phi}\right) \left(\vec{u}^f_{g;(r),\phi} - \vec{\mu}^f_{g;(s),\phi}\right)^{\mathrm{T}}. \tag{34}$$

Here for simplicity we assume that covariance between velocities of different grid nodes is zero. Thus, we define the covariance matrix $\mathbf{p}^f_g$ independently for each grid node.

The ensemble will be very small in the beginning and only becomes a statistically useful sample of realizations after several pulses. In the first pulse of the numerical simulation ($s = 1$), the sample covariance $\mathbf{p}^f_{g;(1),\phi}$ would be equal to zero according to Equation (34). Therefore, the covariance $\mathbf{p}^f_{g;(s),\phi}$ is computed in the following way:

$$\mathbf{p}^f_{g;(s),\phi} = \frac{1}{s}\left(D + \sum_{r=1}^{s}\left(\vec{u}^f_{g;(r),\phi} - \vec{\mu}^f_{g;(s),\phi}\right)\left(\vec{u}^f_{g;(r),\phi} - \vec{\mu}^f_{g;(s),\phi}\right)^{\mathrm{T}}\right), \tag{35}$$

where D is a diagonal matrix whose elements are on order of magnitude larger than the expected covariance one of the specific flow configuration. D ensures the positiveness of $\mathbf{p}^f_{g;(s),\phi}$ at the beginning of the simulation, and then its influence disappears for increasingly larger ensembles.

2.3.3. Data Assimilation Algorithm

The proposed methodology aims at using observed data on a voxel-grid in combination with the forecast solution computed by DNS on a finer computational grid. To this end, the voxels m_v of the voxel grid are overlapped with the computational grid nodes m_g, where the state-vector at each time t_n is defined on each grid node g as $\vec{u}_{g;n} = \{u_x, u_y, u_z\}_{g;n}$. For Cartesian grids, g_v computational grid-nodes will lie inside each voxel v; and it is possible that a grid node g belongs to more than one voxel, i.e., the grid node is located exactly on the borders of adjacent v_g voxels (**Figure 1**).

In the present context, $\vec{d}_{v;(s),\phi}$ is the value that the solution would have on all computational grid nodes g_v lying inside the voxel v, if the data $\vec{d}_{v;(s),\phi}$ was constant over the whole voxel volume. It is clear that this is generally not the case. The discrete form of the observation operator $\mathbf{H}$ that maps the voxel-based data to the grid is a $3m_v \times 3m_g$ matrix assuming the following form:

$$\left[H_{ij}\right]_{v,g} = \phi_{v,g}\delta_{ij} \tag{36}$$

where δ_{ij} is the Kronecker delta, $i, j = 1, 2, 3$ and

$$\phi_{v,g} = \begin{cases} \frac{1}{g_v}, & \text{if } g \text{ lies inside } v, \\ 0, & \text{otherwise.} \end{cases} \tag{37}$$

Solving the analysis step to update the entire state-vector $\vec{u}_{1:m_g;(s),\phi}$ requires the computation on huge matrices $\mathbf{P}$, $\mathbf{R}$ and $\mathbf{H}$ of size $3m_g \times 3m_g$, $3m_v \times 3m_v$, and $3m_v \times 3m_g$, respectively. However, we can exploit the block-structure of $\mathbf{H}$ comprising of blocks $\mathbf{h}$ of size $3 \times 3g_v$ which correspond to single voxels. From an algorithmic point of view, this allows to only use m_v dense matrices $\mathbf{h}$ instead of the huge sparse matrix $\mathbf{H}$ which dramatically reduces the

computational cost. There, the Kalman gain term is written as

$$\vec{k}_{g;(s),\phi} = \sum_{v=1}^{m_v} \Psi_{g,v} \left[\mathbf{p}^f_{1:g_v;(s),\phi} \mathbf{h}^{\mathrm{T}} \left(\mathbf{h} \mathbf{p}^f_{1:g_v;(s),\phi} \mathbf{h}^{\mathrm{T}} + \mathbf{r}_{v,\phi} \right)^{-1} \left(\vec{d}_{v;(s),\phi} - \mathbf{h} \vec{u}^f_{1:g_v;(s),\phi} \right) \right]_g, \tag{38}$$

where $\Psi_{g,1:m_v}$ are weights for interpolating data between the discrete values of the Kalman gain obtained from the different m_v voxels to the grid node g. Since each grid-node solution depends only on the data of the v_g voxels, we define

$$\Psi_{g,v} = \begin{cases} \frac{1}{v_g}, & \text{if } g \text{ lies inside } v, \\ 0, & \text{otherwise.} \end{cases} \tag{39}$$

Finally, the updated solution $\vec{u}^a_{(s),\phi}$ is computed in the analysis step of the SEnKF as

$$\vec{u}^a_{g;(s),\phi} = \vec{u}^f_{g;(s),\phi} + \vec{k}_{g;(s),\phi}. \tag{40}$$

In conclusion, the proposed methodology deals with data obtained by observations on coarse grids, and enhances them by means of the SEnKF algorithm, obtaining a new set of data on finer grids. The entire DA methodology is summarized in the Algorithm 1.

Algorithm 1: Data Assimilation algorithm for computing enhanced volex-based data

- Initialization: $\vec{u}^a_{g;(0),N_\phi} = \vec{u}_{i.c.}$ (initial conditions)
- Data Assimilation:

for s = 1 to p **do**
- $\vec{u}^a_{g;(s),0} = \vec{u}^a_{g;(s-1),N_\phi}$
- **for** ϕ = 1 to N_ϕ **do**
  - $\vec{u}^f_{g;(s),\phi} = \mathbf{DNS}\left(\vec{u}^a_{(s),\phi-1}\right)$
  - $\vec{\mu}^f_{g;(s),\phi} = \frac{1}{s}\sum_{r=1}^{s} \vec{u}^f_{g;(r),\phi}$
  - $\mathbf{p}^f_{g;(s),\phi} = \frac{1}{s}\left(D + \sum_{r=1}^{s} \left(\vec{u}^f_{g;(r),\phi} - \vec{\mu}^f_{g;(s),\phi}\right)\left(\vec{u}^f_{g;(r),\phi} - \vec{\mu}^f_{g;(s),\phi}\right)^{\mathrm{T}} \right)$
  - $\vec{k}_{g;(s),\phi} = \sum_{v=1}^{m_v} \Psi_{g,v} \left[\mathbf{p}^f_{1:g_v;(s),\phi} \mathbf{h}^{\mathrm{T}} \left(\mathbf{h} \mathbf{p}^f_{1:g_v;(s),\phi} \mathbf{h}^{\mathrm{T}} + \mathbf{r}_{v,\phi} \right)^{-1} \left(\vec{d}_{v;(s),\phi} - \mathbf{h} \vec{u}^f_{1:g_v;(s),\phi} \right) \right]_g$
  - $\vec{u}^a_{g;(s),\phi} = \vec{u}^f_{g;(s),\phi} + \vec{k}_{g;(s),\phi}$

for ϕ = 1 to N_ϕ **do**
- **Result**: $\vec{\mu}^a_{g;\phi} = \vec{u}^a\left(\vec{x}_g, t\right) = \frac{1}{p}\sum_{r=1}^{p} \vec{u}^a_{g;(r),\phi}$
- **Result**: $\mathbf{p}^a_{g;\phi} = \langle \vec{u'}^a\left(\vec{x}_g, t\right) \vec{u'}^a\left(\vec{x}_g, t\right)^{\mathrm{T}} \rangle_{g;\phi} = \frac{1}{p}\sum_{r=1}^{p} \left(\vec{u}^a_{g;(r),\phi} - \vec{u}^a_{g;\phi}\right)\left(\vec{u}^a_{g;(r),\phi} - \vec{u}^a_{g;\phi}\right)^{\mathrm{T}}$

2.4. Direct Numerical Simulation

All numerical simulations have been performed using a high-order Navier–Stokes solver for the DNS of incompressible flows. The governing Equations (1) and (2) are discretized on a staggered Cartesian grid using sixth-order finite-difference schemes. A multigrid method is used for solving the Poisson problem and time integration is performed using a three-step Runge–Kutta scheme. Details of the implementation are given in Henniger et al. (31).

The simulations use a combination of periodic boundary conditions and the fringe forcing technique (37) which damps incoming flow disturbances and forces the flow field toward a desired velocity profile by applying a suitable volume force $\vec{f}$ of the right-hand side of the Navier–Stokes (Equation 1). The general form of the fringe forcing is given by

$$\vec{f}\left(\vec{x}, t\right) = \lambda\left(\vec{x}\right)\left(\vec{U}\left(\vec{x}, t\right) - \vec{u}\left(\vec{x}, t\right)\right) \tag{41}$$

where $\lambda\left(\vec{x}\right)$ is the fringe function and $\vec{U}\left(\vec{x}, t\right)$ is the desired velocity to be imposed. The fringe function is non-zero only within the so-called fringe region which is typically located at the edge of the computational domain. In the physically relevant regions of the DNS, the fringe function is zero.

This technique has been exploited to impose inflow velocity profiles, to model outflow conditions and to model complex geometries by setting $\vec{U} = 0$ within immersed objects. The fringe forcing has similarities to the Kalman analysis step (Equation 22), where the Kalman gain K acts like a fringe function and the observation $\vec{d}$ corresponds to the desired velocity $\vec{U}$. However, the fringe forcing is added to the right-hand side of a differential equation and drives the solution toward $\vec{u}$ with a time scale $1/\lambda$, whereas the Kalman update is an algebraic equation which nudges the solution toward the observation at a time scale $\Delta t_{KF}/\|K\|$, where Δt_{KF} is the time between two subsequent analysis steps.

3. RESULTS

In the present study, all observations are available on Cartesian voxel grids and obtained either by experiments or other numerical simulations (synthetic data). In case of synthetic data, the voxel data are extracted from the computational grid, and each voxel comprises multiple g_v grid nodes of the computational grid. The observations have been run for p multiple pulses, and the synthetic voxel data are collected in order to obtain a mean and a covariance estimate in accordance with Equation (11). Each voxel data $\vec{d}_{v;(s),\phi}$ computed in the specific pulse s has an error $\vec{r}_{v;(s),\phi}$ whose covariance will be considered as the result of a voxel-and-phase-average; Equation (26) assumes the

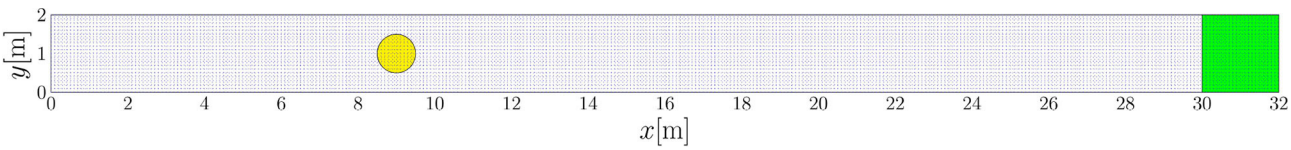

FIGURE 2 | Periodically oscillating flow: configuration of the cylinder confined in the channel. In the green fringe region the inflow is imposed. The cylinder is modeled in the yellow fringe region with $\vec{u} = 0$.

following form:

$$\vec{d}_{v;(s),\phi} \equiv \overline{\vec{u}\left(\vec{x}, t_{(s),\phi}\right)} = \frac{1}{g_v} \sum_{g=1}^{g_v} \vec{u}_{g;(s),\phi}. \tag{42}$$

The methodology has been validated for test problems of increasing complexity, starting with a periodic and non-turbulent configuration, then extending the application of the methodology to a turbulent configuration, and finally applying the methodology to a pulsatile and turbulent configuration. Results have been evaluated comparing global flow-related parameters and local profiles with respect to the ground truth and observed data.

The first flow related parameter that has been chosen is the friction Reynolds number Re_τ which is defined using the friction velocity U_τ,

$$Re_\tau = \frac{U_\tau L_{ref}}{\nu} = U_\tau \frac{Re}{U_{ref}} = Re \sqrt{\frac{1}{Re} \frac{L_{ref}}{U_{ref}} \left| \left\langle \left\langle \frac{\partial u_x(\vec{x}, t)}{\partial y} \right\rangle \right\rangle \right|}, \tag{43}$$

where Re is the Reynolds number based on reference values (U_{ref}, L_{ref}) of the flow configuration, the average $\langle\langle\cdot\rangle\rangle$ is calculated at the specific time t over the wall. The velocity gradient is discretized with a first-order finite difference scheme on the computational grid. Mean velocity and RSS profiles are commonly described in wall units, i.e., by dimensionless variables y^+ and u^+ obtained by normalization with respect to friction velocity U_τ and flow parameters,

$$u^+ = \frac{u}{U_\tau}, \qquad y^+ = \frac{y U_\tau}{\nu}, \tag{44}$$

where y is the distance to the wall and u is the velocity component parallel to the wall.

The turbulent kinetic energy (TKE) is a second parameter used to quantify the turbulence in the bulk flow. We define TKE within a given volume interest V, such that

$$TKE(t) = \frac{1}{2} \overline{\langle u'_x(\vec{x}, t)^2 + u'_y(\vec{x}, t)^2 + u'_z(\vec{x}, t)^2 \rangle} \tag{45}$$

Finally, voxel-and-phase(time)-averaged velocity fields and/or RSS fields are presented for the different configurations.

3.1. Periodically Oscillating Flow

The proposed DA methodology is first validated for an unsteady flow past a cylinder confined in a channel (**Figure 2**). The size of the channel is $32h \times 2h \times h$ where $h = 1$ [m] is the channel half-width. The positive x-direction is the stream-wise direction, the y-axis is perpendicular to the walls at $y = 0$ and $y = 2h$ and the z-axis points in span-wise direction. The diameter of the cylinder is equal to h and its center C has coordinates $(x, y) = (9h, h)$ and an axis parallel to the z-direction. Periodic boundary conditions have been imposed in both the stream-wise and span-wise direction, whereas a no-slip condition is enforced at the top and bottom wall. Fringe forcing at the end of the domain (green region in **Figure 2**) is used to enforce plug flow with velocity $U_x = 1$, $U_y = 0$, $U_z = 0$ [m/s] at the inflow (using $\lambda = 50$ in Equation 41). The presence of the cylinder is modeled by using an another fringe region with $\vec{U} = 0$ and $\boldsymbol{\lambda} = 100$ for the grid nodes within the cylinder (yellow region in **Figure 2**). The combination of the plug flow with the no-slip b.c. will produce a thin boundary layer in the green fringe region. The thickness of this boundary layer will increase and the flow will develop a parabolic profile upstream of the cylinder. The Reynolds number is set equal to 150 based on h and the inflow velocity U_x.

3.1.1. Ground Truth

First, a DNS has been run to obtain the ground truth, using a computational grid of $257 \times 33 \times 3$ grid nodes. At the given Reynolds number, the flow past a confined cylinder presents vortex shedding where the vortices detach periodically with a period of T =1.9951 [s] from either side of the body forming a Von Kármán vortex street in the wake of the cylinder (**Figure 3**).

3.1.2. Data Acquisition

Second, the observation data $\vec{d}_{v;(s),\phi}$ have been extracted from the ground-truth DNS. The period T has been divided in $N_\Phi = 20$ equal time intervals and the data are collected for $p = 500$ periods starting after $100T$ in order to overcome the initial transient leading to the periodic solution. Six different regions of interest (windows) have been selected to sample the data (**Figure 4A**). Window 1 includes the cylinder and the downstream region from where the vortex shedding originates. Window 2 and window 3 are obtained as the left and right half of window 1, respectively, to study the capability of the proposed method to reconstruct the flow downstream of the cylinder with and without the data of the cylinder itself. The windows 1, 2, and 3 have the lengths 4, 2, and 2, h, respectively. Their height is h and they are centered in the y-direction and extend over the whole z-direction. Extending the windows 1,

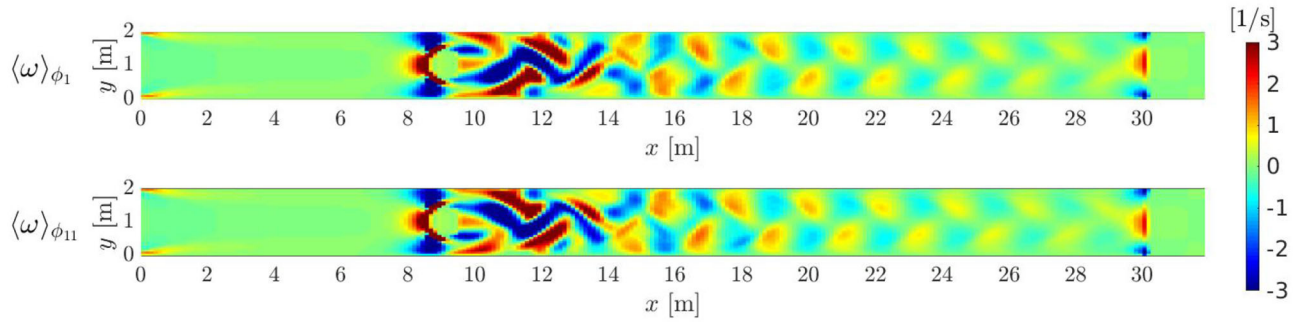

FIGURE 3 | Periodically oscillating flow: vorticity ω fields for two different phase averaging. ϕ_1 corresponds to basic time $t_1 = 0.099755$ [s], while ϕ_{11} corresponds to basic time $t_{11} = 1.097305$ [s]. Von Kármán vortex street develops downstream the cylinder.

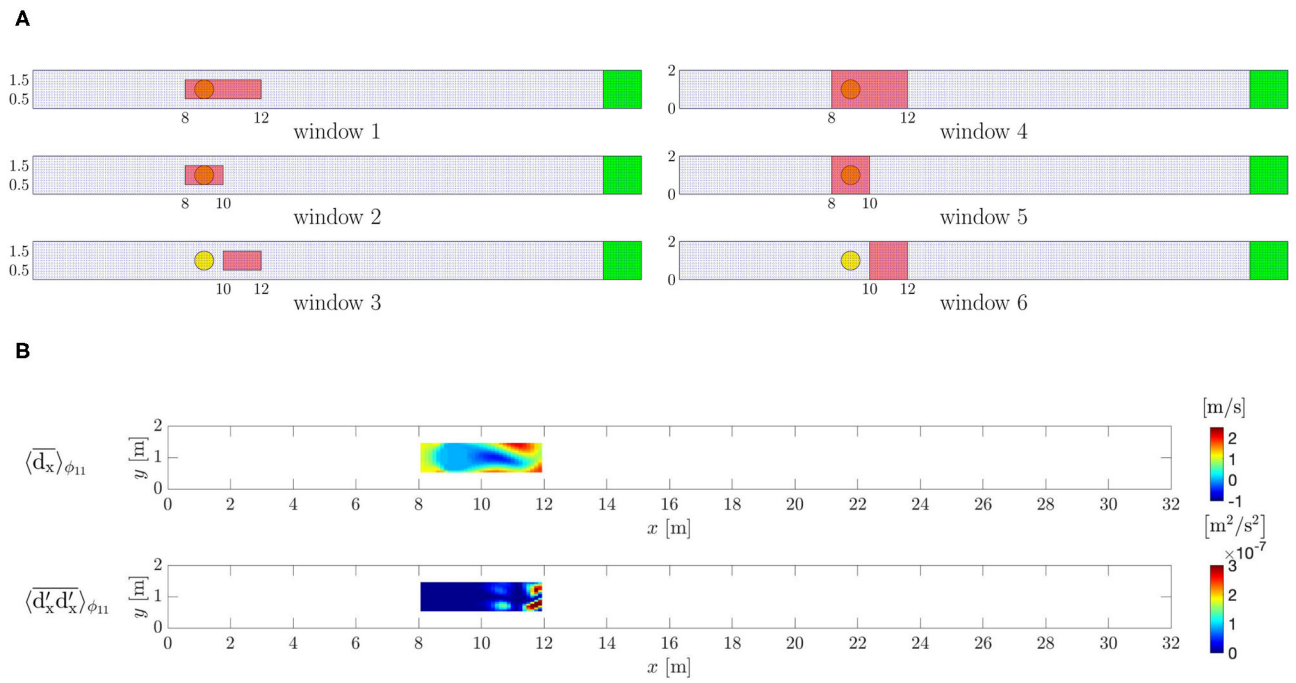

FIGURE 4 | Periodically oscillating flow. **(A)** Windows where the data are extracted from the ground-truth flow field. **(B)** Mean x-velocity and associated xx- covariance component observed from the ground-truth DNS within window 1.

2, and 3 to the overall y-domain leads to the windows 4, 5, and 6, respectively. The choice of window 4, 5, and 6 allows to assess whether the availability of data close to the channel walls will improve the flow reconstruction by using the DA algorithm or not.

Each $\vec{d}_{v;(s),\phi}$ is computed for a voxel formed by $g_v = 2 \times 2 \times 2$ grid nodes by averaging the ground-truth solution of the corresponding g_v nodes. These voxel-averaged values are then further phase-averaged in order to obtain voxel-and-phase averaged data $\vec{d}_{v;\phi}$ and the associated covariances $\mathbf{r}_{v;\phi}$ for all the phases, within the specific window (**Figure 4B**). Because the flow is not turbulent, the covariance will be almost zero and its value will just include the covariance of the numerical error of the DNS solver and the (very low) inaccuracy of the chosen period value T.

3.1.3. Comparison Between Ground Truth and DA Predictions

In the DA predictions only the no-slip b.c. at the walls and the fringe forcing for the inflow are imposed *a priori*. The cylinder fringe region is not used anymore and only the use of the observed data in the SEnKF algorithm, will reconstruct the flow field in the wake of the cylinder. The diagonal matrix $\mathbf{D}$ in Equation (35) is set to $\{D_{ii}\} = 1,000$. Six DA predictions, i.e., DA 1, DA 2, ...DA 6, have been run by using the data set extracted

from the six windows of interest, i.e., window 1, window 2, ... window 6, respectively.

The voxel-and-phase averaged velocity profiles $\langle u_x\left(\vec{x}, t_\phi\right)\rangle_\phi$ computed after $500T$ are shown in **Figure 5A** (left) along a line parallel to the y-axis and crossing the center of the cylinder at $x = 9$ [m]. When the data window includes the cylinder (windows 1, 2, 4, 5) the SEnKF forces the flow velocities to zero, because the data inside the cylinder have mean and covariance both equal to zero. In contrast, the DA predictions using data from window 3 and 6 show a nearly parabolic velocity profile, which is the velocity profile that the flow assumes due to the inflow and boundary conditions. This indicates that the proposed methodology has limitations in propagating the information from the observed data in upstream direction. **Figure 5A** (right) shows the axial velocity profiles at $x = 15$ [m] in the wake of the cylinder: all the DA predictions present good agreement with the ground truth except for the DA prediction performed by using data from window 2. This shows that the window 2 is too small and do not contain enough data to guide the solution of the DA prediction toward the ground truth. **Figure 5B** shows the xx-covariance component profiles at $x = 15$ [m] (right) and at $x = 9$ [m] (left). DA predictions present an error with respect to the ground truth DNS due to the additional uncertainty related to the cylinder boundary condition and to the convergence history of the DA methodology. On the other hand the information is well propagated in downstream direction by the proposed DA methodology as can be seen in **Figure 5C** for all DA predictions. DA 2 presents a phase-shift with respect to the DNS due to the absence of data in the region surrounding the cylinder which apparently led to a counter-phase vortex detachment.

3.2. Turbulent Channel Flow

Hereafter, the DA methodology is extended to turbulent flows, and validated for turbulent channel flow. To this end, the dimensions of the channel are set to $4\pi h \times 2h \times 2\pi h$ according to Kim et al. (38), see **Figure 6**. The laminar Poiseuille flow $\vec{u} = \{[y(2h - y)/h^2]U_x, 0, 0\}$ having maximum velocity $U_x = 1$ [m/s] has been used as initial condition for the velocity field. The Reynolds number (based on the channel half-width $h = 1$ [m] and the initial maximum velocity U_x) is set to $5,000$ which is in the range of the intended final application for blood flow in the aorta (39). Periodic boundary conditions have been imposed in both the stream-wise and span-wise direction, while a no-slip condition is ensured at the top and bottom wall. A constant non-dimensional bulk velocity $U_x^{bk} = 0.667$ [m/s] has been enforced in the stream-wise direction according to Schlatter et al. (40).

3.2.1. Ground Truth

DNS simulations have been run in order to obtain grid-converged solutions that will be considered the ground truth. In order to ensure the transition to turbulence in the channel flow, the initial Poiseuille flow has been perturbed with a two-dimensional (stable) Tollmien–Schlichting (TS) wave with maximum stream-wise velocity amplitude of 3% of the laminar center-line velocity and two superimposed weak oblique (stable) three-dimensional waves with amplitude 0.1% with the same fundamental stream-wise wavelength as the two-dimensional disturbance. The computation of the TS waves was performed using a standard Chebyshev collocation method involving the solution to the Orr–Sommerfeld and Squire equations (41). Sufficient convergence for Re_τ and TKE was achieved for a resolution of $65 \times 65 \times 65$ points.

3.2.2. Data Acquisition

The data $\vec{d}_{v;t}$ to be used in the DA predictions have been extracted from the flow field of the ground-truth DNS starting after 200 [s] when a statistically-steady turbulent flow had been established. The ensemble of states-of-system is chosen in accordance with Equation (9).

Four different windows have been selected (**Figure 7A**). Window 1 has a size of $(\pi/2)\,h$ in x-direction and h in y-direction. It is centered in y-direction. Windows 2 and 3 are obtained by extending the window 1 over the whole y- and x-direction, respectively, in order to evaluate the influence of the amount of available data on the flow reconstruction. Window 4, which covers the whole domain has been chosen to mimic the configuration of clinical applications where the data are available for the entire blood vessels. All windows are spread over the whole domain in z-direction.

Data $\vec{d}_{v;t}$ are collected for $4,000$ [s] in order to compute the covariance $\mathbf{r}_{v;t}$ in an accurate way onto the voxel-grid. Each $\vec{d}_{v;t}$ is obtained by averaging the ground-truth solution over voxels formed by $g_v = 3 \times 3 \times 3$ adjacent grid-nodes; these voxel-averaged values are then further time-averaged in order to obtain time-and-space averaged data. Because the flow is turbulent, the covariance will be not zero and its value will include both the covariance of the numerical error of the DNS solver and the turbulent fluctuations covariance (**Figure 7B**).

3.2.3. Comparison Between Ground Truth and Data Assimilation Predictions

In the DA predictions the contribution of each voxel-based data is spread onto the g_v grid-nodes according to Equation (38). The initial conditions of the velocity are set to Poiseuille flow without any perturbations such that the flow would not show a transition to turbulence without any additional external forcing due to the SEnKF. The diagonal matrix $\mathbf{D}$ in Equation (35) is set to $\{D_{ii}\} = 10$.

Four DA predictions, i.e., DA 1, DA 2, DA 3, DA 4, have been run by using the data set extracted from the four windows of interest, i.e., window 1, window 2, window 3, window 4, respectively.

The results of the DA predictions have been evaluated by comparing the evolution in time of the friction Reynolds number $\langle Re_\tau\rangle$ and $TKE\,(t)$ with the ground truth (**Figure 8**). At the beginning of the DA predictions, filtering the initial Poiseuille flow by the observed data leads to a transient evolution of the flow to the statistically-steady turbulent configuration. This transient is different for each window with regard to the mean value to which the solution tends and the time required to overcome the transient. After this transient, Re_τ present the same qualitative behavior in time of the ground truth, even though with different mean value for the different selected data

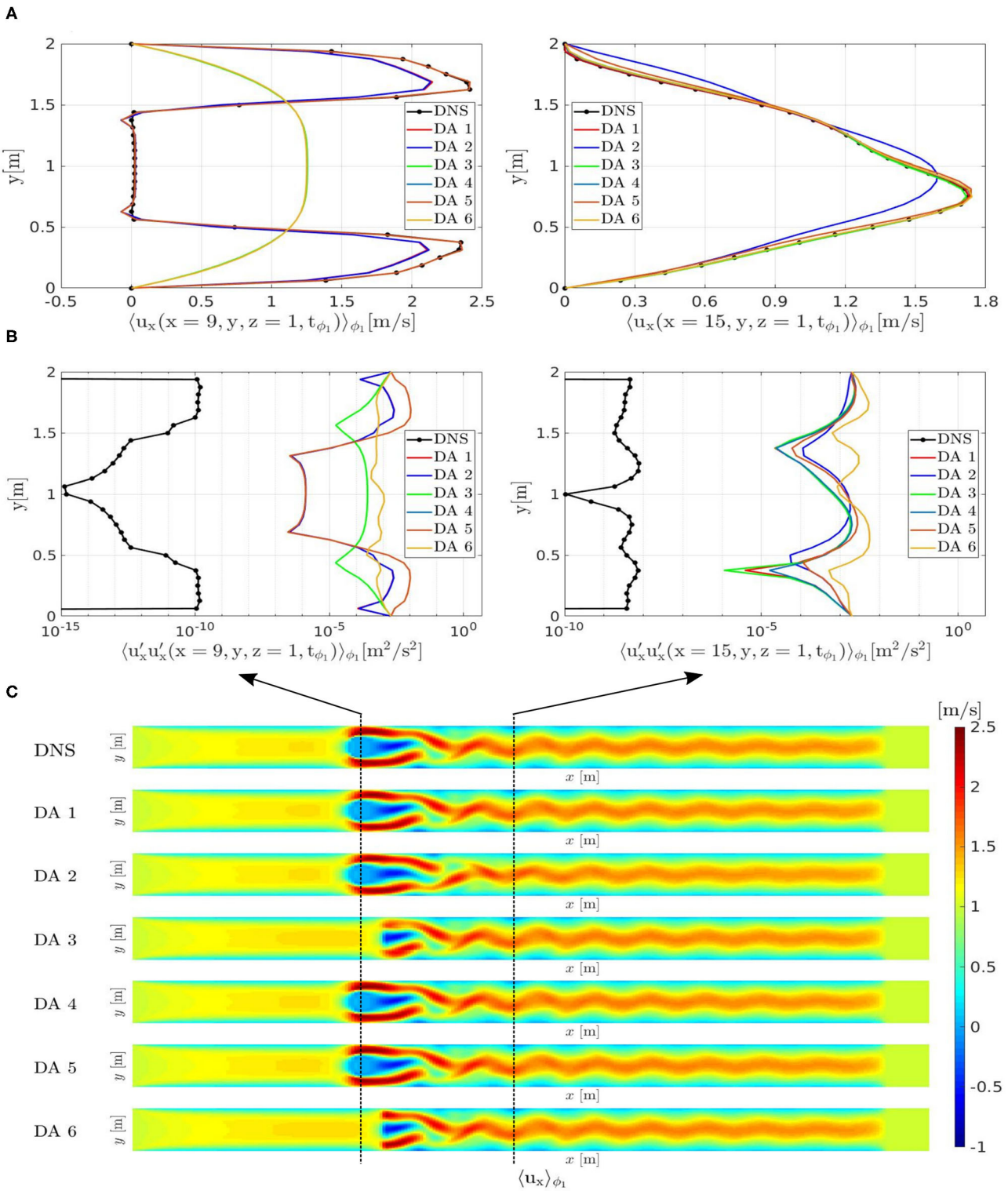

FIGURE 5 | Periodically oscillating flow. Velocity profiles $\langle u_x(\vec{x}, t_{\phi_1})\rangle_{\phi_1}$ **(A)** and *xx*-covariance component profiles $\langle u'_x(\vec{x}, t_{\phi_1})\, u'_x(\vec{x}, t_{\phi_1})\rangle_{\phi_1}$ **(B)** from DNS and from DA predictions: along a line parallel to the *y*-axis crossing the center of the cylinder at $x = 9$ (left); along a line parallel to the *y*-axis crossing the vortex street at $x = 15$ (right). **(C)** Comparison between the flow field of the ground-truth DNS and of the DA predictions: $\langle u_x(\vec{x}, t_{\phi_1})\rangle_{\phi_1}$.

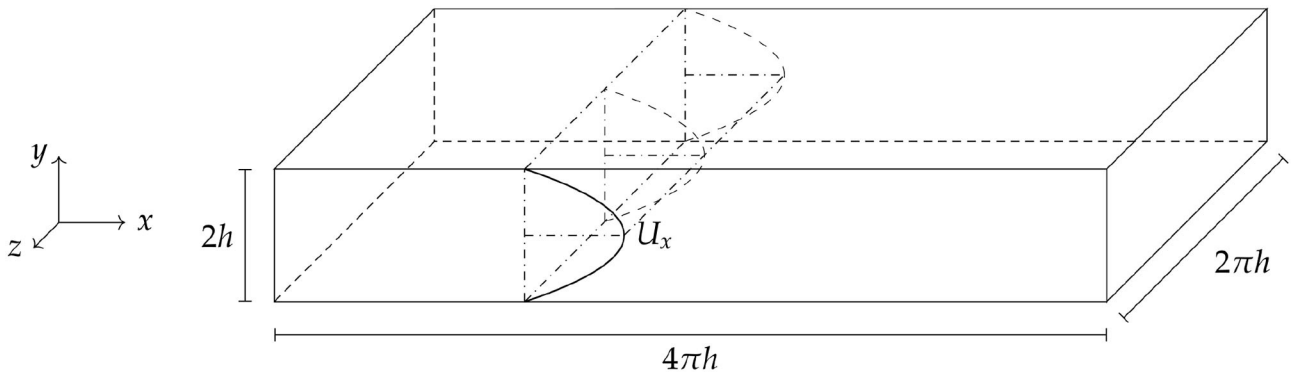

FIGURE 6 | Configuration of the turbulent channel flow. The initial Poiseuille flow has maximum stream-wise velocity U_x.

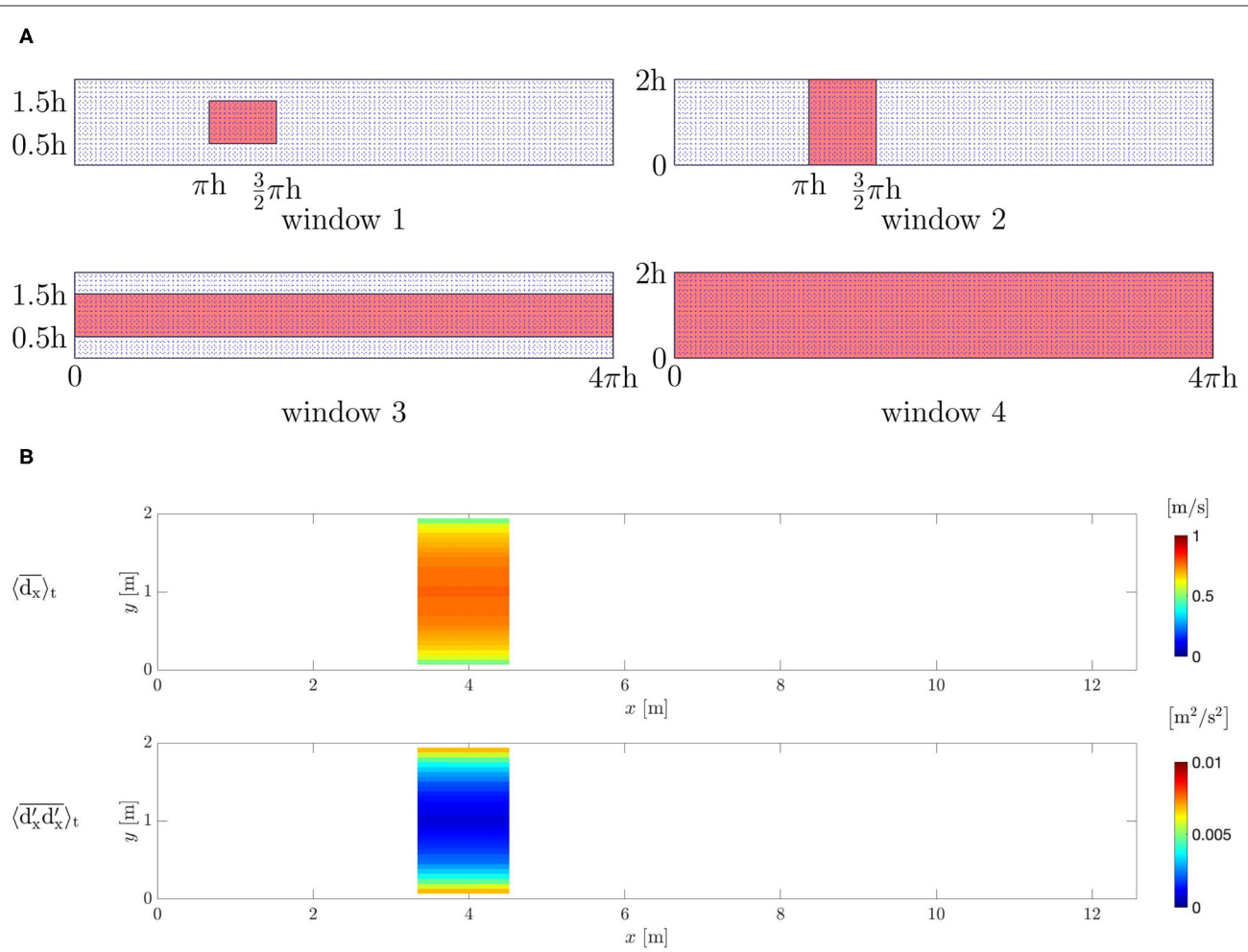

FIGURE 7 | Turbulent channel flow. **(A)** *z*-plane sections of the selected windows in the channel. **(B)** Mean *x*-velocity and associated *xx*- covariance component observed from the ground-truth DNS within window 2.

windows. The results are in good agreement with the ground truth, even though they are slightly underestimated. The value of the *TKE* computed in the DA predictions are also good for all configurations. The values of *TKE* stabilize around 0.55 $[m^2/s^2]$ for all the DA predictions and the more visible differences with respect to the ground truth are in the amplitude of fluctuations. The best agreement is obtained in DA 4. In contrast, the other data windows lead to a loss of accuracy with respect to the ground

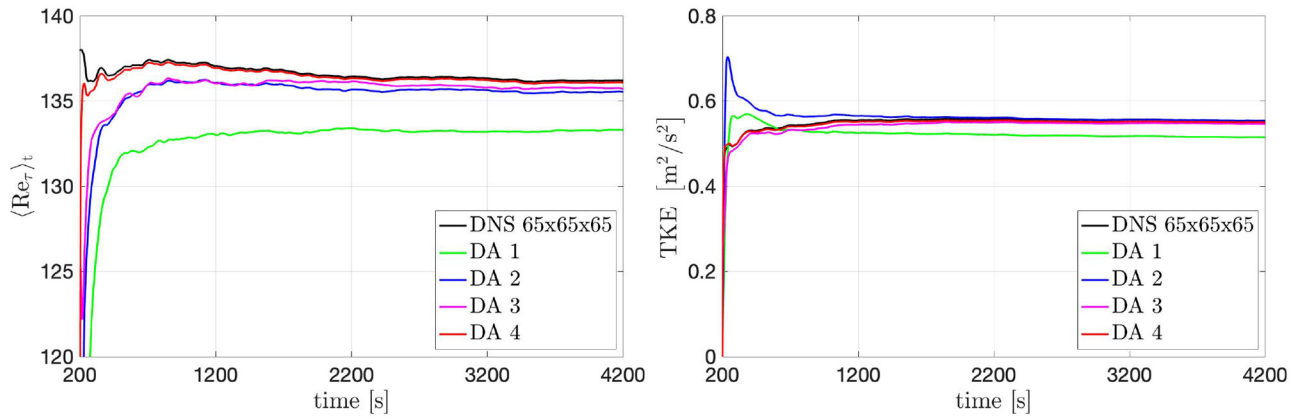

FIGURE 8 | Turbulent channel flow: $\langle Re_\tau \rangle_t$ (left) and TKE(t) (right) evolution over time obtained by using data acquired from different windows.

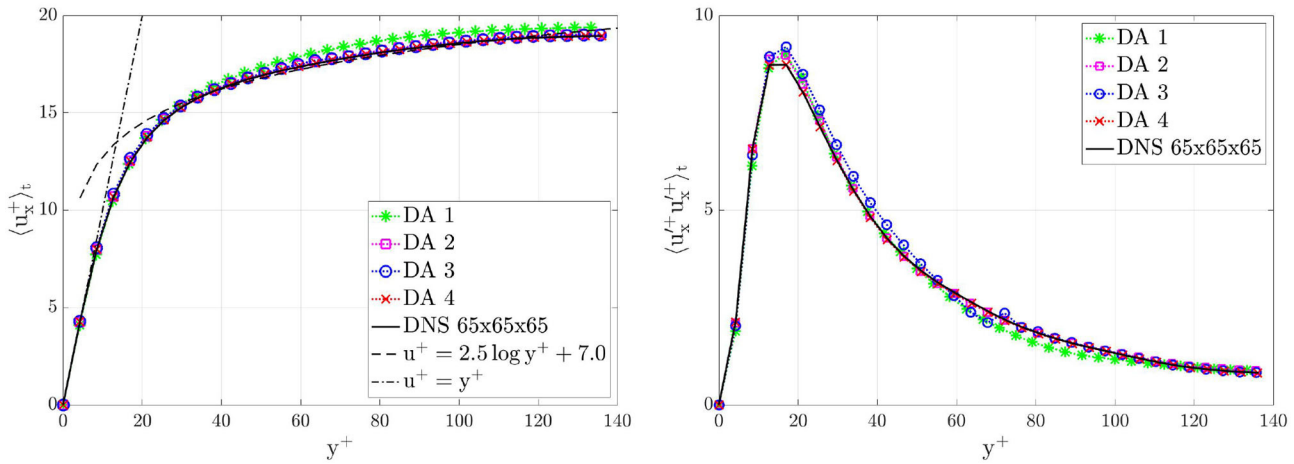

FIGURE 9 | Turbulent channel flow: comparison between DA predictions and ground truth on a line parallel to the y-axis and centered in the z-direction, i.e., $z = \pi h$, for $x = 3\pi h$. Left: stream-wise mean velocity profiles $\langle u_x\,(x = 3\pi h, y, z = \pi h, t)\rangle_t$. Right: RSS profiles $\langle u_x'\,(x = 3\pi h, y, z = \pi h, t)\,u_x'\,(x = 3\pi h, y, z = \pi h, t)\rangle_t$. Results are plotted in wall units and are shown for the bottom half part of the channel, i.e., $y \leq h$.

truth. DA 1 returns the least accurate trends, and extension of the window in x- and y-directions, i.e., DA 2 and DA 3, significantly improves accuracy. This means that larger amounts of available data yields DA predictions that tend closer to the ground truth with a shorter numerical transient. For the same reason, DA 4 returns the most accurate predictions.

The time-averaged velocity $\langle u_x^+\,(\vec{x}, t)\rangle_t$ profiles computed after 4,000 time units are in almost perfect agreement with the ground-truth profile. **Figure 9** shows the comparison between DA prediction and ground truth of the velocity profile $\langle u_x^+\,(\vec{x}, t)\rangle_t$ and the RSS profile $\langle u_x'^+\,(\vec{x}, t)\,u_x'^+\,(\vec{x}, t)\rangle_t$ on a line parallel to the y-axis and centered in the z-direction, for $x = 3\pi h$. The DA predictions recover the logarithmic law of the wall $u^+ = Ay^+ + B$ (42). The precision slightly decreases for DA 1 where not enough data have been used. Moreover, in the boundary region, the RSS profile $\langle u_x'^+\,(\vec{x}, t)\,u_x'^+\,(\vec{x}, t)\rangle_t$ present different peaks in the different DA predictions. The more data are used in DA predictions, the higher the accuracy is. The loss of accuracy for DA 1 is in agreement with the loss of accuracy of the global parameters evolution shown in the **Figure 8**.

3.2.4. Downsampling

In the previous section we evaluated the influence of different window sizes on the accuracy of the results in the DA predictions. Here we want to evaluate the influence of the spatial resolution of the data extracted from the ground-truth solution. To do this, the resolution of the data in window 4 has been down-sampled meaning that the data voxels have a bigger size and the data values are obtained averaging the ground-truth solution over voxels formed by a bigger number of adjacent grid-nodes. The downsampling factor (dw) characterizes the resolution of the data acquisition: for instance, a dw of 2 means that each $\vec{d}_n$ is obtained averaging the ground-truth solution over voxels

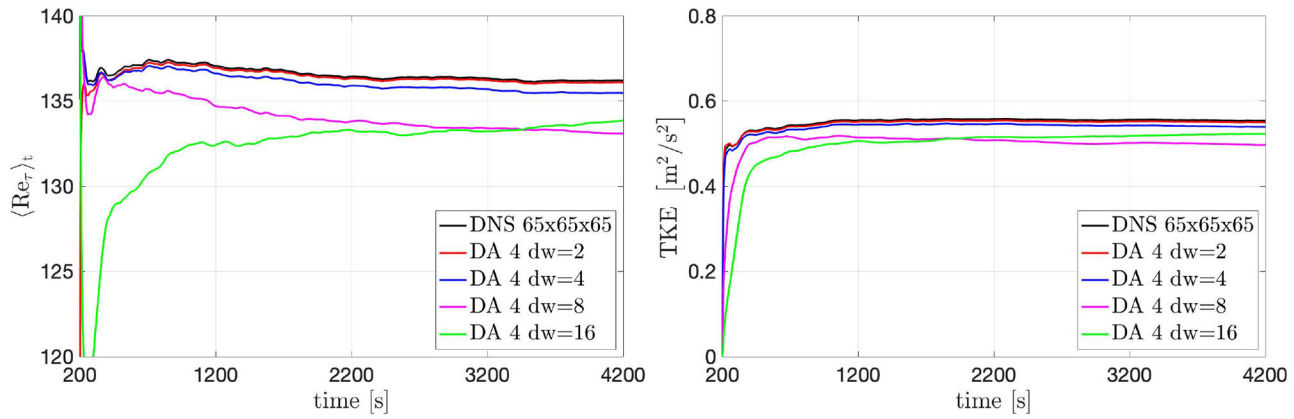

FIGURE 10 | Turbulent channel flow: $\langle Re_\tau \rangle_t$ (left) and *TKE* (t) (right) evolution over time obtained by using data acquired from window 4 with different downsamplings.

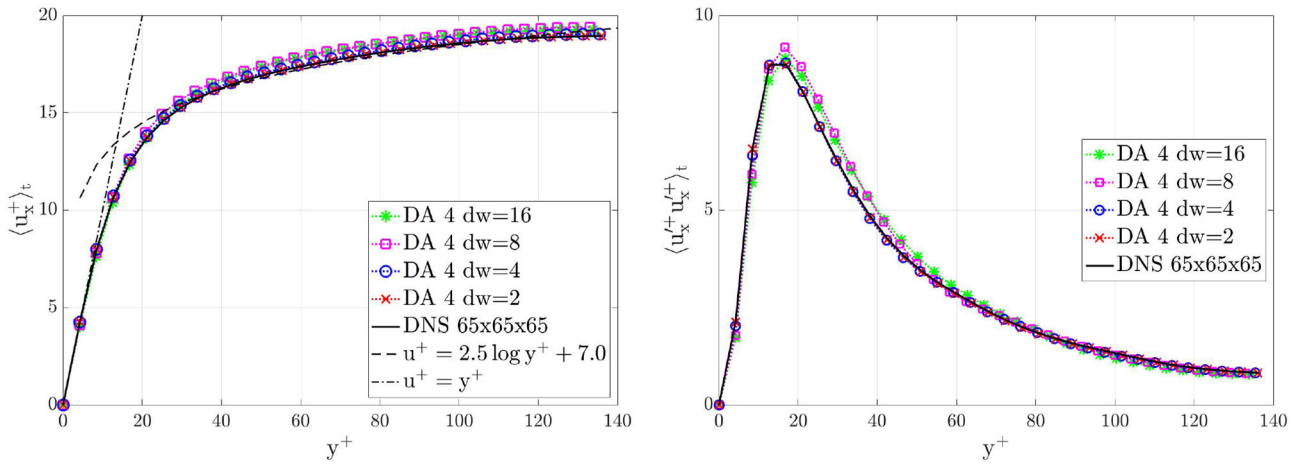

FIGURE 11 | Turbulent channel flow: comparison between DA predictions obtained by using data acquired from window 4 with different downsamplings and ground truth on a line parallel to the y-axis and centered in the z-direction, i.e., $z = \pi h$, for $x = 3\pi h$. Left: stream-wise mean velocity profiles $\langle u_x\,(x = 3\pi h, y, z = \pi h, t)\rangle_t$. Right: RSS profiles $\langle u_x'\,(x = 3\pi h, y, z = \pi h, t)\,u_x'\,(x = 3\pi h, y, z = \pi h, t)\rangle_t$. Results are plotted in wall units and are shown for the bottom half part of the channel, i.e., $y \leq h$.

formed by $(1 + dw) \times (1 + dw) \times (1 + dw)$ adjacent grid-nodes; these voxel-averaged values are then further time-averaged in order to obtain time-and-space averaged data. Here, we analyze the impact of the dw on the results starting from the effect on the $\langle Re_\tau \rangle_t$ and *TKE* (t) evolution, see **Figure 10**. Essentially, a bigger dw (lower data resolution) reduce the accuracy of the solution in the DA predictions: this loose of accuracy is due to the. The results obtained with $dw = 2$ and $dw = 4$ are in a very good agreement with the ground-truth results for both $\langle Re_\tau \rangle_t$ and *TKE* (t).

Figure 11 shows the comparison between DA prediction and ground truth of the velocity profile $\langle u_x^+ (\vec{x}, t)\rangle_t$ profile and the RSS profile $\langle u_x'^+ (\vec{x}, t)\, u_x'^+ (\vec{x}, t)\rangle_t$ on a line parallel to the y-axis and centered in the z-direction, computed after 4,000 time units. Downsampling the data increases the magnitude of the covariance $\mathbf{r}_n$ such that the filter will trust in them less than in the forecast solution given by the numerical solver. The recovery of the log law and the RSS peak predictions slightly deteriorate for higher downsamplings. Even though the unperturbed initial conditions of the flow would not have shown a transition to turbulence without the filter forcing, the boundary conditions are able to maintain the turbulence. After the numerical transient, the loose of accuracy due to the down-sampled data is compensated by the numerical solver. This is an important result because it means that the filter is able to give the correct importance to the two different sources of information.

3.3. Pulsatile Turbulent Flow Downstream a Bioprosthetic Transcatheter Aortic Valve

Here, the configuration setup for a pulsatile turbulent flow past a self-expandable Transcatheter Aortic Valve (TAV) with a heart-rate equal to 70 [beat/min] is investigated in the aortic region

TABLE 1 | Pulsatile turbulent flow downstream a bioprosthetic heart valve: division of the pulse period T in $N_\Phi^{exp} = 22$ intervals and $N_\Phi^{num} = 66$ intervals.

ϕ_i^{exp}	**1**	**2**	**3**	**4**	**5**	**6**	**7**	**8**	**9**	**10**	**11**	
$t_{\phi_i^{exp}}$ [s]	0.05	0.06	0.07	0.08	0.09	0.10	0.11	0.12	0.13	0.14	0.15	
ϕ_i^{exp}	**12**	**13**	**14**	**15**	**16**	**17**	**18**	**19**	**20**	**21**	**22**	
$t_{\phi_i^{exp}}$ [s]	0.16	0.17	0.20	0.25	0.30	0.35	0.40	0.45	0.50	0.60	0.70	
ϕ_i^{exp}	**1**			**2**	…	…	**21**			**22**		
ϕ_i^{num}	**1**	**2**	**3**	**4**	…	…	**61**	**62**	**63**	**64**	**65**	**66**
$t_{\phi_i^{num}}$ [s]	0.05	0.0533	0.0566	0.06	…	…	0.60	0.633	0.666	0.70	0.769	0.838

Numerical time intervals have been obtained by refining by a factor of 3 the temporal resolution of each time interval of the experimental data.

downstream the valve. The positive y-direction define the stream-wise direction, while the x- and z-direction are the span-wise ones. The Reynolds number is set to 4, 900, based on the nominal diameter $d = 23$ [mm] of the TAV, on the peak (systolic) velocity $U_y = 1$ [m/s] and on the kinematic viscosity ν of the fluid. In this case, no ground truth is available but only experimental data. Moreover, blood flow modeling uncertainty has to be taken into account.

3.3.1. Data Acquisition

The generation of the data $\vec{d}_{v;(s),\phi}$ to be used in the DA predictions has been provided by an experimental setup. The TAV was implanted in a quasi-stiff aortic silicon phantom of the aortic root and integrated in a hydraulic pulse duplicator. Tomographic Particle Image Velocimetry (Tomo-PIV) (43, 44) was used to reconstruct the three-dimensional flow fields in the region of interest. The pulse period $T = 60.0/70$ [s] has been divided in $N_\Phi^{exp} = 22$ intervals as described in the **Table 1**.

The experimental grid domain has a size of 35 [mm] × 50 [mm] × 35 [mm] and consists of 42 × 59 × 42 voxels. Each voxel-and-phase-averaged data has been computed by using 24 repetitions of the heart-pulse, and the covariance of the error of the PIV data results from a phase averaging of instantaneous voxel data fields taken at 24 pulses. Outside the region of interest, the data (velocity and corresponding uncertainty) have been set to zero in order to replicate the presence of the aortic walls. Of course there are additional errors due to the PIV methodology itself which are not considered in the present investigation.

3.3.2. Comparison Between Experiments, Direct Numerical Simulation and Data Assimilation Prediction

Two simulations have been performed for a time equal to $120T$: a DNS where the experimental data are used only to impose inflow and wall boundary conditions; and a DA prediction where the experimental data are used also to filter the forecast flow field by using the DA methodology. The pulse period has been divided in $N_\Phi^{num} = 66$ intervals obtained by refining by a factor of 3 the temporal resolution of each time interval of the experimental data, as shown in the **Table 1**.

The computational grid used for both DNS and DA prediction has been obtained by refining the experimental grid by a factor of 2 in each direction and then adding an external padding equal to at least 10% to each side of the three-dimensional domain. The final size of the computational grid domain is 44 [mm] × 60 [mm] × 44 [mm] and consists of 105 × 145 × 105 grid nodes. Mapping the voxel-grid onto the computational grid leads to $g_v = 3 \times 3 \times 3$ grid-nodes lying inside the corresponding voxel. We use periodic boundary conditions for the full computational domain with padding. In both simulations, the presence of the aortic wall and the physical inflow conditions are enforced *via* the fringe forcing method (cf. Section 2.4). The experimental data forced to zero outside the region of interest and the lowest 5 y-plane slices data are used as desired values $\vec{U}$ of the fringe forcing applied in order to impose wall and inflow boundary conditions, respectively. Since the inflow is time dependent, it is not appropriate to use a constant value for λ in the Equation (41). Here, a time-dependent λ has been chosen such that it guarantees the stability condition of the Runge–Kutta time-advancement scheme:

$$\lambda(RK_{substep}, \Delta t) = \frac{1.0}{\alpha(RK_{substep})\Delta t}, \tag{46}$$

where Δt is the numerical time step and α is the first Runge–Kutta coefficient for each Runge–Kutta substep $RK_{substep}$. The inflow boundary conditions for the intermediate numerical time-steps have been imposed by linear interpolation in time of the voxel data. The bulk flow voxel data are used only to perform DA prediction. The initial flow field is set to zero. A sketch of the configuration can be seen in **Figure 12**.

The results obtained by the experiments, DNS and DA prediction have been compared to evaluate the capability of the DA methodology to enhance the spatial and temporal resolution of the observations and to increase the reliability of the characteristic flow patterns captured from the numerical solver. Herein, the systolic phase-averaged velocity $\langle u_y(\vec{x}, t_\phi)\rangle_\phi$ obtained by the Tomo-PIV experiments, DNS and the DA prediction are shown in **Figures 13A,B** for x-plane and z-plane, respectively.

The DNS and DA prediction present an enhancement in time resolution with respect to the experimental data. The boundary conditions extracted by the experimental data drive the flow in the intermediate iterations between two subsequent applications of the filter. This is an important result because it has been possible to simulate the cardiovascular turbulent flow downstream the heart valve numerically without the need for Fluid-Structure-Interaction methods.

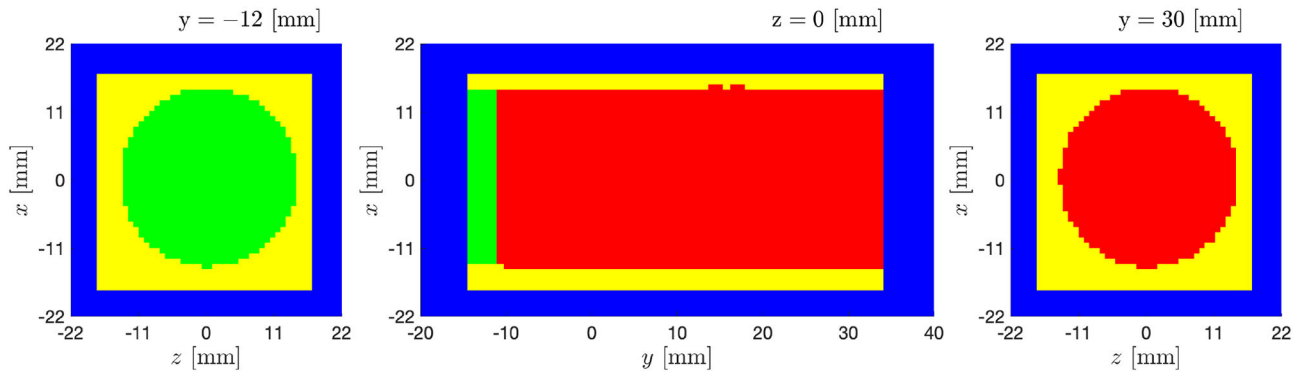

FIGURE 12 | Pulsatile turbulent flow downstream of a transcatheter aortic valve: Numerical setup. The experimental grid is overlapped onto the computational domain (blue). The wall boundary conditions are imposed in the yellow region which includes data masked in the experiments; The inflow boundary conditions are imposed in the green region; DA is performed in the red region.

In the DNS, the results show a global overestimation of the velocity field. This is due to boundary condition uncertainty and blood modeling uncertainty. The DA prediction is affected by the same boundary condition and blood modeling uncertainties but the DA prediction strongly reduces the overestimation of the DNS velocity field. It means that the use of the DA methodology has improved the reliability of the velocity field results. The three leaflet jet coming from the bioprosthetic valve seems to be better defined in DA prediction (see, e.g., $t = 0.175T$ slice, in **Figure 13A**). In the lower part the back flow near the left wall, the DA prediction present a smoother flow field (see **Figure 13B**). This is due to the higher capability of the numerical solver to investigate that region which is, on the contrary, a more difficult challenge for the experimental tool. It is noteworthy that the DA prediction presents a smaller reverse flow region: the filter trust more in the numerical solver and consider the bigger reverse flow region present in the experiments too uncertain with respect to the forecast solution. Moreover, the DA methodology filters the information coming from those voxel data near the wall that are evidently affected by a tool acquisition error. This error is not visible anymore in DA prediction.

Figure 14A shows the evolution of the flow field for increasingly larger number of pulses performed by the DA algorithm. Velocity profiles from DA prediction, DNS, and experiments are compared in **Figure 14B** along two lines parallel to y-axis. The results show that the flow field prediction has reached a good convergence after 120 pulses.

The finer spatial and time resolution obtained in the DA prediction enhanced the flow field of this specific configuration. This is an important and promising result for future applications of the proposed DA methodology on *in vivo* data from Flow-MRI of patient-specific configurations.

4. DISCUSSION

In the present manuscript, a new DA methodology has been presented. The robust theoretical background of the (S)EnKF approaches has been applied to pulsatile and turbulent flow configurations. The different ensemble-averaging approaches, that were presented here, show how the study of turbulent flows can be reduced to the definition and the subsequent investigation of the most important statistical properties of the flow, such as mean velocity and the associated fluctuations covariance.

In the context of turbulent flows, the proposed SEnKF-based methodology states as hypothesis that the "true" state-of-system is the mean velocity field. Turbulent fluctuations are deviations from the ensemble-averaged quantities. This leads to the formal equality between turbulent fluctuations and the observation error $\vec{r}_n$ required in the derivation of a SEnKF.

In the derivation of our DA methodology, the definition of the states of the ensemble allows us to treat the forecast error $\vec{q}_n$ in the proper way: this error has zero mean and the contribution of the covariance of the numerical error $\vec{q}_{n_{NUM}}$ will be negligible compared with the one of the turbulent error $\vec{q}_{n_{TUR}}$ and modeling error $\vec{q}_{n_{MOD}}$. In the first two test cases (sections 3.1, 3.2), the model is well defined and therefore $\vec{q}_{n_{MOD}}$ is zero. In the last test case (section 3.3), DNS and DA predictions are affected by the same $\vec{q}_{n_{MOD}}$. Therefore, only the turbulent error is relevant in the present study.

The choice of the ensemble of states-of-system in the case of pulsatile and turbulent flows allows one to filter the forecast solution at each time t_n with the corresponding data flow field; this yields to an additional but constant computational cost for each pulse interval.

From a numerical point of view, filtering the forecast solution with a forcing term only in nonconsecutive time-step iterations could be seen as forcing the flow field with a temporal Dirac δ function. This would lead to numerical oscillations in the intermediate iterations between two filtering iterations and to a local non-smooth advancement in time of the numerical solution.

First, the DA methodology has been validated vs. an unsteady flow past a cylinder confined in a channel using data acquired

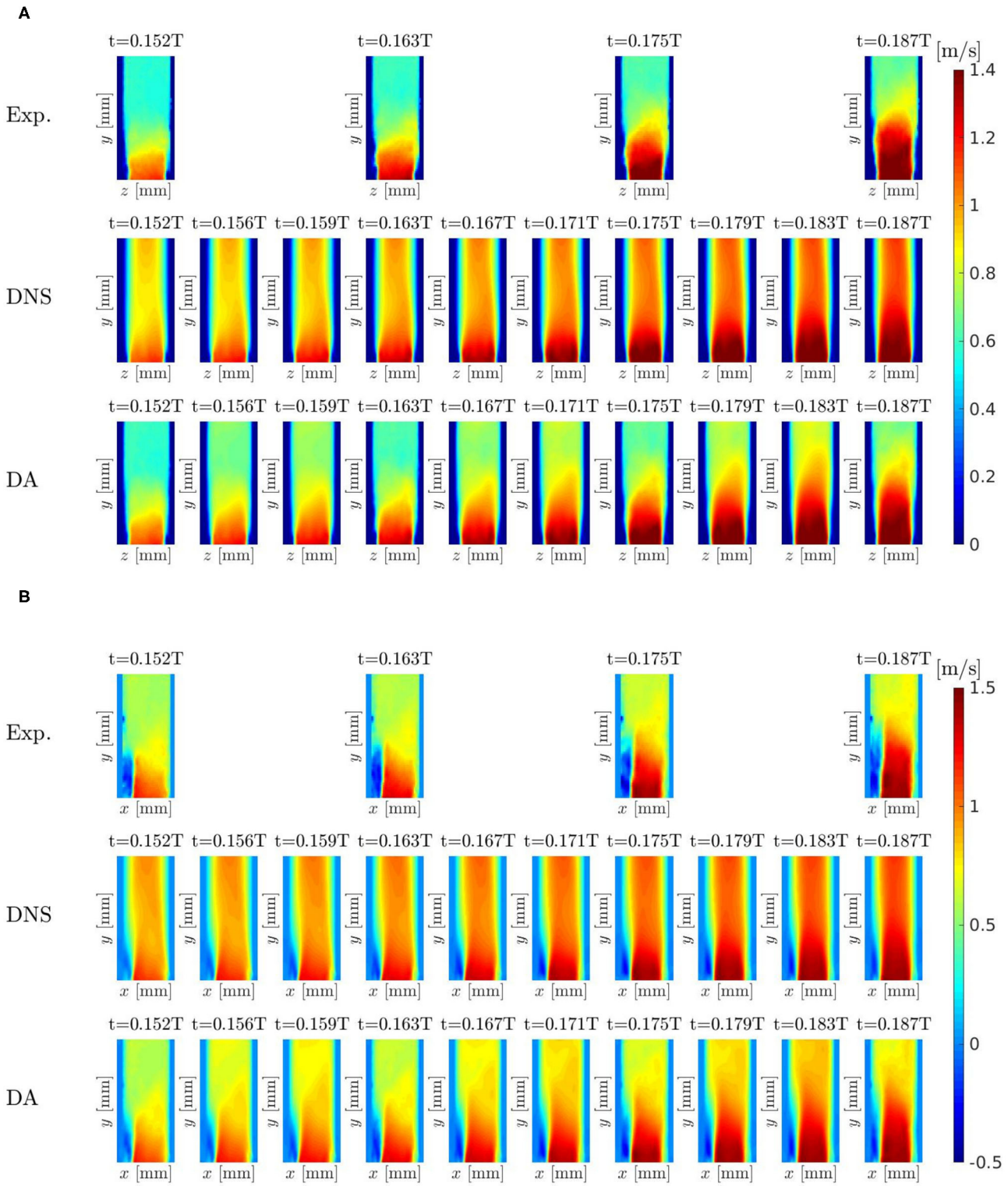

FIGURE 13 | Pulsatile turbulent flow downstream of a transcatheter aortic valve: comparison between experiments, DNS, and DA prediction of velocity field $\langle u_y(\vec{x}, t_\phi)\rangle_\phi$ for $x = 0$ **(A)** and for $z = 0$ **(B)**.

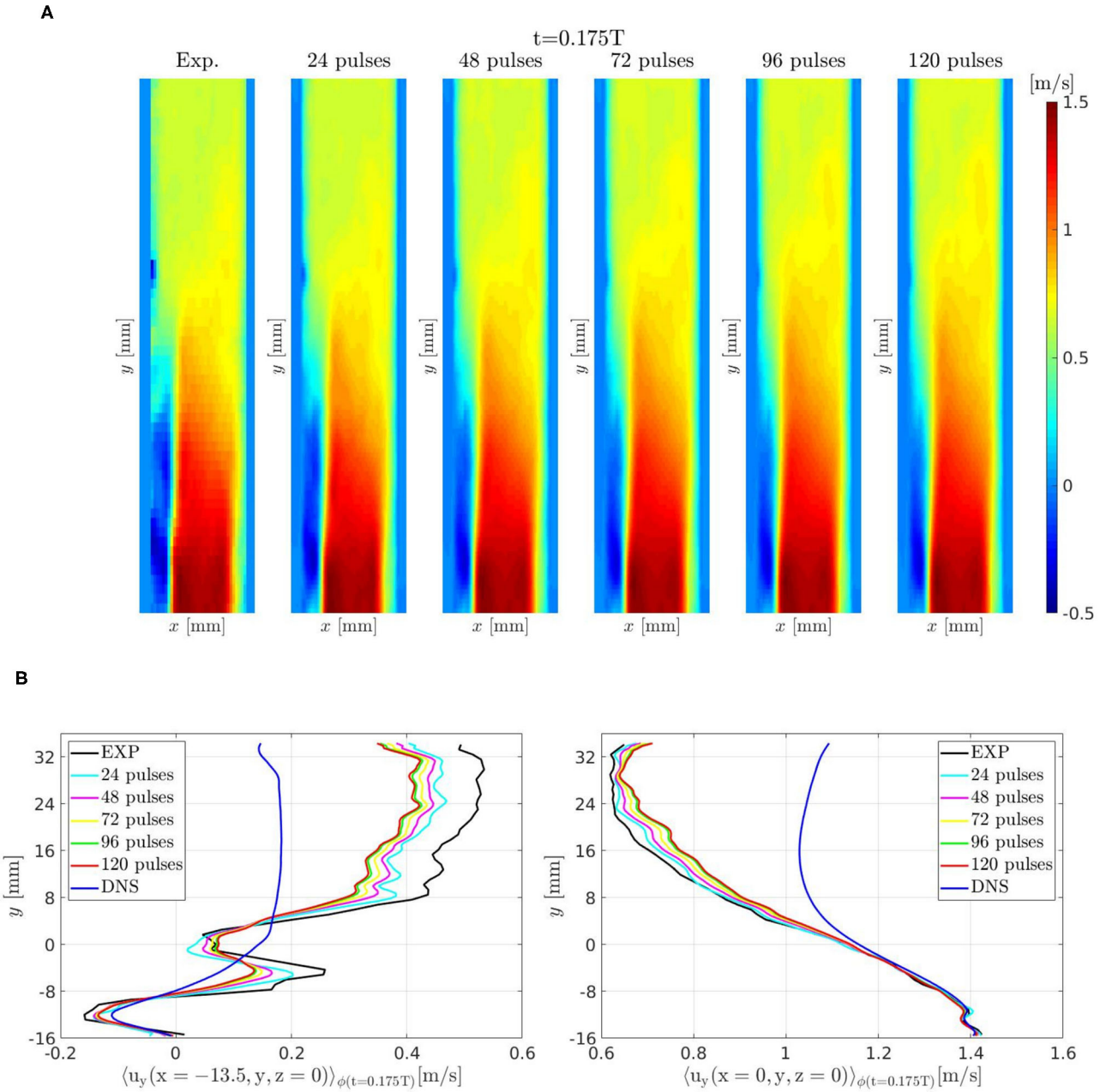

FIGURE 14 | Pulsatile turbulent flow downstream of a transcatheter aortic valve: **(A)** velocity field $\langle u_y\,(x, y, z = 0, t_\phi = 0.175T)\rangle_\phi$ obtained by the DA algorithm for increasingly larger number of pulses. **(B)** Velocity profiles along a line parallel to y-axis and crossing the reverse flow region, $x = -13.5$ mm and $z = 0$, (left) and along the centerline, $x = z = 0$, (right).

from previous numerical simulations. In the DA predictions, the presence of the cylinder was not taken into account by using any boundary conditions but nevertheless the reconstruction of the wake downstream the cylinder has been successfully reconstructed by filtering the forecast solution with the data. The test shows that the DA method, and in particular the proposed choice of the ensemble of states-of-system, copes with unsteady flow field presenting a periodicity in time.

Second, the methodology was extended to turbulent flow applications. The statistically-steady configuration of the wall-bounded turbulent flow shows that the turbulent features can be reconstructed by using the data even though the numerical simulation is initialized with a laminar flow which would not exhibit a transition to turbulence by itself. The effect of the different data configurations on the bulk flow and on the walls has been investigated. Downsampling the resolution of data

acquisition leads to a loss of accuracy in the DA prediction that is limited to 5%.

Finally, the methodology has been applied to pulsatile and turbulent configuration of a flow past a bioprosthetic heart valve. The data of a pulsatile turbulent flow past a TAV, acquired by a Tomo-PIV technique have been used to reconstruct the wake in the aorta in a computational simulation with higher spatial and temporal resolution. The test-case shows how the DA methodology deals with FSI applications even though no structural modeling is required. The results show the capability, the robustness and the accuracy of the proposed methodology to cope with realistic configurations of biomedical applications.

The presented results show that the filter is capable of interpreting the accuracy and reliability of the data with respect to the numerical solution giving locally a different weight to the two different sources of information. A bigger amount of data, although with greater uncertainty, allows to lead the solution of the DA method closer to the true-state of the system. This is useful in heart valve applications where the data acquired by experimental investigations or through 4D Flow MRI techniques suffer from lower accuracy near the walls; these noisy data are filtered and the higher accuracy of the numerical solver will return a better description of the flow field in such regions. On the other hand the available data of the specific-patient configuration will increase the accuracy of the numerical solution in the bulk flow if compared with the solution obtained by using a FSI solver employing a simplified morphology of the aortic valve and aortic root.

A first limitation of the methodology is that we consider the covariance across different voxels to be zero. This is equivalent of assuming that the autocorrelation length is less than the voxel size h. This limitation might be overcome solving with higher computational cost the analysis step by using the global matrices $\mathbf{H}$, $\mathbf{P}^f$ and $\mathbf{R}$ instead of $\mathbf{h}$, $\mathbf{p}^f$ and $\mathbf{r}$. A second limitation of the methodology is represented by the definition of the matrix $\mathbf{D}$ which is required to ensure positiveness of covariance matrix $\mathbf{p}^f$. From a theoretical point of view $\mathbf{D}$ influence disappears for increasingly large ensembles, but the choice of its value strongly affects the convergence history of the DA prediction. For $\mathbf{D}$ too high, the DA prediction will require a larger number of cycles in order to reach a converged solution for both mean velocity and covariance. Moreover, a large value of $\mathbf{D}$ reduces the physical meaning of the matrix $\mathbf{p}^f$ and this will influence the sensitivity of the filter. On the other hand, for $\mathbf{D}$ too low the forecast solution would be considered closer to the "true" state-of-system by the filter even though it cannot be stated a priori. In conclusion, the value of $\mathbf{D}$ has to be chosen high and run the DA prediction for the required number of cylces until convergence is reached. For this reason, in the DA prediction of the pulsatile turbulent flow downstream a bioprosthetic heart valve, 120 pulses (5 times the number of repetitions available by the experiments) have been enough to enhance the description of the mean flow fields with respect to the observations, but have not produced a significant improvement of the *RSS* fields. The investigation of the *RSS* fields requires to collect a larger ensemble for both matching the classical requirements on the ensemble size of turbulent statistics and fully overcoming the influence of $\mathbf{D}$. The sensitivity of the proposed methodology to the matrix $\mathbf{D}$ and the size of ensemble needed for convergence in these cardiovascular applications in the ascending aorta will be further investigated in order to estimate the computational cost required to enhance *RSS* fields. A further limitation is that synthetic experimental data have been created without adding any Gaussian error after spatially averaging inside the voxel, even though this has been previously done in literature. This choice has been made here, because we want to focus our investigations on the effect of turbulent fluctuations (considered as measurement noise). Additional noise may pose additional problems to the described method, in particular, because the real noise in MRI data has a non-Gaussian character. In practice, 4D flow MRI quantification would require more complex methods in order to quantify the effects of these hardware source of errors. Specific methods have been developed for creating synthetic 4D flow MRI data from raw Phase Contrast MRI data to better assess turbulent features, e.g., turbulence intensity and TKE (45–50), and for completely excluding the effects of the hardware source errors by generating synthetic MRI data fields (51).

In conclusion, the results show that the method is promising for future use with *in vivo* data from 4D Flow MRI.

DATA AVAILABILITY STATEMENT

The raw data supporting the conclusions of this article will be made available by the authors, without undue reservation.

AUTHOR CONTRIBUTIONS

DD and DO wrote the manuscript and reviewed the manuscript and designed the data assimilation method. DD implemented the data assimilation method in the numerical solver and performed the simulations. DO supervised the scientific work. Both authors contributed to the article and approved the submitted version.

FUNDING

This research was supported by the Platform for Advanced Scientific Computing (PASC, http://www.pasc-ch.org) under the HPC-PREDICT project (https://www.pasc-ch.org/projects/2017-2020/hpc-predict).

ACKNOWLEDGMENTS

The authors acknowledge Valérie Kulka and Derick Sivakumaran who contributed in developing post-processing tools; David Hasler and Leonardo Pietrasanta who provided the Tomo-PIV experimental data. The authors also acknowledge the support of the Swiss National Supercomputing Center (CSCS, http://www.cscs.ch).

REFERENCES

1. Binter C, Gotschy A, Sündermann SH, Frank M, Tanner FC, Lüscher TF, et al. Turbulent kinetic energy assessed by multipoint 4-dimensional flow magnetic resonance imaging provides additional information relative to echocardiography for the determination of aortic stenosis severity. *Circ Cardiovasc Imaging*. (2017) 10:e005486. doi: 10.1161/CIRCIMAGING.116.005486
2. Kalman RE. A new approach to linear filtering and prediction problems. *J Basic Eng*. (1960) 82:35–45. doi: 10.1115/1.3662552
3. Sorenson HW. *Kalman Filtering: Theory and Application*. IEEE Press (1985).
4. Evensen G. Sequential data assimilation with a nonlinear quasi-geostrophic model using Monte Carlo methods to forecast error statistics. *J Geophys Res*. (1994) 99:10143–62. doi: 10.1029/94JC00572
5. Burgers G, Jan van Leeuwen P, Evensen G. Analysis scheme in the ensemble Kalman filter. *Mon Weather Rev*. (1998) 126:1719–24. doi: 10.1175/1520-0493(1998)126<1719:ASITEK>2.0.CO;2
6. Houtekamer PL, Mitchell HL. Data assimilation using an ensemble Kalman filter technique. *Mon Weather Rev*. (1998) 126:796–811. doi: 10.1175/1520-0493(1998)126<0796:DAUAEK>2.0.CO;2
7. Hœpffner J, Chevalier M, Bewley TR, Henningson DS. State estimation in wall-bounded flow systems. Part 1. Perturbed laminar flows. *J Fluid Mech*. (2005) 534:263–94. doi: 10.1017/S0022112005004210
8. Chevalier M, Hœpffner J, Bewley TR, Henningson DS. State estimation in wall-bounded flow systems. Part 2. Turbulent flows. *J Fluid Mech*. (2006) 552:167–87. doi: 10.1017/S0022112005008578
9. Colburn C, Cessna J, Bewley T. State estimation in wall-bounded flow systems. Part 3. The ensemble Kalman filter. *J Fluid Mech*. (2011) 682:289–303. doi: 10.1017/jfm.2011.222
10. Gu Y, Oliver DS. An iterative ensemble Kalman filter for multiphase fluid flow data assimilation. *SPE J*. (2007) 12:438–46. doi: 10.2118/108438-PA
11. Harlim J, Majda AJ. Filtering turbulent sparsely observed geophysical flows. *Mon Weather Rev*. (2010) 138:1050–83. doi: 10.1175/2009MWR3113.1
12. Suzuki T. Reduced-order Kalman-filtered hybrid simulation combining particle tracking velocimetry and direct numerical simulation. *J Fluid Mech*. (2012) 709:249–88. doi: 10.1017/jfm.2012.334
13. Meldi M, Poux A. A reduced order model based on Kalman filtering for sequential data assimilation of turbulent flows. *J Comput Phys*. (2017) 347:207–34. doi: 10.1016/j.jcp.2017.06.042
14. Foures DP, Dovetta N, Sipp D, Schmid PJ. A data-assimilation method for Reynolds-averaged Navier-Stokes-driven mean flow reconstruction. *J Fluid Mech*. (2014) 759:404–31. doi: 10.1017/jfm.2014.566
15. Symon S, Dovetta N, McKeon BJ, Sipp D, Schmid PJ. Data assimilation of mean velocity from 2D PIV measurements of flow over an idealized airfoil. *Exp Fluids*. (2017) 58:61. doi: 10.1007/s00348-017-2336-8
16. Mons V, Chassaing JC, Gomez T, Sagaut P. Reconstruction of unsteady viscous flows using data assimilation schemes. *J Comput Phys*. (2016) 316:255–80. doi: 10.1016/j.jcp.2016.04.022
17. Gaidzik F, Stucht D, Roloff C, Speck O, Thévenin D, Janiga G. Transient flow prediction in an idealized aneurysm geometry using data assimilation. *Comput Biol Med*. (2019) 115:103507. doi: 10.1016/j.compbiomed.2019.103507
18. Canuto D, Pantoja JL, Han J, Dutson EP, Eldredge JD. An ensemble Kalman filter approach to parameter estimation for patient-specific cardiovascular flow modeling. *Theor Comput Fluid Dyn*. (2020) 34:521–44. doi: 10.1007/s00162-020-00530-2
19. DeVault K, Gremaud PA, Novak V, Olufsen MS, Vernieres G, Zhao P. Blood flow in the circle of willis: modeling and calibration. *Multiscale Model Simulat*. (2008) 7:888–909. doi: 10.1137/07070231X
20. Arnold A, Battista C, Bia D, German YZ, Armentano RL, Tran H, et al. Uncertainty quantification in a patient-specific one-dimensional arterial network model: EnKF-based inflow estimator. *J Verificat Validat Uncert Quant*. (2017) 2:011002. doi: 10.1115/1.4035918
21. Habibi M, D'Souza RM, Dawson ST, Arzani A. Integrating multi-fidelity blood flow data with reduced-order data assimilation. *Comput Biol Med*. (2021). 135:104566. doi: 10.1016/j.compbiomed.2021.104566
22. Arzani A, Dawson ST. Data-driven cardiovascular flow modelling: examples and opportunities. *J R Soc Interface*. (2021) 18:20200802. doi: 10.1098/rsif.2020.0802
23. Rispoli VC, Nielsen JF, Nayak KS, Carvalho JL. Computational fluid dynamics simulations of blood flow regularized by 3D phase contrast MRI. *Biomed Eng Online*. (2015) 14:1–23. doi: 10.1186/s12938-015-0104-7
24. Koltukluoğlu TS, Blanco PJ. Boundary control in computational haemodynamics. *J Fluid Mech*. (2018) 847:329–64. doi: 10.1017/jfm.2018.329
25. Fathi MF, Bakhshinejad A, Baghaie A, Saloner D, Sacho RH, Rayz VL, et al. Denoising and spatial resolution enhancement of 4D flow MRI using proper orthogonal decomposition and lasso regularization. *Comput Med Imaging Graphics*. (2018) 70:165–72. doi: 10.1016/j.compmedimag.2018.07.003
26. Annio G, Torii R, Ariff B, O'Regan DP, Muthurangu V, Ducci A, et al. Enhancing magnetic resonance imaging with computational fluid dynamics. *J Eng Sci Med Diagn Therapy*. (2019) 2:041010. doi: 10.1115/1.4045493
27. Ferdian E, Suinesiaputra A, Dubowitz DJ, Zhao D, Wang A, Cowan B, et al. 4DFlowNet: super-resolution 4D flow MRI using deep learning and computational fluid dynamics. *Front Phys*. (2020). 8:138. doi: 10.3389/fphy.2020.00138
28. Lewis JM, Derber JC. The use of adjoint equations to solve a variational adjustment problem with advective constraints. *Tellus A*. (1985) 37:309–322. doi: 10.3402/tellusa.v37i4.11675
29. Le Dimet FX, Talagrand O. Variational algorithms for analysis and assimilation of meteorological observations: theoretical aspects. *Tellus A*. (1986) 38:97–110. doi: 10.3402/tellusa.v38i2.11706
30. Evensen G, Van Leeuwen PJ. An ensemble Kalman smoother for nonlinear dynamics. *Mon Weather Rev*. (2000) 128:1852–67. doi: 10.1175/1520-0493(2000)128<1852:AEKSFN>2.0.CO;2
31. Henniger R, Obrist D, Kleiser L. High-order accurate solution of the incompressible Navier-Stokes equations on massively parallel computers. *J Comput Phys*. (2010) 229:3543–72. doi: 10.1016/j.jcp.2010.01.015
32. Henniger R, Kleiser L, Meiburg E. Direct numerical simulations of particle transport in a model estuary. *J Turbulence*. (2010) 11:N39. doi: 10.1080/14685248.2010.516257
33. John MO, Obrist D, Kleiser L. Stabilisation of subcritical bypass transition in the leading-edge boundary layer by suction. *J Turbulence*. (2014) 15:795–805. doi: 10.1080/14685248.2014.933226
34. Burns P, Meiburg E. Sediment-laden fresh water above salt water: nonlinear simulations. *J Fluid Mech*. (2015) 762:156. doi: 10.1017/jfm.2014.645
35. Nestola MGC, Becsek B, Zolfaghari H, Zulian P, De Marinis D, Krause R, et al. An immersed boundary method for fluid-structure interaction based on variational transfer. *J Comput Phys*. (2019) 398:108884. doi: 10.1016/j.jcp.2019.108884
36. Becsek B, Pietrasanta L, Obrist D. Turbulent systolic flow downstream of a bioprosthetic aortic valve: velocity spectra, wall shear stresses, and turbulent dissipation rates. *Front Physiol*. (2020) 11:577188. doi: 10.3389/fphys.2020.577188
37. Nordström J, Nordin N, Henningson D. The fringe region technique and the fourier method used in the direct numerical simulation of spatially evolving viscous flows. *SIAM J Sci Comput*. (1999) 20:1365–93. doi: 10.1137/S1064827596310251
38. Kim J, Moin P, Moser R. Turbulence statistics in fully developed channel flow at low Reynolds number. *J Fluid Mech*. (1987) 177:133–66. doi: 10.1017/S0022112087000892
39. Pedley TJ. *The Fluid Mechanics of Large Blood Vessels*. Cambridge: Cambridge Monographs on Mechanics; Cambridge University Press (1980).
40. Schlatter P, Stolz S, Kleiser L. Evaluation of high-pass filtered eddy-viscosity models for large-eddy simulation of turbulent flows. *J Turbulence*. (2005) 6:N5. doi: 10.1080/14685240500103127
41. Schmid P, Henningson DS. *Stability and Transition in Shear Flows*. New York, NY: Springer (2000).
42. Pope SB. *Turbulent Flows*. Cambridge: Cambridge Univ. Press (2011).
43. Hasler D, Landolt A, Obrist D. Tomographic PIV behind a prosthetic heart valve. *Exp Fluids*. (2016) 57:80. doi: 10.1007/s00348-016-2158-0
44. Hasler D, Obrist D. Three-dimensional flow structures past a bio-prosthetic valve in an *in-vitro* model of the aortic root. *PLoS ONE*. (2018) 13:e0194384. doi: 10.1371/journal.pone.0194384

45. Ha H, Lantz J, Haraldsson H, Casas B, Ziegler M, Karlsson M, et al. Assessment of turbulent viscous stress using ICOSA 4D Flow MRI for prediction of hemodynamic blood damage. *Sci Rep*. (2016) 6:1–14. doi: 10.1038/srep39773
46. Ziegler M, Lantz J, Ebbers T, Dyverfeldt P. Assessment of turbulent flow effects on the vessel wall using four-dimensional flow MRI. *Magn Reson Med*. (2017) 77:2310–19. doi: 10.1002/mrm.26308
47. Ha H, Kvitting JP, Dyverfeldt P, Ebbers T. Validation of pressure drop assessment using 4D flow MRI-based turbulence production in various shapes of aortic stenoses. *Magn Reson Med*. (2019) 81:893–906. doi: 10.1002/mrm.27437
48. Ha H, Kvitting JPE, Dyverfeldt P, Ebbers T. 4D Flow MRI quantification of blood flow patterns, turbulence and pressure drop in normal and stenotic prosthetic heart valves. *Magn Reson Imag*. (2019). 55:118–27. doi: 10.1016/j.mri.2018.09.024
49. Walheim J, Dillinger H, Gotschy A, Kozerke S. 5D flow tensor MRI to efficiently map Reynolds stresses of aortic blood flow *in-vivo*. *Sci Rep*. (2019). 9:1–12. doi: 10.1038/s41598-019-55353-x
50. Walheim J, Dillinger H, Kozerke S. Multipoint 5D flow cardiovascular magnetic resonance-accelerated cardiac-and respiratory-motion resolved mapping of mean and turbulent velocities. *J Cardiovasc Magn Reson*. (2019) 21:1–13. doi: 10.1186/s12968-019-0549-0
51. Puiseux T, Sewonu A, Moreno R, Mendez S, Nicoud F. Numerical simulation of time-resolved 3D phase-contrast magnetic resonance imaging. *PLoS ONE*. (2021) 16:e0248816. doi: 10.1371/journal.pone.0248816

Conflict of Interest: The authors declare that the research was conducted in the absence of any commercial or financial relationships that could be construed as a potential conflict of interest.

Publisher's Note: All claims expressed in this article are solely those of the authors and do not necessarily represent those of their affiliated organizations, or those of the publisher, the editors and the reviewers. Any product that may be evaluated in this article, or claim that may be made by its manufacturer, is not guaranteed or endorsed by the publisher.

frontiers in Bioengineering and Biotechnology

ORIGINAL RESEARCH
published: 25 November 2021
doi: 10.3389/fbioe.2021.725121

Left Ventricular Flow Distribution as a Novel Flow Biomarker in Atrial Fibrillation

Hansuk Kim[1,2,3], *Hana Sheitt*[2,3,4,5,6], *Stephen B. Wilton*[3,4], *James A. White*[2,4] *and Julio Garcia*[2,3,4,5,6]*

[1]Biomedical Engineering Graduate Program, University of Calgary, Calgary, AB, Canada, [2]Stephenson Cardiac Imaging Centre, University of Calgary, Calgary, AB, Canada, [3]Libin Cardiovascular Institute, University of Calgary, AB, Calgary, Canada, [4]Department of Cardiac Sciences, University of Calgary, Calgary, AB, Canada, [5]Department of Radiology, University of Calgary, Calgary, AB, Canada, [6]Alberta Children's Hospital Research Institute, University of Calgary, Calgary, AB, Canada

Introduction: Four-dimensional (4-D) flow cardiac magnetic resonance imaging can be used to elegantly describe the hemodynamic efficiency of left ventricular (LV) flow throughout the cardiac cycle. Patients with nonvalvular paroxysmal atrial fibrillation (PAF) may have occult LV disease. Flow distribution analysis, based on 4-D flow, may unmask the presence of LV disease by assessing flow components: direct flow, retained flow, delayed ejection, and residual volume. This study aimed to identify LV hemodynamic inefficiencies in patients with PAF and normal systolic function. We hypothesized that the fraction of direct flow to the total end-diastolic volume would be reduced in patients with PAF compared with controls.

Methods: We used 4-D LV flow component analysis to compare hemodynamics in 30 healthy controls and 50 PAF patients in sinus rhythm.

Results: PAF subjects and healthy controls had similar LV mass, volume, and ejection fraction. Direct flow was lower in the PAF group than in the controls (44.5 ± 11.2% vs. 50.0 ± 12.2%, $p = 0.042$) while delayed ejection was higher in the PAF group (21.6 ± 5.6% vs. 18.6 ± 5.7%, $p = 0.022$).

Conclusion: PAF patients demonstrated a relative reduction in direct flow and elevation in delayed ejection.

Keywords: 4D-flow MRI, flow distribution, magnetic resoance imaging, direct flow, arial fibrillation

OPEN ACCESS

Edited by:
Jolanda Wentzel,
Erasmus Medical Center, Netherlands

Reviewed by:
Fuyou Liang,
Shanghai Jiao Tong University, China
Qiang Chen,
Southeast University, China

***Correspondence:**
Julio Garcia
julio.garciaflores@ucalgary.ca

Specialty section:
This article was submitted to Biomechanics, a section of the journal Frontiers in Bioengineering and Biotechnology

Received: *14 June 2021*
Accepted: *19 October 2021*
Published: *25 November 2021*

Citation:
Kim H, Sheitt H, Wilton SB, White JA and Garcia J (2021) Left Ventricular Flow Distribution as a Novel Flow Biomarker in Atrial Fibrillation. Front. Bioeng. Biotechnol. 9:725121. doi: 10.3389/fbioe.2021.725121

INTRODUCTION

Atrial fibrillation (AF) is a growing epidemic affecting approximately 37.6 million individuals worldwide, and this has increased 33% during the last 20 years (Lippi et al., 2021) and is a significant contributor to disability-adjusted life-years in the elderly (Abbafati et al., 2020). Paroxysmal AF (PAF) is typically initiated by premature atrial ectopic beats originating from the pulmonary veins but is maintained by altered atrial refractoriness related to tissue remodeling (Nattel et al., 2014). In the absence of valvular heart disease, the latter is commonly suspected to be related to abnormal loading of the left atrium (LA) during diastole from apparent or occult left ventricular (LV) dysfunction.

Cardiac magnetic resonance (CMR) is the gold standard for the volumetric evaluation of chamber structure and function (Kawel-Boehm et al., 2015). The more recent availability of four-dimensional

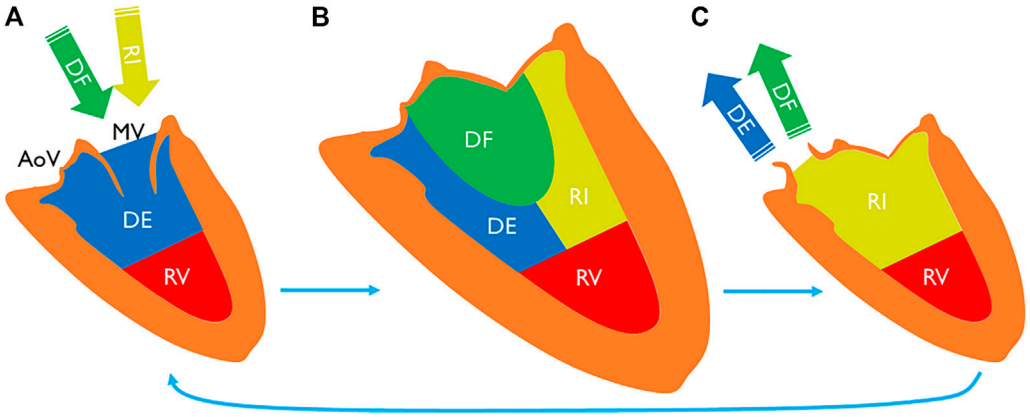

FIGURE 1 | LV blood volume **(A)** at the beginning of diastole, **(B)** at the end-diastole, and **(C)** at the end-systole. End-diastolic volume can be separated into four components. Direct flow is a part of inflow during diastole **(A** to **B)**, exiting the chamber during systole **(B** to **C)**. Retained inflow is another part that remains in the chamber at the end-systole **(C)**. Delayed ejection is a part of LV volume at the beginning of diastole **(A)** that exits during the cycle. Residual volume stays in the chamber for more than one cycle. MV indicates mitral valve; AoV, aortic valve; DF, direct flow; RI, retained inflow; DE, delayed ejection; and RV, residual volume.

(4-D) flow magnetic resonance imaging (MRI) provides a unique ability to assess complex 3-D blood flow patterns *in vivo* and may facilitate gaining insights into complex normal and altered intracardiac hemodynamics otherwise overlooked by standard 2-D imaging techniques (Markl et al., 2016; Garcia et al., 2020).

To date, LV flow component analysis has been largely used to study hemodynamic efficiencies of healthy subjects and patients with heart failure (Eriksson et al., 2010; Stoll et al., 2019). In this method, blood that flows through the LV during a heart cycle is separated into four components (**Figure 1**) (Bolger et al., 2007). Direct flow is the blood that enters and leaves the LV during a cycle. Retained inflow is the blood that enters the LV during diastole and stays in at the end of systole. Delayed ejection is that retained blood at the beginning of diastole, which leaves the LV during systole. Residual volume is that blood stays in the LV for more than one cycle. This method has been applied in AF referral populations to study LV function recovery after cardioversion (Karlsson et al., 2019); however, direct comparison of these novel hemodynamic markers has not been studied between AF patients versus healthy subjects. Given the expanding clinical burden of AF patients' heart failure with preserved ejection fraction (HFpEF) among patients (Savarese and Lund, 2017), a detailed understanding of abnormalities in LV flow distribution within this patient population is strongly justified.

In this study, we aimed to identify the presence of LV hemodynamic inefficiencies in patients with PAF and normal systolic function using flow distribution based on 4-D flow component analysis. We hypothesized that the fraction of direct flow to the total end-diastolic volume is reduced in patients with PAF compared with the healthy controls.

METHODS

Patient Population

A total of 50 patients with PAF with normal systolic function (age = 56 ± 12, female = 16, scanned between July 2017 and August 2019) and 30 healthy controls (age = 50 ± 8, female = 10, scanned between August 2017 and December 2020) were retrospectively selected from our local database. The PAF initial cohort included 103 patients and healthy control cohort 35 subjects. Patients and controls were selected to match by age given that the prevalence of AF increase in parallel with the aging of the population (Lakshminarayan et al., 2006). All patients were enrolled in the Cardiovascular Imaging Registry of Calgary (CIROC) at the time of clinical referral for cardiac MRI prior to consideration of pulmonary vein ablation for PAF. CHA_2DS_2-VASc score of PAF patients was calculated to assess stroke risk level, using patient medical history prior to MRI examination (Pamukcu et al., 2010). A commercial software (cardioDI™, Cohesic Inc., Calgary, Canada) was used to coordinate routine capture of patient informed consent and health questionnaires and for standardized collection of MRI-related variables. Healthy control subjects were older than 18 years of age with no cardiovascular disease and no history of hypertension or diabetes. Patients with significant mitral or aortic valve disease and cases with inappropriate/incomplete image reconstruction were not included. Healthy control screening was performed by a certified research nurse from our institution. The study was approved by the University of Calgary's Conjoint Health Research Ethics Board, and all subjects provided written informed consent. All research activities were performed in accordance with the Declaration of Helsinki.

MRI Data Acquisition

Patients and healthy subjects were required to be in sinus rhythm at the time of CMR imaging. All subjects underwent an identical standardized MRI protocol using 3 T MR scanners Skyra/Prisma (Siemens, Erlangen, Germany) inclusive of standard multi-planar steady-state free-precession (SSFP) cine imaging in four-, three-, and two-chamber, short-axis of the LV at end-expiration, and 3-D magnetic resonance angiography (MRA) of the LA using administration of 0.2 mmol/kg gadolinium contrast (Gadovist®,

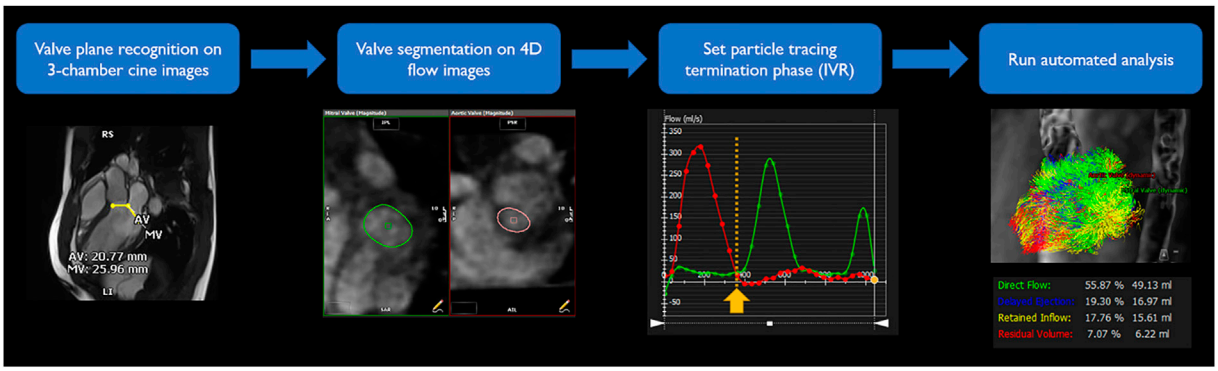

FIGURE 2 | LV flow component analysis workflow. To obtain segmentation of entrance and exit of the LV, valve plane was recognized on three-chamber cine images. Exact shape of the valves was segmented on 4-D flow images for each time frame. Iso-volumetric relaxation phase was identified from time-flow graph, minimizing both flows through the valves. From and to the selected phase, automated simulation traced particles and divided into four components.

Bayer Inc., Mississauga, Ontario, Canada). Approximately 5–10 min following contrast injection, 4-D flow MRI was performed using a prospectively triggered sequence with respiratory navigator-based gating (WIP 785A; n = 68, WIP 1106; n = 12). Whole heart 4-D flow MRI was added at the end of the protocol for the standard cardiac assessment of 3-D intra-cardiac hemodynamics. 4-D flow imaging parameters were as follows: gating = prospective, flip angle = 15°, FOV = 200–420 mm × 248–368 mm, spatial resolution = 2.0–3.5 × 2.0–3.5 × 2.5–3.5 mm; temporal resolution = 25–35 ms, 25–30 phases, and velocity sensitivity = 150–200 cm/s. Total acquisition time varies between 8 and 12 min, depending on heart rate and respiratory navigator efficiency.

MRI Data Processing and Analysis

Volumetric chamber measurements were performed from standard ECG-gated cine images using commercial software (cvi42 v5.11, Circle Cardiovascular Imaging Inc., Calgary, Canada). Short axis cine images were used to obtain LV end-diastolic volume (EDV) (ml), LV end-systolic volume (ESV) (ml), LV stroke volume (SV) (ml), LV mass (g), LV cardiac output (CO) (L/min), LVEDV indexed to BSA (LVEDV/BSA) (ml/m^2), LVESV indexed to BSA (LVESV/BSA) (ml/m^2), LV mass indexed to BSA (LV mass/BSA) (g/m^2), and LV ejection fraction (LVEF) (%). LA volume (ml) and LA volume indexed to BSA (ml/m^2) were measured using the two- and four-chamber views using the biplane area-length method.

4-D flow imaging was analyzed using a dedicated module from cvi42 v5.11. LV flow component analysis is based on a previously presented and validated method (Eriksson et al., 2010; Eriksson et al., 2011). Automated valve tracking was recently incorporated to improve accuracy and reduce variability (Garcia et al., 2021). All data underwent preprocessing to correct for Maxwell terms, eddy current–induced phase offset, and velocity aliasing if necessary. Then, from the long-axis three-chamber cine image, the locations of the aortic and mitral valve planes were automatically recognized on each frame to constrain 4-D flow analysis (**Figure 2**). The exact contour of the valves was refined manually on 4-D flow images. *Trans*-valvular flow was calculated throughout the cycle, and the isovolumetric relaxation (IVR) phase identified where both flows were minimized after systole. From each voxel in the LV segmentation an automated pathline was emitted. Pathline particles were created backward and forward in time until the identified end-systole within the velocity field Runge–Kutta method (Butcher, 2007). Overall pathlines represent the entire cardiac cycle particle tracking, pathline positions relative at the time of end-systole relative to the cardiac chambers are used to separate them into four flow components (**Figure 1**) with both the volume and ratio for each component reported. Flow components in the analyzed heartbeat are defined by direct flow (blood that enters the LV during diastole and leaves the LV during systole), retrained inflow (blood that enters the LV during diastole but does not leave during systole), delayed ejection flow (blood that starts and resides inside the LV during diastole and leaves during systole), and residual volume (blood that resides within the LV, not a component of inflow or ejected volume).

Statistics

Statistics were analyzed using IBM SPSS Statistics for Windows, version 26.0 (IBM Corp., Armonk, N.Y., United States). Continuous variables were tested by the Shapiro–Wilk test to determine if parameters were normally distributed. If parameters were normally distributed, they were presented as mean ± standard deviation, and the independent-samples *t*-test was performed to compare between the PAF and control groups. When the parameters did not satisfy the normality assumption, they were presented as median with (the first quartile - the third quartile), and Mann–Whitney *U*-test was used. A multiple linear regression was performed to assess dependency of flow distribution variables on demographic and conventional LV parameters. The Pearson method was used to assess the correlation and agreement between parameters. Categorical variables are presented by count and frequency and compared using a chi-square test between two groups. For all analyses, two-tailed tests with p-value < 0.05 were considered statistically significant. Propensity score matching was performed to assess baseline confounders and their impact on flow distribution variables.

TABLE 1 | Baseline characteristics.

	Controls (n = 30)	PAF patients (n = 50)	*p*-value
	Mean ± SD, median [range] or count (percent)	Mean ± SD, median [range]or count (percent)	
Age (years)	50 ± 8	56 ± 12	0.009
Sex (female)	10 (33%)	16 (32%)	0.902
Height (m)	1.75 [1.67–1.79]	1.77 [1.70–1.86]	0.062
Weight (kg)	76.0 [61.0–82.2]	81.5 [72.8–100.0]	0.011
BSA (m^2)	1.90 [1.71–2.02]	1.99 [1.84–2.21]	0.016
HR (bpm)	59 [54–66]	63 [55–79]	0.077
Systolic BP (mmHg)	114 ± 12	116 ± 12	0.389
Diastolic BP (mmHg)	70 [55–74]	69 [63–75]	0.806

TABLE 2 | Risk score and factors in PAF group.

	PAF (n = 44)
CHA_2DS_2-VASc	
0	18 (41%)
1	18 (41%)
2	5 (11%)
3	3 (7%)
Risk factors	
CHF/LV dysfunction	2 (6%)
Hypertension	7 (19%)
Aged 75 or over	1 (3%)
Diabetes	2 (6%)
Stroke	0 (0%)
Vascular disease	1 (3%)
Aged 65–74	10 (28%)
Sex category female	13 (36%)

**CHF, congestive heart failure; LV, left ventricle.*

RESULTS

Patient Characteristics

The baseline characteristics of patients and controls are given in **Table 1**. A significant difference was observed in the mean age of the PAF cohort versus controls (56 ± 12 years vs. 50 ± 8 years, p = 0.009). Also, weight and BSA tended to be higher in the PAF group (81.5 kg [72.8–100.0] vs. 76.0 kg [61.0–82.2], p = 0.011 and 1.99 m^2 [1.84–2.21] vs. 1.90 m^2 [1.71–2.02], p = 0.016, respectively). Sex ratio, height, heart rate, and systolic/diastolic blood pressure did not show significant differences. CHA_2DS_2-VASc risk score was 0 or 1 in 82% of PAF subjects (**Table 2**) while five subjects had a score of two, and only three subjects having a score of three. These three latter cases were in two females with age >75 and in a female >65 with hypertension. No patients had score of four or above. Overall, our PAF group mostly consisted of low-risk patients. Standard volume and function measurements of the left ventricle and left atrium are summarized in **Table 3**. LV EDV indexed to BSA was lower in the PAF cohort than in the controls (76.5 [66.4–87.3] vs. 88.8 [77.4–97.0], p = 0.006). There were no other significant differences between the PAF and control groups.

Left Ventricular Flow Distribution

Examples of LV flow component analysis from controls and PAF patients are shown in **Figure 3**. Pathlines show direct flow and retained inflow coming into the LV during diastole, followed by outgoing flow consisting of direct flow and delayed ejection during systole. At end-diastole, when all pathlines reside in the LV, each of the different proportions of flow components are uniquely labeled.

The volume of each flow component and its ratio to the total flow are presented in **Table 4**. The ratio of direct flow to the total flow was significantly reduced (−11%) in the PAF group compared with controls (44.5 ± 11.2 vs. 50.0 ± 12.2, p = 0.042). Delayed ejection was reciprocally increased (+16%) in the PAF group (21.6 ± 5.6 vs. 18.6 ± 5.7, p = 0.022) (**Figure 4**). Observed differences in retained inflow and residual volume were not significant.

To evaluate for independent associations of direct flow (reduction) and delayed ejection (elevation) with known AF diagnosis, two separate multivariable models were constructed adjusting for age, sex, BSA, and hypertension. These variables failed to predict direct flow and delayed ejection statistically significantly, F (4, 46) = 0.685, p = 0.606, R^2 = 0.056, and F (4,46) = 1.712, p = 0.163, R^2 = 0.130, respectively.

Correlation with LV function parameters (SV, LVCO, and LVEF) were also evaluated. LVEF was moderately correlated with both direct flow and delayed ejection (r = 0.432, $p < 0.001$ and r = −0.357, p = 0.001, respectively).

Propensity score matching considered age, weight, and BSA (**Table 1**) for further analysis of flow components. After balancing the comparability of the baseline characteristics between groups, only 18 PAF patients were matched to healthy volunteers. There were no statistical differences between propensity score matched cohorts for flow component parameters.

DISCUSSION

This study compared 4-D flow-derived LV component analysis in patients with PAF and normal LVEF versus healthy controls. Following multivariable adjustment for age, sex, BSA, and hypertension, we identified significant and reciprocal alterations in direct flow (reduced) and delayed ejection

TABLE 3 | Left ventricular and atrial volumes and function.

	Controls (n = 30)	PAF patients (n = 50)	*p*-value
	Mean ± SD, median [range]	Mean ± SD, median [range]	
LV End-Diastolic Volume (ml)	162.6 ± 27.7	159.7 ± 34.4	0.693
LV End-Diastolic Volume indexed to BSA (ml/m^2)	88.8 [77.4–97.0]	76.5 [66.4–87.3]	0.006
LV End-Systolic Volume (ml)	62.5 [45.9–75.8]	61.0 [51.5–79.5]	0.531
LV End-Systolic Volume indexed to BSA (ml/m^2)	33 ± 7.3	31.9 ± 7.7	0.510
LV Mass (g)	103.8 ± 26.1	106.6 ± 27.2	0.658
LV Mass indexed to BSA (g/m^2)	54.6 ± 9.8	52 ± 10.2	0.267
LV Stroke Volume (ml)	101.2 ± 14.7	94.5 ± 23.7	0.121
LV Cardiac Output (L/min)	5.9 ± 0.9	6.0 ± 1.3	0.852
LV Ejection Fraction (%)	61.2 [58.9–68.1]	60.3 [56.9–63.8]	0.061
LA Volume (ml)	69.4 ± 17.5	80.2 ± 26.4	0.054
LA Volume indexed to BSA (ml/m^2)	36.8 ± 9.2	39.5 ± 12.4	0.317

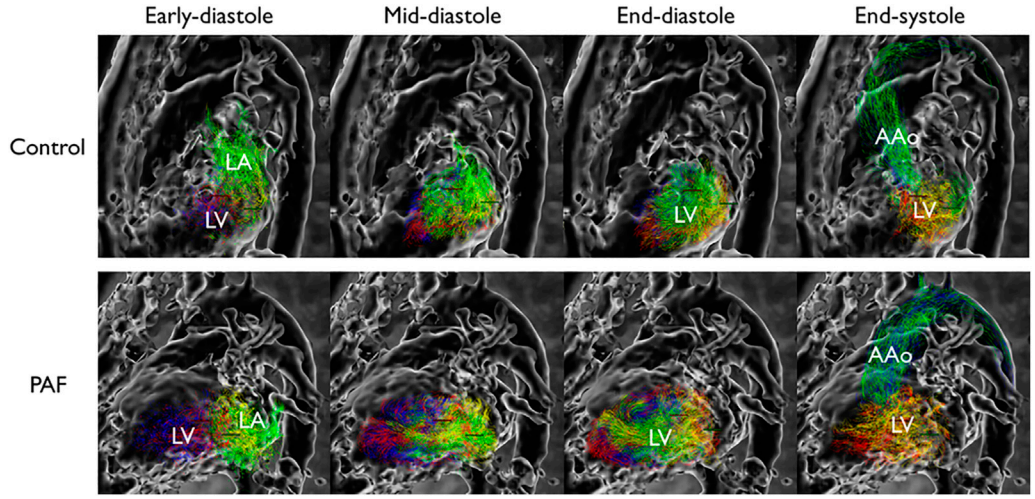

FIGURE 3 | Flow pattern example in left ventricle. Each component is color-coded; green: direct flow, yellow: retained inflow, blue: delayed ejection, red: residual volume. Reduced proportion of direct flow is observed at end-diastolic phase in PAF. LA indicates left atrium; LV, left ventricle; and AAo, ascending aorta.

TABLE 4 | Left ventricular flow distribution.

	Controls (n = 30)	PAF patients (n = 50)	*p*-value
Volumes of flow components			
Direct Flow (ml)	37.4 ± 13.4	33.5 ± 13.1	0.204
Retained Inflow (ml)	18.1 ± 7.0	19.8 ± 9.2	0.348
Delayed Ejection (ml)	15.0 ± 6.6	16.5 ± 7.1	0.390
Residual Volume (ml)	6.6 ± 4.1	7.4 ± 5.5	0.517
Ratio of flow components to the total flow			
Direct Flow (%)	50.0 ± 12.2	44.5 ± 11.2	0.042
Retained Inflow (%)	23.5 ± 5.8	25.3 ± 5.5	0.164
Delayed Ejection (%)	18.6 ± 5.7	21.6 ± 5.6	0.022
Residual Volume (%)	8.0 ± 3.8	8.7 ± 4.1	0.450

(elevated) in patients with AF. This finding provides insights into the unique hemodynamic phenotype of this referral population that may explain their strong predisposition toward HFpEF.

The age difference between study groups is a recognized limitation of this study. Age is one of the most impacting factors on the risk of AF and its complications as well as sex.

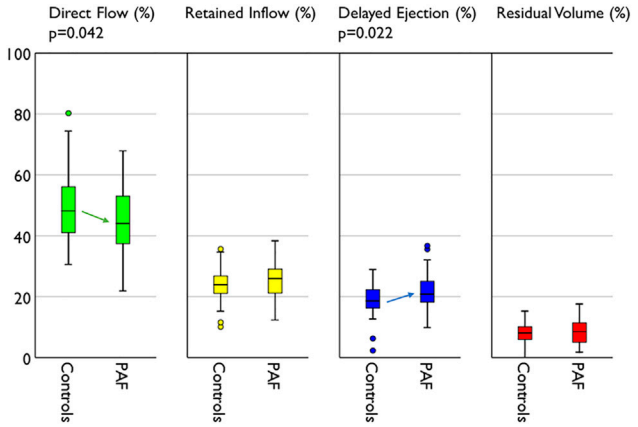

FIGURE 4 | Compare of flow distribution between groups. PAF group represents reduced direct flow and increased delayed ejection compared with controls.

Nevertheless, correlation analysis between age and flow components demonstrated no significant correlation. This revealed flow component analysis is robust to such an external factor, and therefore, the impact from age difference should be limited.

A certain degree of elevated weight and BSA in the PAF group can be explained by the well-known fact that overweight and obesity are associated with the onset of AF (Frost et al., 2005). LV EDV indexed to BSA was rather low in the PAF group but still within normal range. This can be interpreted as AF burden having not yet impacted LV dilation, so normal LV volume size was normalized by elevated BSA. The similarity observed in other LV and LA volume and function parameters indicate that our enrolled group of PAF subjects were a relatively healthy referral population at an early stage of the disease.

Compared with a prior study evaluating LV component analysis in healthy subjects (Stoll et al., 2018), we observed higher direct flow with reduced residual volumes (50 and 8%, respectively). However, it is important to recognize that the previous study used manual segmentation of the LV volume at only the end-diastolic and end-systolic phases; these are used to constrain flow analysis throughout the cardiac cycle. In our study, both mitral and aortic valve planes were dynamically tracked with iterative, phase-adjusted calculation of blood flow through each valve, which improves flow quantification (Garcia et al., 2021). Although, particle tracing near the LV apex of the heart was reduced in most cases, which may cause underestimation of the residual volume and, in consequence, overestimation of the proportion of direct flow. The latter may be due to the particle tracing algorithm used by the vendor and the low velocities near the apex. A recommended validation is based on comparing inflow vs. outflow for every subject. Further investigation into larger cohorts and the sophisticated algorithm will enable clinical use.

Heart failure (HF) and AF often coexist and have worse prognosis than those with isolated HF or AF (Hindricks et al., 2021). The prevalence of both AF and HF also increases with age. AF can promote HF progression through cardiomyopathy characterized by loss of atrial systole, LA dilation, and rapid irregular ventricular rate affecting LV emptying and filling (Olsson et al., 2006). When EF is preserved, the management is mainly based on symptomatic therapy and treatment for comorbidities. In our study, PAF patients had preserved EF and were in sinus rhythm at the time of the scan. Of interest, DF and DE were significantly different in PAF patients as compared with controls. Both reduction of DF and elevation of DE are markers of altered LV emptying and filling and may be able to early characterize the predisposition to HFpEF.

Propensity score matching assessment considered age, weight, and BSA for further analysis of flow components. A matched cohort was reduced to 18 subjects with no significant differences on flow component parameters. The latter may be due to the matched cohort size and highlights the importance of considering baseline cofounding factors in future studies employing flow component analysis.

LIMITATIONS

Although we demonstrate that demographic factors are not correlated with flow distributions, still the age gap between two groups is a potential cofounding factor. Recruiting enough age-matched controls will resolve the bias in the study groups. Blood pressure measurements were not available in some subjects, especially in the control group. Collecting complete data sets will make sure that this flow distribution has not been affected by external factors. We used commercial software for flow distribution analysis. Although it provided a convenient workflow for quantification of flow components, we could not access the raw simulation results to investigate further. The cause of difference in flow proportion with previous studies was postulated but not confirmed. It is important to remark that flow component analysis is sensitive to degraded preprocessing correction, such as eddy currents, concomitant fields, noise, and aliasing corrections. In addition, quality control of the preprocessed data sets is relevant for the careful identification of aberrant pathlines (Eriksson et al., 2010). Pathline common errors include, but they are not limited to, spatial and temporal resolution, interpolation truncation, and implementation algorithms (Chandler et al., 2015). Implementation of flow analysis by our own will allow access to raw results that reveal whether this method reconstructs LV volume successfully, comparison with manual LV volume segmentation method, and also further study such as energy-based analysis. Propensity score matching findings were limited by the number of matching subjects (n = 18). Based on previous studies, a minimum of 30 subjects is needed to detect differences in flow components between groups assuming a power of 80% and type 1 error of 0.5% (p <0 .005) (Eriksson et al., 2010; Eriksson et al., 2011; Kim et al., 2020).

CONCLUSION

This study used LV flow component analysis by 4-D flow MRI to demonstrate occult changes in LV flow efficiency in patients with

PAF and normal systolic function. Hemodynamic alterations were observed showing reduction in direct flow in the absence of additional markers of adverse LV remodeling, such as LV hypertrophy or chamber dilation. Cofounding baseline factors need to be considered for a more representative assessment of flow components. Expanded study into mechanisms underlying reductions in LV efficiency in this patient population and its relevance to future risk of HFpEF is required.

DATA AVAILABILITY STATEMENT

The anonymized raw data supporting the conclusion of this article will be made available on request from the corresponding author.

ETHICS STATEMENT

The studies involving human participants were reviewed and approved by the University of Calgary's Conjoint Health Research Ethics Board. The patients/participants provided their written informed consent to participate in this study.

AUTHOR CONTRIBUTIONS

HK and JG designed the study, analyzed and interpreted the 4D flow data, and drafted the manuscript. HS and JW reviewed standard clinical cardiac MRI. HS, SW, JW, and JG critically revised the manuscript. All authors have read and agreed to the published version of the manuscript.

FUNDING

This research was funded by The University of Calgary, URGC SEM #1054341; JG start-up funding; HK from the Biomedical Engineering graduate program. We acknowledge the support of the Natural Science and Engineering Research Council of Canada/Conseil de recherche en science naturelles et en génie du Canada, RGPIN-2020-04549 and DGECR-2020-00204.

REFERENCES

Abbafati, C., Abbas, K. M., Abbasi-Kangevari, M., Abd-Allah, F., Abdelalim, A., Abdollahi, M., et al. (2020). Global burden of 369 Diseases and Injuries in 204 Countries and Territories, 1990-2019: a Systematic Analysis for the Global Burden of Disease Study 2019. *Lancet* 396 (10258), 1204–1222. doi:10.1016/S0140-6736(20)30925-9

Bolger, A. F., Heiberg, E., Karlsson, M., Wigström, L., Engvall, J., Sigfridsson, A., et al. (2007). Transit of Blood Flow through the Human Left Ventricle Mapped by Cardiovascular Magnetic Resonance. *J. Cardiovasc. Magn. Reson.* 9, 741–747. doi:10.1080/10976640701544530

Butcher, J. (2007). Runge-kutta Methods. *Scholarpedia* 2 (9), 3147. doi:10.4249/scholarpedia.3147

Chandler, J., Obermaier, H., and Joy, K. I. (2015). Interpolation-Based Pathline Tracing in Particle-Based Flow Visualization. *IEEE Trans. Vis. Comput. Graph.* 21 (1), 68–80. doi:10.1109/tvcg.2014.2325043

Eriksson, J., Carlhäll, C. J., Dyverfeldt, P., Engvall, J., Bolger, A. F., and Ebbers, T. (2010). Semi-automatic Quantification of 4D Left Ventricular Blood Flow. *J. Cardiovasc. Magn. Reson.* 12, 1–10. doi:10.1186/1532-429x-12-9

Eriksson, J., Dyverfeldt, P., Engvall, J., Bolger, A. F., Ebbers, T., and Carlhäll, C. J. (2011). Quantification of Presystolic Blood Flow Organization and Energetics in the Human Left Ventricle. *Am. J. Physiol. Heart Circulatory Physiol.* 300 (6), H2135–H2141. doi:10.1152/ajpheart.00993.2010

Frost, L., Hune, L. J., and Vestergaard, P. (2005). Overweight and Obesity as Risk Factors for Atrial Fibrillation or Flutter: The Danish Diet, Cancer, and Health Study. *Am. J. Med.* 118 (5), 489–495. doi:10.1016/j.amjmed.2005.01.031

Garcia, J., Beckie, K., Hassanabad, A. F., Sojoudi, A., and White, J. A. (2021). Aortic and Mitral Flow Quantification Using Dynamic Valve Tracking and Machine Learning: Prospective Study Assessing Static and Dynamic Plane Repeatability, Variability and Agreement. *JRSM Cardiovasc. Dis.* 10, 204800402199990. doi:10.1177/2048004021999900

Garcia, J., Sheitt, H., Bristow, M. S., Lydell, C., Howarth, A. G., Heydari, B., et al. (2020). Left Atrial Vortex Size and Velocity Distributions by 4D Flow MRI in Patients with Paroxysmal Atrial Fibrillation: Associations with Age and CHA 2 DS 2 -VASc Risk Score. *J. Magn. Reson. Imaging* 51 (3), 871–884. doi:10.1002/jmri.26876

Hindricks, G., Potpara, T., Dagres, N., Arbelo, E., Bax, J. J., Blomström-Lundqvist, C., et al. (2021). 2020 ESC Guidelines for the Diagnosis and Management of Atrial Fibrillation Developed in Collaboration with the European Association of Cardio-Thoracic Surgery (EACTS). *Eur. Heart J.* 42 (5), 373–498. doi:10.1093/eurheartj/ehaa612

Karlsson, L. O., Erixon, H., Ebbers, T., Bolger, A., and Carlhäll, C.-J. (2019). Post-cardioversion Improvement in LV Function Defined by 4D Flow Patterns and Energetics in Patients with Atrial Fibrillation. *Front. Physiol.* 10 (MAY), 659. doi:10.3389/fphys.2019.00659

Kawel-Boehm, N., Maceira, A., Valsangiacomo-Buechel, E. R., Vogel-Claussen, J., Turkbey, E. B., Williams, R., et al. (2015). Normal Values for Cardiovascular Magnetic Resonance in Adults and Children. *J. Cardiovasc. Magn. Reson.* 17 (1), 29–33. doi:10.1186/s12968-015-0111-7

Kim, H., Sheitt, H., Jamalidinan, F., Wilton, S., White, J., and Garcia, J. (2020). Left Ventricular Flow Analysis in Atrial Fibrillation. *Annu. Int. Conf. IEEE Eng. Med. Biol. Soc.* 2020, 1182–1185. doi:10.1109/EMBC44109.2020.9175259

Lakshminarayan, K., Solid, C. A., Collins, A. J., Anderson, D. C., and Herzog, C. A. (2006). Atrial Fibrillation and Stroke in the General Medicare Population: a 10-year Perspective (1992 to 2002). *Stroke* 37 (8), 1969. doi:10.1161/01.STR.0000230607.07928.17

Lippi, G., Sanchis-Gomar, F., and Cervellin, G. (2021). Global Epidemiology of Atrial Fibrillation: An Increasing Epidemic and Public Health challenge. *Int. J. Stroke* 16 (2), 217–221. doi:10.1177/1747493019897870

Markl, M., Lee, D. C., Ng, J., Carr, M., Carr, J., and Goldberger, J. J. (2016). Left Atrial 4-Dimensional Flow Magnetic Resonance Imaging. *Invest. Radiol.* 51 (3), 147–154. doi:10.1097/rli.0000000000000219

Nattel, S., Guasch, E., Savelieva, I., Cosio, F. G., Valverde, I., Halperin, J. L., et al. (2014). Early Management of Atrial Fibrillation to Prevent Cardiovascular Complications. *Eur. Heart J.* 35 (22), 1448–1456. doi:10.1093/eurheartj/ehu028

Olsson, L. G., Swedberg, K., Ducharme, A., Granger, C. B., Michelson, E. L., McMurray, J. J., et al. (2006). Atrial Fibrillation and Risk of Clinical Events in Chronic Heart Failure with and without Left Ventricular Systolic Dysfunction: Results from the Candesartan in Heart Failure-Assessment of Reduction in Mortality and Morbidity (CHARM) Program. *J. Am. Coll. Cardiol.* 47 (10), 1997–2004. doi:10.1016/j.jacc.2006.01.060

Pamukcu, B., Lip, G. Y. H., and Lane, D. A. (2010). Simplifying Stroke Risk Stratification in Atrial Fibrillation Patients: Implications of the CHA2DS2-VASc Risk Stratification Scores. *Age Ageing* 39 (5), 533–535. doi:10.1093/ageing/afq059

Savarese, G., and Lund, L. H. (2017). Global Public Health Burden of Heart Failure. *Card. Fail. Rev.* 03 (01), 7. doi:10.15420/cfr.2016:25:2

Stoll, V. M., Hess, A. T., Rodgers, C. T., Bissell, M. M., Dyverfeldt, P., Ebbers, T., et al. (2019). Left Ventricular Flow Analysis. *Circ. Cardiovasc. Imaging* 12 (5), e008130–12. doi:10.1161/CIRCIMAGING.118.008130

Stoll, V. M., Loudon, M., Eriksson, J., Bissell, M. M., Dyverfeldt, P., Ebbers, T., et al. (2018). Test-retest Variability of Left Ventricular 4D Flow Cardiovascular Magnetic Resonance Measurements in Healthy Subjects. *J. Cardiovasc. Magn. Reson.* 20 (1), 15. doi:10.1186/s12968-018-0432-4

Conflict of Interest: The authors declare that the research was conducted in the absence of any commercial or financial relationships that could be construed as a potential conflict of interest.

Publisher's Note: All claims expressed in this article are solely those of the authors and do not necessarily represent those of their affiliated organizations, or those of the publisher, the editors and the reviewers. Any product that may be evaluated in this article, or claim that may be made by its manufacturer, is not guaranteed or endorsed by the publisher.

frontiers in Cardiovascular Medicine

ORIGINAL RESEARCH
published: 30 November 2021
doi: 10.3389/fcvm.2021.727745

Association Between 2D- and 3D-Speckle-Tracking Longitudinal Strain and Cardiovascular Magnetic Resonance Evidence of Diffuse Myocardial Fibrosis in Heart Transplant Recipients

Wei Sun[1,2,3†], *Xuehua Shen*[4,5†], *Jing Wang*[4†], *Shuangshuang Zhu*[1,2,3], *Yanting Zhang*[1,2,3], *Chun Wu*[1,2,3], *Yuji Xie*[1,2,3], *Yun Yang*[1,2,3], *Nianguo Dong*[6], *Guohua Wang*[6], *Yuman Li*[1,2,3], *Qing Lv*[1,2,3], *Bo Liang*[4*], *Li Zhang*[1,2,3*] *and Mingxing Xie*[1,2,3*]

[1] *Department of Ultrasound, Union Hospital, Tongji Medical College, Huazhong University of Science and Technology, Wuhan, China,* [2] *Hubei Province Clinical Research Center for Medical Imaging, Wuhan, China,* [3] *Hubei Province Key Laboratory of Molecular Imaging, Wuhan, China,* [4] *Department of Radiology, Union Hospital, Tongji Medical College, Huazhong University of Science and Technology, Wuhan, China,* [5] *Department of Radiology, The Affiliated Hospital of Guizhou Medical University, Guiyang, China,* [6] *Department of Cardiovascular Surgery, Union Hospital, Tongji Medical College, Huazhong University of Science and Technology, Wuhan, China*

Objective: This study aimed to: (1) evaluate the association between myocardial fibrosis (MF) quantified by extracellular volume fraction (ECV) and myocardial strain measured by two-dimensional (2D)- and three-dimensional speckle-tracking echocardiography (3D-STE) and (2) further investigate which strain parameter measured by 2D- and 3D-STE is the more robust predictor of MF in heart transplant (HT) recipients.

Methods: A total of 40 patients with HT and 20 healthy controls were prospectively enrolled. Left ventricular (LV)-global longitudinal strain (GLS), global circumferential strain (GCS), and global radial strain (GRS) were measured by 2D- and 3D-STE. LV diffuse MF was defined by cardiovascular magnetic resonance (CMR)-ECV.

Results: The HT recipients had a significantly higher native T1 and ECV than healthy controls (1043.8 ± 34.0 vs. 999.7 ± 19.7 ms, $p < 0.001$; 26.6 ± 2.7 vs. 24.3 ± 1.8%, $p = 0.02$). The 3D- and 2D-STE-LVGLS and LVGCS were lower ($p < 0.005$) in the HT recipients than in healthy controls. ECV showed a moderate correlation with 2D-LVGLS ($r = 0.53$, $p = 0.002$) and 3D-LVGLS ($r = 0.60$, $p < 0.001$), but it was not correlated with 2D or 3D-LVGCS, or LVGRS. Furthermore, 3D-LVGLS and 2D-LVGLS had a similar correlation with CMR-ECV ($r = 0.60$ vs. 0.53, $p = 0.670$). A separate stepwise multivariate linear analysis showed that both the 2D-LVGLS ($\beta = 0.39$, $p = 0.019$) and 3D-LVGLS ($\beta = 0.54$, $p < 0.001$) were independently associated with CMR-ECV.

OPEN ACCESS

Edited by:
Juan Carlos Del Alamo, University of Washington, United States

Reviewed by:
Ali Hosseinsabet, Tehran University of Medical Sciences, Iran
Lennart Tautz, Charité—Universitätsmedizin Berlin, Germany

***Correspondence:**
Mingxing Xie
xiemx@hust.edu.cn
Li Zhang
zli429@hust.edu.cn
Bo Liang
xiehelb@sina.com

[†] These authors have contributed equally to this work and share first authorship

Specialty section:
This article was submitted to Cardiovascular Imaging, a section of the journal Frontiers in Cardiovascular Medicine

Received: *19 June 2021*
Accepted: *21 October 2021*
Published: *30 November 2021*

Citation:
Sun W, Shen X, Wang J, Zhu S, Zhang Y, Wu C, Xie Y, Yang Y, Dong N, Wang G, Li Y, Lv Q, Liang B, Zhang L and Xie M (2021) Association Between 2D- and 3D-Speckle-Tracking Longitudinal Strain and Cardiovascular Magnetic Resonance Evidence of Diffuse Myocardial Fibrosis in Heart Transplant Recipients. Front. Cardiovasc. Med. 8:727745. doi: 10.3389/fcvm.2021.727745

Conclusion: CMR marker of diffuse MF was present in asymptomatic patients with HT and appeared to be associated with decreased myocardial strain by echocardiography. Both the 2D- and 3D-LVGLS were independently correlated with diffuse LVMF, which may provide an alternative non-invasive tool for monitoring the development of adverse fibrotic remodeling during the follow-up of HT recipients.

Keywords: heart transplant, diffuse myocardial fibrosis, cardiovascular magnetic resonance, extracellular volume fraction, speckle tracking echocardiography

INTRODUCTION

Heart transplant (HT) is the most effective treatment for patients with end-stage heart failure (1). The outcome of HT has significantly improved owing largely to advances in immunosuppressive therapy and the management of long-term complications. However, myocardial fibrosis (MF) is a commonly demonstrated histopathologic feature and is associated with a higher risk of adverse cardiac events and death after HT (2–9). Therefore, a reliable non-invasive method for monitoring the development of fibrotic remodeling early may be desirable during the follow-up of patients with HT and can assist to risk stratification in HT recipients.

Histological biopsy is the gold standard for the assessment of MF, but it is invasive and not practical for serial follow-up after HT. Besides, the biopsied region only reflects the local pathological information and cannot quantify diffuse MF. However, numerous studies have validated that diffuse MF can be measured non-invasively by extracellular volume fraction (ECV) that was derived from cardiovascular magnetic resonance (CMR) in various cardiovascular diseases (10–13). Furthermore, previous studies have reported that two-dimensional speckle-tracking echocardiography (2D-STE)-derived myocardial strain may be a robust indicator to predict MF (14–16). However, 2D-STE is time-consuming and is affected by the through-plane motion during a cardiac cycle and the transplanted hearts would show noteworthy translational motion during the cardiac phase, which can aggravate the "out-of-plane phenomenon" of 2D-STE. Three-dimensional (3D)-STE can overcome the limitation of plane dependency existing in 2D-STE. Moreover, 3D-STE requires less time to acquire and analyze images (17). Nevertheless, the predictive value of myocardial strain for diffuse MF in HT recipients and whether 3D-STE is superior to 2D-STE remained unknown.

Therefore, this study aimed to: (1) evaluate the association between MF and myocardial strain measured by 2D- and 3D-STE and (2) further investigate which strain parameter measured by 2D- and 3D-STE is the more robust predictor of MF defined by CMR-ECV in HT recipients.

MATERIALS AND METHODS

Study Population

A total of 50 asymptomatic patients with HT who were scheduled for echocardiogram at their routine follow-up examinations were prospectively enrolled in this study. As myocardial edema due to inflammation can expand the extracellular volume and increase native T1 times, patients with acute rejection (AR) at the time of recruitment were excluded. Patients with the following conditions were also excluded: time after HT $<$ 6 months, left ventricular ejection fraction (LVEF) $<$ 50%, significant coronary allograft vasculopathy (CAV), uncontrolled hypertension, uncontrolled blood glucose, renal failure, arrhythmia, and poor image quality. There were 10 patients excluded due to poor echocardiographic image quality ($n = 6$) and arrhythmia ($n = 4$). The remaining 40 patients were included in the final analysis. Demographic data including sex, age, height, and weight at the time of echocardiographic examination were obtained. Clinical data including recipient age, weight at HT, bypass time, ischemia time, donor age, weight, and history of AR and CAV were collected from a medical record review. Additionally, 20 healthy volunteers with a similar distribution of sex and age to the HT group were recruited as the control group. They had no history of hypertension, diabetes mellitus, renal failure, or other organic diseases based on physical examinations, biochemical tests, ECG, and echocardiography that were enrolled as a control group.

This study was approved by the Ethics Committee of Tongji Medical College, Huazhong University of Science and Technology, and all the participants provided a written informed consent.

Conventional 2D Echocardiography

All the 2D, Doppler, and 3D images were acquired by using a commercially available system (EPIQ 7C, Philips Medical Systems, Andover, Massachusetts, USA) with S5-1 and X5-1 transthoracic echocardiography transducers. Four heartbeat images were collected and stored in digital format. All the echocardiographic parameters were acquired according to the published guidelines (18). LV diameter was measured at end-diastole from the parasternal long-axis. Doppler mitral valve peak early (E) and late (A) diastolic velocities and E/A velocity ratio were measured on apical four-chamber view. The mean value of early diastolic mitral annular tissue velocity and left ventricular lateral wall tissue velocity (e') was measured by using tissue Doppler imaging. The LV Tei index was defined as the ratio of isovolumic time divided by ejection time with the use of tissue Doppler of the mitral annulus.

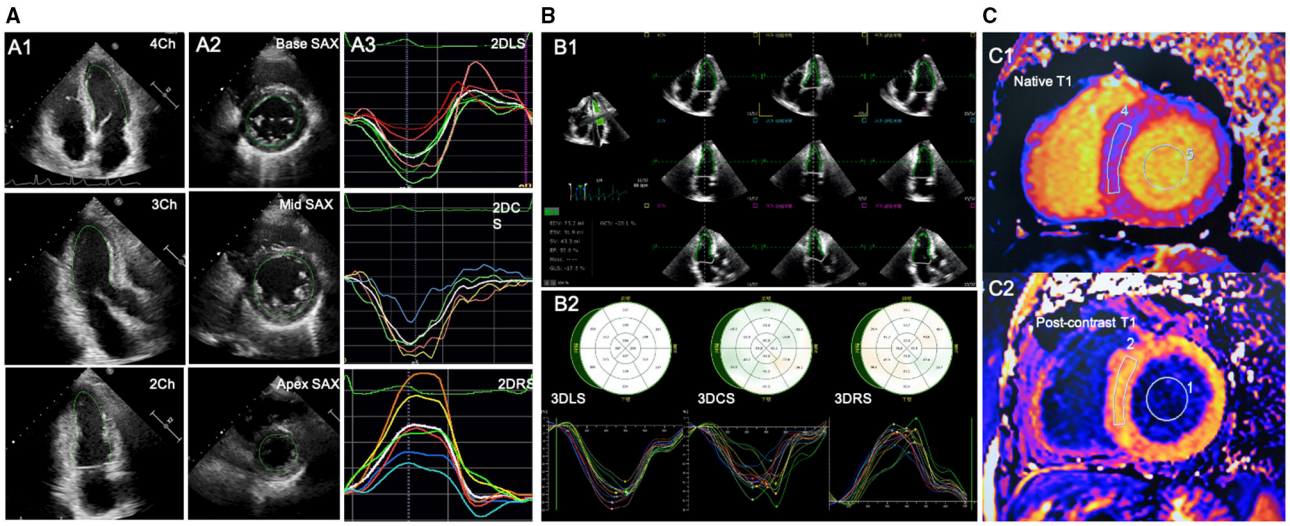

FIGURE 1 | Offline analysis of STE for left ventricular (LV) strain and CMR for LV-ECV. **(A)** 2D-STE offline analysis for LV. A1-A2, LV endocardial tracing in the three LV apical long-axis and three LV short-axis views; A3, LV strain curves; **(B)** 3D-STE offline analysis for LV. B1, LV endocardial tracing at end-diastole and end-systole; B2, 3D-GLS, GCS, and GRS strain curves were generated. **(C)** Offline analysis for CMR-LV-ECV. C1-C2, measurements of native and postcontrast T1 time from LV myocardium and LV blood pool. 2D-STE, two-dimensional speckle-tracking echocardiography; 3D-STE, three-dimensional STE; CMR, cardiovascular magnetic resonance; ECV, extracellular volume fraction; GLS, global longitudinal strain; GCS, global circumferential strain; GRS, global radial strain.

Left Ventricular Myocardial Strain Measured by 2D-STE and 3D-STE

The 2D myocardial strain was performed on the 2D cardiac performance analysis 1.2 software (TomTec Imaging Systems, Unterschleissheim, Germany, UK) in the 2D echocardiographic images with a frame rate of 50–70 MHz. LV longitudinal strain was determined by endocardial tracing in the apical four-, three-, and two-chamber views. LV circumferential and radial strain were measured by endocardial tracing in the basal, middle, and apical level of LV short-axis views on a frame-by-frame basis during one cardiac cycle. If the tracking was suboptimal, manual adjustment was performed. The LV global longitudinal strain (LVGLS), LV global circumferential strain (LVGCS), and LV global radial strain (LVGRS) were defined as the average peak strain values automatically generated from the 16 segmental strain curves by the software (**Figure 1A**).

The 3D-STE was performed on the four-dimensional (4D) LV-Analysis 3.1 Software (TomTec Imaging systems, Unterschleissheim, Germany, UK) in the 3D LV full-volume images with frame rate of 19–23 MHz. After selecting the center of the mitral annulus line and the apex of the left ventricle at end-diastole, the workstation would track the LV endocardium automatically and the manual adjustment was performed in case of unsatisfactory tracking. The same procedure was performed at the end-systolic frame. Subsequently, the software would perform the 3D-STE throughout the cardiac cycle. Ultimately, the 3D-LV-end-diastolic volume (EDV), end-systolic volume (ESV), LVEF, and the myocardial strain would be generated automatically. LVGLS, LVGCS, and LVGRS, respectively, were calculated as the average peak systolic longitudinal, circumferential, and radial strain of all the 16 LV segments (**Figure 1B**). Subjects with two or more inadequately tracked segments were removed from the analysis.

Cardiovascular Magnetic Resonance Images Acquired and Analyzed

Cardiovascular magnetic resonance imaging was performed with a 1.5-Tesla system (MAGNETOM Aera, Siemens Healthineers, Erlangen, Germany, UK). CMR examination was performed within 24 h of the echocardiography examination. Three long axes and a set of contiguous short-axis cine images of LV were acquired with a steady-state free precession sequence during breath-hold of 10–15 s. The cine image parameters were as follows: repetition time (TR)/echo time (TE), 38.09/1.21 ms; slice thickness, 8 mm; field of view, 340 × 255 mm^2; matrix, 256 pixels × 205 pixels; and flip angle, 80°. T1 mapping was performed on three standard LV short-axis slices before and 15 min after the administration of a bolus of gadopentetate dimeglumine contrast agent (0.2 mmol/kg, Magnevist, Bayer Healthcare, Berlin, Germany, UK) by using a modified Look-Locker inversion recovery (MOLLI) sequence with a 5- and 3-sampling scheme. The typical MOLLI sequence parameters were: TR/TE, 255.76/1.01 ms; slice thickness, 8 mm; matrix, 144 × 256 pixels; flip angle, 35°; and scan time, 11 s. The parameters of postcontrast T1 were similar to those of the native T1, except for a TE of 1.12 ms and a TR of 359.76 ms. Image acquisitions at LV basal, middle, and apical short-axis slices in diastole were performed before and 15 min after the injection of gadolinium, respectively.

Cardiovascular magnetic resonance data were analyzed with a commercial software (Argus, Siemens Healthineers, Erlangen, Germany, UK) by an experienced reader blinded to the echocardiographic results. Regions of interest were drawn in the blood and a midwall region of the myocardium and copied between the pre- and postcontrast T1 and ECV maps. To measure the T1 value of blood, a circular region of interest was positioned in the LV cavity, avoiding papillary muscle (**Figure 1C**). Then,

the ECV was calculated from the native and postcontrast T1 time, along with a hematocrit correction that was obtained on the same day of the CMR scanning according to the well-established formula (19).

Reproducibility

To evaluate the reproducibility of 2D-STE and 3D-STE measurements, a total of 20 subjects (including 10 HT recipients and 10 healthy controls) were selected randomly. For intraobserver variability, analysis of the first 2D-STE and 3D-STE data set of the 20 subjects (including 10 HT recipients and 10 healthy controls) was repeated 2–4 weeks later by the same primary investigator. For interobserver variability, the data set was analyzed by two blinded investigators.

Statistical Analysis

Continuous variables are presented as mean ± SD or median [interquartile range (IQR)] and categorical variables are presented as absolute numbers (percentages). The unpaired two-sample *t*-test or the Mann–Whitney *U*-test was used to compare continuous variables and the chi-squared test or the Fisher's exact test was used to compare categorical variables between the HT and control group. Correlations between continuous variables were evaluated with the Pearson's correlation coefficients. Potential predictors (demographic, clinical, LV conventional function parameters, and myocardial strains) of ECV in HT recipients were identified by the univariate linear regression analysis. The variables with univariate $p < 0.10$ were included in the multivariate linear regression analysis. To avoid collinearity issues, the multivariate stepwise linear regression analysis for 2D-LVGLS and 3D-LVGLS (model 1 for 2D-LVGLS and model 2 for 3D-LVGLS) was performed separately, along with those echocardiographic and clinical variables that demonstrated a univariate $p < 0.10$. The interobserver and intraobserver variability of the 10 HT recipients and 10 healthy volunteers were assessed by the intraclass correlation coefficients (ICCs) and the Bland–Altman analyses. Comparison of correlation coefficients was performed with the MedCalc version 19.0.4 (MedCalc Software, Ostend, Belgium, UK). All the statistical analyses, except for the comparison of correlation coefficients, were performed with SPSS Statistics version 23.0 (IBM, Armonk, New York, USA). $p < 0.05$ was considered as statistically significant.

RESULTS

Clinical Characteristics

The baseline clinical characteristics of the 40 patients with HT are given in **Tables 1**, **2**. The most prominent etiology for HT was dilated cardiomyopathy. The echocardiographic studies occurred at a median of 1.2 years after HT (IQR: 1.0–2.9 years). No patients had clinically significant AR or CAV when they were enrolled in this study. Immunosuppression regimens varied, but tacrolimus, mycophenolate mofetil, and prednisone were commonly used. Aspirin and statin were also frequently used.

TABLE 1 | Clinical characteristics of the 40 patients with HT.

Parameters	Value
Characteristics Pre-HT	
Recipient	
Men, *n* (%)	30 (75)
Age, (years)	43 ± 13
Weight, (kg)	58 (50, 65)
Etiology for transplantation, *n* (%)	
Dilated cardiomyopathy	24 (60)
Ischemic cardiomyopathy	8 (20)
Valvular heart disease	3 (7.5)
Hypertrophic cardiomyopathy	1 (2.5)
Complex congenital heart disease	1 (2.5)
Other disease	3 (7.5)
Invasive mPAP, (mmHg)	38 ± 14
Bypass time, (min)	97 (83, 115)
Aortic clamp time (min)	30 (27, 37)
Donor	
Age, (years)	35 ± 10
Weight, (kg)	65 (55, 65)
Weight ratio, (donor/recipient)	1.1 ± 0.3
Ischemic time, (min)	333 (195, 380)
Characteristics at echocardiographic examination	
Time since transplantation, (years)	1.2 (1.0, 2.9)
Surgical technique	
Biatrial technique, *n* (%)	14 (35)
Bicaval technique, *n* (%)	26 (65)
History of AR, *n* (%)	4 (10)
Immunosuppressant medications	
Tacrolimus, *n* (%)	35 (87.5)
Sirolimus/everolimus, *n* (%)	6 (15.0)
Cyclosporine, *n* (%)	5 (12.5)
Mycophenolate mofetil, *n* (%)	37 (92.5)
Prednisone, *n* (%)	32 (80.0)
Aspirin, *n* (%)	26 (65.0)
Statin, *n* (%)	25 (62.5)
ACE inhibitor/ARB, *n* (%)	15 (37.5)
Calcium-channel blocker, *n* (%)	18 (45.0)
Beta-blocker, *n* (%)	18 (45.0)

AR, acute rejection; HT, heart transplant; mPAP, mean pulmonary arterial pressure.

Echocardiographic and CMR Findings

Comparisons of echocardiographic and CMR parameters in the 40 patients with HT and 20 healthy controls are shown in **Table 2**. Compared with healthy controls, patients with HT had a significantly greater E/A ratio of the mitral valve and shorter deceleration time (DT) of E wave, which may suggest impaired LV diastolic function. Concerning LV systolic function, patients with HT had lower 3D-LVEF than the healthy controls (62.4 ± 5.5 vs. 66.1 ± 3.9%, $p = 0.008$), but remained within the normal range. However, HT group showed impaired 2D-LVGLS, 2D-LVGCS, 3D-LVGLS, and 3D-LVGCS. In contrast, the two groups did not differ in 2D- and 3D-LVGRS. Moreover, a weak

TABLE 2 | Demographic information, echocardiographic, and CMR findings of the HT group and control group.

Parameters	Control group ($n = 20$)	HT group ($n = 40$)	*P*-value
Demographic information at echocardiography examination			
Men (%)	14 (70%)	34 (75%)	0.68
Age (years)	45 ± 11	45 ± 14	0.944
Height (cm)	168 ± 8	166 ± 8	0.482
Weight (kg)	65 ± 6	62 ± 13	0.071
BSA (m^2)	1.7 ± 0.1	1.7 ± 0.2	0.118
BMI (kg/m^2)	23 (21, 24)	22 (20, 24)	0.169
Obesity, *n* (%)	3 (15.0)	8(20.0)	0.637
HR (bpm)	67 ± 10	88 ± 7	<0.001
SBP (mmHg)	120 (110, 124)	120 (112, 126)	0.346
DBP (mmHg)	80 (70, 87)	80 (71, 85)	0.766
Echocardiographic findings			
LA, (mm)	33 ± 3	46 ± 7	<0.001
LVd, (mm)	44 ± 2	42 ± 4	0.093
IVST, (mm)	8.9 ± 0.8	9.6 ± 1.3	0.01
LVMI, (g)	72.0 ± 11.1	82.5 ± 17.6	0.007
Mitral valve			
E, (m/s)	0.7 ± 0.2	0.8 ± 0.2	0.366
A, (m/s)	0.6 ± 0.1	0.5 ± 0.1	<0.001
E/A ratio	1.2 ± 0.4	1.8 ± 0.4	<0.001
e', (cm/s)	11 ± 2	11 ± 2	0.528
E/e'	7 ± 2	8 ± 3	0.334
DT, (ms)	210 ± 45	182 ± 34	0.02
Tei index	0.36 ± 0.06	0.52 ± 0.11	<0.001
2D-LVGLS, (%)	−20.0 ± 2.5	−16.9 ± 2.3	<0.001
2D-LVGCS, (%)	−29.1 ± 3.3	−26.6 ± 4.7	0.038
2D-LVGRS, (%)	39.3 ± 6.0	37.8 ± 7.6	0.198
3D-LVEDV, (ml)	90.5 ± 17.8	72.0 ± 19.4	0.001
3D-LVESV, (ml)	30.7 ± 7.3	27.2 ± 9.3	0.013
3D-LVEF, (%)	66.1 ± 3.9	62.4 ± 5.5	0.008
3D-LVGLS, (%)	−20.8 ± 1.5	−17.2 ± 2.3	<0.001
3D-LVGCS, (%)	−31.5 ± 3.7	−28.3 ± 5.1	0.015
3D-LVGRS, (%)	42.3 ± 4.1	40.7 ± 6.3	0.339
CMR findings*			
Native T1 time, (ms)	999.7 ± 19.7	1043.8 ± 34.0	< 0.001
Post-contrast T1 time, (ms)	455.3 ± 24.5	429.8 ± 39.7	0.013
ECV, *n* (%)	24.3 ± 1.8	26.6 ± 2.7	0.002

2D, two dimensional; 3D, three dimensional; A, late diastolic inflow velocity; BSA, body surface area; CMR, cardiovascular magnetic resonance; DBP, diastolic blood pressure; DT, deceleration time of E; E, early diastolic inflow velocity; e', mean value of early diastolic mitral annular tissue velocity and left ventricular lateral wall tissue velocity; ECV, extracellular volume fraction; HR, heart rate; IVST, interventricular septum thickness; LA, left atrial diameter; LVd, left ventricular diastolic diameter; LVMI, left ventricular mass indexed to body surface area; LVEF, left ventricular ejection fraction; LVGLS, left ventricular global longitudinal strain; LVGCS, left ventricular global circumferential strain; LVGRS, left ventricular global radial strain; PA, pulmonary artery; SBP, systolic blood pressure.
**Means that 31 patients with HT and 20 healthy controls had the data of CMR findings.*

to moderate but significant correlation of global strain values between the 2D- and 3D-STE was noted in the entire study population (LVGLS: $r = 0.57$, $p < 0.001$; LVGCS: $r = 0.46$, $p < 0.001$; LVGRS: $r = 0.45$, $p < 0.001$) (**Figure 2**). There were 31 of the 40 patients with HT and all the 20 healthy controls agreed to undergo CMR examination within 24 h of the echocardiography examination. Compared with healthy controls, the HT recipients showed significantly longer native T1 time (999.7 ± 19.7 vs. 1043.8 ± 34.0 ms, $p < 0.001$) and greater ECV (24.3 ± 1.8 vs. 26.6 ± 6.7%, $p = 0.002$).

Relationships Between Diffuse LVMF and Clinical and Echocardiographic Parameters

The diffuse LVMF was defined by CMR-ECV in this study. The correlations between LV myocardial strain and CMR-ECV are shown in **Figure 3**. For 2D-LV myocardial strain, only 2D-LVGLS correlated with ECV ($r = 0.53$, $p = 0.002$), whereas LVGCS and LVGRS showed no correlation with ECV. **Figure 3** also illustrates the association of 3D-LV myocardial strain with CMR-ECV. Similarly, as shown in **Figures 3D–F**, ECV only had correlation with 3D-LVGLS ($r = 0.60$, $p < 0.001$) and not had correlation with 3D-LVGCS or 3D-LVGRS. Moreover, 3D-LVEF did not correlate with CMR-ECV. Furthermore, there was no significant difference between the correlation of 2D-LVGLS with CMR-ECV and the correlation of 3D-LVGLS with CMR-ECV ($r = 0.53$ vs. r $= 0.60$, $p = 0.670$).

Table 3 shows the results of the univariate and multivariate linear regression analyses for the relationship between ECV and the clinical and echocardiographic variables in the HT recipients. The univariate regression analysis revealed that recipient age, time since HT, DT, 2D-LVGLS, and 3D-LVGLS were significantly correlated with ECV. In addition, 2D-LVGLS had correlation with 3D-LVGLS ($r = 0.57$, $p < 0.001$) (**Figure 2**). Therefore, to avoid the problems of collinearity, 2D-LVGLS and 3D-LVGLS were evaluated in two separate models. Finally, the stepwise multivariate regression analysis showed that 2D-LVGLS ($\beta = 0.39$, $p = 0.019$) and 3D-LVGLS ($\beta = 0.54$, $p < 0.001$) both were independently associated with CMR-ECV.

Reproducibility

The measurements obtained by 2D-STE and 3D-STE showed excellent reproducibility. The complete data of interobserver variability and intraobserver variability were shown in **Table 4**.

DISCUSSION

To the best of our knowledge, this is the first study to evaluate the level of diffuse LVMF with non-invasive CMR-ECV, further investigating the predictive value of 3D-STE-derived LV strain for diffuse LVMF in patients with post-HT, and directly compares its utility with that of 2D-STE-derived strains. The main findings of this study were: (1) the level of diffuse MF defined by CMR-ECV was higher even in asymptomatic patients with HT than in healthy controls; (2) the increased LVMF measured by CMR-ECV was correlated with 2D- and 3D-LVGLS, not correlated with LV-GCS, GRS, or ejection fraction (EF); and (3) both the 2D- and 3D-LVGLS were independently correlated with the extent of diffuse LVMF in HT recipients.

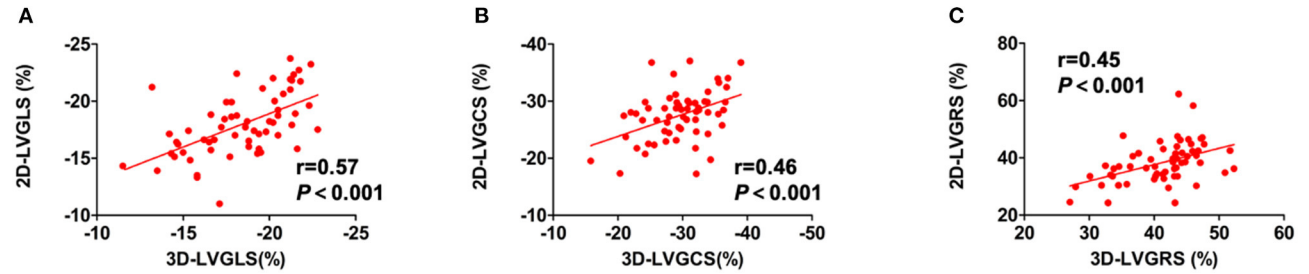

FIGURE 2 | The relationships between LV strain parameters from 2D-STE and 3D-STE. The relationship between **(A)** 2D-LVGLS and 3D-LVGLS, **(B)** 2D-LVGCS and 3D-LVGCS, and **(C)** 2D-LVGRS and 3D-LVGRS. 2D-STE, two-dimensional speckle-tracking echocardiography; 3D-STE, three-dimensional STE; GLS, global longitudinal strain; GCS, global circumferential strain; GRS, global radial strain; LV, left ventricular.

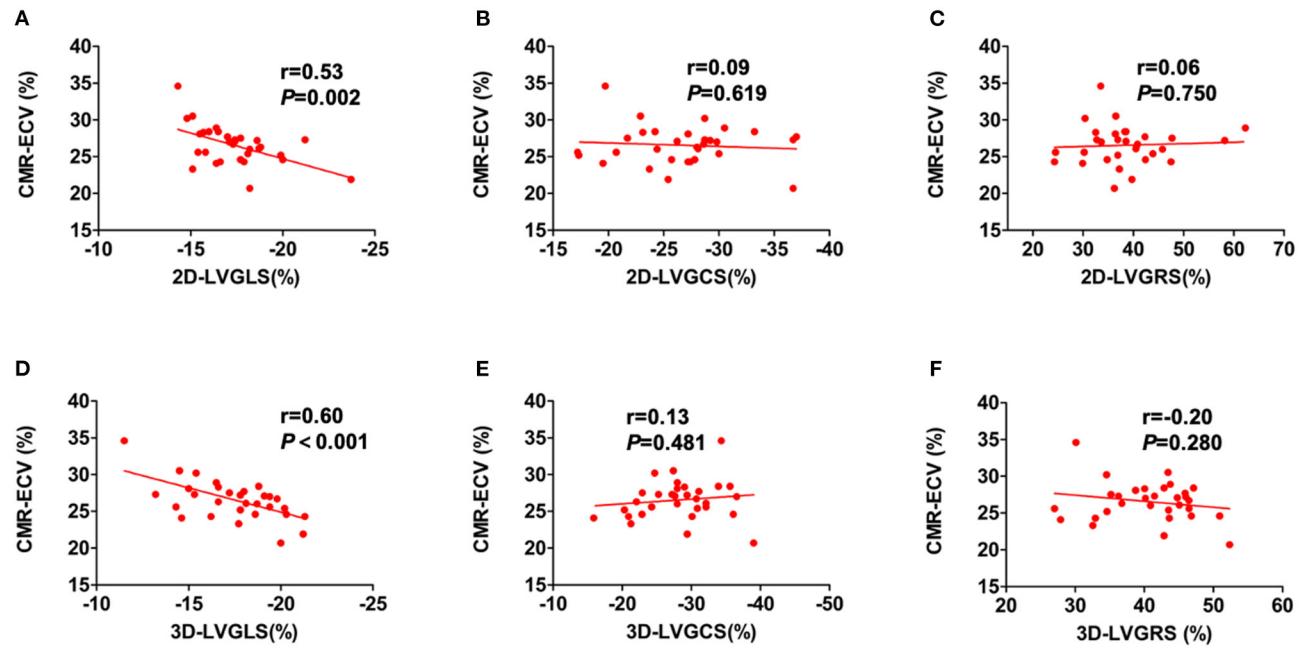

FIGURE 3 | The correlations of CMR-ECV and LV strain parameters. Correlations were showed between CMR-ECV and 2D-LVGLS **(A)**, 2D-LVGCS **(B)**, 2D-LVGRSV **(C)**, 3D-LVGLS **(D)**, 3D-LVGCS **(E)**, and 3D-LVGRSV **(F)**. 2D, two-dimensional; 3D, three-dimensional; CMR, cardiovascular magnetic resonance; ECV, extracellular volume fraction; GLS, global longitudinal strain; GCS, global circumferential strain; GRS, global radial strain; LV, left ventricular.

Left Ventricular MF in Patients With HT

The MF is a commonly demonstrated histopathologic feature in patients with HT and its correlation with a higher risk of adverse clinical outcome has been validated by the previous studies (2–5). Adverse fibrotic myocardial remodeling is a suspected long-term sequela of HT recipients. Therefore, it is clinically crucial to quantify the MF in the transplanted hearts at an early stage.

Histological biopsy is the gold standard for assessing MF, but it is invasive. The myocardial samples by the biopsy cannot accurately assess the diffuse MF. Furthermore, the endomyocardial biopsy is usually performed from the right ventricular side in the transplanted hearts and, thus, can not necessarily reflect LV information (1). Recently, the T1 time and ECV measured by CMR T1 mapping have emerged as a reliable non-invasive method for quantifying diffuse MF. However, previous studies showed high variability in native T1 time for assessing MF (20, 21). However, compared to native T1 time, myocardial ECV, which was derived from myocardial and blood pre- and post-contrast T1 relaxation time changes, has been validated as a preferred non-invasive method for quantifying actual diffuse MF in various cardiovascular diseases (10–13). Therefore, we selected the non-invasive CMR-ECV to measure diffuse MF in the patients after HT. This study proved that ECV was higher even in asymptomatic patients with HT with normal LVEF than in healthy controls, indicating the increased diffuse MF in the transplanted hearts. The increased MF in the transplanted hearts was consistent with a previous study that measured the MF through the histological biopsy or CMR T1 mapping (3–7, 22). AR, CAV, ischemic injure of the donor's heart, and postoperatively immunosuppressive therapy all may lead to

TABLE 3 | Univariate and multivariate linear regression analysis for ECV in patients with HT ($n = 31$).

	Univariate analysis		Multivariate analysis			
			Model 1 + 2D-LVGLS		Model 2 + 3D-LVGLS	
Variables	***β***	***P*-value**	***β***	***P*-value**	***β***	***P*-value**
Pre-HT						
Donor age, (years)	0.21	0.280				
Donor weight, (kg)	−0.08	0.663				
Recipient age, (years)	0.37	0.044	0.18	0.267	0.09	0.543
Recipient weight, (kg)	0.17	0.378				
Weight ratio, (donor/recipient)	−0.02	0.923				
Invasive mPAP, (mmHg)	0.21	0.276				
CPB time, (min)	0.10	0.592				
Aortic clamp time, (min)	0.11	0.559				
Ischemic time, (min)	−0.07	0.737				
Post-HT						
HR, (bpm)	−0.13	0.496				
SBP, (mmHg)	−0.24	0.192				
DBP, (mmHg)	−0.22	0.233				
History of ACR, (yes vs no)	−0.19	0.302				
Time since transplantation, (years)	0.42	0.018	0.24	0.139	0.32	0.022
Mitral valve						
E/A ratio	0.04	0.822				
E/e'	0.17	0.376				
DT, (ms)	−0.32	0.079	−0.23	0.134	−0.29	0.039
LV Tei index	0.16	0.398				
2D-LVGLS, (%)	0.53	0.002	0.39	0.019		
2D-LVGCS, (%)	0.09	0.619				
2D-LVGRS, (%)	0.06	0.750				
3D-LVEF, (%)	0.26	0.151				
3D-LVGLS, (%)	0.60	<0.001			0.54	<0.001
3D-LVGCS, (%)	0.13	0.481				
3D-LVGRS, (%)	−0.20	0.280				
3D-LVEF, (%)	−0.26	0.151				

*Abbreviations as in **Tables 1**, **2**.*

MF of the transplanted hearts (2, 23, 24). Moreover, this study proved that CMR-ECV was positively correlated with time after HT, which corresponded to some other studies that indicated the MF may develop over time (3–5). Additionally, this study also proved that the ECV was correlated with the recipient age, which may suggest that recipient age would affect the allograft remodeling in the transplanted hearts. Furthermore, this study showed that the ECV did not correlate with ischemic time during transplantation, which was not in concordance with the study by Yuan et al. (22) but was in agreement with the study by Ide et al. (7). Therefore, the association between LVMF and the ischemic time needs to be further explored in the multicenter studies among broader research populations in the future.

Correlation Between LV Myocardial Strain and CMR-ECV

The echocardiographic myocardial strain can accurately quantify ventricular mechanical function and it has emerged as a promising modality for predicting MF non-invasively and conveniently (14, 15). However, the correlation between the myocardial strain and MF in patients with post-HT has not been elucidated. Some studies have shown that increased LVMF measured by CMR-ECV was correlated with the decreased LV myocardial strain in a variety of heart diseases (16, 25–27). However, the studies about the association between 2D-myocardial strain and ECV show high variability and studies addressing which strain components might correlate best with ECV have not been seen. This is the first study to reveal the association between CMR-ECV and LV myocardial strain measured by 2D- and 3D-STE simultaneously in patients with HT.

This study showed that CMR-ECV both correlated with the 2D- and the 3D-LVGLS. A possible mechanism linking ECV to reduced systolic strain may be that the increased fibrosis leading to increased LV stiffness, which resulted in reduced

TABLE 4 | Intraobserver and interobserver reproducibility for the parameters of the two-dimensional and the three-dimensional speckle-tracking echocardiography.

	ICC (95% CI)	Bias	Limits of agreement
Intra-observer (*n* = 20)			
2D-LVGLS, (%)	0.95 (0.88-0.98)	0.1	−1.5∼1.7
2D-LVGCS, (%)	0.94 (0.85-0.97)	0.2	−3.0∼3.3
2D-LVGRS, (%)	0.87 (0.71-0.95)	1.0	−6.7∼4.7
3D-LVGLS, (%)	0.97 (0.93-0.99)	0.1	−1.2∼1.2
3D-LVGCS, (%)	0.92 (0.80-0.97)	0.3	−3.7∼3.2
3D-LVGRS, (%)	0.90 (0.78-0.96)	0.8	−3.7∼5.3
Inter-observer (*n* = 20)			
2D-LVGLS, (%)	0.93 (0.83-0.97)	0.1	−1.7∼2.0
2D-LVGCS, (%)	0.90 (0.76-0.96)	1.2	−2.7∼5.3
2D-LVGRS, (%)	0.85 (0.67-0.94)	1.3	−7.3∼4.8
3D-LVGLS, (%)	0.95 (0.88-0.98)	0.1	−1.6∼1.8
3D-LVGCS, (%)	0.87 (0.70-0.95)	0.3	−4.4∼4.0
3D-LVGRS, (%)	0.86 (0.67-0.94)	0.8	−4.6∼6.2

*Abbreviations as in **Table 2**.*
n = 20 means that there were 10 patients with HT and 10 healthy controls data used in this table.

end-diastolic muscle fiber length and, by the Frank–Starling law, reduced cardiac muscle contraction and systolic strain. The significant correlation between MF and GLS in the HT recipients in this study is in agreement with previous studies for other cardiovascular diseases (15, 16, 28). However, the increased ECV was not correlated with GCS or GRS in this study. This is possibly due to the fact that the LS mainly depends on the subendocardial layer and the subendocardial myocardium is sensitive to fibrosis (28). However, the CS mainly reflects the strain in the midmyocardium and RS is a change in the wall thickness of a length of the vertical line from a point on the endocardial border to a cross point on the epicardial border (29). In addition, patients with HT in our study had no severe complications at the time of CMR examination, such as AR and CAV in this study. Therefore, the extent of LV diffuse MF may be relatively mild in our subjects. Moreover, the early stage of MF mainly occurs in the endocardium and only LS can reveal this abnormality (29, 30). We believe that the aforementioned reasons may explain why only decreased GLS had a correlation with the increased ECV in the transplanted hearts.

Theoretically, compared with 2D-STE, 3D-STE is not affected by geometric modeling and out-of-plane motion, and it can evaluate the myocardial deformation in all the three spatial dimensions (17, 31). However, clinical testing and validation are needed to determine whether 3D-STE is superior to 2D-STE. The comparability of 2D- and 3D-STE has been studied extensively in healthy subjects and patients with various other cardiovascular diseases previously (17, 32, 33). However, the comparability of the association between 2D- and 3D-STE-derived strain and CMR evidence of diffuse MF has not been studied in patients post-HT simultaneously. This study made a direct comparison of strain values by 2D and 3D-STE in predicting the MF and revealed that 2D-LVGLS and 3D-LVGLS provides comparable results. The image quality and spatial resolution of 3D-STE are suboptimal than 2D-STE. The lower frame rate of 3D-STE may not be sufficient to accurately capture all the phases of a cardiac cycle. In addition, patients with HT had a higher heart rate. The aforementioned limitations of 3D-STE may lead to the conclusion that it is not superior to 2D-STE in correlation with CMR-ECV.

Clinical Implications

This study proved that the level of diffuse MF defined by CMR-ECV was higher even in asymptomatic patients with HT than in healthy controls. Since MF is an adverse pathologic remodeling and can result in poor clinical outcomes, a reliable non-invasive method to monitor graft fibrosis would be clinically effective for the early identification of higher risk of patients with HT. This study showed that both 2D- and 3D-LVGLS were independently correlated with diffuse MF in HT recipients. Considering the correlation between 2D-STE or 3D-STE derived strain and MF is not robust and only presents up to 36% variations of MF. Therefore, CMR and cardiac biopsy cannot be replaced by these echocardiography modalities. Still this study suggested that measurements of 2D- and 3D-LVGLS may provide a valuable preliminary alternative non-invasive assessment of MF in the transplanted hearts, which may facilitate early risk stratification of HT recipients during follow-up examinations.

Study Limitations

This study is a single-center study and is limited by a relatively small sample size. The HT recipients with AR and CAV at the time of CMR were not included in this study. So, the range of diffuse MF in this study was relatively narrow. In addition, there were no results of the histological biopsy in this study. (Nevertheless, ECV has been validated as a valuable surrogate marker for the assessment for the diffuse MF). Moreover, 3D-STE is highly independent of image quality and its frame rate was lower. Last, as the strain parameters are vendor dependent and not interchangeable, our results may not apply to other software algorithms.

CONCLUSION

This study showed that CMR marker of diffuse MF was present in asymptomatic patients with HT and it was correlated with the 2D- and the 3D-LVGLS, not with LVGCS and LVGRS by echocardiography. The findings highlight the clinical superiority of the 2D- and the 3D-LVGLS over LVGCS, LVGRS, and other conventional parameters in predicting diffuse MF in HT recipients. 2D- and 3D-LVFLS may provide noninvasive tools for monitoring the development of adverse fibrotic remodeling during the serial follow-up of HT recipients.

DATA AVAILABILITY STATEMENT

The raw data supporting the conclusions of this article will be made available by the corresponding authors, without undue reservation.

ETHICS STATEMENT

This study was approved by the Ethics Committee of Tongji Medical College, Huazhong University of Science and Technology. The patients/participants provided their written informed consent to participate in this study.

AUTHOR CONTRIBUTIONS

WS, BL, LZ, and MX: conception and design of study. WS, XS, JW, SZ, YZ, CW, YX, and YY: acquisition of data. WS, XS, JW, ND, GW, YL, and QL: analysis and/or interpretation of data. JW, BL, LZ, and MX: revised the manuscript. WS, XS, and JW: drafting the manuscript. QL, BL, LZ, and MX: revising the manuscript critically for important intellectual content. All authors contributed to the article and approved the submitted version.

FUNDING

This study was supported by the National Natural Science Foundation of China (Grant Numbers: 81922033, 81671705, 81727805, and 81530056) and the Key Research and Development Program of Hubei (Grant Number: 2020DCD015).

REFERENCES

1. Badano LP, Miglioranza MH, Edvardsen T, Colafranceschi AS, Muraru D, Bacal F, et al. European Association of Cardiovascular Imaging/Cardiovascular Imaging Department of the Brazilian Society of Cardiology recommendations for the use of cardiac imaging to assess and follow patients after heart transplantation. *Eur Heart J Cardiovasc Imaging*. (2015) 16:919–48. doi: 10.1093/ehjci/jev139
2. Sade LE, Hazirolan T, Kozan H, Ozdemir H, Hayran M, Eroglu S, et al. T1 mapping by cardiac magnetic resonance and multidimensional speckle-tracking strain by echocardiography for the detection of acute cellular rejection in cardiac allograft recipients. *JACC Cardiovasc Imaging*. (2019) 12:1601–14. doi: 10.1016/j.jcmg.2018.02.022
3. Gramley F, Lorenzen J, Pezzella F, Kettering K, Himmrich E, Plumhans C, et al. Hypoxia and myocardial remodeling in human cardiac allografts: a time-course study. *J Heart Lung Transplant*. (2009) 28:1119–26. doi: 10.1016/j.healun.2009.05.038
4. Armstrong AT, Binkley PF, Baker PB, Myerowitz PD, Leier CV. Quantitative investigation of cardiomyocyte hypertrophy and myocardial fibrosis over 6 years after cardiac transplantation. *J Am Coll Cardiol*. (1998) 32:704–10. doi: 10.1016/S0735-1097(98)00296-4
5. Goland S, Siegel RJ, Burton K, De Robertis MA, Rafique A, Schwarz E, et al. Changes in left and right ventricular function of donor hearts during the first year after heart transplantation. *Heart*. (2011) 97:1681–6. doi: 10.1136/hrt.2010.220871
6. Riesenkampff E, Chen CK, Kantor PF, Greenway S, Chaturvedi RR, Yoo SJ, et al. Diffuse myocardial fibrosis in children after heart transplantations: a magnetic resonance T1 mapping study. *Transplantation*. (2015) 99:2656–62. doi: 10.1097/TP.0000000000000769
7. Ide S, Riesenkampff E, Chiasson DA, Dipchand AI, Kantor PF, Chaturvedi RR, et al. Histological validation of cardiovascular magnetic resonance T1 mapping markers of myocardial fibrosis in paediatric heart transplant recipients. *J Cardiovasc MagnReson*. (2017) 19:10. doi: 10.1186/s12968-017-0326-x
8. Hughes A, Okasha O, Farzaneh-Far A, Kazmirczak F, Nijjar PS, Velangi P, et al. Myocardial fibrosis and prognosis in heart transplant recipients. *Circ Cardiovasc Imaging*. (2019) 12:e009060. doi: 10.1161/CIRCIMAGING.119.009060
9. Pedrotti P, Vittori C, Facchetti R, Pedretti S, Dellegrottaglie S, Milazzo A, et al. Prognostic impact of late gadolinium enhancement in the risk stratification of heart transplant patients. *Eur Heart J Cardiovasc Imaging*. (2017) 18:130–7. doi: 10.1093/ehjci/jew186
10. aus dem Siepen F, Buss SJ, Messroghli D, Andre F, Lossnitzer D, Seitz S, et al. T1 mapping in dilated cardiomyopathy with cardiac magnetic resonance: quantification of diffuse myocardial fibrosis and comparison with endomyocardial biopsy. *Eur Heart J Cardiovasc Imaging*. (2015) 16:210–6. doi: 10.1093/ehjci/jeu183
11. Nakamori S, Dohi K, Ishida M, Goto Y, Imanaka-Yoshida K, Omori T, et al. Native T1 mapping and extracellular volume mapping for the assessment of diffuse myocardial fibrosis in dilated cardiomyopathy. *JACC Cardiovasc Imaging*. (2018) 11:48–59. doi: 10.1016/j.jcmg.2017.04.006
12. Fontana M, White SK, Banypersad SM, Sado DM, Maestrini V, Flett AS, et al. Comparison of T1 mapping techniques for ECV quantification. Histological validation and reproducibility of ShMOLLI versus multibreath-hold T1 quantification equilibrium contrast CMR. *J Cardiovasc MagnReson*. (2012) 14:88. doi: 10.1186/1532-429X-14-88
13. Cui Y, Cao Y, Song J, Dong N, Kong X, Wang J, et al. Association between myocardial extracellular volume and strain analysis through cardiovascular magnetic resonance with histological myocardial fibrosis in patients awaiting heart transplantation. *J Cardiovasc Magn Reson*. (2018) 20:25. doi: 10.1186/s12968-018-0445-z
14. Lisi M, Cameli M, Righini FM, Malandrino A, Tacchini D, Focardi M, et al. RV longitudinal deformation correlates with myocardial fibrosis in patients with end-stage heart failure. *JACC Cardiovasc Imaging*. (2015) 8:514–22. doi: 10.1016/j.jcmg.2014.12.026
15. Cameli M, Mondillo S, Righini FM, Lisi M, Dokollari A, Lindqvist P, et al. Left ventricular deformation and myocardial fibrosis in patients with advanced heart failure requiring transplantation. *J Card Fail*. (2016) 22:901–7. doi: 10.1016/j.cardfail.2016.02.012
16. Cameli M, Mondillo S, Righini FM, Lisi M, Dokollari A, Lindqvist P, et al. Diffuse interstitial fibrosis and myocardial dysfunction in early chronic kidney disease. *Am J Cardiol*. (2015) 115:1311–7. doi: 10.1016/j.amjcard.2015.02.015
17. Saito K, Okura H, Watanabe N, Hayashida A, Obase K, Imai K, et al. Comprehensive evaluation of left ventricular strain using speckle tracking echocardiography in normal adults: comparison of three-dimensional and two-dimensional approaches. *J Am Soc Echocardiogr*. (2009) 22:1025–30. doi: 10.1016/j.echo.2009.05.021
18. Lang RM, Badano LP, Mor-Avi V, Afilalo J, Armstrong A, Ernande L, et al. Recommendations for cardiac chamber quantification by echocardiography in adults: an update from the American Society of Echocardiography and the European Association of Cardiovascular Imaging. *J Am Soc Echocardiogr*. (2015) 28:1–39.e14. doi: 10.1016/j.echo.2014.10.003
19. Flett AS, Hayward MP, Ashworth MT, Hansen MS, Taylor AM, Elliott PM, et al. Equilibrium contrast cardiovascular magnetic resonance for the measurement of diffuse myocardial fibrosis: preliminary validation in humans. *Circulation*. (2010) 122:138–44. doi: 10.1161/CIRCULATIONAHA.109.930636
20. Bull S, White SK, Piechnik SK, Flett AS, Ferreira VM, Loudon M, et al. Human non-contrast T1 values and correlation with histology in diffuse fibrosis. *Heart*. (2013) 99:932–7. doi: 10.1136/heartjnl-2012-303052
21. de Meester de Ravenstein C, Bouzin C, Lazam S, Boulif J, Amzulescu M, Melchior J, et al. Histological validation of measurement of diffuse interstitial myocardial fibrosis by myocardial extravascular volume fraction from Modified Look-Locker imaging (MOLLI) T1 mapping at 3 T. *J Cardiovasc Magn Reson*. (2015) 17:48. doi: 10.1186/s12968-015-0150-0
22. Yuan Y, Cai J, Cui Y, Wang J, Alwalid O, Shen X, et al. CMR-derived extracellular volume fraction (ECV) in asymptomatic heart transplant recipients: correlations with clinical features and myocardial edema.

Int J Cardiovasc Imaging. (2018) 34:1959–67. doi: 10.1007/s10554-018-1421-2
23. Pickering JG, Boughner DR. Fibrosis in the transplanted heart and its relation to donor ischemic time. Assessment with polarized light microscopy and digital image analysis. *Circulation*. (1990) 81:949–58. doi: 10.1161/01.CIR.81.3.949
24. Yamani MH, Haji SA, Starling RC, Tuzcu EM, Ratliff NB, Cook DJ, et al. Myocardial ischemic-fibrotic injury after human heart transplantation is associated with increased progression of vasculopathy, decreased cellular rejection and poor long-term outcome. *J Am Coll Cardiol*. (2002) 39:970–7. doi: 10.1016/S0735-1097(02)01714-X
25. Zeng M, Qiao Y, Wen Z, Liu J, Xiao E, Tan C, et al. The association between diffuse myocardial fibrosis on cardiac magnetic resonance T1 mapping and myocardial dysfunction in diabetic rabbits. *Sci Rep*. (2017) 7:44937. doi: 10.1038/srep44937
26. Kuruvilla S, Janardhanan R, Antkowiak P, Keeley EC, Adenaw N, Brooks J, et al. Increased extracellular volume and altered mechanics are associated with LVH in hypertensive heart disease, not hypertension alone. *JACC Cardiovasc Imaging*. (2015) 8:172–80. doi: 10.1016/j.jcmg.2014.09.020
27. Park SJ, Cho SW, Kim SM, Ahn J, Carriere K, Jeong DS, et al. Assessment of myocardial fibrosis using multimodality imaging in severe aortic stenosis: comparison with histologic fibrosis. *JACC Cardiovasc Imaging*. (2019) 12:109–19. doi: 10.1016/j.jcmg.2018.05.028
28. Wang J, Zhang Y, Zhang L, Tian F, Wang B, Xie Y, et al. Assessment of myocardial fibrosis using two-dimensional and three-dimensional speckle tracking echocardiography in dilated cardiomyopathy with advanced heart failure. *J Card Fail*. (2021) 27:651–61. doi: 10.1016/j.cardfail.2021.01.003
29. Seo Y, Ishizu T, Atsumi A, Kawamura R, Aonuma K. Three-dimensional speckle tracking echocardiography. *Circ J*. (2014) 78:1290–301. doi: 10.1253/circj.CJ-14-0360
30. de Leeuw N, Ruiter DJ, Balk AH, de Jonge N, Melchers WJ, Galama JM. Histopathologic findings in explanted heart tissue from patients with end-stage idiopathic dilated cardiomyopathy. *Transpl Int*. (2001) 14:299–306. doi: 10.1007/s001470100339
31. Yodwut C, Weinert L, Klas B, Lang RM, Mor-Avi V. Effects of frame rate on three-dimensional speckle-tracking-based measurements of myocardial deformation. *J Am Soc Echocardiogr*. (2012) 25:978–85. doi: 10.1016/j.echo.2012.06.001
32. Nagata Y, Takeuchi M, Wu VC, Izumo M, Suzuki K, Sato K, et al. Prognostic value of LV deformation parameters using 2D and 3D speckle-tracking echocardiography in asymptomatic patients with severe aortic stenosis and preserved LV ejection fraction. *JACC Cardiovasc Imaging*. (2015) 8:235–45. doi: 10.1016/j.jcmg.2014.12.009
33. Trache T, Stöbe S, Tarr A, Pfeiffer D, Hagendorff A. The agreement between 3D, standard 2D and triplane 2D speckle tracking: effects of image quality and 3D volume rate. *Echo Res Pract*. (2014) 1:71–83. doi: 10.1530/ERP-14-0025

Conflict of Interest: The authors declare that the research was conducted in the absence of any commercial or financial relationships that could be construed as a potential conflict of interest.

Publisher's Note: All claims expressed in this article are solely those of the authors and do not necessarily represent those of their affiliated organizations, or those of the publisher, the editors and the reviewers. Any product that may be evaluated in this article, or claim that may be made by its manufacturer, is not guaranteed or endorsed by the publisher.

frontiers in Cardiovascular Medicine

METHODS
published: 10 December 2021
doi: 10.3389/fcvm.2021.759675

Mitral Valve Atlas for Artificial Intelligence Predictions of MitraClip Intervention Outcomes

*Yaghoub Dabiri[1], Jiang Yao[2], Vaikom S. Mahadevan[3], Daniel Gruber[4], Rima Arnaout[5,6,7,8,9], Wolfgang Gentzsch[4], Julius M. Guccione[10] and Ghassan S. Kassab[11]**

[1] 3DT Holdings LLC, San Diego, CA, United States, [2] Dassault Systemes Simulia Corp, Johnston, RI, United States, [3] Department of Medicine, University of California, San Francisco, San Francisco, CA, United States, [4] The UberCloud, Sunnyvale, CA, United States, [5] Division of Cardiology, Department of Medicine, University of California, San Francisco, San Francisco, CA, United States, [6] Bakar Computational Health Sciences Institute, University of California, San Francisco, San Francisco, CA, United States, [7] Center for Intelligent Imaging, University of California, San Francisco, San Francisco, CA, United States, [8] Biological and Medical Informatics, University of California, San Francisco, San Francisco, CA, United States, [9] Chan Zuckerberg Biohub, University of California, San Francisco, San Francisco, CA, United States, [10] Department of Surgery, University of California, San Francisco, San Francisco, CA, United States, [11] Department of Medicine, California Medical Innovations Institute, San Diego, CA, United States

OPEN ACCESS

Edited by:
Zahra K. Motamed, McMaster University, Canada

Reviewed by:
Nuno Moreno, Hospital Pedro Hispano, Portugal
Farhad R. Nezami, Brigham and Women's Hospital and Harvard Medical School, United States

***Correspondence:**
Ghassan S. Kassab
gkassab@calmi2.org

Specialty section:
This article was submitted to Cardiovascular Imaging, a section of the journal Frontiers in Cardiovascular Medicine

Received: *16 August 2021*
Accepted: *03 November 2021*
Published: *10 December 2021*

Citation:
Dabiri Y, Yao J, Mahadevan VS, Gruber D, Arnaout R, Gentzsch W, Guccione JM and Kassab GS (2021) Mitral Valve Atlas for Artificial Intelligence Predictions of MitraClip Intervention Outcomes. Front. Cardiovasc. Med. 8:759675. doi: 10.3389/fcvm.2021.759675

Severe mitral regurgitation (MR) is a cardiac disease that can lead to fatal consequences. MitraClip (MC) intervention is a percutaneous procedure whereby the mitral valve (MV) leaflets are connected along the edge using MCs. The outcomes of the MC intervention are not known in advance, i.e., the outcomes are quite variable. Artificial intelligence (AI) can be used to guide the cardiologist in selecting optimal MC scenarios. In this study, we describe an atlas of shapes as well as different scenarios for MC implantation for such an AI analysis. We generated the MV geometrical data from three different sources. First, the patients' 3-dimensional echo images were used. The pixel data from six key points were obtained from three views of the echo images. Using PyGem, an open-source morphing library in Python, these coordinates were used to create the geometry by morphing a template geometry. Second, the dimensions of the MV, from the literature were used to create data. Third, we used machine learning methods, principal component analysis, and generative adversarial networks to generate more shapes. We used the finite element (FE) software ABAQUS to simulate smoothed particle hydrodynamics in different scenarios for MC intervention. The MR and stresses in the leaflets were post-processed. Our physics-based FE models simulated the outcomes of MC intervention for different scenarios. The MR and stresses in the leaflets were computed by the FE models for a single clip at different locations as well as two and three clips. Results from FE simulations showed that the location and number of MCs affect subsequent residual MR, and that leaflet stresses do not follow a simple pattern. Furthermore, FE models need several hours to provide the results, and they are not applicable for clinical usage where the predicted outcomes of MC therapy are needed in real-time. In this study, we generated the required dataset for the AI models which can provide the results in a matter of seconds.

Keywords: mitral valve, finite element method, cardiac imaging, principal component analysis, MitraClip

1. INTRODUCTION

MitraClip (MR) is a percutaneous procedure to treat severe mitral regurgitation (MR), a disease with a prevalence of 4 million in US and an incidence of 250,000 patients each year (1, 2). This intervention is most appropriate for patients who cannot tolerate surgery because of other diseases or poor health conditions (2). The short-term and long-term benefits of MC has been reported in clinical studies (3–5).

Despite the benefits of MC implantation, the positioning of the clips is based on echocardiographic parameters including color doppler which does not accurately predict reduction of MR. Particularly, the location of the MC along the leaflet edges and the number of MCs has a direct role in the effectiveness of MC therapy. Currently, there is no systematic approach to determine the location and number of MCs that minimize MR. On the other hand, leaflet injury can occur as a result of MC intervention (6, 7), which is another consideration for an optimal MC therapy.

An *ad-hoc* approach to implant the MC in an optimal scenario would be to try different locations and number of MC, but this is not practical. Computational modeling including finite element (FE) analysis can be used to create *in-silico* models of MC procedure (8–11). Using FE, different scenarios can be virtually evaluated for a subject, and the best strategy is implemented during the MC intervention. FE computations are time-consuming, however, making FE models inappropriate for clinical usage. Artificial Intelligence (AI) and its subcategory Machine learning (ML) is being used in cardiovascular medicine and technology (12) and presents an opportunity to speed MC simulations compared to FE modeling.

To use AI for MC interventions, an atlas of shapes as well as different scenarios for MC implantation, namely the location and number of MCs is required. Notably, the dataset should cover the diversity in MV geometry for different subjects. The MV geometry can be acquired by different imaging modalities such as magnetic resonance imaging (MRI), CT scan, and echocardiography (Echo). Although Echo modality contains less details compared to MRI and CT scan, it is more convenient for patients. Since there are hand-held Echo imaging devices in development, this imaging modality is more likely to be used in future mobile technologies and internet of things (IoT) technology.

The aim of this paper is to introduce a methodology for creating an atlas that can be used for MV AI applications. Particularly, the data generation methods presented can be used to mine the MC intervention based on AI algorithms. Shapes and FE models of the MV are created where the geometries of the models are based on Echo images of the MV, the morphological data in the literature, principal component analysis (PCA), and generative adversarial networks (GANs). For each geometry, 7 scenarios were created whereby the MR in untreated MV, and 6 locations for the MC were simulated. We also show results for 2 and 3 MCs for comparison.

2. METHODS

2.1. MV Geometry

To create the MV geometries, we morphed a template geometry using data from several key points. The key points were obtained from different sources as described below. The template MV geometry was adopted from another study (13). For morphing the geometry, PyGem, an open-source library in Python was used. We used Radial Basis Functions (RBF) in this package (14). We removed some chords from the original template (888 out of 4,971 total chordal elements). This was necessary to cause MR for some geometries obtained from normal valve data (as described below).

2.1.1. Data From Patients

We obtained 3-dimensional (3D) echocardiographic image data from University of California San Francisco (UCSF). The images obtained were in accordance with UCSF Institutional Review Board (number 19-27738). We used Echo images from UCSF to create a portion of the dataset. An example Echo image is shown in **Figure 1**. We used ImageJ software (version 1.53e, National Institutes of Health) to manually obtain the pixel coordinates of several key points (**Figure 1**) in each image. The pixel data obtained in three views from the images, were used to morph the template geometry (**Figure 2**). In total, we reconstructed geometries from 29 patients.

It should be noted that the MV geometries pertain to patients that were approved for MC intervention at UCSF Medical Center. Thus, the geometries obtained from these images represent pathological MVs that require MC intervention.

2.1.2. Data From Literature

Another source for creating the geometry is from data in the literature. We used the statistics provided by Krawczyk-Ozóg et al. for the leaflets [**Figure 2**; (15)]. A normal distribution for the leaflet parameters was used in our study. Using the mean and standard deviation from the dataset provided by (15), we calculated the respective data for 5, 50, 95% percentile of population. The template geometry was morphed using the data for each datapoint to create respective geometry. The resulting values are shown in **Table 1**. For each of the aorto-mural and inter-commissural diameters, five values were used while other morphological parameters were fixed (**Table 1**).

This part of the dataset represents normal MV morphologies. MV geometries that require MC could have characteristics that are not seen in normal MV (such as the length of leaflets and annulus diameter). In some patients with MR, however, the MV morphology may be normal (16, 17). Unlike imaging data, the geometries created from these data source were not directly obtained from patients. Rather, they were used for data augmentation.

2.1.3. Data From PCA

We used PCA to generate more virtual patients' data using the data we had. The coordinates from UCSF patients' data and data from literature were used for this purpose. We used the following

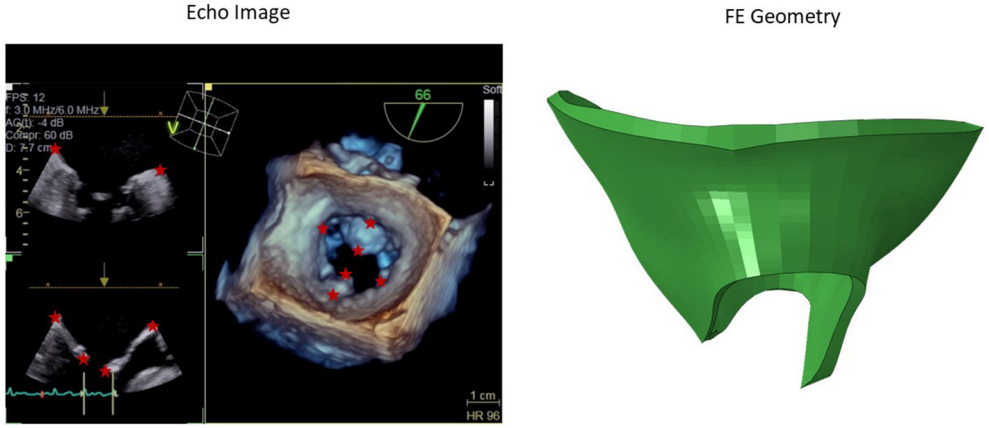

FIGURE 1 | A sample 3D echo image. Six key points used in the morphing are shown with stars. The pixel data from these key points were obtained manually in ImageJ, and they were used to create the respective geometry by morphing a template geometry. The shape on the right is the respective patient geometry after morphing.

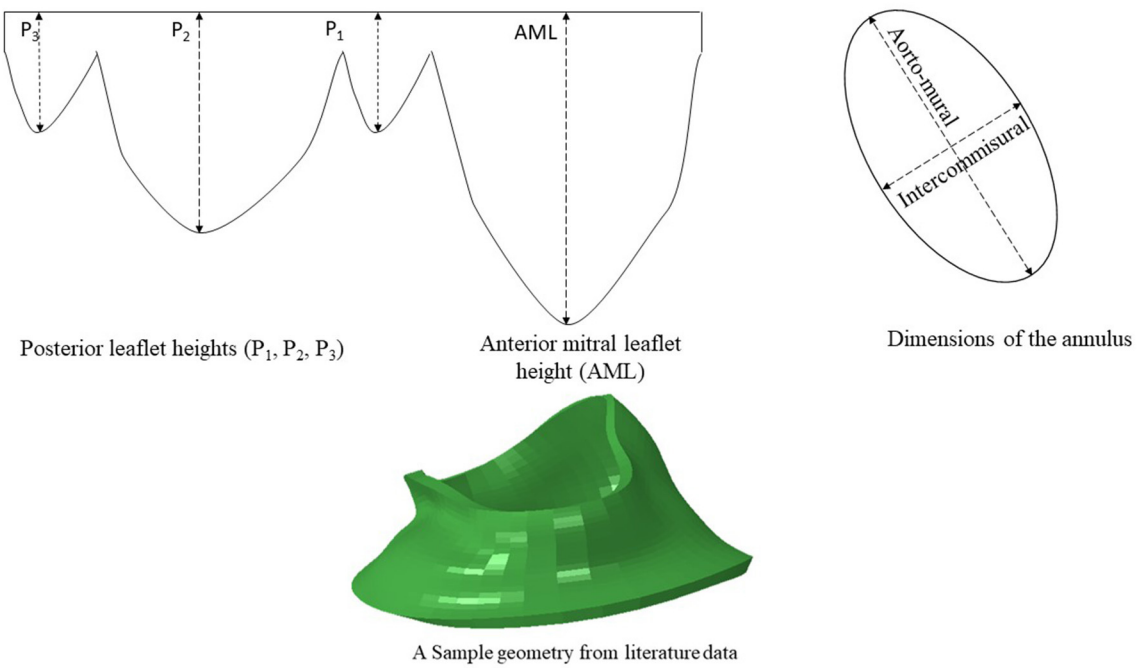

FIGURE 2 | The dimensions of six key points were computed from literature. The diameters of the annulus (two dimensions) and the leaflet edge dimensions (four points) were adopted from data in the literature (15). A sample geometry created from literature data is shown.

equation for this purpose:

$$X \cong X_{PCA} = \bar{X} + \sum_{m=1}^{M} \alpha_m \sqrt{\lambda_m} W_m \tag{1}$$

where $\bar{X}$ is the mean shape, and $\{W_m\}$ and $\{\lambda_m\}$ are the eigenvectors and eigen values of the covariance matrix, respectively, $\{\alpha_m\}$ is the shape code, and M is number of principal components (18–20). We used three components as they could describe over 90% of total shape variation (21). We used linear algebra library in Python to apply singular value decomposition on the MV dataset, and then, PCA computations followed. In total, the valve dataset used for PCA contained 180 shapes.

The geometries obtained from PCA were a combination of MVs from patients and normal MVs. Similar to the geometries created from literature (section Data From Literature), the geometries obtained from PCA were used for data augmentation.

2.1.4. Data From GANs

After creating the dataset from image dataset and literature, we had a dataset from different geometries. Using this dataset, we generated more images using GANs (22). This algorithm has two parts. One part generates the geometries (the generator) and the other part tries to distinguish the generated geometry from a real geometry (discriminator). Initially, the discriminator can recognize the generated image from the real image, but as the generator trains, the discriminator has difficulty in separating the generated image from the real images. To implement this algorithm, we treated the geometries as images. A deep learning (DL) model in TensorFlow was adopted for this purpose (23). We used TensorFlow for computations in Google Collaboratory with Graphics Processing Units (GPUs), with following specifications: name: Tesla P100-PCIE-16GB, driver version: 460.32.03, memory: 16280 MiB.

2.2. Computational Set Up

After the geometries for the MVs were developed, they were used to conduct FE simulations. The FE model included the MV, its chords and the left ventricle (LV), as indicated in **Figure 1**. As mentioned above, the MV geometry was adopted from another study (13). The blood flow was modeled using Smoothed Particle Hydrodynamics (SPH) where particles represent the red blood cells. The MC was simulated by connecting respective points on the MV leaflet edges (**Figure 3**).

The leaflet materials were modeled using hyperplastic fiber-reinforced material, as below (24, 25):

$$\begin{aligned}\Psi_{dev} &= \frac{a}{2b}e^{b(I_1-3)} + \sum_{i=f,t}\frac{a_i}{2b_i}\left\{e^{b_i(I_{4i}-1)^2}-1\right\} \\ &+ \frac{a_{ft}}{2b_{ft}}\left\{e^{b_{ft}(I_{8ft})^2}-1\right\} \\ \Psi_{vol} &= \frac{1}{D}\left(\frac{J^2-1}{2}-\ln(J)\right)\end{aligned} \tag{2}$$

where a and b are isotropic stiffness of the tissue; a_f and b_f are tissue stiffness in the fiber direction, a_t and b_t are tissue stiffness in the (transverse) plane perpendicular to the fiber direction, *and* a_{ft} and b_{ft} are shear rigidity between fibers and transverse plane. I_1, I_{4i} and I_{8ft} are invariants, as follows:

$$\begin{aligned}\mathrm{I}_1 &:= \mathrm{tr}(\mathbf{C}) \\ \mathrm{I}_{4i} &:= \mathbf{C}:(\mathbf{f_0}\otimes\mathbf{f_0}) \\ \mathrm{I}_{8fs} &:= \mathbf{C}:\mathrm{sym}(\mathbf{f_0}\otimes\boldsymbol{t_0})\end{aligned} \tag{3}$$

$\mathbf{C}$ is the right Cauchy-Green tensor, $\mathbf{f}_0$ and $\mathbf{s}_0$ are vectors that define the fiber and trans-fiber directions, respectively. J is the deformation gradient invariant and D is a multiple of the Bulk Modulus K ($\frac{2}{K}$).

TABLE 1 | The values used for the leaflet morphological parameters.

Parameter	Values (mm)
AML	13.63, 20.6, 27.57
P_1	6.85, 11, 15.15
P_2	8.25, 12.9, 17.55
P_3	6.08, 10.4, 14.72
Aorto-mural diameter	21.5, 22.0, 22.5, 23.0, 23.5
Intercommissural diameter	17.65, 18.15, 18.65, 19.15, 19.65

For the variations in diameters, other parameters were fixed at following values: AML = 13.63 mm, P_1 = 6.85 mm, P_2 = 8.25 mm, P_3 = 6.08 mm.

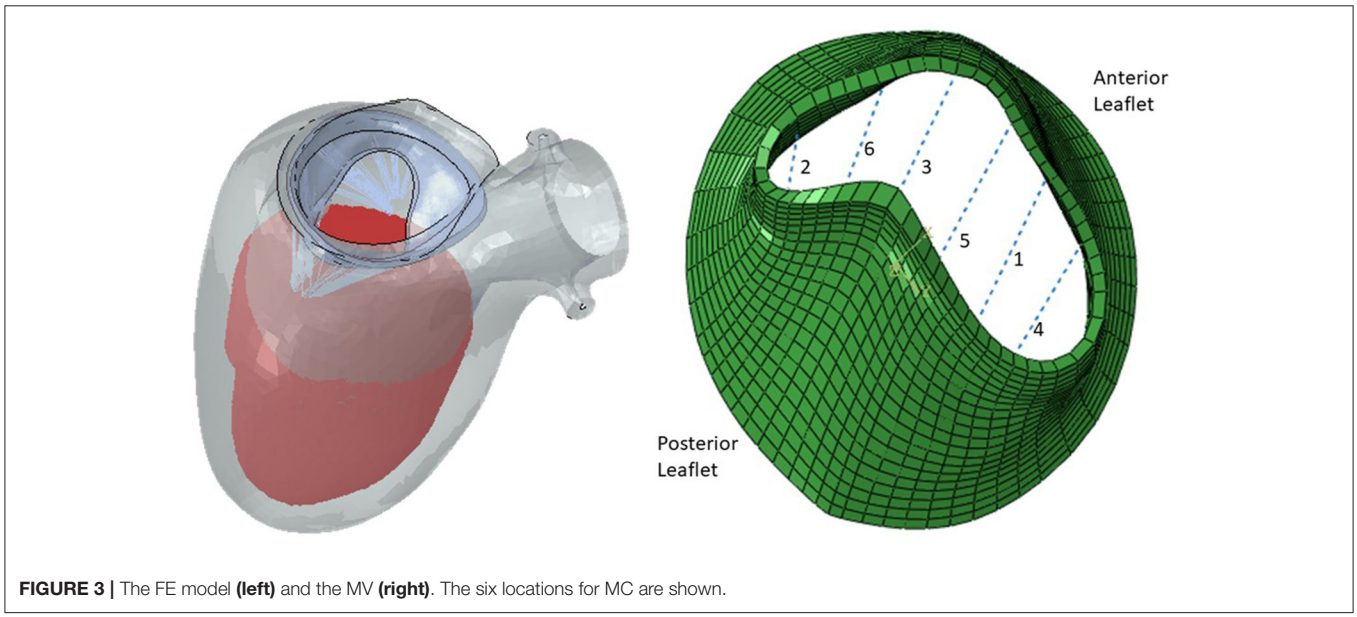

FIGURE 3 | The FE model **(left)** and the MV **(right)**. The six locations for MC are shown.

We used LV (including papillary muscles) as the surrounding geometry for the blood flow and did not consider deformations in the LV nodes. The MV annulus changed for different geometries, but the LV geometry was the same. This caused a mismatch between LV and MV annulus. To avoid leakage between LV and MV due to this mismatch, a surface was placed to seal the gap. This surface did not affect the deformations of the MV and only sealed the gap between MV and LV. The blood flow was enforced by a plate in the LV side of the MV that moved toward the MV. A pressure was applied to the leaflets to close them. The MV annulus motions were adopted from the literature. The SPH methodology is similar to previous publications (24, 26).

The FE simulations were conducted in several steps: (1) SPH particles entered the LV and subsequently the model replicated an LV filled with blood; (2) MC was implemented by connecting respective nodes from two leaflets; (3) Pressure load was applied to close the leaflets; and (4) Particles were forced to move toward the MV, using a plate.

The FE software Abaqus Unified FEA (Part of 3DEXPERIENCE SIMULIA software Suite, Dassault Systemes, Providence, RI, USA) version 2020 was used for computations. For leaflets, we used a material available in Abaqus Living Heart license that is based on Equation 2. The leaflets element type was C3D8I (8-node linear brick, incompatible modes); the chords element type was T3D2 (linear 3-D truss), and the blood particles element type was C3D8R (8-node linear brick, reduced integration with hourglass control). The Abaqus explicit solver was used with automatic time incrementation, and mass scaling was used. The general contact (including self-contact) was used for interaction between the model components including blood particles, leaflets, LV, and the plate which was used to move the particles toward atrium. The FE computations were conducted on the UberCloud platform using Google Cloud Platform computational nodes. We used C2 instances (Cascade Lake) with 30 cores and 240 GB of main memory for computations. The average runtime for each FE model was 6 h.

3. RESULTS

We created 55 geometries from image data, 106 geometries based on leaflet parameters in the literature, and 20 geometries using PCA (**Figure 4**). Although GANs could generate additional shapes (**Figures 5**, **6**), we did not use it to create more geometries, as it required more computational costs. The GANs algorithm required several epochs to generate MV models that were similar to the dataset (**Figure 5**). Although in the initial epochs the geometries provided by GANs were randomly distributed, the generated geometries became closer to the MV (**Figure 5**). The output from GANs was not directly useable for FE modeling, but it provided coordinates of 6 key points which could be used to morph the template FE model (**Figure 6**). The result shown in **Figure 6** was obtained from 81 geometries based on geometrical parameters from the literature.

The blood flow through the MV was simulated by the FE models. The MR was different for different geometries (**Figures 7**–**10**). As well, other parameters were affected including the deformations in the leaflets and stress distributions.

With one MC, with different MC locations, the MR was altered, and the alterations in MR was more noticeable for some MC locations (**Figures 8**, **9**). Other parameters, including the stress distributions and leaflet deformations changes with MC location.

Simulation scenarios with two and three MCs showed the MR with more than one clip. More than one MC led to lower MR compared to one MC, but the reduction in MR depended on the locations of the MCs. When two MCs are used, the locations of the two MCs with respect to each other, affects MR and stresses. The results for three MCs could lower the MR compared to two MCs. The stresses in the leaflets were altered with three MCs (**Figures 10**, **11**). The number of MCs noticeably affected the orifice area. As the number of MCs increased, the MV orifice area became smaller (**Figure 11**).

4. DISCUSSION

We presented a methodology to generate an atlas for prediction of MC intervention outcomes. Our approach is based on different data-generation methods, namely patients' data, literature reports, PCA, and GANs. In case the data from patients is limited, our approach can be used to generate/augment the data. We used echo images as one source of data generation as this modality is more available and safer than other modalities, and it is less expensive. Our FE modeling simulated fluid-structure interaction (FSI) for different scenarios for MC interventions.

The patient data that we used are based on Echo images. There are different modalities for MV imaging including MRI and CT. We used Echo modality because this imaging method is more readily available, less costly and safer. There are patients who cannot tolerate MRI; e.g., those with pacemakers. On the other hand, hand-held Echo cardiac imaging devices are progressing to the clinics (27). Therefore, our approach is compatible with current efforts for personalized imaging methods. These technologies that are integrated in mobile devices will expand Internet of Things (IoT) technologies, providing patient-oriented medicine and more effective treatments. On the other hand, working with Echo images is more complicated than MRI. The Echo images do not come in a regular DICOM format that can be directly used for geometrical reconstruction. Some vendors have provided software modules that makes it possible to convert DICOM data to 3D Cartesian format (Philips), but particularly, Siemens machines do not provide such a module. Our methodology contributes to using Echo images for MV simulations.

The outputs of PCA were directly appropriate for FE modeling (**Figure 4**). The GANs could provide a tool for MV data augmentation. In comparison to PCA, GANs were recently introduced (22). This deep learning algorithm has been used in many domains, particularly for computer vision. The outputs of GANs were not directly appropriate for FE modeling, but they provide the information to generate FE models; e.g., coordinates

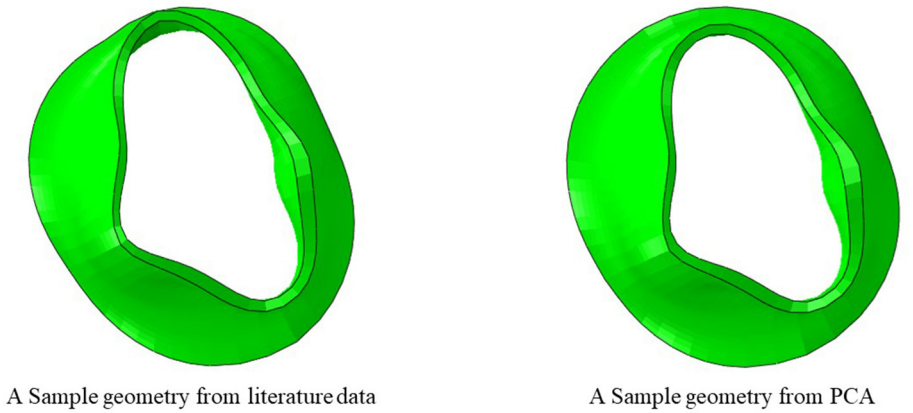

FIGURE 4 | A model created from literature data and a model created using PCA.

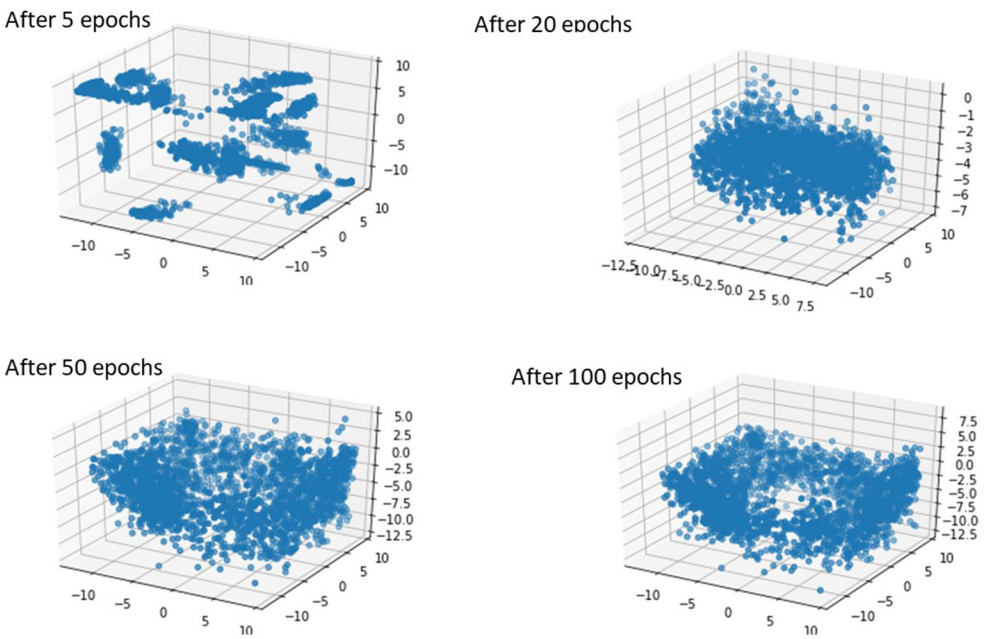

FIGURE 5 | The GAN model was able to produce MV geometries after several epochs.

of key points that we used for morphing. Given that GANs provided the shapes after several epochs (**Figures 5**, **6**), we used PCA for the data generation in this study.

Our study emphasizes using ML analysis for MC intervention optimization. First, it is not feasible to experiment with MC location to determine the optimal MC implantation strategy. Furthermore, stresses in the leaflets cannot be measured experimentally. The FE modeling can be used to virtually simulate the outcomes of different MC intervention scenarios. FE modeling (especially when FSI is considered), however, can be challenging. For some patients, the geometry of the leaflets deviates from a normal geometry such that the distortions in FEs cause numerical instability. This implies that FE modeling is limited in terms of numerical convergence for some patients. Moreover, FE modeling is time-consuming especially when FSI is involved. Even after FE computations are complete, they do not directly lead us to MC intervention improvements. Notably, based on the results, for the same MV geometry the alterations in MR does not follow a pattern that can be intuitively extracted from the data (**Figure 9**). Similar to MR, results for leaflet stresses also do not show a pattern by a simple analysis. In other words, the interplay between factors that affect MR and leaflet stress is complicated, making it difficult to provide a rule of thumb for optimal MC intervention.

On the other hand, ML models do not suffer from FE modeling limitations mentioned above. Once a ML model is

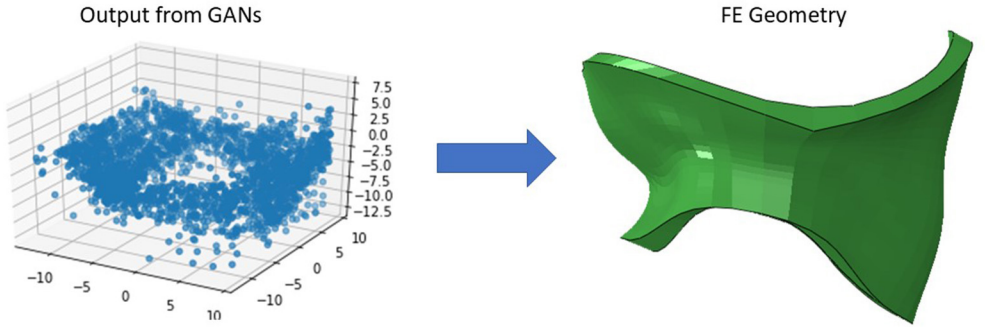

FIGURE 6 | The GAN-generated geometries became more similar to real MVs after several epochs.

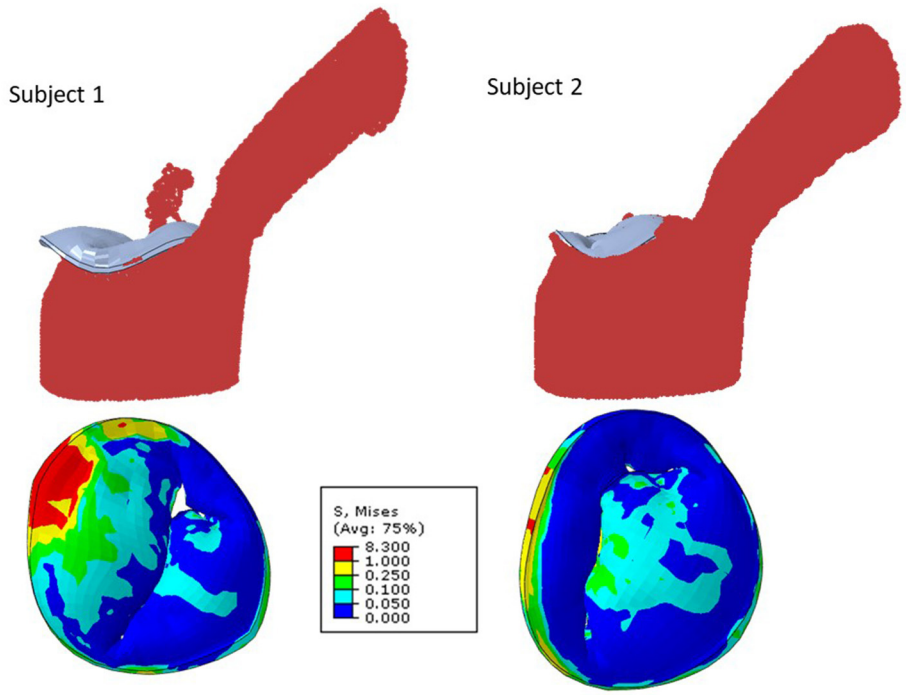

FIGURE 7 | The MR and leaflet stress for two different subjects.

developed, it can provide the results in much shorter time than FE modeling (25, 28), and it can provide the results for the MV parameters that are within the data distribution (results will be provided except for outliers). In this paper, we described data generation, an important step in using ML analysis for MC outcomes prediction.

Because our data generation is founded on FE models, we aimed to use a FE modeling approach that captures import information about MV dynamics and at the same time is computationally efficient. Our FE model has two important aspects that makes it more advanced compared to previous studies. First, it includes the LV as the surrounding geometry for blood whereas in our previous report, we used a cylinder (26). Because FSI models are relatively complex, inclusion of LV is important from a FE modeling standpoint. Second, our FE modeling approach is adaptable for different parameters of the MV, including geometrical parameters. This aspect is important because FSI models are typically sensitive to variations in model parameters. Moreover, we modeled not only the MV and LV but also the MC and different scenarios for MC implantations were considered. The average runtime for our FE models made it possible to use them for our data generation workflow (∼6 h). We are not aware of a previous study that provided a workflow to create a dataset of MV FSI models for different scenarios of the MC intervention.

The MR and leaflet stress are important parameters for MC intervention. In particular, the locations and number of MCs are crucial factors for the outcome of the intervention. Our

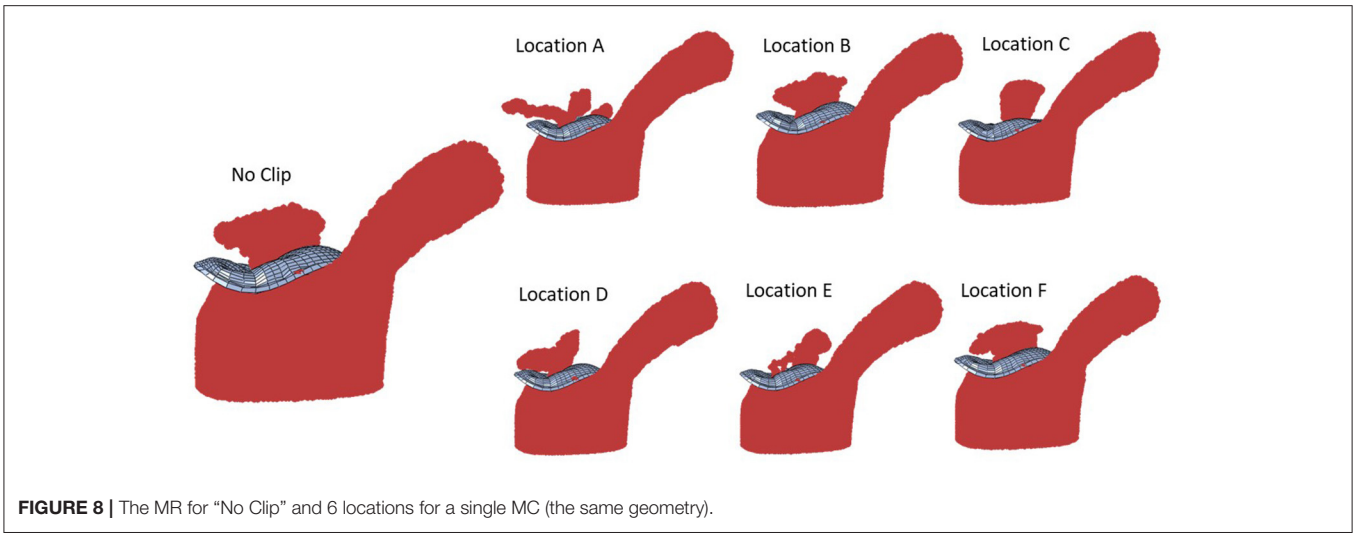

FIGURE 8 | The MR for "No Clip" and 6 locations for a single MC (the same geometry).

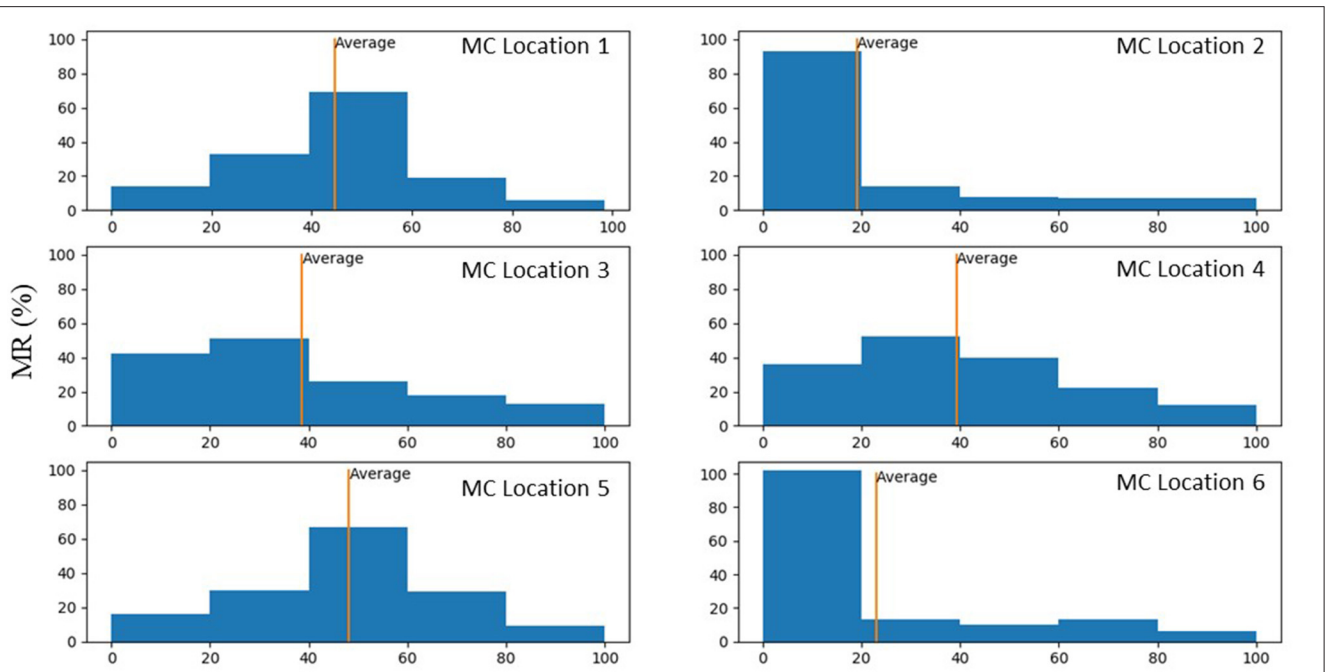

FIGURE 9 | Histograms that show percentage of MR reduction in the MV for each MC location. These histograms were plotted only for scenarios where MR reduced after MC intervention.

simulations show that when one MC is used, the stress and MR is different for each MC location (**Figure 8**). Similarly, when the number of MCs increased to 2 and 3, the MR and stresses were altered (**Figures 10**, **11**). For the model shown in **Figures 10**, **11**, with one clip (location 3), the reduction in MR was 40%, with two clips it was 83% (A) and 61% (B), and with three clips it was 95%. The maximum von Mises stress in the leaflets for one clip was 15.1 MPa, for two clip it was 13.2 MPa (A) and 11.2 MPa (B), and with three clips it was 17.0 MPa. Moreover, the geometry of the MV is another factor that plays a role in the outcomes of MC intervention (**Figure 7**). The maximum von Mises stress was 8.3 and 2.2 MPa for subjects A and B, respectively, in **Figure 7**.

Another important aspect of MC intervention is the alterations in the orifice area caused by MC(s) (29). Based on patient's background and preexisting pressure gradients, typically two or more clips run the risk of causing mitral stenosis (30). Our FE models simulate the effects of MCs on the orifice area as number of MCs change (**Figure 11**). Specifically, for the geometry in **Figure 11**, in relation to one clip scenario, two clips reduced the orifice area by 54% (A) and 23% (B). With respect to one clip, however, three clips reduced the orifice area by 72%.

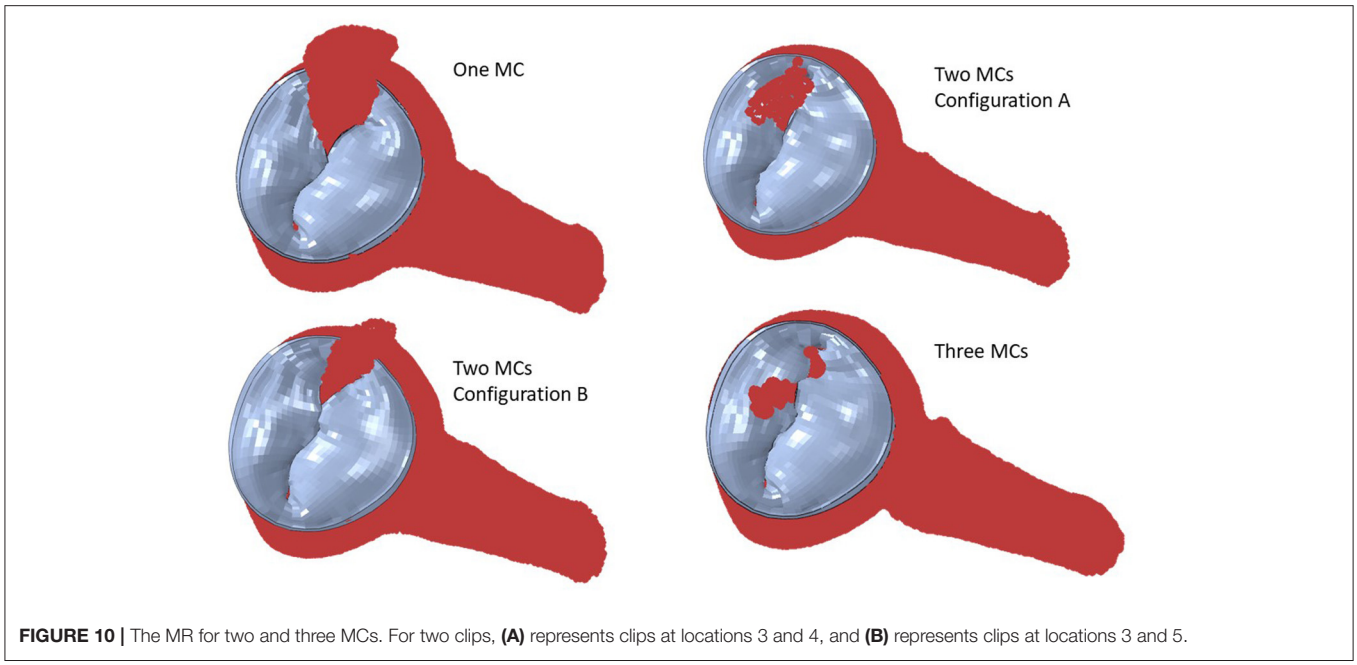

FIGURE 10 | The MR for two and three MCs. For two clips, **(A)** represents clips at locations 3 and 4, and **(B)** represents clips at locations 3 and 5.

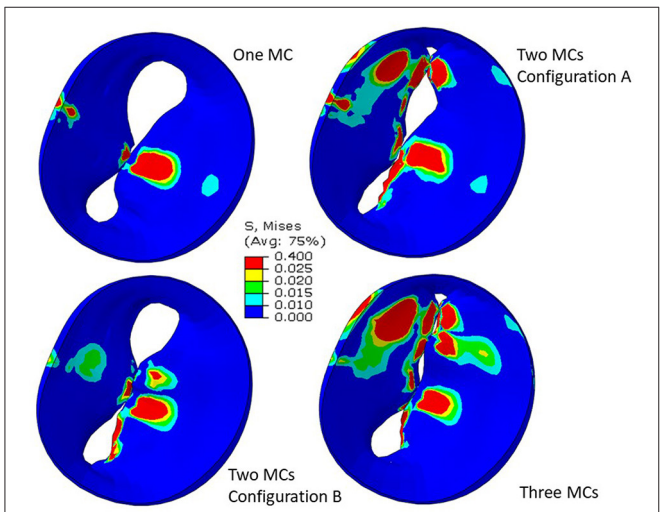

FIGURE 11 | Leaflet von Mises stresses for one, two, and three MCs. These figures show the implantation of the MC. For two clips, **(A)** represents clips at locations 3 and 4, and **(B)** represents clips at locations 3 and 5.

Therefore, our results also show that 3 MCs have noticeably higher effects on the MV orifice area.

The average MR reduction obtained by implanting a MC in locations 1 (45%), 3 (39%), 4 (39%), and 5 (48%) were relatively similar to each other. The average MR reductions obtained by implanting a MC at locations 2 (19%) and 6 (23%), however, were noticeably lower (**Figure 9**). The histograms for MR reductions for locations 2 and 6 are relatively similar. The similarity between MR reduction for locations 2 and 6 can be explained based on the vicinity between these two locations, and that they are both closer to the posterior commissure than the anterior commissure. **Figure 9** demonstrates that the average values of MR should be interpreted with caution. Notably, for some geometries, a MC implanted in location 2 or 6 led to a larger reduction in MR than other locations. As such, it is important to determine the optimal MC scenarios based on each patient's parameters rather than average data.

5. LIMITATIONS

The MV has a wide range of parameters that can be different for each patient. These parameters include (but are not limited to) the geometrical specifications of the annulus and leaflets, the chords, the material properties, and the functional/degenerative type of the disease. The methodology we present in this paper is a proof of concept study that can be used for different types of MV diseases. Once the dimensions of the MV for a patient is extracted from the respective images, they can be used to drive the FE geometry using the morphing process explained in "Methods" section. As mentioned above, FE models do not converge for all geometries, but ML models can provide the results for that patient as long as the geometry distribution is within the dataset distribution range. As such, for a data set generation methodology, it is important to include data with a wide range of variance, as much as information is available.

We presented several methods to create the MV geometries including echo images, morphological data (from literature), PCA, and GANs. Each method provides a different approach to generate data. As such, the proposed methodology can utilize information in the form of either images or MV dimensions to create the dataset and utilize PCA and GANs to augment the data. In this study, the size of available images was limited. As such, morphological data from normal MVs were used to

augment the data. This is a limitation in terms of data distribution because normal MV morphologies can be different from patients' morphologies. This limitation related to the available data, can be addresses as we collect more patient images or morphological data from pathological MVs (that need MC) becomes available. It should be noted that MR can be caused by chordae or papillary muscle rupture (17), in which case the MV morphology might be normal. Therefore, a comprehensive dataset for MC intervention needs to include MVs with normal morphology.

For ML simulations, a larger training data set is generally more desirable. Because the echo images provide the specifications of the patients' geometries directly applicable to MC therapy, there is a need to collect more images from a wide variety of patients. A larger patient images dataset can improve the distribution of geometries and the size of the training dataset. The former will cover more patients' geometries and the latter will improve the ML model accuracy. We are collecting more MV images from patients that need MC intervention.

We did not use GANs for creating additional parts for our dataset in this paper, but we showed that GANs are trainable for generating MV geometries. This result is important because PCA and GANs are two different approaches. The former finds pattern in data by looking at directions of largest orthogonal variances, but the latter finds a complex non-linear function between the inputs and outputs. Therefore, GANs can provide virtual geometries that are not created by PCA. In our future work, GANs can be used to augment geometries from patient data.

An additional limitation is that the LV was considered as the surrounding geometry for the blood flow simulations, which did not consider deformations of the LV; i.e., the LV geometry remained unchanged. In our simulations, we found the FSI convergence is sensitive to the model geometrical specifications. A model that uses a rigid LV geometry is more likely to encounter convergence failure than a model that uses a rigid cylinder. Thus, we included a rigid LV geometry since it is a step closer to a more evolved MV model. Future models require FSI that involves both MV and LV. The LV deformations should be considered in future models where the contraction of the LV will cause the ejection of the blood. This future work can integrate our LV models (25, 28) with our MV and MC modeling approach. The MV will be a part of the LV in such a way that the plate used to seal the gap between MV and LV will not be required. Also, annulus deformations will be caused by LV deformations, and the motions at the annulus will not be applied as boundary conditions. It should be noted that such a model likely requires tremendous computational resources, particularly if it is used for data generation.

Since the effects of MC on MR and MV dynamics do not follow simple patterns or rules, an AI tool is needed for such an analysis. This paper described a methodology to generate the dataset for AI-based tools for MC intervention improvements, but we did not present an AI tool. The next step in the AI analysis is to apply AI models on the data. Analysis of the data and applying AI models for prediction of MC outcomes can be topics of future publications.

DATA AVAILABILITY STATEMENT

The datasets presented in this article are not readily available because of limitations in data access policy in corresponding institutes. Requests to access the datasets should be directed to gkassab@calmi2.org.

AUTHOR CONTRIBUTIONS

YD, JG, and GK designed the study. YD conducted the simulations and analyzed the results. JY contributed to ABAQUS model development. DG and WG contributed to running the models. VM and RA contributed to data preparation and analysis. All authors read and revised the manuscript.

FUNDING

This work was supported in part by the SBIR grant number R43 HL145896.

ACKNOWLEDGMENTS

We thank Dr. Andrew Wisneski in the Department of Surgery, University of California, San Francisco, for assistance with image analysis.

REFERENCES

1. Lloyd-Jones D, Adams RJ, Brown TM, Carnethon M, Dai S, De Simone G, et al. Heart disease and stroke statistics - 2010 update: a report from the American heart association. *Circulation.* (2010) 121:948–54. doi: 10.1161/CIRCULATIONAHA.109.192666
2. St. Goar FG, Fann JI, Komtebedde J, Foster E, Oz MC, Fogarty TJ, et al. Endovascular edge-to-edge mitral valve repair: short-term results in a porcine model. *Circulation.* (2003) 108:1990–3. doi: 10.1161/01.CIR.0000096052.78331.CA
3. Mauri L, Foster E, Glower DD, Apruzzese P, Massaro JM, Herrmann HC, et al. 4-Year results of a randomized controlled trial of percutaneous repair versus surgery for mitral regurgitation. *J Am Coll Cardiol.* (2013) 62:317–28. doi: 10.1016/j.jacc.2013.04.030
4. De Bonis M, Lapenna E, Pozzoli A, Giacomini A, Alfieri O. Edge-to-edge surgical mitral valve repair in the era of mitraClip: what if the annuloplasty ring is missed?. *Curr Opin Cardiol.* (2015) 30:155–60. doi: 10.1097/HCO.0000000000000148
5. Sorajja P, Vemulapalli S, Feldman T, Mack M, Holmes DR, Stebbins A, et al. Outcomes with transcatheter mitral valve repair in the united states: an STS/ACC TVT registry report. *J Am Coll Cardiol.* (2017) 70:2315–27. doi: 10.1016/j.jacc.2017.09.015
6. Rahhab Z, Ren B, Oei F, de Jaegere PPT, Van Mieghem NM. Mitral valve injury after mitraclip implantation. *JACC Cardiovasc Interv.* (2016) 9:e185–6. doi: 10.1016/j.jcin.2016.07.007
7. Maisano F. Leaflet injuries after percutaneous edge-to-edge repair: a challenge to avoid∗. *JACC Case Reports.* (2021) 3:74. doi: 10.1016/j.jaccas.2020.12.003

8. Zhang Y, Wang VY, Morgan AE, Kim J, Handschumacher MD, Moskowitz CS, et al. Mechanical effects of MitraClip on leaflet stress and myocardial strain in functional mitral regurgitation - a finite element modeling study. *PLoS One*. (2019) 14:e0223472. doi: 10.1371/journal.pone.0223472
9. Caballero A, Mao W, McKay R, Hahn RT, Sun W. Comprehensive engineering analysis of left heart dynamics after mitraclip in a functional mitral regurgitation patient. *Front Physiol.* (2020) 11:432. doi: 10.3389/fphys.2020.00432
10. Kong F, Caballero A, McKay R, Sun W. Finite element analysis of MitraClip procedure on a patient-specific model with functional mitral regurgitation. *J Biomech.* (2020) 104:109730. doi: 10.1016/j.jbiomech.2020.109730
11. Al Amri I, Debonnaire P, van der Kley F, Schalij MJ, Bax JJ, Marsan NA, et al. Acute effect of MitraClip implantation on mitral valve geometry in patients with functional mitral regurgitation: insights from three-dimensional transoesophageal echocardiography. *EuroIntervention.* (2016) 11:1554–61. doi: 10.4244/EIJY15M09_09
12. Quer G, Arnaout R, Henne M, Arnaout R. Machine Learning and the future of cardiovascular care: JACC state-of-the-art review. *J Am Coll Cardiol.* (2021) 77:300–13. doi: 10.1016/j.jacc.2020.11.030
13. Votta E, Caiani E, Veronesi F, Soncini M, Montevecchi FM, Redaelli A. Mitral valve finite-element modelling from ultrasound data: a pilot study for a new approach to understand mitral function and clinical scenarios. *Philos Trans R Soc A Math Phys Eng Sci.* (2008) 366:3411–34. doi: 10.1098/rsta.2008.0095
14. Tezzele M, Demo N, Mola A, Rozza G. PyGeM: python geometrical morphing. *Softw Impacts.* (2021) 7:100047. doi: 10.1016/j.simpa.2020.100047
15. Krawczyk-Ozóg A, Hołda MK, Sorysz D, Koziej M, Siudak Z, Dudek D, et al. Morphologic variability of the mitral valve leaflets. *J Thorac Cardiovasc Surg.* (2017) 154:1927–35. doi: 10.1016/j.jtcvs.2017.07.067
16. McCarthy KP, Ring L, Rana BS. Anatomy of the mitral valve: understanding the mitral valve complex in mitral regurgitation. *Eur J Echocardiogr*. (2010) 11:i3–9. doi: 10.1093/ejechocard/jeq153
17. Watanabe N. Acute mitral regurgitation. *Heart.* (2019) 105:671–7. doi: 10.1136/heartjnl-2018-313373
18. Liang L, Liu M, Martin C, Sun W. A deep learning approach to estimate stress distribution: a fast and accurate surrogate of finite-element analysis. *J R Soc Interface.* (2018) 15:20170844. doi: 10.1098/rsif.2017.0844
19. Zhang S, Zhan Y, Metaxas DN. Deformable segmentation via sparse representation and dictionary learning. *Med Image Anal.* (2012) 16:1385–96. doi: 10.1016/j.media.2012.07.007
20. Heimann T, Meinzer HP. Statistical shape models for 3D medical image segmentation: a review. *Med Image Anal.* (2009) 13:543–63. doi: 10.1016/j.media.2009.05.004
21. Liang L, Liu M, Martin C, Elefteriades JA, Sun W. A machine learning approach to investigate the relationship between shape features and numerically predicted risk of ascending aortic aneurysm. *Biomech Model Mechanobiol.* (2017) 16:1519–33. doi: 10.1007/s10237-017-0903-9
22. Goodfellow IJ, Pouget-Abadie J, Mirza M, Xu B, Warde-Farley D, Ozair S, et al. Generative adversarial networks. *Commun ACM.* (2014) 63:139–44. doi: 10.1145/3422622
23. Abadi M, Barham P, Chen J, Chen Z, Davis A, Dean J, et al. *TensorFlow: A System for Large-Scale Machine Learning.* (2016). Available online at: https://research.google/pubs/pub45381/ (accessed June 29, 2020).
24. Dabiri Y, Yao J, Sack KL, Kassab GS, Guccione JM. Tricuspid valve regurgitation decreases after mitraclip implantation: fluid structure interaction simulation. *Mech Res Commun.* (2019) 97:96–100. doi: 10.1016/j.mechrescom.2019.04.009
25. Dabiri Y, Van der Velden A, Sack KL, Choy JS, Kassab GS, Guccione JM. Prediction of left ventricular mechanics using machine learning. *Front Phys.* (2019) 7:117. doi: 10.3389/fphy.2019.00117
26. Kamakoti R, Dabiri Y, Wang DD, Guccione J, Kassab GS. Numerical simulations of mitraclip placement: clinical implications. *Sci Rep.* (2019) 9:15823. doi: 10.1038/s41598-019-52342-y
27. Chamsi-Pasha MA, Sengupta PP, Zoghbi WA. Handheld echocardiography. *Circulation.* (2017) 136:2178–88. doi: 10.1161/CIRCULATIONAHA.117.026622
28. Dabiri Y, Van der Velden A, Sack KL, Choy JS, Guccione JM, Kassab GS. Application of feed forward and recurrent neural networks in simulation of left ventricular mechanics. *Sci Rep.* (2020) 10:22298. doi: 10.1038/s41598-020-79191-4
29. Biaggi P, Felix C, Gruner C, Herzog BA, Hohlfeld S, Gaemperli O, et al. Assessment of mitral valve area during percutaneous mitral valve repair using the MitraClip system: comparison of different echocardiographic methods. *Circ Cardiovasc Imaging.* (2013) 6:1032–40. doi: 10.1161/CIRCIMAGING.113.000620
30. Neuss M, Schau T, Isotani A, Pilz M, Schöpp M, Butter C. Elevated mitral valve pressure gradient after MitraClip implantation deteriorates long-term outcome in patients with severe mitral regurgitation and severe heart failure. *JACC Cardiovasc Interv.* (2017) 10:931–9. doi: 10.1016/j.jcin.2016.12.280

Conflict of Interest: YD is an employee of 3DT Holdings LLC. JG is a consultant for, and JY is an employee of, Dassault Systèmes Simulia Corporation (Johnston, RI, USA). VM is PI for clinical research with Abbott, Edwards Life Sciences and GORE. WG and DG are employees of the UberCloud.

The remaining authors declare that the research was conducted in the absence of any commercial or financial relationships that could be construed as a potential conflict of interest.

frontiers in Bioengineering and Biotechnology

ORIGINAL RESEARCH
published: 13 January 2022
doi: 10.3389/fbioe.2021.725113

Hemodynamic Assessment in Bicuspid Aortic Valve Disease and Aortic Dilation: New Insights From Voxel-By-Voxel Analysis of Reverse Flow, Stasis, and Energetics

Patrick Geeraert[1,2,3†], *Fatemehsadat Jamalidinan*[1,2,3†], *Fiona Burns*[1,2,3], *Kelly Jarvis*[4], *Michael S. Bristow*[1,2,3], *Carmen Lydell*[1,3], *Silvia S. Hidalgo Tobon*[5], *Benito de Celis Alonso*[6], *Paul W. M. Fedak*[1,2], *James A. White*[1,2] *and Julio Garcia*[1,2,3,7*]

[1]Department of Cardiac Sciences, Cumming School of Medicine, University of Calgary, Calgary, AB, Canada, [2]Stephenson Cardiac Imaging Centre, Libin Cardiovascular Institute, Calgary, AB, Canada, [3]Department of Radiology, University of Calgary, Calgary, AB, Canada, [4]Department of Radiology, Northwestern University, Chicago, IL, United States, [5]Department of Physics, Universidad Autonoma Metropolitana, Mexico City, Mexico, [6]Faculty of Mathematical and Physical Sciences, Benemerita Universidad Autonoma de Puebla, Puebla, Mexico, [7]Alberta Children's Hospital Research Institute, University of Calgary, Calgary, AB, Canada

OPEN ACCESS

Edited by:
Seungik Baek,
Michigan State University,
United States

Reviewed by:
Hao Gao,
University of Glasgow,
United Kingdom
Harvey Ho,
The University of Auckland,
New Zealand

***Correspondence:**
Julio Garcia
julio.garciaflores@ucalgary.ca

[†]These authors have contributed equally to this work

Specialty section:
This article was submitted to Biomechanics, a section of the journal Frontiers in Bioengineering and Biotechnology

Received: 14 June 2021
Accepted: 27 December 2021
Published: 13 January 2022

Citation:
Geeraert P, Jamalidinan F, Burns F, Jarvis K, Bristow MS, Lydell C, Hidalgo Tobon SS, de Celis Alonso B, Fedak PWM, White JA and Garcia J (2022) Hemodynamic Assessment in Bicuspid Aortic Valve Disease and Aortic Dilation: New Insights From Voxel-By-Voxel Analysis of Reverse Flow, Stasis, and Energetics. Front. Bioeng. Biotechnol. 9:725113. doi: 10.3389/fbioe.2021.725113

Objectives: Clinical management decisions surrounding ascending aorta (AAo) dilation in bicuspid aortic valve (BAV) disease benefit from personalized predictive tools. 4D-flow MRI may provide patient-specific markers reflective of BAV-associated aortopathy. This study aims to explore novel 4D-flow MRI parametric voxel-by-voxel forward flow, reverse flow, kinetic energy and stasis in BAV disease. We hypothesize that novel parametric voxel-by-voxel markers will be associated with aortic dilation and referral for surgery and can enhance our understanding of BAV hemodynamics beyond standard metrics.

Methods: A total of 96 subjects (73 BAV patients, 23 healthy controls) underwent MRI scan. Healthy controls had no known cardiovascular disease. Patients were clinically referred for AAo dilation assessment. Indexed diameters were obtained by dividing the aortic diameter by the patient's body surface area. Patients were followed for the occurrence of aortic surgery. 4D-flow analysis was performed by a single observer in five regions: left ventricular outflow tract (LVOT), AAo, arch, proximal descending aorta (PDAo), and distal descending aorta (DDAo). In each region peak velocity, kinetic energy (KE), forward flow (FF), reverse flow (RF), and stasis were measured on a voxel-by-voxel basis. T-tests (or non-parametric equivalent) compared flow parameters between cohorts. Univariate and multivariate analyses explored associations between diameter and parametric voxel-by-voxel parameters.

Results: Compared to controls, BAV patients showed reduced stasis ($p < 0.01$) and increased RF and FF ($p < 0.01$) throughout the aorta, and KE remained similar. In the AAo, indexed diameter correlated with age (R = 0.326, $p = 0.01$), FF (R = –0.648, $p < 0.001$), RF (R = –0.441, $p < 0.001$), and stasis (R = –0.288, $p < 0.05$). In multivariate analysis, FF showed a significant inverse association with AAo indexed diameter, independent of age.

During a median 179 ± 180 days of follow-up, 23 patients (32%) required aortic surgery. Compared to patients not requiring surgery, they showed increased KE and peak velocity in the proximal aorta ($p < 0.01$), accompanied by increased RF and reduced stasis throughout the entire aorta ($p < 0.01$).

Conclusion: Novel voxel-by-voxel reverse flow and stasis were altered in BAV patients and are associated with aortic dilation and surgical treatment.

Keywords: 4D-flow imaging, bicuspid aortc valve, reverse flow, kinetic energy, flow stasis, parametric mapping

1 INTRODUCTION

Bicuspid aortic valve (BAV) is considered the most common congenital valvular malformation with an overall prevalence in the general population of 0.5–2% (Siu and Silversides, 2010). BAV disease includes heterogeneous morphological phenotypes of fused cusps and raphe (Sievers and Schmidtke, 2007) which can lead to different pathological and clinical outcomes (Masri et al., 2017). At a population level, BAV is associated with increased risk of aortic dilation (Jamalidinan et al., 2020), requiring surgical intervention in 30–50% of individuals (Branchetti et al., 2014). Despite this, there is still variability in the clinical management guidelines (Baumgartner et al., 2017; Borger et al., 2018) for BAV aortopathy and strategies among cardiovascular surgeons vary substantially (Verma et al., 2013). This may be related to current recommendations relying on binary thresholds of ascending aorta (AAo) diameter to guide timing of proximal aortic aneurysm surgery, though these are recognized as poor predictors of acute aortic events (Pape et al., 2007). Thus, much emphasis has been placed on identifying alternative, patient-specific markers of BAV aortopathy that may provide improved characterization for this patient population.

Abnormal hemodynamics within the aorta related to abnormal valve geometry is considered an important factor in the development of BAV aortopathy (Verma and Siu, 2014). Four-dimensional flow magnetic resonance imaging (4D-flow MRI) has become recognized technique to quantify and characterize abnormal hemodynamics in BAV in a recently published consensus (Michelena et al., 2021). Particularly, wall shear stress (WSS) and flow displacement have shown encouraging associations with aortic dilation (Mahadevia et al., 2013; Guzzardi et al., 2015; Garcia et al., 2016; van Ooij et al., 2017; Rodríguez-Palomares et al., 2018; Dux-Santoy et al., 2019). In addition, other flow-based parameters such as forward flow (FF), reverse flow (RF), and energetics can be easily derived from the 4D-flow MRI velocity field (Harloff et al., 2010; Jamalidinan et al., 2020). However, most of these flow-based parameters are derived using 2D plane-based approaches (Stalder et al., 2008), which have been shown to underestimate true values (Shen et al., 2018), and it does not take advantage of the 3D nature of 4D-flow MRI. Shen et al.(Shen et al., 2018) and Jarvis et al. (Jarvis et al., 2020; Jarvis et al., 2021) recently introduced 3D voxel-by-voxel methods that provide 4D-flow derived parametric mapping of FF, RF, kinetic energy (KE) and stasis in the thoracic aorta. In this study, we applied 4D-flow derived parametric mapping to: (Siu and Silversides, 2010): evaluate differences in 3D-derived aortic parametric voxel-by-voxel hemodynamic markers between BAV patients and healthy controls, (Sievers and Schmidtke, 2007), explore associations between these markers and a structural marker of aortopathy (i.e. aortic diameter), and (Masri et al., 2017) observe differences in these markers for patients progressing to aortic surgery versus patients not requiring surgery during observational follow-up. We hypothesize that novel parametric voxel-by-voxel markers will be associated with aortic dilation and referral for surgery and can enhance our understanding of BAV hemodynamics beyond standard metrics.

2 MATERIALS AND METHODS

2.1 Study Cohort

Aortic 4D-flow MRI was acquired in 73 BAV patients (age = 49 ± 16 years; 21 female) and 23 healthy controls (age = 37 ± 14 years; eight female). Patients were recruited as a pre-defined sub-study of a prospective observational clinical outcomes registry at our institution. The study was coordinated by commercial software (cardioDI^{TM}, Cohesic Inc, Calgary, Alberta) for the routine capture of patient informed consent, health questionnaires and for standardized collection of MRI-related variables. Healthy volunteers ≥18 years of age were recruited and underwent identical workflow and were required to have no known cardiovascular disease, hypertension or diabetes and have no contraindications for MRI (Kramer et al., 2013).

All subjects enrolled to our study were required to be ≥18 years of age and agree to the incremental performance of research pulse sequences inclusive of 4D-flow MRI, and prospective follow-up using electronic health data matching for iterative capture of clinical and procedural events. For this study patients were identified by standardized coding of clinical referral indications for BAV plus confirmation of BAV morphology by MRI. Patients were excluded for the following reasons: history of prior myocardial infarction or known non-ischemic cardiomyopathy, complex congenital heart disease, MRI-coded moderate-severe mitral insufficiency, or a left ventricle ejection fraction (LVEF) < 50%.

The study was approved by the Institutional Review Board (IRB) at our institution and all subjects provided written informed consent. All research activities were performed in accordance with the Declaration of Helsinki.

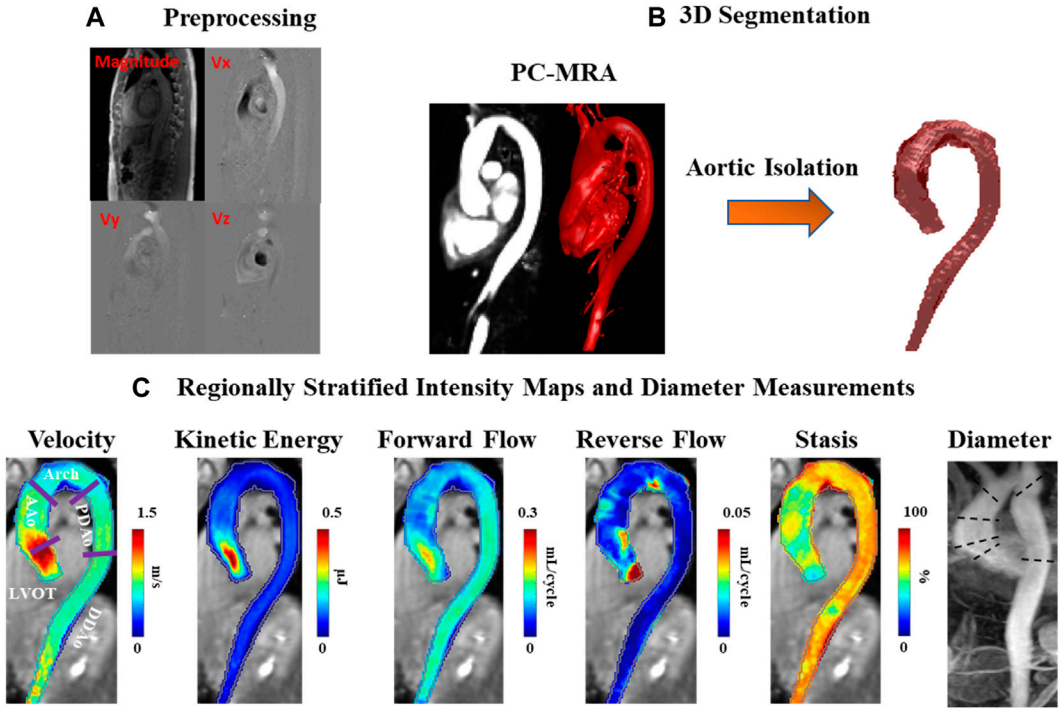

FIGURE 1 | Workflow diagram. **(A)** Preprocessing of the original 4D-flow data, including calculation of 3D PC-MRA from the measured 3D velocities and magnitude. **(B)** 3D segmentation of the thoracic aorta. **(C)** Velocity, kinetic energy, forward flow, reverse flow, and stasis maps stratified by regions: left ventricular outflow tract (LVOT), ascending aorta (AAo), aortic arch (Arch), proximal descending aorta (PDAo) and distal descending aorta (DDAo). Maximum diameter calculated in each region using 2D PC-MRA.

2.2 Cardiac Magnetic Resonance Data Acquisition

All MRI examinations were performed using 3T MRI scanners [Prisma (N = 71) or Skyra (N = 25), Siemens, Erlangen, Germany]. Indication-based protocolling ensured consistent imaging procedures for all subjects. Imaging was performed in accordance with published recommendations (Kramer et al., 2013). Routine, retrospectively-gated balanced steady-state free precession (SSFP) cine imaging was performed in 4-chamber, 3-chamber, and 2-chamber, sequential short axis ventricular views and short axis aortic valve views, the latter to characterize valve morphology. Through-plane 2D phase-contrast (2DPC) flow imaging of the aortic valve was performed at the valve annulus, cusp tips, and 1 cm below the annulus. 3D magnetic resonance angiography (MRA) of the thoracic aorta was performed using administration of 0.2 mmol/kg gadolinium contrast (Gadovist, Bayer, Canada). Approximately 5–10 min following contrast administration, retrospectively ECG-gated 4D-flow MRI (WIP 785A) was acquired during free breathing using navigator gating of diaphragmatic motion (Garcia et al., 2021). 4D-flow imaging parameters were as follows: spatial resolution (row × column × slice) = 2.0–2.5 × 2.0–2.5 × 2.4–3.5 mm^3, temporal resolution = 36.24–40.56 m s, flip angle = 15; field of view (FOV) = 240–350 × 320–400 mm^2, bandwidth = 455–495 Hz/Pixel, velocity sensitivity (Venc) = 150–550 cm/s, echo time = 2.01–2.35 m s, pulse repetition time = 4.53–5.07 m s.

2.3 4D-Flow Analysis

4D-flow MRI analysis was performed using an in-house program developed in MATLAB (2020b) with workflow schematically summarized in **Figure 1**. Workflow consists of a preprocessing step through which raw data are subject to noise masking, velocity anti-aliasing, and corrections for Maxwell terms and eddy currents (Markl et al., 2007) (**Figures 1–A**). A time-averaged 3D phase-contrast MR angiography (PC-MRA) was derived from 4D-flow data, as previously described in the literature (Bock et al., 2007; Markl et al., 2007) to depict the aortic lumen region. Segmentation of the entire aorta was achieved using a semiautomatic software package called "4D-flow Analysis Tool" (Fatehi Hassanabad et al., 2020), which was previously developed in our group and is shown in **Figures 1–B**.

2.4 Data Analysis (Parametric Hemodynamic Maps)

The segmentation results were used to mask the 4D-flow velocity field and perform volumetric hemodynamic analyses. Parametric hemodynamic mapping of FF, RF, flow stasis, and KE was performed using an in-house MATLAB program according to a recently reported workflow (Shen et al., 2018; Jarvis et al., 2020; Jarvis et al., 2021). Briefly, 4D-flow data were interpolated to isotropic voxels (1 mm × 1 mm × 1 mm) using cubic spline interpolation. Each voxel was matched to the nearest plane

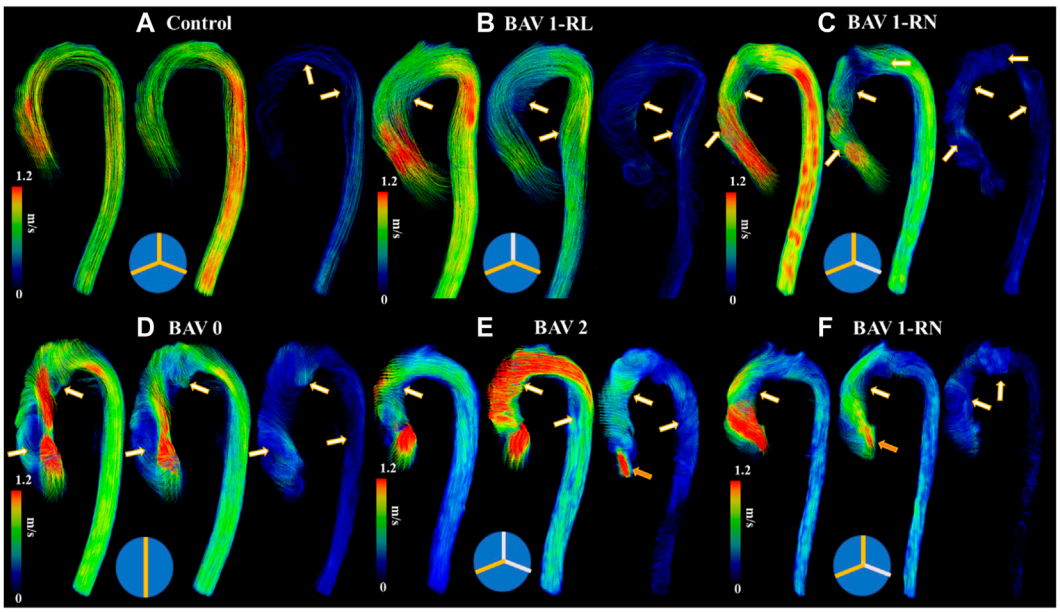

FIGURE 2 | Helical flow patterns throughout the cardiac cycle. Panel **(A)** shows a control. Panel **(B)** shows a bicuspid aortic valve (BAV) with right-left (RL) fusion. Panel **(C)** shows a BAV with right-non coronary (RN) fusion. Panel **(D)** shows a BAV type 0 fusion. Panel **(E)** shows a BAV type 2 fusion with moderate aortic regurgitation. Panel **(F)** shows a BAV RN fusion with mild aortic regurgitation. White-orange arrows point to helical flow patterns and orange arrows to aortic valve regurgitation jet. Note that BAV patients develop reverse helical flow in the ascending aorta. At the bottom of each case a diagram of Sievers fusion type is illustrated.

(based on the shortest 3D distance) along the aortic centerline. Plane position along the centerline was used to define the direction of FF (i.e. flow moving downstream with respect to the plane) and RF (i.e. flow moving upstream with respect to the plane) for each voxel in the aortic volume (Shen et al., 2018). FF and RF were calculated for each aortic voxel, and time-frame, and summed over the cardiac cycle (leading to units of mL/cycle).

Voxel-wise flow stasis was determined as the percent of cardiac time-frames below the threshold value of velocity = 0.1 m/s (which was considered slow flow) (Jarvis et al., 2020). Voxel-wise KE was determined for each time-frame by:

$$KE = \frac{1}{2} \cdot \rho \cdot dV \cdot v(t)^2 \quad (1)$$

with ρ being the blood density (assumed as 1,060 kg/m^3) and dV the unit voxel volume (i.e. 1 mm^3), summed over the cardiac cycle. Peak velocity was the maximum absolute velocity over systole using maximum intensity projections (MIPs) (Rose et al., 2016). Parametric maps were calculated as mean intensity projections for FF, RF, stasis, and KE, **Figures 1–C**.

Regional analysis was performed by dividing the aorta into five volumetric regions based on standard anatomic landmarks recommended in the thoracic aortic disease guidelines and previous studies (Fatehi Hassanabad et al., 2020; Hiratzka et al., 2010; Garcia et al., 2017; Garcia et al., 2015): 1) left ventricular outflow tract (LVOT); 2) ascending aorta (AAo); 3) aortic arch (Arch); 4) proximal descending aorta (PDAo); 5) distal descending aorta (DDAo) (**Figures 1–C**). All aforementioned flow parameters were calculated separately in each of these regions. Reynolds number was calculated at the aortic vena contracta location to assess flow regime (Stalder et al., 2011).

2.5 Valve Phenotypes, Aortic Diameters, and Dilation Patterns

BAV phenotypes were evaluated from aortic valve cine SSFP image acquisitions and categorized according to Sievers' classifications (Sievers and Schmidtke, 2007), as follows: type 0 (no raphe); type 1 RL (one raphe connecting the right coronary and left coronary cusps); type 1 RN (one raphe connecting the right coronary and non-coronary cusps); type 2 (two raphes), **Figure 2**.

Maximum aortic diameters (mm) were measured for each aortic region using 3D contrast-enhanced MRA data, as recommended by published guidelines (Hiratzka et al., 2010). Diameters were indexed to body surface area (BSA) (Gehan and George, 1970) to normalize data across both study and volunteer populations. BSA-indexed diameters have been suggested to offer enhanced prognostic value for BAV patients compared to raw diameter values (Davies et al., 2006).

In keeping with previously used classifications (González-Santos and Arnáiz-García, 2017), patients were stratified by AAo dilation severity, as follows: non-dilated (max AAo diameter <35 mm), moderately dilated (35 mm < max AAo diameter <45 mm), and severely dilated (max AAo diameter >45 mm).

TABLE 1 | Demographics of study cohort.

Parameter	Cohorts									
	All subjects		BAV types			Dilation severity			Outcome	
	Control (*n* = 23)	BAV (*n* = 73)	Type 1-RL (*n* = 36)	Type 1-RN (*n* = 11)	Type 0 (*n* = 19)	Non dilation (*n* = 12)	Mod. Dilation (*n* = 24)	Severe dilation (*n* = 27)	No Surgery (*n* = 49)	Surgery (*n* = 24)
Age (yrs)	37 ± 14	49 ± 16*	49 ± 17	53 ± 14	45 ± 15	38 ± 19	50 ± 13	50 ± 15	48 ± 17	51 ± 13
Female (n)	8 (35%)	21 (29%)	9 (25%)	4 (36%)	5 (26%)	8 (67%)	3 (13%)†	5 (19%)‡	17 (35%)	4 (17%)
BSA (m2)	1.9 ± 0.3	2.0 ± 0.3	2.0 ± 0.2	2.0 ± 0.3	2.0 ± 0.3	1.8 ± 0.3	2.1 ± 0.2†	2.0 ± 0.2‡	2.0 ± 0.3	2.1 ± 0.2
Heart Rate (bpm)	64 ± 11	63 ± 12	65 ± 12	57 ± 5	62 ± 12	62 ± 10	66 ± 14	62 ± 11	63 ± 13	63 ± 9
LVEDV (ml)	167 ± 40	189 ± 63	190 ± 67	177 ± 37	169 ± 56	159 ± 29	198 ± 55	206 ± 73	175 ± 48	210 ± 78*
LVESV (ml)	64 ± 19	76 ± 34	78 ± 33	59 ± 22	68 ± 32	63 ± 16	81 ± 32	85 ± 41	72 ± 29	80 ± 40
LVEF (%)	62 ± 5	60 ± 9	59 ± 10	67 ± 9	61 ± 7	61 ± 4	59 ± 13	60 ± 9	59 ± 10	63 ± 7
LV Mass (g)	103 ± 31	132 ± 49	127 ± 48	164 ± 63	117 ± 32	105 ± 26	142 ± 42	144 ± 61	120 ± 38	153 ± 60*
LVCO (L/min)	6.7 ± 1.7	7.2 ± 2.7	7.3 ± 2.9	6.6 ± 1.4	6.5 ± 1.7	6.0 ± 0.8	7.8 ± 3.0	7.7 ± 3.0	6.5 ± 2.2	8.5 ± 3.0*

*BAV- bicuspid aortic valve, Mod.- moderate, Morpho.—morphotype, BSA-body surface area, LV—center ventricular, LVEDV- center ventricular end-diastolic volume, LVESV—center ventricular end-systolic volume, LVEF—center ventricular ejection fraction, LVCO- center ventricular cardiac output. *p < 0.05 between opposing cohorts, †p < 0.05 between mod. dilation and non-dilation cohorts, and ‡p < 0.05 between severe dilation and non-dilation cohorts.*

2.6 Statistical Analysis

A Shapiro Wilks test was used to determine the normality of each parameter. A student's t-test (or non-parametric equivalent if at least one parameter had a non-normal distribution) was used to evaluate differences in parameter means between two opposing cohorts; when analyzing differences between more than two opposing cohorts, a one-way ANOVA (followed by Tukey's post hoc test) was used.

To determine associations between aortic hemodynamic measures and vessel dilation, we correlated aortic diameters to each hemodynamic parameter within the BAV cohort only. Pearson correlations (or Spearman if at least one parameter had a non-normal distribution) were used and correlations were performed in the AAo region alone.

To further elucidate what hemodynamic parameters are most significantly associated with aortic remodelling in the context of BAV disease, a multivariate model was constructed including BSA-indexed aortic diameter as the dependent variable with age and hemodynamic parameters as independent variables. In each model, hemodynamic parameters were only included if they demonstrated a significant univariate association with the indexed aortic diameter and no multicollinearity with each other; however, age was always included to evaluate its importance in aortic remodelling relative to flow parameters.

For all tests, a p-value ≤ 0.05 was considered statistically significant. For univariate analyses, a correlation coefficient greater than absolute 0.25 was additionally required to be considered statistically significant. All statistical analyses were performed in SPSS 25 (Chicago, IL).

3 RESULTS

3.1 Cohort Assignments

Of the BAV patients, there were: Type 0 ($n = 19$), Type 1 ($n = 47$; 11 RN, 36 RL), Type 2 ($n = 4$), and un-identified ($n = 3$). Patients with type 2 or un-identified valve phenotype were not included in statistical analyses due to the small sample size. Normal aortic valve morphology was confirmed in all healthy volunteers.

Twelve patients (16.4%) had no aortic dilation, 24 (32.8%) met moderate dilation criteria, and 27 (37.9%) met severe dilation criteria. Of those with dilation, a root morphotype was observed in 10 (19.6%) patients, while an ascending morphotype was observed in 13 (25.5%). No aortic dilation criteria was met in any of the health volunteers.

3.2 Subject Demographics and Aortic Dimensions

Baseline patient characteristics are provided in **Table 1**; standard aortic measurements are provided separately in **Table 2**. Compared to healthy volunteers (i.e. percent change in mean value), BAV patients were significantly older ([24%]; $p < 0.01$). However, no significant differences in left ventricle (LV) chamber volumes, mass or function were identified. Aortic measurements showed larger diameters of the AAo ([31%], $p < 0.01$), PDAo ([15%], $p < 0.05$), and DDAo ([11%], $p < 0.01$]) among patients with BAV disease. Once diameter was indexed to BSA, these differences only persisted at the AAo ([24%], $p < 0.01$) location.

Compared to Type 1 BAV subjects, Type 0 BAV subjects were associated with lower indexed diameters of the SOV ([-4%], $p < 0.05$). No other significant differences between valve types were identified. BAV patients with moderate or severe dilation had significantly larger BSAs and a smaller proportion of females when compared with non-dilated BAV patients. There were no other significant differences in baseline characteristics between dilation severity classifications.

3.3.4D-Flow MRI Findings

3.3.1 BAV Patients vs Healthy Controls

It was possible to observe small helical patterns in the arch and in the proximal descending aorta, **Figure 2**. BAV patients exhibited larger helical flow regions with pronounced reverse flow direction

TABLE 2 | Parameter differences between BAV patients and healthy controls at each aortic region.

Parameter	Location									
	LVOT		AAo		Arch		PDAo		DDAo	
	Control	BAV	Control	BAV	Control	BAV	Control	BAV	Control	BAV
Diameter (mm)	28 ± 5	29 ± 4	28 ± 4	40 ± 7**	25 ± 3	26 ± 5	20 ± 3	23 ± 4*	18 ± 3	20 ± 3*
Indexed Diameter (mm/m^2)	15 ± 2	14 ± 2	15 ± 3	20 ± 4**	13 ± 2	13 ± 3	11 ± 2	11 ± 2	10 ± 2	10 ± 2
Peak Velocity (m/s)	1.3 ± 0.2	1.9 ± 1.0*	1.5 ± 0.3	2.6 ± 1.2**	1.2 ± 0.2	1.5 ± 0.8	1.2 ± 0.3	1.3 ± 0.8	1.4 ± 0.4	1.2 ± 0.5
KE (μJ)	1.9 ± 0.5	2.6 ± 1.8	1.8 ± 0.6	2.3 ± 1.2	1.5 ± 0.6	1.7 ± 1.0	1.8 ± 0.7	1.7 ± 1.1	2.0 ± 0.9	1.6 ± 0.9
FF (mL/cycle)	0.18 ± 0.04	0.15 ± 0.06*	0.18 ± 0.04	0.12 ± 0.03**	0.17 ± 0.04	0.14 ± 0.04*	0.19 ± 0.05	0.16 ± 0.05	0.22 ± 0.07	0.17 ± 0.05*
RF (mL/cycle)	0.025 ± 0.01	0.045 ± 0.05*	0.011 ± 0.001	0.039 ± 0.02**	0.010 ± 0.006	0.029 ± 0.02**	0.010 ± 0.01	0.019 ± 0.02**	0.005 ± 0.004	0.015 ± 0.025*
Stasis (%)	33 ± 9	22 ± 12**	50 ± 10	23 ± 11**	52 ± 10	32 ± 16**	53 ± 10	35 ± 18**	43 ± 13	38 ± 17

*Diameter and indexed diameter measurements at the SOV, region are not included. LVOT-center ventricular outflow tract, AAo-ascending aorta, Arch—aorta arch, PDAo-proximal descending aorta, DDAo—distal descending aorta, BAV- bicuspid aortic valve, KE—kinetic energy, FF—forward flow, RF—reverse flow. Values are reported as mean ± stdev. *p < 0.05 and **p < 0.001.*

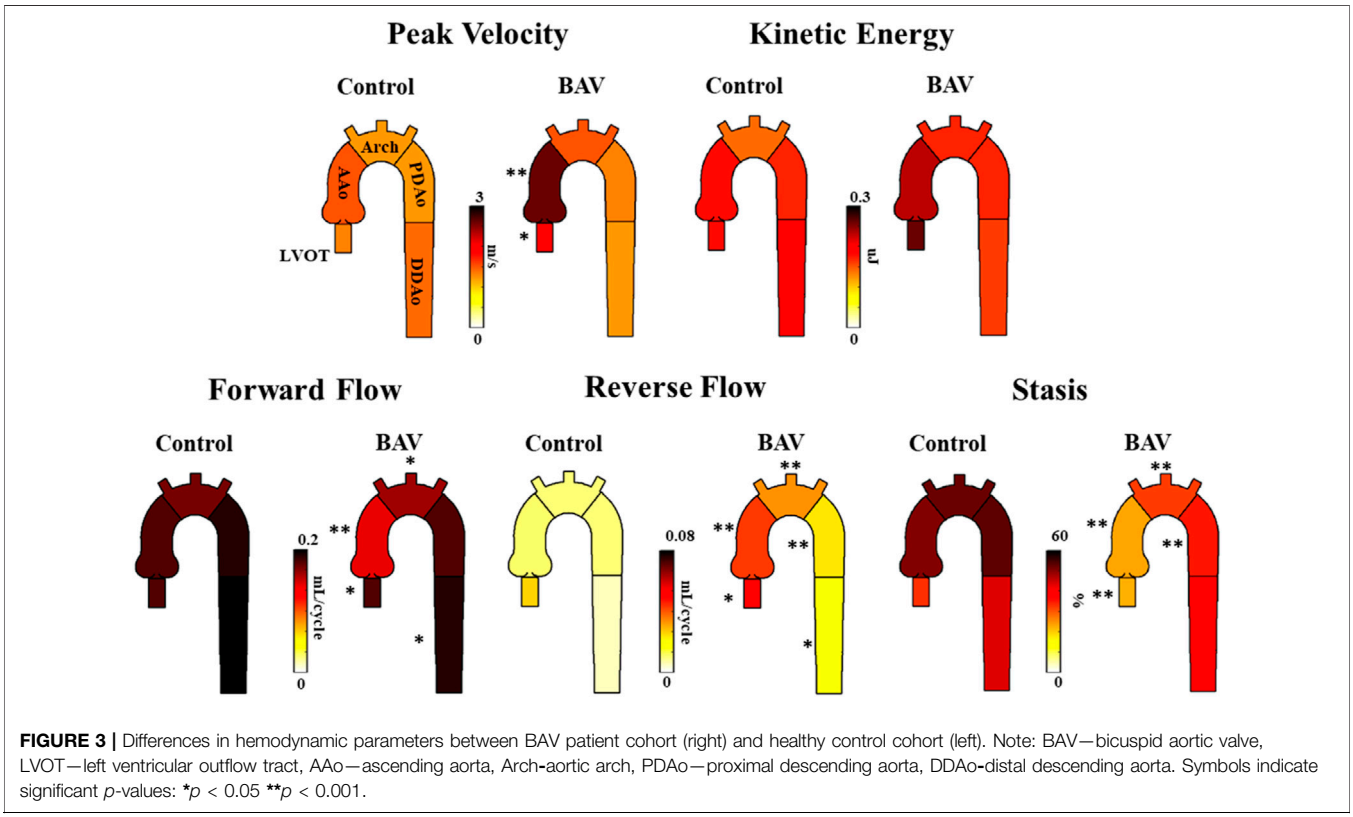

FIGURE 3 | Differences in hemodynamic parameters between BAV patient cohort (right) and healthy control cohort (left). Note: BAV—bicuspid aortic valve, LVOT—left ventricular outflow tract, AAo—ascending aorta, Arch-aortic arch, PDAo—proximal descending aorta, DDAo-distal descending aorta. Symbols indicate significant *p*-values: ***p* < 0.05 ****p* < 0.001.

in the ascending aorta, **Figure 2**-Bottom. Peak velocity measurements were greater in BAV patients at the LVOT ([32%], $p < 0.05$) and AAo ([42%], $p < 0.001$) while FF was lower in the AAo ([-33%, $p < 0.05$) (**Table 2**; **Figure 3**). The BAV cohort also showed significantly elevated RF throughout the entire aorta, with the largest increase being at the AAo ([254%], $p < 0.001$). Stasis levels were significantly lower in BAV patients from the LVOT to PDAo, with the largest decrease being at the AAo ([-54%], $p < 0.001$). Controls had Reynolds numbers in the range of [5,275–1,135] while BAV patients had a range of [5,504–3,0411] at vena contracta; thus indicating the presence of turbulent flow in the ascending aorta.

3.3.2 Bicuspid Aortic Valve Types

Type 0 BAVs exhibited less stasis in the DDAo (30 ± 18% vs 41 ± 16% [-27%]; $p < 0.05$) compared to all Type 1 BAVs together. No other significant difference was found in the comparison of Type 0 and Type 1 valves. When accounting for specific phenotypes of Type 1 BAVs, Type 1-RN possessed the greatest peak velocity in

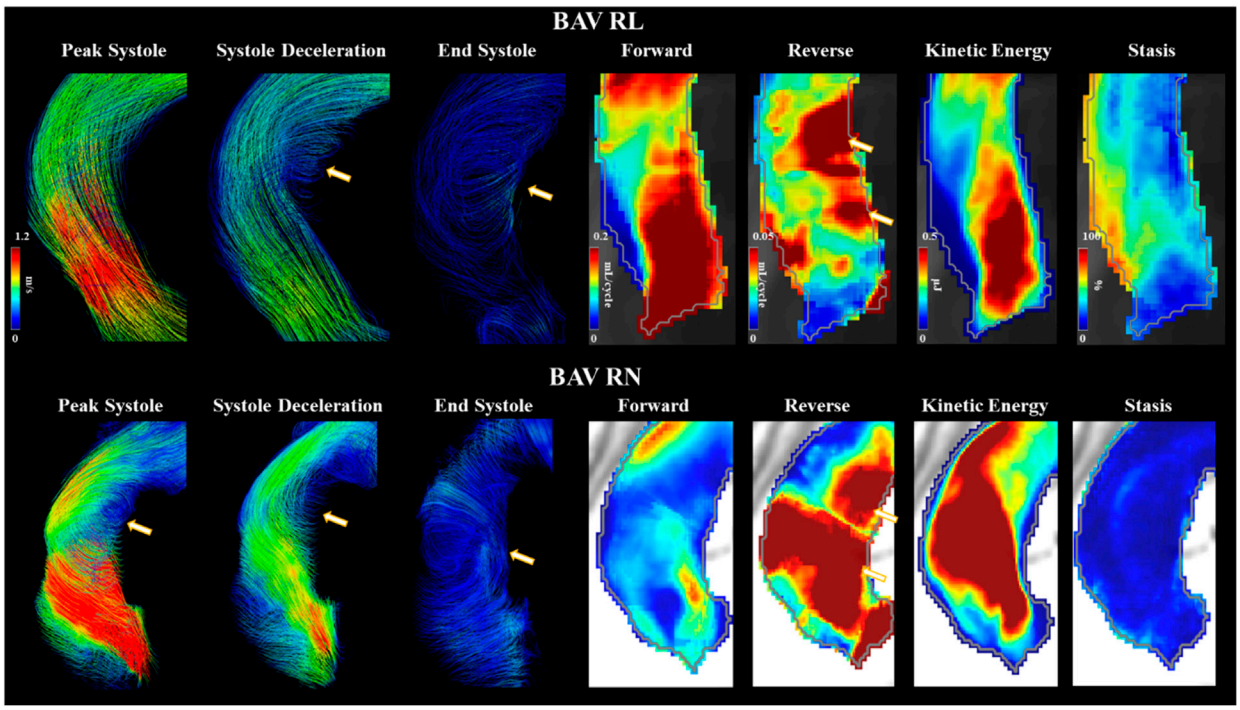

FIGURE 4 | Bicuspid aortic valve cases with right-left and right-non coronary fusion. Arrows point to helical flow patterns. Forward flow, reverse flow, kinetic energy, and flow stasis from each subject are represented using maximum intensity projections. Gray line represents the vessel wall from the aortic segmentation.

TABLE 3 | Parameter differences between BAV dilation severity.

Parameter	AAo			Arch		
	Non-dilated (n = 22)	Mod. dilation (n = 24)	Severe Dilation (n = 27)	Non-dilated (n = 22)	Mod. dilation (n = 24)	Severe Dilation (n = 27)
RF (mL/cycle)	0.033 ± 0.015	0.037 ± 0.016	0.045 ± 0.016*	0.018 ± 0.010	0.027 ± 0.017*	0.039 ± 0.018**
Stasis (%)	31 ± 13	20 ± 9*	19 ± 10**	41 ± 15	33 ± 17	27 ± 14*

*Mod.—moderate; RF- reverse flow. Values are reported as mean ± stdev. *:* p < *0.05 compared with non-dilated, ***p < *0.01 compared with non-dilated.*

the arch when compared to both Type 1-RL (2.1 ± 1.4 m/s vs 1.4 ± 0.5 m/s [50%]; $p < 0.05$) and Type 0 (2.1 ± 1.4 m/s vs 1.4 ± 0.4 m/s [50%]; $p < 0.05$). No other results were statistically significant. An example of Type 1-RL hemodynamics is illustrated in **Figure 4**.

3.3.3 Dilation Severity

Moderately dilated patients showed less stasis in the AAo ([-36%], $p < 0.05$) and more RF in the arch ([83%], $p < 0.05$) compared to non-dilated (**Table 3**). Severely dilated patients showed less stasis in the AAo ([-39%], $p < 0.01$) and arch ([-34%], $p < 0.05$) accompanied by more RF in the arch ([106%], $p < 0.01$) compared to non-dilated patients. No other significant differences in these cohorts were observed.

3.4 Univariate and Multivariate Associations

Indexed AAo diameter correlated positively with age (R = 0.326, $p = 0.01$), but negatively with FF (R = -0.648, $p < 0.001$), RF (R = 0.441, $p < 0.001$) and stasis (R = −0.288, $p < 0.05$). No other significant univariate correlations were found between indexed diameter and hemodynamics at the level of the AAo. Flow-related associations are shown in **Figure 5**.

Multivariate results are shown in **Table 4**. Focusing on the AAo, the model included indexed AAo diameter as the dependent variable and age, AAo FF, AAo stasis, and AAo peak velocity as the independent variables. This model demonstrated an overall R = 0.709 and showed AAo FF (β = -0.492, $p = 0.001$) to be most strongly associated with indexed AAo diameter.

3.5 Surgical Intervention

Twenty-four patients underwent surgical intervention and had a follow-up of 179 ± 180 days. Of these patients, 18 (78%) had an aortic valve replacement, two (9%) had an AAo replacement, and three (13%) had both. Patients who received surgery had larger

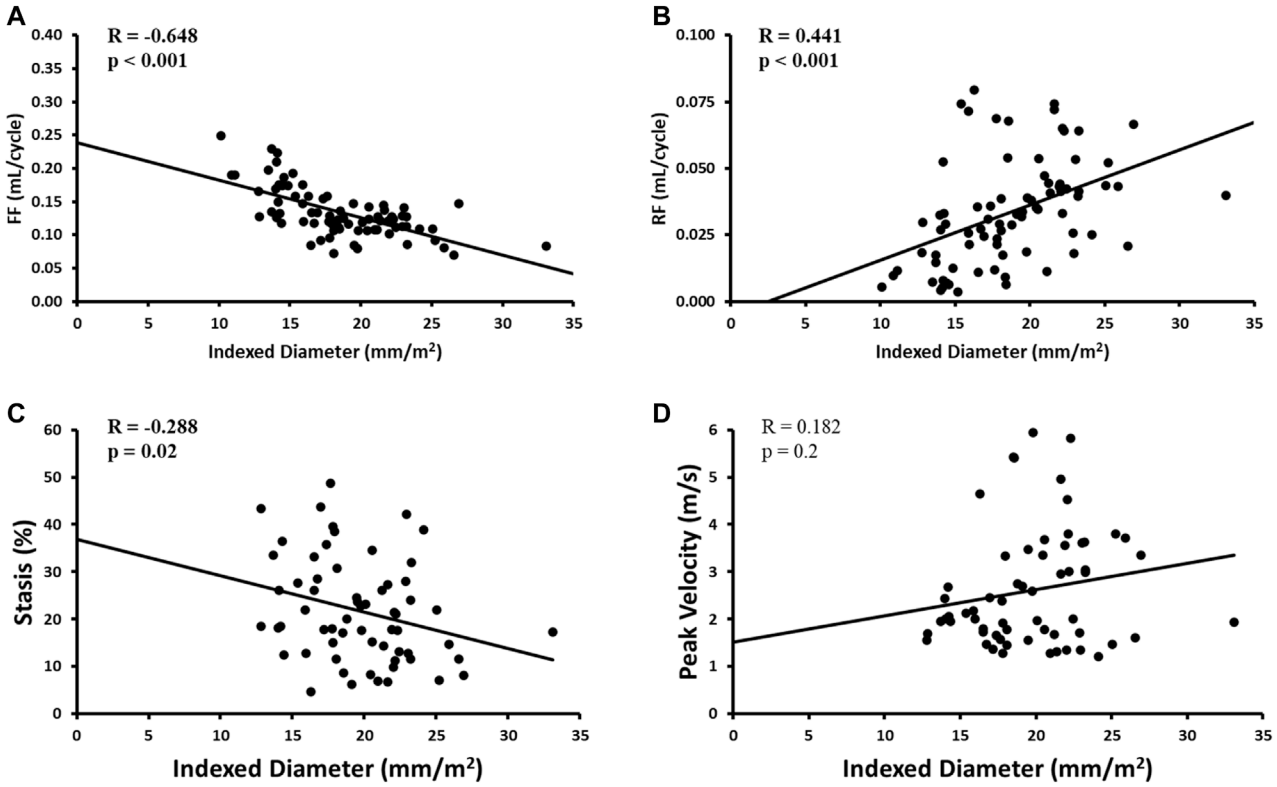

FIGURE 5 | Correlates of aortic diameter in the AAo region only. **Panel A** shows forward flow (FF) plot. **Panel B** shows reverse flow (RF) plot. **Panel C** shows stasis plot. **Panel D** shows peak velocity plot.

diameters at the arch ([14%], $p < 0.01$), greater LV mass ([27%], $p < 0.05$), and greater LVCO ([31%], $p < 0.01$) than those who did not receive surgery. No other significant differences in baseline characteristics were found.

Patients with surgical intervention demonstrated greater KE and peak velocity at the LVOT ([92%], $p < 0.01$ and [84%], $p = 0.01$, respectively), AAo ([61%], $p < 0.001$ and [75%], $p < 0.001$), and arch ([53%], $p < 0.05$ and [56%], $p < 0.001$), as shown in **Figure 6** and **Table 5**. Patients who received surgery also demonstrated significantly elevated RF and decreased stasis throughout the entire aorta, most prominently at the arch ([120%], $p < 0.001$ and [-52%], $p < 0.001$).

TABLE 4 | Multiple linear regression results.

Model	Associations	
	Std. Coef	
AAo diameter indexed	β	*p*
Age	0.174	0.080
AAo FF	–0.492	0.001
AAo RF	0.198	0.151
AAo stasis	–0.008	0.954
AAo Peak Velocity	0.031	0.778

Model only included significant univariate correlations (R > 0.25, p *< 0.01) and no multicollinearity with each other. AAo—ascending aorta, FF- forward flow, RF- reverse flow,* ß *- standardized coefficient, S.E., standard error.*

4 DISCUSSION

This study uses 4D-flow techniques to evaluate thoracic aorta parametric voxel-by-voxel hemodynamics in the context of BAV disease. Our main findings demonstrate that (Siu and Silversides, 2010) 3D-derived aortic peak velocity, FF, RF, and stasis are significantly altered in BAV patients, and (Sievers and Schmidtke, 2007) Peak velocity, KE, FF, RF, and stasis associate with aortic dilation and referral for surgery. Secondary findings suggest that differences in BAV phenotype and dilation severity impact downstream hemodynamics throughout the thoracic aorta.

4.1 Flow Is Abnormal in BAV Patients

Consistent with previous literature (Mathieu et al., 2015; Garcia et al., 2016; Rodríguez-Palomares et al., 2018), we found BAV patients to possess increased peak blood velocity and vessel diameter in the AAo. This is likely due to BAV morphology producing high-velocity jets and BAV patients' increased propensity for AAo dilatation (Siu and Silversides, 2010). In the current study, Reynolds number indicated presence of turbulence in the ascending aorta. Controls in this study exhibited higher *in vivo* Reynolds numbers than controls in Stalder

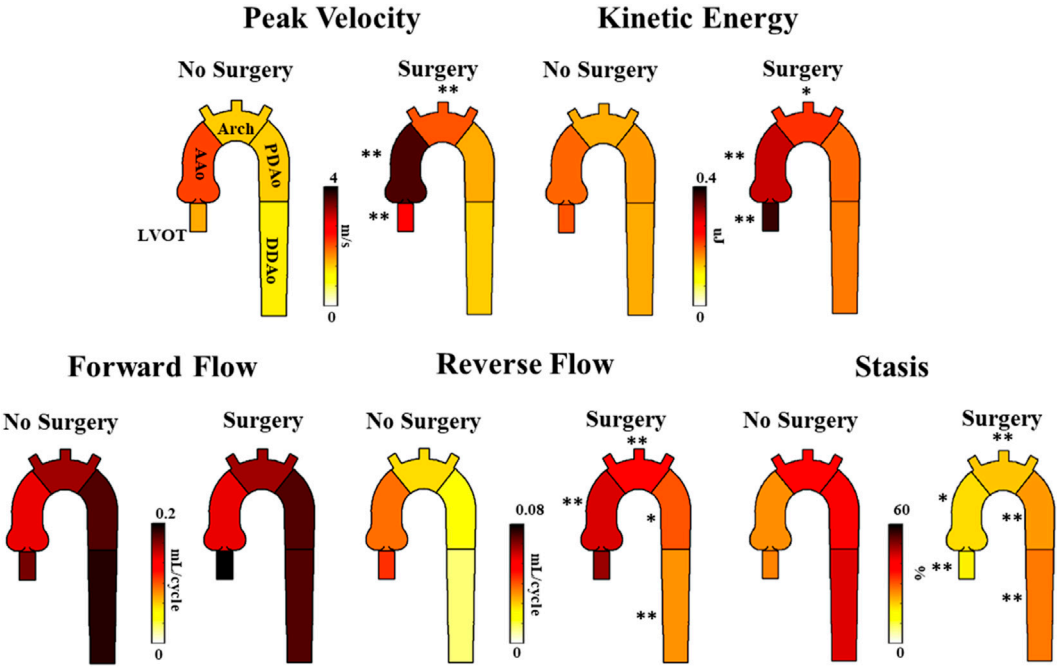

FIGURE 6 | Differences in hemodynamic parameters between BAV patients who received follow-up surgery and BAV patients who did not. Note: BAV—bicuspid aortic valve, LVOT—left ventricular outflow tract, AAo—ascending aorta, Arch—aortic arch, PDAo—proximal descending aorta, DDAo—distal descending aorta. Symbols indicate significant *p*-values: **p* < 0.05 ***p* < 0.001.

TABLE 5 | Parameter differences between BAV patients who did or did not receive aortic surgery following 4D-flow MRI scan.

Parameter	Location									
	LVOT		AAo		Arch		PDAo		DDAo	
	No Surgery (*n* = 49)	Surgery (*n* = 24)	No Surgery (*n* = 49)	Surgery (*n* = 24)	No Surgery (*n* = 49)	Surgery (*n* = 24)	No Surgery (*n* = 49)	Surgery (*n* = 24)	No Surgery (*n* = 49)	Surgery (*n* = 24)
Diameter (mm)	28 ± 4	30 ± 4	38 ± 7	43 ± 6**	25 ± 5	28 ± 4**	22 ± 4	23 ± 3	20 ± 3	21 ± 2
Indexed Diameter (mm/m^2)	14 ± 2	15 ± 2	19 ± 4	21 ± 4	13 ± 3	14 ± 2	11 ± 2	11 ± 1	10 ± 2	10 ± 1
Peak Velocity (m/s)	1.5 ± 0.5	2.7 ± 1.2**	2.1 ± 0.7	3.7 ± 1.3**	1.3 ± 0.4	2.0 ± 1.0**	1.3 ± 0.7	1.5 ± 1.1	1.1 ± 0.4	1.3 ± 0.6
KE (μJ)	2.0 ± 1.0	3.8 ± 2.3**	1.9 ± 0.8	3.1 ± 1.6**	1.5 ± 0.8	2.3 ± 1.1*	1.6 ± 1.0	1.9 ± 1.3	1.5 ± 0.8	1.8 ± 1.2
FF (mL/cycle)	0.15 ± 0.056	0.17 ± 0.062	0.12 ± 0.031	0.12 ± 0.025	0.14 ± 0.041	0.15 ± 0.034	0.16 ± 0.051	0.16 ± 0.036	0.17 ± 0.049	0.16 ± 0.052
RF (mL/cycle)	0.039 ± 0.031	0.057 ± 0.079	0.033 ± 0.013	0.051 ± 0.016**	0.022 ± 0.013	0.045 ± 0.017**	0.014 ± 0.011	0.033 ± 0.026*	0.009 ± 0.0081	0.028 ± 0.032**
Stasis (%)	26 ± 12	16 ± 8**	25 ± 11	18 ± 9*	38 ± 14	20 ± 10**	41 ± 17	24 ± 14**	43 ± 16	27 ± 13**

*LVOT-left ventricular outflow tract, AAo, ascending aorta, Arch - aorta arch; PDAo, proximal descending aorta, DDAo-distal descending aorta, D—Diameter, Di—Dimeter indexed, PV, peak velocity, KE-kinetic energy, FF- forward flow, RF- reverse flow. Values are reported as mean ± stdev. *: p < 0.05 and **p < 0.01.*

et al. who reported a range of [3,357–4,528] using prospectively gated 4D flow (Stalder et al., 2011). Some experimental studies reported a range of [2,400–10,000] in the aorta under normal hemodynamic conditions (Keshavarz-Motamed et al., 2014; Ha et al., 2019).

When compared to controls, BAV patients exhibit significantly elevated RF throughout the entire aorta. The RF findings agree well with previous studies that document increased helical flow and vortices within the AAo of BAV patients compared to healthy volunteers (Faggiano et al., 2012; Rodríguez-Palomares et al., 2018; Shan et al., 2019), which is likely a result of the eccentric off-centered jet produced by a BAV (Rodríguez-Palomares et al., 2018). However, RF differences in the distal aorta are less documented. It is possible that minor helical flow persists in the descending aorta, which would maintain elevated RF levels. Regardless of the underlying mechanism, RF levels in the descending aorta have been

recently implicated in stroke development. Previous studies have demonstrated the presence of retrograde flow in the descending aorta of cryptogenic stroke patients (Harloff et al., 2010), as well as the theoretical ability of this retrograde flow to carry plaques back towards the brachio-cephalic branches in the arch (Harloff et al., 2007). Harloff et al. estimates that this retrograde flow pattern may account for up to 24% of cryptogenic stroke events (Harloff et al., 2010). Thus, our observed increase in descending aorta RF in BAV patients is an intriguing finding with clinical implications that may warrant future research.

BAV patients were also observed to have significantly reduced blood stasis in all aortic regions (except DDAo) compared to healthy controls. There are very few previous studies which provide context to this finding. Hassanabad et al. (Fatehi Hassanabad et al., 2020) demonstrated that BAV patients, in comparison to healthy volunteers, possessed greater pressure drop throughout the entire thoracic aorta. This may imply an association between pressure drop and stasis. However, in this study we did not evaluate pressure drop and parametric voxel-by-voxel markers were not normalized to arterial pressure.

Lastly, KE levels found in BAV patients were similar to those found in healthy controls, even in the AAo. This is unexpected, as the increased blood jet velocity resulting from a BAV would conceivably lead to greater KE values near the valve. However, previous studies, such as that conducted by Elbaz et al. (Elbaz et al., 2019), have also found similar KE levels between controls and BAV patients in the AAo. To interpret these findings, it is important to note that KE is only one aspect of a fluid's total energy cost, which also includes turbulent kinetic energy (TKE), viscous energy loss (EL), and heat. It should also be recognized that BAV patients have consistently been shown to exhibit greater aortic TKE and EL, especially in the AAo (Dux-Santoy et al., 2019; Elbaz et al., 2019). Thus, while BAV patients likely possess significantly elevated KE immediately proximal to the valve, it is possible that much of this KE is subsequently lost in the form of EL and TKE due to chaotic helical flow that develops in the AAo. Thus, when we measure the average amount of KE in the entire AAo region over the cardiac cycle–as we do in this study–it is reasonable that KE measurements may be comparable between healthy controls and BAV patients.

4.2 Aortic Dilation Is Related to Blood Flow

In the AAo, vessel diameter was negatively associated with regionally-matched stasis and FF. This may be due to the increases in helical flow patterns that accompany AAo dilatation (Hope et al., 2007; Bürk et al., 2012; Dux-Santoy et al., 2019), as helical flow patterns leave less opportunity for forward flow and stasis. While it is important to note that our BAV cohort is older than controls, thus age may be a confounding factor in these associations, our multivariate analysis demonstrated both FF and stasis to be stronger independent predictors of diameter than age.

4.3 Ascending Aorta Flow Associates With Surgical Outcomes

No significant difference in aortic diameters was seen between patients who received follow-up surgery and those who did not. Because most of the patients with a surgical event received valvular surgery exclusively, while few patients received AAo replacement surgery, our surgical cohort is mostly characterized by individuals with valvular inefficiencies, rather than aortic aneurysms.

Those who receive surgical intervention exhibited much greater KE, velocity, and RF levels in the proximal aorta. As mentioned above, this is likely a result of the surgical cohort's level of valvular disease severity. Progression of valvular diseases such as calcification, stenosis, and regurgitation increases blood velocity, vorticity, and retrograde flow within the AAo (Garcia et al., 2019), which would conceivably equate to increased levels of KE, velocity, and RF.

Results also demonstrated significantly lower levels of stasis throughout the entire thoracic aorta in patients who received follow-up surgery compared to patients who did not. Alternatively, the elevated peak blood velocities in the surgical cohort may also explain their lower stasis levels. Either way, stasis appears to be a measure of great difference between patients who received follow-up surgery and patients who did not.

4.4 Secondary Findings: Effect of Valve Type and Dilation Severity on Distal Aorta Blood Flow

Previous studies have shown different BAV morphologies and dilation geometries to each possess unique flow characteristics in the AAo (Girdauskas et al., 2012), which may provide great clinical utility in disease severity assessments of BAV patients. Our study has expanded this knowledge by demonstrating that differences in flow patterns between valve phenotypes and dilation severities persist beyond the AAo region into the arch and descending aorta. Thus, it may be of utility for future studies to consider the entire thoracic aorta when characterizing flow patterns of valve types, dilation geometries and aortic arch shape.

4.5 Limitations

This study has several limitations. Patients and control cohorts were not age matched; given that age correlated with several parameters of interest, age may be a confounding variable in our findings. Patients were only included if they underwent clinically-ordered MRI examinations for aortic dilation or significant valvular stenosis and/or insufficiency. Accordingly, our patient cohort had a more severe disease phenotype than prior studies. Due to the localized nature of our voxel-by-voxel approach, it cannot be used to assess standard cardiac output. However, cardiac output can be estimated from an analysis plane at the left ventricle outflow tract, in a similar manner to 2D phase-contrast. As a cross-sectional design looking at the associations of parameters at a single point in time, no causative relationships can be determined from our analyses; future longitudinal studies are needed. Valve type, dilation severity, and surgical outcome cohort sizes were modest, and thus findings drawn from their analyses are limited. The parametric hemodynamic parameters presented in this study were measured over the entire cardiac cycle, rather than at systole or diastole. This reduces the sensitivity of our results and may overlook important

phenomena occurring at specific time points in the cardiac cycle. We did not monitor progression rates over time (i.e. between several serial visits) using parametric voxel-by-voxel markers. Similarly to wall shear stress (van Ooij et al., 2016), voxel-by-voxel markers can be used for generating hemodynamic atlases, which allow a personalized evaluation of disease progression, as recently reported by Soulat's et al. (Soulat et al., 2021).

Lastly, WSS was not included in the analysis for the presented cohort. It may be relevant to explore the association between 3D parametric voxel-by-voxel markers, axial/circumferential WSS (Rodríguez-Palomares et al., 2018), and in-plane rotational flow (Dux-Santoy et al., 2019). Most WSS studies usually report WSS magnitude (Mahadevia et al., 2013; Guzzardi et al., 2015; van Ooij et al., 2016; van Ooij et al., 2017) rather than the WSS vector decomposition. Recent studies reported that increased in-plane rotational flow and higher axial/circumferential WSS may explain aortic dilation morphotypes (Rodríguez-Palomares et al., 2018; Dux-Santoy et al., 2019).

5 CONCLUSION

This study used novel measurement techniques to comprehensively explore thoracic aortic hemodynamics in the context of BAV disease. BAV patients present significantly altered 3D-derived hemodynamics throughout the thoracic aorta compared to healthy controls, some of which are associated with measures of aortic dilation and the need for surgery. Further longitudinal studies are needed to explore these flow parameters in relation to BAV aortopathy, especially stasis and reverse flow, in the effort to provide improved clinical management of BAV patients.

DATA AVAILABILITY STATEMENT

The raw data supporting the conclusion of this article will be made available by the authors, without undue reservation.

ETHICS STATEMENT

The studies involving human participants were reviewed and approved by the Institutional Review Board—University of Calgary. The patients/participants provided their written informed consent to participate in this study.

AUTHOR CONTRIBUTIONS

PG and FJ performed data analysis, data collection, and drafted the initial manuscript. FB performed data segmentation, wrote sections of the manuscript and reviewed statistics. KJ developed flow parametric mapping source code, wrote sections of the manuscript, reviewed data outputs. MB, CL, PF, and JW monitored patients, supervised cardiac scan exam, supervised, and performed clinical reading. SH, BD, and JG performed and reviewed statistical analysis. JG designed the study, supervised students, data analysis, and drafted manuscript. All authors contributed to manuscript revision, read, and approved the submitted version.

FUNDING

JG received funding from the University of Calgary URGC SEM 1054341 and start-up funds. KJ received funding from the National Institute on Aging (T32 AG020506).

ACKNOWLEDGMENTS

We acknowledge the support of the Natural Sciences and Engineering Research Council of Canada/Conseil de recherche en sciences naturelles et en génie du Canada RGPIN-2020-04549 and DGECR-2020-00204.

REFERENCES

Baumgartner, H., Falk, V., Bax, J. J., De Bonis, M., Hamm, C., Holm, P. J., et al. (2017). 2017 ESC/EACTS Guidelines for the Management of Valvular Heart Disease. *Eur. Heart J.* 38 (36), 2739–2791. doi:10.1093/eurheartj/ehx391

Bock, J., Kreher, B. W., Hennig, J., and Markl, M. (2007). "Optimized Pre-processing of Time-Resolved 2D and 3D Phase Contrast MRI Data," in Proceedings of the 15th Annual Meeting of ISMRM (Berlin, Germany.

Borger, M. A., Fedak, P. W. M., Stephens, E. H., Gleason, T. G., Girdauskas, E., Ikonomidis, J. S., et al. (2018). The American Association for Thoracic Surgery Consensus Guidelines on Bicuspid Aortic Valve-Related Aortopathy: Full Online-Only Version. *J. Thorac. Cardiovasc. Surg.* 156 (2), e41–e74. doi:10.1016/j.jtcvs.2018.02.115

Branchetti, E., Bavaria, J. E., Grau, J. B., Shaw, R. E., Poggio, P., Lai, E. K., et al. (2014). Circulating Soluble Receptor for Advanced Glycation End Product Identifies Patients with Bicuspid Aortic Valve and Associated Aortopathies. *Arterioscler Thromb. Vasc. Biol.* 34 (10), 2349–2357. doi:10.1161/atvbaha.114.303784

Bürk, J., Blanke, P., Stankovic, Z., Barker, A., Russe, M., Geiger, J., et al. (2012). Evaluation of 3D Blood Flow Patterns and wall Shear Stress in the normal and Dilated Thoracic Aorta Using Flow-Sensitive 4D CMR. *J. Cardiovasc. Magn. Reson.* 14 (1), 84, 2012 . Available from: http://www.pubmedcentral.nih.gov/articlerender.fcgi?artid=3534249&tool=pmcentrez&rendertype=abstract. doi:10.1186/1532-429x-14-84

Davies, R. R., Gallo, A., Coady, M. A., Tellides, G., Botta, D. M., Burke, B., et al. (2006). Novel Measurement of Relative Aortic Size Predicts Rupture of Thoracic Aortic Aneurysms. *Ann. Thorac. Surg.* 81 (1), 169–177. doi:10.1016/j.athoracsur.2005.06.026

Dux-Santoy, L., Guala, A., Teixidó-Turà, G., Ruiz-Muñoz, A., Maldonado, G., Villalva, N., et al. (2019). Increased Rotational Flow in the Proximal Aortic Arch Is Associated with its Dilation in Bicuspid Aortic Valve Disease. *Eur. Hear. Journal-cardiovascular Imaging* 20 (12), 1407–1417. doi:10.1093/ehjci/jez046

Elbaz, M. S. M., Scott, M. B., Barker, A. J., McCarthy, P., Malaisrie, C., Collins, J. D., et al. (2019). Four-dimensional Virtual Catheter: Noninvasive Assessment of Intra-aortic Hemodynamics in Bicuspid Aortic Valve Disease. *Radiology* 293 (3), 541–550. doi:10.1148/radiol.2019190411

Faggiano, E., Antiga, L., Puppini, G., Quarteroni, A., Luciani, G. B., and Vergara, C. (2012). Helical Flows and Asymmetry of Blood Jet in Dilated Ascending Aorta with Normally Functioning Bicuspid Valve. *Biomech. Model. Mechanobiol* 12, 801, 2012 . Available from: http://www.ncbi.nlm.nih.gov/pubmed/23053594. doi:10.1007/s10237-012-0444-1

Fatehi Hassanabad, A., Burns, F., Bristow, M. S., Lydell, C., Howarth, A. G., Heydari, B., et al. (2020). Pressure Drop Mapping Using 4D Flow MRI in Patients with Bicuspid Aortic Valve Disease: A Novel Marker of Valvular Obstruction. *Magn. Reson. Imaging* 65, 175–182. doi:10.1016/j.mri.2019.11.011

Garcia, J., Beckie, K., Hassanabad, A. F., Sojoudi, A., and White, J. A. (2021). Aortic and Mitral Flow Quantification Using Dynamic Valve Tracking and Machine Learning: Prospective Study Assessing Static and Dynamic Plane Repeatability, Variability and Agreement. *JRSM Cardiovasc Dis.*, 10, 204800402199990, 2021 . Available from: http://journals.sagepub.com/doi/10.1177/2048004021999900.

Garcia, J., Barker, A. J., Collins, J. D., Carr, J. C., and Markl, M. (2017). Volumetric Quantification of Absolute Local Normalized Helicity in Patients with Bicuspid Aortic Valve and Aortic Dilatation. *Magn. Reson. Med.* 78 (2), 689–701. doi:10.1002/mrm.26387

Garcia, J., Barker, A. J., and Markl, M. (2019). The Role of Imaging of Flow Patterns by 4D Flow MRI in Aortic Stenosis. *JACC: Cardiovasc. Imaging* 12 (2), 252–266. Available from: https://linkinghub.elsevier.com/retrieve/pii/S1936878X1831115X doi:10.1016/j.jcmg.2018.10.034

Garcia, J., Barker, A. J., Murphy, I., Jarvis, K., Schnell, S., Collins, J. D., et al. (2016). Four-dimensional Flow Magnetic Resonance Imaging-Based Characterization of Aortic Morphometry and Haemodynamics: Impact of Age, Aortic Diameter, and Valve Morphology. *Eur. Heart J. Cardiovasc. Imaging* 17 (8), 877–884. doi:10.1093/ehjci/jev228

Garcia, J., Barker, A. J., van Ooij, P., Schnell, S., Puthumana, J., Bonow, R. O., et al. (2015). Assessment of Altered Three-Dimensional Blood Characteristics in Aortic Disease by Velocity Distribution Analysis. *Magn. Reson. Med.* 74 (3), 817–825. Available from: http://doi.wiley.com/10.1002/mrm.25466. doi:10.1002/mrm.25466

Gehan, E. A., and George, S. L. (1970). Estimation of Human Body Surface Area from Height and Weight. *Cancer Chemother. Rep.* 54 (4), 225–235.

Girdauskas, E., Disha, K., Borger, M. A., and Kuntze, T. (2012). Relation of Bicuspid Aortic Valve Morphology to the Dilatation Pattern of the Proximal Aorta: Focus on the Transvalvular Flow. *Cardiol. Res. Pract.* 2012, 478259. doi:10.1155/2012/478259

González-Santos, J. M., and Arnáiz-García, M. E. (2017). Wrapping of the Ascending Aorta Revisited-Is There Any Role Left for Conservative Treatment of Ascending Aortic Aneurysm? *J. Thorac. Dis.* 9 (Suppl. 6), S488. doi:10.21037/jtd.2017.04.57

Guzzardi, D. G., Barker, A. J., Van Ooij, P., Malaisrie, S. C., Puthumana, J. J., Belke, D. D., et al. (2015). Valve-Related Hemodynamics Mediate Human Bicuspid Aortopathy. *J. Am. Coll. Cardiol.* 66 (8), 892–900. Available from: http://linkinghub.elsevier.com/retrieve/pii/S0735109715042230. doi:10.1016/j.jacc.2015.06.1310

Ha, H., Kvitting, J.-P. E., Dyverfeldt, P., and Ebbers, T. (2019). 4D Flow MRI Quantification of Blood Flow Patterns, Turbulence and Pressure Drop in normal and Stenotic Prosthetic Heart Valves. *Magn. Reson. Imaging* 55, 118–127. Available from: http://www.ncbi.nlm.nih.gov/pubmed/30266627. doi:10.1016/j.mri.2018.09.024

Harloff, A., Simon, J., Brendecke, S., Assefa, D., Helbing, T., Frydrychowicz, A., et al. (2010). Complex Plaques in the Proximal Descending Aorta: An Underestimated Embolic Source of Stroke. *Stroke*, 41, 1145–1150. Available from: http://www.ncbi.nlm.nih.gov/pubmed/20431080.

Harloff, A., Strecker, C., Frydrychowicz, A. P., Dudler, P., Hetzel, A., Geibel, A., et al. (2007). Plaques in the Descending Aorta: a New Risk Factor for Stroke? Visualization of Potential Embolization Pathways by 4D MRI. *J. Magn. Reson. Imaging* 26 (6), 1651–1655. Available from: http://www.ncbi.nlm.nih.gov/pubmed/18022846.

Hiratzka, L. F., Bakris, G. L., Beckman, J. A., Bersin, R. M., Carr, V. F., Casey, D. E., et al. (2010). ACCF/AHA/AATS/ACR/ASA/SCA/SCAI/SIR/STS/SVM Guidelines for the Diagnosis and Management of Patients with Thoracic Aortic Disease, [Internet]. *J. Am. Coll. Cardiol.* 55 (14), e27–129. Available from: https://linkinghub.elsevier.com/retrieve/pii/S0735109710007151.

Hope, T. A., Markl, M., Wigström, L., Alley, M. T., Miller, D. C., and Herfkens, R. J. (2007). Comparison of Flow Patterns in Ascending Aortic Aneurysms and Volunteers Using Four-Dimensional Magnetic Resonance Velocity Mapping. *J. Magn. Reson. Imaging* 26 (6), 1471–1479. Available from: http://www.ncbi.nlm.nih.gov/pubmed/17968892 doi:10.1002/jmri.21082

Jamalidinan, F., Hassanabad, A. F., François, C. J., and Garcia, J. (2020). Four-dimensional-flow Magnetic Resonance Imaging of the Aortic Valve and Thoracic Aorta. *Radiologic Clin. North America* 58 (4), 753–763. doi:10.1016/j.rcl.2020.02.008

Jarvis, K., Soulat, G., Scott, M., Vali, A., Pathrose, A., Syed, A. A., et al. (2021). Investigation of Aortic Wall Thickness, Stiffness and Flow Reversal in Patients with Cryptogenic Stroke: A 4D Flow MRI Study. *J. Magn. Reson. Imaging* 53 (3), 942–952. Available from: http://www.ncbi.nlm.nih.gov/pubmed/32864836.

Jarvis, K., Pruijssen, J. T., Son, A. Y., Allen, B. D., Soulat, G., Vali, A., et al. (2020). Parametric Hemodynamic 4D Flow MRI Maps for the Characterization of Chronic Thoracic Descending Aortic Dissection. *J. Magn. Reson. Imaging* 51 (5), 1357–1368. Available from: http://www.ncbi.nlm.nih.gov/pubmed/31714648. doi:10.1002/jmri.26986

Keshavarz-Motamed, Z., Garcia, J., Gaillard, E., Maftoon, N., Di Labbio, G., Cloutier, G., et al. (2014). Effect of Coarctation of the Aorta and Bicuspid Aortic Valve on Flow Dynamics and Turbulence in the Aorta Using Particle Image Velocimetry. *Exp Fluids* 55(3):1696, 2014 .Available from: http://link.springer.com/article/10.1007/s00348-014-1696-6. doi:10.1007/s00348-014-1696-6

Kramer, C. M., Barkhausen, J., Barkhausen, J., Flamm, S. D., Kim, R. J., and Nagel, E. (2013). Standardized Cardiovascular Magnetic Resonance (CMR) Protocols 2013 Update. *J. Cardiovasc. Magn. Reson.* 15 (1), 91. doi:10.1186/1532-429x-15-91

Pape, L. A., Tsai, T. T., Isselbacher, E. M., Oh, J. K., Patrick, T. O., Arturo, E., et al. (2007). Aortic Diameter≥ 5.5 Cm Is Not a Good Predictor of Type a Aortic Dissection: Observations from the International Registry of Acute Aortic Dissection (IRAD). *Circulation* 116 (10), 1120–1127. doi:10.1161/CIRCULATIONAHA.107.702720

Mahadevia, R., Barker, A. J., Schnell, S., Entezari, P., Kansal, P., Fedak, P. W. M., et al. (2013). Bicuspid Aortic Cusp Fusion Morphology Alters Aortic 3D Outflow Patterns, Wall Shear Stress and Expression of Aortopathy. *Circulation*, 673–682. Available from: http://www.ncbi.nlm.nih.gov/pubmed/24345403

Markl, M., Harloff, A., Bley, T. A., Zaitsev, M., Jung, B., Weigang, E., et al. (2007). Time-resolved 3D MR Velocity Mapping at 3T: Improved Navigator-Gated Assessment of Vascular Anatomy and Blood Flow. *J. Magn. Reson. Imaging* 25 (4), 824–831. Available from: http://www.ncbi.nlm.nih.gov/pubmed/17345635. doi:10.1002/jmri.20871

Masri, A., Svensson, L. G., Griffin, B. P., and Desai, M. Y. (2017). Contemporary Natural History of Bicuspid Aortic Valve Disease: a Systematic Review. *Heart* 103 (17), 1323–1330. doi:10.1136/heartjnl-2016-309916

Mathieu, P., Bossé, Y., Huggins, G. S., Della Corte, A., Pibarot, P., Michelena, H. I., et al. (2015). The Pathology and Pathobiology of Bicuspid Aortic Valve: State of the Art and Novel Research Perspectives. *J. Path: Clin. Res.* 1 (4), 195–206. doi:10.1002/cjp2.21

Michelena, H. I., Corte, A. D., Evangelista, A., Maleszewski, J. J., Edwards, W. D., Roman, M. J., et al. (2021). International Consensus Statement on Nomenclature and Classification of the Congenital Bicuspid Aortic Valve and its Aortopathy, for Clinical, Surgical, Interventional and Research Purposes. *Radiol. Cardiothorac. Imaging* 3 (4), e200496, 2021 . Available from: http://www.ncbi.nlm.nih.gov/pubmed/34505060. doi:10.1148/ryct.2021200496

Rodríguez-Palomares, J. F., Dux-Santoy, L., Guala, A., Kale, R., Maldonado, G., Teixidó-Turà, G., et al. (2018). Aortic Flow Patterns and wall Shear Stress Maps by 4D-Flow Cardiovascular Magnetic Resonance in the Assessment of Aortic Dilatation in Bicuspid Aortic Valve Disease. *J. Cardiovasc. Magn. Reson.* 20 (1), 28. doi:10.1186/s12968-018-0451-1

Rose, M. J., Jarvis, K., Chowdhary, V., Barker, A. J., Allen, B. D., Robinson, J. D., et al. (2016). Efficient Method for Volumetric Assessment of Peak Blood Flow Velocity Using 4D Flow MRI. *J. Magn. Reson. Imaging* 44 (6), 1673–1682. Available from: http://doi.wiley.com/10.1002/jmri.25305. doi:10.1002/jmri.25305

Shan, Y., Li, J., Wang, Y., Wu, B., Barker, A. J., Markl, M., et al. (2019). Aortic Stenosis Exacerbates Flow Aberrations Related to the Bicuspid Aortic Valve Fusion Pattern and the Aortopathy Phenotype. *Eur. J. Cardio-thoracic Surg.* 55 (3), 534–542. doi:10.1093/ejcts/ezy308

Shen, X., Schnell, S., Barker, A. J., Suwa, K., Tashakkor, L., Jarvis, K., et al. (2018). Voxel-by-voxel 4D Flow MRI-Based Assessment of Regional Reverse Flow in the Aorta. *J. Magn. Reson. Imaging* 47 (5), 1276–1286. doi:10.1002/jmri.25862

Sievers, H.-H., and Schmidtke, C. (2007). A Classification System for the Bicuspid Aortic Valve from 304 Surgical Specimens. *J. Thorac. Cardiovasc. Surg.* 133 (5), 1226–1233. doi:10.1016/j.jtcvs.2007.01.039

Siu, S. C., and Silversides, C. K. (2010). Bicuspid Aortic Valve Disease. *J. Am. Coll. Cardiol.* 55 (25), 2789–2800. Available from: http://www.ncbi.nlm.nih.gov/pubmed/20579534. doi:10.1016/j.jacc.2009.12.068

Soulat, G., Scott, M. B., Allen, B. D., Avery, R., Bonow, R. O., Malaisrie, S. C., et al. (2021). Association of Regional Wall Shear Stress and Progressive Ascending Aorta Dilation in Bicuspid Aortic Valve. *JACC Cardiovasc. Imaging*. Available from: https://linkinghub.elsevier.com/retrieve/pii/S1936878X21005106. doi:10.1016/j.jcmg.2021.06.020

Stalder, A. F., Frydrychowicz, A., Russe, M. F., Korvink, J. G., Hennig, J., Li, K., et al. (2011). Assessment of Flow Instabilities in the Healthy Aorta Using Flow-Sensitive MRI. *J. Magn. Reson. Imaging* 33, 839–846. Available from: http://www.ncbi.nlm.nih.gov/pubmed/21448948. doi:10.1002/jmri.22512

Stalder, A. F., Russe, M. F., Frydrychowicz, A., Bock, J., Hennig, J., and Markl, M. (2008). Quantitative 2D and 3D Phase Contrast MRI: Optimized Analysis of Blood Flow and Vessel wall Parameters, [Internet]. *Magn. Reson. Med.* 60 (5), 1218–1231. Available from: http://www.ncbi.nlm.nih.gov/pubmed/18956416. doi:10.1002/mrm.21778

van Ooij, P., Markl, M., Collins, J. D., Carr, J. C., Rigsby, C., Bonow, R. O., et al. (2017). Aortic Valve Stenosis Alters Expression of Regional Aortic Wall Shear Stress: New Insights from a 4-Dimensional Flow Magnetic Resonance Imaging Study of 571 Subjects. *J. Am. Heart Assoc.* 6 (9), e005959. doi:10.1161/JAHA.117.005959

van Ooij, P., Garcia, J., Potters, W. V., Malaisrie, S. C., Collins, J. D., Carr, J. C., et al. (2016). Age-related Changes in Aortic 3D Blood Flow Velocities and wall Shear Stress: Implications for the Identification of Altered Hemodynamics in Patients with Aortic Valve Disease. *J. Magn. Reson. Imaging* 43 (5), 1239–1249. Available from: http://doi.wiley.com/10.1002/jmri.25081. doi:10.1002/jmri.25081

Verma, S., and Siu, S. C. (2014). Aortic Dilatation in Patients with Bicuspid Aortic Valve. [Internet], *N. Engl. J. Med.* 370, 1920–1929. Available from: http://www.ncbi.nlm.nih.gov/pubmed/24827036.

Verma, S., Yanagawa, B., Kalra, S., Ruel, M., Peterson, M. D., Yamashita, M. H., et al. (2013). Knowledge, Attitudes, and Practice Patterns in Surgical Management of Bicuspid Aortopathy: a Survey of 100 Cardiac Surgeons, [Internet]. *J. Thorac. Cardiovasc. Surg.* 146146 (5), 1033–1040. Available from: http://www.ncbi.nlm.nih.gov/pubmed/23988289 doi:10.1016/j.jtcvs.2013.06.037

Conflict of Interest: The authors declare that the research was conducted in the absence of any commercial or financial relationships that could be construed as a potential conflict of interest.

Publisher's Note: All claims expressed in this article are solely those of the authors and do not necessarily represent those of their affiliated organizations, or those of the publisher, the editors and the reviewers. Any product that may be evaluated in this article, or claim that may be made by its manufacturer, is not guaranteed or endorsed by the publisher.

frontiers in Cardiovascular Medicine

STUDY PROTOCOL
published: 26 January 2022
doi: 10.3389/fcvm.2021.735265

Early Detection of Cardiac Damage by Two-Dimensional Speckle Tracking Echocardiography After Thoracic Radiation Therapy: Study Protocol for a Prospective Cohort Study

Dan Zhu[1†], *Tingcui Li*[1†], *Hongqing Zhuang*[2] *and Ming Cui*[1*]

[1] *Department of Cardiology, Peking University Third Hospital, Beijing, China,* [2] *Department of Radiation Oncology, Peking University Third Hospital, Beijing, China*

OPEN ACCESS

Edited by:
Zahra K. Motamed, McMaster University, Canada

Reviewed by:
Ankush Gupta, Military Hospital Jaipur, India
Alexander E. Berezin, Zaporizhia State Medical University, Ukraine

***Correspondence:**
Ming Cui
mingcui@bjmu.edu.cn

[†] *These authors have contributed equally to this work and share first authorship*

Specialty section:
This article was submitted to Cardiovascular Imaging, a section of the journal Frontiers in Cardiovascular Medicine

Received: *02 July 2021*
Accepted: *31 December 2021*
Published: *26 January 2022*

Citation:
Zhu D, Li T, Zhuang H and Cui M (2022) Early Detection of Cardiac Damage by Two-Dimensional Speckle Tracking Echocardiography After Thoracic Radiation Therapy: Study Protocol for a Prospective Cohort Study. Front. Cardiovasc. Med. 8:735265. doi: 10.3389/fcvm.2021.735265

Background: As one of the important treatment methods for cancer patients, radiotherapy may lead to incidental irradiation of the heart, resulting in radiotherapy-induced heart disease (RIHD) arising many years after radiotherapy. While, there are few studies on early subclinical cardiac damage, which may be essential for the protection of late RIHD. To detect and predict RIHD and early subclinical cardiac damage induced by thoracic radiation therapy, based on two-dimensional speckle tracking echocardiography (2D STE) combined with multiple circulating biomarkers and accurate heart dosimetry.

Methods and Analysis: This is a monocentric prospective cohort study in which 104 patients treated for malignant tumors and with cardiac radiation exposure will be included. All participants will be followed for 12 months after radiotherapy. Echocardiography, 2D STE, and blood samples will be underwent at 5-time points (baseline; after completion of RT; 2, 6, and 12 months after RT). Left ventricular ejection fraction (LVEF); global longitudinal, radial, and circumferential strain; diastolic function parameters; creatine kinase (CK); creatine kinase isoenzyme (CK-MB); cardiac troponin T (cTnT); N-terminal pro-B-type natriuretic peptide (NT-proBNP) and hypersensitive C-reactive protein (hs-CRP) will be measured at baseline and every follow-up time. The incidence of major adverse cardiovascular events will be recorded.

Discussion: This study details the protocol and presents the primary limits and advantages of this single-center project. The inclusion of patients began in 2021, and the results are expected to be published in 2023. This study will be allowed to enhance knowledge on detection and prediction of early subclinical cardiac dysfunction induced by thoracic radiation therapy, based on two-dimensional speckle tracking echocardiography (2D STE) combined with circulating biomarkers and accurate heart dosimetry. Furthermore, we will evaluate risk factors of subtle cardiac damage and identify high-risk groups for early heart damage.

Clinical Trial Registration: ClinicalTrials.gov, identifier: NCT04443400.

Keywords: radiotherapy, radiotherapy-induced heart disease, two-dimensional speckle tracking echocardiography, biomarkers, cardiotoxicity

INTRODUCTION

Cancer is expected to rank as the most critical barrier to increasing life expectancy and the leading cause of death in the world in the twenty-first century. Data from global cancer statistics indicate that there will be about 18.1 million new cancer patients all over the world in 2018 (1, 2). According to statistics, one half of the cancer patients would undergo radiation therapy (RT) as neoadjuvant or adjuvant treatment (3). As an essential treatment modality of comprehensive treatment for cancer patients, radiotherapy can significantly improve the cure rate and survival rate of cancer patients (4). However, RT used to treat carcinomas, especially thoracic cancer, such as Hodgkin lymphoma, lung, breast cancer, etc, carries a high risk of developing cardiovascular side effects.

Heart is inevitably affected during thoracic radiation therapy, resulting in radiotherapy-induced heart damage. Thoracic radiation therapy is associated with long-term increased risk of coronary artery disease, heart failure, myocardial infarction, valvular disease, arrhythmias, pericarditis, and major adverse cardiovascular events many years after RT (5, 6). A meta-analysis of more than 42,000 breast cancer patients in 78 randomized controlled trials showed heart disease mortality increased in patients received RT (rate ratio 1.27, 2p = 0.0001) (7). Several studies confirmed the association between radiotherapy and the increased risk of heart disease, showed the relative risks within the range of 1.18–3.5 (8–11). A retrospective study of 2168 women undergoing radiotherapy for breast cancer showed that the rates of major coronary events increased linearly with the mean dose to the heart by 7.4% per gray (95% confidence interval, 2.9 to 14.5; $P < 0.001$), with no minimum threshold for risk (10). Moreover, a retrospective single-institution study of 415 patients with Hodgkin lymphoma showed that the incidence of coronary artery disease 20 years later to be 10.4% after a median of 9 years after RT treatment (12). In general, compared with non-irradiated patients, patients undergoing thoracic radiotherapy have a 2% higher absolute risk of cardiac morbidity at 5 years and a 23% increased absolute risk after 20 years (4). Radiotherapy-induced heart disease (RIHD) can involve any structure of the heart and has become one of the major complications threatening the survival of post-RT cancer patients (4, 12–14). Heart complications may partially offset the positive effect of radiation therapy on cardiac radiation exposure patients.

Long before the onset of clinically cardiac events occurring, subclinical cardiac changes may occur during the process, after completion, over weeks, months, or first years after RT, that can be detected based on functional dysfunction (15–17). Early detection of RIHD may have important clinical significance for cancer patients, especially young cancer patients. Furthermore, it may be essential for the prediction and protection of late RIHD.

As an essential tool for the assessment of cardiac structure and function, echocardiography has been widely used. However, left ventricular ejection fraction (LVEF) is a relatively insensitive index for detecting subclinical cardiac damage at an early stage (15, 17). It is mainly because no significant change in LVEF occurs until a critical amount of myocardial damage took place and after compensatory mechanisms are exhausted. Recently, two-dimensional speckle-tracking echocardiography (2D STE) has been used for detecting and quantifying subtle cardiac damage induced by RT. Previous studies have shown that when the radiation reaches a specific dose, global longitudinal, circumferential strain, radial strain, and strain rate are substantially decreased, which can be detected by 2D STE before the decrease of LVEF and the appearance of clinical symptoms (16–18). The most recent study included 40 women treated for left breast cancer showed that global longitudinal strain (GLS) significantly decreased during the first year following RT: a decrease in strain was observed at all post-RT time points (18.9 $\pm$ 2 at 6 weeks, 18.9 $\pm$ 3 at 12 months vs. 20.6 $\pm$ 2% before RT, $p < 0.01$) (17). Based on this clinical state, it appeared that early subclinical cardiac dysfunction of RT could be measured by strain, which is consistent with recent recommendations in the evaluation of cardiovascular complications after radiotherapy (19).

Traditional circulating biomarkers, such as creatine kinase (CK), creatine kinase isoenzyme (CK-MB), cardiac troponin T (cTnT), and cardiac troponin I (cTnI) may play an essential role in the detection of acute and late RIHD (20–22). However, early subclinical cardiac damage does not necessarily have an increase in these cardiac biomarkers. Fortunately, many serum biomarkers (e.g., hypersensitive C-reactive protein (hs-CRP) and N-terminal pro-B-type natriuretic peptide (NT-proBNP) have been shown to be potential biomarkers for cardiac damage after RT (22–24). Despite the variability of outcomes, specific serum biomarkers may represent a promising tool for the prediction of early myocardial dysfunction, leading to a more appropriate stratification of those patients who demand closer monitoring. Nevertheless, further studies with more specific biomarkers are certainly needed to empower this association so that patients receive the greatest benefit.

A large number of studies have shown that many chemotherapy drugs can lead to cardiac toxicity (25, 26). Patients with chemotherapy exposure before radiation therapy may be more likely to present radiation-induced heart damage. The history of chemotherapy may be an essential risk factor for radiation-induced heart damage. However, to our knowledge, there is no prospective study on the occurrence of early radiation-induced heart damage in patients with or without a history of chemotherapy. Therefore, this study aims to assess the value of 2D STE combined with the assessment of multiple circulating

biomarkers and accurate heart dosimetry in the detection and prediction of early subclinical cardiac damage induced by thoracic radiation therapy. Risk factors and high-risk groups of subtle cardiac damage and major adverse cardiovascular events (MACE) during the 12 months follow-up will also be evaluated.

METHODS AND ANALYSIS

Study Design

It is a monocenter, prospective cohort study that will include patients who will receive RT. All patients will be followed 12 months after RT. 2D STE parameters and circulating biomarkers will be collected. MACEs were defined as a diagnosis of unstable angina [*International Classification of Diseases, 10th Revision* (ICD-10) codes I20], new arrhythmia (ICD-10 codes I44–I49), acute myocardial infarction (ICD-10 codes I21), heart failure (ICD-10 codes I50), valvular heart disease (ICD-10 codes I08 and I39), acute pericarditis (ICD-10 codes I30), and cardiac death (diagnosis by clinician) in this study. The determination of maces events is based on the patient's clinical symptoms, the results of cardiac damage markers, electrocardiogram (ECG), echocardiography and ambulatory ECG (27–32).

Study Population and Groups

One hundred and four patients with thoracic radiotherapy will be included in Peking University Third Hospital from June 21, 2020 to December 31, 2021. Participants will be recruited based on the eligibility criteria presented in **Table 1**. All of the patients will be included at the baseline before RT and followed for 12 months after RT. Written informed consent will be obtained from all recruited patients. This study was approved by the Ethics Committee of the Peking University Third Hospital and completed under its supervision. Informed consent was signed by all study participants. Our study was in accordance with all the ethical requirements and followed the reporting guideline for case series. Patients or the public were not involved in the design, or conduct, or reporting, or dissemination plans of our research.

Oncologist and cardiologist will present the study to the eligible patients, explaining the study, offering participation, and requesting written informed consent. All patients will be informed that they have no obligation to participate, and they can stop participating at any time and without any consequences for therapeutic schedule and medical follow up.

Follow-Up Strategy

Before radiotherapy, echocardiography, 2D STE, CK, CK-MB, cTnT, NT-proBNP, ECG, hs-CRP, alanine aminotransferase (ALT), aspartate aminotransferase (AST) and creatinine will be detected, and eligible patients will be enrolled. All participants will be followed up after completion of RT (post-RT), 2 months after RT (2-months post-PT), 6 months after RT (6-months post-PT), and 12 months after RT (12-months post-PT). During subsequent follow-up, echocardiography, 2D STE, CK, CK-MB, cTnT, NT-proBNP, ECG, and hs-CRP will be collected at every follow-up time.

Data Collection

A precise description of cancer, treatments for cancer, and information about the main risk factors of a cardiac event is collected at inclusion; details will be shown in **Table 2**. Echocardiography, 2D STE, ECG, and circulating biomarker measurements are detailed in **Table 3**.

Radiation Therapy

All of the patients will be treated with stereotactic body radiotherapy (SBRT). Before radiotherapy, the chest CT

TABLE 1 | Inclusion and exclusion criteria.

Inclusion criteria	Exclusion criteria
With malignant tumors	Satisfactory echocardiographic images could not be obtained
Will receive radiotherapy	Moderate or severe valvular disease
With cardiac exposure during the radiotherapy process	Cardiomyopathy
Could receive regular follow-up for 12 months	Congenital heart disease
Written informed consent	Refractory hypertension
	Coronary artery disease*
	Heart failure
	Arrhythmia requiring intervention
	Pericarditis
	Acute myocarditis
	Participating in other clinical studies of drug intervention
	Severe liver and kidney dysfunction
	Autoimmune disease
	Pulmonary hypertension

*Coronary artery disease: at least 50% stenosis based on previous coronary angiography or coronary CT angiography, or with a history of percutaneous coronary stent implantation. *With LVEF<50%, unstable angina, or acute myocardial infarction within 3 months.*

TABLE 2 | Baseline characteristics.

Characteristic		Value
Age		
Hight		
Weight		
Body mass index (BMI)		
Systolic blood pressure (SBP)		
Diastolic blood pressure (DBP)		
Smoking status		
Hypertension		
Diabetes		
Hyperlipidemia		
Arrhythmia		
Cancer	Type	
	Size	
	Chemotherapy history	
	Mean heart dose	

TABLE 3 | Parameters of echocardiography, 2D STE, ECG and circulating biomarkers.

Parameters
Echocardiography: commercially available ultrasonography systems
LVEF measured by the modified Simpson or the modified Quinones method
LV mass index calculated by the Devereux formula
The degree of aortic and mitral regurgitation classified according to the guidelines of the American Society of Echocardiography
E/A wave ratio
E/e' ratio
Left atrium volume index calculated using the area-length method
Systolic pulmonary arterial pressure
Two-dimensional speckle-tracking echocardiography: TomTec (TomTec Imaging Systems GmbH, Unterschleissheim, Germany)
Global longitudinal strain (GLS)
Global radial strain (GRS)
Global circumferential strain (GCS)
S'
ECG
Heart rate
rhythm
P-R intervals
QRS wave
QTC
S-T segment changes
Circulating biomarkers
CK
CK-MB
cTnT
NT-proBNP
HsCRP

2D STE, two-dimensional speckle tracking echocardiography; ECG, electrocardiogram; LVEF, left ventricular ejection fraction; LV, left ventricular; CK, creatine kinase; CKMB, creatine kinase isoenzyme; cTnT, cardiac troponin T; NT-proBNP, N-terminal pro-B-type natriuretic peptide.

examination will be carried out to locate the target area. According to the location of CT, the treatment target area is gross tumor volume and planning target volume is appropriately expanded on the basis of the anterior target. The treatment plan was made by multiplan 4.6 planning system. After the plan was completed, the plan was verified first, and then the stereotactic radiotherapy robot was used. In the treatment, we use the Xsight-Spinal tracking system, synchronous respiratory tracking mode, or the six-dimensional bed system to control the patient's position and focus perfectly, so as to achieve the effect of precise radiotherapy. According to the treatment plan, the minimum, average and maximum doses of the heart and the V5, V10, V20 and V30 of the heart are counted. To evaluate the effect of radiotherapy dose on heart more accurately, we converted all maximum and mean cardiac doses to the biologically effective doses (BED), assuming an α/β ratio of 3 for the heart, with conversion to an equivalent dose in 2-Gy fractions (EQD2) using the linear quadratic model (33–35). The BED was calculated using the equation $nd[1+d/(\alpha/\beta)]$, the EQD2 was calculated from the dose-volume histograms as $nd[(d+\alpha/\beta) \div (2+\alpha/\beta)]$, n is a number of fractions, d is dose per fraction, and α/β was 3 Gy (36). According to the RTOG 0236 report, the average dose of heart is limited to less than or equal to 30Gy (37). Planning and contouring of the RT and the affected area and dose of heart will be recorded.

Study Endpoints

Primary Endpoint

The primary endpoint is an at least 10% decrease in the global longitudinal, radial, and circumferential strain or strain rate, determined using cardiac 2D STE, compared with the baseline, which can be considered clinically pertinent based on those observed in the previous studies (38).

Secondary Endpoints

CK, CKMB, cTnT and NT proBNP were within the range of normal reference values at baseline, but exceeded the upper limit of normal reference values at follow-up.

ECG indicates new arrhythmia.

Patients had symptoms and signs of heart failure with LVEF decreased by at least 5% and less than 55%, or LVEF decreased by at least 10% and less than 55% without symptoms and signs, or LVEF $< 50\%$, measured by echocardiography (38).

Data Management

Study data will be managed by two study investigators using a predesigned casereport form (Microsoft Office Excel and Word) with double data-entry. Data checks will be regularly performed to ensure data quality. The number of eligible, included and excluded of patients will be recorded. Withdrawals will also record as detailed as possible.

Statistical Analysis

Sample Size Calculation

The sample size was based on a statistical power of 80%, an alpha-risk of 5%, the definition of the primary endpoint (a decrease in the global longitudinal, radial, circumferential strain or strain rate of at least 10%). The baseline value was derived from the literature: mean global longitudinal strain before RT = the post-RT value was derived from the literature: mean global longitudinal strain after RT in patients without a history of chemotherapy $= -17.5 \pm 1.7\%$, mean global longitudinal strain after RT in patients with a history of chemotherapy $= -16.1 \pm 1.9\%$ (39). Taking into account a 20% patients lost, the inclusion of 104 patients is necessary.

Statistics

Continuous variables will be expressed as means $\pm$ standard deviation or median (interquartile range) where appropriate. Categorical variables will be expressed as counts (percentages). Changes regarding early subclinical cardiac damage and biomarkers between the baseline and the follow-up in two groups will be tested with repeated measures analysis of variance. For within-group comparisons, changes in the GLS, GCS, GRS, S', LVEF, and circulating biomarkers between the baseline and the follow-up time points will be analyzed using paired t-test for

parametric variables, and Wilcoxon signed-rank test for non-parametric variables. Chi-square test will be used to compare the occurrence and progression of early subclinical cardiac damage and changes in circulating biomarkers between the two groups. Mixed regression models will be used to investigate the correlation between RIHD and age, blood pressure, BMI, smoking status, hypertension, hypercholesterolemia and heart dose. All statistical analyses will be performed using SPSS 24.0 statistical software, and a $P < 0.05$ will be considered significant.

DISCUSSION

This population-based cohort study aims to estimate the value of 2D STE combined with multiple circulating biomarkers in the detection and prediction of early subclinical cardiac damage induced by thoracic radiation therapy in patients with SBRT. Furthermore, we want to find the risk factors of subtle cardiac damage and to determine the prevalence of MACE within 12 months post-RT.

The study has far-reaching clinical significance. Firstly, the subclinical heart damage reduced by radiotherapy can be identified early by combining 2D STE, echocardiography and a variety of circulating biomarkers. Secondly, the risk factors of RIHD were further identified by prospective cohort study, so as to achieve the early identification of high-risk groups before radiotherapy in the future. Moreover, after detection of RIHD, we will further explore the occurrence mechanism of early RIHD, and explore the prevention and treatment measures through randomized controlled trials, in order to achieve early intervention before the occurrence of clinical symptoms, reduce the incidence of RIHD, alleviate a patient's suffering, improve the quality of patients' life and reduce the economic burden on patients and society. Meanwhile, this study will also provide reference clinical research data for the formulation of guidelines and the detection and protection of RIHD.

Meanwhile, there are some limitations to this study. First, the sample size was small,which might represent a beta error. Second, as the follow-up in this study was limited to 12 months, subclinical cardiac changes may not produce during this period. A larger study with a longer duration of follow-up would be required to validate our current observations and to determine its impact on long-term adverse outcomes. Although these hindrances should be acknowledged, we believe the findings from this study will provide important data, which will help focus on "high-risk" patients for longer follow-ups and take up protective measures.

This study will allow evaluating the advantages of 2D STE combined with circulating biomarkers in early detection and prediction of RIHD and validate risk factors and high-risk groups of subclinical cardiac damage, which will be important for proposing primary and secondary preventive measures and improving patient care and quality of life.

To summarize, this study will elucidate concerns and problems related to RIHD and risk foctors.The findings will form a basis for developing early detection method for subclinical cardiac damage and interventions to alleviate RIHD in people who will receive thoracic radiotherapy in the shaort and long term.

ETHICS STATEMENT

Ethical approval has been obtained for the study procedures by the Ethics Committee of Peking University Third Hospital, China (IRB00006761-M2020074). Any protocol amendments will be submitted to the Ethics Committee of Peking University Third Hospital for ethical approval. Written informed consent will be collected from all participants before entering this study.

AUTHOR CONTRIBUTIONS

MC: conceptualization, supervision, and writing—review and editing. HZ and TL: data curation and formal analysis. DZ and TL: writing—original draft. All authors have read and agreed to the published version of the manuscript.

FUNDING

This study is funded by Peking University Third Hospital (BYSYLXHG2020003). The Peking University Third Hospital has no direct role in the design, conduct, or analysis of this study.

ACKNOWLEDGMENTS

We thank the Department of Cardiology, Peking University Third Hospital for the technical supports. We thank the patients and all the investigators who are participating in this study.

REFERENCES

1. Bray F, Ferlay J, Soerjomataram I, Siegel RL, Torre LA, Jemal A. Global cancer statistics 2018: GLOBOCAN estimates of incidence and mortality worldwide for 36 cancers in 185 countries. *CA Cancer J Clin.* (2018) 68:394–424. doi: 10.3322/caac.21492
2. The L, GLOBOCAN. 2018: counting the toll of cancer. *Lancet.* (2018) 392:985. doi: 10.1016/S0140-6736(18)32252-9
3. Al-Kindi SG, Oliveira GH. Incidence and trends of cardiovascular mortality after common cancers in young adults: analysis of surveillance, epidemiology and end-results program. *World J Cardiol.* (2016) 8:368–74. doi: 10.4330/wjc.v8.i6.368
4. Kesson EM, Allardice GM, George WD, Burns HJ, Morrison DS. Effects of multidisciplinary team working on breast cancer survival: retrospective, comparative, interventional cohort study of 13 722 women. *BMJ.* (2012) 344:e2718. doi: 10.1136/bmj.e2718
5. Wang H, Wei J, Zheng Q, Meng L, Xin Y, Yin X, et al. Radiation-induced heart disease: a review of classification, mechanism and prevention. *Int J Biol Sci.* (2019) 15:2128–38. doi: 10.7150/ijbs.35460
6. Lewis GD, Farach A. Cardiovascular toxicities of radiation therapy. *Methodist Debakey Cardiovasc J.* (2019) 15:274–81. doi: 10.14797/mdcj-15-4-274

7. Clarke M, Collins R, Darby S, Davies C, Elphinstone P, Evans V, et al. Effects of radiotherapy and of differences in the extent of surgery for early breast cancer on local recurrence and 15-year survival: an overview of the randomised trials. *Lancet.* (2005) 366:2087–106. doi: 10.1016/S0140-6736(05)67887-7
8. Giordano SH, Kuo YF, Freeman JL, Buchholz TA, Hortobagyi GN, Goodwin JS. Risk of cardiac death after adjuvant radiotherapy for breast cancer. *J Natl Cancer Inst.* (2005) 97:419–24. doi: 10.1093/jnci/dji067
9. Darby SC, McGale P, Taylor CW, Peto R. Long-term mortality from heart disease and lung cancer after radiotherapy for early breast cancer: prospective cohort study of about 300,000 women in US SEER cancer registries. *Lancet Oncol.* (2005) 6:557–65. doi: 10.1016/S1470-2045(05)70251-5
10. Darby SC, Ewertz M, McGale P, Bennet AM, Blom-Goldman U, Bronnum D, et al. Risk of ischemic heart disease in women after radiotherapy for breast cancer. *N Engl J Med.* (2013) 368:987–98. doi: 10.1056/NEJMoa1209825
11. Wennstig AK, Wadsten C, Garmo H, Fredriksson I, Blomqvist C, Holmberg L, et al. Long-term risk of ischemic heart disease after adjuvant radiotherapy in breast cancer: results from a large population-based cohort. *Breast Cancer Res.* (2020) 22:10. doi: 10.1186/s13058-020-1249-2
12. Hull MC, Morris CG, Pepine CJ, Mendenhall NP. Valvular dysfunction and carotid, subclavian, and coronary artery disease in survivors of hodgkin lymphoma treated with radiation therapy. *JAMA.* (2003) 290:2831–7. doi: 10.1001/jama.290.21.2831
13. Baker JE, Moulder JE, Hopewell JW. Radiation as a risk factor for cardiovascular disease. *Antioxid Redox Signal.* (2011) 15:1945–56. doi: 10.1089/ars.2010.3742
14. Feng M, Moran JM, Koelling T, Chughtai A, Chan JL, Freedman L, et al. Development and validation of a heart atlas to study cardiac exposure to radiation following treatment for breast cancer. *Int J Radiat Oncol Biol Phys.* (2011) 79:10–8. doi: 10.1016/j.ijrobp.2009.10.058
15. Bloom MW, Hamo CE, Cardinale D, Ky B, Nohria A, Baer L, et al. Cancer Therapy-Related Cardiac Dysfunction and Heart Failure: Part 1: Definitions, Pathophysiology, Risk Factors, and Imaging. *Circ Heart Fail.* (2016) 9:e2661. doi: 10.1161/CIRCHEARTFAILURE.115.002661
16. Yu AF, Ho AY, Braunstein LZ, Thor ME, Lee CK, Eaton A, et al. Assessment of Early Radiation-Induced Changes in Left Ventricular Function by Myocardial Strain Imaging After Breast Radiation Therapy. *J Am Soc Echocardiogr.* (2019) 32:521–8. doi: 10.1016/j.echo.2018.12.009
17. Trivedi SJ, Choudhary P, Lo Q, Sritharan HP, Iyer A, Batumalai V, et al. Persistent reduction in global longitudinal strain in the longer term after radiation therapy in patients with breast cancer. *Radiother Oncol.* (2019) 132:148–54. doi: 10.1016/j.radonc.2018.10.023
18. Skytta T, Tuohinen S, Luukkaala T, Virtanen V, Raatikainen P, Kellokumpu-Lehtinen PL. Adjuvant radiotherapy-induced cardiac changes among patients with early breast cancer: a three-year follow-up study. *Acta Oncol.* (2019) 58:1250–8. doi: 10.1080/0284186X.2019.1630751
19. Lancellotti P, Nkomo VT, Badano LP, Bergler-Klein J, Bogaert J, Davin L, et al. Expert consensus for multi-modality imaging evaluation of cardiovascular complications of radiotherapy in adults: a report from the European Association of Cardiovascular Imaging and the American Society of Echocardiography. *J Am Soc Echocardiogr.* (2013) 26:1013–32. doi: 10.1016/j.echo.2013.07.005
20. Skytta T, Tuohinen S, Boman E, Virtanen V, Raatikainen P, Kellokumpu-Lehtinen PL. Troponin T-release associates with cardiac radiation doses during adjuvant left-sided breast cancer radiotherapy. *Radiat Oncol.* (2015) 10:141. doi: 10.1186/s13014-015-0436-2
21. Palumbo I, Palumbo B, Fravolini ML, Marcantonini M, Perrucci E, Latini ME, et al. Brain natriuretic peptide as a cardiac marker of transient radiotherapy-related damage in left-sided breast cancer patients: A prospective study. *Breast.* (2016) 25:45–50. doi: 10.1016/j.breast.2015.10.004
22. Zhang C, Shi D, Yang P, BNP. as a potential biomarker for cardiac damage of breast cancer after radiotherapy: a meta-analysis. *Medicine.* (2019) 98:e16507. doi: 10.1097/MD.0000000000016507
23. Guzhva L, Mendenhall NP, Morris CG, Flampouri S, Hoppe BS. Evaluating cardiac biomarkers after chemotherapy and proton therapy for mediastinal hodgkin lymphoma. *Int J Part Ther.* (2017) 4:35–8. doi: 10.14338/IJPT-D-17-00022
24. Canada JM, Thomas GK, Trankle CR, Carbone S, Billingsley H, Van Tassell BW, et al. Increased C-reactive protein is associated with the severity of thoracic radiotherapy-induced cardiomyopathy. *Cardiooncology.* (2020) 6:2. doi: 10.1186/s40959-020-0058-1
25. Akazawa H. Cardiotoxicity of cancer chemotherapy—mechanisms and therapeutic approach. *Gan To Kagaku Ryoho.* (2017) 44:2058–63.
26. Avila MS, Siqueira S, Ferreira S, Bocchi EA. Prevention and treatment of chemotherapy-induced cardiotoxicity. *Methodist Debakey Cardiovasc J.* (2019) 15:267–73. doi: 10.14797/mdcj-15-4-267
27. Braunwald E, Antman EM, Beasley JW, Califf RM, Cheitlin MD, Hochman JS, et al. ACC/AHA guidelines for the management of patients with unstable angina and non-ST-segment elevation myocardial infarction. A report of the American College of Cardiology/American Heart Association Task Force on Practice Guidelines (Committee on the Management of Patients With Unstable Angina). *J Am Coll Cardiol.* (2000) 36:970–1062. doi: 10.1016/s0735-1097(00)00889-5
28. Chang HM, Okwuosa TM, Scarabelli T, Moudgil R, Yeh ETH. Cardiovascular complications of cancer therapy: best practices in diagnosis, prevention, and management: Part 2. *J Am Coll Cardiol.* (2017) 70:2552–65. doi: 10.1016/j.jacc.2017.09.1095
29. Thygesen K, Alpert JS, Jaffe AS, Simoons ML, Chaitman BR, White HD, et al. Third universal definition of myocardial infarction. *J Am Coll Cardiol.* (2012) 60:1581–98. doi: 10.1016/j.jacc.2012.08.001
30. Ponikowski P, Voors AA, Anker SD, Bueno H, Cleland JGF, Coats AJS, et al. 2016 ESC Guidelines for the diagnosis and treatment of acute and chronic heart failure: the Task Force for the diagnosis and treatment of acute and chronic heart failure of the European Society of Cardiology (ESC) developed with the special contribution of the Heart Failure Association (HFA) of the ESC. *Eur Heart J.* (2016) 37:2129–200. doi: 10.1093/eurheartj/ehw128
31. Nishimura RA, Otto CM, Bonow RO, Carabello BA, Erwin JP 3rd, Guyton RA, et al. 2014 AHA/ACC guideline for the management of patients with valvular heart disease: a report of the American College of Cardiology/American Heart Association Task Force on Practice Guidelines. *J Am Coll Cardiol.* (2014) 63:e57–185. doi: 10.1016/j.jacc.2014.02.536
32. Adler Y, Charron P, Imazio M, Badano L, Barón-Esquivias G, Bogaert J, et al. 2015 ESC Guidelines for the diagnosis and management of pericardial diseases: the Task Force for the Diagnosis and Management of Pericardial Diseases of the European Society of Cardiology (ESC)Endorsed by: The European Association for Cardio-Thoracic Surgery (EACTS). *Eur Heart J.* (2015) 36:2921–64. doi: 10.1093/eurheartj/ehv318
33. Tembhekar AR, Wright CL, Daly ME. Cardiac dose and survival after stereotactic body radiotherapy for early-stage non-small-cell lung cancer. *Clin Lung Cancer.* (2017) 18:293–8. doi: 10.1016/j.cllc.2016.12.007
34. Lebesque JV, Keus RB. The simultaneous boost technique: the concept of relative normalized total dose. *Radiother Oncol.* (1991) 22:45–55. doi: 10.1016/0167-8140(91)90068-r
35. Joiner MC, Bentzen SM. Fractionation: the linear quadratic approach. *Basic Clin Radiobiol.* (2018) 8:102–19.
36. Stam B, Peulen H, Guckenberger M, Mantel F, Hope A, Werner-Wasik M, et al. Dose to heart substructures is associated with non-cancer death after SBRT in stage I-II NSCLC patients. *Radiother Oncol.* (2017) 123:370–5. doi: 10.1016/j.radonc.2017.04.017
37. Xiao Y, Papiez L, Paulus R, Timmerman R, Straube WL, Bosch WR, et al. Dosimetric evaluation of heterogeneity corrections for RTOG 0236: stereotactic body radiotherapy of inoperable stage I-II non-small-cell lung cancer. *Int J Radiat Oncol Biol Phys.* (2009) 73:1235–42. doi: 10.1016/j.ijrobp.2008.11.019
38. Tarantini L, Gulizia MM, Di Lenarda A, Maurea N, Giuseppe AM, Bisceglia I, et al. ANMCO/AIOM/AICO Consensus Document on clinical and management pathways of cardio-oncology: executive summary. *Eur Heart J Suppl.* (2017) 19:D370–9. doi: 10.1093/eurheartj/sux019
39. Tsai HR, Gjesdal O, Wethal T, Haugaa KH, Fossa A, Fossa SD, et al. Left ventricular function assessed by two-dimensional speckle tracking echocardiography in long-term survivors of Hodgkin's lymphoma

treated by mediastinal radiotherapy with or without anthracycline therapy. *Am J Cardiol.* (2011) 107:472–7. doi: 10.1016/j.amjcard.2010.09.048

Conflict of Interest: The authors declare that the research was conducted in the absence of any commercial or financial relationships that could be construed as a potential conflict of interest.

Publisher's Note: All claims expressed in this article are solely those of the authors and do not necessarily represent those of their affiliated organizations, or those of the publisher, the editors and the reviewers. Any product that may be evaluated in this article, or claim that may be made by its manufacturer, is not guaranteed or endorsed by the publisher.

frontiers in Cardiovascular Medicine

BRIEF RESEARCH REPORT
published: 31 January 2022
doi: 10.3389/fcvm.2022.793972

Hybrid CMR- and FDG-PET-Imaging Gives New Insights Into the Relationship of Myocardial Metabolic Activity and Fibrosis in Patients With Becker Muscular Dystrophy

Volker Vehof[1,2], *Florian Büther*[2], *Anca Florian*[1], *Stefanos Drakos*[1], *Bishwas Chamling*[1], *Peter Kies*[2], *Lars Stegger*[2] *and Ali Yilmaz*[1]*

[1] Department of Cardiology I, University Hospital Münster, Münster, Germany, [2] Department of Nuclear Medicine, University Hospital Münster, Münster, Germany

OPEN ACCESS

Edited by:
Marcus R. Makowski,
Technical University of Munich, Germany

Reviewed by:
Ryogo Minamimoto,
National Center for Global Health and Medicine, Japan
Yuetao Wang,
First People's Hospital of Changzhou, China

***Correspondence:**
Ali Yilmaz
ali.yilmaz@ukmuenster.de

Specialty section:
This article was submitted to Cardiovascular Imaging, a section of the journal Frontiers in Cardiovascular Medicine

Received: 12 October 2021
Accepted: 12 January 2022
Published: 31 January 2022

Citation:
Vehof V, Büther F, Florian A, Drakos S, Chamling B, Kies P, Stegger L and Yilmaz A (2022) Hybrid CMR- and FDG-PET-Imaging Gives New Insights Into the Relationship of Myocardial Metabolic Activity and Fibrosis in Patients With Becker Muscular Dystrophy. Front. Cardiovasc. Med. 9:793972. doi: 10.3389/fcvm.2022.793972

Background: Cardiac involvement in patients with Becker muscular dystrophy (BMD) is an important predictor of mortality. The cardiac phenotype of BMD patients is characterized by slowly progressive myocardial fibrosis that starts in the left ventricular (LV) free wall segments and extends into the septal wall during the disease course.

Purpose: Since the reason for this characteristic cardiac phenotype is unknown and comprehensive approaches using e.g. hybrid imaging combining cardiovascular magnetic resonance (CMR) with ^{18}F-fluorodeoxyglucose (FDG) positron emission tomography (PET) are limited, the present study addressed this issue by a comprehensive non-invasive imaging approach.

Methods: Hybrid CMR- and FDG-PET-imaging was performed in $N = 14$ patients with BMD on a whole-body Biograph mMR system (Siemens, Erlangen, Germany). The CMR protocol comprised cine- and late-gadolinium-enhancement (LGE)-imaging. Metabolism was assessed with FDG-PET after oral glucose loading to effect myocardial carbohydrate uptake. PET was acquired for 65 min starting with tracer injection. Uptake values from 60 to 65 min p.i. were divided by the area under the blood activity curve and reported as percentages relative to the segment with maximal myocardial FDG uptake.

Results: A characteristic pattern of LGE in the LV lateral wall was observed in 13/14 patients whereas an additional septal LGE pattern was documented in 6/14 patients only. There was one patient without any LGE. Segmental FDG uptake was 88 ± 6% in the LV lateral wall vs. 77 ± 10% in the septal wall ($p < 0.001$). There was an inverse relationship between segmental FDG activity compared to segmental LGE extent ($r = -0.33$, $p = 0.089$). There were $N = 6$ LGE-positive patients with a segmental difference in FDG uptake of >15% in the LV lateral wall compared to the septal wall = ΔFDG-high group (lateral FDG = 91±3% vs. septal FDG = 69±8%; $p < 0.001$) while the remaining $N = 7$ LGE-positive patients showed a segmental difference in FDG uptake of ≤15% = ΔFDG-low group (lateral FDG = 85±7% vs. septal FDG = 83 ± 5%; $p = 0.37$). Patients in the ΔFDG-high group showed only a minor difference in the LGE extent between the

LV lateral wall vs. septal wall ($p = 0.09$) whereas large differences were observed in the ΔFDG-low group ($p < 0.004$).

Conclusions: Segmental FDG uptake—reflecting myocardial metabolic activity—is higher in the LV free wall of BMD patients—possibly due to a higher segmental work load. However, segmental metabolic activity seems to be dependent on and limited by the respective segmental extent of myocardial fibrosis as depicted by LGE-imaging.

Keywords: CMR, PET, FDG, LGE, muscular dystrophy, cardiomyopathy

INTRODUCTION

Duchenne and Becker muscular dystrophies (DMD and BMD) are the most frequent X-chromosomal recessive neuromuscular disorders and are caused by mutations in the dystrophin gene. Such mutations can either lead to total absence (DMD) or to structural impairment of fragile dystrophin protein (BMD) (1, 2). Since dystrophin is a central protein in the cell membrane of skeletal as well as cardiac muscle cells, particularly BMD patients do not only suffer from skeletal muscle weakness but also from progressive cardiomyopathy (2, 3). Cardiac involvement in BMD patients is characterized by a non-ischemic pattern of left ventricular (LV) myocardial fibrosis starting in the LV free wall and leading to non-ischemic dilated cardiomyopathy (2, 4–6). Heart failure symptoms and ventricular arrhythmias have become a major cause of morbidity and mortality in MD patients (2, 7, 8).

Cardiovascular magnetic resonance (CMR) imaging has developed into the most relevant clinical imaging technique regarding detection of cardiac involvement and monitoring of cardiac disease progression—not only for BMD patients. It cannot only measure shape and function of the heart, but also reveals even subtle structural changes in the myocardium such as fibrosis. Previously, our group described a characteristic pattern of cardiomyopathy in patients with BMD (5), the potential for predicting adverse cardiac events (7) and the detection of diffuse interstitial fibrosis (9) based on multi-parametric CMR data.

Recently, hybrid positron-emission-tomography (PET) magnetic resonance imaging (MRI) systems have been introduced that offer the unique capability of simultaneous PET and MRI for optimal spatial and temporal co-registration. This simultaneous approach is extremely valuable for BMD patients in order to relate different parameters, hitherto acquired separately, with each other on a patient-to-patient and even region-by-region basis. Thereby, the relevance and association of changes in both metabolic and structural abnormalities can be established. Also, simultaneous imaging obviates the need for a second imaging session, a significant relief for the often severely physically impaired patients.

A comprehensive PET-CMR approach in BMD patients to assess different aspects of myocardial changes at the same time in the same cardiac region may well-reveal new insights into pathophysiology of cardiac disease and has not been attempted so far. In this context, we present the first preliminary data of our ongoing PET-CMR-MD research project.

METHODS

Study Population

Fourteen patients with BMD were prospectively enrolled within the scope of the ongoing PET-CMR-MD research project that focuses on cardiac phenotyping of patients with BMD with different severity of myocardial involvement. The diagnosis of BMD was confirmed by skeletal muscle biopsy evaluation with immunohistochemical analysis of the dystrophin protein and/or a genetic work-up with screening for dystrophin gene mutation. Cardiological work-up included (amongst others) physical examination and hybrid PET-CMR imaging. Blood samples were obtained for laboratory studies including measurement of total creatine kinase (CK), high-sensitive troponin-T (hsTnT), NT-pro-brain-natriuretic-peptide (NT-proBNP) apart from others. This study was approved by the local ethics committee and the federal office for radiation protection (BfS). Written informed consent was obtained from each patient prior to inclusion to this study.

CMR Acquisition and Data Analysis

All patients included in this study underwent a simultaneous and comprehensive PET-CMR imaging study. The studies were performed on a 3-T PET-MRI system capable of simultaneous PET and MRI image acquisition (Biograph mMR, Siemens Healthcare). The CMR protocol comprised (amongst others) cine-imaging and late-gadolinium-enhancement (LGE)-imaging, ∼10–15 min after a cumulative gadolinium (Gadovist®) dose of 0.10 mmol/kg. Cine-imaging was performed using a steady-state-free-precession (SSFP) sequence in three long-axis slices (four-, three- and two-chamber) and a stack of short-axis slices completely covering the LV.

Image analysis and interpretation were performed using commercially available software (cvi42, Circle Cardiovascular Imaging, Calgary, Alberta, Canada). Ventricular volumes, ejection fraction and LV mass were derived by contouring endo- and epicardial borders on the short-axis cine images and indexed to body surface area. LGE extent was assessed on the short-axis contrast images and an image intensity level ≥3 SD above the mean of remote myocardium was used to define LGE indicative of damaged myocardium as described previously and expressed as percentage of total LV mass. Based on the 17-segment AHA myocardial segmentation model, we defined a LV "septal wall" as segments 2, 3, 8, 9 and 14, and a LV "lateral wall" as segments 5, 6, 11, 12 and 16.

PET Acquisition and Data Analysis

Metabolism was assessed with FDG-PET after oral glucose loading (50 grams) one hour before tracer injection to effect myocardial carbohydrate uptake, in accordance with clinically established protocols (10). Since diabetes was an exclusion criterion for the study, administration of insulin as recommended in the above guidelines for higher blood glucose levels one hour after glucose loading was not necessary. PET was acquired for 65 min in list-mode, where all events are stored for retrospective sorting into time frames. The tracer (∼185 MBq) was injected as a slow bolus (duration ∼45 s) starting thirty seconds into the list-mode scan. Uptake values from 60 to 65 min were divided by the area under the blood activity curve and reported as percentages relative to the segment with maximal myocardial FDG uptake.

In accordance with our CMR data analyses, we used the same 17-segment AHA myocardial segmentation model for our PET data analyses and defined a LV "septal wall" as segments 2, 3, 8, 9 and 14, and a LV "lateral wall" as segments 5, 6, 11, 12 and 16. Segmental PET analysis was performed using the Cardiac PET tool of the software package PMOD version 3.703 (PMOD Technologies, Zurich).

Statistical Analysis

Statistical analysis was performed with SPSS (version 26.0, IBM Corp., Armonk, NY). Normally distributed variables are expressed as mean ± SD. Skewed variables are expressed as median and range. Categorical variables are expressed as frequency with percentage. Student's *t*-test was used for comparison of groups concerning normally distributed variables, while Mann-Whitney U test was used for comparison of non-normally distributed variables. Non-parametric Kruskal–Wallis test was used in case of multiple comparisons of non-normally distributed variables. Fisher's exact test was used to compare non-continuous variables expressed as proportions. Non-parametric Spearman correlations were used for correlation analysis of non-normally distributed variables. A p-value < 0.05 was considered statistically significant.

RESULTS

Study Population

Patient characteristics as well as major laboratory results are illustrated in **Table 1**. The median age of the present study group of (male) BMD patients was 33 years (19–59 years) and there were only $N = 3$ (21%) patients with loss of walking ability. Median total CK levels were substantially elevated with 858 U/l (374–3.787 U/l) whereas hsTnT levels were only modestly increased. There was no patient with NT-proBNP elevation in our study group.

CMR Findings

Major CMR findings are shown in **Table 2**. Median LV-EF in all $N = 14$ BMD patients was 55% (46–61%) with $N = 6$ (43%) patients showing an impaired LV systolic function with a LV-EF <55%. Median RV-EF was 57% (51–63%) and there was no patient with an impaired RV systolic function (defined as RV-EF <50%). A characteristic pattern of non-ischemic LGE in at least one LV wall segment was observed in $N = 13$ (93%) patients. There was only one patient without any LGE—who also showed a preserved LV and RV systolic function. Presence of any LGE (mostly small areas) in the septal wall was observed in $N = 6$ (43%) compared to $N = 13$ (93%) patients with mostly extensive LGE in the LV lateral wall.

FDG-PET Results in Relation to CMR Findings

Segmental FDG uptake was 88 ± 6% in the LV lateral wall vs. 77 ± 10% in the septal wall in the entire study group ($p < 0.001$). In more detail, segmental FDG uptake in those patients with a total LGE extent of ≤10% was 89 ± 6% in the lateral wall vs. 75 ± 10% in the septal wall ($p = 0.011$). In contrast, there was no significant difference in segmental FDG uptake in those patients with a total LGE extent of >10% (86 ± 8% in the lateral wall vs. 79 ± 8% in the septal wall, p = NS). There was a moderate inverse relationship between segmental FDG activity compared to segmental LGE extent ($r = -0.33$, $p = 0.089$).

There were $N = 6$ LGE-positive patients with a segmental difference in FDG uptake of >15% in the LV lateral wall compared to the septal wall = ΔFDG-high group (lateral FDG = 91 ± 3% vs. septal FDG = 69 ± 8%; $p < 0.001$) while the $N = 7$ LGE-positive patients showed a segmental difference in FDG uptake of ≤15% = ΔFDG-low group (lateral FDG = 85 ± 7% vs. septal FDG = 83 ± 5%; $p = 0.37$). There was no significant difference in "global" as well as "septal" LGE extent between the ΔFDG-high vs. ΔFDG-low group **(Table 2)**. In contrast, there was a substantial difference in "lateral" LGE extent with significantly larger areas of LGE in the ΔFDG-low group.

The single patient without any LGE and preserved LV and RV systolic function showed a balanced FDG uptake when septal segments were compared to lateral ones **(Figure 1)**. Patients in the ΔFDG-high group showed rather small areas of LGE in both the septal as well as the lateral walls without significant differences ($p = 0.09$) and were characterized by the highest segmental FDG uptake values in the LV lateral wall **Table 2**; **Figure 2**. In contrast, patients in the ΔFDG-low group were characterized by rather large areas of LGE in the LV lateral wall compared to the septal wall ($p < 0.004$), but showed less extensive FDG uptake in the lateral wall compared to the ΔFDG-high group **Table 2**; **Figure 3**.

DISCUSSION

To the best of our knowledge, this is the first clinical study that uses simultaneous PET-CMR imaging in patients with BMD in order to assess both metabolic (FDG-PET) and structural myocardial changes (LGE-CMR) at the same time in the same cardiac regions. Based on the presented preliminary data, we hypothesize that (a) segmental FDG uptake (reflecting myocardial metabolic activity) is higher in the LV lateral free wall (compared to the septal wall) of BMD patients possibly due to a higher segmental work load, however, only

TABLE 1 | Patient characteristics.

	BMD (all) *N* = 14	BMDLGE-positiveΔFDG-high *N* = 6	BMD LGE-positive ΔFDG-low *N* = 7	*p*-value
Age, years	33 (19–59)	41 (22–55)	39 (19–59)	0.94
BMI, kg/m²	20 (18–23)	20 (19–21)	20 (18–22)	0.48
CK total, U/l	857 (374–3,787)	958 (374–3,787)	854 (517–1,540)	0.83
hsTrop-T, ng/l	18 (12–50)	23 (16–38)	17 (13–50)	0.77
NT-proBNP elevation (%)	0%	0%	0%	NS
ACE-inhibitor therapy (%)	29%	33%	29%	NS
ß-blocker therapy(%)	14%	17%	14%	NS
Loss of walking ability (%)	21%	33%	14%	NS

TABLE 2 | CMR parameters.

	BMD (all) *N* = 14	BMDLGE-positiveΔFDG-high *N* = 6	BMD LGE-positive ΔFDG-low *N* = 7	*p*-value
LV-EF, %	55 (46–61)	55 (50–61)	53 (46–60)	0.52
LV-EDV index, ml/m²	92 (72–115)	92 (78–99)	95 (72–115)	0.67
LV mass index, g/m²	64 (50–75)	64 (53–72)	65 (50–75)	0.67
RV-EF, %	57 (51–63)	57 (51–62)	57 (53–63)	0.94
RV-EDV index, ml/m²	85 (72–106)	85 (72–100)	91 (74–106)	0.89
LGE presence, n (%)	13 (93)	6 (100)	7 (100)	1.0
Global LGE extent, %	7 (0–47)	6 (3–19)	17 (4–47)	0.09
Septal LGE extent, %	0 (0–36.8)	0 (0–36.8)	1.4 (0–15.1)	0.72
Lateral LGE extent, %	17.8 (0–74.5)	13.3 (3.1–18.9)	36.3 (9.9–74.5)	**0.018**

Bold font indicates a p-value <0.05.

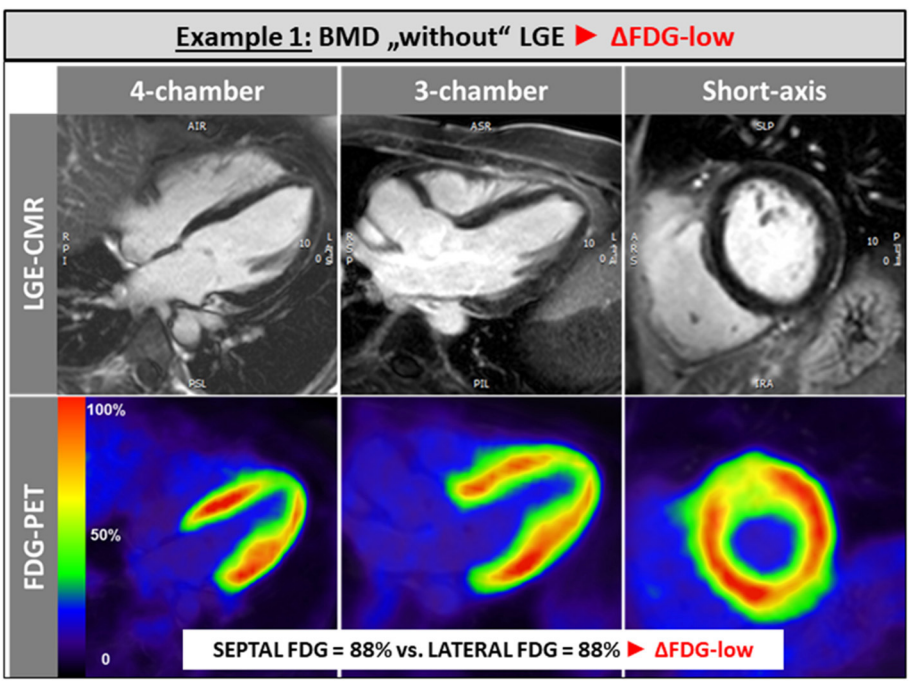

FIGURE 1 | The single patient without any LGE and preserved LV and RV systolic function showed a balanced FDG uptake when septal segments were compared to lateral ones.

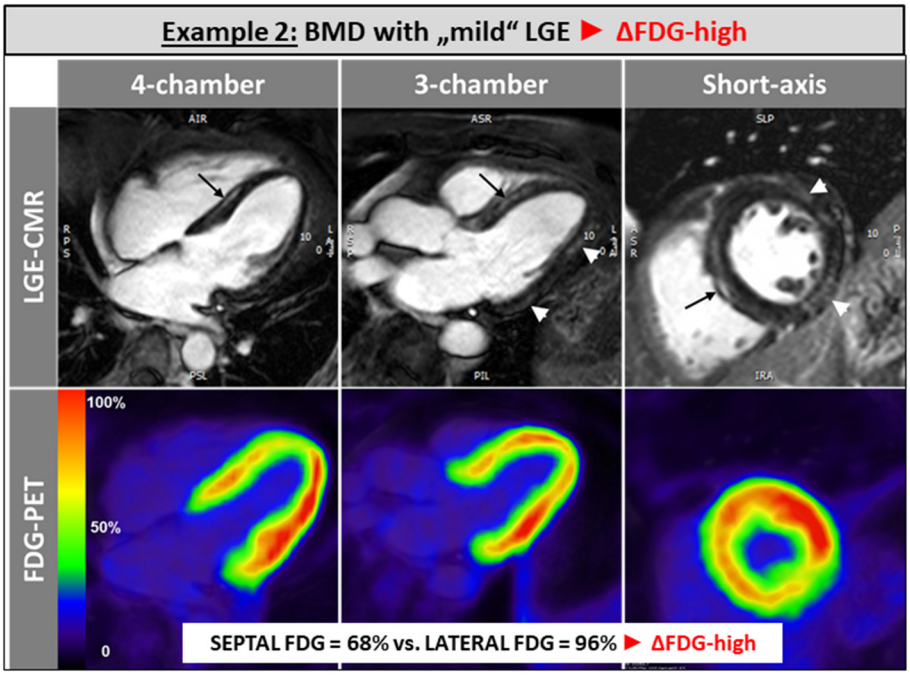

FIGURE 2 | Patients in the ΔFDG-high group showed rather small areas of LGE in both the septal as well as the lateral walls without significant differences and were characterized by the highest segmental FDG uptake values in the LV lateral wall.

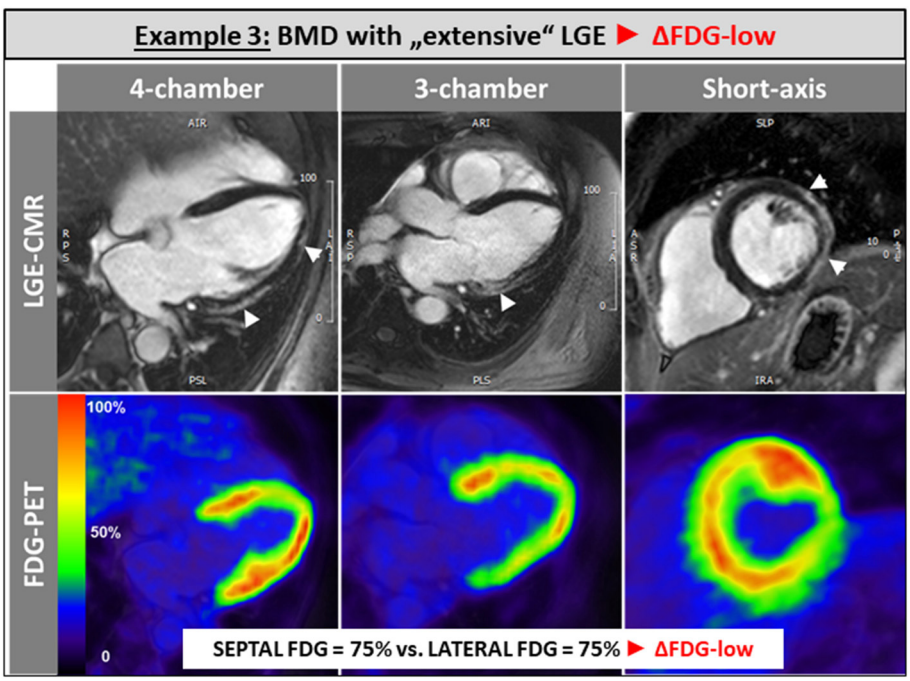

FIGURE 3 | Patients in the ΔFDG-low group were characterized by rather large areas of LGE in the LV lateral wall compared to the septal wall, but showed less extensive FDG uptake in the lateral wall compared to the ΔFDG-high group.

as long as myocardial scarring is limited, and (b) extensive and ongoing myocardial scarring in the LV free wall results in equalization of lateral vs. septal wall FDG uptake by a "relative" decrease in lateral wall FDG uptake due to a decreasing number of "viable" cardiomyocytes whilst growing scars in this region.

Measurement of FDG-uptake—reflecting myocardial glucose metabolism—can be influenced by different patient-specific as well as procedural factors. This important issue was recently addressed in depth by Minamimoto et al. (11) nicely illustrating that "major factors affecting myocardial glucose metabolism include sex differences, aging, obesity, and diabetic mellitus" and that "metabolic change also occurs in pathological states such as obesity, diabetic mellitus, and non-ischemic cardiomyopathy." Moreover, these authors mentioned that "the physiological FDG-uptake … will be poorly-reproducible in the following PET examination" (!). These issues are important limitations of all FDG-PET studies and do not only concern our present study …

The presence of LGE in BMD patients is caused by progressive myocardial fibrosis as a consequence of ongoing cardiomyocyte cell death due to genetic dystrophin-deficiency. Consequently, naturally occurring LGE does not disappear in BMD patients and is rather extending in the further disease course with a continuous shift in the pattern from subepicardial to transmural. Noteworthy, this process of progressive myocardial fibrosis starts in the LV lateral free wall and extends to the septal wall segments during the natural disease course—but is always more pronounced in the LV lateral free wall.

As explained previously, myocardial fibrosis that can be depicted by LGE-imaging preferentially located in the LV free lateral wall of BMD patients is likely (a) due to increased mechanical stress in this region and (b) preceded by adaptive metabolic alterations that occur prior to final cell death. The detailed molecular pathomechanism leading to progressive cardiac contractile dysfunction in BMD patients is still not known. Early alterations in cell metabolism and signal transduction were suggested based on preclinical studies in dystrophin deficient animal models (12). Moreover, excessive intracellular calcium signaling and reactive oxygen species (ROS) generation with breakdown of the mitochondrial membrane potential were described in *in vitro* studies and may constitute the link between the initial sarcolemmal injury due to dystrophin deficiency and mitochondrial dysfunctions (12, 13). In addition, it was demonstrated that even intact dystrophin deficient cardiomyocytes have reduced compliance and increased susceptibility to stretch mediated calcium overload, which in turn lead to cardiomyocyte contracture and cell death. Hence, the fragility of the cell membrane caused by deficient sarcolemmal dystrophin may predispose cardiomyocytes to "metabolic" alterations, which in turn may be enhanced by an excessive susceptibility to mechanical stress. Therefore, it is not surprising that segmental FDG uptake is higher in the LV lateral free wall (compared to the septal wall) of BMD patients—as long as myocardial scarring in these segments is limited.

Future studies with larger sample size need to confirm the present hypothesis-generating preliminary results (and are currently performed at least at our center) using simultaneous PET-CMR imaging. Obviously, a "relatively" increased segmental FDG uptake may reflect "aggravated," however, "reversible" metabolic changes in the myocardium (caused by e.g. disease-specific mechanical stress) and thereby precede irreversible cell death with occurrence of replacement fibrosis. Hence, FDG-PET findings—in addition to simultaneous LGE-CMR findings—may help to detect very early cardiac disease stages and thereby allow to timely start appropriate therapy and to carefully monitor cardiac disease stage.

Limitations

Obviously, the study group was rather small and cautious interpretation of the present data and results is required. However, BMD is an orphan disease and both recruitment of patients as well as conduct of PET-CMR studies are challenging in BMD patients. Noteworthy, this is the first PET-CMR study that was performed in BMD patients so far. Second, myocardial FDG uptake is prone to variations that do not always reflect pathological changes in metabolism (e.g. in case of suboptimal oral glucose loading to effect myocardial carbohydrate uptake). We cannot rule out some "physiological" differences between septal and lateral wall FDG-uptake, but we do not believe that those "physiological" effects may explain the substantial differences observed in the present study. Finally, we have chosen a simplified and targeted approach regarding analysis of FDG-PET data in order to allow a straightforward and categorical comparison of LV lateral vs. septal wall segments—without getting lost in too complex analyses that would not be appropriate in our small study group. It was decided against full quantitation of myocardial glucose utilization since this would require a lengthy glucose clamp procedure (14) considered too time consuming in addition to the already lengthy PET-CMR imaging procedure for this patient group with the risk of early scan termination.

CONCLUSION

Segmental FDG uptake—reflecting myocardial metabolic activity—is higher in the LV free wall of BMD patients—possibly due to a higher segmental work load. However, segmental metabolic activity seems to be dependent on and limited by the respective segmental extent of myocardial fibrosis as depicted by LGE-imaging.

DATA AVAILABILITY STATEMENT

The original contributions presented in the study are included in the article/supplementary material, further inquiries can be directed to the corresponding author.

ETHICS STATEMENT

The study protocol complies with the Declaration of Helsinki and was approved by the Local Ethics Committee (Landesärztekammer Westfalen-Lippe, Reg. No. 2017-175-f-S) and the Federal Office for Radiation Protection (BfS). Written informed consent was obtained from every patient. The patients/participants provided their written informed consent to participate in this study.

AUTHOR CONTRIBUTIONS

VV participated in the CMR and PET exams, performed major analyses of the PET data, and critically reviewed the manuscript. FB participated in the design of this study, performed PET analyses, and critically reviewed the manuscript. AF and SD participated in the CMR exams and in the analysis of the CMR data. BC and PK participated in the analysis of clinical data and critically reviewed the manuscript. LS supported to develop the theoretical framework, participated in the analysis of PET data, and helped shape the research and manuscript. AY designed the project, provided the main conceptual idea, supervised the work, provided critical feedback and helped shape the research, analysis, and manuscript. All authors contributed to the article and approved the submitted version.

FUNDING

This study was funded by a grant from the German Research Foundation (DFG) to LS (STE 1924/2-1) and AY (YI 127/5-1).

REFERENCES

1. Emery AE. The muscular dystrophies. *Lancet.* (2002) 359:687–95. doi: 10.1016/S0140-6736(02)07815-7
2. Yilmaz A, Sechtem U. Cardiac involvement in muscular dystrophy: advances in diagnosis and therapy. *Heart.* (2012) 98:420–9. doi: 10.1136/heartjnl-2011-300254
3. Verhaert D, Richards K, Rafael-Fortney JA, Raman SV. Cardiac involvement in patients with muscular dystrophies: magnetic resonance imaging phenotype and genotypic considerations. *Circ Cardiovasc Imaging.* (2011) 4:67–76. doi: 10.1161/CIRCIMAGING.110.960740
4. Arbustini E, Di TA, Giuliani L, Favalli V, Narula N, Grasso M. Cardiac phenotypes in hereditary muscle disorders: JACC state-of-the-art review. *J Am Coll Cardiol.* (2018) 72:2485–506. doi: 10.1016/j.jacc.2018.08.2182
5. Yilmaz A, Gdynia HJ, Baccouche H, Mahrholdt H, Meinhardt G, Basso C. Cardiac involvement in patients with Becker muscular dystrophy: new diagnostic and pathophysiological insights by a CMR approach. *J Cardiovasc Magn Reson.* (2008) 10:50. doi: 10.1186/1532-429X-10-50
6. Yilmaz A, Gdynia HJ, Mahrholdt H, Sechtem U. Cardiovascular magnetic resonance reveals similar damage to the heart of patients with Becker and limb-girdle muscular dystrophy but no cardiac symptoms. *J Magn Reson Imaging.* (2009) 30:876–7. doi: 10.1002/jmri.21905
7. Florian A, Ludwig A, Engelen M, Waltenberger J, Rösch S, Sechtem U, et al. Left ventricular systolic function and the pattern of late-gadolinium-enhancement independently and additively predict adverse cardiac events in muscular dystrophy patients. *J Cardiovasc Magn Reson.* (2014) 16:81. doi: 10.1186/s12968-014-0081-1
8. Hermans MC, Pinto YM, Merkies IS, de Die-Smulders CE, Crijns HJ, Faber CG. Hereditary muscular dystrophies and the heart. *Neuromuscul Disord.* (2010) 20:479–92. doi: 10.1016/j.nmd.2010.04.008
9. Florian A, Ludwig A, Rosch S, Yildiz H, Sechtem U, Yilmaz A. Myocardial fibrosis imaging based on T1-mapping and extracellular volume fraction (ECV) measurement in muscular dystrophy patients: diagnostic value compared with conventional late gadolinium enhancement (LGE) imaging. *Eur Heart J Cardiovasc Imaging.* (2014) 15:1004–12. doi: 10.1093/ehjci/jeu050
10. Dilsizian V, Bacharach SL, Beanlands RS, Bergmann SR, Delbeke D, Dorbala S, et al. ASNC imaging guidelines/SNMMI procedure standard for positron emission tomography (PET) nuclear cardiology procedures. *J Nucl Cardiol.* (2016) 23:1187–226. doi: 10.1007/s12350-016-0522-3
11. Minamimoto R. Series of myocardial FDG uptake requiring considerations of myocardial abnormalities in FDG-PET/CT. *Jpn J Radiol.* (2021) 39:540–57. doi: 10.1007/s11604-021-01097-6
12. Khairallah M, Khairallah R, Young ME, Dyck JR, Petrof BJ, Des RC. Metabolic and signaling alterations in dystrophin-deficient hearts precede overt cardiomyopathy. *J Mol Cell Cardiol.* (2007) 43:119–29. doi: 10.1016/j.yjmcc.2007.05.015
13. van Westering TL, Betts CA, Wood MJ. Current understanding of molecular pathology and treatment of cardiomyopathy in duchenne muscular dystrophy. *Molecules.* (2015) 20:8823–55. doi: 10.3390/molecules20058823
14. DeFronzo RA, Tobin JD, Andres R. Glucose clamp technique: a method for quantifying insulin secretion and resistance. *Am J Physiol.* (1979) 237:E214–23. doi: 10.1152/ajpendo.1979.237.3.E214

Conflict of Interest: The authors declare that the research was conducted in the absence of any commercial or financial relationships that could be construed as a potential conflict of interest.

Publisher's Note: All claims expressed in this article are solely those of the authors and do not necessarily represent those of their affiliated organizations, or those of the publisher, the editors and the reviewers. Any product that may be evaluated in this article, or claim that may be made by its manufacturer, is not guaranteed or endorsed by the publisher.

frontiers in Cardiovascular Medicine

ORIGINAL RESEARCH
published: 04 March 2022
doi: 10.3389/fcvm.2022.781402

Incremental Prognostic Value of Pericoronary Adipose Tissue Thickness Measured Using Cardiac Magnetic Resonance Imaging After Revascularization in Patients With ST-Elevation Myocardial Infarction

*Yue Ma[1], Quanmei Ma[1], Xiaonan Wang[1], Tongtong Yu[2], Yuxue Dang[1], Jin Shang[1], Guangxiao Li[3] and Yang Hou[1]**

[1] Department of Radiology, Shengjing Hospital of China Medical University, Shenyang, China, [2] Department of Cardiology, Shengjing Hospital of China Medical University, Shenyang, China, [3] Department of Medical Record Management Center, The First Hospital of China Medical University, Shenyang, China

OPEN ACCESS

Edited by:
Marcus R. Makowski, Technical University of Munich, Germany

Reviewed by:
José Tuñón, University Hospital Fundación Jiménez Díaz, Spain
Yuling Zhang, Sun Yat-sen Memorial Hospital, China

***Correspondence:**
Yang Hou
houyang_1973@sina.com

Specialty section:
This article was submitted to Cardiovascular Imaging, a section of the journal Frontiers in Cardiovascular Medicine

Received: 22 September 2021
Accepted: 07 February 2022
Published: 04 March 2022

Citation:
Ma Y, Ma Q, Wang X, Yu T, Dang Y, Shang J, Li G and Hou Y (2022) Incremental Prognostic Value of Pericoronary Adipose Tissue Thickness Measured Using Cardiac Magnetic Resonance Imaging After Revascularization in Patients With ST-Elevation Myocardial Infarction. Front. Cardiovasc. Med. 9:781402. doi: 10.3389/fcvm.2022.781402

Background and Aim: Pericoronary adipose tissue (PCAT) reflects pericoronary inflammation and is associated with coronary artery disease. We aimed to identify the association between local PCTA thickness using cardiac magnetic resonance (CMR) and prognosis of patients with ST-elevation myocardial infarction (STEMI), and to investigate the incremental prognostic value of PCAT thickness in STEMI after reperfusion.

Methods: A total of 245 patients with STEMI (mean age, 55.61 ± 10.52 years) who underwent CMR imaging within 1 week of percutaneous coronary intervention therapy and 35 matched controls (mean age, 53.89 ± 9.45 years) were enrolled. PCAT thickness indexed to body surface area at five locations, ventricular volume and function, infarct-related parameters, and global strain indices were evaluated using CMR. Associations between PCAT thickness index and 1-year major adverse cardiovascular events (MACE) after STEMI were calculated. The prognostic value of the standard model based on features of clinical and CMR and updated model including PACT thickness index were further assessed.

Results: Patients with MACE had a more significant increase in PCAT thickness index at superior interventricular groove (SIVGi) than patients without MACE. The SIVGi was significantly associated with left ventricular ejection fraction (LVEF), infarct size, and global deformation. SIVGi $>$ 4.98 mm/m^2 was an independent predictor of MACE (hazard ratio, 3.2; 95% CI: 1.6–6.38; $p < 0.001$). The updated model significantly improved the power of prediction and had better discrimination ability than that of the standard model for predicting 1-year MACE (areas under the ROC curve [*AUC*] = 0.8 [95% *CI*: 0.74–0.87] *vs*. *AUC* = 0.76 [95% *CI*: 0.68–0.83], $p < 0.05$; category-free net reclassification index [*cfNRI*] = 0.38 [95% *CI*: 0.1–0.53, $p = 0.01$]; integrated discrimination improvement [*IDI*] = 0.09 [95% *CI*: 0.01–0.18, $p = 0.02$]).

Conclusions: This study demonstrated SIVGi as an independent predictor conferred incremental value over standard model based on clinical and CMR factors in 1-year MACE predictions for STEMI.

Keywords: ST elevated myocardial infarction, magnetic resonance imaging, pericoronary adipose tissue, coronary artery disease, prognosis

INTRODUCTION

Effective stratification of residual risk during the early postoperative period is particularly important for the short-term prognosis of patients with acute myocardial infarction (MI) (1). Previous studies have shown that decreased cardiac function, morphological changes of the left ventricle, and large myocardial infarct size evaluated using cardiac magnetic resonance (CMR) imaging are common predictors of adverse events after MI (2). CMR strain indicators, which signal decreased myocardial compliance, have become important prognostic and functional markers for early risk stratification and treatment decisions for survivors of MI (3, 4).

Inflammation has long been postulated to play an important role in the atherosclerotic progression and recurrent major adverse cardiovascular events (MACE) (5, 6). Reportedly, the volume and thickness of epicardial adipose tissue (EAT), as a source of inflammatory cytokines, is associated with the severity of coronary artery disease (CAD) (7–9). Recent evidence demonstrates that the CT attenuation of pericoronary adipose tissue (PCAT) – the EAT directly surrounding the coronary arteries – is associated with cardiac mortality (10, 11). It might imply that the local PCAT might have a more direct and efficient impacts on CAD compared with the global EAT. However, there are only a few studies on the relationship between local PCAT and ST-elevation myocardial infarction (STEMI), and no study has been reported on the incremental prognostic value of PCAT thickness after revascularization in patients with STEMI.

Therefore, the purpose of this study was to evaluate the changes in PCAT thickness at different locations after STEMI, to evaluate the association of PCAT thickness indices with the occurrence MACE, and to determine the effective predictors among PCAT thickness indices to investigate the incremental prognostic value of PCAT thickness index in MACE within 1 year after STEMI.

MATERIALS AND METHODS

Study Group

From April 2017 to December 2019, we retrospectively screened 323 patients who had STEMI for the first time and underwent percutaneous coronary intervention (PCI) therapy at Shengjing Hospital of China Medical University. STEMI was defined according to current definitions (12). We excluded patients who did not undergo contrast CMR imaging within 1 week of PCI, had CMR images of poor quality, or had a history of MI or revascularization. A total of 245 patients met the eligibility criteria and were enrolled in the study (**Supplementary Figure 1**). We also enrolled 35 participants without any known or suspected CAD (based on clinical history) who underwent CMR imaging between December 2019 and July 2020 as control subjects. This study complied with the tenets of the Declaration of Helsinki and was approved by the Shengjing Hospital of China Medical University Research Ethics Committee.

Clinical Assessment and Endpoint

We collected the relevant clinical history data of all patients and controls, including information on baseline clinical characteristics, cardiovascular risk factors, laboratory parameters, current medication, and angiographic information. The follow-up information was obtained from the patients' medical records and from telephone interviews. The endpoint was time to first MACE within the 12-month follow-up period post-revascularization, and included a composite of cardiovascular death, recurrent MI, clinically driven target lesion revascularization, and readmission for heart failure (13). Planned-staged procedures were not counted as MACE.

CMR Imaging and Analysis

All patients were examined using a 3.0-T MR scanner (Ingenia, Philips Healthcare, Best, Netherlands). Anonymized CMR images were analyzed offline using customized software (Circle Cardiovascular Imaging, cvi42®, Calgary, Canada). The images were analyzed by two experienced observers blinded to all patient data. CMR data were prospectively incorporated into the database. The details of the technical aspects of CMR acquisitions, sequences, and quantification have been described previously (14).

Left ventricular ejection fraction (LVEF) (%), left ventricular end-diastolic volume (LVEDV) index (ml/m^2), left ventricular end-systolic volume (LVESV) index (ml/m^2), left ventricular mass index, right ventricular ejection fraction (%), right ventricular end-diastolic volume index (ml/m^2), right ventricular end-systolic volume index (ml/m^2), microvascular obstruction (%), edema size (% of left ventricular mass), infarct size (% of left ventricular mass), and myocardial salvage index (% of left ventricular mass with myocardial edema not showing delayed enhancement) were calculated. Tissue tracking-CMR strain analysis was also performed, and the global strain values (global radial strain [GRS], global circumferential strain [GCS], and global longitudinal strain [GLS]) through the entire cardiac cycle were calculated semi-automatically using the software as previously described (14).

Measurement of PCAT Thickness

Pericoronary adipose tissue thickness was measured using the end-diastolic phase CMR cine images

(**Supplementary Figure 2**). PCAT thickness was defined as the distance between the myocardial surface and the pericardium, which is perpendicular to the pericardium through the center of coronary arteries inside the PCAT. All PCAT measurements were indexed to the body surface area of individual patients to get corrected parameters (right atrioventricular groove PCAT thickness index [RAVGi], anterior interventricular groove PCAT thickness index [AIVGi], left atrioventricular groove PCAT thickness index [LAVGi], superior interventricular groove PCAT thickness index [SIVGi], inferior interventricular groove PCAT thickness index [IIVGi]).

Statistical Analysis

Continuous data were tested for normal distribution using the Kolmogorov–Smirnov test. Normally distributed data were expressed as mean ± SD and compared using Student's *t*-test. Nonparametric data were expressed as medians (interquartile ranges) and compared using the Mann–Whitney *U* test. Categorical variables were expressed as percentages and compared using the chi-square test or Fisher's exact test where appropriate. The correlations between PCAT thickness indices and CMR imaging parameters were evaluated using Pearson's correlation coefficient and the reproducibility was assessed using Bland–Altman analysis and intra-class correlation coefficients.

The time-dependent receiver operating characteristics (ROC) curve analysis was used to assess the performance of the strain indexes and PCAT thickness indexes for the prediction of adverse cardiac events 1-year post STEMI. The areas under the ROC curve (AUCs) and the corresponding 95% *CI* were calculated as well. Meanwhile, the optimal cutoff for each index was determined. Kaplan–Meier curves were used to estimate MACE-free survival rates with respect to high and low level of the PCAT index with best discriminative ability. The comparison of survival rates between groups was examined using the log-rank test.

To facilitate the construction of the Cox regression model, continuous variables were categorized into binary variables using optimal cutoffs, median values, or values of clinical significance, as appropriate. Univariate Cox regression model was used to estimate the risk of adverse events, which were expressed as hazard ratios (*HR*) and 95% *CIs*. Two multivariable Cox regression models were then conducted. Those were the standard model and updated model. The least absolute shrinkage and selection operator (LASSO) strategy, an efficient in handling high-dimensional data (15), was used to select the most useful predictors except for the PCAT thickness indexes in the standard model. The optimal λ in the LASSO Cox regression model was determined by 10-fold cross-validation using the one standard error of the minimum criteria (1-SE criteria). Thereafter, the PACT thickness index with the best performance will be added in to update the standard model. The performances of the two models were further assessed by AUCs. The incremental prognostic value of the updated model was evaluated using delta AUC. The category-free net reclassification improvement (NRI) and integrated discrimination improvement (IDI) were calculated as well (16). NRI is defined as the difference in the proportions of study subjects with events correctly assigned a higher probability and study subjects without events correctly assigned a low probability by an updated model compared with the standard one (16). IDI refers to the extent to which the updated model can improve the average sensitivity but without reducing average specificity as compared with that of the standard model (17). Finally, a nomogram that enables the visualization of the probability of 1-year MACE was drawn to assist risk stratification.

A two-tailed $p < 0.05$ was considered statistically significant. All statistical analyses were conducted using R software (version 3.6.3, Vienna, Austria). The following packages were involved: "timeROC," "survivalROC," "survival," "survminer," "glmnet," and "survIDINRI."

RESULTS

Baseline Characteristics

Table 1 shows the baseline clinical and CMR imaging characteristics of the study population categorized as control vs. patients with STEMI and further stratified according to the occurrence of MACE. There were no significant differences between the patients with STEMI and the control subjects with respect to age and sex. Patients with STEMI were significantly more likely to have traditional cardiovascular risk factors than the control subjects. Compared with patients without MACE, patients with MACE-STEMI had higher Troponin I value. However, there was no significant difference between patient with and without MACE in peak high-sensitivity C-reactive protein (hs-CRP) as a marker of systemic inflammation. Patients with STEMI, especially those with MACE, had a larger chamber size, lower LVEF, larger infarct size, and less deformation, as evaluated using GRS, GCS, and GLS, than the controls (**Table 1**).

Pericoronary Adipose Tissue Thickness Index and Main CMR Parameters

The PCAT thickness indices of patients with STEMI were significantly greater than those of controls at all locations measured, except IIVGi (**Table 1**). However, only SIVGi showed significant difference between patients with MACE and patients without MACE (**Table 1**). We found that only SIVGi was associated with LVEF, infarct size, and the three strain indices in all patients with STEMI (**Table 2**). We also noted a significant increase in SIVGi in patients with lower LVEF, larger infarction size, and less deformation (LVEF≥50%: 4.63 ± 1.47 mm/m^2, LVEF < 50%:5.34 ± 1.63 mm/m^2, $p = 0.001$; infarction size ≤ 13.73%:4.60 ± 1.38 mm/m^2, infarction size > 13.73%:5.37 ± 1.69 mm/m^2, $p < 0.001$; GRS ≥ 22.77%:4.67 ± 1.57 mm/m^2, GRS < 22.77%:5.30 ± 1.55 mm/m^2, $p < 0.01$; GCS ≤ −14.2%:4.71 ± 1.52 mm/m^2, GCS > −14.2%:5.61 ± 1.57 mm/m^2, $p < 0.001$; GLS ≤ −8.6%:4.79 ± 1.61 mm/m^2, GLS > −8.6%:5.26 ± 1.53 mm/m^2, $p = 0.02$) (**Supplementary Table 1**).

TABLE 1 | Baseline characteristics of study population.

Variables	Controls (*N* = 35)	All STEMI (*N* = 245)	*P* value	MACE-STEMI (*N* = 47)	No MACE-STEMI (*N* = 198)	*P* value
Clinical characteristics						
Age (years)	53.89 ± 9.45	55.61 ± 10.52	0.36	56.87 ± 9.99	55.31 ± 10.65	0.36
Male sex (%)	25 (71.43)	197 (80.41)	0.22	38 (80.85)	159 (80.30)	0.93
BMI (kg/m^2)	22.01 ± 3.44	25.87 ± 3.29	<0.001	25.75 ± 3.17	25.91 ± 3.33	0.77
BSA (m^2)	1.71 ± 0.23	1.85 ± 0.18	<0.001	1.84 ± 0.17	1.86 ± 0.18	0.68
Diabetes mellitus (%)	3 (8.57)	62 (25.31)	0.03	9 (19.15)	53 (26.77)	0.28
Hypertension (%)	6 (17.14)	108 (44.08)	<0.01	23 (48.94)	85 (42.93)	0.46
SBP (mm Hg)	119.80 ± 17.28	125.69 ± 21.13	0.12	126.94 ± 19.44	125.40 ± 21.55	0.66
TC (mmol/L)	-	4.88 ± 1.13	-	5.00 ± 1.16	4.85 ± 1.12	0.40
TG (mmol/L)	-	2.00 ± 1.82	-	1.69 ± 1.38	2.08 ± 1.91	0.19
HDL-C (mmol/L)	-	1.02 ± 0.32	-	1.12 ± 0.34	1.00 ± 0.31	0.03
LDL-C (mmol/L)	-	3.01 ± 1.03	-	3.19 ± 0.97	2.97 ± 1.04	0.19
#Dyslipidemia (%)	-	185 (75.51)	-	33 (70.21)	152 (76.76)	0.35
eGFR (ml/min/1.73 m^2)	-	96.33 ± 17.12	-	96.33 ± 16.95	96.33 ± 17.13	1.00
Smoking (%)	7 (20.00)	146 (59.59)	<0.001	30 (63.83)	116 (58.59)	0.51
Heart rate on admission (bpm)	69.63 ± 8.32	78.96 ± 17.72	<0.01	82.34 ± 21.43	78.15 ± 16.69	0.15
Killip class >I (%)	0	35 (14.29)	-	10 (21.28)	25 (12.63)	0.13
Symptom onset to reperfusion time (min)	-	304 (190–535)	-	358 (253–573)	300 (175–529)	0.72
Peak creatine kinase MB (ng/ml)	-	126.00 (79.90–205.35)	-	160.10 (89.30–335.60)	126.00 (79.90–168.30)	0.08
Troponin T (ng/ml)	-	4.08 (1.32–10.0)	-	4.26 (2.13–10.00)	4.08 (1.21–11.34)	0.93
Troponin I (ng/ml)	-	31.60 (9.00–54.83)	-	43.51 (17.65–76.06)	27.35 (8.93–41.54)	<0.01
Peak hs-CPR (mg/dL)	-	5.80 (3.0–10.34)	-	7.00 (3.90–10.80)	5.60 (2.68–10.34)	0.26
Anterior infarction (%)	0	108 (44.08)	-	26 (55.32)	82 (41.41)	0.08
Multivessel disease (%)	0	6 (2.45)	-	1 (2.13)	5 (2.53)	0.87
Initial TIMI flow grade >1 (%)	-	66 (26.94)	-	10 (21.28)	56 (28.28)	0.33
Final TIMI flow grade 3 (%)	-	240 (97.96)	-	45 (95.74)	195 (98.48)	0.23
Medications						
Aspirin (%)	6 (17.14)	244 (99.59)	<0.001	47 (100)	197 (99.49)	0.63
Statins (%)	8 (22.86)	241 (98.37)	<0.001	45 (95.74)	196 (98.99)	0.12
ACEI/ARB (%)	7 (20.00)	223 (91.02)	<0.001	43 (91.49)	180 (90.91)	0.90
βblocker (%)	4 (11.43)	224 (91.43)	<0.001	41 (87.23)	183 (92.42)	0.25
Conventional CMR characteristics						
LVEF (%)	58.49 ± 6.76	50.15 ± 11.93	<0.001	42.36 ± 12.16	51.99 ± 11.13	<0.001
LVEDVi (ml/m²)	69.11 ± 10.72	73.84 ± 14.55	0.07	80.47 ± 16.21	72.27 ± 13.71	<0.001
LVESVi (ml/m²)	29.03 ± 7.46	37.61 ± 14.61	0.001	47.48 ± 17.47	35.26 ± 12.81	<0.001
LV mass index (g/m^2)	52.22 ± 10.58	63.37 ± 11.51	<0.001	65.92 ± 12.93	62.76 ± 11.09	0.09
RVEF (%)	44.18 ± 6.51	37.30 ± 13.51	<0.01	34.00 ± 14.28	38.08 ± 13.24	0.06
RVEDVi (ml/m²)	57.95 ± 12.19	57.59 ± 12.80	0.88	56.83 ± 14.89	57.77 ± 12.28	0.65
RVESVi (ml/m²)	32.69 ± 8.81	35.85 ± 10.23	0.08	37.28 ± 11.73	35.51 ± 9.85	0.29
Edema size (% of LV mass)	-	37.26 ± 13.52	-	38.24 ± 13.89	36.75 ± 13.65	0.50
Microvascular obstruction (%)	-	88 (35.92)	-	20 (42.55)	68 (34.34)	0.29
Infarct size (% of LV mass)	-	13.73 (8.62–19.01)	-	17.04 (11.53–23.78)	12.97 (7.89–18.05)	<0.01
MSI (% of LV mass)	-	22.16 (8.28–33.15)	-	19.25 (3.22–30.14)	23.67 (10.98–33.58)	0.09

(Continued)

TABLE 1 | Continued

Variables	Controls (*N* = 35)	All STEMI (*N* = 245)	*P* value	MACE-STEMI (*N* = 47)	No MACE-STEMI (*N* = 198)	*P* value
Strain characteristics						
GRS (%)	34.09 ± 7.56	23.53 ± 7.98	<0.001	18.96 ± 6.93	24.61 ± 7.85	<0.001
GCS (%)	−20.51 ± 2.86	−15.67 ± 3.49	<0.001	−13.56 ± 3.66	−16.17 ± 3.26	<0.001
GLS (%)	−12.69 ± 2.49	−9.30 ± 2.92	<0.0001	−7.84 ± 2.25	−9.64 ± 2.96	<0.001
PCAT thickness characteristics						
RAVGi (mm/m^2)	4.77 ± 1.15	5.99 ± 1.81	<0.001	6.31 ± 1.78	5.93 ± 1.82	0.19
AIVGi (mm/m^2)	2.27 ± 0.65	2.81 ± 0.84	<0.001	2.66 ± 0.70	2.85 ± 0.86	0.15
LAVGi (mm/m^2)	3.54 ± 0.81	4.82 ± 1.44	<0.001	4.67 ± 1.27	4.85 ± 1.47	0.45
SIVGi (mm/m^2)	3.79 ± 1.11	4.98 ± 1.59	<0.001	5.99 ± 1.55	4.75 ± 1.51	<0.001
IIVGi (mm/m^2)	2.94 ± 0.99	3.10 ± 0.97	0.35	3.18 ± 1.02	3.08 ± 0.96	0.56

ACEi, Angiotensin-converting enzyme inhibitors; AIVGi, Anterior interventricular groove PCAT thickness index; ARB, Angiotensin Receptor Blockers; BMI, Body mass index; BSA, Body surface area; CMR, Cardiac Magnetic Resonance; eGFR, Estimated glomerular filtration rate; GCS, Global circumferential strain; GLS, Global longitudinal strain; GRS, Global radial strain; HDL-C, High-density lipoprotein cholesterol; IIVGi, Inferior interventricular groove PCAT thickness index; LAD, Left anterior descending; LAVGi, Left atrioventricular groove PCAT thickness index; LCX, Left circumflex; LDL-C, Low-density lipoprotein cholesterol; LVEDVi, left ventricular end-diastolic volumeindex; LVEF, Left ventricular ejection fraction; LVESVi, left ventricular end-systolic volumeindex; MACE, Major adverse cardiac events; MSI, Myocardial salvage index; PCAT, Pericoronary adipose tissue; RAVGi, Right atrioventricular groove PCAT thickness index; RCA, Right coronary artery; RVEDVi, Right ventricular end-diastolic volume index; RVEF, Right ventricular ejection fraction; RVESVi, Right ventricular end-systolic volume index; SBP, Systolic blood pressure; SIVGi, Superior interventricular groove PCAT thickness index; STEMI, ST elevation myocardial Infarction; TC, Total cholesterol; TG, Triglycerides; TIMI, Thrombolysis in myocardial infarction. Categorical variables are expressed as absolute number (percentage); Symptom onset to reperfusion time, Peak creatine kinase MB, Troponin T, Troponin I, Peak hs-CPR, Infarct size and Myocardial salvage index are expressed as median (IQR); All other continuous variables are expressed as mean ± SD.

[#]Participants were diagnosed with dyslipidemia if they met any of the following criteria27: TC ≥ 6.22 mmol/L, TG ≥ 2.26 mmol/L, LDL-C ≥ 4.14 mmol/L, HDL-C < 1.04 mmol/L, or patients who were taking lipid-regulating medications.

TABLE 2 | The bivariate Pearson's correlations between pericoronary adipose tissue (PCAT) thickness index and left ventricular ejection fraction (LVEF), infarct size, left ventricular end-diastolic volume index (LVEDVi), left ventricular end-systolic volume index (LVESVi), and strains in all patients with ST elevation myocardial Infarction (STEMI).

Pearson correlations	*RAVGi*	*AIVGi*	*LAVGi*	*SIVGi*	*IIVGi*
LVEF	0.010	0.064	0.034	−0.299***	0.075
Infarct size	0.084	0.041	−0.014	0.299***	0.144*
LVEDVi	0.029	−0.104	−0.003	0.202***	−0.012
LVESVi	0.002	−0.097	−0.034	0.292***	−0.066
GRS	0.066	0.079	0.098	−0.238***	0.065
GCS	−0.035	−0.011	−0.040	0.307***	−0.050
GLS	−0.051	−0.066	−0.054	0.159*	−0.047

*AIVGi, Anterior interventricular groove PCAT thickness index; GCS, Global circumferential strain; GLS, Global longitudinal strain; GRS, Global radial strain; IIVGi, Inferior interventricular groove PCAT thickness index; LAVGi, Left atrioventricular groove PCAT thickness index; LVEDVi, left ventricular end-diastolic volume index; LVEF, Left ventricular ejection fraction; LVESVi, left ventricular end-systolic volume index; PCAT, Pericoronary adipose tissue; RAVGi, Right atrioventricular groove PCAT thickness index; SIVGi, Superior interventricular groove PCAT thickness index; STEMI, ST elevation myocardial Infarction. *Indicates P < 0.05; ***indicates P < 0.001.*

The PCAT Thickness Index With Best Discriminative Ability

During a 1-year follow-up period, 47 patients (19.18%) with STEMI had their first MACE (**Supplementary Table 2**, **Supplementary Figure 5**). For all patients, the time-dependent ROC curve analysis demonstrated that the AUC of 0.73 (95% CI: 0.66–0.80, $p < 0.01$, cutoff value: 4.98 mm/m^2) for SIVGi was the highest among the AUCs of the PCAT thickness indices (**Figure 1B**). Moreover, the Kaplan–Meier event-free survival curve analysis also showed that SIVGi > 4.98 mm/m^2 was associated with poor 1-year MACE-free survival in patients with STEMI (**Figure 2**). Therefore, SIVGi was significant associated with the time to MACE. To avoid variable overfitting, SIVGi was the only PCAT thickness parameter tested in subsequent multivariable analyses.

Similarly, the discriminative ability of different strain characteristics for predicting 1-year MACE was also identified by the time-dependent ROC curve. It was shown that the AUC for GRS was higher among the three parameters, and there was no significant difference compared with the other two AUCs (**Figure 1A**).

Univariate and Multivariable Analysis

Univariate Cox regression analysis was performed to estimate the risk predictors of one-year MACE post-STEMI (**Supplementary Table 3**). It demonstrated that a Troponin *I* > 31.60 ng/ml, a LVEF < 50%, and an infarct size >13.73% were associated with a two- to three-fold increased risk for adverse events, and that a LVESV index > 35.99% ml/m², a GRS < 22.77%, a GCS > −14.2%, and a GLS > −8.6% were associated with an approximately four-fold increased risk for adverse events for all the patients with STEMI (**Supplementary Table 3**). Further, SIVGi > 4.98 mm/m^2 was associated with an approximately five-fold increased risk for MACE (**Supplementary Table 3**).

The standard model in **Table 3** showed that LVESV index, GRS, GCS, and GLS were significantly associated with 1.89-, 1.77-, 1.86-, and 2.03-fold elevated risk of adverse events, respectively (**Supplementary Figure 3**). The addition of SIVGi in the updated model revealed that SIVGi was independently associated with risk of adverse events (*HR* = 3.2, 95% *CI*: 1.6–6.38, $p < 0.001$). Similar results were found when LVESV

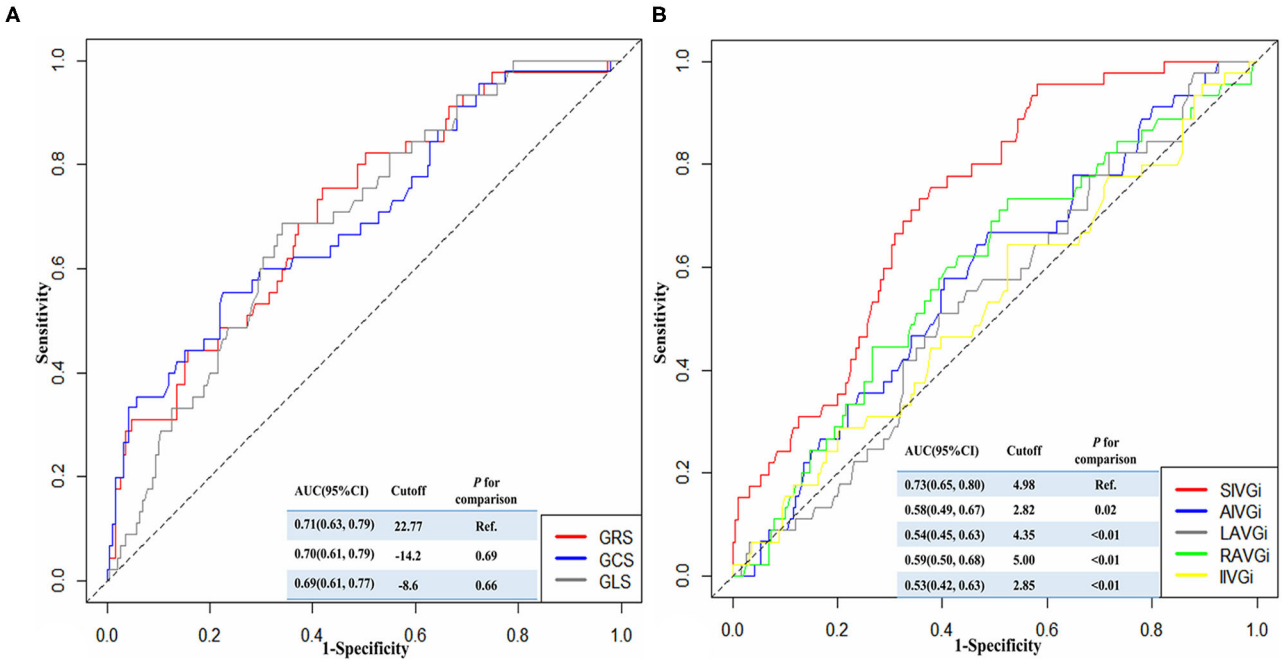

FIGURE 1 | The time-dependent receiver operator characteristic (ROC) curves showing the discriminative ability of different strain characteristics **(A)** and PCAT thickness characteristics **(B)** for predicting 1-year major adverse cardiac events (MACE). AIVGi, Anterior interventricular groove PCAT thickness index; AUC, Areas under the ROC curve; CI, confidence interval; GCS, Global circumferential strain; GLS, Global longitudinal strain; GRS, Global radial strain; IIVGi, Inferior interventricular groove PCAT thickness index; LAVGi, Left atrioventricular groove PCAT thickness index; MACE, Major adverse cardiac events; PCAT, Pericoronary adipose tissue; RAVGi, Right atrioventricular groove PCAT thickness index; ROC, Receiver operator characteristic curve; SIVGi, Superior interventricular groove PCAT thickness index.

index, GRS, GCS, GLS, and SIVGi were enrolled into Cox regression model as continuous variables. There was a 1.49-fold higher risk in adverse events per mm/m^2 increase in SIVGi (**Supplementary Table 4**).

Incremental Discriminatory and Reclassification Performance of SIVGi

As shown in **Table 3**, the discriminative power of the updated model was stronger than that of the standard model (*AUC*: 0.8 *vs*. 0.76). The delta *AUC* and *p*-value were 0.046 and 0.047, respectively. The incremental prognostic value of SIVGi was further confirmed by reclassification analysis. As compared with the standard model, the updated model could more accurately assigned 38% of the participants into the MACE group or non-MACE group (category-free NRI [*cfNRI*] = 0.38, $p = 0.01$), which was consistent with the non-zero IDI value (*IDI* = 0.09, $p = 0.02$). Similar findings were depicted in the sensitivity analysis in which traditional risk factors such as age, sex, smoking, BMI, diabetes mellitus, hypertension, dyslipidemia, eGFR, LVEF, statins, ACEI/ARB, and β blocker were further adjusted (**Supplementary Table 5**).

A higher AUC was also found in the updated model than the standard model when the SIVGi was treated as a continuous variable in Cox regression models (*AUC*: 0.82 vs. 0.74; delta *AUC* = 0.08, $p < 0.01$) (**Supplementary Table 4**). As compared with the standard model, the updated model could more accurately assigned 29% of the participants (*cfNRI* = 0.29, $p = 0.03$). However, we failed to detect a significant IDI value (*IDI* = 0.03, $p = 0.31$).

Based on the updated model, a nomogram that combined all the independent predictors was constructed to predict MACE at 1 year (**Supplementary Figure 4**). In this nomogram, each variable was given a score, and by summing up the total score of each patient, we could predict the possibility of MACE at 1 year.

DISCUSSION

The main finding of the present study was that the increased PCAT thickness at the SIVG was more significant in patients with MACE after STEMI. The SIVGi was significantly associated with LVEF, infarct size and LV global deformation in STEMI. As an independent predictor for 1-year MACE, SIVGi conferred incremental value in predictions for patients with STEMI.

Pericoronary adipose tissue as an organ is anatomically adjacent and functionally interrelated with the myocardium and coronary arteries. Under physiological conditions, PCAT has anti-inflammatory and protective effects and can be used as an energy reservoir to provide fatty acids to the coronary arteries and myocardium (18–20). However, PCAT contains a high density of lymphoid clusters and as a chemical reservoir, can secrete pro-inflammatory cytokines and directly induce adjacent coronary artery inflammation in pathological states, thereby

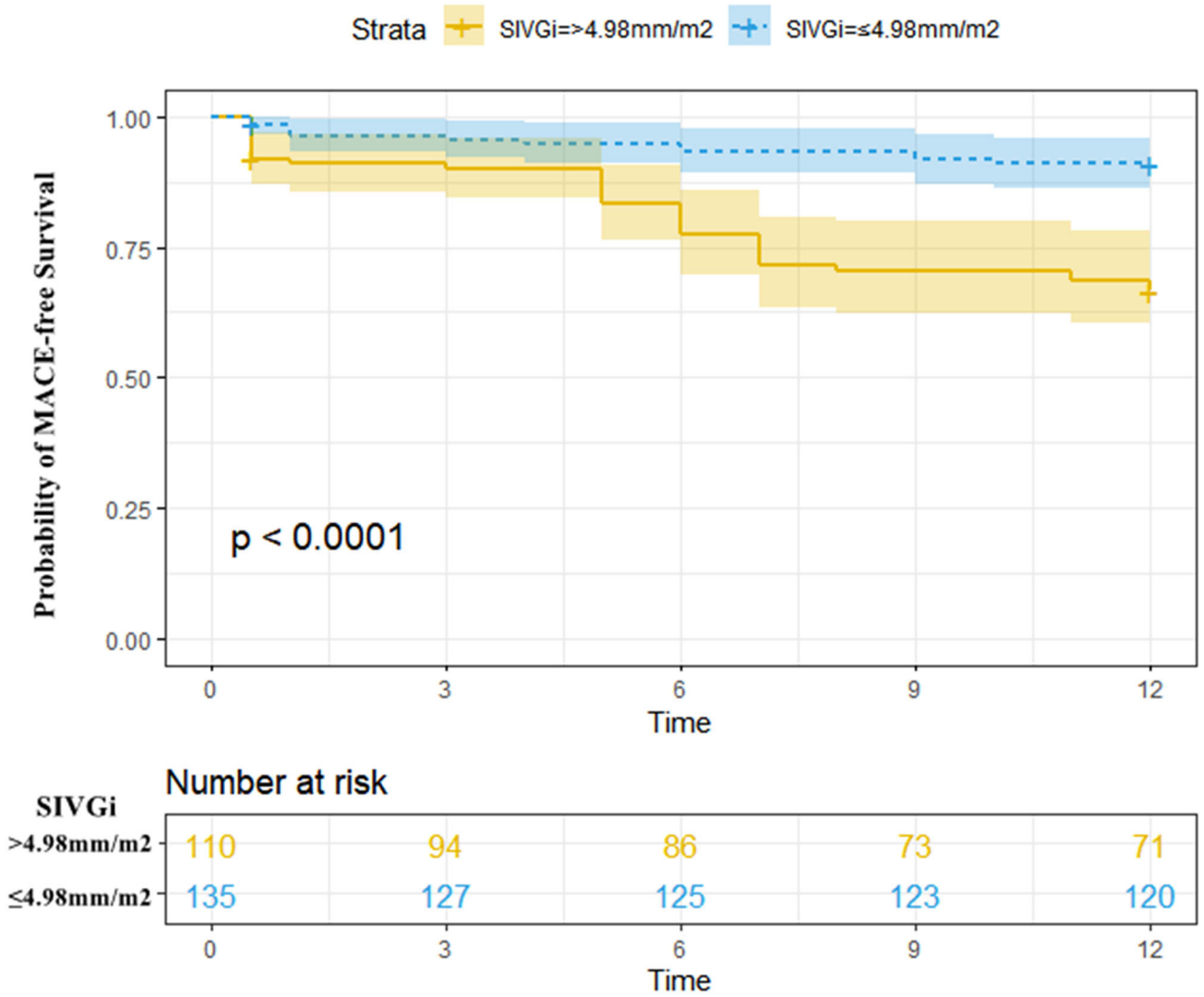

FIGURE 2 | Kaplan–Meier MACE-free survival estimated stratified by SIVGi in all patients with STEMI. Patients with higher SIVGi displayed a significantly higher risk of a first MACE. Central line represented the survival curves and the upper and lower lines of the colored areas correspond to the 95% CI. MACE, Major adverse cardiac events; SIVGi, Superior interventricular groove PCAT thickness index.

promoting the progression of atherosclerosis, plaque rupture, and thrombosis, causing acute MI (9, 21, 22). Acute MI can induce the pathological state of EAT. It is well known that as a cardiovascular disease that increases sympathetic activation, MI is characterized by sustained stimulation of β-adrenoceptors (β-ARs) and activation of the renin-angiotensin-aldosterone system. The vascular dysfunction induced by the overstimulation of β-AR associated with endothelial nitric oxide synthase uncoupling can cause PCAT impairment (23). At the same time, the infarcted myocardium directly secretes inflammatory factors and causes hypoxia in the surrounding microenvironment to promote the inflammatory response of the adjacent EAT, which can promote accumulation and thickening of local EAT (24). The findings of the present study are in accordance with the global and local effects of MI on EAT. We found that for patients with STEMI, PCAT thickened in all locations, and local PCTA at SIVG more significantly thickened in patient with MACE. However, in our study, the peak hs-CPR, as a marker of systemic inflammation, was not significantly increase in patient with MACE compared with patients without MACE. It supported that the local PCAT could be a more direct and efficient indicator on MACE after STEMI compared with global changes.

Previous ultrasound studies have explored the relationship between local EAT thickness and the prognosis of patients with MI (25, 26). Morales-Portano et al. used ultrasound to measure the mean EAT thickness at the right ventricle free wall and the interventricular groove, which showed the good predictive ability for MACE in patients with CAD (25). However, in a 3-year follow-up study of 114 patients with STEMI, Esen et al. found that the EAT thickness at the right ventricle free wall was

TABLE 3 | Comparison of the standard and updated multivariate Cox regression models for predicting 1-year major adverse cardiac events (MACE) post STEMI.

Variables	Standard model		Updated model	
	HR (95%CI)	*P* value	HR (95%CI)	*P* value
LVESVi (>35.99 ml/m²)	1.89 (0.89, 4.00)	0.10	1.87 (0.90, 3.87)	0.09
GRS (<22.77%)	1.77 (0.80, 3.94)	0.16	1.67 (0.75, 3.68)	0.21
GCS (>-14.2%)	1.86 (0.93, 3.71)	0.08	1.53 (0.77, 3.02)	0.23
GLS (>-8.6%)	2.03 (1.03, 4.01)	0.04	1.98 (1.00, 3.90)	0.05
SIVGi (>4.98 mm/m^2)	-	-	3.20 (1.60, 6.38)	<0.001
AUC (95%CI)	0.76 (0.68, 0.83)		0.80 (0.74, 0.87)	
Delta AUC; *P* value	0.046; 0.047			
cfNRI (95%CI); *P* value	0.38 (0.10, 0.53); 0.01			
IDI (95%CI); *P* value	0.09 (0.01, 0.18); 0.02			

AUC, Areas under the ROC curve; cfNRI, category-free net reclassification index; CI, Confidence interval; GCS, Global circumferential strain; GLS, Global longitudinal strain; GRS, Global radial strain.HR, Hazard ratio; IDI, Integrated discrimination improvement index; LVEF, Left ventricular ejection fraction; LVESVi, left ventricularend-systolic volume index; MACE, Major adverse cardiac events; SIVGi, Superior interventricular groove; PCAT thickness index; STEMI, ST elevation myocardial Infarction.

not related to the clinical outcome after PCI (26). Therefore, the prognostic value of local EAT thickness for STEMI remains controversial. In the present study, we found that SIVGi is a stronger predictor of outcome than other PCAT thickness parameters. An SIVGi > 4.98 mm/m^2 was associated with a 4.52-fold increased risk for MACE after STEMI, whereas other PCAT thickness indices were associated with about 1- to 2-fold increased risk for MACE. A previous CT study indicated that PCAT around the left anterior descending (LAD) artery and right coronary artery, but not around the left circumflex coronary artery, is an independent predictor of all-cause and cardiac mortality (11), a finding that supports that of the present study. This is also consistent with the result of another recent MR study, which showed that perivascular EAT at the SIVG is an independent predictor of composite MACE in patients with STEMI (odds ratio, 2.26) after adjustment for age, sex, and LVEF (13).

The findings of the present study and those of previous studies indicate that there are some possible reasons for the significant thickening of PCAT at the SIVG and why it is an independent predictor of MACE. First, the interventricular groove, which is shallow and broad, is where the EAT has the closest contact and is most adjacent to the myocardium, especially the EAT at the SIVG, which is most directly affected by paracrine effects produced by the anterior infarcted myocardium. This could be supported by the significant increase in SIVGi in MACE group, as there were more patients with anterior MI (∼60%) and larger MI sizes in MACE-STEMI compared with no MACE-STEMI in the present study. Second, given that LAD is the main artery of the left ventricle with the most extensive blood supply range, the redistribution of coronary blood flow is most significant after MI. In addition, the damage to the endothelial cells of the LAD can induce more obvious abnormal accumulation of PCAT around the LAD. The effect of PCAT at the SIVG on blood vessels is also stronger and has greater influence on prognosis (27). Third, according to the characteristics of the anatomical location, the measurement value of PCAT thickness at the SIVG is more accurate, more reproducible, and more sensitive to the pathological state of the PCTA than that of other locations. Compared with other PCAT thickness indices, SIVGi had perfect repeatability and the highest AUC value in the present study, a finding that further supports this view. Therefore, it is not appropriate to analyze the overall change in EAT as doing so may dilute the changes controlled by PCAT at the SIVG, which may reduce the ability of PCAT to assess prognosis. Indeed, we found that the higher SIVGi was significantly assistant with lower LVEF, larger LV infarct area, and less deformation, all of which indicate a poor prognosis in patients with STEMI. The deterioration of these parameters may suggest the pathologic effect of PCAT in patients with STEMI.

The results of the present study showed that compared with standard model, the updated model including SIVGi with a cutoff value of 4.98 mm/m^2 had better discrimination and reclassification ability for patients with 1-year MACE after STEMI. The sensitivity analysis in which traditional risk factors were further adjusted also supported this. Interestingly, the most useful predictors (GRS, GCS, GLS, and LVESV) for the standard model are all CMR parameters for myocardial compliance, indicating that myocardial compliance on CMR imaging may have more direct relationship with short-term STEMI prognosis compared with clinical parameters. To our knowledge, this is the first study to show that the simple measurement of PCAT thickness index at the SIVG combined with myocardial compliance indices is a useful marker of MACE after STEMI in the CMR imaging setting. Moreover, PCAT measurement has good reliability and can be completed during routine CMR examination without the need for a special sequence and complex post-processing software. Therefore, the PCAT thickness index is an ideal prognostic indicator.

In this study, the MACE was observed in 19.18% of patients. The similar result is also appeared in recent study from Zhang et al. (28), 1-year follow-up MACE in STEMI patients was 20.4%. However, the incidence of MACE was slightly higher than others. The limited number of cases included in our study and regional differences may be one of the main reasons (29). The wide definition of MACE also increased the incidence, as in this study, patients with heart failure hospitalization were included, accounting for 42%. In addition, more than 75% of patients in this study had dyslipidemia, and 83.27% of patients had pain-to-balloon time more than 120 min, which could lead to a poor prognosis (30, 31).

This study has several limitations. First, the retrospective and observational cohort design of the study makes it challenging to derive causality. Second, PCAT inflammation can be caused by percutaneous endothelium injury during endovascular angioplasty (32). It is difficult to estimate the effect of this procedure on the inflammation of PCAT. However, all the PCAT measurements were taken at different locations; the observed effect of PCAT on MACE could not be explained by the procedure-associated inflammation of PCAT alone. Third, only PCAT thickness was measured in this study. Therefore, the relationship between PCAT thickness and EAT volume needs to be studied further. However, a previous study by Alam et al. showed that the thickness of EAT can reflect myocardial microvascular dysfunction more than the volume of EAT (33). Finally, we used the multivariate analysis method to calculate the 1-year MACE prediction model including PCAT. As the model was obtained from a small sample, its validity needs to be verified further.

CONCLUSION

Patients with MACE have more significant increase in PCAT thickness at SIVG than without MACE after STEMI. PCAT thickness index at the SIVG could possibly be a strong independent predictor of MACE in revascularized patients with STEMI. Compared with standard model based on clinical and CMR parameters, the updated model including SIVGi has significantly improved predictive power for 1-year MACE after STEMI.

DATA AVAILABILITY STATEMENT

The original contributions presented in the study are included in the article/**Supplementary Material**, further inquiries can be directed to the corresponding author.

ETHICS STATEMENT

The studies involving human participants were reviewed and approved by Shengjing Hospital of China Medical University Research Ethics Committee. Written informed consent for participation was not required for this study in accordance with the national legislation and the institutional requirements.

AUTHOR CONTRIBUTIONS

YM, YH, and QM participated in the study design. XW, TY, YD, and JS participated in data collection. GL performed the statistical analysis. YM drafted the article. All authors contributed to the article and approved the submitted version.

FUNDING

This study has received funding by the National Natural Science Foundation of China (Grant Nos. 81901741 and 82071920), the Key Research and Development Plan of Liaoning Province (No. 2020JH2/10300037), and the Talent Project in the Shengjing Hospital of China Medical University.

ACKNOWLEDGMENTS

We thank all of the investigators and patients who participated in this project.

SUPPLEMENTARY MATERIAL

The Supplementary Material for this article can be found online at: https://www.frontiersin.org/articles/10.3389/fcvm.2022.781402/full#supplementary-material

REFERENCES

1. Roe MT, Li QH, Bhatt DL, Bittner VA, Diaz R, Goodman SG, et al. Risk Categorization Using New American College of Cardiology/American Heart Association Guidelines for Cholesterol Management and Its Relation to Alirocumab Treatment Following Acute Coronary Syndromes. *Circulation.* (2019) 140:1578–89. doi: 10.1161/CIRCULATIONAHA.119.042551
2. Eitel I, Stiermaier T, Lange T, Rommel KP, Koschalka A, Kowallick JT, et al. Cardiac magnetic resonance myocardial feature tracking for optimized prediction of cardiovascular events following myocardial infarction. *JACC Cardiovasc Imaging.* (2018) 11:1433–44. doi: 10.1016/j.jcmg.2017.11.034
3. Roffi M, Patrono C, Collet JP, Mueller C, Valgimigli M, Andreotti F, et al. 2015 ESC Guidelines for the management of acute coronary syndromes in patients presenting without persistent ST-segment elevation: Task Force for the Management of Acute Coronary Syndromes in Patients Presenting without Persistent ST-Segment Elevation of the European Society of Cardiology (ESC). *Eur Heart J.* (2016) 37:267–315. doi: 10.1093/eurheartj/ehv320
4. Steg PG, James SK, Gersh BJ. 2012 ESC STEMI guidelines and reperfusion therapy: Evidence-based recommendations, ensuring optimal patient management. *Heart.* (2013) 99:1156–7. doi: 10.1136/heartjnl-2013-304498
5. Hansson GK, Libby P, Tabas I. Inflammation and plaque vulnerability. *J Intern Med.* (2015) 278:483–93. doi: 10.1111/joim.12406
6. Ridker PM, Everett BM, Thuren T, MacFadyen JG, Chang WH, Ballantyne C, et al. Antiinflammatory Therapy with Canakinumab for Atherosclerotic Disease. *N Engl J Med.* (2017) 377:1119–31. doi: 10.1056/NEJMoa1707914
7. Homsi R, Sprinkart AM, Gieseke J, Yuecel S, Meier-Schroers M, Luetkens J, et al. 3D-Dixon cardiac magnetic resonance detects an increased epicardial fat volume in hypertensive men with myocardial infarction. *Eur J Radiol.* (2016) 85:936–42. doi: 10.1016/j.ejrad.2016.02.016
8. Kim HM, Kim KJ, Lee HJ Yu HT, Moon JH, Kang ES, et al. Epicardial adipose tissue thickness is an indicator for coronary artery stenosis in asymptomatic type 2 diabetic patients: its assessment by cardiac magnetic resonance. *Cardiovasc Diabetol.* (2012) 11:83. doi: 10.1186/1475-2840-11-83
9. Horckmans M, Bianchini M, Santovito D, Megens RTA, Springael JY, Negri I, et al. Pericardial Adipose Tissue Regulates Granulopoiesis, Fibrosis, and Cardiac Function After Myocardial Infarction. *Circulation.* (2018) 137:948–60. doi: 10.1161/CIRCULATIONAHA.117.028833
10. Oikonomou EK, Desai MY, Marwan M, Kotanidis CP, Antonopoulos AS, Schottlander D, et al. Perivascular Fat Attenuation Index Stratifies Cardiac Risk Associated With High-Risk Plaques in the CRISP-CT Study. *J Am Coll Cardiol.* (2020) 76:755–7. doi: 10.1016/j.jacc.2020.05.078
11. Oikonomou EK, Marwan M, Desai MY, Mancio J, Alashi A, Hutt Centeno E, et al. Non-invasive detection of coronary inflammation using computed

tomography and prediction of residual cardiovascular risk (the CRISP CT study): a post-hoc analysis of prospective outcome data. *Lancet.* (2018) 392:929–39. doi: 10.1016/S0140-6736(18)31114-0
12. O'Gara PT, Kushner FG, Ascheim DD, Casey DE Jr, Chung MK, de Lemos JA, et al. 2013 ACCF/AHA guideline for the management of ST-elevation myocardial infarction: a report of the American College of Cardiology Foundation/American Heart Association Task Force on Practice Guidelines. *J Am Coll Cardiol.* (2013) 61:e78–e140. doi: 10.1016/j.jacc.2012.11.019
13. Toya T, Corban MT, Imamura K, Bois JP, Gulati R, Oh JK, et al. Coronary perivascular epicardial adipose tissue and major adverse cardiovascular events after ST segment-elevation myocardial infarction. *Atherosclerosis.* (2020) 302:27–35. doi: 10.1016/j.atherosclerosis.2020.04.012
14. Ma Q, Ma Y, Wang X, Li S, Yu T, Duan W, et al. Circulating miR-1 as a potential predictor of left ventricular remodeling following acute ST-segment myocardial infarction using cardiac magnetic resonance. *Quant Imaging Med Surg.* (2020) 10:1490–503. doi: 10.21037/qims-19-829
15. Daghir-Wojtkowiak E, Wiczling P, Bocian S, Kubik Ł, Kośliński P, Buszewski B, et al. Least absolute shrinkage and selection operator and dimensionality reduction techniques in quantitative structure retention relationship modeling of retention in hydrophilic interaction liquid chromatography. *J Chromatogr A.* (2015) 1403:54–62. doi: 10.1016/j.chroma.2015.05.025
16. Thomas LE, O'Brien EC, Piccini JP, D'Agostino RB, Pencina MJ. Application of net reclassification index to non-nested and point-based risk prediction models: a review. *Eur Heart J.* (2019) 40:1880–7. doi: 10.1093/eurheartj/ehy345
17. Li G, Shi C, Li T, Ouyang N, Guo X, Chen Y, et al. A nomogram integrating non-ECG factors with ECG to screen left ventricular hypertrophy among hypertensive patients from northern China. *J Hypertension.* (2021) 40:264–273. doi: 10.1097/HJH.0000000000003003
18. Fitzgibbons TP, Czech MP. Epicardial and perivascular adipose tissues and their influence on cardiovascular disease: basic mechanisms and clinical associations. *J Am Heart Assoc.* (2014) 3:e000582. doi: 10.1161/JAHA.113.000582
19. Siegel-Axel DI, Häring HU. Perivascular adipose tissue: an unique fat compartment relevant for the cardiometabolic syndrome. *Rev Endocr Metab Disord.* (2016) 17:51–60. doi: 10.1007/s11154-016-9346-3
20. Iacobellis G, Bianco AC. Epicardial adipose tissue: emerging physiological, pathophysiological and clinical features. *Trends Endocrinol Metab.* (2011) 22:450–7. doi: 10.1016/j.tem.2011.07.003
21. Guzik TJ, Skiba DS, Touyz RM, Harrison DG. The role of infiltrating immune cells in dysfunctional adipose tissue. *Cardiovasc Res.* (2017) 113:1009–23. doi: 10.1093/cvr/cvx108
22. Vilahur G, Ben-Aicha S, Badimon L. New insights into the role of adipose tissue in thrombosis. *Cardiovasc Res.* (2017) 113:1046–54. doi: 10.1093/cvr/cvx086
23. Victorio JA, Clerici SP, Palacios R, Alonso MJ, Vassallo DV, Jaffe IZ, et al. Spironolactone prevents endothelial nitric oxide synthase uncoupling and vascular dysfunction induced by β-adrenergic overstimulation: role of perivascular adipose tissue. *Hypertension.* (2016) 68:726–35. doi: 10.1161/HYPERTENSIONAHA.116.07911
24. Xu J, Lu X, Shi GP. Vasa vasorum in atherosclerosis and clinical significance. *Int J Mol Sci.* (2015) 16:11574–608. doi: 10.3390/ijms160511574
25. Morales-Portano JD, Peraza-Zaldivar JÁ, Suárez-Cuenca JA, Aceves-Millán R, Amezcua-Gómez L, Ixcamparij-Rosales CH, et al. Echocardiographic measurements of epicardial adipose tissue and comparative ability to predict adverse cardiovascular outcomes in patients with coronary artery disease. *Int J Cardiovasc Imaging.* (2018) 34:1429–37. doi: 10.1007/s10554-018-1360-y
26. Zencirci AE, Zencirci E, Degirmencioglu A, Erdem A, Karakuş G, Özden K, et al. Predictive Value of the No-Reflow Phenomenon and Epicardial Adipose Tissue for Clinical Outcomes After Primary Percutaneous Coronary Intervention. *Hellenic J Cardiol.* (2015) 56:311–319.
27. Liang KW, Tsai IC, Lee WJ, Lin SY, Lee WL, Lee IT, et al. Correlation between reduction of superior interventricular groove epicardial fat thickness and improvement of insulin resistance after weight loss in obese men. *Diabetol Metab Syndr.* (2014) 6:115. doi: 10.1186/1758-5996-6-115
28. Zhang AAY, Chew NWS, Ng CH, Phua K, Aye YN, Mai A, et al. Post-ST-Segment Elevation Myocardial Infarction Follow-Up Care During the COVID-19 Pandemic and the Possible Benefit of Telemedicine: an observational study. *Front Cardiovasc Med.* (2021) 8:755822. doi: 10.3389/fcvm.2021.755822
29. Yu L, Wang T, Bai H, Zhu W, Li Y, Wu J. et al. Association between cytochrome P450 2C19 polymorphism and clinical outcomes in clopidogrel-treated Uygur population with acute coronary syndrome: a retrospective study. *BMC Cardiovasc Disord.* (2021) 21:391. doi: 10.1186/s12872-021-02201-4
30. Simard T, Jung RG, Di Santo P, Harnett DT, Abdel-Razek O, Ramirez FD, et al. Modifiable risk factors and residual risk following coronary revascularization: insights from a regionalized dedicated follow-up clinic. *Mayo Clin Proc Innov Qual Outcomes.* (2021) 5:1138–52. doi: 10.1016/j.mayocpiqo.2021.09.001
31. Zahler D, Rozenfeld KL, Pasternak Y, Itach T, Lupu L, Banai S, et al. Relation of Pain-to-Balloon Time and Mortality in Patients With ST-Segment Elevation Myocardial Infarction Undergoing Primary Percutaneous Coronary Intervention. *Am J Cardiol.* (2022) 163:38–42. doi: 10.1016/j.amjcard.2021.09.039
32. Takaoka M, Suzuki H, Shioda S, Sekikawa K, Saito Y, Nagai R, et al. Endovascular injury induces rapid phenotypic changes in perivascular adipose tissue. *Arterioscler Thromb Vasc Biol.* (2010) 30:1576–82. doi: 10.1161/ATVBAHA.110.207175
33. Alam MS, Green R, de Kemp R, Beanlands RS, Chow BJ. Epicardial adipose tissue thickness as a predictor of impaired microvascular function in patients with non-obstructive coronary artery disease. *J Nucl Cardiol.* (2013) 20:804–12. doi: 10.1007/s12350-013-9739-6

Conflict of Interest: The authors declare that the research was conducted in the absence of any commercial or financial relationships that could be construed as a potential conflict of interest.

frontiers in Cardiovascular Medicine

ORIGINAL RESEARCH
published: 28 March 2022
doi: 10.3389/fcvm.2022.763073

Surgical Restoration of Antero-Apical Left Ventricular Aneurysms: Cardiac Computed Tomography for Therapy Planning

Natalia Solowjowa[1], *Olena Nemchyna*[1], *Yuriy Hrytsyna*[1], *Alexander Meyer*[1,2], *Felix Hennig*[1,3], *Volkmar Falk*[1,2,3,4] *and Christoph Knosalla*[1,2,3]*

[1] Department of Cardiothoracic and Vascular Surgery, German Heart Center Berlin, Berlin, Germany, [2] DZHK (German Centre for Cardiovascular Research), Partner Site Berlin, Berlin, Germany, [3] Charité – Universitätsmedizin Berlin, Berlin, Germany, [4] Eidgenössische Technische Hochschule Zürich, Department of Health Sciences and Technology, Translational Cardiovascular Technology, Zurich, Switzerland

OPEN ACCESS

Edited by:
Zahra K. Motamed,
McMaster University, Canada

Reviewed by:
Filippo Cademartiri,
Gabriele Monasterio Tuscany Foundation (CNR), Italy
Patrick Klein,
St. Antonius Hospital, Netherlands

***Correspondence:**
Christoph Knosalla
knosalla@dhzb.de

Specialty section:
This article was submitted to Cardiovascular Imaging, a section of the journal Frontiers in Cardiovascular Medicine

Received: 23 August 2021
Accepted: 21 February 2022
Published: 28 March 2022

Citation:
Solowjowa N, Nemchyna O, Hrytsyna Y, Meyer A, Hennig F, Falk V and Knosalla C (2022) Surgical Restoration of Antero-Apical Left Ventricular Aneurysms: Cardiac Computed Tomography for Therapy Planning. Front. Cardiovasc. Med. 9:763073. doi: 10.3389/fcvm.2022.763073

Background: Surgical ventricular restoration (SVR) leads to functional improvement by volume reduction and restoration of left ventricular (LV) geometry. Our purpose was to refine the planning for SVR using cardiac computed tomography (CCT).

Methods: The possibility to anticipate the postoperative residual LV volume was assessed using CCT in 205 patients undergoing SVR combined with coronary artery bypass grafting (77%), mitral valve repair/replacement (19%) and LV thrombectomy (19%). The potential of CCT to guide the procedure was evaluated. Additionally, the predictive value of CCT characteristics on survival was addressed.

Results: 30-day, 1- and 5-year survival was 92.6, 82.7, and 72.1%, respectively, with a marked reduction of NYHA class III-IV quota after surgery (95.1% vs. 20.5% in the follow-up). Both pre- and postoperative LV end-systolic volume index (LVESVI) were predictive of all defined endpoints according to the following tertiles: preoperative: <74 ml/m², 74–114 ml/m² and >114 ml/m²; postoperative: <58 ml/m², 58–82 ml/m² and >82 ml/m². On average, a 50 ml/m² increase of preoperative LVESVI was associated with a 35% higher hazard of death ($p = 0.043$). Aneurysms limited to seven antero-apical segments (1–7) were associated with a lower death risk ($n = 60$, HR 0.52, CI 0.28–0.96, $p = 0.038$). LVESVI predicted by CCT was found to correlate significantly with effectively achieved LVESVI ($r = 0.87$ and $r = 0.88$, respectively, $p < 0.0001$).

Conclusions: CCT-guided SVR can be performed with good mid-term survival and significant improvement in HF severity. CCT-based assessment of achievable postoperative LV volume helps estimate the probability of therapeutic success in individual patients.

Keywords: heart failure, myocardial infarction, aneurysm, imaging—computed tomography, cardiac computed tomography, surgical ventricular reconstruction

INTRODUCTION

Chronic ischemic heart failure (HF) after myocardial infarction (MI) is an important indicator of poor prognosis despite advances in drug and device therapy (8). The development of therapeutic concepts addressing ischemic left ventricular (LV) remodeling due to scar formation is essential to improve survival and amelioration of HF symptoms in this patient cohort.

Surgical ventricular restoration (SVR) of anterior LV aneurysms (9–11) is an established treatment option for LV remodeling after MI. It can be performed, if required, in combination with revascularization and mitral valve (MV) repair/replacement (1, 12, 13). Despite disillusioning reports from the STICH trial (2) with its known methodological limitations (14), other studies report excellent outcomes for acute reverse remodeling following SVR. Essential factors of clinical success are appropriate patient selection (15, 16) combined with adequate surgical volume reduction and reshaping of the LV (3, 17).

The analysis of LV volume, scar localization and extension as well as the amount of geometrical distortion play a key role in the preoperative assessment for SVR. Image guidance and a tailored surgical procedure are of paramount importance for a successful SVR. With its high spatial resolution of up to 0.4 mm and an acceptable time resolution of up to 75 ms, cardiac computed tomography (CCT) enables the analysis of a primarily acquired three-dimensional data set, the detailed examination of the cardiac anatomy and the assessment of the functional and geometrical remodeling of the cardiac chambers, based on exact true volume detection, with very high accuracy (4). Advanced CCT software tools allow for analyzing LV segmental wall motion abnormalities (WMA) and estimating the aneurysm volume.

This study aimed to refine surgical planning for SVR and to investigate factors that allow for predicting whether the therapeutic goals (sufficient volume reduction, sufficient residual volume, improved ventricular geometry) can be successfully achieved using the volumetric, geometric and functional tools of CCT. We analyzed our single-center early and mid-term results and the factors determining survival and improvement in HF symptoms after CCT-guided SVR for anterior LV aneurysms.

MATERIALS AND METHODS

Study Design

Using a modified Dor technique in most cases, SVR was performed in patients with severe HF symptoms, well-defined antero-septal LV akinesia or dyskinesia and preserved contractility of residual myocardium after anterior MI. The procedure was combined with coronary revascularization, MV repair or replacement and LV thrombectomy, when indicated. Endpoints were 30-day mortality, death from any cause in the follow-up period, implantation of a LV assist device and heart transplantation.

The diagnosis of LV aneurysm was made by echocardiography or angiography and confirmed by CCT. Echocardiography and CCT were repeated during the first postoperative week. The pre- and postoperative data were analyzed and compared retrospectively. Clinical, demographic and procedural data were retrospectively collected.

Study Population

We retrospectively analyzed the data of 205 consecutive patients with coronary artery disease who underwent SVR for anterior LV aneurysms in our hospital between November 2005 and January 2016. All patients had a previous anterior MI with severe LV systolic dysfunction and symptomatic HF.

Written informed consent for surgery was obtained from all patients or their representatives. The study was performed according to the principles of the Declaration of Helsinki and approved by the ethics committee of the Charité – Universitätsmedizin Berlin (EA2/177/20).

Surgical Technique

All SVR procedures were performed through a median sternotomy approach under cardiopulmonary bypass (CPB). After coronary artery bypass grafting (CABG), LV repair and MV repair or replacement were performed. Antero-apical SVR was routinely performed using a modified Dor procedure with several Fontan sutures along the aneurysm perimeter without patch application to exclude the aneurysm and restore LV geometry (9). This technique enables the effective exclusion of scarred area, achieving the required target LV volume and reconstruction of the LV apex. Only few patients (12.2%) with specific local findings, for example a ventricular septal defect after a huge antero-apical MI, required a patch repair.

Intraoperative transesophageal echocardiography was routinely performed to assess the adequacy of LV repair. Mitral surgery was performed in patients with echocardiographically proven MR grade $\geq$2. All surgeons had access to the complete preoperative CCT assessment.

MSCT Measurements

LV Volumetric Study

CCT measurements have been extensively described previously (5). The data were obtained and analyzed in a single lab by use of the uniform protocols. In brief, contrast-enhanced ECG-triggered cardiac scanning was performed using a first- or second-generation dual-source scanner (Somatom Definition, Somatom Definition Flash, Siemens AG, Erlangen, Germany). To study the anatomy and geometry of the LV, the data set was reconstructed with a slice thickness of 0.75 mm and reconstruction increment of 0.4 mm, from early systole to end diastole in steps of 10%. LV volumes and systolic function were assessed using a dedicated CCT evaluation software (syngo.via Cardiac Function, Siemens AG) and applying a 3D threshold segmentation algorithm. The timepoints of the end diastole and end systole were estimated automatically and adjusted by the investigator if required.

LV end-diastolic and end-systolic volume (LVEDV, LVESV) were obtained (**Figure 1**) and then indexed to body surface area (LVEDVI/LVESVI). Stroke volume (SV) was calculated by subtracting LVESV from LVEDV; left ventricular ejection fraction (LVEF) was obtained by dividing SV by LVEDV; cardiac output (CO) was calculated as a product of SV and cardiac rate.

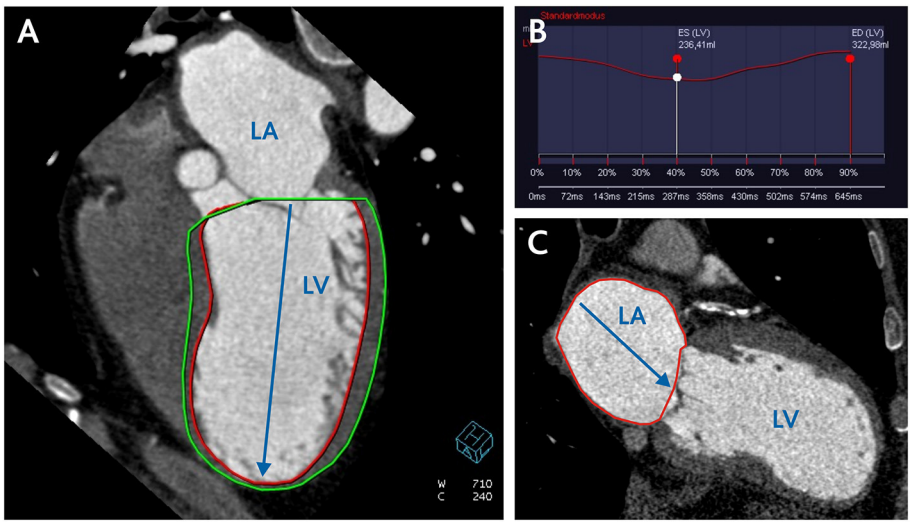

FIGURE 1 | CCT assessment of left ventricular and left atrial volume. **(A)** CCT reconstruction of four-chamber view for semi-automatic measurement of LV volume and calculation of LV volumetric sphericity index (LVSI) according to the formula LVSI = LV Volume/LV long axis $3 \times \pi/6$. **(B)** filling curve of LV. **(C)** two-chamber view for measurement of LA area and calculation of LA volume according to the formula $(0.85 \times A1 \times A2)/L$. LV, left ventricle; LA, left atrium; A1 and A2, LA area in two- and four-chamber view; L, length of the left atrium.

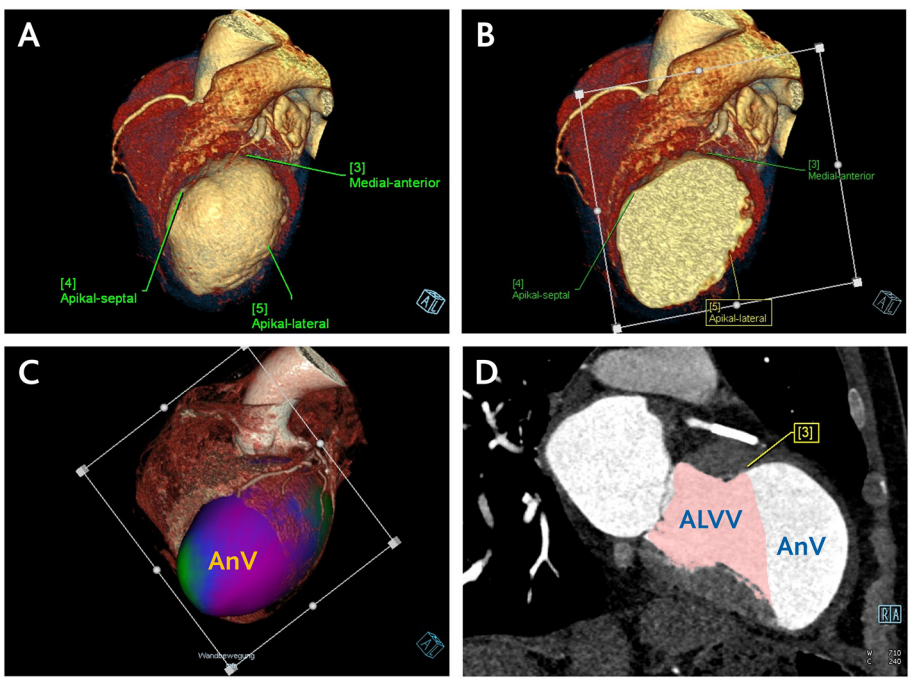

FIGURE 2 | Central Picture. CCT assessment of anticipated residual LV volume and aneurysm volume. **(A)** Definition of three landmarks on the borders of scarred to intact LV myocardium. **(B)** Positioning of the plane determined by the defined landmarks. **(C)** Separation of the aneurysm volume in a three-dimensional data set using the defined plane in the systole and diastole. **(D)** Estimation of the anticipated postoperative LV volume by means of manually corrected LV borders along the defined plane using the same CCT volumetric software tool. Subsequent calculation of the aneurysm volume through subtraction of anticipated from original LV volume. ALVV, anticipated left ventricular volume; AnV, aneurysm volume.

Assessment of the Anticipated Residual LV Volume and Aneurysm Volume

To separate the aneurysm volume in diastole and systole, a plane determined by three landmarks on the borders of scarred to intact LV myocardium (antero-septal, lateral and inferior) was used. The residual volumes were then assessed using the same CCT evaluation software tool (**Figure 2**). This enabled the estimation of the anticipated postoperative

LVEDV/LVEDVI and LVESV/LVESVI. Aneurysm volume (AnV/AnVI) was then calculated as the subtraction of anticipated from original volumes.

Analysis of LV Segmental WMA

Local WMA were estimated semiquantitatively using a 17-segment model with separate assessment of papillary muscles. Akinetic or dyskinetic segments involved in an aneurysm or scar formation of other localizations were detected.

Automated cluster analysis was performed to establish the different scar patterns. The identified clusters were then tested for their influence on survival after SVR.

Patients were divided into defined subgroups according to their LVA localization and extension: antero-apical LVA (segments 7, 8, 13, 14, 15, 16, 17)—subgroup1; antero-apical and basal septal or basal anterior LVA (plus segments 1 or 9)—subgroup 2; antero-apical LVA and additional scar of any other localization—subgroup 3.

Morphological characteristics of the aneurysm in terms of myocardial disruption, apposition of thrombotic masses and pericardial effusion were also evaluated.

TABLE 1 | Baseline patient characteristics and perioperative data.

Variable	All patients ($n = 205$)
Mean age, y	63.4 ± 11.2
Male sex	151 (73.6%)
Diabetes mellitus	62 (30.2%)
Arterial hypertension	140 (68.3%)
Hypercholesterolemia	139 (67.8%)
Peripheral artery disease	20 (9.7%)
Renal failure	32 (15.6%)
Atrial fibrillation	23 (11.2%)
NYHA class	
II	10 (4.9%)
III	179 (87.3%)
IV	16 (7.8%)
Median LV EF (%, Echo) (range)	30 (11–70)
Mitral regurgitation ≥2+	36 (17.6%)
Coronary lesion	
Single vessel	34 (16.6%)
Double vessel	43 (21%)
Triple vessel	112 (54.6%)
No lesion	16 (7.8%)
Perioperative data	
Concomitant CABG	158 (77.1%)
Median no. of grafts performed (range)	2 (0–5)
Concomitant MV repair/replacement	39 (35/4) (19%)
Linear repair	180 (87.8%)
Patch repair	25 (12.2%)
LV thrombectomy	39 (19%)
Median CBP time, min (range)	131 (40–693)
Mean cross-clamp time, min	79.7 ± 35
IABP support	38 (18.5%)
Switch to LVAD	7 (3.4%)
Postoperative complications	
Reexploration for bleeding	15 (7.3%)
Stroke	1 (0.4%)
Sepsis	8 (3.9%)
Renal failure	6 (2.9%)
Hospital (30-day) mortality	15 (7.3%)

LV Volumetric Sphericity Index

The systolic and diastolic LV volumetric sphericity index (LVSI) was calculated on the basis of end-diastolic and end-systolic LV volume and LV long axis length in two-chamber view according to the empiric formula (7) (**Figure 1**),

$$\text{LVSI} = \text{LV volume}/\text{LV long axis}^3 \times \pi/6.$$

Left Atrium Volume

The left atrium (LA) volume was calculated at the end systole on the basis of planimetric measured LA area in two-chamber view (A1) and four-chamber view (A2) and LA length (L) according to the simplified empiric formula (6) (**Figure 1**),

$$(0.85 \times A1 \times A2)/L.$$

Follow-Up Data Collection

Follow-up was performed in 94.6% of the cases, either during a routine clinical evaluation in our outpatient department or by telephone contact using the short form Health Survey (SF-12) (18). In patients, in whom the follow-up was not possible, national death registry check was performed. Mean follow-up time in the overall population was 1,600 ± 1,106-days. Median follow-up time was 1,528-days.

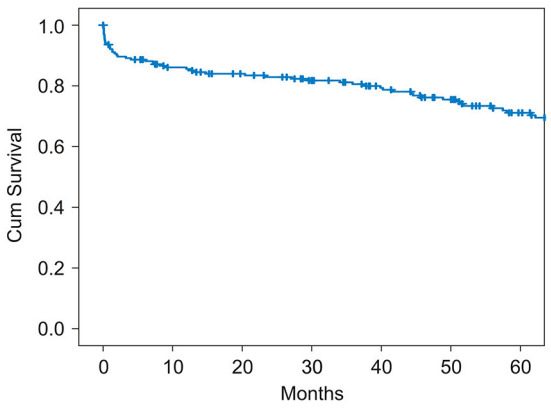

Months	0	12	24	36	48	60
Patients at risk	205	165	150	134	113	91

FIGURE 3 | Kaplan-Meier survival curve for all-cause mortality for the overall population.

Statistical Analysis

Continuous variables are presented as mean ± SD. Parametric and non-parametric tests were used where required. For parametric variables, means were compared with the paired, two-tailed student *t*-test. Categorical variables are presented as numbers with percentages and compared using chi-square tests. Actuarial survival curves were produced using the Kaplan-Meier analysis with a long-rank test. For the evaluation of survival differences dependent on LV volumetric parameters, the patient population was subgrouped according to tertiles of LVESVI with further application of survival analysis. A cluster analysis of scarred ventricle segments detected in CCT was performed using nearest neighbor algorithm to reveal patterns of segmental wall motion abnormalities associated with better or worse survival.

Cox proportional hazard regression modeling was applied, and both univariable and multivariable hazard ratios were calculated to assess independent predictive factors of combined endpoint of all-cause mortality, implantation of a LV assist device and heart transplantation. A p-value <0.05 was considered statistically significant. The data were analyzed with SPSS 23 (SPSS, Chicago, IL, USA).

RESULTS

Preoperative patient characteristics are presented in **Table 1**. There were 10 (4.9%) patients in New York Heart Association (NYHA) class II of HF, 179 (87.3%) in class III and 16 in class IV (7.8%); the mean NYHA class was 3.02 ± 0.35. The median preoperative LVEF, estimated via echocardiography, was 30% (11–70). 36 (17.6%) patients had a concomitant MR of grade ≥2.

A modified Dor procedure without patch application was performed in 180 patients (87.8%). while 25 patients underwent SVR with patch. One hundred and fifty eight patients (77.1%) had associated myocardial revascularization. Thirty nine patients (19%) underwent concomitant MV surgery (MV repair in 35 and MV replacement in four patients). LV thrombectomy was performed in 39 patients (19%).

Fifteen patients (7.3%) died in hospital within 30-days due to multiorgan failure ($n = 9$), septic shock ($n = 4$), electromechanical dissociation ($n = 1$) or stroke ($n = 1$). The operative and postoperative data are summarized in **Table 1**.

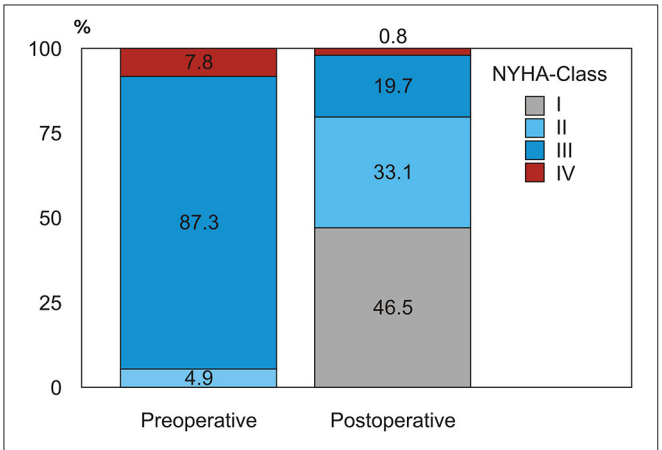

FIGURE 4 | Redistribution of NYHA functional class before and after SVR in the surviving population.

TABLE 2 | Multivariate logistic regression analysis for an adverse outcome (all-cause death, ventricular assist device or heart transplantation).

Variable	Hazard ratio	95% Confidence interval	*p-Value*
Preoperative LVEDD, mm	1.035	1.008–1.063	0.011
LAVI, ml/m^2	1.023	1.008–1.038	0.003
Age at operation, y	1.032	1.002–1.063	0.039
Diabetes mellitus	2.223	1.27–3.9	0.039
Renal failure	2.3	1.2–4.4	0.012

LVEDD, LV end diastolic diameter; LAVI, left atrium volume index.

Early and Late Outcomes

The median survival period was 51.1 months (range between 1-day and 121.4 months) and the mean survival time was 51.6 ± 37.8 months. Overall, 30-day mortality was 7.3% ($n = 15$). One- and 5-year survival was 82.7 and 72.1%, respectively (**Figure 3**).

NYHA Class Change in Survivors

During follow-up we observed a remarkable improvement in HF symptoms after SVR, with a positive redistribution of NYHA class in the whole population in the sense of a strong reduction of NYHA class III-IV quota after surgery in survivors (from 95.1% preoperatively to 20.5% in the early follow-up, $p < 0.001$) (**Figure 4**).

Predictive Factors of 30-Day Mortality

Hospital and 30-day mortality were identical in our series. Thirteen of the 15 patients who died in hospital underwent combined SVR and CABG surgery, six underwent combined SVR, CABG and valvular surgery, and 10 required an intra-aortic balloon pump (IABP). Univariate logistic regression revealed factors potentially predictive of 30-day mortality: long CPB time and cross-clamp time, requirement of IABP or other temporary mechanical circulatory support systems, urgent surgery, postoperative sepsis and renal failure contributed to the higher 30-day mortality rate (**Supplementary Table 1**). Multivariate logistic regression showed that CPB time ($p < 0.001$) and postoperative LVEF ($p < 0.001$) were independent predictive factors of 30-day mortality. CPB time longer than 163 min was associated with an adverse outcome (sensitivity 0.765, specificity 0.789, AUC=0.890). Severity of preoperative HF, preoperative LVEF and CCT LV volumetric parameters did not play a substantial role in 30-day mortality.

Late Mortality and Survival Determinants

Univariate logistic regression showed a potential predictive role in all-cause 5-year mortality of such factors as diabetes mellitus, peripheral artery disease, renal failure and atrial fibrillation. Preoperative MR ≥2+, preoperative LAVI, SVI, CI and postoperative LVEDVI, LVESVI and LAVI also had a potential predictive role in all-cause mortality (**Supplementary Table 2**). The multivariate regression analysis revealed that preoperative

LVEDD and preoperative LAVI as well as patient age, presence of diabetes mellitus and renal failure were independent significant predictive factors of all adverse outcomes (**Table 2**).

There was no difference in survival between men and women as shown by the Kaplan-Meier analysis ($p = 0.593$) and by the univariate regression analysis (male sex $HR = 0.87$; 95%CI 0.52–1.45).

Changes in LV Geometry and Function

The changes in LV geometric and functional parameters measured by echocardiography and CCT after SVR are presented in **Table 3**.

TABLE 3 | LV dimensions measured by echocardiography and in CCT before and after SVR.

Parameter	Preoperative	Postoperative	*p* Value
Echocardiography (*n* = 205)			
LVEDD, mm	60.1 ± 9.95	55.1 ± 8.9	<0.001
LVEF, %	32.3 ± 10.6	39.5 ± 10.9	<0.001
MR, whole population	1.02 ± 0.8	0.36 ± 0.45	<0.001
MR, without MV surgery	0.79 ± 0.56	0.37 ± 0.44	<0.03
CCT (*n* = 160)			
LVEDVI, ml/m^2	146 ± 52.4	97.3 ± 35.6	<0.001
LVESVI, ml/m^2	100 ± 49.6	59.2 ± 33.4	<0.001
LAVI, ml/m^2	60.7 ± 19.2	50.6 ± 18.7	<0.001
SVI, ml/m^2	45.3 ± 11.7	37.6 ± 10.1	<0.001
LVEF, %	34.1 ± 12.1	43.1 ± 13.9	<0.001
CI, l/min/m^2	3.08 ± 0.79	3.29 ± 0.75	0.022
LVSI, diastolic	0.40 ± 0.10	0.52 ± 0.18	<0.001
LVSI, systolic	0.31 ± 0.10	0.36 ± 0.17	<0.001

LVEDD, LV end diastolic diameter; LVEF, LV ejection fraction; MR, mitral regurgitation; LVEDVI, LVESVI, LV end diastolic and end systolic volume index; LAVI, left atrium volume index; SVI, stroke volume index; CI, cardiac index; LVSI, LV sphericity index.

LV volumetric parameters measured in CCT in 160 patients were significantly reduced after SVR: LVEDVI decreased about 33.0 ± 17.0% ($p < 0.001$) and LVESVI about 40.8 ± 21.5% ($p < 0.001$). LVEF measured in CCT increased significantly from 34.1 ± 12.1% to 43.1 ± 13.9% ($p < 0.001$) after SVR. The diastolic LV SI increased from 0.40 ± 0.10 to 0.52 ± 0.18 ($p < 0.001$); the systolic LV SI increased from 0.31 ± 0.10 to 0.36 ± 0.17 ($p < 0.001$).

Survival Stratified by Preoperative LVESVI and Postoperative LVESVI

Survival stratification according to tertiles of preoperative LVESVI revealed a significantly higher survival rate in the lower tertile group (≤74 ml/m^2) than in the groups with a LVESVI of 74–114 ml/m^2 and ≥114 ml/m^2 ($p = 0.048$). Five-year survival in the group with LVESVI ≤74 ml/m^2 was 83.4% compared to 67.3 and 64.3% in the two other groups. An average 50 ml increase of preoperative LVESVI was associated with a 35% increase of the hazard of death ($p = 0.043$) (**Figure 5A**).

Survival stratification according to tertiles of the postoperative LVESVI demonstrated a significant difference in survival between tertiles ($p = 0.016$), with the lowest survival rate of 60.2% in the highest tertile of postoperative LVESVI (>66.2 ml/m²) compared to the survival rates of 84.6 and 85.3% in the middle (41.6–66.2 ml/m²) and lowest (<41.6 ml/m^2) teriles, respectively (**Figure 5B**).

Correlation Between Anticipated and Achieved Residual LV Volume and Estimated Aneurysm Volume

We observed a significant correlation between anticipated and effectively achieved postoperative LVEDV and LVESV ($r = 0.903$ and $r = 0.904$, respectively, $p < 0.0001$), and their indexed values ($r = 0.87$ and $r = 0.88$, respectively, $p < 0.0001$) (**Figure 6**). Anticipated LVEDVI was only 7.2 ± 18.0 ml/m^2

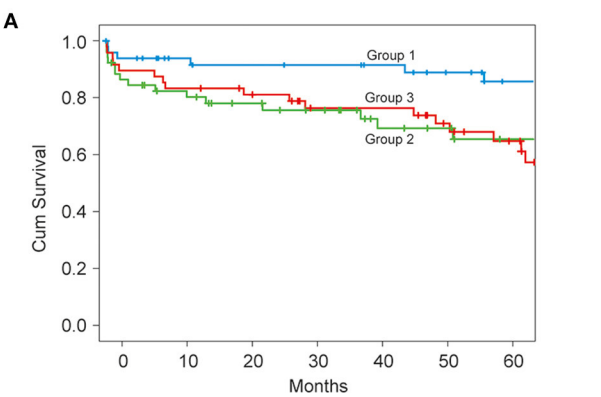

Months	0	12	24	36	48	60
Group 1 < 74 ml/m²	49	40	38	37	32	25
Group 2 - 74-114 ml/m²	52	38	31	26	19	15
Group 3 > 114 ml/m²	48	40	36	30	26	19

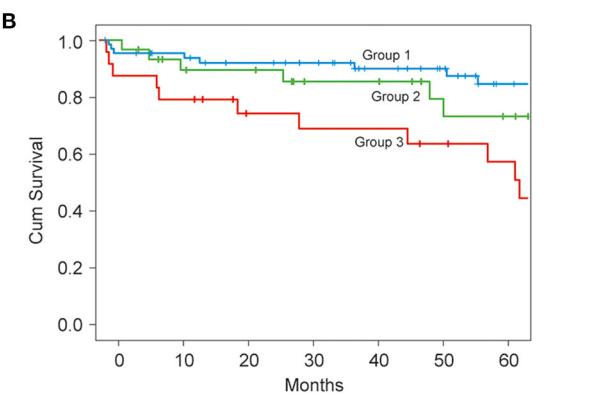

Months	0	12	24	36	48	60
Group 1< 58ml/m²	65	57	52	46	38	27
Group 2 - 58-82 ml/m²	30	24	22	18	14	11
Group 3 > 82 ml/m²	24	19	14	13	11	9

FIGURE 5 | (A) Kaplan-Meier survival curves stratified by preoperative LVESVI. **(B)** Kaplan-Meier survival curves stratified by achieved postoperative LVESVI.

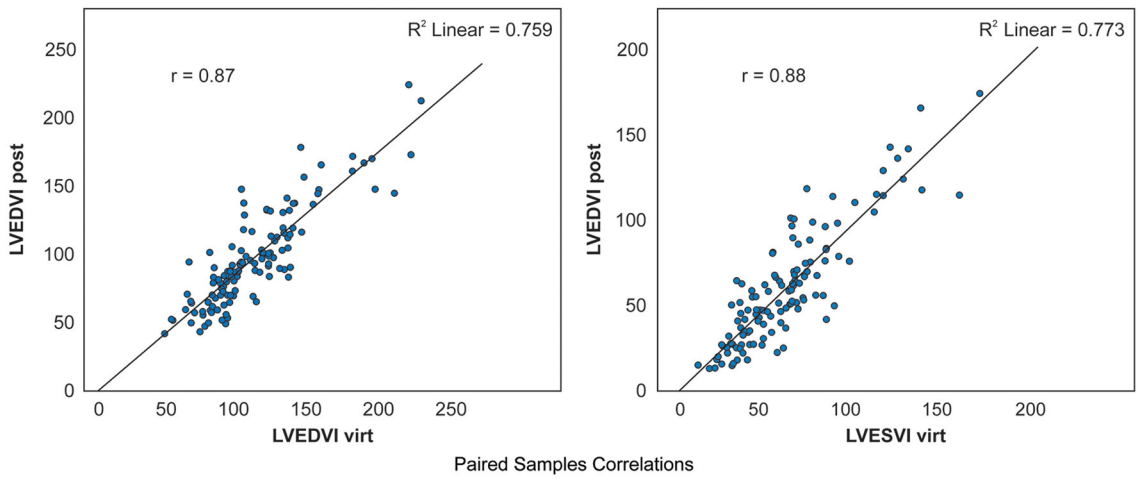

Paired Samples Correlations

		N	Correlation	Sig.
Pair 1	LVEDV virt & LVEDVpost	124	.903	.000
Pair 2	LV ESV virt & LVESVpost	122	.905	.000
Pair 3	LVEDVIvirt & LVEDVIpost	124	.871	.000
Pair 4	LVESVIvirt & LVESVIpost	123	.879	.000

FIGURE 6 | Correlation between anticipated and postoperatively achieved LVEDVI and LVESVI.

TABLE 4 | Difference between anticipated and achieved postoperative LV Volumes.

Parameter	Anticipated	Achieved	Mean difference	*p-Value*
LVEDV, ml	203.3 ± 76.1	190.6 ± 78.5	12.7 ± 34.1	<0.001
LVESV, ml	119.9 ± 63.3	115.1 ± 70.7	4.8 ± 30.2	0.08
LVEDVI, ml/m^2	104.6 ± 34.9	97.4 ± 35.9	7.2 ± 18	<0.001
LVESVI, ml/m^2	61.6 ± 30.3	59.3 ± 33.7	2.3 ± 16.1	0.109

LVEDV, LVESV, LV end diastolic and end systolic volume; LVEDVI, LVESVI, LV end diastolic and end systolic volume index diastolic and systolic.

TABLE 5 | Five-year survival rates in defined subgroups of patients according to their LVA localization and extension.

Group	*N*	5-year Survival
1 Antero-apical LVA (segments 7,8,13,14,15,16,17)	60	84.7 % (71.3–92.1)
2 Antero-apical LVA + segment 1 or 9	9	62.2% (21.3–86.4)
3 Antero-apical LVA + any other segments involved	85	63.7% (50.8–74.1)
2+3 Groups	94	64 % (50.8–74.6)

Group 1—antero-apical LVA (segments 7, 8, 13, 14, 15, 16, 17); Group 2—antero-apical LVA + segment 1 or 9; Group 3—antero-apical LVA + any other segments involved. Bold values represents Group 1, Group 2, Group 3 and Group 2+3 respectively.

higher than achieved LVEDVI ($p = 0.00002$), and anticipated LVESVI was only 2.3 ± 16.1 ml/m^2 higher than achieved LVESVI ($p = 0.109$) (**Table 4**).

Mean estimated diastolic and systolic AnV were 88.5 ± 54.2 ml and 80.5 ± 56.4 ml, respectively. The relation of the estimated AnV to the actual preoperative LVEDV and LVESV was 28.9 ± 11.3% and 37.8 ± 14.7%, respectively. This relation closely matched with the effectively postoperative achieved relation of excluded part of LV volume to the whole LV volume—LVEDV by 33.1 ± 1.6% and LVESV by 41.2 ± 21.7%.

Analysis of LV Segmental WMA

Aneurysms limited to seven antero-apical segments (1–7)—group 1—were associated with a lower death risk ($n = 60$, HR 0.52, CI 0.28–0.96, $p = 0.038$). The Kaplan-Meier analysis showed significantly better survival in these patients compared to all other patients ($p = 0.035$)—group 2 and 3—with a 5-year survival rate of 84.7% (95% CI 71.3–92.1) vs. 64% (95% CI 50.8–74.6) (**Table 5**).

Furthermore, an automated cluster analysis based on the frequency of segment involvement and its impact on survival after SVR allowed for identifying the similar scar pattern (Cluster 1) with a significantly better outcome (**Figure 7**) compared to all other patients with HR 0.491 (0.263–0.916, $p = 0.025$) and a 5-year survival rate of 82.2% vs. 63.7% in all other patients ($p = 0.022$).

Left Atrium Volume

LAVI decreased significantly from 60.7 ± 19.2 ml/m^2 to 50.6 ± 18.7 ml/m^2 ($p < 0.001$). Dividing by tertiles of preoperative LAVI revealed that patients in the lowest tertile (<49.5 ml/m^2) had a lower risk of death than patients in the middle (49.5–67.6 ml/m^2) and in the highest tertile (>67.6 ml/m^2) of LAVI (long rank $p = 0.005$), with a 5-year survival in patients with LAVI<49.5 ml/m^2 of 83.4% compared to the survival rate of patients in the middle and highest tertiles of 71.6 and 60.8%, respectively.

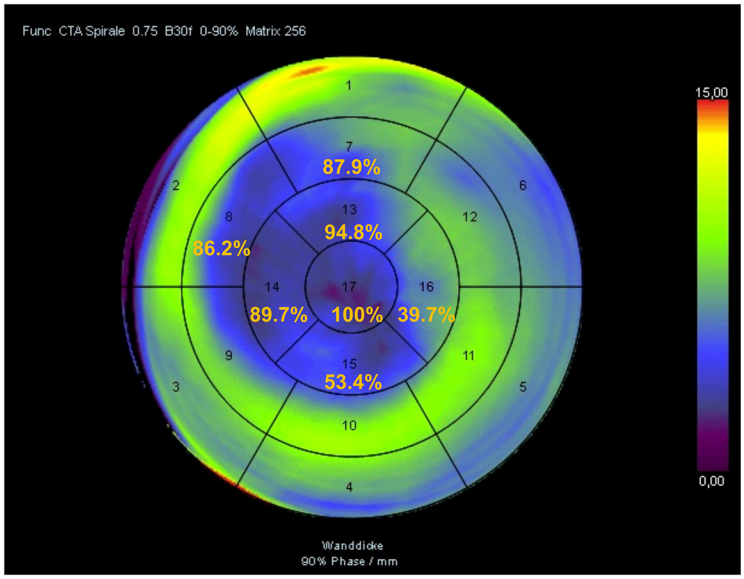

FIGURE 7 | Automated cluster analysis based on the frequency of segment involvement allowed for identifying the scar pattern (Cluster 1) with a significantly better outcome compared to all other patients.

Mitral Regurgitation

MR was reduced after surgery from 1.02 ± 0.80 to 0.36 ± 0.45 ($p < 0.001$) in the whole population and from 0.79 ± 0.56 to 0.37 ± 0.44 ($p < 0.001$) in patients without concomitant MV surgery.

Role of LVSI

Both systolic and diastolic SI increased significantly in all patients after SVR (**Table 3**) due to a substantial shortening of the LV long axis in relation to the LV volume reduction. However, the multivariate regression analysis (χ^2 =1.7, $p = 0.428$) provided no evidence for an effect of pre-operative diastolic SI on survival.

DISCUSSION

This study is based on our experience of SVR performed between 2005 and 2016, since the modified Dor procedure was implemented as a standard technique in our institution.

The main results of the present analysis are that both CCT-derived preoperative and postoperative LVESVI are predictive for mid-term survival. The possibility to predict the volume reduction following SVR through the separation of the aneurysm volume using a commercially available CCT evaluation software tool allows for better therapy planning and patient selection. The CCT-based analysis of local WMA provides additional information for risk assessment: aneurysms limited to seven antero-apical segments were associated with a lower risk of mortality. The follow-up analysis shows a remarkable positive improvement in NYHA class after surgery as evidence for an improvement in HF symptoms.

Diagnostic Testing

Accurate assessment of the LV geometrical distortion, aneurysm localization and extension, and viability of the remaining myocardium is decisive for a successful SVR (19, 20). The most advanced imaging modality with excellent standardized approaches for these purposes is cardiac magnetic resonance imaging (MRI) (19); however, an increasing number of patients with ischemic cardiomyopathy become carriers of implantable devices (in our cohort up to 40%), limiting the applicability of MRI.

Despite excellent spatial and temporal resolution, echocardiography depends highly on exact geometric alignment, patient anatomical characteristics and the operator's skills, and it often has limitations in the visualization of the apical region. Furthermore, 2D echocardiography only allows for calculating the ventricle volume based on the empiric approximated formula, and 3D real-time volume detection is not widespread or sufficiently validated. In this study we complementarily employed echocardiography to evaluate the LV diameters, systolic function and severity of MR. The profound analysis of further echocardiographic data in the represented patient cohort, especially the prognostic role of speckle-tracking echocardiography (LV global longitudinal and basal longitudinal strain), is presented separately (21).

Our reasons to use CCT for SVR planning were the possibility of exact true volume detection and geometrical analysis in primarily acquired three-dimensional data sets combined with a short examination time and lack of technical restrictions even in critical patients. Previous studies (4, 22) demonstrated that CCT is a valuable tool to evaluate LV and MV geometry and function. In our previous study (5) we showed that CCT data enable the precise analysis of LV volume, geometry and local WMA as well as the reliable recognition of aneurysm borders, thrombotic apposition and presence of LV pseudoaneurysm. This study focuses on prognostic important volumetric and functional characteristics and on the validation of the CCT-based separation

of the aneurysm volume from the residual LV volume and thereby on improvement of the therapy targeting, with the further aim to avoid the restrictive residual LV volume.

However, we are well aware that CCT has clear limitations in detecting scar transmurality and viability of the remaining myocardium compared to MRI.

Thirty-Day Mortality

In our series the overall 30-day mortality was 7.3%. Dor et al. (19) found hospital mortality rates of 8.1 and 4.8% in early and late series of patients who underwent SVR. Garatti et al. (23) reported a 30-day mortality of 8.3% in patients after SVR for anterior aneurysm. Jeganathan et al. (13) reported a hospital mortality of 13.3% in patients who underwent combined SVR and MV surgery. Their group identified NYHA class IV symptoms, preoperative atrial fibrillation, previous cardiac surgery and presence of ischemic MR as significant risk factors for increased hospital mortality. In our study, multivariate logistic regression showed that CPB time ($p < 0.001$) and postoperative LV EF ($p < 0.001$) but not the severity of preoperative HF, preoperative LV EF or CCT LV volume were independent predictive factors of 30-day mortality.

Late Mortality and Survival Determinants

In our study population, 1- and 5-year actuarial survival rates were 82.7 and 72.1%, which is comparable to most published studies. A multivariate regression analysis revealed that preoperative LVEDD and LAVI as well as the patient's age, presence of diabetes mellitus and renal failure were independent significant predictive factors of all adverse outcomes (**Table 2**).

Efficient LV volume reduction toward a physiological range of a LVESVI of <60–70 ml/m^2 is essential to improve survival after surgical repair. Di Donato et al. (7) showed that a postoperative LVESVI of >60 ml/m^2 is an independent predictor of mortality. The analysis of the STICH trial data (2) showed that a statistically significant reduction in mortality was achieved only in patients attaining an LVESVI of <70 ml/m^2. In our study group, both the preoperative and the postoperative LVESVI had a strong effect on survival. A cut-off point of ≤74 ml/m^2 for preoperative LVESVI revealed the best 5-year survival rate of 86% (**Figure 5A**). An average 50 ml increase of preoperative LVESVI was associated with a 35% increase of the hazard of death ($p = 0.043$). A postoperative LVESVI of ≥82 ml/m^2 was strongly predictive of all-cause mortality, with a lowest 5-year survival rate of 49% (**Figure 5B**).

The other important task is to avoid the restrictive residual LV volume after surgery. There were five patients with LVESVI<20 ml/m^2 after surgery in our series, only one of them showed no improvement in HF symptoms during follow-up.

In this context, the possibility to predict the volume reduction using CCT volumetric tools is extremely valuable for better therapy planning and appropriate patient selection.

A CCT-based analysis of LV segmental WMA yielded additional valuable findings; it showed that the scar pattern typically involving seven antero-apical segments is associated with a better 5-year survival rate of 82.2% compared to 63.7% in all other patients with more segments involved ($p = 0.022$).

We observed a significant reduction of LAVI as immediate effect of SVR, probably through the improvement in LV diastolic function after SVR and/or in correlation with the reduction of MR, both in the whole population and in patients who underwent SVR only (**Table 2**). Preoperative LAVI was identified as an independent significant predictive factor of all adverse outcomes with a 5-year survival in patients with LAVI< 49.5 ml/m^2 of 83.4%, compared to a survival rate of 71.6 and 60.8% in patients in the middle and highest tertiles, respectively.

In our series both diastolic and systolic LVSI increased immediately after surgery due to a substantial shortening of the LV long axis in relation to LV volume reduction, but it is not clear whether this effect is necessarily negative. In the follow-up study of the STICH trial, Choi et al. (17) also reported a postoperative increase of the SI in the CABG+SVR group and an association of higher baseline SI with poorer postoperative survival both in CABG and CABG+SVR groups. In our series, multivariate proportional hazards regression modeling ($\chi 2 = 1.7$, $p = 0.428$) revealed no evidence for an effect of pre-operative diastolic SI on survival.

Study Limitations

First, the study is subject to the usual limitations inherent to a retrospective analysis of prospectively collected data sets. Second, CCT imaging data were not available in all patients. Third, postoperative CCT data were obtained only several days after surgery and documented the immediate effects of SVR on LV volumes and function. However, they do not reflect the effects of subsequent ventricular reverse remodeling. Fourth, CCT-based assessment of local WMA as semiquantitative detection of akinetic or dyskinetic myocardial segments involved in an aneurysm or scar formation of other localizations is dependent on the operator's skills and only offers rough scar detection. Due to the high radiation burden, we did not consider the use of CCT-based viability assessment. The CCT-based strain analysis has clear limitations because of the low temporal resolution. The analysis of systolic and diastolic LV function, myocardial dyssynergy and viability based on a two-dimensional speckle-tracking echocardiography is not included in this study. Fifth, the provided CCT-based procedure to separate the aneurysm volume using a plane determined by three landmarks on the borders of scarred to intact LV myocardium and subsequent estimation of residual volumes using the commercially available CCT volumetric tool only allows for an approximate estimation of the possible volume reduction and does not incorporate the modeling of the surgical procedure in the sense of the creation of a neoapex.

CONCLUSIONS

The results of this study suggest that CCT-guided SVR can be performed with good mid-term survival and significant relief of HF symptoms due to LV volume reduction, reverse remodeling and functional improvement. The modified Dor procedure is an adequate surgical approach to achieve the therapeutic goals of SVR. CCT as an alternative modality to MRI can deliver relevant data for surgical planning as well

as important predictive parameters for adverse outcome. The provided possibility to predict the achievable volume reduction through the separation of the aneurysm volume using a commercially available CCT volumetric tool allows for better therapy planning and patient selection.

DATA AVAILABILITY STATEMENT

The data analyzed in this study is subject to the following licenses/restrictions: anonymized data. Requests to access these datasets should be directed to Natalia Solowjowa, solowjowa@dhzb.de.

ETHICS STATEMENT

The study was performed according to the principles of the Declaration of Helsinki and approved by the ethics committee of the Charité – Universitätsmedizin Berlin (EA2/177/20). Written informed consent for surgery was obtained from all patients or their representatives.

AUTHOR CONTRIBUTIONS

NS performed the MSCT examinations, designed the study, analyzed and interpreted the data, and wrote the manuscript. ON and YH analyzed and interpreted the data and helped writing the manuscript. AM helped design the study, analyzed and interpreted the data, and helped writing the manuscript. FH and VF performed surgery and revised the manuscript critically for important intellectual content. CK performed surgery, conceived and designed the study, analyzed and interpreted the data, and wrote the manuscript. All authors contributed to the article and approved the submitted version.

FUNDING

This work was supported by the DZHK (German Centre for Cardiovascular Research) and the BMBF (German Ministry of Education and Research).

ACKNOWLEDGMENTS

We thank Hannah Laumann for editorial assistance and Helge Haselbach as well as Nadja Kugler for graphics.

SUPPLEMENTARY MATERIAL

The Supplementary Material for this article can be found online at: https://www.frontiersin.org/articles/10.3389/fcvm.2022.763073/full#supplementary-material

REFERENCES

1. Prucz RB, Weiss ES, Patel ND, Nwakanma LU, Baumgartner WA, Conte JV. Coronary artery bypass grafting with or without surgical ventricular restoration: a comparison. *Ann Thorac Surg.* (2008) 86:806–14; discussion −14. doi: 10.1016/j.athoracsur.2008.05.009
2. Michler RE, Rouleau JL, Al-Khalidi HR, Bonow RO, Pellikka PA, Pohost GM, et al. Insights from the stich trial: change in left ventricular size after coronary artery bypass grafting with and without surgical ventricular reconstruction. *J Thorac Cardiovasc Surg.* (2013) 146:1139–45 e6. doi: 10.1016/j.jtcvs.2012.09.007
3. Menicanti LA. Reduce or reshape, this is the question! *Eur J Cardiothorac Surg.* (2015) 47:480–1. doi: 10.1093/ejcts/ezu254
4. Asferg C, Usinger L, Kristensen TS, Abdulla J. Accuracy of multi-slice computed tomography for measurement of left ventricular ejection fraction compared with cardiac magnetic resonance imaging and two-dimensional transthoracic echocardiography: a systematic review and meta-analysis. *Eur J Radiol.* (2012) 81:e757–62. doi: 10.1016/j.ejrad.2012.02.002
5. Solowjowa N, Penkalla A, Dandel M, Novikov A, Pasic M, Weng Y, et al. Multislice computed tomography-guided surgical repair of acquired posterior left ventricular aneurysms: demonstration of mitral valve and left ventricular reverse remodelling. *Interact Cardiovasc Thorac Surg.* (2016) 23:383–90. doi: 10.1093/icvts/ivw137
6. Lester SJ, Ryan EW, Schiller NB, Foster E. Best method in clinical practice and in research studies to determine left atrial size. *Am J Cardiol.* (1999) 84:829–32. doi: 10.1016/S0002-9149(99)00446-4
7. Di Donato M, Castelvecchio S, Menicanti L. End-systolic volume following surgical ventricular reconstruction impacts survival in patients with ischaemic dilated cardiomyopathy. *Eur J Heart Fail.* (2010) 12:375–81. doi: 10.1093/eurjhf/hfq020
8. Ponikowski P, Voors AA, Anker SD, Bueno H, Cleland JGF, Coats AJS, et al. ESC scientific document group 2016 esc guidelines for the diagnosis and treatment of acute and chronic heart failure: The task force for the diagnosis and treatment of acute and chronic heart failure of the european society of cardiology (ESC) developed with the special contribution of the Heart Failure Association (HFA) of the ESC. *Eur Heart J.* (2016) 37:2129–200. doi: 10.1093/eurheartj/ehw128
9. Dor V, Civaia F, Alexandrescu C, Sabatier M, Montiglio F. Favorable effects of left ventricular reconstruction in patients excluded from the surgical treatments for ischemic heart failure (stich) trial. *J Thorac Cardiovasc Surg.* (2011) 141:905–16:16 e1–4. doi: 10.1016/j.jtcvs.2010.10.026
10. Dor V, Saab M, Coste P, Kornaszewska M, Montiglio F. Left ventricular aneurysm: a new surgical approach. *J Thorac Cardiovasc Surg.* (1989) 37:11–9. doi: 10.1055/s-2007-1013899
11. Jatene AD. Left ventricular aneurysmectomy. Resection or reconstruction. *J Thorac Cardiovasc Surg.* (1985) 89:321–31. doi: 10.1016/S0022-5223(19)38781-1
12. Castelvecchio S, Parolari A, Garatti A, Gagliardotto P, Mossuto E, Canciani A, et al. Surgical ventricular restoration plus mitral valve repair in patients with ischaemic heart failure: risk factors for early and mid-term outcomesdagger. *Eur J Cardiothorac Surg.* (2016) 49:e72–8; discussion e8–9. doi: 10.1093/ejcts/ezv478
13. Jeganathan R, Maganti M, Badiwala MV, Rao V. Concomitant mitral valve surgery in patients undergoing surgical ventricular reconstruction for ischaemic cardiomyopathy. *Eur J Cardiothorac Surg.* (2013) 43:1000–5. doi: 10.1093/ejcts/ezs499
14. Buckberg GD. Surgical ventricular restoration after flawed stich trial: results when guidelines followed. *Eur J Cardiothorac Surg.* (2016) 50:702–3. doi: 10.1093/ejcts/ezw133
15. Calafiore AM, Iaco AL, Kheirallah H, Sheikh AA, Al Sayed H, El Rasheed M, et al. Outcome of left ventricular surgical remodelling after the stich trial. *Eur J Cardiothorac Surg.* (2016) 50:693–701. doi: 10.1093/ejcts/ezw103
16. Castelvecchio S, Menicanti L, Ranucci M. Development and validation of a risk score for predicting operative mortality in heart failure patients undergoing surgical ventricular reconstruction. *Eur J Cardiothorac Surg.* (2015) 47:e199–205. doi: 10.1093/ejcts/ezv023
17. Choi JO, Daly RC, Lin G, Lahr BD, Wiste HJ, Beaver TM, et al. Impact of surgical ventricular reconstruction on sphericity index in patients with ischaemic cardiomyopathy: follow-up from the stich trial. *Eur J Heart Fail.* (2015) 17:453–63. doi: 10.1002/ejhf.256

18. Ware J, Kosinski M, Keller S. *Sf-12: How to Score the sf-12 Physical and Mental Health Summary Scales*. Boston, MA: The Health Institute, New England Medical Center (1995).
19. Dor V, Sabatier M, Montiglio F, Civaia F, DiDonato M. Endoventricular patch reconstruction of ischemic failing ventricle. A single center with 20 years experience. Advantages of magnetic resonance imaging assessment. *Heart Fail Rev.* (2004) 9:269–86. doi: 10.1007/s10741-005-6804-5
20. Schuster A, Morton G, Chiribiri A, Perera D, Vanoverschelde JL, Nagel E. Imaging in the management of ischemic cardiomyopathy: special focus on magnetic resonance. *J Am Coll Cardiol.* (2012) 59:359–70. doi: 10.1016/j.jacc.2011.08.076
21. Nemchyna O, Solowjowa N, Dandel M, Hrytsyna Y, Knierim J, Schoenrath F et al. Predictive value of two-dimensional speckle-tracking echocardiography in patients undergoing surgical ventricular restoration. *Front Cardio Med.* (2022) 9:824467.
22. Debonnaire P, Palmen M, Marsan NA, Delgado V. Contemporary imaging of normal mitral valve anatomy and function. *Curr Opin Cardiol.* (2012) 27:455–64. doi: 10.1097/HCO.0b013e328354d7b5
23. Garatti A, Castelvecchio S, Bandera F, Guazzi M, Menicanti L. Surgical ventricular restoration: is there any difference in outcome between anterior and posterior remodeling? *Ann Thorac Surg.* (2015) 99:552–9. doi: 10.1016/j.athoracsur.2014.07.076

Conflict of Interest: VF disclosed financial relationships with the following entities: Medtronic GmbH, Biotronik SE & Co, Abbott GmbH & Co KG, Boston Scientific, Edwards Lifesciences, Berlin Heart, Novartis Pharma GmbH, JOTEC GmbH, and Zurich Heart.
The remaining authors declare that the research was conducted in the absence of any commercial or financial relationships that could be construed as a potential conflict of interest.

frontiers | Frontiers in Cardiovascular Medicine

ORIGINAL RESEARCH
published: 10 May 2022
doi: 10.3389/fcvm.2022.779528

Fractal Geometry Illustrated Left Atrial Appendage Morphology That Predicted Thrombosis and Stroke in Patients With Atrial Fibrillation

Chuxiang Lei[1], Qi Gao[2], Runjie Wei[3], Qijie Li[3], Xingli Liu[3], Lingmin Wu[1], Yan Yao[1], Hongguang Fan[1] and Zhe Zheng[1]**

[1] State Key Laboratory of Cardiovascular Diseases, Department of Cardiac Surgery, National Center for Cardiovascular Diseases, Fuwai Hospital, Peking Union Medical College and Chinese Academy of Medical Sciences, Beijing, China, [2] School of Aeronautics and Astronautics, Institute of Fluid Engineering, Zhejiang University, Hangzhou, China, [3] Hangzhou Shengshi Technology Co., Ltd., Hangzhou, China

OPEN ACCESS

Edited by:
Zahra K. Motamed,
McMaster University, Canada

Reviewed by:
Ernst Wellnhofer,
Charité – Universitätsmedizin Berlin, Germany
Annagrazia Cecere,
University of Padua, Italy
Natallia Maroz-Vadalazhskaya,
Belarusian State Medical University, Belarus

***Correspondence:**
Hongguang Fan
fanhongguang@fuwai.com
Zhe Zheng
zhengzhe@fuwai.com

Specialty section:
This article was submitted to Cardiovascular Imaging, a section of the journal Frontiers in Cardiovascular Medicine

Received: 19 September 2021
Accepted: 28 March 2022
Published: 10 May 2022

Citation:
Lei C, Gao Q, Wei R, Li Q, Liu X, Wu L, Yao Y, Fan H and Zheng Z (2022) Fractal Geometry Illustrated Left Atrial Appendage Morphology That Predicted Thrombosis and Stroke in Patients With Atrial Fibrillation. Front. Cardiovasc. Med. 9:779528. doi: 10.3389/fcvm.2022.779528

Background: This study aims to correlate the morphological complexity of left atrial appendage (LAA) with thrombosis and stroke in patients with atrial fibrillation (AF).

Methods: The training cohort consisted of 46 patients with AF (age 55.8 ± 7.2 years, 73.9% men) who were referred for radiofrequency catheter ablation. An independent validation cohort consisting of 443 patients with AF was enrolled for further verification. All patients in the training cohort underwent both transesophageal echocardiography (TEE) and enhanced computed tomography (CT). Fractal dimension (FD) analysis was performed to evaluate the morphological complexity of LAAs quantitatively. Clinical and imaging manifestations, FD of LAAs, and diagnostic accuracy were investigated and compared between patients with AF in both training and validation cohorts.

Results: In the training cohort, LAAs (n = 22) with thrombi had significantly higher FD than those without thrombi (n = 24) h 0.44 ± 0.07 vs. 2.35 ± 0.11, p = 0.003). Receiver-operating characteristic (ROC) analysis suggested that the diagnostic accuracy of FD combined with a CHA_2DS_2-VaSc score was significantly higher than that of the CHA_2DS_2-VaSc score alone in low- to moderate-risk patients with AF (area under the curve 0.8479 vs. 0.6958, p = 0.009). The results were also validated in an independent external validation cohort and demonstrated that increased FD was associated with stroke. Hemodynamic analysis revealed that LAAs with thrombi and high FD were prone to blood stasis and lower blood flow rate.

Conclusion: LAA morphological complexity is closely associated with thrombosis and stroke in patients with paroxysmal AF. A new risk assessment system combining CHA_2DS_2-VaSc score and FD has a higher diagnostic accuracy in predicting LAA thrombosis.

Keywords: left atrial appendage, fractal dimension, morphological complexity, thrombosis, atrial fibrillation

INTRODUCTION

Atrial fibrillation (AF) is the most common clinically significant cardiac arrhythmia characterized by the presence of irregular fibrillatory waves. The incidence of AF increases markedly with age and approximately doubles with each decade (1, 2). AF is associated with an increased risk of thrombosis in the left atrial (LA), and it has been reported that the left atrial appendage (LAA) is suspected to be a vital source of cerebral emboli and may lead to ischemic stroke (3, 4). Previous studies suggested that, among all cardiogenic strokes, more than 90% of the emboli were from LAA. Furthermore, the risk of stroke increases nearly fivefold when AF is present, and so does the mortality in patients with AF and thrombosis (5).

According to Virchow's triad, thrombosis is determined by stasis of blood flow, endothelial injury, and hypercoagulability. At present, the CHA_2DS_2-VaSc score is the most widely used model for assessing the risk of cerebrovascular events. This index includes age, congestive heart failure, sex, diabetes, hypertension, stroke, and vascular disease. Although it covers the assessment of the endothelial function and coagulability status, it does not reflect the blood flow stasis in LA or LAA. When AF occurs, LAA fails to contract effectively and leads to slow blood flow or stasis in LAA, which eventually results in thrombosis. It is obvious that the morphology of LAA has a significant impact on the blood flow. In contrast, studies suggest that the shape and structure of LAA are complex and diverse among the population. Cardiac computed tomography (CT) imaging has been widely used in the evaluation of cardiovascular diseases, including heart structures evaluation, calcium score in risk stratification, and coronary artery disease assessment (6, 7). For example, the coronary artery calcium score, which is readily detected on CT images, represents a surrogate marker of the presence and extent of coronary artery disease (8). In addition, cardiac CT is used to analyze the morphology and function of the heart. Several studies reported that the risk score based on cardiac CT could categorize disease severity and predict outcomes, including mitral annular and coronary artery calcification (7, 9). Moreover, multidetector CT scan image LAA at high resolution (10), and the existing classification criteria of LAA morphology according to these images are used to describe the anatomical shapes (5). However, none of them are able to characterize the internal morphological features. Therefore, the blood flow stasis is extremely difficult to assess.

To quantitatively describe the morphological complexity of LAA, we introduced the box-count dimension in the fractal geometry. Fractal dimension (FD) is the most crucial concept and content in the fractal geometry theory. Box-counting dimension is a commonly used parameter in FD, where it can evaluate the complexity and irregularity of a real object or a fractal object quantitatively. Fractal geometry analysis has been applied in many fields such as the dimensionless measurement of trabeculation complexity. Furthermore, it has been used to evaluate the left ventricular (LV) trabeculation quantitatively in LV non-compaction patients and define the normal FD range of LV trabeculation (11). Similarly, the fractal analysis can assess the correlation between the complexity of right ventricle trabecula and hemodynamic parameters in patients with pulmonary hypertension and identify retinal microvascular changes in the early stage of patients with type 2 diabetes (11–13). Our study first applied FD calculated by enhanced CT image of LAA to evaluate its complexity and further revealed the association between thrombosis and shape complexity of LAA.

MATERIALS AND METHODS

Patients' Enrollment

This is a retrospective cohort study that included all consecutive patients with AF who were first admitted to Fuwai Hospital and scheduled to undergo radiofrequency ablation from January 2010 to December 2017. According to the 2020 European Society of Cardiology guideline (14), the diagnosis of AF was determined by a standard 12-lead ECG showing heart rhythm with no discernible repeating P waves and irregular RR intervals. All the patients enrolled in this study should have undergone the multidetector computed tomography (MDCT) of the LA. For patients with paroxysmal AF, the CT images used for 3D reconstruction were collected during the diastolic phase, whereas for patients with persistent AF, the images were collected during the whole cardiac cycle due to the inability to distinguish between systolic and diastolic phases. Transesophageal echocardiography (TEE) was also required for patients in the training cohort to determine the presence of LAA thrombosis. In the training cohort, all patients did not take anticoagulants at any time before the corresponding examination and had their imaging examination performed before the anticoagulation treatment they would have undergone prior to radiofrequency ablation. An independent external validation cohort consisted of patients with AF who were examined by LA MDCT over the same period of time. Similar inclusion criteria, except for the use of anticoagulants and TEE examination, were applied for these patients (not receiving regular anticoagulation within 1 year prior to imaging), and these patients were divided into two groups based on whether they had the stroke. Patients with low MDCT image quality during AF rhythm were excluded, as well as patients who had undergone MDCT without contrast enhancement because of renal dysfunction. Other exclusive criteria included organized thrombus in LAA, severe chronic kidney disease (stage 4 or 5 or end-stage chronic kidney disease), other anticoagulant indications in the past 30 days (including deep vein thrombosis/pulmonary embolism, hip/knee replacement, femur/tibia/patella fracture, thrombectomy, or chronic hypercoagulable state), and poor CT or echocardiographic image quality. Eventually, a total of 46 patients were enrolled in the training cohort, and 443 patients were assigned to validation cohort. The overall flowchart of this study is shown in **Figure 1**. Approval to conduct this study was obtained from the Institutional Review Board, Fuwai Hospital. All patients signed an informed consent form using their clinical data for research, and patients were not involved in the study design, data analysis, and other research processes. All the data used in this study were necessary examinations for patients.

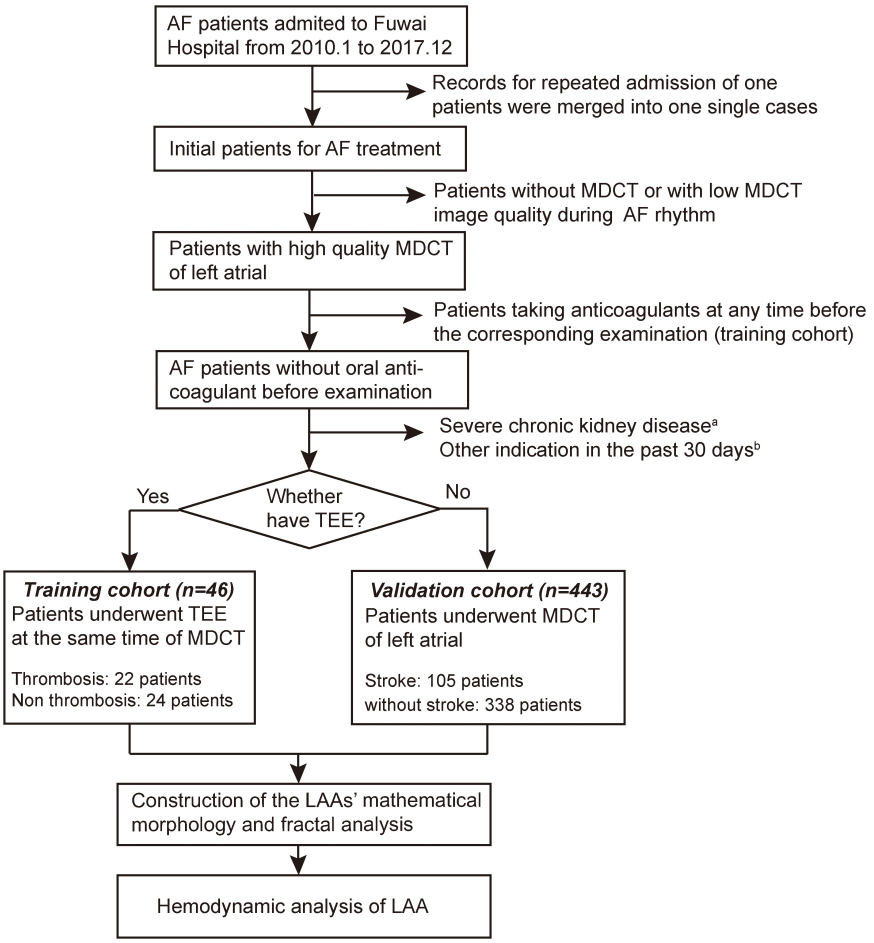

FIGURE 1 | Flowchart of the study. (a) Stage 4 or 5 or end-stage chronic kidney disease. (b) Deep vein thrombosis/pulmonary embolism, hip/knee replacement, femur/tibia/patella fracture, thrombectomy, or chronic hypercoagulable state.

Echocardiographic Data Analysis

See **Supplementary Material**.

Cardiac Computed Tomography Scan and Image Analysis

See **Supplementary Material**.

Classification of Left Atrial Appendage s' Morphology

See **Supplementary Material**.

Construction of Left Atrial Appendage s' Mathematical Morphology

To further analyze the LAA morphology, it is necessary to separate LAA from LA. To cut the LAA accurately and objectively, we introduced erosion-dilation image processing (15) (**Figure 1**) technology to prevent cutting LAAs from subjective interference (16). The morphology of the LAA was assessed with reconstructed three-dimensional (3D) data, and LAA orifice diameters were measured in both the long and short axes. The specific technical route was as follows: first, to determine the position of the aorta, this study used the Hough transform to detect the circle method. Next, the aorta and LV tissues and organs were separated, and tissue model 1 was obtained as shown in **Figure 2A**. The corrosion operation on tissue model 1 was performed, and only a part of the left atrium tissue was retained as shown in **Figure 2B**. The dilate operation of the tissue shown in **Figure 2B** was done to obtain the approximate position of the left atrium in **Figure 2C**. Then, the corresponding left atrium position in tissue model 1 was cleared, and LAA and left atrium were separated as shown in **Figure 2D**. Finally, the LAA model was retained as shown in **Figure 2E**.

Fractal Analysis

Based on an adaption of the methodology described by Captur et al. (11, 17), FD (18) was calculated from the reconstructed 3D volume of LAA *via* an in-house fractal analysis program in MATLAB (MathWorks Inc., Natick, MA, United States). The roughness/curvature of the LAA surface is associated with the complexity of the LAA volume, which can be quantitatively indicated by the value of FD. For a reconstructed LAA within a

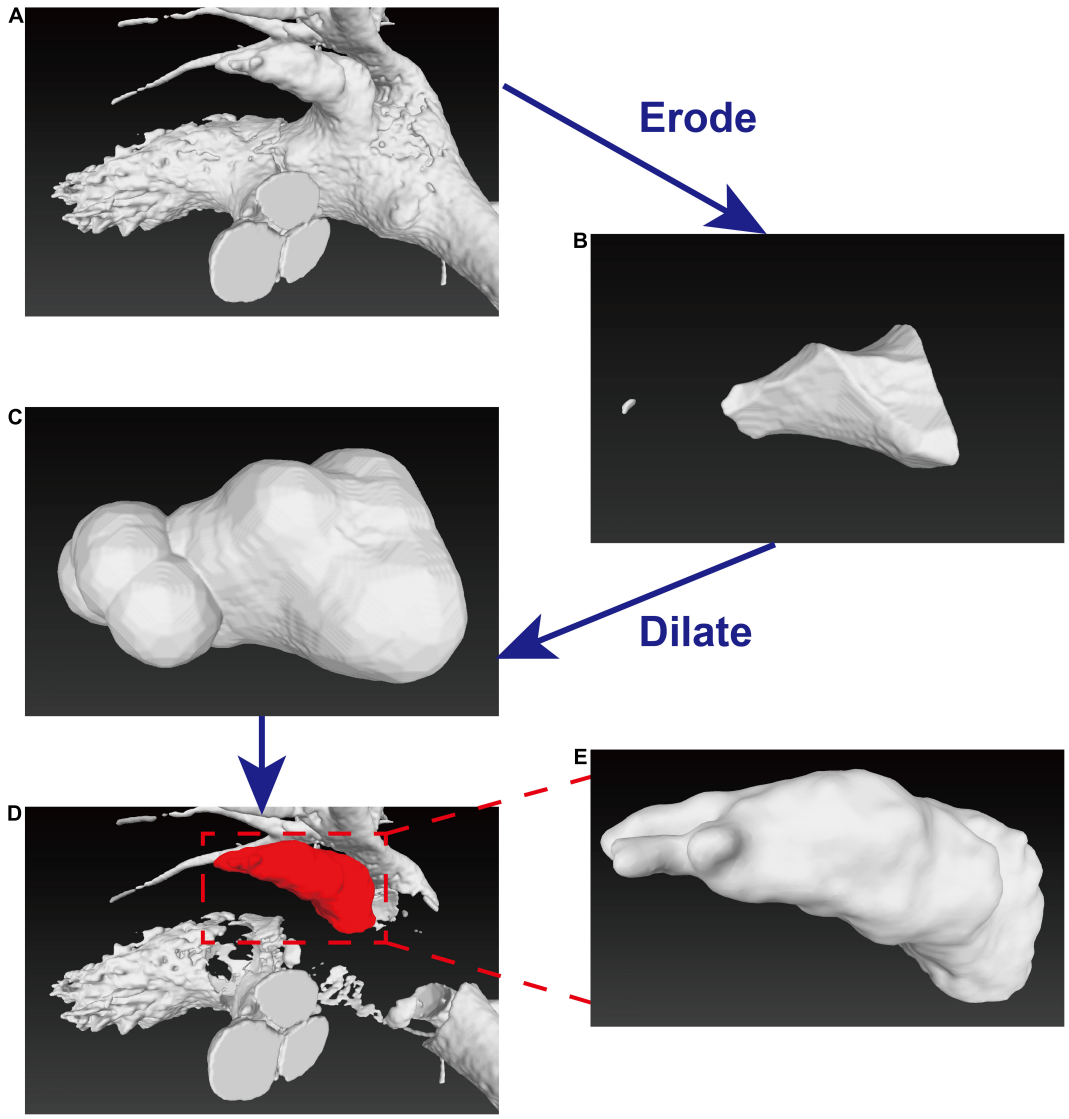

FIGURE 2 | Diagram of erosion-dilation image processing. **(A–C)** Process of erode-dilation operation to obtain the approximate position of the left atrium. **(D)** Separation of the LAA and the left atrium were separated. **(E)** The LAA model used for further analysis.

volume of $M \times M \times M$, we partition the 3D space into boxes with side size of r. The minimum number of *b*oxes that can cover the entire volume of LAA is named $N(r)$, which is a function of r. Therefore, the box FD (19) D_B, one of the most commonly used FDs, is calculated as

$$D_B = \lim_{r \to 0} \left[logN(r)/log(\frac{1}{r}) \right]$$

Hemodynamic Analysis

The 3D morphological structure models of LA and LAA were obtained *via* an in-house image processing algorithm. The 3D models were discretized to consecutive mesh by using the open-source library "snappyHexMesh" for the subsequent computational fluid dynamics simulations. A pressure waveform was imposed at the inlet (i.e., pulmonary veins) (17). At the outlet (i.e., mitral valve), a time-varying velocity waveform was applied to simulate AF condition. In this study, the maximum instantaneous velocity at mitral valve was measured by echocardiography at the diastole. For patients with AF, Iosifescu (18) derived blood velocity profile across the mitral valve orifice by dividing the instantaneous flow rate by the orifice area, in which the flow rate across the mitral valve was derived from the international regulation ISO5840-1:2015 (19). Therefore, using maximum instantaneous velocity and blood velocity profile, patient-specific velocity profile at mitral valve can be identified by scaling proportionally. Rigid and no-slip conditions were set at the wall boundary.

Blood flow was numerically modeled by solving the Navier-Stokes and continuity equations using the open-source library OpenFOAM version 18.04. Blood was assumed to be an incompressible and Newtonian fluid with density

TABLE 1 | Clinical characteristics of patients with AF and with and without thrombosis.

	Total	AF without thrombosis	AF with thrombosis	*P*-value
N	46	24	22	
Age, years	55.8 ± 7.2	54.9 ± 5.9	56.7 ± 8.4	0.398
Sex, *n* (%)				
Female	12 (26.1)	8 (33.3)	4 (18.7)	0.242
Male	34 (73.9)	16 (66.7)	18 (81.8)	
Type of AF, *n* (%)				
Paroxysmal	24 (52.2%)	13 (54.2%)	11 (50.0%)	0.777
Persistent	22 (47.8%)	11 (45.8%)	11 (50.0%)	
Height, m	1.72 (1.64, 1.76)	1.69 (1.62, 1.75)	1.75 (1.70, 1.76)	0.155
Weight, kg	76.3 ± 13.6	72.8 ± 13.2	80.1 ± 13.3	0.071
BMI, kg/m^2	26.1 ± 3.4	25.3 ± 3.0	27.0 ± 3.7	0.105
Duration of AF, years	3.0 (2.0, 6.0)	4.0 (2.0, 6.0)	3.0 (1.8, 4.3)	0.219
Laboratory findings				
Triglyceride, mmol/L	1.7 ± 0.9	1.6 ± 0.7	1.8 ± 1.1	0.638
Total cholesterol, mmol/L	4.6 ± 1.2	4.6 ± 1.2	4.5 ± 1.3	0.783
Image examination				
LA diameter, mm	40.0 ± 5.4	38.6 ± 4.6	41.5 ± 5.9	0.069
LVEF, %	62.7 ± 6.3	63.5 ± 5.6	61.7 ± 6.9	0.332
Mean LAA orifice diameter, mm	24.0 ± 5.8	22.6 ± 6.5	25.6 ± 4.6	0.078
LAA orifice area, mm^2	1821.7 (1122.5, 2508.9)	1331.5 (764.5, 2455.6)	2052.0 (1653.1, 2533.3)	0.082
LAA volume, cm^3	8.2 (5.2, 11.2)	6.2 (4.6, 9.4)	10.2 (7.7, 12.0)	0.059
Hypertension, *n* (%)	18 (39.1)	6 (25.0)	12 (54.5)	0.040*
Hyperlipidemia, *n* (%)	10 (21.7)	3 (12.5)	7 (31.8)	0.159
Diabetes mellitus, *n* (%)	3 (6.5)	0 (0)	3 (13.6)	0.101
Stroke, *n* (%)	8 (17.4)	1 (4.2)	7 (31.8)	0.020*
CAD, *n* (%)	3 (6.5)	1 (4.2)	2 (9.1)	0.600
Smoke, *n* (%)	18 (39.1)	7 (29.2)	11 (50.0)	0.148
Warfarin use†, *n* (%)	42 (91.3)	22 (91.7)	20 (90.9)	1.000
CHA_2DS_2-VaSc score, *n* (%)				
High risk: ≥ 2	11 (23.9)	2 (8.3)	9 (40.9)	0.010*
Moderate risk: = 1	21 (45.7)	10 (41.7)	11 (50.0)	0.571
Low risk: = 0	14 (30.4)	12 (50.0)	2 (9.1)	0.003*

Values are expressed in mean ± SD, number (percentage, %) or median (Q1, Q3).
**Marked significant differences.*
† "Warfarin use" refers to the use of warfarin after obtaining the image data required for the study rather than warfarin on admission.
AF, atrial fibrillation; BMI, body mass index; LA, left atrium; LVEF, left ventricle ejection fraction; LAA, left atrial appendage; CAD, coronary artery disease.

(ρ 1, 060 kg/m^3) and viscosity (μ 0.0035 Pa · s). The interfoam solver was used to analyze the blood flow process. The duration of each cardiac cycle was 0.8 s. Five complete cardiac cycles were taken to simulate the blood flow. Subsequently, the results in the last cardiac cycle were selected for statistical data analysis. Furthermore, to quantitatively characterize the blood washout in LAA, the blood in LA and LAA was considered as phase 1 at the end of one filling phase, whereas phase 2 was regarded as the blood flowing into the LA from the pulmonary veins at the following cardiac cycles. Then, the volume-of-fluid model was applied to estimate the volume fraction of blood residual and locate the residual blood at the end of each cardiac cycle. Finally, through the parameterization study of the morphological structure and hemodynamics index for the LAA, the essential hemodynamic characteristics, such as velocity, were obtained (20–22). We introduced residual blood flow fraction to describe the blood flow stasis. BL1/BT1 was defined as the ratio of residual blood volume to LAA/LA volume at the end of the first cardiac cycle. Additionally, more advanced hemodynamics descriptors potentially associated with the risk of thrombosis are estimated. They are time-averaged wall shear stress (TAWSS), oscillatory shear index (OSI), relative residence time (RTT), and endothelial cell activation potential (ECAP) (23–25).

Statistical Analysis

The distribution of all continuous variables was assessed for normality using the Shapiro-Wilk test and presented as mean ± standard deviation (SD) or median (Q1, Q3), appropriately. Independent *t*-tests or Mann-Whitney *U*-tests were performed appropriately to compare the differences of scale or ordinal variables between groups. For nominal variables, the *chi*-square test and Fisher's exact test were performed to compare them between groups. A comparison of echocardiographic, CT variables, and box-counting dimension between four types of

LAA morphology was performed by one-way ANOVA followed by Tukey's *post-hoc* test. Receiver-operating characteristic (ROC) curve analysis with the use of Youden's index was conducted to obtain the optimum cutoff for the box-counting dimension. The comparison of the area under the curve (AUC) in ROC analysis was conducted by DeLong test (26). ANOVA was used to test whether the regression coefficient in linear regression equation is 0. Two-sided p-values < 0.05 were considered statistically significant. All statistical analyses were conducted with the SPSS software (version 24.0, IBM SPSS Statistics) and Stata/SE software (version 14.1, TX, United States).

RESULTS

Relevant Clinical Characteristics

As shown in **Table 1**, a total of 46 patients were enrolled in this study as the training cohort. All 46 patients were divided into two groups based on the presence of LAA thrombi. The general baseline characteristics were compared between the two groups. Overall, the mean age was 55.8 ± 7.2 years, and 34 (73.9%) were men, with a sex ratio of 2.8:1. There were 24 patients with paroxysmal AF and 22 with persistent AF, which did not present a significant difference in the two groups. Mean body mass index (BMI) of the patients with AF and with and without thrombosis were 27.0 ± 3.7 and 25.3 ± 3.0, respectively. No statistical difference was observed in the duration of AF between the two groups of patients.

Patients with AF and thrombosis had a larger LA diameter and less left ventricle ejection fraction (LVEF) numbers, whereas neither of them was significant. However, the prevalence of hypertension was markedly lower among patients with AF and without thrombosis than that among patients with thrombosis (25.0% vs. 54.5%, $p = 0.040$). The incidence of hyperlipidemia and diabetes mellitus also manifested as such a trend, but no significant difference was observed between the two groups.

According to the CHA_2DS_2-VaSc score, all patients with AF were evaluated as high risk (≥ 2), moderate risk ($= 1$), or low risk ($= 0$). The rate of thrombosis in patients with AF was significantly different in both high-risk and low-risk patients. However, for moderate-risk patients, the CHA_2DS_2-VaSc score did not present any difference between the two groups. In addition, warfarin was used in 42 (91.3%) patients in the follow-up treatment, including 22 (91.7%) patients without LAA thrombi.

Comparison Between Four Types of Left Atrial Appendage Morphology and Fractal Dimension

The box-counting dimensions of LAAs were compared to test the hypothesis that patients with AF and thrombosis would have a higher FD. The results suggested that the LAA FD of patients with AF and thrombi was significantly higher than those of patients without thrombi (2.42 ± 0.072 vs. 2.35 ± 0.109, $p = 0.003$) (**Figure 3A**). To further investigate the potential differences between four types of LAA morphology, we compared the crucial imaging parameters and box-counting dimensions (**Figure 3** and **Supplementary Table 1**). None of the echocardiographic and CT variables were significantly different among the four groups, nor was thrombosis and the box-counting dimension (**Figure 3A**), indicating that this classification might not reflect LAA complexity. In addition, we compared LAA volume, orifice area, and CHA_2DS_2-VaSc score between the four morphological classifications and between the groups divided by FD quartiles. Interestingly, the volume and orifice area of LAA markedly increased in the group with higher FD; however, they did not differ significantly among the four LAA morphological classifications (**Figures 3C,D**). In addition, the CHA_2DS_2-VaSc score was dramatically higher in Q4 than that in Q1, while there seemed to be no difference among the four LAA morphological classifications (**Figure 3B**).

Fractal Dimension Demonstrated the Relationship Between Morphological Complexity and Stroke

To further illustrate the profound relationship between LAA morphological complexity and the long-term prognosis of patients with AF, an independent validation cohort were enrolled and were divided into two groups based on whether they had stroke after the diagnosis of AF. There were 338 patients without stroke and 105 patients with stroke (**Table 2**). The median age of patients with AF and stroke was markedly lower than that of patients without stoke [55.0 (45.0, 64.0) vs. 58.0 (51.0, 63.0), $p = 0.045$]. In addition, there were no statistical differences in gender composition and the incidences of hypertension, diabetes, and vascular disease between the two groups. CHA_2DS_2-VaSc score was significantly different between the two groups. Interestingly, the average box-counting dimension of patients with stroke was dramatically higher than that of patients without stroke (2.45 ± 0.08 vs. 2.41 ± 0.09, $p = 0.001$), further suggesting that the degree of morphological complexity of LAA might be closely related to cerebral infarction complicated by AF.

Diagnostic Accuracy of Box-Counting Dimension in Training and Validation Cohorts

To further investigate the relationship between thrombosis and LAA morphology complexity, ROC analysis was performed to reveal the accuracy of box-counting dimensions in diagnosis of LAA thrombus and stroke in the training and validation cohort, respectively (**Table 3** and **Figure 4**). The optimum diagnostic thresholds for thrombosis and stroke in patients with AF were 2.426 and 2.438, respectively (**Figures 4A,C**). Through ROC analysis, the AUC of the box-counting dimension was 0.7462. The AUC of FD was slightly lower than that of the CHA_2DS_2-VaSc score (0.7462 vs. 0.7689, $p = 0.811$). However, for low- to moderate-risk patients, the diagnostic accuracy of FD was higher than the CHA_2DS_2-VaSc score (AUC 0.7622 vs. 0.6958, $p = 0.545$) (**Figure 4B**). We consequently combined the shape complexity of LAA and CHA_2DS_2-VaSc and made it into a new risk scoring system. To be specific, box-counting dimensions greater than 2.426 were awarded 1 point in the training cohorts, otherwise 0

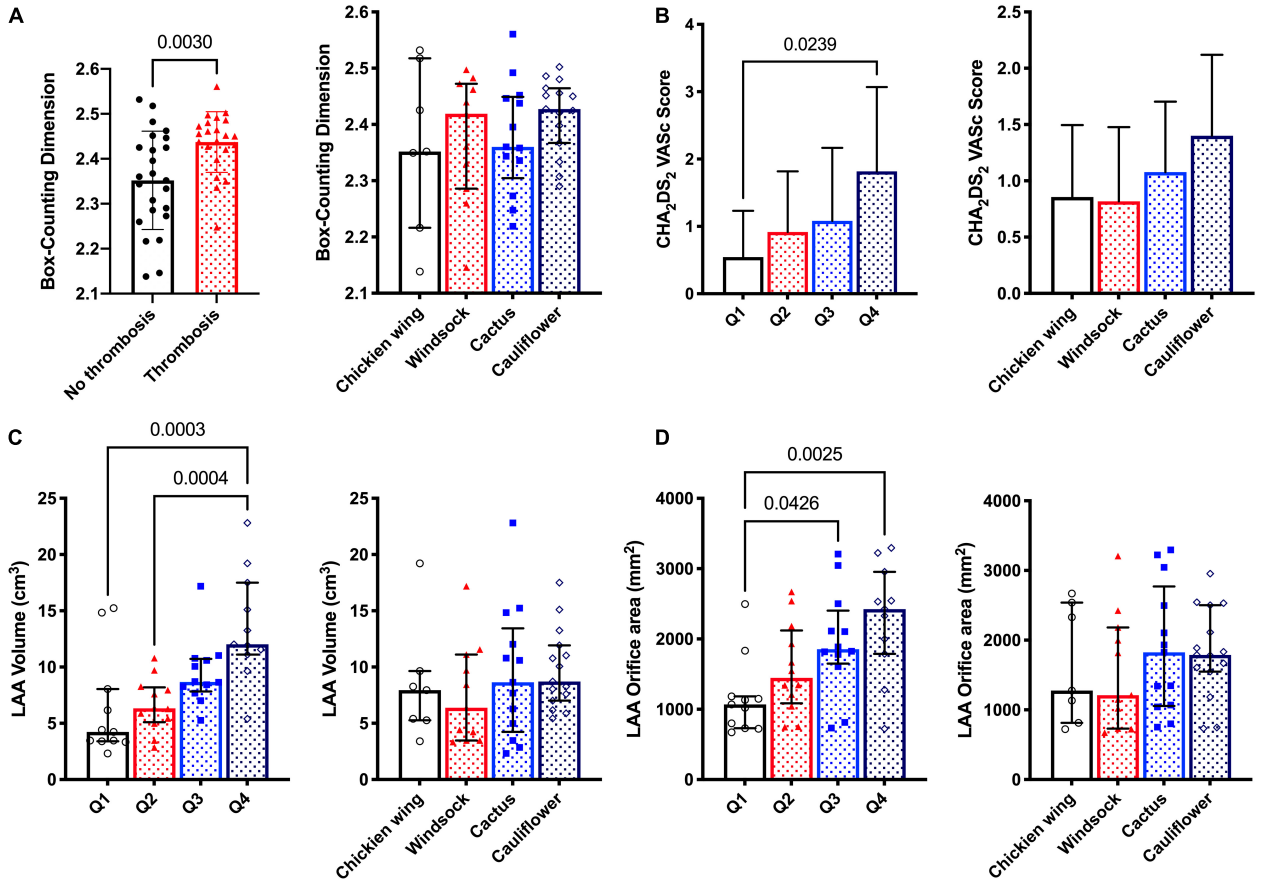

FIGURE 3 | Comparison of box-counting dimension and other LAA parameters. **(A)** The LAA box-counting dimension of patients with AF and thrombi was significantly higher than that of patients without thrombi ($p = 0.003$), yet the box-counting dimension was not statistically different between the four types of LAA. **(B)** Comparison of CHA_2DS_2-VaSc between four groups divided by quartile indicated that the CHA_2DS_2-VaSc score was markedly higher in Q4 group compared to Q1 group, while it appeared no significant difference between four types of LAA. **(C)** LAA volumes of patients in Q4 were dramatically larger than those of patients in the Q1 and Q2 groups, and no difference was observed in four types of LAA. **(D)** Similar to LAA volume, the LAA orifice area was also significantly larger in the Q4 group.

TABLE 2 | Clinical characteristics of patients with AF and with and without stroke.

	Total	AF without stroke	AF with stroke	*P*-value
N	443	338	105	
Age, years	58.0 (50.0, 63.0)	58.0 (51.0, 63.0)	55.0 (45.0, 64.0)	0.045*
Sex, *n* (%)				
Female	135 (30.5)	110 (32.5)	25 (23.8)	0.089
Male	308 (69.5)	228 (67.5)	80 (76.2)	
Hypertension, *n* (%)	212 (47.9)	159 (47.0)	53 (50.5)	0.538
Congestive heart failure, *n* (%)	23 (5.2)	16 (4.7)	7 (6.7)	0.436
Diabetes mellitus, *n* (%)	75 (16.9)	63 (18.6)	12 (11.4)	0.085
Vascular disease, *n* (%)	39 (8.8)	26 (7.7)	13 (12.4)	0.139
CHA_2DS_2-VaSc score, *n* (%)				
High risk: ≥ 2	245 (55.3)	147 (43.5)	98 (93.3)	<0.001*
Moderate risk: = 1	114 (25.7)	109 (32.2)	5 (4.8)	<0.001*
Low risk: = 0	84 (19.0)	82 (24.3)	2 (1.9)	<0.001*
Box-counting dimension	2.43 ± 0.09	2.41 ± 0.09	2.45 ± 0.08	0.001*

Values are expressed in mean ± SD, number (percentage, %) or median (Q1, Q3).
**Marked significant differences.*
AF, atrial fibrillation.

TABLE 3 | ROC analysis of patients with AF in the training and validation cohorts.

	Training cohort (n = 46)			Validation cohort (n = 443)		
		P-value			P-value[#]	
	AUC (95% CI)	Compared to 0.5	Compared to AUC of CHA_2DS_2-VaSc	AUC (95% CI)	Compared to 0.5	Compared to AUC of CHA_2DS_2-VaSc
All patients						
FD	0.746 (0.599, 0.893)	0.004*	0.811	0.602 (0.541, 0.663)	0.002*	<0.001*
CHA_2DS_2-VaSc	0.769 (0.643, 0.895)	0.002*	-	0.856 (0.817, 0.895)	<0.001*	-
Combined[†]	0.842 (0.732, 0.952)	<0.001*	0.063	0.863 (0.827, 0.899)	<0.001	0.427
Low to moderate risk						
Number of patients n (%)	35 (76.1)			198 (44.7)		
FD	0.762 (0.592, 0.932)	0.005*	0.545	0.696 (0.568, 0.823)	0.079	0.171
CHA_2DS_2-VaSc	0.696 (0.548, 0.843)	0.056	-	0.572 (0.388, 0.756)	0.519	-
Combined[†]	0.848 (0.733, 0.963	0.001*	0.009*	0.747 (0.608, 0.886)	0.026*	<0.001*

p-Values were obtained by z-test.
**Marked significant differences.*
[†]If the box-counting dimension value is greater than threshold (2.426 in the training cohort; 2.438 in the validation cohort), one point will be added to CHA_2DS_2-VaSc system, and the new risk score was assessed by ROC analysis.
[#]The DeLong test was used to compare the AUCs.
AUC, area under the curve; CI, confidential interval; FD, fractal dimension (represented by box-counting dimension).

point. The combined risk score was significantly more accurate in the diagnosis of LAA thrombus than the CHA_2DS_2-VaSc scoring system alone in low- to moderate-risk patients (AUC 0.8479 vs. 0.6958, $p = 0.009$). The same trend was also observed among all patients, whereas it was not statistically significant. Similarly, box-counting dimensions more than 2.438 were given one more point to be added to the CHA_2DS_2-VaSc score. In addition, the ROC analysis indicated that the diagnostic accuracy of combined risk score was higher than that of CHA_2DS_2-VaSc score alone among all patients and low- to moderate-risk patients (**Figures 4C,D**).

Relationship Between Fractal Dimension and Left Atrial /Left Atrial Appendage Parameters

We found that the morphological complexity of LAA was positively correlated with LAAs' orifice area and volume (**Figures 3C,D**). We plotted a scatter diagram to reflect this trend (**Figures 5A,C**). It shows that, with an increase in the volume of LAA, the degree of morphological complexity gradually increases in both training and validation cohorts, so does the risk of thrombosis and stroke (**Figures 5B,D**). Furthermore, we performed simple linear regression for FD and LA/LAA parameters (**Figures 6A,B**). FD showed significant positive correlation with the area of LAA entrance, LAA, and LA volume (**Figure 6A**), yet the correlation of FD and the blood flow velocity inside LAA was not identified (**Figure 6B**).

Hemodynamic Characteristics of Left Atrial Appendage and Thrombosis

To further evaluate the hemodynamic characteristics in LAAs of patients with AF and with and without thrombi, we obtained a hemodynamic model of the LAA through parameterization studies. It suggested that LAAs with thrombi and higher FD were prone to blood stasis and lower blood flow rate (**Supplementary Figure 2** and **Figure 5**). Furthermore, the residual blood volume in LAAs of patients without thrombosis was lower than those of patients with thrombosis after the sixth cardiac cycle, and the distribution of residual blood volume was more dispersed in LAAs without thrombi (**Supplementary Figure 3**). Linear regression between FD and BL1% or BT1% indicates the markedly positive correlation (**Figure 6C**). In addition, TAWSS was negatively correlated with FD, whereas the linear correlations between FD and OSI, RRT, and ECAP were not significant (**Figure 6D**).

DISCUSSION

Our study takes the first step in assessing the thrombosis and stroke among patients with AF from the perspective of LAA morphological complexity, which was quantitatively analyzed by means of fractal geometry. It is technically feasible to calculate FD of LAAs through enhanced CT images of patients with AF. Our data suggested that patients with AF having higher box-counting dimension were more prone to LAA thrombi and stroke. Furthermore, FD of LAA showed more exceptional ability to diagnose thrombosis and stroke than the CHA_2DS_2-VaSc scoring system among low- to moderate-risk patients with AF. In addition, hemodynamic analysis of LAAs indicated that blood flow rate was lower in LAAs with thrombi and higher with box-counting dimension. This study revealed the relationship between the thrombosis and morphological complexity of LAA in patients with AF and provided additional clinical implications for risk stratification.

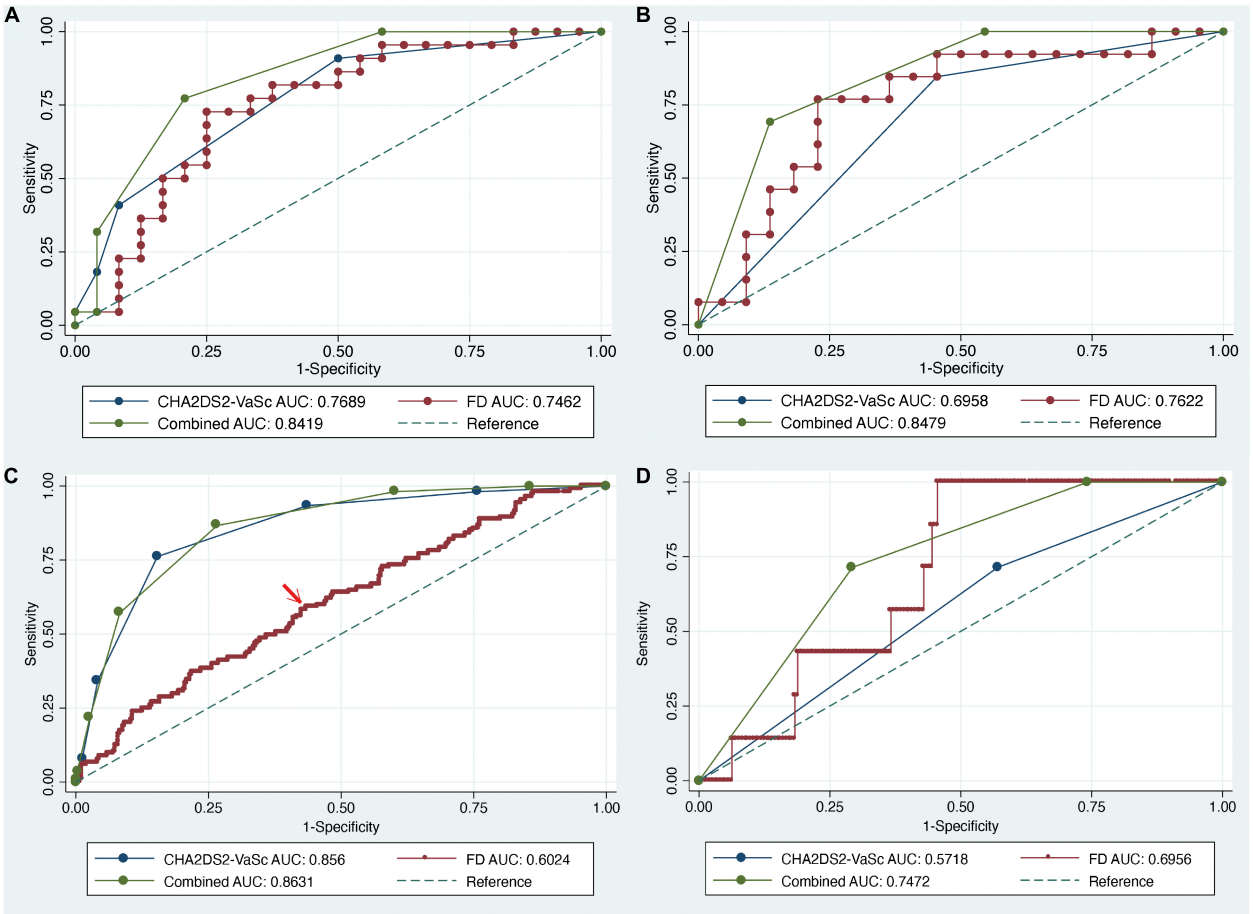

FIGURE 4 | ROC analysis of FD and CHA_2DS_2-VaSc score in training and validation cohorts. **(A)** ROC curve for assessing the patients in the training cohorts. **(B)** ROC analysis of low- to moderate-risk patients with AF. Both AUC of FD and combined scoring system were significantly larger than that of CHA_2DS_2-VaSc score (p = 0.005 and 0.001, respectively). **(C)** ROC analysis of FD and CHA_2DS_2-VaSc score among all patients in the validation cohort. **(D)** ROC analysis in low- to moderate-risk patients in the validation cohort.

The relationship between the shape of LAAs and thrombosis has been explored for a long time, and previous studies have reached a consensus that LAA morphology is correlated with the risk of thrombus formation and stroke or transient ischemia attack in patients with AF (27–29). It has been reported that LAA volume, LAA empty velocity, and LAA orifice area could be used to predict thrombus formation (27, 29), yet these parameters did not present significant differences between the two groups in our cohort. Interestingly, according to the study by Yamamoto et al. (27), most of the patients with LAA thrombus had $\geq$ 3 LAA lobes, whereas the thrombi were observed in only 0.7% of patients with AF and with one or two LAA lobes. These studies indicated that thrombosis was closely related to the complexity of the LAA. Correspondingly, our data quantitatively evaluated the morphological complexity of LAA and further confirmed the correlation between the LAA thrombosis and morphological complexity. In contrast, Fukushima et al. demonstrated the relationship between LAA flow velocity (LAAFV) and LAA morphology in patients with paroxysmal AF based on the four-type classification system of LAA morphology, indicating that LAAFV was significantly higher in patients with chicken wing LAA (5). Likewise, another study pointed out that patients with chicken wing morphology were less prone to cerebral embolic events (28), which indicated that the higher LAAFV might be associated with less thrombus formation and stroke. These data suggest that LAA morphology can significantly affect the state of blood flow within LAA, and thus further lead to thromboembolism (30, 31). The traditional four-type morphological classification of LAA can reflect the association between LAA morphology and thrombosis or embolic event. However, this classification system cannot quantitatively assess the complexity of LAA, thus there were contrary conclusions about the relationship between LAA morphology and thrombosis or stroke in the previous studies. Consequently, we provided a novel method to evaluate the morphological complexity of both outer and internal sides of LAA (5, 28, 32, 33).

The fractal geometry analytic method proposed in this study can accurately quantify the morphological complexity of LAAs. A recent study revealed that complex LAA morphology

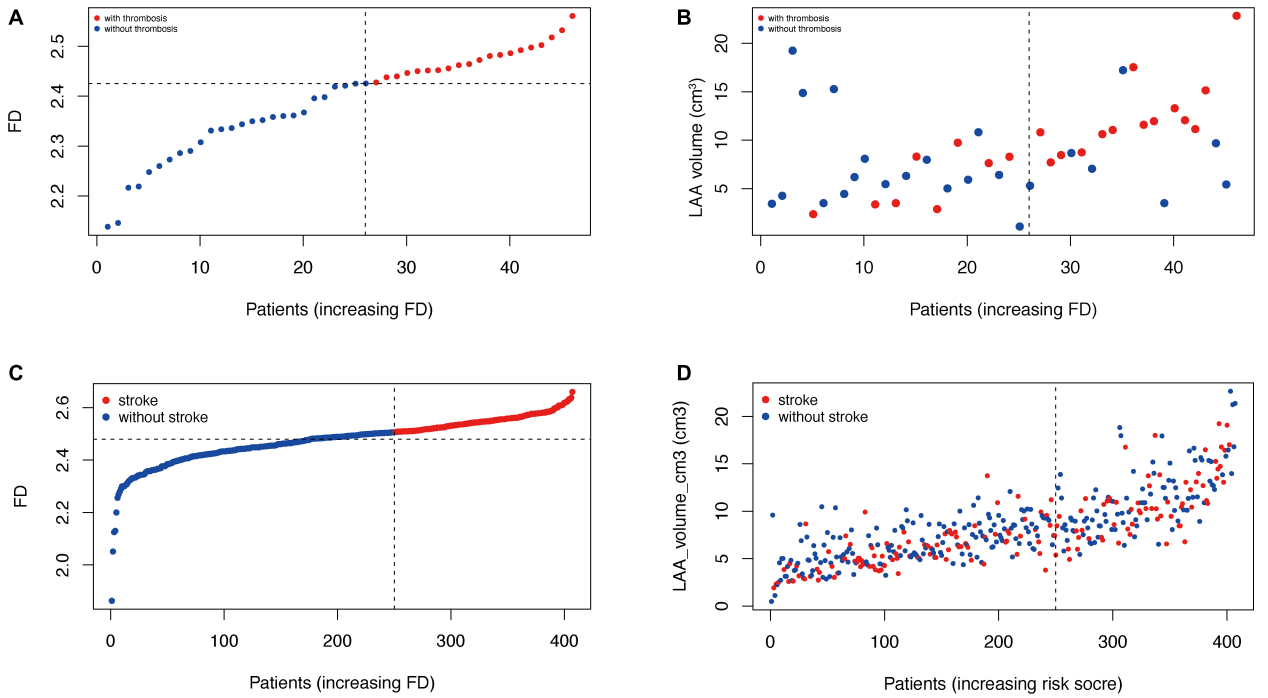

FIGURE 5 | Risk plot of training and validation cohort. **(A,C)** LAA box-counting dimension of each patient is plotted and presents the cutoff value that defines high- and low-risk patients in the training and validation cohorts, respectively. **(B,D)** Each patient's LAA volume is plotted with its box-counting dimension, suggesting the positive correlation between LAA volume and morphological complexity.

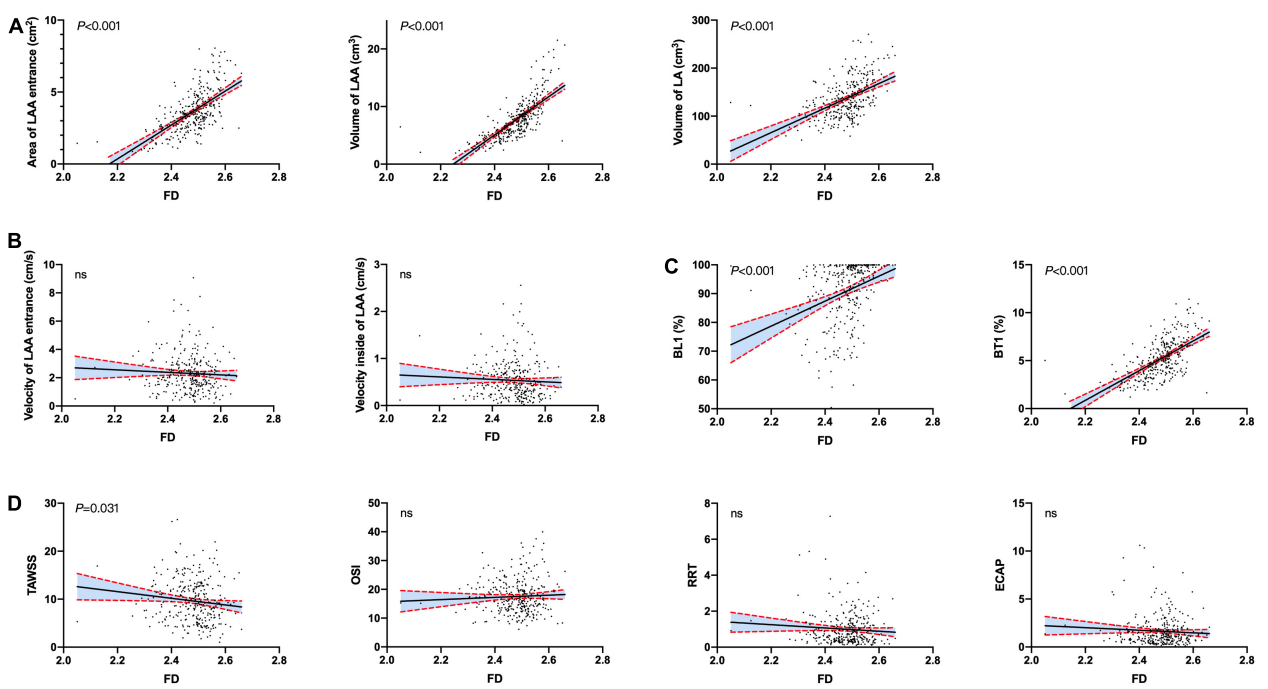

FIGURE 6 | Linear regression of FD and hemodynamic parameters. **(A)** The correlation between FD and LAA/LA morphological parameter. **(B)** The correlation between FD and blood flow velocity in LAA. **(C)** FD was positively related to the ratio of residual blood volume to LAA/LA volume at the end of the first cardiac cycle. **(D)** FD was markedly negatively related to TAWSS. BL1%: Ratio of the volume of blood remaining in the LAA to the volume of the LAA at the end of first cardiac cycle. BT1%: Ratio of the volume of blood remaining in the LAA to the volume of the entire left atrium at the end of the first cardiac cycle.

characterized by an increased number of LAA lobes was associated with the presence of LAA thrombi and was an independent predictive factor in thrombosis (27). Blood stasis caused by more lobes of LAA may be an essential factor in the formation of thrombosis. Accordingly, the morphological complexity inside the LAA, which directly determines the hemodynamic state of blood in the LAA, might reflect the relationship between LAA morphology and blood flow more intuitively. Moreover, the hemodynamic model of LAAs reached a similar conclusion: the blood flow in the LAA with a high FD and thrombosis was slower, prone to stasis and higher RRT, and residual blood volume fraction in the LAA after six cardiac cycles was higher than that of the control group.

Through ROC analysis, we identified the cutoff values of box-counting dimension as 2.426 and 2.438 in training and validation cohorts, indicating that patients with FD values higher than thresholds should be considered for active treatment, including anticoagulant therapy. The CHA_2DS_2-VaSc score system, widely used to evaluate the thrombosis risk among patients with AF, was reported to have limited efficacy in predicting thrombosis and stroke in patients with AF and low to moderate risk of thrombosis (34, 35). Therefore, it remains controversial whether active treatment should be performed among these patients. Our findings imply that FD had more potency to evaluate the possibility of both thrombosis and stroke in low- to moderate-risk patients with AF, which might be a clinical parameter that can be used to assess these patients. Besides, FD indirectly compensates for blood flow stasis that is not covered by the CHA_2DS_2-VaSc score, and the novel scoring system, combining the FD and CHA_2DS_2-VaSc score, presents higher accuracy in diagnosis of LAA thrombosis.

At present, patients with AF are routinely treated with antiplatelet or anticoagulant therapy, and 41 (91.3%) patients in our study took warfarin. To altogether remove the site of thrombus, some other patients underwent LAA. Although a vital part of LA, LAA is involved in the contraction and endocrine function of LA. Considering the side effects of warfarin and the decreased LA compliance after LAA (33), anticoagulation or surgery needs to be implemented more cautiously in patients with AF. The FD of LAA can be added to the CHA_2DS_2-VaSc scoring system to more accurately stratify patients with stroke and guide treatment decisions. Therefore, further research is needed to confirm clinically that the LAA FD is related to the occurrence of stroke.

There are several limitations to our study. First, the relatively small sample size collected from our single center and the retrospective nature might cause some bias in the comparison results. The starting point of the disease course of patients with AF is mainly through the patient's recollection and health examination report, which may have an impact on the course of the patient's illness. Secondly, the diagnosis of LAA thrombus in the training cohort largely depends on TEE images rather than pathological or surgical examination. Poor quality ultrasound images of patients cannot determine whether the patients had LAA thrombi, thereby leading to a certain amount of error. Due to the limitations of retrospective data acquisition, the division of patients in the two cohorts is not random, which may lead to a certain selection bias. In addition, the onset and duration of patients with persistent atrial fibrillation (PAF) could not be accurately recalled and recorded by these patients, which may also affect the results to some extent. Moreover, an absence of anticoagulants in the treatment of included patients before CT or TEE could be a confounding factor in the thrombosis and stroke. In addition, because the contrast agent may not be completely adherent during scanning, the 3D reconstructed model cannot wholly reflect the internal shape of the patient's LAA. Therefore, a prospective study, including large samples, should be conducted to reduce the biases of the result and to verify the conclusion of this study further.

CONCLUSION

The LAA morphological complexity is closely associated with thrombosis and stroke in patients with AF. It can be quantitatively evaluated with box-counting dimension calculated by enhancing the CT image and our fractal analysis approaches. Moreover, FD presented higher accuracy than the CHA_2DS_2-VaSc score in the diagnosis of LAA thrombosis and stroke in low- to moderate-risk patients with AF. Furthermore, preliminary hemodynamic studies have confirmed that complicated LAA morphology is more likely to cause blood flow stasis and thrombosis. The threshold of the box-counting dimension was defined, and a new combined scoring system was established for better risk assessment, potentially providing an efficient approach that may better assess the necessity for anticoagulation in low- to moderate-risk patients with AF.

DATA AVAILABILITY STATEMENT

The raw data supporting the conclusions of this article will be made available by the authors, without undue reservation.

ETHICS STATEMENT

The studies involving human participants were reviewed and approved by Institutional Review Board at the FuWai Hospital. Written informed consent for participation was not required for this study in accordance with the national legislation and the institutional requirements. Written informed consent was obtained from the individual(s) for the publication of any potentially identifiable images or data included in this article.

AUTHOR CONTRIBUTIONS

ZZ, HF, and YY participated in the design of the study. CL, QG, RW, and QL conducted the statistical analysis and drafted the

manuscript. XL and LW participated in hemodynamic analysis and helped to draft the manuscript. RW carried out important literature review and modified the manuscript. All authors read and approved the final manuscript.

FUNDING

This study was supported by the Ministry of Science and Technology of China and the Prevention and Control Project of Major Chronic Non-ons study Disease during the 13th 5-year plan period (no. 2016YFC1302000) and Beijing Municipal Science and Technology Commission (no. D171100002917001).

SUPPLEMENTARY MATERIAL

The Supplementary Material for this article can be found online at: https://www.frontiersin.org/articles/10.3389/fcvm.2022.779528/full#supplementary-material

REFERENCES

1. Falk RH. Atrial fibrillation. *N Engl J Med.* (2001) 344:1067–78. doi: 10.1056/nejm200104053441407
2. Zimetbaum P. Atrial fibrillation. *Ann Intern Med.* (2017) 166:Itc33–48. doi: 10.7326/aitc201703070
3. Atrial Fibrillation Investigators. Risk factors for stroke and efficacy of antithrombotic therapy in atrial fibrillation. Analysis of pooled data from five randomized controlled trials. *Arch Intern Med.* (1994) 154:1449–57. doi: 10.1001/archinte.154.13.1449
4. Mahajan R, Brooks AG, Sullivan T, Lim HS, Alasady M, Abed HS, et al. Importance of the underlying substrate in determining thrombus location in atrial fibrillation: implications for left atrial appendage closure. *Heart.* (2012) 98:1120–6. doi: 10.1136/heartjnl-2012-301799
5. Fukushima K, Fukushima N, Kato K, Ejima K, Sato H, Fukushima K, et al. Correlation between left atrial appendage morphology and flow velocity in patients with paroxysmal atrial fibrillation. *Eur Heart J Cardiovasc Imaging.* (2016) 17:59–66. doi: 10.1093/ehjci/jev117
6. Sala ML, Bizino MB, Amersfoort J, de Roos A, Lamb HJ. Computed tomography evaluation of cardiac structure and function. *J Thorac Imaging.* (2014) 29:173–84. doi: 10.1097/rti.0000000000000080
7. Wu YJ, Mar GY, Wu MT, Wu FZ. A LASSO-derived risk model for subclinical CAC progression in Asian population with an initial score of zero. *Front Cardiovasc Med.* (2020) 7:619798. doi: 10.3389/fcvm.2020.619798
8. Channon KM, Newby DE, Nicol ED, Deanfield J. Cardiovascular computed tomography imaging for coronary artery disease risk: plaque, flow and fat. *Heart.* (2022). doi: 10.1136/heartjnl-2021-320265 [Epub ahead of print].
9. Guerrero M, Wang DD, Pursnani A, Eleid M, Khalique O, Urena M, et al. Tomography-based score to categorize mitral annular calcification severity and predict valve embolization. *JACC Cardiovasc Imaging.* (2020) 13:1945–57. doi: 10.1016/j.jcmg.2020.03.013
10. Patel A, Au E, Donegan K, Kim RJ, Lin FY, Stein KM, et al. Multidetector row computed tomography for identification of left atrial appendage filling defects in patients undergoing pulmonary vein isolation for treatment of atrial fibrillation: comparison with transesophageal echocardiography. *Heart Rhythm.* (2008) 5:253–60. doi: 10.1016/j.hrthm.2007.10.025
11. Captur G, Muthurangu V, Cook C, Flett AS, Wilson R, Barison A, et al. Quantification of left ventricular trabeculae using fractal analysis. *J Cardiovasc Magn Reson.* (2013) 15:36. doi: 10.1186/1532-429X-15-36
12. Cai J, Bryant JA, Le TT, Su B, de Marvao A, O'Regan DP, et al. Fractal analysis of left ventricular trabeculations is associated with impaired myocardial deformation in healthy Chinese. *J Cardiovasc Magn Reson.* (2017) 19:102. doi: 10.1186/s12968-017-0413-z
13. Chen Q, Ma Q, Wu C, Tan F, Chen F, Wu Q, et al. Macular vascular fractal dimension in the deep capillary layer as an early indicator of microvascular loss for retinopathy in type 2 diabetic patients. *Invest Ophthalmol Vis Sci.* (2017) 58:3785–94. doi: 10.1167/iovs.17-21461
14. Hindricks G, Potpara T, Dagres N, Arbelo E, Bax JJ, Blomström-Lundqvist C, et al. 2020 ESC guidelines for the diagnosis and management of atrial fibrillation developed in collaboration with the European association for cardio-thoracic surgery (EACTS): the task force for the diagnosis and management of atrial fibrillation of the European society of cardiology (ESC) developed with the special contribution of the European heart rhythm association (EHRA) of the ESC. *Eur Heart J.* (2020) 42:373–498. doi: 10.1093/eurheartj/ehaa612
15. Miura N, Taneda A, Shida K, Kawashima R, Kawazoe Y, Fukuda H, et al. Automatic brain tissue extraction method using erosion-dilation treatment (BREED) from three-dimensional magnetic resonance imaging T1-weighted data. *J Comput Assist Tomogr.* (2002) 26:927–32. doi: 10.1097/00004728-200211000-00012
16. Serra J. *Image Analysis and Mathematical Morphology*. New York, NY: Academic Press (1982).
17. Captur G, Radenkovic D, Li C, Liu Y, Aung N, Zemrak F, et al. Community delivery of semiautomated fractal analysis tool in cardiac Mr for trabecular phenotyping. *J Magn Reson Imaging.* (2017) 46:1082–8. doi: 10.1002/jmri.25644
18. Iosifescu M. Fractals – form, chance, and dimension – mandelbrot, Benoit B. *Int Stat Rev.* (1979) 47:299–299. doi: 10.2307/1402650
19. Fractal Geometry. *Mathematical Foundations and Applications*. Hoboken, NJ: Wiley (2003).
20. Bosi GM, Cook A, Rai R, Menezes LJ, Schievano S, Torii R, et al. Computational fluid dynamic analysis of the left atrial appendage to predict thrombosis risk. *Front Cardiovasc Med.* (2018) 5:34. doi: 10.3389/fcvm.2018.00034
21. Masci A, Alessandrini M, Dede L, Forti D, Menghini F, Tomasi C, et al. Development of a computational fluid dynamics model of the left atrium in atrial fibrillation on a patient specific basis. In: *Proceedings of the 2017 Computing in Cardiology*. (Los Alamitos, CA: IEEE) (2017). doi: 10.22489/CinC.2017.004-429
22. Otani T, Al-Issa A, Pourmorteza A, McVeigh ER, Wada S, Ashikaga H. A computational framework for personalized blood flow analysis in the human left atrium. *Ann Biomed Eng.* (2016) 44:3284–94. doi: 10.1007/s10439-016-1590-x
23. Koizumi R, Funamoto K, Hayase T, Kanke Y, Shibata M, Shiraishi Y, et al. Numerical analysis of hemodynamic changes in the left atrium due to atrial fibrillation. *J Biomech.* (2015) 48:472–8. doi: 10.1016/j.jbiomech.2014.12.025
24. Garcia-Isla G, Olivares AL, Silva E, Nunez-Garcia M, Butakoff C, Sanchez-Quintana D, et al. Sensitivity analysis of geometrical parameters to study haemodynamics and thrombus formation in the left atrial appendage. *Int J Numer Method Biomed Eng.* (2018) 34:e3100. doi: 10.1002/cnm.3100
25. Olivares AL, Silva E, Nunez-Garcia M, Butakoff C, Sanchez-Quintana D, Freixa X, et al. Silico analysis of haemodynamics in patient-specific left atria with different appendage morphologies. In: Pop M, Wright GA editors. *Functional Imaging and Modelling of the Heart*. (Cham: Springer International Publishing) (2017). doi: 10.1007/978-3-319-59448-4_39
26. DeLong ER, DeLong DM, Clarke-Pearson DL. Comparing the areas under two or more correlated receiver operating characteristic curves: a nonparametric approach. *Biometrics.* (1988) 44:837–45.
27. Yamamoto M, Seo Y, Kawamatsu N, Sato K, Sugano A, Machino-Ohtsuka T, et al. Complex left atrial appendage morphology and left atrial appendage thrombus formation in patients with atrial fibrillation. *Circ Cardiovasc Imaging.* (2014) 7:337–43. doi: 10.1161/circimaging.113.001317
28. Di Biase L, Santangeli P, Anselmino M, Mohanty P, Salvetti I, Gili S, et al. Does the left atrial appendage morphology correlate with the risk of stroke

in patients with atrial fibrillation? Results from a multicenter study. *J Am Coll Cardiol.* (2012) 60:531–8. doi: 10.1016/j.jacc.2012.04.032
29. Khurram IM, Dewire J, Mager M, Maqbool F, Zimmerman SL, Zipunnikov V, et al. Relationship between left atrial appendage morphology and stroke in patients with atrial fibrillation. *Heart Rhythm.* (2013) 10:1843–9. doi: 10.1016/j.hrthm.2013.09.065
30. Fatkin D, Kelly RP, Feneley MP. Relations between left atrial appendage blood flow velocity, spontaneous echocardiographic contrast and thromboembolic risk in vivo. *J Am Coll Cardiol.* (1994) 23:961–9.
31. Kamp O, Verhorst PM, Welling RC, Visser CA. Importance of left atrial appendage flow as a predictor of thromboembolic events in patients with atrial fibrillation. *Eur Heart J.* (1999) 20:979–85. doi: 10.1053/euhj.1998.1453
32. Kimura T, Takatsuki S, Inagawa K, Katsumata Y, Nishiyama T, Nishiyama N, et al. Anatomical characteristics of the left atrial appendage in cardiogenic stroke with low CHADS2 scores. *Heart Rhythm.* (2013) 10:921–5. doi: 10.1016/j.hrthm.2013.01.036
33. Bai W, Chen Z, Tang H, Wang H, Cheng W, Rao L. Assessment of the left atrial appendage structure and morphology: comparison of real-time three-dimensional transesophageal echocardiography and computed tomography. *Int J Cardiovasc Imaging.* (2017) 33:623–33. doi: 10.1007/s10554-016-1044-4
34. Fang MC, Go AS, Chang Y, Borowsky L, Pomernacki NK, Singer DE. Comparison of risk stratification schemes to predict thromboembolism in people with nonvalvular atrial fibrillation. *J Am Coll Cardiol.* (2008) 51:810–5. doi: 10.1016/j.jacc.2007.09.065
35. Daccarett M, Badger TJ, Akoum N, Burgon NS, Mahnkopf C, Vergara G, et al. Association of left atrial fibrosis detected by delayed-enhancement magnetic resonance imaging and the risk of stroke in patients with atrial fibrillation. *J Am Coll Cardiol.* (2011) 57:831–8. doi: 10.1016/j.jacc.2010.09.049

Conflict of Interest: RW, QL, and XL were employed by the Hangzhou Shengshi Technology Co., Ltd.

The remaining authors declare that the research was conducted in the absence of any commercial or financial relationships that could be construed as a potential conflict of interest.

Publisher's Note: All claims expressed in this article are solely those of the authors and do not necessarily represent those of their affiliated organizations, or those of the publisher, the editors and the reviewers. Any product that may be evaluated in this article, or claim that may be made by its manufacturer, is not guaranteed or endorsed by the publisher.

frontiers | Frontiers in Cardiovascular Medicine

TYPE Original Research
PUBLISHED 22 July 2022
DOI 10.3389/fcvm.2022.809688

OPEN ACCESS

EDITED BY
Grigorios Korosoglou,
GRN-Klinik Weinheim, Germany

REVIEWED BY
Andrew Kahn,
University of California, San Diego, United States
Enrique Garcia-Sayan,
University of Texas Health Science Center at Houston, United States

*CORRESPONDENCE
Qi Yang
qiyangcy@163.com
Xiaojuan Guo
xjuanguo@163.com

†These authors share last authorship

SPECIALTY SECTION
This article was submitted to Cardiovascular Imaging, a section of the journal Frontiers in Cardiovascular Medicine

RECEIVED 05 November 2021
ACCEPTED 29 June 2022
PUBLISHED 22 July 2022

CITATION
Li W, Liu M, Yu F, Zhu W, Yu X, Guo X and Yang Q (2022) Detection of left atrial appendage thrombus by dual-energy computed tomography-derived imaging biomarkers in patients with atrial fibrillation.
Front. Cardiovasc. Med. 9:809688.
doi: 10.3389/fcvm.2022.809688

Detection of left atrial appendage thrombus by dual-energy computed tomography-derived imaging biomarkers in patients with atrial fibrillation

Wenhuan Li[1], Mingxi Liu[1], Fangfang Yu[1], Weiwei Zhu[2], Xianbo Yu[3], Xiaojuan Guo[1*†] and Qi Yang[1*†]

[1]Department of Radiology, Beijing Chao-Yang Hospital, Capital Medical University, Beijing, China, [2]Department of Echocardiography, Heart Center, Capital Medical University, Beijing, China, [3]CT Collaboration, Siemens Healthineers Ltd., Beijing, China

Aims: This study aimed to assess the diagnostic performances of dual-energy computed tomography (CT)-derived iodine concentration and effective atomic number (Z_{eff}) in early-phase cardiac CT in detecting left atrial appendage (LAA) thrombus and differentiating thrombus from spontaneous echo contrast (SEC) in patients with atrial fibrillation using transesophageal echocardiography (TEE) as the reference standard.

Methods and results: A total of 389 patients with atrial fibrillation were prospectively recruited. All patients underwent a single-phase cardiac dual-energy CT scan using a third-generation dual-source CT. The iodine concentration, Z_{eff}, and conventional Hounsfield units (HU) in the LAA were measured and normalized to the ascending aorta (AA) of the same slice to calculate the LAA/AA ratio. Of the 389 patients, TEE showed thrombus in 15 (3.9%), SEC in 33 (8.5%), and no abnormality in 341 (87.7%) patients. Using TEE findings as the reference standard, the respective sensitivity, specificity, positive predictive value, and negative predictive value of the LAA/AA HU ratio for detecting LAA thrombus were 100.0, 96.8, 55.6, and 100.0%; those of the LAA/AA iodine concentration ratio were 100.0, 99.2, 83.3, and 100.0%; and those of the LAA/AA Z_{eff} ratio were 100.0, 98.9, 79.0, and 100.0%. The areas under the receiver operator characteristic curve (AUC) of the LAA/AA iodine concentration ratio (0.978; 95% CI 0.945–1.000) and Z_{eff} ratio (0.962; 95% CI 0.913–1.000) were significantly larger than that of the LAA/AA HU ratio (0.828; 95% CI 0.714–0.942) in differentiating the thrombus from the SEC (both $P < 0.05$). Although the AUC of the LAA/AA iodine concentration ratio was larger than that of the LAA/AA Z_{eff} ratio, no significant difference was found between them ($P = 0.259$).

Conclusion: The dual-energy CT-derived iodine concentration and the Z_{eff} showed better diagnostic performance than the conventional HU in early-phase cardiac CT in detecting LAA thrombus and differentiating the thrombus from the circulatory stasis. However, these results need to be validated in large-cohort studies with late-phase images.

KEYWORDS

left atrial appendage thrombus, left atrial thrombus, computed tomography, dual-energy CT (DECT), atrial fibrillation (AF)

Introduction

Left atrial (LA) thrombus is common in patients with atrial fibrillation, with a prevalence of 13–15%, and most frequently occurs in the left atrial appendage (LAA) (1–3). The presence of thrombus in LA or LAA is considered to be a contraindication to electrical or pharmacological cardioversion or catheter ablation in patients with atrial fibrillation (4). Transesophageal echocardiography (TEE) is the gold standard in detecting or excluding LA or LAA thrombus before catheter ablation (5, 6). However, this technique is semi-invasive and carries physical discomfort for patients (7). Significantly, during the coronavirus disease 2019 pandemic, the performance of TEE carries a heightened risk for transmission of this viral infection, especially in non-intubated patients, secondary to the aerosolization of a large amount of virus due to coughing or gagging (7, 8). Therefore, it is important to develop a valid imaging modality alternative to TEE to exclude LAA.

Computed tomography (CT) is routinely performed before catheter ablation, as it provides the exact anatomical details of the LA and pulmonary veins (9–11). Indeed, a uniphasic standard CT cannot discriminate thrombus from flow stasis or stagnation when an iodine contrast-filling defect is present in LAA, owing to the lack of organized LA and LAA contraction in patients with atrial fibrillation (10, 12). The term spontaneous echo contrast (SEC) was coined to refer to this flow stasis visualized by echocardiographic examination (8). To overcome the issue of delayed filling due to stasis, a two-phase scan protocol was proposed, in which a second set of images is acquired following a short time delay after the initial scan (13). A meta-analysis showed that when delayed imaging was performed by this two-phase scan protocol, the specificity increased from 92 to 99% and the positive predictive value (PPV) increased from 41 to 92% (14). Likewise, a double-contrast single-phase scan has shown promising results despite a double-contrast load (15, 16). But, the two-phase scan protocol and double-contrast single-phase scan protocol are only applicable for some LAA stasis, owing to their limited ability to discern tissue characteristics.

The recently introduced dual-energy CT-derived iodine concentration can differentiate iodine from other materials through the material decomposition method. This is valuable for differentiating non-enhancing thrombus from other iodine-enhancing phenomena, such as SEC. Nevertheless, there exists an absolute measurement error in iodine quantification, especially when measured at lower iodine concentrations, such as severe SEC or patients with large-body type (17–19), which weaken the ability to distinguish thrombus. Another dual-energy CT-derived imaging biomarker called effective atomic number (Z_{eff}) can chemically qualify the type of material. Previous studies have shown the potential of this technique in pilot populations enrolled for various disorders (20–24). Nevertheless, its abilities to detect LAA thrombus and differentiate LAA thrombus from circulatory stasis are unclear.

Thus, this study aimed to assess the diagnostic performances of dual-energy CT-derived iodine concentration and Z_{eff} in detecting LAA thrombus and differentiating thrombus from SEC in patients with atrial fibrillation using TEE as the reference standard.

Materials and methods

Patient selection

From January 2017 to May 2019, we prospectively enrolled consecutive patients with atrial fibrillation referred for catheter ablation. **Figure 1** outlines the study protocol. All patients underwent TEE for the exclusion of LAA thrombi before undergoing catheter ablation and underwent cardiac dual-energy CT for anatomical assessment of the pulmonary veins, LA, and LAA. The interval time between dual-energy CT and TEE was less than 48 h. This study was approved by the

Abbreviations: AUC, area under the receiver operating characteristic curve; CT, computed tomography; HU, Hounsfield units; Z_{eff}, effective atomic number; TEE, transesophageal echocardiography; LAA, left atrial appendage; AA, ascending aorta; SEC, spontaneous echocardiographic contrast.

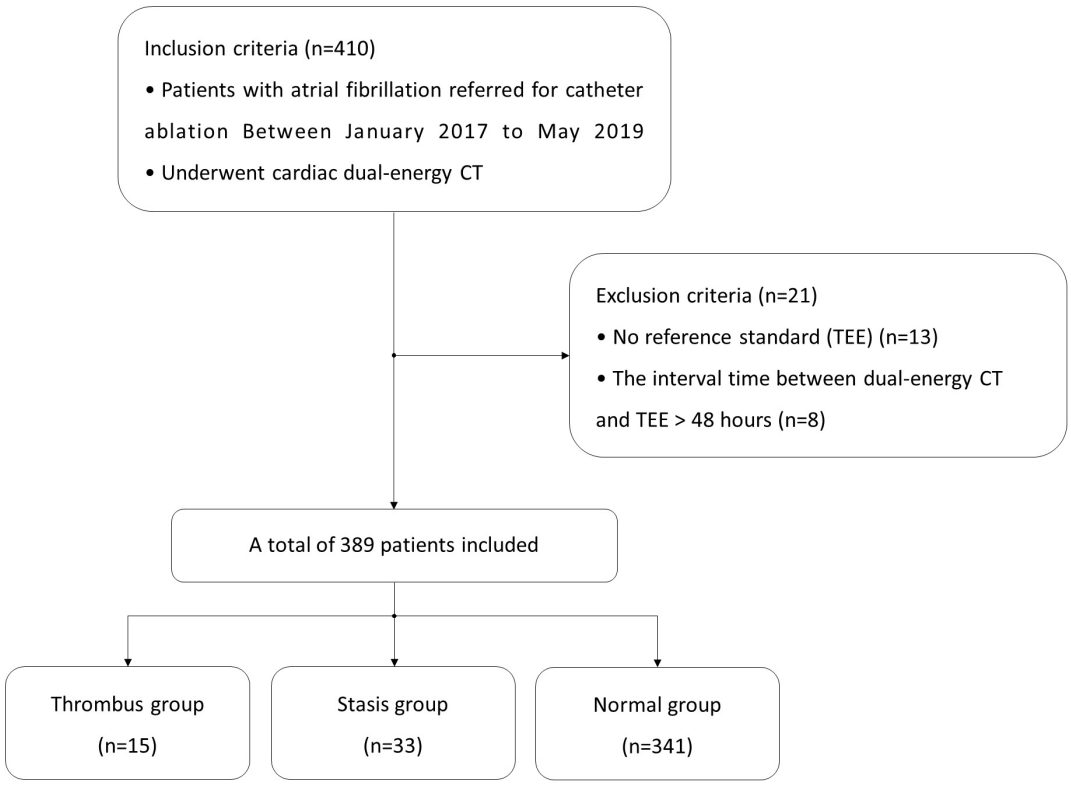

FIGURE 1
Flowchart for patient enrollment.

institutional ethics committee, and written informed consent was obtained from each patient.

Dual-energy cardiac computed tomography examination

Computed tomography was performed by a third-generation dual-source CT (SOMATOM Force; Siemens Healthineers, Forchheim, Germany) in dual-energy mode prospective ECG-gating technique. The CT scan parameters were as follows: 2 mm × 64 mm × 0.6 mm acquisition collimation with z-flying focal spot technique. An automated tube current modulation (Care Dose 4D, Siemens Healthcare) was used in scanning. One tube of the dual-source CT system was operated with 127 reference mAs per rotation at Sn 150 kV, and the second tube was automatically operated with 444 reference mAs per rotation at 70 kV. All CT scans were performed in cranio-caudal direction at a supine position during a mid-inspiratory breath-hold.

Contrast media were injected by a dual-syringe injector (Stellant D, Medrad, Indianola, MS, United States) using an 18-gauge intravenous needle placed in the right antecubital vein. A triphasic injection protocol was used. Firstly, 40 mL of contrast agent (Iopromide, Ultravist 370, 370 mg/ml, Bayer-Schering Pharma, Berlin, Germany) was administered. Thereafter, there was a 15-s delay before administration of the second bolus of contrast agent (40 ml). Finally, 30 ml of saline was administered. The injection rates were 4 ml/s for all phases. Contrast agent application was controlled by a bolus tracking technique. After the second bolus injection, there was a 5-s delay before the monitoring scan. A region of interest was placed in LA, and image acquisition was automatically started 7 s after the attenuation reached the predefined threshold of 100 HU.

Dual-energy cardiac computed tomography image post-processing and evaluation

A dual-energy CT post-processing was performed by a dedicated clinical radiology workstation (Syngo Via, VB10, Siemens Healthcare). The acquired 70 kV and Sn150 kV images were transferred to the workstation and loaded into the dual-energy application software. This software allows the automated derivation of iodine maps and effective atomic number maps and obtains quantitative iodine concentration (in mg/ml) and

effective atomic number values within a user-designated region of interest (ROI).

All CT images were assessed by two experienced readers who were blinded to echocardiographic and clinical information. Disagreements between readers were settled by consensus. If the entire LAA was not fully opacified with contrast media by visual assessment, a filling defect was deemed to be present. We then placed an ROI inside the filling defect in the LAA to determine the iodine concentration and Z_{eff}. To account for hemodynamic inter-patient variations, all the measured parameter values in the ROI of the lesion were normalized to the ascending aorta (AA) in the same axial plane.

Transesophageal echocardiography examination

A TEE was performed using commercially available echocardiograms (Toshiba Nemio, Tokyo, Japan) with a 5.0-MHz multiplane transducer. With the patient lying in the left lateral decubitus position and monitored by means of a three-lead electrocardiogram, the TEE probe was introduced into the esophagus with the transducer facing anteriorly (25). The LAA was imaged by placing the probe at the level of the mid-esophagus including 0, 45, 90, and 135 angled views. A thrombus was defined as an "echo-dense mass" that was distinct from the adjacent normal tissue without any detectable Doppler flow velocity and signs of vascularization on color doppler in the LAA. SEC was defined as hyperechogenic sparkling that could not be eliminated by adjusting the gain settings in the presence of residual flow velocity in the LAA (10). SEC was not regarded as a thrombus. The severity of SEC was classified according to the following criteria: grade 0, no echogenicity was observed (normal group); grade 1 (mild), minimal echogenicity, imperceptible at "normal" gain settings, may be detectable only transiently during the cardiac cycle, located in the left atrial appendage, or sparsely distributed in the left atrial cavity; grade 2 (mild to moderate), more dense swirling pattern, detectable without increased gain settings, with a similar distribution to mild; grade 3 (moderate), dense swirling pattern in the left atrial appendage, generally associated with somewhat lesser intensity throughout the main left atrial cavity, and may fluctuate in intensity but is detectable constantly throughout the cardiac cycle; and grade 4 (severe), intense echodensity and very slow swirling patterns in the left atrial appendage, usually with similar density in the main cavity (26).

Statistical analysis

All statistical analyses were performed using SAS version 9.4 (SAS Institute Inc., Cary, NC, United States) or MedCac version 11.4.1 (Medcalc Software, Mariakerke, Belgium). Continuous variables were expressed as mean ± SD, and categorical variables were expressed as frequencies or percentages. Student's *t*-test and the Wilcoxon test were performed for normally and non-normally distributed variables, respectively.

Using TEE as the reference standard for the diagnosis of a thrombus formation, the sensitivity, specificity, PPV, negative predictive value (NPV), and accuracy of iodine quantification and Z_{eff} for the detection of LAA thrombi were calculated. Additionally, using TEE as the reference standard for the diagnosis of a thrombus formation, the diagnostic performance was quantified using receiver operating characteristic (ROC) analysis, and the areas under the curves (AUCs) were compared using the DeLong method. A two-tailed p-value < 0.05 was considered to be statistically significant. Intraclass correlation coefficients were used to assess intraobserver and interobserver agreements in the measurements of iodine concentration and Z_{eff} in 10 randomly selected patients.

Results

The characteristics of the study population are summarized in **Table 1**. A total of 389 patients (219 men and 170 women, 61.7 ± 8.2 years) were enrolled and analyzed. In all cases, the interval time between dual-energy CT and TEE was less than 48 h and within 24 h in 80% of the cases. The image quality of all dual-energy CT and TEE examinations was considered acceptable for evaluation. The mean estimated radiation effective dose was 2.2 ± 0.4 mSv (dose–length product × 0.014 mSv/mGycm).

Of the 389 enrolled patients, TEE demonstrated thrombus in 15 (3.9%), SEC in 33 (8.5%), and no abnormality in 341 (87.7%) patients. The resultant severity of SEC was categorized as severe in 4 patients, moderate in four patients, mild to moderate in 10 patients, and mild in 15 patients on TEE. All thrombi were located in the LAA. On dual-energy CT, the mean LAA/AA

TABLE 1 Characteristics of the study population (n = 389).

Characteristics	Value
Age (years) [mean ± SD]	61.7 ± 8.2
Sex [male/female]	219/170
BMI [kg/m^2; mean ± SD]	25.3 ± 3.9
CHA2DS2-VASc score [mean ± SD]	1.4 ± 1.1
Hypertension (%)	120 (31%)
Hypercholesterolemia (%)	85 (22%)
Diabetes mellitus (%)	89 (23%)
Current or prior cigarette smoking (%)	97 (25%)
Warfarin	46 (12%)
NOAC	311 (80%)

Values are n (%).
SD, standard deviations; BMI, body mass index; NOAC, novel oral anticoagulants.

iodine concentration ratio was −0.23 ± 0.14 for the thrombus group, 0.09 ± 0.13 for the SEC group, and 0.80 ± 0.29 for the normal group (no thrombus or SEC). The mean LAA/AA Z_{eff} ratio was 0.53 ± 0.07 for the thrombus group, 0.69 ± 0.11 for the SEC group, and 0.98 ± 0.19 for the normal group. The mean LAA/AA Z_{eff} ratio and the LAA/AA iodine concentration ratio were significantly different among the three groups ($p < 0.001$).

Using TEE findings as the reference standard, the sensitivity, specificity, PPV, and NPV of the LAA/AA HU ratio were 100.0, 96.8, 55.6, and 100.0%, respectively, in detecting the LAA thrombus (**Table 2**) by using the LAA/AA iodine concentration ratio, were 100.0, 99.2, 83.3, and 100.0%; and by using the LAA/AA Z_{eff} ratio, were 100.0, 98.9, 79.0 and 100.0%, respectively (**Table 2**).

In the ROC analysis, the AUCs of the LAA/AA iodine concentration ratio (AUC 0.978; 95% CI 0.945–1.000) and the LAA/AA Z_{eff} ratio (0.962; 0.913–1.000) were significantly larger than that of the LAA/AA HU ratio (0.828; 0.714–0.942) in differentiating thrombus from SEC (both $p < 0.05$; **Figure 2**). Although the AUC of the LAA/AA iodine concentration ratio was larger than that of the LAA/AA Z_{eff} ratio (0.978 vs 0.962), no significant difference was found between them ($p = 0.259$). The best cutoff values for detecting an LAA thrombus and differentiating thrombus from SEC were -0.09 for the LAA/AA iodine concentration ratio, 0.61 for the LAA/AA Z_{eff} ratio, and 0.33 for the LAA/AA HU ratio. **Figure 3** shows representative dual-energy CT images from a patient with LAA thrombus and SEC, and **Figure 4** shows representative dual-energy CT images from a patient with LAA SEC.

Intraobserver and interobserver agreements for the measurement of the LAA/AA iodine concentration ratio (ICC = 0.88, ICC = 0.81) and LAA/AA Z_{eff} ratio (ICC = 0.86, ICC = 0.82) were all excellent.

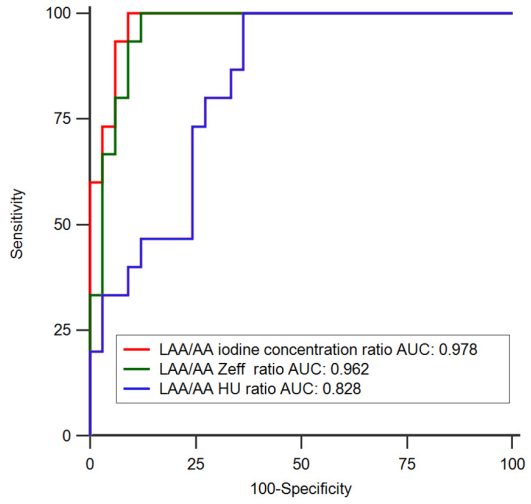

FIGURE 2
Receiver operating-characteristic curve (ROC) analysis in differentiating thrombus from circulatory stasis using transesophageal echocardiography (TEE) as the reference standard. The areas under the ROC (AUC) of LAA/AA iodine concentration ratio (0.978; 0.945–1.000) and LAA/AA Z_{eff} ratio (0.962; 0.913–1.000) showed significantly larger than that of LAA/AA HU ratio (0.828; 0.714–0.942) ($P < 0.05$).

Discussion

This study was conducted to assess the diagnostic performances of dual-energy CT-derived iodine concentration and Z_{eff} in detecting LAA thrombus and differentiating thrombus from SEC in patients with atrial fibrillation using TEE as the reference standard. This study demonstrated that the diagnostic performances of iodine concentration and Z_{eff} were superior to conventional HU in detecting LAA thrombus and differentiating thrombus from circulatory stasis. Although the diagnostic performance of iodine concentration measurements was better than that of Z_{eff} measurements, no significant difference was found between them.

Recent studies have shown that conventional CT has high sensitivity and NPV, but poor specificity and PPV in detecting LAA thrombus because CT has a limited capacity in differentiating thrombus from circulatory stasis when an LAA-filling defect is present (10, 12, 27). Kim et al. (28) reported that

TABLE 2 Statistical results for the detection of left atrial appendage (LAA) thrombus (n = 389).

Image series	Accuracy	Sensitivity	Specificity	PPV	NPV
LAA/AA iodine concentration ratio	99.2 (386/389) [97.8–99.8]	100.0 (15/15) [78.2–100]	99.2 (371/374) [97.7–99.8]	83.3 (15/18) [58.6–96.4]	100.0 (371/371) [99.0–100]
LAA/AA Z_{eff} ratio	99.0 (385/389) [97.4–99.7]	100.0 (15/15) [78.2–100]	98.9 (370/374) [97.3–99.7]	79.0 (15/19) [54.4–94.0]	100.0 (370/370) [99.0–100]
LAA/AA HU ratio	96.9 (377/389) [94.7–98.4]	100.0 (15/15) [78.2–100.0]	96.8 (362/374) [94.5–98.3]	55.6 (15/27) [35.3–74.5]	100.0 (362/362) [99.0–100]

Values are% (raw data) [95% CI].
PPV, positive predictive value; NPV, negative predictive value.

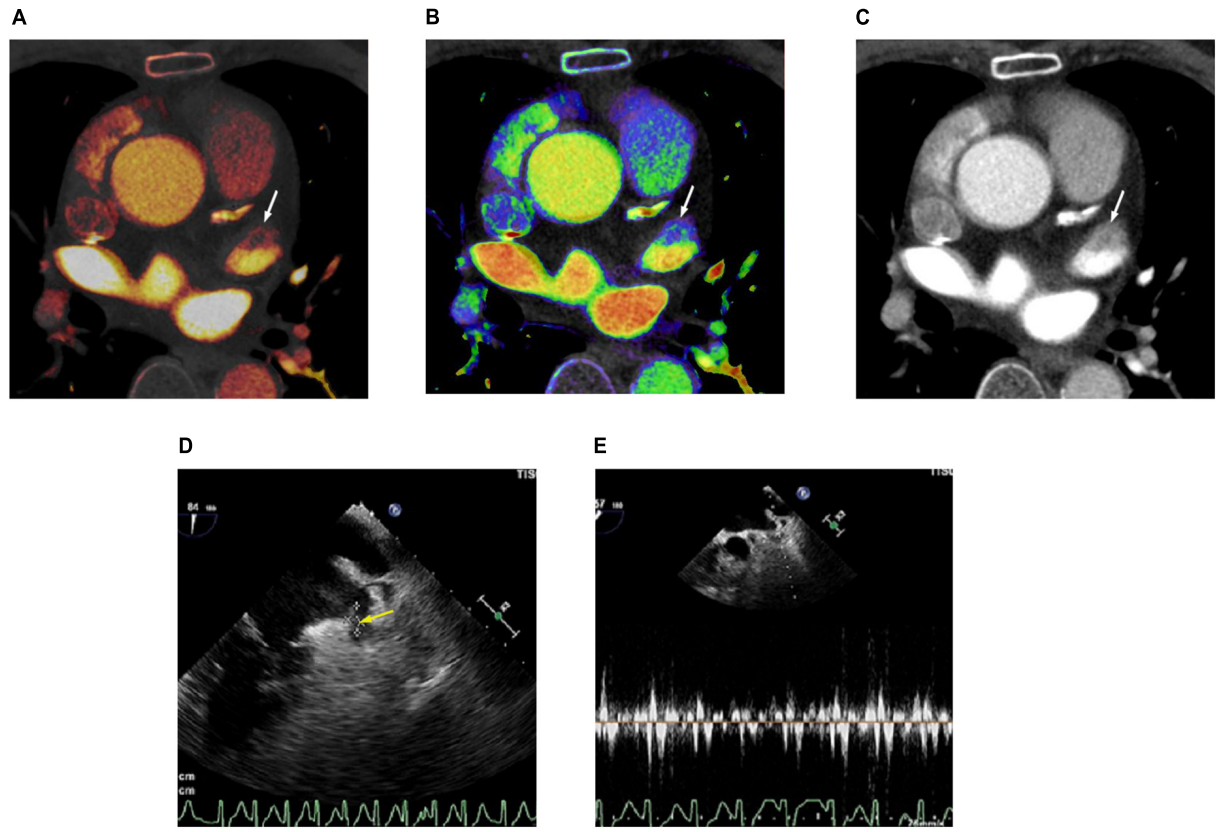

FIGURE 3
Cardiac computed tomography (CT) and transesophageal echocardiography (TEE) images in 78-year-old man with left atrial appendage (LAA) thrombus and spontaneous echo contrast (SEC). **(A)** Dual-energy CT-derived iodine map shows filling defect in LAA (arrow), with LAA/AA iodine concentration ratio of −0.18 (true positive finding). **(B)** Dual-energy CT-derived Z_{eff} image shows filling defect in LAA (arrow), with LAA/AA Z_{eff} ratio of 0.54 (true positive finding). **(C)** Conventional CT image shows filling defect in the LAA (arrow) with LAA/AA HU ratio of 0.11 (true positive finding). **(D)** TEE image demonstrates thrombus (arrow) and SEC in LAA. **(E)** Doppler flow measurement of TEE shows reduced emptying velocity of 38 cm/s in LAA besides the thrombus. For quantitative assessment, LAA/AA iodine concentration ratio ≤ −0.09, LAA/AA Z_{eff} ratio of ≤0.61 and LAA/AA HU ratio of ≤0.33 was considered positive for thrombus.

the PPV and NPV of conventional CT measurements (HU) for the detection of severe spontaneous echo contrast and thrombus were 31 and 99%, respectively. Budoff et al. (29) reported that the PPV and NPV of conventional CT for the detection of LAA thrombus were 51.6 and 100%, respectively. Compared with previous studies, the PPV of this study was slightly higher (55.6%), which may be due to the use of the double-contrast single-phase scan protocol. The double-contrast single-phase scan protocol is an alternative protocol to improve the ability to detect LAA thrombus, involving only one-phase CT scan after two separate injections of contrast agent without delayed CT scan. Teunissen et al. (30) reported a PPV of 7.7% when using two contrast boluses (30 and 70 ml) with 25-s inter-bolus delay. However, another study by Hur et al. (15) showed a PPV of 100% when using two contrast boluses (50 and 70 ml) with 180-s delayed acquisition after the test bolus (first bolus). This may indicate that the two contrast boluses combined with the optimal interval time between injections or optimal delayed acquisition time is of great significance in improving the ability to detect LAA thrombus.

Another CT protocol designed to improve the diagnostic ability to detect LAA thrombus is the two-phase scan protocol, in which the second set of images is acquired following a short time delay after the initial scan, recommended using a 60-s delay from contrast peak detected by bolus tracking (13). A recent meta-analysis showed that the specificity increased from 92 to 99% and the PPV increased from 41 to 92% by using the two-phase scan protocol with delayed imaging (14). Notably, for the two-phase scan protocol, an optimal acquisition time for the second scan is most crucial but difficult aspects because the circulation time depends on the individual involved. If the acquisition time is not properly chosen, the contrast medium will run out or will not be fully filled in LAA. Moreover, the double-contrast single-phase protocol and the two-phase scan protocol are only applicable for some LAA stasis, owing to their limited ability to discern the tissue characteristics.

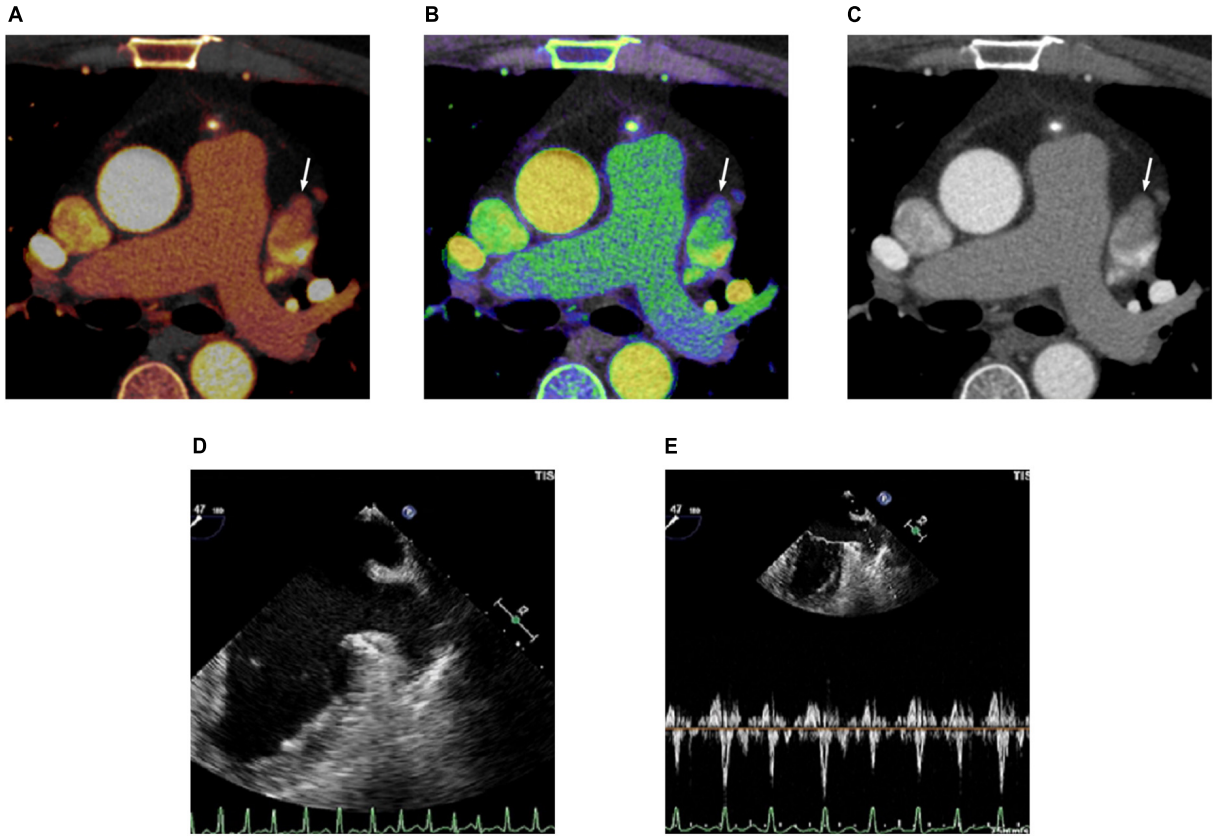

FIGURE 4
Cardiac computed tomography (CT) and transesophageal echocardiography (TEE) images in 48-year-old man with spontaneous echo contrast (SEC). **(A)** Dual-energy CT-derived iodine map shows filling defect in the left atrial appendage (LAA) (arrow) with LAA/AA iodine concentration ratio of 0.13 (true negative finding). **(B)** Dual-energy CT-derived Z_{eff} image shows filling defect in the LAA (arrow) with LAA/AA Z_{eff} ratio of 0.68 (true negative finding). **(C)** Conventional CT image shows filling defect (arrow) in the LAA with LAA/AA HU ratio of 0.24 (false positive finding). **(D)** TEE image demonstrates SEC in LAA. **(E)** Doppler flow measurement of TEE shows reduced emptying velocity of 37 cm/s but measurable flow throughout the LAA.

Compared with conventional single-energy CT, dual-energy CT is not only a powerful technique to obtain material-specific information by adding a second set of data to the same scanned material but it also reduces beam-hardening artifacts (31, 32). Our study further enhanced the advantages of dual-energy CT. In our study, dual-energy CT-derived iodine quantification (AUC 0.978 ± 0.017 vs 0.828 ± 0.058, $p < 0.05$) and Z_{eff} (AUC 0.962 ± 0.025 vs 0.828 ± 0.058, $p < 0.05$) showed significantly higher diagnostic ability than conventional HU measurements in the detection of LAA thrombus. Such observations are caused by using materials with different elemental compositions that can represent the same CT values (HU), making the differentiation and classification of different tissues extremely challenging. Moreover, the conventional HU measurements may be affected by confounding factors characterized by both the unenhanced CT attenuation densitometry and the contrast-enhanced densitometry. Conversely, the iodine quantification, unaffected by unenhanced CT attenuation densitometry, has great potential to differentiate non-enhancing thrombi from enhancing intracardiac blood pools. In line with current observation, our group reported that iodine concentration measurements based on dual-energy dual-source CT were superior to conventional HU measurements (33) in detecting LAA thrombus. Moreover, Hur et al. (34) have reported that iodine concentration measurements based on single-source dual-energy CT with a fast-kilovoltage-switching technique were better than conventional HU measurements in distinguishing thrombus from circulatory stasis.

Dual-energy CT-derived Zeff is a quantitative parameter that represents the mean atomic number of compounds or mixtures of various materials in tissue, rather than the absolute value of pure single chemical substance (35). Zeff describes the electronic changes at the atomic level. It can show subtle amount of iodine with higher sensitivity than CT attenuation in Hounsfield units (20, 21, 24). In our study, this electronic contribution from subtle amounts of iodine within a pseudo–filling defect provides useful information about the presence and accumulation of contrast material by chemically qualifying the

focused type of material. Even if the manufacturer states that the Z_{eff} results for materials with a higher atomic number may not be correct, recent data are not in conflict with the manufacturer statement because the recent data are based on distinguishing the materials with different contents of higher atomic number and not based on the quantification of the absolute Z_{eff} value.

Z_{eff} measurements were compared with iodine measurements in our study. Interestingly, the diagnostic performance of iodine concentration measurements was better than that of Z_{eff} measurements in the detection of LAA thrombus, but without significant (AUC 0.978 vs 0.962, $p > 0.05$). Of 374 patients without thrombus, four were misdiagnosed with thrombus by Z_{eff} measurements and severe SEC were detected by TEE in these cases. The false-positive cases may be due to the iodine concentration being not measurable in the LAA at the time of data acquisition because contrast opacification might take longer in patients with atrial fibrillation who have very low filling and emptying velocities than in individuals in sinus rhythm. Likewise, these situations may also negatively affect the diagnostic performance of iodine concentration measurements in detecting LAA thrombus. Of 374 individuals without thrombus, three were misdiagnosed with thrombus by iodine concentration measurements and TEE showed severe SEC. However, undoubtedly, iodine concentration measurements and Z_{eff} measurements are more sensitive than conventional HU measurements in detecting the iodine presence and are relatively less affected by the scan time.

In this study, to minimize the variations of circulation status and scanning time in different patients, all the measured parameter values in the ROI of the lesion were normalized to the AA in the same axial plane. Additionally, to achieve a sufficient attenuation difference between iodine-enhancing and non-enhancing phenomena, a dual-enhanced protocol involving two injections of iodinated contrast media was followed, and a short delay time was used between administering the first and second contrast boluses.

Nowadays, although a few studies have evaluated the potential of dual-energy CT-derived Z_{eff} in pilot populations enrolled for various disorders (20–24), the ability for differentiation of LAA thrombus and circulatory stasis remains unclear. To the best of our knowledge, the application of Z_{eff} in detecting LAA thrombus has never been reported. The finding of this study can be considered a proof of concept of the feasibility of this novel technology in detecting LAA thrombus. Taken together, these study results suggest the potential of dual-energy CT as a promising non-invasive method for the identification of individuals with LAA thrombus.

Limitations

This study has several limitations. First, this was a single-center analysis with a relatively small number of positive cases. Although small, the results are encouraging but require further studies with larger cohorts to validate. Second, TEE was used as the reference standard and the presence or absence of LAA thrombus was not confirmed by direct visual surgical specimens or inspection of the anatomy. Third, although the intervals between dual-energy CT and TEE were within 48 h, the risk of "new" thrombus formation would be low. We cannot entirely erase the possibility that this did occur between the two examinations. Fourth, we did not perform the two-phase CT scan protocol and the dual-energy CT-derived iodine concentration and Zeff were only compared with HU from early-phase CT instead of late-phase images. Future studies including the comparison with the two-phase scan protocol with late-phase images are required. Finally, the study was performed in a cohort with relatively low CHA2DS2-VASc score, which may limit generalizability.

Conclusion

Dual-energy CT-derived iodine concentration and Z_{eff} showed better diagnostic performance than conventional HU in early-phase cardiac CT in detecting LAA thrombus and differentiating thrombus from circulatory stasis. However, these results need to be validated in large cohort studies with late-phase images.

Data availability statement

The raw data supporting the conclusions of this article will be made available by the authors, without undue reservation.

Ethics statement

The studies involving human participants were reviewed and approved by Institutional Review Board, Beijing Chao-Yang Hospital, Capital Medical University. The patients/participants provided their written informed consent to participate in this study. Written informed consent was obtained from the individual(s) for the publication of any potentially identifiable images or data included in this article.

Author contributions

WL: writing – original draft preparation, conceptualization, methodology, and software. ML: data curation. FY: visualization and investigation. WZ: software and validation. XG and QY: project administration and supervision. All authors contributed to the article and approved the submitted version.

Conflict of interest

XY was employed by CT Collaboration, Siemens Healthineers Ltd.

The remaining authors declare that the research was conducted in the absence of any commercial or financial relationships that could be construed as a potential conflict of interest.

Publisher's note

References

1. Heeringa J, van der Kuip DA, Hofman A, Kors JA, van Herpen G, Stricker BH, et al. Prevalence, incidence and lifetime risk of atrial fibrillation: the Rotterdam study. *Eur Heart J.* (2006) 27:949–53. doi: 10.1093/eurheartj/ehi825

2. Lloyd-Jones DM, Wang TJ, Leip EP, Larson MG, Levy D, Vasan RS, et al. Lifetime risk for development of atrial fibrillation: the Framingham heart study. *Circulation.* (2004) 110:1042–6. doi: 10.1161/01.CIR.0000140263.20897.42

3. Achenbach S, Sacher D, Ropers D, Pohle K, Nixdorff U, Hoffmann U, et al. Electron beam computed tomography for the detection of left atrial thrombi in patients with atrial fibrillation. *Heart.* (2004) 90:1477–8. doi: 10.1136/hrt.2003.027805

4. Kirchhof P, Benussi S, Kotecha D, Ahlsson A, Atar D, Casadei B, et al. 2016 ESC guidelines for the management of atrial fibrillation developed in collaboration with EACTS. *Europace.* (2016) 18:1609–78. doi: 10.1093/europace/euw295

5. Hindricks G, Potpara T, Dagres N, Arbelo E, Bax JJ, Blomstrom-Lundqvist C, et al. 2020 ESC guidelines for the diagnosis and management of atrial fibrillation developed in collaboration with the European association for cardio-thoracic surgery (EACTS): the task force for the diagnosis and management of atrial fibrillation of the european society of cardiology (ESC) developed with the special contribution of the European heart rhythm association (EHRA) of the ESC. *Eur Heart J.* (2021) 42:373–498. doi: 10.1093/eurheartj/ehaa612

6. Douglas PS, Garcia MJ, Haines DE, Lai WW, Manning WJ, Patel AR, et al. ACCF/ASE/AHA/ASNC/HFSA/HRS/SCAI/SCCM/SCCT/SCMR 2011 appropriate use criteria for echocardiography. *J Am Coll Cardiol.* (2011) 57:1126–66. doi: 10.1016/j.jacc.2010.11.002

7. Hilberath JN, Oakes DA, Shernan SK, Bulwer BE, D'Ambra MN, Eltzschig HK. Safety of transesophageal echocardiography. *J Am Soc Echocardiogr.* (2010) 23:1115–27. doi: 10.1016/j.echo.2010.08.013

8. Achilleos S, Quattrocchi A, Gabel J, Heraclides A, Kolokotroni O, Constantinou C, et al. Excess all-cause mortality and COVID-19-related mortality: a temporal analysis in 22 countries, from January until August 2020. *Int J Epidemiol.* (2022) 51:35–53. doi: 10.1093/ije/dyab123

9. Beigel RM, Wunderlich NCM, Ho SYM, Arsanjani RM, Siegel RJM. The left atrial appendage: anatomy, function, and noninvasive evaluation. *JACC Cardiovasc Imaging.* (2014) 7:1251–65. doi: 10.1016/j.jcmg.2014.08.009

10. Romero J, Cao JJ, Garcia MJ, Taub CC. Cardiac imaging for assessment of left atrial appendage stasis and thrombosis. *Nat Rev Cardiol.* (2014) 11:470–80. doi: 10.1038/nrcardio.2014.77

11. Chen J, Yang Z, Xu H, Shi K, Long Q, Guo Y. Assessments of pulmonary vein and left atrial anatomical variants in atrial fibrillation patients for catheter ablation with cardiac CT. *Eur Radiol.* (2017) 27:660–70. doi: 10.1007/s00330-016-4411-6

12. Feuchtner GM, Dichtl W, Bonatti JO, Jodocy D, Muller S, Hintringer F, et al. Diagnostic accuracy of cardiac 64-slice computed tomography in detecting atrial thrombi. Comparative study with transesophageal echocardiography and cardiac surgery. *Invest Radiol.* (2008) 43:794–801. doi: 10.1097/RLI.0b013e318184cd6c

13. Korsholm K, Berti S, Iriart X, Saw J, Wang DD, Cochet H, et al. Expert recommendations on cardiac computed tomography for planning transcatheter left atrial appendage occlusion. *JACC Cardiovasc Interv.* (2020) 13:277–92. doi: 10.1016/j.jcin.2019.08.054

14. Romero J, Husain SA, Kelesidis I, Sanz J, Medina HM, Garcia MJ. Detection of left atrial appendage thrombus by cardiac computed tomography in patients with atrial fibrillation: a meta-analysis. *Circ Cardiovasc Imaging.* (2013) 6:185–94. doi: 10.1161/CIRCIMAGING.112.000153

15. Hur J, Pak HN, Kim YJ, Lee HJ, Chang HJ, Hong YJ, et al. Dual-enhancement cardiac computed tomography for assessing left atrial thrombus and pulmonary veins before radiofrequency catheter ablation for atrial fibrillation. *Am J Cardiol.* (2013) 112:238–44. doi: 10.1016/j.amjcard.2013.03.018

16. Hur J, Kim YJ, Lee HJ, Nam JE, Ha JW, Heo JH, et al. Dual-enhanced cardiac CT for detection of left atrial appendage thrombus in patients with stroke: a prospective comparison study with transesophageal echocardiography. *Stroke.* (2011) 42:2471–7. doi: 10.1161/STROKEAHA.110.611293

17. Euler A, Solomon J, Mazurowski MA, Samei E, Nelson RC. How accurate and precise are CT based measurements of iodine concentration? A comparison of the minimum detectable concentration difference among single source and dual source dual energy CT in a phantom study. *Eur Radiol.* (2019) 29:2069–78. doi: 10.1007/s00330-018-5736-0

18. Koonce JD, Vliegenthart R, Schoepf UJ, Schmidt B, Wahlquist AE, Nietert PJ, et al. Accuracy of dual-energy computed tomography for the measurement of iodine concentration using cardiac CT protocols: validation in a phantom model. *Eur Radiol.* (2014) 24:512–8. doi: 10.1007/s00330-013-3040-6

19. Jacobsen MC, Schellingerhout D, Wood CA, Tamm EP, Godoy MC, Sun J, et al. Intermanufacturer comparison of dual-energy CT iodine quantification and monochromatic attenuation: a phantom study. *Radiology.* (2018) 287:224–34. doi: 10.1148/radiol.2017170896

20. Mileto A, Allen BC, Pietryga JA, Farjat AE, Zarzour JG, Bellini D, et al. Characterization of incidental renal mass with dual-energy CT: diagnostic accuracy of effective atomic number maps for discriminating nonenhancing cysts from enhancing masses. *AJR Am J Roentgenol.* (2017) 209:W221–30. doi: 10.2214/AJR.16.17325

21. Nakajima S, Ito H, Mitsuhashi T, Kubo Y, Matsui K, Tanaka I, et al. Clinical application of effective atomic number for classifying non-calcified coronary plaques by dual-energy computed tomography. *Atherosclerosis.* (2017) 261:138–43. doi: 10.1016/j.atherosclerosis.2017.03.025

22. Yang Z, Zhang X, Fang M, Li G, Duan X, Mao J, et al. Preoperative diagnosis of regional lymph node metastasis of colorectal cancer with quantitative parameters from dual-energy CT. *AJR Am J Roentgenol.* (2019) 213:W17–25. doi: 10.2214/AJR.18.20843

23. Ju Y, Liu A, Dong Y, Liu Y, Wang H, Sun M, et al. The value of nonenhanced single-source dual-energy CT for differentiating metastases from adenoma in adrenal glands. *Acad Radiol.* (2015) 22:834–9. doi: 10.1016/j.acra.2015.03.004

24. Deniffel D, Sauter A, Fingerle A, Rummeny EJ, Makowski MR, Pfeiffer D. Improved differentiation between primary lung cancer and pulmonary metastasis by combining dual-energy CT-derived biomarkers with conventional CT attenuation. *Eur Radiol.* (2021) 31:1002–10. doi: 10.1007/s00330-020-07195-9

25. Aschenberg W, Schluter M, Kremer P, Schroder E, Siglow V, Bleifeld W. Transesophageal two-dimensional echocardiography for the detection of left atrial appendage thrombus. *J Am Coll Cardiol.* (1986) 7:163–6. doi: 10.1016/s0735-1097(86)80275-3

26. Fatkin D, Loupas T, Jacobs N, Feneley MP. Quantification of blood echogenicity: evaluation of a semiquantitative method of grading spontaneous echo contrast. *Ultrasound Med Biol.* (1995) 21:1191–8. doi: 10.1016/0301-5629(95)02006-3

27. Hur J, Kim YJ, Nam JE, Choe KO, Choi EY, Shim CY, et al. Thrombus in the left atrial appendage in stroke patients: detection with cardiac CT angiography–a preliminary report. *Radiology.* (2008) 249:81–7. doi: 10.1148/radiol.2491071544

28. Kim YY, Klein AL, Halliburton SS, Popovic ZB, Kuzmiak SA, Sola S, et al. Left atrial appendage filling defects identified by multidetector computed tomography in patients undergoing radiofrequency pulmonary vein antral

isolation: a comparison with transesophageal echocardiography. *Am Heart J.* (2007) 154:1199–205. doi: 10.1016/j.ahj.2007.08.004

29. Budoff MJ, Shittu A, Hacioglu Y, Gang E, Li D, Bhatia H, et al. Comparison of transesophageal echocardiography versus computed tomography for detection of left atrial appendage filling defect (thrombus). *Am J Cardiol.* (2014) 113:173–7. doi: 10.1016/j.amjcard.2013.09.037

30. Teunissen C, Habets J, Velthuis BK, Cramer MJ, Loh P. Double-contrast, single-phase computed tomography angiography for ruling out left atrial appendage thrombus prior to atrial fibrillation ablation. *Int J Cardiovasc Imaging.* (2017) 33:121–8. doi: 10.1007/s10554-016-0973-2

31. Almeida IP, Schyns LE, Ollers MC, van Elmpt W, Parodi K, Landry G, et al. Dual-energy CT quantitative imaging: a comparison study between twin-beam and dual-source CT scanners. *Med Phys.* (2017) 44:171–9. doi: 10.1002/mp.12000

32. Mccollough CH, Leng S, Yu L, Fletcher JG. Dual- and Multi-Energy CT: principles, technical approaches, and clinical applications. *Radiology.* (2015) 276:637–53. doi: 10.1148/radiol.2015142631

33. Li W, Yu F, Zhu W, Zhang W, Jiang T. Detection of left atrial appendage thrombi by third-generation dual-source dual-energy CT: iodine concentration versus conventional enhancement measurements. *Int J Cardiol.* (2019) 292:265–70. doi: 10.1016/j.ijcard.2019.04.079

34. Hur J, Kim YJ, Lee HJ, Nam JE, Hong YJ, Kim HY, et al. Cardioembolic stroke: dual-energy cardiac CT for differentiation of left atrial appendage thrombus and circulatory stasis. *Radiology.* (2012) 263:688–95. doi: 10.1148/radiol.12111691

35. Gonzalez-Perez V, Arana E, Barrios M, Bartres A, Cruz J, Montero R, et al. Differentiation of benign and malignant lung lesions: dual-energy computed tomography findings. *Eur J Radiol.* (2016) 85:1765–72. doi: 10.1016/j.ejrad.2016.07.019

Advantages of publishing in Frontiers

OPEN ACCESS
Articles are free to read for greatest visibility and readership

FAST PUBLICATION
Around 90 days from submission to decision

HIGH QUALITY PEER-REVIEW
Rigorous, collaborative, and constructive peer-review

TRANSPARENT PEER-REVIEW
Editors and reviewers acknowledged by name on published articles

Frontiers
Avenue du Tribunal-Fédéral 34
1005 Lausanne | Switzerland

Visit us: www.frontiersin.org
Contact us: frontiersin.org/about/contact

REPRODUCIBILITY OF RESEARCH
Support open data and methods to enhance research reproducibility

DIGITAL PUBLISHING
Articles designed for optimal readership across devices

FOLLOW US
@frontiersin

IMPACT METRICS
Advanced article metrics track visibility across digital media

EXTENSIVE PROMOTION
Marketing and promotion of impactful research

LOOP RESEARCH NETWORK
Our network increases your article's readership